N84-10115

NASA Conference Publication 2283
Part 1

Shuttle Performance: Lessons Learned

Compiled by
James P. Arrington and Jim J. Jones
NASA Langley Research Center
Hampton, Virginia

Proceedings of a conference held at
NASA Langley Research Center
Hampton, Virginia
March 8-10, 1983

NASA
National Aeronautics
and Space Administration

Scientific and Technical
Information Branch

1983

1. Report No.	2. Government Accession No.	3. Recipient's Catalog No.
NASA CP-2283, Part 1		

4. Title and Subtitle	5. Report Date
SHUTTLE PERFORMANCE: LESSONS LEARNED	October 1983
	6. Performing Organization Code: 506-51-13-06

7. Author(s)	8. Performing Organization Report No
James R. Arrington and Jim J. Jones, Compilers	L-15673
	10. Work Unit No.

9. Performing Organization Name and Address	11. Contract or Grant No.
NASA Langley Research Center Hampton, Virginia 23665	
	13. Type of Report and Period Covered: Conference Publication

12. Sponsoring Agency Name and Address	14. Sponsoring Agency Code
National Aeronautics and Space Administration Washington, DC 20546	

15. Supplementary Notes

16. Abstract

Full texts are included of papers presented at a conference held at Langley Research Center, March 8-10, 1983. The purpose of the conference was to evaluate data obtained during the first flights of the Space Shuttle, to compare the data to design or preflight predictions, and to assess improvements in the state of the art which could be incorporated into any new space transportation system design. The areas considered were ascent aerodynamics; entry aerodynamics; aerothermal environment; thermal protection; guidance, navigation, and control; and measurement and analysis techniques. Papers were contributed from several NASA centers, the Air Force, industries, and universities. Also included are summary comments by the chairpersons of the sessions.

17. Key Words (Suggested by Author(s))	18. Distribution Statement
Space Shuttle Flight data Aerodynamic performance Convective heat transfer Thermal protection systems	Unclassified - Unlimited Subject Category 16

19. Security Classif. (of this report)	20. Security Classif. (of this page)	21. No. of Pages	22. Price
Unclassified	Unclassified	660	A99

For sale by the National Technical Information Service, Springfield, Virginia 22161

PREFACE

Beginning with the first orbital flight of the Space Shuttle, a great wealth of flight data became available to the aerospace community. These data were immediately subjected to analyses by several different groups with different viewpoints and motivations.

The contractors, represented primarily by the prime contractor, Rockwell International, were concerned with verifying subsystems and correcting any deficiencies to make the vehicle operational. Having spent a decade or more in vehicle design and testing, the contractors were anxious to assess the quality of their product.

The contractors' counterparts within the NASA organization and its Project Office had a similar investment, and NASA immediately began to assess the measured performance of the vehicle against the wind tunnel data base and previous predictions. The primary motivation, in most cases, was the necessity to certify the vehicle for operational status.

Researchers at several NASA centers and elsewhere in the organization were anxious to reduce and analyze the data. They regarded the Shuttle as though it were a research vehicle, and the cornucopia of data from the Orbital Flight Test program was viewed as a magnificent opportunity to assess the state of the art in predicting the performance of a complex configuration throughout the speed range from entry to touchdown. Through the Orbiter Experiments Program, the researchers proposed and developed several instruments and experiments to supplement the basic developmental flight instrumentation. In some cases, the researchers were successful in having these instruments and experiments installed during the OFT flights.

The Air Force was also intensely interested in evaluating the flight data and independently assessed the Shuttle to ensure that it met their needs. Future launches from the Western Test Range will require greater crossrange than Kennedy-launched missions. Therefore, the Air Force was anxious to assess these first flights and their implications for higher crossrange on future entries.

Frequent telephone conferences were held during the Orbiter Flight Test program among representatives of each of the participating groups. Aerodynamics and the aerothermal performance were principal disciplines represented, and a general picture began to emerge in these areas. The vehicle's overall performance was well predicted in the design phase, but a number of discrepancies existed which warranted further investigation.

Although some of the results of these flight data analyses began to appear in AIAA conferences, papers in these conferences were usually intermixed with other papers and thus failed to give an overview of the vehicle's performance. Further, only a fraction of the interested parties described earlier were present to hear and discuss these papers.

We, at Langley, believed that it was an appropriate time to have a general convocation devoted to the interpretation of the Shuttle data and that this meeting would help provide a mechanism to collect and to distribute the results in a single publication. The conference was held at Langley on March 8-10, 1983, a little over 3 months after STS-5. Papers were solicited in the subject areas of ascent and entry

aerodynamics; guidance, navigation, and control; aerothermal environment prediction; thermal protection systems; and measurement techniques.

These volumes contain not only the contributed papers but also the invited papers by Mr. Robert Hoey of the Air Force Flight Test Center at Edwards Air Force Base, Major Steven Nagel of the Astronaut Office at Johnson Space Center, and Mr. [illegible] Silveira of NASA Headquarters. We have also included a few other papers that were not given orally but that contribute to the overall understanding of Shuttle performance.

The use of trade names or names of manufacturers in this report does not constitute an official endorsement of such products or manufacturers, either expressed or implied, by the National Aeronautics and Space Administration.

CONTENTS

ENTRY AERODYNAMICS I

Chairpersons: James C. Young, NASA Johnson Space Center
Bernard Spencer, Jr., NASA Langley Research Center

ENTRY AERODYNAMICS II

Chairpersons: Donald C. Schlosser, Rockwell International
George M. Ware, NASA Langley Research Center

*Part 2 is presented under separate cover.

AEROTHERMAL ENVIRONMENT II

Chairpersons: John J. Bertin, University of Texas at Austin
E. Vincent Zoby, NASA Langley Research Center

THERMAL PROTECTION

Chairpersons: Howard E. Goldstein, NASA Ames Research Center
Richard E. Snyder, NASA Langley Research Center

MEASUREMENTS AND ANALYSIS

Chairpersons: Ernest R. Hillje, NASA Johnson Space Center
Harold R. Compton, NASA Langley Research Center

SUMMARY SESSION

Chairpersons: James P. Arrington, NASA Langley Research Center
Jim J. Jones, NASA Langley Research Center

PLUME BASE FLOW SIMULATION TECHNOLOGY

Barney B. Roberts and Rodney O. Wallace
NASA Lyndon B. Johnson Space Center
Houston, Texas

Joseph L. Sims
Georgia Institute of Technology
Huntsville, Alabama

ABSTRACT

This study was intended to pursue a combined analytical/empirical approach in an effort to define the plume simulation parameters for base flow. For design purposes, rocket exhaust simulation (i.e., plume simulation) is determined by wind tunnel testing. Cold gas testing was concluded to be a cost - and schedule-effective data base of substantial scope. The results fell short of the target, although work conducted was conclusive and advanced the state of the art. Comparisons of wind tunnel predictions with Space Transportation System (STS) flight data showed considerable differences. However, a review of the technology program data base has yielded an additional parameter that may correlate flight and cold gas test data. Data from the plume technology program and the NASA test flights are presented to substantiate the proposed simulation parameters.

INTRODUCTION

The wind tunnel simulation of exhaust plume effects on the aerodynamics of rocket-powered launch vehicles has historically been accomplished by using cold gases (usually, unheated air). Although accurate simulation with hot gases is current state of the art, the cost and schedule impacts are one to two orders of magnitude greater than for testing with cold gases. In addition, data quality for hot gas testing is limited extensively because of the short duration of steady-state flow (10 - 100 m/sec). Thus, the choice to be made was between hot gas simulation, a costly, low quality data base of reduced scope, and cold gas simulation, a cost - and schedule-effective data base of substantial scope. Cold gas testing was the preferred choice by a wide margin, even though the scaling parameters required to make cold gas simulate hot gas are not well understood.

Rocket exhaust extensively affects the base drag of a launch vehicle. For design purposes, the effects are determined by wind tunnel testing. The following factors must be considered for any aerodynamic test:

1. Geometrically scaled model

2. Free-stream Mach number

3. Boundary layer development (Reynolds number)

However, if the rocket exhaust gases are to be simulated as well, additional factors must be considered. The exhaust plume phenomena vary with increasing rocket engine chamber pressure (Figure 1). The plume diameter is initially too small to significantly alter the forebody pressure. Thus, the primary effect is the entrainment of the base flow by the high-velocity gases in the boundary of the plume and the subsequent reduction of power-off base pressure. As the plume grows in size, it begins to block the base and increase the base pressure. Ultimately, the boundary layer will separate, and a recirculating pattern will develop. For multiple engines, the plumes will impinge upon each other and deflect exhaust flow into the base. Three or more engines can reverse enough mass into the base to choke the volume enclosed by the engines. The effect of the plumes can actually increase base pressure above the power-off level.

The following design options are available for use in plume simulation:

1. Hot gas, by combustion

2. Cold or warm/heated gas

3. Solid-body simulator

Hot gas testing can be eliminated as a viable option when cost and complexity are considered. A hot gas model costs 3 to 10 times more than a cold gas model. Short-duration techniques (detonation/shock tubes or small solid-propellant wafers) are required to generate the hot gas, and only three to five data points may be obtained for each shift in the test facility. Short-duration pressure data are always of lower quality than continuous pressure data. In addition, specialized support personnel are needed to implement the short-duration techniques required for hot gas testing.

The use of a solid-body simulator can also be eliminated from consideration. The base environment is not known before the testing. Therefore, the configuration of the plume shape cannot be determined to enable design of the solid body. In addition, a solid-body configuration cannot respond to changes in angle of attack or sideslip; and finally, entrainment of the free-stream flow and aspiration of the base cannot be simulated.

Cold gas testing is used almost exclusively for launch vehicle plume simulation. A cold gas model can be operated continuously to obtain 70 to 100 data points per shift in the test facility. Therefore, the Space Shuttle Program chose this technique to determine launch vehicle plume effects because of cost and schedule effectiveness.

This paper discusses the development of the technology correlation techniques used to define the plume simulation parameters and the impact of the flight data on this technology program.

BACKGROUND

In 1972, NASA initiated the planning phase for the first wind tunnel test of the Space Shuttle Launch Vehicle (SSLV). At this time, the technical archives were surveyed to determine the appropriate rocket exhaust simulation techniques. Those data accumulated through experience with the Saturn launch vehicle were chosen for study. A comparison of the wind tunnel predictions with the Saturn flight data indicated a deficiency in the technology at that time. The base drag was substantially overestimated by the predictions from wind tunnel testing (Figure 2). Finally, the surveys concluded that the simulation techniques and the simulation parameters were not well understood. Therefore, in planning the testing for the SSLV, the following approach was adopted.

1. For the initial SSLV test, model nozzles were designed and test conditions were chosen such that the cold gas plume shape matched the analytical estimates of flight plume shape.

2. Simultaneously, a technology program was initiated to enable understanding of the flow phenomena and develop a set of simulation parameters.

3. These findings were input into subsequent SSLV tests.

The current status of the technology program is best described as "terminated incomplete." The technology program (Figure 3) yielded substantial knowledge on how to correlate the cold gas base pressure. The simultaneous evolvement of the technology program and the SSLV program are shown in Table I. Note that the last output from the technology program did not feed into the SSLV test program, a circumstance of the technology learning curve and the SSLV test program timing. Therefore, only an assessment of the latest technology could be made at that time. The result was a substantial difference between the predicted and the actual flight SSLV base pressure.

TECHNOLOGY PROGRAM

The objective of the technology program was to determine a set of functions that would correlate base pressure data generated by wind tunnel cold gas tests with full-scale flight base pressure. A substantial empirical data base was obtained using generic models with some geometry variations to assess configuration effects on the base pressure. The key independent variables were simulated gas, nozzle geometry, and geometric configuration. Hot, warm, and cold gases were used. In most cold and warm gas technology tests, air was the simulated gas; in some instances, however, Freon (CF_4) was used because its variation of the ratio of specific heats through the exhaust plume was similar to a prototype full-scale rocket engine. The hot gases for the technology tests were generated by burning solid propellant charges in the models. Simulated model nozzle area ratios and nozzle lip angles varied from test to test, assuring that internal geometry was not an explicit contributor to the correlation functions. The external configurations (Figure 3) consisted of:

1. Cone or ogive noses and cylindrical afterbodies with single or triple nozzle bases.

2. A triple-body configuration, used to assess the effects on the center body (similar to the External Tank on the Space Shuttle).

Difficulties were encountered in correlating the plume technology test data because of limited variations in nozzle geometry and test conditions. Therefore, the decision was made to supplement the data base with analysis.

The Addy program[1] was used as a controlled experiment to generate additional data. The substantial empirical and analytical data base generated throughout this technology program was then analyzed for correlation by plotting the base pressure data as a function of reasonable candidate simulation parameters. The successful simulation parameters were those that would coalesce the base pressure data to a simple function of the assumed simulation parameter. An example of a "winning" set of parameters is shown in Figure 4. These parameters are defined in Figure 5.

The results from the Addy program (Figure 6) demonstrate the failure of the initial expansion angle, δ_j, to correlate the data. If the plume boundary Mach number, M_j, is introduced into the simulation parameter, the correlation is remarkably improved (Figure 6(b)). However, all cases shown in these two figures have the same one-dimensional exit Mach number, M_{ex}. Notice in Figure 6(c) how the data are once again uncorrelated when M_{ex} is allowed to vary. Obviously, the correlation parameter must also contain M_{ex} as a variable. This approach was continued until it became apparent that the simulation had the form

$$\frac{M_j \delta_j}{M_{ex}^{a} \gamma_j^{b}}$$

This knowledge was then applied to the technology program test data.

Proceeding in a similar manner with the technology test data, the results (Figure 7a) show only a fair correlation with δ_j. The results plotted in Figure 7(b) show that $M_j \delta_j$ correlates the data with the same exit Mach number. The effect of the exponent for γ_j equal to unity is shown in Figure 7(c). Assigning 0.5 as the value of this exponent results in the excellent correlation quality previously shown in Figure 4.

The final result of this analysis was the preparation of a preliminary table of simulation parameters (Table II) for the SSLV. The caveat, however, is that neither the hot gas technology test nor the hot gas analytical data from the Addy program agree with the SSLV parameters in Table II.

Much of the hot gas test data was of questionable quality and had to be discarded; however, the few data points available show a definite offset from the cold and warm gas data (Figure 8). This effect was substantiated with the Addy program (Figure 9). Obviously, an additional function of $(T_c/T_{t\infty})^c$ is required to fully correlate the data. These data came too late in the program to impact any SSLV testing; furthermore, the data points were too spotty to extrapolate to all Mach numbers and base configurations.

A temperature correction was not incorporated in the SSLV aerodynamic data base; the effect of excluding this correction would be an under prediction of the flight base pressure with a resulting underestimate of vehicle performance and a conservative prediction for SSLV performance design. The SSLV cold gas data base was not updated for the temperature effects noted in Figures 8 and 9 because of SSLV schedule and resource restrictions and because the hot gas effect is conservative. Temperature correlation is further discussed in Flight Data Comparison.

SSLV TEST DATA CORRELATION

The SSLV test data was acquired in the Unitary Plan Wind Tunnel (UPWT) at Ames Research Center (ARC), Moffett Field, California. The facility has the capability to supply secondary air at a flow rate of 10,342.5 kilopascals (1500 psi) and 36.3 kg/sec (80 lb/sec) for propulsion system simulation. In Figure 10, the model is shown installed in the ARC UPWT 11 by 11 test section. Condensation in the gas caused the simulated exhaust to be visible in the photograph.

Unfortunately, the key to the technique of base pressure correlation is that the simulation parameters (Table II) are a function of the base pressure itself. For example, δ_j and M_j are dependent on the Prandtl-Meyer expansion at the nozzle lip and therefore, proportional to the base pressure and the square root of the base pressure respectively. Consequently, if the base pressure is not known a priori, the correct simulation in the wind tunnel is impossible to establish. The technique used to establish the base pressure is as follows.

1. A variation of the base pressure is obtained by a variation of the simulated air stagnation pressure and the tunnel total pressure.

2. The variation of the base pressure from the wind tunnel test is plotted as a function of the simulation parameter. See curve A in Figure 11.

3. A similar curve can be analytically derived for the full scale prototype by assuming a base pressure (curve B, Figure 11). This curve represents the loci of possible values of the similarity parameters for the prototype as a function of base pressure.

4. Where the curve of prototype possibilities is equal to the wind tunnel test data, the similarity is matched, and the resulting base pressure is the design value.

This technique evolved from the plume technology program and the early SSLV tests and has been incorporated into the JANNAF Rocket Exhaust Plume Technology Handbook.[2] The final results of applying this technique to the SSLV are shown in Figure 12.

FLIGHT DATA COMPARISONS

As expected, the flight base pressure data from STS-2, 3, and 5 were greater than predicted. A comparison of the predicted data and the flight data is shown in

Figure 13. The total integrated effect of this difference is equivalent to an additional 453.6 kilograms (1000 pounds) of payload that can be delivered to low Earth orbit (i.e., a circular orbit of 277.8 kilometers (150 nautical miles)).

The discovery was made late in the technology program that a temperature correction was needed to fully correlate the base pressure data. The technology data was reprocessed to determine if introduction of the temperature effect into the correlation would result in matching flight and test data. Using the data in Figure 8, a temperature correlation factor of $(T_c T_{t\infty})^{0.081}$ was determined and applied to the SSLV wind tunnel test data as shown in Figure 14. (The correction could only be applied to the solid rocket booster (SRB) base because of the limited technology hot gas data and the limited SSLV wind tunnel test data.) The effect of the correction and the comparison with the flight data for the SRB base, at Mach = 1.25, are shown in Figure 15. On this figure, the original pre-flight data acquired in the wind tunnel is the lower plot labeled "SSLV SRB base pressure test data". The flagged circles are the actual data acquired in that test. Note that the last test data point was taken at a value of 85 for the similarity parameter. Although the original data completely brackets the original cold flow possibility curve, extrapolation is required to intersect the new possibility curve with the hot gas correction. When this hot gas correction is applied to the SRB prediction across the Mach range for which data is available, the wind tunnel predictions more closely match the flight data as shown in Figure 15.

Now, the obvious thing to do would be to revisit the plume technology and cold gas wind tunnel test programs, and complete the base flow technology, so that this information would not be lost. More specifically, additional hot gas data on the technology models, analysis and correlation of this data to obtain the hot gas correction terms, and a SSLV cold gas test to confirm the simulation of the flight base pressures in the wind tunnel is needed. To date, resources have not been sufficient to support a proposal of this magnitude; however, some additional testing with the SSLV configuration has been accomplished. The objective of these tests was to vary the plume simulation and model nozzle parameters until the flight base pressures were recreated in the wind tunnel.

The data from this test were in analysis at the time of this publication and only preliminary results are available. These results are plotted on Figure 15. First, note that the new data was intended to bracket the flight data (indicated by a band of values on Figure 14). This results in a much higher value for the simulation parameter. Second, note that the low values of SSME simulation (which are consistent with the original SSLV test) justify a linear extrapolation of the original SRB base pressure for increasing SRB simulation parameter. And last, there can be a far more significant effect of the SSME on SRB base pressure than was originally expected, especially at low values of the SRB similarity parameter where the SSME can become the dominant influence. All these effects cannot be clearly untangled from each other without some additional plume simulation technology development. However, the trends do support the temperature correction developed from the limited hot gas technology data.

CONCLUSIONS/RECOMMENDATIONS

The optimum similarity parameter for wind tunnel testing for launch vehicle base pressure measurements is:

$$\frac{M_j \delta_j}{M_{ex}^{\ a} \gamma_j^{\ b}} \left(\frac{T_c}{T_{t\infty}} \right)^c$$

where a, b, and c are weak functions of geometry.

The following recommendations are made.

1. The technology program should be revived to generate a more extensive data base for the purpose of assessing the variables a, b, and especially c.

2. Upon completion of the technology program, the SSLV model should be retested at the ARC UPWT to confirm that the simulation parameters will indeed recreate the flight base pressures.

SYMBOLS

C Coefficient
f function of
F force
M Mach number
N nozzle
P pressure
T temperature
γ ratio of specific heats
δ initial expansion angle of gas
Θ lip angle

Superscripts:
a,b,c undetermined exponents, functions of geometric configuration

Subscripts:
A axial
B base
c chamber
ex exit
j plume boundary
N nozzle
p pressure
t total of stagnation
∞ free stream

REFERENCES

1. Addy, A. L.: Analysis of the Axisymmetric Base Pressure and Base Temperature Problem with Supersonic Interacting Freestream Nozzle Flows Based on the Flow Model of Korst, et al, Part III: A Computer Program and Representative Results for Cylindrical, Boatailed, or Flared Afterbodies. Army Missile Command Report No. RD-TR-69-14, Feb. 1970.

2. Rocket Exhaust Plume Technology, JANNAF Handbook. Chemical Propulsion Information Agency (CPIA) publication 263, ch. 5, sec. 5.8, July 1981, pp. 5.8-1 to 5.8-39.

TABLE I. EVOLVEMENT OF PLUME TECHNOLOGY AND THE SSLV PROGRAM

Development phase	Correlation parameters	SSLV test identification
History and intuition	Plume shape	1A2, 1A7, 1A12B, 1A12C, 1A19
Plume technology tests and analyses		
o Cold gas o Warm gas o CF_4 o Single body o Single and multi-nozzle	δ_j, δ_j/γ_j	1A8O, 1A82B, 1A82C, 1A72
o Triple body o Solid propellants	$\delta_j \gamma_j^b$	1A119, 1A138
o Triple body with solid propellants	$f(\delta_j, M_j, M_{ex}, T_c, T_{t\infty})$	Assessment of effects only

TABLE II. CORRELATION PARAMETERS

M_∞	Configuration		
	Single body, single nozzle	Single body, triple nozzle	Triple body
0.9	$\frac{M_j \delta_j}{M_{ex}^{0.25} \gamma_j}$	$\frac{M_j \delta_j}{M_{ex}^{0.25} \gamma_j}$	$\frac{M_j \delta_j}{M_{ex}^{0.25} \gamma_j}$
1.2	$\frac{M_j \delta_j}{M_{ex}^{0.25} \gamma_j^{0.5}}$	$\frac{M_j \delta_j}{M_{ex}^{0.25} \gamma_j}$	$\frac{M_j \delta_j}{M_{ex}^{0.25} \gamma_j}$
1.46	$\frac{M_j \delta_j}{M_{ex}^{0.25} \gamma_j^{0.5}}$	$\frac{M_j \delta_j}{M_{ex}^{0.25} \gamma_j}$	-
3.48	$\frac{M_j \delta_j}{\gamma_j}$	$\frac{M_j \delta_j}{\gamma_j}$	

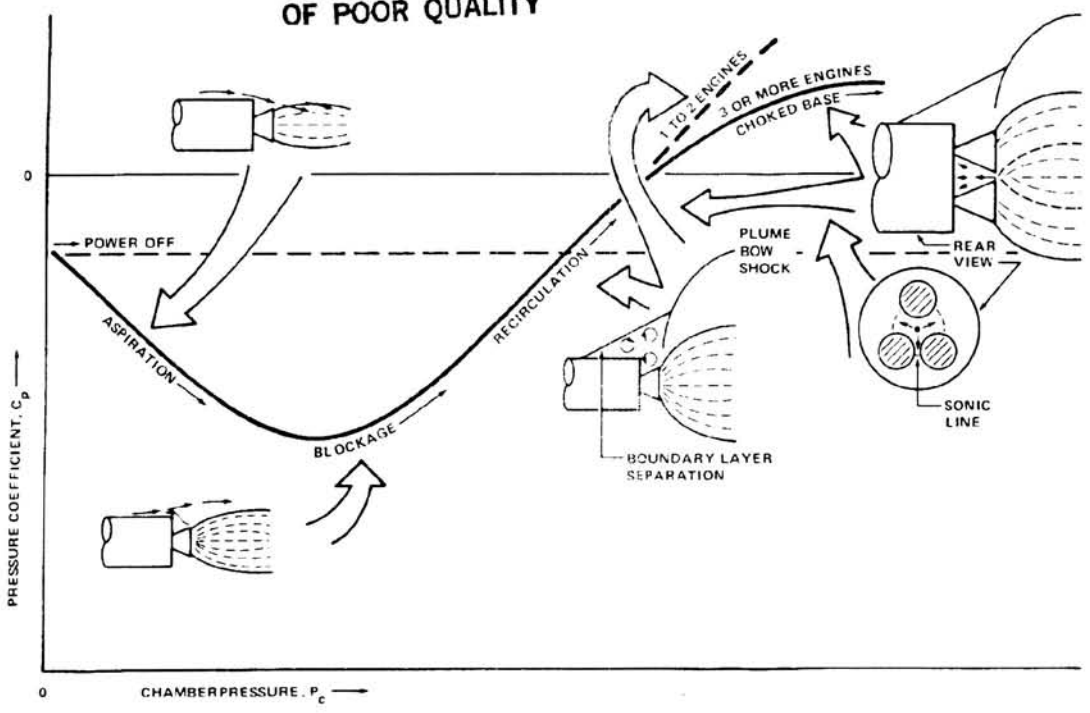

Figure 1.- Base flow - exhaust plume phenomena.

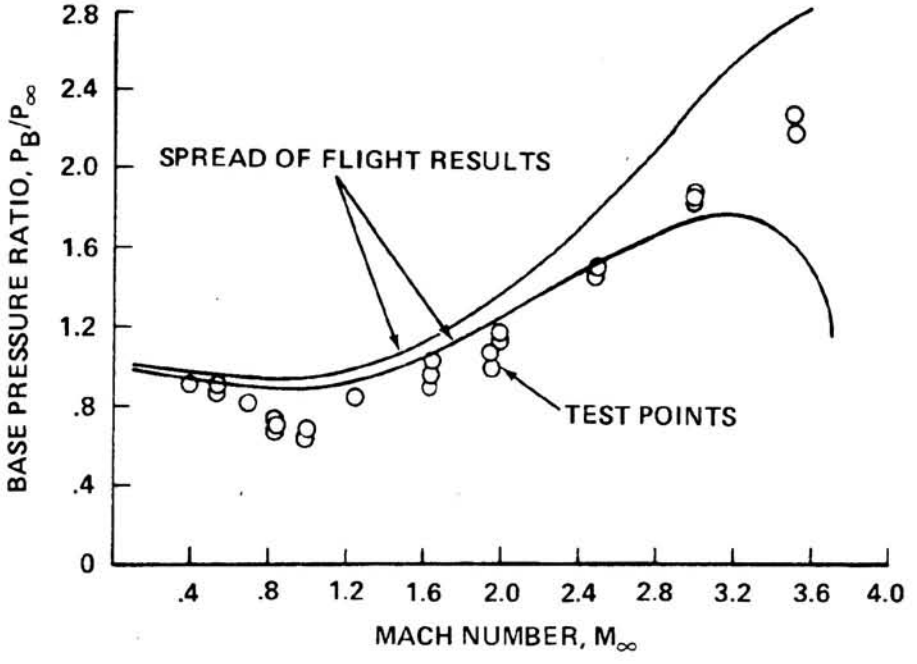

Figure 2.- Comparison of Saturn V test and flight data.

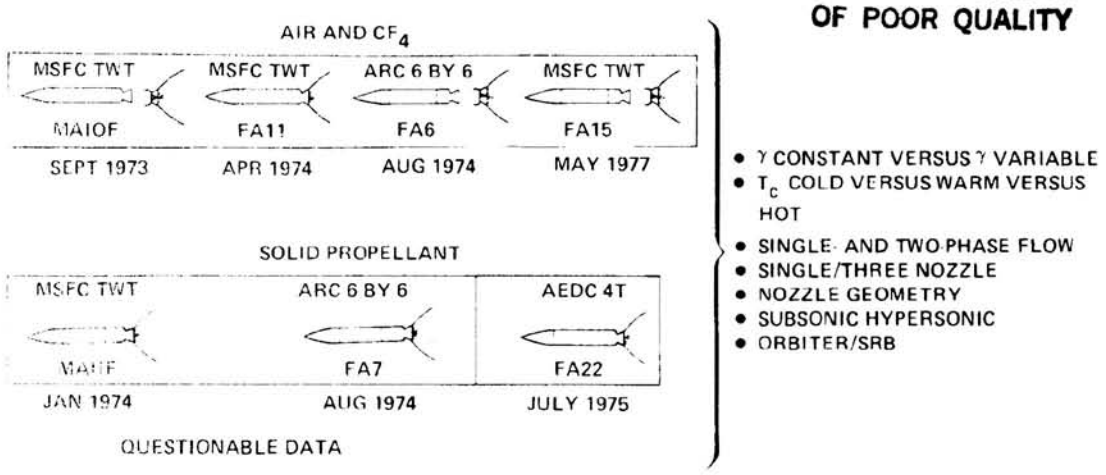

(a) Basic test program.

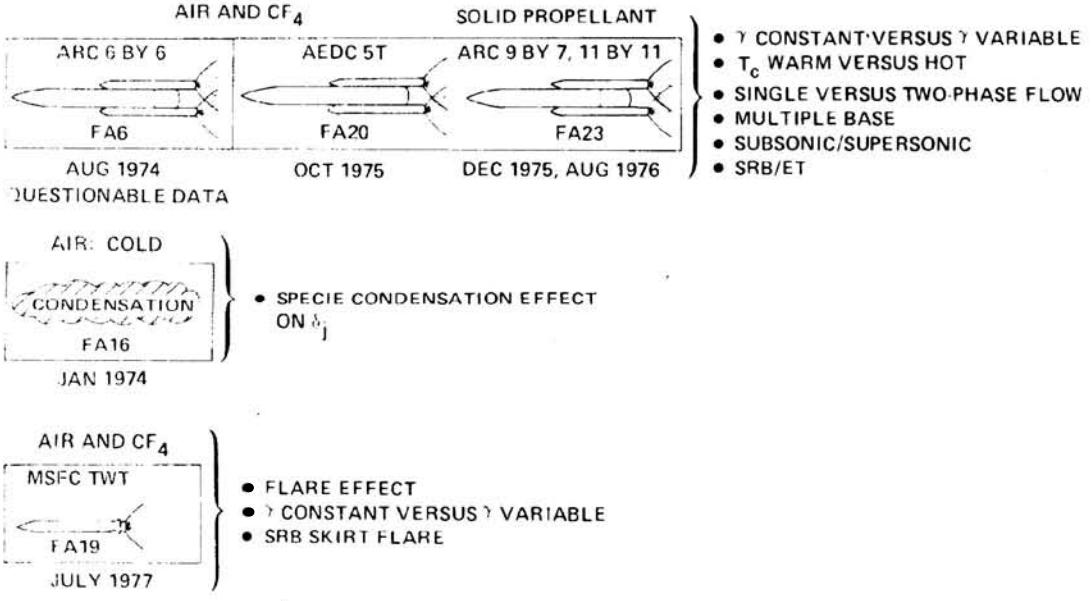

(b) Supplementary test program.

Figure 3.- SSLV plume simulation program.

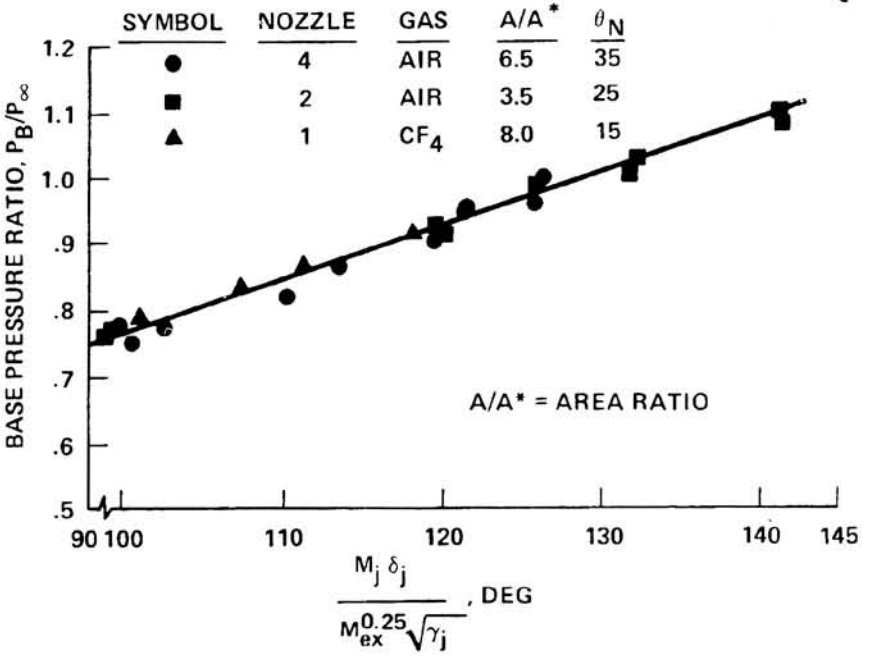

Figure 4.- Example of a successful simulation parameter: $M_\infty = 1.46$.

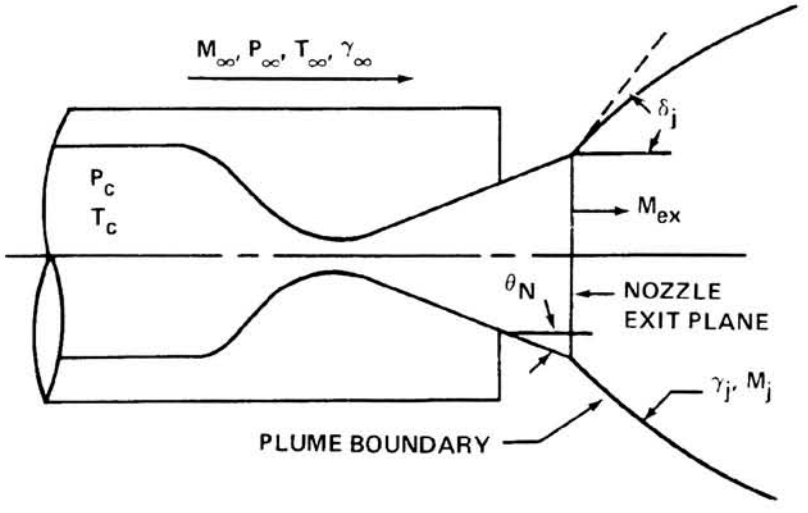

Figure 5.- Definition of the parameters.

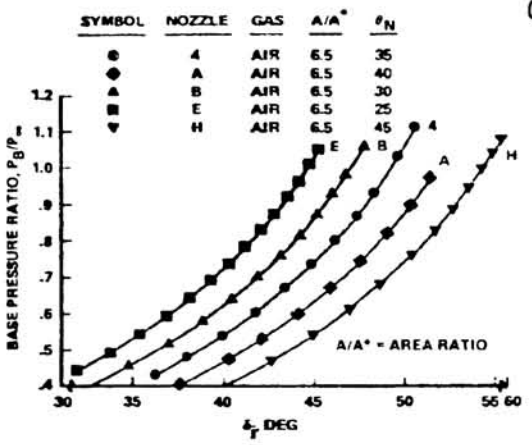

(a) Initial plume angle correlation.

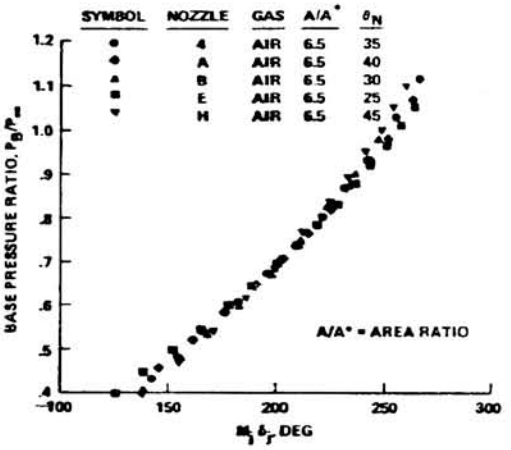

(b) Correlation of wall angle effect.

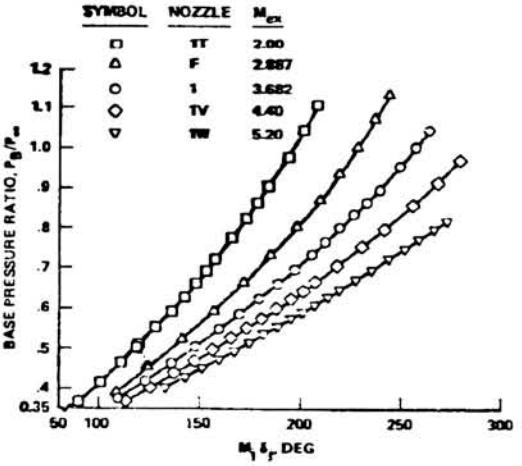

(c) Exit Mach number, M_{ex}, effects: $\gamma = 1.4$, $\theta = 15°$.

Figure 6.- Addy program results: $M_\infty = 2.00$.

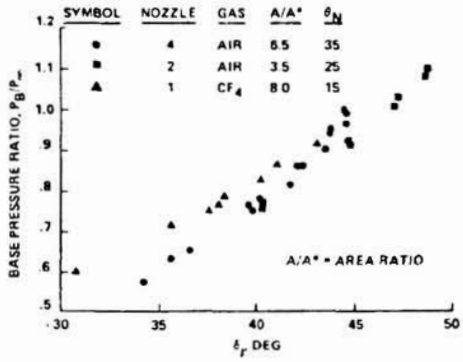

(a) Correlated with initial expansion angle, δ_j.

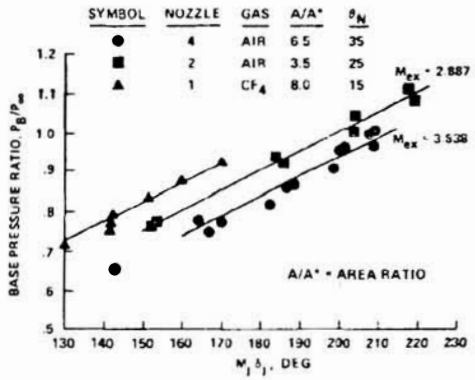

(b) Correlated with the exit Mach number.

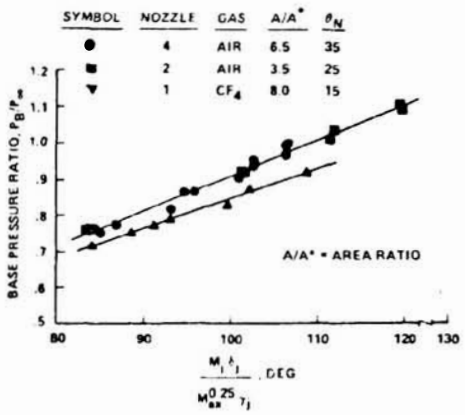

(c) Effect of the exponent of δ_j equal to unity.

Figure 7.- Experimental data results: $M_\infty = 1.45$.

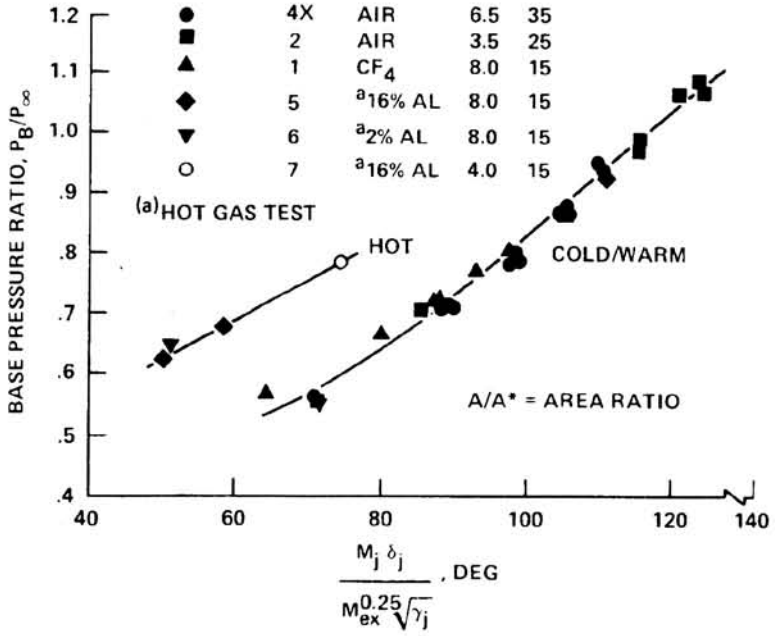

Figure 8.- Experimental data results: $M_\infty = 1.2$.

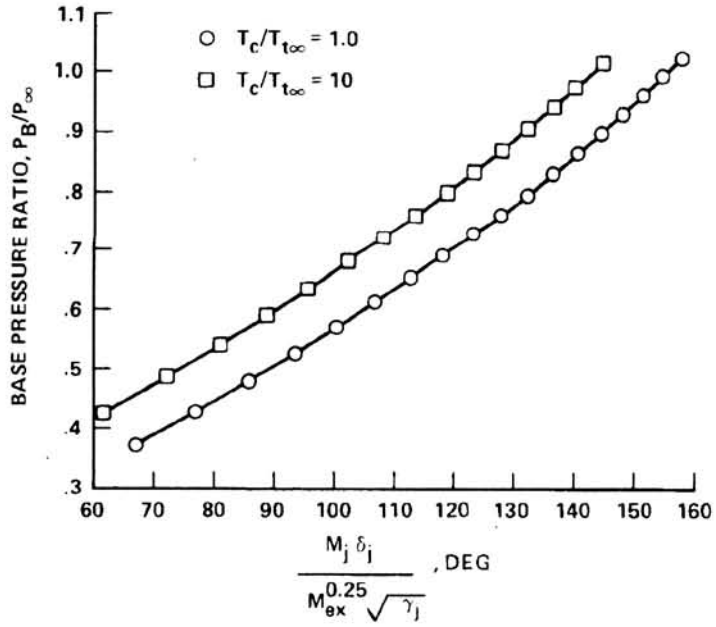

Figure 9.- Addy program results - chamber temperature effect.

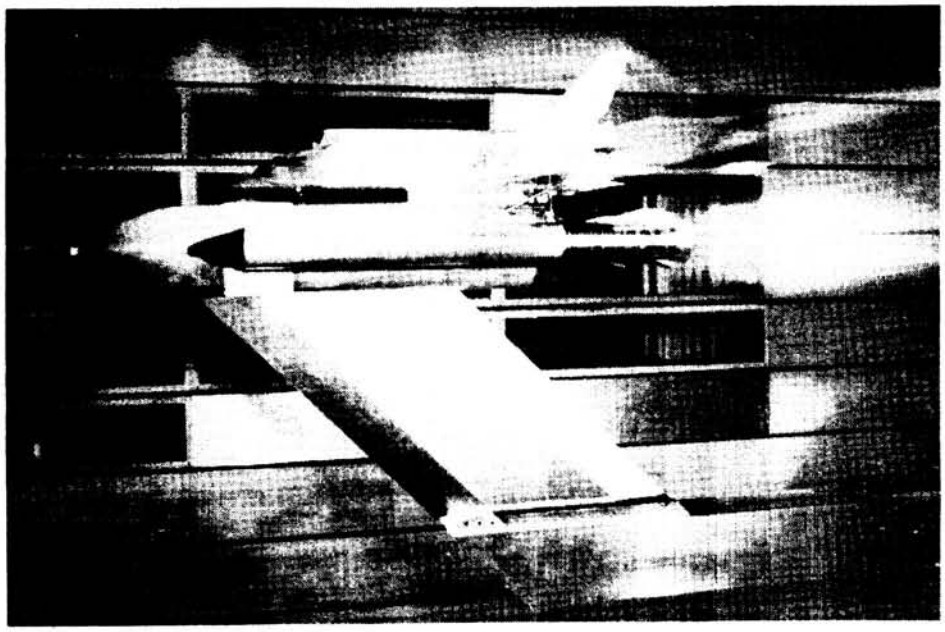

Figure 10.- Plume test showing the model installed in the ARC UPWT 11 by 11 transonic wind tunnel.

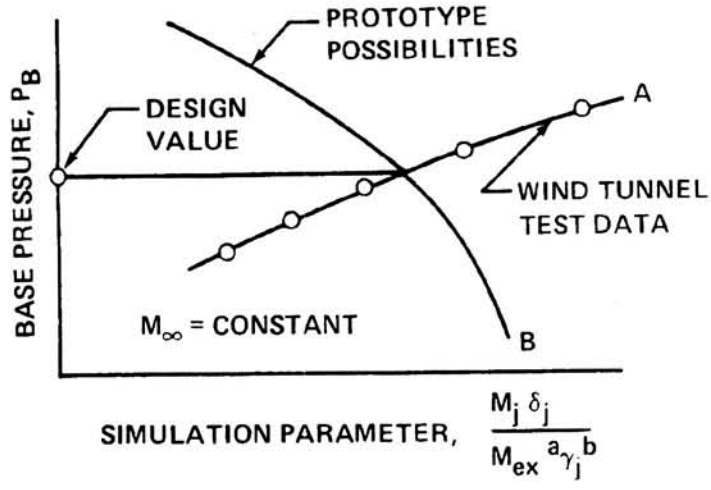

Figure 11.- Plot of the technique for determining the design value for base pressure.

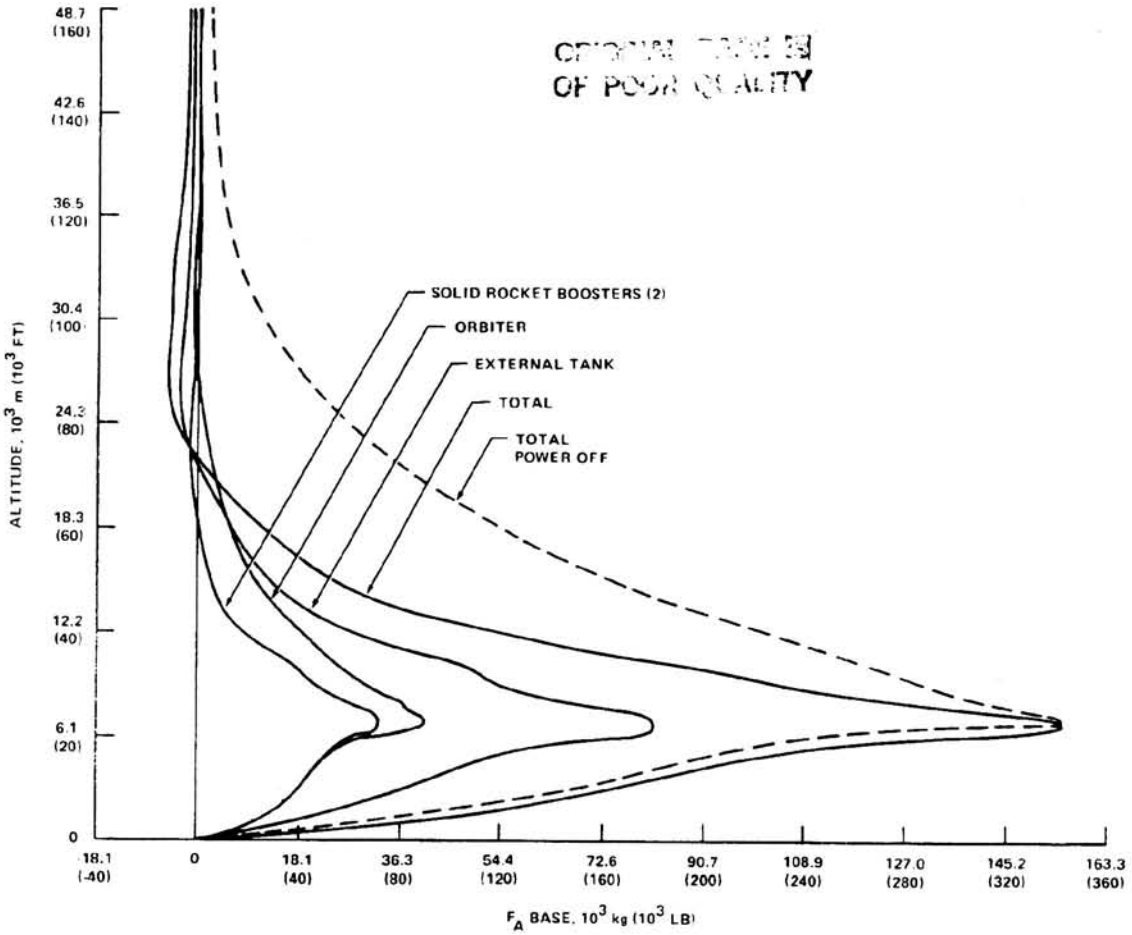

Figure 12.- Power effects on base axial force.

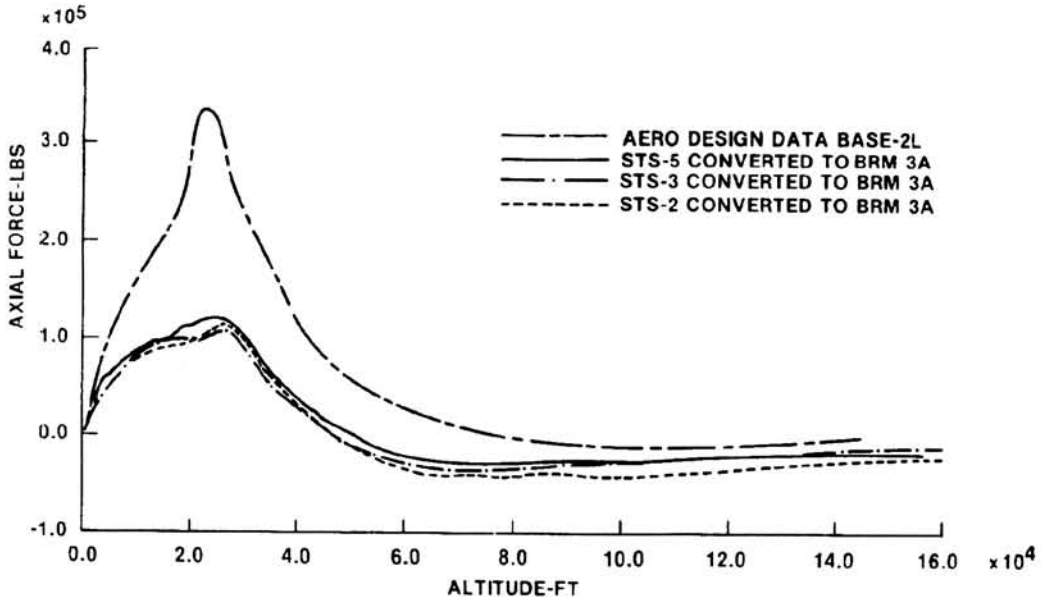

Figure 13.- First stage vehicle base force - flight versus prediction comparison.

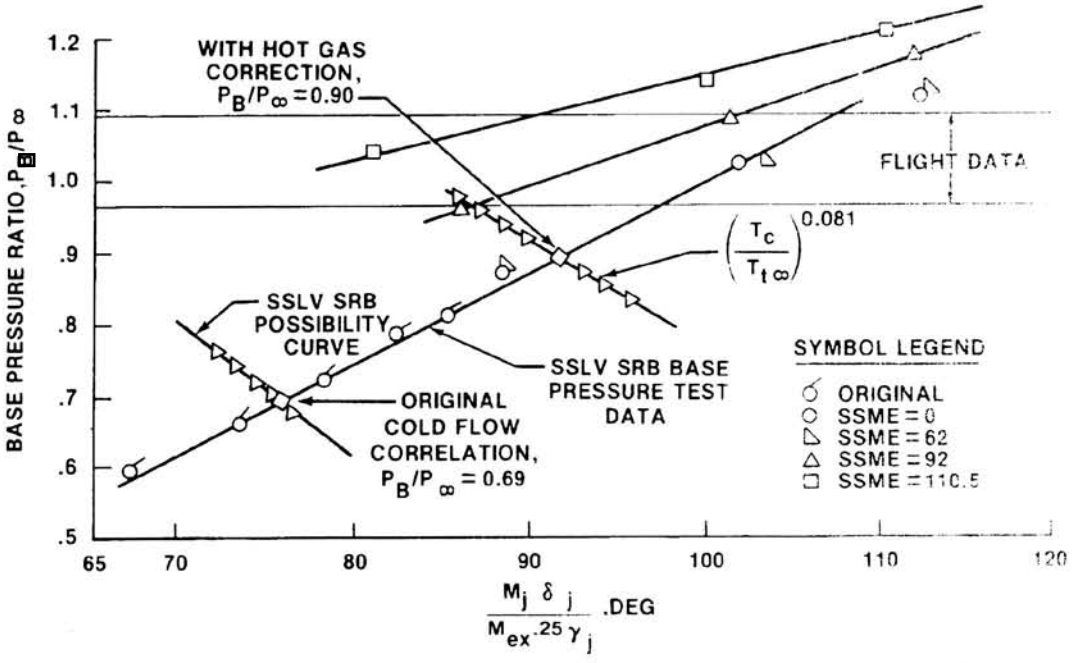

Figure 14.- SSLV experiment data results and flight comparison.

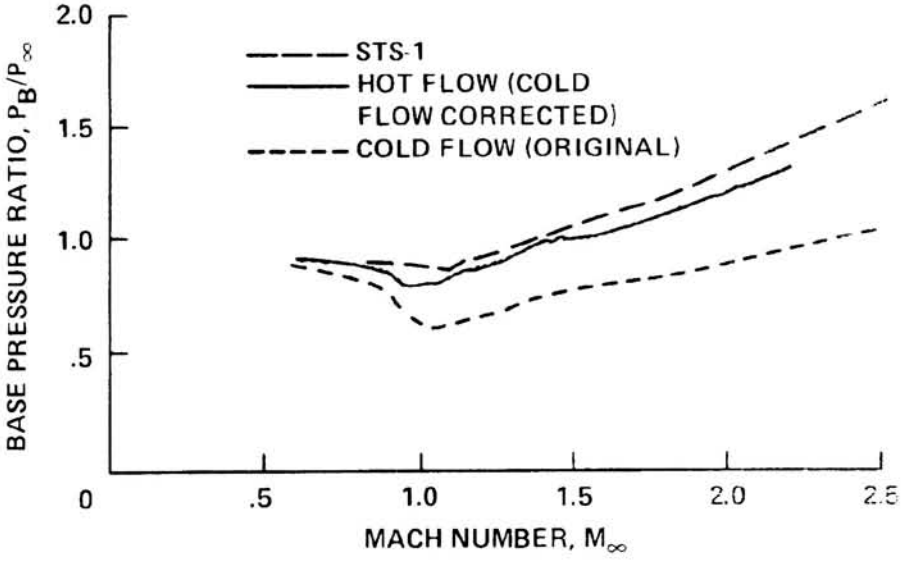

Figure 15.- STS-1 SRB base pressure compared to cold- and hot-flow predictions.

LAUNCH VEHICLE AERODYNAMIC DATA BASE DEVELOPMENT COMPARISON WITH FLIGHT DATA

J. T. Hamilton
Space Transportation and Systems Group
Rockwell International
Downey, California

R. O. Wallace
Systems Engineering Division
NASA Johnson Space Center
Houston, Texas

C. C. Dill
Aerophysics Division
NASA Marshall Space Flight Center
Huntsville, Alabama

SUMMARY

The aerodynamic development plan for the Space Shuttle integrated vehicle had three major objectives. The first objective was to support the evolution of the basic configuration by establishing aerodynamic impacts to various candidate configurations. The second objective was to provide continuing evaluation of the basic aerodynamic characteristics in order to bring about a mature data base. The third task was development of the element and component aerodynamic characteristics and distributed air loads data to support structural loads analyses. The complexity of the configurations rendered conventional analytic methods of little use and therefore required extensive wind tunnel testing of detailed complex models. However, the ground testing and analyses did not predict the aerodynamic characteristics that were extracted from the Space Shuttle flight test program. Future programs that involve the use of vehicles similar to the Space Shuttle should be concerned with the complex flow fields characteristic of these types of complex configurations.

INTRODUCTION

The Space Shuttle aerodynamic data base development was initiated in the early 1970's. Systems requirements defined aerodynamic inputs for vehicle performance analyses, structural loads analyses, separation systems analyses, aeroheating analyses, and more detailed inputs for tile loads and venting. This paper discusses the development of the Space Shuttle aerodynamic data base for vehicle performance and structural loads analyses.

SYMBOLS

Values are given in both the International System of Units (SI) and U. S. customary units. The measurements and calculations were made in U. S. customary units.

C	typical aerodynamic coefficient
i	incidence angle between orbiter and external tank (ET), deg (deg)
$\bar{q}$	dynamic pressure, kg/m^2 (lbs/ft^2)
X	station, along axial axis, m (in.)
Z	station along vertical axis, m (in.)
α	angle of pitch, deg (deg)
β	angle of sideslip, deg (deg)
ϕ	circumferential angle, deg (deg)

Subscripts:

o	orbiter
T	external tank

SPACE SHUTTLE CONFIGURATION EVOLUTION

Evolution of the physical characteristics of the Space Shuttle is shown in figure 1 with major changes noted. The changes shown were not restricted to aerodynamic considerations alone; however, the emphasis from an aerodynamic viewpoint was to reduce wing loads, reduce interference effects, reduce drag, and reduce plume effects. Therefore, the initial wind tunnel tests were designed to provide parametric studies which would yield aerodynamic inputs for the configuration evolution.

DATA BASE DEVELOPMENT

Initial emphasis was placed on the total vehicle aerodynamic forces and moments. Preliminary tests were run at the Marshall Space Flight Center's Trisonic Wind Tunnel (MSFC TWT) facility using several 0.4 percent models. These early tests included various parametric studies to determine an acceptable configuration of the elements. These studies included solid rocket booster (SRB) placement (fig. 2), SRB aft skirt outer moldline (OML) geometry (fig. 3), external tank (ET)/SRB nose profiles (fig. 4), orbiter incidence and initial vertical placement relative to the ET centerline (fig. 5), and model sting placement (fig. 6).

As the design of the vehicle evolved, the need for higher fidelity models, more instrumentation, and a higher degree of data accuracy increased. The increased emphasis on the aerodynamic data base was prompted by several design problems. Typical of these problems were: wing/elevon loads, attach structure loads, vertical tail loads, venting, and local pressure definition. These problems prompted emphasis of the aerodynamic definition to be moved from the total vehicle to the elements (orbiter, ET, and SRB's) and components (wing, elevon, and vertical tail), providing their respective forces, moments, and pressure distributions where applicable.

In 1976, a series of wind tunnel tests were performed at the Ames Research Center's Unitary Plan Wind Tunnel (ARC UPWT) facility using a 3.0-percent model which was supported by four stings (fig. 7). In this series, forces, moments, and pressure distributions were determined for the orbiter, ET, SRB's, wing, elevons, and vertical tail. Since the total vehicle forces and moments were not measured directly, a series of tests were conducted at the Langley Research Center (LaRC) Eight-Foot Wind Tunnel and at the Unitary Plan Wind Tunnel facilities using a 1.0-percent model which was supported by a single sting through the base of the orbiter model (located for least interference as determined from earlier studies). Differences were noted in the forces and moments measured directly in the LaRC test relative to the sum of the elements from the ARC test. Analysis attributed these differences to sting interference and blockage from the four stings and the close proximity of the sting mounting hardware to the base of the model in the ARC test.

The LaRC tests also measured elevon hinge moments along with the shear, bending, and torsion of the wing panel. During this period of time, loads analysis of the wing showed that the elevon actuator capability was exceeded as a result of the magnitude of the elevon hinge moment. This required analysis of data from the wind tunnel data bases to find a way to relieve the problem. An elevon deflection schedule was derived as a result of this analysis which would maintain the elevon hinge moment near zero and, at the same time, keep the wing panel loads within limit (fig. 8). As a safety measure, an active load relief system was designed which would maintain the hinge moment level within the actuator capabilities.

Since sting interference was affecting the aerodynamics of the total vehicle, emphasis was placed on designing models which could be mounted from a single sting through the orbiter base and have the capability of measuring the total vehicle, element, and component forces, moments, and base pressures simultaneously (fig. 9). One such model was initially fabricated to a 1.0-percent scale and tested at the ARC UPWT facility. This test demonstrated the feasibility of the design concept as well as verified the prognosis of the sting interference affecting the aerodynamics. However, some problems existed with this new model due primarily to its scale, e.g., balance fouling and instrumentation routing. These problems were significantly reduced in the 2.0-percent high-fidelity version of this design. A test was conducted in the 16T Propulsion Wind Tunnel facility at Arnold Engineering Development Center (AEDC) utilizing this 2.0-percent model. Examination of the resulting data revealed problems with the flow angularity encountered from the 16T facility quick-turn sting mounting system (fig. 10). A flow angularity test was conducted, and the problem was eradicated (fig. 11).

These problems were not peculiar to the force and moment models only. The pressure models were also susceptible to similar problems which rendered the pressure distribution data base questionable until model and facility corrections were made. The sting interference problem was resolved by mounting the model on two stings, one in the base of each SRB. A three-percent high-fidelity pressure model was designed which incorporated some of the concepts used in the two percent model (fig. 12). This allowed the orbiter and component forces and moments to be measured simultaneously with approximately 1500 pressure measurements covering the total vehicle. The sting interference question was thus eliminated relative to the orbiter. The only problem encountered on the new three-percent model was with balance stiffness, which caused an orbiter roll misalignment. The two- and three-percent models were tested at AEDC and ARC to obtain the aerodynamic force/moment and pressure distribution power-off data bases for the first Space Transportation System (STS-1) flight.

Coincident with the power-off testing program was the power-on program which was initiated with a plume technology study at MSFC to define plume similarity parameters for use in plume simulation tests on the Space Shuttle. The resulting similarity parameters were incorporated in the wind tunnel model nozzle design and test planning. Several cold-flow plume tests were conducted to define the solid rocket motor (SRM) and Space Shuttle main engine (SSME) plume effects on the vehicle pressure distributions. Data obtained from these tests included base pressures, nozzle airloads, forebody plume effects, throttling, and angle-of-attack/sideslip effects. The test results indicated that the only significant effect to forebody aerodynamics was on the inboard elevons (fig. 13). These data were formatted, along with the power-off data, for use by the various design disciplines for structural and trajectory design analyses leading to the first Space Shuttle launch.

POSTFLIGHT COMPARISONS

Postflight extraction of the aerodynamic forces and moments from STS-1 revealed that significant differences existed from the baseline longitudinal forebody and base aerodynamics (figs. 14 through 17). These differences caused the SRB's to be staged at a higher altitude than expected on STS-1 and STS-2. Reconstructed trajectory parameters, incorporating extracted aerodynamics for STS-1 and STS-2, agreed very well with the flight-derived trajectory parameters. Analyses of these differences uncovered deficiencies in the wind tunnel simulation of plumes and Reynold's number effects and their interaction. The results from STS-1 were modeled as biases to be applied as a function of Mach number and released for initialization of STS-3 flight control parameters. The extraction of aerodynamics from a vehicle of this complexity leads to many questions about the inclusion of all factors in the extraction process. Nevertheless, approximately the same biases were repeated from flight to flight. After STS-4, the current Space Shuttle aerodynamic data base was modified to include the first four flight results. Gradient and intercept analyses of the derivatives ($\partial C/\partial \beta$ and $\partial C/\partial \alpha$) indicated that the wind tunnel data base derivatives and absolute levels were incorrect as shown in figures 18 and 19 and, therefore, required revision.

Other questions still exist. Since the forebody aerodynamics changed significantly, confidence in the wind-tunnel-derived external pressure distribution decreased. STS-1 through STS-3 provided only base pressure information, except for one row of wing pressure instrumentation. These measurements indicated that the base and wing pressures were significantly higher than predicted but with no net load change on the wing at the measured station (fig. 20). Strain gauge data on the wing indicated that the total wing loads increased (fig. 21).

The fact that the vehicle pressure distributions are questioned causes problems concerning go/no-go launch decisions since these data are inputs to the load indicator equations used for this decision. The first attempt to model the strain gauge data into pressure distributions resulted in a model which did not match the gauge data to the preferred accuracy (fig. 22 through 24). However, the gauge data was questioned and a check calibration performed after STS-5 revealed that several key gauges had either the wrong scaling factors or reversed polarity. Incorporation of the corrections along with more pressure data received from STS-4 and STS-5 into a new model is now being accomplished. These last two flights have also provided pressure data on the fuselage which verifies the higher pressures on the lower surface.

A wind tunnel test program to simulate flight base pressures with cold gas SRM and SSME plumes was recently completed. The data from this test verified that the trends and levels of the pressure distribution model currently being completed are correctly synthesized.

LESSONS LEARNED

The development of the Shuttle integrated aerodynamic data base has provided a learning experience which applies to any launch vehicle. The wind tunnel programs must pay special attention to sting effects and Reynold's number simulation. Recent knowledge obtained from plume simulation wind tunnel testing will aid in accurate prediction of plume effects for future vehicles. In the preliminary design of any multibody or winged launch vehicle, the sensitivity of vehicle attach loads and components to aerodynamics must be understood in order to avoid vehicle constraints which may limit the flight performance and structural envelopes. Finally, the planning of the flight test program, from an aerodynamic viewpoint, must devote special attention to instrumentation locations, accuracy, and calibration with emphasis on the measurement of thrust and thrust vectors for powered flights since these highly influence the aerodynamic data extraction process.

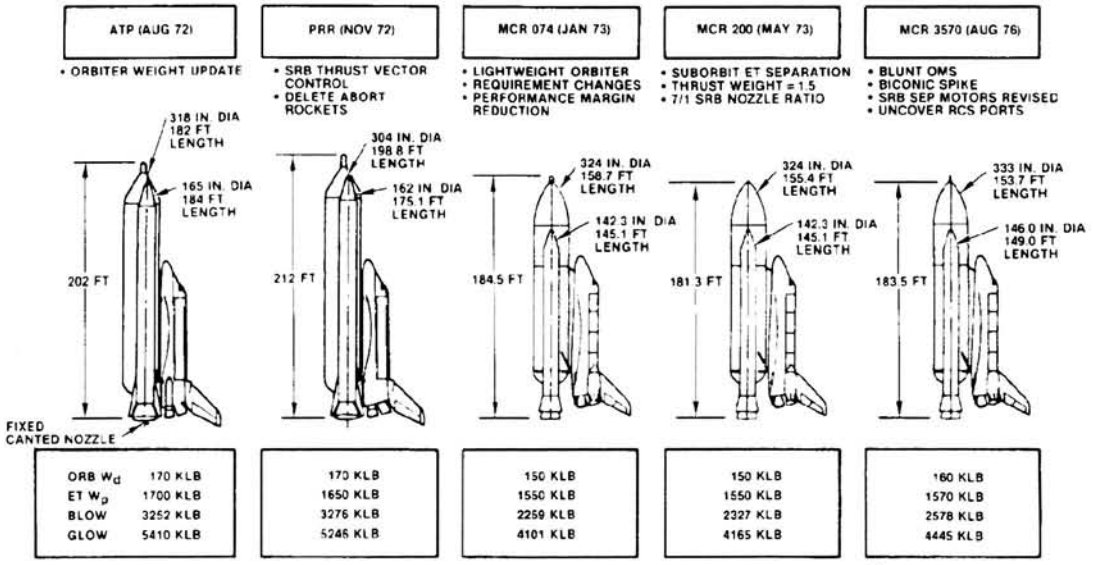

Figure 1.- Space Shuttle design evolution.

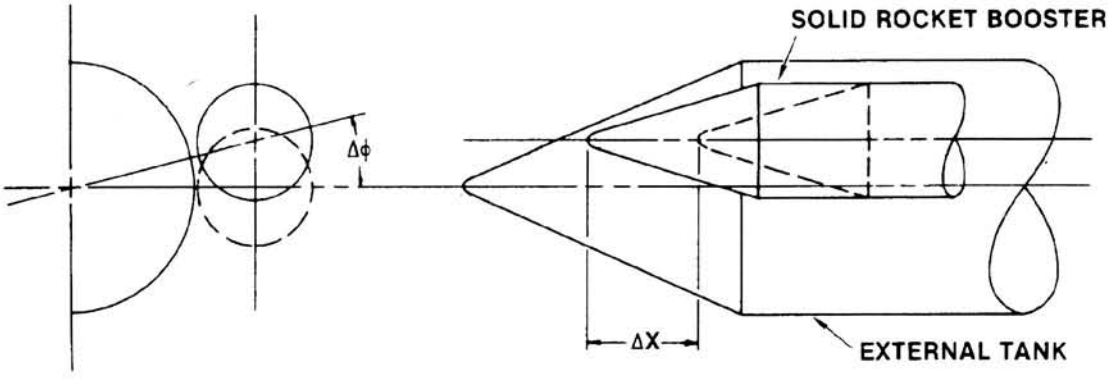

Figure 2.- Solid rocket booster placement.

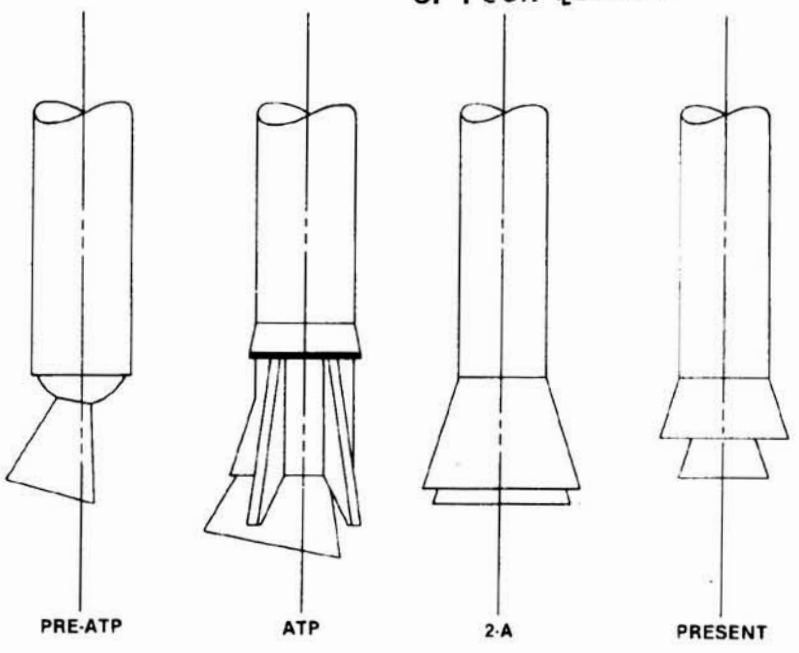

Figure 3.- Solid rocket booster aft skirt outer moldline geometry.

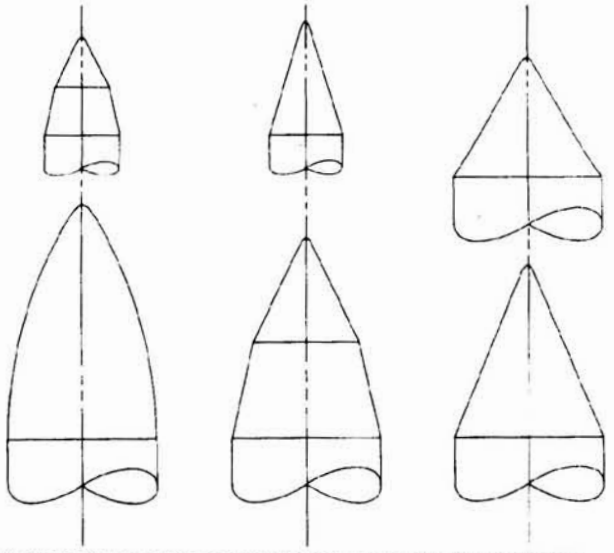

Figure 4.- External tank/solid rocket booster nose profiles.

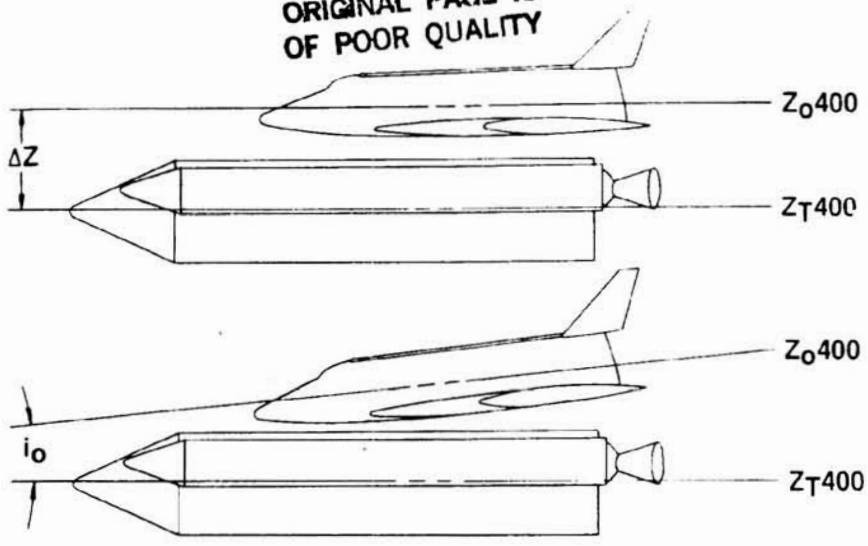

Figure 5.- Orbiter incidence and vertical placement from external tank.

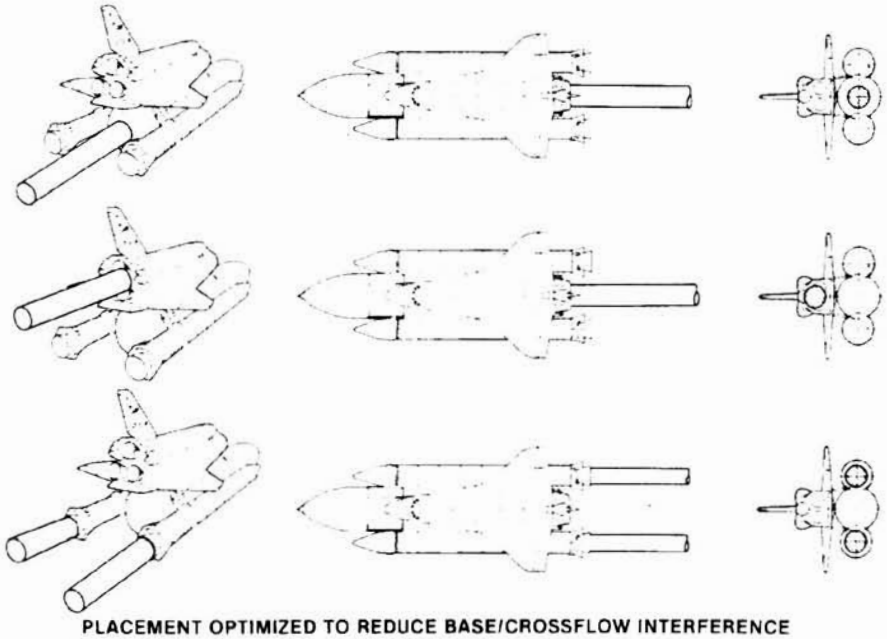

PLACEMENT OPTIMIZED TO REDUCE BASE/CROSSFLOW INTERFERENCE

Figure 6.- Wind tunnel model sting placement.

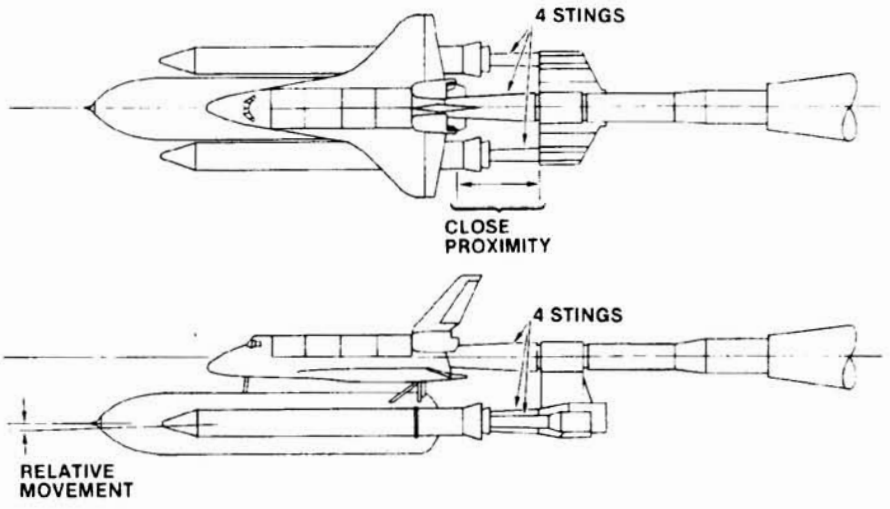

CLOSE PROXIMITY OF STING SUPPORT CAUSED BLOCKAGE. FOUR STINGS AND THEIR PLACEMENT CAUSED INTERFERENCE/ CROSSFLOW PROBLEMS. FOUR STINGS ALSO ALLOWED EXCESSIVE MOVEMENT OF MODEL COMPONENTS WITH RESPECT TO EACH OTHER

Figure 7.- Model support system for early loads tests.

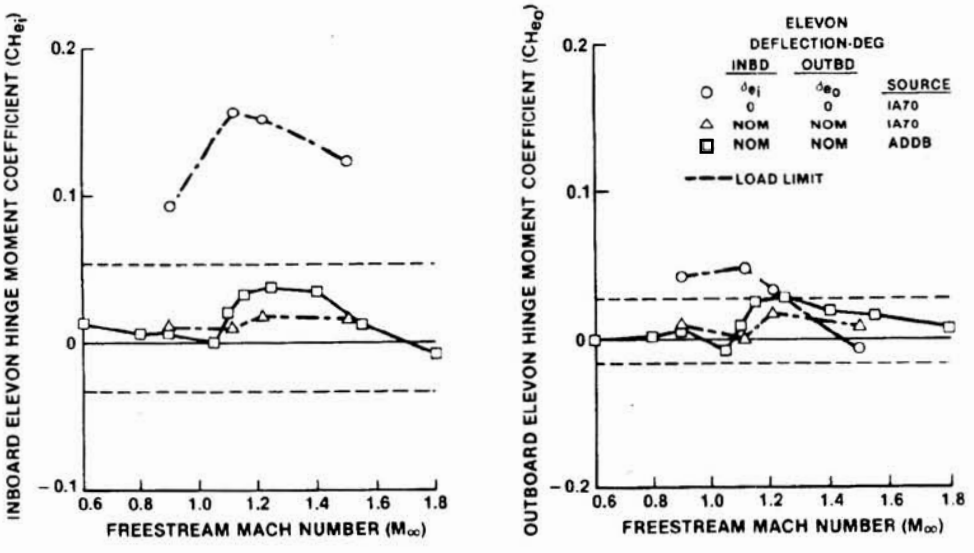

Figure 8.- Elevon schedule effect on hinge moments.

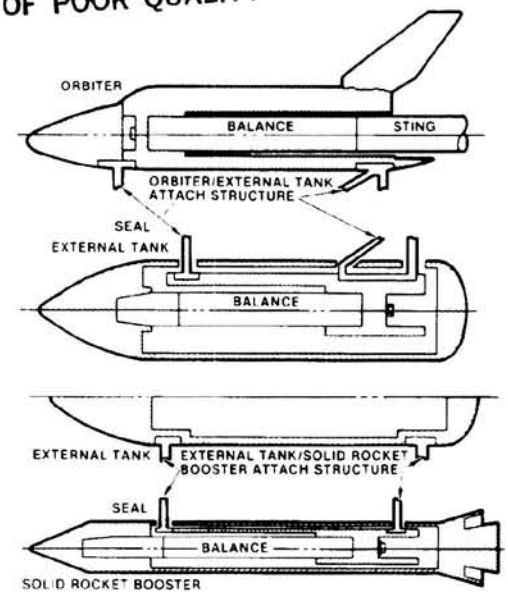

Figure 9.- Multiple-balance layout for single-sting installation.

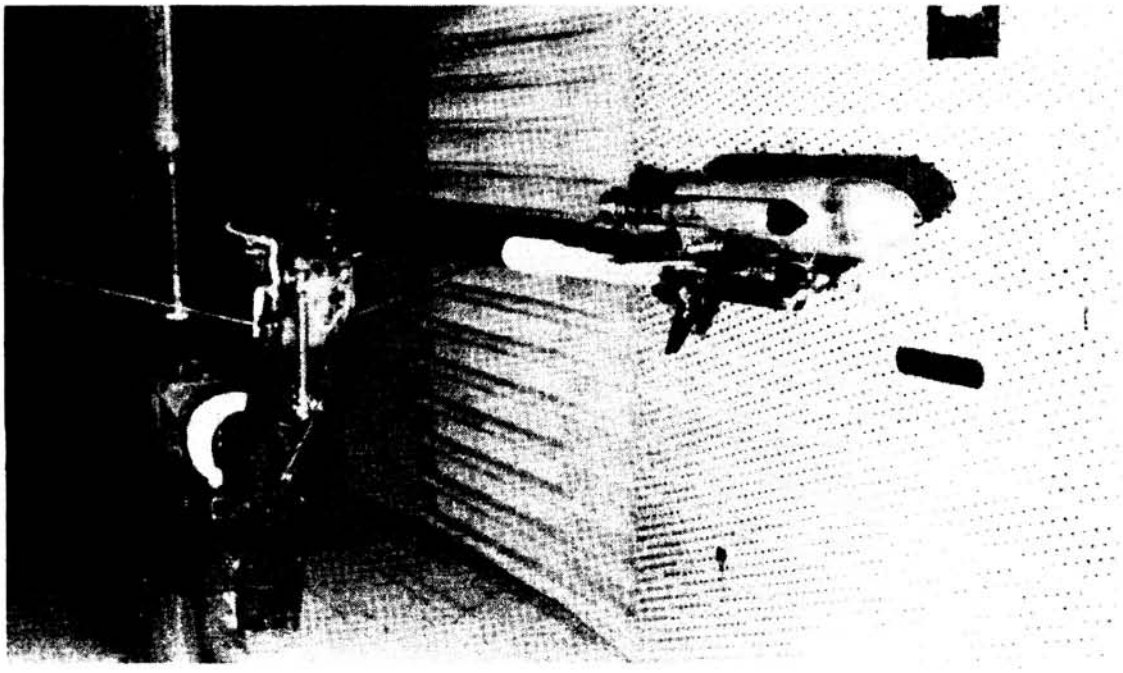

Figure 10.- Installation of model in ADEC 16T on quick-turn mounting system.

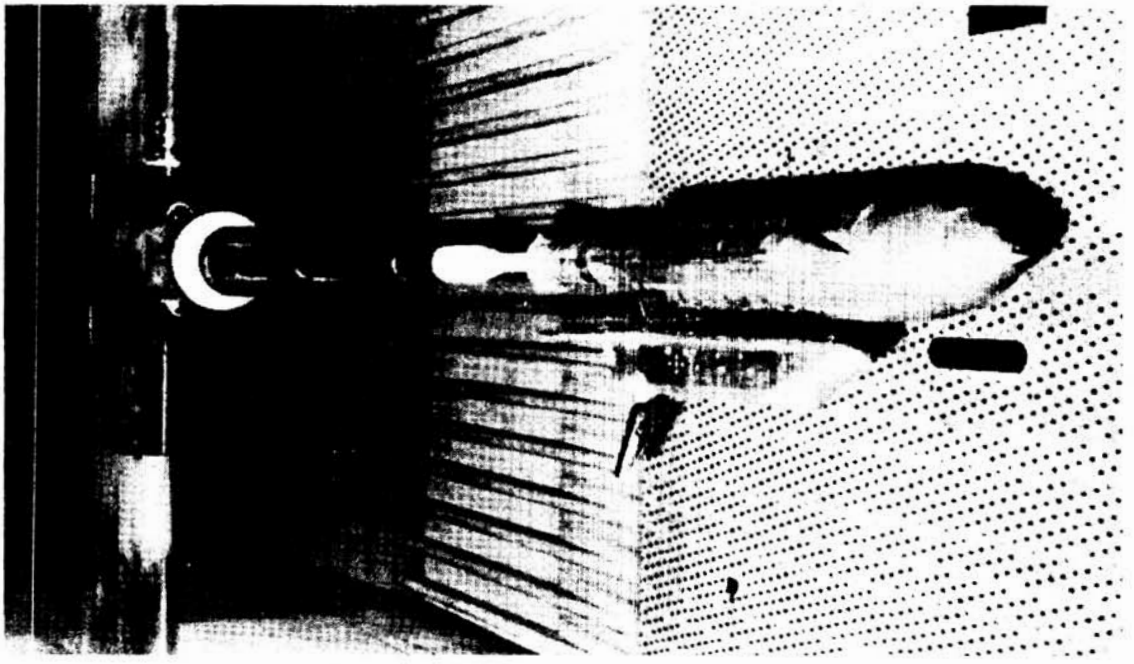

Figure 11.- Installation of model in ADEC 16T on straight-sting mounting system.

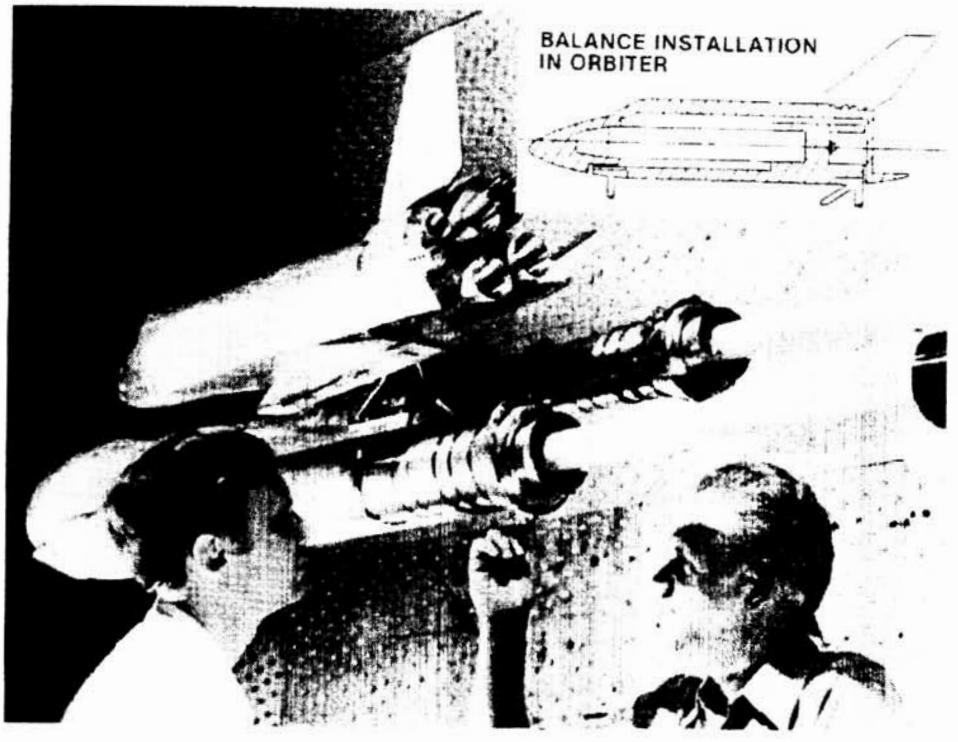

Figure 12.- View of three-percent high-fidelity model in ADEC 16T facility.

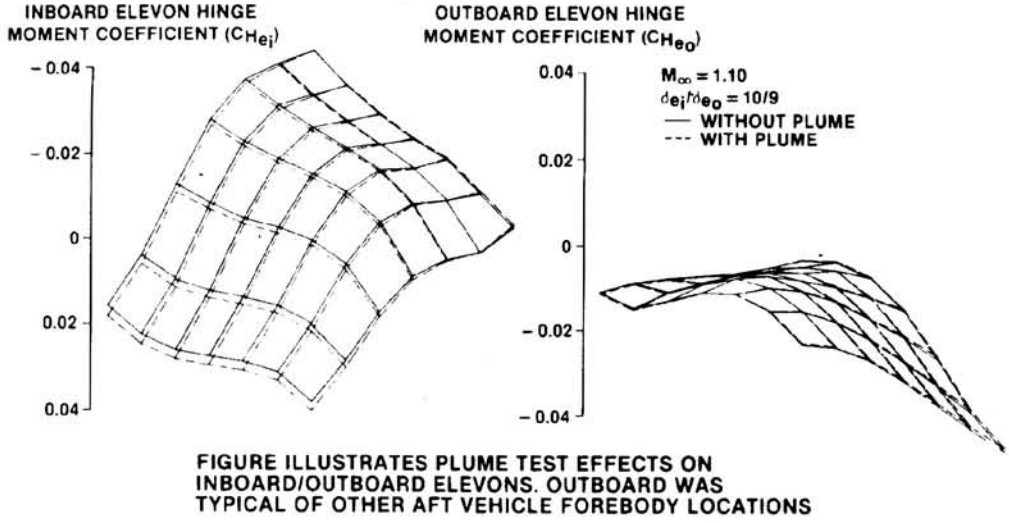

Figure 13.- Forebody plume effects on elevon hinge moment.

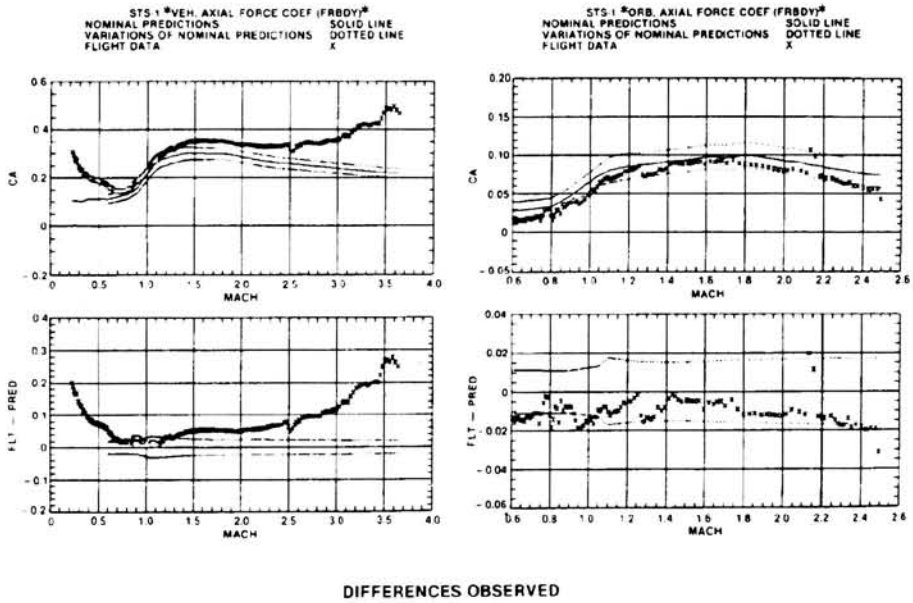

Figure 14.- Postflight extracted axial-force comparison with predicted data.

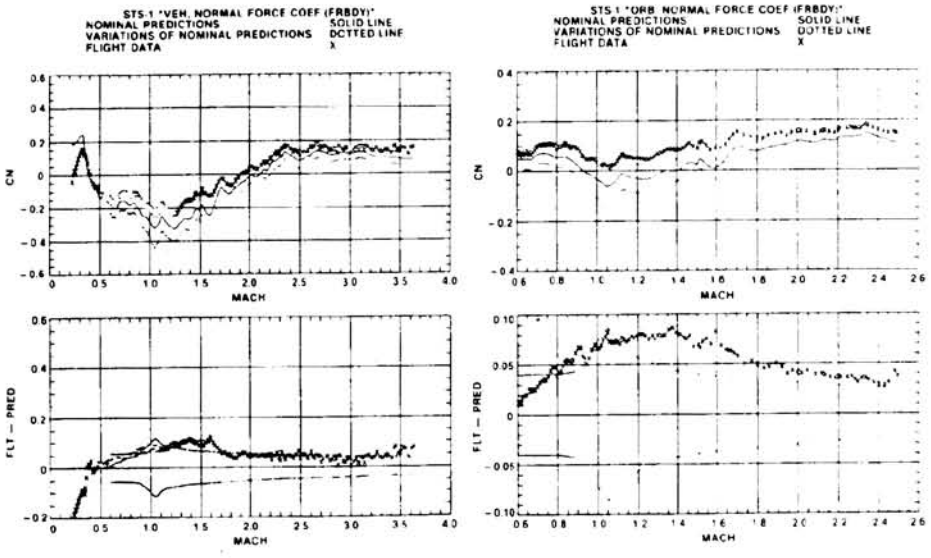

Figure 15.- Postflight extracted normal-force comparison with predicted data.

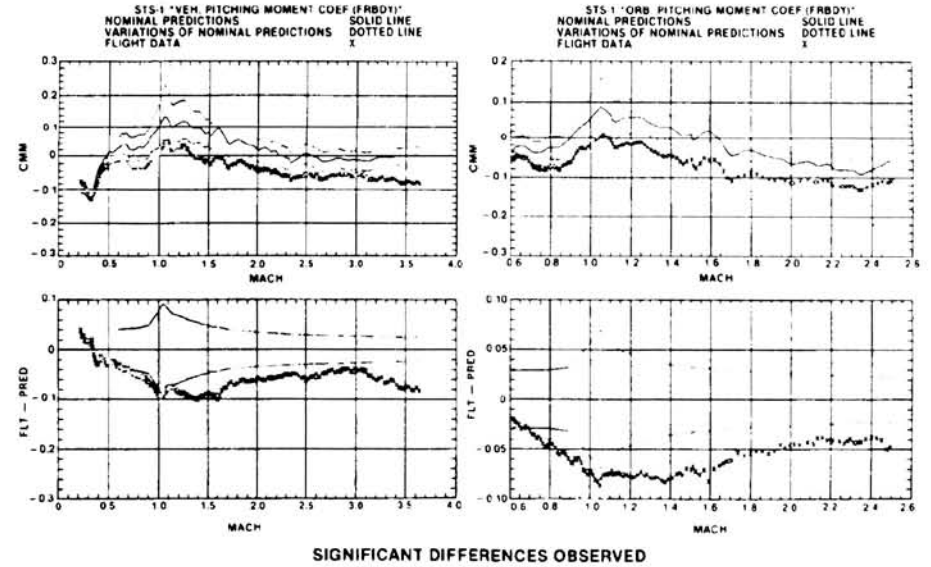

Figure 16.- Postflight extracted pitching moment comparison with predicted data.

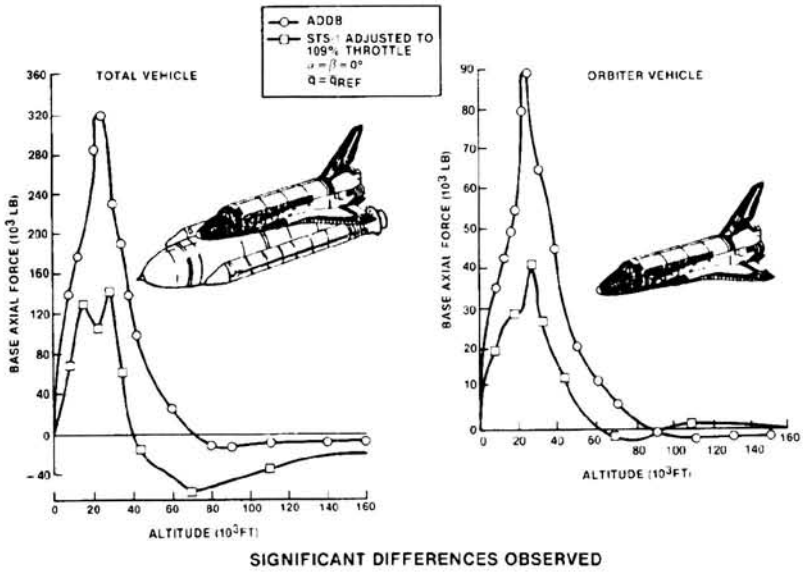

Figure 17.- Postflight extracted base axial-force comparison with predicted data.

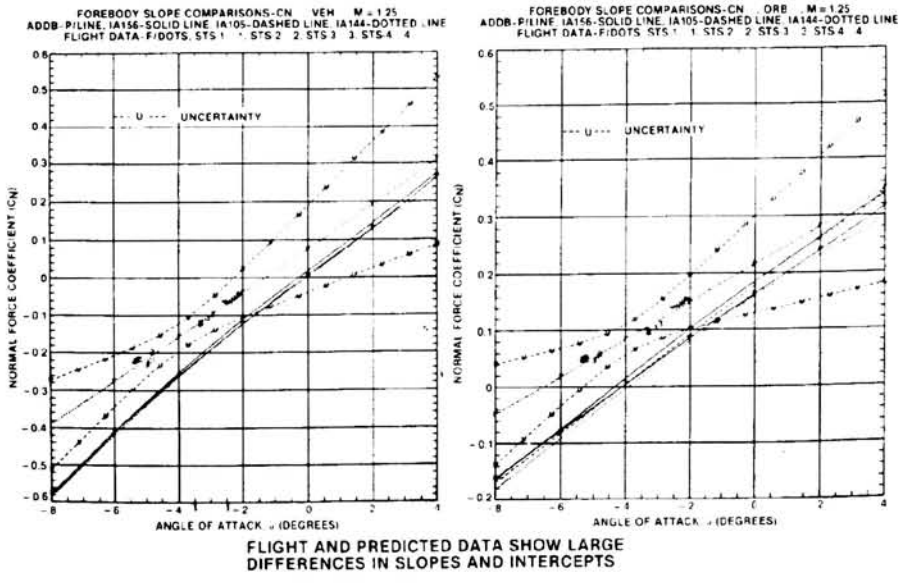

Figure 18.- Normal-force gradient comparison.

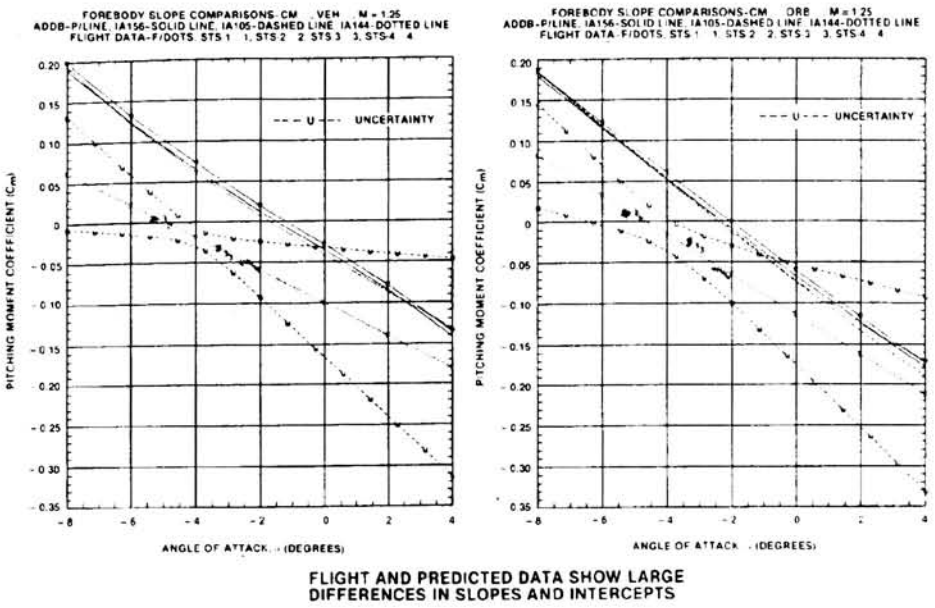

Figure 19.- Pitching moment gradient comparison.

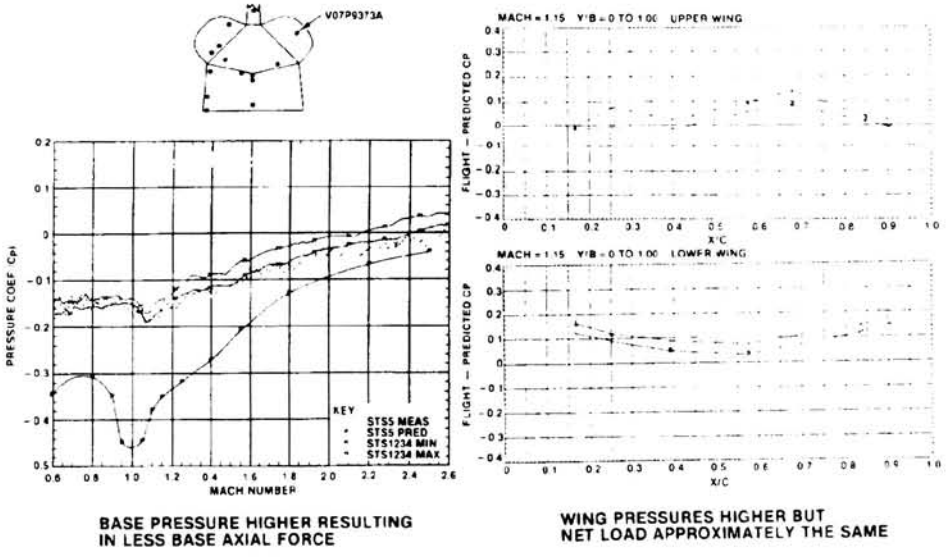

Figure 20.- Flight and predicted pressure data comparison.

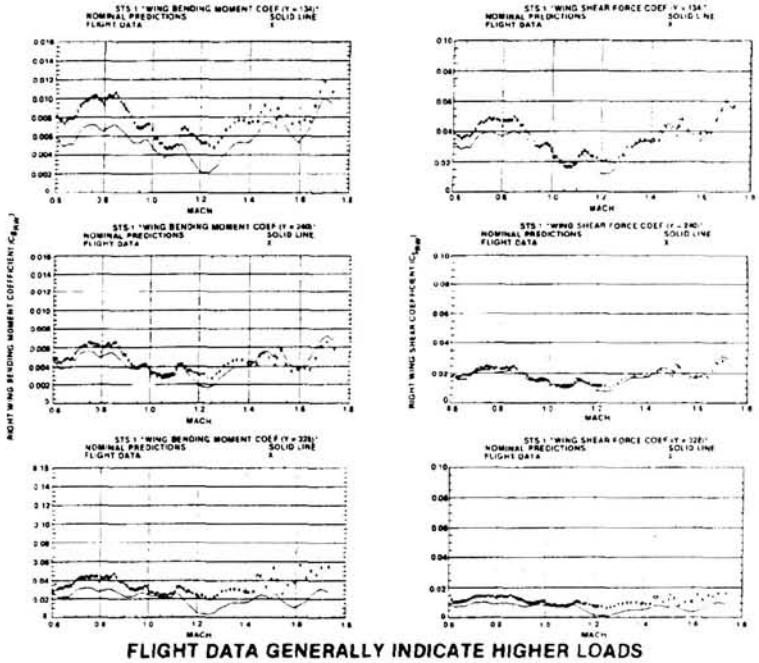

Figure 21.- Wing strain gauge flight data.

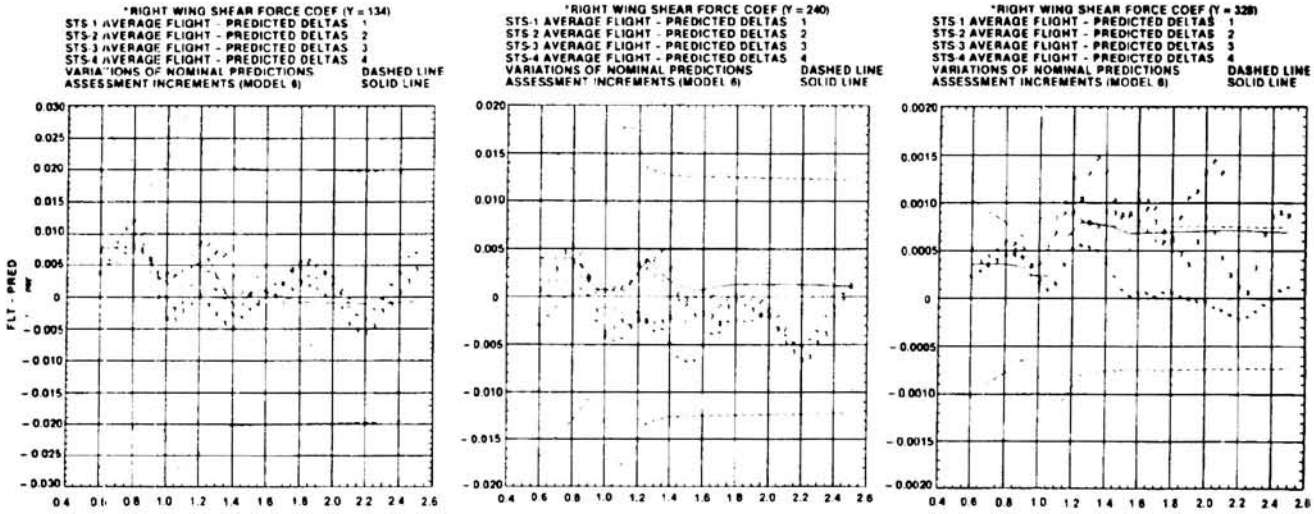

MODEL PREDICTION OF SHEAR ACCEPTABLE

Figure 22.- Wing strain gauge comparison with integrated pressure distribution model for wing shear.

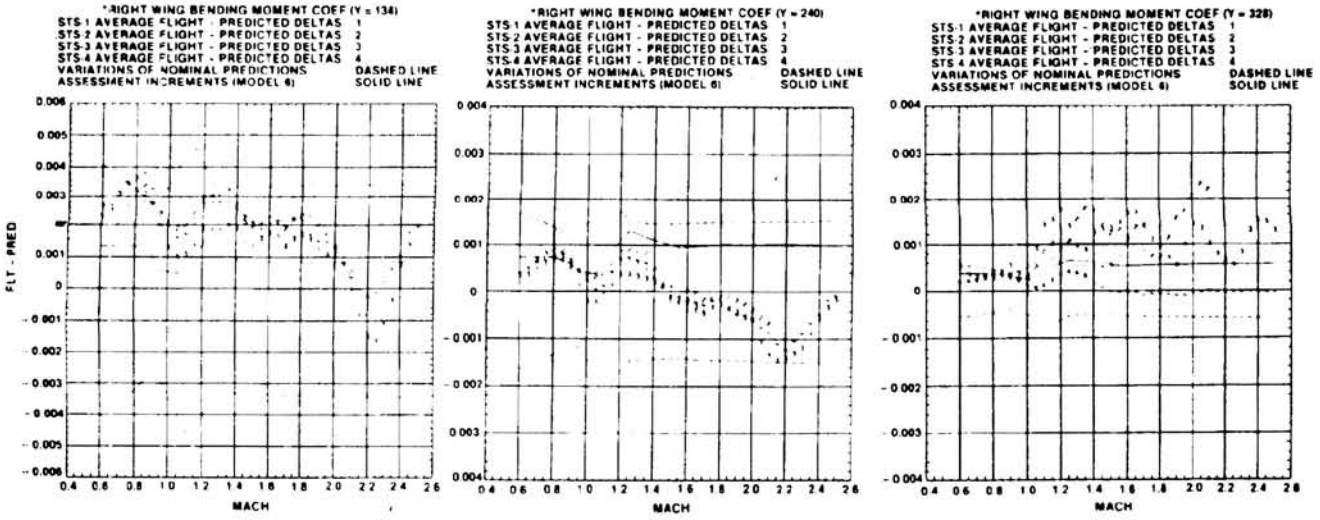

MODEL PREDICTION OF BENDING NOT ACCEPTABLE

Figure 23.- Wing strain gauge comparison with integrated pressure distribution model for wing bending.

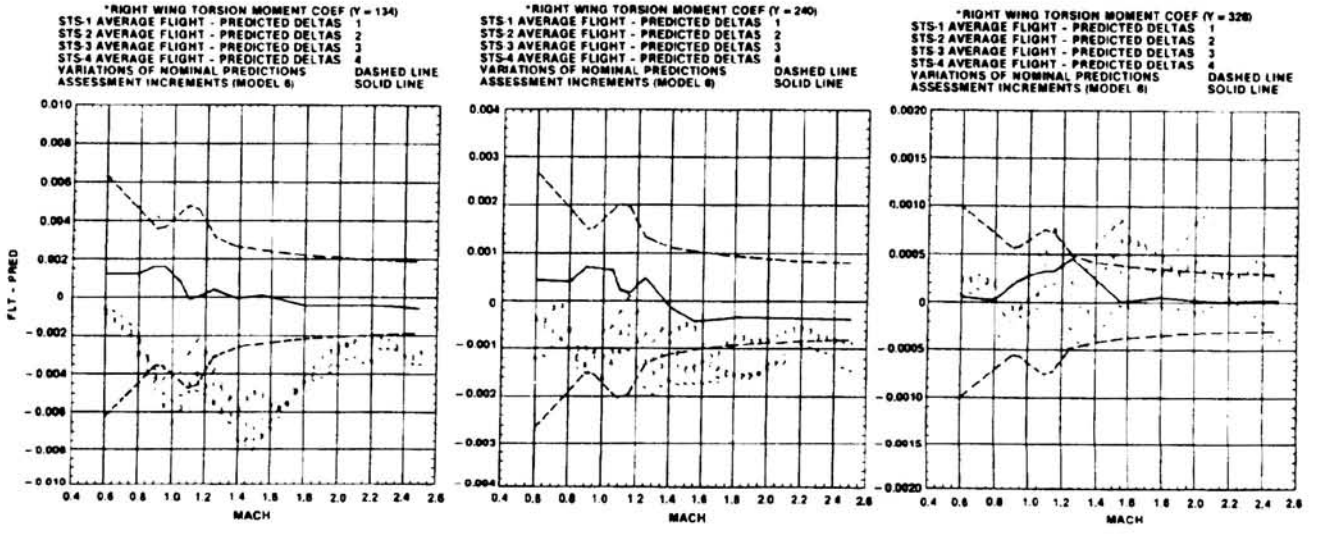

MODEL PREDICTION OF TORSION NOT ACCEPTABLE (TORSION WAS NOT CONSIDERED IMPORTANT IN FORMULATION OF MODEL)

Figure 24.- Wing strain gauge comparison with integrated pressure distribution model for wing torsion.

SPACE SHUTTLE LAUNCH VEHICLE AERODYNAMIC UNCERTAINTIES: LESSONS LEARNED

J. T. Hamilton
Space Transportation and Systems Group
Rockwell International
Downey, California

SUMMARY

This paper presents the chronological development and evolution of an uncertainties model which defines the complex interdependency and interaction of the individual Space Shuttle element and component uncertainties for the launch vehicle. Emphasis is placed on user requirements which dictated certain concessions, simplifications, and assumptions in the analytical model. The use of the uncertainty model in the vehicle design process and flight planning support is discussed. The terminology and justification associated with tolerances as opposed to variations are also presented. Comparisons of and conclusions drawn from flight minus predicted data and uncertainties are given. Lessons learned from the Space Shuttle program concerning aerodynamic uncertainties conclude this paper.

INTRODUCTION

The Space Shuttle is a complex flight vehicle comprised of four major elements: orbiter, external tank (ET), and two solid rocket boosters (SRBs) plus orbiter/ET/SRB attachment structures, miscellaneous protuberances, and components such as the wing, elevons, vertical, and body flap. In order to insure that the design of a vehicle of this complexity is adequate, uncertainties must be defined for each of the above items, and an analytical model must be devised where required. This paper discusses the development of the Space Shuttle aerodynamic uncertainties for application to vehicle performance and structural loads analyses.

DATA BASE DEVELOPMENT

Initial requirements for uncertainties surfaced in the early 1970's. Emphasis was placed on definition of tolerance uncertainty levels for the total vehicle forces and moments for use in trajectory dispersion studies. The magnitude of these uncertainties, expressed as percentages of the aerodynamic coefficients, was based on early test data and engineering judgement without any statistical basis. As the design of the Space Shuttle matured, emphasis shifted from the

total vehicle to element and component uncertainty definition. Parallel to this requirement was the need to account for model-to-full-scale data differences. This need was fulfilled with the introduction of "variations" as opposed to "tolerances." Variations accounted for the difference between model and full-scale data, whereas tolerances provided the uncertainty on the model or predicted data. In order to generate variation levels, one usually researches the differences between model and flight-extracted data for configurations and conditions similar to the required configuration. Unfortunately, no such information existed for something similar to the launch vehicle; however, data did exist for configurations similar to the isolated orbiter. Using relationships based on isolated orbiter variation-to-tolerance ratios, launch vehicle as well as element variations were defined. Uncertainties for the elements, components, and the total vehicle were then ready to be generated.

Due to the large number of element, component, and total vehicle aerodynamic coefficients, the need for a consistent method of developing uncertainties arose. Further complexity became apparent since a limited number of tests and conditions were available. Uncertainties were generated based on two tests and the spread of the data therein. Incremental uncertainties were estimated for model-to-full-scale configuration differences, Reynolds number effects, and instrumentation inaccuracies. Also introduced at this time were the concepts of "channel flow," "transfer term," and "common cause." A very complex model was conceived with a minimum amount of data as a basis. More testing was accomplished to increase the accuracy, fidelity, and amount of data for use in the design verification. These data allowed the formulation of a new generation of uncertainties comprised of a somewhat simplified model, fewer terms, semistatistical basis, and a refined output format allowing the users to obtain a less conservative and more accurate definition of aerodynamic uncertainty effects on design and payload capabilities.

Certain specialized and isolated needs arose concerning the use of the uncertainties prior to STS-1 and in preparation for subsequent flights. Of primary importance was the day-of-launch load indicator margins assessment criteria with respect to uncertainties. Up to this point in time, variation levels had been used for all aerodynamic uncertainty definitions, and these were applicable primarily to ascent trajectory dispersion studies, structural fitting/strut member loads analyses, and Monte Carlo day-of-launch criteria. A specialized set of uncertainties was generated for the Monte Carlo studies which were only a function of Mach number. Use of these uncertainties became complicated when the need for distributed values was required. Several models were tried, and the current model, which uses basically a partial-to-total-load ratio at the station in question, was the best overall. The distributed uncertainties and the results of the load indicator dispersion studies revealed that the aerodynamic uncertainties were large percentages of the allowable load margins. Several indicators, especially on the components and the wing in particular, showed levels that exceeded design flag loads when aerodynamic uncertainties were used. Several values were eliminated to levels below variations, but the levels of values greater than tolerances and problems diminished.

LESSONS LEARNED

The OFT flight program has revealed large differences in the longitudinal aerodynamics between predicted data and flight data. These differences were deemed responsible for what is termed the "lofting anomaly." Variations limits were exceeded slightly but were probably responsible for the adequacy of the design, and so no structural failures occurred. Information extracted from flight data has enabled a new technique to be utilized in the definition of aerodynamic uncertainties. Treatment of the data through the use of "Student-t" methodology has enabled the possible generation of a statistical uncertainties data base in which the preliminary evaluation indicates significant reductions of uncertainty levels. Currently, definition of an "operational data base" is being accomplished. The uncertainties model is being formalized, and the values established. These data will be used for all flights beyond STS-6.

The development of the Space Shuttle integrated aerodynamic uncertainties data base has provided a learning experience which applies to any launch vehicle. The use of so-called "variations" provided the needed capability in terms of flight control profiles to preclude structural failures on a vehicle of this type. Careful attention to the complex flow phenomena must be adhered to in the formulation of an uncertainties model which must predict levels dependent on the interaction between not only the coefficients but also the vehicle components.

LAUNCH VEHICLE AERODYNAMIC FLIGHT TEST RESULTS

L. M. Gaines,
W. L. Osborn,
and
P. D. Wiltse

Space Transportation and Systems Group
Rockwell International
Downey, California

SUMMARY

This paper presents the aerodynamic flight test procedures and results for the Space Shuttle orbiter. The aerodynamic characteristics used in testing were determined from flights STS-1 through STS-4.

Normal force and pitching moment were different than predicted, suggesting an unanticipated aerodynamic force acting upward on the aft end of the orbiter. However, lateral-directional aerodynamic characteristics were in good agreement with predictions. The flight-measured aerodynamics are repeatable and show good correlation with angle of attack and angle of sideslip.

INTRODUCTION

Early in the Space Shuttle program, a requirement was identified for Rockwell to verify the first-stage aerodynamic data base within the defined uncertainties level during the flight test program. It was a goal of the verification process to establish flight data within these uncertainties. This objective would assure satisfactory subsystem operation and performance since the Space Shuttle vehicle (SSV) had been designed to accommodate the defined uncertainties. A program to accomplish these objectives was developed several years before the first flight. The data requirements, including instrumentation accuracy needs, were established. The accuracy of each parameter was estimated and verified by an engineering review conducted by the Ascent Flight System Integration Working Group (AFSIG). This group reviewed the product of the data extraction procedure with respect to estimated input parameters; thus, they identified the significant flight measurements that were critical to achieving the original goal of the program. Effort and resources were committed to improve or add additional data as a result of these combined engineering and programmatic reviews.

SYMBOLS

$\ddot{R}_I$	measured acceleration (ft/sec^2)
ρ	position vector from accelerometers to Space Shuttle vehicle center of gravity
p	roll rate (rad/sec)
q	pitch rate (rad/sec)
r	yaw rate (rad/sec)
B	force due to base pressure (lb)
T	total thrust due to Space Shuttle main engines and solid rocket boosters (lb)
I	moment of inertia (slug-ft^2)
L	rolling moment (ft-lb)
M	pitching moment (ft-lb)
N	yawing moment (ft-lb)

Subscripts:

x	forward
y	right
z	down
J	jet damping
b	base pressure
T	thrust

ANALYSIS DEVELOPED TO EXTRACT AERODYNAMIC CHARACTERISTICS FROM FLIGHT MEASUREMENTS

A fairly large computer program was developed prior to the flight test program to extract aerodynamic characteristics from flight measurements and provide comparisons with wind tunnel predictions. Six-component body axis force and moment coefficients are extracted by solving the equations of motion at each instant in time throughout the first stage using known mass properties, measured accelerations, thrust for each of the five engines, engine gimbaling, and interface loads for the orbiter external tank (ET) and for the solid rocket booster (SRB) and the ET based on flight measurements.

The flight data analysis procedures were as follows:

- Launch vehicle
  - Measure all forces and moments (except aerodynamics) acting on the SSV, mass, and accelerations
    - Linear and angular accelerations, angular rates, mass properties, Space Shuttle main engine (SSME) and SRB thrust magnitude and direction
    - Calculate aerodynamic forces and moments
- Orbiter
  - Same as SSV except:
    - Add orbiter and ET interface loads
    - SRB thrust magnitude and direction not needed

Figure 1 also summarizes this concept.

The equations used to calculate the six SSV ascent aerodynamic force and moment coefficients are listed below:

$$C_A = \frac{-M[\ddot{R}_x - \rho_x (q^2 + r^2) - \rho_y (\dot{r} - pq) + \rho_z (\dot{q} + pr) - B_x - T_x}{q\,S}$$

$$C_y = \frac{M[\ddot{R}_y + \rho_x (\dot{r} + pq) - \rho_y (p^2 + r^2) - \rho_z (\dot{p} - qr) - T_y}{q\,S}$$

$$C_N = \frac{-M[\ddot{R}_z - \rho_x (\dot{q} - pr) + \rho_y (\dot{p} + qr) - \rho_z (p^2 + q^2) - B_z - T_z}{q\,S}$$

$$C_l = \frac{I_{xx}\,\dot{p} + qr\,(I_{zz} - I_{yy}) - I_{xz}\,(\dot{r} + pq) + \dot{I}_{xx}\,p - \dot{I}_{xz}\,r + L_J - L_T}{q\,Sl}$$

$$C_m = \frac{I_{yy}\,\dot{q} + pr\,(I_{xx} - I_{zz}) - I_{xz}\,(r^2 - p^2) + \dot{I}_{yy}\,q + M_J - M_b - M_T}{q\,Sl}$$

$$C_n = \frac{I_{zz}\,\dot{r} + pq\,(I_{yy} - I_{xx}) - I_{xz}\,(\dot{p} - qr) + \dot{I}_{zz}\,r - \dot{I}_{xz}\,p + N_J - N_T}{q\,Sl}$$

where C_A, C_N, C_y are the axial, normal, and side force coefficients and C_l, C_m, C_n are the rolling, pitching, and yawing moment coefficients, respectively. The symbol S denotes the reference area.

The basic program extracted the aerodynamic coefficients for the first-stage vehicle and the orbiter element, and provided comparisons with wind tunnel data. An auxiliary program was developed to extract the aerodynamics for the SRB elements. Thus, the aerodynamic characteristics for each element of the stack could be determined from these programs.

The program also calculated the uncertainties associated with each coefficient, based on estimates of accuracies for each measurement. These data were used before the flight program to estimate the number of flights required to provide the desired accuracy in the extracted aerodynamics. They were also used to select accelerometers to increase accuracy in the results. The procedure used to calculate these uncertainties is given below:

$$C_N = \frac{M[\ddot{R}_Z - \rho_x(\dot{q}-pr) + \rho_y(\dot{p} + qr) - \rho_z(p^2 + q^2)] - B_Z - T_Z}{\bar{q}\ S}$$

- Uncertainties are due to measurement accuracies of R_Z, mass (M), center of gravity (C.G.), location (ρ_x, ρ_y, ρ_z), angular acceleration ($\dot{q}$ and $\dot{p}$), angular rates (p, q, and r), base pressure (B_Z), thrust and thrust alignment (T_Z), and dynamic pressure ($\bar{q}$).

- Uncertainty due to a particular measurement = $(\partial C_N/\partial x)\cdot$(measurement uncertainty in x).

- Total uncertainty in the coefficient is root sum square (RSS) of individual uncertainties (22 terms):

$$\Delta C_N = \sqrt{\Sigma[(\partial C_N/\partial_x)(\Delta x)]^2}$$

- Uncertainty equations have been developed and programmed for all six aerodynamic components, i.e.:

$$C_N,\ C_M,\ C_A,\ C_\eta,\ C_\ell,\ C_y$$

INSTRUMENTATION AND DATA PROCESSING

In addition to the main aerodynamic extraction program, several auxiliary programs were developed to handle flight measurements that required postflight processing to achieve the necessary precision. The development of these postflight processing subroutines required venturing into areas normally foreign to the traditional aerodynamicist, but knowledge of these areas was absolutely necessary to achieve the confidence ir the significant measurements required to realize the final accuracy of the flight-extracted aerodynamic data.

One example is the measurement of the deflection angle of the SSME thrust vector. This measurement consisted of an approximation of the angle by a linear relation between the actuator extension and the nozzle angular position. In addition, the gimbal and gimbal actuator attach points deflected under load and acceleration. The subroutine developed to postflight process these measurements had to work backwards through the measured angular approximation to determine the extension of the actuator, then determine the angular deflection due to the thrust loads and accelerations and, finally, to recalculate the correct thrust vector angle for every data point for each engine.

The procedure for calculating the SRB and solid rocket motor (SRM) gimbal angles was developed using data obtained during a series of static firings. Empirical equations were developed relating the thrust angle obtained from the test stand to the thrust vector control actuator strokes and chamber pressure in the rocket motor case.

The need to isolate orbiter aerodynamics from the remaining portion of the launch vehicle added a requirement to determine the interface forces between the two elements. The interface struts consist of a forward bipod and a more complex massive structure consisting of five struts on the aft end of the vehicle, as illustrated in figure 2. A system of four strain gages on each strut was installed, and a precise calibration of each of the orthogonal forces was conducted on the flight test strut assemblies. The results of these structural calibrations were reduced to a set of matrix coefficients using linear curve fitting procedures. These coefficients became the principal elements of a postprocessing subroutine to determine the forces on orbiter fittings. The attach struts also support the large liquid oxygen (LOX) feed line with a 12,000-lb column of LOX, as well as the lesser hydrogen line and the various umbilical disconnects. A subroutine using dynamic pressure and accelerations was developed to correct the measurement system data output to reflect only the forces at the orbiter fittings.

Estimates of the accuracy of the system were verified by monitoring the main propulsion tests conducted in the test stands at Bay St. Louis, Mississippi. These tests also provided valuable experience in working with a data system used on the flight ET's.

The data used for the flight analysis were reduced by averaging the output of the four gauges on each strut and then solving a two-by-two matrix for the forward struts and a five-by-five matrix for the aft struts. A bad or failed measurement required throwing out the diagonally opposite measurement to eliminate bending effects. This 50 percent reduction in the measurement system prompted the development of a pseudo matrix procedure which utilized all of the gauges in a nonsquare or 5 by 20 matrix; then, if a gauge failed, only the contribution of the single gauge was missing from the flight evaluation process. A typical product of this subprogram is shown in figures 3, 4 and 5. In addition, computer files were created for easy access to the measured data. Comparisons with preflight estimates, as well as historical comparisons with previous flights, were made to determine valid interface forces going into the flight analysis process.

Several accelerometers were installed on the orbiter and on both SRB's. Locations of the accelerometers are indicated in figure 6. With several accelerometers, those that were out of agreement with the majority could be discarded. Biases were applied to the measurements based on comparisons of the measurements with the should-have-read values before main engine start with the vehicle on the pad. A computer program was developed to utilize the multiple measurements. This program provided accelerations at the vehicle C.G. based on the position of the instruments with respect to the vehicle C.G. A least-squares process was used in the analysis. Typical results are indicated in figure 7. The accelerometer measurements were filtered with a fourth-order Butterworth filter which made two passes, one forward and one backward, to avoid any inadvertent time shift in the filtered data.

These accelerometers were aligned with the body axis. However, the orbiter fuselage does experience some bending deflection due to thrust and aerodynamic loads. Analysis of the bending effects indicated that corrections to the normal acceleration measurements did not provide significant changes in the extracted aerodynamic normal force.

An air data probe was installed on the tip of the ET (fig. 8). Pressure orifices in a cone were used to determine angle of attack and sideslip and total pressure using a calibration from a wind tunnel test program. Static pressure was determined from tracking and meteorological data. See reference 1 for further details.

The wind tunnel data (compiled in the ADDB (e.g., ref. 2)) was also mechanized as a subroutine to the extraction program to provide comparisons of wind tunnel prediction with aerodynamics extracted from flight measurements. Angle of attack, angle of sideslip, Mach number, dynamic pressure from air data system measurements, and aeroelastic elevon deflections from actuator position and pressure differential measurements are used to provide wind tunnel coefficients corrected for aeroelasticity at the flight condition. Finally, a series of trials and verification assessments prior to the first flight established that the analytical process was correct and that the flight data could be retrieved within the goals of the original requirements.

FLIGHT RESULTS

With first Space Shuttle flight, the aerodynamic data extraction program was immediately called upon to provide important programmatic answers. The first-stage trajectory was steeper than expected (lofted), resulting in staging about 10,000 ft higher than predicted (fig. 9). Comparisons of the SSV normal force and pitching moment characteristics measured during the first flight with wind tunnel data are shown in figure 10. The coefficients, extracted using the flight measurements, are shown as dotted lines. The Aerodynamic Data Book prediction, (ref. 2) based on the wind tunnel test results, is shown as the middle solid line. Each point on the solid line is the Aerodynamic Data Book prediction for the angle of attack, angle of sideslip, elevon position, and Mach number measured in flight. The Aerodynamic Data Book uncertainties are also shown. It was noted that the variation in the measured coefficients over short periods of time followed predictions fairly well, lending confidence to the instrumentation and analytical procedure. The analysis

revealed greater first-stage positive normal force and negative pitching moment (nose-down direction) than predicted. These differences from the wind tunnel prediction were a primary contributor to the loft anomaly (fig. 11). After the first flight, an assessment package that included the incremental changes in the longitudinal coefficients was released and used in trajectory predictions for subsequent flights to correct this loft anomaly.

Analysis of data from STS-2, -3, and -4 confirmed the STS-1 results. Figure 12 shows the differences between the flight-measured normal force coefficient and the Aerodynamic Data Book prediction for the first four flights (ref. 2). Similar differences in pitching moment coefficient are shown in figure 13. Although the expanded scales emphasize the data scatter, the results show that the flight data average is clearly different than the prediction, since a zero difference in the flight-minus-Aerodynamic Data Book coefficient (ΔC_N) would represent agreement between the flight and wind tunnel results. Beyond Mach 1.0, the flight-measured normal force and pitching moment coefficient differences exceeded the published prediction uncertainties.

The extracted longitudinal aerodynamic characteristics for the orbiter element differed from predictions in the same direction as those of the first stage. The observed differences for the orbiter normal force and pitching moment made up a large part of those differences observed for the entire launch vehicle, as shown in figures 14 and 15. These data indicate that the unpredicted aerodynamic force acts largely on the orbiter near its aft end.

STS-4 was deliberately flown at a less negative angle of attack, as shown in figure 16, to evaluate angle of attack effects on the aerodynamic characteristics. Figure 17 shows a typical correlation of flight-measured normal force and pitching moment coefficients with angle of attack. The data points in this figure represent all the data taken at ten samples per second between Mach 1.075 and 1.125, at 0.1-second intervals. The data points are corrected to Mach 1.1 and β = 0 using Aerodynamic Data Book trends (ref. 2). The results show a surprisingly good correlation with angle of attack, confirming the accuracy of the measured flight results. Regression analysis of data from the first four flights showed that the slopes, $C_{n\alpha}$ and $C_{m\alpha}$, were slightly less than predicted.

The flight data shown in figure 17 (and repeated in fig. 18) have also been used to assess the uncertainty in the flight results. The solid line in figure 17 was determined by a linear regression analysis and represents the estimate of the mean of the C_N versus α curve, based on measurements from four flights. The "Students T" distribution defines the statistical limits on the true mean of C_N versus α curve, given a number of samples and a confidence level. Figure 18 shows the limits on the true C_n versus α curve, for four samples, with a confidence of 0.997. This bound can be considered the uncertainty in the flight-measured C_n versus α curve.

A total of six flights are planned with instrumentation for the determination of aerodynamic characteristics. With six flights (or samples), the statistical limits reduce to about one-half of those shown for four samples. If the scatter in the data for the two additional flights does not change from current results, the uncertainties of the aerodynamic characteristics determined from flight measurements will be within the original program goals set several years ago.

The lateral-directional aerodynamic characteristics have also been extracted from flight measurements. In general, the lateral-directional characteristics are in very good agreement with the Aerodynamic Data Book (ref. 2). Figures 19 and 20 are typical illustrations of this. The side force, rolling moment, and yawing moment coefficients are correlated with sideslip angle and, although some scatter is apparent, the correlation with sideslip angle and the agreement with the Aerodynamic Data Book are very good.

SUMMARY AND CONCLUSIONS

The Space Shuttle aerodynamic data base included a definition of uncertainties of the aerodynamic characteristics. The Shuttle design accommodated these uncertainties. During the flight program it was not only necessary to verify the aerodynamic data base, but also to determine the uncertainties in the aerodynamic characteristics with a goal of reducing uncertainties to a predetermined level. The necessary instrumentation was identified and provided and the analysis tools developed. The first flight occurred and the aerodynamic data extraction program was immediately called upon to provide important programmatic answers as to why the first-stage trajectory was higher than predicted. Comparisons of aerodynamic characteristics (measured during the first flight) with wind tunnel data revealed greater first-stage normal force and negative pitching moment than predicted. These differences from the wind tunnel data were a primary contributor to the loft anomaly. Analysis of data from succeeding flights confirmed the first flight results. The lateral-directional aerodynamic characteristics were also extracted from flight measurements and showed very good agreement with wind tunnel results. The aerodynamic characteristics measured in flight showed surprisingly good correlation with angle of attack and sideslip. A statistical procedure was used to evaluate the uncertainty in the aerodynamic characteristics measured in flight. The aerodynamic characteristics have been determined based on the results of the first four flights and it is anticipated that when the six-flight program is completed, the aerodynamic uncertainties will meet the program goals.

REFERENCES

1. Hillje, E. R., and Nelson, R. L.: Ascent Air Data System Results From the Space Shuttle Flight Test Program. Shuttle Performance: Lessons Learned, NASA CP-2283, Part 1, 1983, pp. 187-230.

2. Aerodynamic Design Data Book, vol. 2, Launch Vehicle, Report No. SD72-SH-0060-2J, Rockwell International, Aug. 1978.

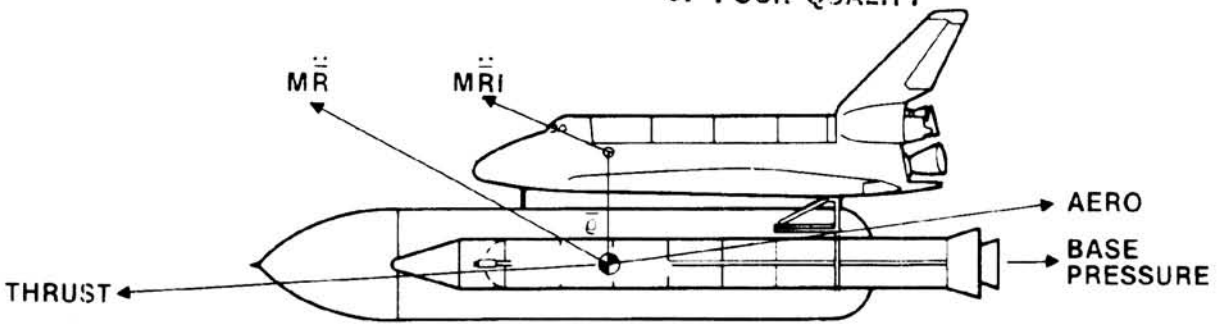

$$\text{TOTAL APPLIED FORCE} = \text{THRUST} + \text{AERO} + \text{BASE PRESSURE}$$
$$= M\ddot{\bar{R}} = M\left[\ddot{\bar{R}}_I + \dot{\bar{\omega}} \times \bar{\rho} + \bar{\omega} \times (\bar{\omega} \times \bar{\rho})\right]$$
$$\text{AERO} = M\ddot{\bar{R}} - \text{THRUST} - \text{BASE PRESSURE}$$
$$\text{TOTAL APPLIED TORQUE} = \bar{M}_{\text{THRUST}} + \bar{M}_{\text{AERO}} + \bar{M}_{\text{BASE PRESSURE}}$$
$$= I\dot{\bar{\omega}} + I\dot{\bar{\omega}} + \bar{\omega} \times I\dot{\bar{\omega}} + \bar{M}_{\text{JET DAMPING}}$$
$$M_{\text{AERO}} = I\dot{\bar{\omega}} + \dot{I}\omega + \bar{\omega} \times I\bar{\omega} + \bar{M}_{\text{JET DAMPING}} - \bar{M}_{\text{THRUST}} - \bar{M}_{\text{BASE PRESSURE}}$$

Figure 1.- Space Shuttle aerodynamic forces and moments.

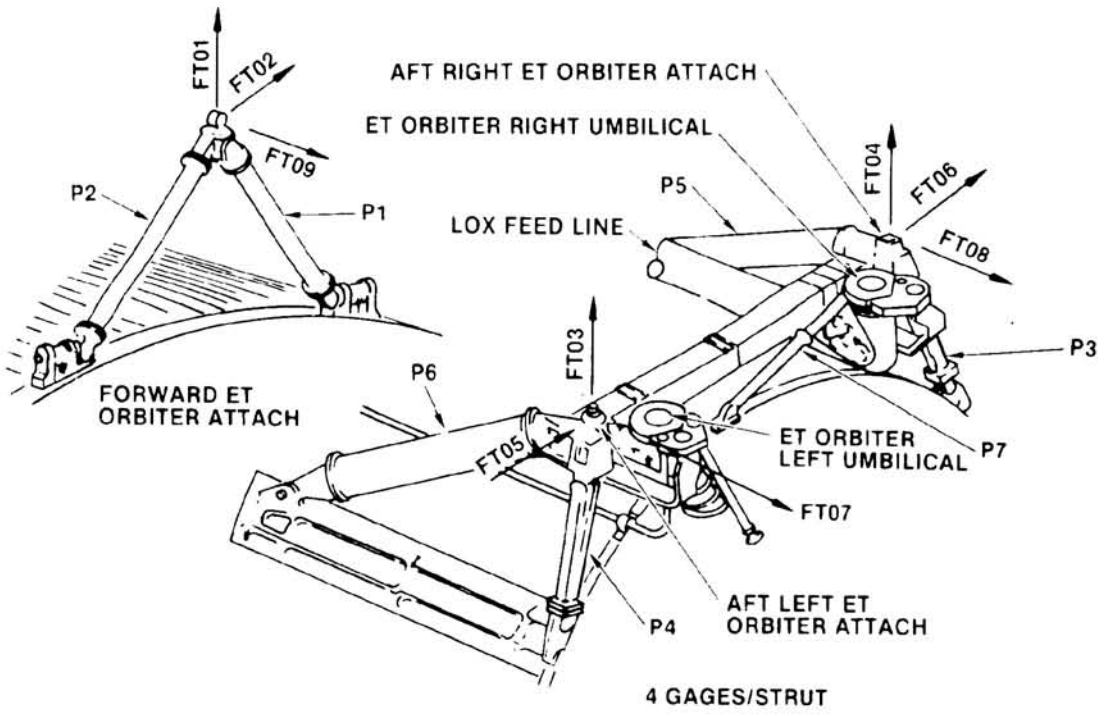

Figure 2.- Orbiter external tank attach strut configuration.

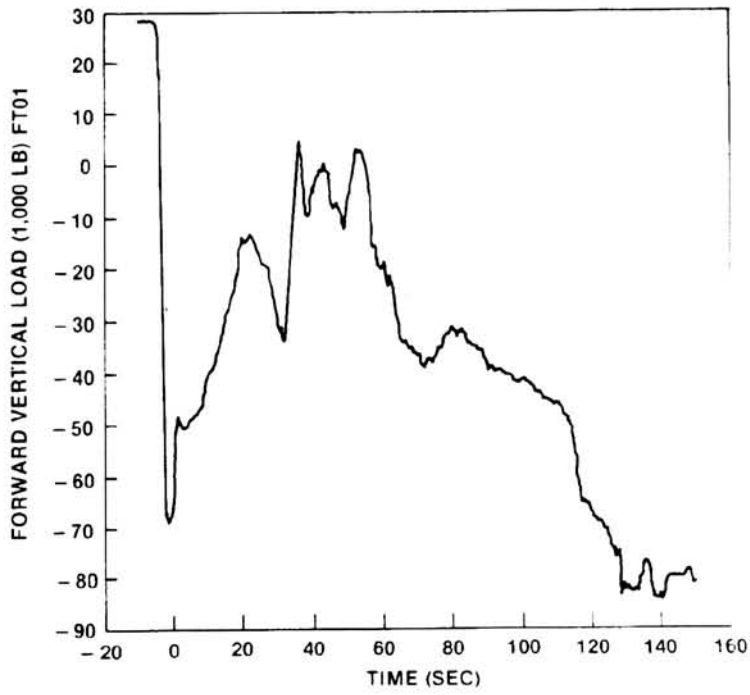

Figure 3.- STS-3 flight interface loads - forward vertical load.

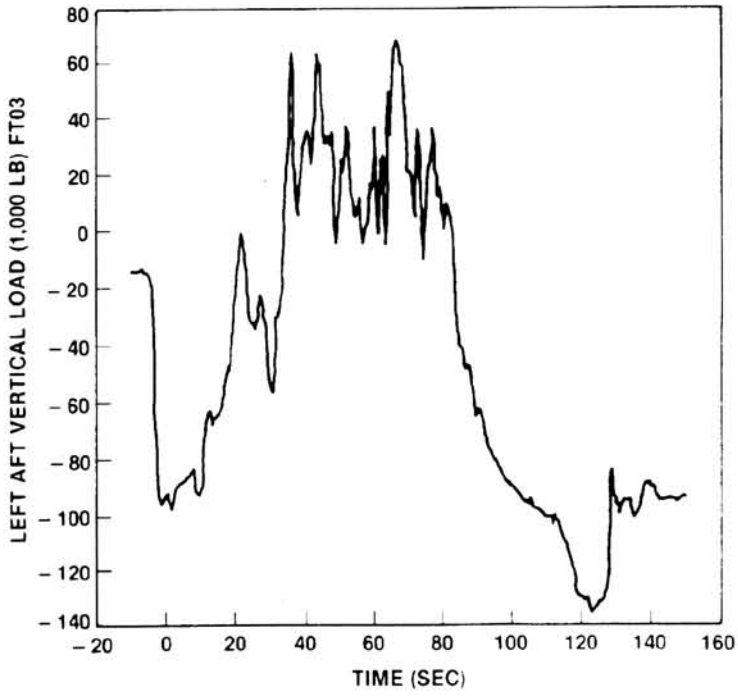

Figure 4.- STS-3 flight interface loads - left aft vertical load.

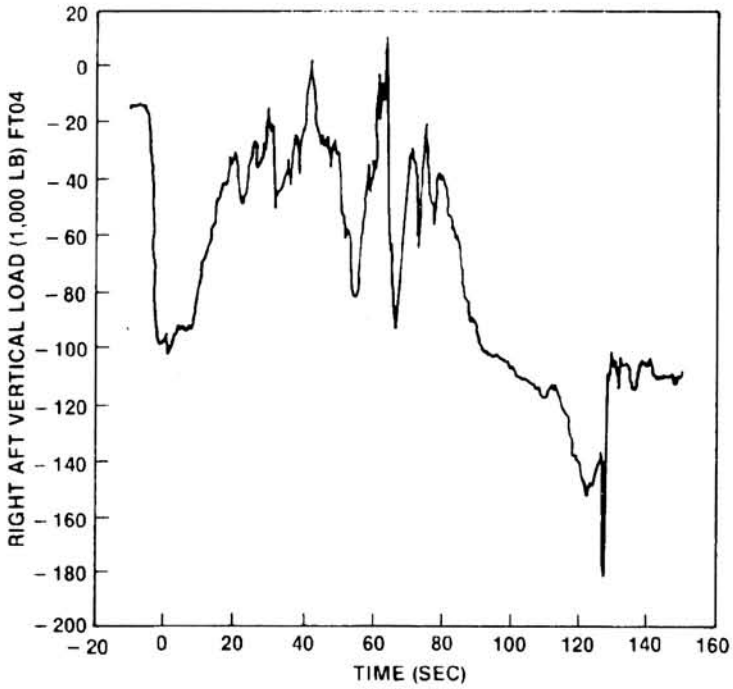

Figure 5.- STS-3 flight interface loads - right aft vertical load.

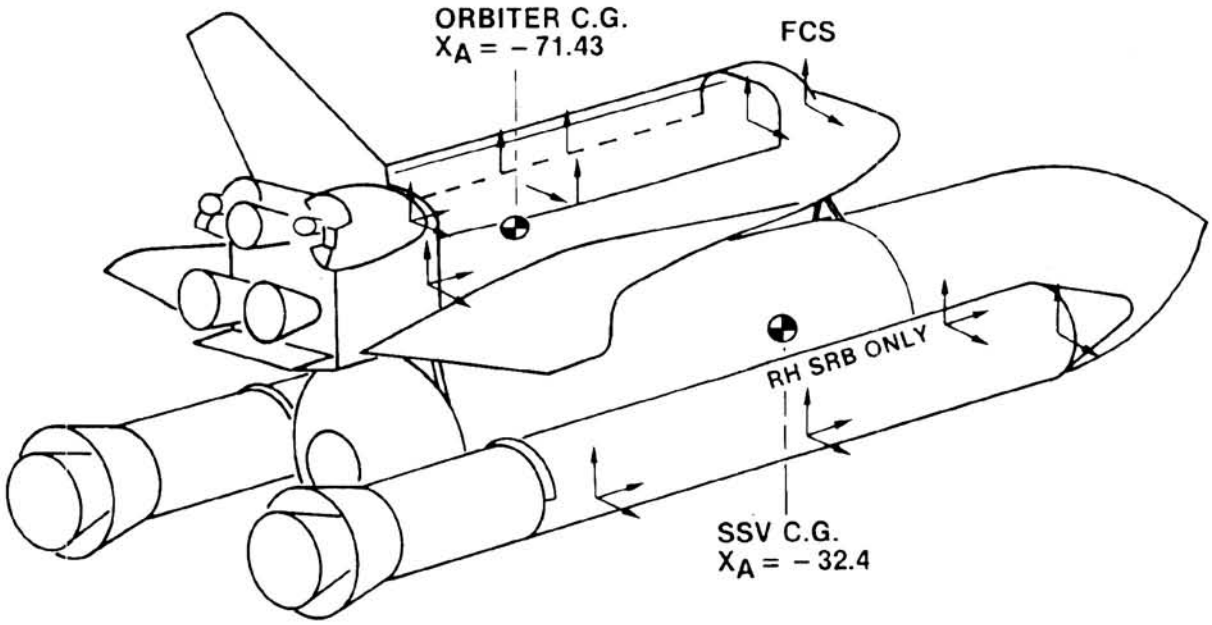

Figure 6.- Linear accelerometers.

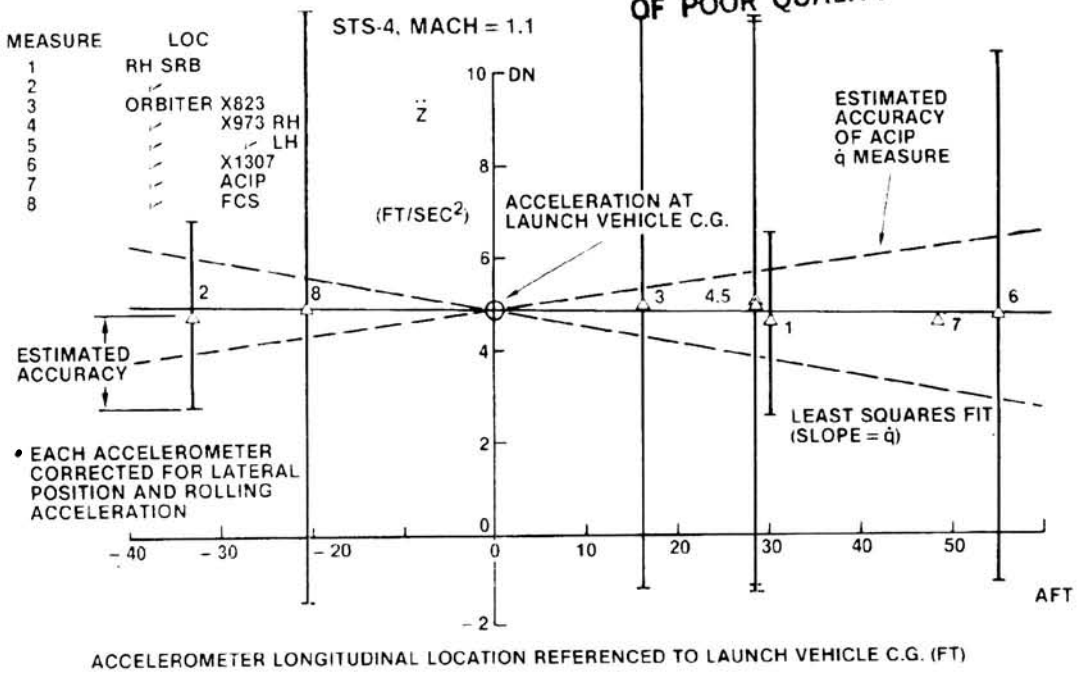

Figure 7.- Comparison of accelerometer measurements with multiple accelerometer analysis result.

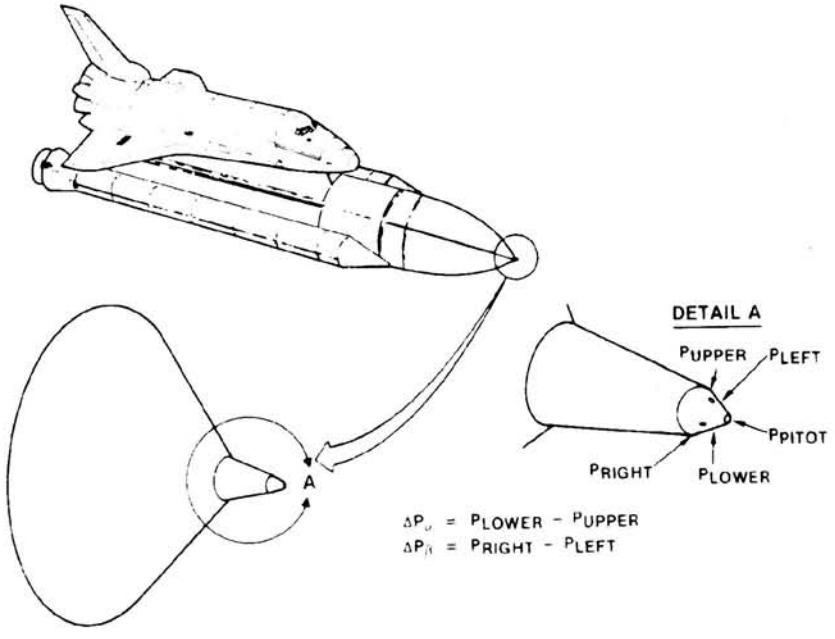

Figure 8.- Ascent air data system.

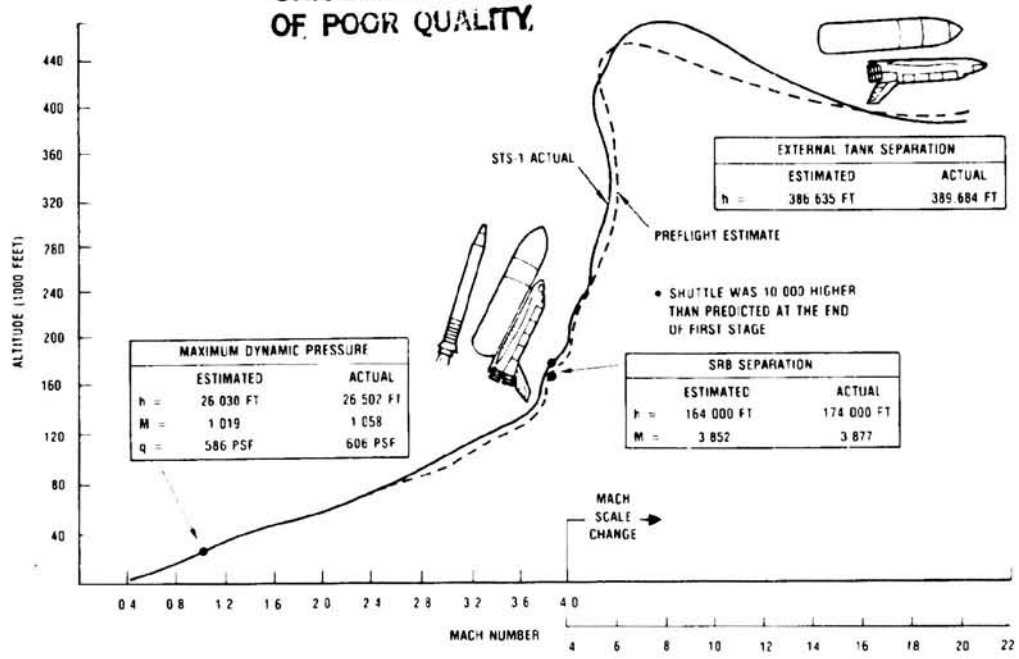

Figure 9.- STS-1 trajectory loft anomaly.

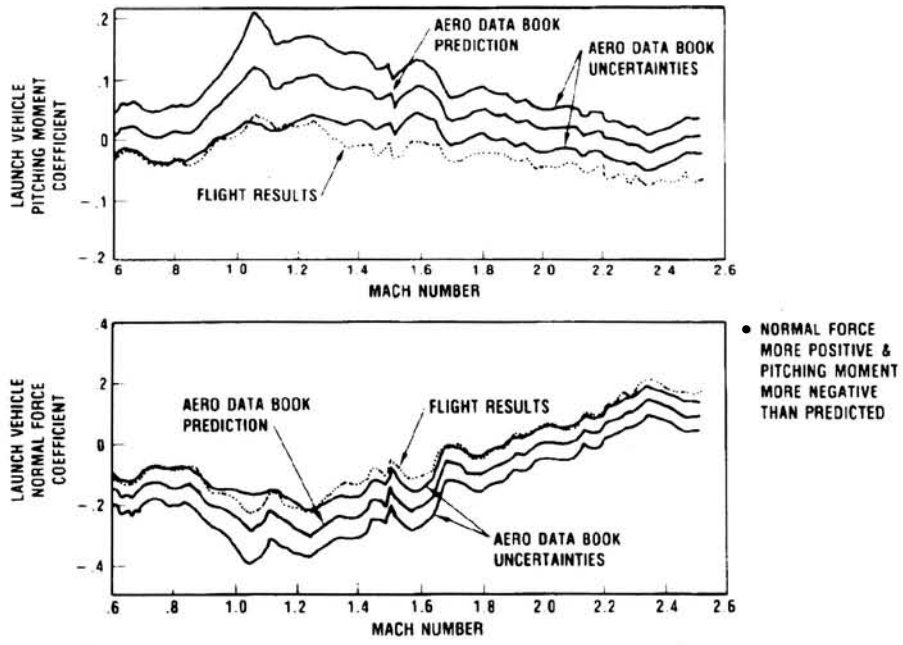

Figure 10.- STS-1 measured longitudinal aerodynamics.

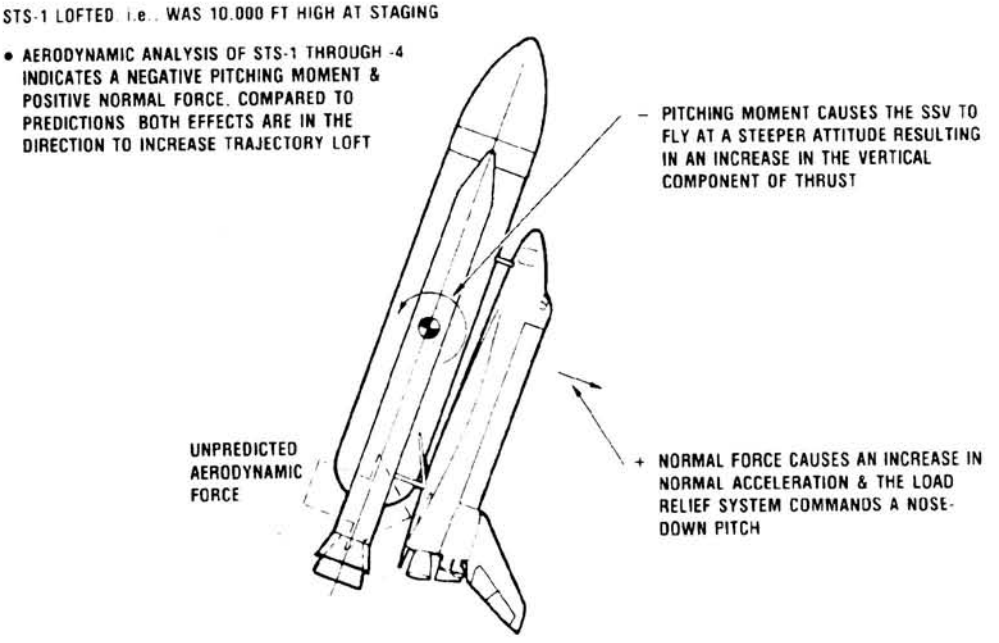

Figure 11.- Ascent aerodynamic loft anomaly effect of pitching moment and normal force on trajectory loft.

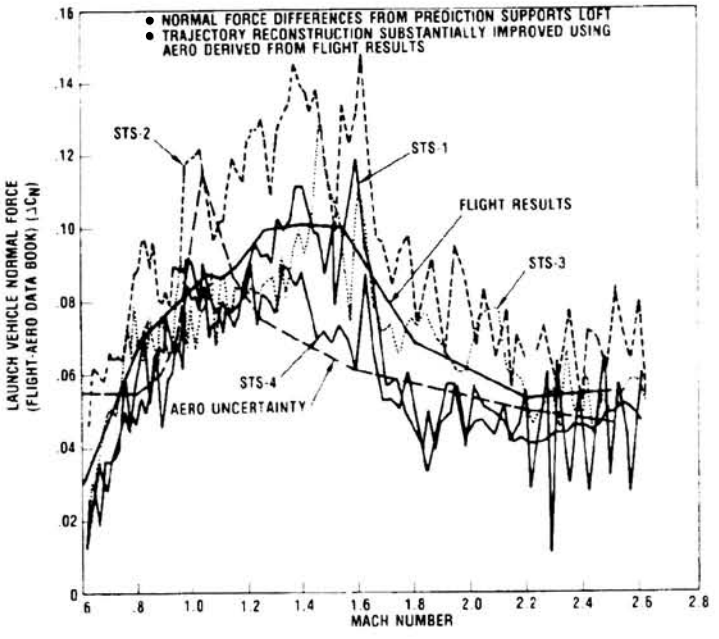

Figure 12.- Launch vehicle normal force.

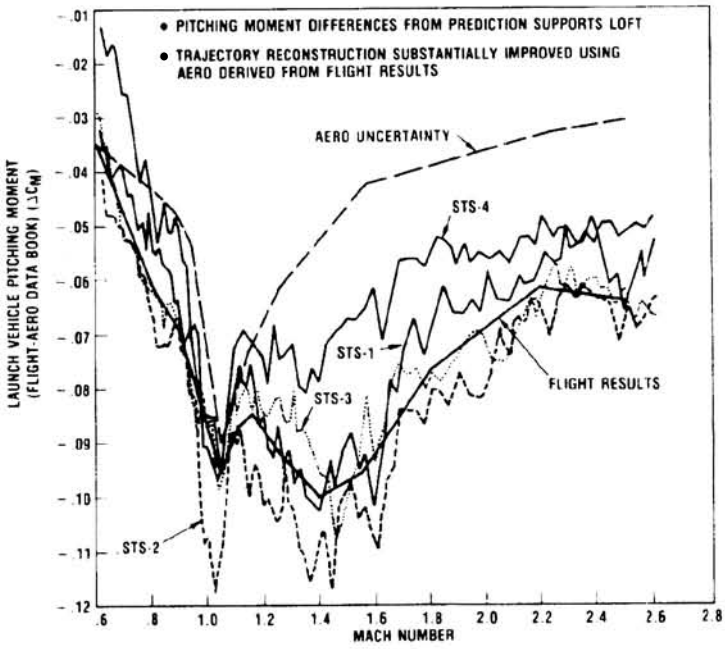

Figure 13.- Launch vehicle pitching moment.

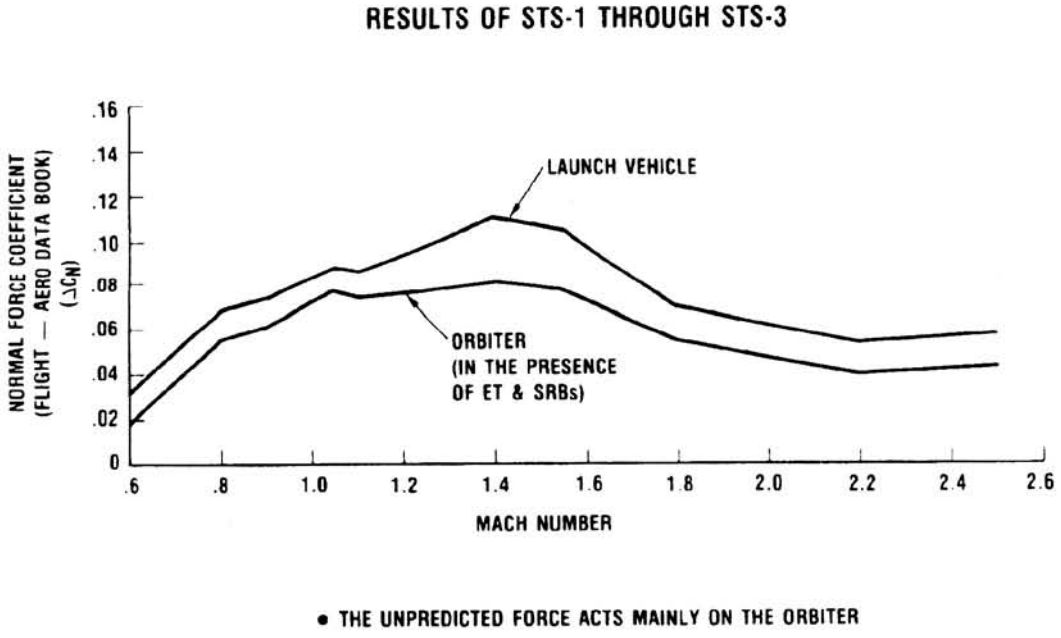

Figure 14.- Comparison of launch vehicle and orbiter differences from predictions - normal force.

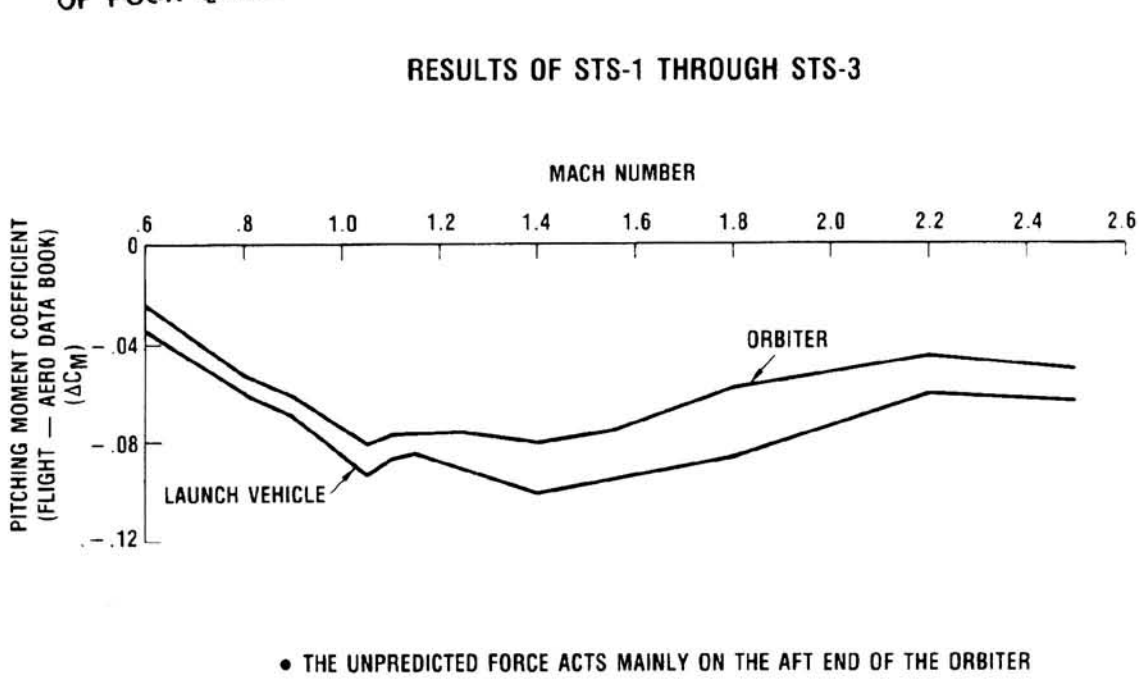

Figure 15.- Comparison of launch vehicle and orbiter differences from predictions - pitching moment.

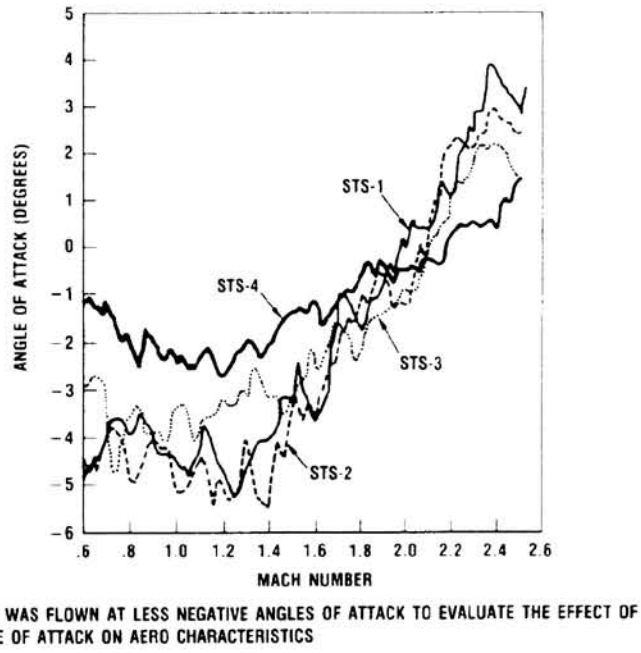

Figure 16.- Comparison of STS-1 through -4 angle of attack.

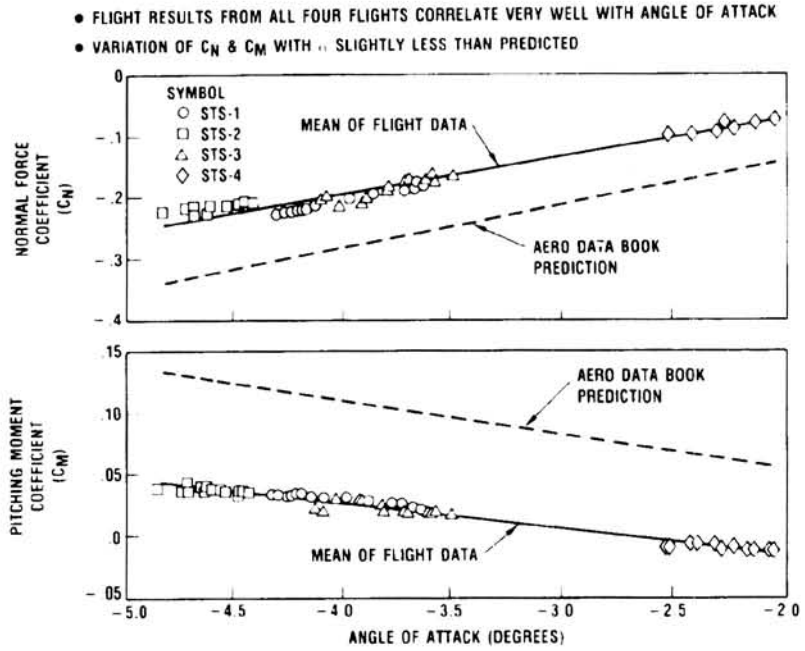

Figure 17.- Effect of angle of attack on launch vehicle aerodynamic characteristics (Mach 1.1, typical).

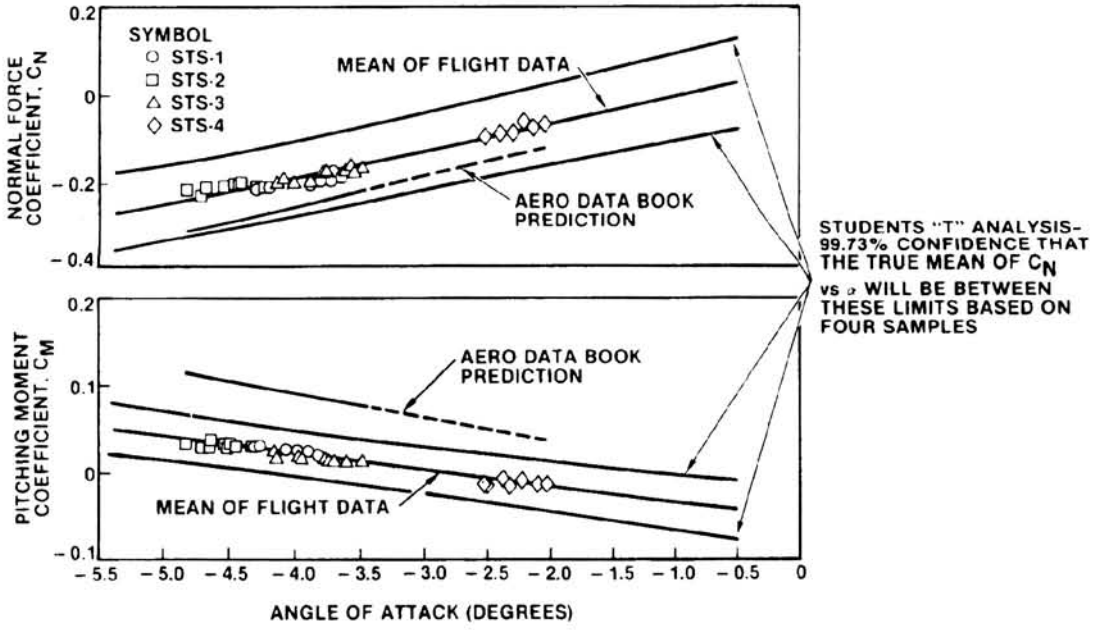

Figure 18.- Uncertainties in normal force and pitching moment measured in flight (Mach = 1.1, typical).

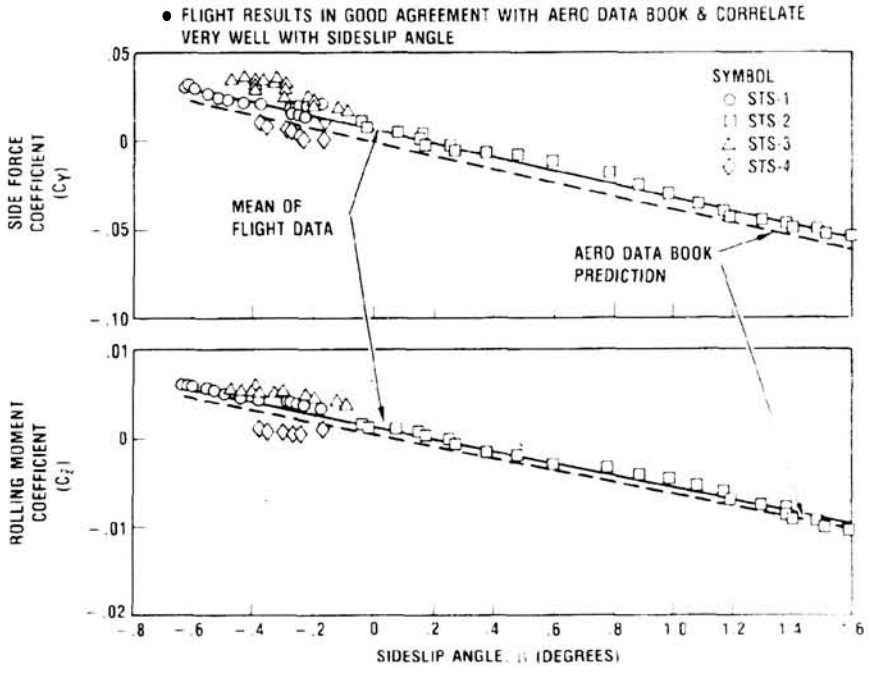

Figure 19.- Launch vehicle lateral directional flight results - side force and rolling moment (Mach = 1.1, typical).

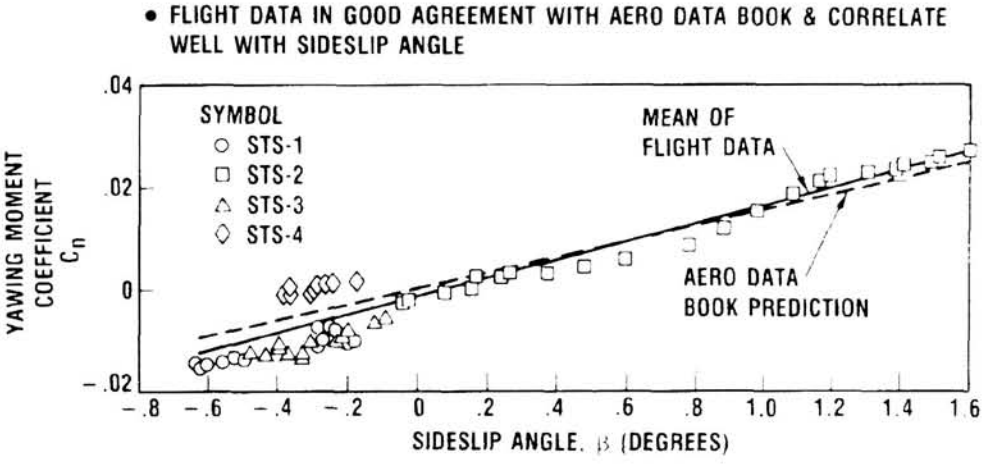

Figure 20.- Launch vehicle lateral directional flight results - yawing moment (Mach = 1.1, typical).

AERODYNAMIC ANALYSIS OF THE LOFT ANOMALY OBSERVED ON ORBITAL FLIGHT TESTS OF THE SPACE SHUTTLE

T. E. Surber and J. S. Stone
Space Transportation & Systems Group
Rockwell International
Downey, California

SUMMARY

This paper describes the loft anomaly observed during the launch phase of the orbital flight tests (OFT) of the Space Shuttle and presents evidence that the loft anomaly resulted from previously unobserved aerodynamic phenomena. The anomaly was that the altitude at staging was higher than anticipated. The anticipated altitude profile was predicated on wind tunnel test results that did not accurately simulate the flow between the orbiter vehicle and external tank and did not adequately simulate the engine plumes and thus the base pressures. An analogy is used to relate the flow between the orbiter and external tank to the flow in a two-dimensional channel. Plume simulation is identified as a major goal during wind tunnel testing, and a wind tunnel test that was conducted to provide the best possible representation of the plume effect on the channel flow field is described.

INTRODUCTION

The initial launch of the Space Shuttle resulted in a trajectory wherein the launch vehicle attained a higher altitude at solid rocket booster (SRB) separation than had been predicted. This altitude discrepancy (or loft) was attributed, in part, to apparent inaccuracies in the wind tunnel based predicted aerodynamic characteristics. An effort to define the cause and isolate the contributing parameters was initiated immediately.

On-board flight instrumentation data were reduced to provide comparison data with the pre-flight estimates. One of the first actions taken was trajectory reconstruction utilizing the variation levels (allowance for possible differences between wind tunnel predictions and full-scale flight parameters) for aerodynamic pitching moment uncertainty. The reconstruction, using the maximum negative pitching moment uncertainty, yielded an SRB separation altitude of 171,907 feet as compared to the measured value of 173,957 feet. A second reconstruction, using one degree of Space Shuttle main engine (SSME) thrust misalignment in addition to the pitching moment due to aerodynamic uncertainties, produced a separation altitude of 173,293 feet, which was within 664 feet of the measured value. It was concluded that the aerodynamic characteristics played a significant role in the discrepancies between the actual flight and estimated trajectories. Subsequent investigations of the measured aerodynamic coefficients for the launch vehicle and the orbiter in the presence of the external tank and SRB's revealed a favorable comparison between flight and predicted values of the lateral-directional coefficients whereas the comparison of the measured longitudinal coefficients did not compare very well with the estimates.

The next step in the investigation was to examine the flight data in detail. The analysis of the extracted aerodynamic data indicated that normal force and pitching moment were the primary contributors to the loft anomaly. The analysis also showed that incremental loads acting on the aft portion of the vehicle contributed to the loft and that these loads originated primarily on the orbiter vehicle. Flight data also indicated that launch vehicle base pressures and wing loads were considerably higher than had been estimated. These same observations were repeated for all subsequent OFT flights.

Since the loft anomaly was repeated on all flights and the extracted aerodynamics were reasonable and repeatable, it remained to develop a flow model to account for the observed aerodynamic effects. The first item investigated was the flow between the orbiter lower surface and the external tank and solid rocket booster upper surfaces. Results of this investigation showed that the "channel" flow could account for approximately 50 percent of the normal force and 40 percent of the pitching moment increment between pre-flight predictions and flight measurements. A math model of the channel flow between the orbiter and external tank and the unanticipated strong influence of the jet plumes on the forebody forces and moments will be described and the influence of each of these aerodynamic effects on the loft anomaly will be discussed. This paper also discusses plans for early wind tunnel testing of a jet plume model with increased plume simulation capability.

SPACE SHUTTLE VEHICLE

Configuration

The Space Shuttle launch configuration is shown in figure 1. The launch configuration is composed of the orbiter vehicle mounted on top of a nonrecoverable liquid oxygen-hydrogen external tank (ET) to which are also attached two solid rocket boosters (SRB), which are recoverable for refurbishing and reuse. Propulsion for the Shuttle is provided by three liquid propellant engines positioned on the orbiter base and two solid propellant rocket boosters mounted on either side of the external tank.

Flight Environment

The launch phase of a Space Shuttle mission exposes the vehicle to subsonic, transonic, and hypersonic flow regimes. A trajectory profile for the first mission is presented in figure 2, which shows the flight altitude varying from near sea level to approximately 400,000 feet at orbital insertion. Vehicle configuration changes during launch result from SRB separation during the transition from first to second stage and external tank separation prior to on-orbit operation. Vehicle aerodynamic forces and moments are the result of vehicle motion plus the effect of engine plumes on the vehicle forebody and base.

Observed Anomaly

During the first two Space Shuttle missions, the launch vehicle was observed to fly a trajectory that was higher than predicted. The difference between the flight and predicted altitudes for the first Shuttle flight is shown in figure 2. Flights 3 and 4 of the flight test program included an update to the flight control variables to account for these differences. This eliminated the loft phenomenon. The cause of the trajectory anomaly remains, however, and is the subject of this analysis.

PREDICTED DATA AND FLIGHT DATA

Flight Data Base

The predicted flight data base was derived exclusively using wind tunnel test data. Standard force and moment aerodynamic characteristics were obtained for the complete launch vehicle as well as for each component of the vehicle (ref. 1). Airload distributions were established from pressure data obtained on highly pressure-instrumented airloads models (ref. 2). The wind tunnel derived airloads data were modified so that integration of these data would yield the predicted force and moment data. Wing loads and elevon hinge moments were obtained from strain gauge wind tunnel model instrumentation. The effects of SRB and SSME engine plumes were obtained through cold plume wind tunnel testing using a pressure-instrumented launch vehicle test model.

Flight Measurements

Flight aerodynamic data were derived from acceleration data taken for the launch vehicle and strain gauge data obtained from the orbiter-ET attach hardware. The launch vehicle aerodynamics were thus divided between the orbiter and lower stack (ET plus two SRB's). Wing loads and elevon hinge moments were derived from strain gauge measurements. Flight base pressures were obtained from transducer pressure measurements taken on the base of the vehicle components.

Analysis

Longitudinal aerodynamic flight data did not agree with the predicted data of the Aerodynamic Design Data Book (ref. 1). The orbiter vehicle normal force and pitching moment terms extracted from flight measurements are presented in figure 3. The normal force was more positive than predicted while the pitching moment was more negative than predicted. The differences between flight and predicted normal force and pitching moment for the launch vehicle were caused, almost completely, by differences in orbiter loads. The distribution of flight-minus-predicted normal force and pitching moment increments between the orbiter vehicle and the complete launch vehicle is presented in figure 4.

The longitudinal load increments that were measured on the orbiter were substantiated using wing shear and elevon hinge moment flight data. The wing shear was more positive than predicted. The inboard elevon hinge moments generally indicated a positive load was acting on the elevon. Figure 5 presents the wing panel load terms.

Flight base pressures from each component of the launch vehicle were found to be higher than the predicted value obtained from wind tunnel test data. The difference between flight and predicted base pressures is shown in figure 6 in terms of the launch vehicle base axial force.

The differences between flight and predicted pitching moment and normal force had a direct influence on the vehicle lofting. A negative aerodynamic pitching moment increment caused the engines to gimbal for trim resulting in a negative normal force component of thrust. Since the vehicle is inverted (tail down) during launch, the resultant thrust-induced normal force in the vertical direction forced the vehicle to higher altitudes. The positive aerodynamic normal force increment also caused vehicle accelerations that the flight control system attempted to eliminate by further engine gimballing to create an additional thrust-induced negative normal force. Hence, the vehicle response to an aerodynamic-induced negative pitching moment and positive normal force was to force the vehicle higher. In addition, base axial force, being less than predicted, also contributed to the lofting by an increase in vehicle performance.

The flight data anomalies indicated that the flow between the orbiter and the ET may not have been simulated properly during the wind tunnel tests. Since the center of pressure of the flight-minus-predicted longitudinal load increments was determined to be on the aft portion of the launch vehicle, the effect of the plume-induced ET base pressures was concluded to have a strong influence on the flow in the channel area. Higher than predicted ET base pressures could feed forward between the orbiter and ET and induce the more positive normal force and more negative pitching moment. The development of an analytical model was initiated to further understand this phenomenon. Assessment of the accuracy of the flight-extracted longitudinal data, however, remained.

Flight Data Credibility

Various flight-derived sources of error were investigated to determine the magnitude of each term, as well as a total error sum, to be compared with the flight-minus-predicted increments. Figure 7 shows a bar graph for each pertinent source of normal force and pitching moment measurement error plus a root sum square (RSS) value representing a total error. It was concluded that the measured data were larger than the various sources of error. The aerodynamic measurements were also found to correlate well with angle of attack and, when combined with all other sources of error that affect vehicle performance, provided good trajectory reconstruction. It was concluded that the flight measurements were reasonable and repeatable.

RESULTS AND DISCUSSION

Flow Field Modeling

A simplified description of the flow field was developed from known fluid flow characteristics for simple geometries. A theoretical model was then defined to provide an analytical basis for the flow description.

The flow between the orbiter and ET was considered similar to that found in a channel with a downstream constriction. As the flow accelerated through the orbiter-ET "channel," at sufficiently high flight Mach numbers, choking occurred in the vicinity of the orbiter-ET aft attach hardware. A normal shock formed in front of the attach hardware resulting in a supersonic/subsonic flow discontinuity at the shock location. A sketch of this flow field is presented in figure 8 with photographs of the aft attach hardware to illustrate the constriction problem.

The three-dimensional nature of the flow in the channel suggested that a better analogy would be that of the flow entering an engine inlet. To control the amount of injested mass, a throat could be located downstream of the inlet opening. Figure 9 shows the general configuration where the nozzle throat is representative of the openings in the orbiter-ET attach hardware shown in figure 8. The choking would probably occur at subsonic channel Mach numbers as shown in figure 9. This flow phenomenon would thus be present throughout a major portion of the launch profile.

It remained to develop an analytical model to describe the relationship between the measured base pressures, the flow properties between the orbiter and ET, and the vehicle longitudinal characteristics. Figure 10 shows a summary of the differences obtained between the flight and model test vehicles. The effects of vehicle boundary layer were considered before the model was developed.

Boundary Layer Simulation

The boundary layer thickness on each body was an additional contributing factor in the position of the shock between the orbiter and the ET. The boundary layers become thicker as they progress along each body until separation pressure gradients are encountered. These separation gradients are created by the structural cross beam on the orbiter and the presence of the attach structure on the ET. In addition, the resultant shock structure could induce a surface flow separation, so the position of this shock becomes important. The general flow situation is illustrated in figure 11.

It became apparent that boundary layer simulation on the wind tunnel models could affect the position of the channel shock. The thick boundary layer on the wind tunnel model would produce a cross-sectional area in the channel that was smaller than that on the flight vehicle. Hence, the shock would be farther forward on the model than on the flight vehicle. This in effect created a channel pressure distribution discrepancy between the flight vehicle and the model tested, and the separated flow aft of the shock created a means by which ET base pressure effects could be transmitted into the channel.

The resultant shock-induced flow separation would allow ET base pressures to influence the channel pressures; however, the effects of vehicle boundary layer are considered secondary to the influence of plume simulation and model geometry and were not, therefore, included in the development of the analytical model.

Channel Flow Analysis

A typical plot of the pressure distribution (C_p) along the external tank centerline at M = 1.10 is shown in figure 12. Several observations concerning the flow between the ET and orbiter can be made. Starting at the ET nose, the decrease in C_p implies a continuing acceleration until the flow encounters the strong nose shock from the orbiter at X/L = 0.23. The flow then decelerates (C_p increases) until the pressure field of the forward attach bipod is encountered. The flow accelerates around the bipod and then decelerates aft of the bipod. In the "channel" from X/L = 0.56 to X/L = 0.80, the flow decelerates because of the blockage from the aft attach cross beam hardware. This second supersonic region is terminated by another strong shock that brings the pressure back to the base pressure level. The static pressure plot also shows that essentially the same flow characteristics are observed on the orbiter bottom centerline. As mentioned earlier, the flow between the top of the ET and the bottom of the orbiter is somewhat analogous to flow through a nozzle.

In flight, the pressurization of the base due to the engine plumes is postulated to force the second shock to jump forward and merge with the first shock in front of the attach hardware. The resulting flow separation causes a completely subsonic flow behavior down the channel to the exit. The shock jump generates a pressure increase resulting in a positive normal force discontinuity (ΔC_N) and a corresponding stabilizing pitching moment discontinuity ($-\Delta C_m$) because the positive pressure jump occurs aft of the moment reference point. The next step in the analysis was to derive some fundamental relationships relating the "inlet" and "exit" conditions of the channel. These relationships permitted the calculation of properties within the channel, which led to a quantitative evaluation of the forces causing the loft.

Assume that the channel is defined as shown at the top of figure 12 and that the channel flow has the characteristics represented by the lower portion of figure 12. Assume also that the "inlet" is represented by the constriction produced by the aft attach hardware and the inlet "cowl" is represented by the channel between the forward attach point and the aft attach point. Assume that the inlet shock is pushed upstream by a pressure pulse from the engine plumes until the inlet blocks. Some of the mass will accumulate upstream of the point of blockage. The pressure in that region will rise, resulting in a forward motion of the shock. This motion is unstable and the flow begins to spill out of the "channel" laterally. After the entering flow has been blocked (by the forward motion of the shock), the momentum of the air column in the "channel" sustains its downstream motion for a time and results in a low pressure region at the "exit" (aft attach hardware). At the same time, the mass flow entering the "channel" begins to decrease as soon as the "inlet" blocks. The pressure downstream of the blockage point, therefore, begins to drop as soon as the inlet blocks.

The next significant event is a large drop in inlet pressure caused by restarting of supercritical flow. Since the "channel" pressure is low, the inlet flow quickly becomes supersonic. As mass accumulates in the "channel," the pressure rises and the shock wave moves upstream. The jump in "channel" pressure corresponds to the first impulsive entrance of mass into the "inlet" and the "inlet" pressure drops when supercritical flow is established. The entire process is seen to be time-dependent. The "channel" essentially "fills" and "spills" as the shock blocks the inlet and the inlet subsequently restarts. After the inlet becomes supercritical, an approximate calculation of fill-up time can be made based on "engine" volume and known rates of mass flow into the inlet and out of the exit.

The mass flow, $\dot{m}$, through the sonic area, S*, can be expressed in terms of the stagnation pressure and temperature

$$\dot{m} = \left[\left(\frac{\gamma + 1}{2}\right)^{\frac{-(\gamma+1)}{2(\gamma-1)}} \sqrt{\frac{\gamma}{R}}\right] S^* \frac{P_s}{\sqrt{T_s}} \tag{1}$$

The time rate of mass accumulation within the "engine" is the difference between the inlet and exit flow rates

$$\frac{d\dot{m}}{dt} = \left(\frac{\gamma + 1}{2}\right)^{\frac{-(\gamma+1)}{2(\gamma-1)}} \sqrt{\frac{\gamma}{R}} \frac{1}{\sqrt{T_{s_\infty}}} \left(S^*_\infty P_{s_\infty} - S^*_2 P_{s_2}\right) = V\left(\frac{dP_{s_2}}{dt}\right) \tag{2}$$

where V is the total volume of the "engine."
The density change can be eliminated by using the thermal equation of state

$$\frac{d\rho_{s_2}}{dt} = \frac{1}{RT_{s_\infty}} \frac{dP_{s_2}}{dt} \tag{3}$$

Substitute equation (3) into equation (2):

$$\frac{dP_{s_2}}{dt} = \left(\frac{\gamma + 1}{2}\right)^{\frac{-(\gamma+1)}{2(\gamma-1)}} \frac{\sqrt{\gamma RT_{s_\infty}}}{V} \left[S^*_\infty P_{s_\infty} - S^*_2 P_{s_2}\right] \tag{4}$$

The effective length, ℓ, for the "engine" is defined by

$$\ell \equiv \frac{V}{S_2}$$

Equation (4) becomes

$$\frac{d(P_{s_2}/P_{s_\infty})}{dt} = \left(\frac{\gamma + 1}{2}\right)^{\frac{-(\gamma + 1)}{2(\gamma - 1)}} \frac{a_{s_\infty}}{\ell} \left[\left(\frac{S^*}{S}\right)_\infty \frac{S_\infty}{S_2} - \left(\frac{S^*}{S}\right)_e \frac{S_e}{S_2} \frac{P_{s_2}}{P_{s_\infty}}\right] \tag{5}$$

where the subscript, e, refers to the "engine" exit conditions.
Equation (5) is a first-order differential equation whose solution is of the form:

$$y = \frac{Q}{P} + ce^{-bPt} \tag{6}$$

where

$$Q = \left(\frac{S^*}{S}\right)_\infty \frac{S_\infty}{S_2}$$

$$P = \left(\frac{S^*}{S}\right)_e \frac{S_e}{S_2}$$

$$b = \left(\frac{\gamma + 1}{2}\right)^{\frac{-(\gamma + 1)}{2(\gamma - 1)}} \frac{a_{s_\infty}}{\ell}$$

thus

$$y = \frac{P_{s_2}}{P_{s_\infty}}$$

The stagnation pressure ratio across the channel is obtained from equation (5) and is presented in figure 13.

The "channel" pressure coefficient variation with time was calculated using the derived model for Mach 1.1 (STS-4 trajectory). These data are presented in figure 14. For comparison, the flight pressure coefficient, measured from pressure tap V07P9484A (lower fuselage, forward of attach hardware), has a value of 0.325. As shown in figure 14, the "channel" flow model predicts a maximum time dependent difference from flight of $\Delta C_p = 0.135$ (t = 0.1 sec.). However, the model channel pressure is in good agreement with the flight value for the steady state (t = 0 second) case (C_p FLIGHT=0.325, C_p MODEL= 0.301). The conclusion is that the "channel" pressure response time may be too short for the flight instrumentation to give a reliable measurement. Although the pressure transducer samples at a rate of ten cycles per second, it lacks the time response characteristics to measure the predicted transient pressure pulse.

The predicted vehicle pressures came from wind tunnel test IA105 (ref. 2). The IA105 pressure value corresponding to the flight point in question at Mach 1.1 is $C_p = 0.25$. If the transient pressure pulse does exist, then the incremental pressure (difference between the analytical model and IA105) will have a magnitude of $\Delta C_p = 0.21$ (0.46 - 0.25). This pressure, when integrated from $X_o = 1200$ to the body flap hinge line, yields a normal force of 52 percent of the flight-minus-predicted increment and 43 percent of the pitching moment coefficient. These results indicate that the "channel" flow increment may be a significant contributor to the loft anomaly.

Additional Wind Tunnel Testing

Power-on base pressures and forebody plume effects were generated using cold plume wind tunnel tests. Plume simulation parameters were used in an effort to have the cold plume model base pressures equal those to be encountered in flight. However, the component base pressures from the wind tunnel model were much lower than occurred in flight. An explanation for these lower pressures is that the simulation parameters that were used generated undersized plumes during the wind tunnel tests.

The large flight plumes tended to block freestream flow and/or recirculate SRB plume gases into the ET base region earlier in the trajectory than would have been predicted from the test data. This resulted in higher than predicted ET base pressures, which affected the flow in the orbiter-ET channel. Previous plumes tests used an air supply strut between the orbiter and ET to enclose pressure lines. This strut not only affected the flow field simulation in this area but also altered the plume effect pressure distribution on the bottom of the orbiter fuselage and wing lower surface. At the time, these models were primarily used to obtain base pressures. The air strut was considered to have a negligible effect on base pressures, with a secondary effect on forebody plume pressure increments. However, this strut would greatly influence the orbiter-ET channel pressures. An additional cold plumes wind tunnel test will be run to update the power-on base pressure data base and obtain channel pressures without the air supply strut.

Wind tunnel test IA300 was recently run to obtain forebody base plume effect pressure data. Plumes were scaled so that actual component flight base pressures could be obtained. SSME plume air for the 1 percent scale model was routed through the top of the orbiter with the orbiter-ET channel area clean (to resemble the launch configuration). Pressure distributions were obtained on the wing lower surface and fuselage as well as ET base and other launch vehicle components.

The results of test IA300 will be influenced by model scaling and the use of air plumes as the jet gas. However, the effects of the simulated base pressures in relation to the forebody loads should be adequate to verify the suggested model. The resultant load distributions will be used to develop the forebody pressures so that the integrated, predicted loads produce the flight longitudinal data.

CONCLUDING REMARKS

The loft anomaly has been attributed, in part, to underprediction of launch vehicle plume effects on longitudinal aerodynamics. Flight-extracted normal force and pitching moment data were checked and found to be reasonable and repeatable and, in addition, provided good trajectory reconstruction. The lack of flow simulation between the orbiter and ET, associated with higher than predicted ET base pressures, is considered to be the cause of the longitudinal aerodynamic discrepancies.

An analytical model has been developed to describe the flow in the channel between the orbiter and ET. The pressures in this area were found to be time dependent and influenced by ET base pressures. Calculations using the derived model, but without the time dependency, produce channel pressure levels that agree with flight measured pressures. The time dependence of the plume effect on ET base pressures is a possible cause of the pressure difference and was not measured during flight tests due to instrumentation limitations. The differences between the channel model and test results can account for 52 percent of the flight/predicted normal force increment and 43 percent of the pitching moment increment.

Verification of the predicted channel flow analytical model will be established using the results of an additional cold plume wind tunnel test. This test, designated IA300, uses a previously tested plumes model, but will test without the orbiter-ET blade strut used in other plumes tests. This feature, plus the duplication of flight base pressure using cold gas plumes, will provide the required representation of the plume effect on the channel flow field.

REFERENCES

1. SD 72-SH-0060-2L, "Aerodynamic Design Data Book, Volume 2, Launch Vehicle," Space Division, Rockwell International, Downey, California, 1981.

2. DMS DR 2398, "Results of Tests Using a 0.03-Scale Model (47-OTS) of the Space Shuttle Integrated Vehicle in The AEDC 16-Foot Transonic Propulsion Wind Tunnel (IA-105A)," Space Division, Chrysler Corporation, New Orleans, Louisiana, Nov. 1981.

SYMBOLS

a	speed of sound, feet per second
C_m	pitching moment coefficient, pitching moment/$qS_{ref}\ell_{ref}$
C_p	pressure coefficient, $\Delta P/q$
ℓ	effective length, feet
M	Mach number
$\dot{m}$	mass flow rate, slugs per second
P	pressure, pounds per square foot
q	dynamic pressure, pounds per square foot
R	universal gas constant, foot-pounds/slug deg Rankins
S	cross-section area of stream tube, square feet
T	temperature, deg Rankins
t	time, seconds
V	total internal volume of channel model, S_2
γ	specific heat ratio
ρ	density, slug/cubic foot

Subscripts:

∞	freestream conditions
1	entrance to diffuser
2	end of subsonic diffuser
e	channel model exit
ref	reference
s	local stagnation conditions

Superscript:

*	local sonic conditions

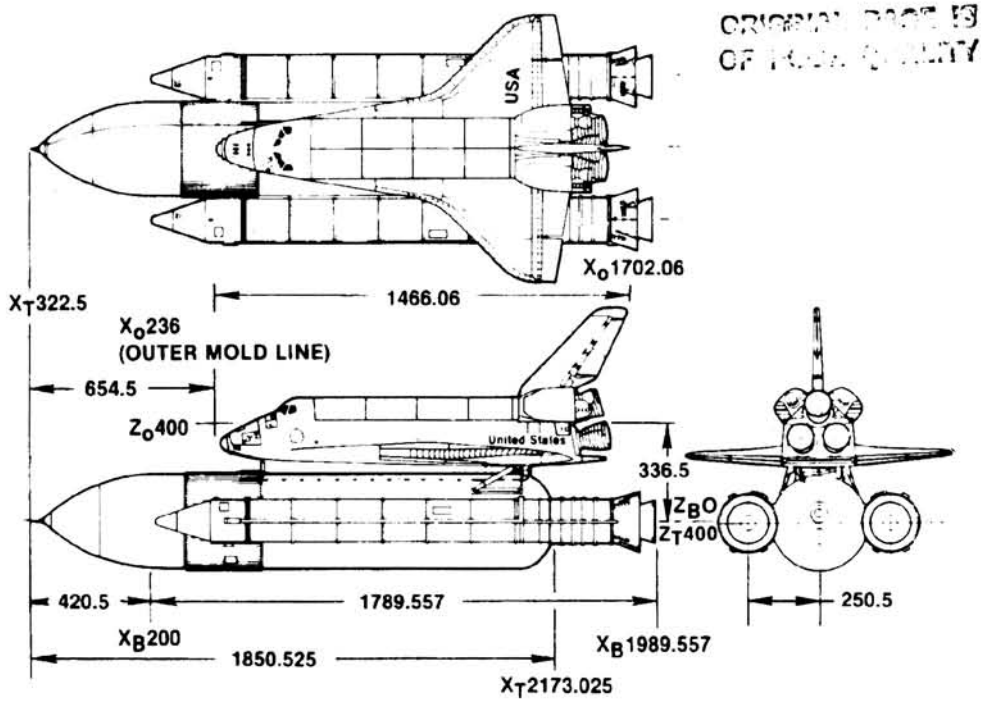

Figure 1.- Launch vehicle geometry.

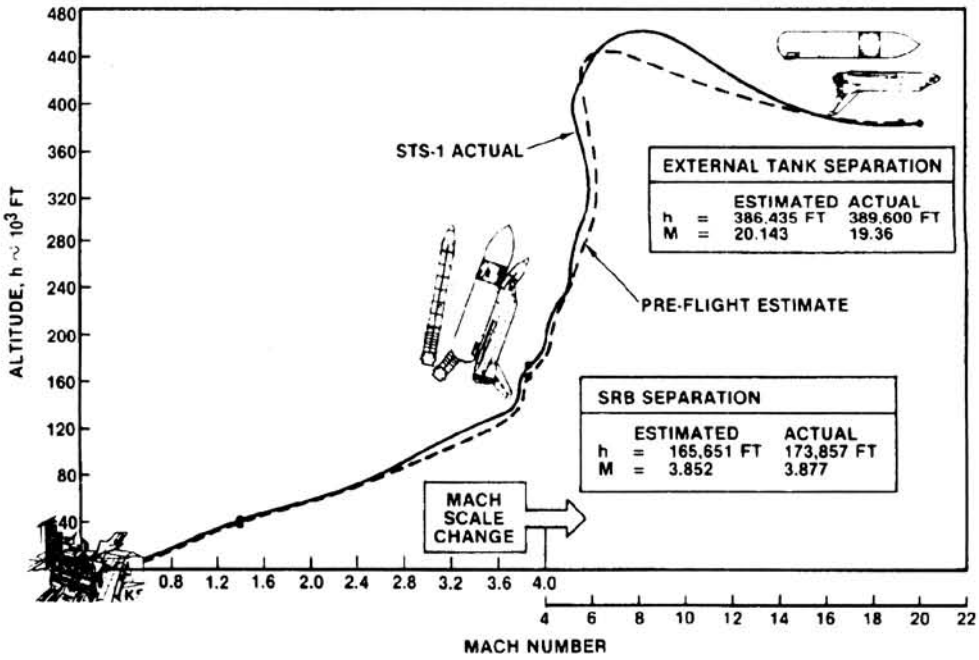

Figure 2.- STS-1 launch vehicle altitude-Mach profile.

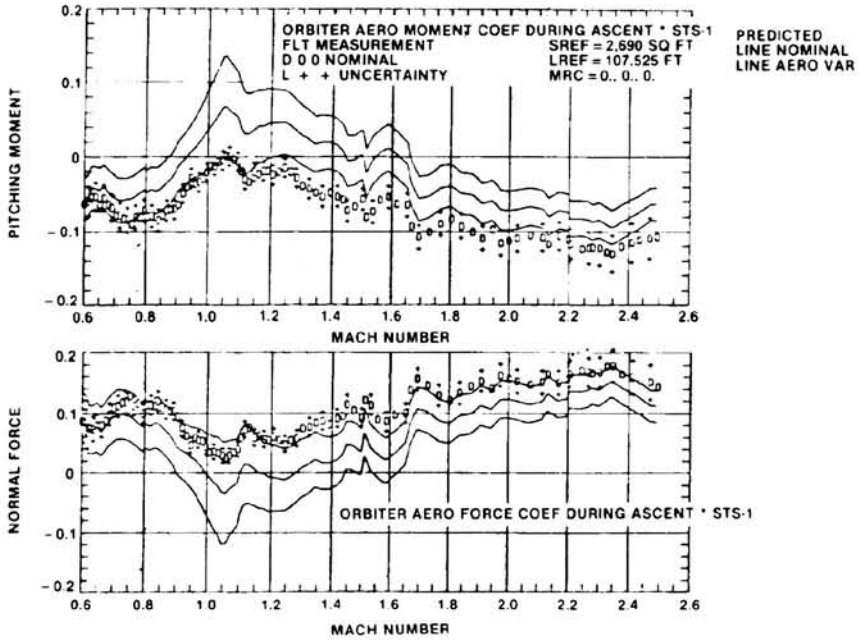

Figure 3.- Flight extracted aerodynamics.

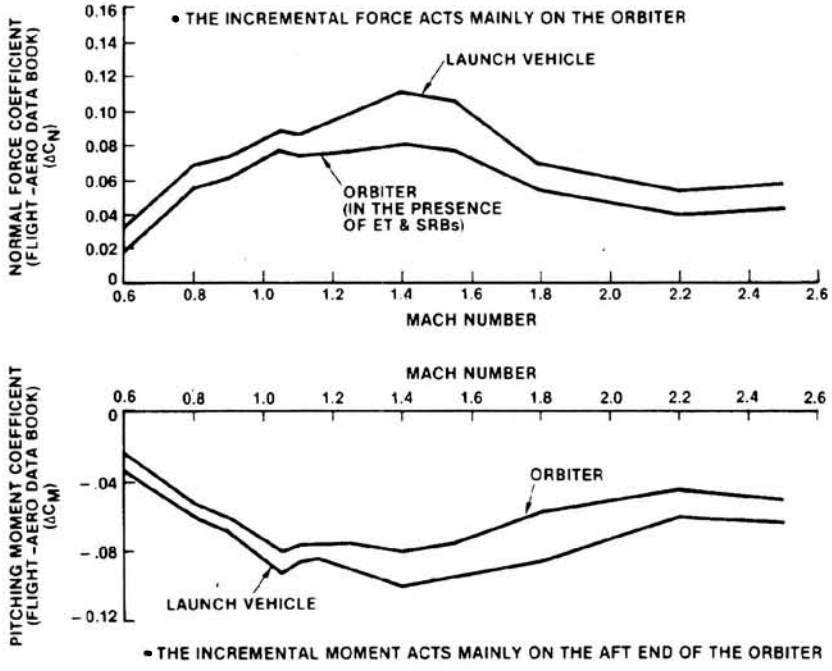

Figure 4.- Comparison of launch vehicle and orbiter differences from predictions.

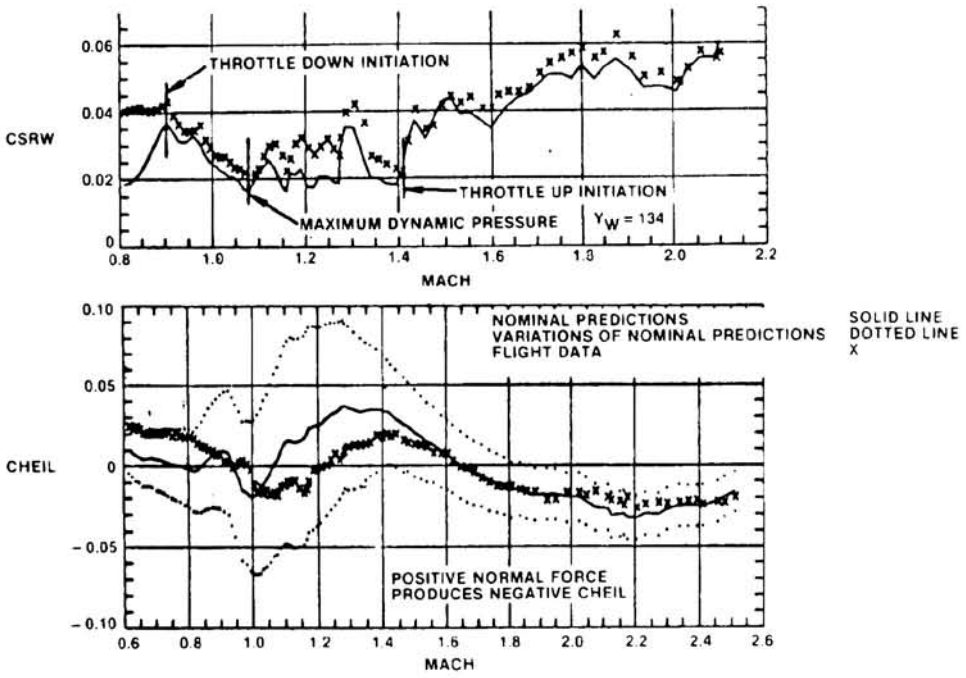

Figure 5.- Wing and elevon loads from STS-2.

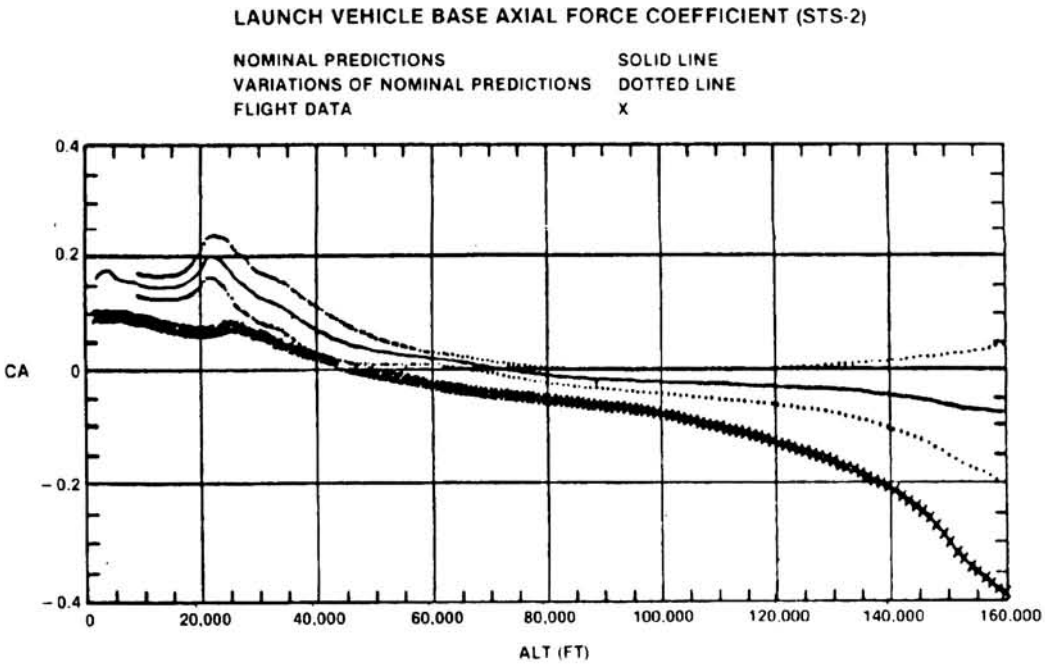

Figure 6.- Launch vehicle base axial force from STS-2.

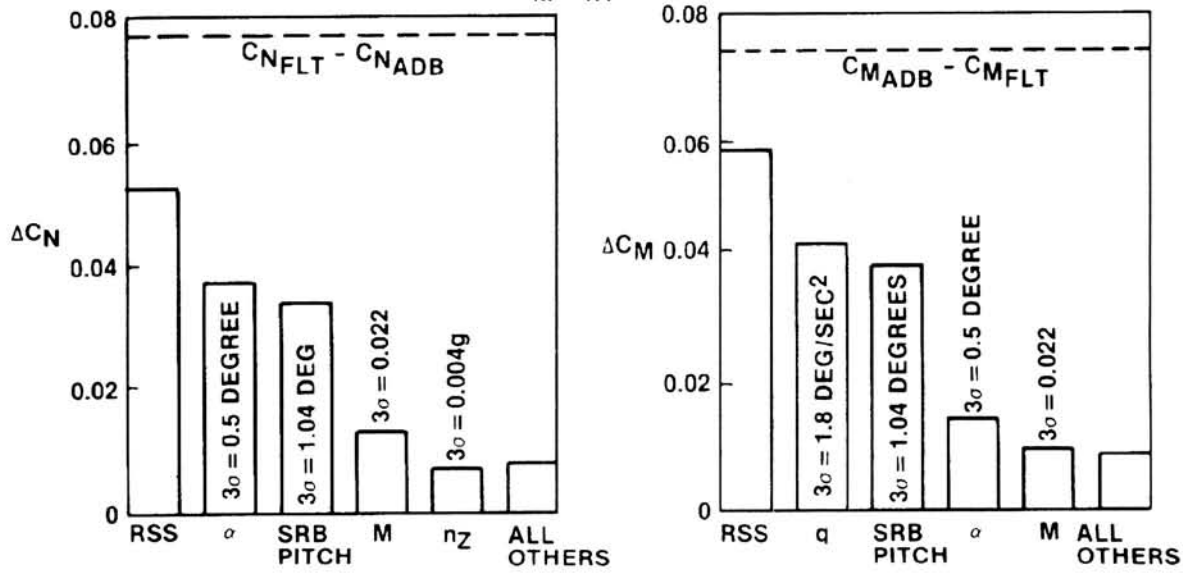

Figure 7.- Effect of potential instrument errors on extracted coefficients.

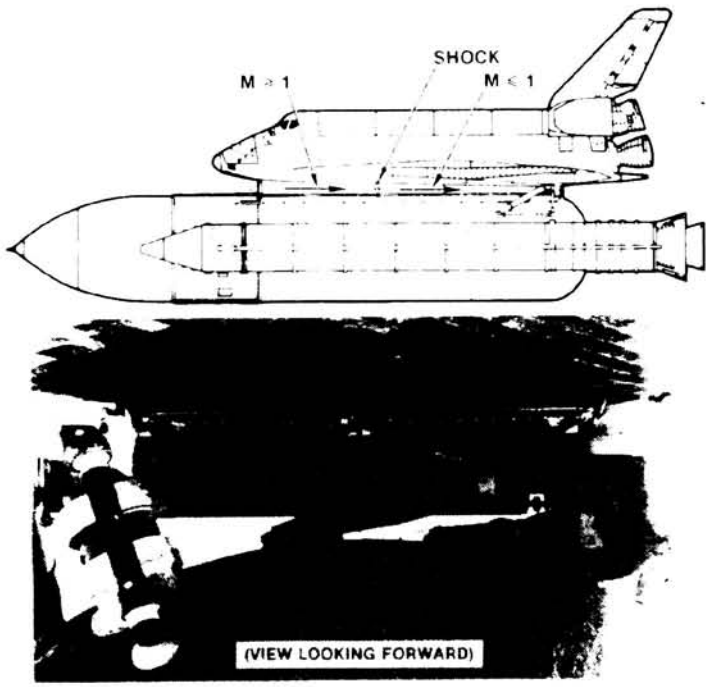

Figure 8.- Flow field model and orbiter-external tank aft attach hardware.

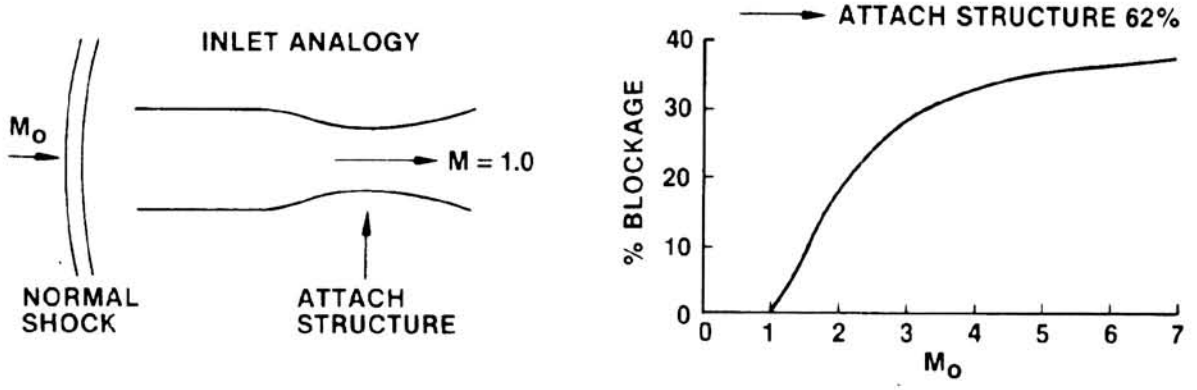

Figure 9.- Channel flow inlet analogy - theoretical model.

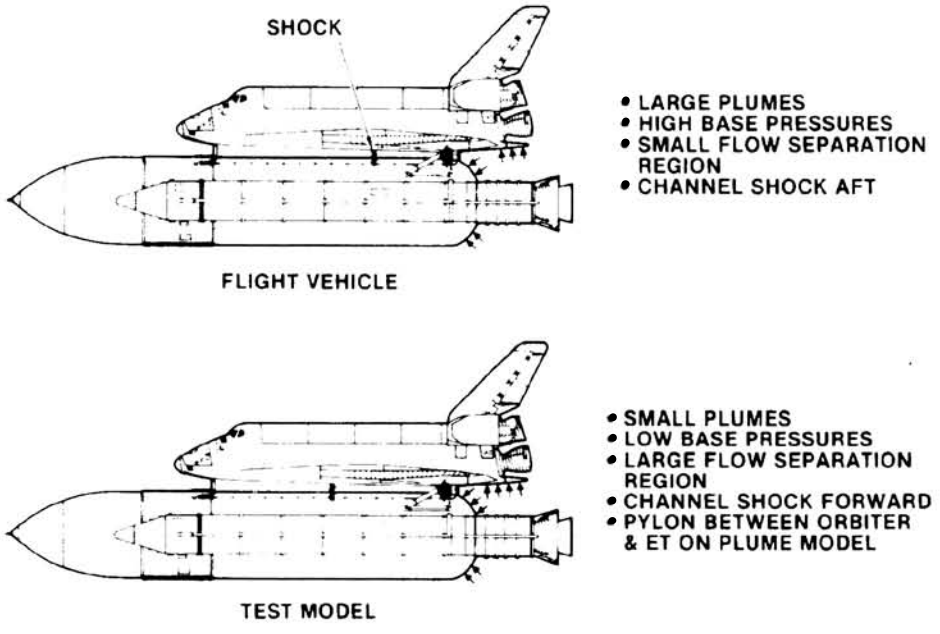

Figure 10.- Differences between full scale and model scale.

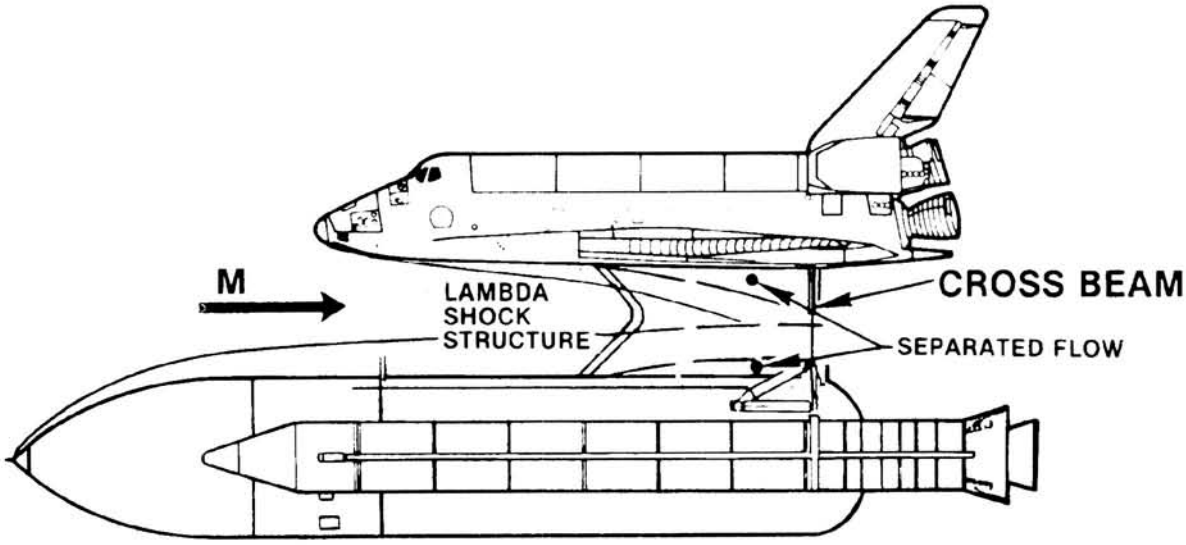

Figure 11.- Orbiter-external tank shock structure development.

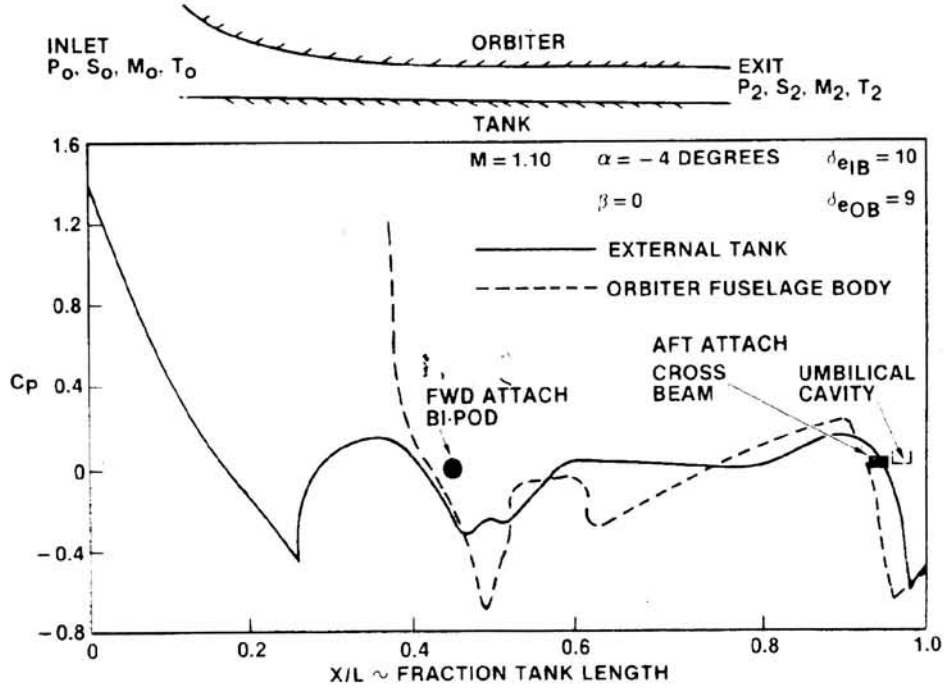

Figure 12.- Channel flow analogy and external tank and lower fuselage pressure.

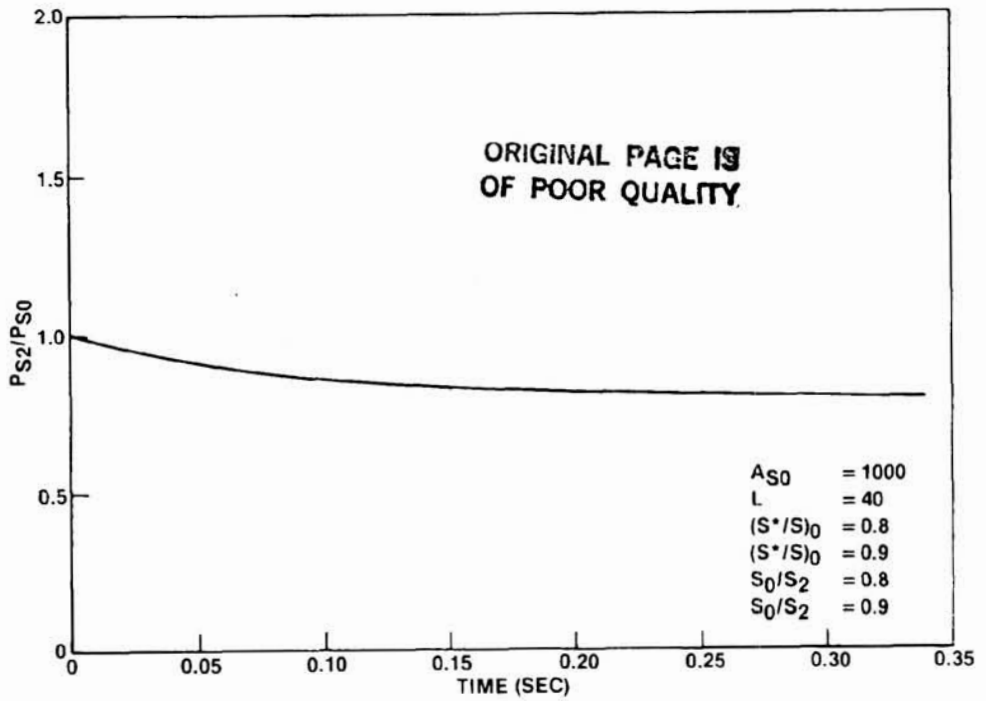

Figure 13.- Channel flow.

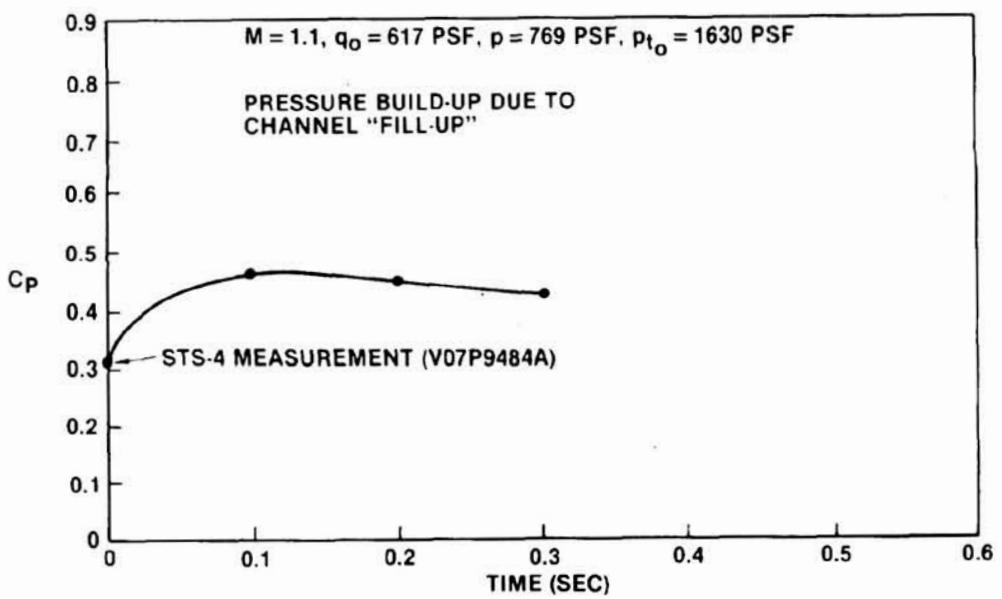

Figure 14.- Channel flow characteristics - variation of C_p with time.

TECHNIQUES FOR ASSESSMENT OF ASCENT AERODYNAMIC CHARACTERISTICS OF THE SPACE SHUTTLE LAUNCH SYSTEM

Kenneth S. Leahy
McDonnell Douglas Technical Services Co.
Houston, Texas

SUMMARY

In order to investigate the impact of ascent element aerodynamics on the flight constraints of the Space Shuttle, a system of programs was developed which allowed the assessment of wind-tunnel data, the extraction of aerodynamic coefficients, the identification of critical structural load indicators and their margins, the calculation of mission-unique shaping parameters and the evaluation of prelaunch wind measurements.

INTRODUCTION

The Space Shuttle is a highly complex launch configuration, wherein four separate elements are essentially flown in formation in a high dynamic pressure environment. This dictated development of a system of unique analysis tools provides visibility into the element interface loading and their sensitivities to aerodynamic and environmental characteristics. During development and subsequent application of these tools (computer programs) we learned that the interface loads are the result of relatively small differences in large numbers (airloads). Thus the effects of element aerodynamic uncertainties and in-flight winds produce profound deviations in the interface loads. These potential deviations must be accounted for in determining how to fly the vehicle to minimize risk of exceeding interface design requirements while realizing the maximum possible launch system performance capability. Accordingly, the system of programs that was developed allowed:

1) assessment of preflight wind tunnel test data and its processing into a component design data base,

2) determination of mission unique trajectory shaping parameters,

3) identification of critical structural load indicators, their margins and their sensitivities to element aerodynamic uncertainties, system dispersions and in-flight winds,

4) evaluation of prelaunch wind measurements for go/no go decisions and,

5) postflight extraction of vehicle and component aerodynamic coefficients.

OVERVIEW

The body of this paper will concern itself with the identification of critical load indicators and how they are used to determine shaping parameter requirements. The other topics mentioned in the Introduction will be covered briefly in the Applications Section.

First the basic interface loads calculation technique will be discussed which forms the backbone of the entire system of assessment programs. Then this technique is used in the development of uncertainty models which are a basic input to the Capability Box program. This process is depicted in Figure 1 and will be explained in its own section.

INTERFACE LOAD CALCULATION TECHNIQUE

In order to develop a tool with which to investigate Space Shuttle ascent flight constraints, an approach was adopted whereby the Orbiter, right and left solid rocket boosters (SRB) were "isolated upon," each in its turn. By this it is meant that the equations of motion were written for each element under consideration as if it were an isolated body. The driving functions for these equations are the external forces on the element itself (aerodynamics, thrust, gravity) and the contributions from the interface fitting/strut loads. This has the effect of transforming an internal reaction type force (interface load) into an external driving function. These equations take the form:

$$\begin{aligned} M_i \ddot{\vec{R}}_i &= \vec{F}_{AERO_i} + \vec{F}_{THRUST_i} + \sum_{j=1}^{N_i} \vec{F}_{STRUT_{ij}} + \vec{G}_i \\ I_i \dot{\vec{\omega}}_i + \vec{\omega}_i \times I\vec{\omega}_i &= \vec{M}_{AERO_i} + \vec{M}_{THRUST_i} + \sum_{j=1}^{N_i} (\vec{R}_{STRUT} \times \vec{F}_{STRUT})_{ij} \end{aligned} \qquad (1)$$

where N_i is the number of interface loads for element i and G_i is the gravity term. Usually equations of motions are set up to be integrated for unknown positions and rates. In our application however, the inertia (acceleration) and thrust terms are assumed to be known in order to solve for either the interface loads or the aerodynamic forces and moments.

These equations can be solved for the preflight component and interface loads using the wind tunnel element aerodynamic data base. Two points are worth noting:

1) The orbiter is attached to the External Tank (ET) by means of seven struts (see Fig. 2) but Eqs. (1) provide only six relationships between them. This then is an underdetermined structure and a seventh "redundancy" equation has been provided by a detailed structural analysis program.

2) Each SRB attaches to the ET at a forward ball joint and at three locations near station 1078 (see Fig. 2). Allowing a triad of three orthogonal loads to represent the forward thrust fitting, the six Eqs. (1) are sufficient for a solution.

UNCERTAINTY MODELS

With the general purpose loads calculation tool in hand, it was necessary to assess the full spectrum of uncertainties which logically fall into two (2) categories, deterministic and probabilistic.

Deterministic Errors - measured atmospheric data, including winds, for which measured data existed and which would be sampled many times prior to launch.

Probabilistic Errors - these are composed of: 1) subsystem dispersions, 20 contributors composed predominantly of autopilot dispersions and SRB propellant temperature variations, 2) element aerodynamic uncertainties, and 3) a wind persistence effect.

Our standard six degree-of-freedom (DOF) Space Shuttle simulation was interfaced with the element aerodynamic data base and the loads equations. It was used to produce nominal and dispersed load values which will be discussed.

The uncertainty group termed subsystem dispersions was run in the 6 DOF simulator and the load histories for each simulation stored on permanent disc. At the completion of this series, the delta load histories (dispersed-nominal) were computed and then reduced using root sum square (rss) across the group. These rss delta load histories due to subsystem dispersions were then stored for future use. See Figure 1.

A program was written to calculate the delta loads due to all element aerodynamic uncertainties as a whole. First, the matrix of sensitivities of interface loads to element aero coefficients is determined (Δ load$_i$/Δ coefficient$_j$). Then using uncertainties from the Space Shuttle Ascent Aerodynamic Data Book (Ref. 1) in both coefficient value and point of application, a combinational technique is employed to obtain a set of total delta loads. See Table 1 for a look at these equations and Table 2 for sample program output.

Sets of 150 measured wind profiles representing a realistic statistical sampling (Ref. 2) are available for every month of the year for both the Eastern and Western Test Ranges (ETR and WTR). Six DOF trajectory simulation runs have been made for selected months at ETR for 150 winds sets and the interface load histories saved. An empirically determined factor was then multiplied by the standard deviations of the load histories to obtain a 3-hour wind persistence effect. This time interval was chosen as it corresponds to the last time prior to an actual launch that wind data can be taken for assessment. At this point, the delta loads due to subsystem dispersions, aerodynamic uncertainties and wind persistence are reduced using the rss to obtain the probabilistic effect. See Figure 1.

THE "CAPABILITY BOX" PROGRAM

In order to make prelaunch determinations and predictions it was desired to separate the probabilistic effects above from the deterministic wind contribution. The point of departure for this operation is a set of limit load values supplied to the Ascent Flight Systems Intergration Group by the Rockwell International Structures Division. A parameter called the wind allowable is obtained by diminishing the limit load by the rss of the three probabilistic effects: subsystem dispersion, element aerodynamic uncertainty and wind persistence. Quantities like limit load do not refer to ultimate capability but to a load that may be reached before there would be any concern for the integrity of the structure. Thus, the wind allowable is the amount of protection that remains against a severe or unlikely wind after everything else statistically has been taken into account.

The next consideration was to find parameters common to all the interface loads in terms of which boundaries could be established. In keeping with industry practice, dynamic pressure times angle of attack ($q\alpha$) and angle of sideslip ($q\beta$) were deemed

appropriate. In order to calculate values for these parameters, the following scenario was devised. The α,β coverage in the element aerodynamic data base is $-8 \text{ deg} \leq \alpha \leq +4 \text{ deg}$ and $-6 \text{ deg} \leq \beta \leq +6 \text{ deg}$, each in two degree increments. This is equivalent to the matrix of the perimeter points which are shown in Fig. 3 with center at $\alpha = -2$ deg, $\beta = 0$ deg. In order to investigate the trends in the loads, a full set of trajectory conditions corresponding to a particular Mach number were fed into the Capability Box program. The program calculates the loads at the (-2,0) point and at the perimeter point and at a point halfway in between. These three points constitute a ray through which a parabola is passed to determine the radial distance required to obtain the wind allowable value. The radial distance along the ray is then reconverted to an α and β and multiplied by the dynamic pressure appropriate to that ray. A sinusoidal curve with offset is used to describe the variation of q with wind azimuth. This process is continued at each of the 28 rays around the perimeter. The locus of points in the $q\alpha$ - $q\beta$ plane is termed the capability curve for the particular load. The capability curves for all of the fitting, strut, and component load indicators are superimposed and the odd-shaped figure interior to all the curves simultaneously is called the capability box (Fig. 4). This analysis is repeated at 12 selected Mach numbers spanning the high dynamic pressure portion of first stage flight.

In the course of evaluating the perimeter of the data matrix described above, many highly off-nominal α, β, q sets are encountered. A unique feature of this program makes adjustments to the trajectory data to account for the aerodynamics at these arbitrary perimeter test points. The approach is to calculate the total thrust moment required to balance the aerodynamic moment and produce the same vehicle motion. The mixing logic of the flight control software is used to apportion control authority to the main engines and the solid rocket boosters; an iteration scheme is employed to converge on a solution. Thus, all five engines are "regimbaled" in both pitch and yaw to accomplish the moment-balance. This accurately compensates for the high angles of attack and sideslip encountered while scanning the data matrix.

The ($q\alpha$, $q\beta$) pairs are stored for the several Mach numbers of interest from the large data set accumulated during the trajectory sims of the 150 measured winds for the appropriate month. An off-line program is used to calculate characteristics of ellipses which encompass a certain percentile (say 95th) of the data. See Fig. 5 for examples. These ellipses are transfered onto transparencies and used in conjunction with the capability boxes to identify the upper to lower $q\alpha$ travel and right to left $q\beta$ travel (Fig. 6). This information is put into the form of a Mach history of $q\alpha$ and $q\beta$ corridors through which the particular mission can be flown. Midway through this envelop gives the mission-unique shaping parameters which minimize the probability of violating the structural constraints of the Shuttle Launch System. These shaping parameters can be converted to "I-loads" and subsequently stored in the on-board flight software to provide first stage steering commands.

APPLICATIONS

Day-of-Launch Wind Monitoring

A series of programs have been organized and used in conjunction with each of the Shuttle flights. These programs accept a wind altitude profile measured just hours (or days) before the launch and fly it in the 6 DOF simulator. There the interface loads are calculated and plotted in comparison with the wind allowables. Any exceedance of a wind allowable due to a measured wind represents a possible launch hold. For this purpose the Launch Systems Evaluation Advisory Team immediately

is made aware of these determinations.

Aerodynamic Model Rapid Impact Assessment

During the wind tunnel testing for element aerodynamic coefficients in the late 1970's, it became advantageous to develop a tool to be used for rapid assessment of these several data bases. For this purpose, a version of the basic loads program was assembled to evaluate the various indicators at 51 points around $q\alpha$, $q\beta$ wind response loci (known across the Shuttle program as "squatcheloids"). These results at various Mach numbers represented a significant swath through the data base for inspection. Figure 7 shows cases where shifts and inconsistencies were spotlighted for further investigation.

In other instances the load calculations have been used to quickly analyze the data in different ways. With an element data base in the neighborhood of a half-million values, this can be a lifesaver. For example, the Integrated Vehicle Baseline Coefficients, Cycle 2 (IVBC-2) was a highly touted data base derived largely from the IA-135 wind tunnel test results and from manipulation techniques thought to be state of the industry at the time. However, the calculation of the forward pitch-plane orthogonal orbiter/ET load (FT01) often demonstrated unrealistic sensitivity to inboard and outboard elevon deflections (see Figure 8). As a consequence of these results it was learned that there must be a reasonableness constraint applied when smoothing the wind tunnel test data as a function of elevon deflection: the aerodynamic center ($\Delta C_{m_e} / \Delta C_{N_e}$) of the elevon must remain consistent with its physical location.

Postflight Aerodynamic Data Extraction

Looking back at the isolation equations (1) it can be seen that all terms except the aerodynamic ones can be supplied directly or derived from flight instrumentation: angular accelerations and rates along with preflight mass properties yield the left sides of the equations while engine chamber pressure, propellant flow rates and strut strain gauge measurements cover the terms on the right side. This allows the equations to be solved for the aerodynamic forces and moments (six equations in six unknowns) and finally for the aerodynamic coefficients. This aerodynamic data extraction process has been exercised using sensor data from the first four Shuttle flights at nine Mach numbers across the high dynamic pressure regime. At each Mach number the coefficient data were fitted with least-squares curves (see Figure 9). The slopes and intercepts of these linear curve fits were used to obtain deltas with which the standard aerodynamic data base was adjusted.

CONCLUDING REMARKS

The interface/component/strut loads discussed throughout this paper, while being valid concepts worthy of consideration, are a macroscopic effect. The fittings and struts are structures in themselves, capable of more detailed analysis. Algorithms have been developed and mechanized to describe the stresses and strains in these members. These new indicators have been monitored for each of the Shuttle flights and are being incorporated into an upgraded version of the Capability Box program. The ultimate goal of this and related exercises is to reduce the amount of work required to assess a wind measured prior to a Shuttle launch.

REFERENCES

1. Aerodynamic Design Data Book, Element Component. Vol II - Launch Vehicle, Rept. No. SD72-SH-0060-2L, Rockwell International, 1981.

2. Smith, O.E.: MSFC Jimsphere Wind Data Tape for Design Verification. MSFC Memorandum S & A-AERO-YA-98-71, April 1976.

TABLE 1.- TYPICAL ATTACH LOAD COMBINATIONAL EQUATIONS

Δ ATTACH LOADS DUE TO NORMAL FORCE UNCERTAINTY

$$\Delta FTIX)_{\Sigma\Delta C_N} = \pm \left\{ \left[\frac{\partial FTIX}{\partial C_{N_o}} + \frac{\partial FTIX}{\partial C_{m_o}} \left(\frac{C_{m_\alpha}}{C_{N_\alpha}} \right)_o \right]^2 \Delta C_{N_o}^2 + \left[\frac{\partial FTIX}{\partial C_{N_{ET}}} + \frac{\partial FTIX}{\partial C_{m_{ET}}} \left(\frac{C_{m_\alpha}}{C_{N_\alpha}} \right)_{ET} \right]^2 \Delta C_{N_{ET}}^2 \right.$$
$$\left. + \left[\frac{\partial FTIX}{\partial C_{N_{BL}}} + \frac{\partial FTIX}{\partial C_{m_{BL}}} \left(\frac{C_{m_\alpha}}{C_{N_\alpha}} \right)_{BL} + (0.194) \frac{\partial FTIX}{\partial C_{\ell_{BL}}} \right]^2 \Delta C_{N_{BL}}^2 + \left[\frac{\partial FTIX}{\partial C_{N_{BR}}} + \frac{\partial FTIX}{\partial C_{m_{BR}}} \left(\frac{C_{m_\alpha}}{C_{N_\alpha}} \right)_{BR} - (0.194) \frac{\partial FTIX}{\partial C_{\ell_{BR}}} \right]^2 \Delta C_{N_{BR}}^2 \right\}^{1/2}$$

Δ ATTACH LOADS DUE TO PITCHING MOMENT UNCERTAINTY

$$\Delta FTIX)_{\Sigma\Delta C_m} = \pm \left\{ \left(\frac{\partial FTIX}{\partial C_{m_o}} \right)^2 \left[\Delta C_{m_o}^2 + C_{N_o}^2 \left(\Delta \frac{C_{m_\alpha}}{C_{N_\alpha}} \right)_o^2 \right] + \left(\frac{\partial FTIX}{\partial C_{m_{ET}}} \right)^2 \left[\Delta C_{m_{ET}}^2 + C_{N_{ET}}^2 \left(\Delta \frac{C_{m_\alpha}}{C_{N_\alpha}} \right)^2 \right] \right.$$
$$\left. + \left(\frac{\partial FTIX}{\partial C_{m_{BL}}} \right)^2 \left[\Delta C_{m_{BL}}^2 + C_{N_{BL}}^2 \left(\Delta \frac{C_{m_\alpha}}{C_{N_\alpha}} \right)^2 \right] + \left(\frac{\partial FTIX}{\partial C_{m_{BR}}} \right)^2 \left[\Delta C_{m_{BR}}^2 + C_{N_{BR}}^2 \left(\Delta \frac{C_{m_\alpha}}{C_{N_\alpha}} \right)^2 \right] \right\}^{1/2}$$

Δ ATTACH LOADS DUE TO POWER-ON AERO UNCERTAINTIES

$$\Delta FTIX)_{\Sigma PWR} = \pm \left\{ \left[\left(\frac{\partial FTIX}{\partial C_{A_o}} + 0.2608 \frac{\partial FTIX}{\partial C_{m_o}} \right) \Delta C_{A_{b_o}} + \left(\frac{\partial FTIX}{\partial C_{N_o}} - 1.0 \frac{\partial FTIX}{\partial C_{m_o}} \right) \Delta C_{N_{b_o}} \right]^2 \right.$$
$$\left. + \left(\frac{\partial FTIX}{\partial C_{A_{ET}}} \right)^2 \Delta C_{A_{b_{ET}}}^2 + \left[\frac{\partial FTIX}{\partial C_{A_{BL}}} - (0.194) \frac{\partial FTIX}{\partial C_{n_{BL}}} \right]^2 \Delta C_{A_{b_B}}^2 + \left[\frac{\partial FTIX}{\partial C_{A_{BR}}} + (0.194) \frac{\partial FTIX}{\partial C_{n_{BR}}} \right]^2 \Delta C_{A_{b_B}}^2 \right\}^{1/2}$$

RSS COMBINATIONS

$$FTIX = \pm \left\{ \Delta FTIX_{\Sigma C_N}^2 + \Delta FTIX_{\Sigma C_y}^2 + \Delta FTIX_{\Sigma C_A}^2 + \Delta FTIX_{\Sigma C_m}^2 + \Delta FTIX_{\Sigma C_n}^2 + \Delta FTIX_{\Sigma C_\ell}^2 + \Delta FTIX_{\Delta PWR}^2 \right.$$
$$\left. + 2 \left[\frac{\partial FTOX}{\partial C_{n_B}} (0.194) \Delta C_{A_B} \right]^2 + 2 \left[\frac{\partial FTOX}{\partial C_{n_B}} (0.194) \Delta C_{A_{b_B}} \right]^2 + 2 \left[\frac{\partial FTOX}{\partial C_{\ell_B}} (0.194) \Delta C_{N_B} \right]^2 \right\}^{1/2}$$

TABLE 2.- STRUT LOAD SENSITIVITIES TO ORBITER AERODYNAMIC COEFFICIENTS

ITEM	CA	CY	CN	CLL	CLM	CLN
P1	-7.17	41.16	-41.07	-3.89	-87.53	61.90
P2	-7.17	-41.13	-41.07	2.97	-87.56	-61.84
P3	33.02	11.71	56.03	508.41	345.59	-160.44
P4	32.98	-20.50	55.96	-522.23	345.43	92.70
P5	-64.63	-20.33	-18.68	165.56	-61.15	-127.49
P6	-64.66	20.65	-18.72	-167.25	-61.20	128.53
P7	-0.02	32.32	-0.05	70.76	-0.04	252.32
P8	15.46	-15.55	202.52	-1518.11	-37.78	342.75
P9	9.89	-49.26	-228.17	3398.73	248.13	531.48
P10	13.78	43.40	85.45	-5849.86	-728.68	-224.56
P11	15.55	15.02	203.23	1519.20	-37.02	-344.45
P12	10.08	48.72	-229.59	-3401.47	247.02	-533.47
P13	13.67	-43.42	87.98	5854.29	-726.45	224.77
2010	41.72	347.94	0.97	52.59	3.22	640.86
3031	50.07	420.48	1.16	63.25	3.86	772.66

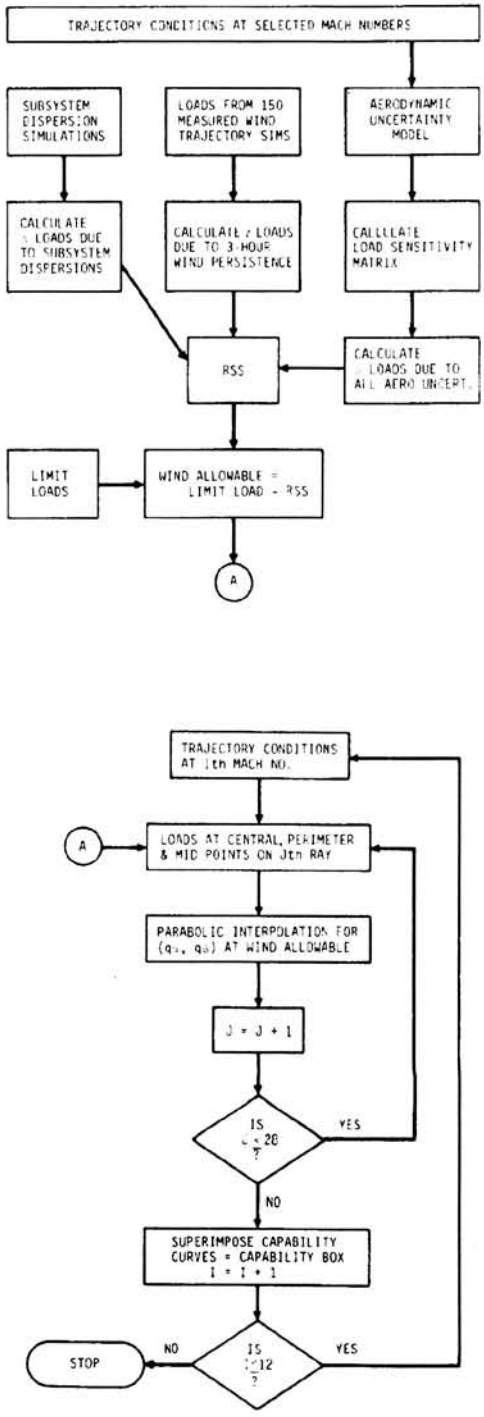

Figure 1.- Capability box flow diagrams.

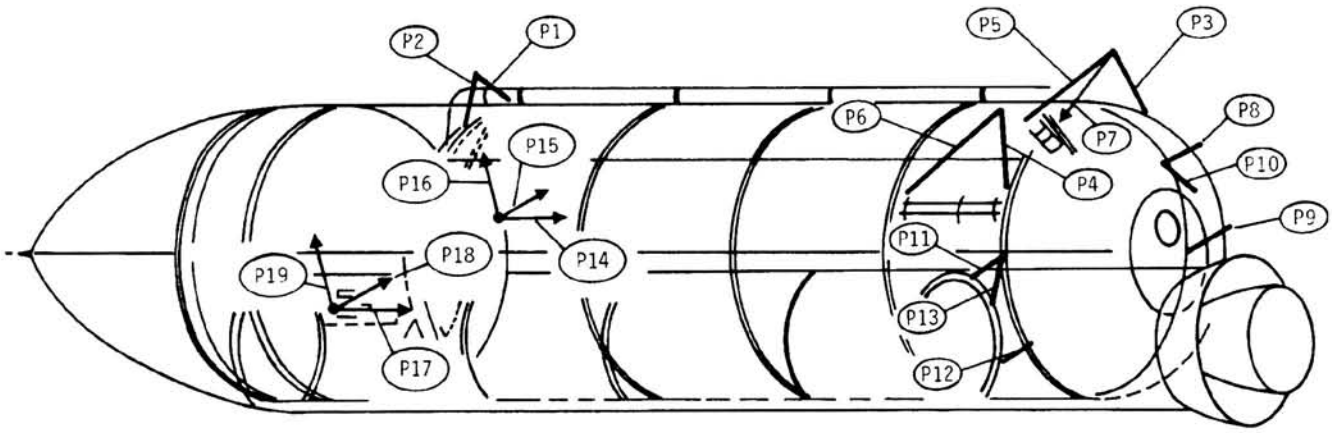

Figure 2.- Interface strut identification.

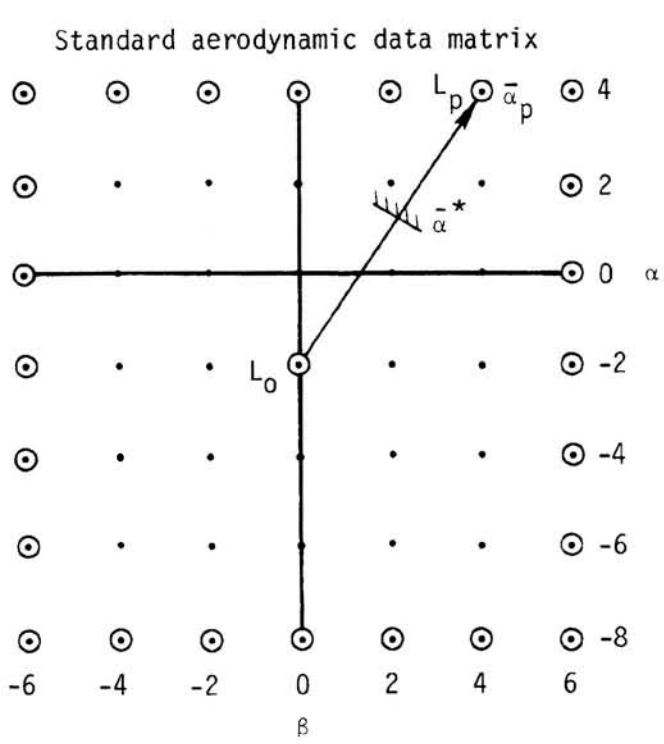

$$\bar{\alpha}^* = \frac{L_{wa} - L_o}{L_p - L_o} \bar{\alpha}_p$$

$$L_{wa} = L_{limit} - \Delta L_{RSS}$$

$$\Delta L_{RSS} = \left(\Delta L^2_{AERO} + \Delta L^2_{S/D} + \Delta L^2_{W/p}\right)^{1/2}$$

$$\bar{\alpha}_p = \left[(\alpha_p + 2)^2 + \beta^2_p\right]^{1/2}$$

$$\alpha^* = \frac{\alpha_p + 2}{\bar{\alpha}_p} \bar{\alpha}^* - 2$$

$$\beta^* = \frac{\beta_p}{\bar{\alpha}_p} \bar{\alpha}^*$$

Figure 3.- Aerodynamic data matrix.

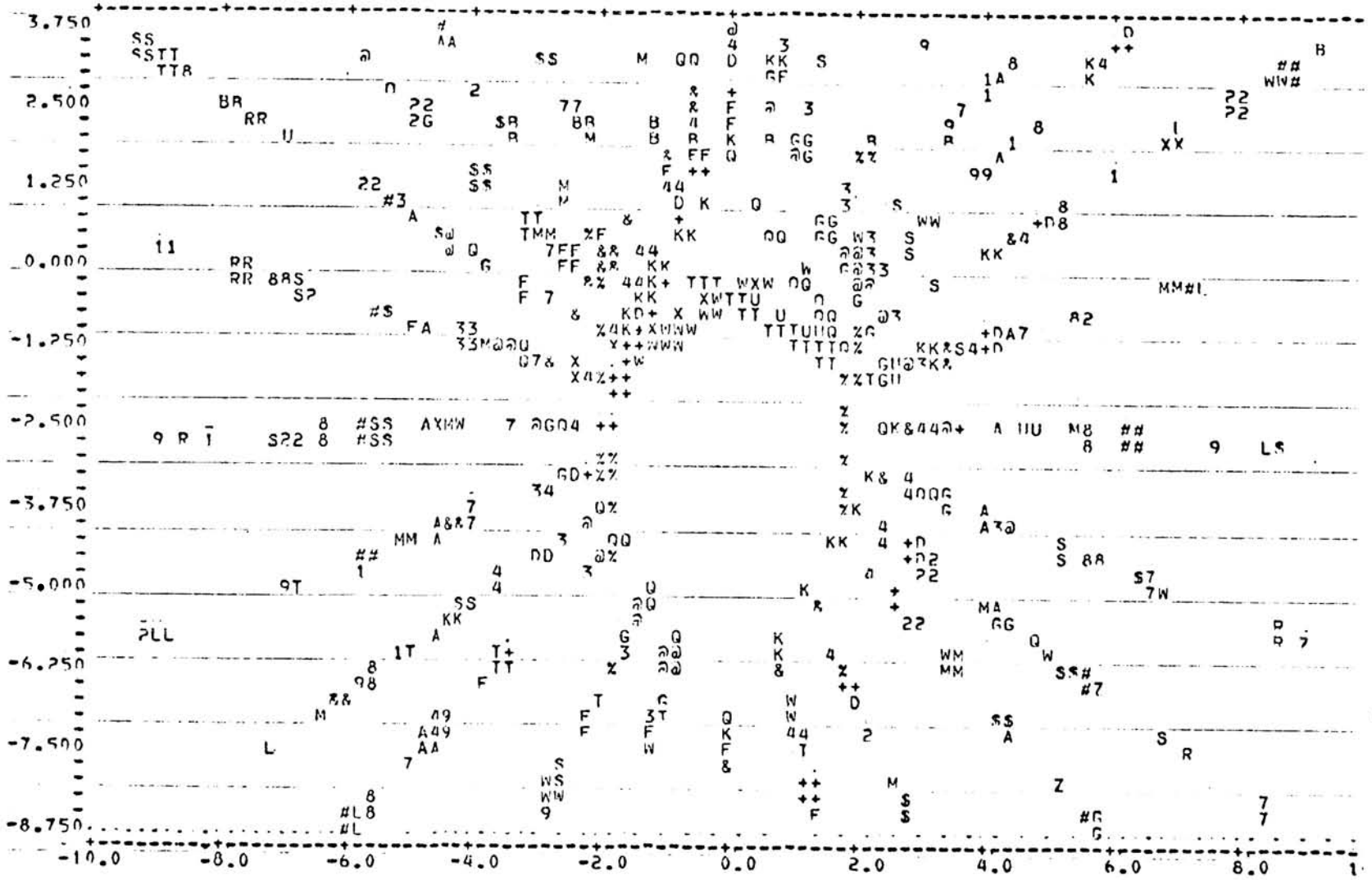

Figure 4.- Sample capability box.

Figure 5 - Sample Wind Roses.

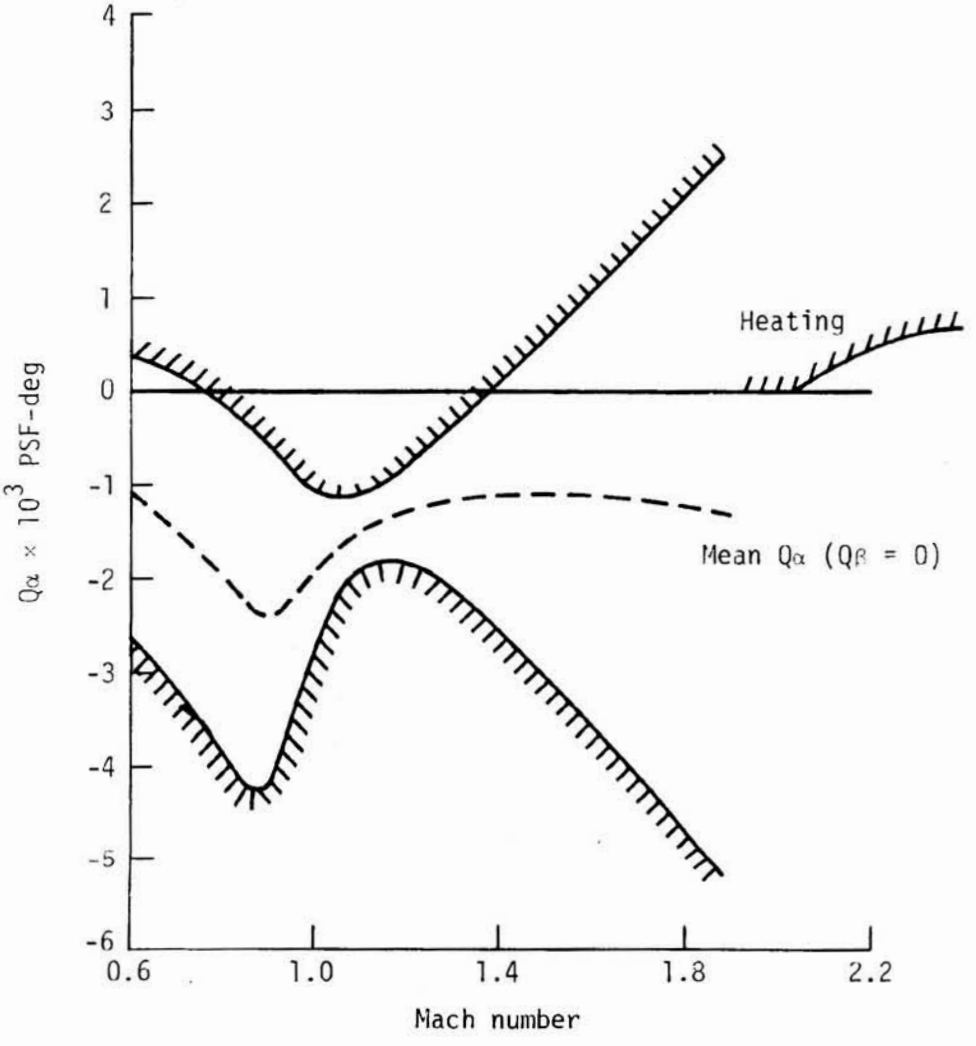

Figure 6.- STS-1 $Q\alpha$ flight constraint profile.

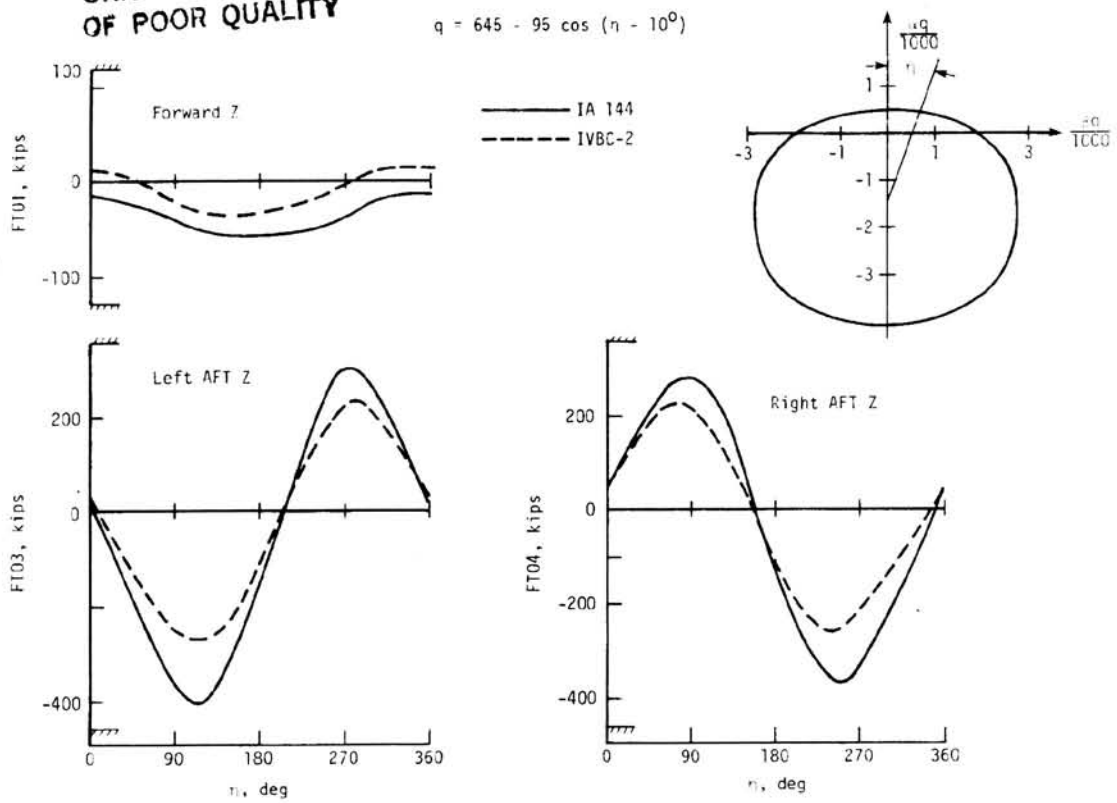

(a) Rigid body orbiter/ET attach load indicators; M = 1.25.

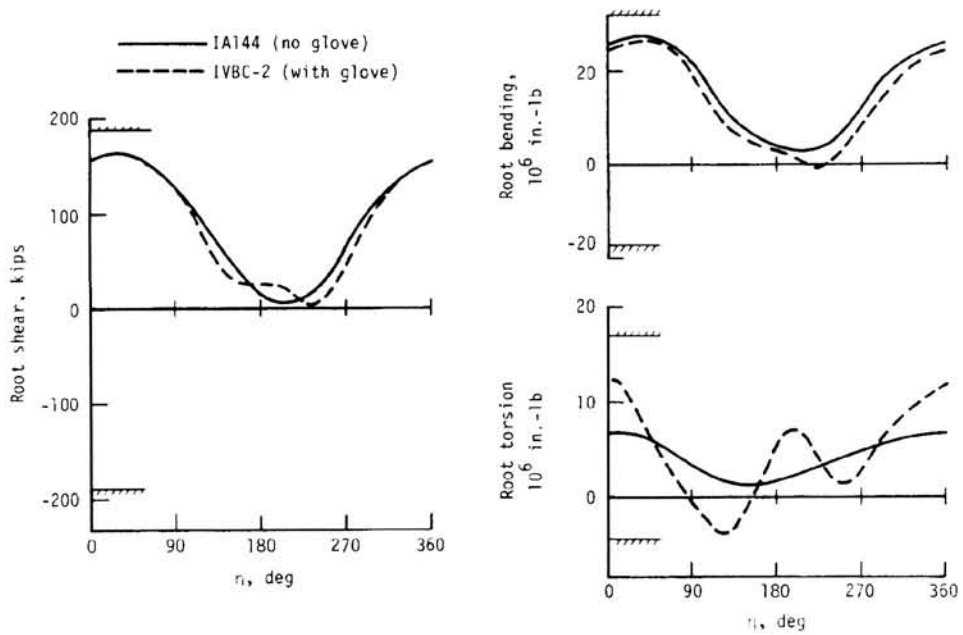

(b) Right wing root load indicators.

Figure 7.- Sample load indicators.

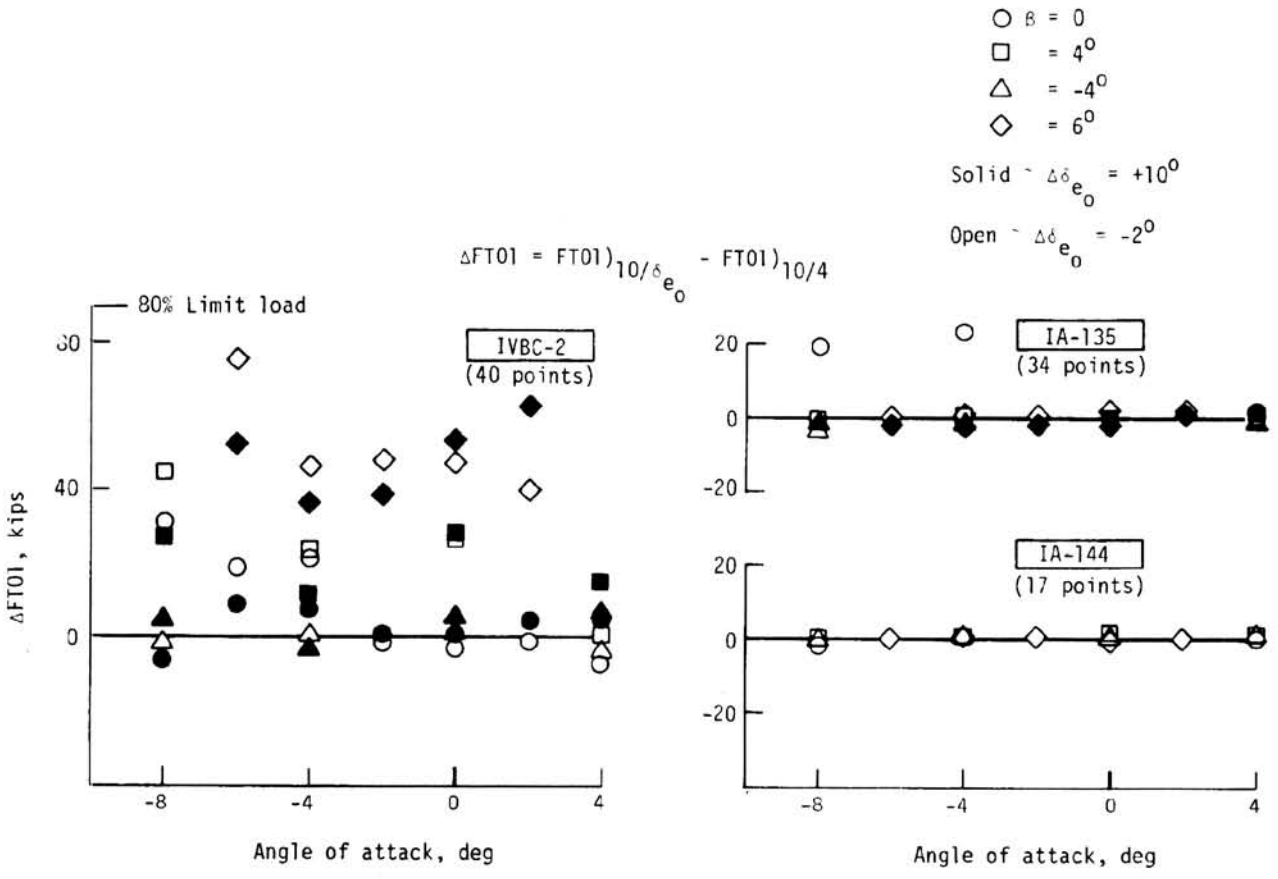

Figure 8.- Effect of $\pm 6^{o}$ outboard elevon deflection on FTO1; $M = 1.25$, $q = 700$, $\delta_{e_i} = 10^{o}$.

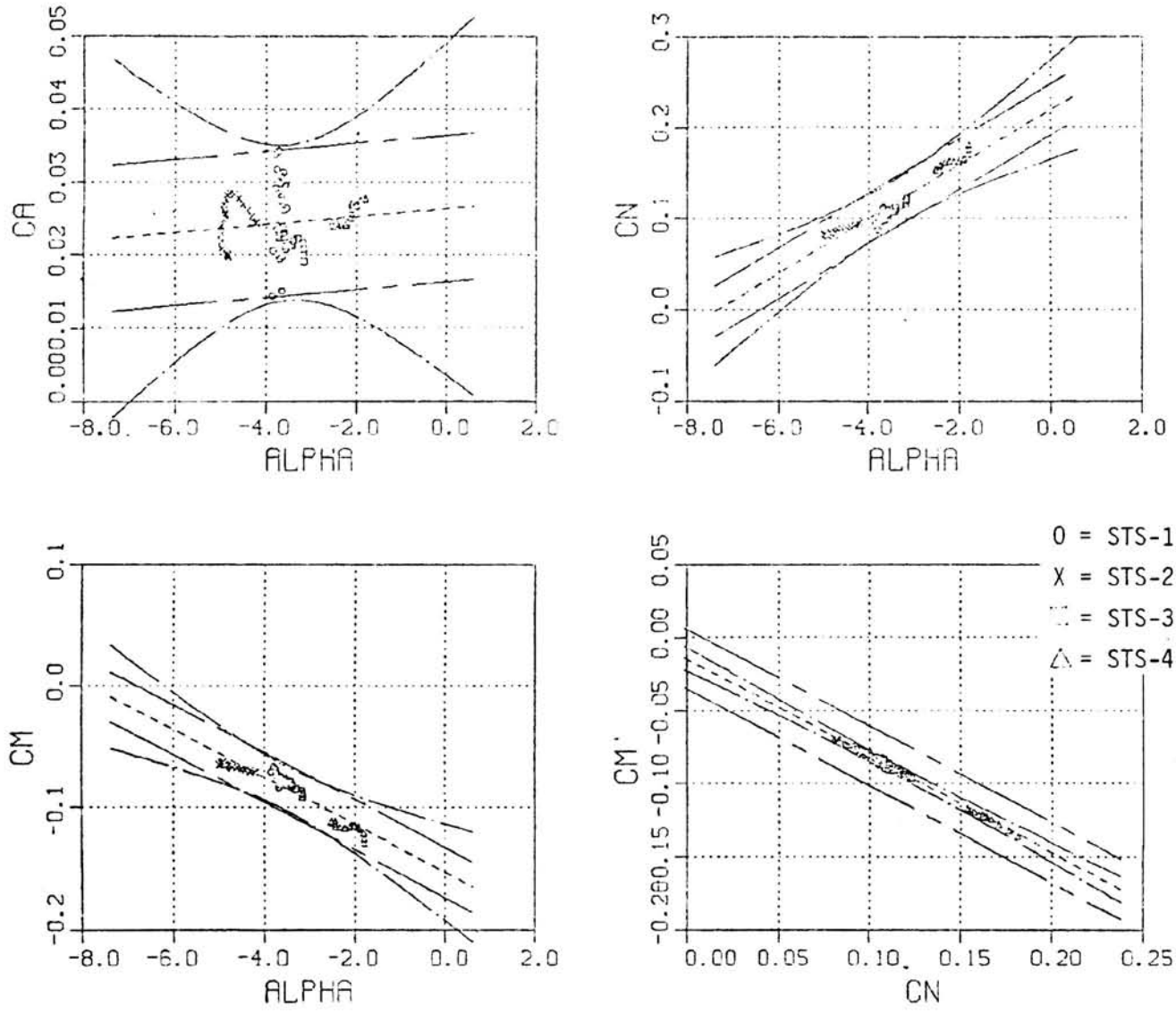

Figure 9.- Least squares curve fits of shuttle flight data.

SUPERSONIC LOADS DUE TO SHUTTLE-ORBITER/ EXTERNAL-TANK ATTACHMENT STRUCTURES

C. L. W. Edwards, P. J. Bobbitt, and W. J. Monta
NASA Langley Research Center
Hampton, Virginia

SUMMARY

A large variety of tests were conducted during development of the Space Shuttle to determine the strength, fatigue, and thermal characteristics of the thermal-protection system of the orbiter. The present paper describes the research and analysis carried out to accurately define and simulate the flow characteristics immediately ahead of the external-tank attachment structures. The highest known acoustic pressure loads occur in these regions and tests to insure the ability of the tiles to withstand these acoustic loads, plus those due to pressure gradient, were thought necessary. First flight-critical wind-tunnel tests were therefore conducted in the Langley 8-Foot Transonic Pressure Tunnel (8-Ft. TPT), which simulated the time histories of Shuttle ascent loads on tile arrays bonded to structures which accurately duplicated those of the Shuttle. The time-varying free-stream conditions were provided by controlling the deflection-angle history of diffuser spoiler flaps in an automated way. Time histories of the critical-load parameters imposed on the tile arrays in the tunnel are compared with those expected in flight.

INTRODUCTION

A large variety of tests were conducted to determine the strength, fatigue, and thermal characteristics of the thermal-protection system of the Shuttle orbiter. Included were tests of the individual components, single-tile systems, and tile arrays. Materials, vibroacoustic, aerodynamic load, and aerodynamic heating tests were conducted with models of varying size and complexity in the laboratory, in flight, and in many types of wind tunnels. The present paper describes supersonic wind-tunnel tests which were conducted to define flow details and aid in the establishment of the appropriate conditions for the simulation in the Langley 8-Foot Transonic Pressure Tunnel of the time histories of Shuttle ascent loads on tiles bonded to realistic structures. This type of test, designated herein as the Combined Loads Orbiter Tests (CLOT), had never before been attempted in a wind tunnel of this size (ref. 1).

The primary objectives of the 8-Ft. TPT tests were to verify that the tiles would remain attached to the flight structures under the simulated flight conditions, to compare measured and predicted tile and strain-isolation-pad (SIP) loads and responses, and to determine tile roughness characteristics after single- and repeated-ascent missions. The process for determining the time-varying aerodynamic environment on the tile array (called panel) just ahead of the forward external-tank/Shuttle-orbiter attachment yoke is described subsequently. This process required the use of previously acquired pressure data on the ascent configuration,

as well as data from supersonic wind-tunnel tests of a subscale bipod carried out as a separate part of this program. Precalibration and calibration panels used to obtain detailed loads data, to calibrate the instrumentation, and to ascertain and modify the actual pressure environment in the tunnel are also briefly discussed. Finally, the methodology used to provide the required time-varying free-stream and local conditions is described.

SYMBOLS

C_p	$= \frac{p - p_\infty}{q_\infty}$
D	diameter of bipod legs, in.
h	height of bipod yoke, in. (= 1.205D)
L	length of Shuttle orbiter, in.
L_{SEP}	length of separation ahead of bipod, in.
M	Mach number
p	static pressure, psi
P_{SCALE}	nondimensional quantity used in correlating pressure data ahead of bipod
P_t	total pressure, atm
q	dynamic pressure, $1/2\ \rho V^2$, psf
t	time, sec
V	velocity, ft/sec
X	dimensional distance measured forward from center of bipod, in.
X_{SCALE}	nondimensional quantity used in correlating pressure data ahead of bipod
X_{SEP}	dimensional distance to separated flow footprint measured forward from center of bipod, in.
x	distance measured rearward along centerline of Shuttle from nose of Shuttle, or distance measured rearward along false floor from leading edge, in.
x'	distance measured forward from face of bipod, in.

y	lateral distance measured from centerline of Shuttle, in.
γ	ratio of specific heats (= 1.4 in this study)
δ	dividing streamline angle, deg
δ_F	diffuser-flap deflection angle, deg
ϕ	meridian angle defining separated-flow footprint, deg
ρ	density, slugs/ft^3
ΔX_{SHOCK}	shock detachment distance measured at intersection of base flange with bipod leg, in.
Δp_{SHOCK}	pressure jump across bow shock ahead of bipod

Subscripts:

LOCAL	quantity measured in separated-flow region ahead of bipod
ONSET	quantity measured immediately ahead of separated-flow region ahead of bipod
PLATEAU	value of pressure in plateau region just downstream of flow-separation point ahead of bipod
1	value at a single point (for panel 20C, 4 bipod diameters ahead of face of bipod (12 in. for a half-scale bipod))
∞	free-stream conditions

Abbreviations:

CLOT	combined loads orbiter tests
DFI	diagnostic flight instrumentation
OFPL	overall fluctuating pressure level, dB
PCF	pounds per cubic foot
rms	root mean square
SIP	strain isolation pad
STS-1	first flight of space transportation system

UPWT Langley Unitary Plan Wind Tunnel

8-Ft. TPT Langley 8-Foot Transonic Pressure Tunnel

TEST-PANEL SELECTION

A total of four separate areas on the bottom of the Shuttle were considered at various times for testing, but simulation concepts and hardware were developed for only three. Near the end of the program one of these was dropped, leaving the two panels which had previously been declared critical for the first flight to be tested. The latter two panels are located ahead of and behind the forward external-tank/Shuttle-orbiter connection bipod (yoke) and are among the most critical panels on the Shuttle. Local laminar heating rates during entry are extremely high, and if the tile loads during ascent cause the surface to become rough, then premature transition to turbulent flow could occur. Consequently, the heat of entry is increased over the downstream areas, and the structural integrity of the orbiter could be jeopardized. The third panel, for which a simulation concept and hardware were developed, was located just ahead of the inboard aileron hinge and was chosen because of large predicted inplane deflections (which were later found to be overly conservative) and lift-off acoustic pressures. Sketches showing the location and geometry of the three panels are given in figures 1 and 2. Panel 20A, shown in the lower middle of figure 1, is located about 2 feet behind the bipod; panel 20C whose flow environment and simulation criteria are the primary subjects of this paper, is just ahead of the bipod and includes a portion of the landing-gear doors; and panel 20D (fig. 2) is positioned at the rear of the wing ahead of the elevon hinge line. Panel 20D, which includes the tile array in the "test area" in figure 2, has a width of 49 inches and a length of 65 inches. A fourth panel (20B), which is shown on the bottom right-hand side of figure 1, was dropped early in the program, because the ascent environment for panel 20A was considered to be more severe.

The panel ahead of the bipod (20C) includes, as noted previously, a portion of the doors of the forward landing-gear compartment. These doors are constructed of a thick honeycomb sandwich material (see fig. 3) and are so rigid that structural vibrations were not a concern. However, buffet loads due to extremely high unsteady-pressure levels caused by the bow shock ahead of the bipod at supersonic speeds and the possibility of increased surface roughness due to repeated loads were concerns.

SHUTTLE TRAJECTORIES

The level and distribution of static pressures over the orbiter, the intensity and distribution of dynamic pressures, and the position and strength of shocks all depend on free-stream Mach number and static-pressure levels provided by the trajectory as well as vehicle attitudes (angles of attack and sideslip) which result from control inputs and winds. Over the years, prior to the STS-1 flight, hundreds of trajectories were postulated to examine the effects of various wind

profiles, payloads, orbital parameters, and uncertainties in thrust levels and aerodynamic coefficients. For the CLOT, the time-varying environments were based on the STS-1 nominal-trajectory quantities shown in figure 4. Note that time starts at 30 seconds in this plot, which corresponds to a Mach number of 0.6, a dynamic pressure of 350 psf, and a static pressure of 11 psi. Dynamic pressure reaches a maximum of approximately 580 psf at 45 seconds and remains nearly constant for the next 25 seconds. It was assumed in the CLOT program that trajectories with higher or lower maximum dynamic pressure could be simulated in the wind tunnel by raising or lowering the pressure level (total head) at which the test was run.

The symbols in figure 4 represent the values of p_∞, q_∞, and M_∞ actually obtained in the flight of STS-1. Static pressure was slightly overpredicted for early times and underpredicted for later times; Mach number was in excellent agreement up until about 45 seconds, when flight values began to exceed those of the predicted nominal. These small differences in Mach number are amplified into larger differences in dynamic pressure by the dependence of dynamic pressure on Mach number squared. The agreement between the predicted and flight trajectories shown in figure 4 clearly indicates that simulations based on the predicted STS-1 nominal trajectory were well-founded.

PRESSURE DISTRIBUTIONS

A number of wind-tunnel tests were carried out by the Shuttle Project on pressure models of the Shuttle orbiter and ascent configuration. However, most were conducted for the purpose of obtaining structural loads, and not TPS tile loads. The latter requires significantly more resolution, not only to obtain accurate pressure levels and gradients, but also for shock strengths and shock locations. At the start of the CLOT program, the only data available were from wind tunnel tests denoted as IA105A, IA105B, and IA81. Figure 5 shows centerline pressure distributions from these tests for Mach numbers from 0.6 to 1.4. It should be noted that the circle symbols, denoted as IA105A data, are not all actual data points, but points taken from previously established fairings of the data. Another test (OA253) which included transonic data had been run, but the data were not yet available. A special effort was undertaken by Rockwell to provide OA253 data for comparison. Test OA253, which has much higher resolution in many areas on the Shuttle, was most helpful in resolving the uncertainties. The large changes in the character and levels of pressure obtained in OA253, ahead of and behind the bipod, were in agreement with data from a Langley small transonic tunnel. Thereafter data from test OA253 were coupled with IA105A and IA81 data to provide a simulation standard particularly for onset flow conditions approaching the bipod. The solid lines in figure 5 are illustrative of the actual fairings used.

Even with the higher resolution of the OA253 test pressure data, many important features of the flow field could not be determined. In addition, detailed supersonic data are required ahead of the bipod for panel 20C, while OA253 tests were carried out only at transonic speeds. Variations of pressure in the lateral direction, separated-flow boundaries, and shock locations are all features of the flow field that existing data did not define with the precision required to assure an accurate

simulation. Consequently, both transonic and supersonic tests of subscale bipods were undertaken. Results from these tests later proved indispensable. In subsequent paragraphs, the features of the supersonic portion of these additional tests are described.

SUPERSONIC TESTS OF SUBSCALE BIPODS

The main source of loads of panel 20C was the unsteady pressure under the bow shock ahead of the Shuttle bipod. The magnitude of these loads varies directly with the strength of the shock and is a maximum for free-stream Mach numbers approaching 2.5. However, the Mach number just ahead of the bipod, M_{ONSET}, governs the bow-shock strength, and this is the flow condition that one would like to simulate in the tunnel. Because it was expected that the highest Mach number achievable in the 8-Ft. TPT would not be much in excess of 1.5, and this with a subscale bipod, a large amount of additional information had to be developed to formulate an acceptable simulation.

A general description of the flow character ahead of the bipod is illustrated in figure 6. The free stream flow is stagnated on the orbiter nose and then expanded over the lower surface of the orbiter. This downstream flow is labelled "onset flow" in the sketch. At the ascent flight conditions of interest, near maximum loads, the boundary layer is turbulent. This turbulent boundary layer is separated ahead of the bipod attachment structure (yoke). An oblique shock is formed at the beginning of separation creating a secondary or local flow which governs the standoff distance and pressure rise across the normal shock sustained ahead of the bipod. Since the main concerns are the acoustic loads at the foot of this normal shock, the local flow conditions, the location of the normal shock, and the pressure rise across it must be accurately determined to conduct a proper simulation.

In order to provide realistic insight into the nature of the flow ahead of the bipod, a 0.22-scale bipod was mounted on a flat plate as illustrated in figure 7 and tested in the Langley Unitary Plan Wind Tunnel (UPWT) over a range of Mach numbers from 1.5 to 2.5. Boundary layer trips were employed to insure a turbulent boundary layer. Surface pressures (on the plate) were measured through 51 orifices to define the boundary layer separation point as well as the local flow conditions ahead of the bipod. Thirty-three of the orifices were located along the centerline of the plate; 9, along a ray emanating from the center of the bipod at a 30° angle to the plate center; and the remaining 9, along a similar 60° ray. In addition, the bipod was subsequently mounted at a second longitudinal location 3.5 inches aft of the position shown in figure 7. The effective number of orifices was thereby increased to 102, 66 along the plate centerline and 36 others to define the lateral pressures ahead of the bipod.

Surface oil flows were also employed to study the longitudinal and lateral extent of separation. Schlieren and shadowgraph photographs were employed to define the average position of the bow shock at each Mach number. The pressure and flow visualization data were analyzed rather extensively to understand the flow mechanics and to establish correlations wherever possible so that the flow conditions in flight could be properly simulated without necessarily duplicating

the flight environment. Subsequent discussions will cover the supersonic wind tunnel tests, the analysis of those data, and their application to the static and dynamic simulations required for the Combined Loads Orbiter Tests (CLOT) conducted in the Langley 8-Foot Transonic Pressure Tunnel (8-Ft. TPT).

FLOW AHEAD OF THE BIPOD AT SUPERSONIC MACH NUMBERS

As stated earlier, the subscale bipod was tested at two longitudinal locations on the flat plate; however, the forward location had been originally anticipated to be sufficient and the aft position was included during the UPWT tests. The forward bipod location and distribution of orifices were based on pressure distributions from existing data as previously indicated in figure 5 as well as pressure distributions ahead of vertical fins with cylindrical leading edges (ref. 2) previously tested in the UPWT. A typical pressure distribution ahead of a vertical cylinder is presented in figure 8. The pressure interaction extends approximately 3 diameters ahead of the cylinder at this Mach number (~2.3) while a set of pressure orifices covering that same nondimensional distance ahead of the bipod does not come close to measuring the pressure interaction. The derivation of the pressure correlation curve shown in this figure to illustrate the true extent of interaction ahead of the bipod for this Mach number will be discussed in the following paragraphs.

A typical pressure distribution resulting from both longitudinal locations of the subscale bipod on the flat plate is presented in figure 9. The onset Mach number (2.1) for this test corresponds to the flight Mach number where maximum pressure rise across the normal shock ahead of the bipod occurs. The pressure interaction extends approximately 6 bipod diameters upstream. This is slightly larger than the predicted extent indicated in figure 8 but is consistent with the decrease in Mach number from 2.3 to 2.1.

The schlieren photograph on the left side of the figure corresponds to the square symbol pressure data obtained with the bipod mounted aft and the shadowgraph on the right side corresponds to the circular symbol data obtained with the bipod in the forward position. The oblique shock which occurs at the beginning of interaction (or separation) as well as the normal shock ahead of the bipod legs are clearly visible in both types of flow visualization. Also noted on this figure is the relatively constant (or plateau) pressure region which occurs just downstream of the initial pressure rise. This parameter is the basis of the correlations developed during this study.

The centerline pressure distributions ahead of the bipod for the Mach number range ($1.5 \leqslant M_{ONSET} \leqslant 2.5$) of the UPWT tests are presented in figure 10. The nondimensional pressure ratio P_{LOCAL}/P_{ONSET} has been reduced by unity for convenience in subsequent correlations. The interaction length ahead of the bipod has been nondimensionalized by the height of the bipod yoke h because this is the key geometric parameter governing the extent of separation. It can be seen that the basic pressure levels can vary by as much as 100 percent and the interaction length by 25 percent over this Mach number range.

Because the plateau pressures are a specific feature of separated flow regions, this parameter was chosen to correlate the pressures. The plateau pressures in this study agree well with values obtained ahead of two-dimensional forward-facing steps as illustrated in figure 11. Between onset Mach numbers of 0 to 6, these data are reasonably well represented by the following linear function of onset Mach number:

$$\frac{P_{PLATEAU}}{P_{ONSET}} = 0.56\ M_{ONSET} + 0.80 \tag{1}$$

When this pressure ratio is reduced by unity, it becomes an effective inverse scaling function. The scaled pressure data from figure 10 is presented in figure 12 where

$$P_{SCALE} = \left[\frac{P_{PLATEAU}}{P_{ONSET}} - 1\right]^{-1} = \left[0.56\ M_{ONSET} - 0.2\right]^{-1} \tag{2}$$

The overall pressure levels are in better agreement and the scaled plateau pressures are approximately equal to 1 as they should be; however, the disparity in extent of interaction with Mach number becomes even more obvious when the pressure level has been scaled.

The extent of interaction along the centerline was also correlated primarily as a function of plateau pressure as illustrated in figure 13. It was assumed that the dividing streamline of the separated flow ahead of the bipod was straight, that the flow was two-dimensional, and that the average pressure over this separated region was equal to the plateau pressure. Once the onset Mach number has been chosen the plateau pressure ratio can be determined from equation (1). Oblique shock relations can then be used to determine the turning (or wedge) angle δ required to generate that plateau pressure. The following relation was taken from reference 3:

$$\tan\delta = \frac{2\gamma M_{ONSET}^2 - (\gamma - 1) - (\gamma + 1)\left(\frac{P_{PLATEAU}}{P_{ONSET}}\right)}{(\gamma + 1)\left(\frac{P_{PLATEAU}}{P_{ONSET}}\right) + (\gamma - 1)} \left[\frac{\gamma M_{ONSET}^2 - \left(\frac{P_{PLATEAU}}{P_{ONSET}}\right) + 1}{\left(\frac{P_{PLATEAU}}{P_{ONSET}}\right) - 1}\right]^{-1} \tag{3}$$

Since the dividing streamline reattaches at the top of a forward-facing step, an extent of separation L_{SEP} can be calculated as a simple trigonometry function for a given step height h:

$$L_{SEP} = \frac{h}{\tan\delta} = X_{SCALE} \tag{4}$$

This calculated separation length was used to scale the nondimensional lengths of figure 12 and the results are presented in figure 14. The centerline pressure distributions appear to be well correlated and the resulting pressure curve shown in figure 15 was tabulated and adopted as the basic pressure curve to be scaled to other test conditions and bipod sizes as required.

The pressure orifices located off the centerline were too sparse to accurately define the lateral variation and extent of the pressure interaction. The lateral variation in extent of separation with Mach number was determined from oil flow photographs such as those presented in figure 16. The outline of panel 20A and 20C with its dashed lines representing the forward landing gear doors have been overlayed on the oil flow photographs for reference. The separated flow footprints at each of four Mach numbers were fitted with parabolas whose eccentricities were correlated with onset Mach number and meridian angle ϕ as previously shown in figure 13. The general equation for the parabolas is

$$1.205\left(\frac{y}{h}\right)^2 = \left(2p\right)\left(\frac{X_{SEP} - X}{h}\right) \tag{5}$$

where $2p$ is a linear function of onset Mach number given by

$$2p = -5.24\ M_{ONSET} + 21.74 \tag{6}$$

and X_{SEP} is equal to the centerline extent of separation L_{SEP} plus half of the bipod yoke thickness, 0.346h, or

$$X_{SEP} = L_{SEP} + 0.346h \tag{7}$$

With equations (5), (6), and (7), the intersection (X, y) of any given meridian with the parabolic footprint can be determined algebraically. The extent of the pressure curve presented in figure 15 can then be properly scaled by the distance along the meridian between the face of the bipod and the parabolic footprint as given by

$$X_{SCALE} = \sqrt{\left(\frac{y}{h}\right)^2 + \left(\frac{X}{h}\right)^2} - 0.346\ \sec\phi \tag{8}$$

For meridian angles less than or equal to 30°, the decrease in pressure with increasing meridian angle is negligible; however, the primary pressure distribution of interest for this study was the centerline value.

The importance of these pressure distributions obtained at supersonic Mach numbers in the UPWT can be illustrated to some degree by applying the correlations to produce a pressure distribution at the highest Mach number of existing data previously presented in figure 5(d). The free stream Mach number is 1.4 and the onset Mach number based on the pressures from figure 5(d) is approximately 1.2. The comparative pressure distribution from the correlations developed in this study are presented in figure 17. The character of the pressure distribution is considerably different, both in magnitude and extent of pressure. The extrapolation of the UPWT data down to an onset Mach number of 1.2 are probably more tenuous in predicted extent than in pressure levels; however, both parameters should be reasonably accurate. In any event, the pressure rise across the normal shock at this local Mach number is very small, and at onset Mach numbers above 1.5 where the fluctuating pressures are significant, the correlations are very reliable.

Once the local pressure distribution has been established, the local Mach number can be determined from the following relations which were taken from reference 3. Local Mach numbers greater than unity are determined

$$M_{LOCAL} = \sqrt{\frac{M_{ONSET}^2 (6 \xi_{LOCAL} + 1) - 5(\xi_{LOCAL}^2 - 1)}{\xi_{LOCAL} (\xi_{LOCAL} + 6)}} \tag{9}$$

where ξ_{LOCAL} is simply the pressure ratio p_{LOCAL}/p_{ONSET}. When the local Mach number becomes less than one, it is determined from

$$M_{LOCAL} = \sqrt{\frac{\xi_{LOCAL} + 6}{7 \xi_{LOCAL}}} \tag{10}$$

With the local pressures and Mach numbers now defined, the remaining aerodynamic parameters of interest such as local dynamic pressure and pressure rise across the normal shock ahead of the bipod when the local flow is supersonic can be readily determined from

$$q_{LOCAL} = \frac{\gamma}{2} p_{LOCAL} M_{LOCAL}^2 \tag{11}$$

and

$$\frac{\Delta p_{SHOCK}}{p_{ONSET}} = \frac{2\gamma}{(\gamma + 1)} \xi_{LOCAL} \left(M_{LOCAL}^2 - 1\right) \tag{12}$$

Of equal importance with the magnitude of fluctuating normal-shock pressures is the location where they occur, i.e., the location of the normal shock. It was assumed that the shock standoff distance ahead of the bipod would be similar to that ahead of a cylinder mounted normal to the flow. The standoff distance would then be characterized by the diameter of the bipod, D, the local Mach number, and the density ratio across the normal shock. However, the density ratio across the shock is only a function of local Mach number when specific heats are constant.

For this study, an attempt was made to correlate the shock standoff distances measured from enlarged shadowgraphs similar to those previously presented in figure 9 as a function of bipod diameter and onset Mach number in the following manner. It was assumed that the shock standoff distance ΔX_{SHOCK}, when non-dimensionalized by the bipod diameter D, could be adequately represented by simple functions of the density ratio K and the onset Mach number M_{ONSET}. For air with $\gamma = 1.4$, the density ratio is given by

$$K = \frac{M_{ONSET}^2 + 5}{6 M_{ONSET}^2}$$

The functional relationship employed for K was $\left[\frac{1-f(K)}{f(K)}\right]$ where

$$f(K) = \frac{K}{1-K} \sinh^{-1}\left[\frac{1-K}{\sqrt{K(2-K)}}\right] \tag{14}$$

as developed by Li and Geiger in reference 4. It was hoped that this relation would be sufficient to produce a correlation similar to the following

$$\frac{\Delta X_{SHOCK}}{D}\left[\frac{1-f(K)}{f(K)}\right] = \text{Constant} \tag{15}$$

When the measured shock standoff distances were applied to equation (15) it was found that the right-hand side was not a constant, but instead was a function of onset Mach number which resulted in the following relationship for shock standoff distance

$$\frac{\Delta X_{SHOCK}}{D}\left[\frac{1-f(K)}{f(K)}\right] = \ln\left(\frac{3.171}{M_{ONSET}^{0.536}}\right) \tag{16}$$

An indication of the effectiveness of equation (16) in predicting shock standoff distance is given in figure 18. The vertical dashed lines represent the locations predicted from equation (16). The left side of the figure shows the normal shock ahead of the subscale bipod used in the UPWT tests at the onset Mach number where the maximum shock pressures during STS-1 ascent occur. The right side of the figure (from ref. 2) shows the normal shock ahead of a vertical cylinder which has nearly twice the diameter of the bipod and was tested at a higher onset Mach number. The accuracy is considered quite acceptable in both cases. With the inclusion of equation (16), all the necessary correlations were available to accurately define the static or steady-state environments necessary to produce an accurate simulation of flight in the Langley 8-Foot Transonic Pressure Tunnel.

STATIC SIMULATION

With the correlation equations (1) through (16) available, the pressure distribution for any size bipod can be calculated given the onset Mach number and pressure. The application of these correlation relations to the generation of flight shock strengths (3.78 psi at $M_{ONSET} = 2.1$) with subscale bipods at lower Mach numbers (in this case, half-scale and three-quarter-scale bipods at $M_{ONSET} = 1.65$ and seven-eighth-scale bipod at $M_{ONSET} = 1.80$) is illustrated by the pressure distributions in figure 19. Note the increase in total pressure required at lower Mach numbers to achieve the desired shock strength. Obviously, the levels of static pressure are also increased and flow separation occurs closer to the bipod. Figure 20 can be used to illustrate this effect more graphically. It shows the flow-separation boundaries for a full-scale bipod at

the free-stream conditions that provide the maximum shock strength compared with that for subscale bipods at representative wind-tunnel conditions. The subscale bipods are positioned to give the same bow-shock locations as the full-scale bipod.

Another valuable piece of diagnostic information obtained from the UPWT tests was the measurement of the detachment distance of the bow shock on the bipod as a function of Mach number. The variation of shock-detachment distance (measured at the top of the bipod flange located near the bottom of the bipod) with Mach number is shown in figure 21. These data were useful for two very distinct purposes: (1) they provided the information needed to move a subscale bipod so that its bow shock could be located in the same place (as a function of time) as that for the full-scale bipod and (2) they provided another method of estimating the effective free-stream conditions in the 8-Ft. TPT where there were significant Mach number gradients ahead of the panel. Given that the important tile-load contributors are pressure gradients (especially those associated with shocks), time-varying pressure levels, and unsteady pressures associated with flow separation and shock movement, it is clear from figures 19 and 20 that the use of a half-scale bipod significantly reduced the area over which realistic tile loads can be simulated. It should also be pointed out that when the total pressure of the onset flow is raised to provide the same bow-shock strength for a half-scale bipod at an onset Mach number of 1.65 as that obtained in flight for an onset Mach number of 2.1, then the oblique shock from the leading edge of the separated-flow regions (see fig. 6) is much stronger than that encountered in flight at the same conditions.

TIME-VARYING ENVIRONMENTS

The time-varying free-stream conditions of figure 4 can be used with the pressure distributions obtained in the wind-tunnel tests of IA105A and B, IA81 and OA253, and on the subscale bipods at transonic and supersonic speeds to define the pressure distributions around the bipod at specific points in time. These data can also be used to provide a continuous time history of the static pressure, dynamic pressure, and Mach number at a specific point on the surface. If one is reasonably sure that, on the basic of favorable comparisons of pressure distributions obtained in complete model tests with those obtained in the wind tunnel where the bipod was the dominant feature, the latter provides accurate pressure distributions, then time histories at a single point can be used to effect the simulation of pressures for a much larger area. This is the situation that existed following the completion of the subscale bipod tests; consequently, most of the time simulations were done on the basis of those measured at a single representative point. The point chosen for panel 20C was 12 inches ahead of the bipod, where both unsteady- and steady-pressure data were available from the calibration panels.

Variations of the flow parameters with time ahead of the full-scale bipod are plotted in figures 22 to 25. Free-stream, onset, and point values for a point 24 inches ahead of the bipod in the region of the pressure plateau are presented. The Mach number at this point increases continuously with time but at a lower rate than in the free stream. Dynamic pressure on the other hand has two maxima, one at 45 seconds and another at 81 seconds. Note that the second maximum is much larger than the first and occurs at a free-stream Mach number near 2.0.

Figure 24 is presented to show the variation with time of the pressure jump across the bow shock ahead of the bipod as well as the pressure jump across a normal shock with M_∞ as the onset Mach number. The quantity Δp_{SHOCK} peaks at a value of 3.82 psi at 90 seconds into the flight, where the onset Mach number is 2.1 and the free-stream Mach number is 2.5. Some appreciation for the strength of the bow shock can be obtained from the fact that in the transonic speed range no shocks stronger than 2.2 psi are expected. Shock-detachment distance as a function of time is given in figure 25. The shock first starts to form around 70 seconds and moves steadily closer to the bipod. At the time when the pressure rise across the shock is at the maximum, the detachment distance is just over 3 inches.

SPECIAL PROBLEMS IN PANEL 20C SIMULATION

Because the free-stream Mach numbers required to generate the shock strengths (fig. 24), could not be achieved with a full-scale bipod in the 8-Ft. TPT, a great amount of difficulty was encountered in effecting an accurate simulation of the flow field over panel 20C. Even with a subscale bipod (or no bipod), there was never an expectation that the 8-Ft. TPT could be modified to achieve an onset Mach number of 2.1. The hope was that the right combination of bipod size and supersonic nozzle could be found to achieve an onset Mach number greater than 1.6. With this Mach number, the total pressure in the tunnel could be raised relative to that in flight so that the required shock strength could be obtained. The nozzle required to accelerate the flow to supersonic speeds was provided by building up the sides and ceiling of the tunnel with fiberglass-coated, contoured blocks in the throat region and z-bar-reinforced aluminum sheets upstream and downstream. This was to provide as gradual a contraction and expansion as possible. The sides of the nozzle diffuser extended downstream to about the middle of panel 20C, while the top-side fairing terminated about a foot beyond the bipod. In the tunnel-empty configuration (with the bipod removed), the supersonic nozzle yielded an onset Mach number of close to 1.8. With two-third-scale and half-scale bipods (with truncated legs), the maximum Mach numbers achievable were approximately 1.35 and 1.65, respectively. Clearly, the half-scale bipod had to be used to simulate the maximum shock jumps and associated unsteady pressures encountered in flight.

With the aid of the supersonic UPWT data previously described, time histories of onset Mach number and local values of static and dynamic pressure could be determined that would yield the required shock-pressure jumps. Since a half-scale bipod was employed in the tests, a point closer to the bipod than the 24 inches chosen for the full-scale bipod (figs. 19, 22, and 23) had to be used to monitor the time variation of p_l, M_l, and q_l. A point 12 inches ahead of the bipod was selected. Onset Mach number versus time is plotted in figure 26 for the 8-Ft. TPT simulation and for the Shuttle in flight. The variation of dynamic pressure with time at the 12-inch point for the 8-Ft. TPT simulation and the Shuttle STS-1 flight is given in figure 27. The Mach number short fall (1.65 versus 2.1) at the point of maximum shock strength requires that the wind tunnel be run at a total pressure of approximately 1.0 atm instead of the flight value which is slightly above 0.6 atm. The adverse effect of running at this higher total pressure is that the point values of dynamic pressure (fig. 27) are much higher than the flight levels and persist for a longer time. This phenomenon stimulated a quick look at what

happens when the dynamic pressure is matched (at the 12-inch point) instead of Δp_{SHOCK}. The result is shown in figure 28 and indicates that a far weaker shock is generated than that desired and for a much shorter time.

It can be expected, with the use of a half-scale bipod and a maximum tunnel Mach number of 1.65, that the movement of the bow shock will be less than that for the full-scale bipod at flight Mach numbers. Furthermore, when the Mach number in the tunnel decreases for times greater than 90 seconds (in order to continue to match the STS-1 shock strength), then the bow shock moves away from the bipod instead of moving closer as it does in flight. The above deficiencies are abundantly clear in figure 29, which shows the STS-1 shock standoff distances and those incurred for a fixed half-scale bipod. Early and late in the Δp_{SHOCK} pulse, the half-scale bipod shock position is in error by about 3 inches with a "zero error" at the cross-over point at 92 seconds. The desirability of being able to move the bipod to position the shock in the "right" location is apparent. Consequently, the bipod was mounted on a hydraulic ram with a stoke of 6 inches. The position of the ram was automatically controlled and coordinated with the diffuser-flap movement.

TEST SETUP IN 8-Ft. TPT

The time-varying free-stream conditions are provided by controlling the deflection angle of the diffuser flaps in a prescribed way. When the tunnel is started, prior to the start of a simulation, the flaps are positioned at their full-in position, which is about 33° from the wall. This flap position yields a test-section Mach number of about 0.6. Dynamic pressure and Mach number are increased by moving the flap toward the tunnel wall. Maximum conditions are usually achieved when the flap is within 5° or 6° of the wall; further decreases are ineffective. The maximum angular rate for moving the flap was about 1.5° per second.

The false floor was originally constructed much like an airfoil with a flat bottom and was mounted on streamlined supports about 2 inches high. This permitted the onset boundary layer to pass beneath the floor. Consequently, the boundary layer just ahead of the panels was kept thin - about the same thickness as that on the Shuttle. Also, it was initially thought that the diffuser would operate more efficiently with the bypass and that the diffuser flap would be more effective in controlling the flow as well. It was found through trial and error after the floor was installed that the performance of the tunnel was, in fact, improved with the bypass closed. Further improvement in tunnel performance was achieved by the installation of vortex generators on the false floor several feet downstream of the panel trailing edge. Boundary-layer thicknesses were measured on the false floor with the bypass closed for panel 20C installation. The measurement was taken 4 inches from the centerline and 1 foot downstream of the leading edge of the panel. The boundary-layer thickness ranged from 0.5 to 0.7 inches. These values are in good agreement with those predicted for the Shuttle under similar conditions.

Figure 30 is a photograph of the test panel installed in the false floor. This photograph of panel 20C was taken looking downstream. Faintly visible in the background are the diffuser flaps at the downstream edge of the false floor. The housing aft of the bipod is for the hydraulic ram used to translate the bipod.

FEATURES OF CALIBRATION AND TEST PANELS

The general arrangement for panel 20C is shown in figure 31. Panel 20C is covered with both silica tiles and polyurethane foam. Only three rows of real tiles were installed on panel 20C, and these are contained within the heavy dark line in the figure. The first row of tiles on the doors and those adjacent to the center edge of the door are comprised of 22-PCF silica tiles; those outside these regions on the second and third rows are 9-PCF densified tiles. Two of the real tiles contain DFI and are so labeled.

Panel 20C has two instrumented tiles; one is in the first row of tiles on the door and to the right of the bipod, and the second is to the left of the centerline in the second row of tiles on the door. Part of the special instrumentation was the installation of mini Coe sensors (ref. 5) distributed in three rows on the bottom of the tile. These sensors consist of a strain gage bonded to a diaphragm, which in turn is bonded to the bottom side of the adhesive which holds the strain isolation pad to the aluminum surface. Once installed, the face of the diaphragm is flush with the aluminum surface. Normal force and pitching and rolling moments which are applied to the tile can be determined through an appropriate calibration of the sensor outputs (ref. 6).

SIMULATION METHODOLOGY

Prior to starting the simulation process, it is necessary to define the time varying environment to be simulated. For panel 20C, the primary parameters are the pressure rise across the bow shock Δp_{SHOCK} and the shock standoff distance ΔX_{SHOCK}, ahead of the bipod. In flight, the shock pressure jump becomes discernible at a free-stream Mach number of 1.5 (~70 seconds into ascent), increases steadily until it reaches a maximum at a free-stream Mach number of 2.5 (~90 seconds), and then decreases steadily until it becomes negligible at a free-stream Mach number of 4.0 (~120 seconds) as the vehicle continues to accelerate to orbital speeds. The shock standoff distance during this same interval (between 70 and 120 seconds of ascent) decreases continually beginning with a value of about 10 inches at a free-stream Mach number of 1.5.

The Mach number capability of a transonic wind tunnel is limited to low supersonic speeds; therefore, the maximum levels of pressure jump across the bow shock must be achieved through tunnel operating pressure rather than Mach number. Operating pressure, on the other hand, cannot normally be varied rapidly enough to reflect the changes in shock pressures during flight and must be controlled by some other means which in this case was the limited range of supersonic Mach numbers available in the tunnel. In addition, the shock standoff distances are inversely proportional to Mach number so that as the Mach number is cycled to produce a Δp_{SHOCK} pulse similar to flight, the bow shock would move toward the bipod as the Mach number increased and away from it as Mach number decreased. Therefore, it was necessary to devise a means of independently translating the bipod to hold the bow shock in the correct location.

PANEL 20C SIMULATION

Prior to starting the simulation process, it is necessary to define the time-varying environment to be simulated. The procedure for doing this is discussed in a preceding section, where it was shown that by using static data for various wind-tunnel tests, the time variations of dynamic pressure and Mach number at any point on the panel could be determined. For panel 20C, a point 12 inches ahead of the bipod was chosen as the "representative" point. Results from this process are plotted in figures 22 through 25 and are repeated in the upper left-hand corner of figure 32. It should be noted that when the flight flow variables are matched at the representative point, they are also in good agreement in the surrounding area.

The problem now is to determine the diffuser flap-angle time histories that will give a good approximation of these time variations. To accomplish this, a series of runs are made at discrete flap-angle settings to construct curves such as those shown schematically in the upper right-hand corner of figure 32. Each value of M_{ONSET}, ΔX_{SHOCK}, and Δp_{SHOCK} can be related to a flap angle and to time. Consequently, the flap-angle time history needed to yield the correct shock pressure time history as well as the bipod translation schedule to maintain correct shock locations (upper left-hand corner) can now be constructed. The sketch in the lower right-hand corner of figure 32 depicts this result. A dynamic run is then made with the calculated flap and bipod translation time histories and the resulting shock induced pressures and bipod shock standoff (and Mach number) time histories are compared with that desired. If the simulation is not satisfactory, either the flap-angle or bipod translation time history is adjusted, taking into consideration any new information, and the process is repeated. If the rate of change of the shock pressure jumps require a larger rate of change of the flap angle than the maximum available, 1.5° per second, then the maximum rate is used until the flight and predicted values come back into agreement. Adjustments in the level of onset pressure can be made by changing the stagnation-pressure level at which the test is run.

Prior to making simulation runs, a series of tests were conducted to determine the time lags in the tunnel circuit, i.e., the time it takes a flap-angle change to be felt in the test section. Sawtooth time variations of the flap angle were used with several different amplitudes of the sawteeth. The lags determined using these data were factored into the initial guess or first iteration of the flap-angle time history.

Shock-detachment distances were also measured in the 8-Ft. TPT precalibration (precal) tests and compared with those measured on 0.22-scale bipods in the subscale tunnel experiment to determine an effective onset Mach number. In addition, measured plateau and onset pressures were used in correlation equation (1) to calculate onset Mach number as a check on the values determined from shock-detachment-distance measurements. Figures 33(a) and 33(b) are shadowgraph and schlieren photographs for a Mach number of approximately 1.6 taken in the UPWT and the 8-Ft. TPT, respectively. A corner fillet obscures the flow at the bottom of the bipod in the 8-Ft. TPT schlieren. As previously indicated, the shock-detachment distances in the 8-Ft. TPT schlieren are about 3 inches, which correspond to a

Mach number of approximately 1.6 for a half-scale bipod. The maximum Mach number attained in the 20C simulation was 1.66. This was based on plateau pressures and was roughly confirmed by schlieren photographs.

Three iterations of the flap-angle time history were necessary to achieve a satisfactory Δp_{SHOCK} simulation. (See fig. 34). The first iteration shown in figure 34 yielded a Δp_{SHOCK} pulse that was much too broad with a maximum Δp_{SHOCK} of 3.63. The second iteration gave rise to the Δp_{SHOCK} pulse that was only slightly too broad but did not reach the desired Δp_{SHOCK} of 3.78. The broadness of Δp_{SHOCK} pulses was attributed, in part, to the inadequacy of the diffuser-flap drive motors to move the flap back out into the high-dynamic-pressure flow at the required rate. The third iteration in figure 34 was formulated with the hope that by bringing the flap back closer to the wall (between 85 and 90 seconds) and into the low-energy boundary layer, it would move away with more momentum and, consequently, maintain the desired rate of flap deflection through the higher flap angles. The desired width or broadness of the pulse was roughly maintained, but the maximum Δp_{SHOCK} achieved was higher than required. No further improvements were attempted because of schedule commitments.

As noted in the key of figure 35, the data obtained in the tunnel simulations were translated 3.5 seconds in order to provide the best fit to the Δp_{SHOCK} pulse. It was not necessary to modify the flap time history to adjust for this lag, since the primary concern was to have a realistic Δp_{SHOCK} pulse during each load cycle. It should also be pointed out that the Δp_{SHOCK} values plotted in figure 35 were derived using an onset Mach number based on the average shock-detachment distances measured from schlieren photographs for six of the early load cycles. A plot of this average curve is given in figure 36 and confirms that a maximum Mach number of approximately 1.66 was obtained.

Concern for the location of the bow shock on the panel ahead of the half-scale bipod was noted previously. A hydraulic ram was provided to translate the half-scale bipod in order to have its shock location match that of a full-scale bipod for as long as possible. The most complete match would have required the half-scale bipod to be moved forward of its normal position early in the Δp_{SHOCK} pulse; however, the unsteady-pressure levels just ahead of the bipod were found to be extremely high ($\sim$172 dB), even though they dropped off rapidly. Therefore, it was decided not to move the bipod ahead of its normal position and put an unrealistically high load on those tiles immediately ahead of the bipod. Once the maximum Mach number was reached and the bow shock reached its most rearward position, with the bipod fixed, the bipod was translated rearward to keep the shock moving toward the rear, similar to flight, for as long as possible. The bipod was translated 2 inches (4 inches out of the 6 inches available was originally allotted to a planned forward translation) over a period of about 16 seconds and remained there for the remainder of the load cycle (fig. 37).

The variations of bow-shock location with time for six load cycles, relative to the position of the face of the fixed full-scale bipod, are bounded by the shaded band in figure 38. The data from seven of the earlier runs have been plotted at 3.5 seconds later, which is the same translation as that for the Δp_{SHOCK} pulse in

figure 35. At times near 90 seconds, where Δp_{SHOCK} is a maximum, the STS-1 curve and the experimental band cross. Overall, the agreement is good considering the limited translation employed.

Panel 20C was tested for 25 missions (100 cycles) using the setup described previously. At the start of the 26th mission, one of the supports of the top-wall nozzle fairing gave way. A number of attempts were made to resore the wall to its original configuration without tearing it down, but they were not successful. Finally, a new and more substantial top wall was installed; a number of unsuccessful adjustments were made in striving to achieve the performance of the original wall. In all, 14 missions (56 cycles) were run at maximum onset Mach numbers from 1.5 to 1.55 as various adjustments were made to the top wall. All the tests of panel 20C were carried out at a tunnel stagnation pressure of 1.0 atm.

UNSTEADY-PRESSURE ENVIRONMENTS

The severe bow-shock-induced unsteady pressures on panel 20C are peculiar to configurations with attachment structures nearly normal to the flow. These pressures are not as well understood. Overall fluctuating pressure level (OFPL) data obtained in an investigation by Hanly (ref. 7) on a 0.035-scale model of the Shuttle ascent vehicle denoted (IS-2) provided the first quantitative results for the bipod area. Indeed, these data provided much of the justification for the panel 20C test.

Sound pressure levels encountered in front of the bipod on panel 20C are plotted in figure 39. Also shown are data points from the IS-2 tests and the STS-1 flight. Panel 20C and the IS-2 data indicate that the highest values of unsteady pressure are immediately ahead of the bipod and fall off rapidly with increasing distance from the bipod face. Ahead of the flow-separation line, which is roughly 24 inches ahead of the bipod face for a half-scale bipod, sound-pressure levels are negligible. The points taken from the IS-2 tests (complete model tests) show a lower OFPL away from the bipod, which probably is a reflection of the differences in local dynamic and static pressure (fig. 19) between the CLOT test and the full-scale bipod in flight. Also, the interaction of the oblique shock with the separated-flow wedge (fig. 6) gives rise to high sound-pressure levels. Since the oblique shock in the CLOT tests is much stronger than that for STS-1 because of the higher stagnation-pressure levels, the sound-pressure levels near the separation line tend to be higher than those for STS-1 in the same location. As noted in previous discussions (fig. 20), the separation zone and the associated oblique shock for a full-scale bipod would be much further forward on the panel than that for the half-scale bipod. Only one data point is available in this region from STS-1, and it is about 13 inches ahead of the bipod face. It is about 2 dB lower than the precal panel results.

The test panel for configuration 20C had a surface Kulite gage placed about 1 inch ahead of the bipod and a fraction of an inch off the centerline. Maximum rms pressure levels from a number of runs range from 170 to 173 dB, which is in qualitative agreement with the precal panel results. The IS-2 point plotted at $x = 3$ inches may be in better agreement with the CLOT results than is readily apparent if the averaging effect that the gage has in a high gradient flow is considered. The diameter of the Kulite gages used on the IS-2 model, when scaled to full-scale dimensions, is approximately 6 inches.

Generally, it is felt that close to the bipod, say the first 8 to 10 inches, the CLOT environment was a good simulation of that provided by the STS-1 nominal trajectory. Further away, the rms pressure levls are 3 to 4 dB too high and correspond more to the tile design-load levels rather than to those encountered in the nominal STS-1 trajectory. More details on the vibroacoustic and buffet simulations for panel 20C are contained in a paper by Schuetz, et al (ref. 8).

CONCLUDING REMARKS

The present paper describes the procedures and equipment used to provide a realistic time-varying environment for arrays of Shuttle tiles bonded to structures which accurately duplicate those on the Shuttle. Special problems which were encountered because of the blockage of the bipod and the high Mach numbers required for panel 20C were overcome with the aid of correlations of data from additional supporting tunnel tests. The panel was subjected to at least 100 load cycles with no apparent structural degradation. Since panel 20C tests were first-flight critical, it was particularly gratifying during the tests that, after one Shuttle mission (4 load cycles), the panel appeared to be flawless.

Several "lessons learned" from this study appear to be worthy of note: For example, the maximum aerodynamic loads and acoustic pressures in the vicinity of attachment structures, ramps, cones, and forward-facing steps may well occur at supersonic speed rather than the customary highest free-stream dynamic pressure conditions which occur at transonic speed. The flows in these regions tend to be characterized by high pressures and severe pressure gradients. Therefore, the resolution of pressure data in areas where there are attachment structures, etc., must be considerably higher than those data requirements for determining structural loads in uncluttered relatively flat areas. Definition of the flow in vicinity of these protuberance-type geometries can be carried out through localized testing if the tests are based on appropriate local flow conditions approaching the protuberance which can be significantly different from the corresponding free-stream conditions. It has been demonstrated that these localized tests can be scaled to a variety of other conditions required for either flight or wind-tunnel simulations and although not essential to success, good correlations of these data can be invaluable scaling aids, particularly when establishing dynamic simulations such as the 8-Ft. TPT tests described in this paper.

REFERENCES

1. Bobbitt, Percy J.; Edwards, C. L. W.; and Barnwell, Richard W.: Simulation of Time-Varying Ascent Loads on Arrays of Shuttle Tiles in a Large Transonic Wind Tunnel. NASA TM-84529, November 1982.

2. Price, Earl A., Jr. and Stallings, Robert L., Jr.: Investigation of Turbulent Separated Flows in the Vicinity of Fin-Type Protuberances at Supersonic Mach Numbers. NASA TN D-3804, February 1967.

3. Ames Research Staff, Equations, Tables and Charts for Compressible Flow, NACA Rep. 1135, 1953.

4. Li, T. Y. and Geiger, R. E.: Stagnation Point of a Blunt Body in Hypersonic Flow. Journal of Aeronautical Sciences, Vol. 24, No. 1, January 1957, pp 25-32.

5. Coe, Charles F.: Buffet Loads on Shuttle Thermal-Protection-System Tiles. Shock & Vib. Bull., Bull. 52, Pt. 2, U.S. Dep. Def., May 1982, pp 147-155.

6. Rummler, Donald R. and Pinson, Larry D.: Static Calibration for Measurement of Loads in Wind Tunnel Tests on Shuttle Surface Tiles. A Collection of Technical Papers - AIAA/ASME/ASCE/AHS 23rd Structures, Structural Dynamics and Materials Conference, Part 1, May 1982, pp 374-380. (Available as AIAA-82-0754).

7. Hanly, Richard D.: Surface-Pressure Fluctuations Associated With Aerodynamic Noise on the Space Shuttle Launch Configuration at Transonic and Supersonic Speeds. Proceedings - AIAA/ASME/SAE 17th Structures, Structural Dynamics and Materials Conference, May 1976, pp 241-247.

8. Schuetz, P. H.; Pinson, L. D.; and Thornton, H. T., Jr.: Unsteady Environments and Responses of the Shuttle Combined Loads Orbiter Test. Shock & Vib. Bull., Bull. 52, Pt. 2, U.S. Dep. Def., May 1982, pp 157-163.

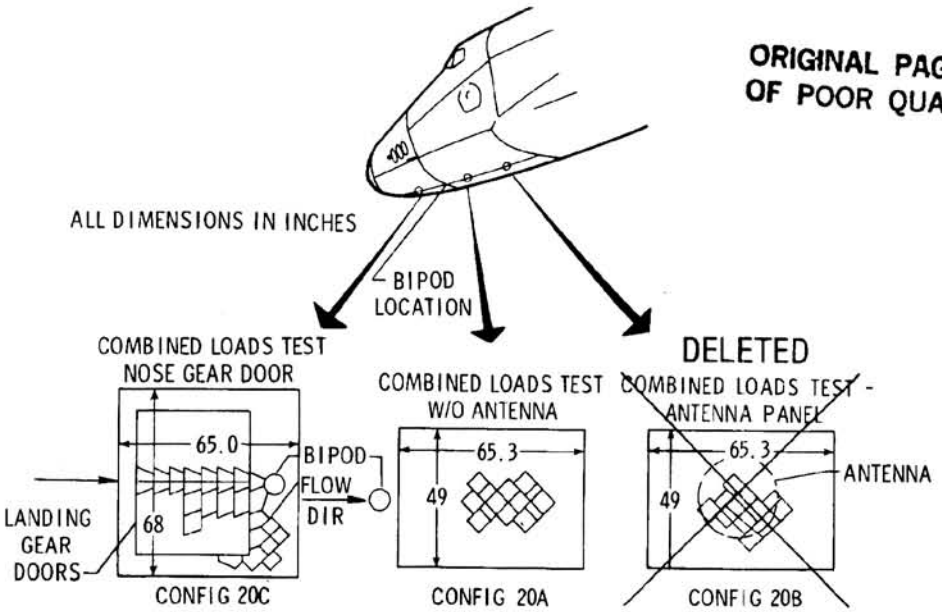

Figure 1.- Sketches showing locations and dimensions of panel configurations 20A, 20B, and 20C.

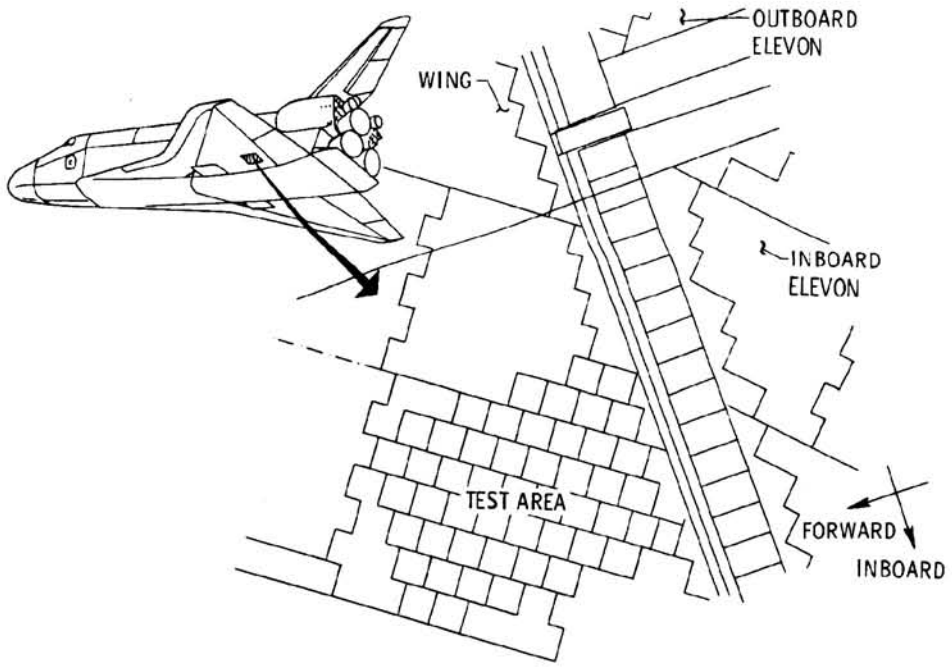

Figure 2.- Sketch showing location of panel 20D.

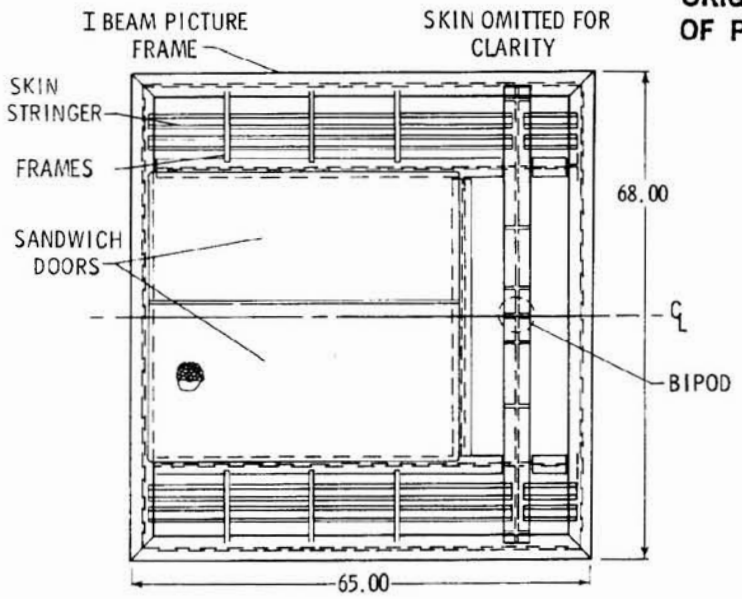

Figure 3.- Structural features of panel 20C.
All dimensions are in inches.

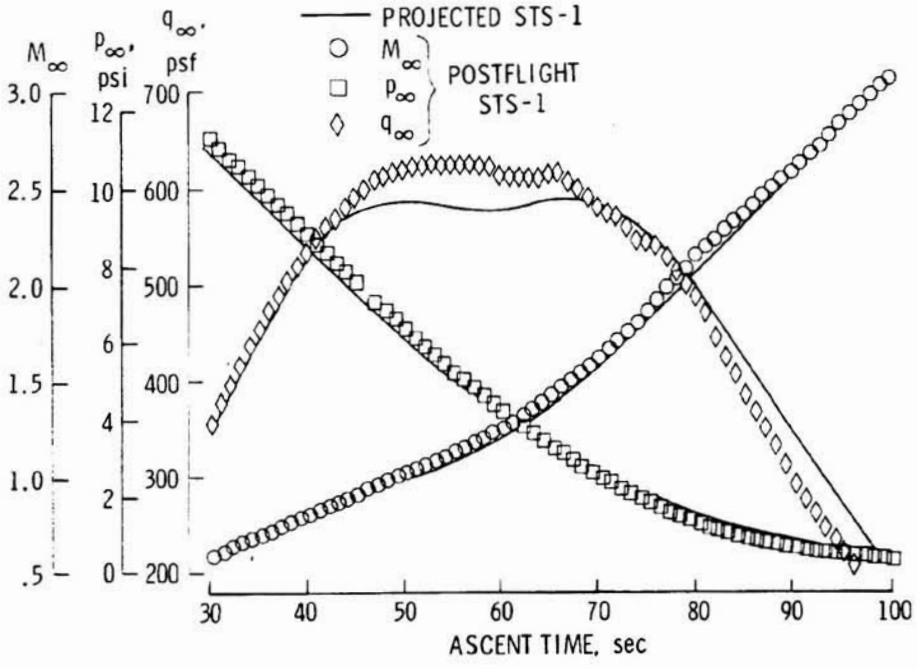

Figure 4.- Variation with time of free-stream Mach number, static pressure, and dynamic pressure for nominal STS-1 trajectory.

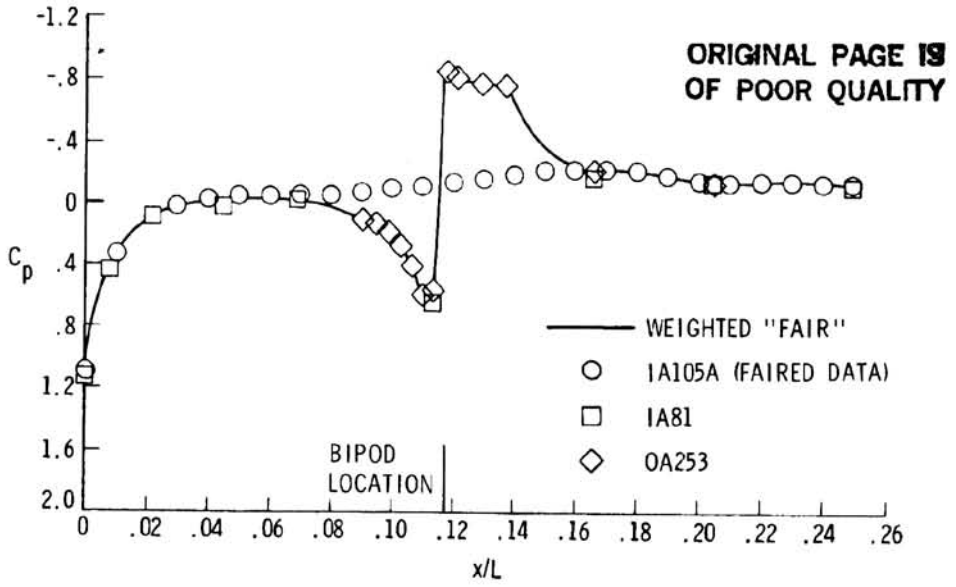

(a) $M_\infty = 0.60$.

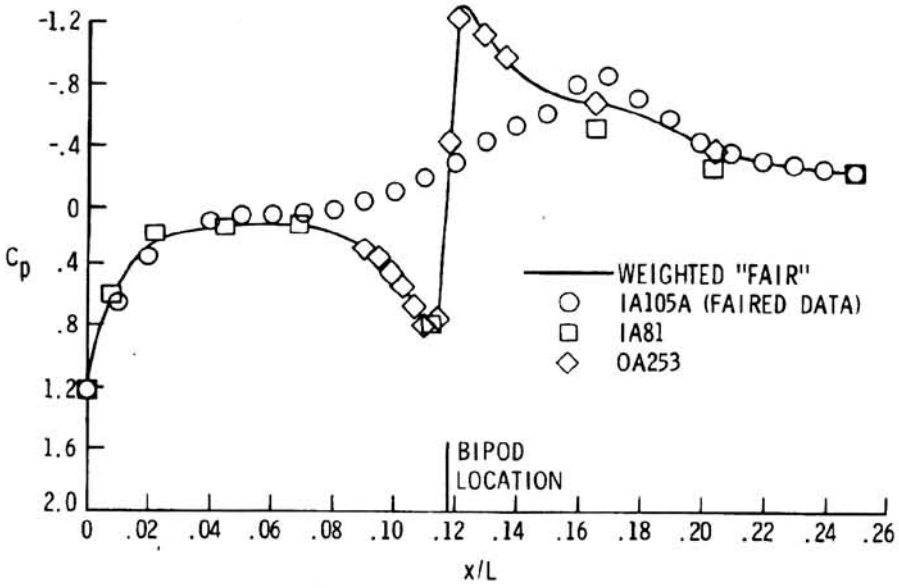

(b) $M_\infty = 0.90$.

Figure 5.- Longitudinal variations of pressure along centerline of Shuttle for four Mach numbers.

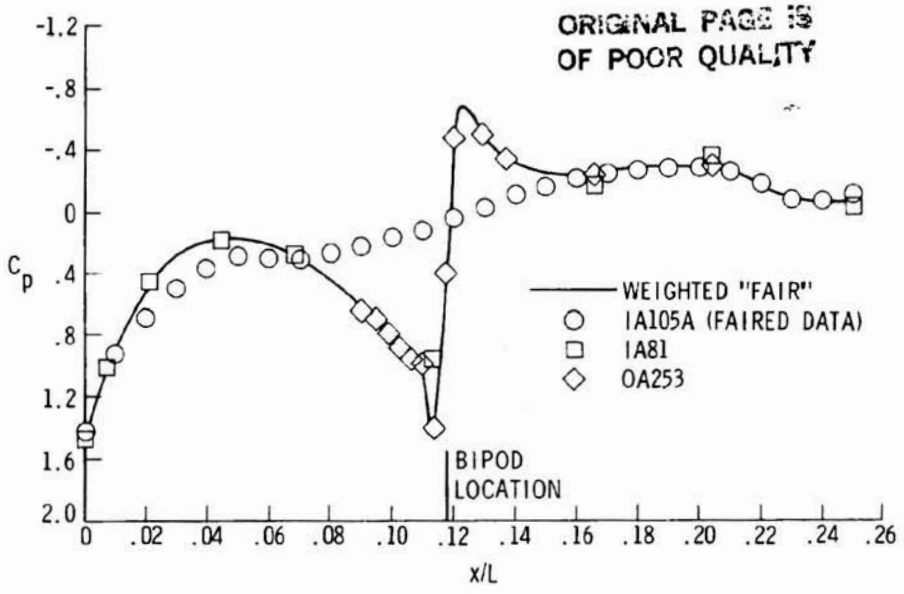

(c) $M_\infty = 1.25$.

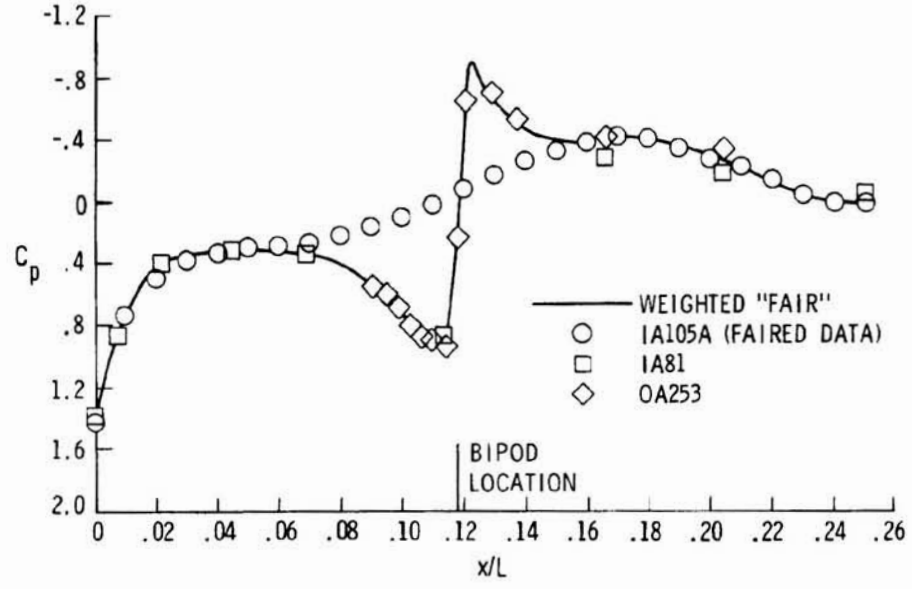

(d) $M_\infty = 1.40$.

Figure 5.- Concluded.

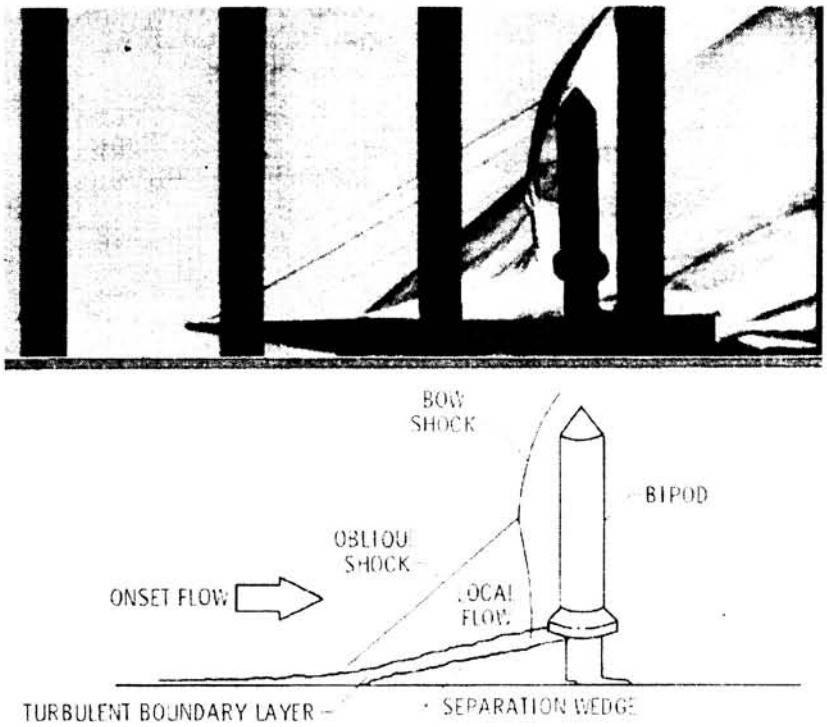

Figure 6.- Sketch and shadowgraph showing features of flow ahead of bipod.

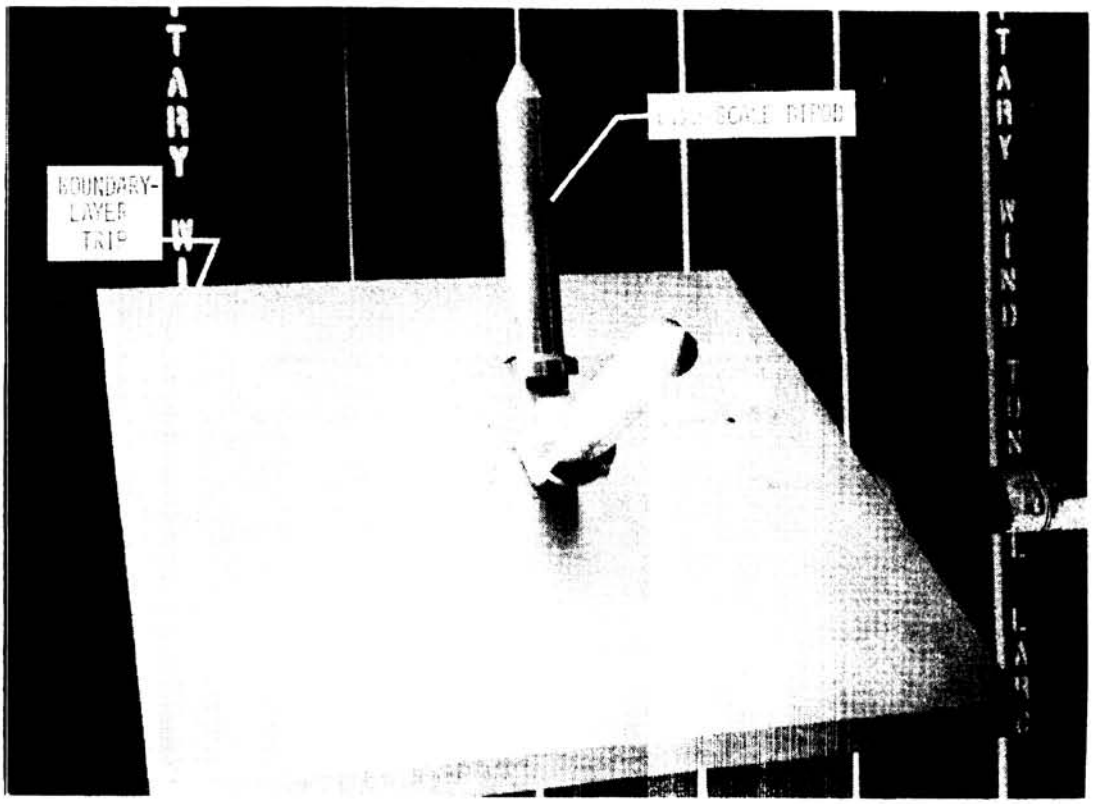

Figure 7.- The 0.22-scale bipod mounted on flat plate used in supersonic Mach number tests in UPWT.

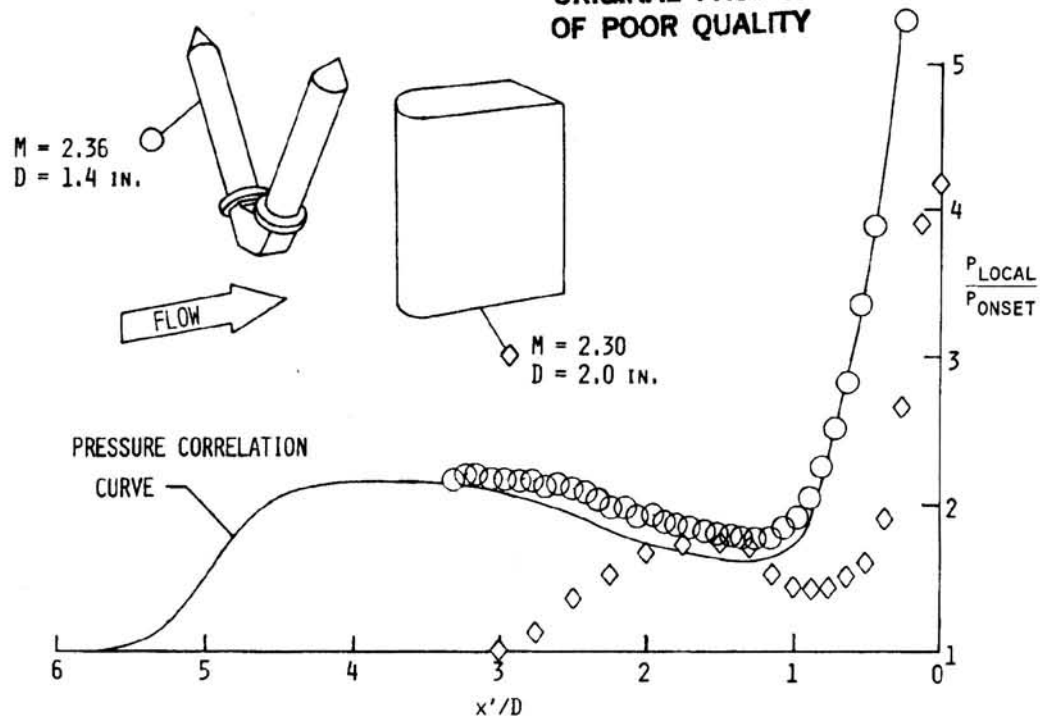

Figure 8.- Comparison of pressure interaction ahead of vertical cylinder and subscale Shuttle bipod.

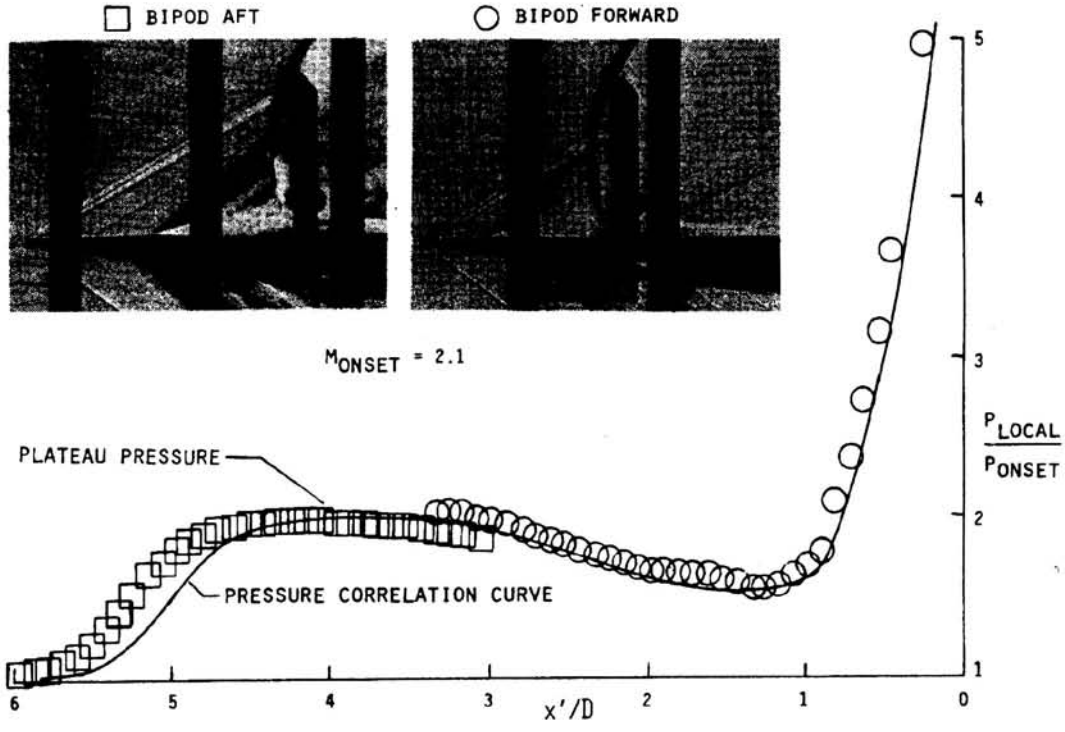

Figure 9.- Typical pressure distribution ahead of Shuttle bipod at supersonic Mach number corresponding to maximum bow shock pressure rise.

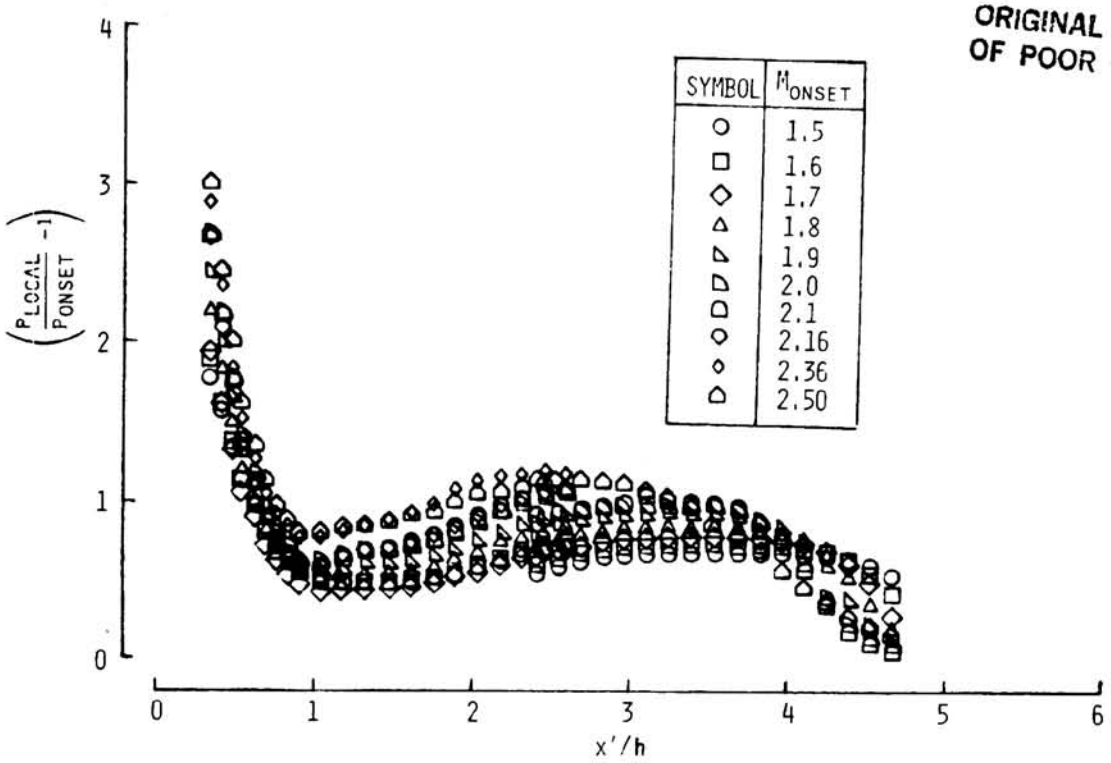

Figure 10.- Centerline pressure distributions ahead of Shuttle bipod over test range of supersonic Mach numbers in UPWT.

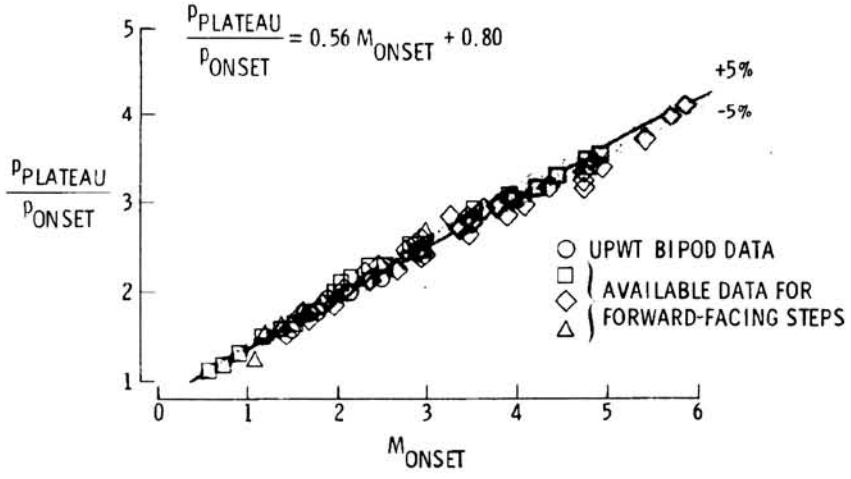

Figure 11.- Variation of ratio of $P_{PLATEAU}$ to P_{ONSET} with M_{ONSET} including comparison of empirical expression with experimental data.

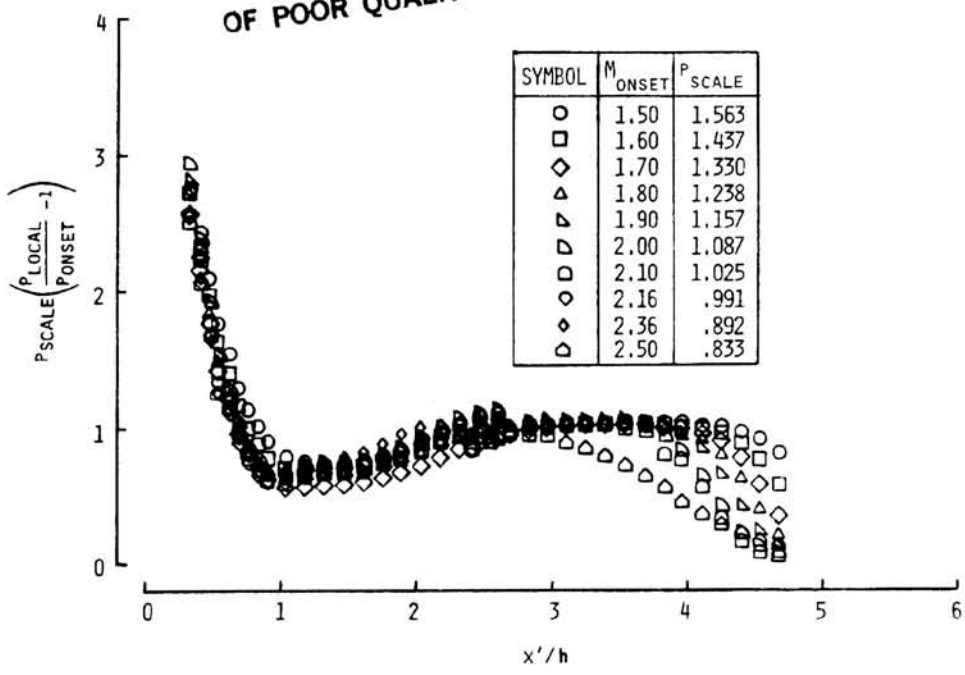

Figure 12.- Variation of nondimensional correlated centerline pressure with distance for M_{ONSET} = 1.5 to 2.5.

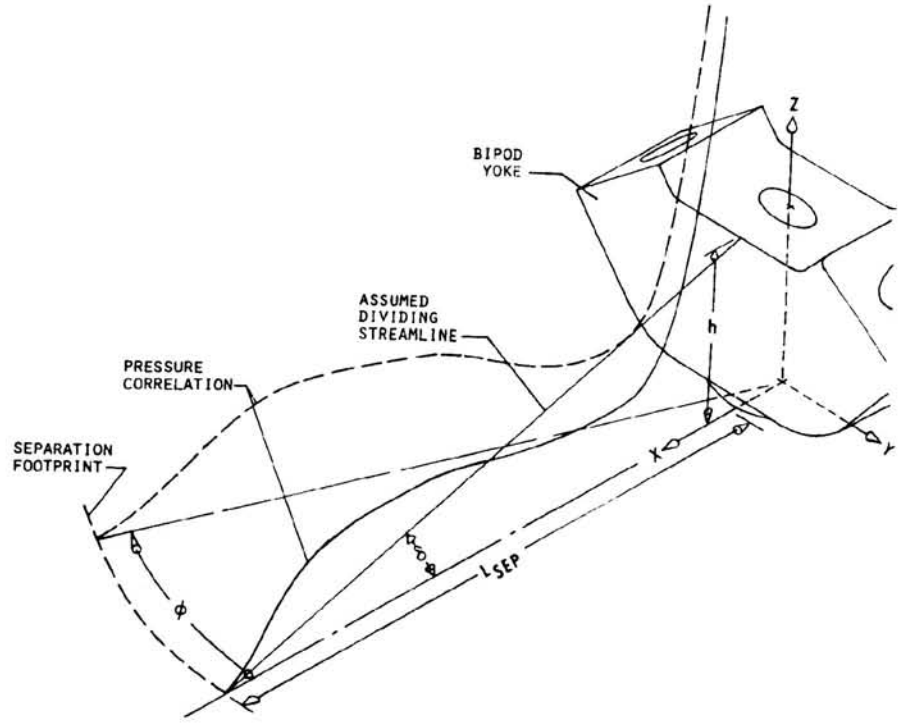

Figure 13.- Parameters correlating extent of separation ahead of Shuttle bipod at supersonic Mach numbers.

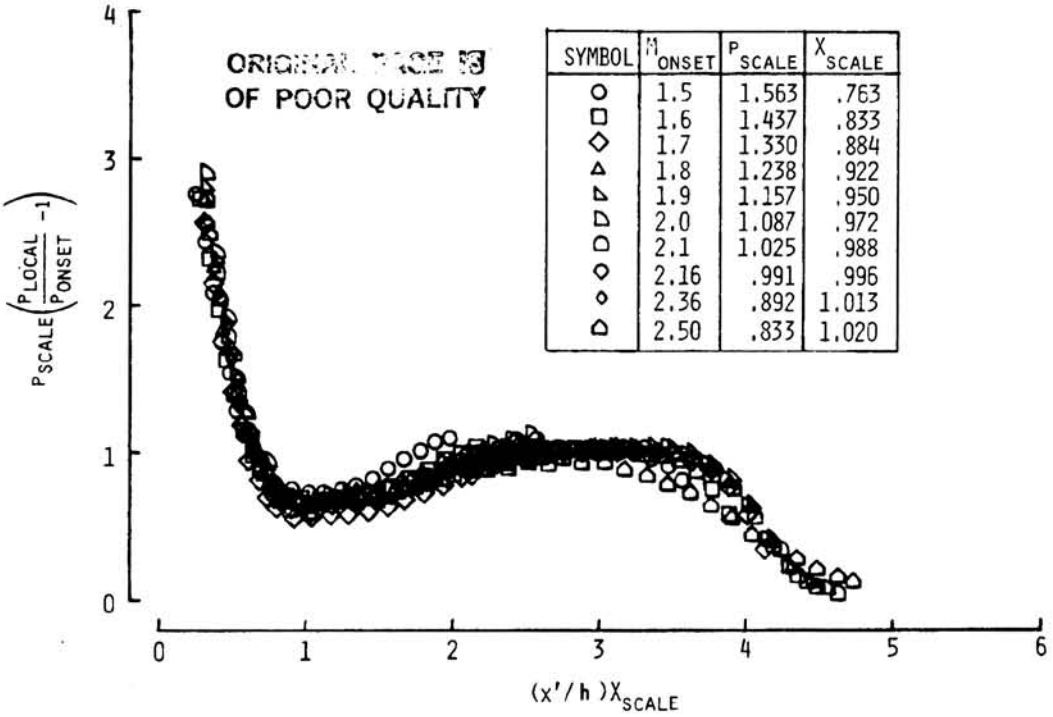

Figure 14.- Correlated variation of nondimensional pressure with nondimensional distance ahead of bipod for M_{ONSET} = 1.5 to 2.5.

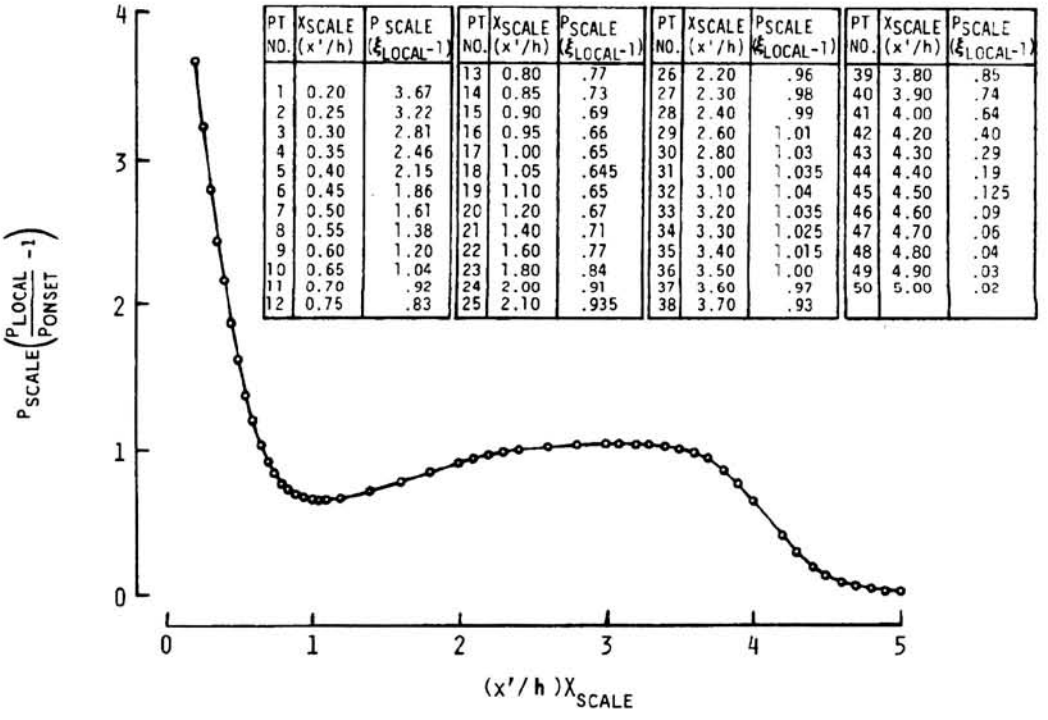

PT NO.	X_{SCALE} (x'/h)	P_{SCALE} (ξ_{LOCAL}-1)	PT NO.	X_{SCALE} (x'/h)	P_{SCALE} (ξ_{LOCAL}-1)	PT NO.	X_{SCALE} (x'/h)	P_{SCALE} (ξ_{LOCAL}-1)	PT NO.	X_{SCALE} (x'/h)	P_{SCALE} (ξ_{LOCAL}-1)
			13	0.80	.77	26	2.20	.96	39	3.80	.85
1	0.20	3.67	14	0.85	.73	27	2.30	.98	40	3.90	.74
2	0.25	3.22	15	0.90	.69	28	2.40	.99	41	4.00	.64
3	0.30	2.81	16	0.95	.66	29	2.60	1.01	42	4.20	.40
4	0.35	2.46	17	1.00	.65	30	2.80	1.03	43	4.30	.29
5	0.40	2.15	18	1.05	.645	31	3.00	1.035	44	4.40	.19
6	0.45	1.86	19	1.10	.65	32	3.10	1.04	45	4.50	.125
7	0.50	1.61	20	1.20	.67	33	3.20	1.035	46	4.60	.09
8	0.55	1.38	21	1.40	.71	34	3.30	1.025	47	4.70	.06
9	0.60	1.20	22	1.60	.77	35	3.40	1.015	48	4.80	.04
10	0.65	1.04	23	1.80	.84	36	3.50	1.00	49	4.90	.03
11	0.70	.92	24	2.00	.91	37	3.60	.97	50	5.00	.02
12	0.75	.83	25	2.10	.935	38	3.70	.93			

Figure 15.- Incremental pressure correlation curve for separated flow ahead of bipod derived from UPWT data.

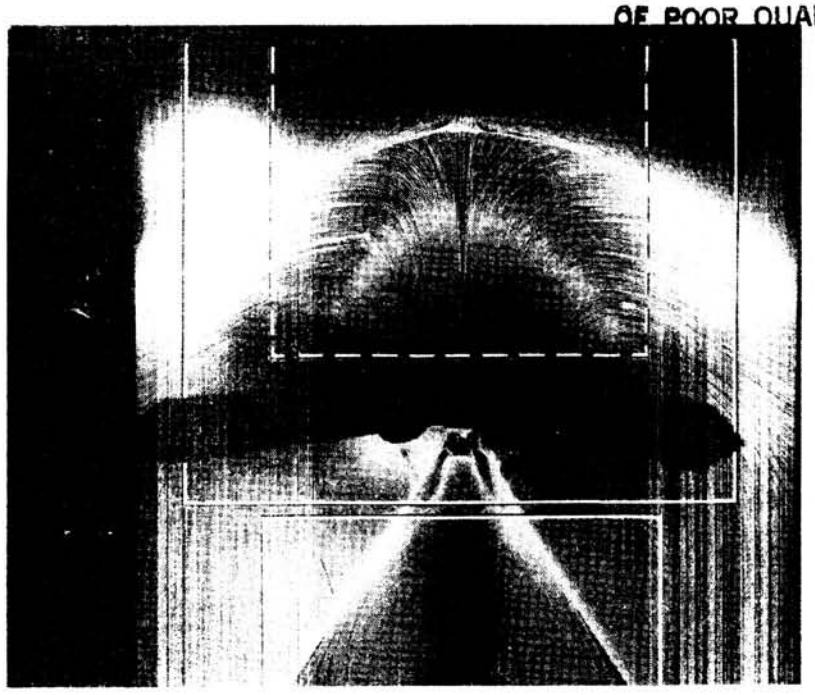

(a) $M_{ONSET} = 1.5$.

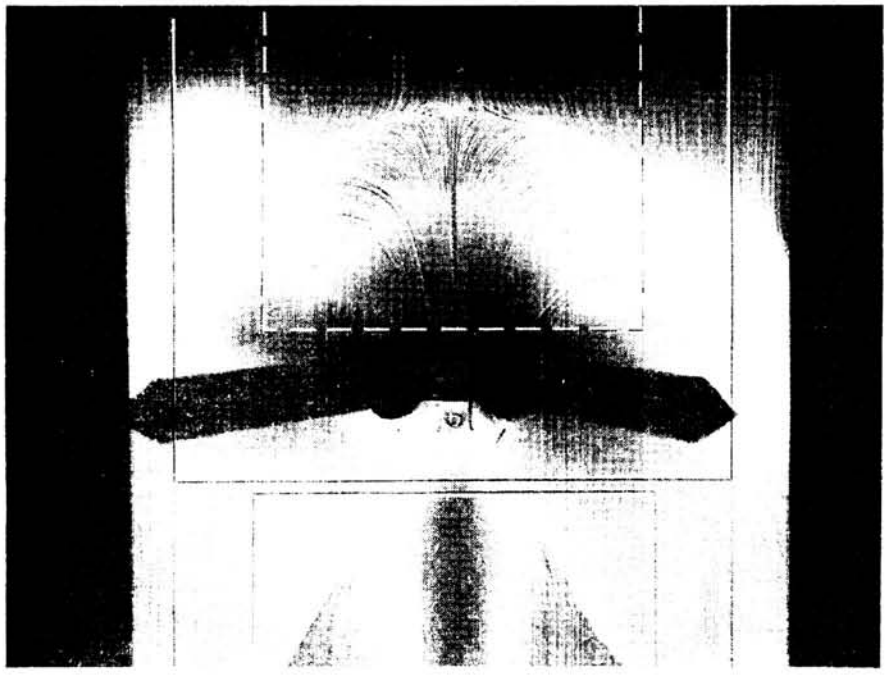

(b) $M_{ONSET} = 1.8$.

Figure 16.- Oil flow photographs used to correlate lateral characteristics of separated-flow region ahead of bipod.

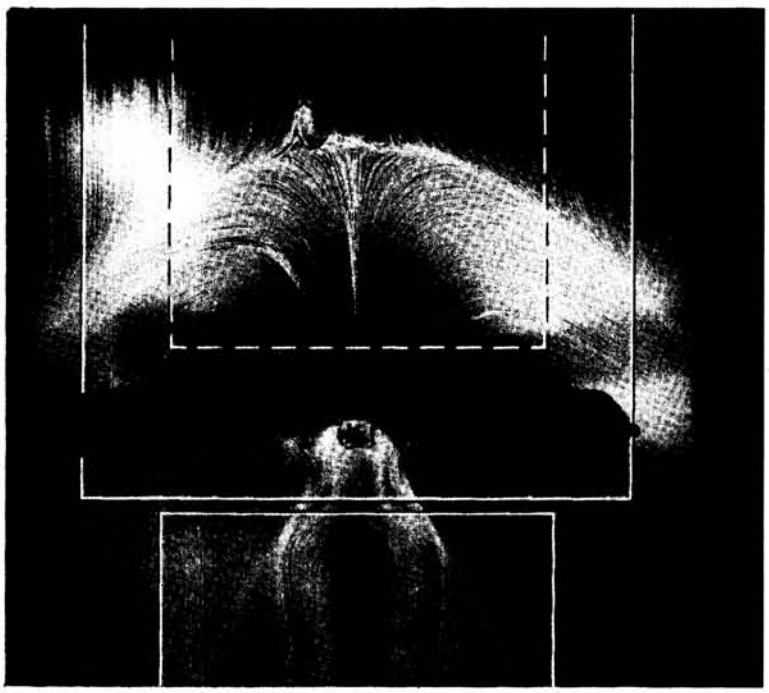

(c) $M_{ONSET} = 2.1$.

Figure 16.- Concluded.

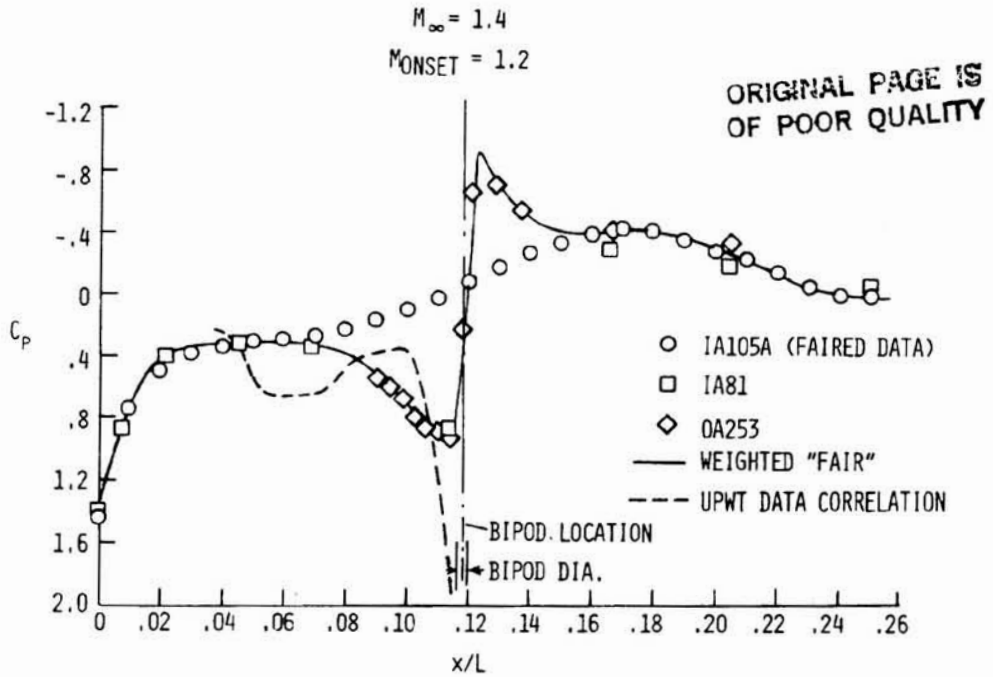

Figure 17.- Comparison of centerline pressure data on Shuttle orbiter surface in vicinity of bipod attachment structure between orbiter and external tank.

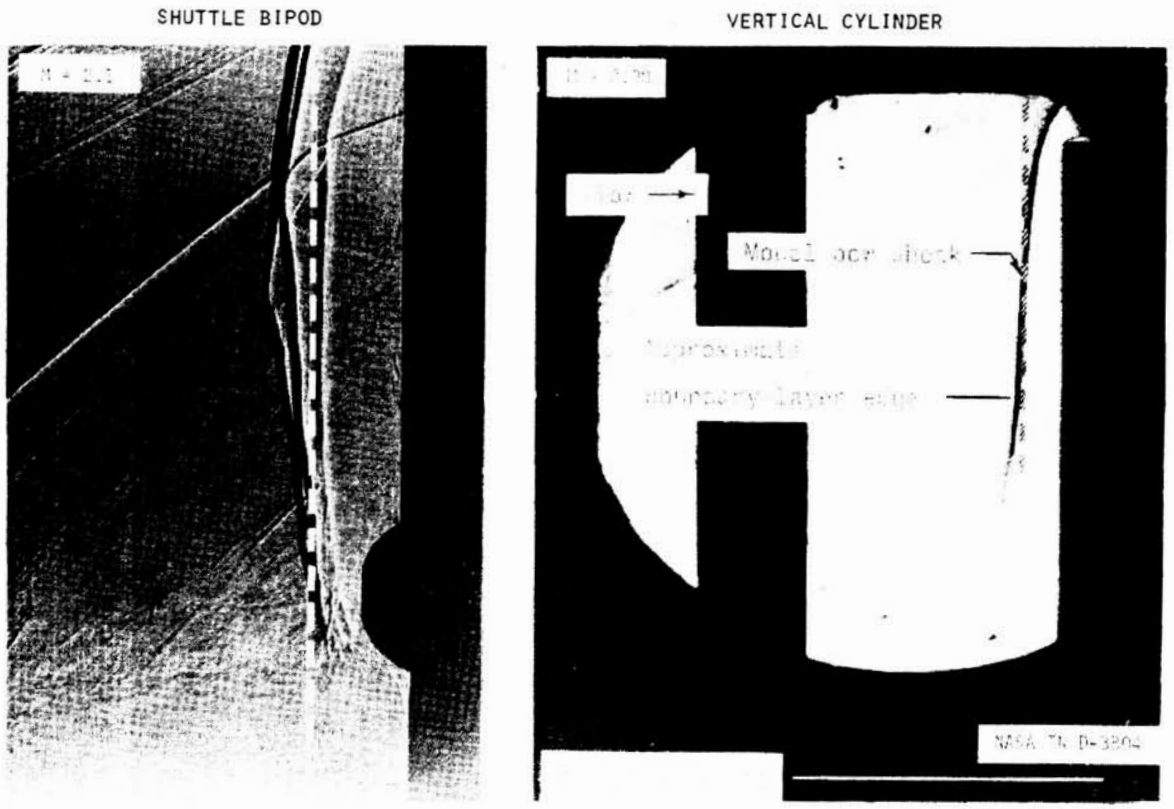

Figure 18.- Assessment of validity of shock standoff distance correlation developed from UPWT tests of 0.22-scale bipod.

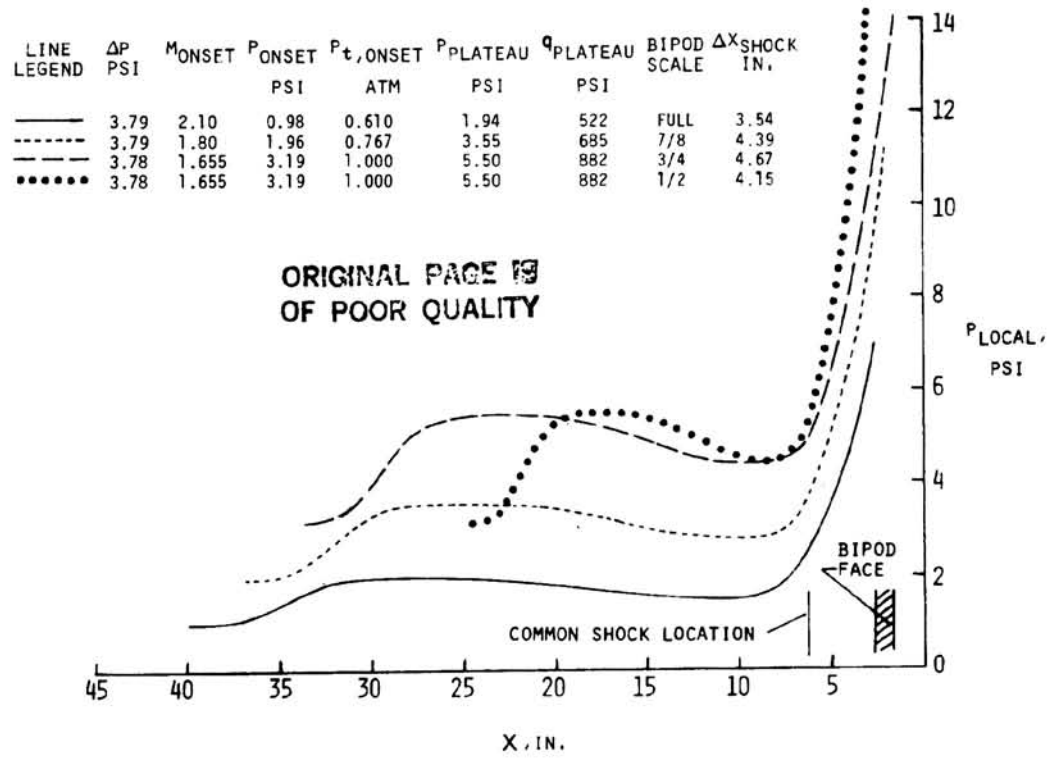

Figure 19.- Comparison of equal bow-shock-strength pressure distributions ahead of bipod, including full-scale bipod at flight condition and subscale bipods at Mach numbers corresponding to 8-Ft. TPT.

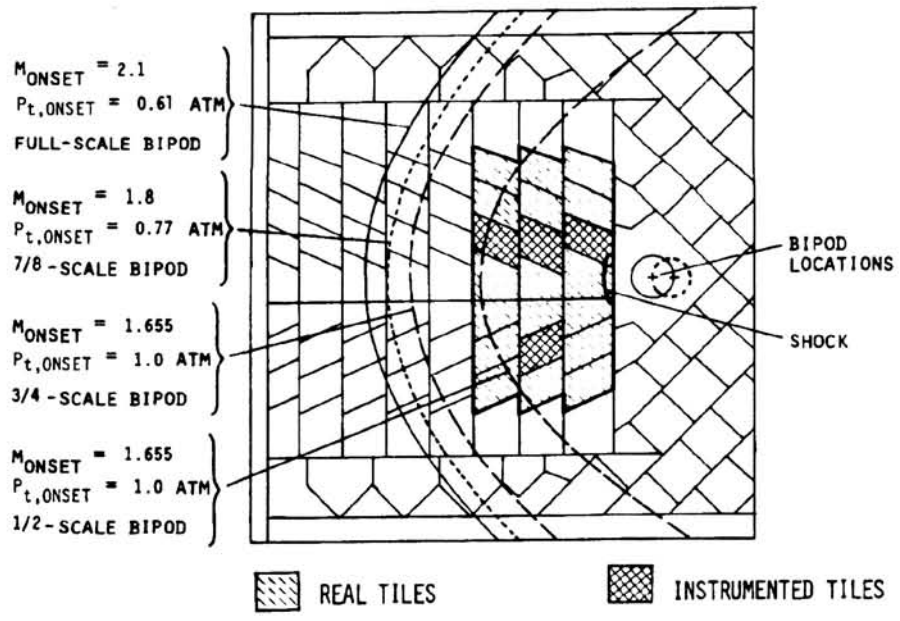

Figure 20.- Separated-flow footprints on panel 20C for various scale bipods with identical shock strengths and longitudinal locations.

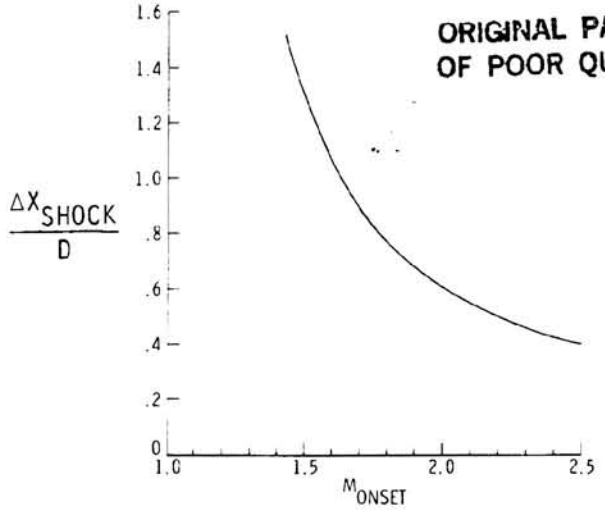

Figure 21.- Variation of detachment distance for bipod bow shock with onset Mach number.

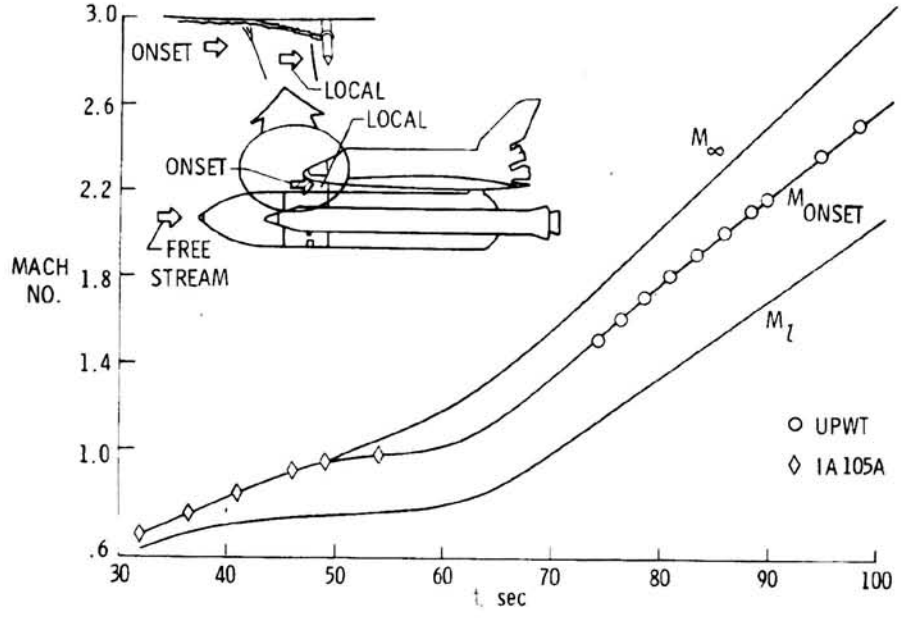

Figure 22.- Variations of free-stream, onset, and local Mach numbers with time for panel 20C simulation.

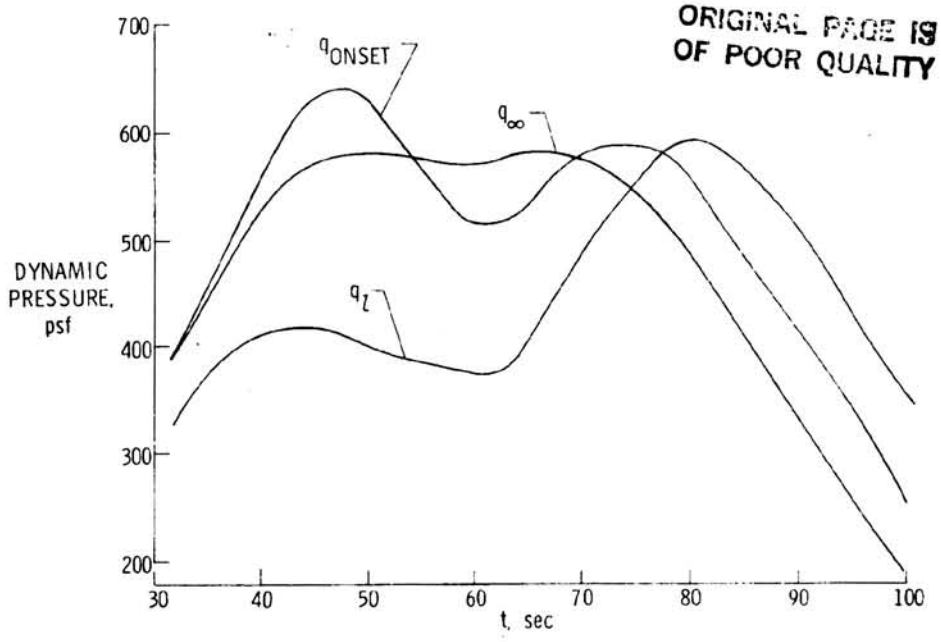

Figure 23.- Variation of free-stream, onset, and local dynamic pressures with time for panel 20C simulation.

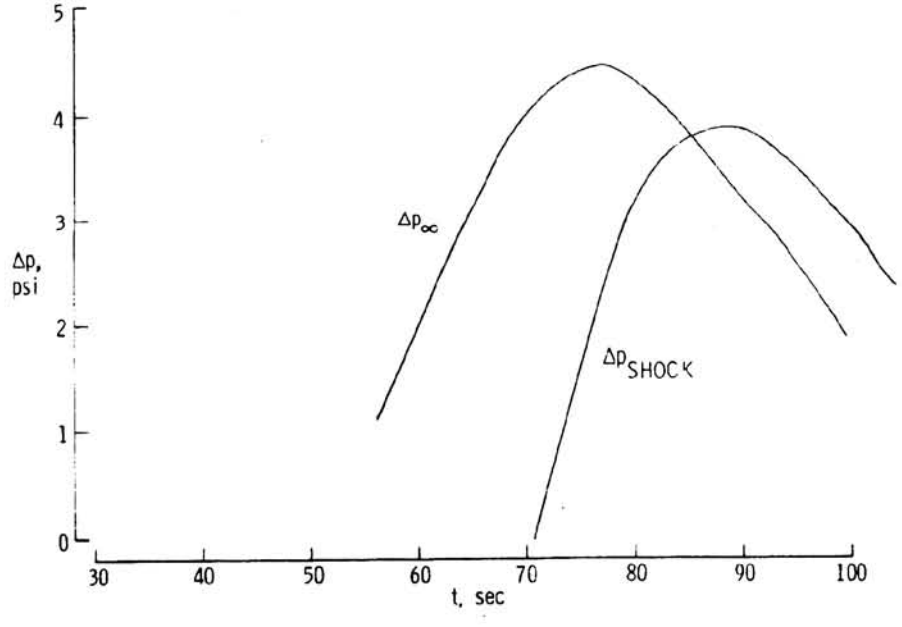

Figure 24.- Variation of pressure jump across bipod bow shock with time compared with that for a normal shock with free-stream onset conditions.

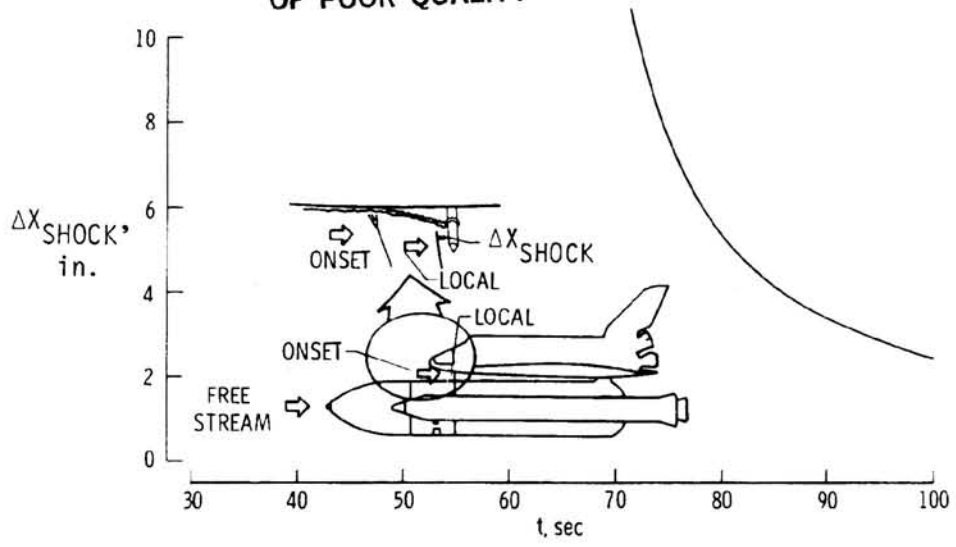

Figure 25.- Variation of bow-shock detachment distance with time for STS-1.

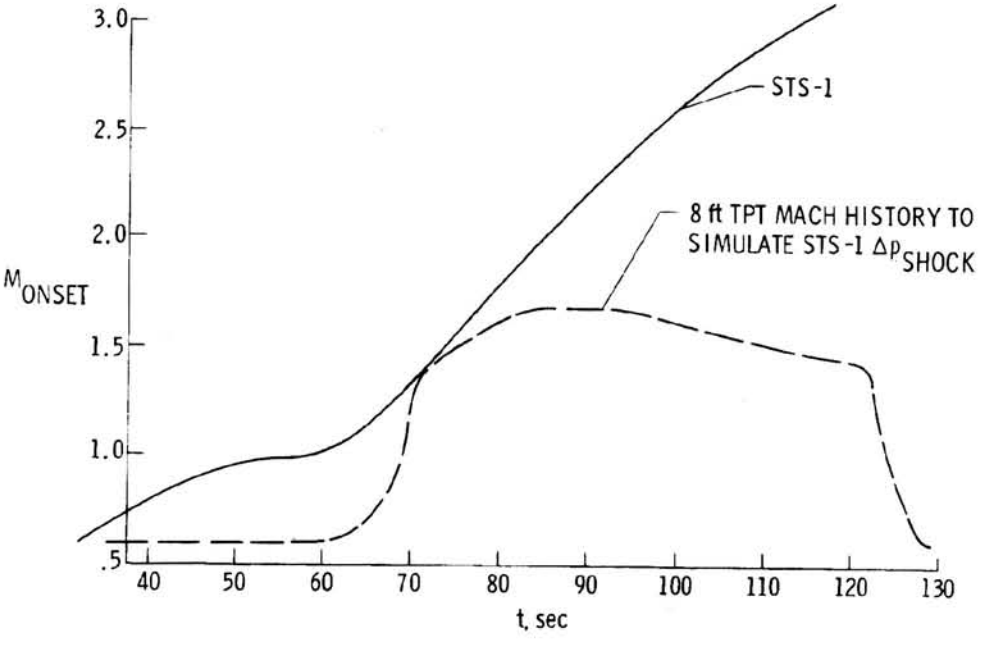

Figure 26.- Time variation of STS-1 onset Mach number compared with that required in 8-Ft. TPT simulation to match STS-1 bow-shock pressure jumps.

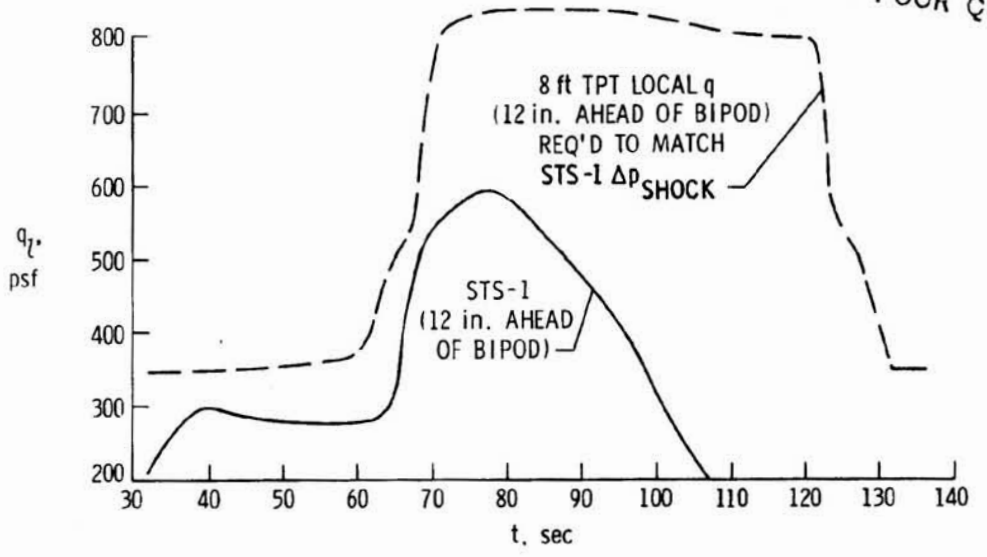

Figure 27.- Comparison of time variations of dynamic pressure at point 12 in. ahead of full-scale bipod for STS-1 trajectory with that 12 in. ahead of half-scale bipod in 8-Ft. TPT when simulating STS-1 Δp_{SHOCK} time history.

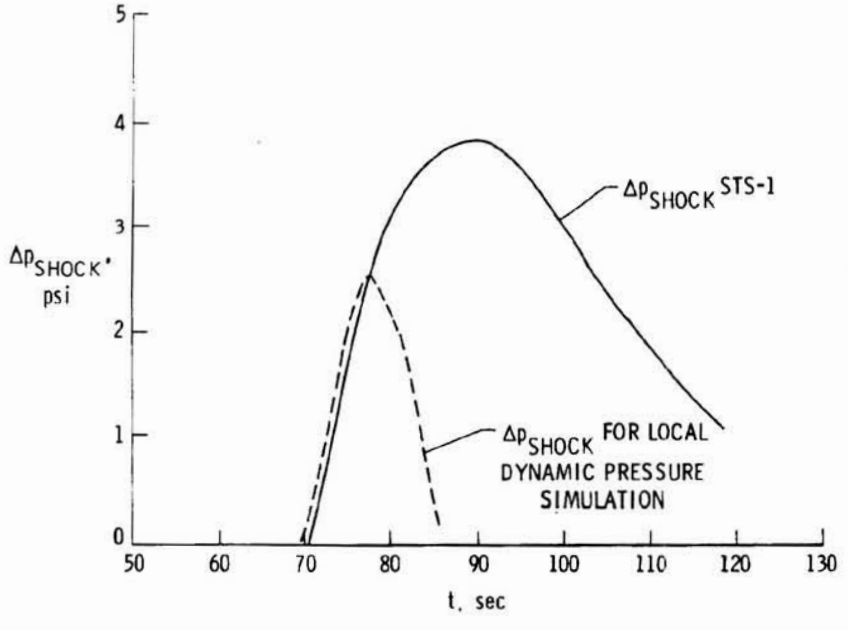

Figure 28.- Shock-pressure jump versus time for STS-1 trajectory and for 8-Ft. TPT when simulating time variation of point dynamic pressure q_l.

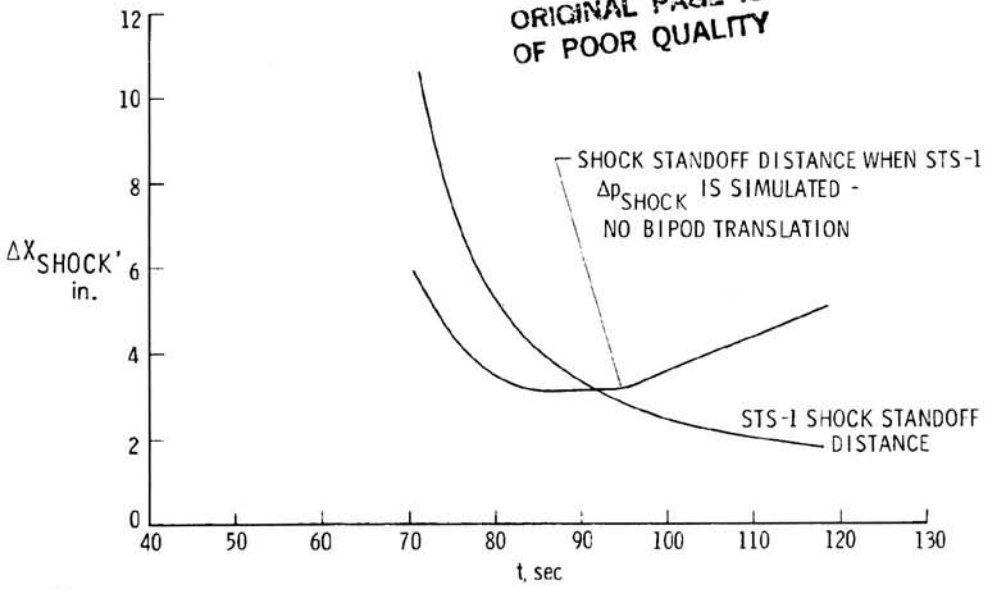

Figure 29.- Variation of shock standoff distance for STS-1 trajectory with time compared with that for fixed half-scale bipod in 8-Ft. TPT during simulation of STS-1 Δp_{SHOCK} time variations.

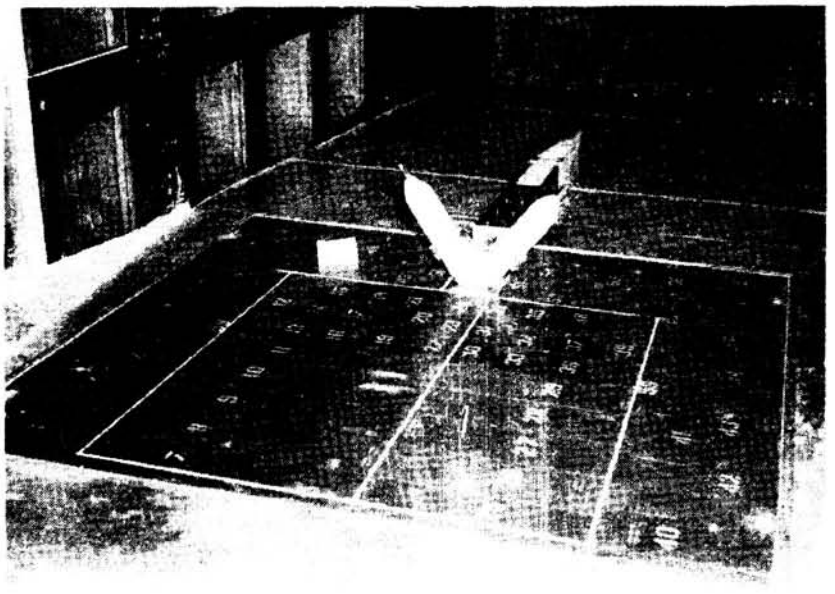

Figure 30.- Photograph of panel 20C installed in false floor in 8-Ft. TPT test section.

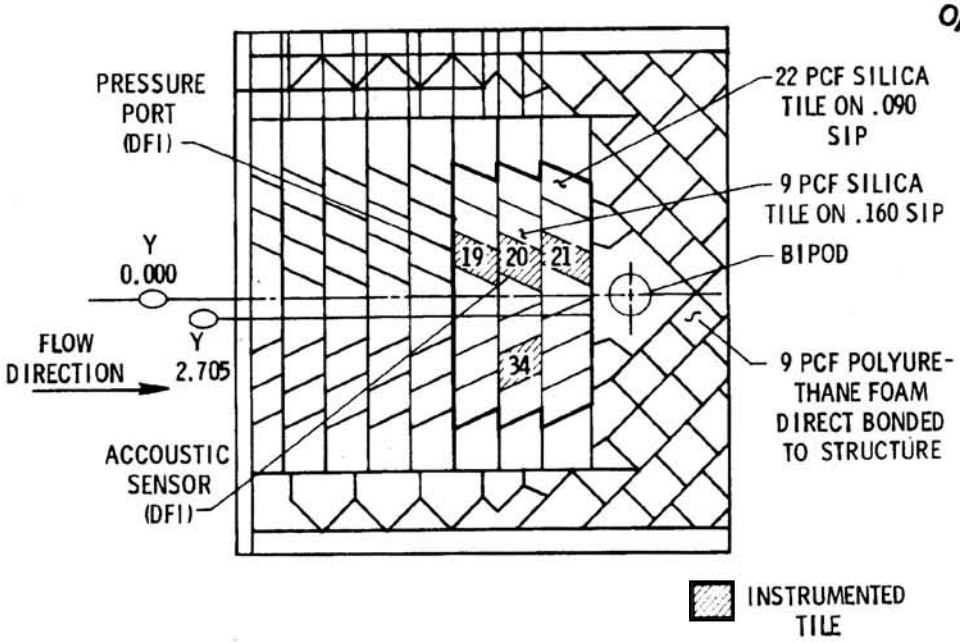

Figure 31.- Sketch showing location of instrumented tiles and types of tiles installed on test panel for configuration 20C.

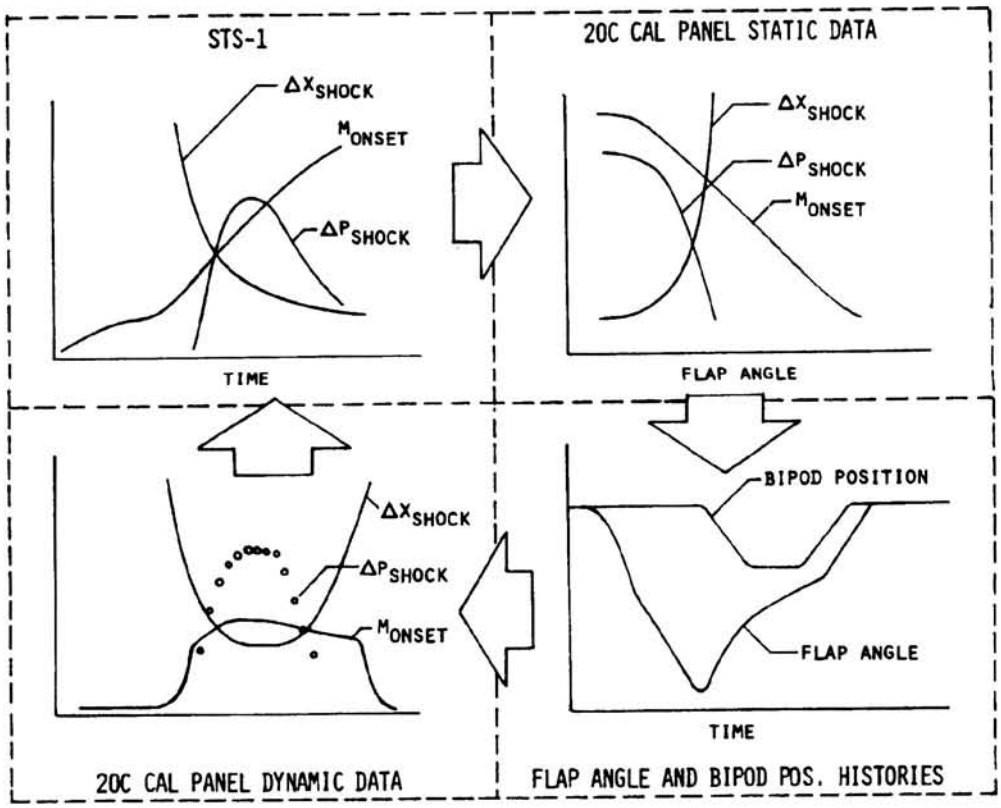

Figure 32.- Schematic illustrating steps required to simulate STS-1 time variations of bow-shock-induced pressures and shock standoff distances for panel 20C.

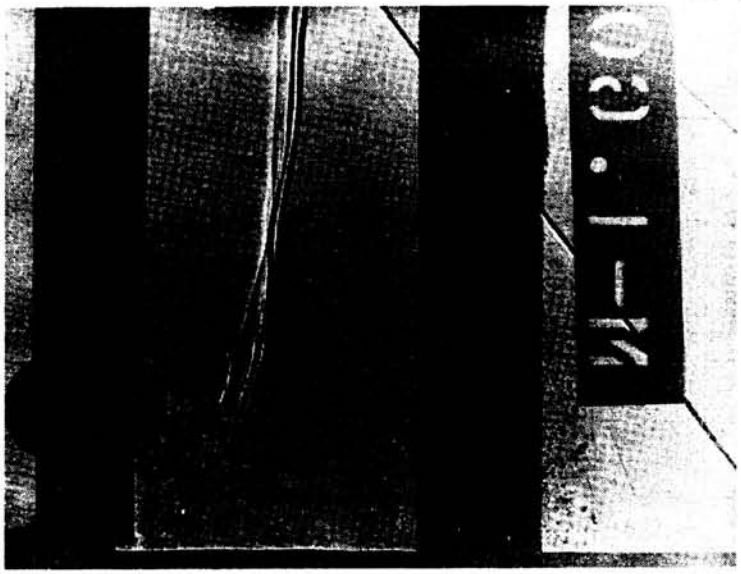

(a) Langley Unitary Plan Wind Tunnel.

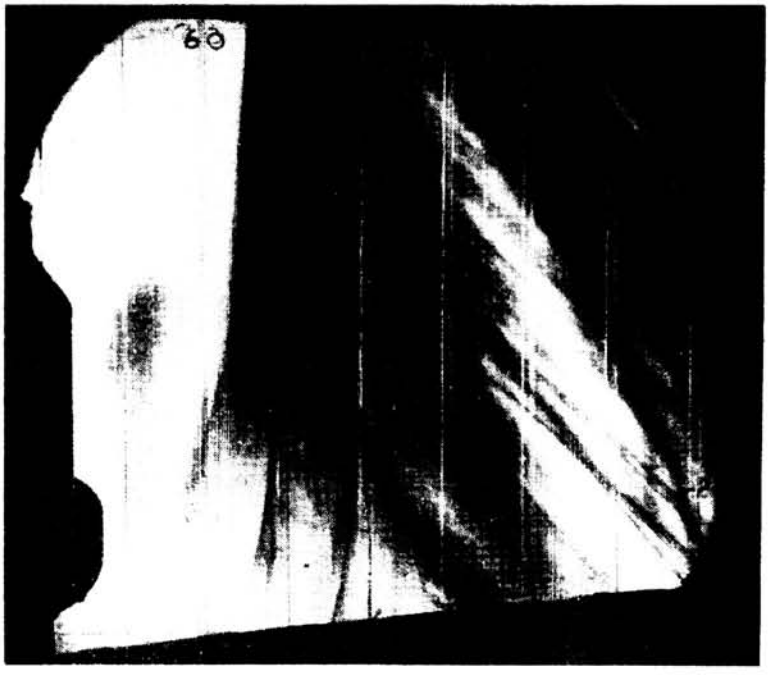

(b) Langley 8-Foot Transonic Pressure Tunnel.

Figure 33.- Shadowgraph and schlieren photographs from UPWT and 8-Ft. TPT at Mach number of approximately 1.6.

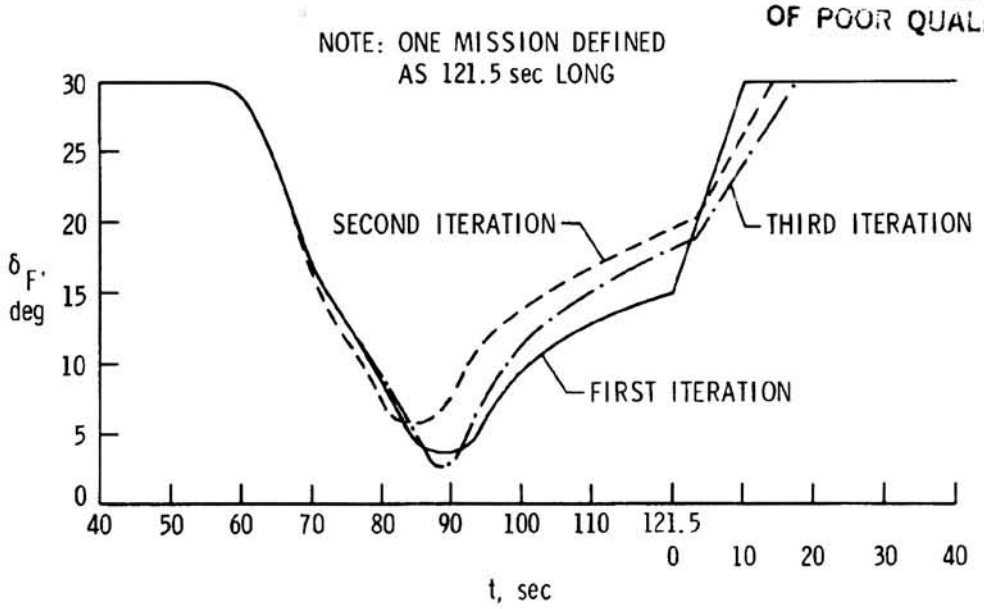

Figure 34.- Time variations of diffuser-flap angle for three iterations attempted.

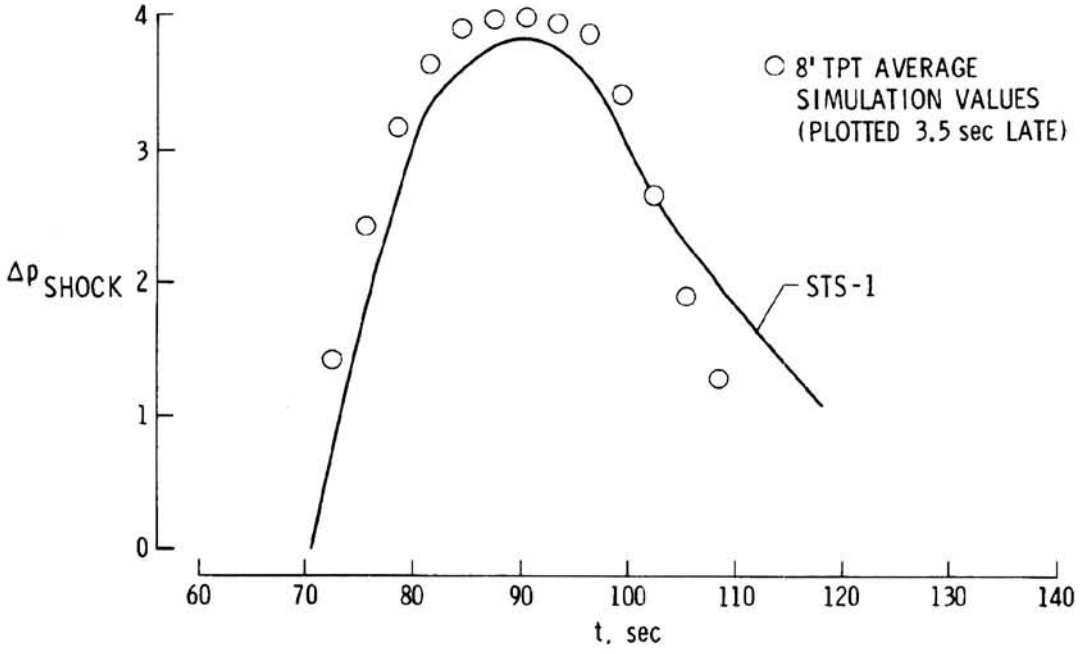

Figure 35.- Variations of bow-shock pressure jump Δp_{SHOCK} with time for STS-1 and for 8-Ft. TPT simulation.

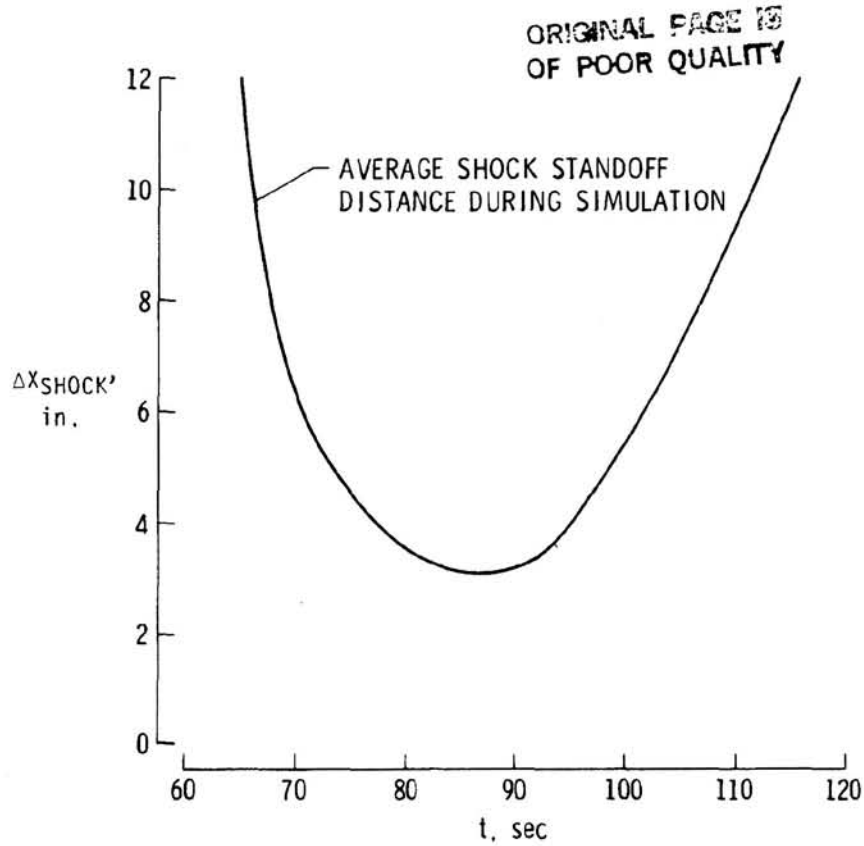

Figure 36.- Variation of average shock-detachment distance with time based on six load cycles.

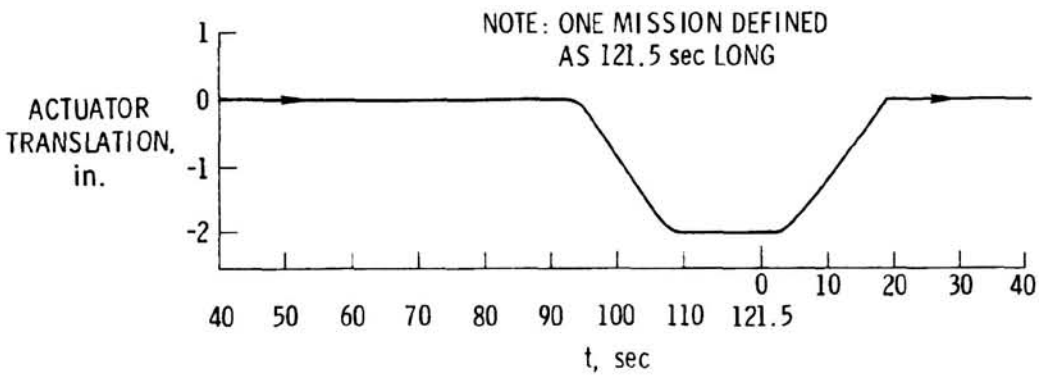

Figure 37.- Variation of position of half-scale bipod with time.

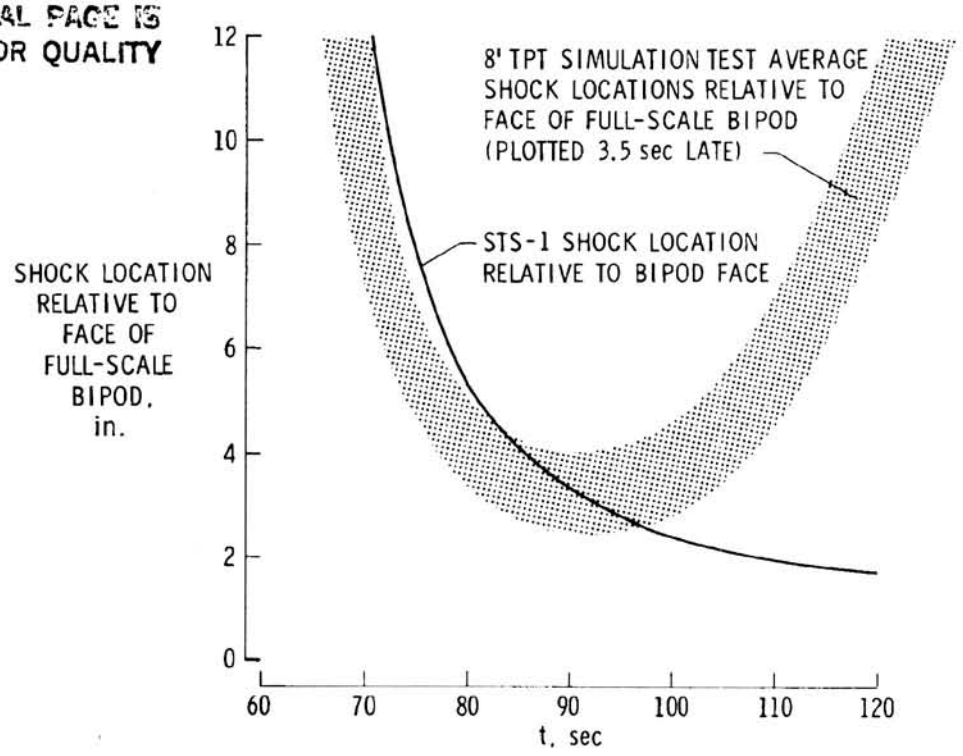

Figure 38.- Comparison of time variation of location of STS-1 bow shock relative to face of bipod with location of shock in 8-Ft. TPT simulation.

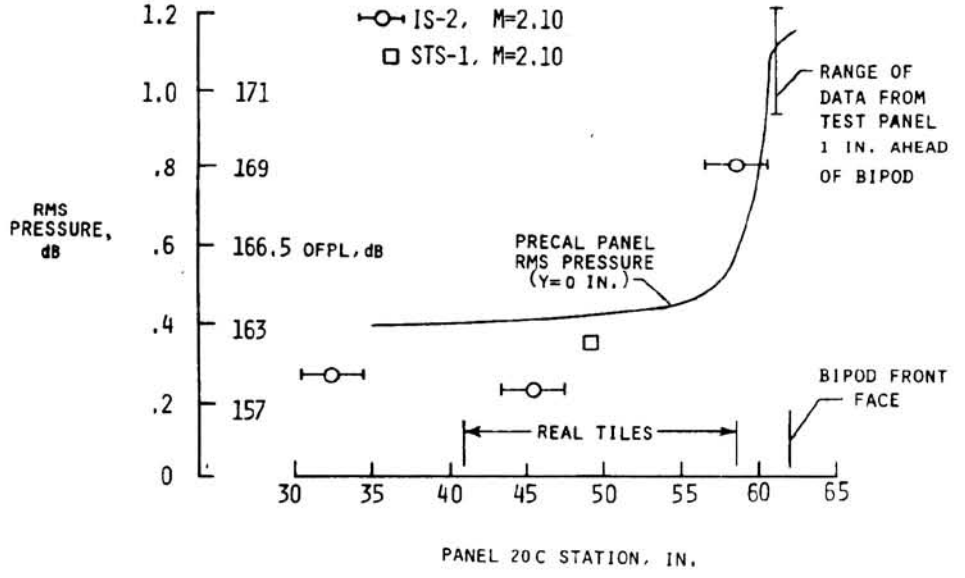

Figure 39.- Variation of rms sound pressures ahead of bipod from panel 20C tests compared with IS-2 and STS-1 results.

SHUTTLE BOOSTER SEPARATION AERODYNAMICS

Mark K. Craig
NASA Johnson Space Center
Houston, Texas

Henry S. Dresser
Rockwell International Corp.
Downey, California

SUMMARY

A wind tunnel test program of some complexity was used to define the aerodynamic forces exerted on the space shuttle solid rocket boosters and orbiter/external tank during staging. In these tests, problems associated with the use of up to three models in close proximity and with the need to simulate high pressure separation motor plumes were handled in a unique and effective manner. A new method was developed for efficiently organizing data which is a function of a large number of independent variables. Data derived from the test program drastically reduced previous estimates of aerodynamic uncertainties and allowed certification of the separation system at the design maximum staging dynamic pressure. Reduction of flight data has implicitly verified the staging aerodynamics data base and its associated uncertainties.

INTRODUCTION

Staging of the space shuttle's solid rocket boosters (SRB's) occurs under conditions which produce significant aerodynamic forces on both the separating SRB's and the remaining orbiter/external tank (OET). An accurate definition of these forces is essential to the design of the separation system because of the stringent motion constraints imposed by the shuttle's unique asymmetric configuration. During staging, the SRB's must translate aft without adverse displacements or rotations to avoid recontact with the external tank in the yaw plane and with the orbiter's wings in pitch. This paper will address the strategy developed to define these aerodynamic forces, will discuss the final wind tunnel test (IA193) undertaken to establish a data base, will discuss the effects of the data on separation clearance analyses, and will present flight data supporting data base verification.

SYMBOLS

C_N	normal force coefficient
C_Y	side force coefficient
C_l	rolling moment coefficient
C_m	pitching moment coefficient
C_n	yawing moment coefficient
d_j	nozzle throat diameter
h	geodetic altitude
h_{MD}	jet Mach disk height
M	Mach number
MW	molecular weight
p_o	static pressure
$\bar{q}$	dynamic pressure
R	universal gas constant
S_{REF}	reference area
T	temperature
t	time
V_{REL}	earth-relative velocity
α	angle of attack
β	angle of sideslip
γ	specific heat ratio
Δx	longitudinal displacement of SRB from mated position
Δy	lateral displacement of SRB from mated position

Δz	normal displacement of SRB from mated position
$\Delta\alpha$	SRB pitch angle relative to OET
$\Delta\beta$	SRB yaw angle relative to OET
θ_j	nozzle lip angle
ϕ	momentum

Subscripts:

FLT	flight
ISOL	isolated vehicle
j	jet
OT	orbiter/external tank
PROX	proximity
RSRB	right-hand SRB
TUN	wind tunnel
o	stagnation condition

BOOSTER SEPARATION

The shuttle solid rocket boosters (SRB's) are separated at burnout from the launch vehicle by means of two basic phenomena. Longitudinal separation is achieved as a result of the higher axial acceleration of the orbiter/external tank (OET). Lateral and normal separation is achieved, however, by the application of thrust and aerodynamic forces to the SRB's. Unlike previous cylindrical launch vehicles, control of these non-longitudinal forces is critical to assure that no recontact occurs. Separation motion is initiated by the firing of eight solid propellant booster separation motors (BSM's) on each SRB, four forward in the SRB nose frustrum and four aft on the base skirt. The motors produce 21,700 lbs thrust each over a very short burn time (0.68 sec) which was selected to minimize impingement of the exhaust plume on the sensitive orbiter thermal protection tiles. Orientation of the BSM's (figure 1) was also selected to minimize impingement; the motors' nozzles are canted 40° from vertical away from the orbiter in pitch and 20° toward the orbiter in roll. This unusual impingement-avoiding motor orientation has two direct effects on separation aerodynamics. The first, and most obvious, is that a severe disturbance of the vehicle flowfield (figure 2) can be anticipated as a result of the forward-facing jet. The second effect

is that the energy of this jet, and its resulting disturbance, will be greater than otherwise required because the BSM thrust must be elevated to account for cosine losses associated with the 40° pitch cant and the shallow 20° inboard roll.

Staging occurs under supersonic conditions with Mach numbers in the range of 4.0 to 4.5 and dynamic pressures up to a design limit of 75 psf. Typical conditions are as follows:

t	= 126 sec	$\bar{q}$	= 32 psf
V_{REL}	= 4,600 fps	α	= 2°
h	= 154,000 ft	β	= 0°
M	= 4.3		

WIND TUNNEL TEST APPROACH

Three basic aerodynamic phenomena must be modeled in determining separation aerodynamics through test: (1) the proximity effect of one vehicle's flowfield on those of nearby vehicles, (2) the jet interaction effect of the BSM plumes on the flowfield surrounding all of the vehicles, and (3) the effect of direct BSM plume impingement on the external tank. Each of these phenomena is a function of the orientation of the OET with respect to the freestream flow and the relative displacements and orientations between the vehicles. The jet interaction and plume impingement effects are also a function of a plume scaling parameter. This knowledge defines the set of eight independent variables which must be simulated in a separation wind tunnel test (figure 3). The effects of Mach number and Reynolds number have been found from previous tests to be second order over the range of anticipated flight conditions and were thus included in the data base uncertainty. The dependent variables, or aero coefficients, derived from the test take the form of BSM plume-on and plume-off proximity increments, that is, coefficient increments to be added to SRB and OET freestream aerodynamic data.

Data Organization

The use of eight independent variables in a data base can present severe difficulties if a standard square data grid is used. The most obvious difficulty is that the number of test data points required to fill the grid will be quite large since it is a function of the number of tested values of each independent variable raised to the eighth power. The squareness of the grid in 8-dimensional space will also assure that most of the data points are far-removed from areas of interest and, in fact, that many data points will be required in

locations which are physically unrealizeable due to model or sting interference. This can be most easily seen in the proximity independent variables Δx, Δy, Δz, $\Delta\alpha$, and $\Delta\beta$. At a large Δx the required range of the other variables will be large due to the need to account for separation motion dispersions. At $\Delta x = 0$, however, the other proximity variables have only the value of zero since this constitutes the SRB's mated position. To superimpose the grid required at a large Δx on $\Delta x = 0$ would require that data be taken at positions involving model interference and would result in most, if not all, of the data being far removed from the only point of interest, the mated position.

These difficulties have been circumvented by developing a unique data organization concept to handle the five proximity independent variables. This new approach, designated the "hypercube" format, allows data to be placed only along required separation paths. At each Δx to be tested two 4-dimensional hypercubes are situated so as to encompass anticipated dispersions in Δy, Δz, $\Delta\alpha$, and $\Delta\beta$; an outer cube encompasses all dispersions, including system failures, while an inner cube includes the nominal separation path with 3σ dispersions. These hypercubes are not constrained to have parallel opposite sides so that they can be shaped to match physical constraints (figure 4). Data points are taken at the vertices of the hypercubes; in addition, an interior point is placed within each hypercube to increase the data density in a region of interest. The Δx values at which hypercubes are placed were selected to maintain constant time increments at the separation relative longitudinal acceleration rather than constant length increments. This increases the data density early in the motion when trends are being established.

The use of this approach has provided a much higher data density along separation trajectory paths while reducing the required number of data points by a factor of at least 20 from a squared grid. A special algorithm has been developed which transforms these 4-dimensional arbitrary shapes into 4-dimensional cubes so that a low order polynomial can be easily fit to the vertices and interior point, thus providing interpolation. Interpolation in the remaining independent variables α, β, and the plume scaling parameter is handled in a similar manner, although the organization of these variables is based initially on 3-dimensional cubical shapes since there are no physical interference constraints to be taken into account.

In addition to hypercube data, test points were also established to support the definition of data uncertainties. One class of points constitute alternate paths through the hypercubes and are also representative of separation motion (figure 5). As will be discussed later, the difference between data obtained at these points and that predicted by the interpolator constitutes a data use error due primarily to data non-linearity. A second class of test points was obtained with the SRB's in asymmetric positions with respect to the OET to evaluate the error associated with assembling the data base assuming symmetry.

Model Configuration

All testing used to define the SRB separation aero data base was conducted in the U. S. Air Force Arnold Engineering and Development Center/Von Karman Facility tunnel "A" using a 1% scale model of the space shuttle vehicle. This facility was selected because of its efficient captive trajectory system (CTS) which provides rapid computerized movement of models in the tunnel without interrupting the primary tunnel airflow.

In BSM plume-on testing, the OET was placed on the CTS sting and the two SRB's were placed on a specially designed screw-jack adapter to the primary sting. This adapter allowed automatic movement of the SRB's in the yaw plane but required manual placement in pitch. The BSM plume-on test installation is shown in figure 6. Separate lines were provided to supply plume air to plenum chambers for the forward and aft nozzle clusters in each SRB. The forward clusters were fed by air flowing through the balances. Care was taken to balance the plenum chamber pressures between forward and aft jets and between left and right SRB's by means of orifice meters in the individual supply lines. In plume-on testing, previous experience has shown that it is necessary to account for SRB-to-SRB flow interference as well as for the mutual coupling of the SRB's plume interference effects on the flowfield surrounding the OET. Hence, the use of both SRB's is required.

In plume-off testing, a single SRB was mounted on the CTS and moved through the hypercube matrix of points representing relative positions and attitudes of the SRB with respect to a fixed OET. The model installation is shown in figure 7. Although forces and moments were measured on both models, axial force and rolling moment were not measured on the SRB. The SRB model was equipped with a flow-through balance for use in plume-on testing making it impossible to measure axial force with any degree of accuracy. Rolling moment was also eliminated from the balance readings since it is negligible as a result of SRB body symmetry. Previous plume-off test experience indicated that SRB-to-SRB effects are minimal and that SRB effects on the OET are additive, thus justifying the use of a single SRB test procedure.

Plume Scaling

Technology studies (reference 1, et al.) conducted in the 1970's indicated that the appropriate BSM plume scaling parameter was jet-to-freestream momentum flux ratio ($\bar{q}_j/\bar{q}_\infty$). Plume interaction with a freestream crossflow, as depicted in figure 8, is then defined by the following empirical relationship for Mach disk height:

$$h_{MD} = \left[\frac{2\left(1+\frac{\gamma_j-1}{2}M_j^2\right)}{\gamma_j^2 M_j(\gamma_j+1)}\right]^{0.25}\left[\frac{1.25(1+\gamma_\infty)\gamma_\infty M_\infty^2}{(1-\gamma_\infty)+2\gamma_\infty M_\infty^2}\right]^{0.5}\left[\frac{\bar{q}_j}{\bar{q}_\infty}\right]^{0.5}\left\{\frac{d_j}{(1+\cos\theta_j)}\right\}$$

Scaling $\bar{q}_j/\bar{q}_\infty$ in a separation wind tunnel test was not possible, however, due to constraints on plume gas supply pressure (1,500 psi) and the prohibitively small nozzle sizes required (1/32 inch throat diameter). As a result, jet-to-freestream momentum ratio (ρ_j/ϕ_∞) was selected over $\bar{q}_j/\bar{q}_\infty$ as the plume scaling parameter. This choice preserved the geometric scaling of h_{MD} but removed any dependence on nozzle size, d_j:

$$h_{MD} = \left[\frac{2\left(1+\frac{\gamma_j-1}{2}M_j^2\right)}{\gamma_j^2 M_j(\gamma_j+1)}\right]^{0.25}\left[\frac{1.25(1+\gamma_\infty)\gamma_\infty M_\infty^2}{(1-\gamma_\infty)+2\gamma_\infty M_\infty^2}\right]^{0.5}\left[\left(\frac{4S_{REF}}{\pi}\right)\left(\frac{\phi_j}{\phi_\infty}\right)\right]^{0.5}\left\{\frac{1}{1+\cos\theta_j}\right\}$$

Using momentum ratio scaling, nozzle throat size was doubled to minimize the chance of nozzle plugging and the chamber pressure was reduced to within plant gas supply limits. Model nozzle area ratio was adjusted to obtain a good match of plume cross-sectional area and hence proper simulation of the blockage associated with flowfield interaction effects.

Plume gas temperature and molecular weight affect jet/flowfield interaction by strongly influencing the external flow separation distance upstream of the nozzle for low molecular weight or high temperature transverse jets. This effect is correlated by the "RT" ratio as follows:

$$\tau = \frac{(RT_o)_j}{(RT)_\infty} = \frac{(T_o/MW)_j}{(T/MW)_\infty}$$

"RT" simulation provides the rationale for using air as the injectant gas in wind tunnel plume testing. Reference 2 indicates that "RT" effects are negligible for $\tau < 7$. Since the values for flight ($\tau = 2.91$) and test with air ($\tau = 4.6$) are below this limit, unheated air was selected to simulate the BSM exhaust product plume. A summary of nozzle design and plume simulation parameters is presented in table 1. The simulation values representing matched conditions between flight and test are noted.

Tunnel operating conditions resulting from ϕ_j/ϕ_∞ plume scaling with unheated air are presented in figure 9. The operational test region is defined by two boundaries. The upper boundary is determined by the maximum plume operating pressure in the tunnel, that is, the air supply limit. The tunnel lower operating boundary represents a facility primary airflow limitation with no consideration given to model and plume blockage effects. The inclusion of blockage effects determined from previous testing moves this lower curve up to the designated "tunnel operating curve." The separation design limit boundary ($\bar{q}$ = 75 psf) was established by SRB separation system design requirements and is not a test limitation.

The tunnel operating curve in figure 9 provides the information required to select the two jet operating pressures to be used in the test: 900 psi corresponds to the separation design limit $\bar{q}$ = 75 psf and 1,500 psi, corresponding to $\bar{q}$ = 45 psf, is the highest pressure obtainable within facility constaints. It should be noted that the minimum simulated dynamic pressure of 45 psf is well above the nominal 33 psf value. Extrapolation to this value will not be required, however, as previous testing has shown that higher ϕ_j/ϕ_∞ values do not significantly affect separation aerodynamics; the flowfield has been disturbed to the greatest extent possible.

WIND TUNNEL TEST RESULTS

Hypercube Data

As might be expected, the hypercube data base geometry does not permit the parametric plotting of data as a function of single independent variables; rather, paths through the data base must be constructed by, for example, connecting corresponding hypercube corners at successive Δx's. The incremental proximity pitching moment coefficient data for a representative trajectory path through the data base is plotted in figure 10 as a function of Δx. The proximity increment is defined as the difference between proximity and isolated aerodynamic coefficients. In accordance with the proximity increment definition, for BSM plume-on data $\Delta C_{m_{OET}}$ approaches zero as the SRB moves away. $\Delta C_{m_{SRB}}$, on the other hand, approaches a value representing the plume/flowfield interaction effect on the SRB. For plume-off data, $\Delta C_{m_{SRB}}$ approaches zero as it leaves the OET flowfield. Note that the separation aero data base extends back in Δx only to a value of 1,700 inches full scale; this represents the point at which the SRB nose clears the aft end of the OET and, thus, the terminus of separation.

The use of aero coefficient proximity increments as dependent variables was selected to eliminate the need for generating a new separation aero data base each time a change was made to vehicle outer moldlines. Since the total aerodynamic coefficients are obtained by combining isolated aero coefficients with proximity increments, effects of minor configuration changes are adequately reflected in updates to the isolated aero only. The effect on the proximity increments is negligible.

Data Uncertainties

The uncertainties associated with the SRB separation aero data base are composed of three components: an error resulting from the

hypercube interpolation process, an error due to the asymmetry of the motion of the two SRB's with respect to the OET, and an error associated with scaling the BSM plumes. The total coefficient uncertainties were obtained by root-sum-squaring the contribution of these three components. Tables 2 and 3 present a summary of these uncertainties for the BSM plume-on and plume-off data, respectively, which are assumed to be at a 3σ level.

The uncertainty component associated with interpolation error accounts for the inability of the hypercube interpolator polynomials to exactly model the data and for the fact that the data base was generated at a constant value of Mach number. This term was evaluated by comparing interpolator outputs to test data points established along representative trajectory paths within, but not coincident with the hypercubes, and therefore not in the data base. Three trajectory paths were chosen to provide a reference data point within the inner cube, within the outer cube, and in an area of motion close in to the OET (figure 5). Data along these uncertainty paths was taken at a Mach number of 4.0, whereas the hypercube data was taken at Mach 4.5. The interpolation error component was obtained by differencing the interpolated aero coefficient values and the tested values (figure 10) and integrating the difference over time to obtain a path average. Points at Δx's corresponding to $t \leq 0.5$ seconds were given a higher weighting because of the importance of first motion. The largest integrated error from the three paths is used as the coefficient uncertainty.

The uncertainty component associated with asymmetric SRB motion accounts for the error incurred in performing all plume-on testing with the SRB's in symmetric positions with respect to the OET. Asymmetry is not applicable to the plume-off data since only one SRB was used. SRB asymmetry modifies plume-on aerodynamics by establishing unequal impingement of the BSM plumes on the external tank and by causing an asymmetric interaction of the plumes with the freestream flow. This term was evaluated by differencing test data obtained in two representative asymmetric configurations from data obtained with the SRB's in the corresponding symmetric positions in the data base; the largest difference for each coefficient is defined to be the uncertainty.

The third aero uncertainty component results from errors in plume scaling, that is, errors incurred by using the jet-to-freestream momentum ratio as the plume simulation parameter. Sources of this error include test-to-flight differences in BSM nozzle geometry, atmospheric conditions (Reynolds number), and exhaust plume characteristics (specific heat ratio, chemical constituents). Lack of sufficient data on the shuttle precluded evaluation of this error directly for the SRB aero. An estimate of the SRB uncertainty was made, however, by evaluating test and flight data available from a military missile with a transverse jet used for attitude control. The difference between test and flight data for this missile was converted to an error in momentum ratio which in turn was converted into an SRB aero coefficient error. Adequate flight data was available from the shuttle to assess the OET aero plume scaling error. Values were

deduced from comparisons between flight and dynamics math model OET yaw and roll rates during BSM firing. The level of the aerodynamic uncertainties used in the math model was varied until a good flight-math-model rate comparison was achieved. To be conservative, all of this uncertainty was assumed to be accounted for by an error in plume scaling.

A comparison of the plume-on aero uncertainties derived from test IA193 by the procedure outlined above with the values from previous tests for the first manned orbital flight (FMOF) is presented in figure 11. Previous uncertainty values were determined by root-sum-squaring the worst-case values of each of 16 individual components. Most of these components are accounted for in the current procedure's interpolation error and are more realistically dealt with in the integration process now used. The tests on which FMOF uncertainties were based had certain facility difficulties which also increased the uncertainty levels. A comparison of the previous and updated plume-off uncertainties is presented in figure 12.

Effects on Separation Dynamics

Separation aerodynamics have a strong influence on separation motion and the vehicle-to-vehicle clearances which result from that motion. Figure 13 presents the minimum clearance which exists between a strut stub on the external tank and the barrel of the SRB body as a function of staging dynamic pressure. This particular clearance is usually the most critical in defining a safe separation. At the dynamic pressures encountered during the orbital flight test program recontact was not predicted and, based on an analysis of flight data, was not encountered. Using the aero uncertainties available at the time of STS-1 (FMOF), however, a safe separation could not be demonstrated at the separation system design limit dynamic pressure of 75 psf. The uncertainties outlined above from test IA193 have alleviated this situation and allowed system certification to the design limit.

Flight data has served to implicitly validate these uncertainties. Figure 14 presents the difference between vehicle yaw rates measured in flight and those predicted by the separation dynamics math model. The bands of 0.05 deg/sec for the OET and 0.40 deg/sec for the SRB represent typical flight minus predicted differences when the prediction is based on nominal separation aerodynamics without uncertainties. The use of both the IA193 and FMOF uncertainties to generate the predicted values causes a deviation from flight experience; the deviation is especially pronounced for the FMOF uncertainties. The IA193 uncertainties appear to be slightly conservative.

CONCLUDING REMARKS

A complex wind tunnel test program has been completed to define the aerodynamics associated with SRB separation. The program has

developed unique and effective approaches to the use of multiple wind tunnel models in close proximity, the scaling of high energy forward facing jet effects, and the organization and use of n-dimensional data which is severely constrained in terms of geometry and density. Flight experience has verified the validity of the program.

REFERENCES

1. Cohen, Leonard S., Coulter, Lawrence J., and Egan, William J.: Penetrations and Mixing of Multiple Gas Jets Subjected to a Cross Flow. AIAA Journal, Vol. 9, No. 4, 1971.

2. Thayer, W. J. III and Corlett, R. C.: Gas Dynamic and Transport Phenomena in the Two-Dimensional Jet Interaction Flowfield. AIAA Journal, Vol. 10, No. 4, 1972.

TABLE 1.- BSM PLUME SIMULATION SUMMARY

PARAMETER		FLIGHT (OPS)	MODEL DESIGN
FREESTREAM			
DYNAMIC PRESSURE	q_∞	55.0 PSF	165.6 PSF
MACH NUMBER	M_∞	4.46	4.5
*REYNOLDS NUMBER	R_{eN}	6.95×10^6	1.62×10^6
ALTITUDE	h	142,830 FT	
BSM JET CHARACTERISTICS			
CHAMBER PRESSURE	P_C	1800 PSIA	1134 PSIA
CHAMBER TEMPERATURE	T_C	5435°R	530°R
AVERAGE SPECIFIC HEAT	γ	1.22	1.4
EXPANSION RATIO	ϵ	5.826	3.00
NOZZLE LIP ANGLE	θ_P	8°	13°
EXIT AREA	A_e	44.94 IN^2	0.01157 IN^2
EXIT MACH NUMBER	M_J	2.94	2.64
EXIT PRESSURE	P_J	44.50 PSIA	53.40 PSIA
MASS FLOW RATE	$\dot{m}_J$	181.1 LB_m/SEC	0.1009 LB_m/SEC
MOMENTUM	$\dot{m}_J U_J$	20,000 LB_f	6.03 LB_f
THRUST	T	22,000 LB_f	6.647 LB_f
JET TO FREESTREAM ($S_{REF} = 1\ FT^2$) FS			
THRUST RATIO	$T/q_\infty S_{REF}$	400	401.4
MOMENTUM RATIO (ϕ_J/ϕ_∞)	$\frac{\dot{m}_J U_J}{2q_\infty S_{REF}}$	182	182
MASS FLOW RATIO	$\frac{\dot{m}_J}{\rho_\infty V_\infty S_{REF}}$	252	224
PRESSURE RATIO	P_J/P_∞	1704.3	658.4
MOMENTUM FLUX RATIO (AT NOZZLE EXIT)	q_J/q_∞	613	225.6
MACH DISK HEIGHT (FULL SCALE)	h_{MD}	23.82 IN.	23.57 IN.

*REYNOLDS NUMBER BASED ON ORBITER LENGTH, $L_B = 107.5$ FT

TABLE 2.- BSM PLUME-ON PROXIMITY AERO 3σ UNCERTAINTIES

	OET					RSRB			
UNCERTAINTY	C_N	C_m	C_Y	C_n	C_ℓ	C_N	C_m	C_Y	C_n
INTERPOLATION	0.0350	0.0201	0.0145	0.0096	0.0022	0.0064	0.0009	0.0105	0.0043
ASYMMETRY	0.0677	0.0256	0.0732	0.0101	0.0029	0	0	0	0
PLUME SIMULATION	0.0155	0.0074	0.0410	0.0093	0.0008	0.0085	0.0004	0.0035	0.0034
RSS TOTAL	0.0778	0.0334	0.0851	0.0167	0.0037	0.0106	0.0010	0.0111	0.0055

TABLE 3.- BSM PLUME-OFF PROXIMITY AERO 3σ UNCERTAINTIES

	OET					RSRB			
UNCERTAINTY	C_N	C_m	C_Y	C_n	C_ℓ	C_N	C_m	C_Y	C_n
INTERPOLATION	0.0198	0.0075	0.0160	0.0054	0.0016	0.0112	0.0037	0.0121	0.0041
ASYMMETRY	0	0	0	0	0	0	0	0	0
PLUME SIMULATION	0	0	0	0	0	0	0	0	0
RSS TOTAL	0.0198	0.0075	0.0160	0.0054	0.0016	0.0112	0.0037	0.0121	0.0041

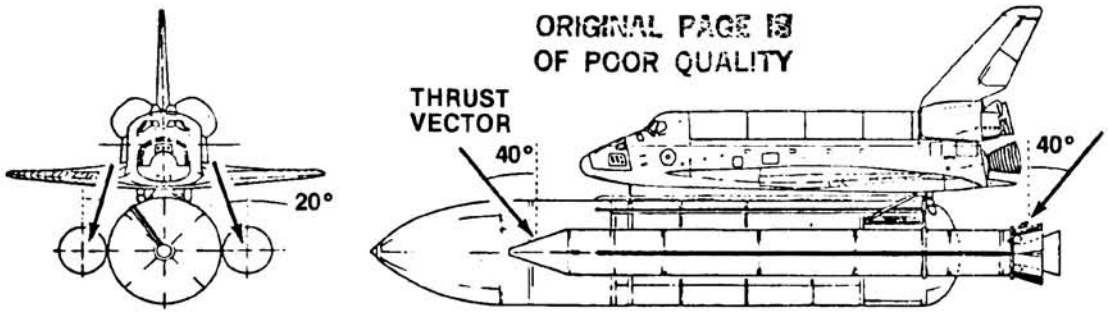

- **FOUR BSMs FORWARD AND FOUR AFT**
- **PERFORMANCE**
  - **WEB ACTION TIME ~ 0.68 SECONDS**
  - **VACUUM THRUST/MOTOR ~ 21,000 POUNDS**
  - **AVERAGE OPERATING PRESSURE = 1700 PSI**

Figure 1.- Booster separation motor configuration.

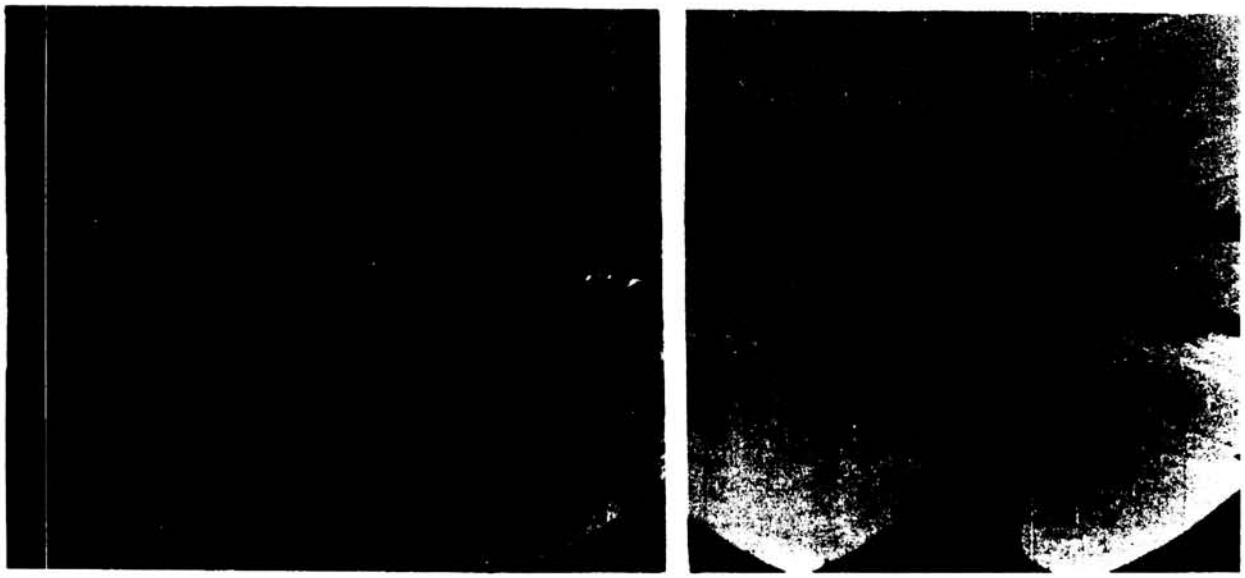

Plume off Plume on

Figure 2.- Separation motor disturbance of vehicle flowfield.

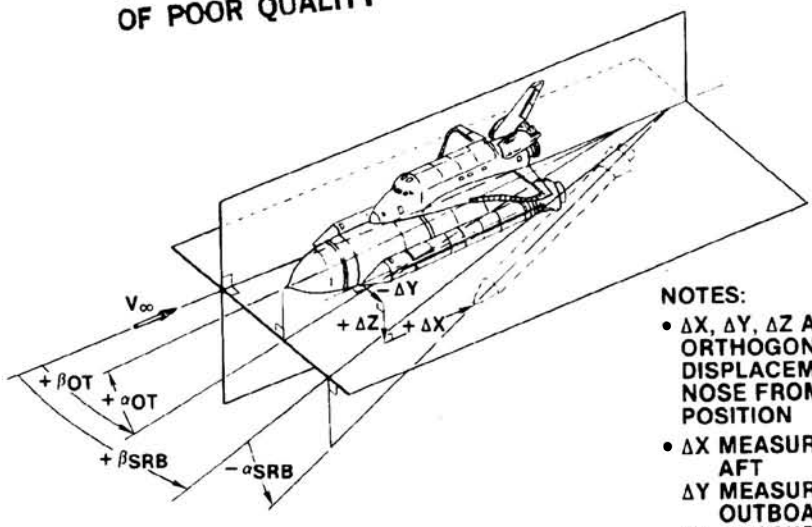

NOTES:

- ΔX, ΔY, ΔZ ARE ORTHOGONAL DISPLACEMENTS OF SRB NOSE FROM ITS MATED POSITION
- ΔX MEASURED POSITIVE AFT
  ΔY MEASURED POSITIVE OUTBOARD RIGHT
  ΔZ MEASURED POSITIVE DOWN
- $\Delta\alpha \equiv (\alpha_{SRB} - \alpha_{OT})$
  $\Delta\beta \equiv (\beta_{SRB} - \beta_{OT})$
- SEPARATION MOTOR JET-TO-FREESTREAM MOMENTUM RATIO IS ALSO INDEPENDENT VARIABLE

Figure 3.- SRB separation aerodynamics independent variables.

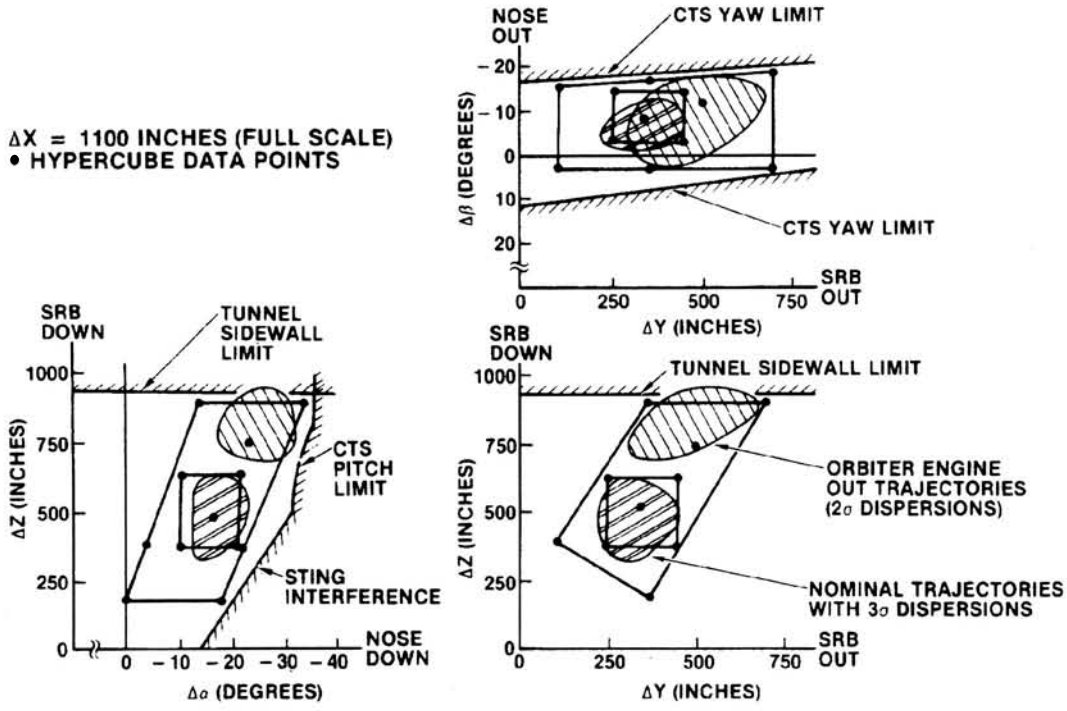

Figure 4.- Separation trajectory envelope cross section.

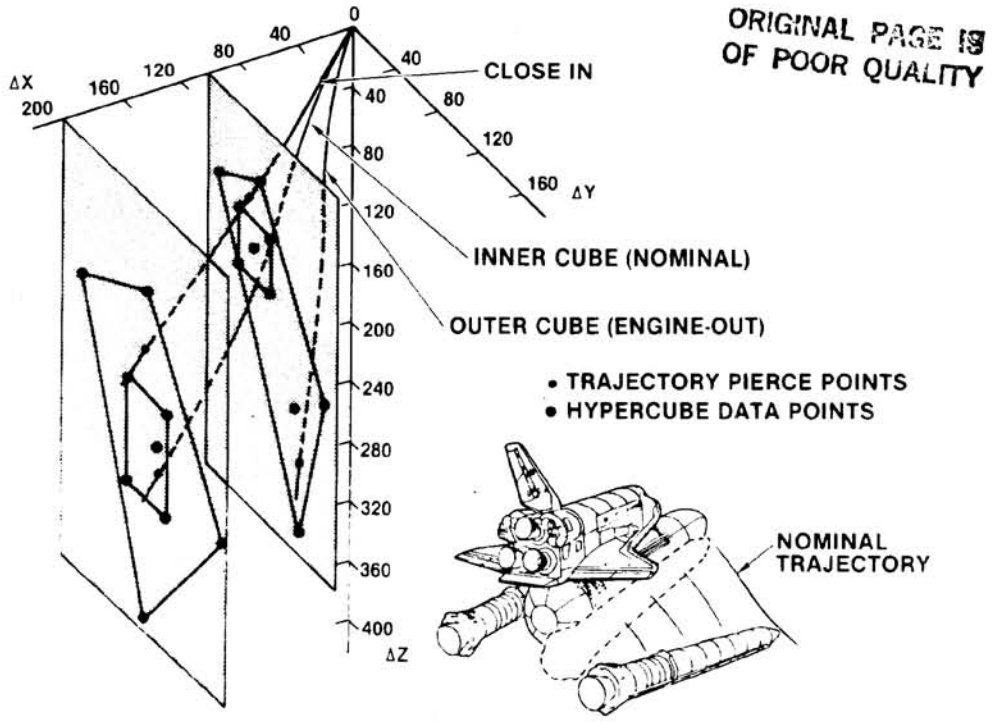

Figure 5.- Separation trajectory path through hypercubes.

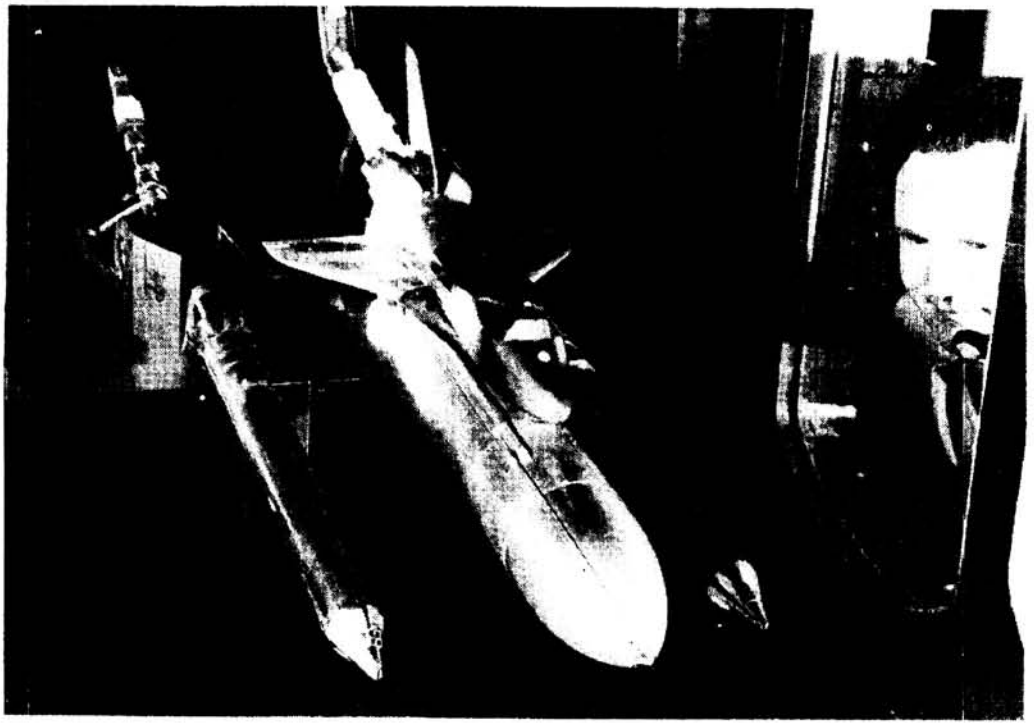

Figure 6.- BSM plume-on test configuration.

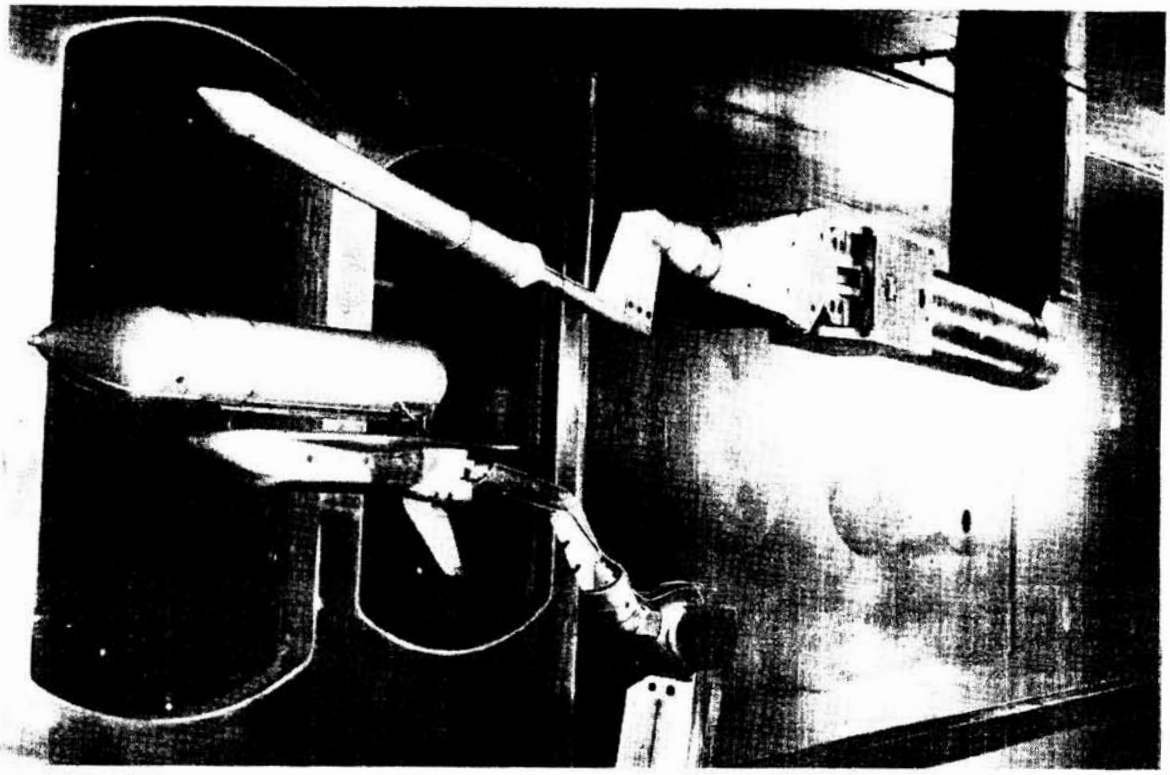

Figure 7.- BSM plume-off test configuration.

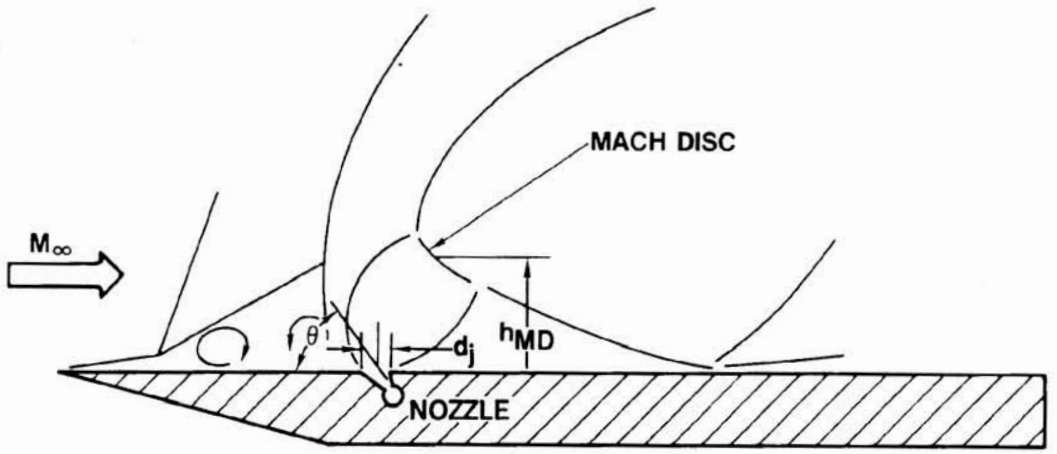

Figure 8.- Transverse firing jet flow mechanism.

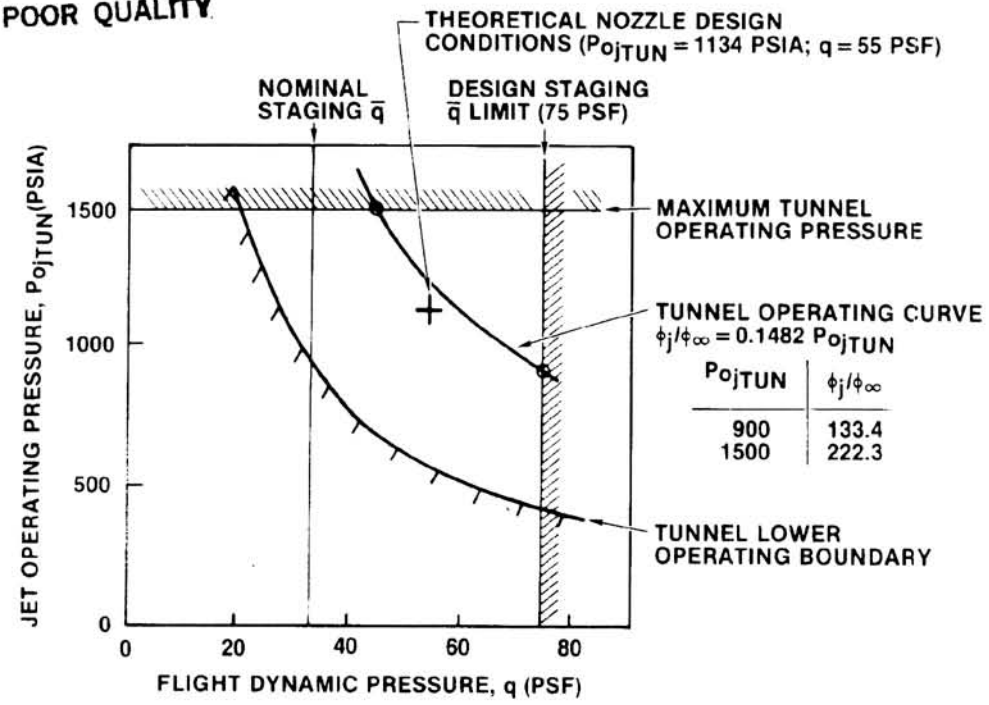

Figure 9.- BSM plume simulation envelope.

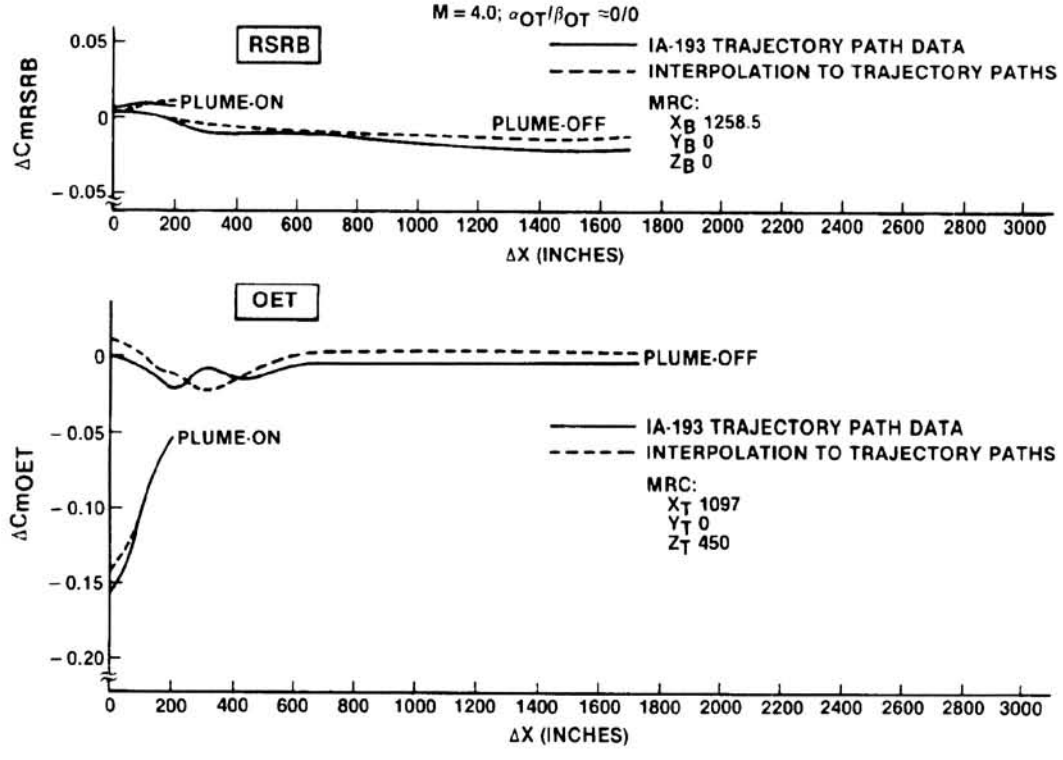

Figure 10.- Proximity aero trends.

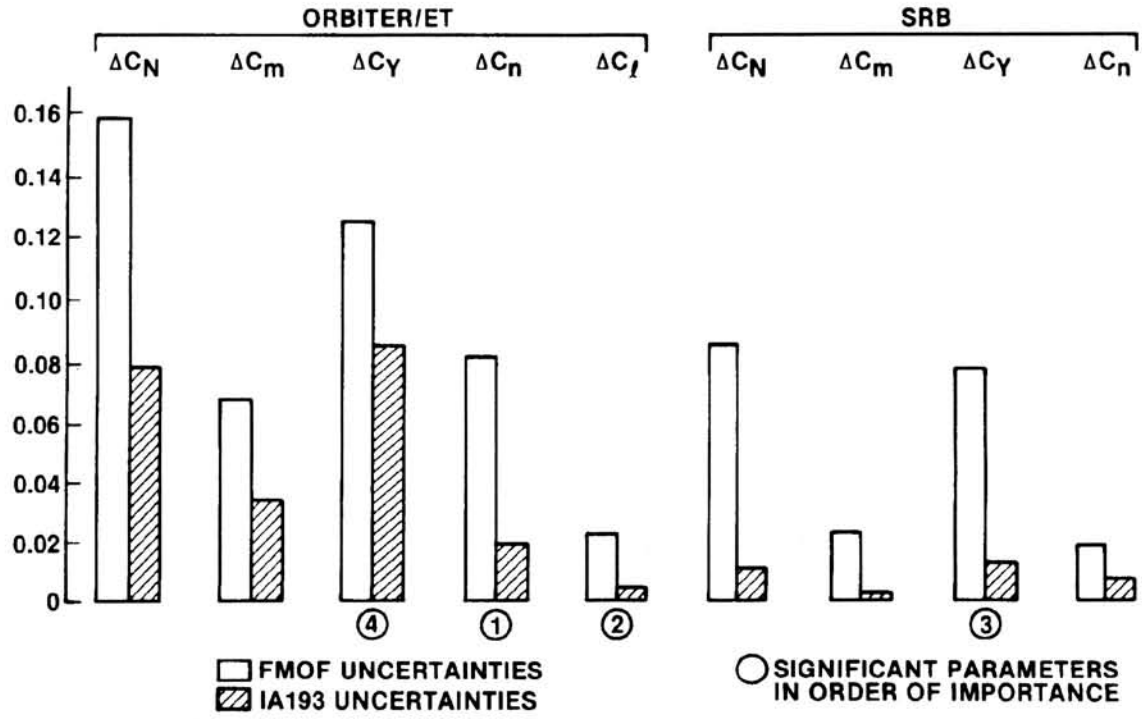

Figure 11.- BSM plume-on 3σ uncertainties comparison.

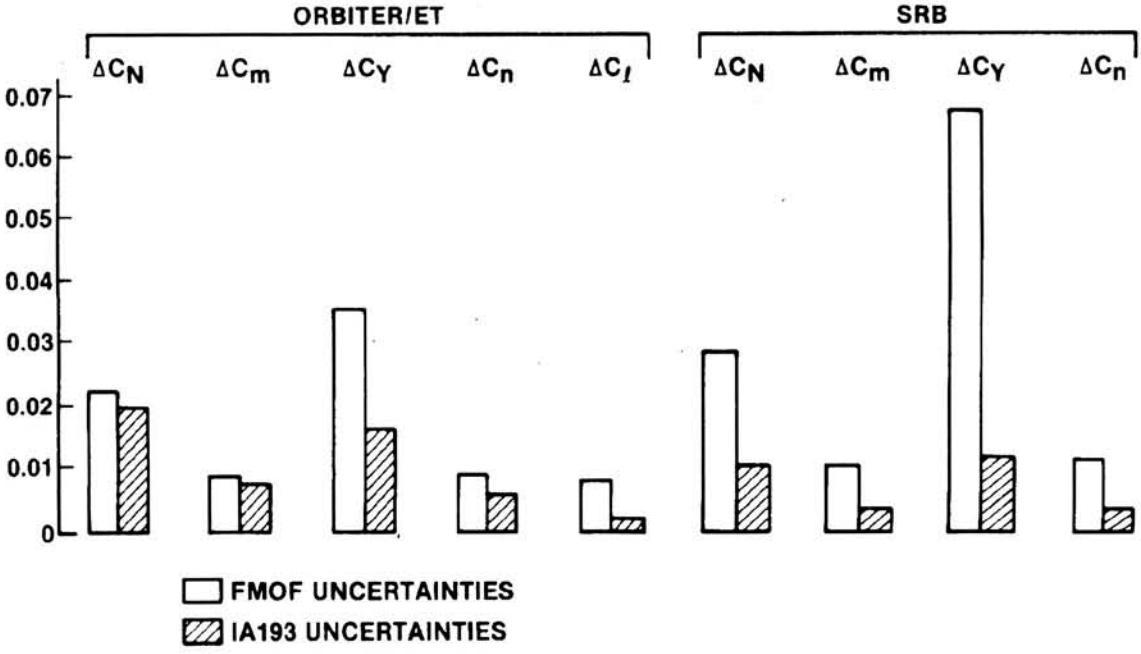

Figure 12.- BSM plume-off 3σ uncertainties comparison.

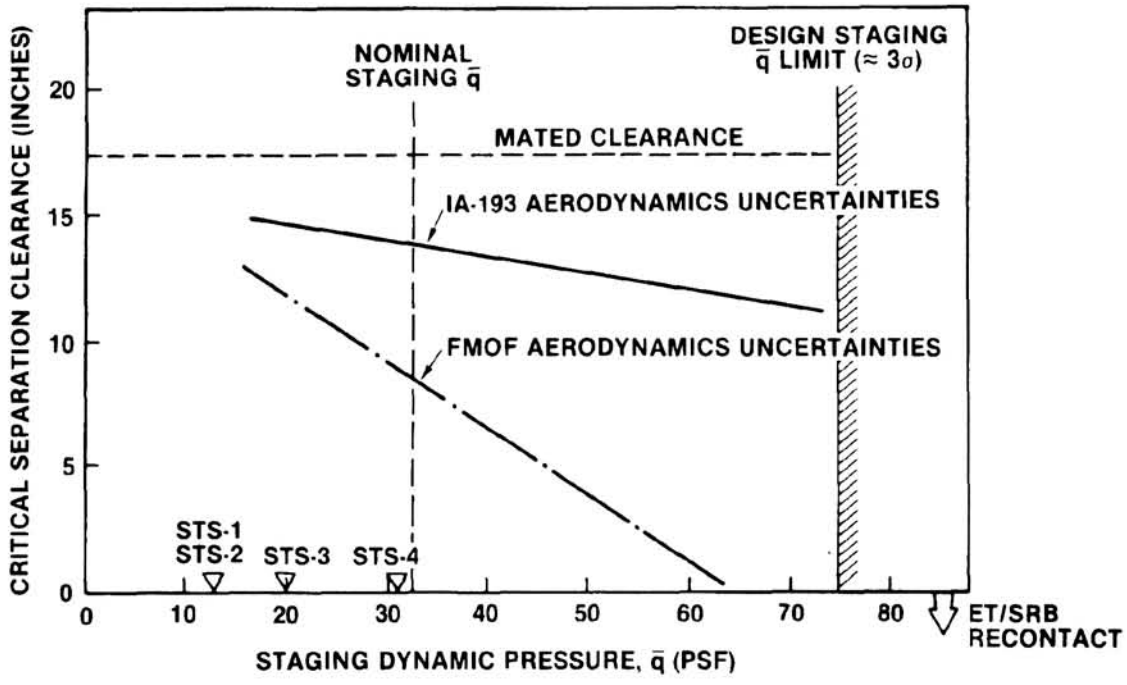

Figure 13.- Effect of separation aerodynamics on clearances.

Δ RATE = SIMULATION (DISPERSED AERODYNAMICS) MINUS SIMULATION (NOMINAL AERODYNAMICS)
= FLIGHT MINUS SIMULATION (NOMINAL AERODYNAMICS)

3σ COMPOSITE UNCERTAINTY
≈ WORST-ON-WORST COMBINATION OF 2σ INDIVIDUAL AERODYNAMIC COEFFICIENT UNCERTAINTIES

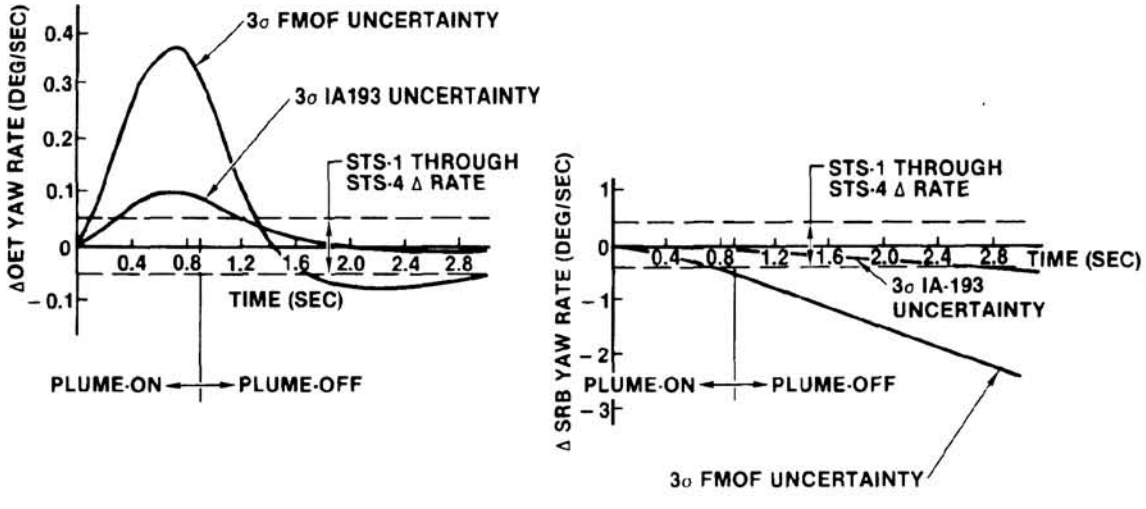

Figure 14.- Aero uncertainty effects on separation dynamics.

SHUTTLE LAUNCH DEBRIS --

SOURCES, CONSEQUENCES, SOLUTIONS

Mark K. Craig
NASA Johnson Space Center
Houston, Texas

SUMMARY

Following the first space shuttle flight, the shuttle program established a team to identify and eliminate sources of debris which had caused serious damage to the orbiter thermal protection tiles. An approach was developed for debris identification which involved pre- and post-flight vehicle and pad inspections, analytic assessment of debris transport and impact phenomena, and analysis of various photographic records of the flight. Debris sources identified by this approach were classified as being either hazards to flight or sources of damage which increased vehicle refurbishment costs without having any safety implications. As a result of this assessment, all known hazardous debris sources on the launch vehicle and pad have been eliminated; other sources are being removed in a cost-effective manner as appropriate.

INTRODUCTION

The space shuttle vehicle is susceptible to the adverse effects of lift-off and ascent debris to a degree unknown on previous launch vehicles. This results from the fact that a significant portion of the launch vehicle, the orbiter, also serves as an entry vehicle and, as such, is covered with mechanically fragile thermal protection system (TPS) tiles. The shuttle program recognized this susceptibility early-on and instituted a program to minimize what was felt to be the chief launch debris threat, ice formation on the vehicle's external tank (ET). This effort was pursued with particular vigor on the nose region of the tank where analytic transport studies indicated a definite possibility that debris released in ascent would strike the orbiter windows and TPS tiles. The principal ice source on the nose was eliminated by covering the tank vent louvers in the nosecap with a facility vent hood, a "beanie cap," to duct away the cold vent vapors. The hood is retracted two minutes before launch to minimize ice and frost buildup. Analytic transport studies of the tank barrel section were inconclusive, but considerable effort was expended by the ET project to minimize ice formation on the tank lines and protuberances. The first shuttle flight, STS-1, was flown with this "minimum ice" configuration, although somewhat more ice than anticipated was located on the nosecap vent louvers due to a failure of the "beanie cap" dock seals. Following the flight, orbiter TPS damage was found to be significant in terms of both the number of debris impacts (hundreds) and in terms of the severity of the largest damage sites. To

investigate the sources of STS-1 debris damage and to make recommendations to reduce damage on future flights, the Shuttle Program Manager established a Debris Assessment Team headed by the Johnson Space Center (JSC), with members from JSC, the Marshall Space Flight Center, the Kennedy Space Center, Rockwell International Corp., and the Martin Marietta Co. This paper will address the approach used by this team to assess debris sources and debris-related TPS damage, will present conclusions resulting from the team's effort, and will summarize vehicle and launch pad modifications undertaken to minimize damaging debris.

APPROACH

Methods available for identification of debris sources fall into three major categories: pre- and post-flight inspections of the launch pad and vehicle, analytic treatment of transport and impact damage phenomena, and analysis of flight film and crew voice records. Pre-launch inspections of the vehicle and pad are conducted to document the system configuration and to identify changes implemented since the previous flight. The final pre-launch inspection is conducted approximately two hours before launch, after the external tank has been filled, for the purpose of documenting ice/frost formations and tank insulation anomalies (if any). The principal ice/frost formations, to date, have been found on the ET feedline and protuberances and in the orbiter umbilical area. After launch, the pad is inspected after it has been safed (launch + 3 hours) to identify facility damage which may have produced debris. The pad grounds are searched for evidence of this debris as well as for evidence of vehicle damage which may have been sustained at launch. This inspection produced the first evidence on STS-3 that tiles had been lost at lift-off as several fragments were found on the pad apron. The SRB's are inspected for possible debris sources immediately upon their removal from the water after being towed to port. Loss of insulation from the nose frustrums has been the only debris source of concern identified on the SRB. The orbiter is inspected after it has been placed in the Mate-Demate Device at the landing site. Detailed maps of tile damage are made and the most significant damage sites are photographed and measured. The most significant concentrations of damage have been found on the upper nose surface and around the windows, on the right-hand wing chine and inboard wing and elevon underside, around the umbilical wells, on the body flap underside, and on the base between the engines. Samples of material imbedded in tiles and window wipes are taken for later chemical analysis.

Two areas of analytical effort have been useful in understanding the debris source and damage data obtained from these inspections. Transport studies were undertaken for the nose and barrel sections of the ET to identify probable debris impact locations on the orbiter. The results of ET nose transport studies have shown that debris striking the orbiter upper nose surface and around the windows must have originated ahead of ET station 500. ET barrel transport studies

have indicated that it is unlikely that debris originating on the ET barrel will strike the orbiter as the result of inter-vehicle pressure gradients. Debris from the barrel which does strike the orbiter must, therefore, do so as the result of other localized effects (SRB bow wave impingement, ET drag strut upflow). Impact studies were undertaken to identify incident energy thresholds corresponding to tile coating cracking for various debris materials. These studies have shown that the ET acreage foam insulation, with a density of about 2 lb/cu. ft., will not damage tiles under any but the most severe impact conditions. The ET nosecap insulation, at 19 lb/cu. ft., will damage the tiles over a wide range of impact conditions. Impact studies also indicated that high velocity ice impacts on the orbiter windows were sufficient to cause catastrophic damage.

Review of the flight film and crew voice records has been very useful in establishing a correlation between debris sources and vehicle damage. Film from cameras in the immediate vicinity of the launch pad has identified the ablative insulation applied to the hold-down posts as a prime source of severe vehicle damage. These films have also aided in the definition of pad flow phenomena which direct debris objects back toward the orbiter. On-board films of SRB and ET separation taken from the orbiter umbilical wells have aided in establishing debris sources on both vehicles. Much of the ice on the ET lines and protuberances survives ascent intact without becoming debris. On several flights large pieces of air-load reduction ramps on the ET have been lost in flight. All flight crews have reported seeing a large quantity of debris throughout ascent, much of it striking the windows. All of it has been reported as being white in color.

STS-1 AND STS-2 DEBRIS EXPERIENCE

TPS Damage Due to Debris

Debris damage to the orbiter TPS tiles on STS-1 was significant in terms of both the number of debris impacts (hundreds) and in terms of the severity of the largest damage sites. The most alarming damage was located on the right-hand nose gear door and consisted of a gouge approximately 12 inches long and 1 inch deep in several damage-resistant, high density TPS tiles (figures 1 and 2). Severe damage was also inflicted on a low density tile on the underside of the body flap (figures 3 and 4); this damage site was enlarged significantly by melting of the tile substrate material during entry. Extensive, though less severe, damage was observed on the right-hand inboard elevon near the hinge line (figure 5); approximately 25 sq. in. of tile coating was removed by an impact with very little loss of depth. These large damage sites were very atypical. The average impact damage size was less than 1/8 inch and exhibited no depth other than that associated with loss of the tile coating. This type of damage was particularly evident on the nose upper surface and right-hand side.

Although no severe damage was sustained on the orbiter nose, STS-2 experienced debris damage which was similar to STS-1. Damage to the body flap was significant and exhibited the substrate melting as before. The number of damage sites was roughly comparable to STS-1. The only area which was damaged in a different fashion was the base tile array between the three main engines (figure 6). A number of small damage sites were present as on STS-1 but, in addition, on STS-2 there was a long scrape or compression which damaged seven adjacent tiles. A summary of the locations of noteworthy TPS damage due to debris on flights STS-1 and STS-2 is presented in figures 7 and 8.

The role of entry heating in modifying impact damage characteristics can be dramatic. As noted above, this effect has been observed on both STS-1 and STS-2 at body flap damage sites. Figure 9 presents a summary of TPS tile sensitivity to damage incurred before entry. Flight and arc-jet experience has revealed that on regions of the vehicle where surface temperatures exceed approximately 2200°F (figure 10) significant growth of larger damage sites can be expected due to shrinkage of the substrate silicon matrix. This knowledge is useful in both reconstructing the appearance of the original damage, which aids in identifying the damage source, and in anticipating the consequences of damage. Body flap temperatures on STS-1 and STS-2 were relatively low (2300°F) compared to their design values (2500°F). This was fortunate in that the higher temperatures may well have resulted in a burn-through. Shrinkage of the STS-1 nose gear door tile damage was minimal because of the higher density of the tiles, even though the temperatures were also higher (2400°F).

Debris Sources

Three potential sources of the debris causing the nose gear door tile damage (figure 2) were hypothesized. The first, and most likely, was that a section of the ET lightning band had dislodged and been transported to the orbiter. The lightning band consists of a graphite-loaded epoxy material which is applied on the external surface of the tank insulation in a strip about 6 inches wide; it can be seen circling the tank nose in figure 11. Photographs taken of the ET immediately after its separation from the orbiter revealed that large sections of the band were missing. At a density of over 100 lb/cu. ft., the lightning band material certainly would have caused significant tile damage on impact. Another potential source of the damage was ice on the ET nose. As was mentioned earlier, the facility "beanie cap" failure resulted in the formation of ice on the ET liquid oxygen (LOX) dump vent louvers; figure 12 shows a typical build-up observed during a tanking test. These louvers are within 10° of the ET lateral plane, though, so that transport to the orbiter is unlikely. Several thermal shorts which produced frost balls at the nosecap/insulation interface (the forward lightning band) can also be seen in figure 12. This frost certainly would have been transported to the orbiter (to the right but not shown in figure 12) but probably would not have had the density required from the unique characteristics of the

damage. As can be seen in figure 2, the damage had a V-shaped cross section which is maintained along its entire length. Near the end of its course, one would expect the cross section to moderate as damage inflicted on the debris by the tile increased. Because this did not happen the debris would appear to have been very hard with a square corner to form the "V." Some problems had been experienced in tank operations with the retention of phenolic spacer blocks in the cable tray running up the right-hand side of the ET nose (figure 11). Although no proof exists that any blocks were lost, they must also be considered a candidate for causing this damage.

The severe damage to the body flap (figure 4) was conclusively shown to have been the result of impacts by an ablative insulation applied to the pad SRB hold-down posts. Significant amounts of this insulation were observed in launch films to be released in the first few seconds after SRB ignition. The loss of this material can be observed in figure 13. The north posts, those on the left, experience a much more severe environment than do the south posts because they are overflown by the very abrasive SRB exhaust plumes as the vehicle heads initially north. The south posts, for all extents and purposes, represent the pre-ignition configuration of insulation on the north posts. Several films revealed that pieces of this material were caught in plume flow reflected upward from the top of the structure supporting the posts and impacted the orbiter body flap and aft fuselage. The calculated impact velocity was 100 fps; the density of the material is over 100 lb/cu. ft.

The damage area on the inboard elevon (figure 5) was probably the result of an impact by a large piece of ET insulation since it exhibited little depth. The damage mechanism involved only the shattering of the tile coating. Many of the small tile damage sites were also a result of ET insulation impacts; on-orbit photos revealed that the insulation surface contained many inch-size divots. Several large pieces of insulation (1-2 feet) were observed to be missing from load alleviation ramps in proximity to external lines.

The remainder of the damage was caused by ice released from the ET feedline and anti-geyser line which run down the right side of the tank (figure 11). This ice, which is produced at exposed cold-points along the lines, was anticipated and waived as acceptable prior to flight. Typical damage resulting from ice consisted of long, shallow grooves which would be expected from high velocity, low angle impacts (figure 5).

Modifications to Reduce Debris

Following STS-1, several steps were taken to reduce the debris hazards discussed above. The lightning bands which had been installed on the ET were removed for STS-2 and all subsequent vehicles pending identification of a material which would not generate debris (figure 14). The dock seals on the facility "beanie cap" were modified to eliminate leaks and prevent ice formation on the vent louvers (figure 14). Although no direct evidence of loss existed, provisions were

made in the ET cable tray design to physically constrain the phenolic spacer blocks. In addition to these changes, updated aerodynamic load analyses indicated that some of the insulation used in load alleviation ramps could be eliminated. About 70 running feet of these ramps were removed from the hydrogen tank.

Debris experience gained from STS-2 resulted in several changes to the launch pad. The most significant change was the removal of a substantial portion of the SRB hold-down post ablative insulation; material was retained on the base of the posts but was stripped from other areas. An attempt was also made to improve the procedure by which the material was bonded to the post to assure its retention. During several inspections the debris team found evidence of loose material on the launch platform immediately before launch. Detailed inspection and clean-up procedures were initiated to alleviate this problem. On the external tank, thermal shorts which had existed at the nosecap/insulation interface were eliminated to preclude the formation of frost balls. Two debris-producing agents on the orbiter on STS-2 were also eliminated. A more secure method of retaining orbiter umbilical well baggie fragments was found to prevent these fragments from damaging tiles immediately behind the umbilical well opening on the underside. In addition, tire pressure monitoring wires which sever on landing at tire spin-up were provided with quick-disengage connectors to prevent the wires from being thrown up into underside tiles.

STS-3 DEBRIS EXPERIENCE

As a result of the vehicle and pad modifications described above, no hazardous debris damage was experienced on STS-3. The number of debris damage sites, though, was comparable to those on STS-1 and STS-2. The only new damage characteristic was observed on the orbiter upper nose surface (figure 15) and around the windows (figure 16). In this area six large shallow gouges about 1 inch wide and 4 inches long were found on the left-hand side. One gouge of this type was found in this area on STS-1. No connection could be found between this impact damage and the loss of a number of tiles from the upper nose surface. The tile loss, which was caused by bondline failures, did result, however, in some impact damage around the windows.

The damage to the nose upper surface was particularly enigmatic because transport studies showed that the only possible source was the forward portion of the ET nose. On the ET nose, however, there are no protuberances on the left-hand side to serve as debris generators. It was finally concluded that the most probable source was an area of hand-packed insulation on the nosecap which had demonstrated bond problems during ET build-up operations. The density of this hand-pack (20 lb/cu.ft.) is more than adequate to have caused the observed damage. STS-3, for the first time, afforded a good opportunity to assess the extent of ice sources on the ET protuberances because the insulation was no longer painted white but allowed to retain its

natural brown color. Figure 17 shows the ice formations on the anti-geyser line rainshields and the LOX feedline brackets and line bellows. Although much of this ice remains in place throughout ascent, a significant portion is dislodged and impacts the orbiter nose and wing chine (because of SRB bow wave impingement) and the wing and elevon (because of upflow at the aft orbiter/ET attachments). A debris source noted on STS-3 continued to be the hold-down posts. The pre- and post-launch configurations of post M-3 are shown in figures 18 and 19, respectively. Large amounts of insulation were again lost from the base although, fortunately, no vehicle impacts were observed. Also missing after launch were the box covers placed over the tops of the post struts. These were found at great distances from the pad. For the first time a significant debris source was noted on the SRB's in that large sections of nose frustrum insulation were missing upon recovery. No specific tile damage sites could be attributed to this debris, however.

Several modifications to the vehicle and pad were undertaken to eliminate these debris sources. On the external tank, a small thermal short which formed a button of ice on a line mount at the ET nosecap was foamed over. Efforts were again made to reduce the amount of insulation on the hold-down posts and to improve application techniques to assure retention of the material during launch. In addition, some insulation was added to the tops of the post strut covers to protect the bolts holding them in place. On the SRB, the frustrum insulation application technique was revised to prevent material debond.

STS-4 DEBRIS EXPERIENCE

Debris damage to TPS tiles on STS-4 was roughly comparable to that on STS-3 in terms of number of impacts. STS-4 did not experience significant damage on the left-hand side of the nose and the damage on the upper nose was less severe. There were, however, several large damage sites on the right-hand underside of the vehicle (figure 20). A gouge about 9 inches long and 2 inches wide was induced on the right side wing chine by the impact of a fairly large object (figure 21). A series of scrapes was formed on the aft wing and inboard elevon underside by the high velocity, low angle impact of a number of objects (figure 22). Several of the scrapes line up and indicate that the major dimension of the impacting debris was about 1 inch.

Sources of damaging debris were similar to those encountered on previous flights. The gouge on the right-hand wing chine was caused by a piece of ET insulation about 18 inches long which was lost during ascent from a load alleviation ramp on the hydrogen tank (figure 23). Several such pieces were lost and may also account for the damage to the wing and inboard elevon. Another candidate for the wing damage is ice from the anti-geyser line. Most of this ice, however, as seen in figure 23, has been retained to orbit insertion. Ice observed on acreage areas of the insulation in this photo is air ice produced by foam venting in second stage flight; it is not believed to represent a

debris hazard. The hold-down posts continued to generate debris but, fortunately, none of the material hit the orbiter. Figures 24 and 25 present a pre- and post-launch view of north post M-7. Note that substantial amounts of the white insulation material are missing in figure 25 from the post base. One such piece (figure 26) was observed on film moving up out of the flame hole but away from the orbiter at approximately 1 second after ignition when the vehicle had risen about 5 feet. Figure 25 shows a clear view of the post support structure and the flat top plate which deflects SRB plume flow, and debris, upward toward the vehicle. The post strut covers survived launch intact due to the application of insulation over their placement bolts (figure 24) but many were loose and could be lifted off without resistance.

Two modifications were made to the pad as a result of STS-4 debris experience. Hold-down post insulation was reduced to minimal levels. The insulation which was packed at the post base was replaced with a steel belly band and that on the base webs was eliminated. The strut covers were modified to accept internally penetrating bolts and were faired so as to lower the incident flow heating induced as the SRB plumes passed overhead. An important change was made to the ET following STS-4 in that the principal source of ice on the launch vehicle, the anti-geyser line, was eliminated. Studies had shown that propellant geysering would not occur in its absence, so it was removed to reduce ET weight and eliminate an important debris source.

STS-5 DEBRIS EXPERIENCE

The damage patterns established on STS-5 are important because they reflect representative damage for future flights unless additional modifications are made to reduce debris sources. STS-5 was also important because it allowed five flights worth of tile damage to be viewed simultaneously in that the gray tile repairs are easily visible. The most extensive damage was experienced on the right-hand lower side of the nose (figure 27). Those damage repairs seen in this figure which are essentially circular are associated with hail damage experienced by the vehicle on the pad immediately prior to STS-4. New debris damage sites are easily visible, though, as are many repaired debris impact streaks. An area that exhibited substantially less debris damage on STS-5 was the right wing and onboard elevon underside. This can be attributed directly to the removal of the ET anti-geyser line and its associated ice (compare figure 28 to figure 17). All other debris damage was representative of that experienced on previous flights.

The debris damaging the orbiter right-hand nose was ET insulation from either the intertank/upper hydrogen tank areas or from the nose of the LOX tank. Intertank debris is transported to this region by flow resulting from impingement of the SRB bow shock on the ET. Nose debris receives sufficient momentum to cross streamlines and reach the orbiter as the result of being accelerated over the ogive of the LOX tank. No significant insulation degradation on the ET can be observed

in these areas (figure 29) which is consistent with the fact that the maximum debris dimension as inferred from the damage is approximately 1 inch. Pad debris cannot be shown to have produced any tile damage on STS-5. The amount of hold-down post insulation applied for this flight was greatly reduced and was placed in an area where the majority of it would be physically retained (figure 30). Post-flight inspection, however, revealed that several inch-sized pieces were lost during launch. The major pad debris source which remains unresolved is the hold-down shoe shim material. The epoxy-based shim is poured around the SRB support pads after they have been installed in the shoe; the shim is designed to be retained firmly in the shoe, but this has not always occurred (figure 31). Because the shoe serves as a source of upward plume reflection the shim material has the potential of impacting the orbiter if it is released.

The only major debris-reducing modification to the vehicle undertaken after STS-5 was an improvement of the insulation placed over the thermal short on a line mount at the ET nosecap. This short had been foamed over initially for STS-4 but that was not totally effective in preventing ice formation. An effort has also been made to improve the retention characteristic of the hold-down shoe shim material by improving the application procedure.

CONCLUDING REMARKS

Figure 32 presents a summary of the principal orbiter TPS tile debris damage regions experienced on each of the first five space shuttle flights. The only potentially catastrophic damage was encountered on flights STS-1 and STS-2 as the result of ET lightning band or cable tray debris and pad hold-down post insulation debris. The elimination of these sources as well as the principal source of ice on the launch vehicle, the ET anti-geyser line, has resulted in a fairly repeatable and well understood debris damage pattern. STS-5 was typical of debris damage which can be expected on future flights unless spallation of the ET insulation can be eliminated. Five flights worth of repaired debris damage can be observed on the left-hand side of the orbiter nose (figure 33) where hail damage was minimal and around the right-hand umbilical well (figure 34). Debris moving near the lower surface of the vehicle is brought into impact with the orbiter just forward and outboard of the umbilical wells by upflow around the aft orbiter/ET attach structure.

A summary of potentially damaging debris produced by the launch vehicle and pad is presented in figure 35. The debris is categorized by its potential damage severity which may or may not coincide with damage which it has actually caused to date. "Safety of flight" severity is assigned to debris which potentially could damage the orbiter windows or TPS tiles to the point that either the mission or the vehicle was lost. All known "safety of flight" debris sources have been eliminated. "Significant" severity is based on either the size or extent of damage. Figure 36 summarizes steps taken to date to eliminate these sources.

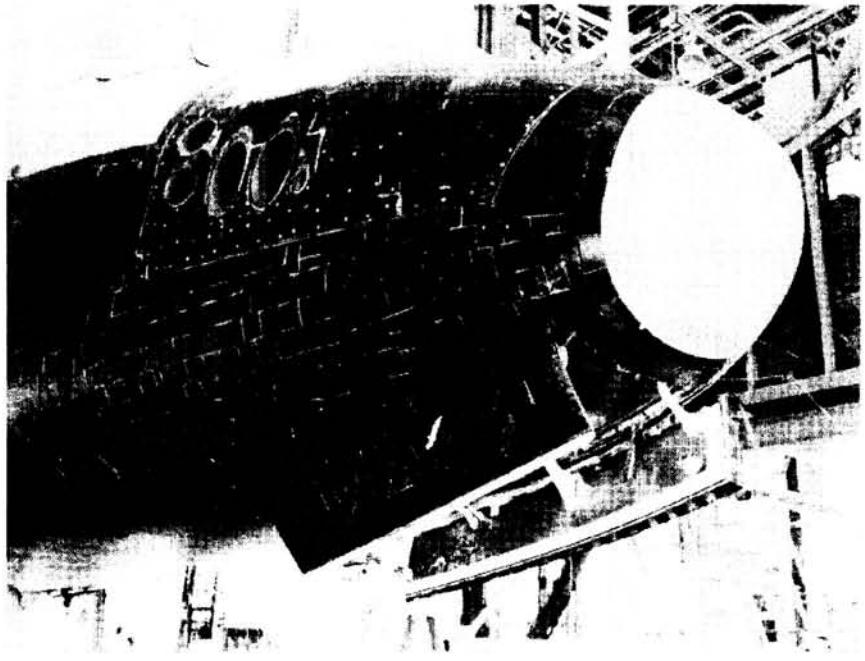

Figure 1.- Nose gear door tile damage (STS-1).

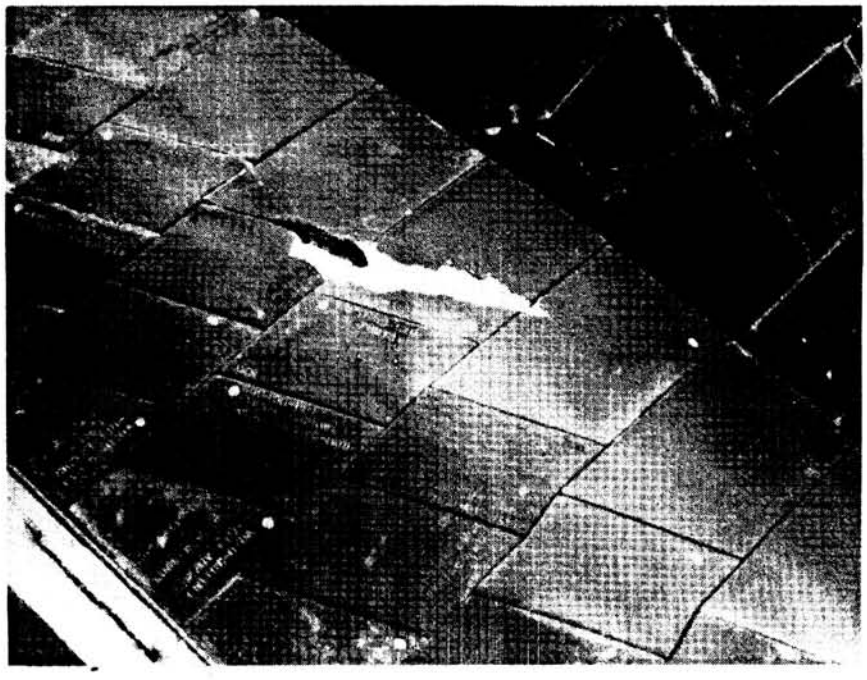

Figure 2.- Close-up of nose gear door tile damage (STS-1).

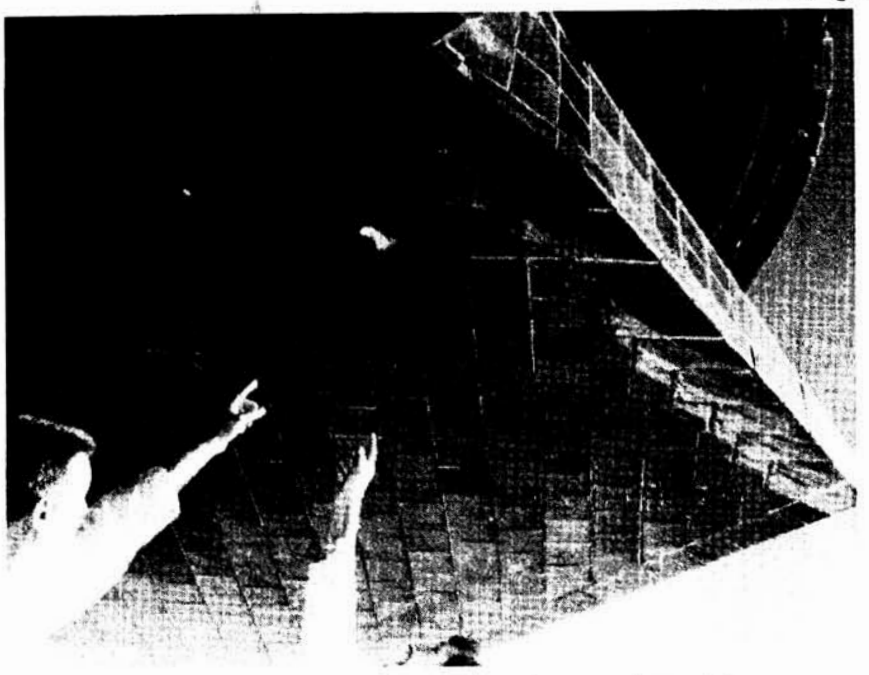

Figure 3.- Body flap tile damage (STS-1).

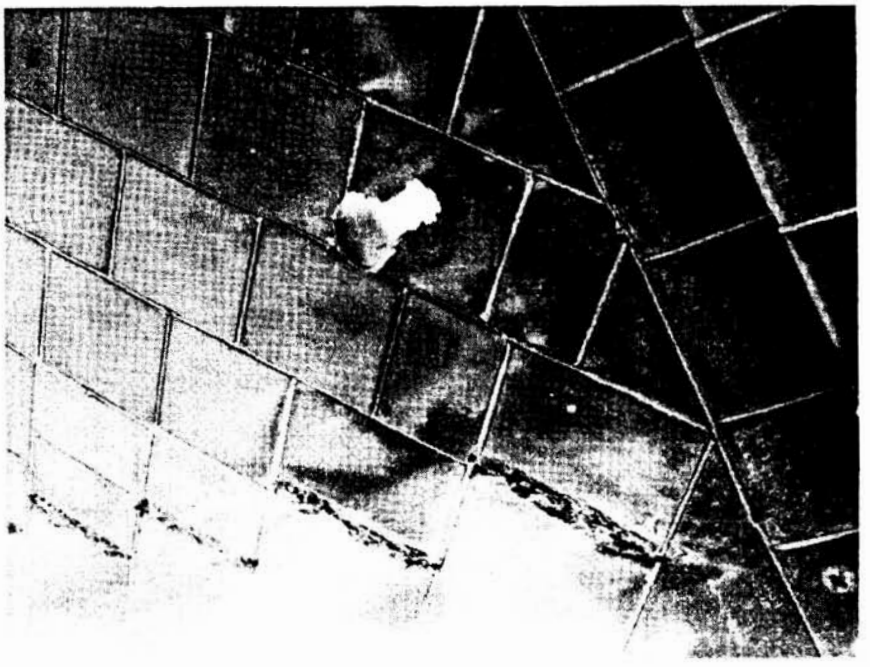

Figure 4.- Close-up of body flap tile damage (STS-1).

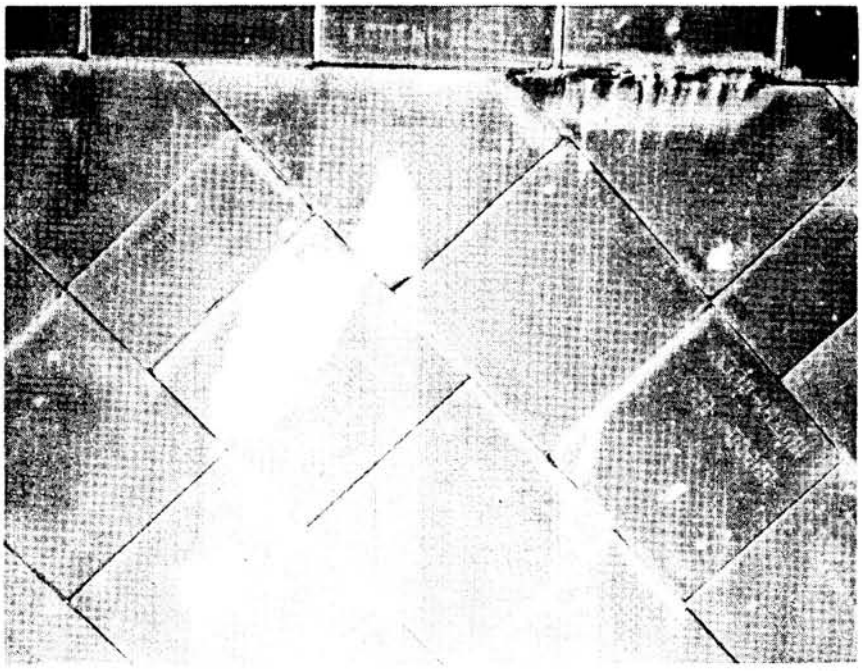

Figure 5.- Right-hand inboard elevon tile damage (STS-1).

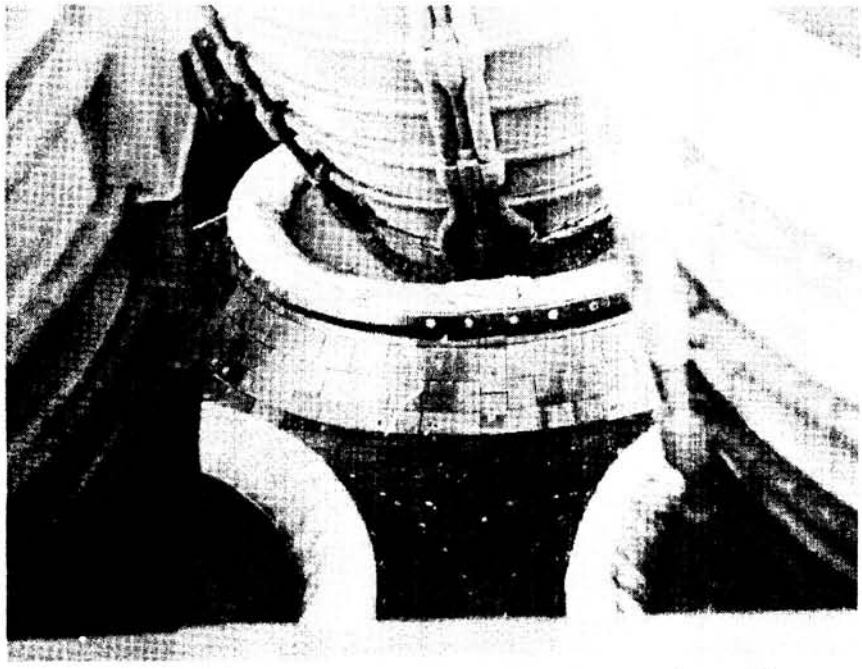

Figure 6.- Base heat shield tile damage (STS-2).

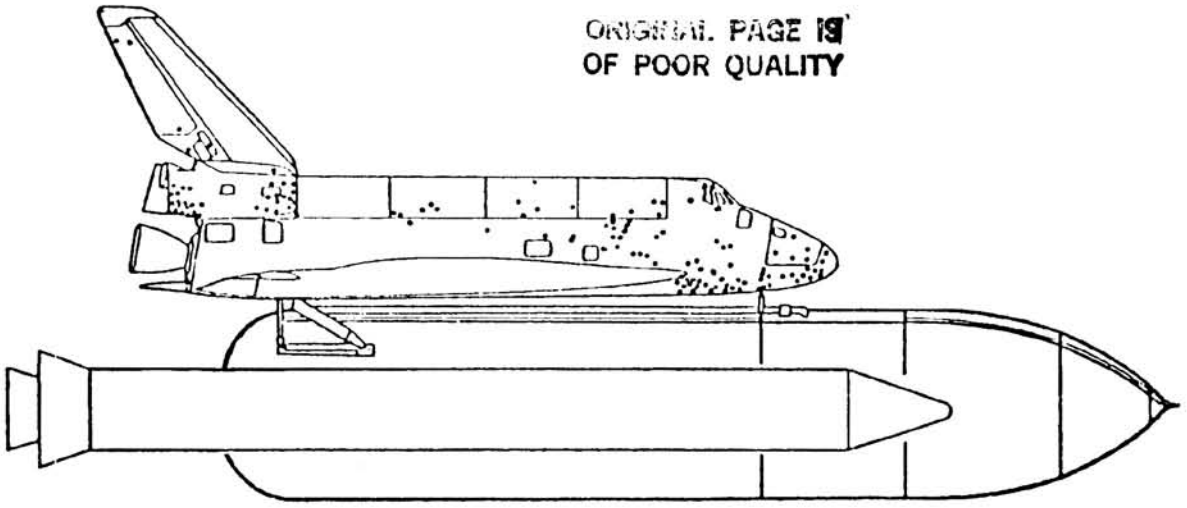

Figure 7.- STS-1 and STS-2 right-side debris damage composite.

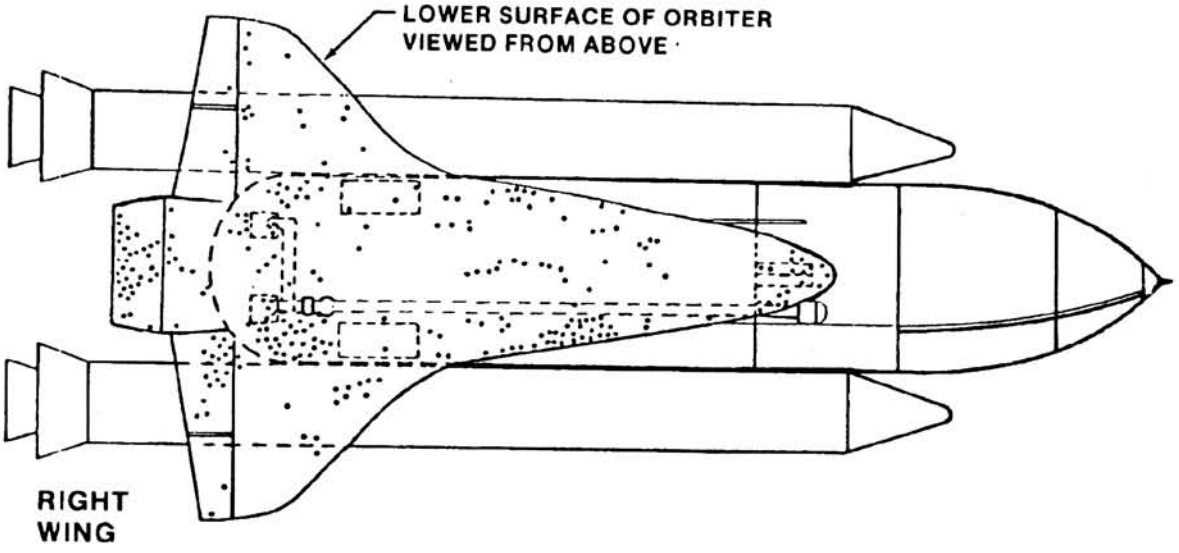

Figure 8.- STS-1 and STS-2 lower surface debris damage composite.

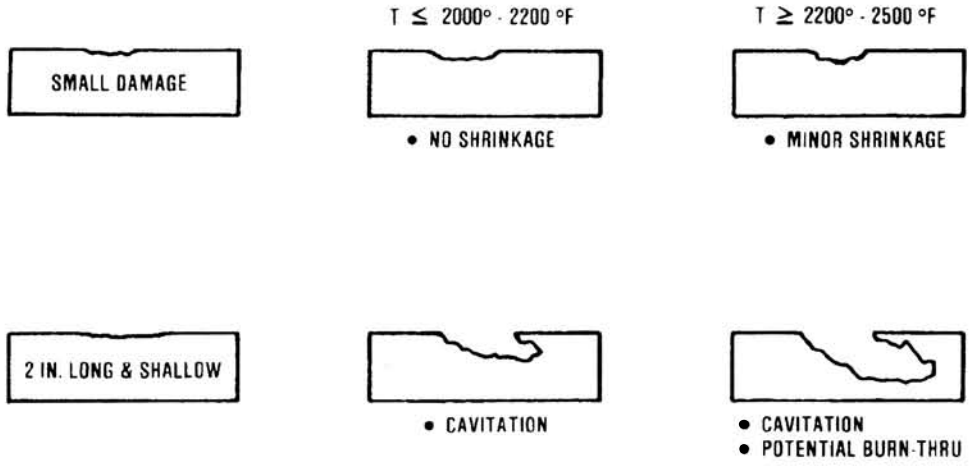

Figure 9.- TPS tile sensitivity to debris damage.

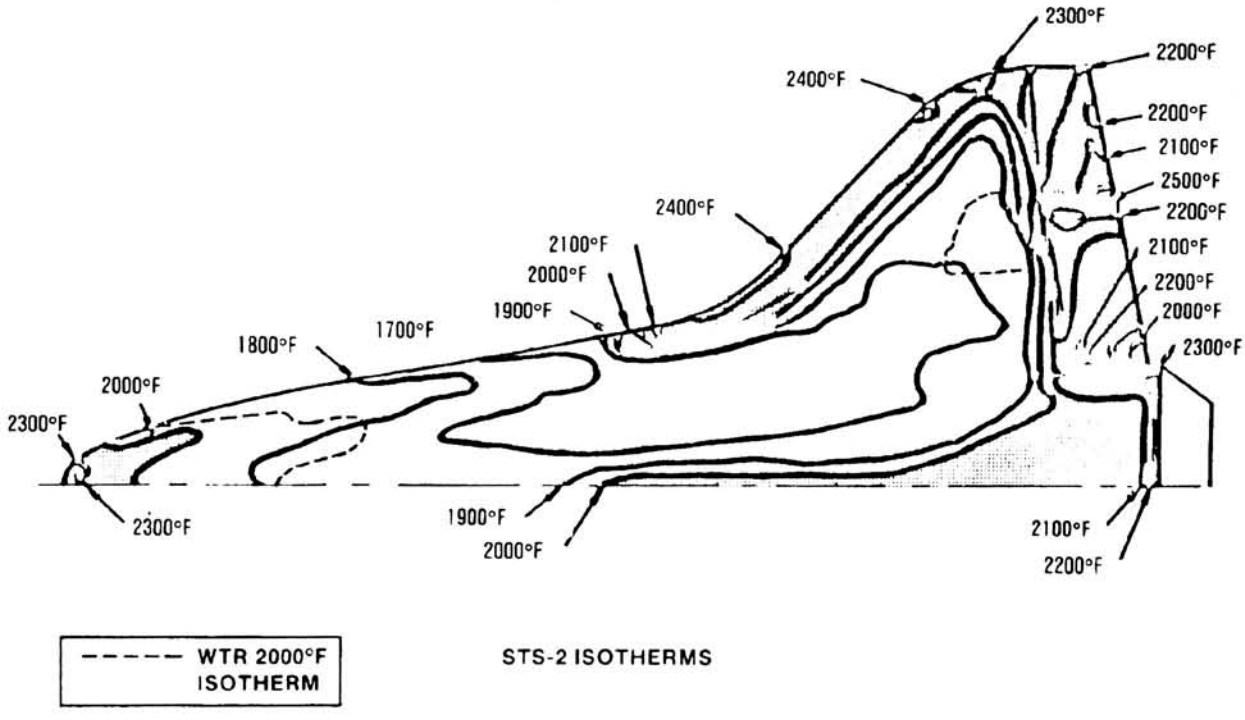

Figure 10.- Orbiter lower surface isotherms (STS-2).

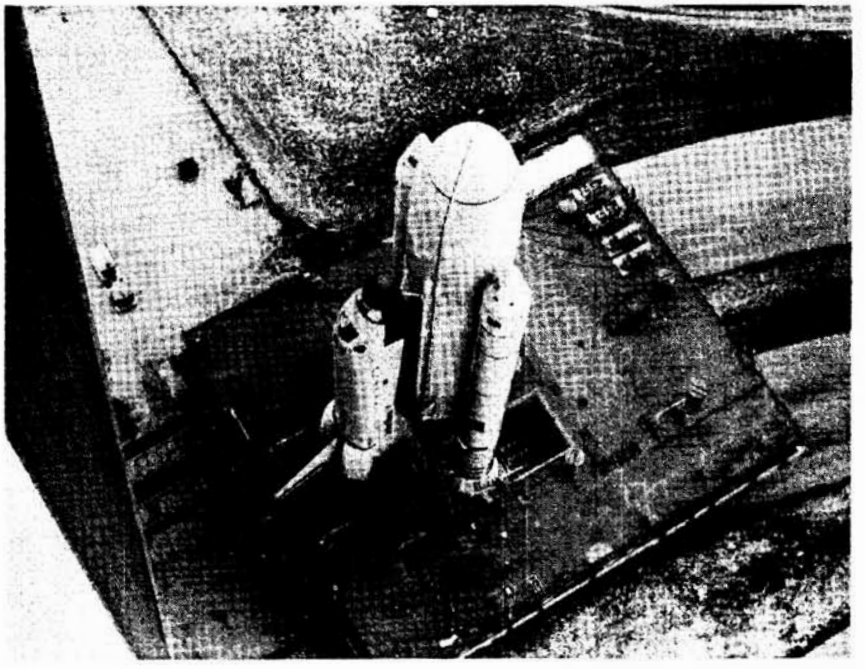

Figure 11.- Launch vehicle configuration (STS-1).

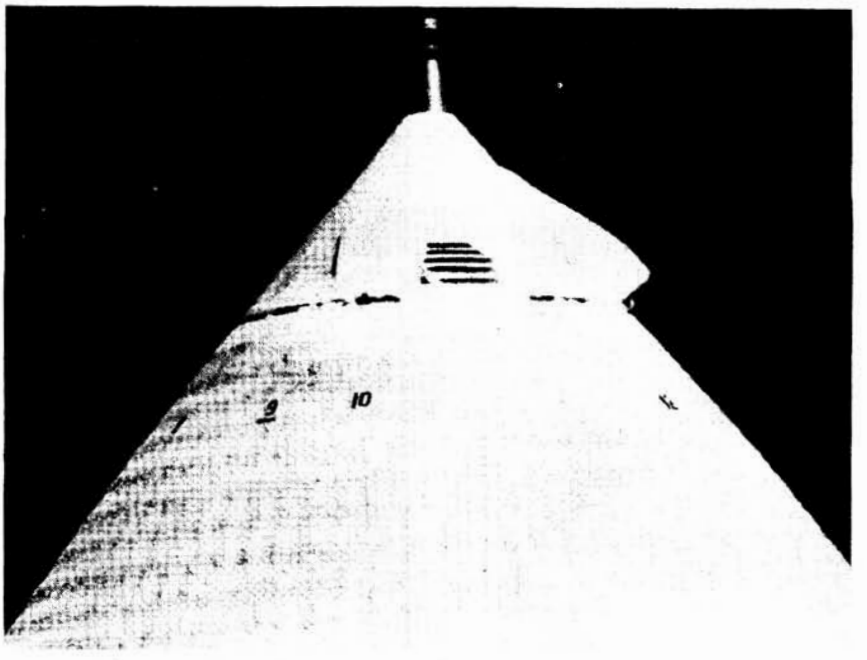

Figure 12.- Representative ET vent louver ice configuration (STS-1).

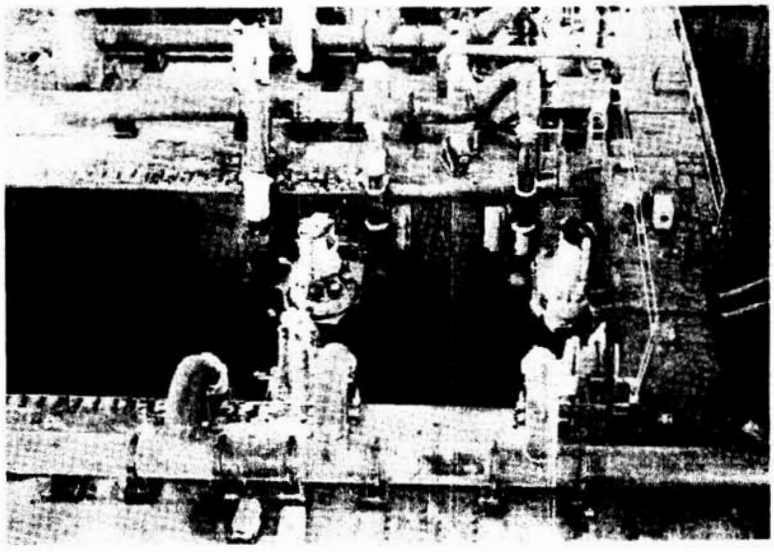

Figure 13.- Post-launch pad damage (STS-2).

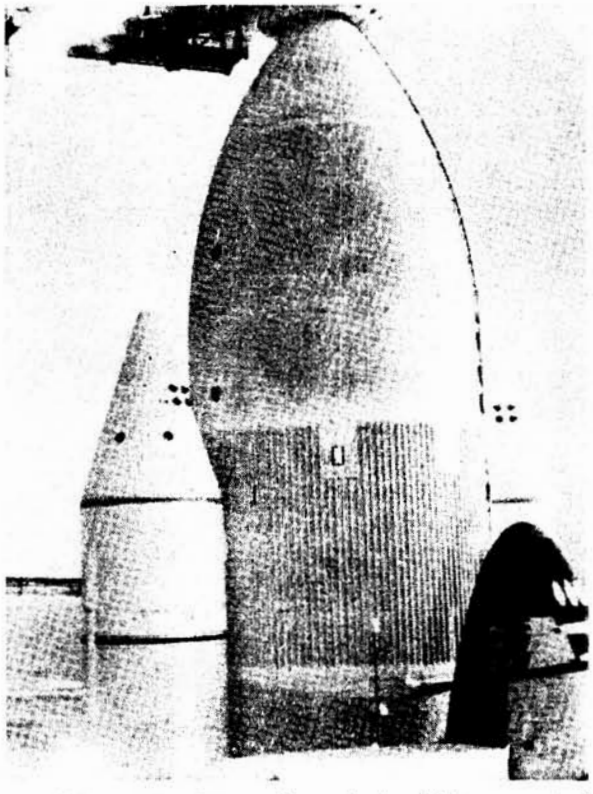

Figure 14.- ET LOX tank and facility vent hood during tanking (STS-2).

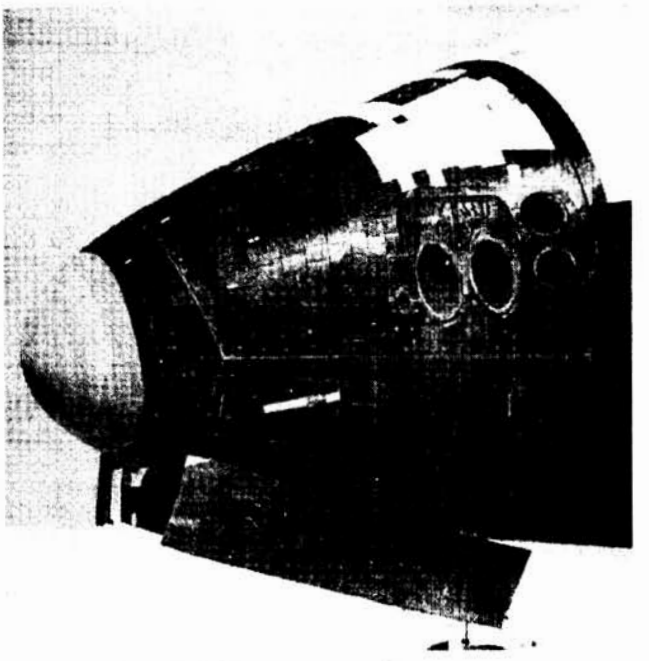

Figure 15.- Orbiter nose tile damage (STS-3).

Figure 16.- Window periphery tile damage (STS-3).

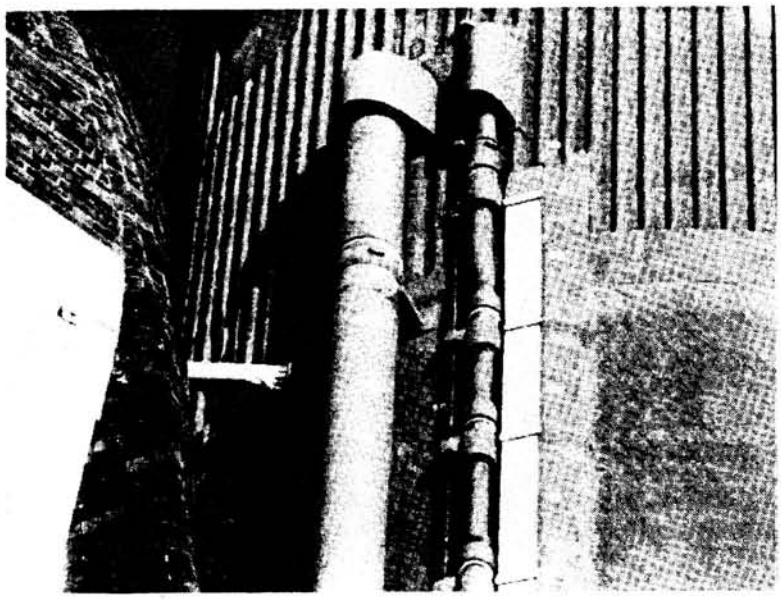

Figure 17.- ET feedline and anti-geyser ice after tanking (STS-3).

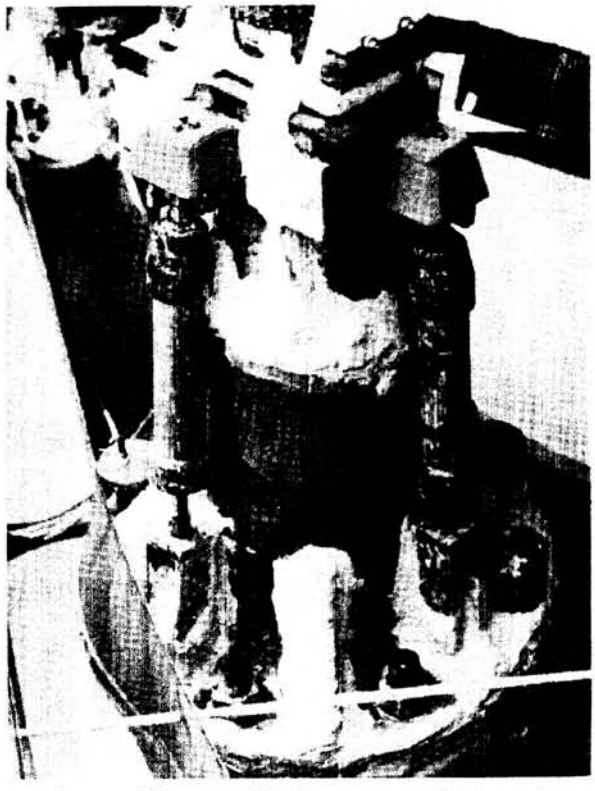

Figure 18.- Hold-down post M-3 prior to launch (STS-3).

Figure 19.- Hold-down post M-3 after launch (STS-3).

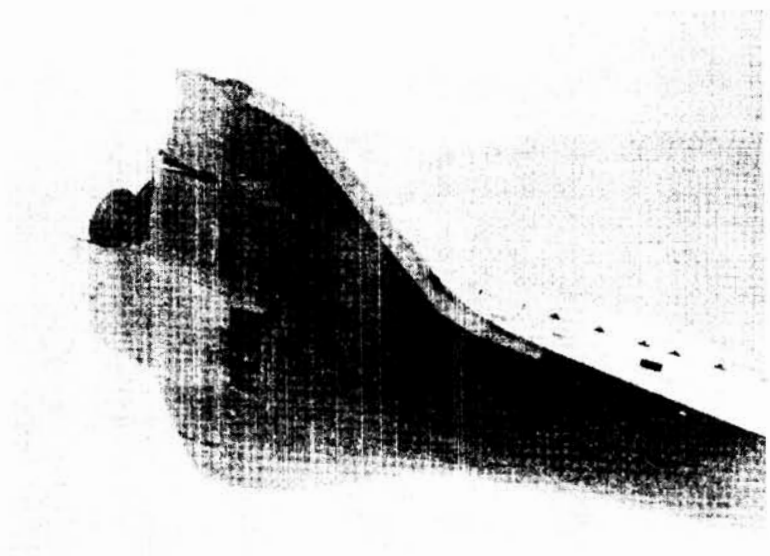

Figure 20.- Orbiter underside tile damage (STS-4).

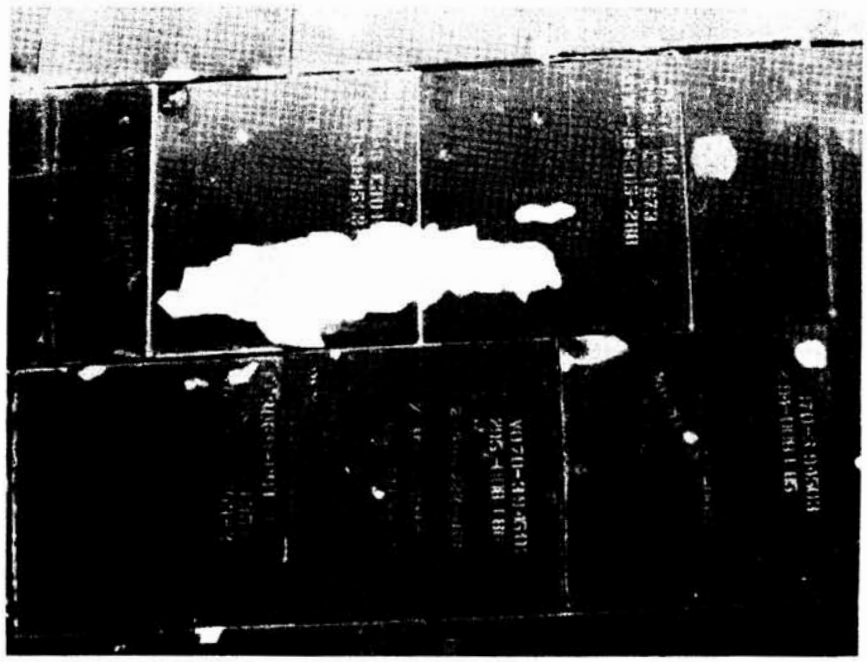

Figure 21.- Orbiter right-hand wing chine tile damage (STS-4).

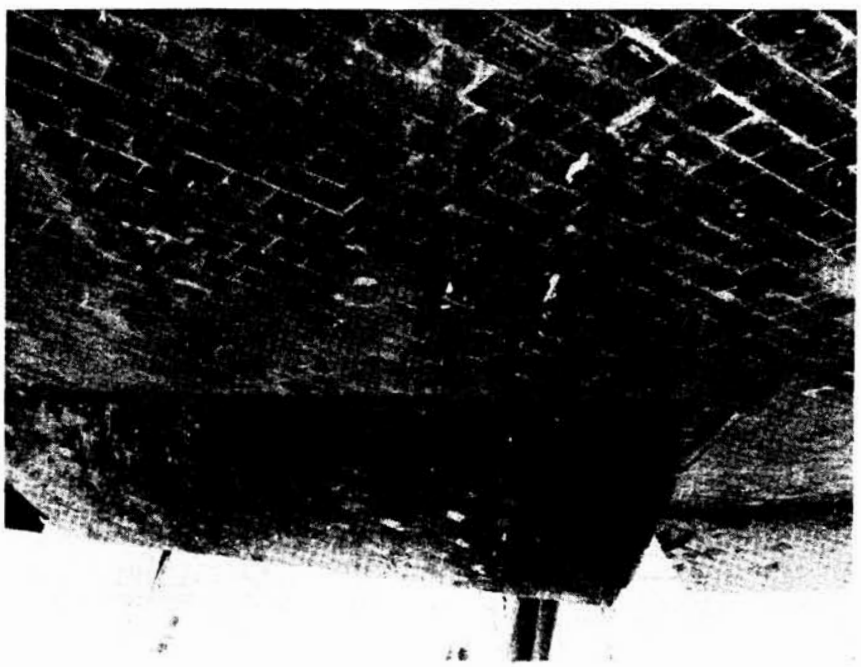

Figure 22.- Right-hand wing and inboard elevon tile damage (STS-4).

Figure 23.- ET during separation from the orbiter (STS-4).

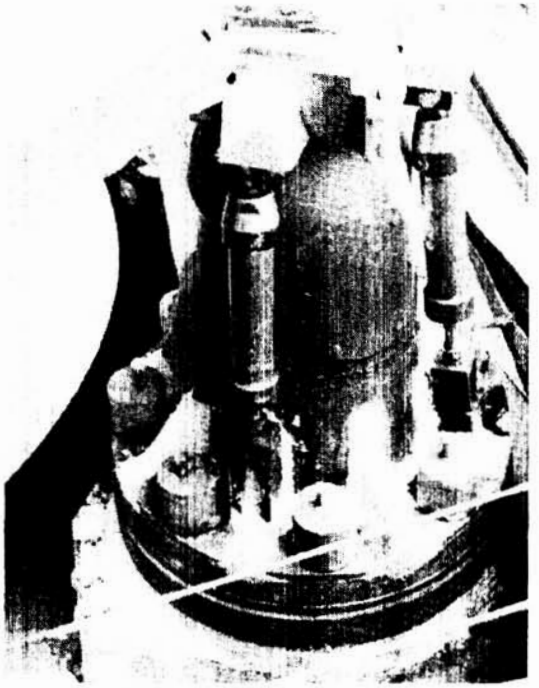

Figure 24.- Hold-down post M-7 prior to launch (STS-4).

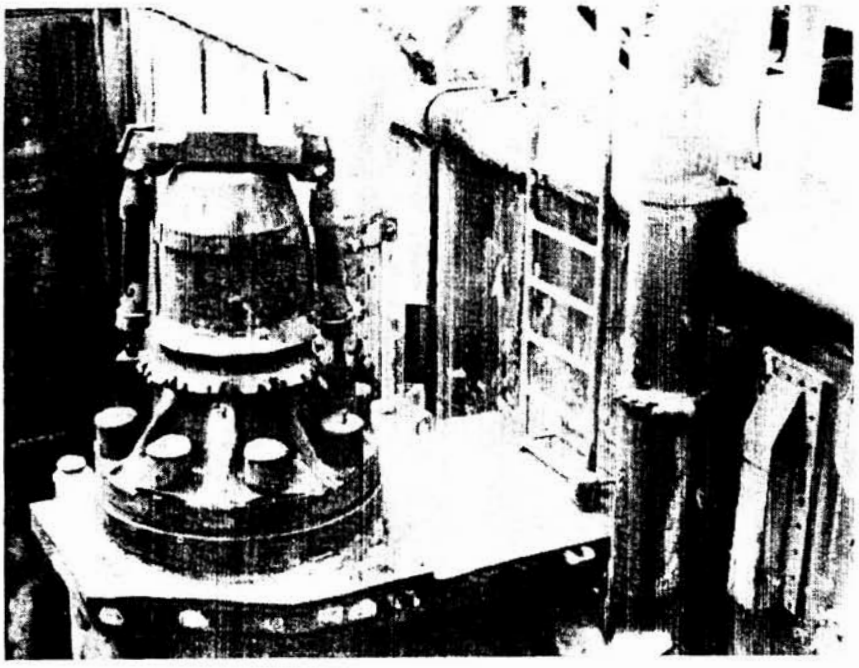

Figure 25.- Hold-down post M-7 after launch (STS-4).

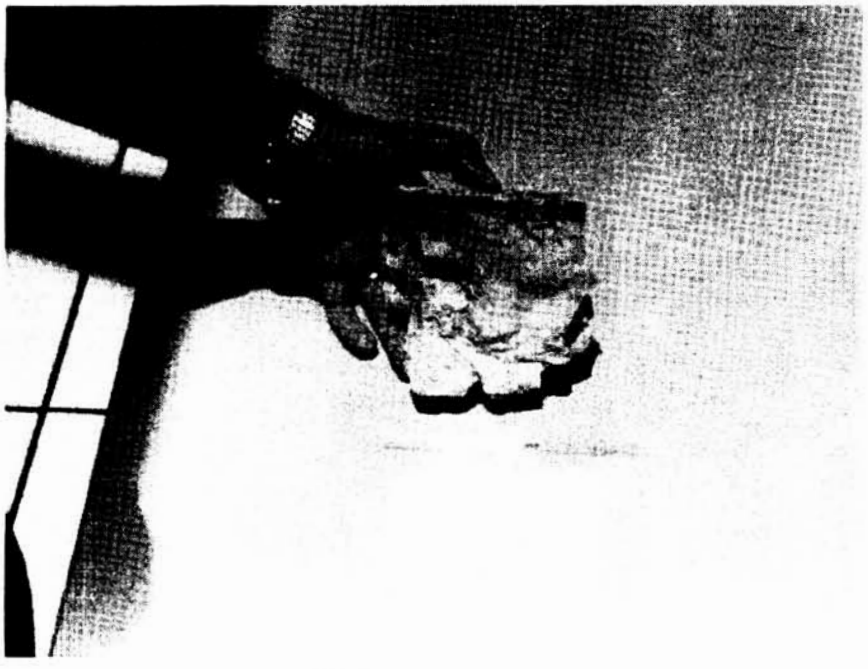

Figure 26.- Hold-down post insulation fragment released from post M-7 (STS-4).

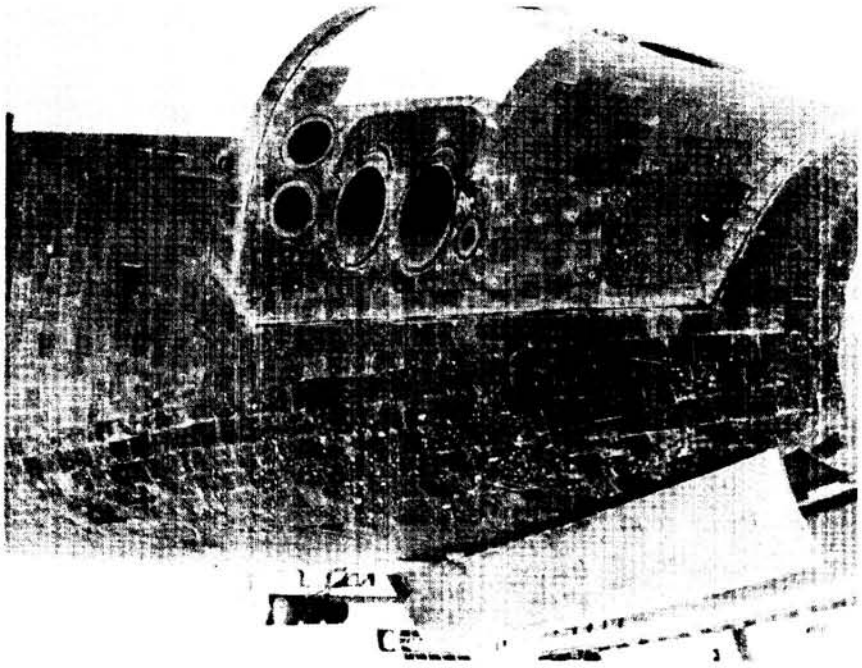

Figure 27.- Nose tile damage (STS-5).

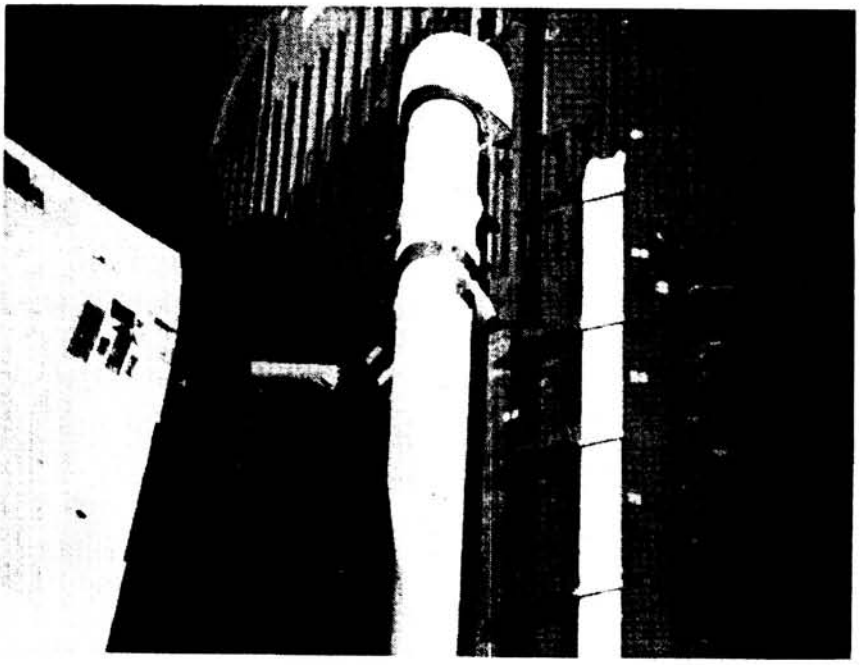

Figure 28.- Lightweight tank protuberance configuration (STS-5).

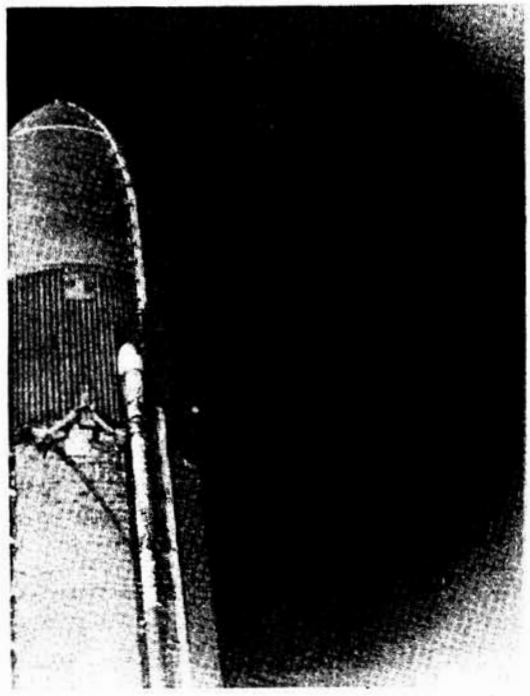

Figure 29.- ET during separation from the orbiter (STS-5).

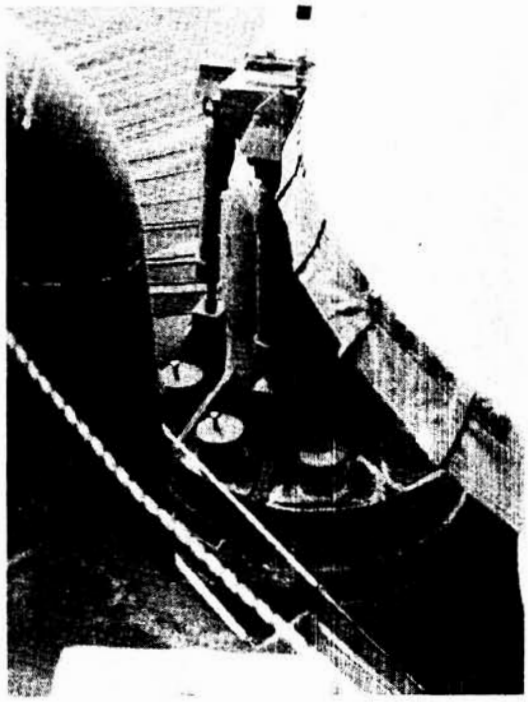

Figure 30.- Hold-down post M-3 prior to launch (STS-5).

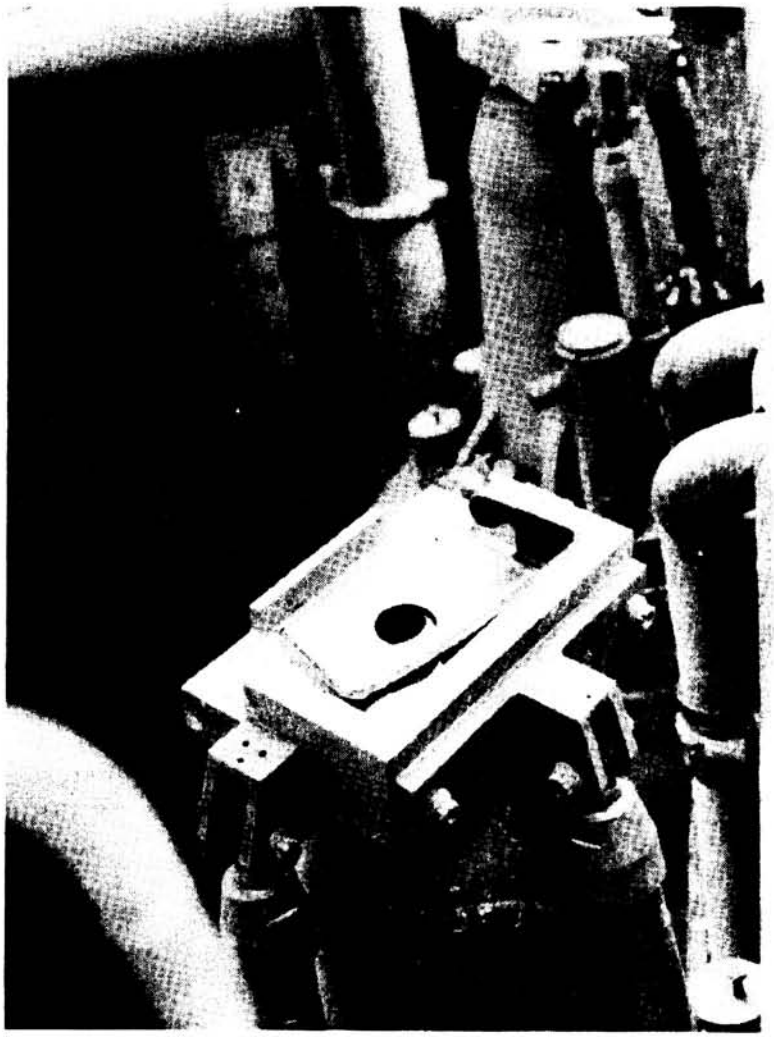

Figure 31.- Hold-down post shoe shim material after launch (STS-5).

PRINCIPAL DEBRIS DAMAGE REGIONS	STS-1	STS-2	STS-3	STS-4	STS-5
UPPER NOSE SURFACE AND AROUND WINDOWS	√		√	√	√
RIGHT SIDE OF NOSE AND WING CHINE	√	√	√	√	√
LEFT SIDE OF NOSE AND WING CHINE			√		√
AROUND UMBILICAL WELLS		√	√	√	√
RIGHT WING AND INBOARD ELEVON UNDERSIDES	√	√	√	√	
AFT FUSELAGE AND BODY FLAP UNDERSIDES	√	√	√	√	
BASE	√	√	√	√	√

Figure 32.- Orbiter TPS debris damage summary.

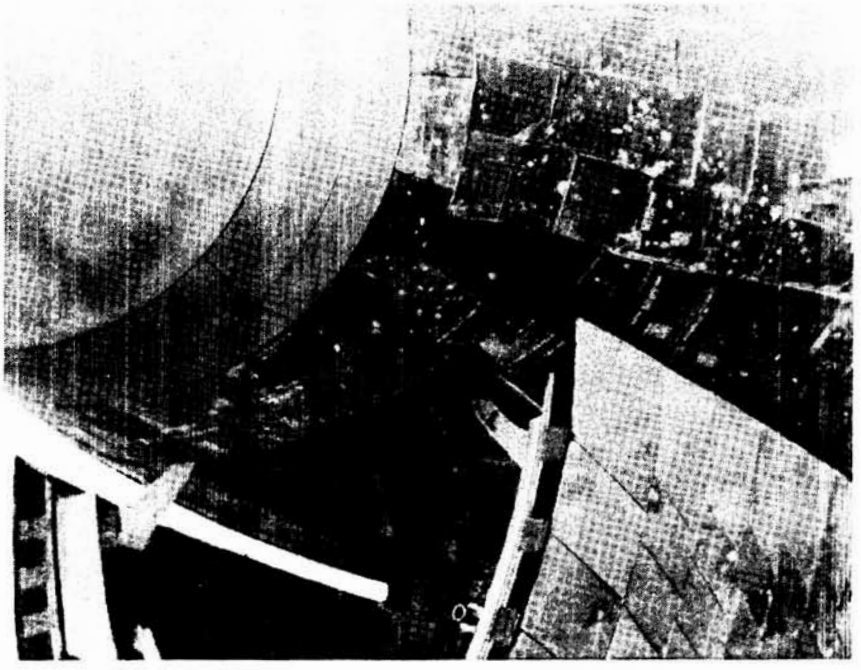

Figure 33.- Repaired debris damage on orbiter nose tiles (STS-5).

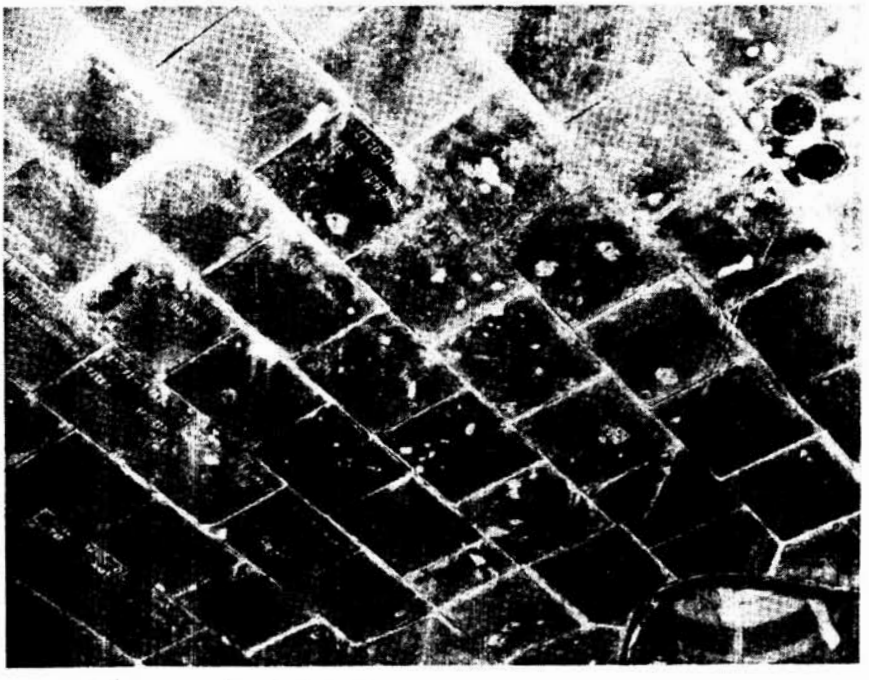

Figure 34.- Repaired debris damage at umbilical well (STS-5).

POTENTIAL DAMAGE SEVERITY

DEBRIS SOURCES	SAFETY OF FLIGHT	SIGNIFICANT	MINOR
ORBITER		TILE FRAGMENTS UMBILICAL H_2O ICE	TIRE STRAIN GAUGE WIRE UMBILICAL BAGGIE REMNANTS TILE SPACER SHIMS
ET	LIGHTNING BANDS VENT LOUVER ICE LOX PRESS LINE MOUNT ICE NOSECAP/OGIVE INTERFACE ICE	NOSECAP SLA PAL RAMP FRAGMENTS FEEDLINE & A/G LINE ICE* SOFI FRAGMENTS	TUMBLE VALVE COVER
SRB		FRUSTRUM INSULATION THROAT PLUG FRAGMENTS	STRUT BAGGIES* ET/SRB CONNECTOR PIECES*
PAD	HOLD-DOWN POST RTV POST STRUT COVERS	SHOE LINER MATERIAL	WATER TROUGH FRAGMENTS

*WAIVED FROM NO DEBRIS REQUIREMENT AS ACCEPTABLE

Figure 35.- Debris source summary.

- **FOR STS-2 AND SUBS**
  - ET LIGHTNING BANDS REMOVED
  - ET CABLE TRAY PHENOLIC SPACERS REDESIGNED TO ASSURE RETENTION
  - FACILITY BEANIE - CAP MODIFIED TO PREVENT ICE ON ET VENT LOUVERS
  - LH_2 PRESS LINE LOAD ALLEVIATION RAMPS REMOVED
- **FOR STS-3 AND SUBS**
  - USE OF HOLD-DOWN POST ABLATIVE INSULATION DRASTICALLY REDUCED
  - THERMAL SHORTS FORMING ICE AT ET NOSECAP/OGIVE INTERFACE ELIMINATED
  - ORBITER UMBILICAL BAGGIES RETAINED BY CLIPS RATHER THAN DRAWSTRING
  - TIRE PRESSURE STRAIN GAUGE WIRES MODIFIED TO ASSURE CLEAN RELEASE AT SPIN-UP
  - RIGOROUS PAD CLEAN-UP PROCEDURE INSTITUTED
- **FOR STS-4 AND SUBS**
  - THERMAL SHORT ON LOX PRESSURIZATION LINE MOUNT FOAMED OVER
  - SRB FRUSTRUM INSULATION APPLICATION TECHNIQUE REVISED TO PREVENT SPALLATION
- **FOR STS-5 AND SUBS**
  - HOLD-DOWN POST STRUT COVERS MODIFIED TO ELIMINATE EXPOSED BOLTS TO ASSURE RETENTION
  - HOLD-DOWN POST RTV INSULATION MINIMIZED
  - ET ANTI-GEYSER LINE REMOVED
- **FOR STS-6 AND SUBS**
  - THERMAL SHORT ON LOX PRESSURIZATION LINE MOUNT FOAMED OVER

Figure 36.- Summary of modifications to reduce debris.

N84 10125

ASCENT AIR DATA SYSTEM RESULTS FROM THE SPACE SHUTTLE FLIGHT TEST PROGRAM

Ernest R. Hillje and Raymond L. Nelson
NASA Lyndon B. Johnson Space Center
Houston, Texas

SUMMARY

The ascent air data system of the Space Shuttle consists of a simple biconic spike probe on the nose of the external tank. Pressure measurements were calibrated in a wind tunnel to obtain vehicle attitude and speed (relative to the air) and dynamic pressure. The wind tunnel test data analysis and the calibration are discussed in terms of test problems and calibration parameter formulation. The flight pressures are traced from telemetry data to final air data products. Analysis of the flight results showed that static pressure could not be accurately determined at the higher Mach numbers (above ≈2.0). By replacing static pressure with data from a postflight estimated trajectory the ascent air data system performance met the user requirements. Lessons learned are enumerated, the most important being the need for a thorough systems integration effort.

INTRODUCTION

The Space Shuttle vehicle is the major space transportation system that will carry payloads to low Earth orbit. During the ascent phase of each mission, the vehicle is subjected to its highest aerodynamic loading; it also encounters critical localized aerothermodynamic heating. To perform postflight assessments of the structural and heating conditions as well as the related aerodynamic characteristics and performance, analysts need to know the vehicle's attitude and environment (see tables I and II). These assessments will, in turn, allow expansion of the flight envelope during the orbital flight test (OFT) series. Obtaining this data for the post-flight analyses is the purpose of the ascent air data system (AADS).

The AADS consists of a $30^{\circ}/10^{\circ}$ biconic spike, or probe, mounted on the tip of the external tank (ET). Located on the spike are five pressure ports that are sensitive to pitch and yaw attitude, total pressure, and static pressure. For the Space Shuttle OFT series, data were obtained and used in conjunction with wind tunnel calibrations to determine the vehicle angle of attack, angle of sideslip, static pressure, and total pressure. The last two terms were then used to calculate the vehicle Mach number and dynamic pressure. The wind tunnel calibrations span the Mach number range 0.5 to 4.63, the region of most interest to postflight system analysts because it contains

maximum dynamic pressure as well as transonic flow. Initial results from the AADS were compared with reconstructed trajectory (digital simulation) data. Later, comparisons were made with a "best estimate trajectory" (BET), which was also used to supplement the AADS results.

The objective of this paper is to describe the AADS hardware, the wind tunnel data analysis, the calibration formulation, the post-flight data processing, and to assess the flight results.

NOMENCLATURE

Symbols and Abbreviations

M	Mach number
P	Ambient, or free-stream, pressure
PAVE	Averaged bottom and upper pressures
PB, P_{BOTTOM}	Bottom orifice pressure (or Z port)
PL, P_{LEFT}	Left orifice pressure
PR, P_{RIGHT}	Right orifice pressure
PS	Static pressure
PT, P_{PITOT}	Total orifice pressure
PU, P_{UPPER}	Upper orifice pressure
$\bar{q}$	Dynamic pressure
α	Angle of attack (pitch)
β	Angle of sideslip (yaw)
$\Delta P\alpha$	Differential pitch pressure, $P_{BOTTOM} - P_{UPPER}$
$\Delta P\beta$	Differential yaw pressure, $P_{RIGHT} - P_{LEFT}$
CPSD	Static pressure calibration parameter, or decrement
C_N	Normal force coefficient
C_m	Pitching moment coefficient
CPTD	Total pressure calibration parameter, or decrement
CPα, CPA	Angle of attack (α) calibration coefficient
CPβ, CPB	Angle of sideslip (β) calibration coefficient
CPM	Mach calibration coefficient
PT1	Total pressure ahead of shock
PT2	Total pressure behind shock
CPASL	Slope calibration parameter for angle of attack
CPBSL	Slope calibration parameter for angle of sideslip
γ	Ratio of specific heats
X	Longitudinal axis
Δ	Incremental quantity

Subscripts

∞	Free-stream
WT	Wind tunnel related data
FLT	Flight data
SLOPE	Calibration parameter slope term
INT	Calibration parameter intercept term
PROX	Orbiter proximity effect on angle of attack
MSL	Misalignment

Abbreviations

AADS	Ascent Air Data System
ET	External Tank
NASA	National Aeronautics and Space Administration
SRB	Solid rocket booster
WT	Wind tunnel
OFT	Orbital flight test
BET	Best estimate trajectory
PS BET	BET static pressure override data
STS-N	Nth orbital flight of the Space Transportation System
STA	Longitudinal station on the external tank
WIG	Whichever is greater
TM	Telemetry
T	Time
QL	Quick-look (data)
CCT	Computer compatible tape
CDC	Control Data Corporation
RI	Rockwell International
MMC	Martin Marietta Company
JSC	Johnson Space Center
MSFC	Marshall Space Flight Center
STD	Standard
STS	Space Transportation System
MSID	Measurement stimulus ID
FTS	Federal Telecommunication System
SSME	Space Shuttle main engine
NAV	Navigation
SIM	Simulated (trajectory data)

ASCENT AIR DATA SYSTEM DESCRIPTION

In early 1975, technical integration managers saw that accurate definition of the launch vehicle attitude and of certain air data parameters during the ascent phase of flight was needed for postflight evaluation of the structural, heating, and aerodynamic performance of the Space Shuttle. Several early configurations of the ascent air data system were considered[1], and in late 1977 a $30^{\circ}/10^{\circ}$ biconic configuration, shown in figure 1, was recommended and accepted. This

biconic spike is mounted on a 40° nose cone that mates to the ET ogive. The AADS spike also serves as a lightning rod.

Details of the AADS spike are shown in figures 2 and 3. The AADS spike is attached to the forward tip of the ET. Five pressure orifices are located on the 30° conical section of the AADS spike as shown. Four pressure transducers are housed in the 40° conic section of the tank nose cap and are used to sense the orifice pressures. The pitot (PT) orifice pressure (the indicator of total pressure) and the bottom (PB) orifice pressure are read by absolute pressure transducers (0 to 15 psia). The differential pitch pressure ($\Delta P\alpha$) and the differential yaw pressure ($\Delta P\beta$) are read by differential pressure transducers (+/-2 psi). These flight pressure transducers are calibrated in a laboratory before ET assembly and check-calibrated before flight. The basic transducer calibrations are obtained at various environmental temperatures to provide accurate pressure measurements at temperatures typical for the pressure transducer housing during launch. In flight, a temperature sensor installed in the proximity of the pressure transducers will monitor the temperature environment within the 40° portion of the nose cap during ascent.

The AADS spike is subject to two alignments. The first is between the $30^{\circ}/10^{\circ}$ spike and the 40° nose cone. Mating procedures were developed using tapered shims between these two sections to accommodate manufacturing differences, thereby reducing alignment errors. The second alignment is performed after the assembled nose cone is mounted on top of the ET. A transit setup is used to determine the plane of a slice through a lower section of the ET. (The station 2048 ring frame that contains the rear Orbiter attach point was used.) This plane is compared to a plane established at the spike using a clinometer and a special fixture that sits on the spike tip and affords a horizontal surface. Because any misalignment at this point is not adjustable, the measurements are recorded and used as a bias adjustment to the calculated pitch and yaw attitudes.

WIND TUNNEL CALIBRATION

Wind Tunnel Test Data Analysis

There is much experimental data on the flowfield around cones. There also exists theoretical data on this subject. Both of these sources of data were used to evaluate the AADS configuration and to estimate attitude sensitivity levels. However, detailed pressure data for the Space Shuttle AADS must be obtained from wind tunnel testing. The proximity of the Orbiter and the two solid rocket boosters (SRB's), and the cable tray fairing that extends along the ET all the way up to the AADS spike (resulting in an asymmetric configuration), cause disturbances in the local flow that must be accounted for. This

is particularly true in the important transonic flight regime where the vehicle loads are the greatest.

A wind tunnel test series was conducted that covered the Mach number region of interest, from Mach = 0.55 to Mach = 4.63, as shown in table III. Verification tests were run, as "piggy-back" tests to airloads testing, up to Mach = 2.5. For the AADS wind tunnel data base, the basic test series was conducted using a 7 percent scale forebody model (see fig. 4), in order to allow for a reasonable size for the AADS spike. A previous test, using a 0.4 percent model of the launch configuration, was run to determine the effect of the elements (Orbiter and SRB's) on the AADS spike measurements. The results of this test showed no effect in the yaw, or sideslip, direction; the SRB left and right elements evidently canceled each other. In the pitch, or angle of attack, direction the Orbiter caused the effect shown in figure 5. Note that the effect is a maximum at Mach = 0.5 and disappears at Mach = 1.2.

A problem that was encountered during the calibration of the Orbiter air data system was that of the uncertainty of the facility test conditions[2]. In order to circumvent this potential problem a flight test probe model (see fig. 4(c)) was used as a calibration standard to compare with both the facility indicated total pressure and the AADS measurement. Subsonically the facility and the AADS pressures showed good agreement. At some of the higher Mach numbers where the facility data deviated from the calibration standard (and the AADS probe showed good agreement) the AADS probe total pressure was considered accurate enough to use in the post-test data correction process. Figure 6 compares the theoretical value of the pressure ratio across a normal shock (PT2/PT1) to the measured values (AADS PT2 to facility PT1).

During the test program many problems occurred such as an erroneous right port reading in early tests, sting balance problems, poor transducer performance and pressure leaks. As a result corrections were made where possible, or data was discarded. In most cases flow tares were determined by running the model upright and inverted. Where available, facility standard tares were used. Many repeat runs were made to ascertain a test data uncertainty level. Also data were obtained in separate facilities at "overlap" Mach numbers of 1.55, 2.5 and 3.5. Where possible, Reynolds number effects were determined experimentally. Analytical studies had shown negligible effects, and this was supported by the experimental data in that any differences noted were within the wind tunnel data uncertainties. Early testing with the cable tray fairing on and off showed signficant effects and consequently a correction is included to account for this. Where each of these aformentioned testing irregularities appeared, a level of uncertainty was included in the overall AADS uncertainty analysis.

The probe pressure orifice locations were selected based on early parametric testing to allow the most accurate determination of the desired air data system products of Mach number (M), dynamic pressure

($\bar{q}$), angle of attack (α) and angle of sideslip (β). Compromises were necessary because probe locations for pitch and yaw attitudes were not compatible with those for static pressure. The pitch-plane and yaw-plane differential pressures, $\Delta P\alpha$ and $\Delta P\beta$, are highly linear with respect to the angle of attack and angle of slideslip, respectively. An example of this, for α, is shown in figure 7. Mach number is functionally related to PT and the average of PB and PU (upper orifice pressure) and static pressure is related to the latter (i.e., the average). This is indicated in figure 8 where CPM is the ratio of PT over PAVE. The analysis of the wind tunnel testing results showed that all of the AADS calibration parameters (needed to determine the air data products) were dependent on Mach number, angle of attack, and angle of sideslip. These however are also in the list of the desired air data products. Therefore an independent set of dimensionless calibration coefficients was required in order to avoid an extensive iteration scheme. The complete set follows:

Mach calibration coefficient $= CPM = \frac{PT}{PAVE}$

Angle of attack calibration coefficient $= CP\alpha = \frac{\Delta P\alpha}{PT}$

Angle of sideslip calibration coefficient $= CP\beta = \frac{\Delta P\beta}{PT}$

where $PAVE = PB - 1/2\ \Delta P\alpha$.

These coefficients can be obtained directly from the flight measurements and used in conjunction with a wind tunnel determined set of calibration curves.

AADS Calibration Formulation

The relationship between the wind tunnel calibration and the "calibration-corrected" flight data is shown schematically in figure 9. Briefly, in the wind tunnel, the forebody model of the ET containing the spike probe is subjected to the wind tunnel free-stream conditions (data subscripted WT). These data and the probe measurements are used to obtain the wind tunnel calibration coefficients and calibration parameters. After the flight, the flight air data products (M, $\bar{q}$, α, β) are desired (subscripted FLT). The flight probe measurements are recorded and used as the input to the wind tunnel calibration formulas to obtain α, β, PT and PS (static pressure). The last two calibration-corrected terms are then used to calculate Mach number (M) and dynamic pressure ($\bar{q}$). What remains to be defined is the formulation of the calibration parameters for PS, PT, α, and β.

To determine the static and total pressures the classic "decrement" style of formulation was used where:

Static pressure calibration parameter $= CPSD = \frac{PAVE - PS}{PAVE}$

Total pressure calibration parameter $= CPTD = \frac{PT - PT2}{PT}$

Early in the program it was felt that the most difficult term to determine would be static pressure, partly because the orifices used (PB and PU) were on a 30° cone, and partly because the pressure ratio formulation tends to blow up at high altitudes (and high Mach numbers) where the static pressure is very low. (This was substantiated with the early flight data from STS-1 and alternate data was used as discussed in "Flight Results and Discussion"). The variation of CPSD with the angle of attack calibration coefficient, CPA, and the angle of sideslip calibration coefficient, CPB, was seen to be parabolic in nature. This is shown in figure 10, for CPB, for several CPM's (subsonic). The variation of CPSD with CPM is much more nonlinear as shown in figure 11. Curve fit analyses, to obtain a reasonable fit with CPM, reduced the 3 sigma error from approximately 0.12 to 0.02 by using a three part calibration.

For total pressure, CPTD showed the effect of α and β only below $M \approx 1.5$, or CPM = 1.35. Above this Mach number the probe measures PT2 directly (i.e. CPTD = 0). At subsonic speeds ($PS/PT2 > 0.5283$) the calibration - corrected pressure is PT1. Here the isentropic equation is used, where:

$$M = \sqrt{5\left[\left(\frac{PT1}{P_\infty}\right)^{2/7} - 1\right]},$$

P_∞ = PS = ambient pressure,

and PT1 = total pressure ahead of the shock. Above Mach 1.0, the Rayleigh pitot formula is used, where:

$$\frac{PT2}{P_\infty} = \left(\frac{6M^2}{5}\right)^{7/2}\left(\frac{6}{7M^2-1}\right)^{5/2}$$

The dynamic pressure, $\bar{q}$, is calculated using the equation for a thermally perfect gas:

$$\bar{q} = \frac{\gamma}{2}(P_\infty)(M)^2,$$

where the ratio of specific heats, γ, is taken as 1.4 and P_∞ = PS.

The angle of attack, α, and angle of sideslip, β, were calculated from calibration parameters defined using a slope and intercept concept because of the high degree of linearity in the data, shown previously in figure 7. For the slopes,

$$\alpha \text{ slope calibration parameter} = CPASL = \left[\frac{\Delta P\alpha/\bar{q}}{\Delta\alpha}\right]_{WT}$$

$$\beta \text{ slope calibration parameter} = CPBSL = \left[\frac{\Delta P\beta/\bar{q}}{\Delta\beta}\right]_{WT}$$

In order to obtain flight data from these calibration parameters, the equations are inverted to obtain the α and β slope terms, thusly:

$$\alpha_{SLOPE} = \frac{\Delta P\alpha/\bar{q}}{CPASL} = \frac{(CP\alpha)(PT)/\bar{q}}{CPASL}$$

$$\beta_{SLOPE} = \frac{\Delta P\beta/\bar{q}}{CPBSL} = \frac{(CP\beta)(PT)/\bar{q}}{CPBSL}$$

For the magnitudes of the intercept terms (α_{INT} and β_{INT}), the above slope equations are evaluated at $\alpha = 0$ and $\beta = 0$, respectively. An additional term ($\Delta\alpha_{PROX}$) is needed in the pitch plane to account for the proximity effect of the Orbiter on the $\Delta P\alpha$ measurements (see fig. 5). The variation of the slope and intercept terms with Mach number (for α) are shown in figures 12 and 13, respectively. Both are fairly well behaved with non-linearities in the Mach 1.3 to 1.8 region. Note that above this region both terms are nearly constant. Angle of sideslip slopes were similar but the intercept term was quite different due to the asymmetry caused by the cable tray fairing.

The flow of the AADS calculations is shown in figure 14. Note that after the Mach number (M) and dynamic pressure ($\bar{q}$) are determined they can be used directly to obtain α and β. The angle of attack and angle of sideslip calculations both require an additional term (MSL) determined from an alignment check after nose cone installation on the ET (see "Ascent Air Data System Description").

FLIGHT DATA

The heart of the AADS flight instrumentation package is the four pressure transducers mounted on a bulkhead inside the 40° nose cone on the tip of the ET (fig. 3). The pneumatic lines are short, which reduces the lag factor to a negligible quantity. The pressure transducers are bench calibrated by the manufacturer twice, with a vibration test done in between. Each calibration starts at a zero point, goes to full scale in 12.5 percent increments, then is decremented in the same steps to reach the starting point. Recordings are made at each step. This procedure is repeated twice at five different control temperatures ranging from 50° to 240° Fahrenheit. The nominal calibration was for 150°F with temperature compensation made for any deviations using a polynomial that was a function of both the temperature difference and the percent of full scale pressure level. The allowable transducer calibration error was 1/2 percent of

full scale. The uncertainty would approximately double without temperature compensation. The digitization of the flight pressures was done using 252 counts for the full scale range, resulting in a data granularity of 0.0595 psia for the absolute pressures (PT and PB) and 0.0159 psia for the differential pressures ($\Delta P\alpha$ and $\Delta P\beta$).

The flight data for the AADS were available from the Orbiter telemetry (TM) system as well as from the on-board recorder. Plans for postflight analyses included using both sources. The planned AADS postflight data flow is shown in figure 15. The TM data for "Quick Look" analyses was generally available 24 hours after launch as part of the Marshall Space Flight Center (MSFC) Shuttle Data Base. Tracing the "Quick Look" path, the data was converted from volts to counts using the nominal calibration curve ($T = 150^{\circ}F$), then converted from counts to pressures in engineering units and loaded into both the Martin Marietta (MMC) data base at Slidell, LA and into the MSFC data base. The data were then transmitted to the Space Shuttle prime contractor in California for conversion to the air data products. The basic differences in the "Final" data were temperature compensation, and use of best estimated trajectory (BET) data for comparison purposes. Two additions were made to the AADS data processing system for the STS-1 postflight analysis. The first was the capability to access the STS data base directly from the NASA-Johnson Space Center using a remote terminal and an existing 1200 BAUD FTS telephone line. The second difference was the use of reconstructed trajectory simulation data for "Quick Look" analyses.

Samples of the basic flight data measurements are shown in figures 16 through 19. Figure 16 shows that the nose cap temperature was approximately 30° lower than estimated and dropped approximately 11° during ascent. The time history of the total pressure is shown in figure 17. Data levels obtained for pre-launch conditions, shown in figure 17(b) (see fig. 18 for bottom pressure) were adjusted to the static pressure at the ET tip elevation (approximately 280 feet above mean sea level), obtained from local meteorological measurements just prior to lift off. Figure 19 represents the differential pressure in pitch ($\Delta P\alpha$), where the preflight level seen in figure 19(b) shows the zero adjustments that had to be made. Note the data granularity, previously mentioned, that is shown graphically in figures 16, 17(b), 18 and 19(b). Note also that the pressure data sample rate was 10 samples per second with the exception of the bottom pressure which was at 1 sample per second. This caused some problems when combining this data with the $\Delta P\alpha$ data to obtain PAVE. Other data problems that occurred early in the program were the use of incorrect transducer calibrations, reverse polarity of the pitch-plane differential pressure ($\Delta P\alpha$), data timing discrepancies, and data smoothing and merging.

ESTIMATED SYSTEM PERFORMANCE

Preflight estimates of the AADS product uncertainties were made and are shown in figure 20. The estimates shown are for end-to-end systems performance and include the uncertainties resulting from wind tunnel calibration (including curve fit), pressure calibration data transmission, AADS spike manufacturing, and AADS alignment. The user requirements, designated by crosshatching, are superimposed on the figure for comparison purposes. There is no defined subsystem (or user) requirement for Mach number; however, because it can indirectly affect look-up values in the wind tunnel calibrations and other postflight user analyses, it was included for completeness. There is a peak in the uncertainty estimate for α and β near a Mach number of 1.6, which indicates a pressure discontinuity caused by a shock wave passing over the 30° cone pressure orifices. All of the uncertainty estimates can be seen to increase at the higher Mach numbers. The estimated uncertainty increases because, while the uncertainties in the pressure measurements remain essentially constant, the trajectory pressures are decreasing exponentially. The data of figure 20 show that the estimated attitude uncertainties are well below the requirements for the major portion of the flight. The user requirement for $\bar{q}$ is exceeded by the estimated uncertainty below a Mach number of approximately 1.2.

FLIGHT RESULTS AND DISCUSSION

Early Analyses and Procedures

The first Space Shuttle OFT lifted off on April 12, 1981. Flight data in the form of ground station recorded telemetry were available in 24 hours as advertised. An early calculation of the AADS air data products (circle symbols) is given in figure 21. The AADS data was available much sooner than the BET would be, therefore the early analyses used the available reconstructed trajectory simulation data (solid line) for comparison. The reconstructed trajectory contains merged meteorological data (winds and atmosphere), MSFC SRB-quick look thrust, SSME gimbal angle bias, elevon deflection angle bias and ascent aerodynamic variations for C_N, C_m and base pressure coefficient. During these early analyses of the STS-1 data many problems surfaced (basic data problems were mentioned in "Flight Data") in the process of calculating the AADS air data products. The basic data were smoothed, filtered, merged, etc. using many methods until one was chosen that satisfied the data reduction process without compromising the accuracy of the data. The comparison shown in figure 21 is the first "quick-look" data set that was published. There are obvious discrepancies between the two sets of data. The AADS Mach number diverges quite rapidly after T=80 seconds. The AADS dynamic pressure shows a large peak in the T=50 second region and an apparent data time shift past 70 seconds. The AADS α time history looked good up to approximately 80 seconds. Continuing data analyses showed the

AADS static pressure to be difficult to calculate accurately at the higher Mach numbers (actually at a low pressure, or an altitude effect). This was not unexpected from experience during the wind tunnel program and was actually predicted as shown in the "Estimated System Performance" section (albeit at higher Mach numbers). AADS data calculations were made subsequently using the static pressure from the reconstructed trajectory. This method of overriding the static pressure became standard procedure for the final AADS data calculations with the exception of the BET data being considered the best source for static pressure. Figure 22 shows the air data products for STS-1 using the BET for comparison purposes. (The BET uses a regression analysis program to solve for modeled systematic errors. The noise and remaining systematic errors are "fit" in a weighted least-squares sense. Input to this program includes ground tracking, meteorological, and navigation systems data.) Included in the comparison is the onboard navigation system (NAV) generated data. A thorough discussion of this flight data can be found in reference 3. It should be pointed out that comparison with the AADS calculations for STS-1 revealed an error in the wind direction that was resident in this set of BET data, as shown graphically on the figures. The BET was subsequently corrected.

Flight Data Comparisons

Comparison sets of the air data products for the OFT series (STS-1 through -4) are given in figures 23 through 26 for M, $\bar{q}$, α, and β, respectively. The reader is reminded that the data labeled "AADS" on these sets actually used the PS from the BET (i.e., conversely PT, $\Delta P\alpha$, $\Delta P\beta$ are from the AADS data). Also data labeled "EX42 SIM" is the previously described simulation data. The comparisons of the data indicate random differences flight to flight, with no consistent quantitative trends showing up.

Mach number comparisons in figure 23 show deviations of approximately 3 percent or less near Mach 2.0, and greater deviations (up to 6 percent) at the highest Mach numbers for all flights. In general this is considered very good agreement. For dynamic pressure in figure 24 the "AADS-BET" differences were less than 20 psf for all flights and were a maximum of approximately 3 percent in the critical transonic Mach number region.

The angle of attack and sideslip comparisons in figures 25 and 26 again show the randomness of the data. Static pressure had little effect on these calculations (as shown in comparing to figures 22(c) and 22(d)), so that using PS from the BET is of no consequence. The predicted divergence at the higher Mach numbers is again prevalent. The AADS data is felt to be the best data source for α and β because of the fact that the AADS spike is measuring wind effects real time whereas the other sources are using meteorological data taken slightly prior to (or slightly after) lift-off. In general the AADS gave overall results that satisfied the user requirements for postflight systems analyses.

LESSONS LEARNED

To ensure that the end-to-end accuracy of the calculated air data products meet the user requirements, the many sources of potential data uncertainties must be investigated, assessed (as to the error magnitude), and either accepted or improved upon. For the AADS, user requirements were established early (the requirement for angle of attack and sideslip for structural loads analyses was originally 0.2°, but was later increased to 0.5° based on the Orbiter air data system flight results). The several areas needing investigation as error sources were the wind tunnel test program, the calibration formulation, and the flight hardware/data processing system.

For the wind tunnel test program, procedures instituted during the Orbiter air data system tests[2] were used. In spite of using high quality instrumentation, consistent test procedures and calibration standards for facility test conditions, the scatter in the wind tunnel data accounted for over one-half of the estimated air data product error. Very little can be done about this without expending large amounts of time and money for additional verification testing using many models in many facilities. The increased accuracy would be in the form of higher probability with the increased sample of data.

The calibration formulation had two aspects to it. One was the curve fit, which is again a statistical quantity. For this the AADS polynomial was expanded to minimize these errors to a reasonable level. The second aspect was the calibration parameters used. As it turned out, many other data combinations of measured (AADS spike) and known (wind tunnel), or desired (flight), pressures were looked at, plotted, and analyzed prior to the selection of those used. A better set probably could have been found if time and the data manipulation effort were no object. Again the question is: Is the additional effort worth the increased data accuracy? In this case it probably was not.

The flight hardware, including instrumentation, was a mixed set. The AADS spike was manufactured to very high tolerances and was aligned accurately, both the $10^{\circ}/30^{\circ}$ conic sections and the spike to the 40° nose cone. The flight pressure transducer error, however, was a major contributor to the estimated system errors. This could have been circumvented by using dual-range transducers or transducer pairs with a switching device, but we are again talking about increased costs. In our case the user requirements at the higher Mach numbers (lower pressures) did not warrant the increased costs. A source of error that should have been avoided was the data sample rate. All pressure data was at a rate of 10 samples/second except PB which was at 1 sample/second. The lower rate tends to smooth the absolute pressure measurement, and when combining it with the $\Delta P\alpha$ measurement to obtain PAVE, results in unnecessary data uncertainties.

All of the above comments point to the fact that a thorough integration and error analysis of all of the involved systems should: 1) be done, and 2) be done early. This way, areas that are large potential error sources can be identified and possibly avoided.

CONCLUDING REMARKS

The ascent air data system was designed to obtain data to support postflight analyses of the Space Shuttle orbital flight test series. Pressure data were obtained for flights STS-1 through -4, and were then converted to the desired air data products through use of the wind tunnel calibration data base.

Results showed that the flight static pressure calculation diverged at the higher Mach numbers. It was therefore replaced by static pressure from a "best-estimated" (postflight) trajectory (BET). When comparing flight AADS data calculated in this manner with the BET data, Mach number showed very good agreement, dynamic pressure was within 3 percent in the critical transonic region, and angle of attack and sideslip compared well. The AADS α and β are considered the best source of attitude data because they measure real-time winds and are essentially unaffected by flight static or total pressures. In general the AADS performance was essentially as estimated preflight and the results satisfied the user requirements.

Lessons learned include the importance of obtaining a good estimate of the end product data uncertainties for the system so that weak areas can be strengthened. As with most multi-disciplined systems, the defined error sources can be improved on, but only by extending test/analysis time, or with increased costs or both. Another major area of improvement would have been to have a thorough systems integration effort that started at the beginning of the AADS program and continued through to the end.

REFERENCES

1. Hillje, Ernest R.; and Tymms, David E.: The Ascent Air Data System for the Space Shuttle. AIAA Paper 80-0422, March 1980.
2. Hillje, Ernest R.; and Tymms, David E.: Wind Tunnel and Flight Calibration of the Shuttle Orbiter Air Data System. AIAA Paper 78-792, April 1978.
3. Hillje, Ernest R.; and Nelson, Raymond L.: Post Flight Analysis of the Space Shuttle Ascent Air Data System. AIAA Paper 81-2457, November 1981.

TABLE 1.- FLIGHT TEST REQUIREMENTS FOR ASCENT AIR DATA

FLIGHT TEST REQUIREMENT NO.	SUBSYSTEM	FLIGHT TEST REQUIREMENT OBJECTIVE
07VV002	AERODYNAMICS	● LAUNCH VEHICLE POWER-ON BASE DRAG DETERMINE LAUNCH VEHICLE BASE DRAG DURING FIRST AND SECOND STAGE ASCENT
07VV001	AERODYNAMICS	● ASCENT AERODYNAMICS ESTABLISH THE EXTERNAL AIRLOAD ENVIRONMENTS, VERIFY AERODYNAMIC CHARACTERISTICS, AND PROVIDE AERODYNAMIC MEASUREMENTS FOR PROGRAM DIAGNOSIS
MC-1	MISSION CAPABILITY	● ASCENT PERFORMANCE VERIFICATION VERIFY SPACE SHUTTLE VEHICLE PERFORMANCE (INJECTED WEIGHT) IN THE FLIGHT ENVIRONMENT
47VB018	SOLID ROCKET BOOSTER SEPARATION PERFORMANCE	● SOLID ROCKET BOOSTER SEPARATION PERFORMANCE VERIFY THE SYSTEM PERFORMANCE
48VT013	EXTERNAL TANK SEPARATION PERFORMANCE	● EXTERNAL TANK SEPARATION PERFORMANCE VERIFY THE SYSTEM PERFORMANCE (RETURN TO LAUNCH SITE PHASE ONLY)
08VV001	STRUCTURES	● LOAD AND STRESS EVALUATION DETERMINE SPACE SHUTTLE FLIGHT LOADS AND LOAD SPECTRA
07VV020	THERMODYNAMIC	● ASCENT AERO HEATING VERIFICATION VERIFY THE SHUTTLE VEHICLE ASCENT AERO-THERMAL DESIGN ENVIRONMENT

TABLE 2.- AADS ACCURACY REQUIREMENTS

PARAMETER	MACH	VALUE	AREA OF EVALUATION
α, β	0.6 - 2.0	$\pm 0.5^\circ$ OR 10%	STRUCTURAL LOADS
	0.6 - 2.0	$\pm 0.5^\circ$	AERODYNAMICS
	2.0 - 4.3 4.3 - 5.0	$\pm 0.5^\circ$ $\pm 1.0^\circ$	AEROHEATING
$\bar{q}_\infty$	0.6 - 2.0	$\pm 3\%$	STRUCTURAL LOADS

TABLE 3.- AADS WIND TUNNEL PROGRAM

TEST	MODEL SCALE		M RANGE	FACILITY
	EXTERNAL TANK	PROBE		
I	0.07 (FOREBODY)	10° CONIC	0.55→1.15	ARC 14'
II	0.004 INTEGRATED VEHICLE	40° PROBE AFT FAIRING	0.6→1.2	MSFC 14"
III*	0.07 (FOREBODY)	30°/10° CONIC	0.6→1.55	AEDC 16T
IV*	0.07 (FOREBODY)	30°/10° CONIC	1.55→2.5	ARC 9 x 7'
V*	0.07 (FOREBODY)	30°/10° CONIC	2.5→3.5	ARC 8 x 7'
VI*	0.07 (FOREBODY)	30°/10° CONIC	3.5→4.63	LRC UPWT
VII**	0.03 INTEGRATED VEHICLE	30°/10° CONIC	0.6→1.55	AEDC 16T
VIII**	0.03 INTEGRATED VEHICLE	30°/10° CONIC	1.55→2.5	ARC 9 x 7'

*BASIC TEST DATA
**VERIFICATION TEST DATA

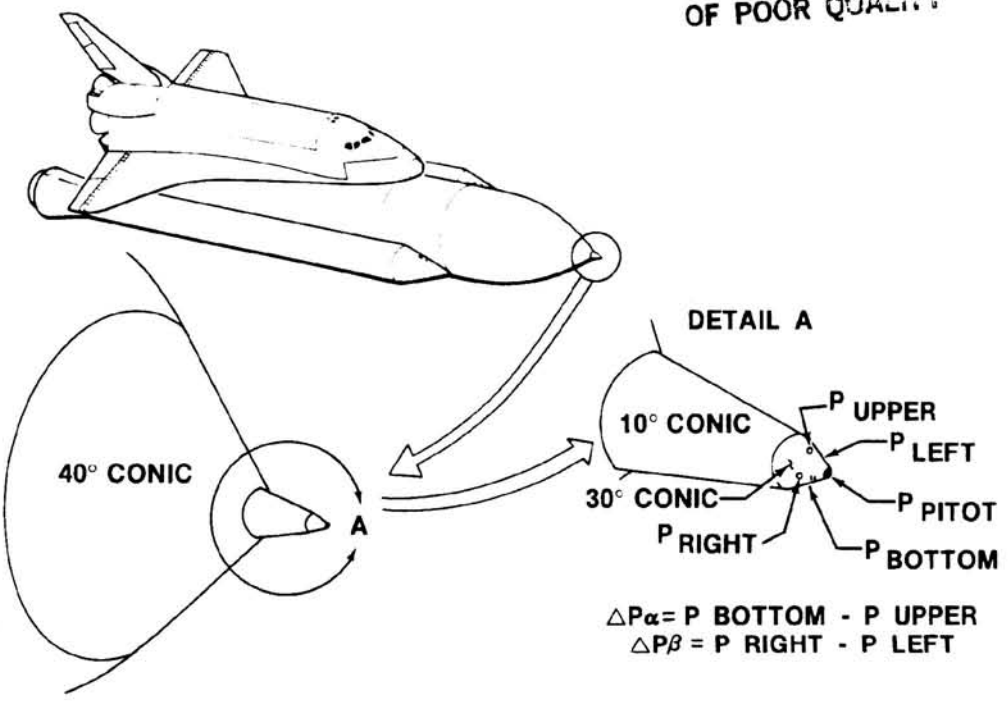

Figure 1.- Ascent air data system flight configuration.

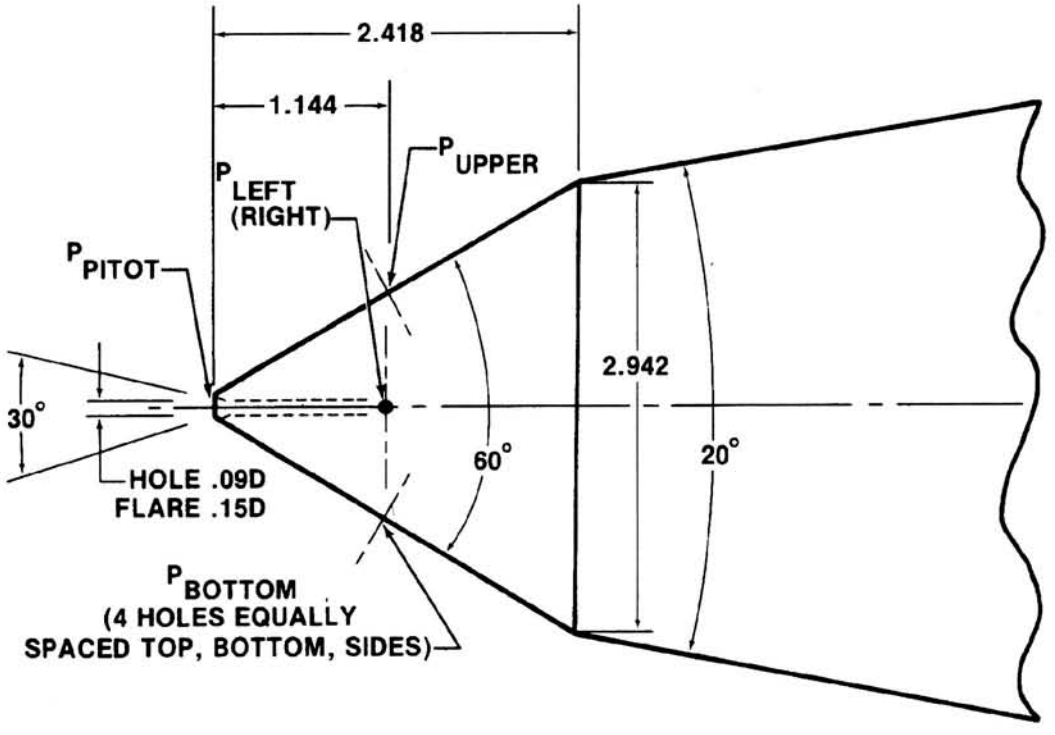

Figure 2.- AADS spike pressure port details. (All linear dimensions in inches.)

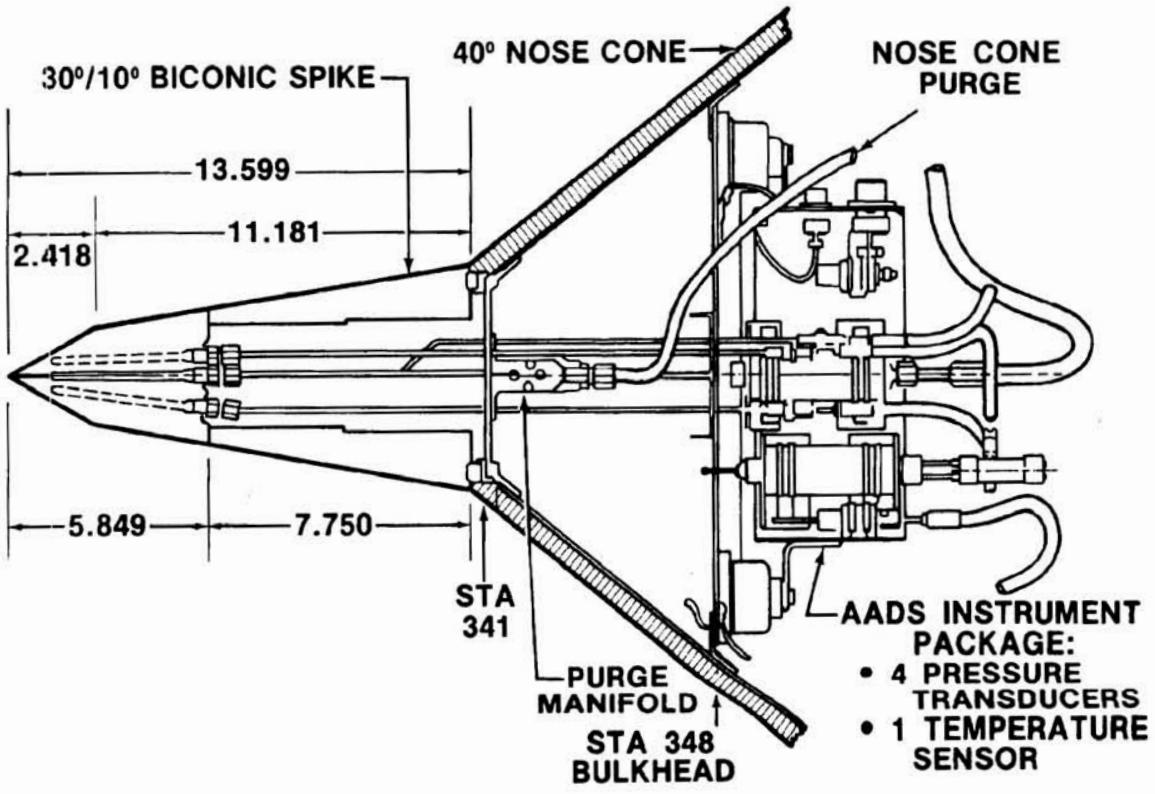

Figure 3.- AADS hardware arrangement. (All linear dimensions in inches.)

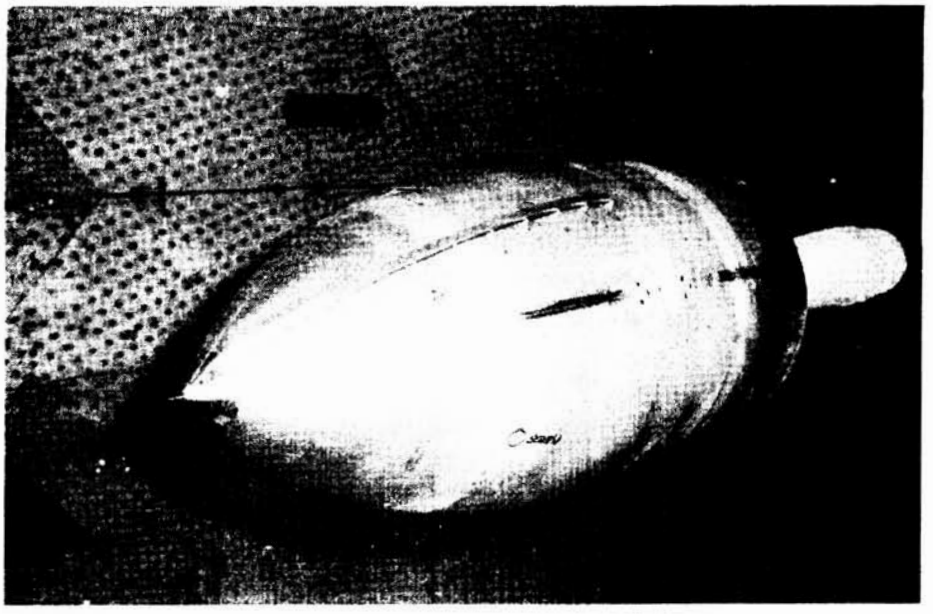

(a) Seven percent forebody model - front quarter view.

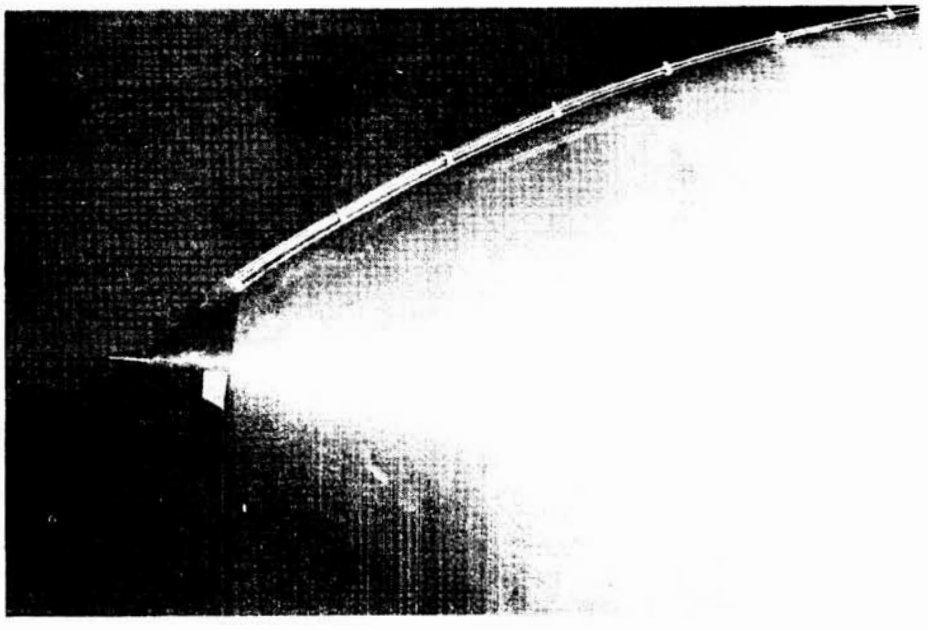

(b) Seven percent forebody model - side view showing cable tray fairing.

Figure 4.- AADS wind tunnel models.

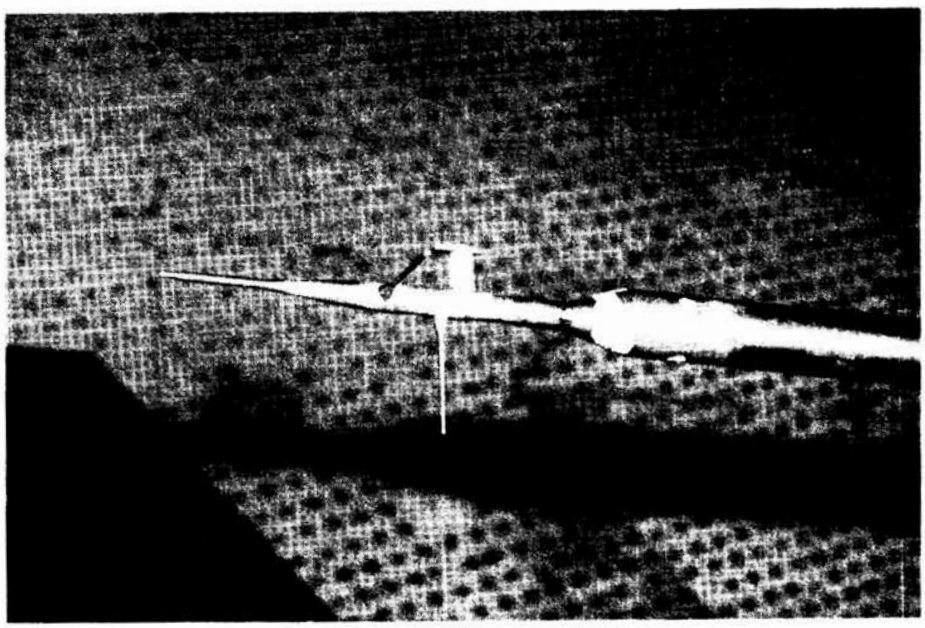

(c) Flight test boom - used as calibration standard.

Figure 4.- Concluded.

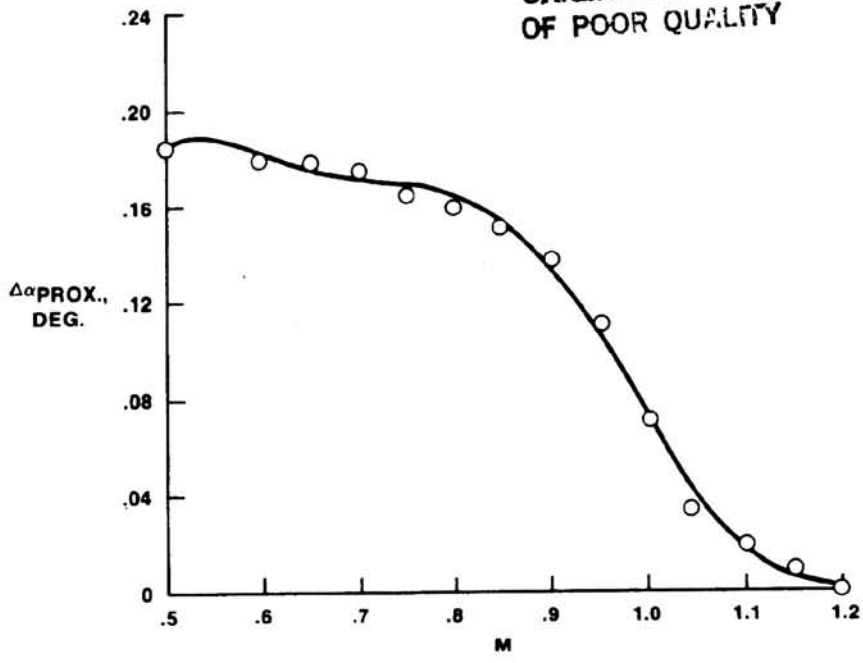

Figure 5.- Effect of Orbiter and SRB on the AADS angle of attack.

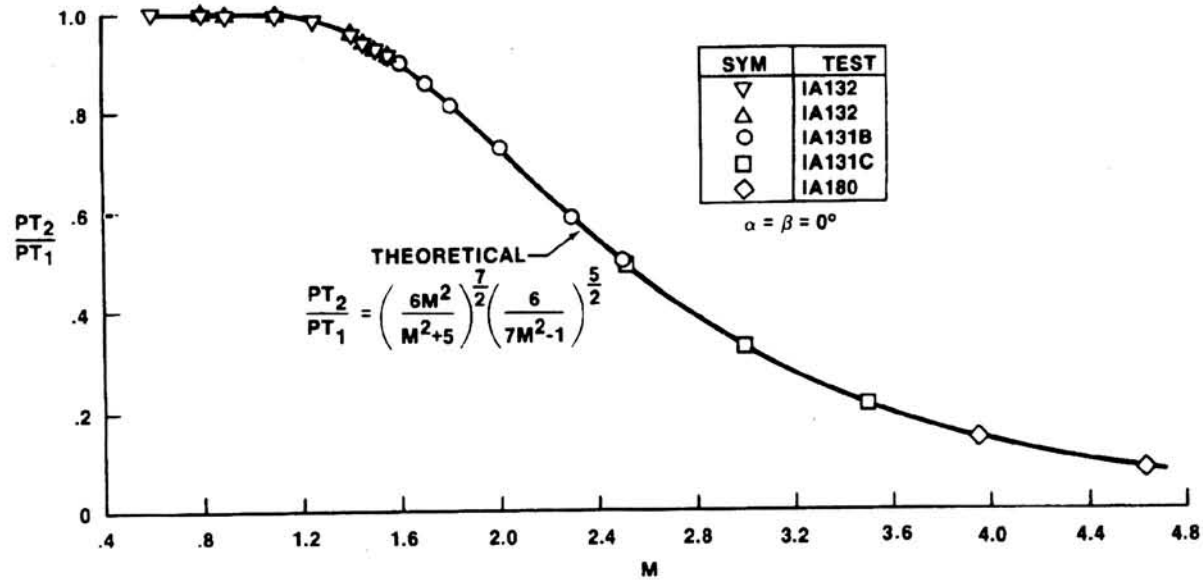

Figure 6.- Comparison of measured and theoretical pressure ratios.

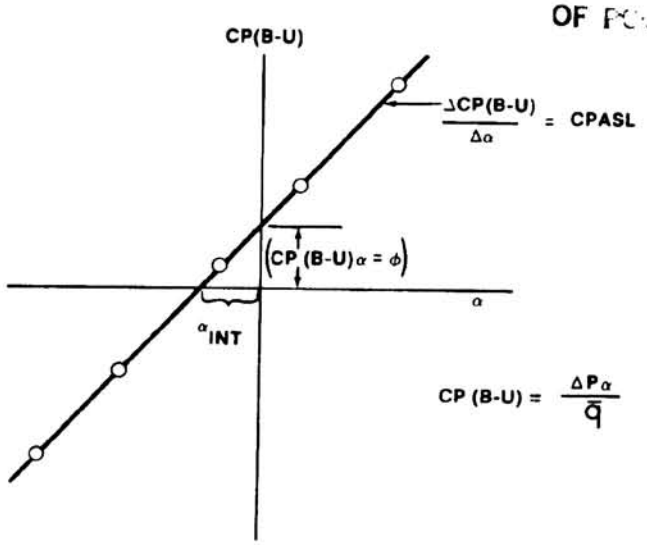

Figure 7.- Wind tunnel pitch plane coefficient versus angle of attack.

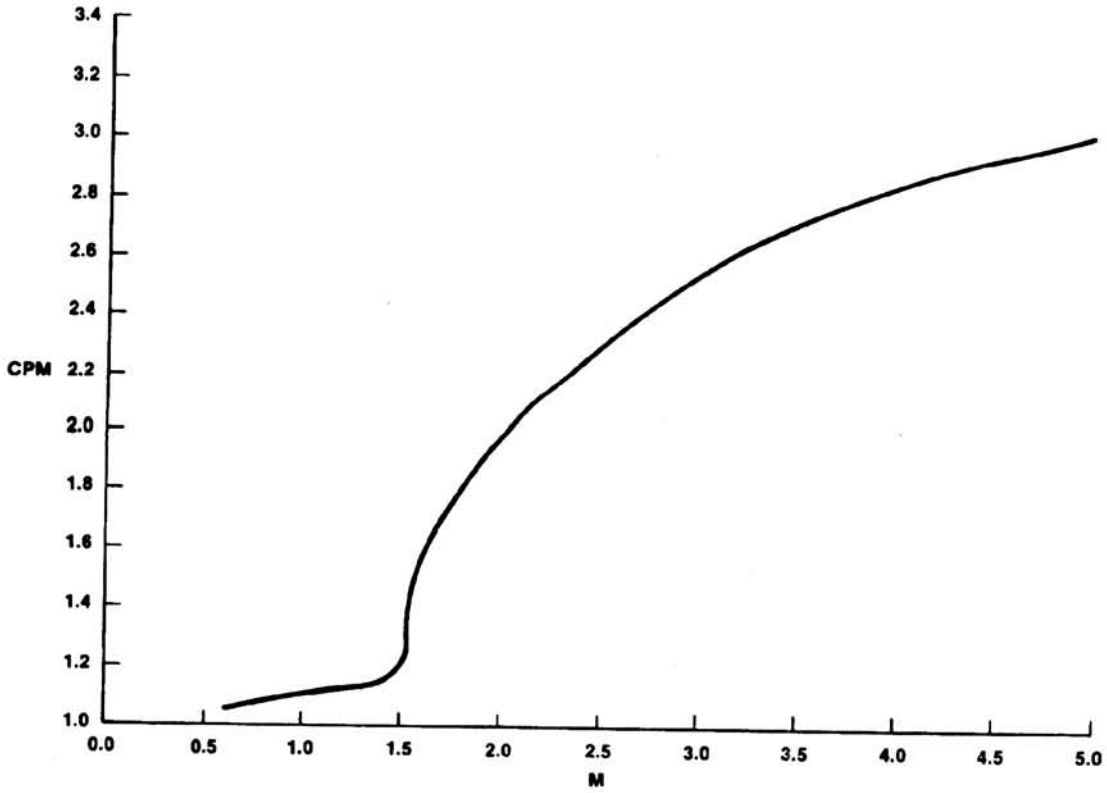

Figure 8.- Mach calibration coefficient (CPM) versus Mach number.

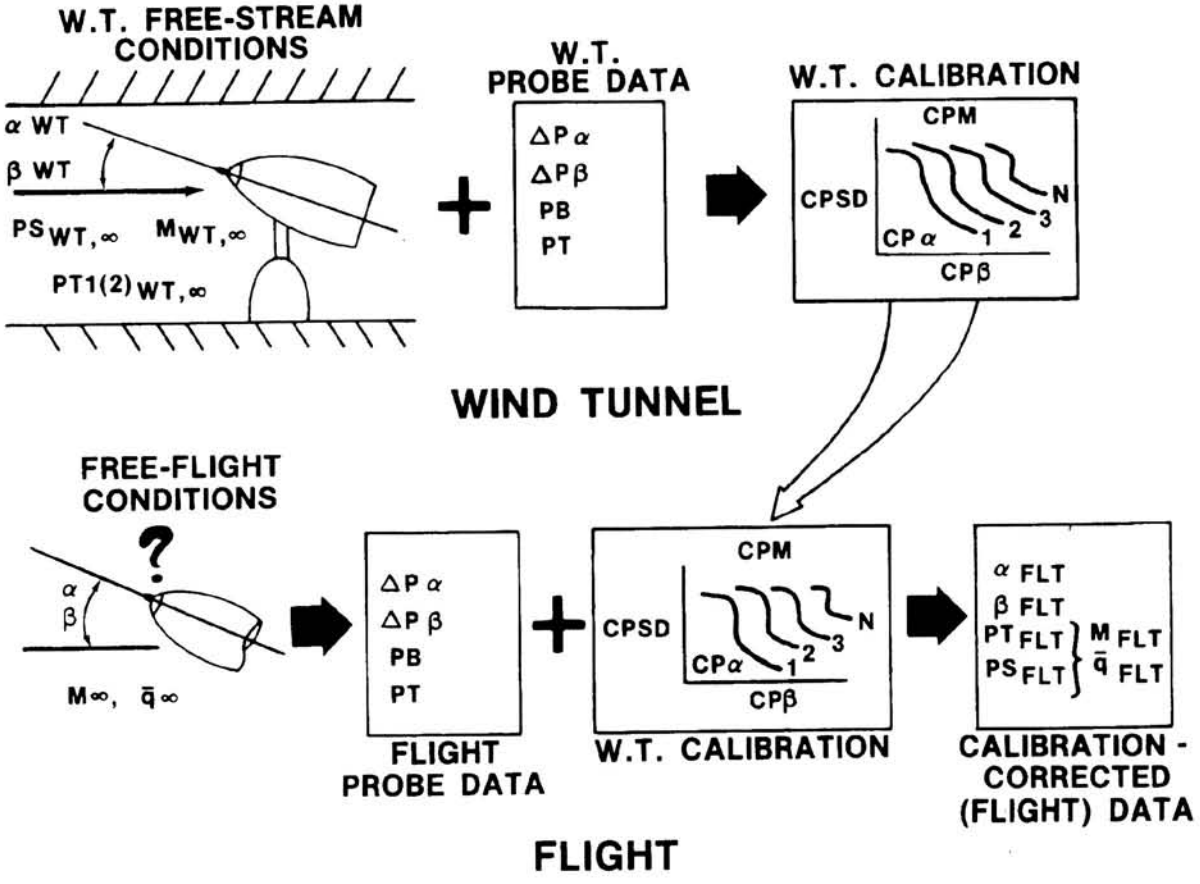

Figure 9.- Example of wind tunnel calibration/flight relationship.

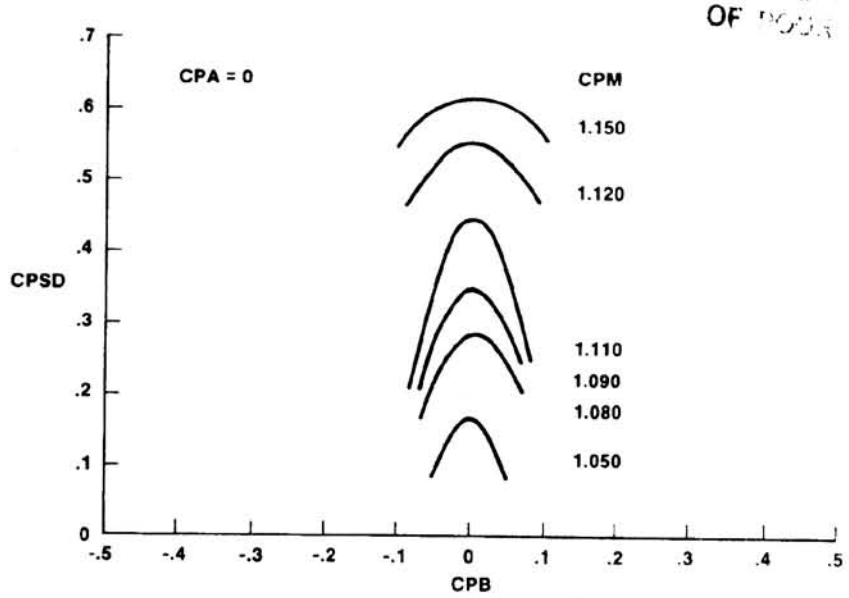

Figure 10.- Static pressure decrement (CPSD) versus angle of sideslip calibration coefficient (CPB).

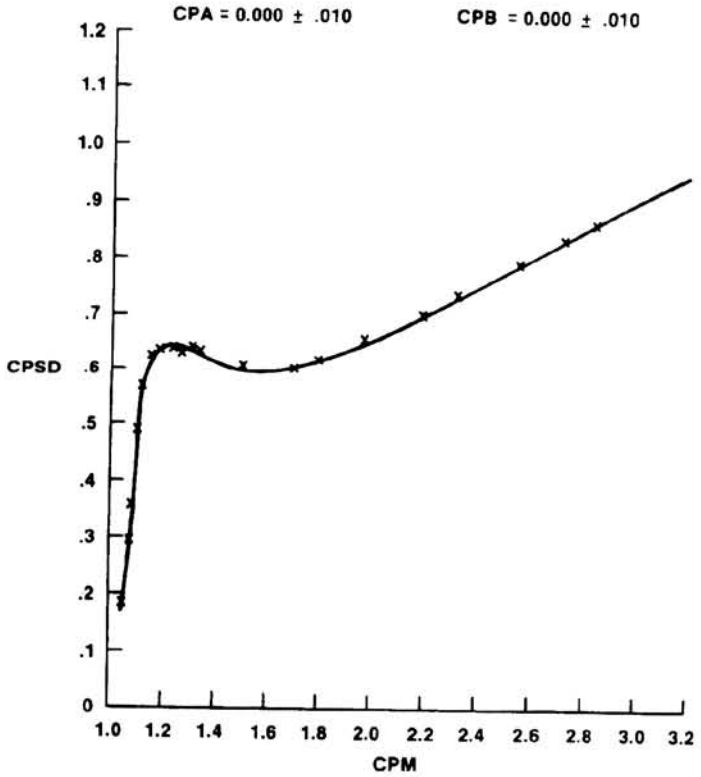

Figure 11.- Static pressure decrement (CPSD) versus Mach calibration coefficient (CPM).

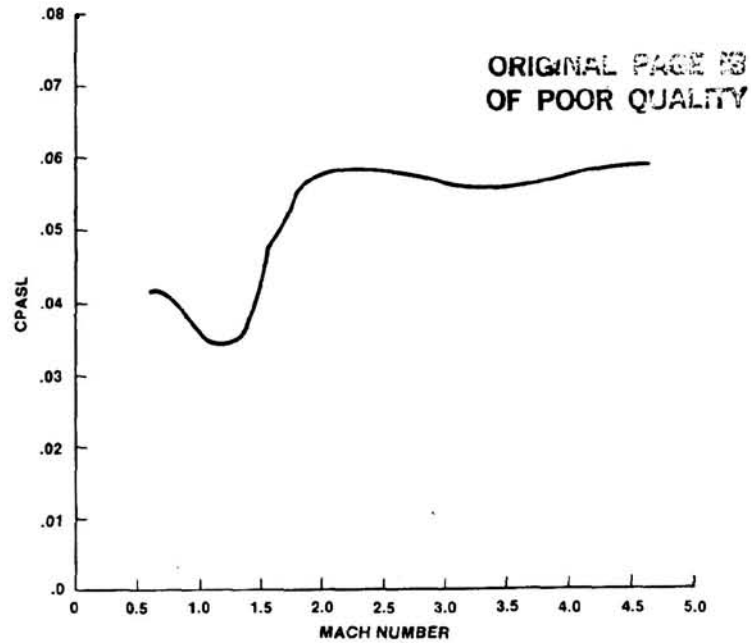

Figure 12.- Slope calibration parameter for α (CPASL) versus Mach number.

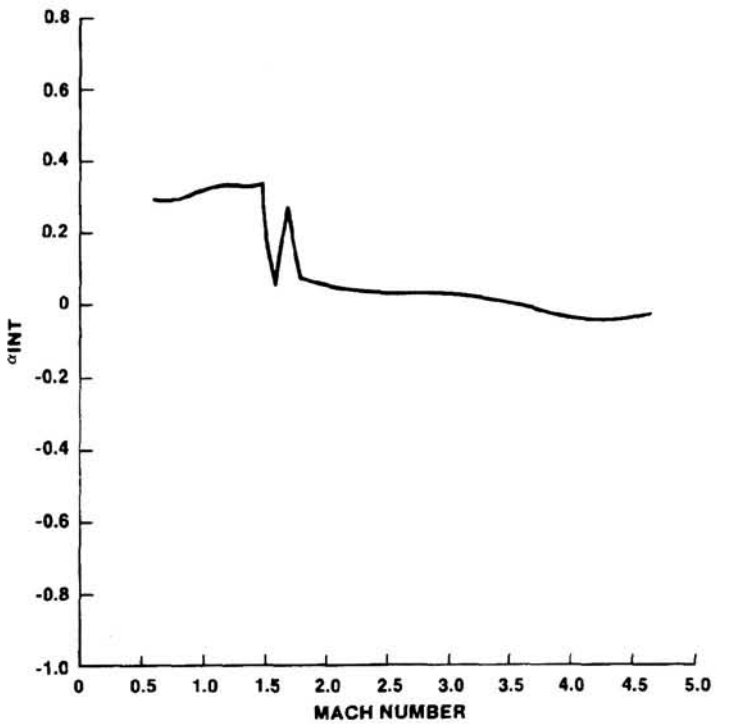

Figure 13.- Angle of attack calibration parameter intercept term (α_{INT}) versus Mach number.

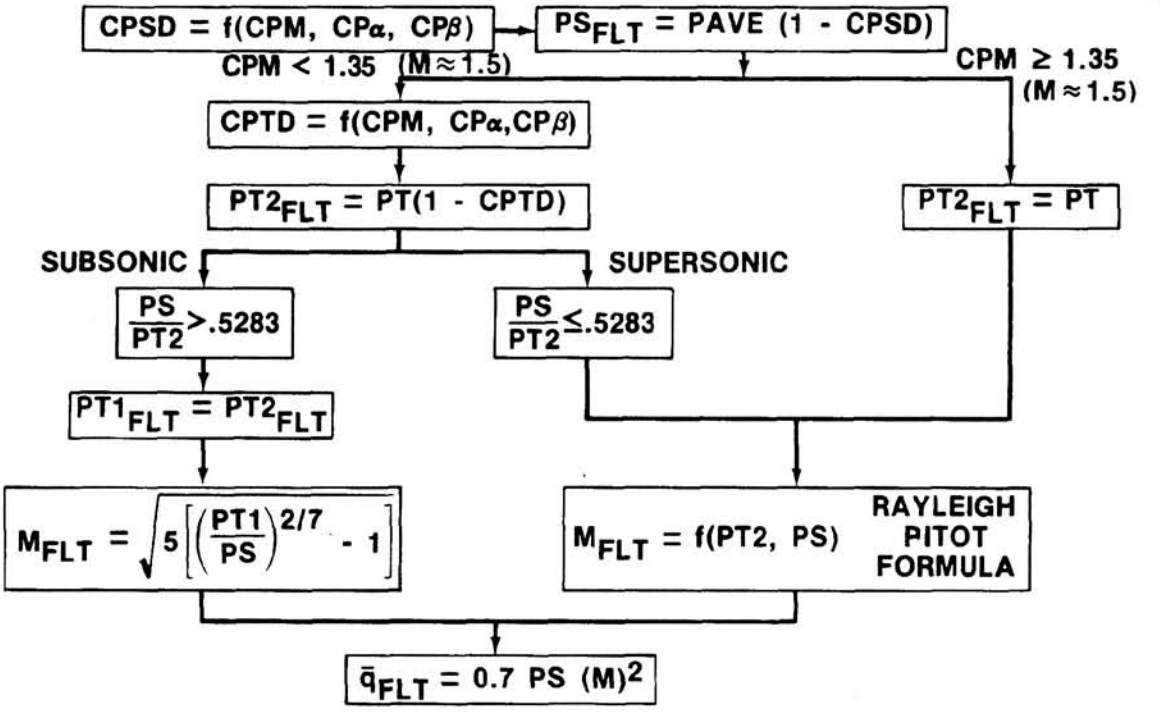

(a) Static and total pressure, Mach number, and dynamic pressure.

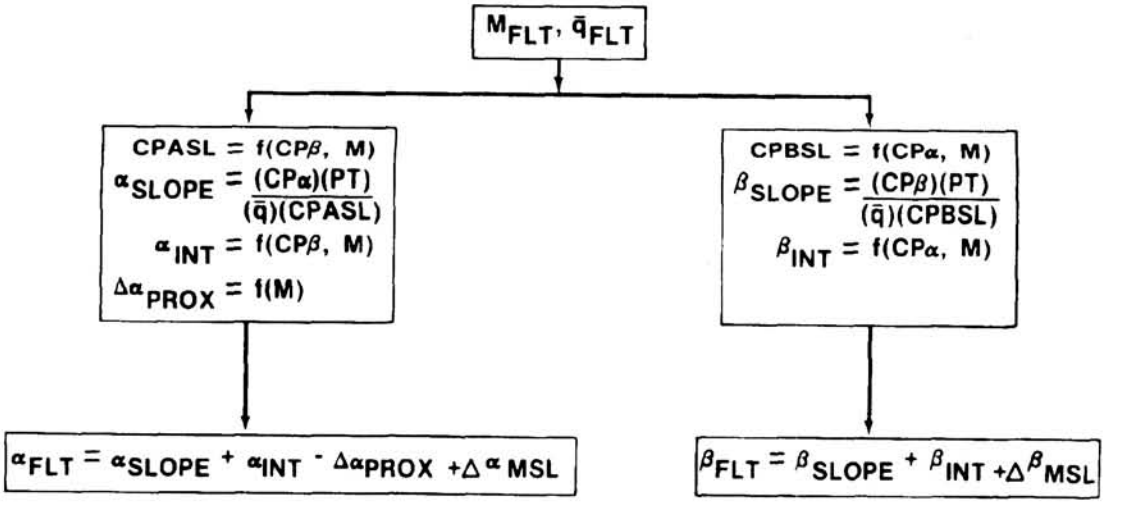

(b) Angles of attack and sideslip.

Figure 14.- AADS air data product calculation procedure.

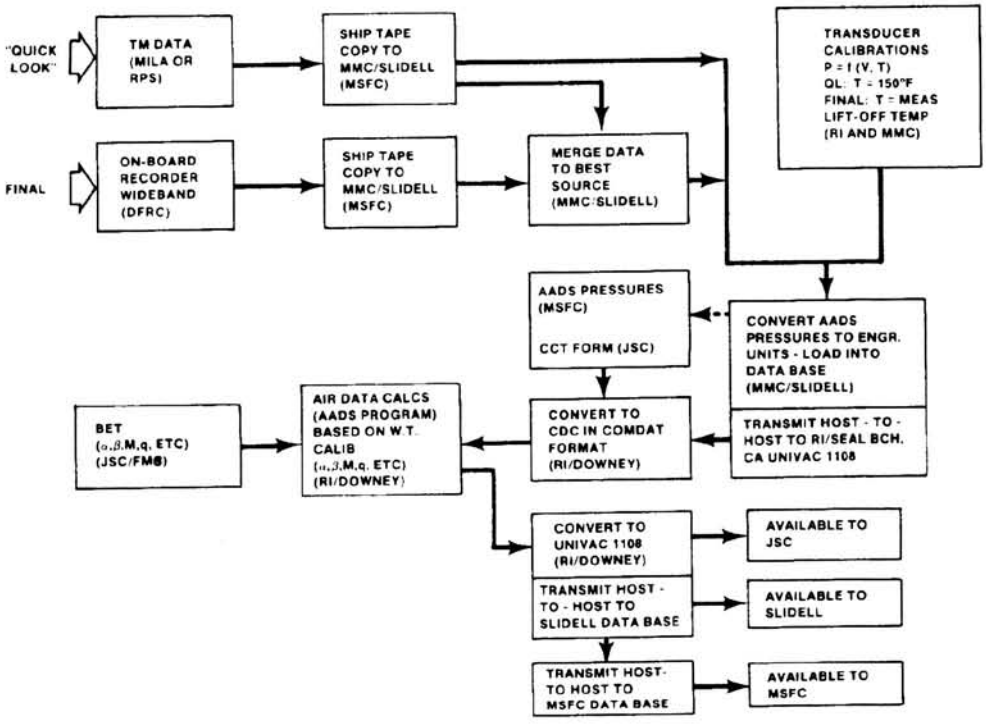

Figure 15.- AADS postflight pressure data acquisition.

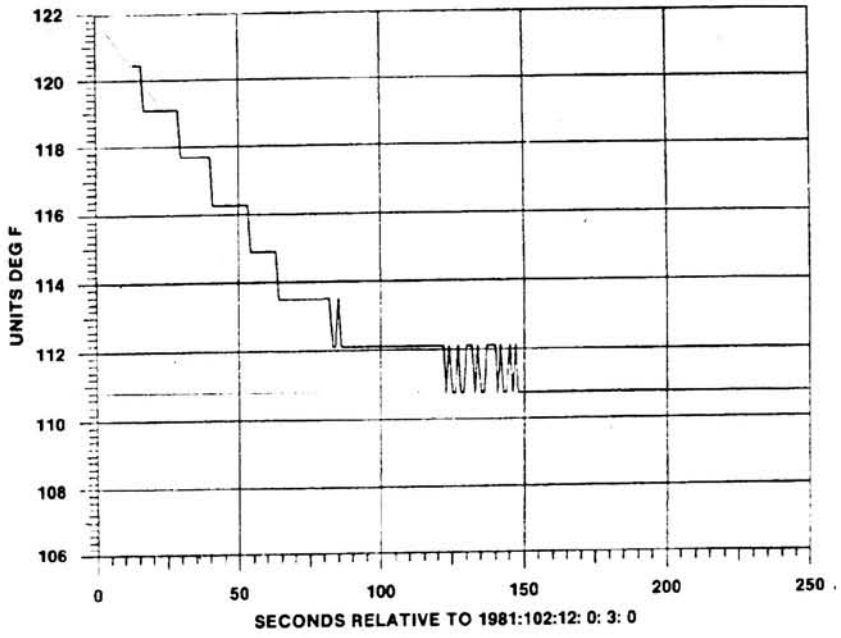

Figure 16.- AADS basic measurement data - nose cap AADS package temperature. STS-1 data.

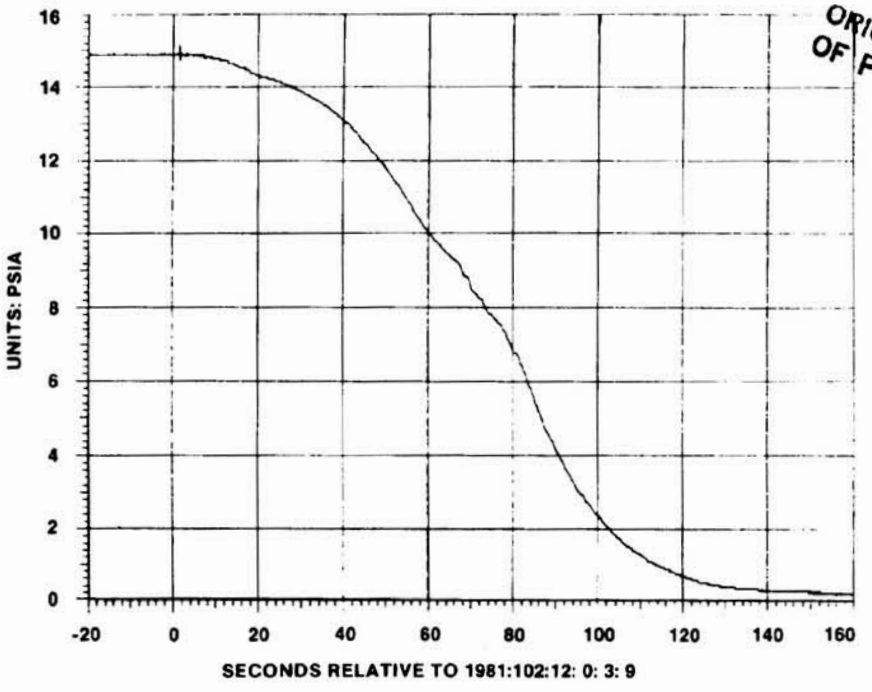

(a) Ascent flight phase.

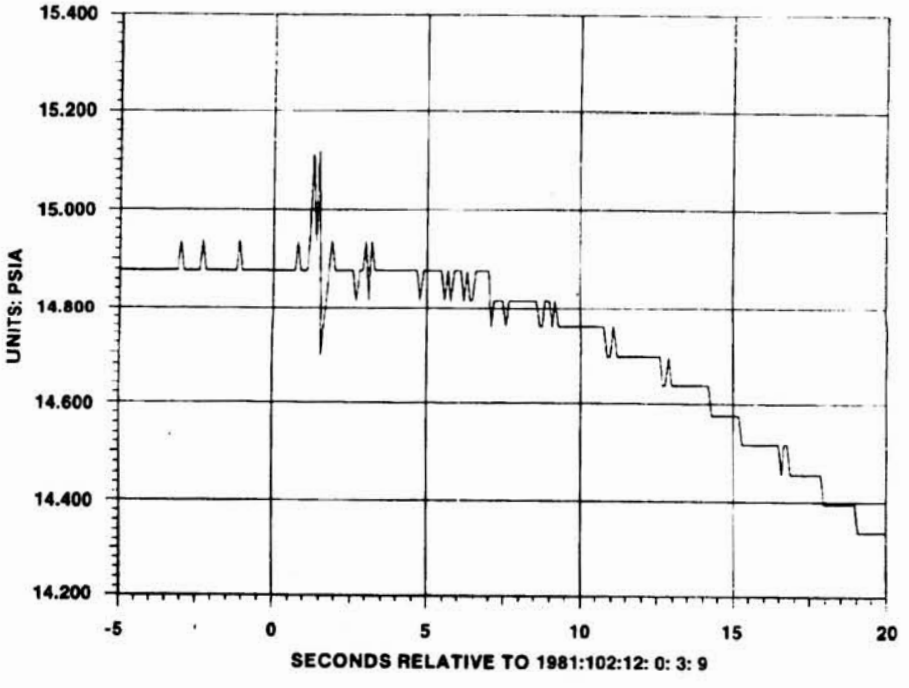

(b) Near lift-off.

Figure 17.- AADS basic measurement data - nose cap total pressure (PT).

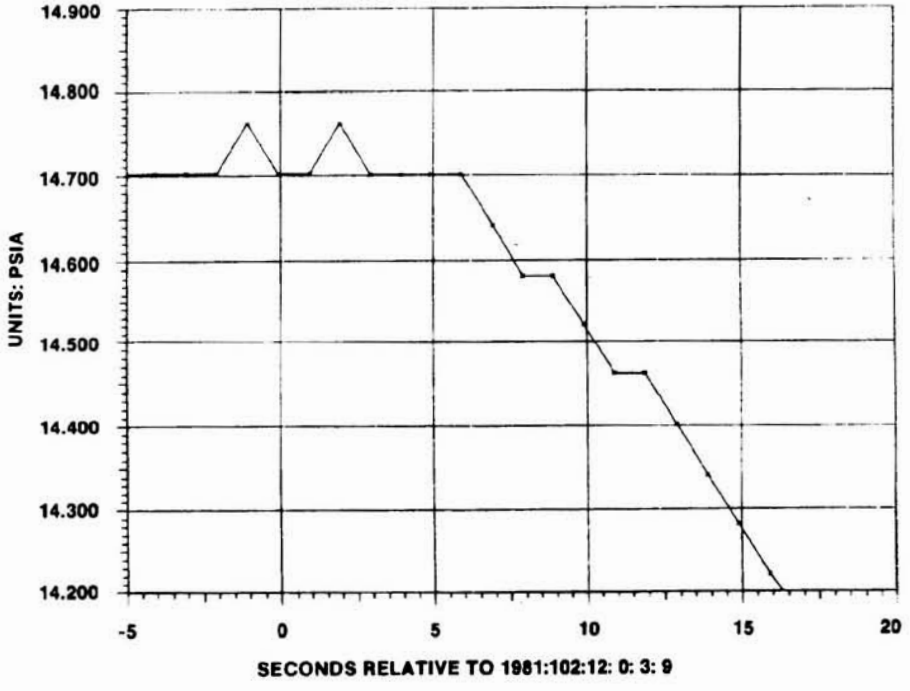

Figure 18.- AADS basic measurement data - nose cap pressure - Z port (PB) - near lift-off.

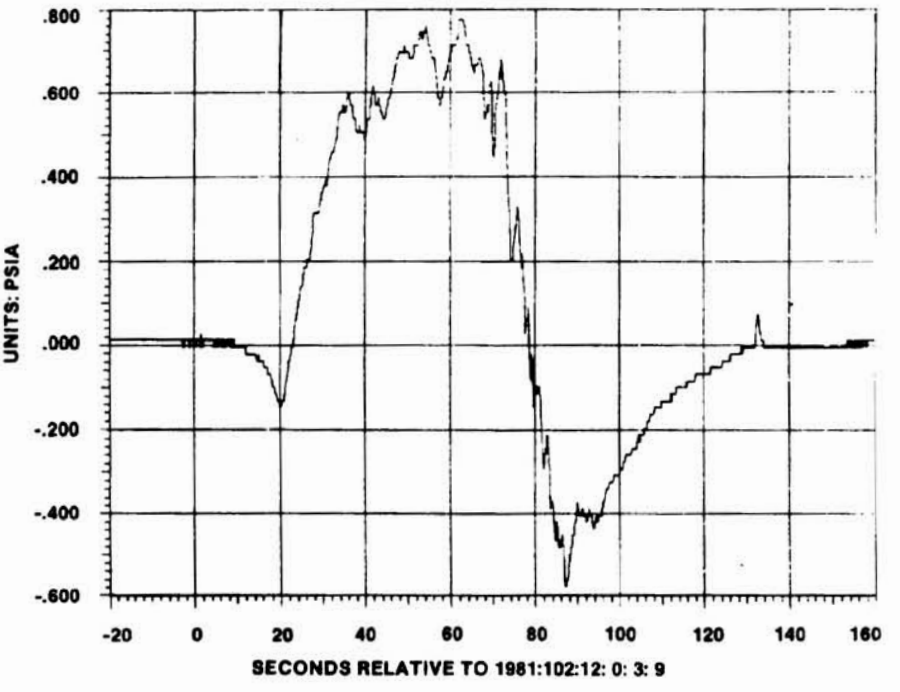

(a) Ascent flight phase.

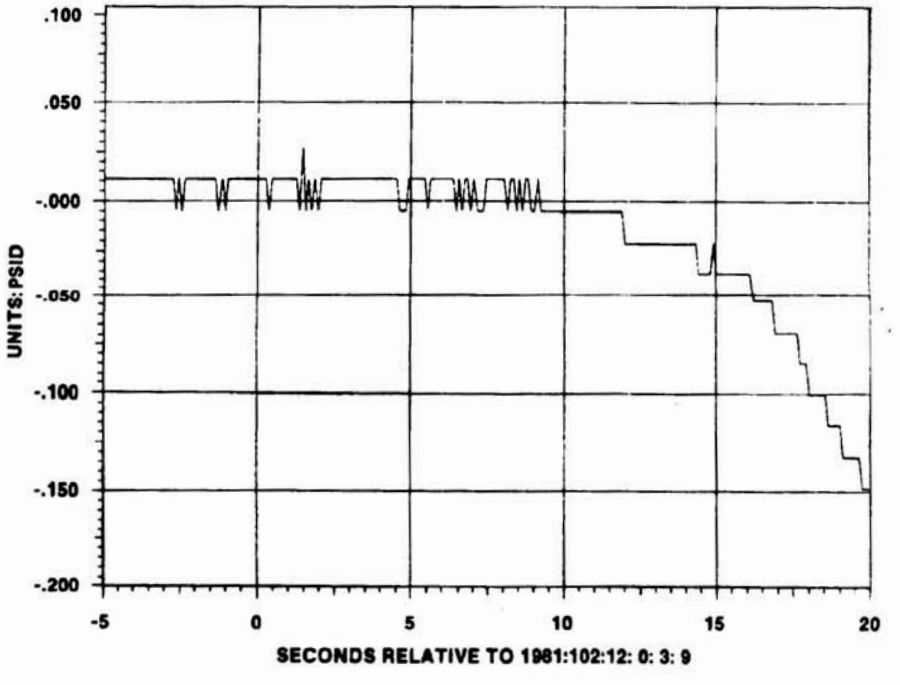

(b) Near lift-off.

Figure 19.- AADS basic measurement data - nose cap differential pressure-pitch ($\Delta P\alpha$).

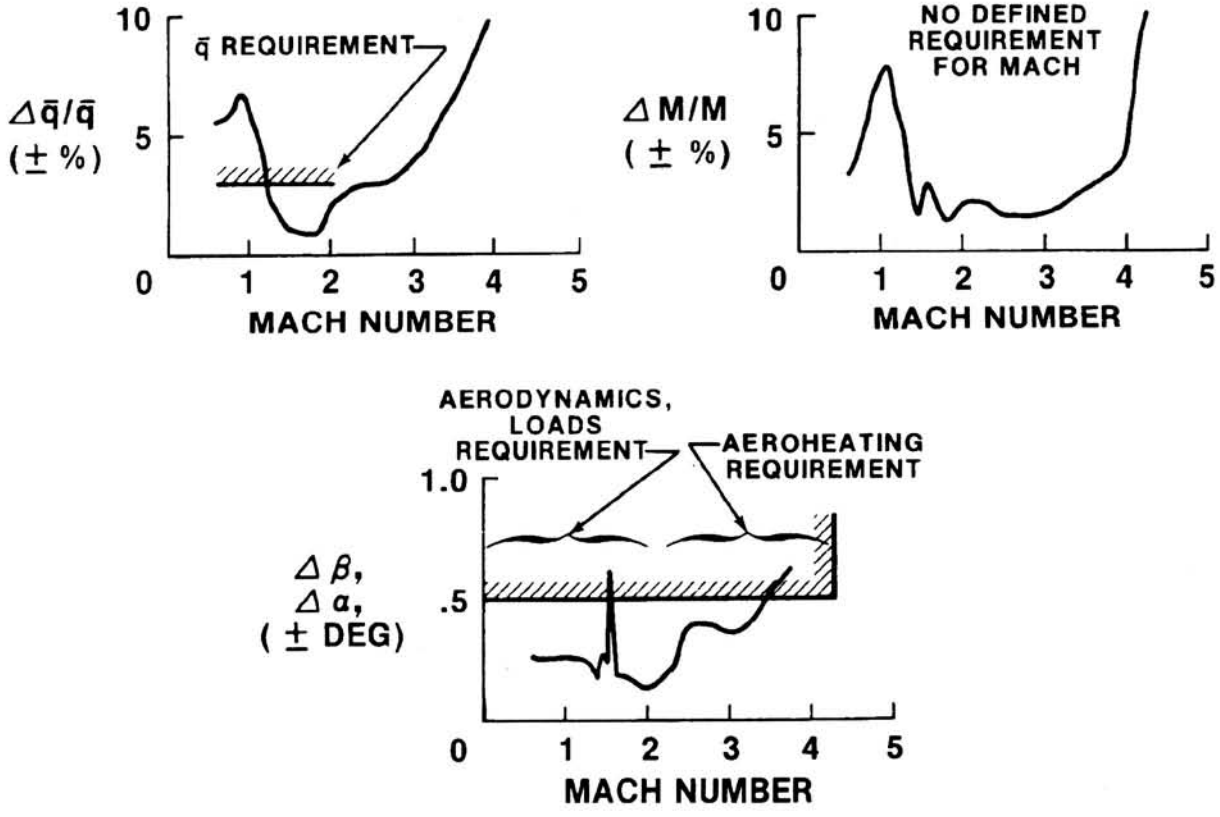

Figure 20.- Estimated AADS air data product uncertainties.

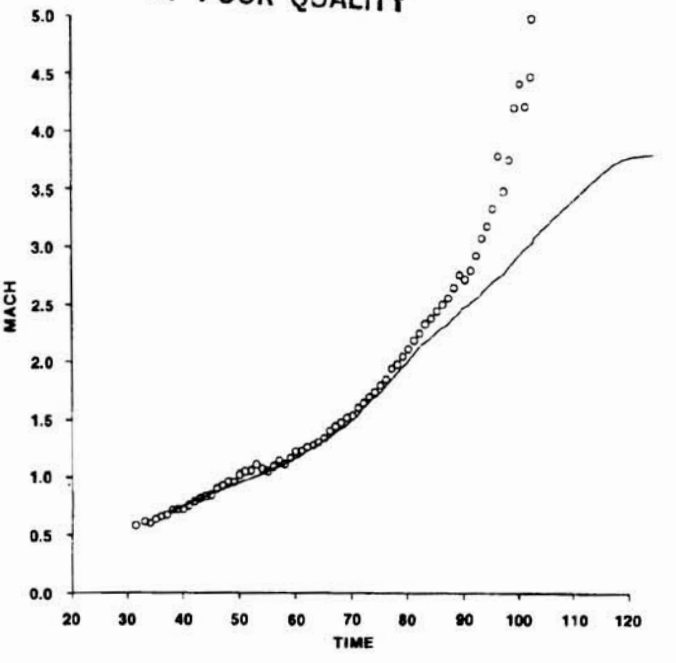

(a) Mach number versus time from lift-off.

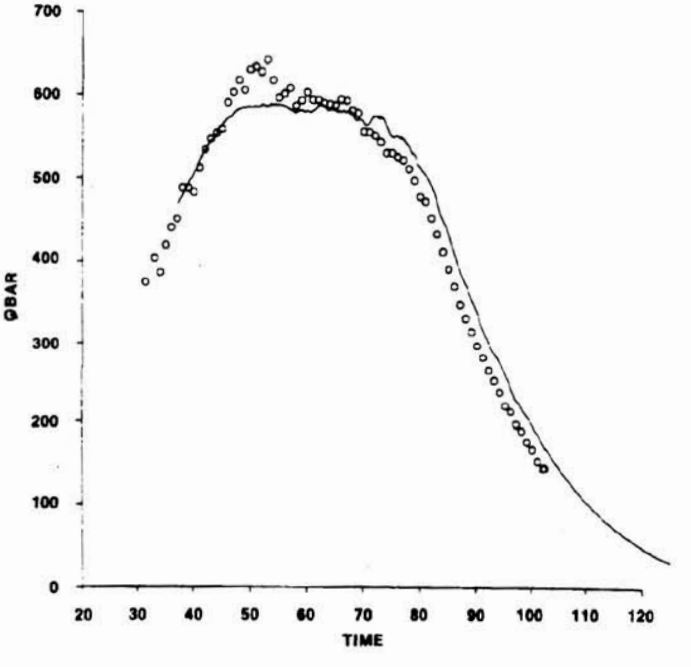

(b) Dynamic pressure (QBAR) versus time from lift-off.

Figure 21.- "Quick-Look" STS-1 AADS air data calculations (circles) compared with simulated reference trajectory data (solid line).

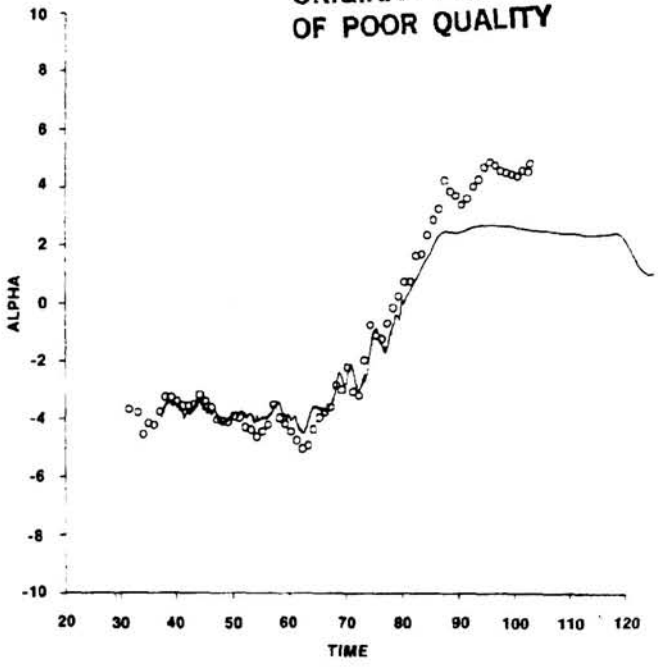

(c) Angle of attack (ALPHA) versus time from lift-off.

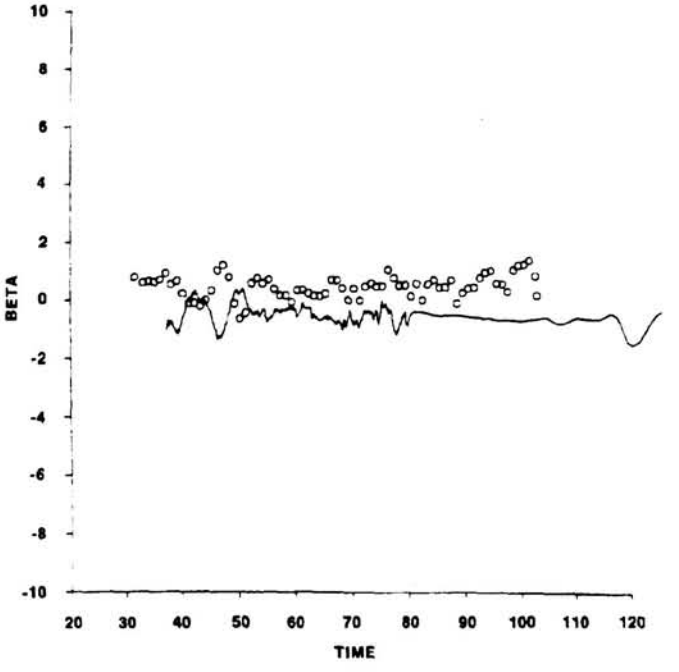

(d) Angle of sideslip (BETA) versus time from lift-off.

Figure 21.- Concluded.

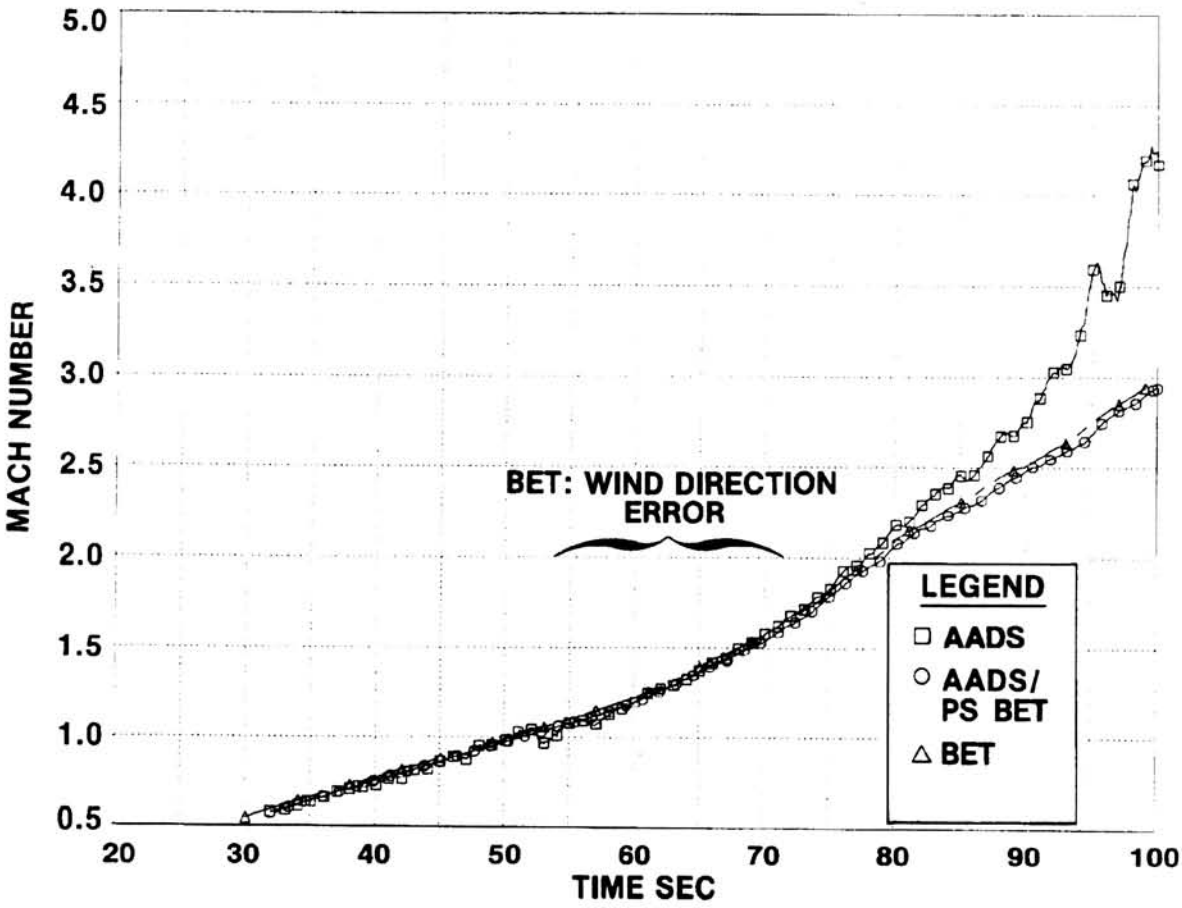

(a) Mach number versus time from lift-off.

Figure 22.- Preliminary STS-1 AADS air data calculations compared with alternate data sources.

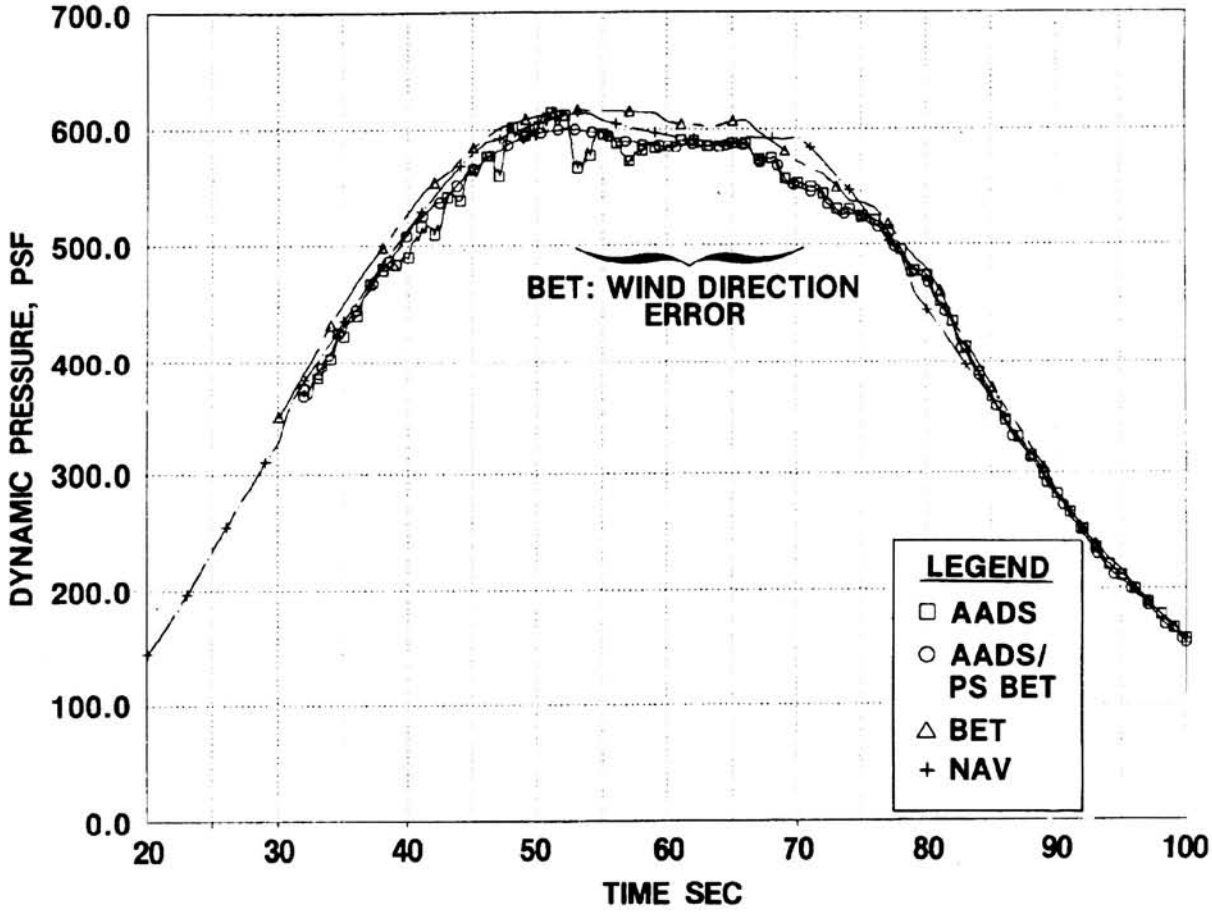

(b) Dynamic pressure versus time from lift-off.

Figure 22.- Continued.

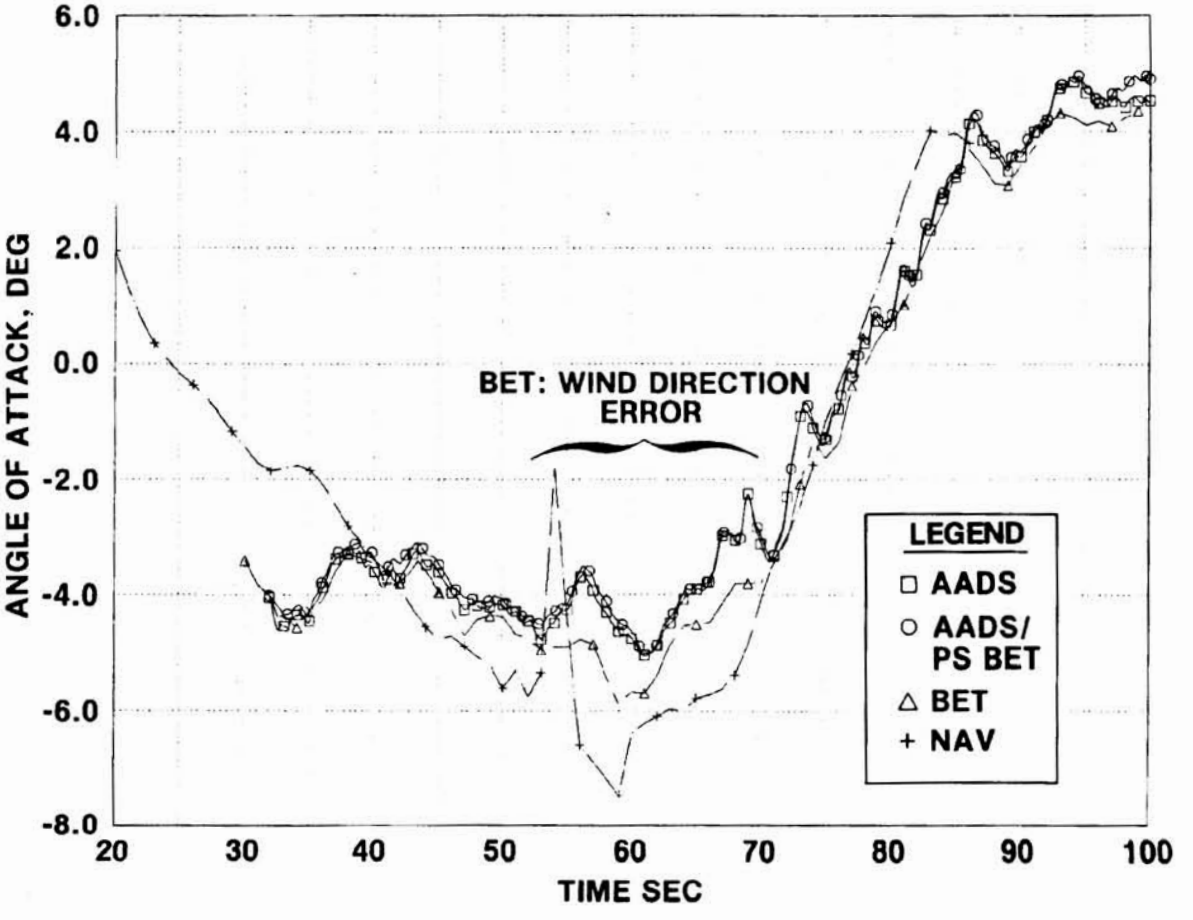

(c) Angle of attack versus time from lift-off.

Figure 22.- Continued.

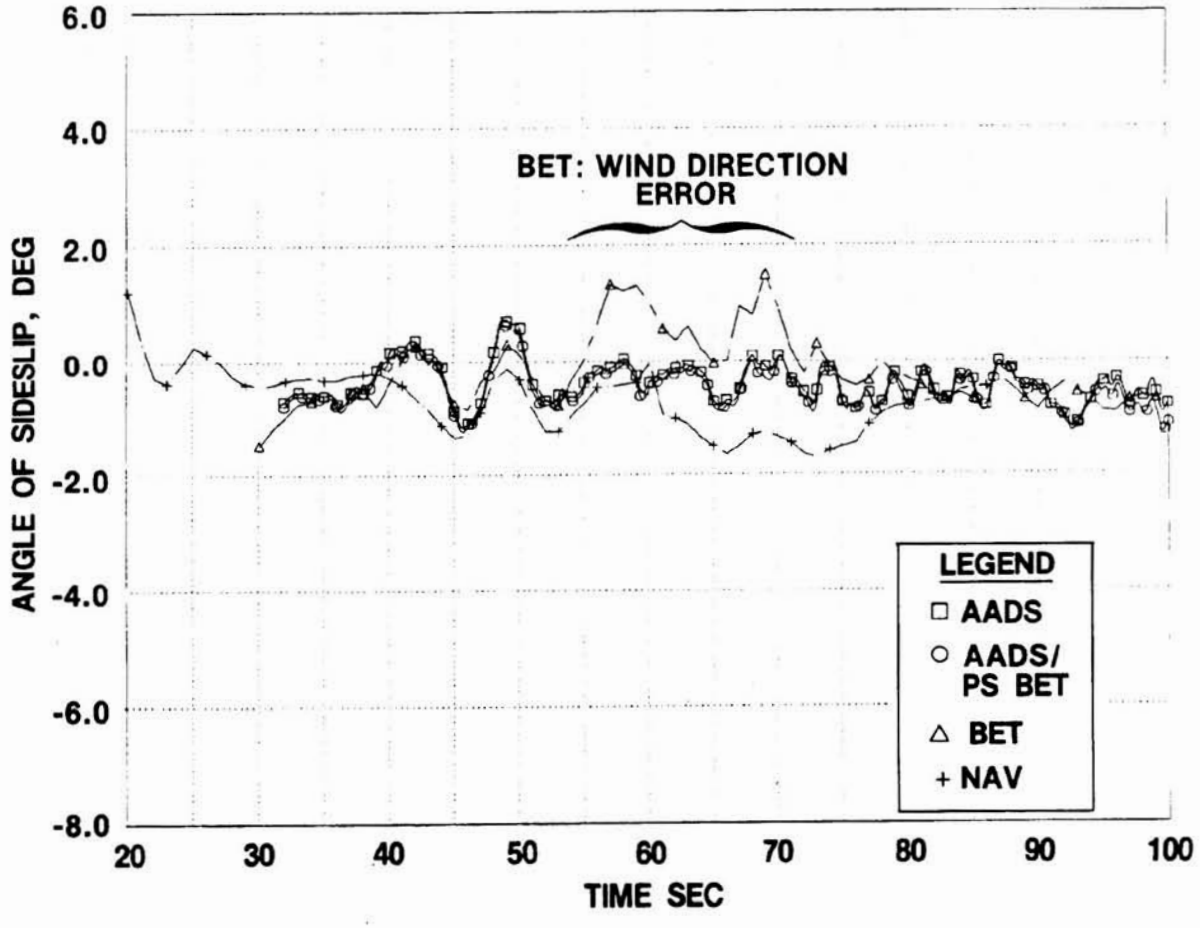

(d) Angle of sideslip versus time from lift-off.

Figure 22.- Concluded.

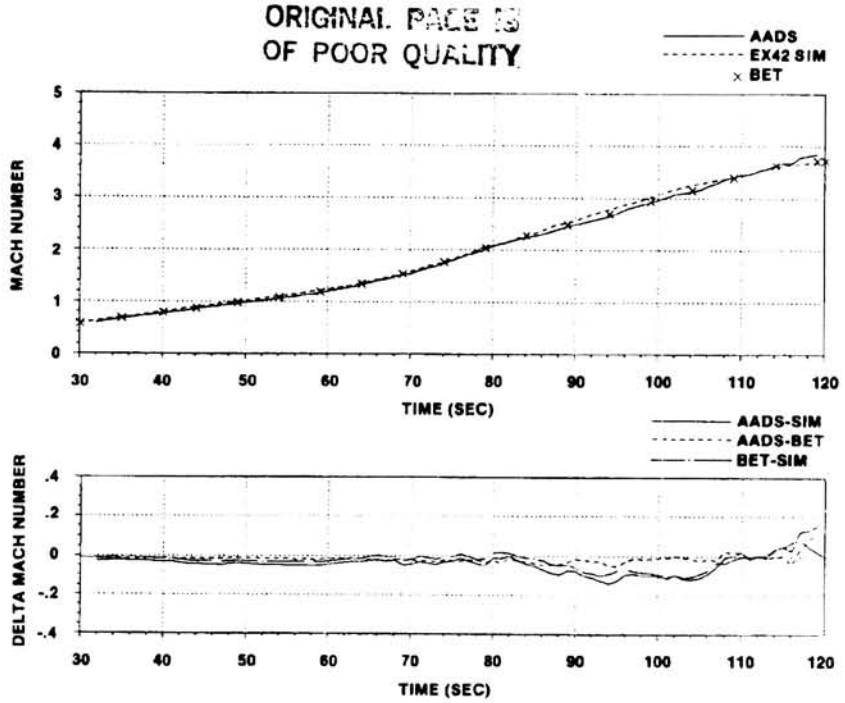

(a) STS-1.

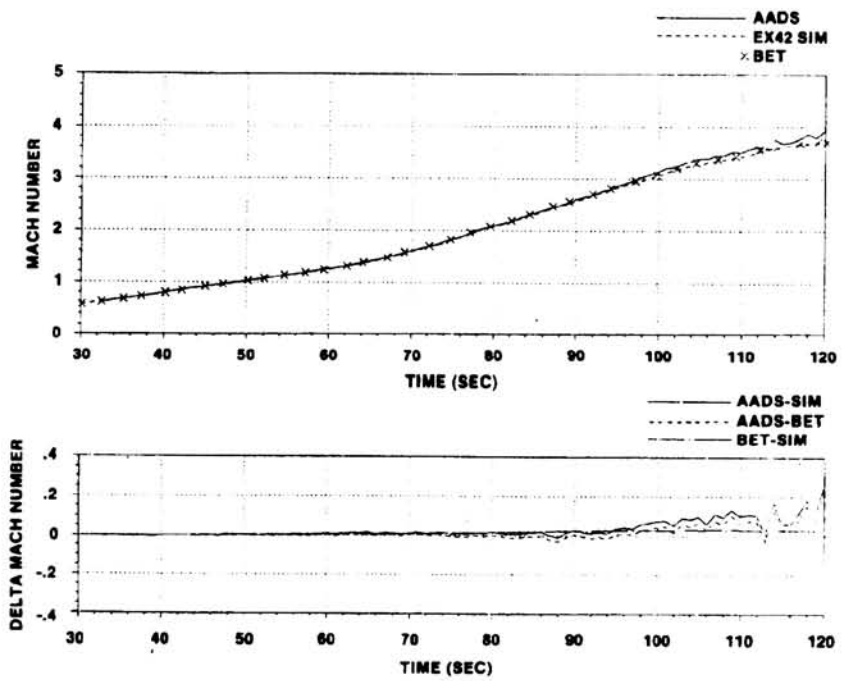

(b) STS-2.

Figure 23.- Final AADS air data comparisons and differences for Mach number (M).

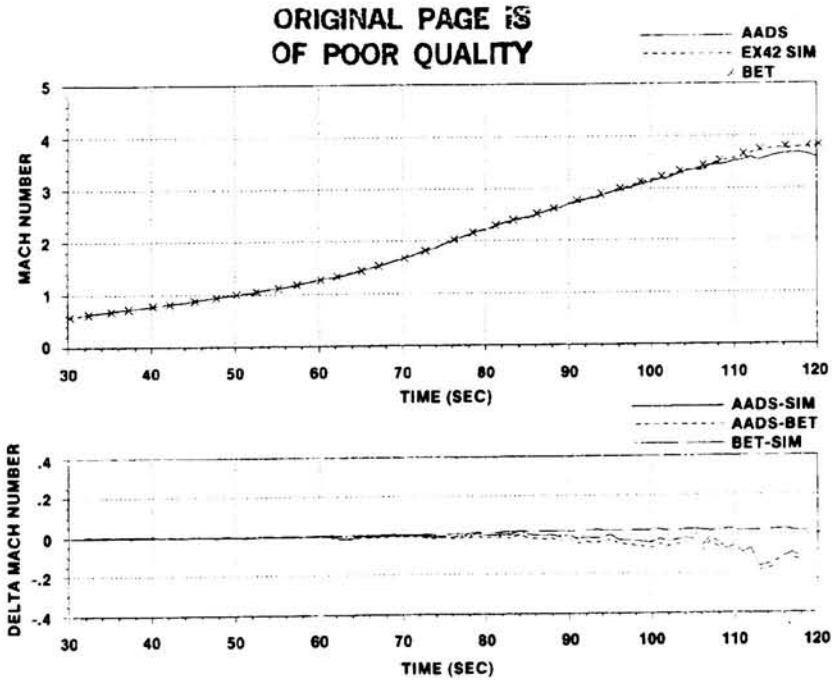

(c) STS-3.

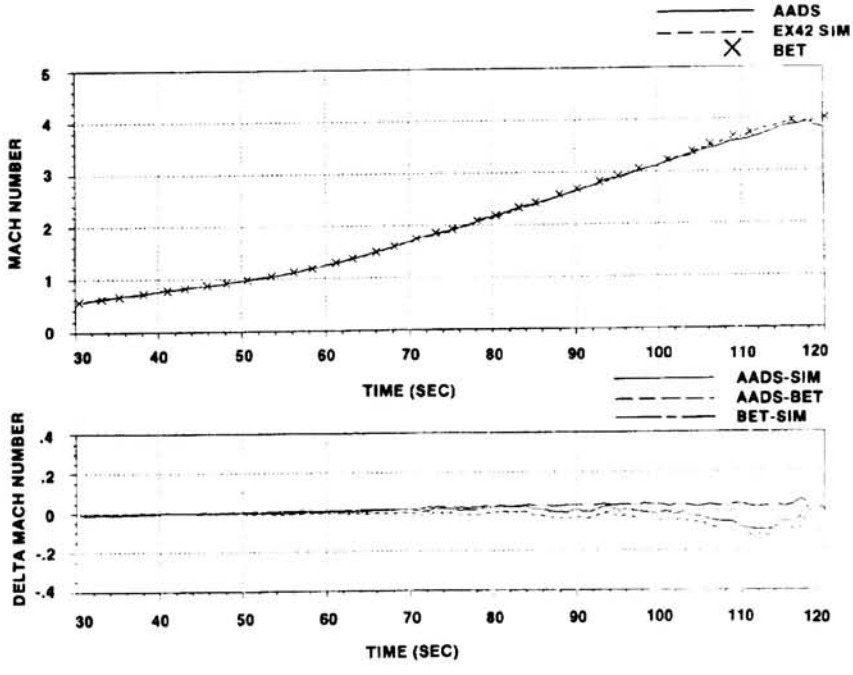

(d) STS-4.

Figure 23.- Concluded.

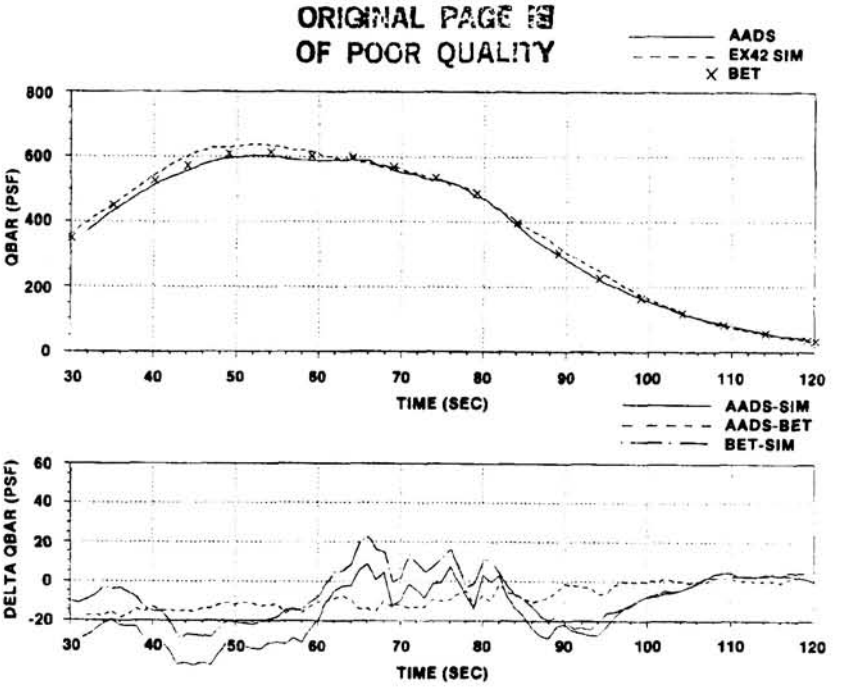

(a) STS-1.

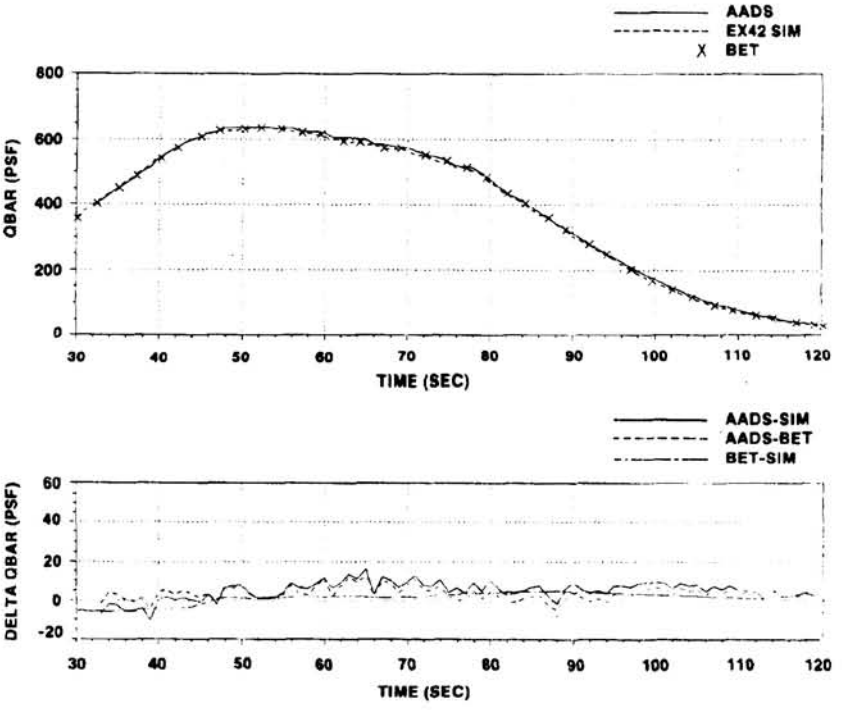

(b) STS-2.

Figure 24.- Final AADS air data comparisons and differences for dynamic pressure (QBAR).

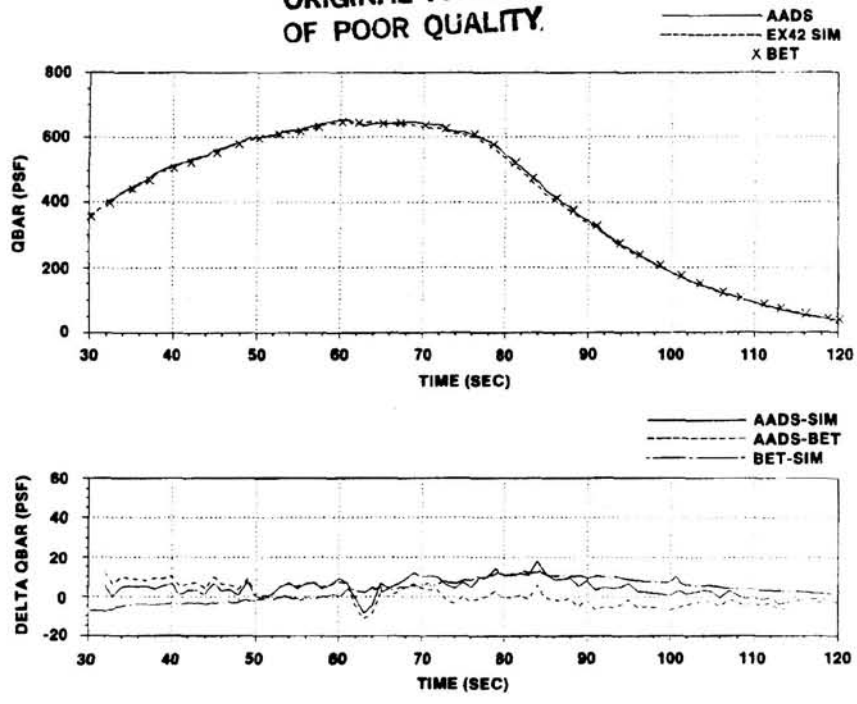

(c) STS-3.

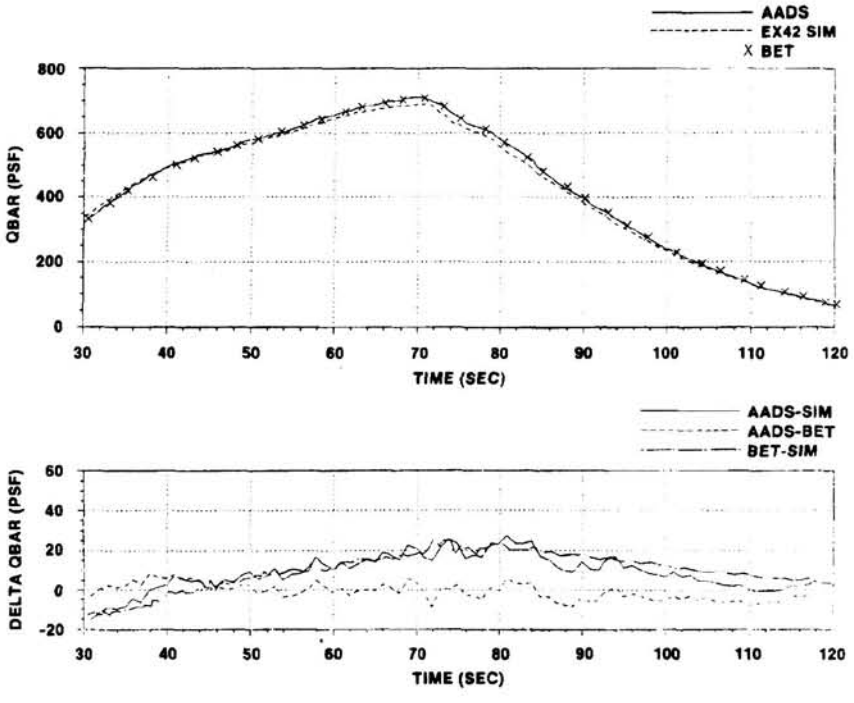

(d) STS-4.

Figure 24.- Concluded.

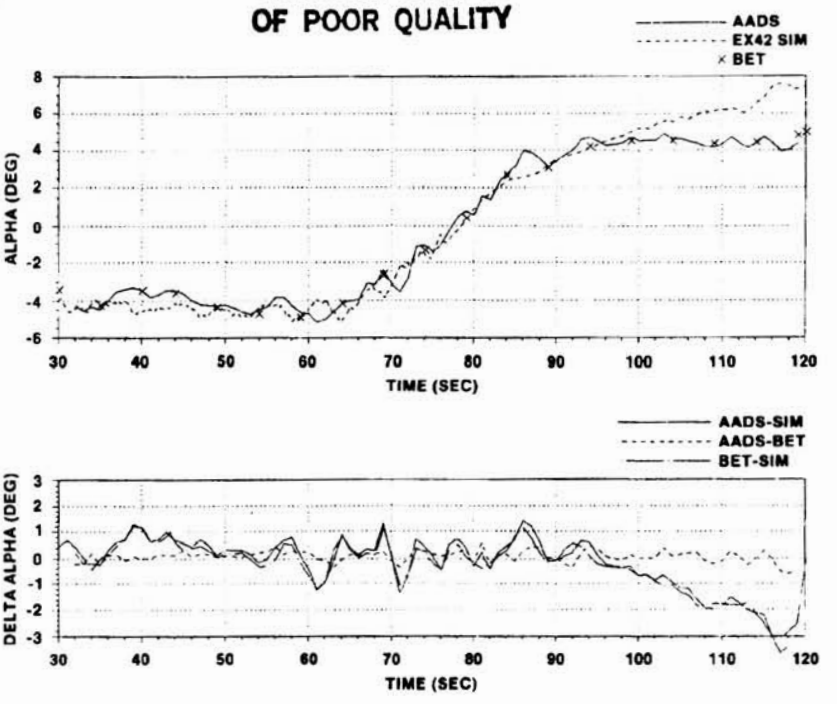

(a) STS-1.

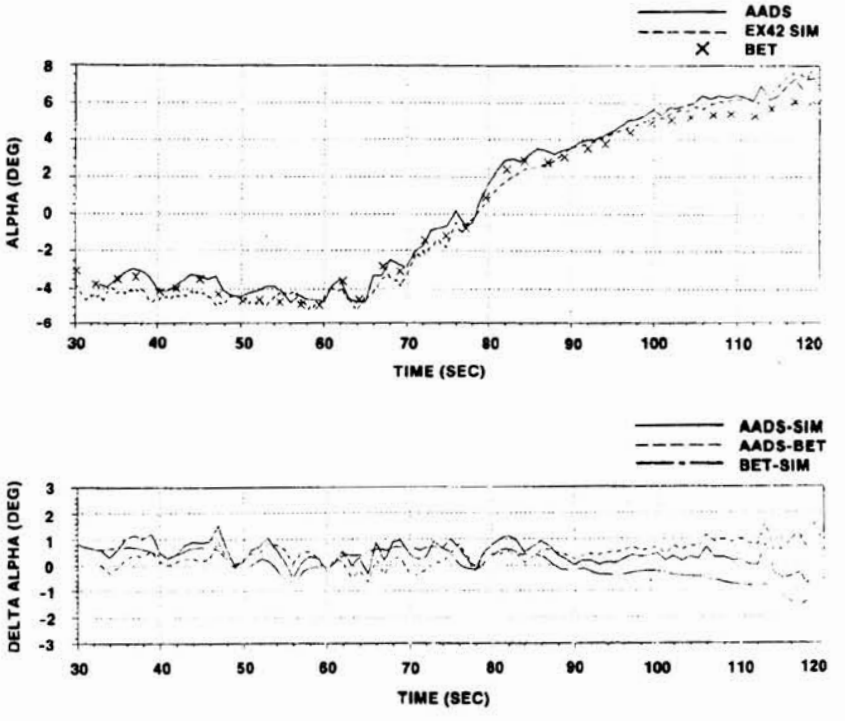

(b) STS-2.

Figure 25.- Final AADS air data comparisons and differences for angle of attack (ALPHA).

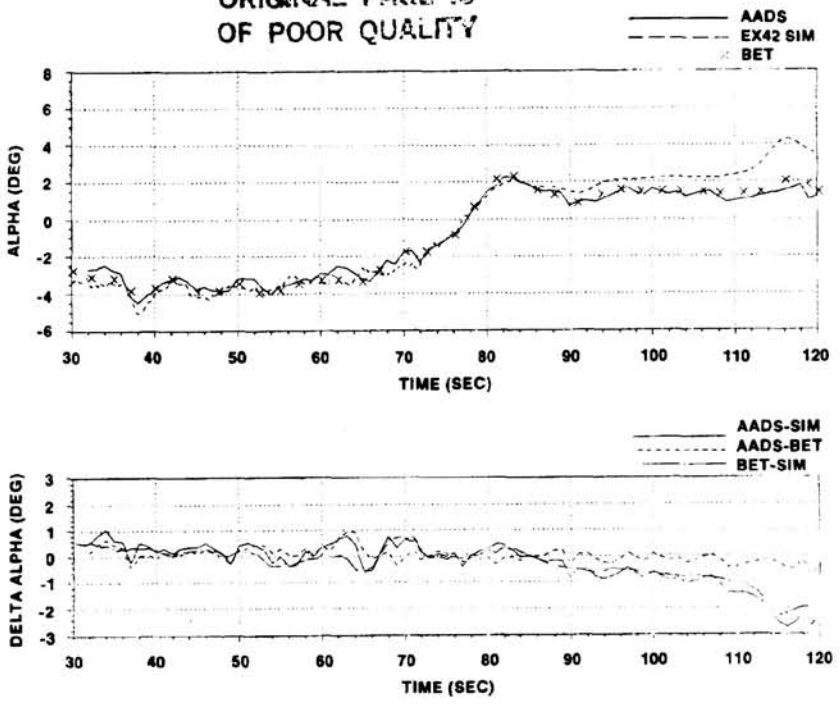

(c) STS-3.

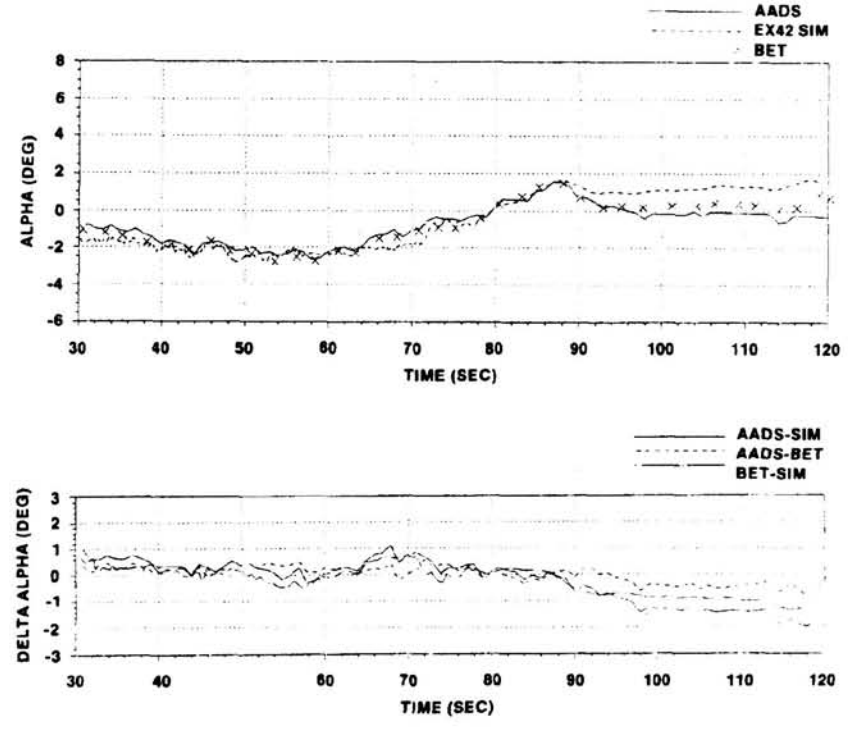

(d) STS-4.

Figure 25.- Concluded.

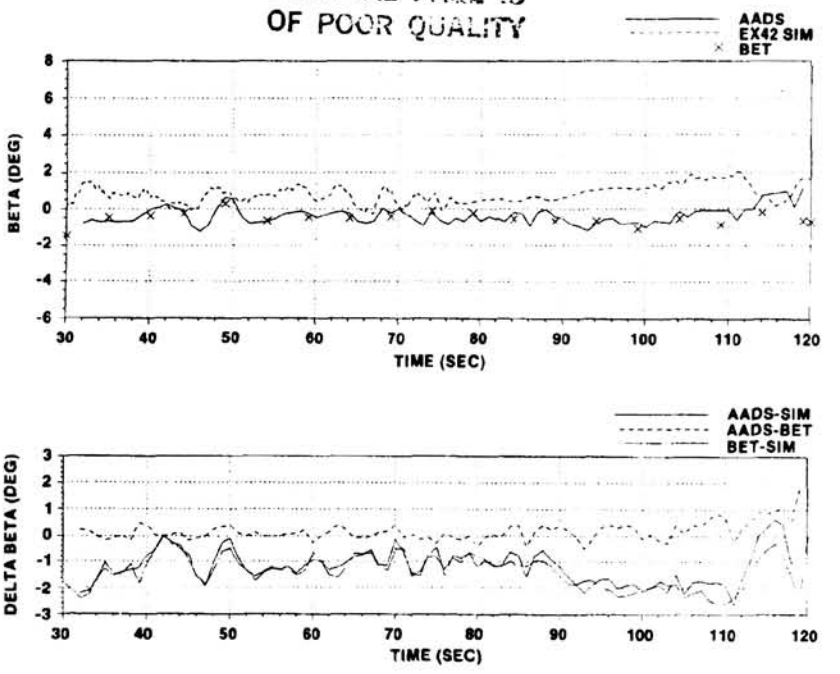

(a) STS-1.

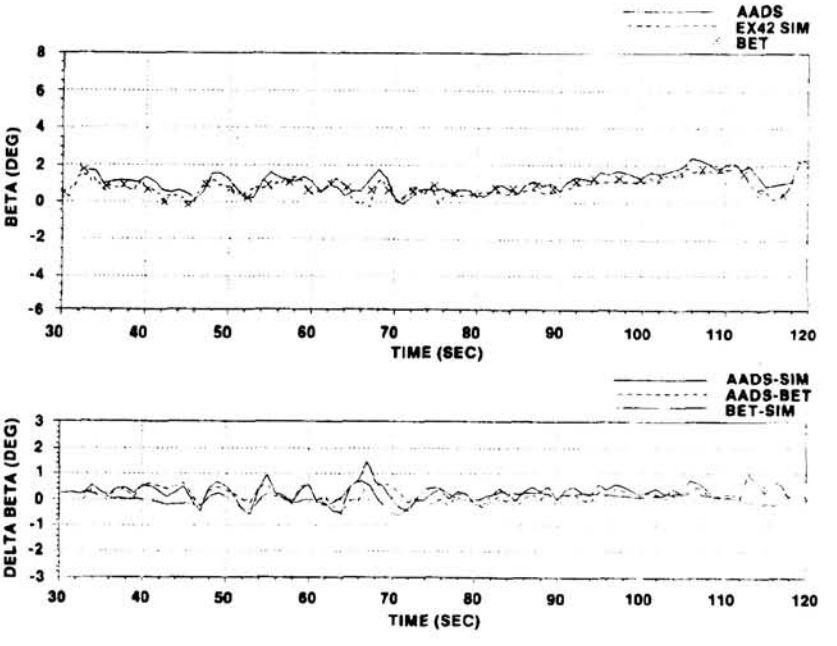

(b) STS-2.

Figure 26.- Final AADS air data comparisons and differences for angle of sideslip (BETA).

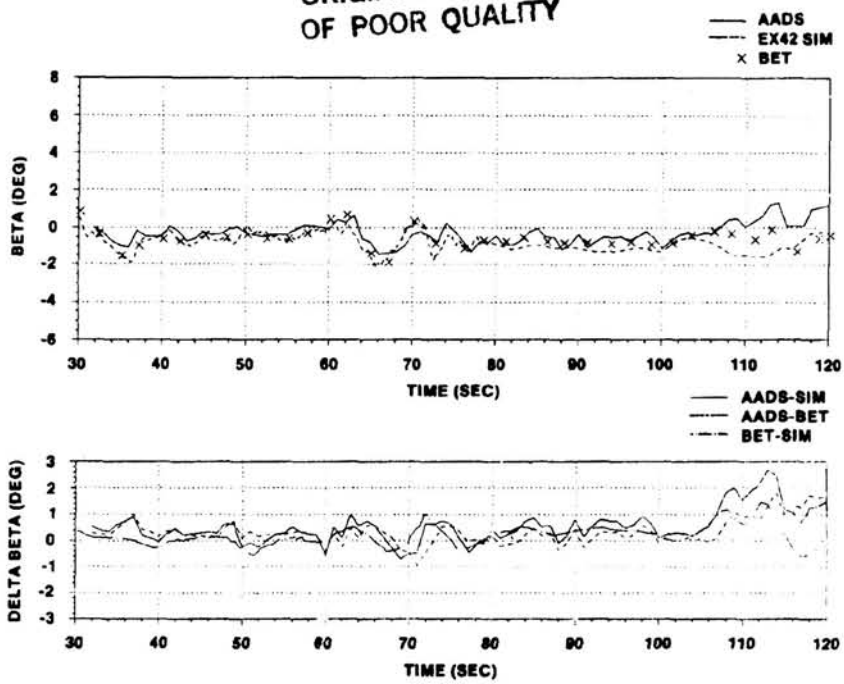

(c) STS-3.

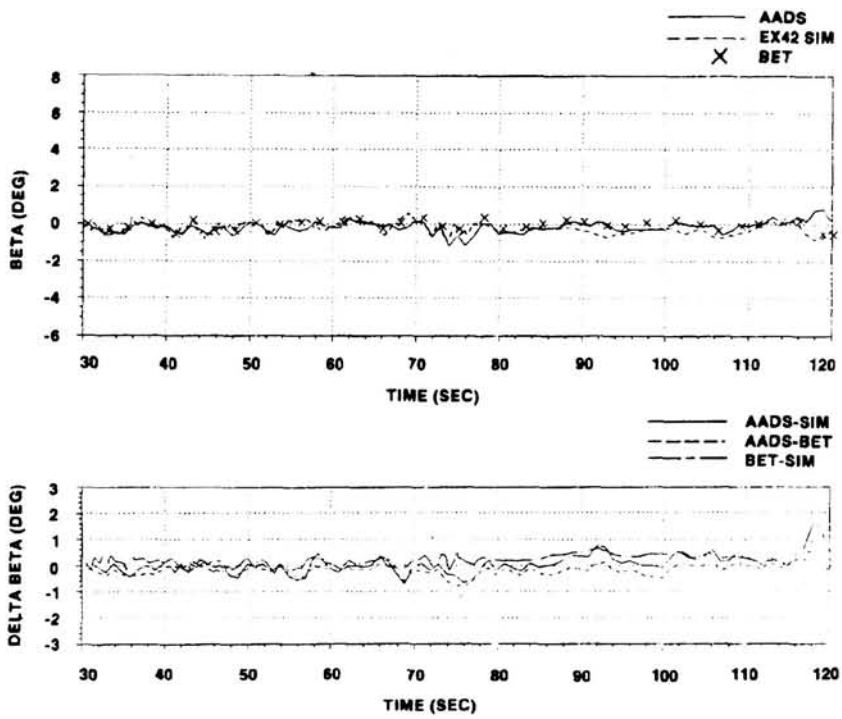

(d) STS-4.

Figure 26.- Concluded.

SPACE SHUTTLE ORBITER VENTING - LESSONS LEARNED

H. S. Lutfi
Rockwell International
Downey, California

Raymond L. Nieder
NASA Johnson Space Center
Houston, Texas

SUMMARY

The orbiter vent system provides dedicated vent areas to permit the gases trapped inside the vehicle to escape during ascent. The same vent system also repressurizes the vehicle during entry. The vent system is one of six systems that constitutes the purge, vent and drain subsystem. The orbiter active vent system has been very adaptable to the changing requirements that have occurred during the development of the Space Shuttle orbiter.

Good correlation has been obtained between predicted and measured compartment pressures during the orbital flight test (OFT) program. An investigation of the flight data showed that the difference between preflight prediction and the measured values were primarily due to the difference between the baseline external pressures, which was based on subscale wind tunnel test data, and the actual vehicle local external pressures measured during the flight. The current predictions are based on flight derived vent port pressure coefficients since the wind tunnel data does not adequately define the orbiter ascent pressure environment.

Recommendations for future vehicle vent systems include designing for large vent areas, providing for sufficient flight instrumentation, performing structural leakage testing, and avoiding external vent ports in close proximity to one another.

ORBITER ACTIVE VENT SYSTEM

The Space Shuttle orbiter purge, vent and drain (PVD) subsystem consists of six basic systems whose primary function is the environmental control of the orbiter unpressurized structural compartments. One of these is the vent system which provides dedicated vent areas to control the gases entering and exiting from the various compartments during ascent, on-orbit, entry and ground purging. The orbiter active vent system maintains acceptable structural differential pressures through controlled venting during ascent depressurization and descent repressurization. The system also provides for on-orbit molecular venting to assist the thermal control subsystem insulation blankets in reaching maximum efficiency and to provide reduced vent port area so that the purge system can maintain a positive differential pressure for moisture and hazardous gas control.

The active vents are equipped with electromechanical doors which are located on both sides of the orbiter as shown in figure 1. There are nine active vent doors of which three are independently actuated while the remainder are actuated in groups of two. Each vent system consists of an independently powered redundant motor drive, the vent doors and associated hinges, linkages, torque shafts, and gear boxes.

Three main factors determined the location of the orbiter active vents. The first consideration was orbiter internal compartmentation which established isolated volumes or compartments requiring dedicated vents. The second factor was sensitivity of the internal compartment pressures, during ascent and descent venting, to the external aerodynamic pressure. The external pressure varies greatly depending on the velocity, yaw and angle of attack of the vehicle. In order to reduce the internal compartment pressure sensitivity to fluctuations in the external pressures, regions of the orbiter were identified where the external aerodynamic pressures remained relatively constant despite changes in yaw and angle of attack. The orbiter active vent locations were located in areas exhibiting the least sensitivity to pressure variation as illustrated in the isobar contour plot included as figure 2. Once the vent locations were established, the total required vent area was divided between the left and right sides of the orbiter in order to reduce the compartment pressure sensitivity due to yaw. The third factor was the magnitude of the internal compartment pressures. The internal pressure will follow the local external pressure at the vent port. Thus, if it is desired to have a low compartment pressure, the vents must be located in a low external pressure region. For the orbiter, it was desired to maintain a low pressure differential across the compartment external skin panels, so the compartment vents were located very close to those compartment external skin panels. The three factors are mutually dependent and can be fully understood only from a total vehicular viewpoint.

ORBITER COMPARTMENTS

The early venting design goal of the orbiter was to minimize the effect on compartment pressure due to minor changes in vent or leakage areas, and due to trajectory parameter variations such as angle of attack and angle of sideslip. Because of the different types of venting volumes, three different vent system designs were used on the orbiter. These three types of vent compartments are the self-vented, passive-vented, and control-vented compartments. The self-vented compartments consist of the nose cap, body flap, and wing leading edges. The venting area requirements for these compartments are provided by intentional gaps between the reinforced carbon-carbon panels. The elevons, rudder/speedbrake and window cavities comprise the orbiter passive-vented compartments. These compartments are vented through passive vents with self contained heat sinks which absorb thermal energy from the hot reentry gases to maintain compartment temperatures at low levels. The remaining orbiter compartments are the control-vented compartments which are vented through the active vent doors. These vent doors are opened and closed during flight to provide the required vent areas when needed, and by closing during entry, they prevent the ingestion of hot gases into the compartments. A schematic diagram of the orbiter vehicle compartments is illustrated in figure 3.

VENT SIZING

Very early orbiter venting analysis established the vent sizing criteria based on the volume of air vented and the desire to maintain a low differential pressure loading across the compartment bulkheads and skin panels. The initial sizing criteria for the active vent ports was established as 0.06 square inches of vent area per cubic foot of compartment volume to be vented. A similar vent area criteria had proven successful in venting the second stage of the Apollo/Saturn launch vehicle. This number was arrived at by determining the maximum differential pressure that would exist in a compartment of one cubic foot volume with various vent areas. These cases were analyzed with the venting analysis digital computer program for a typical ascent and descent trajectory, and the results from the various cases (plotted in figure 4) showed that very small vent areas resulted in large differential pressures while small differential pressures would occur for large vent areas. The curve is nonlinear for the area-to-volume ratios presented and shows that for small area-to-volume ratios, minor changes in vent area cause very large changes in differential pressures. Thus, to minimize the compartment differential pressure loading across the external skin panels as well as to reduce the sensitivity due to vent area changes, an ascent vent area design criteria of 0.06 square inches per cubic foot of compartment volume was established. The descent vent area criteria was established as 0.03 square inches per cubic foot. For reliability and mechanical simplicity, the orbiter descent vent area to compartment volume ratio was established at the larger ascent value. This criteria automatically gave the resulting orbiter vent system the capability to withstand large variation in compartment leakage areas and also to withstand any single failure of the electromechanical vent door to operate properly.

VENT SYSTEM OPERATION TIMELINE

During the evolution of the orbiter, the active vent system operation timeline has changed significantly. Due to the inherent flexibility that was initially designed into the system, the orbiter vent system has adapted to these changes in operations and requirements with very little impact to the system software or to the resulting structural differential pressures. For the STS-1 flight, since there was no payload, it was decided to open all vents prior to lift-off in order to measure the internal acoustic levels and also to provide protection against vent doors failing to open during ascent. The measured acoustic levels were all below the payload bay design criteria and thus, the nominal ascent vent door operation is to verify that all vent doors are fully open prior to ignition of the Space Shuttle main engines start. Also for the STS-1 flight, it was decided to not close the aft fuselage vent doors from 80 to 100 seconds after lift-off. This decision was made so that gas sample bottles located in the aft fuselage could obtain compartment gas samples during the time period that the hydrogen rich engine exhaust gases were expected to be ingested and thus, verify whether a potential hazard really existed. Subsequent analysis of these gas samples showed that hydrogen gas existed in the aft fuselage, along with air, but in concentrations that were significantly below the flammability limits. Since the data measured during the STS-1 flight showed no significant hydrogen concentrations, the proposed ascent vent door management operation was never implemented. The nominal ascent vent door operation timeline now verifies that all vent doors are open prior to engine ignition. All vents were kept in their full open position until just prior to entry at which time the vent doors were closed. The open vent area, while in orbit, provides more than sufficient vent area

to satisfy the thermal control subsystem molecular venting requirement that the compartment pressure be below 5×10^{-5} torr within 12 hours after launch. In addition, leaving the vent doors open also provides some capability to withstand subsystem gas leakages into the various compartments due to line or tank leaks. Prior to entry, the vent doors were closed and were not reopened until the vehicle velocity was below 2400 feet per second. This normally occurs between 80,000 and 85,000 feet altitude. For maximum dispersed trajectories and worst case system measurement errors, the vent doors could open as low as 70,000 feet or as high as 95,000 feet. After landing, the vent doors are cycled to their purge position and the post landing purge starts to cool the vehicle internal structure and to purge any hazardous gases that might have been ingested during descent.

VENTING ANALYSIS

The orbiter internal compartments contain large volumes of gases which undergo considerable variations in pressure during launch and reentry. It is necessary to predict accurately the internal compartment pressure-time histories in order to verify that the differential pressure loadings across the compartment skin panels, bulkheads and doors are within their structural capabilities. These pressures are readily predictable by computing the mass flow and energy transfer between compartments that are connected by a wide range of conductor types. These conductors range from the simple orifices used to model the Orbiter active vents, to the pipes used in the window cavity conditioning system venting analysis. Each type of orifice has its own experimentally derived flow discharge coefficient which is used to correct the computed theoretical mass flow rate to account for gas viscosity, stream contraction, orifice geometry and external gas cross-flow effects. The pipe flow analysis is corrected similarly for pipe inlet and exit geometry resistance as well as for the resistance of pipe joints and bends by using pipe flow resistance coefficients.

The extensive computations required for an orbiter venting analysis are performed with the multicompartment venting computer programs that were developed independently at Rockwell International and at the NASA Johnson Space Center. Both computer programs were developed and used extensively during the Apollo/Saturn program and then adapted for use in analyzing the Space Shuttle. The compartments can be treated as adiabatic or be forced to follow prescribed temperature or heat transfer time histories. The gas flow through the pipes can be treated as adiabatic, isothermal or be subjected to heat transfer due to differences between the gas temperature and the pipe wall temperature. The pipe wall temperature can be specified as being constant or vary with distance along the pipe and/or with time.

The importance of accurate computations of compartment pressures cannot be over-emphasized. This is especially shown by the fact that prelaunch venting analyses are an integral part of the day of launch structural loads evaluation program in which critical structural loads and compartment pressures are computed based on the latest prelaunch flight trajectories. These trajectories are predicted by using the upper atmosphere wind profiles measured on the day of launch as well as the latest SRB bulk propellant temperatures and other parameters that affect the ascent flight trajectory. If any of the computed loads or differential pressures exceed preset "red-line" values, structural analysts at NASA JSC, Rockwell International and other support contractors are notified of the exceedances. Additional analysis and evaluation of the orbiter structural capability are then conducted that will result in a recommendation to NASA and Rockwell International upper management to launch or to hold the launch until the conditions improve.

VENTING ANALYSIS DATA REQUIREMENTS

Before either the Rockwell or NASA JSC venting computer programs can be used to predict the orbiter internal compartment pressure time histories, various data must be obtained and transformed to meet the computer program input requirements. These data requirements include the compartment volume, vent and leakage area definition, external aerodynamic data bases, flight trajectory parameters and standard atmosphere tables.

For the orbiter, the compartment volumes, vent and leakage area definition is provided by the Rockwell Purge, Vent, and Drain Subsystem Group. This group monitors all activities that could result in changes to the compartment venting characteristics. The detailed definition of vent and leakage areas for each orbiter compartment is provided to the venting analysts in the format shown in figure 5. With these data, the venting analyst can define the venting math model to be used in the computer program. In addition, the locations of all external vent ports and structural leakage areas are used to extract, from the total orbiter aerodynamic data base, the local pressure coefficients as a function of Mach number, control surface deflection, angle of attack and angle of sideslip. This reduced set of aerodynamic data is referred to as the venting aero data base. The required trajectory parameters include altitude, vehicle velocity, dynamic pressure, Mach number, angle of attack, angle of sideslip, and the various control surface deflections, all as functions of time. Once the altitude-time history is defined, standard atmosphere tables are interrogated to obtain the ambient pressure and temperature time history profiles. The remaining trajectory parameters are used to interrogate the venting aero data base to define the local pressure time history at each external vent port and structural leakage area location.

VENTING ANALYSIS TECHNIQUE

Once the necessary data has been obtained, the orbiter internal compartment pressure-time histories are predicted by computing the mass and energy transfer between compartments that are interconnected by a wide range of conductor types. The analysis requires that the compartment volume and vent areas are shown as a function of time as well as the initial pressure, temperature and gas composition for each compartment. The net flow of mass and energy from each compartment can then be accurately computed throughout the flight time interval specified. The computations performed in the computer program are described briefly as follows:

The analytical approach to the venting problem is to compute the compartment initial conditions and then determine the rate of mass flow and energy transfer through the conductors. The actual mass flow rate through an orifice or pipe is a function of the pressures that exists on both sides of the orifices, the orifice geometry and the gas thermodynamic properties. The theoretical mass flow rate through an orifice is computed using the inviscid compressible isentropic one-dimensional flow equation. The effects of viscosity, orifice geometry, and stream contraction are then accounted for by using the appropriate experimentally derived discharge coefficient. The actual mass flow rate is thus determined by multiplying the theoretical mass flow rate and the discharge coefficient. Using the initial conditions specified for each compartment, the initial gas mass and internal energy are computed with equations 1 and 2:

$$m = PV/RT \tag{1}$$

$$u = m\, C_V\, T \tag{2}$$

The compartment pressure time history can be predicted by the repetitive solution of a series of thermodynamic equations that determines the mass and energy transfer across each vent or structural leakage area during a very small time interval.

The mass flow rate equation used for choked flow is

$$\dot{m} = \frac{C_D\, A\, P_T}{\sqrt{RT}_{T/\gamma}} \left(\frac{\gamma + 1}{2}\right)^{\frac{\gamma + 1}{2(1 - \gamma)}} \tag{3}$$

or for unchoked flow:

$$\dot{m} = \frac{C_D\, PAM}{\sqrt{RT}_{T/\gamma}} \sqrt{1 + \left(\frac{\gamma - 1}{2}\right) M^2} \tag{4}$$

The rate of change for the internal energy is computed as:

$$\dot{u} = \dot{m}\, C_p\, T_T \tag{5}$$

Equations 3 through 5 are solved for each vent port or leakage area and then the net mass flow and energy transfer for each compartment is computed by summing the individual changes, i.e.:

$$\dot{m}_T = \sum_{i=1}^{N} \dot{m}_i \tag{6}$$

$$\dot{u}_T = \sum_{i=1}^{N} \dot{u}_i \tag{7}$$

The compartment mass and internal energy can now be calculated at time = $t + \Delta t$ by adding the incremental change in mass and internal energy to the values that existed at time = t. That is:

$$m_{t+\Delta t} = m_t + \dot{m}_T \, \Delta t \tag{8}$$

$$u_{t+\Delta t} = u_t + \dot{u}_T \, \Delta t \tag{9}$$

The new compartment pressure and temperature are now computed using equations 10 and 11:

$$T = u_{T+\Delta t}/c_V \, m_{t+\Delta t} \tag{10}$$

$$P = RT \, m_{t+\Delta t}/V \tag{11}$$

Equations 3 through 11 are solved repetitively until some specified termination condition (such as time or pressure) is attained.

The prediction of compartment pressure reduces essentially to the accurate prediction of mass flow and energy transfer rates between compartments, containing the same or various gas mixtures, connected by orifices or pipes. These predictions have been shown, during the Apollo/Saturn program, to be very accurate when compared to flight data if a well defined venting math model is used together with an accurate definition of the location and distribution of the structural leakage areas, and an accurate knowledge of the external pressure environments. For the Space Shuttle program, extensive structural leakage testing was performed on the orbiter and the results incorporated into the venting math models, while the venting aero data bases were generated using the best Space Shuttle wind tunnel test data available.

STRUCTURAL LEAKAGE TESTS

Unlike the dedicated vent port area whose dimensions and locations can be defined accurately, the structural leakage could only be estimated prior to building the orbiter. After the orbiter was built, structural leakage testing was performed to determine the structural leakage distribution and also to verify that the leakage was not concentrated in extremely high or extremely low pressure fields on the orbiter. The tests were conducted just prior to rollout from the Orbiter Processing Facility and were one of the last ground tests performed prior to flight. This ensured that all equipment, seals, and hatches were installed in the actual flight configuration.

The structural leakage test is conducted by pressurizing a selected compartment and accurately measuring the gas mass flow rate required to maintain the compartment pressure at a constant level. Knowing the mass flow rate and the compartment pressure, the total structural leakage can be calculated. The next step is to pressurize an adjacent compartment so that the differential pressure across the bulkhead between the compartments is zero. The gas mass flow rate into the selected compartment is accurately measured and a new structural leakage area calculated. The difference between the two calculated leakage area is the bulkhead leakage area. After all bulkhead leakage areas are determined, any area not accounted for is due to leakage through the outer moldline (OML) for that compartment.

The location and distribution of the external structural leakage is very important to the venting analyst. This could not be measured but was estimated by locating the outflow locations while the compartment was pressurized. By feeling the outflow locations, the proportion of the outflow at each location is estimated. This proportion is then used to allocate the measured compartment OML leakage area and arrive at the leakage area distribution to be used in the venting analysis.

Several of the orbiter structural leakage tests conducted for the OV-102 vehicle were not the detailed leakage tests as previously described, but were instead a simplified version to reduce the impact on rollout schedules and reduce costs. For these simplified tests, only the compartment total leakage area was determined by pressurizing each compartment individually. It was assumed that bulkhead leakage areas did not change from the detailed tests. Thus, any change was assumed to be due to OML leakage area changes. The location and distribution of the revised OML leakage area was again determined by locating where the purge gas was flowing out and estimating the proportions of outflow.

Results from all of the OV-102 structural leakage tests have shown insignificant leakage area variations that can be attributed to inflight loading. All of the variations measured to date can be explained either by the changes made to the vehicle while on the ground or accuracy of the test.

ORBITER INFLIGHT VENTING

Prior to the first orbiter flight, the only source of external pressure coefficient data available for analyzing the compartment's external pressure environment was the orbiter subscale wind tunnel tests. Any new concept or study regarding the orbiter vent system (e.g., vent doors management, doors failure, subsystem leakage) relied heavily on the wind tunnel data in order to predict the effects of any changes on the total orbiter pressure loading.

VERIFICATION OF VENT MATH MODEL

In order to justify using the venting program results for verification of the orbiter design data, it was important to demonstrate that the results adequately represented the vehicle pressure environment. During the orbiter approach and landing test (ALT) program, two absolute pressure transducers were located in the nose and in a main landing gear compartment in order to measure the landing gear wheel well pressure environments. Comparisons were made between the analytical prediction and the measured data obtained from the orbiter fifth free flight, and are shown as figures 6 and 7. The comparisons show good agreement, with some minor deviation which was attributed to the fact that the math model used in the ALT analysis did not account for leakage areas or interaction between adjoining compartments. Thus, the results were encouraging.

POST STS-1 ANALYSIS

Once the flight data from the first Space Shuttle flight had been received and reviewed, it readily became apparent that the preflight predictions differed considerably from the measured data. This was true of all of the internal pressure measurements as well as the external pressures, and was dramatically evidenced by the considerable lofting variation in the ascent trajectory. Figure 8 shows the comparison between the STS-1 flight measured and the preflight prediction for the payload bay. The comparison is presented as the payload bay internal pressure relative to ambient since an absolute pressure comparison does not readily show the variation between the data or the areas of mismatch. The data comparison for the other compartments showed a range of poor to fair correlation.

The predicted values utilized the best reconstructed ascent trajectory, measured structural leakage areas, and the best available wind tunnel data for the pressure coefficients, while the measured data was corrected to account for the transducer zero shift by adjusting the data to the measured ambient pressure at the time of lift-off. As is obvious from figure 8, there is considerable differences in the magnitude and the timing of the peaks in the payload bay differential pressure. By a process of elimination of the variables in the venting analysis, the external vent port pressure coefficients were quickly identified as causing the differences between the preflight predicted and the measured internal pressures. This conclusion was also consistent with the ascent trajectory lofting phenomena which was indicative of a major change in the external pressure environment. To test this theory, the measured vent port pressures were converted into pressure coefficients for input to a revised venting analysis. Figures 9 through 12 show comparisons for the four payload bay vent ports local pressure coefficients between the measured STS-1 flight data and the baseline wind tunnel test data. The differences between the measured and the data base pressures at the transducer locations are quite large

in some regions. Some of these differences can be attributed to the plume effects which were improperly simulated in the wind tunnel tests. The measured pressures for transducers on the aft section of the vehicle were higher than the predicted values. Another explanation for the significant difference between the measured and predicted wind tunnel test data is the scarcity of the wind tunnel test points. Noted on figure 9 are the Mach numbers at which the actual wind tunnel tests were conducted. As can be seen, the wind tunnel test correlates well with the measured data at each of the supersonic Mach numbers tested. Other more localized pressure differences result from full scale to model boundary layer differences, pressure transducer line leakage at the thermal protection system (TPS) tile/strain isolation pad (SIP) interface, and influence of the vent mass outflow on nearby pressure transducers. These effects are localized and are definitely small when compared to the pressure differences actually seen during flight.

The measured base pressures were similarly converted into pressure coefficients. Figure 13 shows the comparison between the flight measured data on the orbiter base heat shield and the wind tunnel test derived predicted values. The comparison shows a considerable difference between the two data sets which could be caused by the cold-flow plumes simulation during the wind tunnel tests. The base pressure environment is used in establishing the design data for the aft fuselage and orbital maneuvering system (OMS) Pod base heat shields. Furthermore, the aft fuselage and OMS Pod internal pressures are influenced by the base pressure due to the large concentration of leakage area in the orbiter base around the engine seals and engine domes.

The results from the venting analysis using the measured vent port and base heat shield pressure coefficients is shown in figure 14 for the payload bay. The remarkable change in the predictions from figure 8 which used wind tunnel data to figure 14 which used flight measured vent pressures demonstrated conclusively that the wind tunnel data was in error. All of the other orbiter compartments demonstrated similar improvements in the analysis prediction correlation with the measured data.

The vent analysis correlation has been improved even more by slight modifications to the flight measured vent port pressure. This slight modification accounts for some of the errors included in the measured pressure. Such as, vent gas outflow, tile penetration leakage and structural leakage.

The vent outflow source of error in the measured pressure is due to the fact that the orbiter vent port pressure measurements are, unfortunately, located either ahead of, or behind the vent. Depending on the measurement location, the vent gas outflow can distort the measurement reading by causing a higher reading than the actual pressure at the vents if the measurement is in front of the vent or a lower reading if it is behind the vent. The readings from measurements located ahead of the vent will be affected for short time periods during flight and will be dependent on the mass flow rate out of the vents, the local velocity perpendicular to the vents and the distance of the pressure tap from the vent. Measurements behind the vent will be affected anytime that there is vent outflow.

Several of the external pressure measurements had special penetrations through the TPS tiles. These transducers had a thin glass tube that provided the flow path between the pressure sensor and the external location at which it was desired to measure the pressure. During tile pull testing that was performed to verify the tile bonding, the seal between the tube, SIP, and the tile were broken. Thus, the measured pressure was a combination of the SIP internal pressure and the external pressure. For most ascent, these two pressures are nearly the same due to the very rapid venting characteristics of the tile/SIP combination. The only time that there is a significant difference is when a steep pressure gradient or shock wave exists across the instrumented tile. Thus, even though there is a tile penetration leakage effect for several of the external pressure measurements, the effect tends to be evident for only short periods of time and represents a small error source.

The third deviation source is actually more a correlation analysis procedure error rather than an error in the external pressure measurement. The only measured external pressure data that was available, and that was meaningful to the vent correlation analysis, was that measured at the vent ports which are located along the sides of the vehicle. The external structural leakage areas in the venting analysis continued to rely on the questioned wind tunnel data because there was no data that could be used to update the structural leakage pressure coefficients. The correlation procedure adjusted the vent port pressure coefficients in order to obtain a better correlation between the predicted and measured compartment pressures. Thus, some of the correction done to the vent ports will actually tend to correct for the errors introduced into the analysis due to the continued reliance on wind tunnel data for the structural leakage areas. The continued use of wind tunnel data for the structural leakage areas is acknowledged as an error source but this is considered to have a minor effect on the predictions of compartment pressures.

The flight derived vent port pressure coefficients were used to predict the compartment pressures for Shuttle flights 2 through 5. In all cases, the derived pressure coefficients have provided a much better correlation with the measured flight data than with the wind tunnel pressure coefficients. Figures 15 through 18 show the comparison between measured and predicted for several of the orbiter compartments utilizing the flight derived vent port pressure coefficients.

ENTRY CORRELATION

Unlike ascent, the comparisons between predicted and measured pressures for entry has shown good correlation both for the internal and external pressure measurements. Comparisons of several external pressure measurements are shown in figures 19 through 23, and for several of the orbiter compartments as figures 24 through 27.

RECOMMENDATIONS AND LESSONS LEARNED

During the evolution of the orbiter vent system, several items were discovered that are worthy of comment and are recommended for application to future vehicles.

The first of these is to use large external vent areas. That is, design for large vent area to compartment volume ratios instead of small values of the ratio. Inherent in this design is the capability to have wide variation in structural leakage areas and vent door operation failures without significantly changing the structural differential pressure loading. After all, it is the structural loading that is important to the vehicle and whatever can be done to reduce its sensitivity due to uncontrollable leakage areas and failures should be incorporated.

Structural leakage testing should be planned for, and performed on, all new vehicles. Besides providing much improved venting math models, structural leakage tests also verify the sealing integrity of the vehicle. It also provides verification that the necessary leakage or vent area does exists. A perfectly sealed (or close to it) bulkhead or skin panel is not necessarily good for structural loading consideration. For example, during the structural leakage verification test performed on the second orbiter (i.e., OV-099), it was found that the leakage between the main wing box and the outboard elevons was far less than that measured on the first orbiter. Based on the OFT flight correlation experience, the venting analysis updated for the OV-099 structural leakage areas indicated a substantial increase in the wing rear spar differential pressure loading that would exceed the design values. Additional vent area was provided in the OV-099 wing rear spar to reduce the predicted differential pressures to the OV-102 values. Future structural leakage tests will specifically check and verify that a minimum of leakage exists in this spar. The current orbiter structural leakage tests could be improved by performing the tests at higher pressures than currently done, except that the purge gas supply source is currently the limiting factor. The higher test pressures would provide a more accurate leakage area calculation as well as permit a better identification of the leakage location. Once the leakage test is performed, that configuration should be maintained throughout the flight. A structural leakage test that is performed before seals are installed or with nonflight article doors is not meaningful and should not be accepted by the venting analysts unless an accurate definition of the out-of-flight configuration is provided. Granted, some items of a nonflight nature will be required for the tests but these should be minimized as much as possible.

Instrumentation location, especially on the external surface, is very important and can cast doubt on the validity of the measured data, such as happened with the orbiter data. The pressure measurements which are located near the vent ports should either be located above or below the ports in order to reduce the effect of the vent port outflow on the measured pressures. The measurements should never be located behind the vent port as this yields a completely distorted view of the surface pressure distribution. Locations ahead of the vent port are acceptable but there will be some period of time during which the vent outflow disturbance may cause a small error in the reading. These readings will tend to be slightly higher than with the undisturbed flow.

Another problem encountered with the orbiter pressure measurements was the quoted accuracy. Only total pressure transducers were used on orbiter 102 and these are quoted as being accurate to within 5 percent of full scale (i.e., 0.75 psi). Some

of this error was reduced by using individual calibration data for each transducer and biasing the measured data to account for the zero shift. The potential error is still significant in trying to reconcile the compartment pressure. This error is effectively doubled when 2 total pressure measurements are differenced to determine the differential pressure existing across a bulkhead or skin panel. For much of the orbiter internal structure, this instrumentation error is as large as the bulkhead design pressure loading. The best solution to this problem is the installation of differential pressure sensors across the various bulkheads and critical skin panels. Total pressure measurements are still mandatory in order to define the compartment pressure while differential pressure measurements are required to accurately measure bulkhead loading. For the orbiter program, the OV-102 vehicle will continue flying with a full compliment of total pressure measurements while the OV-099 vehicle will have a limited number of differential pressure sensors.

A problem with the orbiter active vent system that was identified during the OFT flights was due to the fact that the OMS Pod vent port was located immediately behind the larger aft fuselage vent. The problem with this configuration is the same as that discussed earlier concerning the location of pressure measurements, namely that the gas outflow from the front vent causes a low pressure environment across the rear vent. So instead of both compartments being at similar pressures, there is a significant difference in the two pressures. This effect was especially noticeable with the OMS Pod since its vent was located just behind the aft fuselage vent. It was also seen to a lesser extent with the forward fuselage due to the outflow from the forward RCS vent. The influence is less for the forward vents since these vents were angled instead of being directly behind and the larger vent was located behind the smaller one. For future vehicles, if vent ports are to be located close to each other, one should be located above the other so that the outflow from one vent does not impinge on the other.

CONCLUSIONS

The orbiter active vent system has shown itself to be very adaptable to the changing requirements of the Space Shuttle Program. The system is capable of withstanding vent door failures without significantly impacting structural differential pressure loading. The active vent system is designed such that any single failure will still permit proper operation of the system. Even with two failures in the same vent door system, the redundancy built into the system would provide adequate compartment vent area.

During the orbiter OFT Program, several problems were encountered that affected the orbiter vent system and should be remembered when designing vent systems for future vehicles. The biggest problem encountered was the large difference between the wind tunnel predicted pressure distribution and the orbiter measured pressures. Other minor problems encountered were with the location of the external pressure transducers and instrumentation accuracy.

Items that had significant impact on the success of the orbiter vent system include the initial design requirement of large vent areas, redundant vent paths and good structural leakage testing. The combination of these items have resulted in a system that lends itself to accurate analysis.

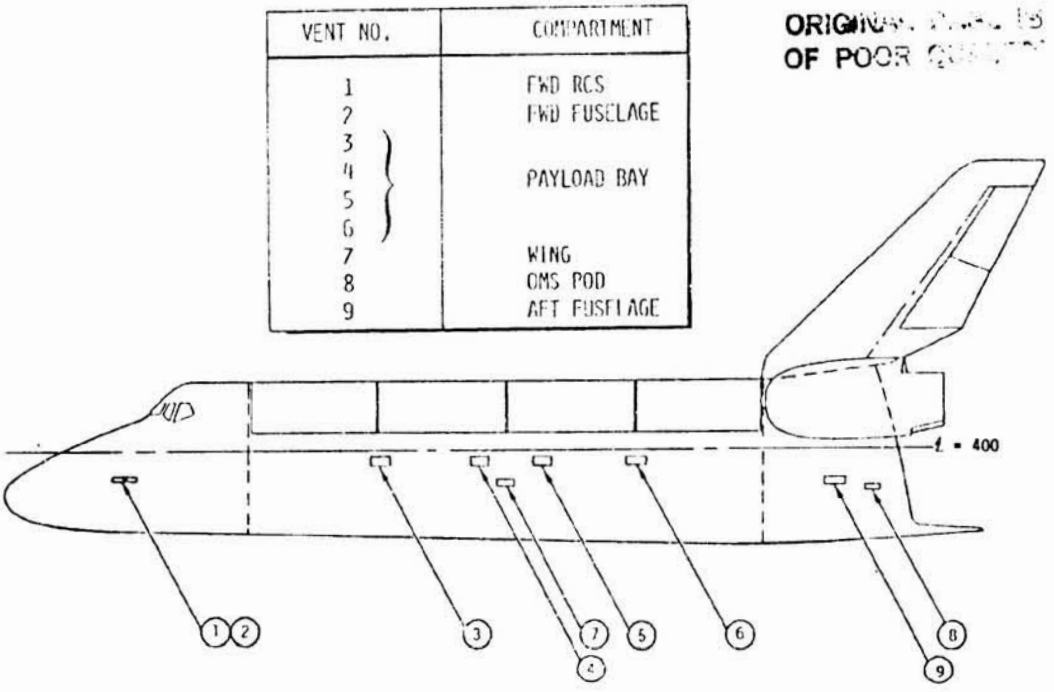

Figure 1.- Active vent door locations.

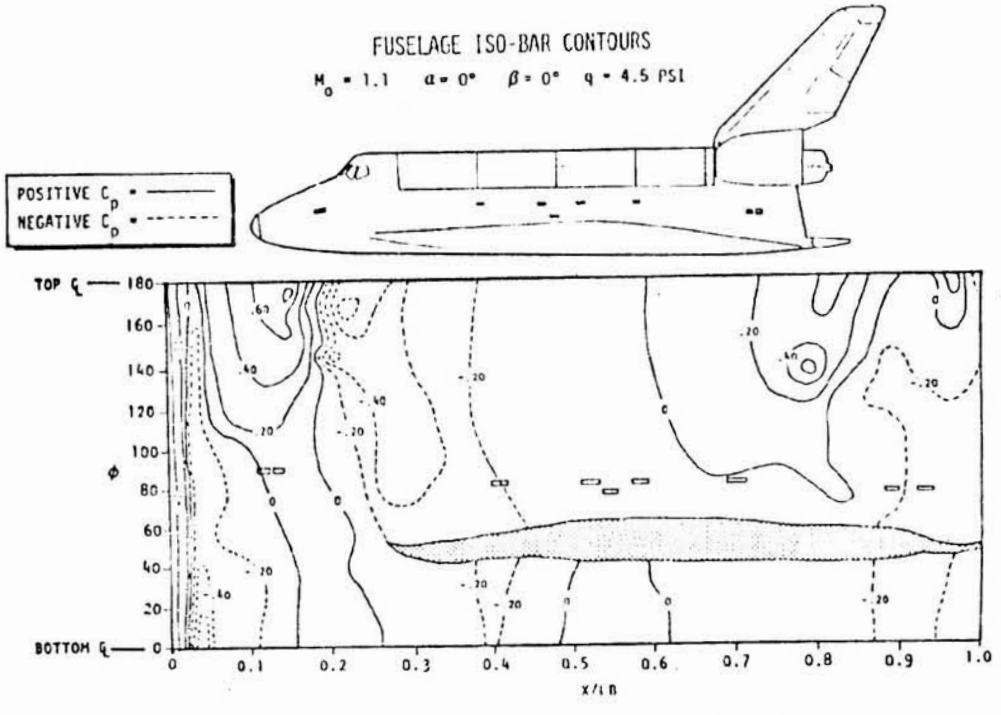

Figure 2.- Orbiter external pressure distribution.

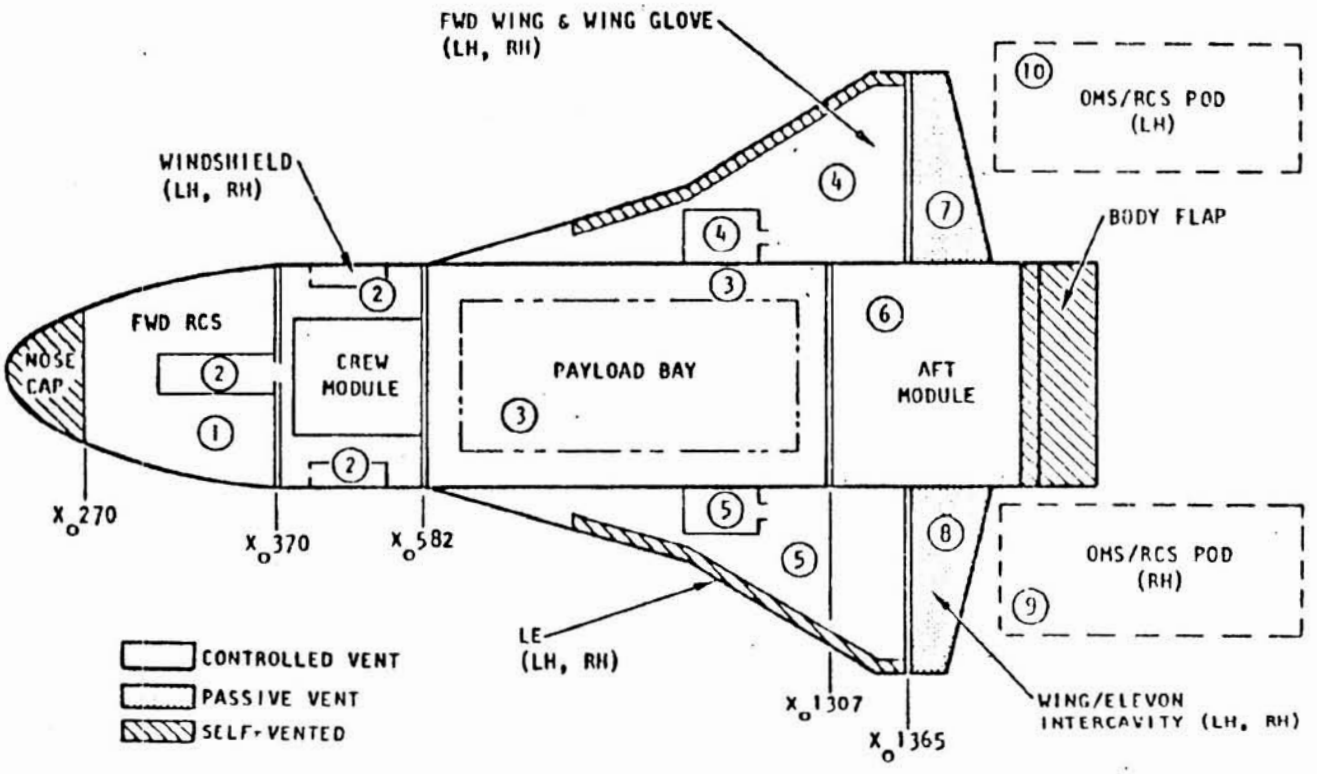

Figure 3.- Space Shuttle orbiter compartmentation.

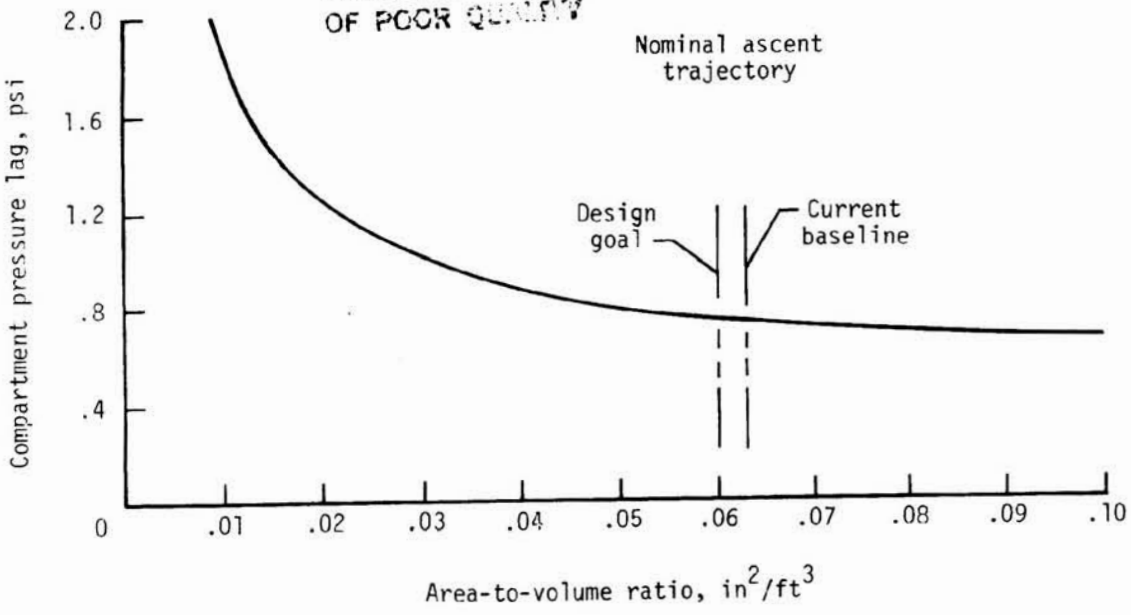

(a) Ascent.

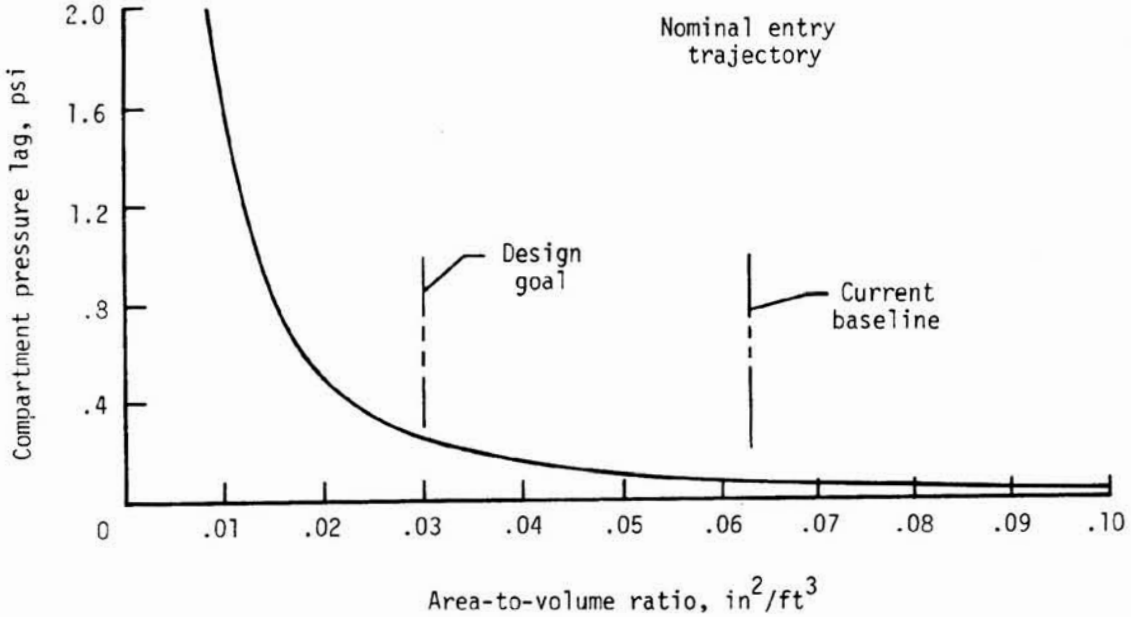

(b) Entry.

Figure 4.- Area-to-volume ratio curve.

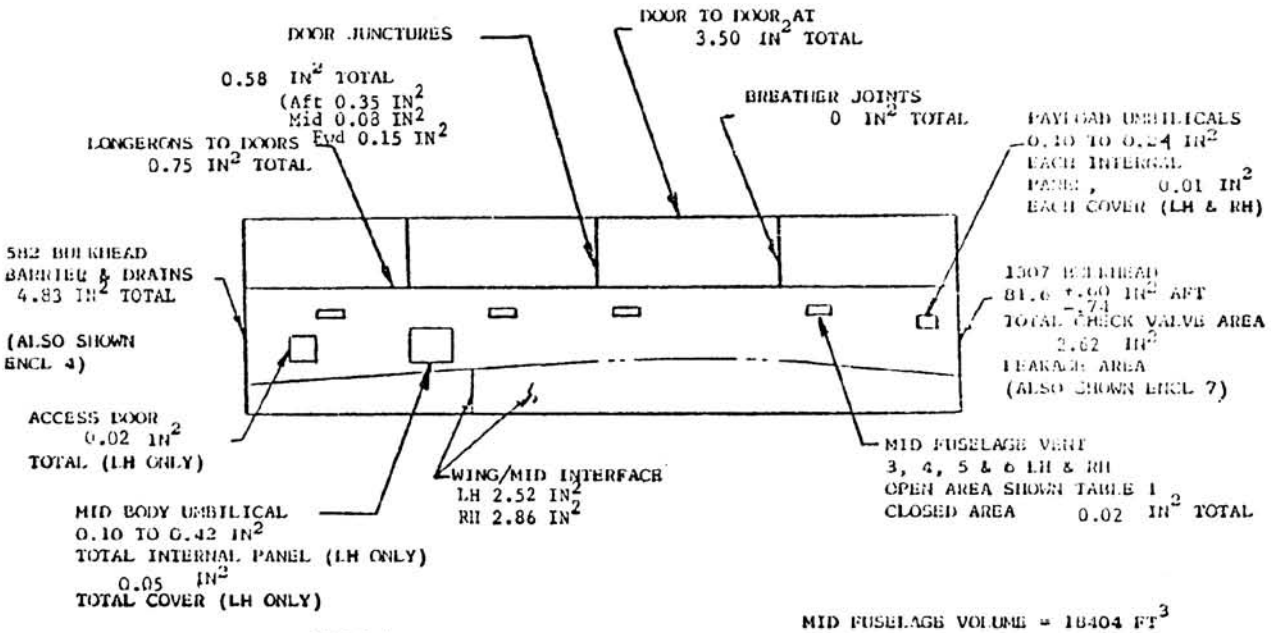

MID FUSELAGE VOLUME = 18404 FT³

TABLE 1

VENT	OPEN AREA PER VENT
3	156.58 IN²
4	144.01 IN²
5	169.10 IN²
6	122.38 IN²

TOTAL OIL LEAKAGE
4.93 IN²
DOORS & VENTS CLOSED

Figure 5.- OV-099 payload bay integrated vent model.

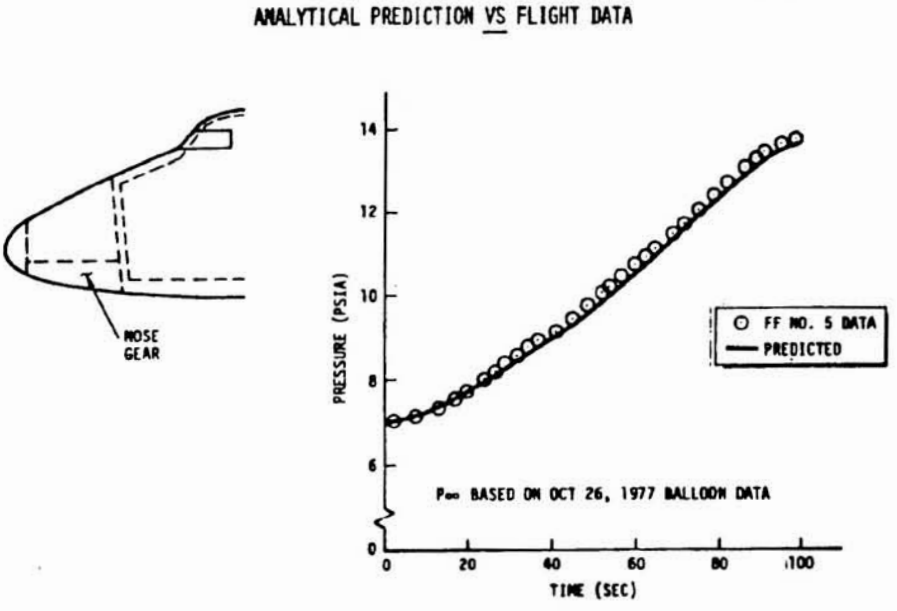

Figure 6.- Orbiter nose gear internal pressure.

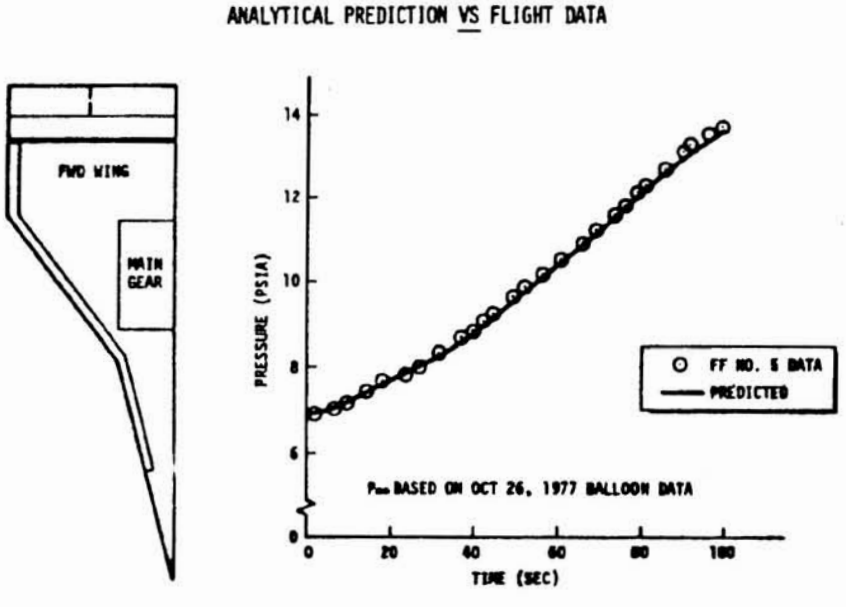

Figure 7.- Orbiter main gear internal pressure.

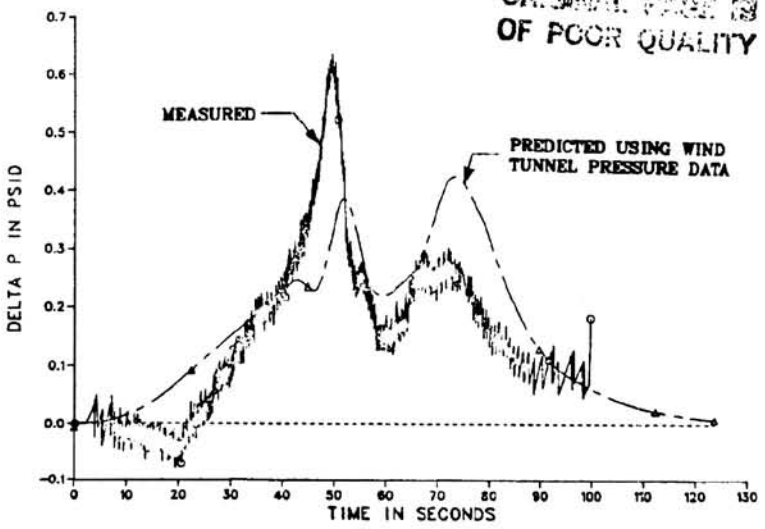

Figure 8.- STS-1 correlation results. Payload bay to ambient differential pressure.

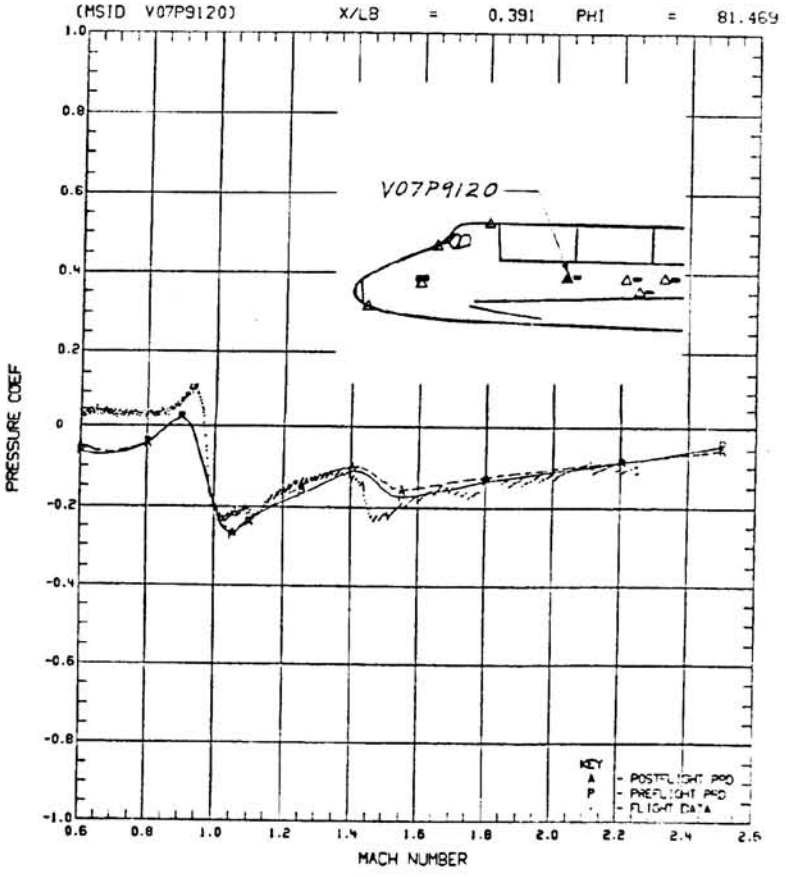

Figure 9.- STS-1 orbiter vent port 3 external pressure comparison.

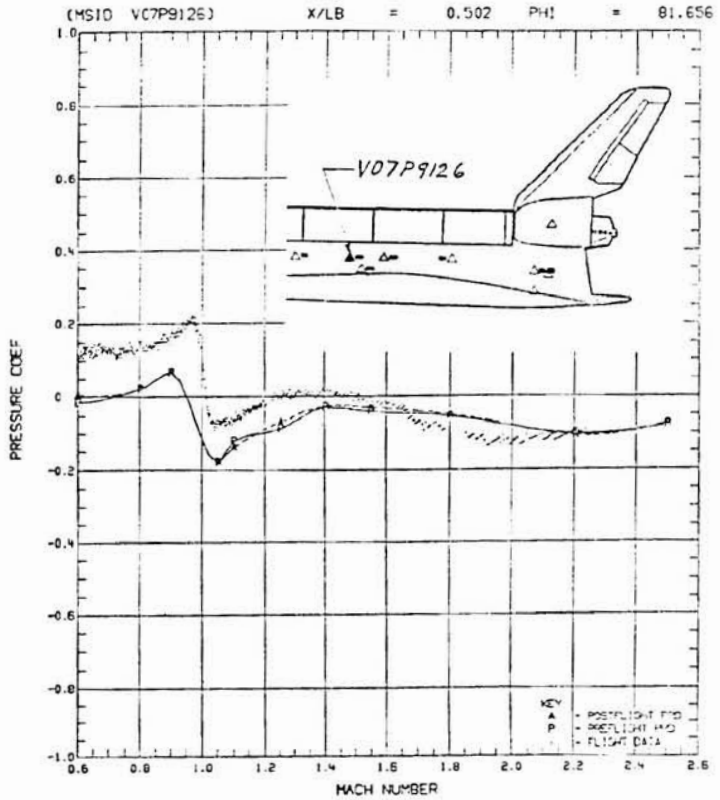

Figure 10.- STS-1 orbiter vent port 4 external pressure comparison.

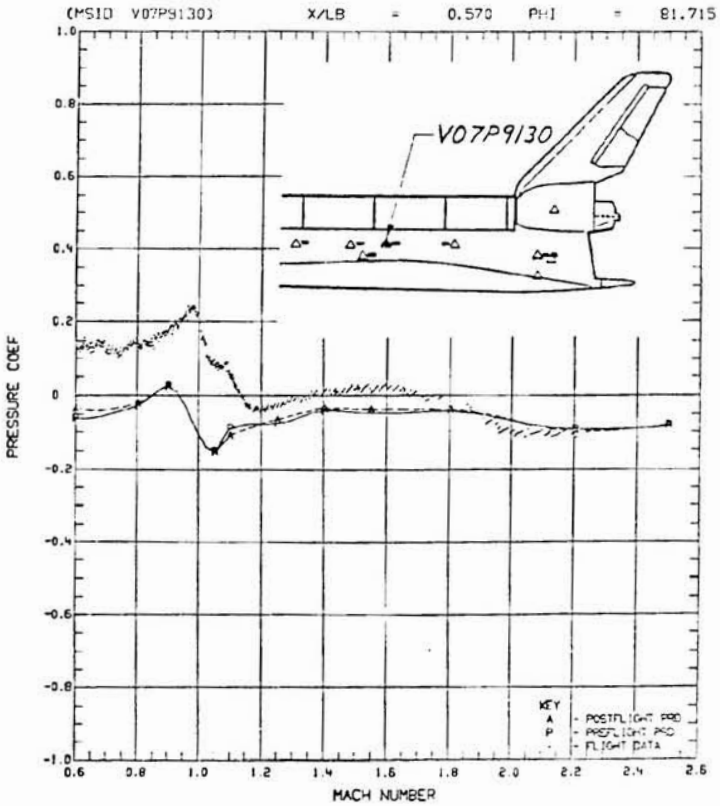

Figure 11.- STS-1 orbiter vent port 5 external pressure comparison.

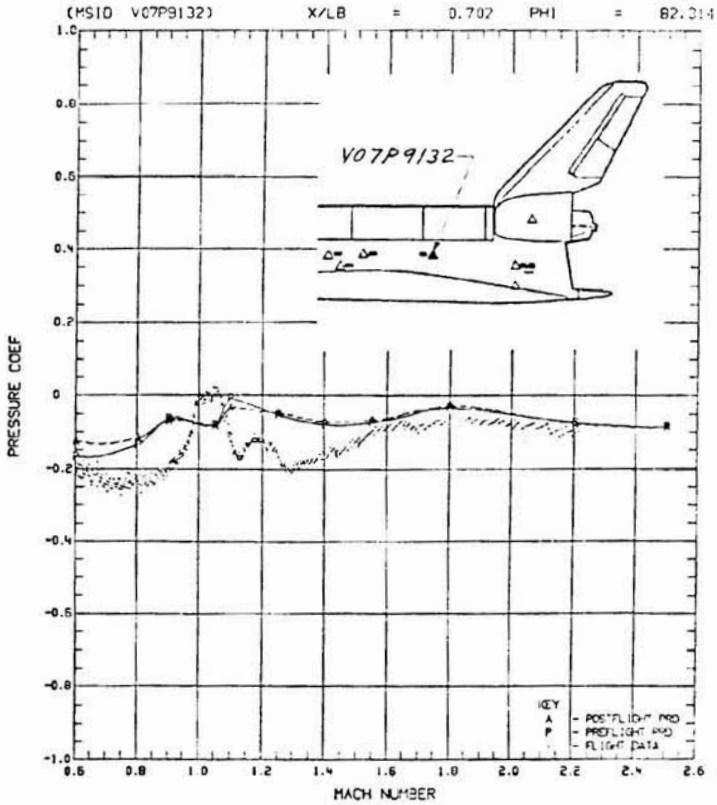

Figure 12.- STS-1 orbiter vent port 6 external pressure comparison.

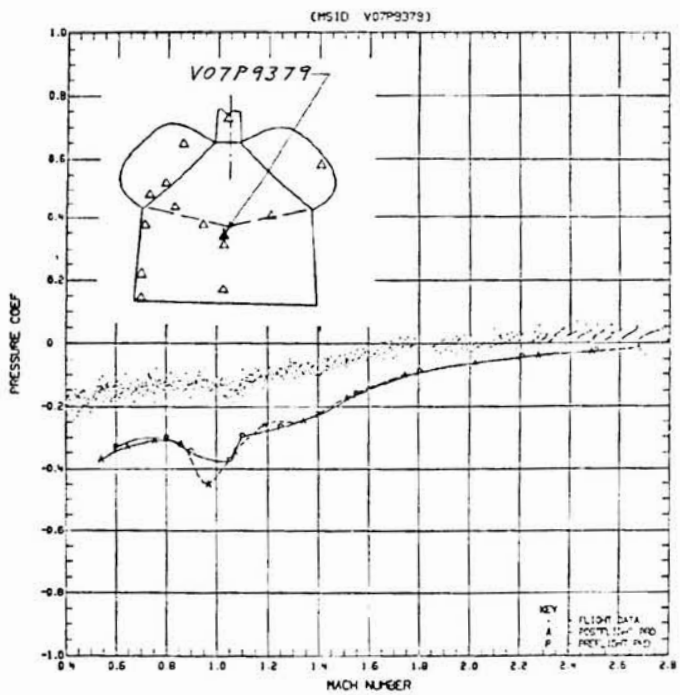

Figure 13.- STS-1 orbiter base external pressure comparison.

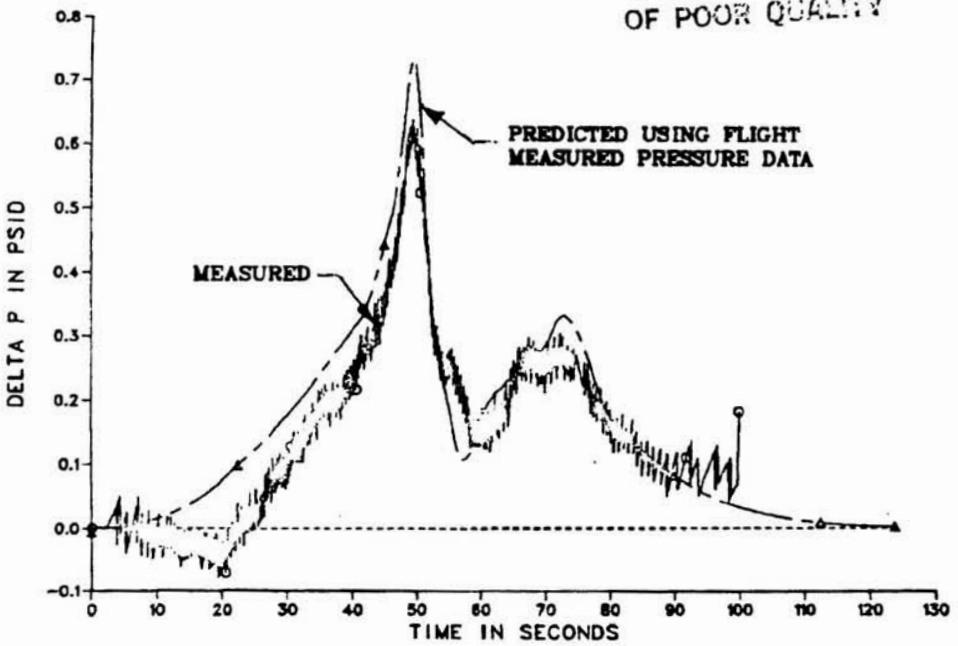

Figure 14.- STS-1 correlation results. Payload bay to ambient differential pressure using flight measured pressure data.

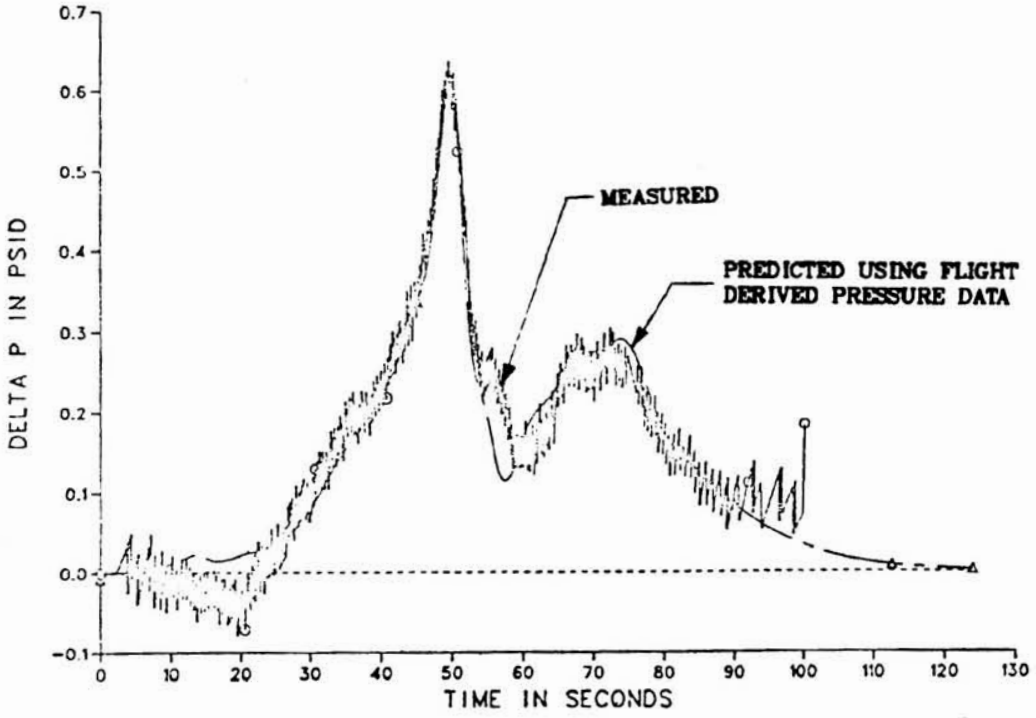

Figure 15.- STS-1 correlation results. Payload bay to ambient differential pressure using flight derived pressure data.

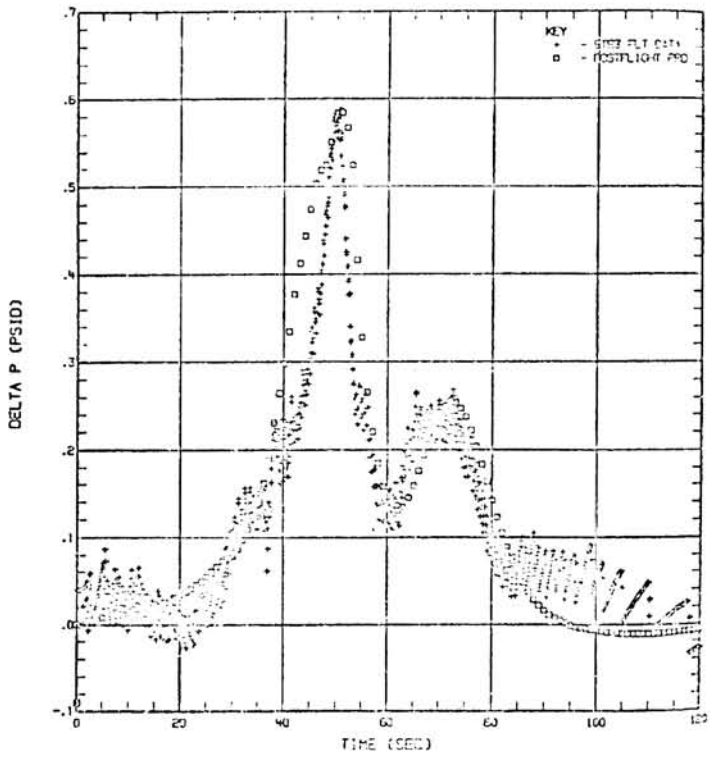

Figure 16.- STS-3 ascent correlation results. Payload bay to ambient differential pressure.

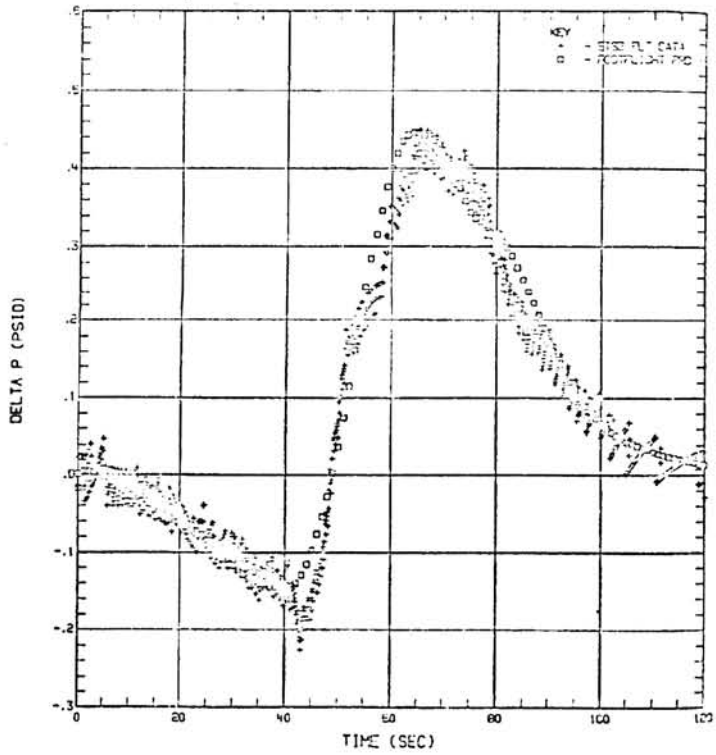

Figure 17.- STS-3 ascent correlation results. Aft fuselage to ambient differential pressure.

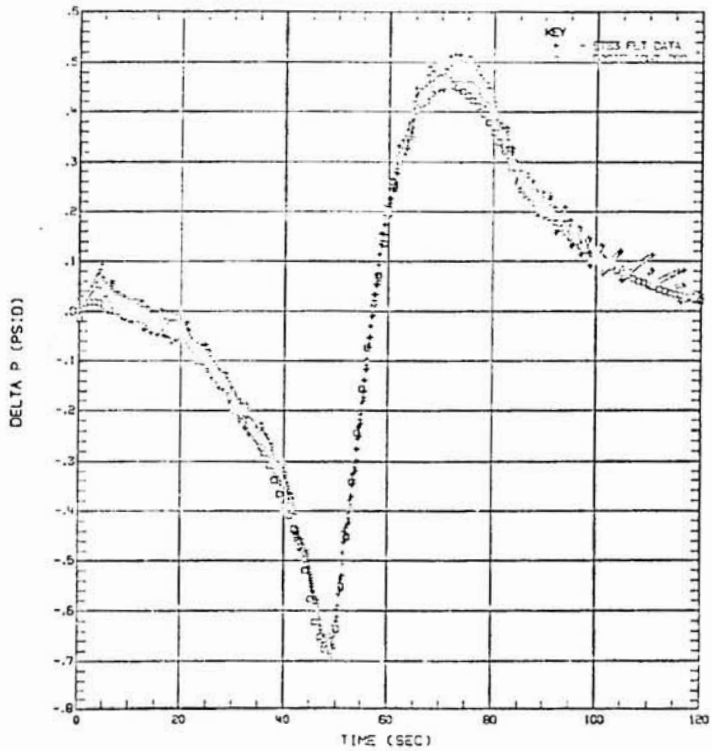

Figure 18.- STS-3 ascent correlation results. OMS pod to ambient differential pressure.

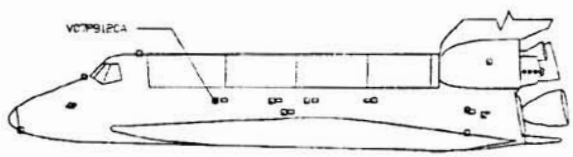

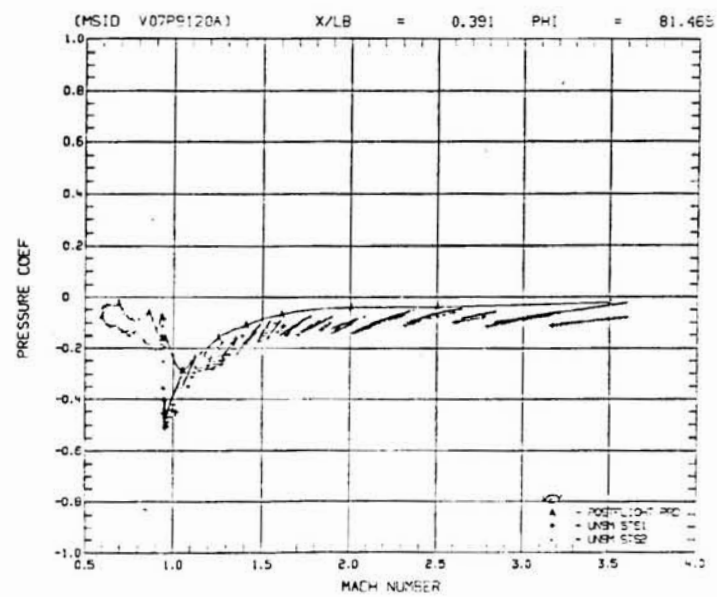

Figure 19.- STS-2 entry. Orbiter vent port 3 external pressure comparison.

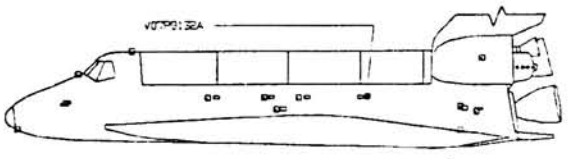

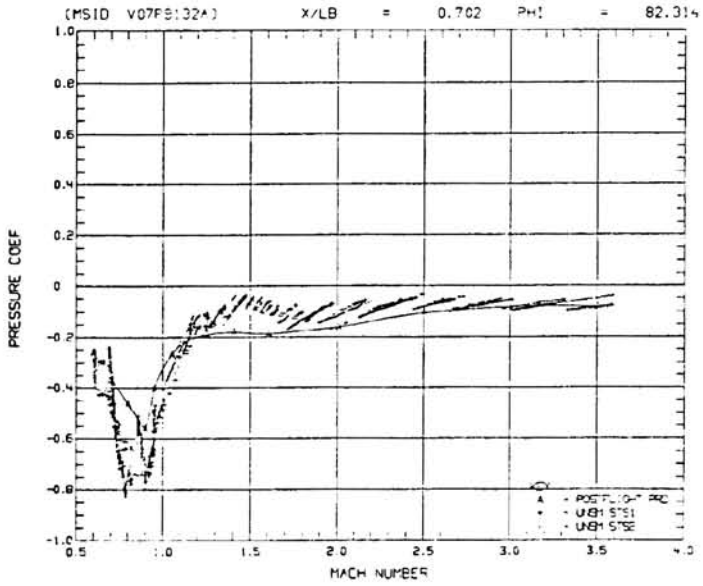

Figure 22.- STS-2 entry. Orbiter vent port 6 external pressure comparison.

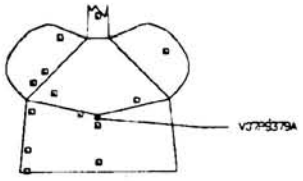

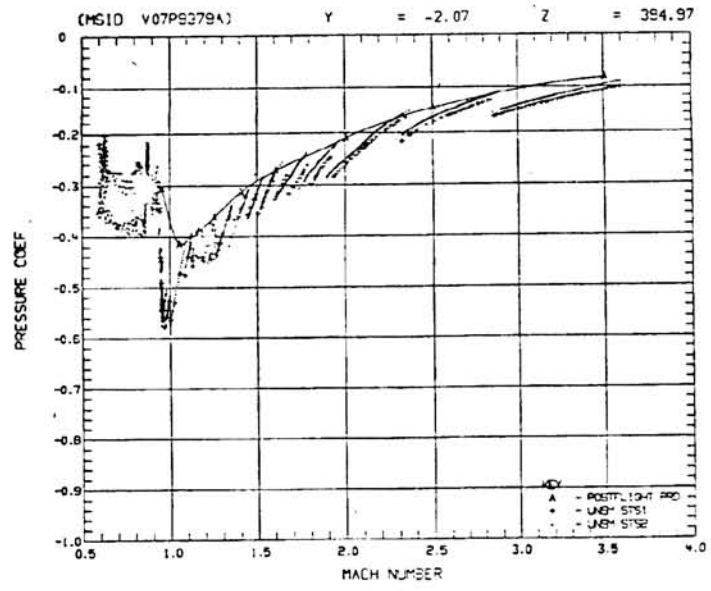

Figure 23.- Orbiter base external pressure comparison.

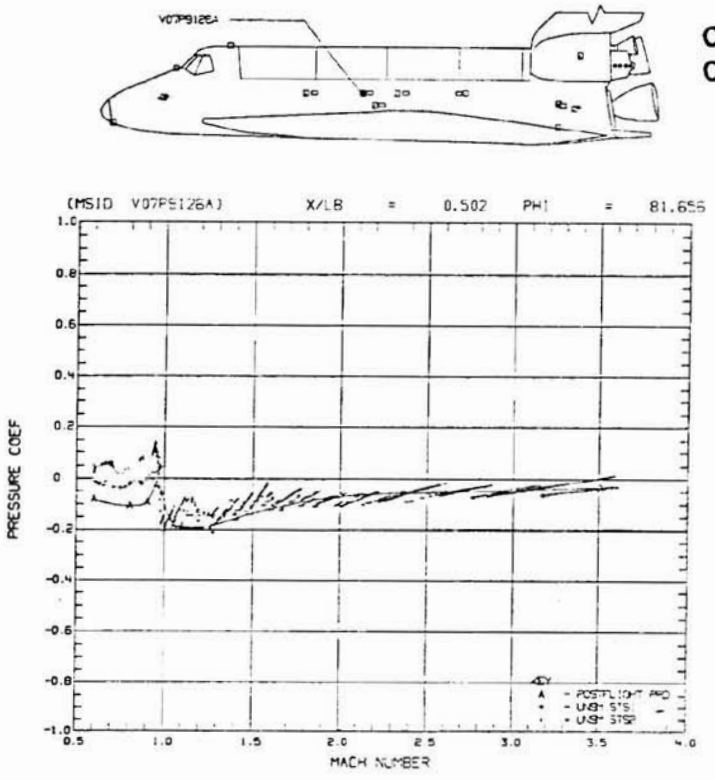

Figure 20.- STS-2 entry. Orbiter vent port 4 external pressure comparison.

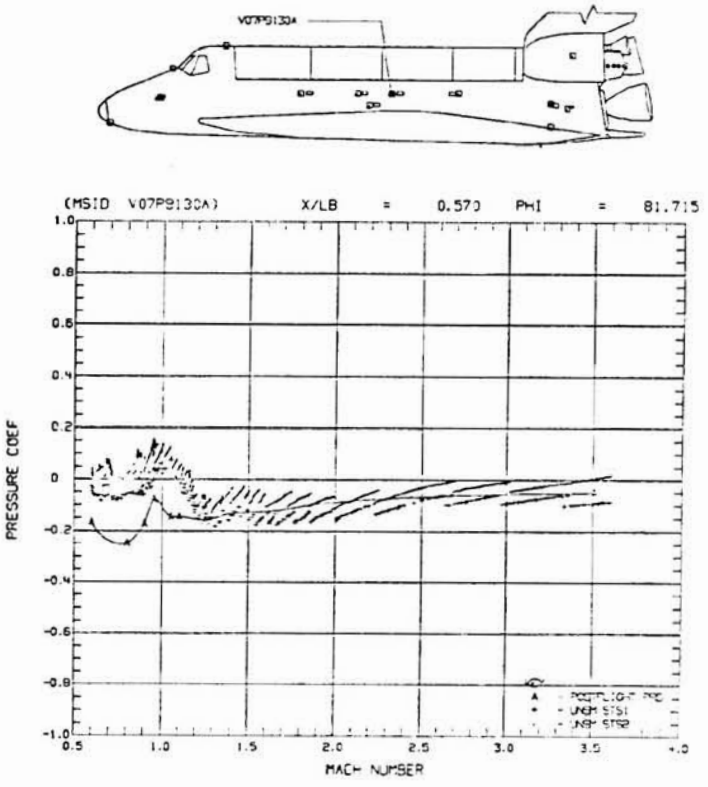

Figure 21.- STS-2 entry. Orbiter vent port 5 external pressure comparison.

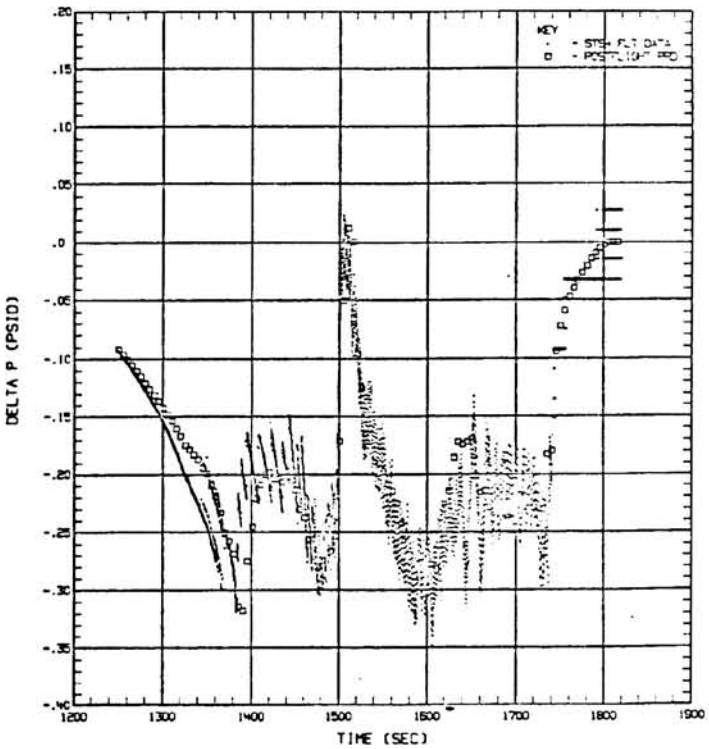

Figure 24.- STS-4 entry correlation results. Wing to ambient differential pressure.

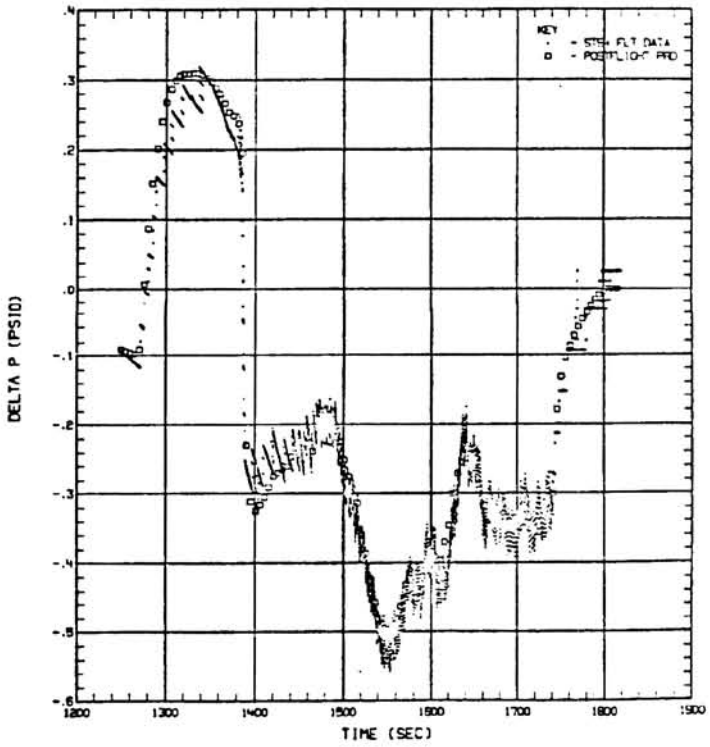

Figure 25.- STS-4 entry correlation results. Aft fuselage to ambient differential pressure.

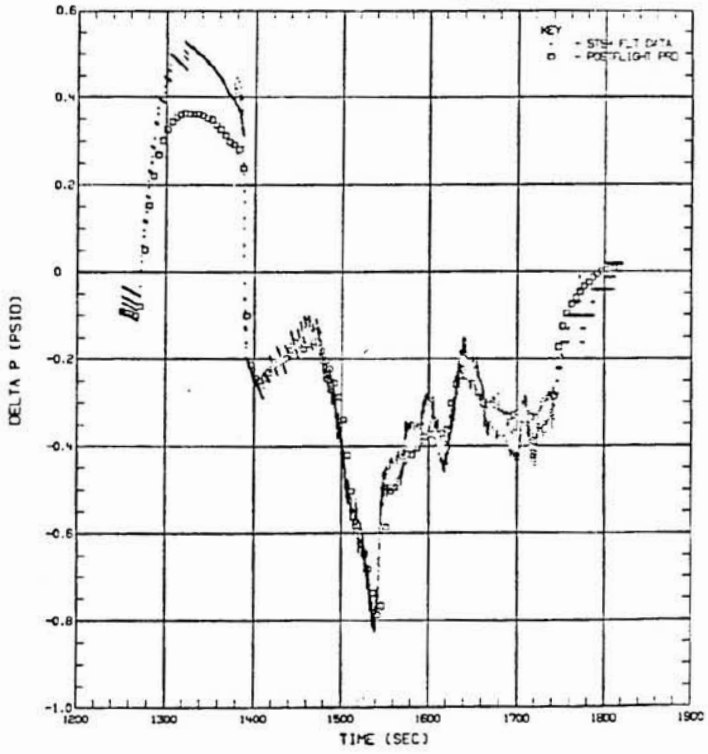

Figure 26.- STS-4 entry correlation results. OMS pod to ambient differential pressure.

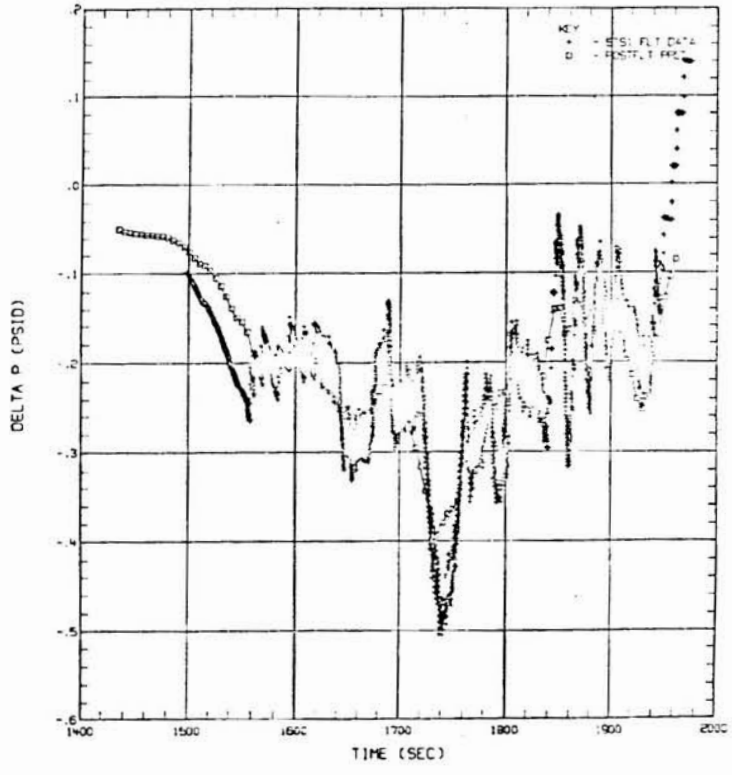

Figure 27.- STS-2 entry correlation results. Payload bay to ambient differential pressure.

DEVELOPMENT OF SPACE SHUTTLE IGNITION OVERPRESSURE ENVIRONMENT AND CORRELATION WITH FLIGHT DATA

S. Lai
Space Transportation and Systems Group
Rockwell International
Downey, California

ABSTRACT

The Space Transportation System (STS) launch vehicles are more complex than other launch vehicles. A comprehensive analysis of the lift-off event is required so that the responses of the vehicle and payloads can be predicted. The transient overpressure induced by ignition of the solid rocket motors (SRM's) is one of the critical design factors assessed for lift-off. The STS-1 ignition overpressure design environment was developed from 6.4-percent scale-model tests in which the Tomahawk solid rocket motors were used to simulate the start-up process of the SRM's. The overpressures measured during STS-1 lift-off were much more severe than predicted. The reasons for this anomaly are discussed in this paper. The 6.4-percent scale model was redesigned and used as a tool to develop an effective ignition overpressure suppression system for STS-2 and subsequent flights. Also presented are advancements in subscale-model simulation and theoretical understanding of this transient overpressure phenomenon that led to the successful development of the fix.

NOMENCLATURE

a_∞	ambient speed of sound
A	duct cross-sectional area
A*	nozzle throat area
E_o	energy released during rocket ignition transient
f	frequency
h_c	specific enthalpy of rocket motor chamber
K_f	empirical constant pertaining to jet momentum
K_m	empirical constant pertaining to jet mass
m	mass flow rate
P	transient pressure
P_∞	ambient pressure

ΔP	pressure disturbance, $P-P_\infty$
P_c	rocket-motor chamber pressure
$\dot{P}_c$	rate of change of chamber pressure $^{d}P_c/dt$
t	time
T	temperature
U_e	exhaust-gas velocity
ρ_{e_∞}	density of exhaust gas at ambient pressure
γ	ratio of specific heats
τ	time interval of ignition transient

INTRODUCTION

During the start-up process of a rocket motor, transient pressure waves are generated that propagate to the rocket's vicinity. The source of this pressure disturbance is the sudden displacement of ambient air by the combustion products flowing from the rocket nozzle during ignition transients. As the air is displaced by the increasing flow rate of exhaust gases, compression and expansion pressure waves are generated. These pressure waves propagate outward from the disturbed region and interact with the launch facilities and the launch vehicle, resulting in a spatial and time-dependent pressure disturbance. The pressure disturbance (ΔP) is defined as

$$\Delta P(x,y,z,t) = P(x,y,z,t) - P_\infty \tag{1}$$

where $P(x,y,z,t)$ is the transient pressure at location x,y,z and time (t), and P_∞ is the ambient pressure. This pressure disturbance resulting from rocket ignition is called ignition overpressure.

The Titan and Minuteman weapon systems, in which the missiles were fired from underground launchers, experienced high levels of overpressure during the engine-starting transient (ref. 1). The Titan III launch vehicle, with two strap-on solid rocket motors, also experienced a significant overpressure environment during lift-off, although the launch vehicle used a surface-type launch pad (ref. 2).

The STS launch vehicle employs two SRM's in addition to its liquid-fueled main engines. Thus, it was recognized early in the development program that the overpressure environment induced by the SRM ignitions should be considered for lift-off loads analysis. The prediction of the STS overpressure environment induced by the SRM start-up process relied on the 6.4-percent scale-model test conducted at NASA's MSFC Acoustic Model Test Facility (AMTF). Flight data measured during STS-1 lift-off indicated that the overpressure environment was much more severe than predicted. As a result, the vehicle responses at body flap, elevons, cargo bay, and crew cabin were excessively large. The 6.4-percent scale model was redesigned and then used as a tool to develop an effective ignition overpressure suppression system for STS-2 and subsequent flights.

This paper identifies the causes of the STS-1 ignition overpressure anomaly and discusses the advancements made after STS-1 that led to the successful development of a fix for STS-2 and subsequent flights.

SUBSCALE-MODEL TESTING AND THEORIES

6.4-Percent Scale-Model SRM Ignition Overpressure Test

Because of the complexity of the ignition overpressure phenomenon, the prediction of the STS overpressure environment induced by the SRM start-up process relies on subscale-model tests. Conducting a dynamically similar subscale-model simulation of SRM ignition overpressure requires the subscale model to fulfill a set of scale parameters, as shown in table I.

The Tomahawk motor was selected to simulate the SRM in the 6.4-percent scale-model acoustic tests conducted at the AMTF. The Tomahawk motor was the best available production motor for matching nominal SRM characteristics (table II). However, for the subscale ignition overpressure test, in addition to the nominal features, simulation of the motor start-up characteristics (primarily chamber pressure) was also important. Figures 1 and 2 show typical comparisons of the Tomahawk motor chamber-pressure characteristics with those of the SRM's during ignition transient. The maximum chamber-pressure rise rate ($\dot{P}_c$) for the Tomahawk motor is about 0.3 to 0.5 of what is required, and the ignition transient characteristic time (determined by the time interval between the first and second $\dot{P}_c$ maximum) for the Tomahawk motor is approximately twice what is required for proper simulation of the SRM ignition overpressure pulse amplitude and frequency. Thus, to predict the SRM ignition overpressure from the 6.4-percent scale-model tests, the subscale-model test results must be corrected to account for these differences.

Broadwell and Tsu Theory

The principal theoretical guidance available before the STS-1 flight was developed by Broadwell and Tsu to compute the rocket ignition overpressure for silo launchers such as Titan II and Minuteman (ref. 1). In their analysis, the SRM constitutes a mass and momentum source at the silo (fig. 3). The mass source generates compression waves into the launch and exhaust ducts. The momentum source generates a compression wave into the exhaust duct and an expansion wave into the launch duct.

The pressure waves propagating from the source region are given by

$$\frac{\Delta P}{P} = \frac{1}{2}\left[\left(\frac{\gamma \dot{m}}{a_\infty \rho e_\infty A}\right) K_m \pm \left(\frac{2\, U_e\, \dot{m}}{A}\right) K_f\right] \tag{2}$$

The plus sign is for the exhaust duct and the minus sign is for the launch duct. The subsequent propagation of these waves is treated by one-dimensional linear theory. Once the empirical constants, K_m and K_f, are fixed in the theory, the results agree with empirical observations made inside the Titan II and Minuteman launchers.

Application of this theory results in

$$\Delta P \sim \dot{P}_c \tag{3}$$

Since the Tomahawk motor $\dot{P}_c$ maximum is approximately one third of what is required for the SRM simulation, the STS-1 SRM ignition overpressure environment was predicted by multiplying the 6.4-percent scale-model test data by three. No attempt was made to adjust the frequency.

Comparison of Predicted and STS-1 Measured Data

As shown in table III, the overpressures measured during STS-1 are much more severe than predicted. As a result, the overpressure on the orbiter base heat shield (2.1 psid) exceeded the design limit of 1.32 psid. The frequency of the overpressure measured is also significantly higher than predicted. More importantly, the structural responses on the orbiter elevons, body flap, crew cabin, and cargo bay at lift-off were excessive. Figure 4 compares the predicted and measured accelerations inside the crew cabin and cargo bay. The accelerations measured inside the cargo bay are considered unacceptable to the remote manipulator system and many future payloads.

Reconstruction of the STS-1 lift-off events based on the flight data indicated that the SRM ignition overpressures were the major cause of excessive vehicle responses. Therefore, the 6.4-percent scale-model test program was quickly designed and conducted to evaluate various practicable fix concepts for the launch pad to suppress the ignition overpressure environment for STS-2 and subsequent flights.

As shown in figures 1 and 2, the left and right SRM ignition transients for STS-1 are almost identical (<3 milliseconds time lag). On the other hand, when two Tomahawk motors were fired during each test, the ignition transient time lag between the motors was as long as 150 milliseconds (full-scale equivalent), even though the firing commands for the two motors were issued simultaneously. This uncontrollable ignition transient time skew between the Tomahawk motors resulted in drastic distortion of the waveform and the amplitude of overpressures measured during the 6.4-percent scale-model tests (as illustrated in fig. 5). Furthermore, the spatial distributions of the overpressures on the orbiter model were also distorted significantly from the flight data measured during STS-1.

Two Tomahawk motors were also used to simulate the ignition overpressure environment induced by the two strap-on SRM's in the 7.5-percent scale-model tests of the Titan III used to support STS studies. The Titan III SRM $\dot{P}_c$ maximum is approximately equal to 7.5 percent of the Tomahawk motor $\dot{P}_c$ maximum. Therefore, the overpressures measured during these 7.5-percent scale-model tests should be approximately equal to those measured at Titan III lift-off. Nevertheless, the magnitude of the overpressures measured at Titan III lift-off are about two to four times greater than those measured during the 7.5-percent scale-model tests (ref. 2). Again, this discrepancy is believed to be a result of the relatively large mismatch of the ignition transients between the two Tomahawk motors used in the tests.

Redesign of 6.4-Percent Scale Model

Difficulties associated with the 6.4-percent scale-model testing cast some doubt on the value of using the Tomahawk motor as a tool to develop the SRM ignition overpressure suppression system. To overcome the problems associated with the Tomahawk motor ignition transient uncertainties, the 6.4-percent scale-model test was redesigned after STS-1 (ref. 3). Instead of firing two Tomahawk motors during each test, only one motor was used. A smooth flat plate, called a splitter plate, was placed in the center between the left and right sides of the vehicle, extending above and below the mobile launch platform (MLP), as shown in figure 6. The interactions of the incident waves and reflected waves from the splitter plate simulated two SRM's with identical ignition transients firing simultaneously.

Figure 5 illustrates a typical comparison of the overpressure wave characteristics measured during the redesigned test with splitter plate/single-motor-firing configuration and those measured during previous tests using dual-motor firings. The redesigned model tests provided overpressure data with larger amplitudes and higher signal-to-noise ratios.

Ried's Scaling Relationship

Meanwhile, efforts were devoted to investigating the mechanism of the overpressure formation and its propagation characteristics. While there are many fruitful results from various investigators, this paper describes only Ried's formulation because of its engineering application in bridging the gap between subscale test data and flight data. SRM start-up times are characteristically short. For the Tomahawk motor, the start-up time is about 0.05 sec, while the SRM start-up time is approximately 0.35 sec. The fast start-up resembles an explosion, and the ignition overpressure can be analyzed in this way. Ried considers the SRM ignition overpressure phenomenon analogous to the blast-wave phenomenon whereby the energy is released instantaneously (ref. 3). Therefore, the overpressure (ΔP) is related to the energy (E_o) released during the start-up by

$$\Delta P \sim \frac{E_o}{V_{A+B}} \tag{4}$$

where V_{A+B} is the affected volume, as shown in figure 7.

For a rocket motor, the total energy released during start-up is determined by

$$E_o \sim A^* \sqrt{h_c} \int_{t=0}^{\tau} P_c dt \tag{5}$$

where τ is the start-up time for the rocket motor, h_c is the enthalpy of the gases in the combustion chamber, and A* is the nozzle throat area. The ignition overpressure for one-, two-, and three-dimensional flow fields can be expressed, respectively, as

$$\Delta P \sim \frac{\sqrt{h_c P_c}}{a_\infty} \tag{6}$$

$$\Delta P \sim \frac{\sqrt{A^* h_c P_c}}{a^2_\infty} \tag{7}$$

$$\Delta P \sim \frac{A^* \sqrt{h_c} (\dot{P}_c)^2}{a^3_\infty P_c} \tag{8}$$

STS-1 OVERPRESSURE RECONSTRUCTION THROUGH 6.4-PERCENT SCALE-MODEL TESTS

To identify a fix that could be implemented to suppress the overpressure environment on STS-2, it was important to demonstrate that the results from the redesigned 6.4-percent scale-model test adequately represented the full-scale vehicle overpressure environment.

Typical Tomahawk motor combustion chamber pressure characteristics are shown in figure 8. Typical overpressure waveforms measured during the 6.4-percent scale-model tests representing the STS-1 launch pad configuration are illustrated in figures 9 and 10. The SRM chamber pressure characteristics measured during STS-1 are shown in figures 11 and 12, and the typical overpressure waveforms measured on the orbiter base, the lower surface of the orbiter fuselage, and the upper surface of the orbiter fuselage are depicted in figures 13, 14, and 15, respectively.

The pressure waveforms measured on the 6.4-percent scale model are similar to those measured during STS-1. The overpressure wave period derived from this model is approximately twice that measured during STS-1. Examination of the difference in chamber pressure characteristics between the Tomahawk motor and the SRM shows that the characteristic time for the Tomahawk is also twice what is required for proper simulation of the SRM. Therefore, to predict the SRM overpressure pulse frequency (f) based on the 6.4-percent scale model, the following relationship can be used:

$$(f)_{\text{full scale}} = (f)_{\text{model}} \times 0.064 \times 2 \qquad (9)$$

Correlations of Overpressure and $\dot{P}_c$

Broadwell and Tsu's theory implies that $\Delta P \sim \dot{P}_c$, whereas Ried's theory indicates $\Delta P \sim (\dot{P}_c)^2/P_c$ for a three-dimensional flow field. Thus, the magnitude of overpressure and the $\dot{P}_c$ can be expressed by the general relationship

$$\Delta P \sim (\dot{P}_c)^m \qquad (10)$$

where m represents the slope in a log-log scale plot of ΔP versus $\dot{P}_c$. Note that the $\dot{P}_c$ maximum for STS-1 was approximately 8,900 psi/sec. The equivalent 6.4-percent scale-model $\dot{P}_c$ maximum for STS-1 is 139,000 psi/sec. Figures 16 and 17 suggest that $\Delta P \sim (\dot{P}_c)^2$ is a reasonably accurate approximation.

Overpressure Wave Attenuation

When the overpressure waves propagate outward from the source, the magnitude of each wave attenuates. The attenuation of these waves can be described by the general relationship

$$\Delta P = C\, X^{-m} \qquad (11)$$

where m is dependent on the geometry involved and the strength of the waves, X is the distance from the source, and C is a constant. When the magnitude of a wave is large enough to classify the overpressure as a blast or strong compression wave, the exponent m equals 3. For a weak pressure wave, m equals 0, 0.5, and 1 for one-, two-, and three-dimensional wave propagations, respectively.

The overpressure wave attenuation characteristics observed for STS-1 and the 6.4-percent scale-model tests simulating the STS-1 launch pad configuration are depicted in Figures 18 and 19. The 6.4-percent scale-model test data were adjusted by the $\Delta P \sim (\dot{P}_c)^2$ relation. These data show that the overpressure wave attenuation characteristics approach those of a three-dimensional weak pressure wave propagation as the overpressure waves approach the nose regions of the Space Shuttle. These data also demonstrate that the attenuation characteristics and the distribution of overpressure measured on the 6.4-percent scale model are similar to the data measured in flight. When corrected for the P_c discrepancy between the model and the SRM by the $\Delta P \sim (\dot{P}_c)^2$ relation, the magnitudes of overpressure derived from the 6.4-percent scale-model test approximate the magnitudes measured during STS-1. This suggests that, in a subscale-model ignition overpressure test, the splitter plate/single-motor-firing configuration is the correct approach for simulating the dual-motor launch vehicle ignition overpressure.

STS-2 FIX AND RESULTS

The overpressure suppression system developed for STS-2 consisted of a water injection system and water trough covers in the SRM exhaust holes. For each SRM, the water injection system (fig. 20) injected a total of 378,540 liters (100,000 gal) of water per minute at two elevations below the nozzle exit plane. The initial velocity of the water jet was approximately 9.14 m/sec (30 ft/sec). The primary purpose of this water injection was to quench the SRM exhaust plume. The water troughs, as shown in figure 21, were filled with a 30.48-cm (12-in.) depth of water, covering the SRM exhaust hole at the nozzle exit plane level. There was an opening of approximately 5.01 m^2 (54 ft^2) surrounding the SRM nozzles for lift-off clearance. The purpose of the water troughs was to block the overpressure wave path and to absorb the wave energy. The water troughs were made of fabric that could be burned easily without the threat of hard debris impact on the thermal protection system tiles.

A typical comparison of the overpressure measured during STS-1 and -2 is shown in figure 22. Figure 23 shows a typical comparison of the STS-1 and -2 vehicle responses to overpressure waves. STS-2 overpressures and vehicle responses were significantly less than those of STS-1. As indicated in figure 24, the overpressure suppression system provided an overall reduction of 50 to 80 percent in the amplitudes of the overpressure wave measured on the orbiter. Figure 25 shows that the predicted STS-2 overpressures are approximately 30 to 70 percent higher than measured. However, the predicted magnitudes of STS-2 overpressure are 0.05 to 0.12 psi higher than measured and are similar to accuracies obtained from the test for reconstructing the STS-1 overpressure environment.

CONCLUSIONS

STS-1 postflight data analysis revealed an anomaly in SRM ignition overpressure that was much more severe than predicted. The cause of this anomaly was attributed to unsatisfactory subscale simulation due to the nonrepeatability of the Tomahawk motor start-up process and lack of analytical understanding of this transient phenomenon induced by rocket ignition.

The splitter plate/single-motor-firing simulation technique developed after STS-1 resulted in improved data quality compared to the previous technique of firing two motors during each test. This technique also reduced the complexity and cost of conducting the tests. Ried's scaling relation, derived from the three-dimensional blast-wave theory, was shown to be applicable to the STS Eastern Test Range type of launch pad configurations. By using the splitter plate/single-motor-firing simulation technique in conjunction with Ried's scaling relation, the STS-1 overpressure environment was accurately reconstructed with the 6.4-percent scale model.

An effective overpressure suppression system has been developed for the STS Eastern Test Range launch pad through 6.4-percent scale-model tests. A similar system is being developed for the Vandenberg Air Force Base STS launch mount.

The advancements made in the subscale simulation technique and analytical understanding of the transient phenomenon of rocket ignition should result in improvements in the design of future space transportation systems.

REFERENCES

1. Broadwell, J. E., and C. N. Tsu: An Analysis of Transient Pressure due to Rocket Starting in Underground Launchers. Space Technology Laboratories, Inc., 7103-0028-MU-00 (June 1961).

2. Walsh, E. J., and P. M. Hart: Flight-Measured Lift-off Ignition Overpressure--A Correlation With Subscale Model Tests. AIAA Paper 81-2458.

3. Lai, S.: 6.4 Percent Scale Model SSV SRM Ignition Overpressure Testing for STS-2, Vol. II, Results of Analysis. Space Systems Group, Rockwell International, STS 81-0665 (Jan. 1982).

TABLE I.-ROCKET MOTOR IGNITION OVERPRESSURE SIMULATION PARAMETERS

Parameter	Full Scale	Model
Pressure	P	P
Velocity	u	u
Density	ρ	ρ
Temperature	T	T
Flow rate	m	$m \times S^2$
Thrust	F	$F \times S^2$
Mach number	M	M
Length	L	$L \times S$
Area	A	$A \times S^2$
Time	t	$t \times S$
Frequency	f	f/S

Note: S indicates scale factor.

TABLE II.- TOMAHAWK AND SRM NOMINAL MOTOR CHARACTERISTICS

Parameter	Tomahawk		SRM
	Actual (6.4% Scale)	Full-Scale Equivalent (100% Scale)	
Sea level thrust (kg-lb)	4,808.16 (10,600)	1,179,360 (2,600,000)	1,202,040 (2,650,000)
Weight flow (kg/sec-lb/sec)	19.86 (43.8)	4,850.79 (10,694)	4,989.6 (11,000)
Specific impulse (sec)	242	242	240.9
Chamber pressure (psia)	1,200	1,200	840
Chamber temperature (°R)	6,413	6,413	6,178
Exit Mach number	2.95	2.95	3.00
Expansion ratio	6.66	6.66	7.16
Exit area (m^2-ft^2)	0.036 (0.396)	8.893 (96.7)	10.748 (115.7)
Specific heat ratio	1.18	1.18	1.18
Nozzle exit 1/2 angle (deg)	15	15	11.2

TABLE III.- PREDICTED AND MEASURED STS-1 IGNITION OVERPRESSURE

Measurement No.	Orbiter Coordinate System			Predicted Overpressure (psi)	STS-1 Measured Overpressure (psi)
	X-orb	Y-orb	Z-orb		
V08Y9196A	1534.1	-84.4	290.0	0.1790	1.9
V08Y9202A	407.2	-8.9	436.7	0.1050	0.4
V08Y9204A	532.1	0.0	500.0	0.1080	0.5
V08Y9206A	373.4	-5.1	290.0	0.1050	0.4
V08Y9207A	499.3	-9.5	280.0	0.1070	0.5
V08Y9210A	546.3	-104.1	419.9	0.1090	0.5
V08Y9402A	1281.4	4.3	500.0	0.1480	0.77
V08Y9404A	1284.5	-6.0	260.0	0.1490	1.05
V08Y9681A	1410.7	-115.4	336.5	0.1620	0.9
V08Y9686A	1499.6	-2.4	384.9	0.1730	2.1
V08Y9687A	1340.0	-125.0	470.0	0.1540	0.7
V08Y9734A	1342.1	-379.0	315.7	0.1540	0.55
V08Y9735A	1317.7	-363.7	292.8	0.1510	0.55
V08Y9772A	1498.4	-33.0	568.5	0.1730	0.6
V08Y9774A	1638.4	-10.0	795.0	0.1950	0.3

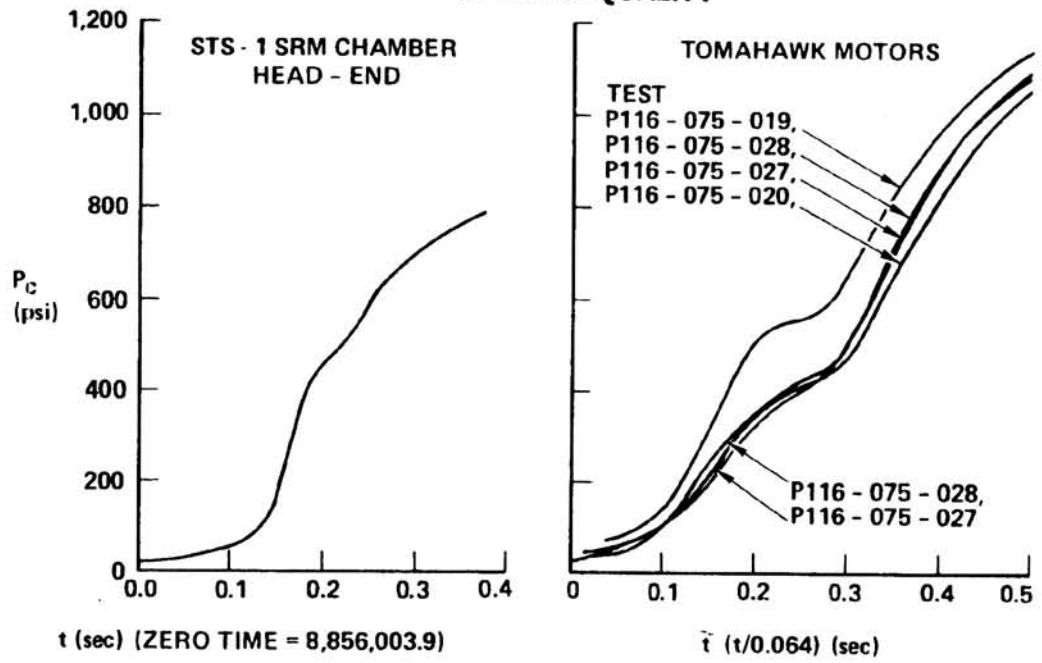

Figure 1.- Comparison of SRM and Tomahawk motor chamber pressure.

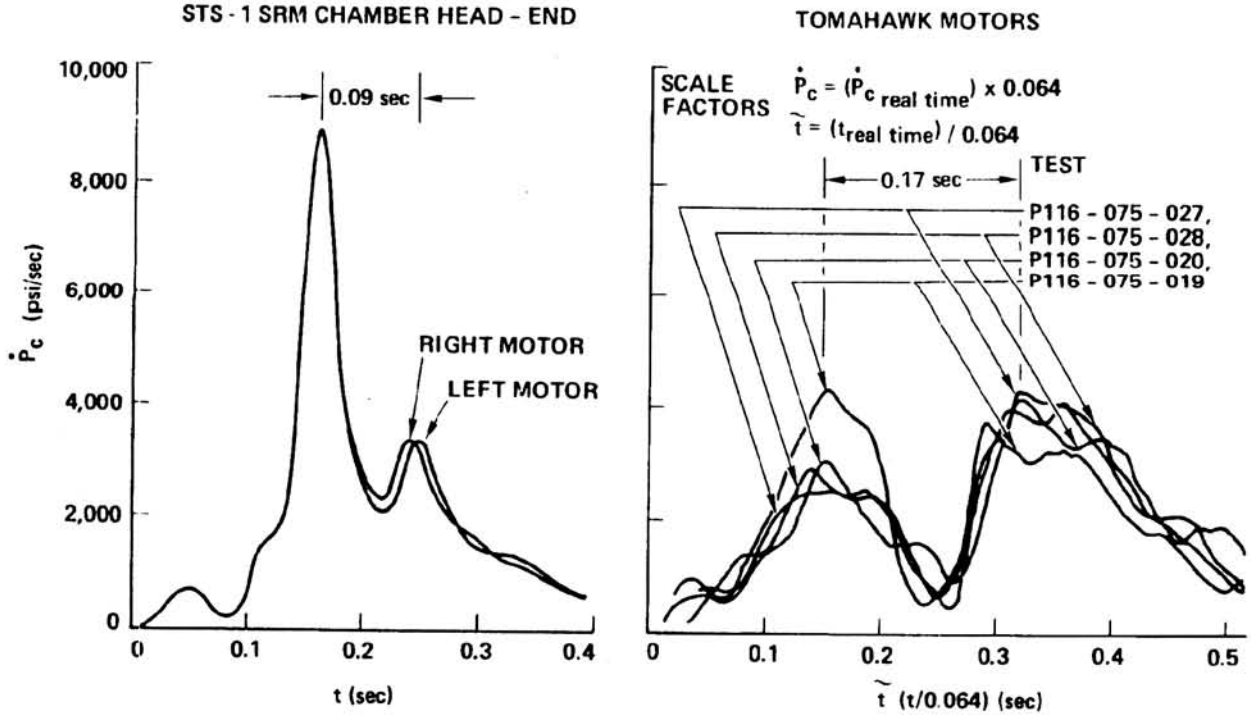

Figure 2.- Comparison of SRM and Tomahawk motor chamber pressure rise rate.

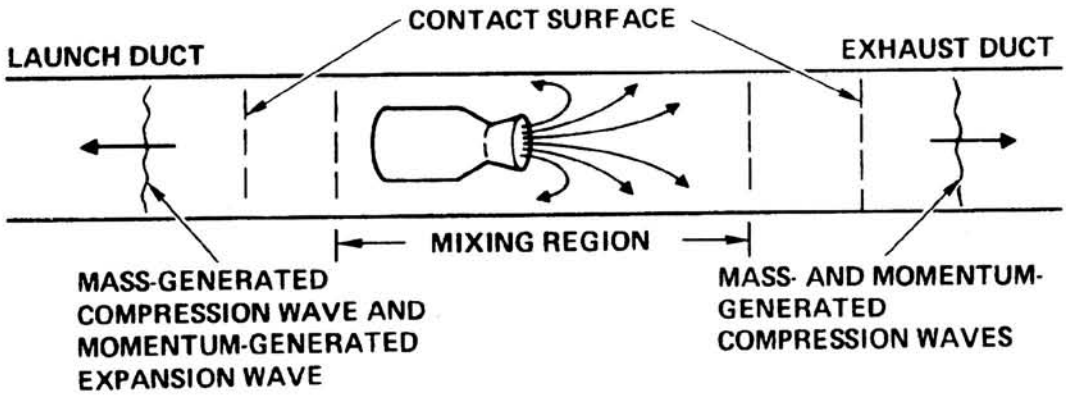

Figure 3.- Ducted launcher control volume.

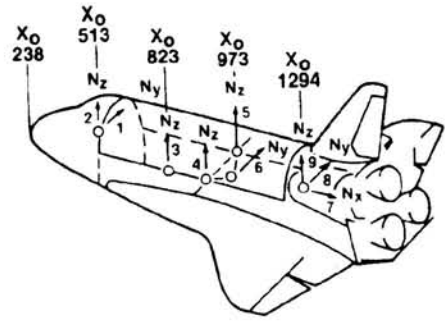

ACCELEROMETER			MEASURED ACCELERATION (g)	PREDICTED ACCELERATION (g)
NUMBER	LOCATION X_o (INCH)	DIRECTION		
1	511	NY	0.19	0.87
2	511	NZ	3.5	1.43
3	825	NZ	2.8	1.85
4	974	NZ	2.9	1.75
5	974	NZ	2.9	1.83
6	973	NY	0.4	0.45
7	1294	NX	2.1	2.41
8	1294	NY	0.25	0.66
9	1294	NZ	1.25	0.95

Figure 4.- Predicted and measured STS-1 lift-off accelerations.

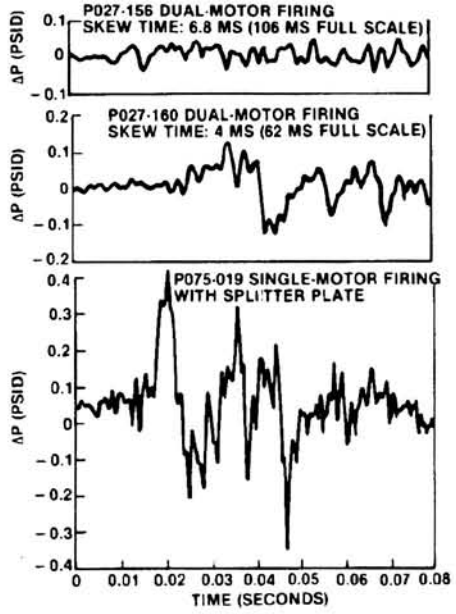

Figure 5.- Effects of ignition transient mismatch on overpressure wave characteristics.

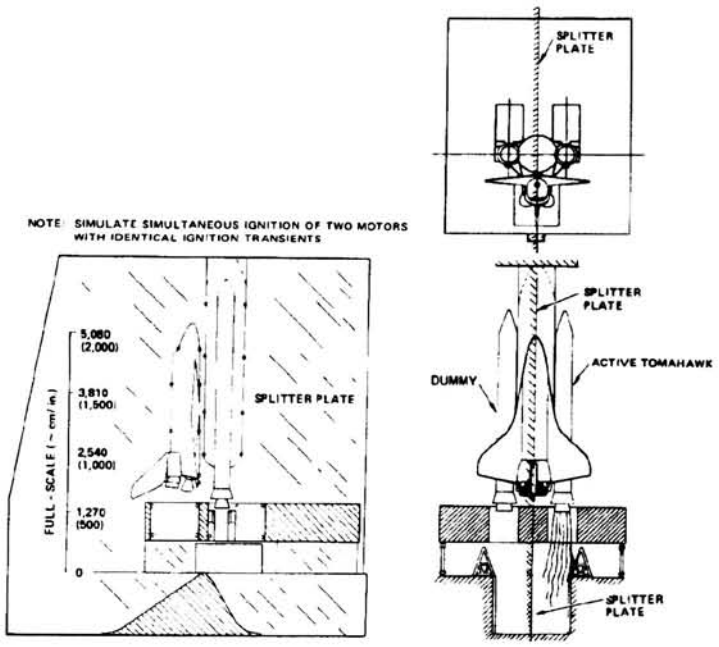

Figure 6.- Post STS-1 6.4-percent scale model arrangement.

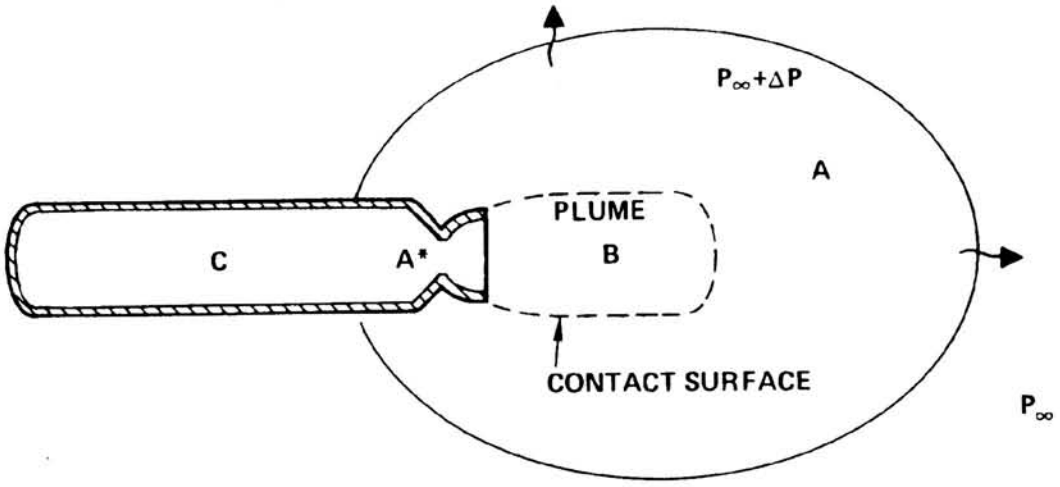

Figure 7.- Blast wave analogy of ignition overpressure phenomenon.

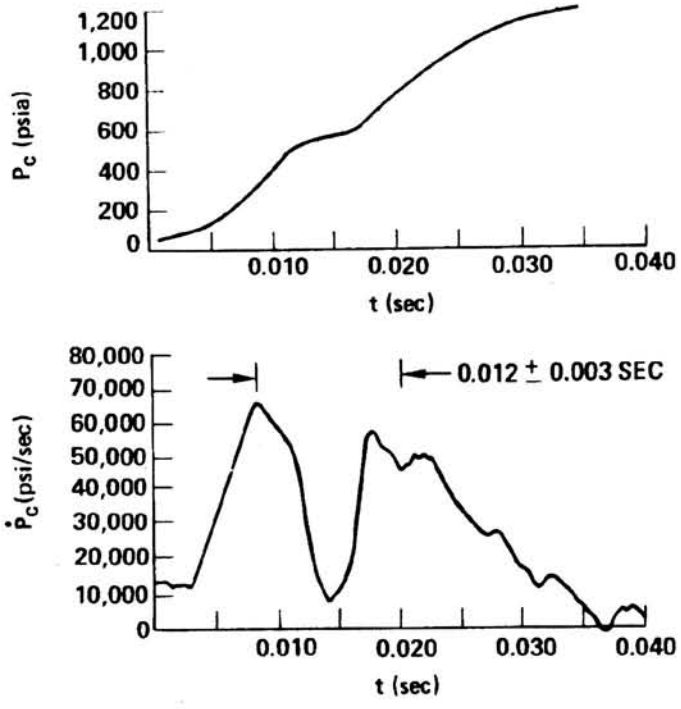

Figure 8.- Chamber pressure and chamber pressure rise rate for Tomahawk motor (test no. P116-075-019).

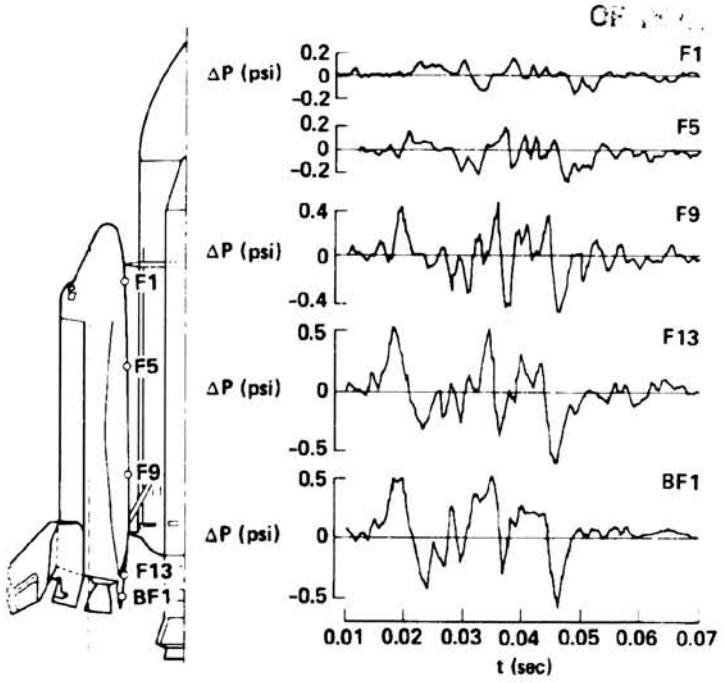

Figure 9.- Typical overpressure wave characteristics on lower surface of orbiter fuselage (test no. P116-075-019).

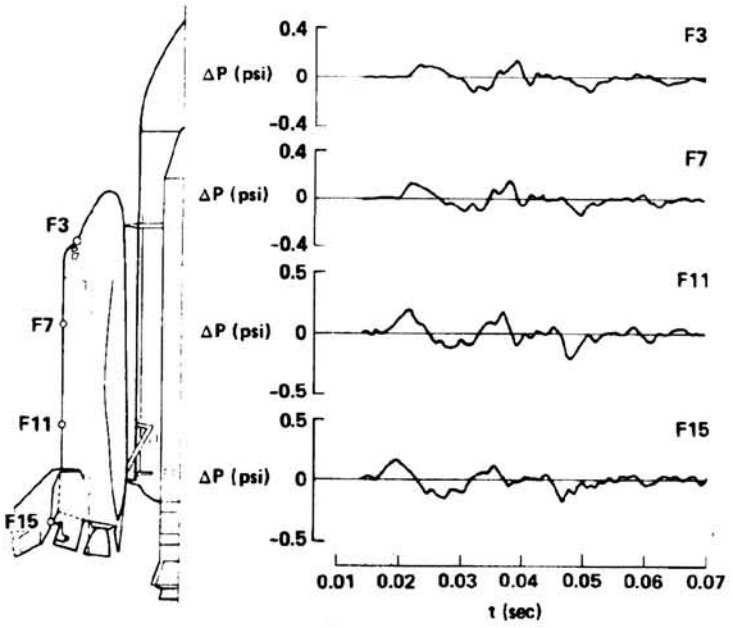

Figure 10.- Typical overpressure wave characteristics on upper surface of orbiter fuselage (test no. P116-075-019).

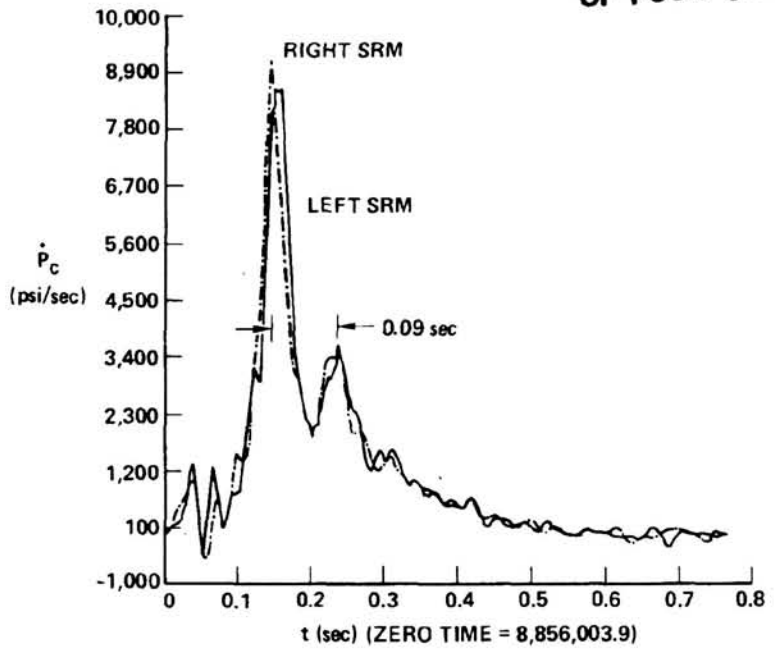

Figure 11.- SRM head-end chamber pressure from STS-1 flight data.

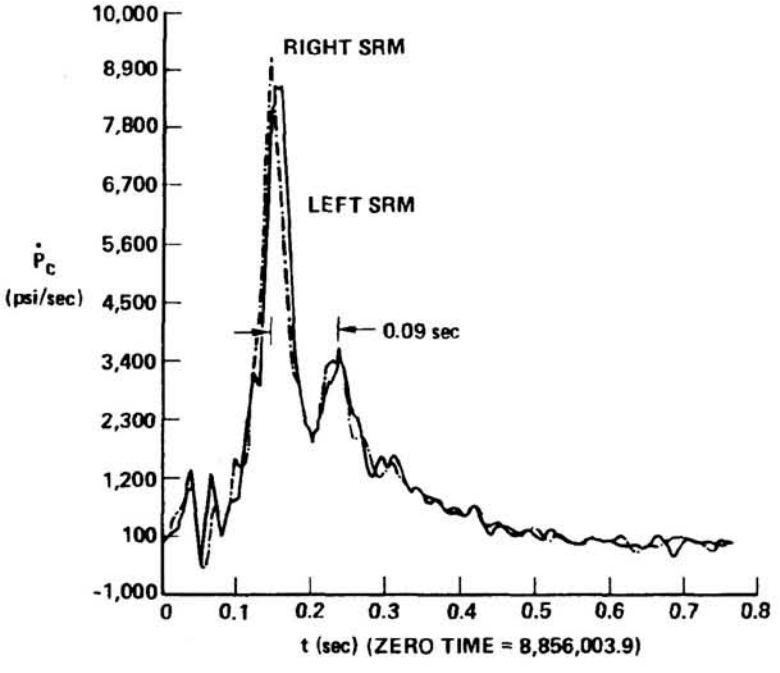

Figure 12.- SRM head-end chamber pressure rise rate for STS-1 flight data.

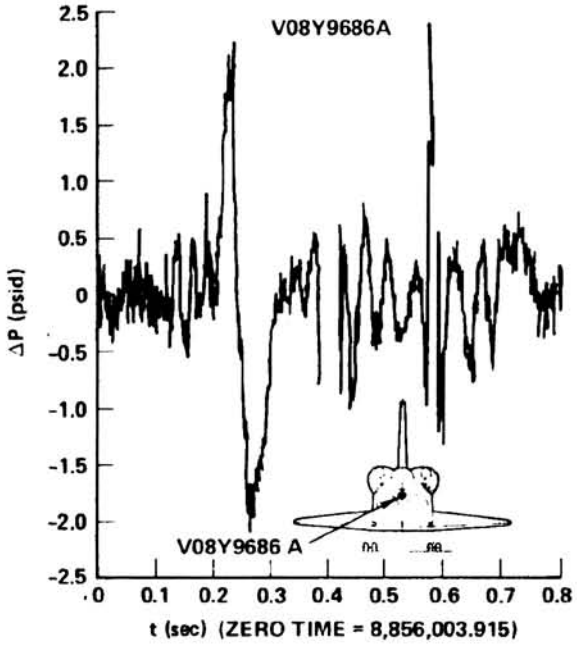

Figure 13.- STS-1 SRM ignition overpressure on orbiter base.

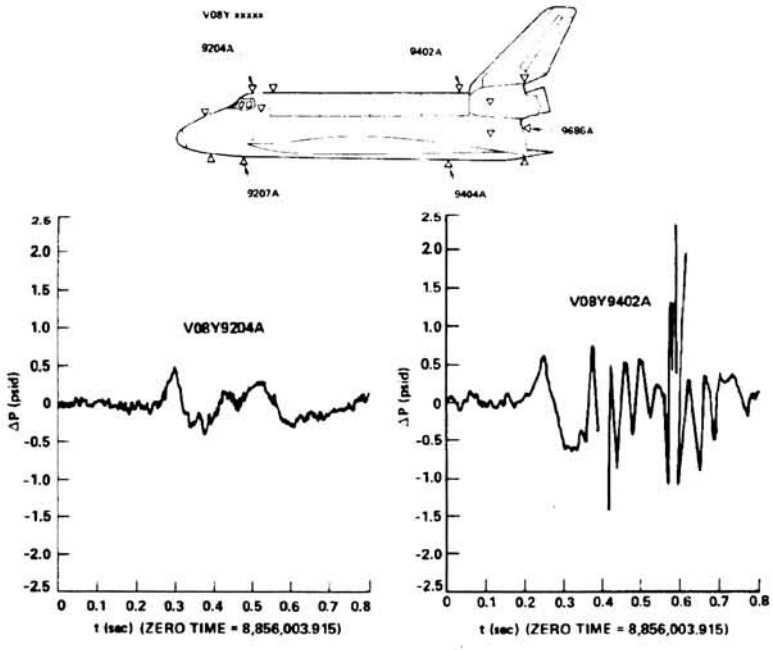

Figure 14.- STS-1 SRM ignition overpressure on lower surface of orbiter fuselage.

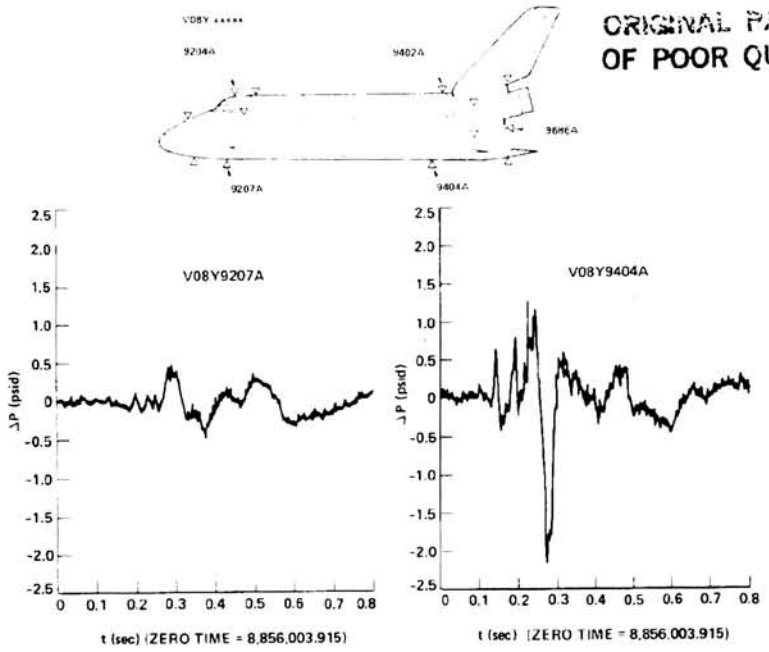

Figure 15.- STS-1 SRM ignition overpressure on upper surface of orbiter fuselage.

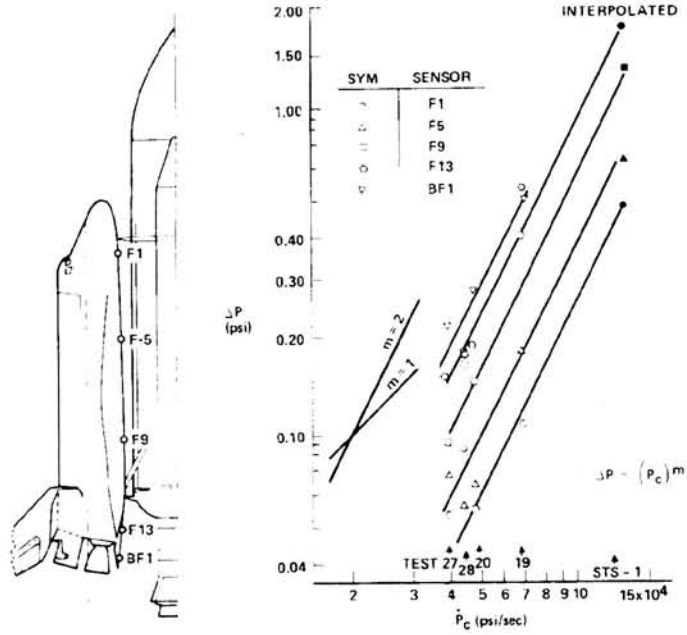

Figure 16.- Correlation of overpressure versus chamber pressure rise rate. Lower surface of orbiter fuselage.

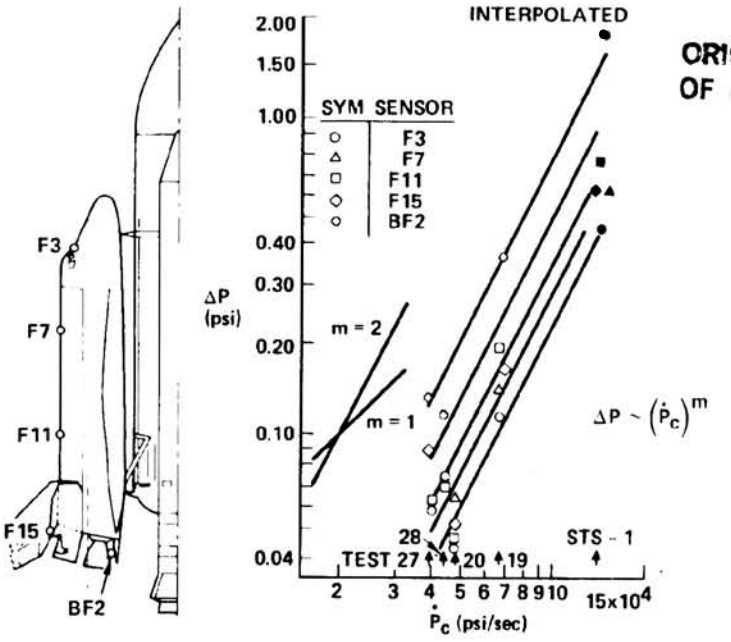

Figure 17.- Correlation of overpressure versus chamber pressure rise rate. Upper surface of orbiter fuselage.

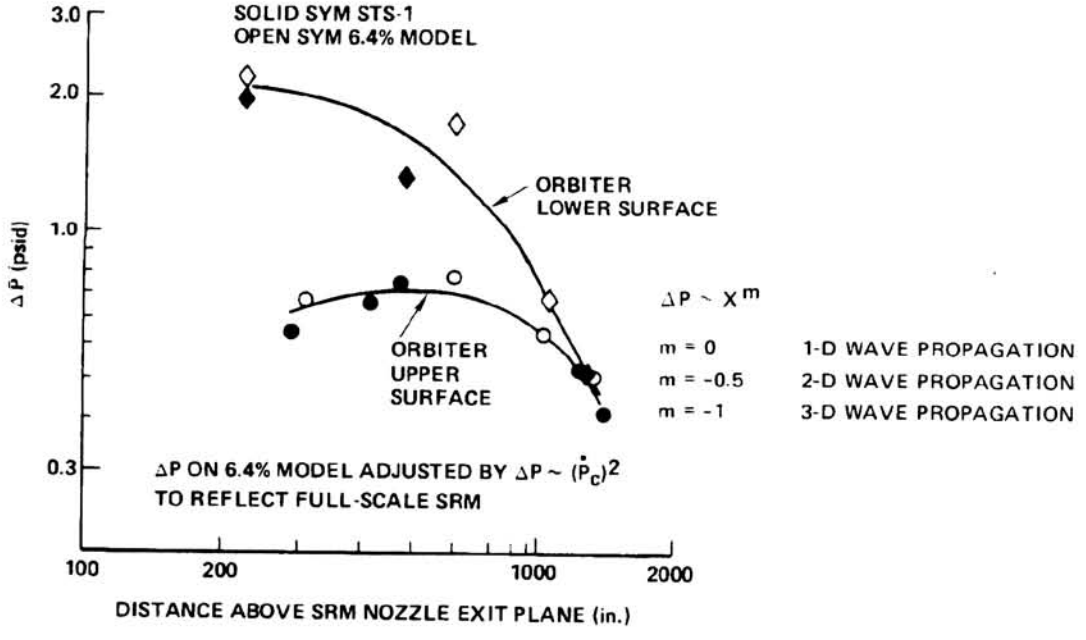

Figure 18.- Comparison of overpressures measured on STS-1 and reconstructed from 6.4-percent scale model test.

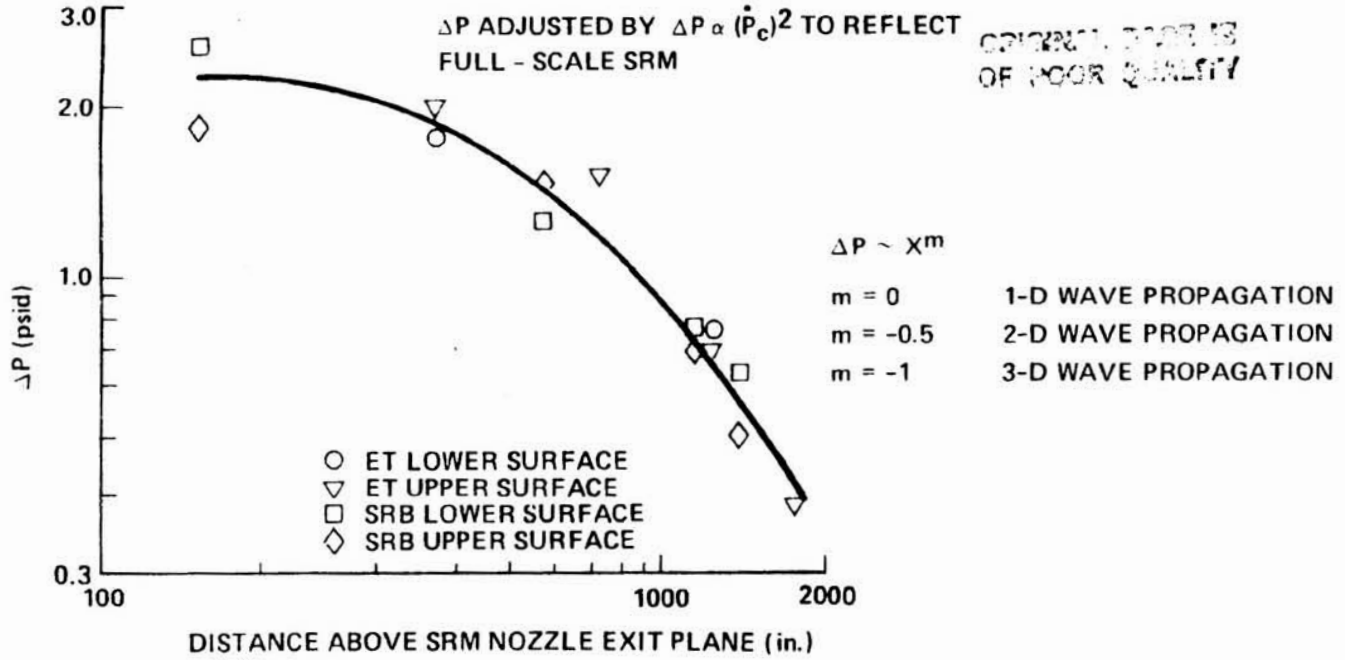

Figure 19.- Overpressure attenuation characteristics from 6.4-percent scale model test. ET, SRB.

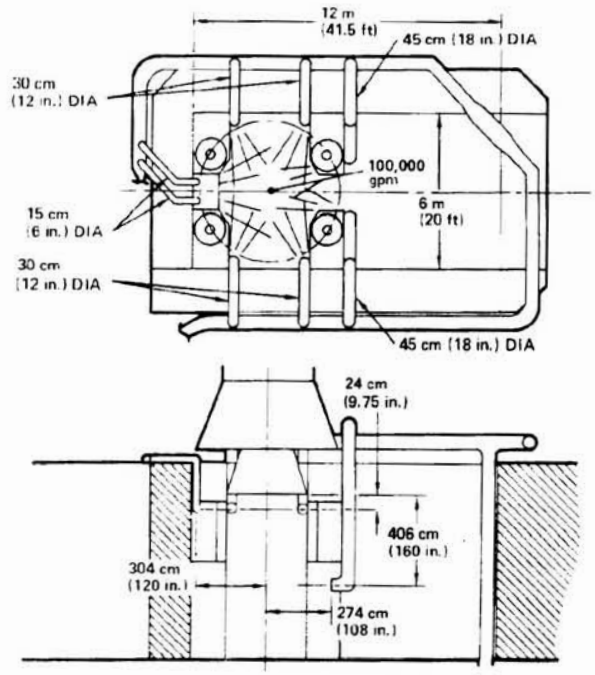

Figure 20.- STS-2 water injection system.

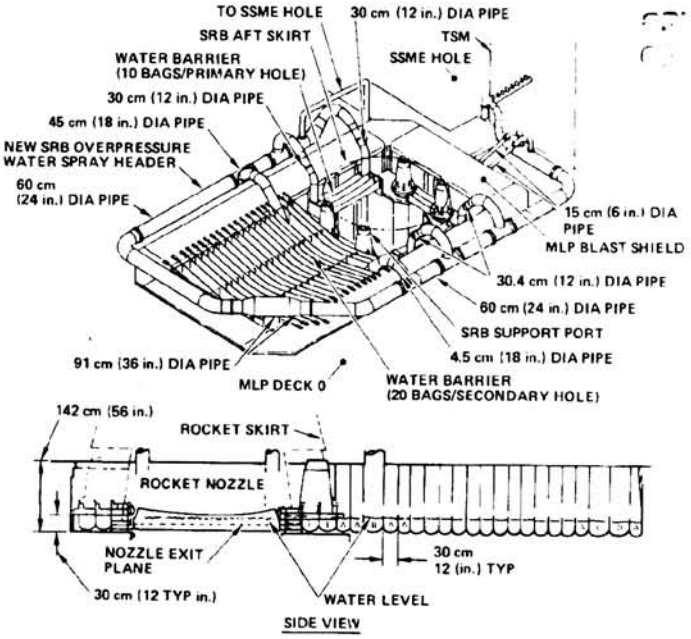

Figure 21.- STS-2 water trough covers.

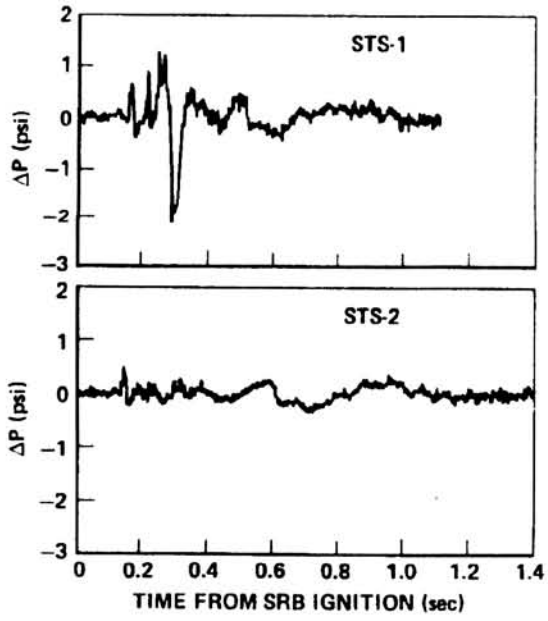

Figure 22.- Typical comparison of overpressure on STS-1 and STS-2.

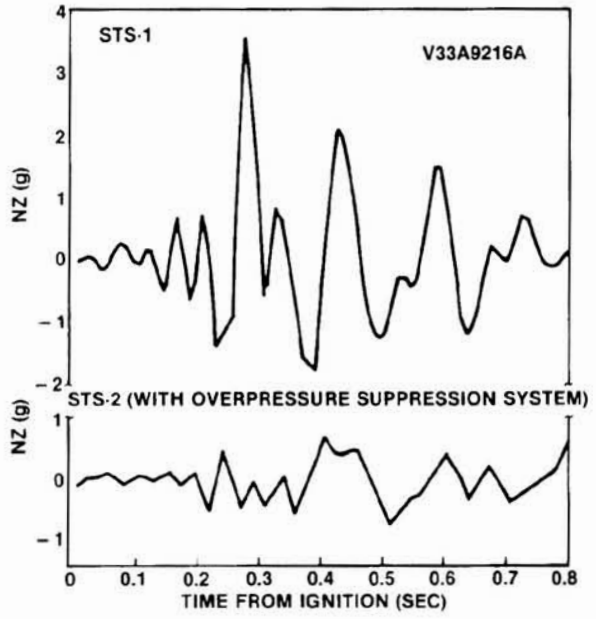

Figure 23.- Typical comparison of acceleration measured on STS-1 and STS-2.

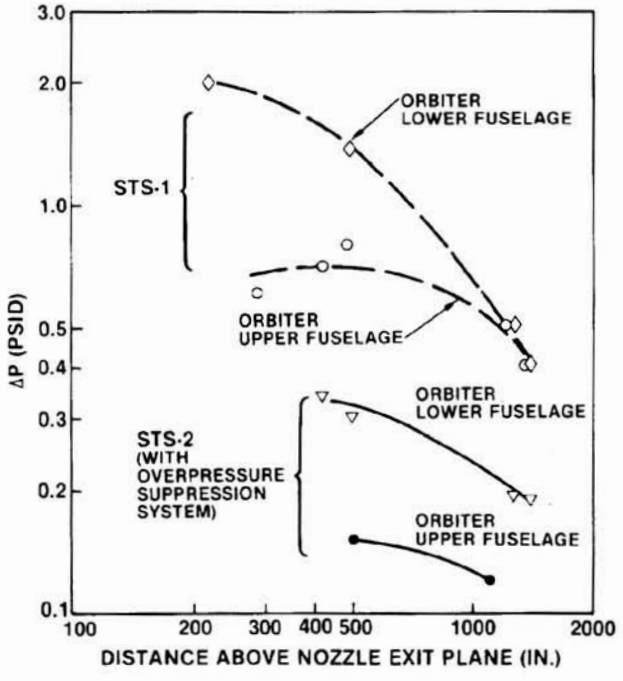

Figure 24.- Comparison of overpressures measured on STS-1 and STS-2.

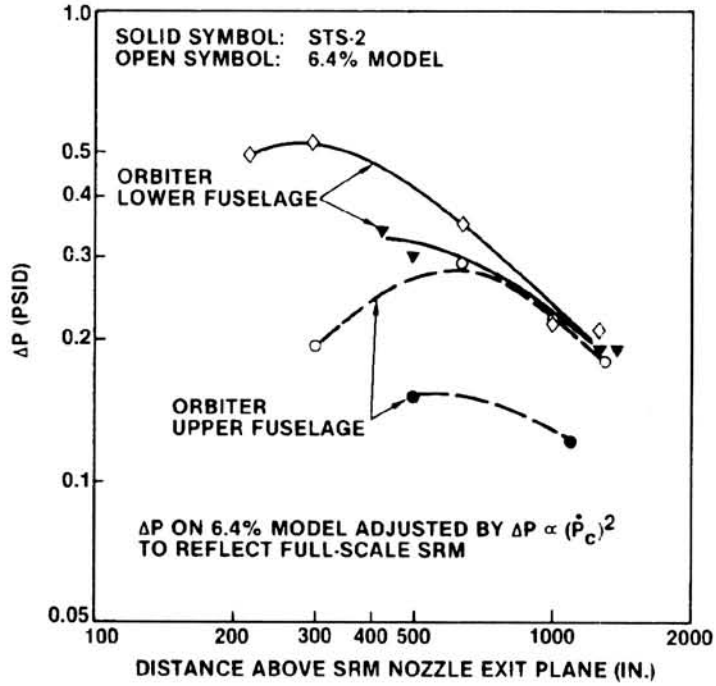

Figure 25.- Comparison of predicted and measured overpressures on STS-2.

SPACE SHUTTLE ENTRY LONGITUDINAL AERODYNAMIC COMPARISONS OF FLIGHTS 1-4 WITH PREFLIGHT PREDICTIONS

Paul O. Romere and A. Miles Whitnah
NASA Johnson Space Center
Houston, TX

ABSTRACT

The Space Shuttle orbiter flight test program has required the aerodynamicist to take a new approach in determining flight characteristics. A conventional flight test program of slowly and cautiously approaching more severe flight conditions was not possible with the orbiter. On the first four orbital flights, the orbiter entered the atmosphere at approximately Mach 29 and decelerated through the Mach range (the subsonic portion of flight had also been flown by another orbiter vehicle during the Approach and Landing Test Program). Certification for these flights was achieved by an extensive wind tunnel test and analysis program. The initial series of flights of the orbiter were heavily instrumented for the purpose of obtaining accurate aerodynamic data. The flight data derived from the entry Mach range provided comparisons between flight and wind tunnel derived predicted data in the areas of both aerodynamic performance and longitudinal trim. The second and fourth orbital flights incorporated several maneuvers which were beneficial to the analysis of the hypersonic aerodynamic performance and the hypersonic longitudinal trim.

NOMENCLATURE

A	Area
b	Wingspan
C´	Proportionality factor for the linear viscosity - temperature relationship
C_A	Axial force coefficient
C_m	Pitching moment coefficient
h	Altitude
h/b	Ratio of altitude from aft fuselage lower trailing edge to wingspan
IML	Interface mold line
L_B	Reference body length
L/D	Lift-to-drag ratio
M	Mach number

MAC	Mean aerodynamic chord
PUPO	Pullup/pushover
$\bar{q}$	Dynamic pressure
Re	Reynolds number based on L_B
S_{REF}	Reference area
$\bar{V}'_\infty$	Viscous interaction parameter, $= M_\infty\sqrt{\frac{C'_\infty}{Re}}$
X_{CP}/L_B	Center of pressure in body length
α	Angle of attack, degrees
δ_{SB}	Speedbrake deflection angle, degrees
ϕ	Roll angle, degrees

Subscripts

∞	Free stream

Test Facilities Abbreviations

AEDC	Arnold Engineering and Development Center
ARC	Ames Research Center
Calspan	Calspan Corporation
HST	Hypersonic Shock Tunnel
4 x 4 HSWT	High Speed Wind Tunnel
LaRC	Langley Research Center
LTV	LTV Aerospace Corporation
NSWC	Naval Surface Weapons Center
8-ft TPT	8-Foot Transonic Pressure Tunnel
UPWT	Unitary Plan Wind Tunnel
16T	16-Foot Transonic

INTRODUCTION

Obtaining flight test data over a wide range of flight conditions through a traditional graduated flight test program is not economically feasible on a large, unpowered, gliding flight vehicle such as the Space Shuttle orbiter. Therefore, an extensive wind tunnel test and analysis program was undertaken to provide a high level of confidence in the aerodynamic predictions. Also, both the Approach and Landing Test Program (ALT) and the current orbital flight test program have been severely restricted with respect to angle of attack and center of gravity location to account for uncertainties in the predicted data base, thus assuring a minimum-risk flight test program. The vehicles were extensively instrumented to obtain flight data. This approach resulted in both high-quality flight test data and an extensive wind tunnel data base. Thus, the aerodynamicist has been given the unique opportunity to compare state-of-the-art prediction techniques with flight data over an extensive range of entry flight conditions.

The Space Shuttle Program's first and third flights, designated Space Transportation System (STS-1 and -3), did not contain any specifically designed performance data extraction maneuvers; however, the second (STS-2) and fourth (STS-4) did incorporate many data extraction maneuvers. Several involved pullup/pushovers (PUPO) and bodyflap pulses, which are most useful in the flight data analysis effort towards the steady-state aerodynamic performance, longitudinal trim characteristics, and control surface effectiveness.

This paper presents an overview of the current analyses of the aerodynamic performance, longitudinal trim, and control surface effectiveness which have been conducted using STS-2 and -4 flight data results. Those analyses were directed towards comparisons and correlations of flight data and predicted data with emphasis on those areas in which differences were significant.

SPACE SHUTTLE ORBITER DESIGN CHARACTERISTICS

The physical characteristics of the Space Shuttle orbiter are illustrated in figure 1. The bodyflap is the predominant longitudinal trim device, while the wing-mounted elevons are used for longitudinal stability and as ailerons for lateral trim and control. The vertical tail consists of the fin and a combination rudder/speedbrake, with the speedbrake providing lift-to-drag ratio modulation during the terminal area energy management and the approach and landing phases of the flight. Aft-mounted side-firing reaction control jets are used to supplement yaw stability from entry down to Mach 1.0.

The Space Shuttle orbiter is designed to perform an unpowered, gliding entry from orbit at an angle of attack of 40 degrees, which is modulated depending upon crossrange requirements. A gradual pitchdown is initiated at Mach 14 and is completed at Mach 2. From Mach 2 to touchdown, more conventional angles of attack, 3 to 10 degrees, are flown. At the beginning of entry, downrange modulation is achieved by periodically performing roll reversals across the prescribed ground track. STS-1 through -4 entry flight conditions are illustrated in figures 2a through 2d.

Aerodynamically, during the major portions of the flight from entry to touchdown, the vehicle is longitudinally and laterally stable. In certain flight regimes where the vehicle is statically unstable, the stability is artificially provided by the flight control system. The design concept of using a stability augmented flight control system has increased the need to accurately define the aerodynamic characteristics beyond those for a conventional aircraft development program.

PREFLIGHT PREDICTIONS

The preflight aerodynamic predictions[1] are built on a foundation of 27,000 occupancy hours of wind tunnel testing. This testing program utilized state-of-the-art facilities, as seen in table 1.

In general, wind tunnel data cannot be used directly for prediction; the most valid set of wind tunnel results must be adjusted for unsimulated conditions. The major adjustments applied to the Space Shuttle wind tunnel data base involved corrections for nonsimulation of structural deformation, flow field parameters, and the profile drag due to thermal protection system roughness and minor protuberances. The process of establishing the preflight predictions is discussed subsequently.

Experts from Langley and Ames Research Centers were called upon to join with the prime contractor and the Johnson Space Center in a cooperative effort to establish the most valid set of wind tunnel tests results. These results were established through a team analysis effort in which the most representative tests were selected, scrutinized for blockage and sting effects, and integrated into an overall data base. The data base was then reviewed and approved by this team of experts.

The traditional free-stream Reynolds number was selected for the flow field scaling parameter below Mach 15, while a viscous interaction parameter ($\bar{V}_\infty'$) was utilized at higher Mach numbers. Since the test facilities were able to provide near-flight Reynolds number simulations over a large Mach number range (as illustrated in fig. 2d), no corrections to the wind tunnel results were required. At lower Mach numbers, the traditional adjustments were applied for Reynolds effect on friction drag. Additional adjustments were applied to the profile drag to account for the added roughness of the thermal protection system tiles and for minor protuberances which could not be simulated on the wind tunnel test models.

In the rarefied atmosphere above Mach 15, $\bar{V}_\infty'$ was selected as the scaling parameter. This is appropriate when the boundary layer thickness becomes significant with respect to the shock stand-off distance.[2] The selection was further based upon the assumption that simulation of the shock boundary layer interaction with the flow on the windward side of the vehicle also provides adequate flight-to-wind-tunnel correlation for the lee-side flow field. An examination of flight conditions with respect to this scaling parameter (fig. 2d), shows that no adjustments are necessary. The wind tunnel data were not adjusted for real-gas effects.

In general, no attempt was made to obtain a wind tunnel simulation of the effects of structural deformation on the longitudinal aerodynamics through testing of an aeroelastic or deformed model. Since at higher dynamics pressures ($\bar{q}$) these effects

are significant, some adjustment to the wind tunnel data to account for structural deformation must be made to provide adequate estimates of the flight aerodynamics. The approach used to evaluate the aeroelastic effects is unqiue. These effects were derived using a sensitivity analysis performed with the aid of a structural/aerodynamic analysis program.[3,4] The program was used to stiffen systematically various portions of the vehicle structure and evaluate analytically the effect of the stiffness changes on the aerodynamics. The results indicated that the major longitudinal aeroelastic effects were produced by deformation of the elevon about its hinge line as a result of the aerodynamic hinge moments. The effect was modeled by combining a rotary spring constant, as determined from vehicle loading tests, with wind tunnel derived aerodynamic hinge moment characteristics to produce an elastically deformed elevon deflection angle. The elastic elevon angle is subsequently used with the rigid aerodynamic characteristics in determining the vehicle longitudinal aeroelastic characteristics.

As a result of the Space Shuttle Program management's desire to desensitize the flight control system with respect to the aerodynamics, uncertainties (defined as variations) were provided for use with the preflight predictions. These variations[1] are based upon historical predicted-to-flight differences of similar configurations and on engineering judgement.

COMPARISONS OF STS-2 AND -4 FLIGHT TO PREDICTED DATA

The aerodynamic analyst is faced with a dilemma in the comparison of preflight predictions and flight data. In wind tunnel testing, which is the basis of the preflight predictions, the independent parameters are known precisely while the aerodynamics are questionable. In flight testing, the aerodynamics are known exactly, by definition, but the accuracy of the independent parameters may be in question. To minimize the impact of this dilemma, the aerodynamic comparisons were selected such that errors in the flight-independent parameters are minimized.

Lift-to-drag ratio (L/D) was selected for comparisons of predicted and flight aerodynamic performance since it is independent of flight dynamic pressure ($\bar{q}$). As may be seen in figures 3 and 4, the preflight predictions agreed well with flight L/D above Mach 1. Below Mach 1, the flight exhibited higher L/D than predicted.

At a Mach number of approximately 21 during the STS-2 entry and approximately 12 during the STS-4 entry, pullup/pushover (PUPO) maneuvers were executed in which angle of attack varied from 32 to 45 degrees. During this maneuver, the only control surface movement involved that of the elevons to drive the vehicle through the angle-of-attack sweep from approximately 32 to 45 degrees. Figure 5 presents the correlation of flight to predictd L/D for the PUPO maneuvers. The correlation is excellent, with a maximum difference being

approximately 1-½ percent. The predicted variations in this region are approximately 10 percent.

The longitudinal aerodynamic center of pressure (X_{CP}/L_B), which is also independent of $\bar{q}$, was selected for trim comparisons. For a trimmed vehicle, the longitudinal center of pressure (the imaginary point on the vehicle where the pitching moment is zero) coincides with the center of gravity. Figures 6 and 7 present a comparison of the flight and predicted centers of pressure. As can be seen in figures 6b and 7b, at Mach numbers above 10 the predicted center of pressure is more aft by 0.7 percent of the reference body length (1.9 percent of the mean aerodynamic chord) than the flight data would indicate. For the Mach range where the Reynolds number was simulated ($2.0 < M < 10$; fig. 2d), trim was predicted more precisely even though unusually high angles of attack between 15 and 30 degrees were flown. The predictions for the transonic and subsonic range were less than satisfactory although they were within the predicted variations. The slight difference between STS-2 flight and predicted in the Mach 2 to 10 range of figure 6b was not noted in STS-1[5] and -4 results and can be attributed to a possible uncertainty in the center of gravity location for STS-2.

In addition, axial force coefficient (C_A) comparisons have been made. Two observations can be made from the C_A comparisons of figures 8 and 9. The underprediction of subsonic L/D previously reported was largely influenced by the overprediction of C_A in the same Mach range. Figures 8b and 9b indicate that the viscous interaction parameter ($\bar{V}_\infty'$), which is used above Mach 15, was a wise choice of scaling parameters for C_A. The higher flight C_A seen at Mach 12 to 14 of STS-2 and -4 corresponds to a flight control system update which involved an aileron input, possibly causing a control-surface-induced laminar-to-turbulent boundary layer transition.

Longitudinal Trim Difference Analysis

Upon examination of the X_{CP}/L_B correlations (fig. 10) derived from the previously mentioned pullup/pushover maneuvers, the STS-2 M=21 data indicate a very good straight-line correlation which is parallel to but biased from the perfect correlation line by approximately 0.0075, while the STS-4 M=12 data indicate a bias of approximately 0.004. The data being essentially parallel to the perfect correlation line indicates that the effects of angle of attack and elevon effectiveness are as predicted and the bias is probably the result of not correctly predicting the basic vehicle pitching moment or underprediction of the body flap by approximately 50 percent. Illustrated in figure 11 are the X_{CP}/L_B correlations of data taken during body flap pulse maneuvers at Mach numbers of approximately 21,

17, and 12.5 for STS-2. During those maneuvers the angle of attack was near constant with only the body flap and elevons moving.

Each body flap maneuver of figure 11 illustrated a generally straight line correlation which was parallel to the perfect correlation line and biased in the same manner as the PUPO maneuvers. The inference here is that both the body flap and elevon effectiveness are as predicted. The ratio of the change in elevon deflection to the change in body flap deflection from the flight data is as was predicted. This lends additional strength to the inference that both body flap and elevon effectiveness were well predicted. Therefore, one would conclude that the most probable cause for the hypersonic trim discrepancy would be an error in the predicted basic pitching moment of the vehicle. The wind tunnel results were reexamined to insure that no data were overlooked which would better reflect the flight data results. None were found.

One must conclude that the proper scaling was not realized for the hypersonic trim characteristics, either because the scaling parameter was improperly selected or because the test facilities were not capable of reproducing the proper environment. Because the discrepancy is indicated to result from a basic pitching moment error, the probable cause is due to the test facilities not reproducing the proper environment, namely to simulate real-gas effects. Because real-gas effects can not be simulated in ground-based test facilities, real-gas effects, which primarily affect the pitching moment, were analytically derived and included in the predicted data base. However, due to the uncertainties associated with the analytically derived effects, they were applied to the predicted moment uncertainties or variations mentioned previously. It should be noted that the analytically derived real-gas effects do give the correct trends and approximate magnitudes required to better predict the flight characteristics.

Subsonic Performance Difference Analysis

As a result of the discrepancy between flight performance and predicted performance in the subsonic range, the Space Shuttle orbiter was analyzed with respect to drag and speedbrake effectiveness. Data from flights 4 and 5 of the Approach and Landing Test Program (ALT 4 and ALT 5) and STS-1, -2, -3, and -4 were used. The drag analysis was centered on the axial force coefficient and included only the flight data taken with a speedbrake deflection of less than 30 degrees, with the landing gear retracted, and above the region of ground effects (i.e. $h/b > 1.5$). Correlation plots of flight to predictd data are presented in figure 12 and indicate an overprediction of C_A by a constant 40 counts ($C_A = 0.004$) for all flight data sets, with the exception of that for the final data reduction of STS-1 and -4, which indicates an overprediction of approximately 70 counts. No explanation for the STS-1 and -4 discrepancy is available at the present time. A significant improvement in the correlations resulted from correcting the predicted profile drag by -40 counts (see

fig. 13). The data presented in figures 12 and 13 are for Mach ≈ 0.47 to 0.5.

For the analysis of speedbrake effectiveness, flight test data were selected where body flap deflection was approximately zero degrees and the speedbrake was swept through a large deflection range. ALT 4 and 5 and STS-1 and -2 reflect those conditions. The flight data were then corrected to an angle of attack of 5 degrees and an elevon deflection of 5 degrees through the use of the coefficient slopes as determined from the predicted data base. The resultant effectiveness with respect to axial force coefficient is presented in figure 14 as an increment about the baseline speedbrake deflection of 25 degrees. For STS-1 and -2, the effectiveness was underpredicted by approximately 60 counts at a 55-degree speedbrake deflection angle.[6] Results from ALT 4 and 5 do not indicate this underprediction. Resolution of this flight data inconsistency will require further analysis.

CONCLUDING REMARKS

The completion of the first four flights of the Space Shuttle orbiter has given aerodynamicists the first opportunity to test their prediction skills over diverse flight conditions. The performance predictions were in excellent agreement with flight performance above Mach 1; however, drag was overpredicted at the subsonic Mach numbers.

The trim characteristics were predicted adequately in the Mach range of 2 to 10; however, above Mach 10 and below Mach 2, the predictions were less than satisfactory. Analysis results of the STS-2 and -4 maneuvers during entry indicate that the hypersonic trim discrepancy is due to an error in prediction of the basic vehicle pitching moment and not to an error in prediction of the elevon and body flap effectiveness.

REFERENCES

1. "Aerodynamic Design Data Book, Volume 1, Orbiter Vehicle 102," SD72-SH-0060, Volume 1M, November 1980, Space Division, Rockwell International.

2. Cox, R. N. and Crabtree, L. F., "Elements of Hypersonic Aerodynamics," Academic Press, New York, 1965.

3. "Aerodynamic Preliminary Analysis System, Part I-Theory," NASA CR-145284, April 1978.

4. "Aerodynamic Preliminary Analysis System, Part II-User's Manual and Program Description," NASA CR- 145300, April 1978.

5. Young, J. C., Perez, L. F., Romere, P. O., and Kanipe D. B., "Space Shuttle Entry Aerodynamic Comparisons of Flight 1 with Preflight Predictions," AIAA 81-2476, paper presented at AIAA/SEPT/SFTE/SAE/ITEA/IEEE 1st Flight Testing Conference at Las Vegas, Nevada, November 11-13, 1981.

6. Romere, P. O. and Young, J. C.: "Space Shuttle Entry Aerodynamic Comparisons of Flight 2 with Preflight Predictions," AIAA 82-0565, paper presented at AIAA 12th Aerodynamic Testing Conference at Williamsburg, Virginia, March 22-24, 1982.

Table 1 - Shuttle Wind Tunnel Utilization Summary

Test Identification	Facility	Model Scale
Transonic		
0A145A	ARC 11 x 11 ft	.05
0A270A	LaRC 16T	.05
0A270B	LaRC 16T	.02
LA70	Calspan 8 ft	.015
LA76	LTV 4 x 4 HSWT	.015
LA77	ARC 11 x 11 ft	.015
LA111	LaRC 8-ft TPT	.015
LA115	LaRC 8-ft TPT	.015
Supersonic		
0A145B	ARC 9 x 7 ft	.05
0A145C	ARC 8 x 7 ft	.05
0A109	AEDC "A"	.02
LA63A	LaRC UPWT-1	.015
LA63B	LaRC UPWT-2	.015
LA75	LaRC UPWT-2	.015
LA76	LTV 4 x 4 HSWT	.015
LA101	LaRC UPWT-1	.015
LA110	LaRC UPWT-1	.015
LA114	LaRC UPWT-2	.02
LA125	LaRC UPWT-2	.02
LA131	LaRC UPWT-2	.02
LA144	LTV 4 x 4 HSWT	.02
0A258	AEDC "B"	.02
0A259	AEDC "B"	.01
0A257	LaRC 20 in. Mach 6	.01
Hypersonic		
0A113	Calspan HST (48 in.)	.01
0A171	NSWC Tunnel 9	.02

GEOMETRY	COMPONENT	
	WING	VERTICAL TAIL
AREA	2690 FT^2 (249.9092 m^2)	413.25 FT^2 (38.3922 m^2)
SPAN	936.68 (23.8425)	315.72 (8.0193)
ASPECT RATIO	2.265	1.675
TAPER RATIO	0.2	0.404
SWEEP (LE)	81/45 DEG	45 DEG
DIHEDRAL	3.5	— —
INCIDENCE	0.5 DEG	— —
MAC	474.81 (12.0602)	199.81 (5.0752)

NOTE: UNLESS OTHERWISE NOTED, ALL DIMENSIONS ARE IN INCHES (METERS)

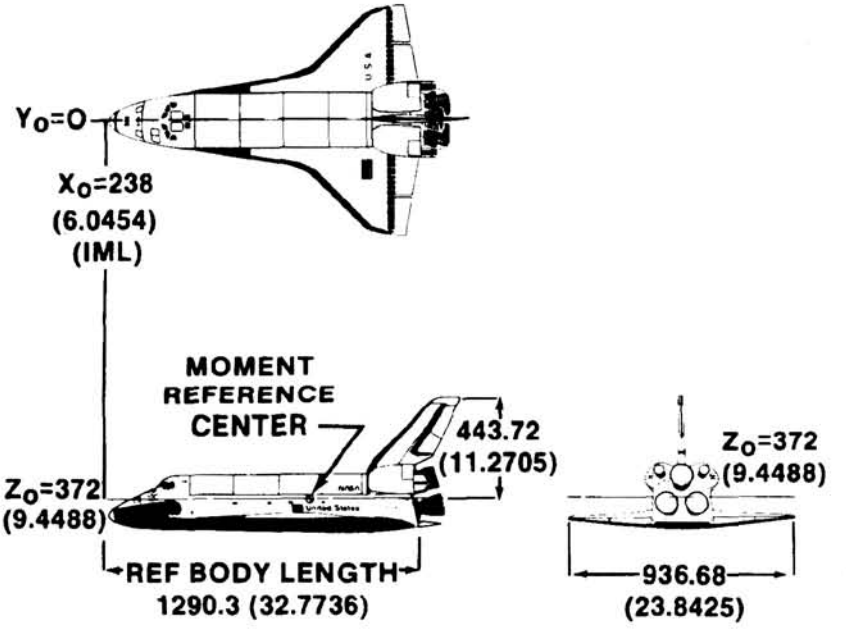

Figure 1.- Space Shuttle orbiter configurations.

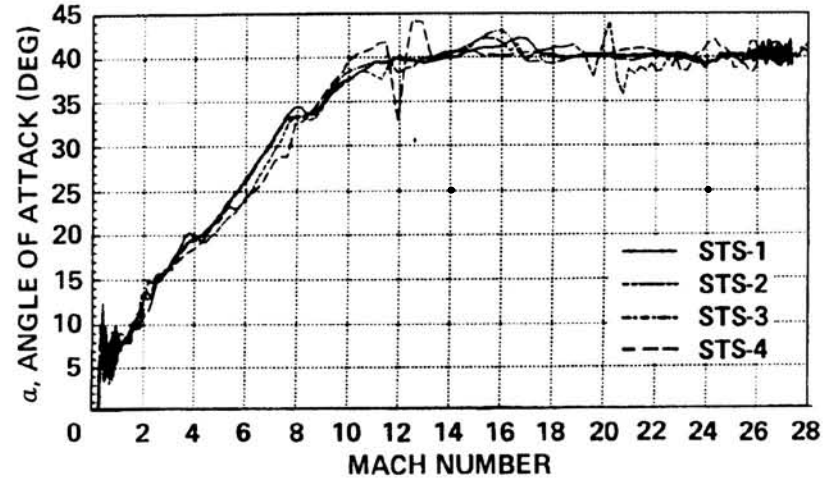

(a) Angle of attack.

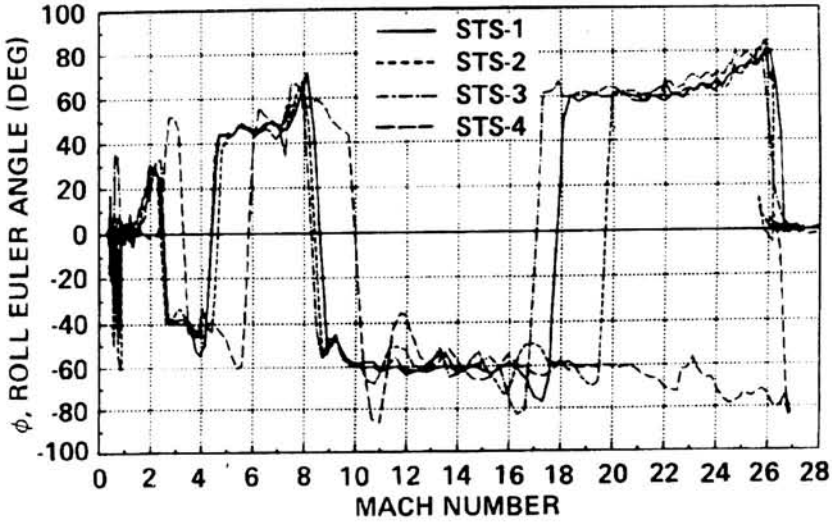

(b) Roll angle.

Figure 2.- STS-1 through -4 entry flight conditions.

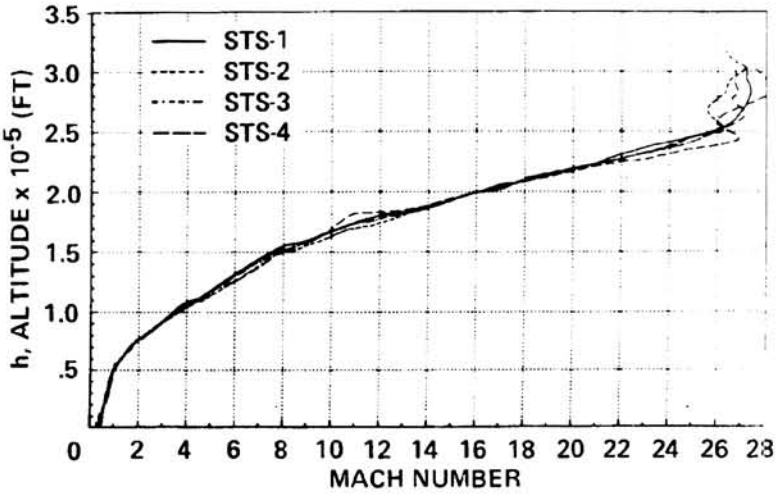

(c) Altitude.

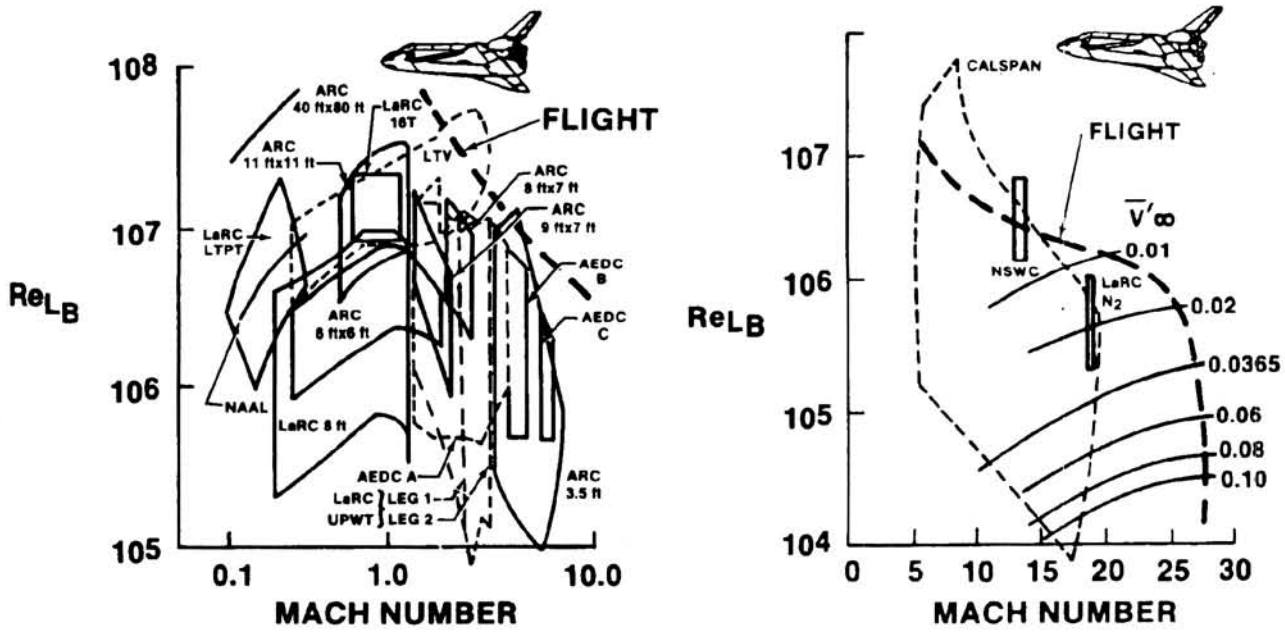

(d) Reynolds number simulation.

Figure 2.- Concluded.

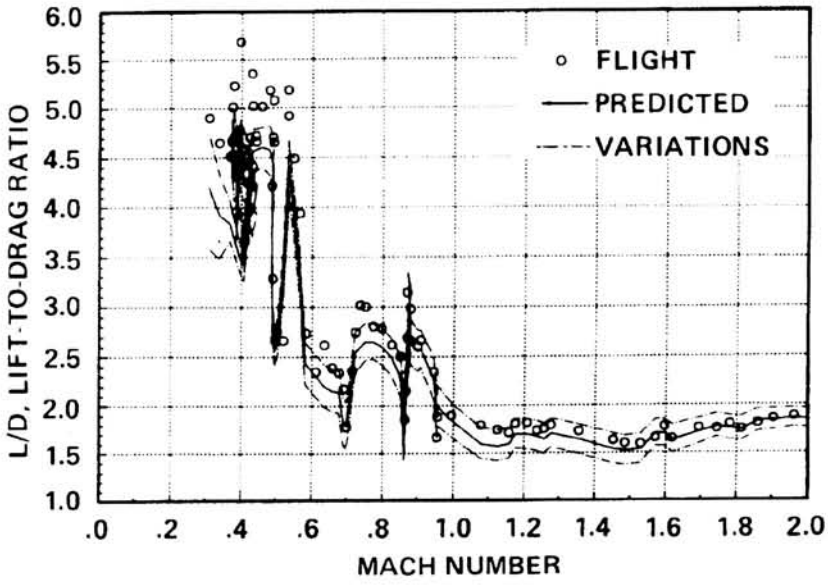

(a) Mach 0.0 to 2.0.

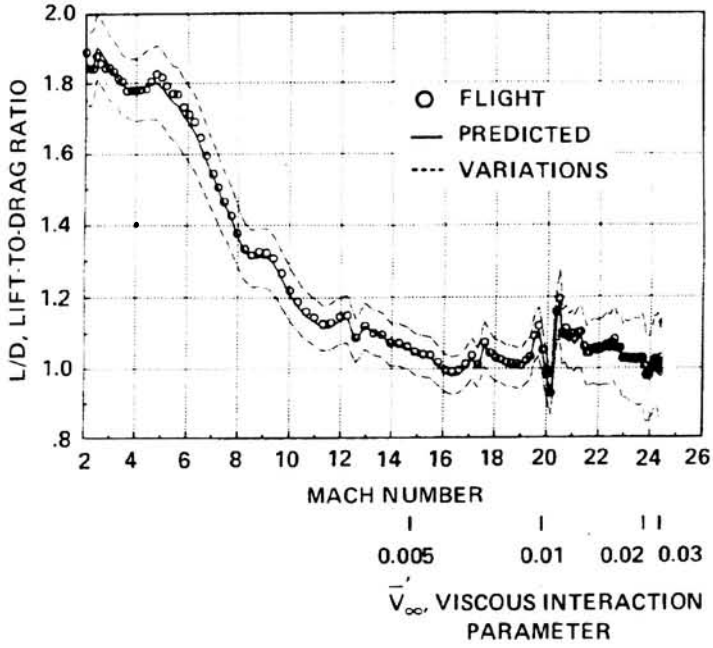

(b) Mach 2.0 to 26.0.

Figure 3.- STS-2 aerodynamic performance comparison.

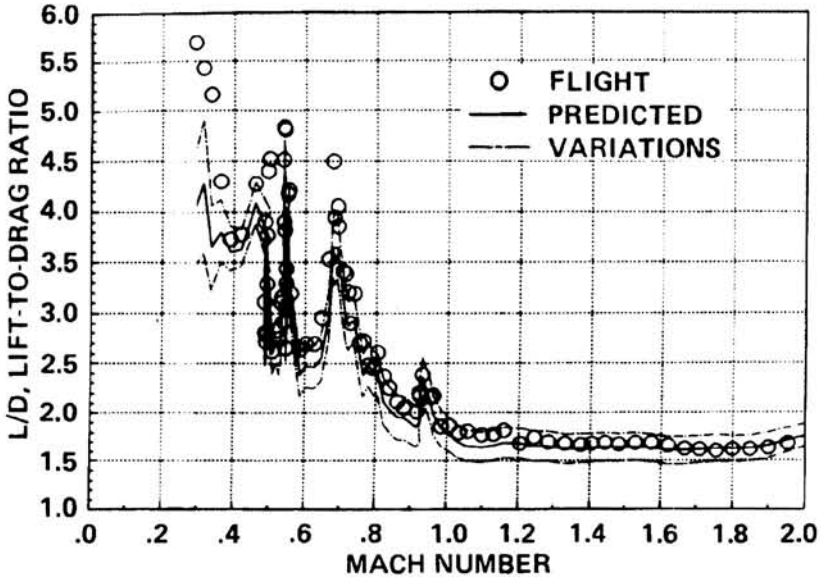

(a) Mach 0.0 to 2.0.

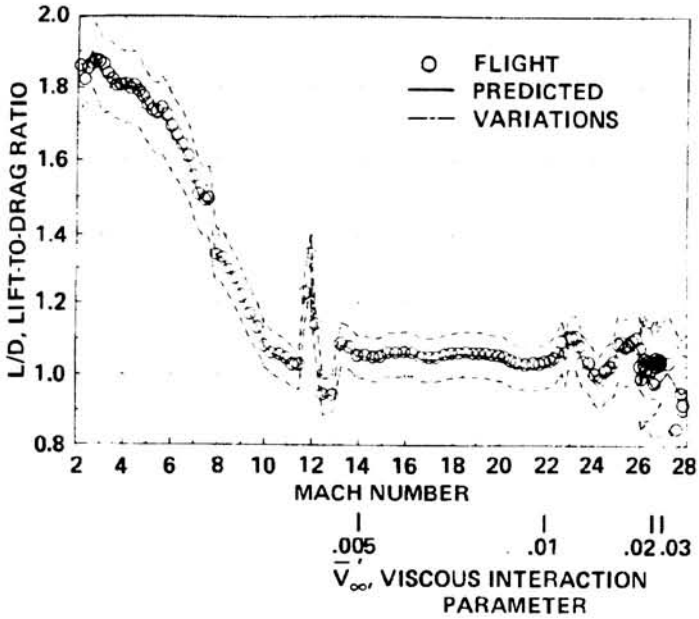

(b) Mach 2.0 to 28.0.

Figure 4.- STS-4 aerodynamic performance comparison.

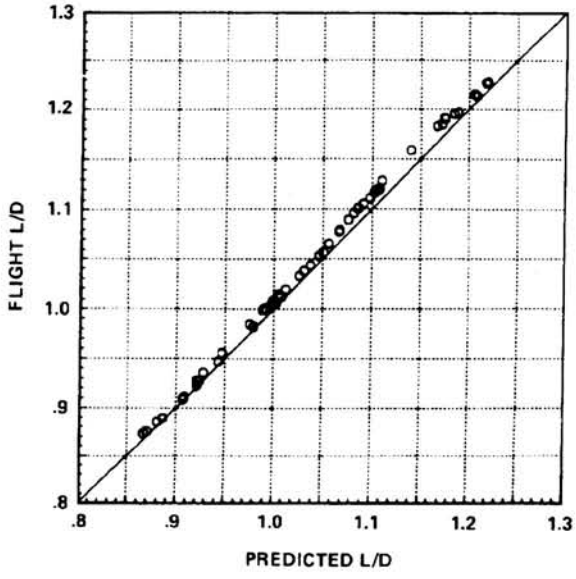

(a) STS-2; M = 21.

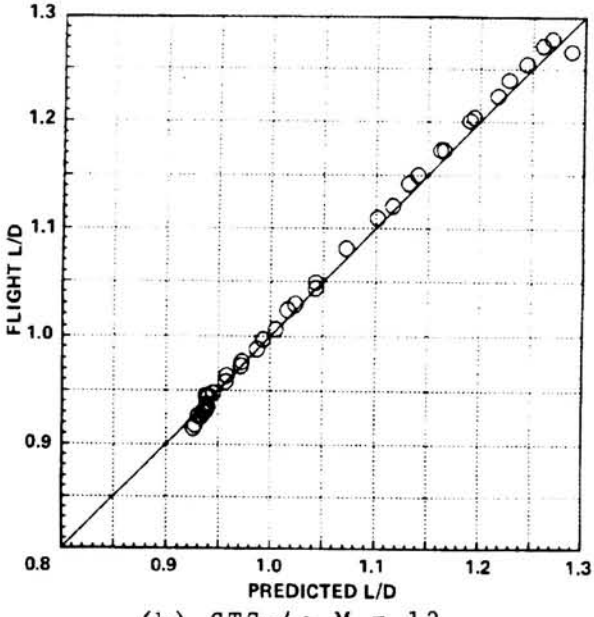

(b) STS-4; M = 12.

Figure 5.- Hypersonic lift-to-drag ratio correlation of flight with predicted data for pullup/pushover maneuvers.

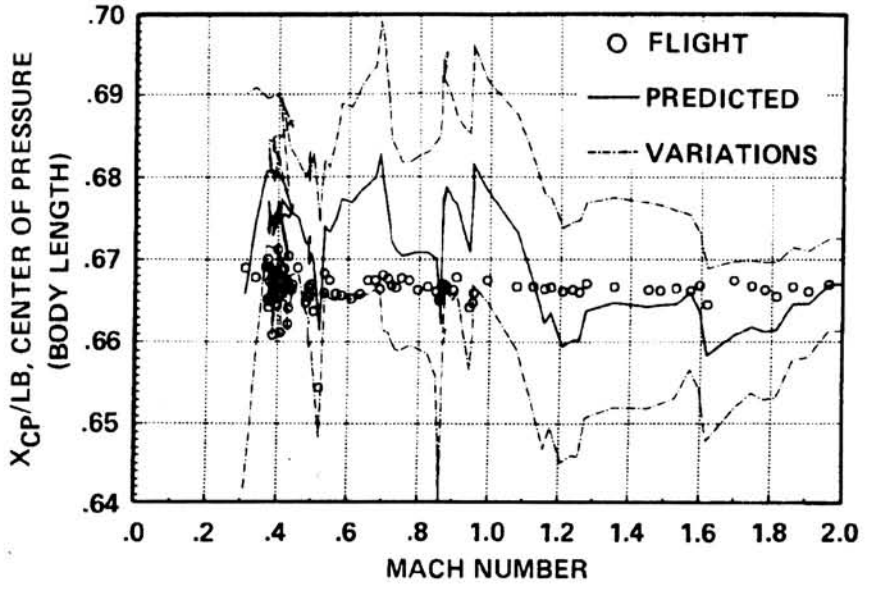

(a) Mach 0.0 to 2.0.

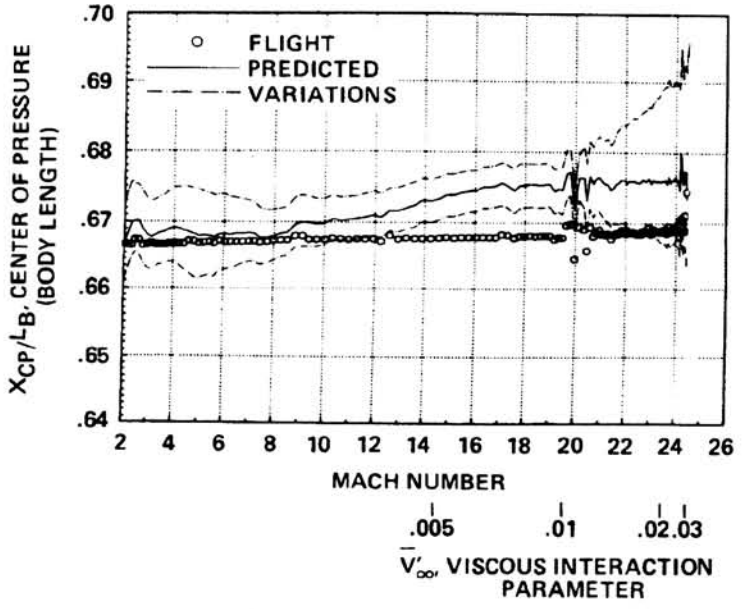

(b) Mach 2.0 to 26.0.

Figure 6.- STS-2 longitudinal aerodynamic center of pressure location comparison.

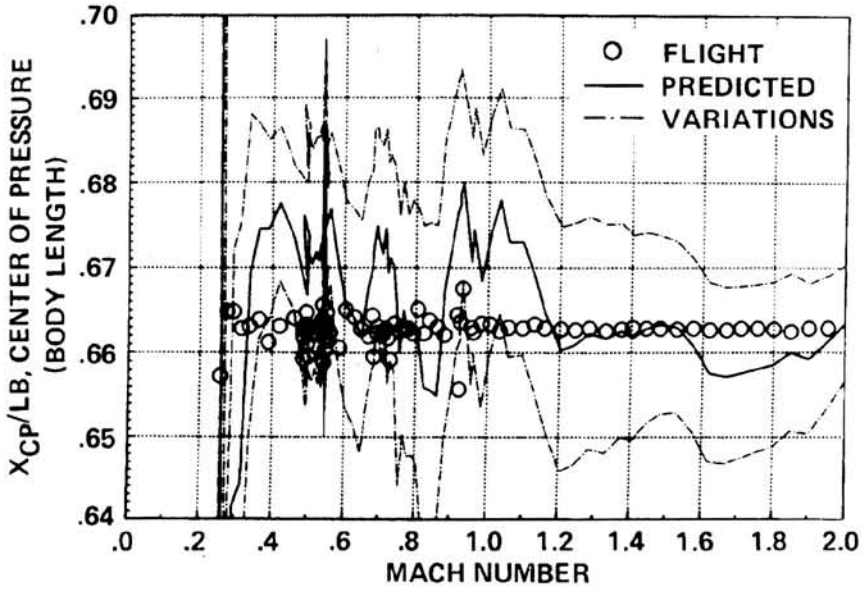

(a) Mach 0.0 to 2.0.

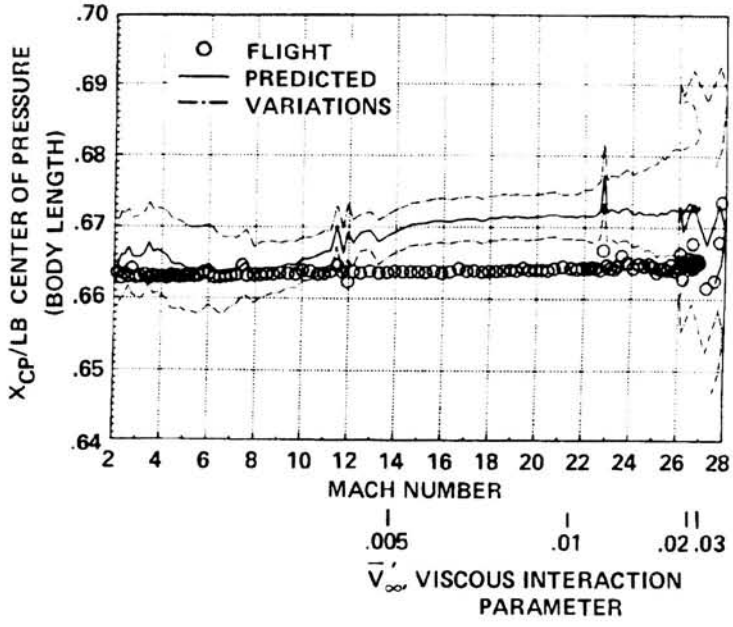

(b) Mach 2.0 to 28.0.

Figure 7.- STS-4 longitudinal aerodynamic center of pressure location comparison.

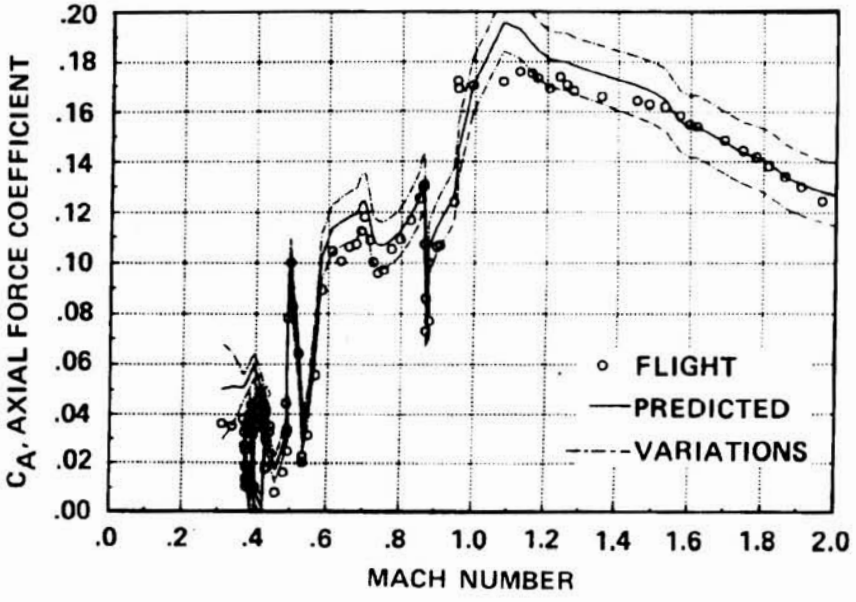

(a) Mach 0.0 to 2.0.

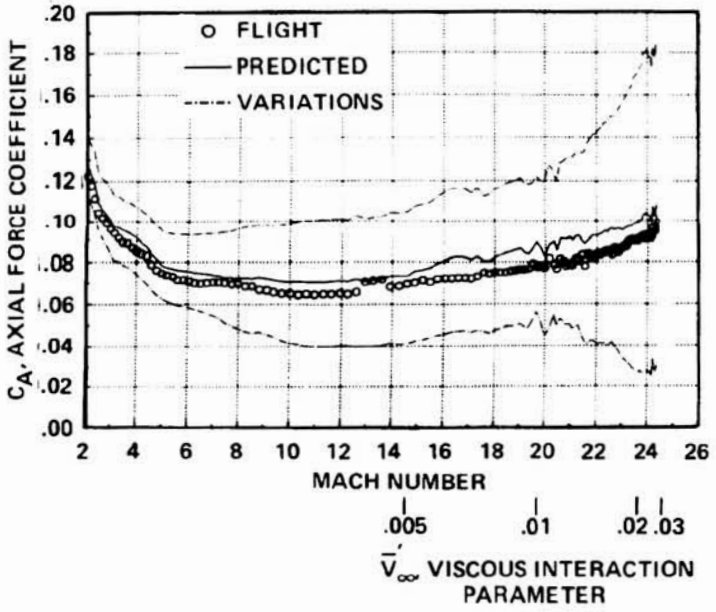

(b) Mach 2.0 to 26.0.

Figure 8.- STS-2 axial force coefficient comparison.

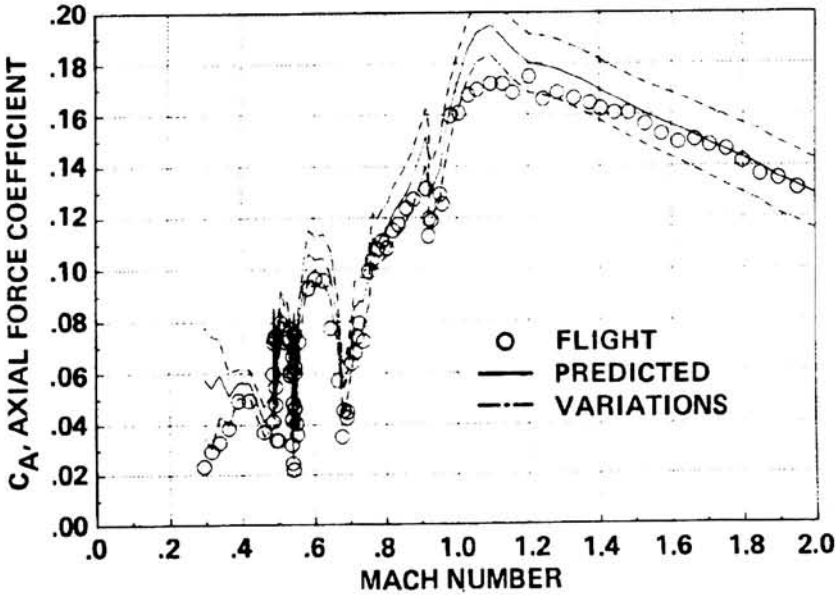

(a) Mach 0.0 to 2.0.

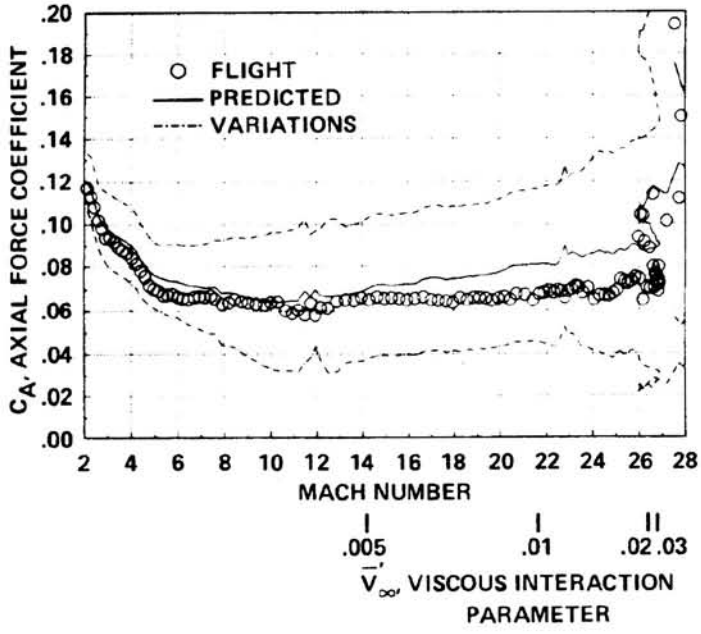

(b) Mach 2.0 to 28.0.

Figure 9.- STS-4 axial force coefficient comparison.

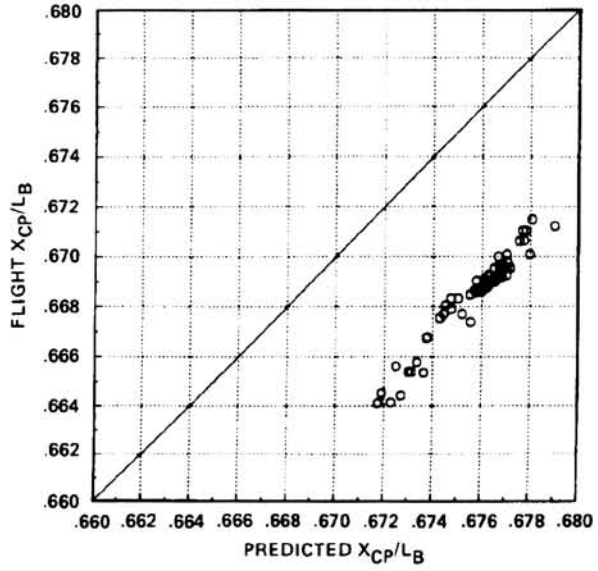

(a) STS-2; M = 21.

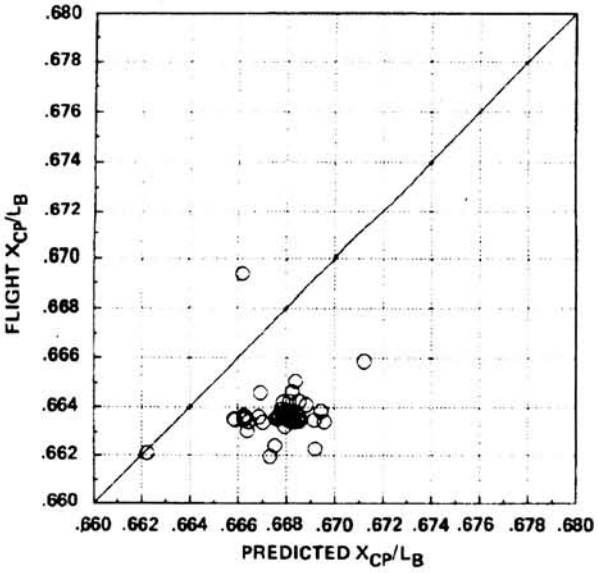

(b) STS-4; M = 12.

Figure 10.- Hypersonic longitudinal aerodynamic center of pressure correlation of flight with predicted data for pullup/pushover maneuvers.

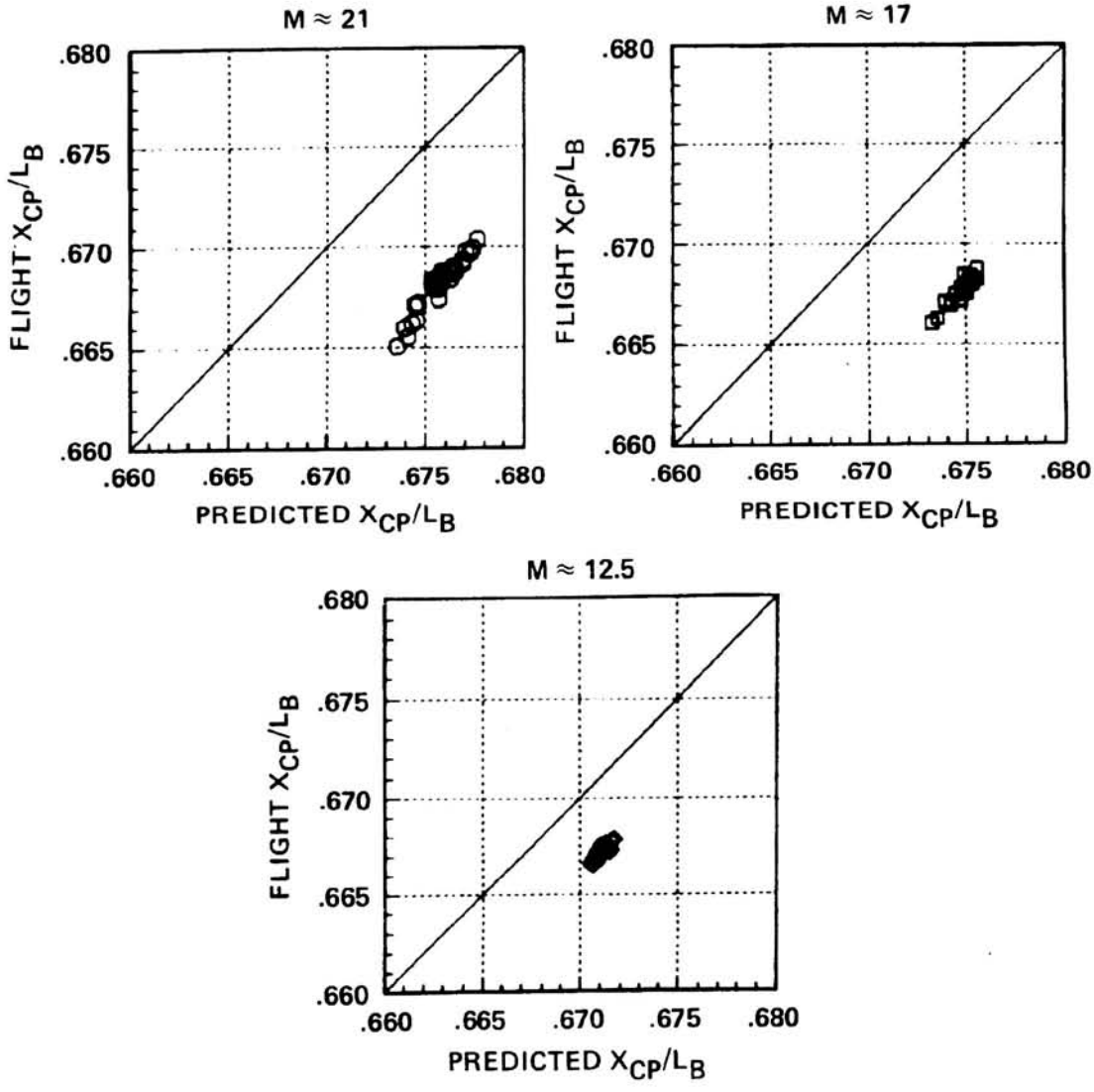

Figure 11.- STS-2 hypersonic longitudinal aerodynamic center of pressure correlation of flight with predicted data for body flap pulse maneuvers.

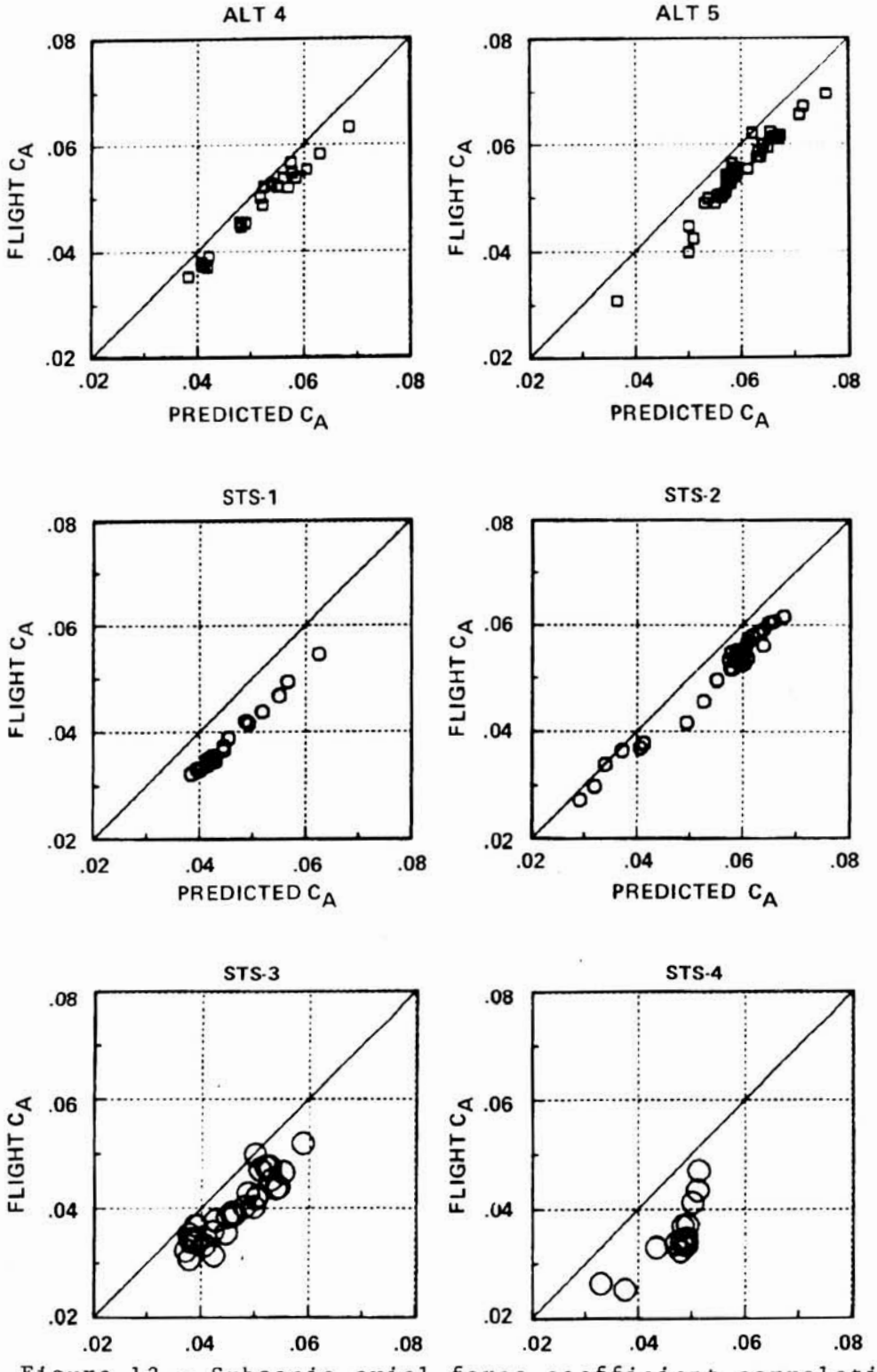

Figure 12.- Subsonic axial force coefficient correlations of flight with predicted data.

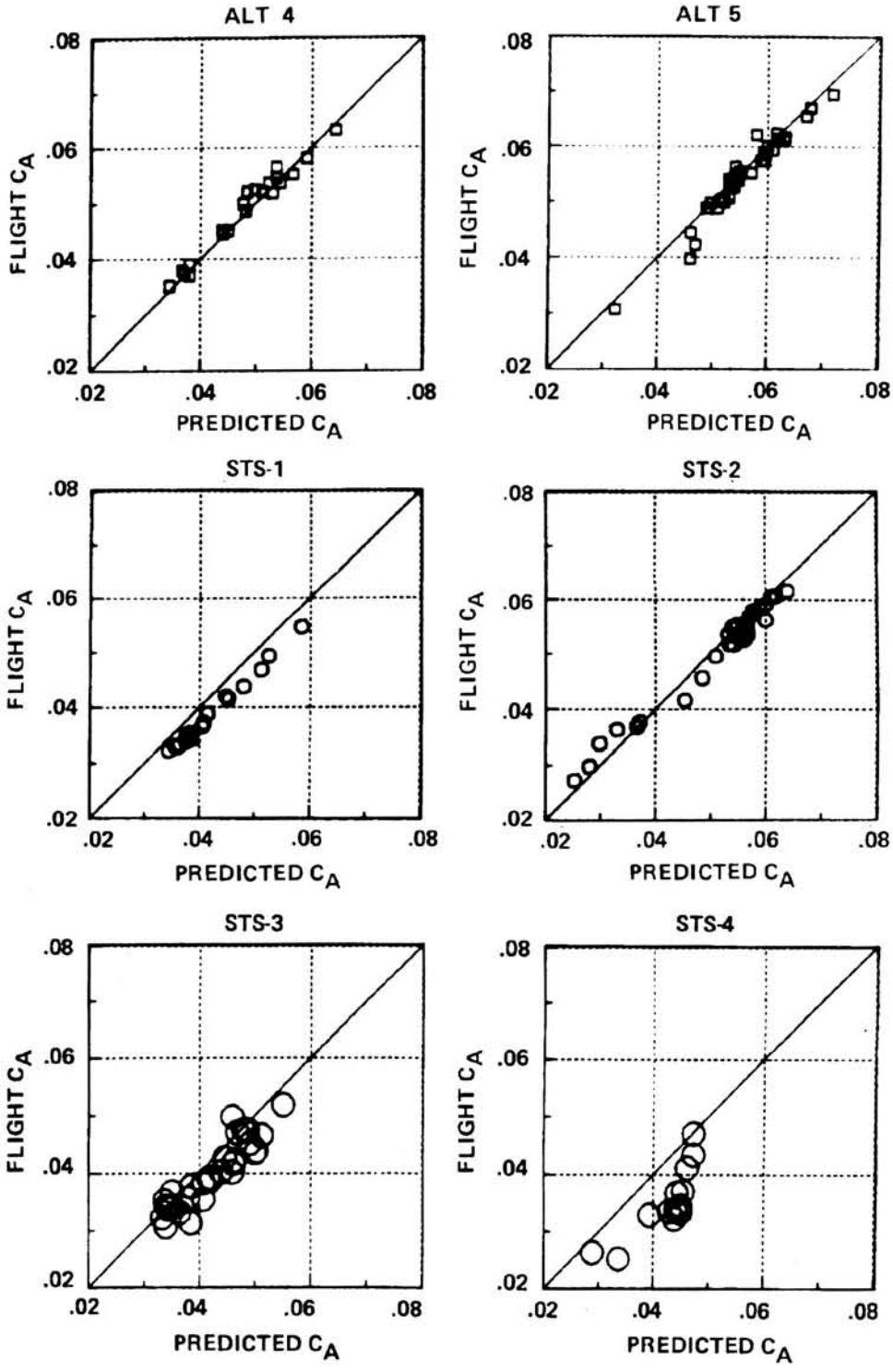

Figure 13.- Subsonic axial coefficient correlations of flight with predicted data corrected by -40 counts.

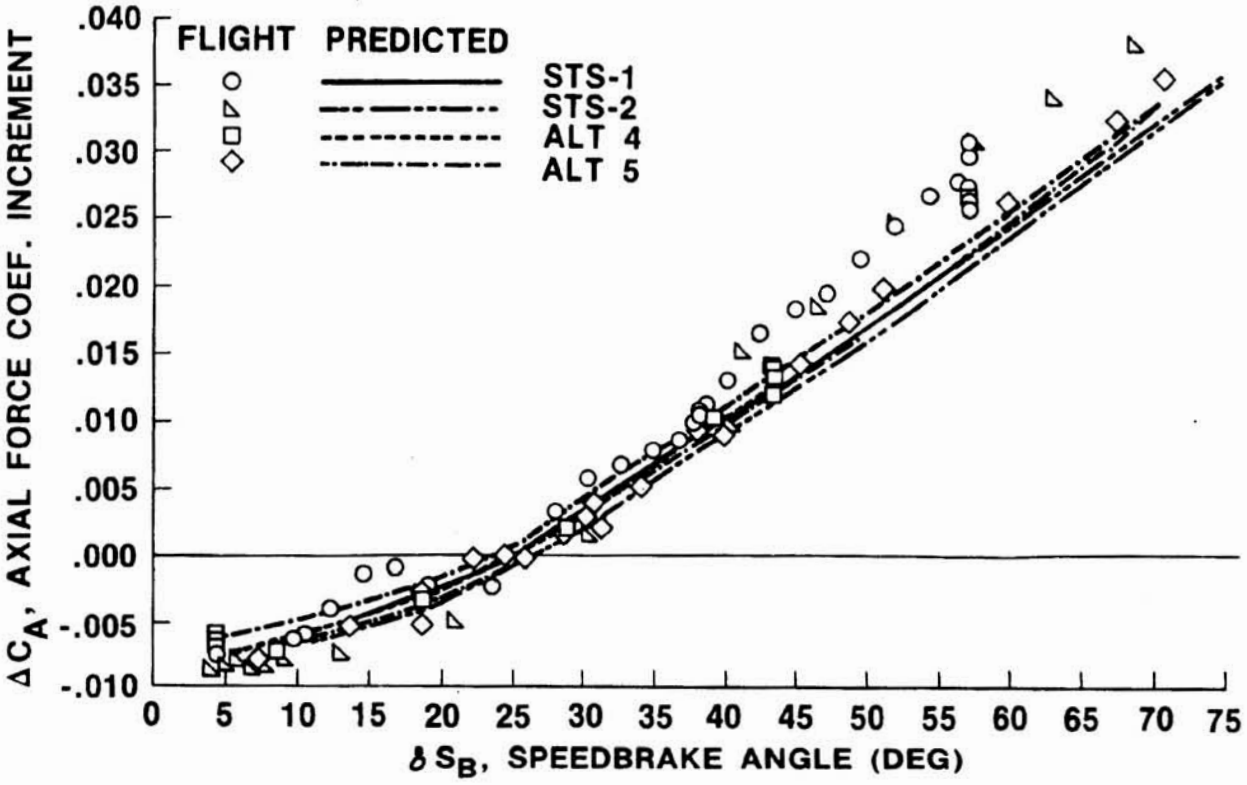

Figure 14.- Subsonic axial force coefficient increment due to speedbrake deflection.

A REVIEW OF PREFLIGHT ESTIMATES OF REAL-GAS EFFECTS ON SPACE SHUTTLE AERODYNAMIC CHARACTERISTICS

W. C. Woods, J. P. Arrington, and H. H. Hamilton II
NASA Langley Research Center
Hampton, Virginia

SUMMARY

Preflight estimates of the hypersonic aerodynamic characteristics of the Shuttle orbiter were based on a diverse series of research studies using state of the art techniques developed by basic research in the 60's and 70's. Real-gas viscous calculations on simple shapes that were used to evaluate correlation parameters indicated that real-gas effects reduce aerodynamic forces and moments. Inviscid calculations on winged lifting shapes indicated reduced forces and a slight nose-up pitch resulted because of real-gas effects. Analysis of the extensive wind tunnel data base indicated viscous correlation parameters provided the most appropriate extrapolation technique for estimating flight aerodynamics. Variations because of changes in the ratio of specific heats, which was the only available experimental tool for evaluating real-gas effects, indicated that reduced loads and nose-up pitching moments would occur at high altitudes and Mach numbers but that the values would not exceed the tolerances and variations established about the aerodynamic design data book values derived from viscous correlations. During STS-1, nose-up pitching moments exceeded the established variations. Whereas all preflight estimates indicate real-gas effects will cause nose-up pitch, comparison of STS-1 flight data to selected hypersonic wind-tunnel tests indicate the state of the boundary layer and its effect on body-flap effectiveness may be an important contributor to the so called "hypersonic anomaly."

INTRODUCTION

The state of the art knowledge of the effect of real-gas dynamics on the trimmed performance, stability, and control of winged, lifting, entry vehicles has not changed for about 15 years. This is not true of simpler, planetary entry research shapes. The state of the art in real-gas chemistry and real-gas effects for the pressure and heating distributions of blunt bodies entering planetary atmospheres has steadily progressed such that a reasonable level of confidence exists when this technology is applied in the design for survivability of planetary probes. With the growth in main-frame computers and vector processors, advanced numerical techniques have been applied to accurately determine loads and heating on blunt bodies of revolution with sonic corners and slightly blunted slender bodies of revolution in real-gas environments. In the latter case, stagnation point mass addition is frequently employed to reduce shape change and heating, and this phenomenon has been analytically modeled. Whereas this ability to model complex real-gas effects on the aerothermodynamics of bodies of revolution has been applied to predicting local pressure and heating on complex, winged, lifting configurations, it has not been applied in an integrated manner to determine overall vehicle aerodynamic coefficients of the Space Shuttle. This has been due in part to the geometry of the vehicle. For example, for wing sweeps less than approximately 50° and angles of attack above 25°-30° (Space Shuttle entry conditions) subsonic flow pockets occur on the windward side and until recently codes could not compute

through these areas. The main complicating factor has been the overall complexity of the problem of analytically and/or experimentally modeling low density, viscous, real-gas environments on both windward and leeward surfaces on three-dimensional shapes with any degree of confidence. This problem is faced by the developers of advanced space transportation systems today as the Shuttle developers faced it in the early seventies. Data from the first 5 Shuttle flights have indicated where deficiencies exist in Shuttle predicted aerodynamics. Hopefully, with the Shuttle system returning to Earth on a fairly routine basis, sufficient data will be accumulated to establish a flight data base and to develop empirical models of the vehicle's performance, stability, and control limits at entry Mach numbers. In the interim, a look back at the validity of the various assessments conducted in the past 12 years can place in perspective the state of the art of real-gas effects on static aerodynamic stability and trim characteristics of current and future space transportation systems. This paper will summarize the preflight attempts to access real-gas effects on orbiter entry aerodynamics.

SYMBOLS AND ABBREVIATIONS

C_∞ Chapman-Rubesin viscosity coefficient evaluated in the free stream based on wall conditions, $\frac{\mu_\infty}{\mu_w}\frac{T_w}{T_\infty}$

C'_∞ Chapman-Rubesin viscosity coefficient evaluated in the free stream based on reference temperature conditions, $\frac{\mu_\infty}{\mu'}\frac{T'}{T_\infty}$

C'_l Chapman-Rubesin viscosity coefficient evaluated at local conditions based on reference temperature conditions, $\frac{\mu_l}{\mu'}\frac{T'}{T_l}$

C_A axial-force coefficient, $\frac{\text{axial force}}{q_\infty S}$

C_{A,q_l} axial-force coefficient based on local conditions, axial force/$q_l S$

C_D drag coefficient, drag/$q_\infty S$

$C_{D,L^2(\min)}$ minimum-drag coefficient referenced to length, $\frac{\text{minimum drag}}{q_\infty L^2}$

$C_{D,V}$ viscous-drag coefficient, viscous drag/$q_\infty S$

C_L lift coefficient, lift/$q_\infty S$

C_m pitching-moment coefficient, pitching moment/$q_\infty SL$

C_{m,q_l} pitching-moment coefficient referenced to local dynamic pressure conditions, pitching moment/$q_l SL$

C_N normal-force coefficient, normal force/$q_\infty S$

C_{N,q_l} normal-force coefficient based on local dynamic pressure conditions, normal force/$q_l S$

C_p pressure coefficient, $\frac{p-p_\infty}{q_\infty}$

c_f skin friction coefficient

L/D lift-to-drag ratio, C_L/C_D

L reference length

M_∞ freestream Mach number

M_l local Mach number

p pressure

p_∞ freestream static pressure

q_∞ freestream dynamic pressure

q_l local dynamic pressure

R_∞ freestream Reynolds number, $\frac{\rho_\infty V_\infty L}{\mu_\infty}$

R_l local Reynolds number, $\frac{\rho_l V_l L}{\mu_l}$

R_n nose radius

S reference area

T_w wall temperature

T_∞ freestream temperature

T' reference temperature

V velocity

$\bar{v}_\infty$ slip parameter evaluated at freestream conditions based on wall temperature, $\frac{M_\infty\sqrt{C_\infty}}{\sqrt{R_\infty}}$

$\bar{v}'_\infty$ slip parameter evaluated at freestream conditions, $\frac{M_\infty\sqrt{C'_\infty}}{\sqrt{R_\infty}}$

$\bar{v}'_l$ slip parameter evaluated at local conditions based on reference temperature, $\frac{M_l\sqrt{C'_l}}{\sqrt{R_l}}$

X spanwise coordinate measured from centerline

Z axial coordinate measured from nose

δ_{BF} body flap deflection angle, deg

μ	viscosity
ρ	density
$\bar{\chi}'_\infty$	viscous interaction parameter evaluated at freestream conditions based on reference temperature, $\frac{M_\infty^3 \sqrt{C'_\infty}}{\sqrt{R_\infty}}$

Abbreviations:

ADDB	Aerodynamic Design Data Book (refs. 14, 27, 38, 39)
AEDC	Arnold Engineering Development Center
ARC	Ames Research Center
CALSPAN	Arvin Calspan Advanced Technology Center
JSC	Johnson Space Center
LA46,0A20C, etc.	Shuttle wind-tunnel tests
LaRC	Langley Research Center
LTV	Ling Tempco Vaught Corporation
MDB	Minimum Drag Body
NSWC	Naval Surface Weapons Center

REAL-GAS/HIGH-ALTITUDE/LOW-DENSITY EFFECTS

The state of the art analysis of real-gas effects in the sixties was adequately depicted by Nagel and Thomas[1]. This treatment places emphasis on heating and pressure distributions; hence simulation capability was measured in terms of Mach number and velocity (or total enthalpy). Stagnation point simulation was judged insensitive to Mach numbers in excess of 8-10, but no mention was made of the importance of stagnation point density ratio. Ground facilities were judged incapable of simulating real-gas effects over an entire configuration and were judged adequate only to about 10,000 fps velocity. These observations were based on flow analysis about body shapes amenable to reliable calculation (sharp and blunt delta wings, sharp leading edge flat plates with trailing-edge flaps, etc.), and overall integrated aerodynamics were not considered.

During the same pre-Shuttle time frame, NASA and the Air Force were testing entry shapes classed according to trimmed L/D capability and considering ways to correlate the aerodynamic characteristics across large Mach number and Reynolds number ranges as a means of extrapolating ground facility data to flight. Whitfield and Griffith[2] studying viscous drag effects on blunted slender cones postulated using Tsien's[3] "slip parameter," $\bar{V} \sim M(R)^{-1/2}$, to correlate viscous drag and performance (L/D). These authors, perhaps noting the similarity to the hypersonic viscous interaction parameter of Lees and Probstein[4] ($\bar{\chi} \sim M^3(R)^{-1/2}$) referred to $\bar{V}$ as the hypersonic viscous parameter. Sieron[5], Bertram[6-8], and others across the

aerospace community were examining $\bar{\chi}$, $\bar{V}$, and a host of other parameters to correlate Mach number, Reynolds number, and temperature ratio effects upon skin friction, boundary layer transition, local pressure and heating, and aerodynamic characteristics. The high Mach number low-density (low Reynolds number) regime characterized by these studies is the same regime where real-gas dynamics occur in flight. Therefore, many people, including the authors, have some difficulty distinguishing between low-density and real-gas effects. When the Shuttle was born in the late sixties, researchers were calculating real-gas effects on simple shapes and correlating ideal-gas ground facility data on more complicated shapes with the hope of using both techniques to get a focused view of real-gas aerodynamics.

ILRV/PHASE B-C SHUTTLE

Early Shuttle activity (entitled "Integral Launch and Reentry Vehicle Studies") involved widely diverse configurations (straight wing, delta wing, lifting bodies, etc.) and concepts (2 stage, stage and a half, triamese, etc.) with specifications such as gross lift-off weight, payload size, staging velocity, and cross range as open issues. Therefore, gray areas such as low-density, real-gas, viscous-dominated flight conditions received little attention. Assessment of these various configurations, however, required an intensive wind tunnel test program. Tests were conducted across the entire continuum flight range for both ascent and entry (including hypersonic) conditions[9,10].

By mid-1971, economic factors were beginning to drive the Shuttle concept toward the eventual choice of a double-delta orbiter with an external fuel tank using solid-rocket boosters. Researchers were able to direct their efforts to using the generated data and the existing technology base from the 60's to investigate issues such as low-density effects and correlation parameters.

In a treatment of the "Operational Aspects of Shuttle", Holloway[11] discussed the high-altitude effects on entry operations. The assumed area of concern is shown in figure 1 to be for $\bar{V}'_\infty > 0.007$ which, for the assumed trajectory, occurred at an altitude of 240,000 ft. For $\bar{V}'_\infty < 0.007$, aerodynamic evaluations being conducted in ground facilities were believed sufficient. Emphasis was, therefore, placed where the behavior of aerodynamic characteristics was and still is relatively uncertain. Past work indicated that serious performance degradation can occur in this region. Therefore, initial estimates of the high-altitude aerodynamics were made by applying the Hypersonic Arbitrary-Body Program[12] to the phase B North American 134D orbiter (figure 2). As indicated on the figure, various combinations of viscous and inviscid analytical techniques were used to verify the numerical model against the wind tunnel data base and then to calculate the high-altitude effects where no data existed. Figure 3 indicates the performance degradation and trim changes that were predicted with these methods for conditions from M=6 at 120,000 ft. altitude ($\bar{V}'_\infty$=0.0007) to M=25 at 400,000 ft. altitude (free-molecular flow). A point of interest is that, excluding the free-molecular region, trim angle of attack variation is only about 5° and the sense of the variation is toward nose-up pitch going from M=6 and h=120,000 ft. to M=22 and h=300,000 ft. ($\bar{V}'_\infty$=0.017). With this analysis as a quantifying guide to high-altitude degradation of aerodynamic characteristics, an extremely conservative model was formulated for trajectory analysis purposes. The results indicated that these effects would not have significant impact. The primary cause of concern was the lack of knowledge concerning this region[11].

By the 1972-1973 time frame, the program had moved in the final design-procurement cycle. Love[13] in his 1973 von Karman lecture on "Advanced Technology

and the Space Shuttle" reaffirmed the indicated usefulness of $\bar{V}'_\infty$ as a reliable guide to aerodynamic coefficient degradation because of high-altitude effects using examples from the HL-10 experience and general hypersonic body shaping research programs of the 60's. He stated that "prudent application of correlation techniques can be beneficial in defining hypersonic aerodynamics."

DEVELOPMENT OF THE AERODYNAMIC DESIGN DATA BOOK AND ESTABLISHMENT OF THE AD HOC PANEL ON HYPERSONIC AERODYNAMICS

Through 1973 a fairly large aerodynamic data base was being generated from an extensive wind tunnel test program being conducted by NASA and Rockwell International. The contractor used this data base to develop an Aerodynamic Design Data Book (ADDB)[14] representative of the orbiter's aerodynamic characteristics across the speed range. This activity was monitored closely by the NASA-JSC Orbiter Aerodynamics manager through a system of periodic reviews and critiques by the various NASA Centers and contractors. Differences of opinion were expressed in writing in a "Review Item Disposition" (RID), and over a period of days a negotiated position on the data book was reached. Real-gas and viscous-interaction effects were treated in this process.

An early '73 ADDB[14] used $\bar{V} \approx M(R)^{-1/2}$ as a correlation for high-altitude viscous effects. After a review at LaRC, a recommendation was made that $\bar{V}'_\infty = M_\infty (C'_\infty / R_\infty)^{1/2}$ be used based on results of the general hypersonic body shaping work presented in reference 13. This work, summarized in figure 4 (fig. 17, ref. 13) showed clearly the importance of utilizing correlation parameters in their defined entirety and not approximations thereof. For example, in figure 4, drag results for a series of n-power bodies (radius=length^n) and a classical minimum drag body (MDB) are presented versus $M(R)^{-1/2}$ and $\bar{V}'_\infty$. The open flagged symbols are experimental results for M=10.3 in air at one test condition. The open symbols are experimental results in helium at $M \approx 20$ for a range of Reynolds numbers, and theoretical inviscid calculations are indicated by the closed symbols at $M(R)^{-1/2} = \bar{V}'_\infty = 0$. It is easily seen that whereas $M(R)^{-1/2}$ does not correlate the data, $\bar{V}'_\infty$ does. It should be noted that $C'_\infty \approx 1$ for the air data, $\bar{V}'_\infty \approx 0.008 \approx M(R)^{1/2}$. Accordingly, researchers in air ground facilities had used this simplification for years. This assumption negates the correlation capability of the parameter when a wide range of free-stream conditions, including different test gases as well as free-flight conditions, is considered.

By investigating the variation of C'_∞ (fig. 5) for such a range of conditions, one sees that for γ=1.4 facilities (air and nitrogen) and M=6 → 20, C'_∞ is greater than 0.7; but for the same Mach number variation and characteristic helium tunnel and flight conditions, C'_∞ varies from 0.2 at M=20 to 0.8 at M=6. Admittedly, this is not a rigorous treatment, but it is a clear indication of the importance of including the Chapman-Rubesin viscosity coefficient (C'_∞) as an integral part of the $\bar{V}'_\infty$ correlation parameter.

Love[13] had cautioned that correlation parameters such as $\bar{V}'_\infty$ may not necessarily apply to all vehicles. Therefore, while these perturbations on the ADDB were being recommended, it was recognized that parameters derived from laminar boundary layer viscous-dominated flows were being used in low-density real-gas regimes. Amplifying the questionable use of continuum parameters were data obtained in impulse facilities which indicate large center-of-pressure changes on the orbiter for M=20 low-density conditions. A reassessment of correlation parameters was requested by the aerodynamics manager. Additionally, in late '73 the Shuttle Progam

Office requested that Langley accept an action item to examine Mach/Reynolds number effects for $5 \geq M \geq 20$ and (early '74) participate in an Ad Hoc Working Group for Orbiter Hypersonic Aerodynamics to determine real-gas and viscous-interaction effects. These actions initiated agency-wide activity to resolve the issue of real-gas effects. At Langley, the action item and working group activities shared similar problem areas; therefore, both were included in one study of Mach/Reynolds number, inviscid/viscous, ideal/real-gas effects on Shuttle orbiter aerodynamics.

Probstein's weak interaction theory[15] was utilized early in the study to evaluate ideal-gas viscous effects and correlation parameters on several cones for a wide range of test and flight conditions (M_∞=8 to 30, $R_{\infty,l}$=0.001 × 10^6 to 68 × 10^6, and γ=1.4 and 1.667). The conditions selected were representative of facilities of interest for Shuttle orbiter testing at high Mach numbers (Calspan; LaRC M=19, N_2; and LaRC M=20, He) and a current design trajectory (8922). Probstein's theory was selected for this initial effort because it is based on a tangent-cone flow model (verified as a good approximation for orbiter lower surface flow along the centerline[16]), the inviscid and viscous drag components are easily separated, and a large number of variables could be included (M, R, T_w, γ, etc.). Although several cone angles were evaluated, the present results (figure 6) are for a 15° cone. The axial-force coefficients shown were determined by dividing the total cone axial force by surface area, applying this unit axial force over the lower surface of the orbiter, and dividing by the orbiter reference area and free-stream dynamic pressure. The magnitude of the calculated coefficients corresponds to that of an orbiter in hypersonic tunnels at α=30°. The results have been plotted versus several correlation parameters.

The classical hypersonic viscous interaction parameter, $\bar{\chi}'_\infty = M_\infty^3 \sqrt{C'_\infty} / \sqrt{R_{\infty,L}}$, is normally used to correlate local effects (pressure, heating, skin friction, etc.). When the total integrated axial-force coefficient is presented as a function of $\bar{\chi}'_\infty$, a separate trend appears to be established for each facility and for the entry condition. The large variation indicated for Calspan conditions can be attributed to the extreme range of operating conditions and the use of different nozzles to obtain these conditions.

The slip parameter, $\bar{V}_\infty = M_\infty \sqrt{C_\infty} / \sqrt{R_\infty}$, does correlate results for the wind-tunnel test conditions, but for entry flight conditions, a different trend is established. The Chapman-Rubesin viscosity coefficient, C_∞, is nearly 1.0 in most air facilities. Therefore, in many instances, it is assumed to be 1.0; and data are then correlated by $M_\infty / \sqrt{R_\infty}$. The present results presented in this manner show the same trend as obtained with $\bar{V}_\infty$. Ground facility results establish one trend and entry conditions another. The parameter $\bar{V}'_\infty = M_\infty \sqrt{C'_\infty} / \sqrt{R_\infty}$, where C'_∞ is based on a reference temperature, T' (using Monoghan's reference conditions), correlates the present results for both ground facility and entry conditions (ideal gas). Therefore, for this simplistic analysis, $\bar{V}'_\infty$ appeared capable of correlating hypersonic data for wind-tunnel and flight conditions.

The Ad Hoc Working Group concentrated its efforts on resolving the paradox of using continuum viscous parameters to correlate real-gas aerodynamic characteristics. The general lack of knowledge about combined viscous interaction and real-gas effects produced an environment of no practical means, either experimental or analytical, to study these combined effects on the complex orbiter shape at high angles of attack. A wide variety of parameters were considered using both free-stream and local conditions without much success. A complete real-gas/viscous code for the Shuttle geometry (and α) did not exist. Therefore, a three-part study (fig. 7) using existing analytical tools and experimental data was initiated to

define Shuttle trim and control boundaries in the hypersonic regime. The initial step was to use calculated flow fields on 30° and 40° blunted cones[17,18] and to apply the results to the lower half only (representative of orbiter at entry angles of attack) for conditions that simulate entry flight and several ground facilities. The results were used to determine the magnitude of real/ideal and viscous/inviscid effects and to evaluate correlation parameters. The second step involved an extensive wind tunnel test program that covered a range of hypersonic Mach numbers, Reynolds numbers, and ratios of specific heats to simulate the real-gas, viscous flow on the orbiter shape in ideal-gas ground facilities. Correlation parameters identified by the cone studies were applied to the results obtained from these tests and the available results from all of the other hypersonic tests conducted in the Shuttle program. The third step utilized an inviscid analytical program, developed by Grumman for NASA in support of the Shuttle program, to determine the magnitudes of inviscid real- and ideal-gas effects on complex 3-D (Shuttle-type) configurations.

Figure 8 shows the flow models considered for the viscous, real-gas analytical calculations. For the Shuttle at high angles of attack, normal forces are mainly due to pressure and axial forces are mainly due to skin friction with lift, drag, and pitching moment due to a combination of the two. The contractual study (NAS1-11728) calculated complete flow fields on 30° and 40° blunted cones at α=0°. (Thus, $C_N=C_L=0$, $C_m=0$, and $C_A=C_D=f(C_p,C_f)$.) The approach adopted by the working group was to apply these existing flow fields to half cones, assuming pressure and friction on the upper surface were zero as depicted on the lower right of the figure. Thus, the flow model used consisted of a pure conical flow field over a half cone such that lift, drag, and pitching moment were a function of pressure and friction forces on the curved lower surface. The objective of this effort was to either verify the use of $\bar{V}'_\infty$ or determine parameters that would correlate the forces and moments produced by the real- and ideal-gas flow models, apply this technique to the hypersonic wind tunnel data on the orbiter, and, if successful, extrapolate to real-gas flight conditions.

In all cases, inviscid flow fields were calculated first and then partially coupled to viscous flow fields by iterating on the boundary-layer momentum flux (iterated on the boundary layer but not the shock layer). Inviscid ideal-gas and equilibrium flow fields were calculated by the inverse blunt-body solution matched to the method of characteristics (fig. 9). These in turn were partially coupled to viscous codes developed by Cebeci[19,20] for the ideal-gas cases and a modification of Blottner's nonequilibrium code[21] for the equilibrium-flow cases. Finite rate flow fields were determined by the methods of Curtis and Strom[22] for the inviscid properties and Blottner for the viscous solutions. All codes were modified somewhat for reasons of economy, ease of handling, system interface, and so forth[17,18].

The analytical models for producing flight results were 30° and 40° slightly blunted cones, (R_n/L=0.2) with 100 ft. slant heights so relative surface lengths would correspond to the orbiter. Flight conditions included altitudes from 210,000 ft. to 275,000 ft. for both equilibrium and nonequilibrium chemistry. These results were compared to ideal-gas/viscous calculations performed on 6-inch cones for four wind tunnel test conditions covering a Mach number range of 6.2 to 20 and ratios of specific heats (γ) from 1.12 to 1.667. Note that although discrete points are depicted, these results are theoretical calculations at specific conditions.

Initial comparisons of the viscous component of drag (fig. 10a) indicated that $\bar{V}'_\infty$ correlates all the data except those calculated for hypersonic nitrogen wind tunnel conditions. A continuing dialog within the working group had discussed the use of local parameters for real-gas data correlation. Figure 10b shows that

$\bar{V}'_l$ does indeed correlate the viscous drag. Because previous correlations had indicated $\bar{V}'_\infty$ could correlate the viscous force component in ideal-gas conditions (i.e. nitrogen tunnel) the data of figure 10 was reexamined. It was discovered the original study used the classical Sutherland law for the nitrogen temperature-viscosity relationship. Bertram[23] recommended Keyes'[24,25] T-μ (temperature-viscosity) relationship as providing a better fit to the existing T-μ data base over a wide temperature range such as encountered in nitrogen tunnels. Keyes' relationship had been used in the earlier correlations (fig. 6), and, when applied to calculate $\bar{V}'_\infty$ for the data of figure 10, the correlation with $\bar{V}'_\infty$ and $\bar{V}'_l$ became identical (fig. 11). The effort under the existing contract was concluded and is summarized in reference 26. A new contract was extended to McDonald Douglas (NAS1-13868) to recompute the flow fields for the nitrogen tunnel and air tunnel conditions using state-of-the-art transport properties and to extend the calculations to 300,000 ft. altitude. The results are summarized in figures 11-14 using selected results to emphasize significant conclusions.

The viscous component of forces and moments was correlated by both $\bar{V}'_\infty$ and $\bar{V}'_l$ as shown by figure 11. However, the pressure component accounted for the majority of the total force and dominated the correlation as shown in figure 12 for both the 30° and 40° cone calculations. The calculated value of C_D for wind tunnel conditions correlated with $\bar{V}'_\infty$, and C_D calculated for flight conditions (nonequilibrium and equilibrium) correlated with $\bar{V}'_\infty$. However, wind tunnel calculations and real-gas flight calculations did not correlate with each other. Using local conditions in the hypersonic viscous parameter $(\bar{V}'_l)$ produced the same results (fig. 13).

Variable γ because of real-gas chemistry has a strong effect on shock location and stagnation-point standoff distance for blunt bodies, which greatly affects local flow conditions. Hunt[26] postulated that for these reasons force and moment coefficients based on local dynamic pressure should correlate with local Mach number. The present calculated results for these two 30° and 40° half cones indicated relatively good correlations of lift and drag using this approach. There was a small amount of scatter in pitch (fig. 14). When wind tunnel results were treated in this fashion, as will be subsequently shown, a local Reynolds number effect was apparent. The correlations for the cones were re-examined, and this local Reynolds number effect was indicated (shown by the points with the numbers indicating local Reynolds number in thousands). This assessment indicated that, for local Reynolds numbers greater than 150,000, coefficients based on local dynamic pressure will correlate with local Mach number for 30° and 40° half cones.

Orbiter Tests Analyzed

As the final design phase of the Shuttle continued, a decision was made to construct high-fidelity wind tunnel models for the most relevant wind tunnel tests for preflight data book verification. Because funds were limited, all model requests could not be met. Therefore, high fidelity 2-percent and 5-percent models were constructed to produce accurate wind tunnel data for supersonic to landing conditions. The decision was made to utilize data on the existing 140A/B and 140C configurations to supplement the hypersonic analysis. These data covered $M \approx 5 \rightarrow 20$ in a variety of facilities (figure 15) both within and outside NASA to cover a range of parameters of interest including $\gamma = 1.12 \rightarrow 1.667$.

Since real-gas viscous calculations indicated correlations based on local M and q might relate wind tunnel data to flight results, attempts were made to apply this correlation to the hypersonic data base. Tangent-cone relationships[15] (with the

small-disturbance approximations removed) were used to determine local conditions (M_l, R_l, $\bar{V}'_l$, etc.). Figure 16 presents the results for the 140A/B and 140C models with zero control deflections. Extensive scatter is seen, particularly in the axial-force coefficient. Examination of the data indicated that tests in which large viscous interaction effects occurred contributed to the scatter. When the data were grouped according to local Reynolds number, a local Reynolds number effect was indicated (fig. 17). For a fairly large range (R_l=2 × 10^6 - 40 × 10^6) little local Reynolds number effect is indicated. As the local Reynolds numbers decrease (0.5 × 10^6 → 1 × 10^6), a shift in the trend is indicated. The lower values of Reynolds number that indicate large viscous-interaction effects did not cover a sufficient range in local Mach number to adequately determine trends. As previously mentioned, the analytical results of figure 14 were re-examined for local Reynolds number effects and both the lowest density wind tunnel results and flight results indicated possible local Reynolds number effects for values of R_l less than about 10^6.

In conjunction with the working group activity, Langley analyzed Mach and Reynolds number effects for $M \geq 5$ by using the continuum parameters M_∞, R_∞, and $\bar{V}'_\infty$. The experimental longitudinal aerodynamic characteristics were correlated with $\bar{V}'_\infty$ at α=20°, 30°, and 40° for control settings of δ_e/δ_{BF}=-40°/-11.7°, 0°/0°, and 10°/16.3°. The selected results presented (figs. 18-21) indicated the trends obtained in this portion of the study. The open symbols represent data on 0.010 and 0.015 scale 140A/B orbiters, and the shaded symbols represent data for a single 0.004-scale 140C orbiter mounted on a single balance-sting combination in five different facilities.

In general, the C_A (fig. 18) results remain within a band of approximately ±0.005 in C_A (exception, not shown for δ_e/δ_{BF} 10°/16.3° at α=40°, has a width of ±0.01) and exhibits a definite trend with $\bar{V}'_\infty$. Over a range of $\bar{V}'_\infty$ from 0.005 to 0.07, the level of C_A approximately doubles which reflects the impact of viscous interaction effects. Compared with the magnitude of these viscous effects, the results obtained over a range of the ratios of specific heats (γ=1.667 for helium, 1.4 for air and nitrogen, and 1.12 for CF_4) indicate little effect on C_A.

The C_N results (fig. 19) generally remain within a band of ±0.03 and are relatively constant over the $\bar{V}'_\infty$ range of interest. Also, the relatively large change in γ has little effect on C_N.

The C_m results (fig. 20) do not correlate as well with $\bar{V}'_\infty$, and the trends are not as well defined. The width of the data band is on the order of ±0.007 to ±0.01, and the results obtained over the γ range generally remain within this band.

Figure 21 is an attempt to summarize results of this extensive data base. In general, the data scatter appears to be bounded as previously mentioned. Ground facility tests with γ variations (1.667 → 1.12), exceeding those encountered in flight, produced data that remained within the overall scatter band. Finally, the ADDB[27] at the time was a line fairing that did not necessarily represent the overall data pattern, and recommendations were made to modify the data book to more representative values.

Real/Ideal-Gas Inviscid Calculations

Inviscid calculations on simple shapes were being continually utilized to provide some insight to real- vs ideal-gas effects. For example, figure 22

(blunt-body method of characteristics) indicates varying M from 6-20 has little effect on pressure coefficient for blunted 30° cones. The same results presented to show γ effects at constant Mach number (fig. 23) show higher pressure at the nose and lower pressure on the afterbody for γ varying from 1.667 → 1.12. For a constant distribution of planform area, a nose-up pitch for decreasing γ is indicated.

A more rigorous analysis was utilized in the final part of the working group's three-part study. This analysis utilized the most advanced codes (available) to indicate the magnitude of inviscid real/ideal gas effects on Shuttle-like configurations (fig. 24). Calculations were performed on a modified 140C Shuttle orbiter at α=25° using the Supersonic Three-Dimensional External Inviscid (STEIN) flow-field code to determine the effect of real gas on aerodynamics.[28,28] Two ideal-gas conditions (γ=1.4, M_∞= 10.29 and γ=1.12, M_∞=26.1) and one real-gas condition (equilibrium air, M_∞=26.1, and altitude=240,000 ft.) were calculated. The geometry of the orbiter was modified by increasing the wing sweep to 55° to eliminate a pocket of subsonic flow near the wing tip which would have prevented completion of the calculations. Pressure distributions, shock shapes, and aerodynamic coefficients were compared to quantify inviscid real-gas effects. The results are summarized in figures 25-27.

The pressure coefficients in the windward symmetry plane for the γ=1.4 and the equilibrium air cases are shown in figure 25. In the recompression region (Z=360-525 in), the pressure coefficients are higher for the equilibrium air, but in all other regions--and notably in the strong expansion region toward the rear of the vehicle (Z>1050 in)--the pressure coefficients are lower for equilibrium air. Additional unpublished results indicate that there is little Mach number effect in the above results as was shown on blunt cones (fig. 22).

Integrating these results in a longitudinal manner placed in perspective where differences in pressure distribution affected pitching moment (figs. 26 and 27). The increased C_p at the nose when γ decreased from 1.4 to 1.12 affected pitch little. Pitch differences were primarily due to reduced C_p near the rear of the body with calculations for assumed equilibrium air having the least afterbody C_p and the most indicated nose-up pitch. A direct comparison of the integrated aerodynamic coefficients (fig. 27) for the STEIN code with ideal-gas flow modeled by using low γ (1.12) indicates approximately the same results as using equilibrium air at flight conditions. The differences between M=10.3 ideal-air wind tunnel conditions and equilibrium-air entry conditions produced reductions in force coefficients on the order of 10 percent and a nose-up pitching-moment change of 0.023. Axial force coefficient experienced virtually no change as should be expected. Two important points should be made at this time. First, these are inviscid calculations, and viscous effects will cause a nose-down pitch. Second, the indicated γ and/or real-gas effects were on the same order as the repeatability and/or scatter in the data band supporting the data book. Therefore, trim and control boundaries were established on the data base with real-gas effects considered ill defined but indicated to be on the same order as the data scatter.

ADDB for the Hypersonic Regime

The Ad Hoc Working Group was dissolved after exercising all available tools to resolve the issue of real-gas effects on orbiter aerodynamics with the main question still unanswered. Many issues were resolved such as the importance of utilizing the correct form of correlation parameters, and state-of-the-art transport properties of gases. Gamma effects were indicated to be within the wind tunnel data base scatter

by both experimental data and real-gas inviscid calculations. The ADDB had been modified to be more representative of these results. Recommendations were made to upgrade real-gas codes so the actual Shuttle geometry and angle of attack could be treated analytically and to obtain additional hypersonic wind tunnel data at flight Reynolds numbers. In the interim, $\bar{V}'_\infty$ correlations with an uncertainty band for data scatter should still be used. In addition, the personnel involved (in the Ad Hoc Working Group) were requested to monitor the continuing work and interact with the program office and prime contractor in maintaining a current data book on real-gas effects.

As previously mentioned, funding limitations prevented the fabrication of high-fidelity models for hypersonic testing. However, the 2-percent "hi-fi" model was not too large for testing in the Naval Surface Weapons Center (NSWC) Tunnel 9. This facility is capable of matching flight Reynolds number with the 2-percent orbiter at M=13.5 and has sufficient operational range to produce $\bar{V}'_\infty$=0.01 data. Therefore, tests were recommended to produce what was expected to be the data most representative of high Mach number continuum flight conditions and an anchor point for high-altitude estimates.

These tests were conducted in the spring of '78 and integrated into the data book with AEDC Tunnels A and B[30] data on the same 2-percent model and CALSPAN Hypersonic Shock Tunnel[31] tests on a 1-percent model. The results on the basic aerodynamics are shown in figures 28-30. Overall, normal-force coefficient was presumed to be only a function of α and independent of Mach number and $\bar{V}'_\infty$ for $M \geq 10$ (fig. 28). In instances of high $\bar{V}'_\infty$, where the data book might not represent the data, the total data base was considered, and engineering judgment was applied.

Axial-force coefficient was considered constant with Mach for $10 < M < 20$ and a function of α only (fig. 29). For $\bar{V}'_\infty \geq 0.01$, C_A was considered a function of $\bar{V}'_\infty$ and α, with the CALSPAN data, experience from past correlations, and engineering judgment guiding the functional relationship. Pitching-moment coefficient was considered a function of α only for $M \geq 10$ (fig. 30). Langley researchers conducted an extensive analysis of the AEDC and NSWC data in the continuum regime which indicated control effectiveness was additive and that increments added to the basic aerodynamics produced agreement with tests of combined control deflections. For the CALSPAN data, various combinations of control setting were not tested, and data repeatability showed the characteristic scatter generally attributed to impulse facilities. Therefore, a similar analysis was not possible. However, body flap extremes for zero elevons, elevon extremes for zero body flap, and full maximum controls were tested.

Figure 31 shows an example of the application of the CALSPAN data to provide data-book values. Pitching-moment coefficient is presented for the various control combinations at α=40°. The solid lines for δ_{BF}=0° and δ_e=-40°, 0°, and 12.35°, and for δ_e=0 and δ_{BF}=-11.7 and -16.3 represent basic fairings of the data including interpolation from one set to another. The solid lines for the bottom portion of the figure having combined controls are not fairings but the sum of the fairings in the top two portions. Many iterations on this procedure were taken at each angle of attack before curves considered representative of the total data base were produced. Figure 32 shows the final result in the form of pitching-moment coefficient increment due to body-flap deflection as a function of α and $\bar{V}'_\infty$. These were applied to the basic stability levels for zero control to produce the ADDB for combined controls in the real-gas regime.

Approximately 10 years of work by a host of engineers using state of the art experimental and analytical techniques were applied to estimate orbiter aerodynamics

in the hypersonic real- and ideal-gas regimes. As the first flight approached, real-gas effects producing variable shock-density ratios (therefore variable γ) appeared to fall within the scatter of the wind tunnel data base and were accounted for by acceptable tolerances and variations established by the program office. Systematic variations of the aerodynamics in the high-altitude real-gas regime were accounted for by correlations with the viscous/slip parameter $\bar{V}'_\infty$ based on the best available model of free-stream conditions (atmosphere).

Comparison to Flight

Substantial analyses of Shuttle flight data have been conducted for the past 2 years, and this activity will continue for some time as the flight data base grows and the Shuttle orbiter experiments program (OEX) produces more flight results. In addition, analytical techniques have been recently developed at LaRC to treat the orbiter inviscid real-gas flow field and integrate the results to produce real-gas performance estimates. An evaluation of the adequacy of preflight predictions of real-gas effects, however, depends upon results of the first 5 flights. Young et al.[32] concluded that performance predictions were adequate throughout the speed range with forces generally predicted within 10 percent in the hypersonic regime, but trim (or basic pitching moment) predictions were less than satisfactory above Mach 10. For example, aerodynamics in the ADDB indicated a 7.5 degree deflection of the body flap would be required for trim for the center-of-gravity location and vehicle configuration for STS-1. In reality, the body flap had to deflect to much larger values ($\delta_{BF} \approx 16°$) to maintain trim at the proper angle of attack (α=40°). This "hypersonic anomaly" is shown in figure 33 by comparing body flap deflections from STS-1 to the nominal ADDB value. For Mach numbers above 18, δ_{BF} was generally greater than 15. As the vehicle decelerated below M=18, the required trim deflection gradually decreased until M=8 where flight and ADDB values agreed.

In general, Shuttle flight data have been analyzed by spotting wind tunnel points on the flight data. For the present study the opposite approach of spotting flight values on specific wind tunnel data produced some interesting results. Initial comparisons were made with preliminary flight data, an assumed 67 percent c.g. location, and wind tunnel control settings. These rough comparisons implied some low density wind tunnel data indicated large body flap deflections might be required for trim in the real-gas regime.

These comparisons were re-examined after STS-1 final pass flight data was available by transferring the wind tunnel results to the best estimated c.g. (66.55 percent L) and using linear interpretation of the wind tunnel data to produce estimates of the aerodynamic coefficients vs α at the exact flight control settings. Three particular tunnel tests (LA 79, 0A109, 0A171)[33-35] were used for comparison. The results (fig. 34) indicated there was good agreement between wind tunnel data and flight for axial-force coefficient and lift-drag ratio. Lift, drag, and normal-force coefficients were overpredicted by about 10 percent (fig. 34). These results were consistent for all three sets of wind tunnel data. The interpolated wind tunnel data for pitching-moment coefficient in helium at M=20 (γ=1.667, 0A109),[33] indicated flight control deflections would produce trim at about α=20° with a pitch decrement between wind tunnel and flight of about +0.0235. The low density results ($\bar{V}'_\infty$ = 0.035/LA79)[34] in nitrogen indicated flight controls would trim the vehicle at α=35° with a pitch decrement of +0.014 at actual flight trim conditions. But the data projected to be the most accurate before the flight (NSWC 9, 0A171)[35] indicated flight controls would not trim the vehicle for α=20° → 50° and showed a pitch decrement of +0.0302 at flight trim conditions.

These comparisons for particular wind tunnel tests could be fortuitous, but examination based on knowledge of the origin of preflight estimates and results from STS-1 support the following analysis. Preflight predictions indicated boundary layer transition would occur on the orbiter near Mach 16. STS-1 heating measurements indicated boundary layer transition did not occur until Mach numbers on the order of 10 were reached. Therefore, for most of the hypersonic portion of entry the body flap was immersed in a laminar boundary layer. As previously mentioned, the Mach 13.5 tests were conducted in NSWC Tunnel 9 for the express purpose of producing an anchor point for the hypersonic continuum data book because flight Reynolds numbers could be obtained and control effectiveness data in a turbulent boundary layer would be produced. As has been shown, these data indicated 7.5 degrees deflection on the body flap were required for trim.

Theoretical analysis (fig. 27) had previously indicated nose-up pitch of 0.023 to 0.025 for γ variations from 1.4 to flight. The ideal-gas helium data (M=20, γ=1.667, $\bar{V}'_\infty \approx 0.008$, laminar boundary layer) showed the same degree of nose-up pitch for a wider range of γ. The ideal-gas low-density nitrogen data (M=18, γ=1.4, $\bar{V}'_\infty \approx 0.035$, laminar boundary layer) produced trim angles closest to flight values with pitch differences within data accuracy. Therefore, this simplified analysis based on only 3 data points postulates that, although real-gas effects account for some of the "hypersonic anomaly" in terms of a small nose pitch as indicated by preflight estimates, about 50 percent is due to reduced control effectiveness because the boundary layer was laminar instead of turbulent as expected.

After STS-1, a concerted effort was made to upgrade real-gas computer codes as a flight data analysis tool. A preliminary version of the HALIS code[36] being developed at Langley was used in an analysis of STS-3 pressure measurements. Figure 35 compares an orbiter windward centerline pressure distribution computed by HALIS (assuming γ=1.4 and γ=1.18) with pressure measurements from STS-3. The HALIS pressure distributions were used as initial conditions for computing 2-D oblique shock jump conditions to define theoretical pressure levels for a 10° body flap (STS-3 conditions). The pressure rise is different for γ=1.4 and γ=1.18 conditions but the nondimensional pressure level on the body flap appears the same for both and is in proximity with the flight levels. This analysis indicates pitch differences are due to pressure levels ahead of the body flap in the expansion region as has been previously stated. This analysis is admittedly limited, but HALIS development has progressed and is presently being applied to calculate the complete real-gas inviscid flow field over the orbiter.

CONCLUDING REMARKS

Preflight estimates of the real-gas effects on the hypersonic aerodynamic characteristics of the Shuttle orbiter were based on a diverse series of research studies. Real-gas viscous calculations on simple shapes attempted to quantify real/ideal viscous/inviscid effects. The results indicated that inviscid pressure dominated the force system, and viscous correlation parameters could not relate wind tunnel data to flight values. Real-gas effects were indicated to reduce forces and moments. Inviscid calculations on winged lifting shapes indicated reduced forces and a slight nose-up pitch resulted because of real-gas effects.

Analysis of the extensive wind tunnel data base indicated viscous correlation parameters provided the most appropriate extrapolation technique for estimating flight aerodynamics. Differences in the aerodynamics produced by varying the range of ratios of specific heats, which was the only tool available for attempting to

experimentally model real-gas effects, appeared to fall within the tolerances and variations established about the ADDB derived from viscous correlations. Therefore, an extensive three-part study using state of the art techniques produced conflicting results.

Placing Shuttle real-gas aerodynamics in the context of the subject conference is somewhat preliminary; however, some lessons have been learned. First, it has been shown that correlations should be used in complete form along with state of the art transport properties of the fluid medium (flight or test gas). Second, real-gas effects do cause some nose-up pitch because of the expansion characteristics at the rear of the vehicle. However, the state of the boundary layer and its effect on control effectiveness may be a contributor to the longitudinal hypersonic trim anomaly. Third, the development of codes such as HALIS is critical to resolving these issues. However, since HALIS is an inviscid code, researchers will still have no complete model of high-altitude real-gas effects on Shuttle-like vehicles.

Five data points (five flights) do not make a data base, so the learning process continues. Hopefully, with the Shuttle returning to Earth on a fairly routine basis, sufficient data will be accumulated to complement advanced computer codes such as HALIS in upgrading the state of the art of real-gas effects on the aerodynamic stability and trim characteristics of current and future space transportation systems.

REFERENCES

1. Nagel, A. L.; and Thomas, A. C.: Analysis of the Correlation of Wind Tunnel and Ground Test Data to Flight Test Results. AIAA/NASA Flight Testing Conference in Huntsville, Ala, February 15-17, 1965.

2. Whitfield, J. D.; and Griffith, B. J.: Hypersonic Viscous Drag Effects on Blunt Slender Cones. AIAA Journal, vol. 2, no. 10, October 1964.

3. Tsien, Hsue-Shen: Superaerodynamics, Mechanics of Rarefied Gases. Journal of the Aeronautical Sciences, pp. 653-664, December 1946.

4. Lees, L.; and Probstein, R. F.: Hypersonic Viscous Flow Over a Flat Plate. Rept. No. 195, Dept. Aero. Eng., Princeton Univ., Princeton, N.J., 1952.

5. Sieron, Thomas R.; and Martinez, Conrad, Jr.: Effects and Analysis of Mach Number and Reynolds Number on Laminar Skin Friction at Hypersonic Speeds. Technical Report No. AFFDL-TR-65-5, April 1965.

6. Bertram, M. H.: Boundary Layer Displacement Effects in Air at Mach Numbers of 6.8 and 9.6. NASA TR R-22, 1959.

7. Bertram, M. H.; and Henderson, A.: Effects of Boundary Layer Displacement and Leading Edge Bluntness on Pressure Distribution, Skin Friction and Heat Transfer of Bodies at Hypersonic Speeds. NACA TN 4301, July 1958.

8. Bertram, Mitchel H.: Hypersonic Laminar Viscous Interaction Effects on the Aerodynamics of Two-Dimensional Wedge and Triangular Planform Wings. NASA TN D-3523, August 1966.

9. Space Transportation System Technical Symposium. NASA TMX 52876, vol. 1, July 1970.

10. NASA Space Shuttle Technology Conference, vol. 1, Aerothermodynamics, Configurations and Flight Mechanics. NASA TMX 2272. March 1, 1971.

11. Holloway, Paul F.: Operational Aspects of Space Shuttle. Presented at the short course High Altitude Aspects of Lifting Reentry Vehicles, Rhodes Saint-Genese, Belgium, May 24-27, 1971.

12. Gentry, A. E.: Hypersonic Arbitrary-Body Aerodynamic Computer Program. Douglas Aircraft Corporation Report 61552, April 1968.

13. Love, Eugene S.: Advanced Technology and the Space Shuttle. 10th Von Karman Lecture, AIAA Paper No. 73-31, January 1973.

14. Aerodynamic Design Data Book. Volume I - Orbiter Vehicle, Rept. No. SD72-SH-0060-1C, Rockwell International, April 1973.

15. Probstein, Ronald F.: Interacting Hypersonic Flow Over a Cone. Tech. Report AF 2798, Division of Engineering, Brown University, Providence, Rhode Island, March 1955.

16. Ashby, G. C., Jr.: Experimental Boundary Layer Edge Mach Numbers for Two Space Shuttle Orbiters at Hypersonic Speeds, NASA TN D-6574, February 1972.

17. Fivel, H. J.; Masek, R. V.; and Mockapetris, L. J.: Analytical Comparison of Hypersonic Flight and Wind Tunnel Viscous/Inviscid Flow Fields. NASA CR-2489, February 1975.

18. Fivel, H. J.; and Masek, R. V.: Analytical Comparison of Hypersonic Flight and Wind Tunnel Viscous/Inviscid Flow Fields Check Case and Users Manual. NASA CR-132359, July 1973.

19. Cebeci, T., Smith, A. M. O.; and Wang, L. D.: A Finite-Difference Method for Calculating Compressible Laminar and Turbulent Boundary Layers. McDonnell Douglas Report DAC-67131, Part I, March 1969.

20. Cebeci, T.; Smith, A. M. O.; and Mosinskis, G.: Calculation of Compressible Adiabatic Turbulent Boundary Layers. AIAA Paper No. 69-687, June 1969.

21. Blottner, F. G.: Chemical Nonequilibrium Boundary Layer. AIAA Paper No. 63-443, August 1963.

22. Curtis, J. T.; and Strom, C. R.: Computations of the Nonequilibrium Flow of a Viscous, Radiating Fluid About a Blunt Axisymmetric Body, Volume I: Equations and Results. AFFDL-TR-67-40, Vol. 1, June 1967.

23. Bertram, Mitchel H.: Comment on "Viscosity of Air." Journal of Spacecraft, page 287, vol. 4, no. 2, February 1967.

24. Keyes, F. G.: A Summary of Viscosity and Heat Conduction Data for He, A, H_2, O_2, N_2, CO, CO_2, H_2O, and Air, Trans. Am. Soc. Mech. Engrs., Vol. 73, 1951, pp. 589-596.

25. Keyes, F. G.: The Best Conductivity, Viscosity, Specific Heat and Prandtl Number for Thirteen Gases. Project Squid, Massachusetts Institute of Technology, TR 37, 1952.

26. Hunt, J. L.; Jones, R. A.; and Woods, W. C.: Investigation of Real-Gas and Viscous Effects on the Aerodynamics Characteristics of a 40° Half-Cone With Suggested Correlations for the Shuttle Orbiter. NASA TN D-8418, June 1977.

27. Aerodynamic Design Data Book. Volume I - Orbiter Vehicle. Rept. No. SD72-SH-0060-1J, Rockwell International, Dec. 1975.

28. Marconi, Frank; Salas, Manuel; and Yaeger, Larry: Development of a Computer Code for Calculating the Steady Super/Hypersonic Inviscid Flow Around Real Configurations. Volume I - Computational Technique. NASA CR-2675, 1976.

29. Marconi, Frank; and Yaeger, Larry: Development of a Computer Code for Calculating the Steady Super/Hypersonic Inviscid Flow Around Real Configurations. Volume II - Code Description. NASA CR-2676, 1976.

30. Milam, M. D.; Vaughan, J. E.; and Moser, M. M., Jr.: Results of Investigations on a 0.015 Scale 140 A/B Configure Space Shuttle Vehicle. NASA CR-134429, Jan. 1975.

31. Burrows, R.; Marroquin, J.; Rogers, C. E.; Sarver, D. A.; and Vaughan, J. E.: Wind Tunnel Test 0A113 of the 0.01 Scale Space Shuttle Orbiter Model 51-0 on the CALSPAN Hypersonic Shock Tunnel. NASA CR-141574, July 1975.

32. Young, James C.; Jones, C.; Romere, Paul O.; and Kanipe, David B.: Space Shuttle Entry Aerodynamic Comparisons of Flight, With Preflight Predictions. AIAA Paper 81-2476, Nov. 1981.

33. Hawthorne, P. J.; Sarver, D. A.; and Love, R. B.: Results of a 0.004-Scale 140C Modified Configuration Space Shuttle Vehicle Orbiter Model (74-0) in the Langley Research Center Hypersonic Helium Tunnel. NASA CR-141532, May 1975.

34. Keel, A. G., Jr.; and Knott, J.: Static-Stability Testing of the 0.004-Scale Space Shuttle Orbiter in the White Oak Mach 18 Hypervelocity Research Tunnel. Naval Surface Weapons Center, White Oak Laboratory Wind-Tunnel Report No. 109, Jan 1976.

35. Daileda, J. J.; Woods, W. C.; Ashby, G. C., Jr.; Hersey, D. W.; and McDonald, G. G.: Results of Tests Using a 0.020 Scale Model (105-0) of the Space Shuttle Vehicle Orbiter in the Naval Surface Weapons Center Hypervelocity Tunnel 9. NASA CR-151764, Oct. 1978.

36. Weilmuenster, K. James; and Hamilton, H. Harris, II: High Angle of Attack Inviscid Flow Calculations Over Shuttle Like Vehicles With Comparisons to Experimental Data. NASA TP-2103, 1983.

37. Lomax, H.; and Inouye, M.: Numerical Analysis of Flow Properties About Blunt Bodies Moving at Supersonic Speeds in an Equilibrium Gas. NASA TR-R-204, July 1964.

38. Aerodynamic Design Data Book. Vol. I - Orbiter Vehicle 102, Rept. No. SD72-SH-0060-1K, Rockwell International, Nov. 1977.

39. Aerodynamic Design Data Book. Vol. I - Orbiter Vehicle 102, Rept. No. SD72-SH-0060-1L, Rockwell International, Oct. 1978.

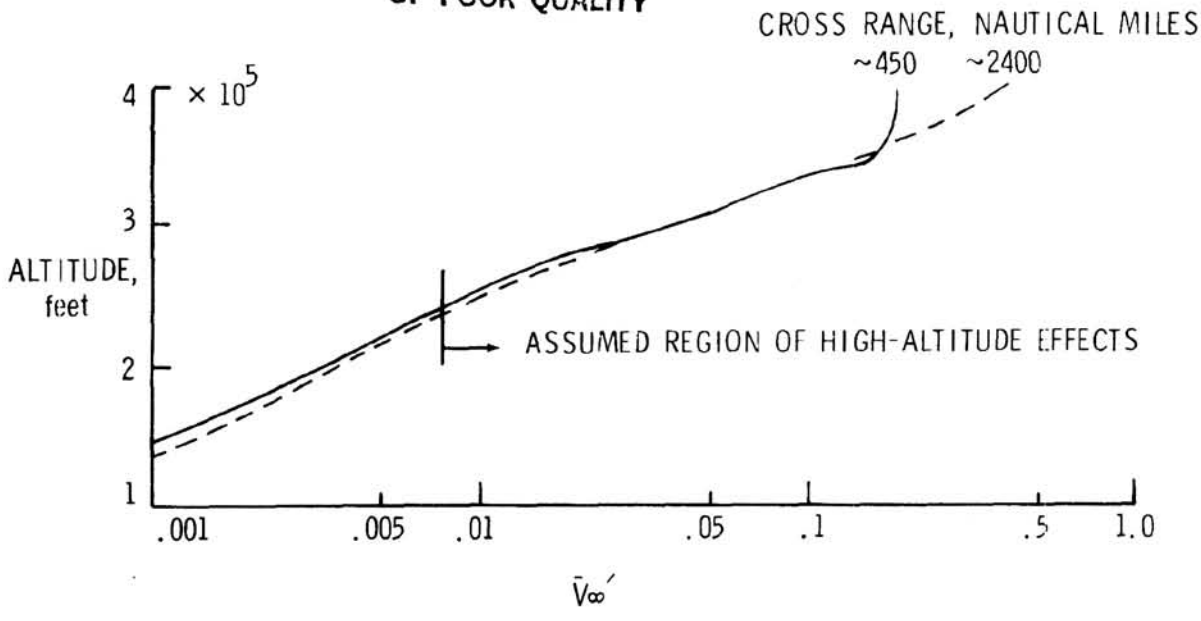

Figure 1.- Variation of correlation parameter during entry.

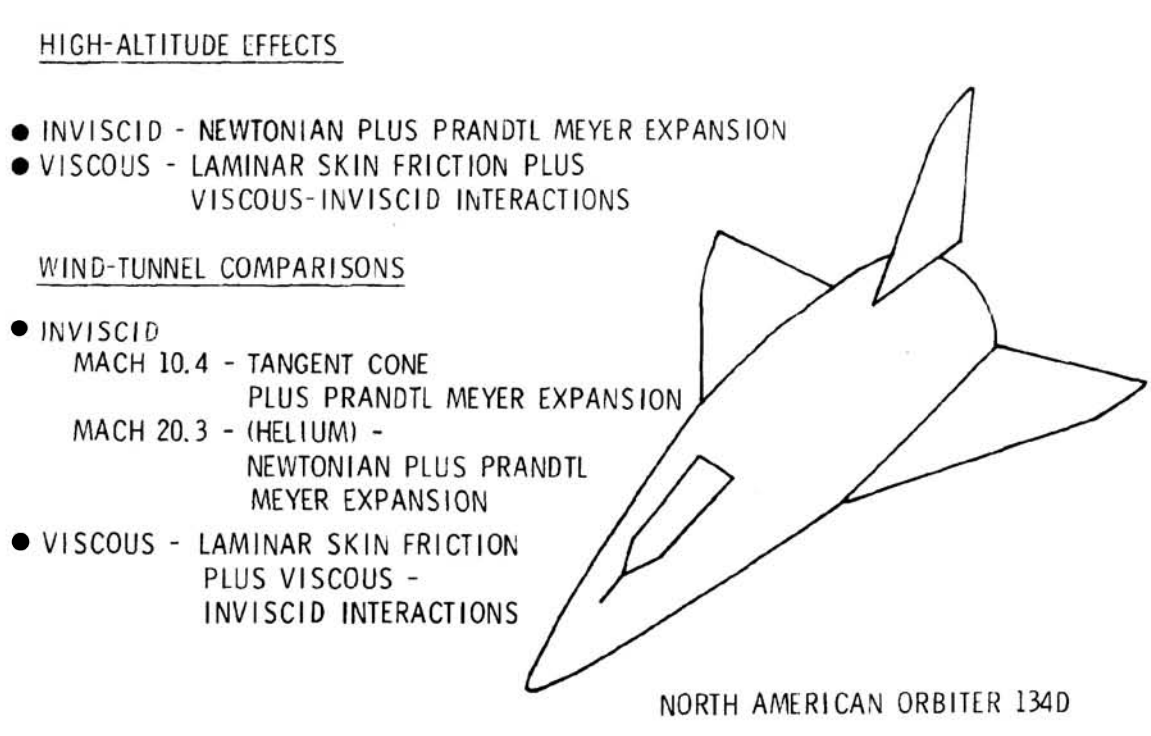

Figure 2.- Approach for determining high-altitude effects.

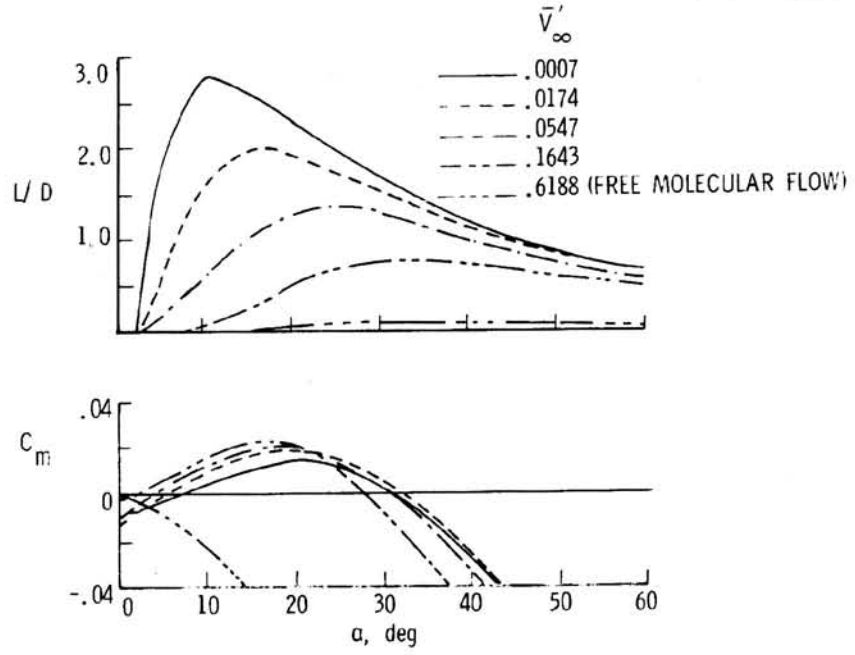

Figure 3.- Predicted performance variation at high altitude.

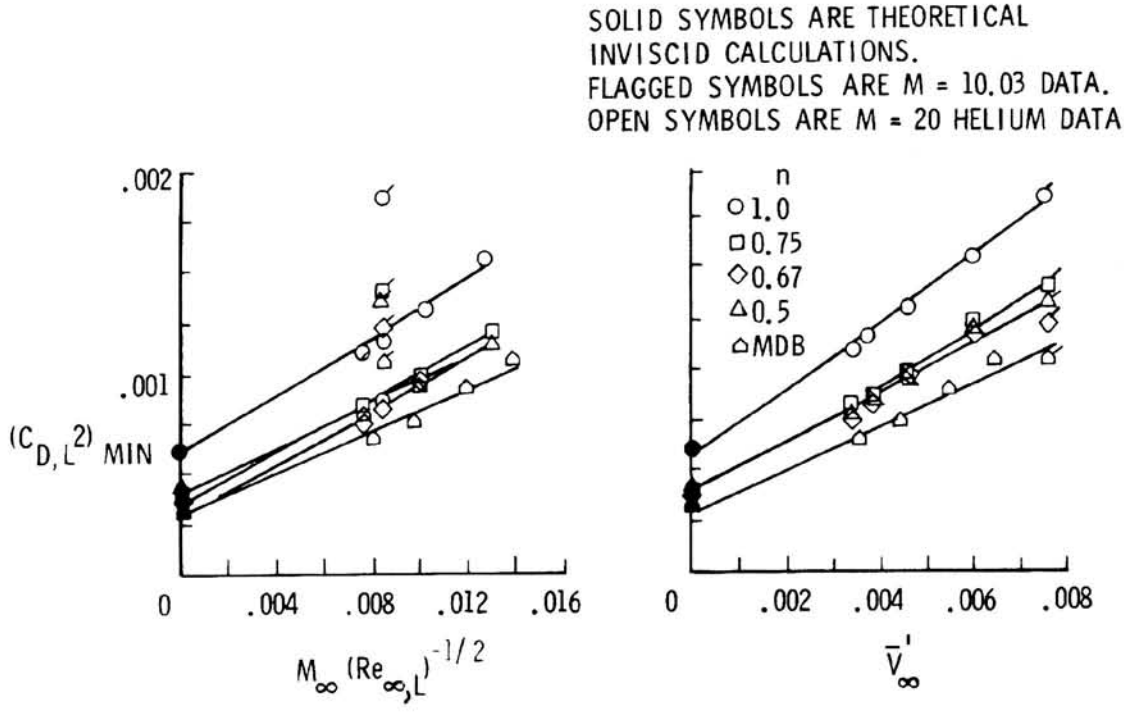

Figure 4.- Drag correlation using $\bar{V}'_\infty$. (From ref. 13.)

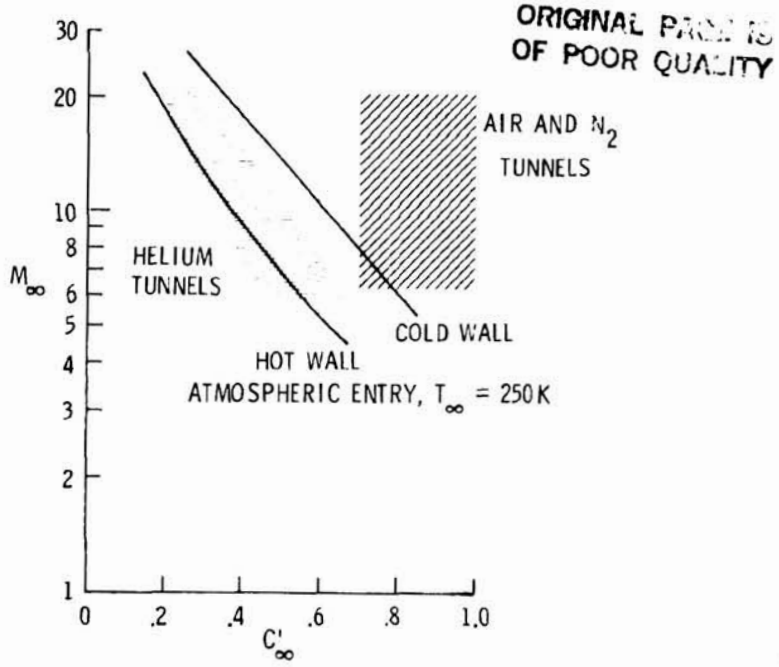

Figure 5.- Variation of C'_∞ with Mach number for ground facilities and flight.

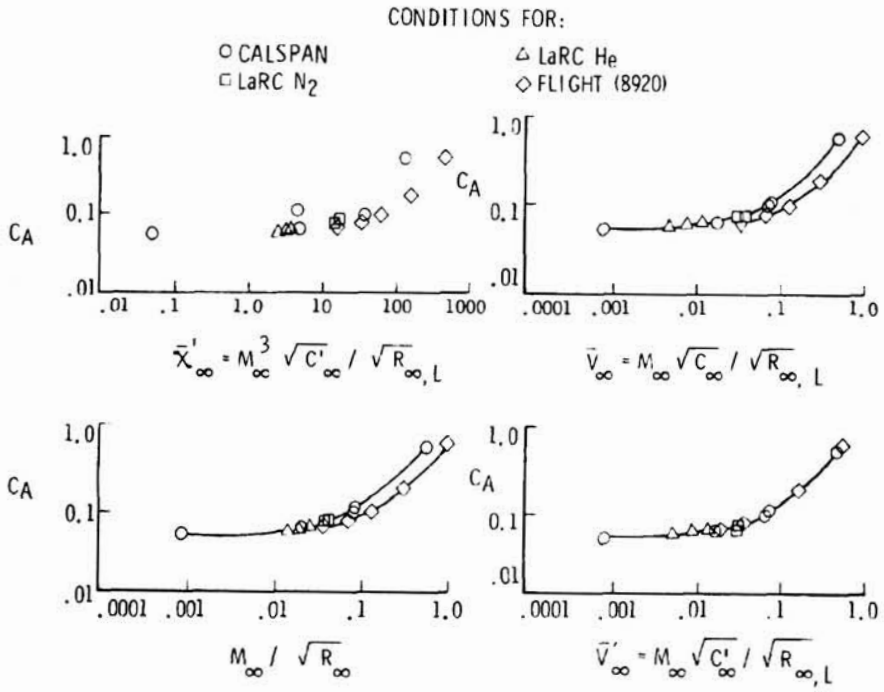

Figure 6.- Correlation of estimated Shuttle axial-force coefficient based on 15° cone axial force per unit surface area nondimensionalized by orbiter reference conditions.

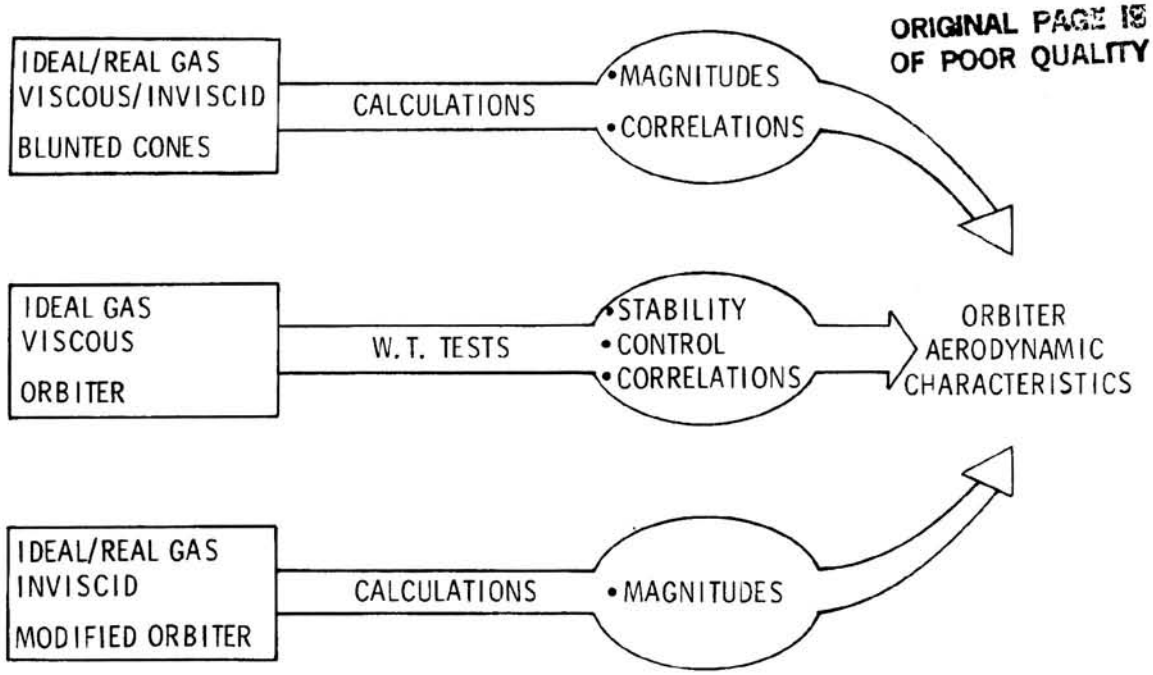

Figure 7.- Investigation of combined real-gas viscous-interaction effects on orbiter aerodynamic conditions.

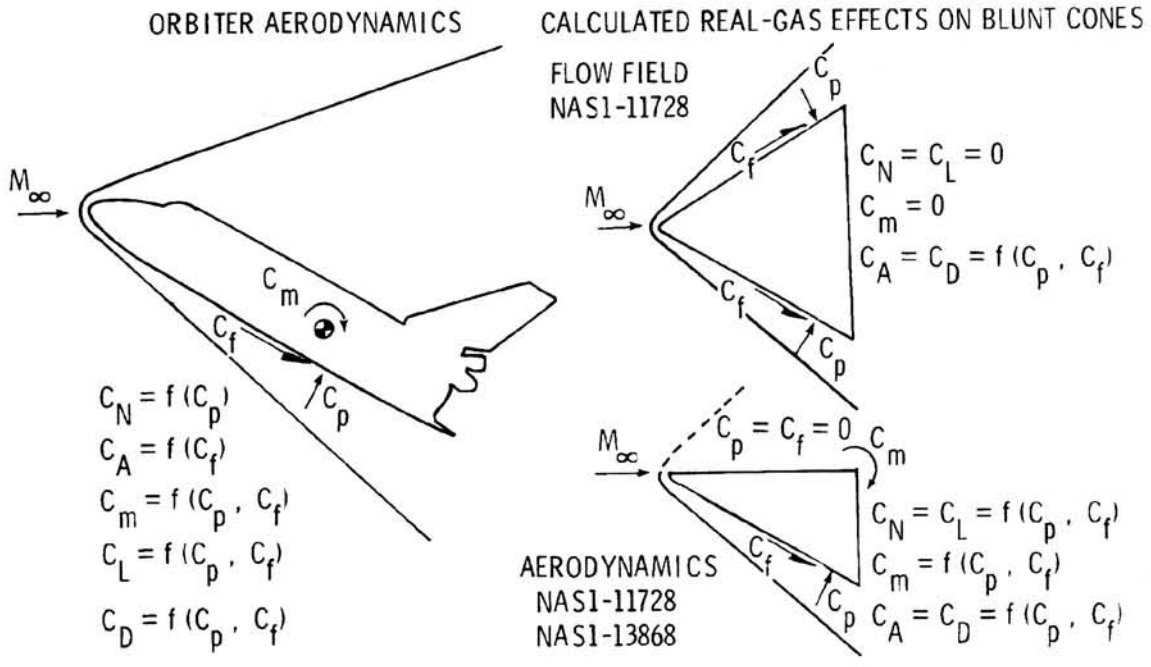

Figure 8.- Flow models considered by Ad Hoc Working Group.

INVISCID

- IDEAL-GAS AND EQUILIBRIUM FLOW FIELDS
  LOMAX AND INOUYE[37]
- FINITE-RATE FLOW FIELDS
  CURTIS AND STROM[22]

VISCOUS

- IDEAL-GAS FLOW FIELDS
  CEBECI[19,20]
- EQUILIBRIUM AND FINITE-RATE FLOW FIELDS
  BLOTTNER[21]

Figure 9.- Computer codes utilized in the blunt cone analytical investigation.

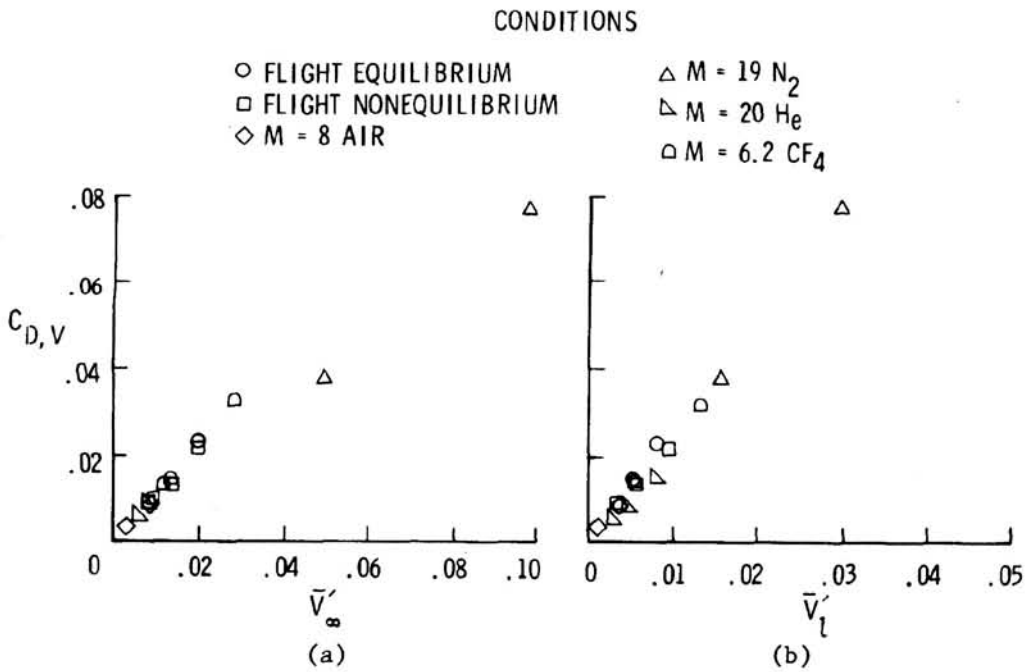

Figure 10.- Correlation of C_D due to skin friction with viscous parameter (using Sutherland's T-μ relationship for air and nitrogen).

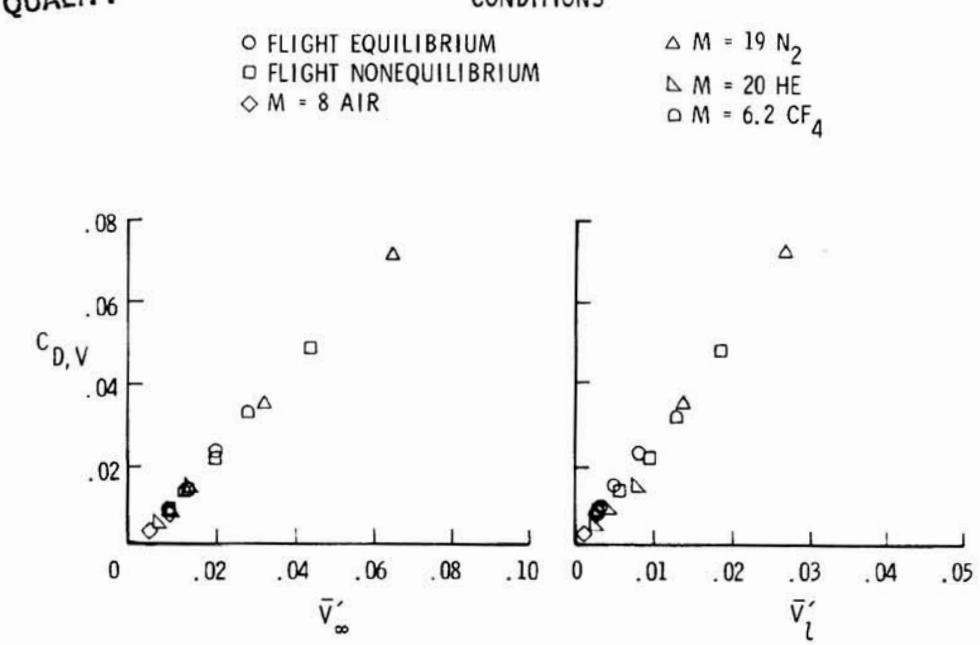

Figure 11.- Correlation of C_D due to skin friction with viscous parameter (using Keyes' T-μ relationship for air and N_2).[24,25]

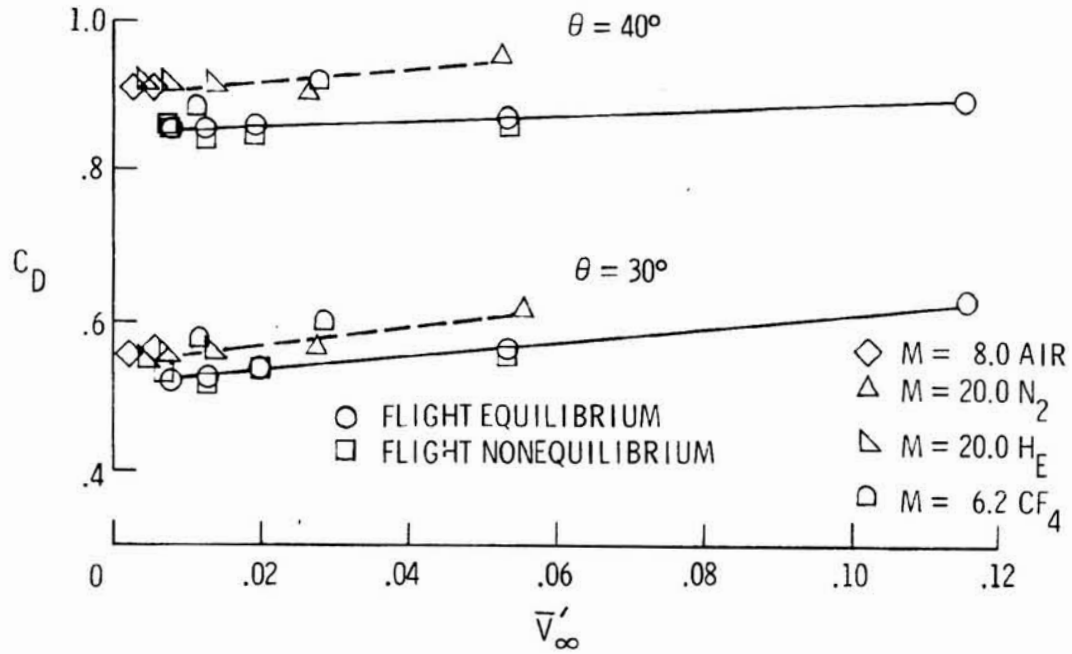

Figure 12.- Correlation of C_D with $\bar{V}'_\infty$.

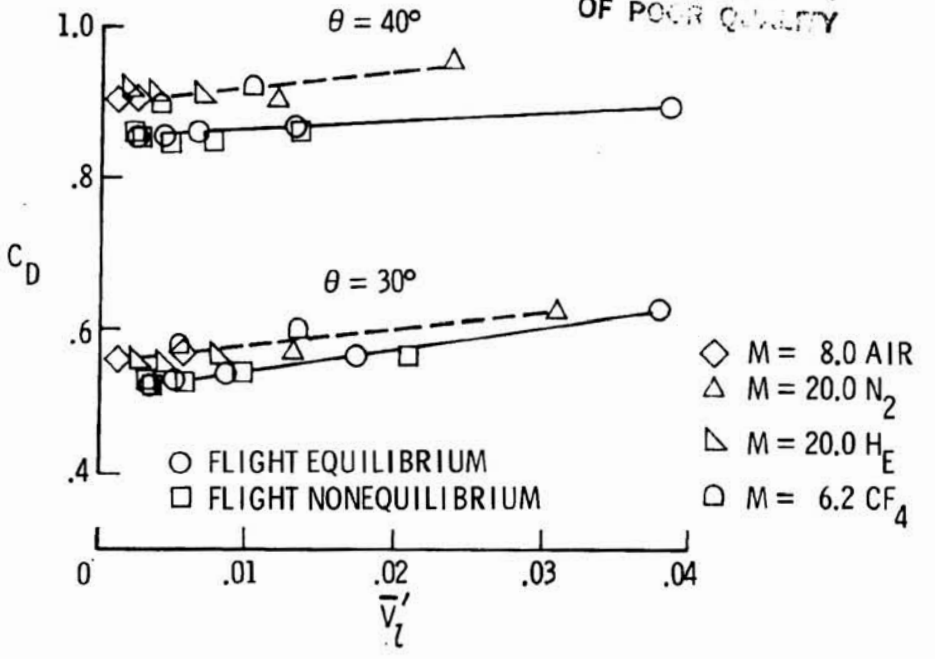

Figure 13.- Correlation of C_D with $\bar{V}_l'$.

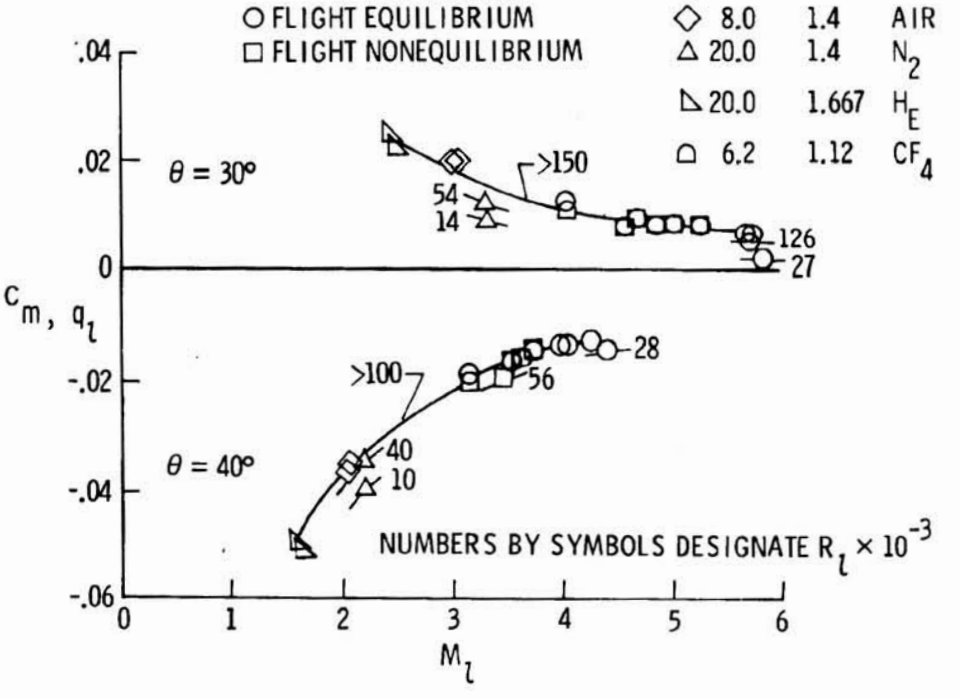

Figure 14.- Correlation of C_{m,q_l} with M_∞ for blunt-cone calculations.

TEST	M_∞	MODEL/ SCALE	FACILITY	CAPABILITY R_∞/ FT $\times 10^{-6}$	TEST $R_{\infty,L} \times 10^{-6}$	TEST $V_\infty \times 10^3$
140A/ B CONFIGURATION						
LA46	4.6	LaRC/ .010	LaRC UPWT	0.1 - 8.0	2.15	2.96
LA52	6.0	↓	LaRC 20"	1.0 - 10	6.0 - 6.7	2.25 & 2.36
LA47	10.3		LaRC CFHT	0.5 - 2.5	1.0	9.0
OA20C	4.6	49-0/ .015	LaRC UPWT	0.1 - 8.0	2, 4, & 8	1.5 - 3.1
OA84	4.6	↓	LTV 4'	11 - 22	24.6 & 34.9	0.7 & 0.9
OA87	5.3		ARC 3.5'	0.2 - 5.0	1.8 & 3.0	2.8 & 3.6
OA77	6.0		AEDC B	0.3 - 4.7	1.6, 3, & 7.5	2.0 - 4.4
OA77	8.0		AEDC B	0.3 - 3.6	0.8, 3, & 5.6	3.1 - 8.2
OA78	10.0	↓	AEDC C	0.3 - 2.4	1.3 & 3.0	5.3 & 7.8
OA87	10.3	49-0/ .015	ARC 3.5'	0.06 - 2.0	3.0	5.5
OA90	10.3	72-0/ .010	LaRC CFHT	0.5 - 2.5	0.6, 1, & 1.3	8 - 11
OA81	16	51-0/ .010	AEDC F	0.5 - 1.7	0.5 & 1.2	12 & 26
OA113	10	51-0/ .010	CALSPAN	.03 - 13+	0.3 & .6	14 & 45.9
OA113	16		CALSPAN	.04 - 1.2	.04 & .09	41 & 68
OA160	19	51-0/ .010	AEDC F	0.5 - 1.7	0.1 & 0.3	30 & 50
140C CONFIGURATION						
LA53	6.1	74-0/ .004	LaRC CF_4	0.3 - 0.5	0.14 & 0.21	15.1 & 12.5
LA54	6.0	↓	LaRC 20"	1.0 - 10	0.5	7.8
OA89	19.8		LaRC N_2	0.5 - 0.8	0.17	41
OA109	20.	74-0/ .004	LaRC He	1.6 - 11.3	0.7, 1.1 & 1.9	6.5 - 10
LA79	18	74-0/ .004	NSWC 8A	0.23 - 0.7	0.26	35

Figure 15.- Orbiter tests analyzed.

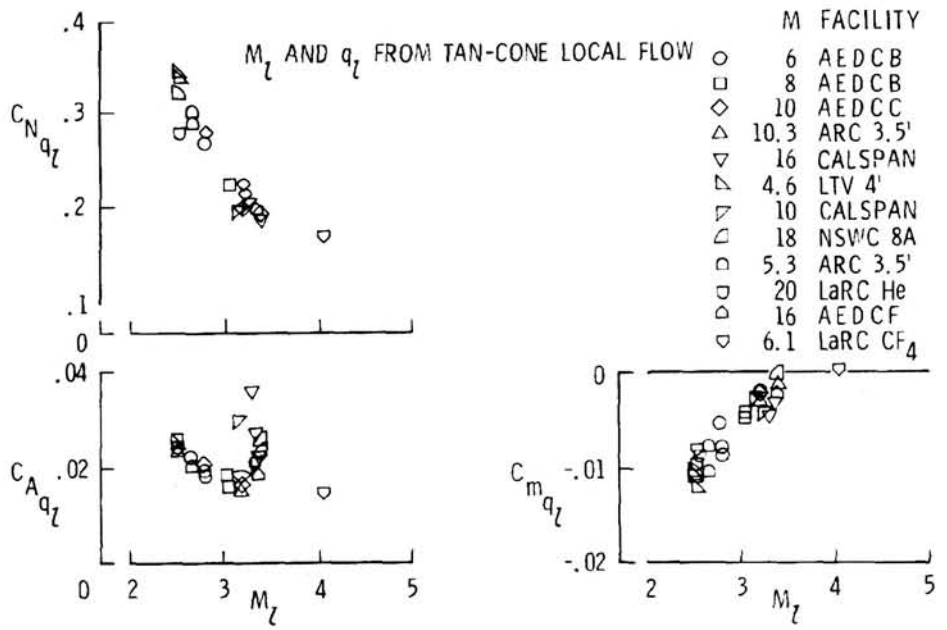

Figure 16.- Orbiter hypersonic data correlation. 140A/B and 140C at $\alpha = 30^\circ$, $\delta_e = 0^\circ$, $\delta_{BF} = 0^\circ$.

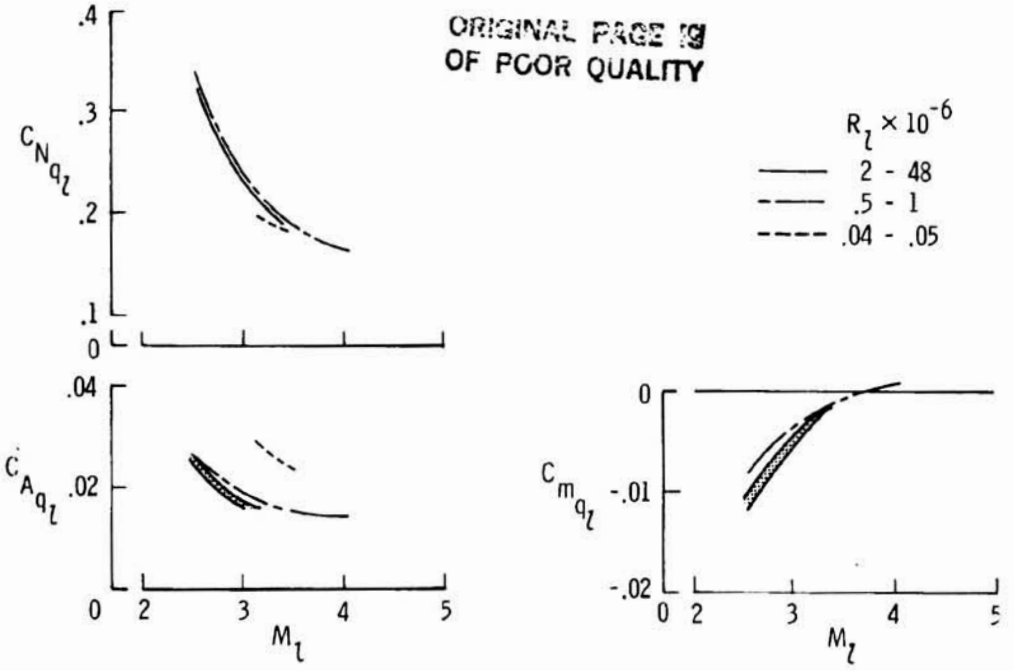

Figure 17.- Orbiter hypersonic data correlation. 140A/B and 140C at $\alpha = 30^{o}$, $\delta_e = 0^{o}$, $\delta_{BF} = 0^{o}$.

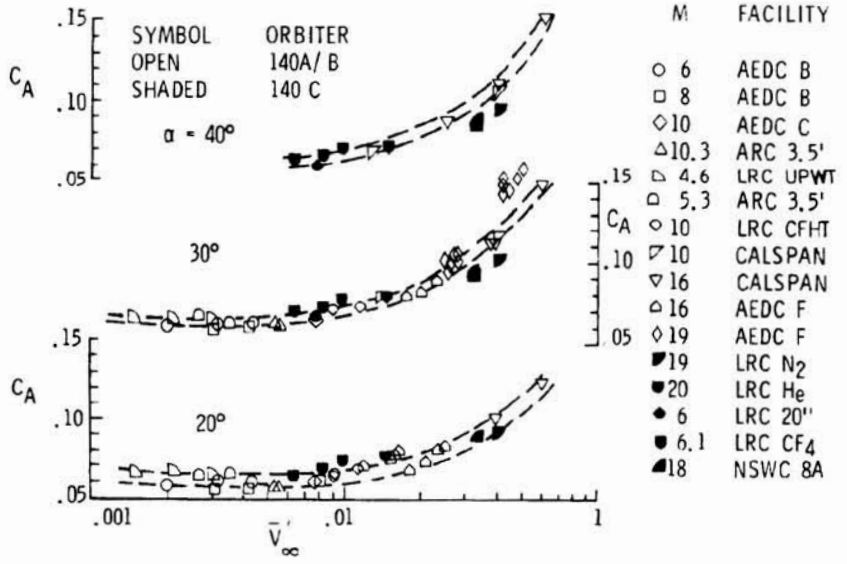

Figure 18.- Orbiter C_A data correlation. $\delta_e = 0^{o}$, $\delta_{BF} = 0^{o}$.

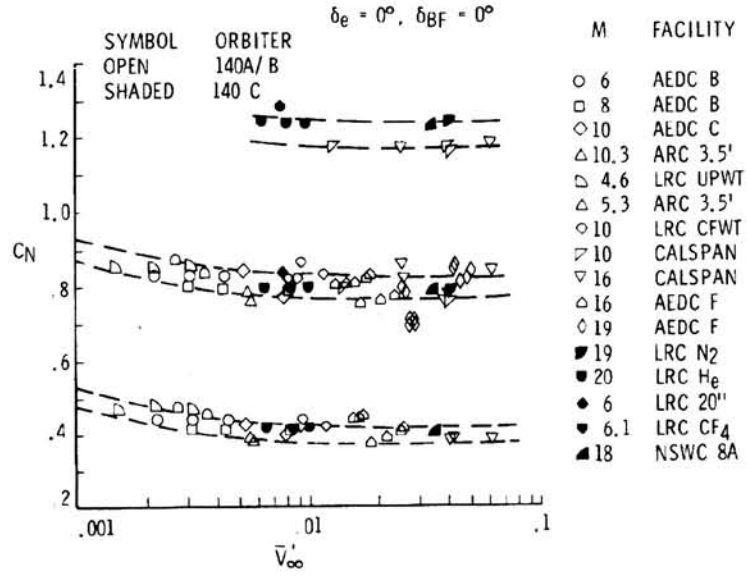

Figure 19.- Orbiter C_N data correlation.
$\delta_e = 0°$, $\delta_{BF} = 0°$.

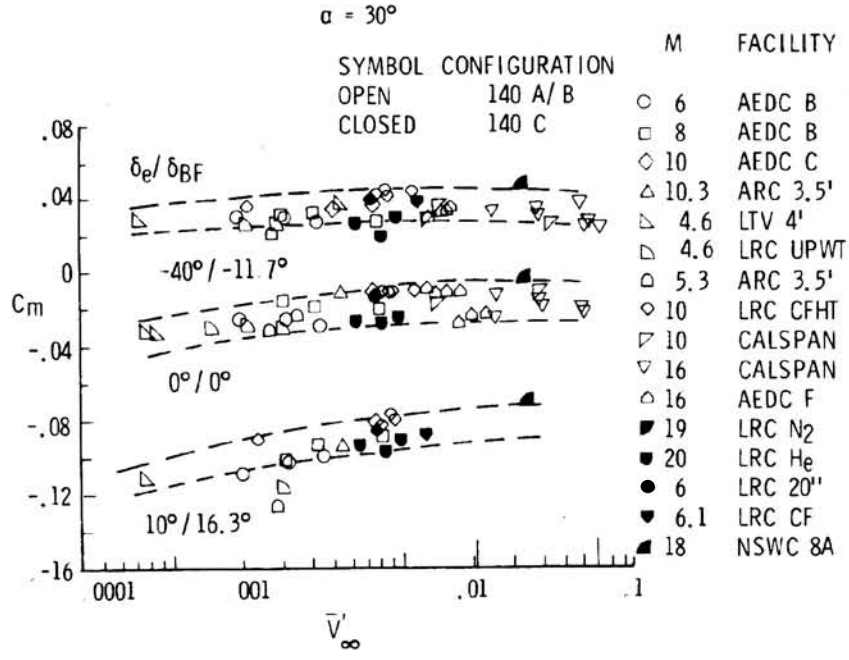

Figure 20.- Baseline C_m data correlation. $\alpha = 30°$.

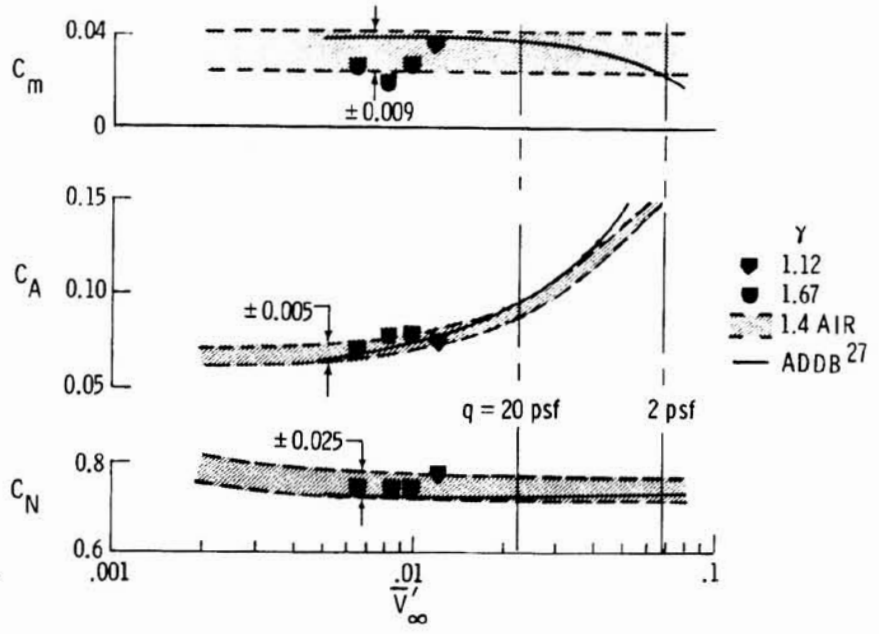

Figure 21.- Orbiter data correlation with $\bar{V}'_\infty$.
$\alpha = 30^\circ$, $\delta_e/\delta_{BF} = -40^\circ/-11.7^\circ$.

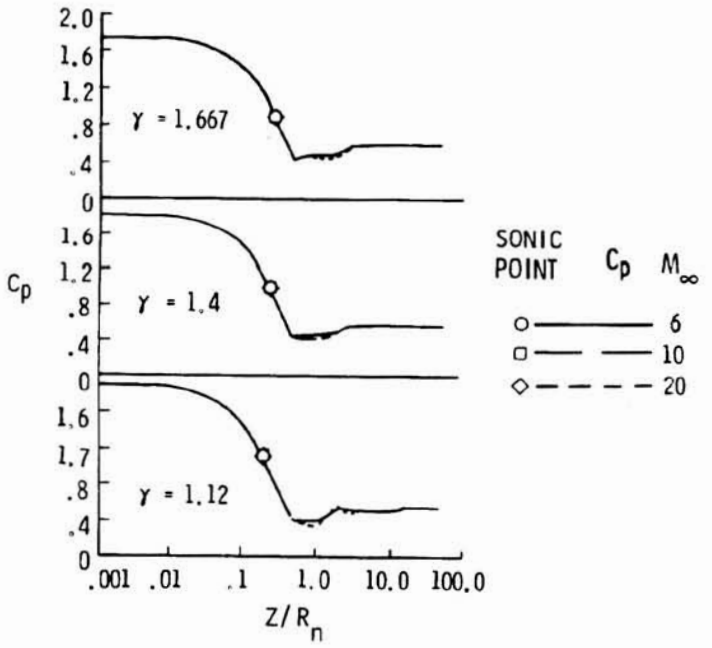

Figure 22.- Effect of M_∞ on C_p for constant γ.

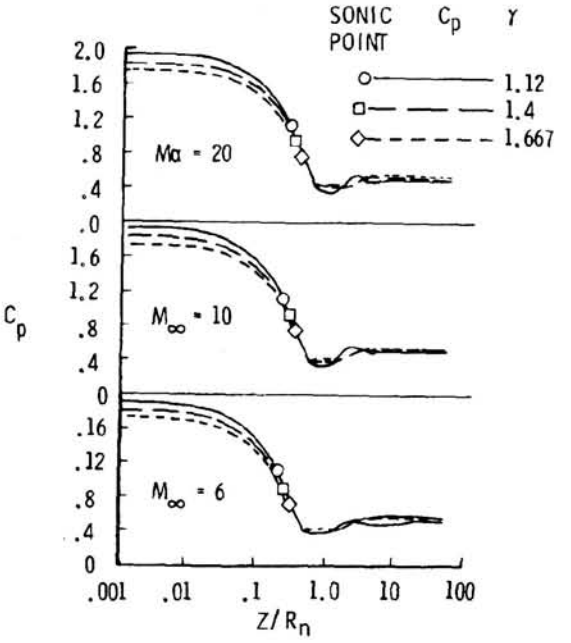

Figure 23.- Effect of γ on C_p for constant M_∞.

- APPROACH

  COMPUTE INVISCID FLOW FIELD OVER "MODIFIED" 140-C SHUTTLE ORBITER USING GRUMMAN 3-D INVISCID CODE (STEIN)[28,29] @ $\alpha = 25°$, ALTITUDE = 240000 FEET FOR FOLLOWING CONDITIONS

  (a) $\gamma = 1.4$, $M_\infty = 10.29$
  (b) $\gamma = 1.12$, $M_\infty = 26.1$
  } IDEAL GAS

  (c) EQUILIBRIUM AIR CHEMISTRY, $M_\infty = 26.1$

- CONFIGURATION

  MODIFIED 140-C SHUTTLE ORBITER ($\Lambda = 55°$)

- RESULTS

  COMPARISON OF PRESSURE DISTRIBUTIONS, SHOCK SHAPES, AND AERODYNAMIC COEFFICIENTS

Figure 24.- Investigation of real-gas effects on Shuttle orbiter.

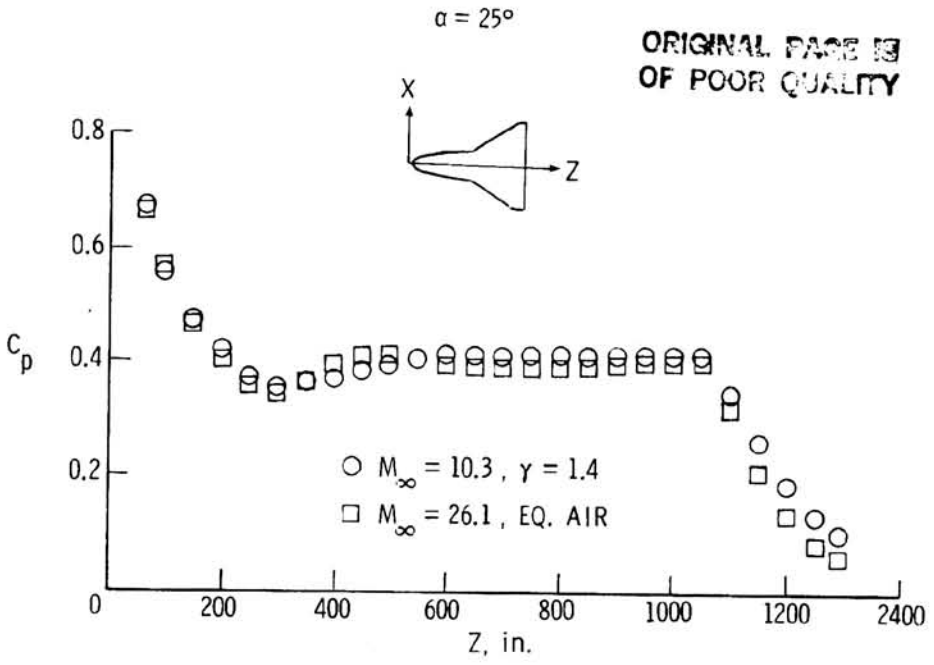

Figure 25.- Windward symmetry plane pressure distribution.

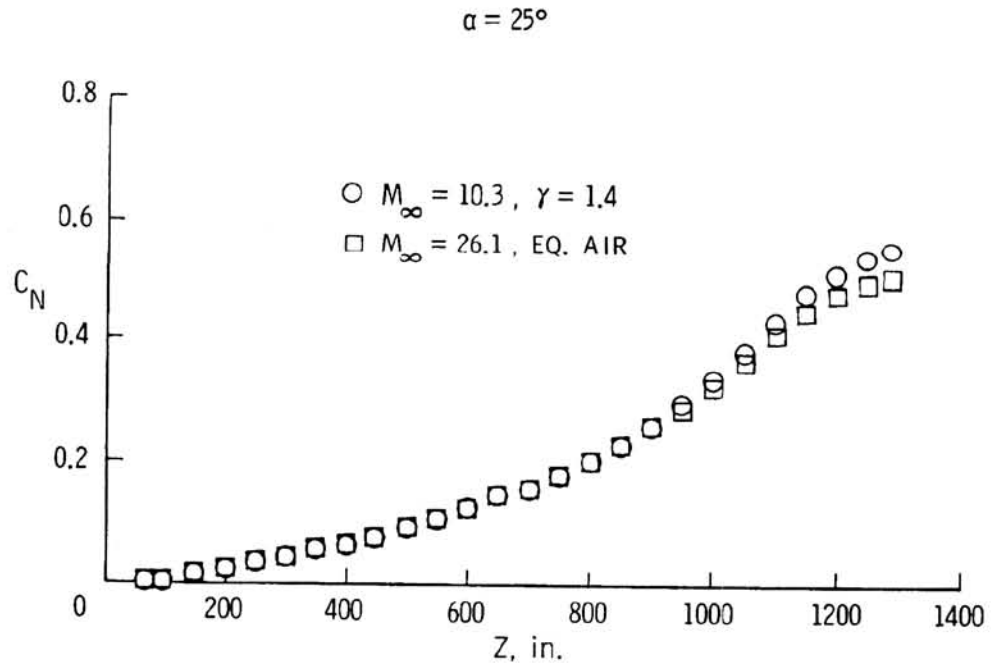

Figure 26.- Integrated normal-force coefficient.

	$\gamma = 1.4$ $M_\infty = 10.3$	$\gamma = 1.12$ $M_\infty = 26.1$	EQ. AIR $M_\infty = 26.1$
C_L	0.479	0.430	0.434
C_D	0.276	0.252	0.255
C_M	-0.037	-0.012	-0.014
C_N	0.550	0.495	0.501
C_A	0.050	0.049	0.049

Figure 27.- Summary of aerodynamic characteristics. Modified 140C Shuttle orbiter, $\alpha = 25°$.

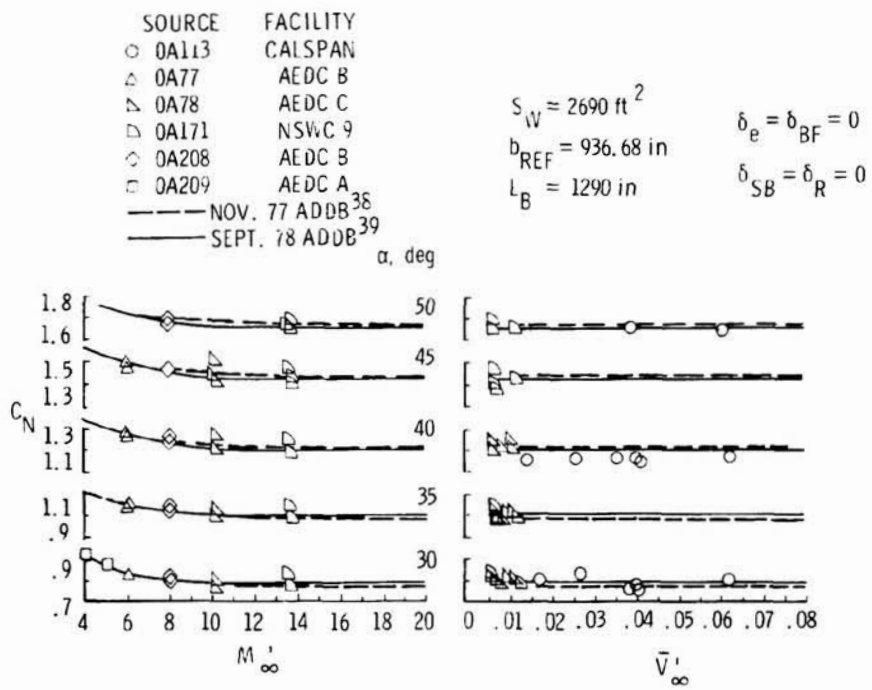

Figure 28.- Normal-force coefficient variation with M_∞ and $\bar{V}'_\infty$.

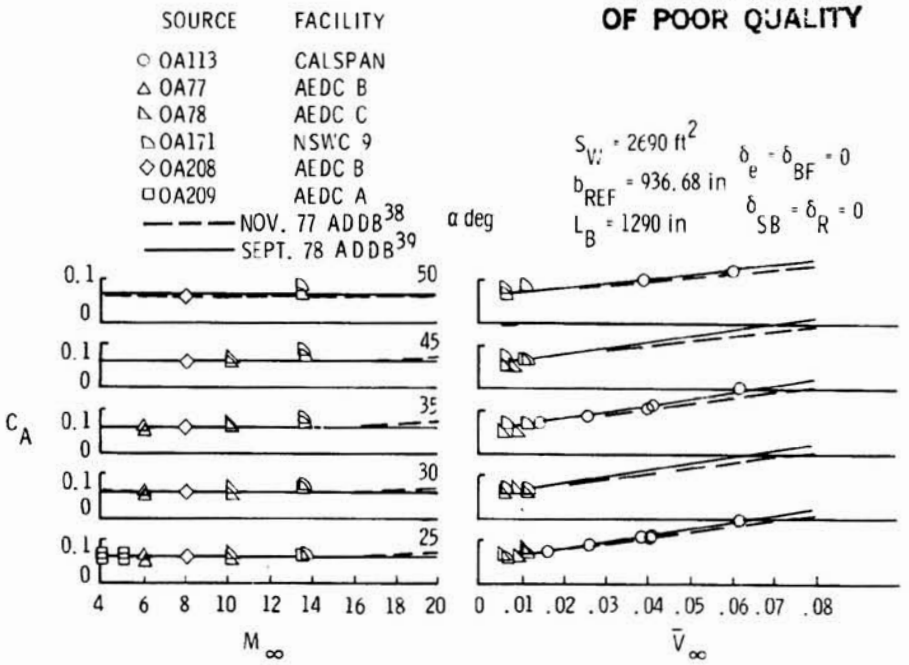

Figure 29.- Axial-force coefficient variation with M_∞ and $\bar{V}'_\infty$.

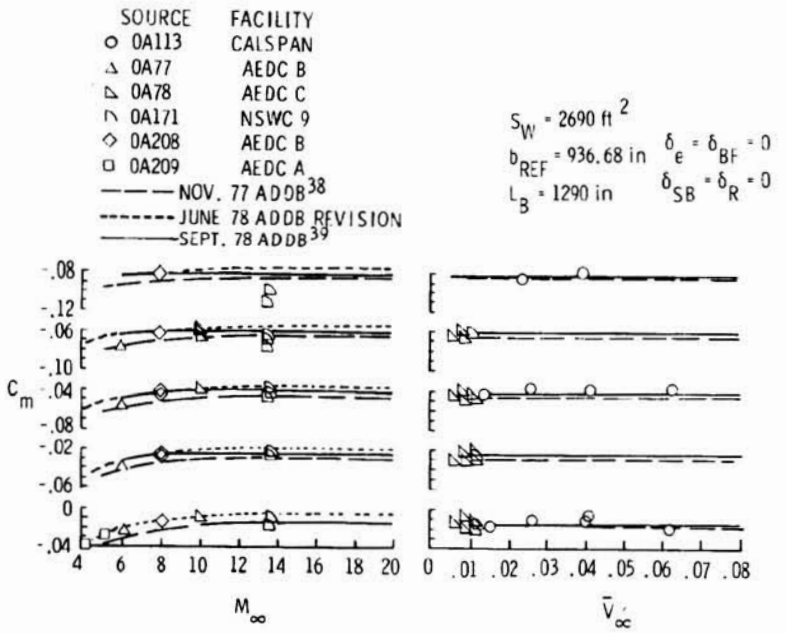

Figure 30.- Pitching-moment coefficient variation with M_∞ and $\bar{V}'_\infty$.

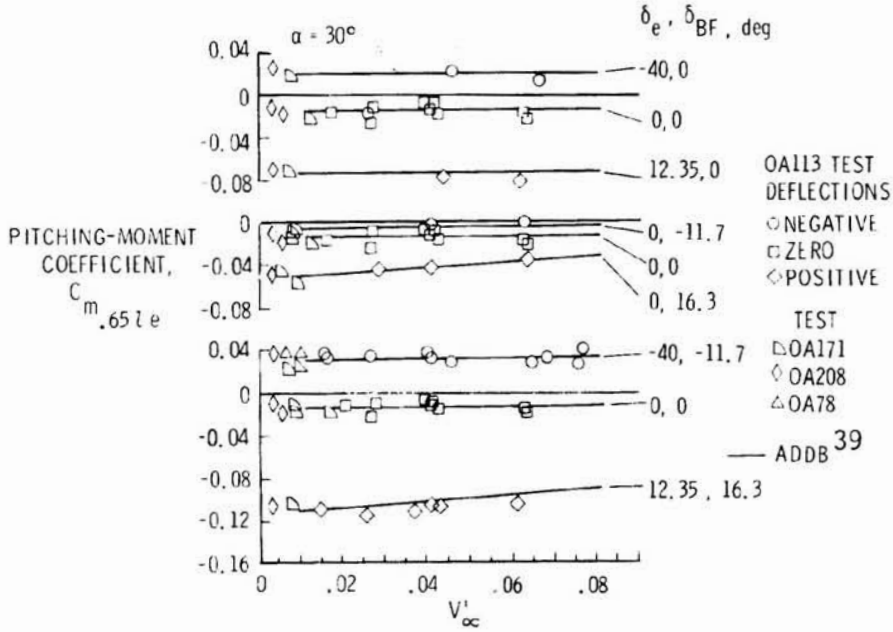

Figure 31.- Pitching-moment coefficient, $C_{m_{0.65L}}$.

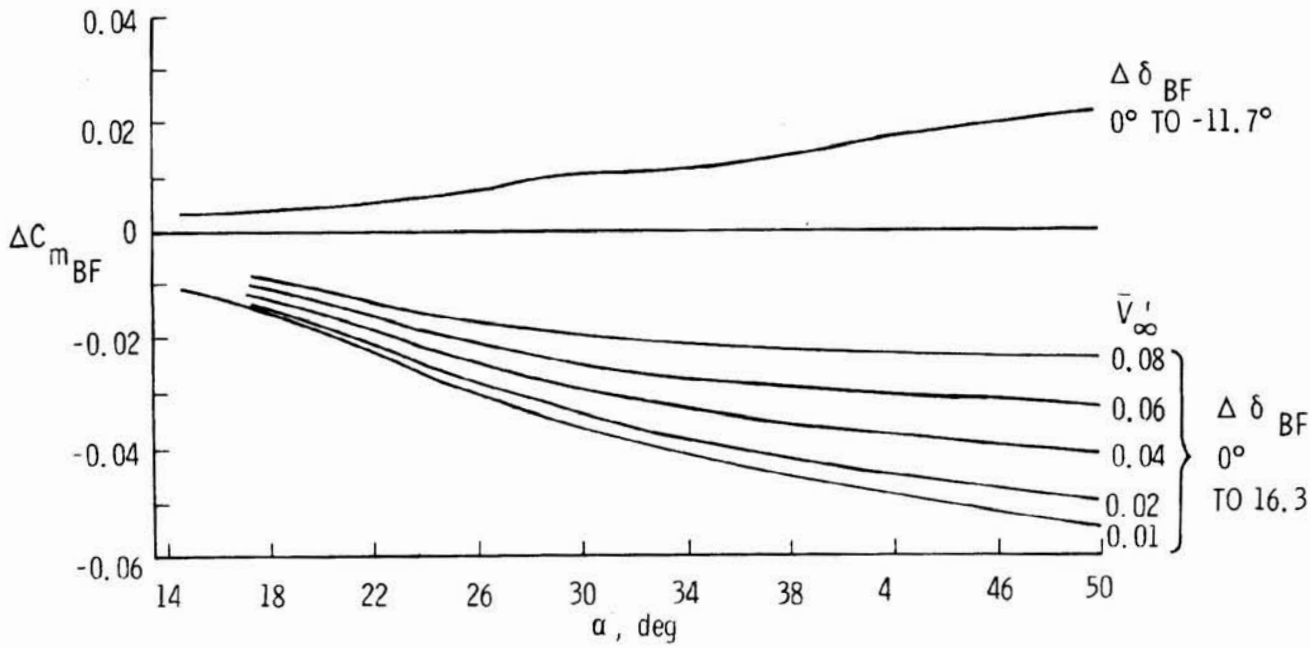

Figure 32.- ADDB values for hypersonic body flap effectiveness.

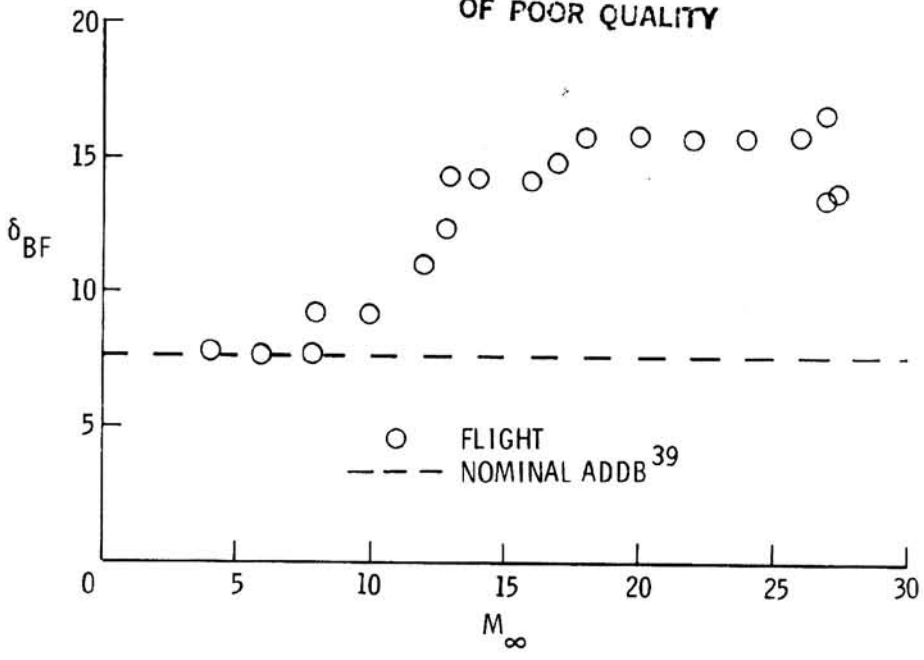

Figure 33.- Body flap deflection for STS-1.

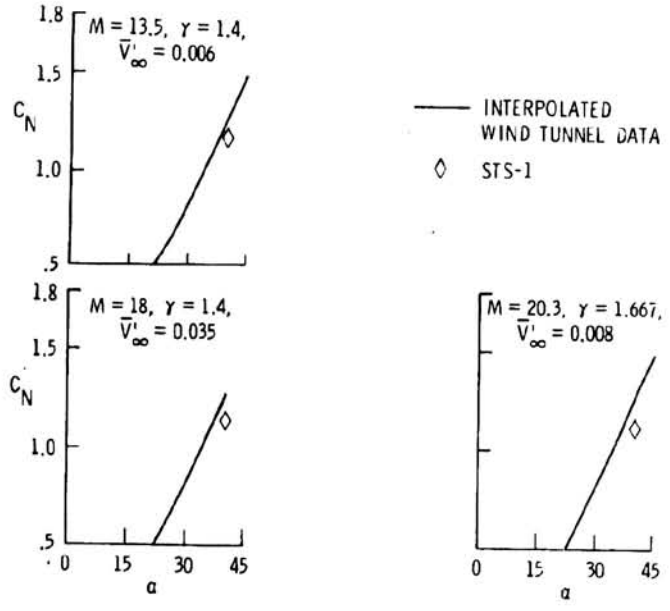

(a) Normal-force coefficient.

Figure 34.- Postflight comparison of STS-1 aerodynamics with interpolated wind tunnel data.

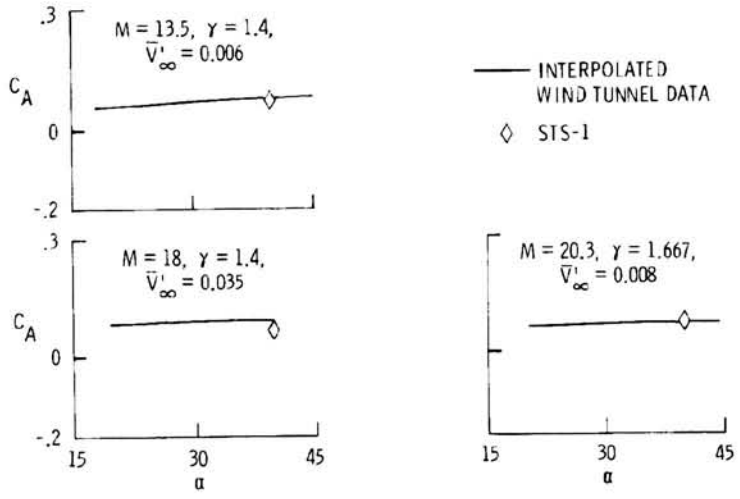

(b) Axial-force coefficient.

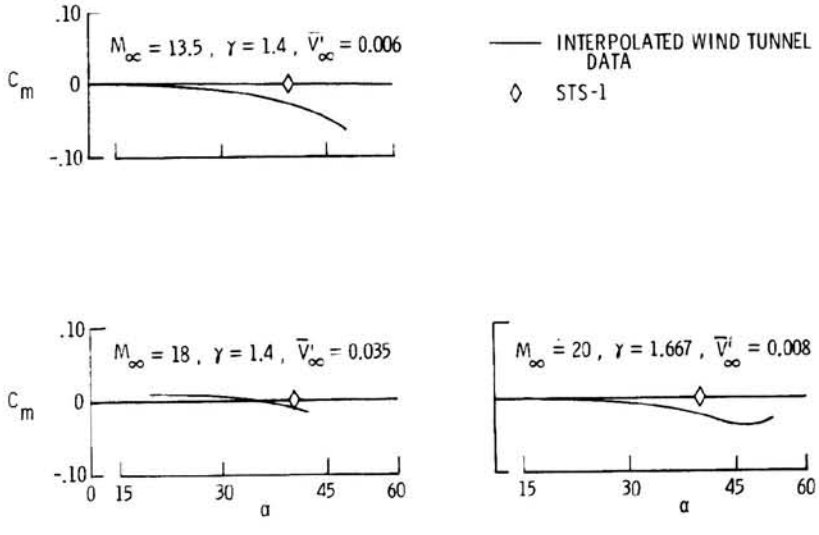

(c) Pitching-moment coefficient.

Figure 34.- Continued.

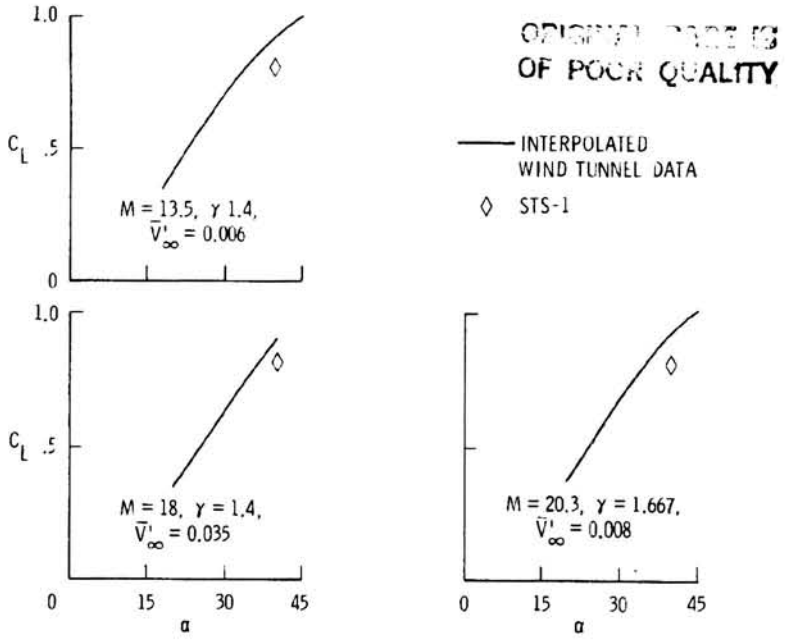

(d) Lift coefficient.

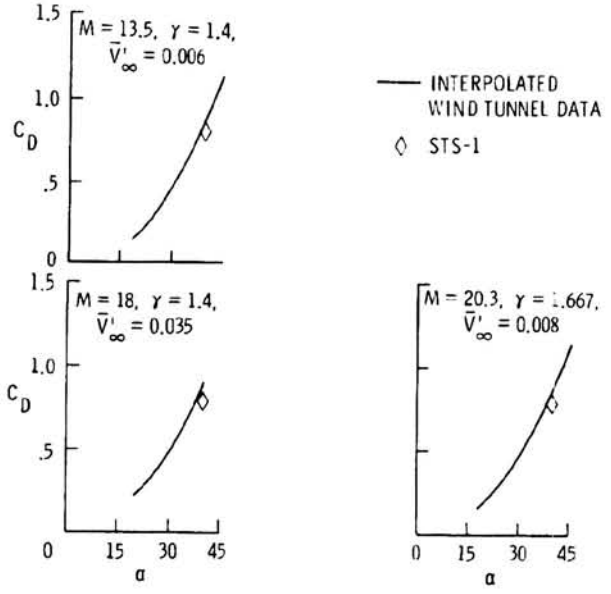

(e) Drag coefficient.

Figure 34.- Continued.

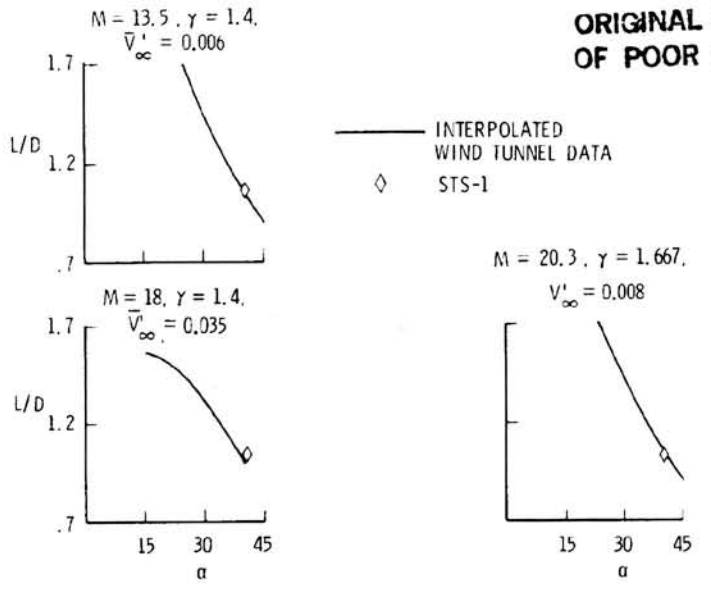

(f) Lift-to-drag ratio.

Figure 34.- Concluded.

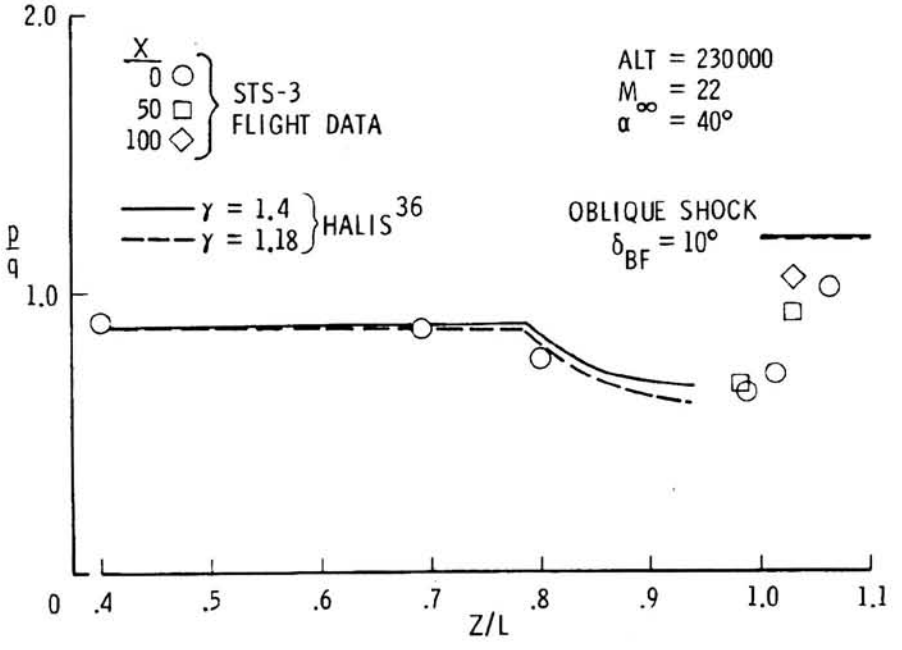

Figure 35.- Comparison of flight windward centerline pressure distribution with calculation.

EXPLANATION OF THE HYPERSONIC LONGITUDINAL STABILITY PROBLEM - LESSONS LEARNED*

B. J. Griffith and J. R. Maus
Calspan Field Services, Inc./AEDC Division
Tullahoma, Tennessee

J. T. Best
U. S. Air Force, Analysis and Evaluation Division
Arnold Air Force Station, Tennessee

SUMMARY

Inviscid and viscous CFD codes have been applied to a modified Space Shuttle orbiter geometry to investigate differences between preflight aerodynamic predictions and aerodynamic data from hypersonic reentry flight. Flow field solutions were obtained for wind tunnel conditions and flight conditions to assess Mach number, real-gas, and viscous effects on the reentry aerodynamics of the orbiter. Based on the CFD studies, a methodology model has been developed to 1) extrapolate wind tunnel data to flight conditions and 2) calculate a DCM for use with the Aerodynamic Design Data Book. Comparisons are made with selected flight data. Results of the study indicate that the differences between flight and pre-STS-1 predictions of hypersonic pitching moment are primarily due to Mach number and real-gas effects.

INTRODUCTION

The flight test program for the Space Shuttle (figure 1) has been remarkably successful overall; however, aerodynamic anomalies have arisen that require further investigation. For example, results from the Space Shuttle flights have shown a significant difference between preflight prediction of hypersonic pitching moment and values inferred from flight data (refs. 1,2). These differences have resulted in body flap deflections (required to maintain trim) more than twice those predicted prior to STS-1.

The preflight predictions of the orbiter aerodynamics were based primarily on ground test data obtained in a very extensive wind tunnel test program. In an effort to resolve this discrepancy, the present study addresses, through the use of Computational Fluid Dynamics (CFD) codes, some of the fundamental flow modeling necessary to extrapolate ground test data to hypersonic flight conditions. In particular, this paper examines the high Mach number, real-gas, and viscous effects on the orbiter aerodynamics.

---

*The work reported herein was performed by the Arnold Engineering Development Center (AEDC), Air Force Systems Command. This study was sponsored by the U.S. Air Force Space Division, NASA/JSC and AEDC. Work and analysis were done by personnel of Calspan Field Services, Inc./AEDC Division, operating contractor for Aerospace Flight Dynamics Testing, and the Air Force's Analysis and Evaluation Division (DOFAA).

The effects of Mach number were assessed by parametrically varying free-stream Mach number and angle of attack in a series of inviscid, perfect-gas computations carried out on a modified orbiter geometry. Real-gas effects were explored by making calculations at specific points of the reentry trajectory using equilibrium air thermodynamics and comparing with the corresponding perfect-gas computations. Viscous effects on the orbiter aerodynamics were determined by an analysis of wind tunnel heat transfer and viscous drag data supplemented by several viscous computations for a modified Shuttle geometry at low angles of attack.

The effects discussed above have been incorporated into a methodology model to (1) extrapolate high Mach number wind tunnel data from AEDC Hypersonic Wind Tunnel (B) to flight conditions and (2) calculate a DCM that can be used with the Aerodynamic Design Data Book (ADDB). Comparisons are made with selected flight data. Precision problems with the flight data, ADDB values, and CFD results are addressed.

NOMENCLATURE

A	reference area, 250 m^2 (2690 ft^2)
C_A	axial-force coefficient, F_A/Aq_∞
C_f	skin friction coefficient
C_M	pitching-moment coefficient, $M_o/\bar{c}Aq_\infty$
C_N	normal-force coefficient, F_N/Aq_∞
CG	center of gravity
C_p	pressure coefficient $(p - p_\infty)q_\infty$
C_∞	Chapman-Rubesin constant, $(\mu_w T_\infty)/\mu_\infty T_w)$
$\bar{c}$	reference chord length, 12.06 m (474.8 in.)
DCM	moment to be added to Aerodynamic Design Data Book (ADDB) (ref. 3) for flight agreement
F_A	axial shear drag
F_N	normal force
K	empirical constant
K_r	Reynolds analogy factor
L	lift force or body length
L/D	lift-to-drag ratio
M	Mach number

M_o	total moment about Z_o = 94.0 cm (37.0 in.) and noted flight axial CG
P	pressure
POPU	pushover-pull-up manuver
PR	Prandtl number
$\dot{Q}$	heat-transfer rate
q	dynamic pressure
Re	free-stream Reynolds numbers per meter
$Re_{\infty,L}$	free-stream Reynolds number based on model length
S	area
St	Stanton number
T	temperature
V	velocity
$\overline{V}_\infty$	viscous parameter, $M_\infty\sqrt{C_\infty}/\sqrt{Re_{\infty,L}}$
X_{ST}	station at which blunt body code is used to start primary code
x,y,z	Cartesian coordinates
Z	average distance from CG to lower surface
α	angle of attack
Δ	difference
δ	deflection angle
γ	specific heat ratio
ρ	density
ϕ	circumferential angle

Subscripts:

AEDC	Arnold Engineering Development Center
BB	basic body ($\delta_e = \delta_{bf} = 0$)
bf	body flap
CFD	computational fluid dynamics
c.p.	center of pressure
e	elevon

FLT	flight
o	stagnation point
V	viscous
WET	wetted area
w	wall
∞	free-stream conditions

Acronyms:

ADDB	Aerodynamic Design Data Book (ref. 3)
AIR3D	Navier Stokes Blunt Body Code (ref. 4)
CFD	Computational Fluid Dynamics
CM3DT	Blunt Body Euler Code (ref. 5)
PNS	Parabolized Navier Stokes Code (ref. 6)
QUICK	Geometry Modeling Code (ref. 7)
STEIN	Inviscid Space Marching Code (ref. 8)

INVISCID COMPUTATIONS

Approach

Advanced CFD codes CM3DT (ref. 5) and STEIN (ref. 8) have been applied to a modified orbiter geometry to obtain detailed inviscid flow field solutions for both wind tunnel test conditions and hypersonic flight conditions. Figure 2 illustrates the geometry for which the computations were performed. The major differences between the computational model geometry and the actual orbiter geometry shown in figure 1 are: (1) the wing sweep back angle has been increased from 45^{o} to 55^{o}, (2) the wing thickness of the model is about twice that of the orbiter, (3) the computational geometry is squared off at the body flap hinge line, and (4) the rudder and OMS pods are not included in the model geometry. The projected planform area of the computational geometry is about two percent less than the orbiter projected area, and the centroid of the computational projected area is approximately two percent of model length further aft than for the orbiter. All coefficients, however, are based on the actual orbiter reference values for consistency.

CM3DT and STEIN are both interfaced with the QUICK (ref. 7) geometry routines which specify the body shape and compute geometrical parameters on the surface. Both codes employ conformal mapping to transform physical space between the body and the bow shock into a simple computational domain.

The time-dependent Euler solver CM3DT was used to obtain flow field solutions in the transonic forebody region of the orbiter. These solutions provide initial

conditions for the inviscid space marching code STEIN, which was used to compute the flow field for the supersonic afterbody portion of the vehicle. Calculated surface pressures were integrated over the body to obtain aerodynamic forces and moments acting on the vehicle.

Both CM3DT and STEIN can be used either for perfect-gas or equilibrium-air calculations. Tabulated thermodynamic properties, in conjunction with table look-up routines, are used for equilibrium air computations.

Comparison with Wind Tunnel Data

To establish credibility of the CFD results and to assess the effect of geometrical differences on the aerodynamic parameters, initial computations with CD3DT and STEIN were made to compare with wind tunnel results. The specific wind tunnel data used in this comparison are from AEDC Tunnel B (refs. 9, 10) since these data are some of the most reliable high Mach number data available for the Space Shuttle orbiter.

Figure 3 shows a comparison of computed and measured pressure coefficients along the windward centerline at $M_\infty = 8$ for two angles of attack. The computed pressure distribution, although slightly overpredicting the pressures in the midbody region, generally agrees very well in distribution and level with the experimental values.

A comparison of computed and experimental normal-force coefficients is shown in figure 4. The reference area used to nondimensionalize the calculated values is the actual orbiter wing area, $A = 250\ m^2$ ($2690\ ft^2$). The agreement shown, as good as it is, would be even better had the reference area been reduced by two percent to account for the difference in projected planform area.

Predicting pitching moment is a severe test of any CFD code. Figure 5 shows a comparison of computed pitching-moment coefficient with experimental values for the basic orbiter geometry. The maximum deviation, which occurs at an angle of attack of about 30°, corresponds to a difference in center of pressure of only 0.3 percent of the body length, indicating that the computational model is a realistic representation of the actual Space Shuttle orbiter.

The results of the above comparisons give confidence in the applicability of the computational code to the complex model orbiter geometry. These CFD codes and a set of high-quality Mach 8 tunnel data are the tools used to predict flight aerodynamics in this paper.

Mach Number and Real-Gas Effects

Effects on the orbiter aerodynamics attributable to hypersonic Mach number and equilibrium-air thermodynamics were investigated by carrying out a series of CFD solutions using CM3DT and STEIN for the matrix of conditions shown in table I. As indicated in this table, difficulties were encountered in obtaining solutions at the highest angle of attack, $\alpha = 40^\circ$. Nonetheless, it is believed that the consistency of the results is such that values at high angles of attack can be extrapolated without great risk. More detail on the computational results is given in ref. 10.

The effect of real-gas thermodynamics on the surface pressure distribution is illustrated in figure 6 by comparing the pressure distribution for a perfect gas at

M_∞ = 23 with an equilibrium-air calculation for conditions at a point on the reentry trajectory corresponding approximately to the same Mach number. Note that the real-gas pressures are slightly higher than the perfect-gas pressures in the forebody region and somewhat lower on the afterbody. These distributions indicate that an effect of real gas will be to produce a more positive (nose-up) pitching moment.

Real-gas effects on the normal-force coefficient of the Shuttle orbiter model are illustrated in figure 7. The Mach numbers for the real-gas computations in this figure correspond to points of the reentry trajectory given in table I. Figure 7 indicates a slight decrease in normal-force coefficient attributable to real-gas effects caused by the lower pressures on the aft part of the orbiter.

Real-gas effects on pitching moment are illustrated for the high-velocity, high-altitude case in figure 8 by comparing the results for perfect-gas computations with those for equilibrium-air thermodynamics. This figure reveals that the real-gas effects drive C_M more positive with the effects being most significant at higher angles of attack. The equivalent effects of Mach number and real gas on center-of-pressure location are shown in figure 9.

VISCOUS ANALYSIS

The analysis of the viscous effects on the Space Shuttle orbiter aerodynamics was pursued using two complementary approaches: (1) fully viscous computations for a modified orbiter geometry using a parabolized Navier Stokes computer code and (2) the development of simple analytical expressions for the viscous contribution to C_A and C_M from theoretical considerations and experimental data.

PNS Computations

The main emphasis of this part of the program was to obtain laminar viscous flow field solutions for a model orbiter geometry employing an existing parabolized Navier Stokes computer code (PNS) originally developed by Schiff and Steger (ref. 6). Further developmental work on this code is currently being sponsored by AFWAL/FIMG. Some of the more recent modifications are described in ref. 11. It should be noted that it is a perfect-gas code at the present time.

The model geometry for which these computations were carried out is similar to the inviscid computational geometry shown in figure 2 and described in the section entitled INVISCID COMPUTATIONS. The principal difference between the two computational models is that the upper surface of the viscous geometry is approximated by ellipses as indicated by the dashed line in figure 2.

The PNS code uses a starting solution on an initial data surface where the inviscid flow is supersonic. The embedded subsonic region over the nose requires a three-dimensional time-dependent Navier-Stokes code for the blunt-body nose solutions. The full three-dimensional time-dependent thin-layer Navier-Stokes code (AIR3D) developed by Kutler et al. (ref. 4) is used here to obtain the blunt-nose solution and initial data for starting the parabolized Navier-Stokes code.

Obtaining solutions on the Shuttle-like geometry was not an easy task. A number of modifications to the code, described in more detail in ref. 12, were required to march the solution to the end of the body. In particular, stability problems were encountered to about x/L = 0.6 where the wing flare occurs. At this point, it was

found necessary to delete the lee side from the flow field, replacing the lee pitch plane symmetry condition by a supersonic outflow condition just above the wing. The solution on the windward side could then be continued to the end of the body for low angles of attack ($<20^{o}$).

Numerical solutions of three-dimensional parabolized Navier-Stokes equations were obtained for the Shuttle-like geometry at Mach 23 over a pressure altitude range of 52.4 and 86 km (172,000 and 282,000 ft) at an angle of attack of 20° in order to illustrate the application of the technique. The Shuttle angle of attack at Mach 23 during flight is about 40^{o}, a more difficult computation. A numerical solution of an AEDC Tunnel B test condition at Mach 8 and 25° angle of attack was also obtained. Free-stream conditions for the test cases are given in table II.

Figure 10 shows a comparison of computed heat transfer distribution along the windward centerline with data from AEDC Tunnel B (ref. 12). The PNS code slightly overpredicts the data, but the agreement is considered to be good.

Figure 11 presents the surface pressure along the body surface at windward ($\phi = 0$) and leeward ($\phi = 180^{o}$) planes for two different Reynolds numbers. The pressure on the lee side after $x/L = 0.2$ is very low and should have little effect on the aerodynamic coefficients. The PNS results approach the inviscid STEIN results as the free-stream Reynolds number is increased.

Figures 12 and 13 present the theoretical pitching-moment and axial-force contributions attributable to direct viscous shear and induced pressure effects as a function of viscous interaction parameter, $\overline{V}_{\infty}$. The viscous contribution to C_M or C_A is the value at $\overline{V}_{\infty}$ minus the value at $\overline{V}_{\infty} = 0$. The shear force on the wind surface causes a nose-down pitching moment as shown in figure 12, decreasing the amount of elevon or body flap deflection necessary to trim the vehicle.

Semi-Theoretical Analysis

It is well-known that for fully attached flow, the local skin friction coefficient and the Stanton number can be related through Reynolds analogy:

$$C_{f_{\infty}} = K_r \, St_{\infty} \tag{1}$$

where K_r is the Reynolds analogy factor ($K_r = 2 \, Pr^{1/2}$ for laminar flow over a flat plate). It is assumed that at high angles of attack, all of the viscous forces act on the lower surface of the vehicle. It is further assumed that the average skin friction on the windward surface is proportional to an average Stanton number. Then, the total viscous axial-force coefficient can be expressed as

$$\Delta C_A = \left(C_{f_{\infty}}\right)_{AVG} \left(\frac{S_{WET}}{A}\right) = \left(K_r S_{t_{\infty}}\right)_{AVG} \left(\frac{S_{WET}}{A}\right) \tag{2}$$

Introducing the viscous parameter

$$\overline{V}_{\infty} = \frac{M_{\infty} \sqrt{C_{\infty}}}{\sqrt{Re_{\infty,L}}}$$

into eq. (2) yields

$$\Delta C_A = \left(St_\infty\right)_{AVG} \sqrt{Re_{\infty,L}} \frac{K_r \bar{V}_\infty}{M_\infty \sqrt{C_\infty}} \frac{S_{WET}}{A} \tag{3}$$

Heat transfer data (Test OH-11) obtained on the orbiter configuration in AEDC Hypervelocity Wind Tunnel (F) (ref. 13) were used to define the variation of $(St_\infty)_{AVG}(Re_{\infty,L})$ as a function of M_∞ and α (see figure 14):

$$\left(St_\infty\right)_{AVG} \sqrt{Re_{\infty,L}} = M_\infty \sin \alpha \tag{4}$$

Using this relation in eq. (3) gives

$$\Delta C_A = \bar{V}_\infty \sin \alpha \frac{K_r S_{WET}}{\sqrt{C_\infty} A} \tag{5}$$

Theoretical calculations on an earlier Space Shuttle design using a quasi-three-dimensional boundary layer code developed by Adams and Martindale (ref. 14) indicate that the Reynolds analogy factor, K_r, for the windward side depends on angle of attack (see figure 15):

$$K_r(\alpha) = K(\cos \alpha)^{1.75} \tag{6}$$

Substituting in eq. (5) gives

$$\Delta C_A = \bar{V}_\infty \sin \alpha \, (\cos \alpha)^{1.75} \frac{K S_{WET}}{\sqrt{C_\infty} A} \tag{7}$$

Evaluating the constants

$$C_\infty = 0.932 \text{ (tunnel conditions)}$$

$$K = 1.99, \quad \frac{S_{WET}}{A} = 1.695$$

yields

$$\Delta C_A = 3.63 \, \bar{V}_\infty \sin \alpha \, (\cos \alpha)^{1.75} \tag{8}$$

Recalling the assumption that the viscous drag acts only over the windward surface of the orbiter, the above expression can also be used to obtain an approximation to the viscous contribution to pitching moment. Referring to figure 16 shows that multiplying eq. (8) by an effective lever arm, the distance from the assumed center of gravity to the windward surface, appropriately nondimensionalized, gives an approximate expression for ΔC_M. Taking Δz to be 254 cm gives

$$\Delta C_M = -0.765 \, \bar{V}_\infty \sin \alpha \, (\cos \alpha)^{1.75} \tag{9}$$

Figure 17 shows a comparison of the viscous contribution to C_A and C_M as obtained from eqs. (8) and (9) with corresponding PNS solutions and experimental data (ref. 15) from AEDC Tunnel F at 20^o angle of attack. The various experimental points during a given Tunnel F run are data taken at different test times during the run where the Reynolds number and Mach number are changing because of a decreasing stagnation pressure and generally a changing stagnation temperature. Inviscid values of 0.0520 (C_A) and +0.0010 (C_M) were subtracted from the tabulated experimental data in ref. 15 to obtain ΔC_A and ΔC_M. The empirical equations (8) and (9) give a very good representation of the viscous influence predicted by the PNS solution and displayed by the experimental data at this angle of attack.

DEVELOPMENT OF METHODOLOGY MODEL

In order to make comparisons with flight results, aerodynamic coefficients for the Space Shuttle orbiter under flight conditions were obtained by extrapolating wind tunnel data for $M_\infty = 8$. The methodology that was employed in this extrapolation is illustrated in figure 18. The Mach number and real-gas effects were obtained from the computational results previously described. The viscous effects indicated in figure 18 were derived from a combination of computational results using a parabolized Navier-Stokes code and a semi-theoretical analysis as described in the previous section. The summation of the Mach number, real-gas and viscous effects is equal to the AEDC DCM described in the following section.

For the comparisons made in this paper, the contribution of the control surface deflections was assumed to be as predicted before flight. In other words, it was assumed that the tunnel-derived control surface effectiveness was not further degraded by viscous effects nor substantially changed by Mach number and real-gas effects. This assumption appears to be satisfactory for the comparisons made here, but further analysis of Mach number, real-gas, and viscous effects of the elevons and body flap is needed.

An example of the buildup of flight C_M for the basic body is given in figure 19 for a high-altitude point on the flight trajectory. This plot depicts the Mach 8 Tunnel B data and the Mach number, real-gas, and viscous effects derived from CFD computations to arrive at the basic body C_M for flight conditions. Also shown in this figure are the pre-flight predictions (ref. 3) of C_M for similar conditions. Note that the basic body values of C_M based on the present results are 0.02 or more greater than the preflight predictions.

Figure 20 shows a comparison of the results of the methodology model with the first body flap sweep of STS-2, where the body flap and elevons were deflected simultaneously to maintain the orbiter in trim. Displayed in figure 20 is the elevon deflection as a function of body flap angle obtained by using the $M_\infty = 8$ basic-body pitching-moment data. This dashed curve is very close to the preflight prediction. In addition, figure 20 shows the relationship between body flap deflection and elevon deflection during this sweep as computed by the present methodology and the corresponding flight data. The agreement is excellent.

DCM COMPUTATIONS

Computations at various Mach numbers, altitudes, and angles of attack using the methodology model were made. A series of these computations is presented in figures 21 through 26. The data are presented as a $(DCM)_{CFD}$ to be added to the Mach 8 ADDB basic body pitching moment.

The $(DCM)_{CFD}$ decreases as the angle of attack of the orbiter decreases. However, the effective center-of-pressure shift increases at the lower angles of attack as noted in figure 9. The $(DCM)_{CFD}$ also decreases slightly as altitude increases because of the nose-down moment caused by the increasing viscous forces on the lower surface. Additional PNS solutions are needed at higher angles of attack in order to improve or validate the methodology model.

PROBLEM AREAS

The previous sections attempt to give an explanation of the longitudinal stability DCM problem that caused the additional body flap deflection for trim. This section briefly outlines some of the problem areas encountered in flight data reduction, tunnel and ADDB data, and the CFD computations.

Comparison of DCM_{CFD} With Reduced STS-3 and STS-4 DCM_{FLT}

Figure 27 presents the definition of DCM as derived from flight and CFD computations. A comparison of these DCM's for flights STS-3 and STA-4 is given in figure 28. The DCM_{CFD} underpredicts the flight DCM between 0.0030 and 0.0060 above 56.4 km (185,000 ft). Similar agreement is noted when data from STS-1 and STS-2 are analyzed.

Flight/ADDB Problems

An accurate DCM from flight depends upon both good flight data and accurate mass properties, plus a data base that describes the aerodynamic parameters of the body flap and elevon as a function of Mach number, altitude, and attitude.

The incremental differences between flight and computer DCM are presented in figure 29 as a function of altitude. The figure also shows the sensitivity of the difference to the flight CG. A 5.08-cm (2-inch) forward error in the noted center of gravity of STS-3 will bring the flight and computed DCM into agreement above 55 km (180,000 ft).

Another problem that needs to be considered is the variation of the body flap and elevon effectiveness with the flight parameters. Figure 30 shows the shock shape along the wind surface for a Mach 8 ideal-gas and a Mach 23 equilibrium-air solution. The effectiveness of the body flap should be influenced by the significant difference in the shock shapes. Figure 30b presents the difference between flight (STS-1 to 4) and the DCM_{CFD} as a function of body flap deflection for an altitude of 73.1 km (240,000 ft). The DCM should not be a function of body flap deflection; however, a definite trend is shown, indicating a possible error in the ADDB high Mach number, body flap effectiveness. However, a 2.54-cm (1-inch) error

in CG for any of the flights would alter the trend. Figure 31 shows the velocity profiles from the PNS solutions entering the body flap on the wind plane of symmetry for several altitudes at Mach 23 and 20° angle of attack. The projections of the body flap into the flowstream for 5° and 8° deflections are also given in this figure. The results clearly show that the viscous influence on the body flap effectiveness at 20° angle of attack should be considered.

Atmospheric unknowns are always present in flight data to some degree. Figure 32 gives a comparison of the flight normal force (C_N) and the computed normal force. The calculation of C_N should be the most accurate of all the aerodynamic parameters since C_N does not significantly vary with Reynolds number, and the body flap and elevon contributions are not large. Considerable variation, however, is noted between the various flights. This variation is most likely due to inaccuracies in the determination of local atmospheric density.

A summary of the various problem areas is given in figure 33. Each of these should be considered in any flight analysis.

CFD and Empirical Computations

The ability to make CFD calculations on flight configurations has advanced at a rapid pace in the last few years. Problems, however, still exist in computing the flow over complex configurations such as the Space Shuttle. The validation of computed real-gas effects in ground test facilities is very difficult. Computing the flow over the exact Space Shuttle geometry is not yet possible. The numerics of the code can influence the answer in some situations. Finally, solutions from several codes are required (see figure 34) to develop a methodology model, plus some empirical work. A few of these problems are discussed in the following paragraphs.

One computational parameter that could not be held constant for all calculations was X_{ST}, the station at which blunt body (CM3DT) solution was used to start STEIN solution (see figure 34). The flow must be fully supersonic at this plane, and the windward-side sonic line moves aft as angle of attack increases. Thus, with changing angle of attack, X_{ST} must be changed. There is some arbitrariness in the selection of X_{ST} just as there is some arbitrariness in the number of mesh points used. Generally speaking, X_{ST} was chosen just downstream of the windward-side sonic point to take maximum advantage of the more efficient STEIN computation. The table in figure 34 shows the effect of X_{ST} changes on the computed C_M at $\alpha = 30^{\circ}$. More importantly, note that the effect on ΔC_M is less than 0.0001. Based on a series of such computations the uncertainty in ΔC_M for Mach number and real-gas effects is estimated to be no greater than ±0.0008.

A comparison of the basic-body axial force between flight and the CFD calculations is given in figure 35 for STS-3 and figure 36 for STS-4. In order to minimize the influence of unknown atmospheric and control variations, the following procedure was used:

$$C_{A_{BB}} = (C_{A_{FLT}}) \frac{C_{N_{AEDC}}}{C_{N_{FLT}}} - \Delta C_A \, (\delta_{bf}, \, \delta_e, \, \text{ADDB}) \qquad (10)$$

Several conclusions can be drawn from an analysis of figures 35 and 36. These are: (1) the poor agreement between the flight C_N and computed C_N indicates that a problem

with the STS-4 atmosphere may exist above 60 km (200,000 ft), (2) the basic body flight C_A (eq. (10)) between STS-3 and STS-4 is in excellent agreement, and (3) AEDC modeling of the axial force above 64 km (210,000 ft) does not match the flight data. Additional PNS solutions at higher angles of attack are needed as an aid in explaining the higher altitude disagreement. The prediction from the ADDB is shown in figure 35 for reference.

The L/D ratio for STS-3 is presented in figure 37. The AEDC methodology model is in excellent agreement with the flight data. Above 64 km (210,000 ft) the flight L/D is about one percent higher than the AEDC computed value. The disagreement between the flight C_A and computed C_A in this region is the reason for the disagreement.

Finally, figure 38 summarizes the major problem areas in the CFD computations. It should be noted that the term CFD in this paper includes the semi-empirical work on the shear drag as presented in the section on viscous analysis.

LESSONS LEARNED

Advanced CFD codes have been applied to a modified Space Shuttle orbiter geometry to obtain inviscid and viscous flow field solutions for both wind tunnel and hypersonic flight conditions. Based on the CFD studies, a methodology model has been developed to extrapolate wind tunnel data to flight conditions and to calculate the DCM that should be used with the ADDB for better flight predictions. The results of this investigation led to the following lessons learned:

1. Wind tunnel data can be used with the state-of-the-art CFD computations for improved flight predictions.

2. Real-gas and high Mach number effects are important for most high Mach number reentry vehicles, especially the Space Shuttle.

REFERENCES

1. Young, J. C.; Perez, L. F.; Romere, P. O.; Janipe, D. B.: Space Shuttle Entry Aerodynamic Comparisons of Flight 1 with Preflight Predictions. AIAA 81-2476, Nov. 1981.

2. Underwood, J. M.; and Cooke, D. R.: A Preliminary Correlation of the Orbiter Stability and Control Aerodynamics from the First Two Space Shuttle Flights (STS-1 & 2) with Preflight Predictions. AIAA-81-0564, AIAA 12th Aerodynamic Testing Conference, Mar. 1982.

3. Russell, W. R., ed.: Aerodynamic Design Data Book, Volume 1, Orbiter Vehicle. Rockwell International, SD72-SD-00601L, Oct. 1978.

4. Kutler, P.; Pedelty, J. A.; and Pulliam, T. H.: Hypersonic Flow over Three-Dimensional Ablated Nosetips Using an Unsteady Implicit Numerical Procedure. AIAA Paper 80-0063, Jan. 1980.

5. Hall, D. W.: Inviscid Aerodynamic Predictions for Ballistic Reentry Vehicles with Ablated Nosetips. SAI-79-506-VF, Science Applications, Inc., Feb. 1979.

6. Schiff, L. B.; and Steger, J. L.: Numerical Simulation of Steady Supersonic Viscous Flow. AIAA Paper 79-0130, Jan. 1979.

7. Vachris, A. F.; and Yeager, L. S.: Quick Geometry - A Rapid Response Method for Mathematically Modeling Configuration Geometry. NASA SP-390, 1975.

8. Marconi, F.; Salas, M.; and Yaeger, L.: Development of a Computer Code for Calculating the Steady Super/Hypersonic Inviscid Flow Around Real Configurations. NASA CR-2675, Apr. 1976.

9. Martindale, W. R.; and Carter, L. D.: Flow-Field Measurements in the Windward Surface Shock Layer of Space Shuttle Orbiter Configuration at Mach Number 8. AEDC-TR-75-5 (AD-A012875), July 1975.

10. Maus, J. R.; Griffith, B. J.; Szema, K. Y.; and Best, J. T.: Hypersonic Mach Number and Real Gas Effects on Space Shuttle Orbiter Aerodynamics. AIAA Paper 83-0343, Jan. 1983.

11. Chaussee, D. S.; Patterson, J. L.; Kutler, P.; Pulliam, T. H.; and Steger, J. L.: A Numerical Simulation of Hypersonic Viscous Flows over Arbitrary Geometries at High Angles of Attack. AIAA Paper 81-005, Jan. 1981.

12. Szema, K. Y.; Griffith, B. J.; Maus, J. R.; and Best, J. T.: Laminar Viscous Flow-Field Predictions of Shuttle Like Vehicle Aerodynamics. AIAA Paper No. 83-0211, Jan. 1983.

13. Results of Tests of a Rockwell International Space Shuttle Orbiter in AEDC Tunnel F to Determine Hypersonic Heating Effects. Report DMS-DR-2141, Data Management Services, Chrysler Corporation, June 1975.

14. Adams, J. C., Jr.; and Martindale, W. R.: Hypersonic Lifting Body Windward Surface Flow-Field Analysis for High Angles of Incidence. AEDC-TR-73-2 (AD756499), Feb. 1973.

15. Results of an Investigation of Hypersonic Viscous Interaction Effects on an 0.01 Scale Shuttle Orbiter 51-0 Model in the AEDC-VKF Hypersonic Wind Tunnel. Data Management Services, Chrysler Corporation, Report DMS-DR-2152, Jan. 1976.

16. Results of Tests Using a 0.02 Scale Model of the Space Shuttle Vehicle Orbiter in the AEDC Supersonic Tunnel A and Hypersonic Tunnel B. Report DMS-DR-2415, Data Management Services, Chrysler Corporation, Jan. 1980.

Table I Matrix of Conditions for Inviscid Computations

α, deg	Gas	Mach Number			
		8	13	18	23
20	Ideal	v	v	v	v
	Real				v
25	Ideal	v	v	v	v
	Real				v
30	Ideal	v	v	v	v
	Real	v	v	v	v
35	Ideal	v	v	v	v
	Real	v	v	v	v
40	Ideal	x	v	v	v
	Real		x	x	x

v - Computation Completed

x - Computation Failed

Real-Gas Conditions

$M_\infty = 8$ V_∞ = 2622 m/sec (8600 ft/sec) Altitude = 46.3 km (152,000 ft)

$M_\infty = 13$ V_∞ = 4268 m/sec (14,000 ft/sec) Altitude = 57.3 km (188,000 ft)

$M_\infty = 18$ V_∞ = 5488 m/sec (18,000 ft/sec) Altitude = 64.6 km (212,000 ft)

$M_\infty = 23$ V_∞ = 6707 m/sec (22,000 ft/sec) Altitude = 73.2 km (240,000 ft)

Table II Viscous Test Case Conditions

	Case				
	1	2	3	4	5
α, deg	25	20	20	20	20
M_∞	7.92	23.0	23.0	23.0	23.0
T_∞, K	52.7	234	234	234	234
T_w, K	300	1111.1	1111.1	1111.1	1111.1
Re, m^{-1}	18.23×10^5	7.87×10^4	1.57×10^4	3.02×10^3	3.93×10^5

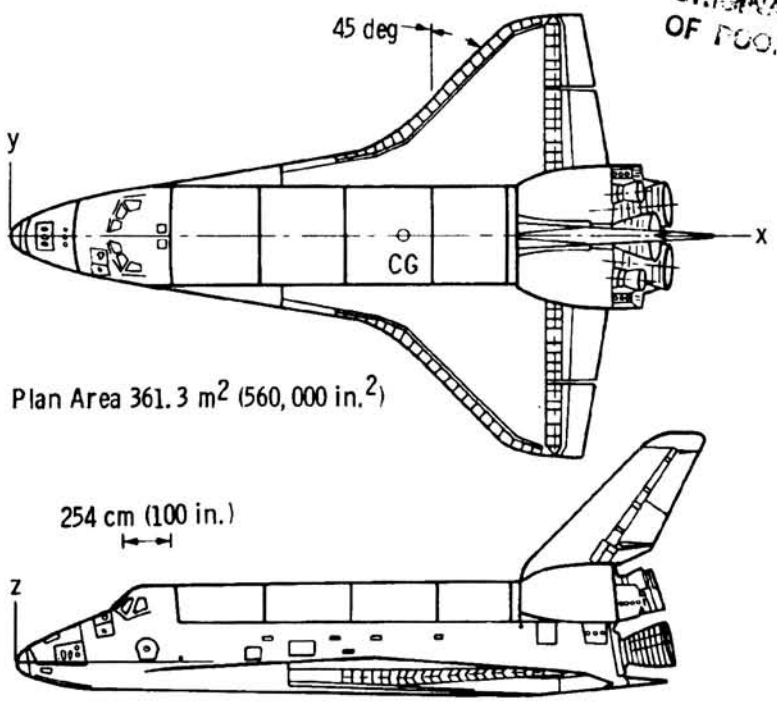

Figure 1.- Shuttle orbiter geometry.

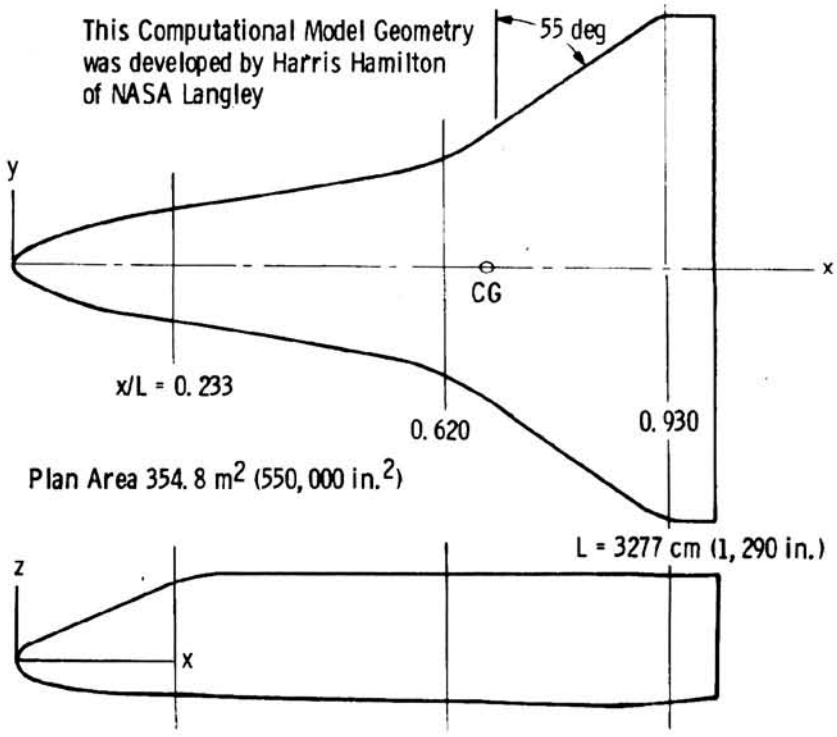

Figure 2.- Computational model geometry.

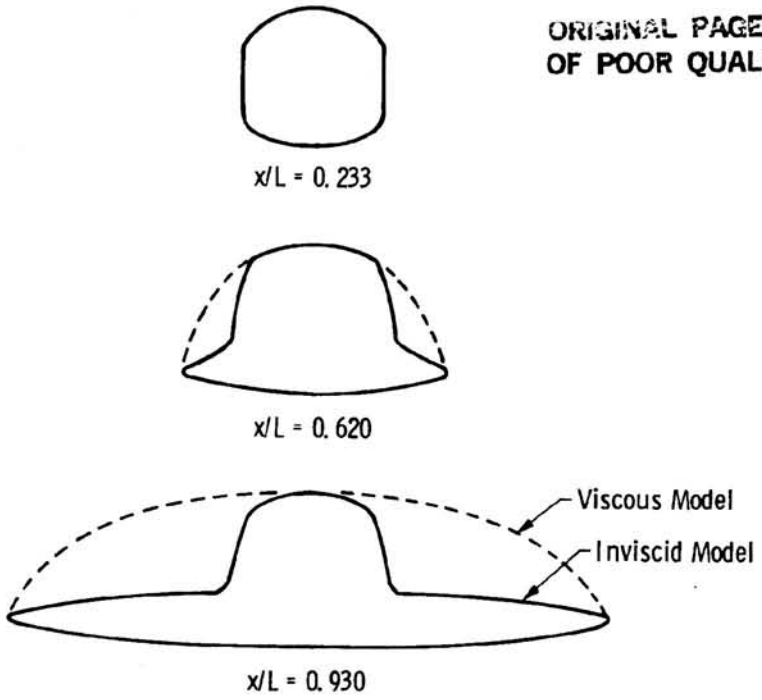

Figure 2.- Concluded.

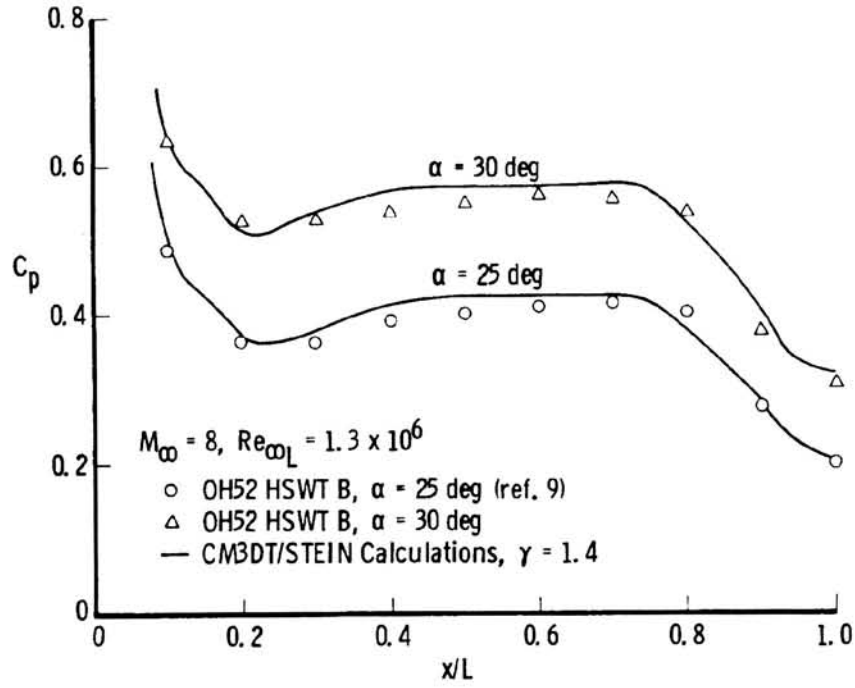

Figure 3.- Comparison of pressure distributions on windward centerline with experimental data.

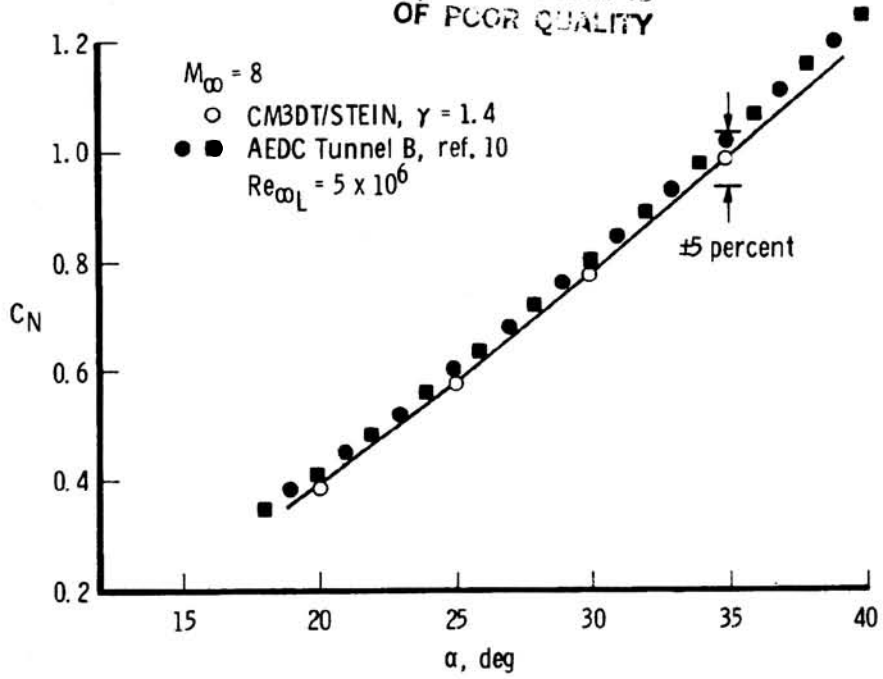

Figure 4.- Comparison of computed normal-force coefficient with experimental data.

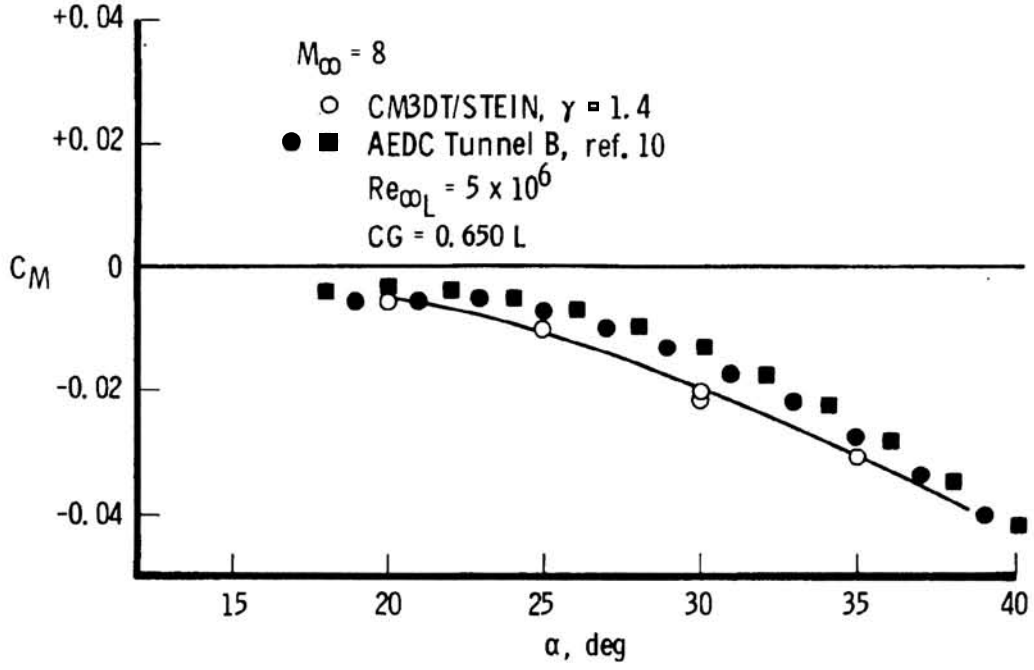

Figure 5.- Comparison of computed pitching-moment coefficient with experimental data.

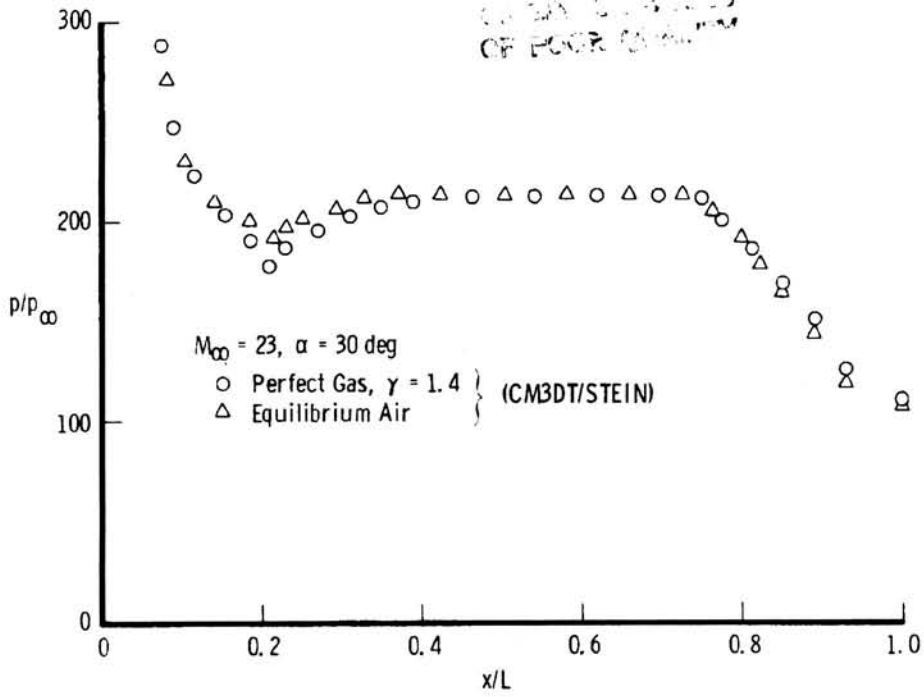

Figure 6.- Real-gas effect on windward centerline pressure distribution.

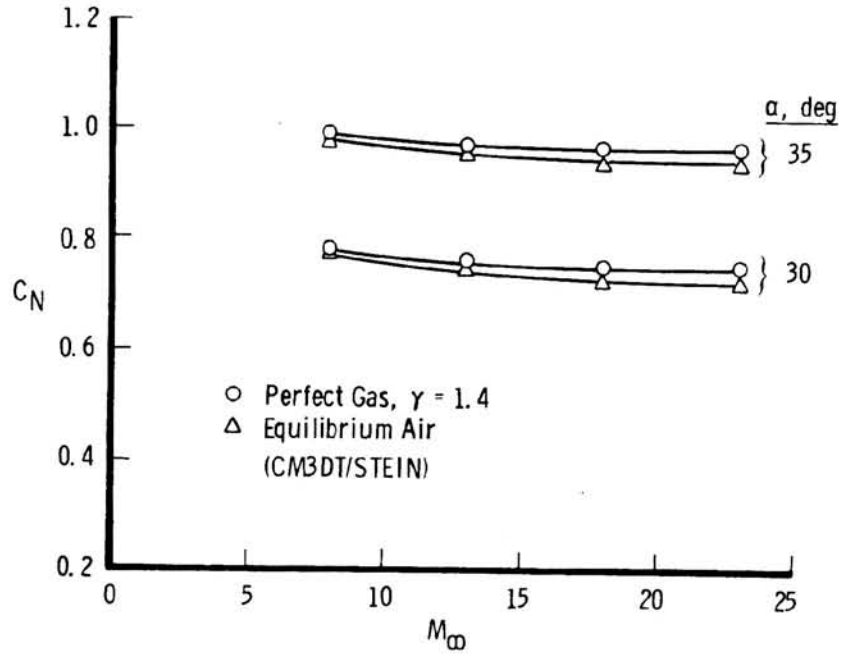

Figure 7.- Real-gas effect on normal-force coefficient.

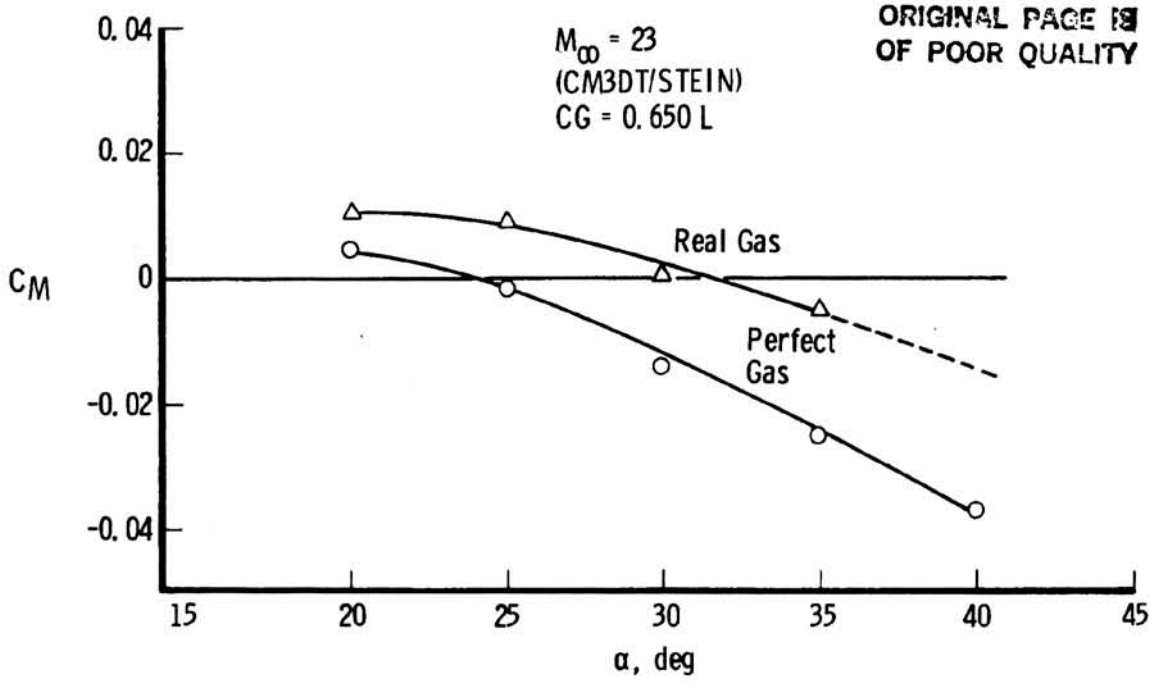

Figure 8.- Real-gas effect on pitching-moment coefficient.

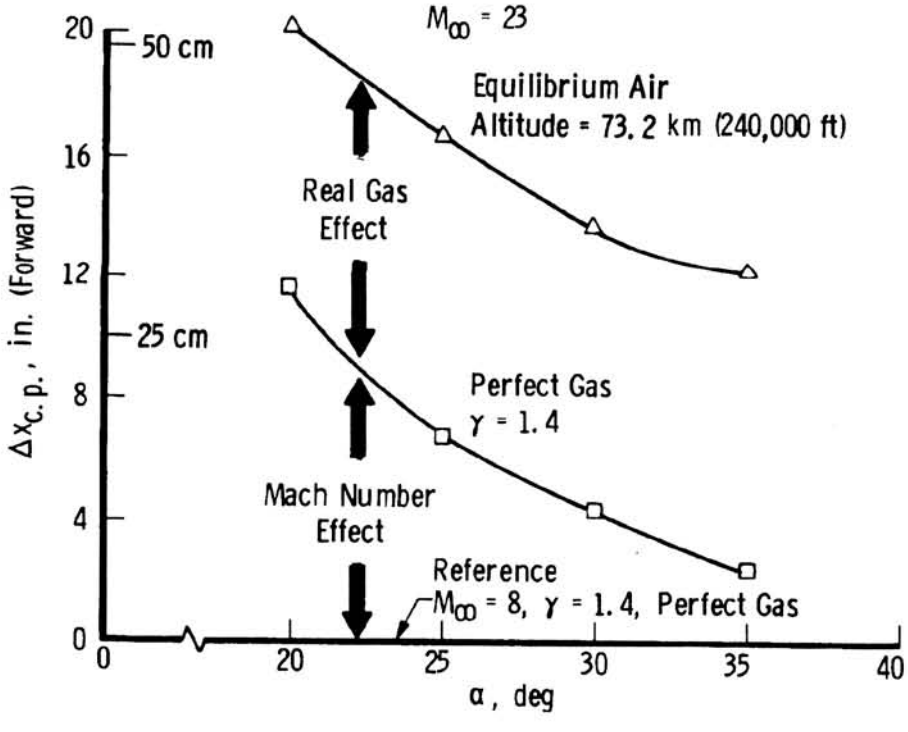

Figure 9.- Combined Mach number and real-gas effects on center-of-pressure location.

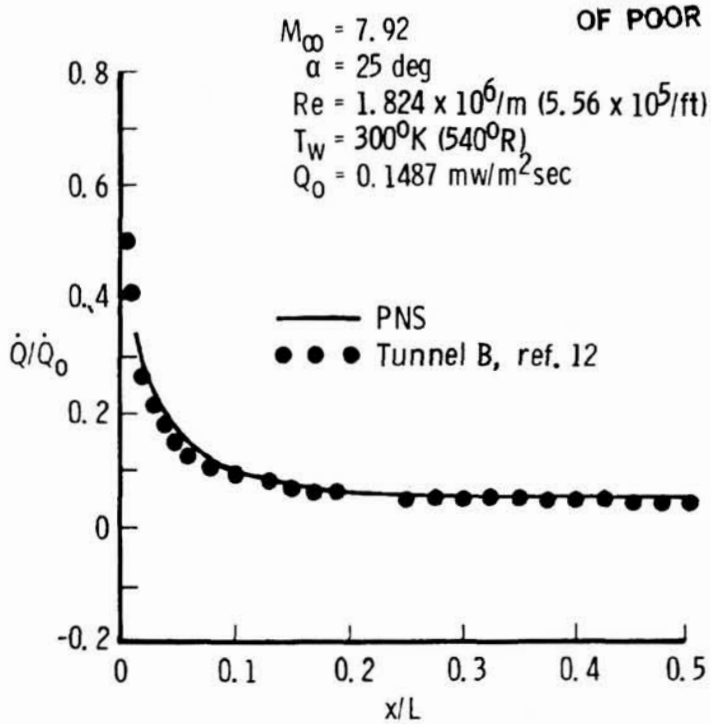

Figure 10.- Comparison of theoretical and experimental heating rates on the windward-side pitch plane.

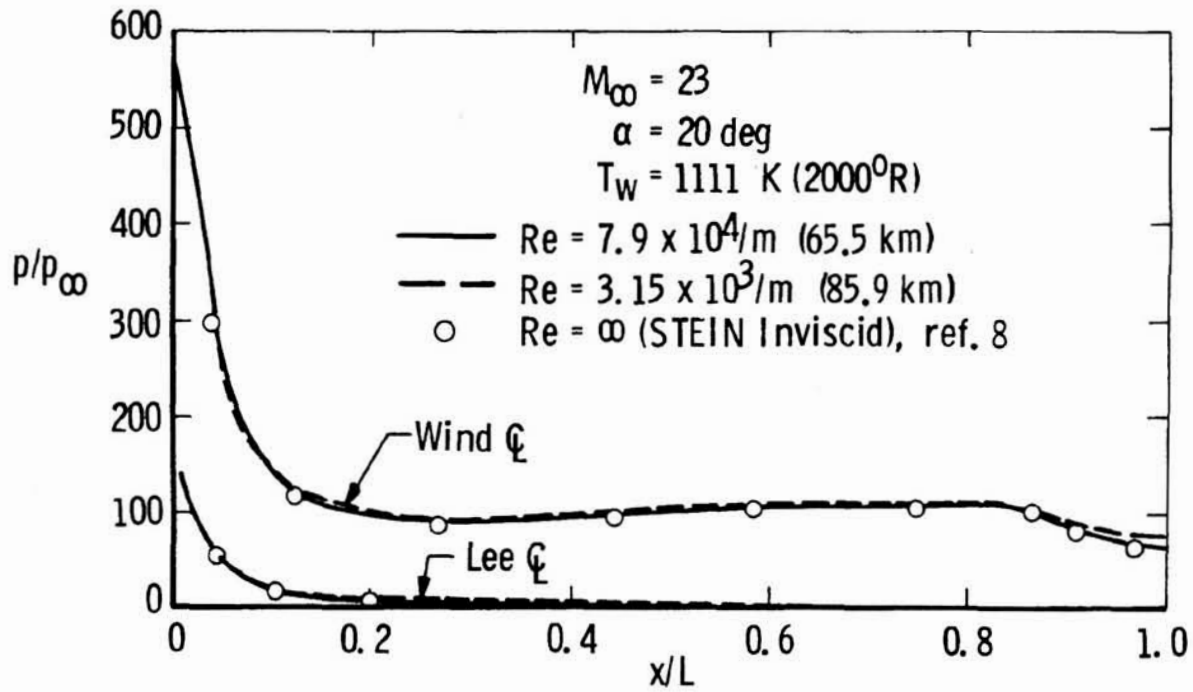

Figure 11.- Surface pressure distribution.

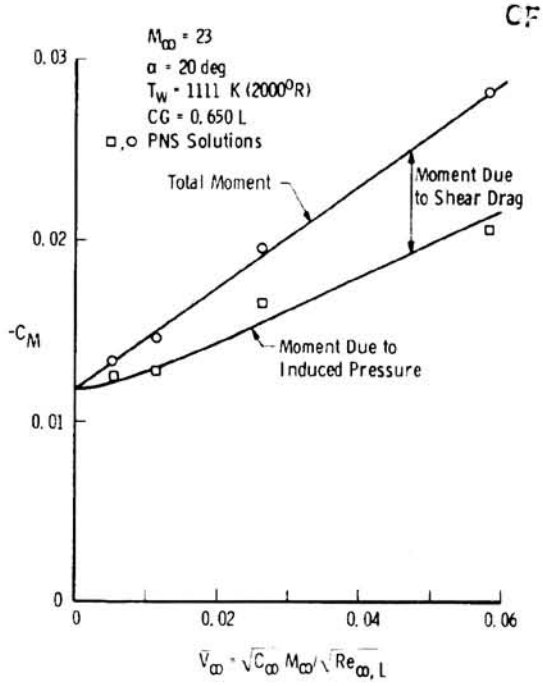

Figure 12.- Pitching-moment coefficient.

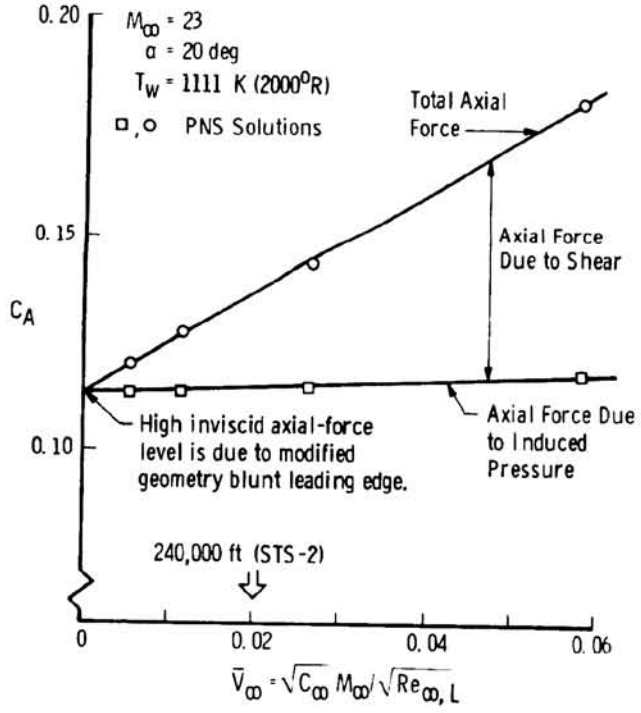

Figure 13.- Axial-force coefficient.

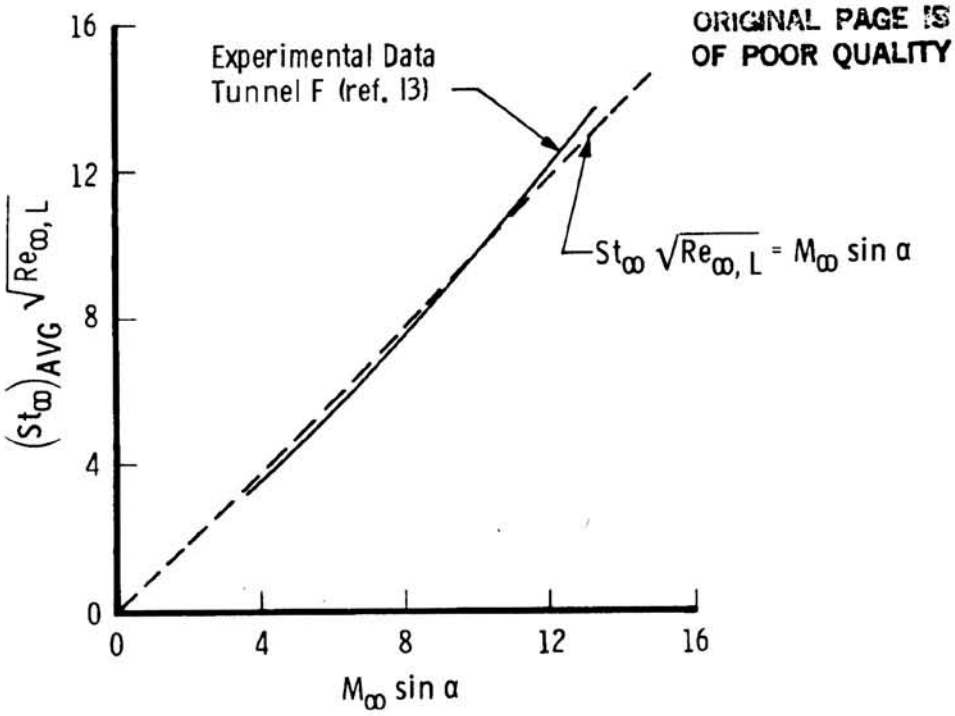

Figure 14.- Experimental variation of $(St_\infty)_{AVG}\sqrt{Re_{\infty,L}}$ with $M_\infty \sin \alpha$.

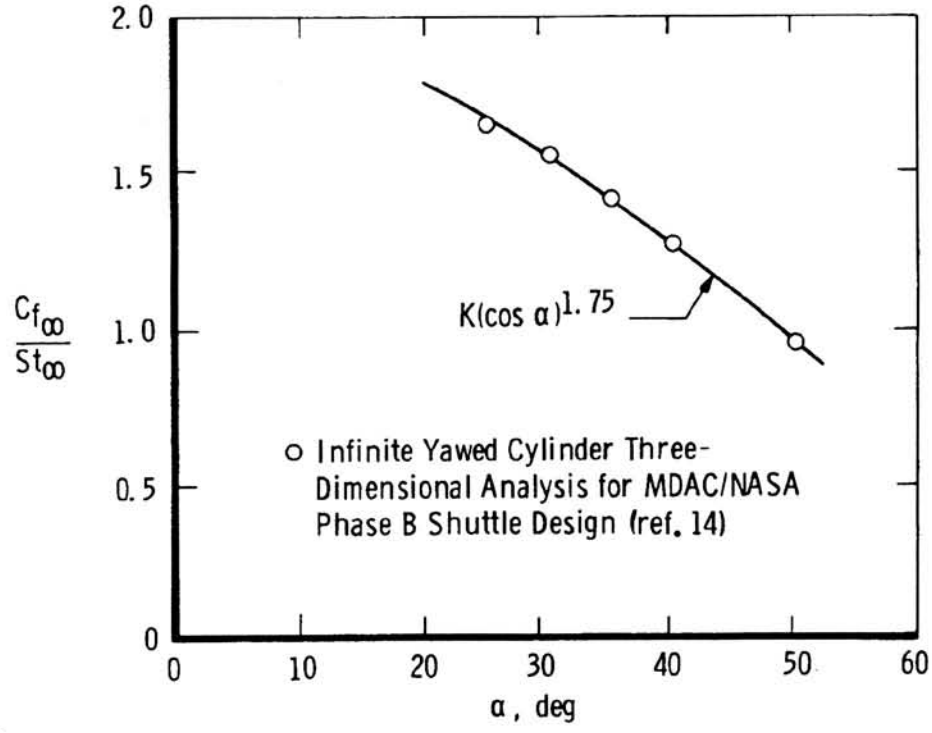

Figure 15.- Theoretical variation of C_{F_∞}/St_∞ at high angle of attack.

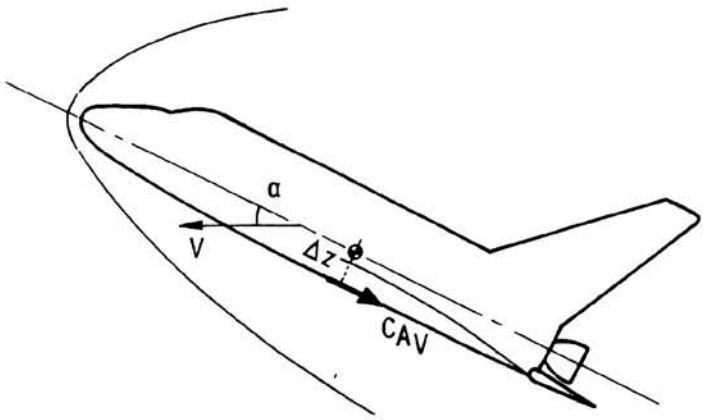

Analytical Approach

*Assumption

+ Viscous Drag and Viscous Moment Comes from Lower Surface Only.

+ Viscous Moment Can Be Expressed in Terms of Viscous Drag.

$$\Delta C_{M_V} \simeq -C_{A_V} \cdot \frac{\Delta z}{\bar{c}}$$

$$\simeq -0.765\, \bar{V}_\infty \sin\alpha\, (\cos\alpha)^{1.75}$$

Figure 16.- Viscous contribution to pitching moment.

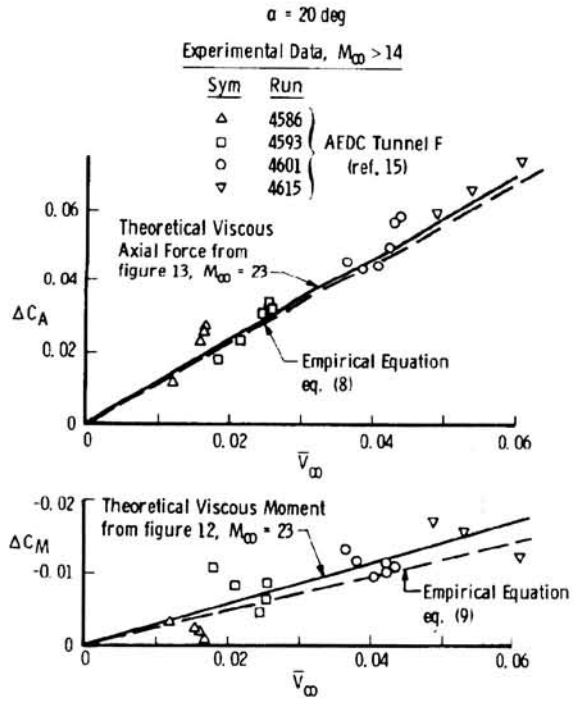

Figure 17.- Comparison of theoretical empirical, and experimental viscous drag and moment data.

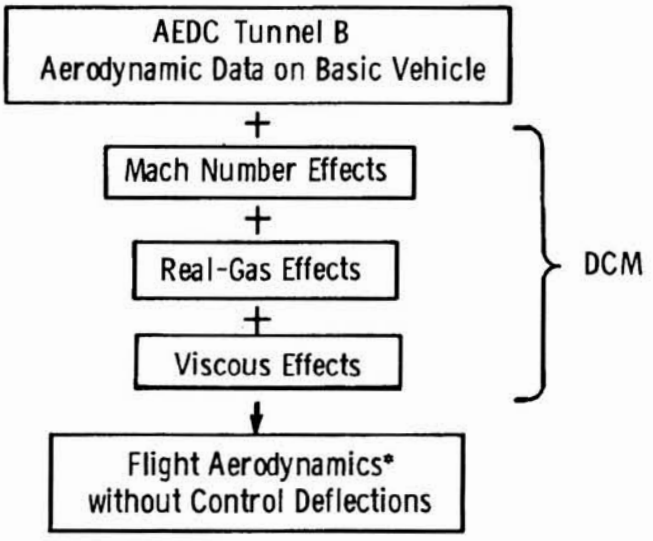

*For this study, the effectiveness of the control surfaces (body flap and elevon) was taken from the Aerodynamic Design Data Book (ref. 3).

Figure 18.- Methodology for extrapolation to flight conditions.

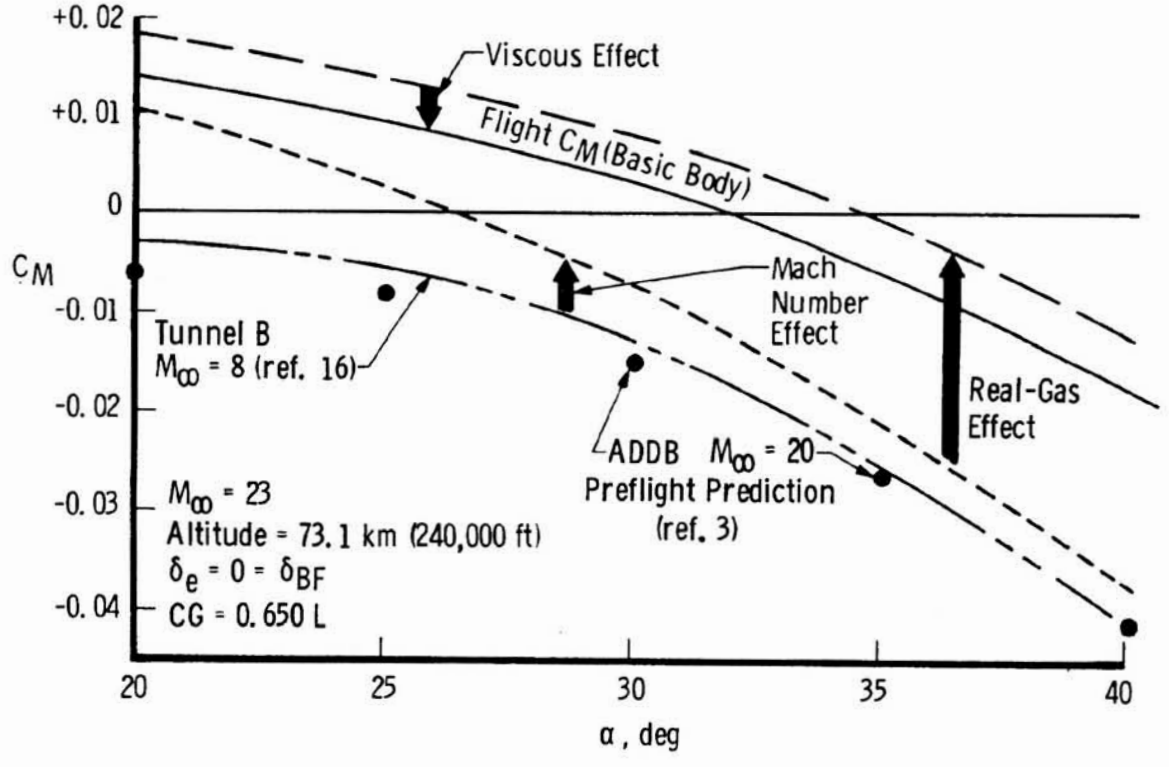

Figure 19.- Build-up of flight C_M using methodology model.

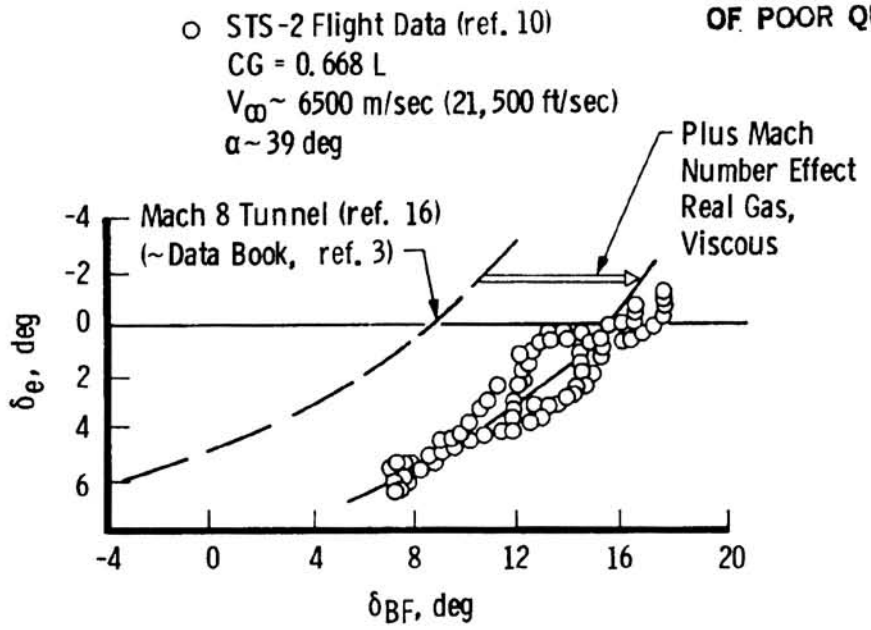

Figure 20.- Comparison of present results for first body flap sweep with flight data.

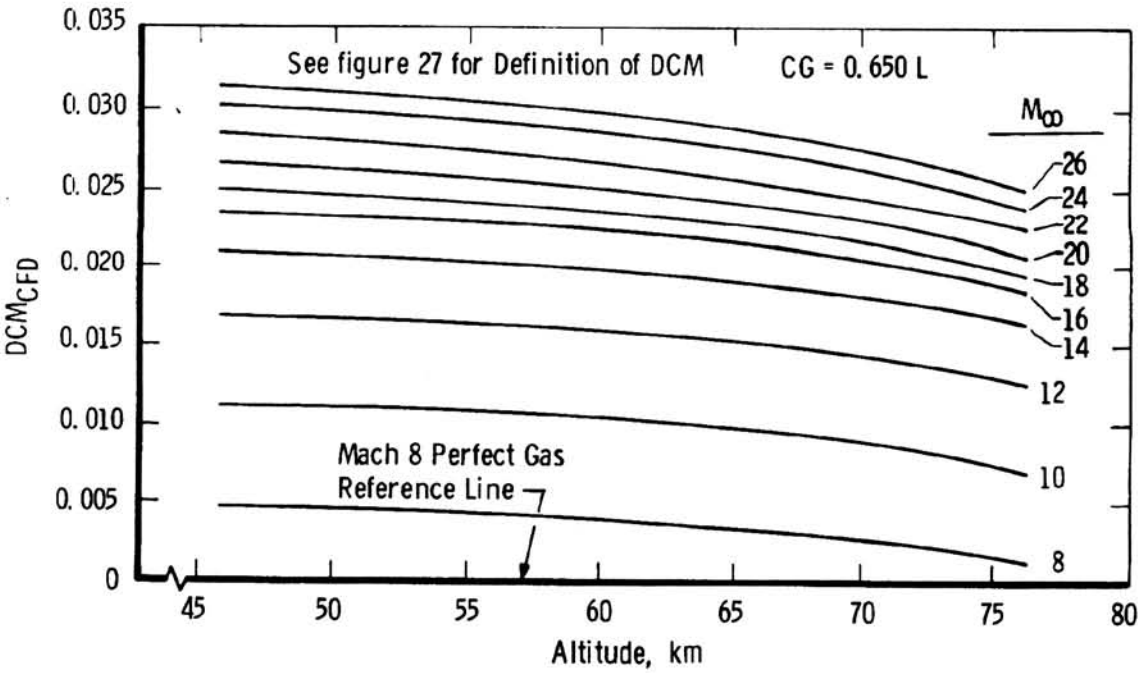

Figure 21.- Computed DCM, laminar flow, $\alpha = 45^\circ$.

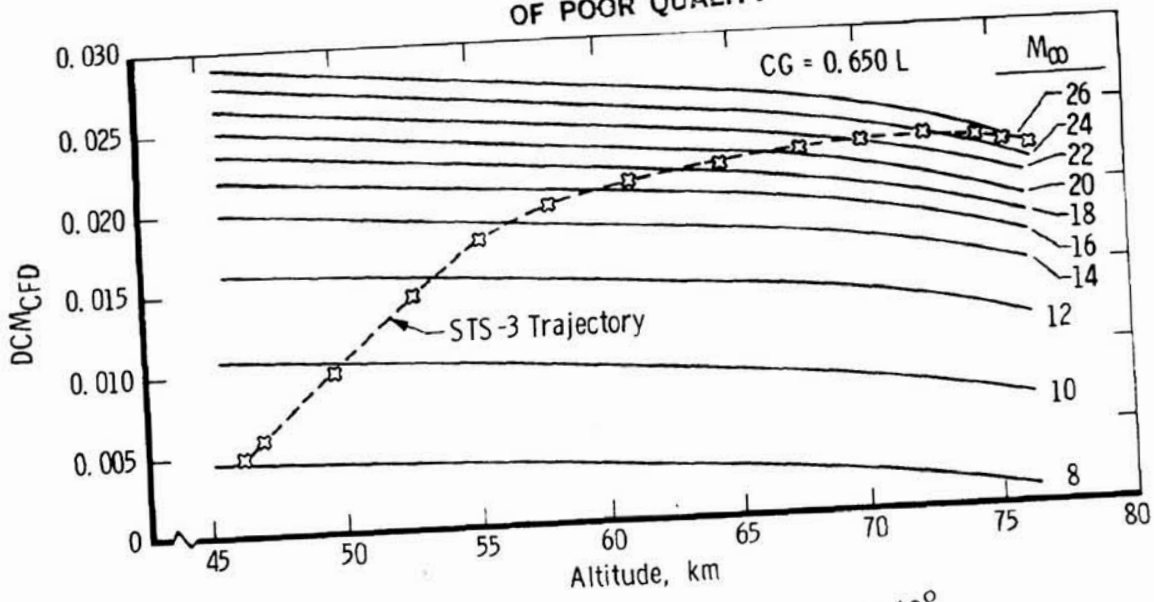

Figure 22.- Computed DCM, laminar flow, $\alpha = 40^{o}$.

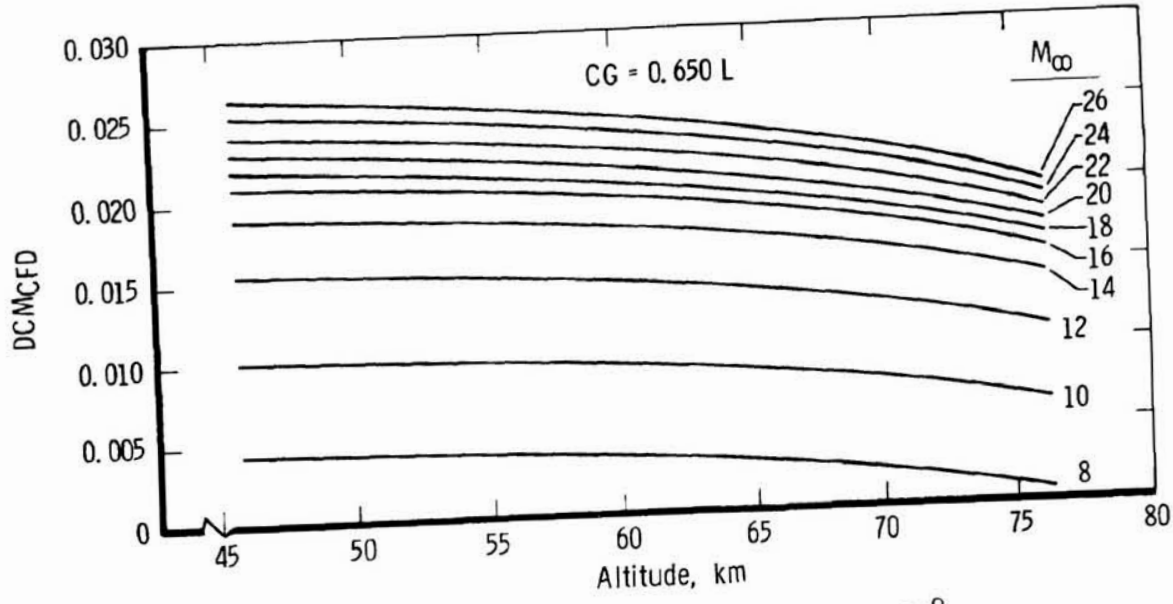

Figure 23.- Computed DCM, laminar flow, $\alpha = 35^{o}$.

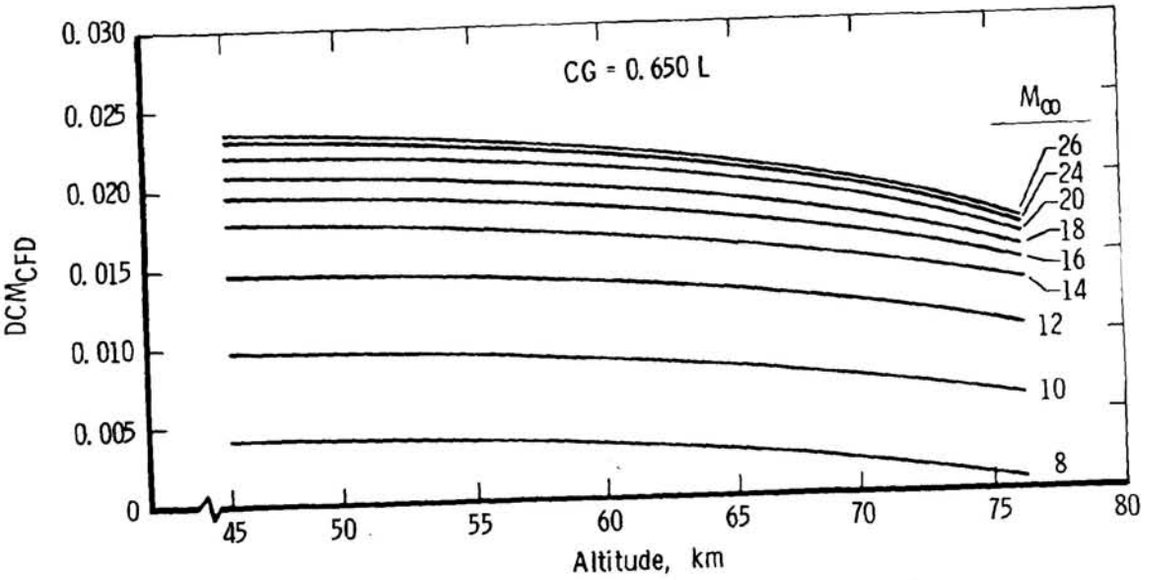

Figure 24.- Computed DCM, laminar flow, $\alpha = 30^\circ$.

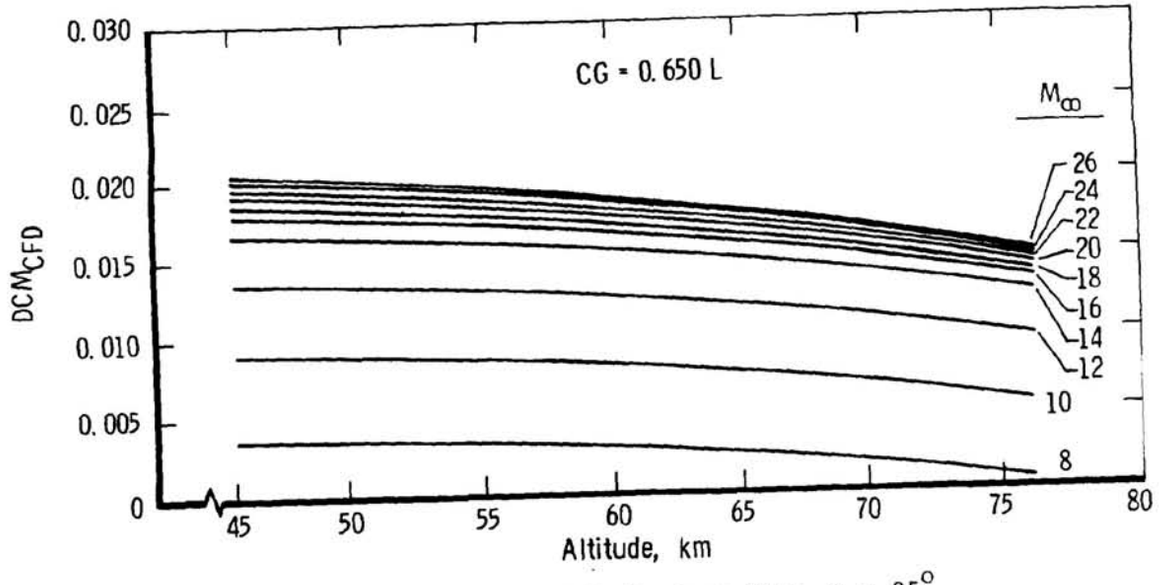

Figure 25.- Computed DCM, laminar flow, $\alpha = 25^\circ$.

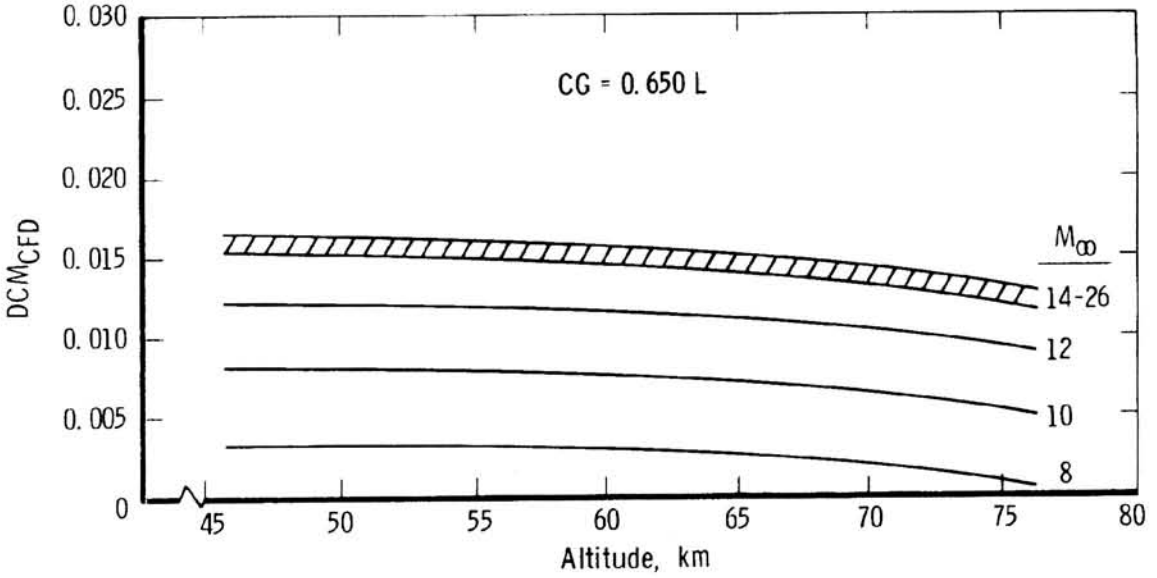

Figure 26.- Computed DCM, laminar flow, $\alpha = 20^{\circ}$.

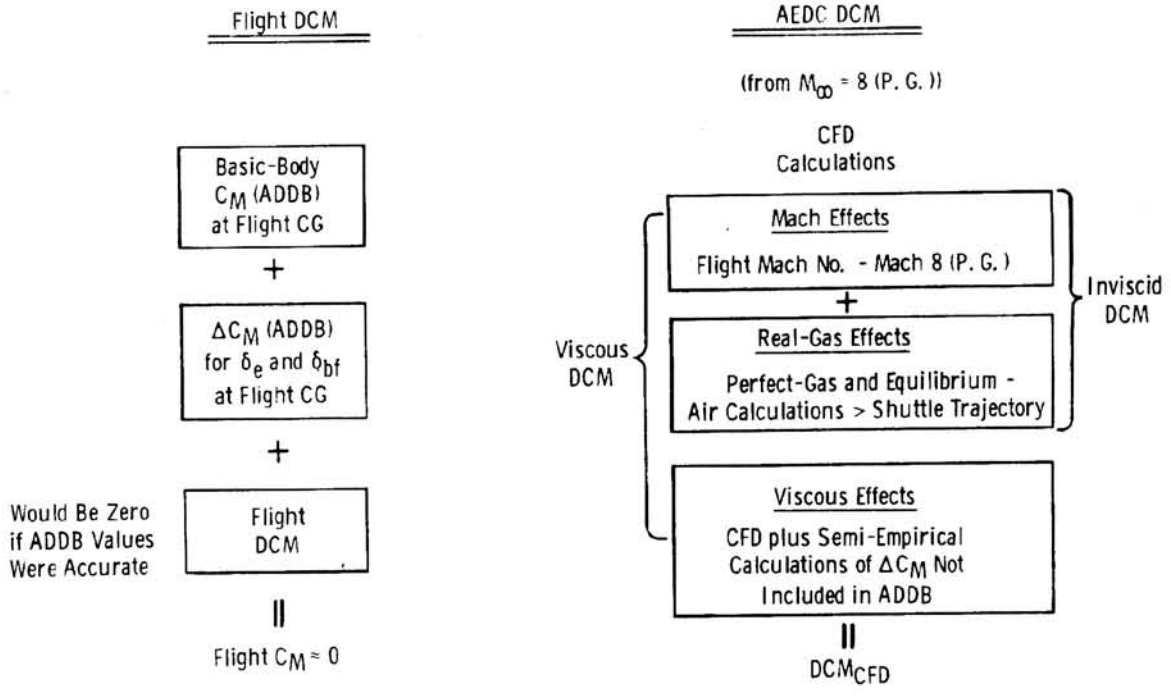

Figure 27.- Definition of DCM.

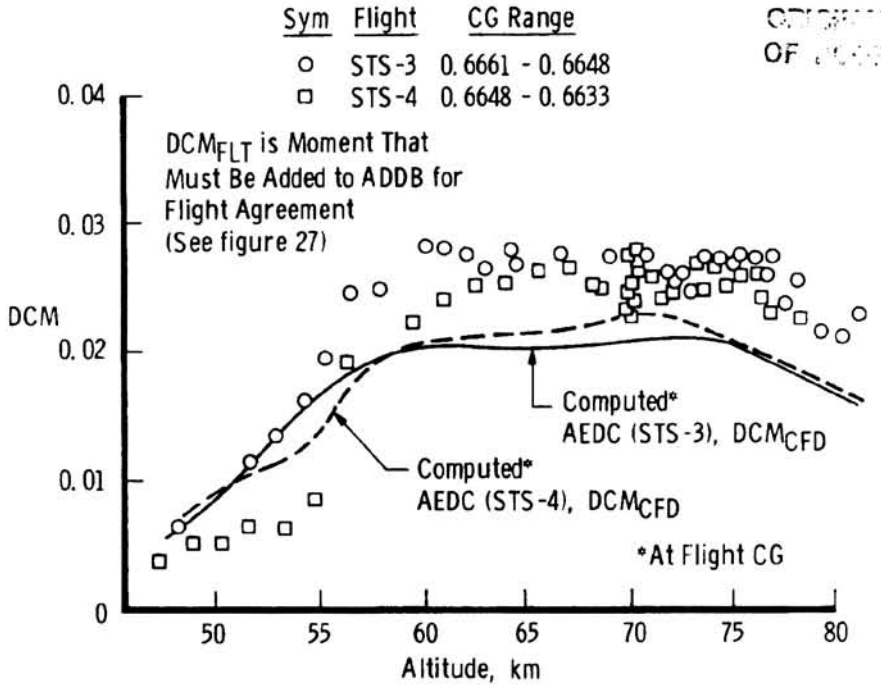

Figure 28.- DCM comparisons, CFD, and flight.

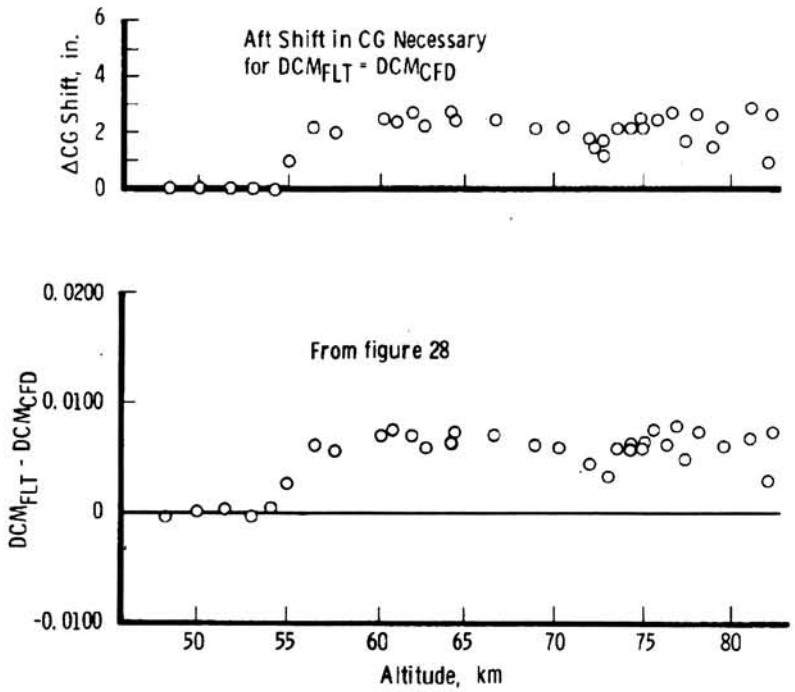

Figure 29.- Sensitivity of flight DCM to flight CG, STS-3.

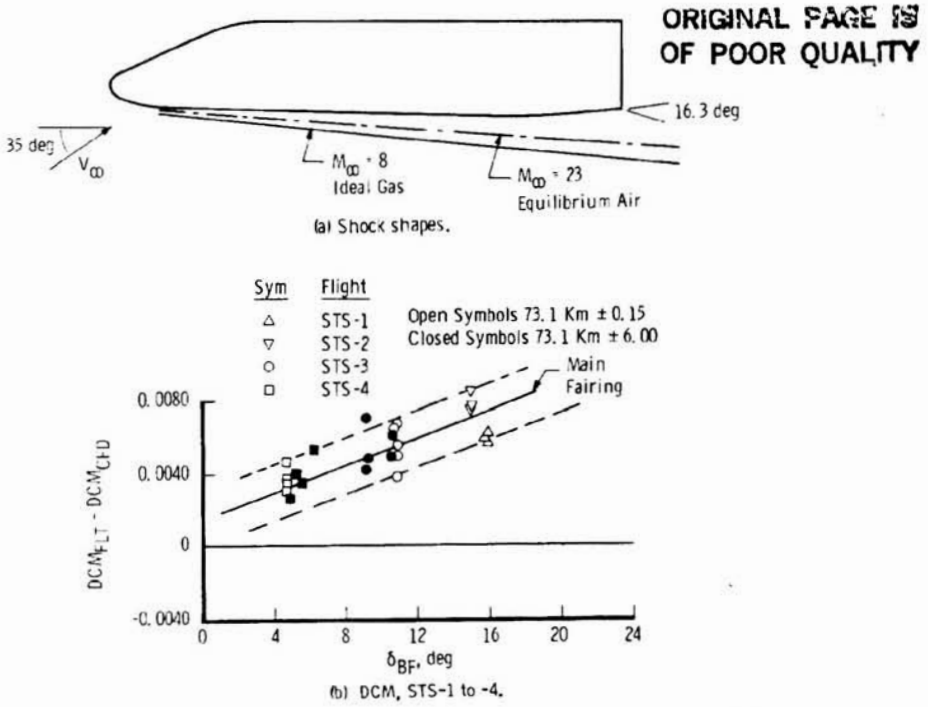

Figure 30.- Possible Mach number, real-gas, and viscous effects on body flap effectiveness.

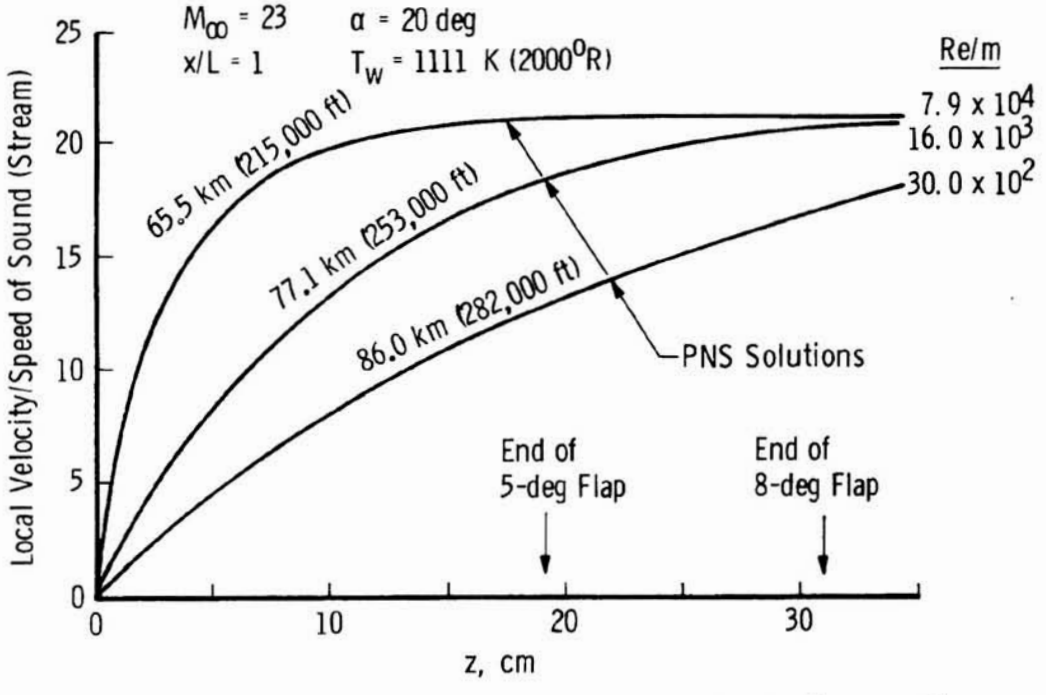

Figure 31.- Velocity profiles entering the body flap on the windward plane of symmetry.

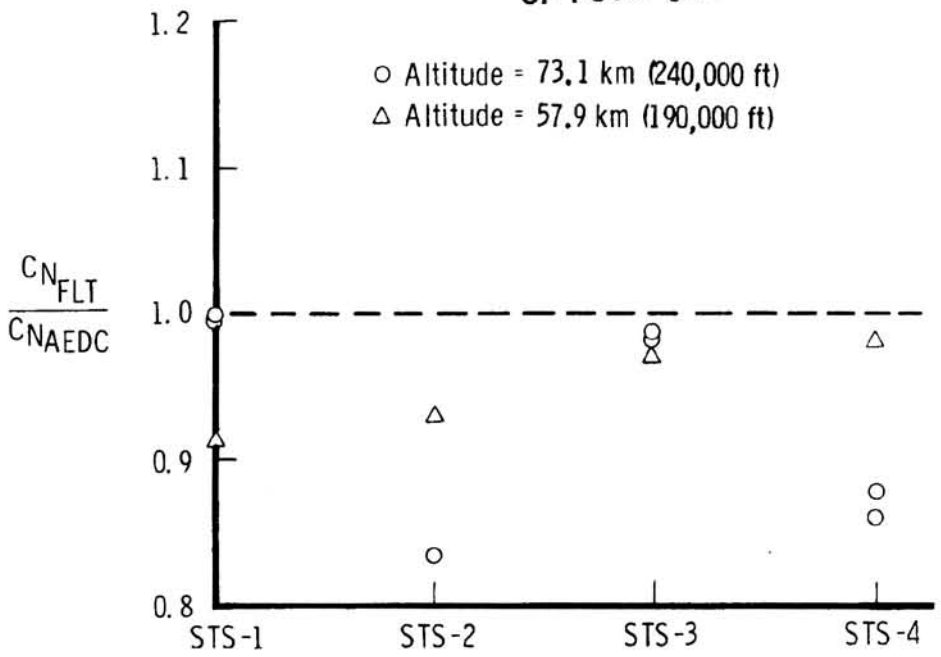

Figure 32.- Variation of flight and computed C_N at 57.9 km (190,000 ft) and 73.1 km (240,000 ft).

- ATMOSPHERIC UNKNOWNS
- ORBITER CENTER OF GRAVITY NOT AS ACCURATE AS DESIRED.
- POSSIBLE SLIGHT CONFIGURATION DIFFERENCE BETWEEN FLIGHT ORBITER AND WIND TUNNEL MODELS. HOWEVER, GREAT CARE WAS TAKEN TO MAKE SURE TUNNEL CONFIGURATIONS WERE CORRECT.
- PRECISE DETERMINATION OF PARAMETERS AS $\alpha, \delta_{BF}, \delta_e, C_N, C_M$, AND C_A.
- AERODYNAMICS OF BODY FLAP AND ELEVONS AT HIGH MACH NUMBERS ESPECIALLY UNDER HIGHLY VISCOUS CONDITIONS MAY BE DIFFERENT THAN ADDB.

Figure 33.- Summary of selected flight and data book uncertainties.

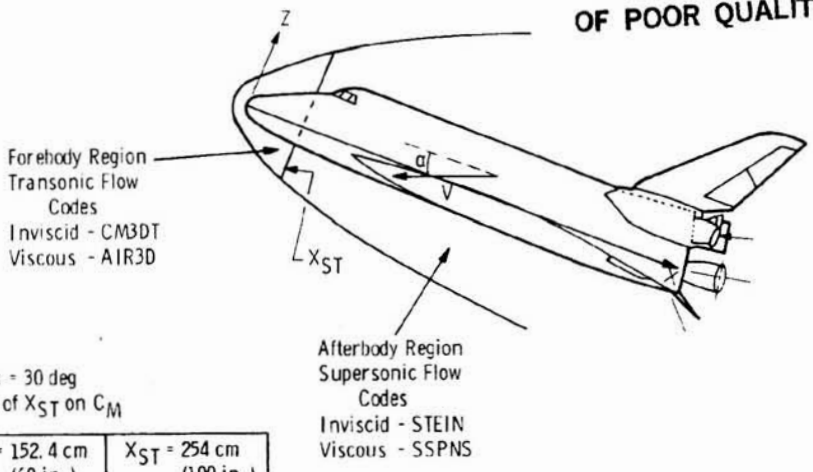

α = 30 deg
Effect of X_{ST} on C_M

Condition	X_{ST} = 152.4 cm (60 in.)	X_{ST} = 254 cm (100 in.)
M_∞ = 8 Ideal Gas	C_M = -0.02536	C_M = -0.02196
M_∞ = 23 Real Gas	C_M = -0.00290	C_M = +0.00045
ΔC_M	+0.02246	+0.02241

Estimated Uncertainty in ΔC_M Due to Variation of $X_{ST} \sim \pm 0.0008$ Based on a Series of Computations

Figure 34.- Code matching analysis.

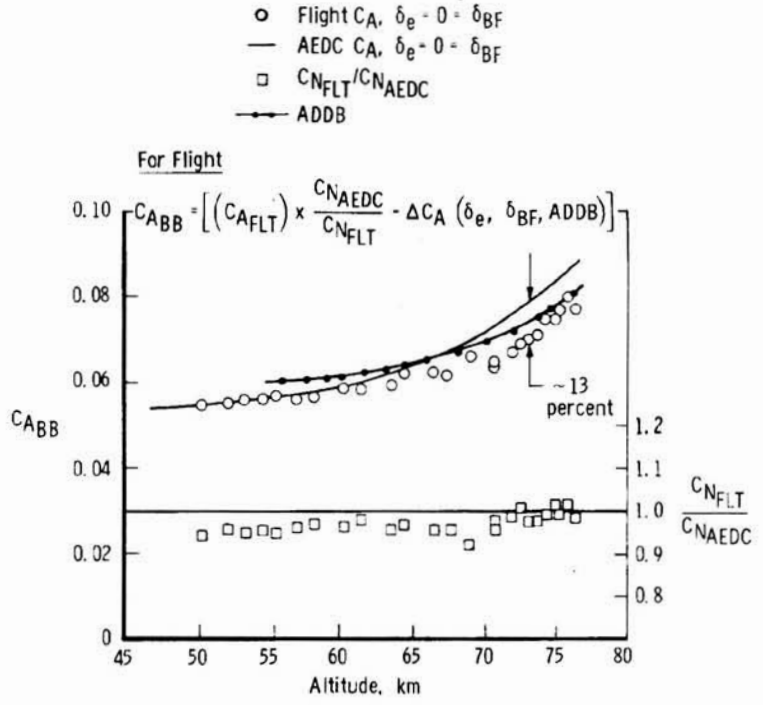

Figure 35.- Comparison of flight C_A and C_N with CFD calculations, STS-3.

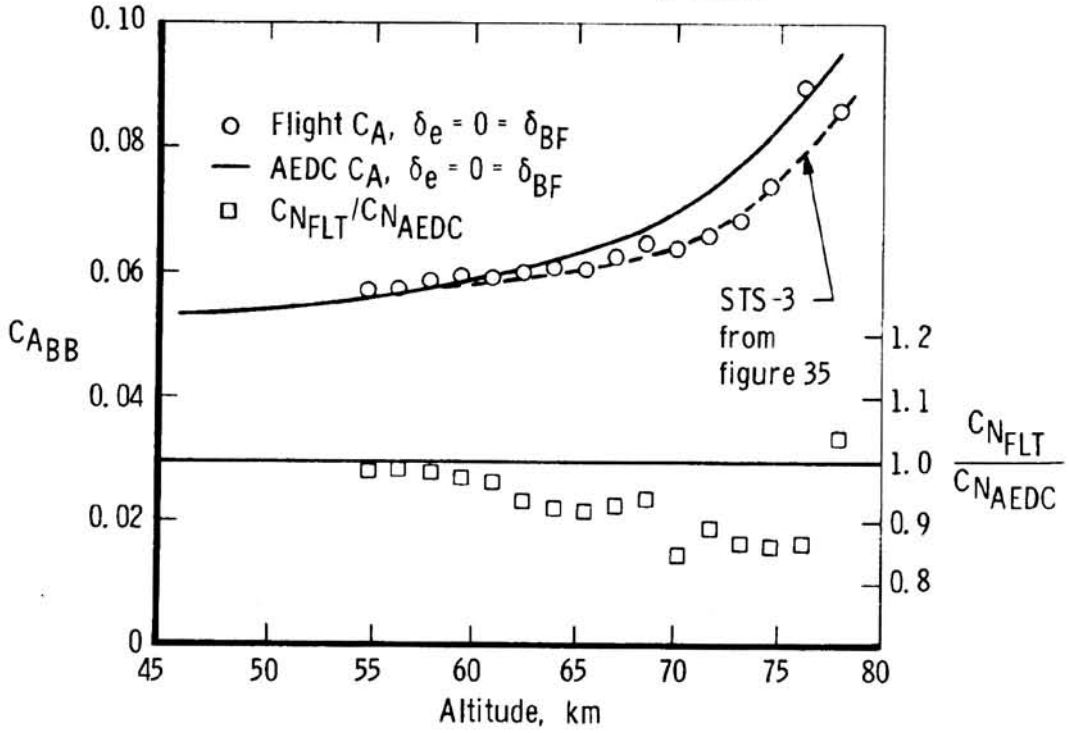

Figure 36.- Comparison of flight C_A and C_N with CFD calculations, STS-4.

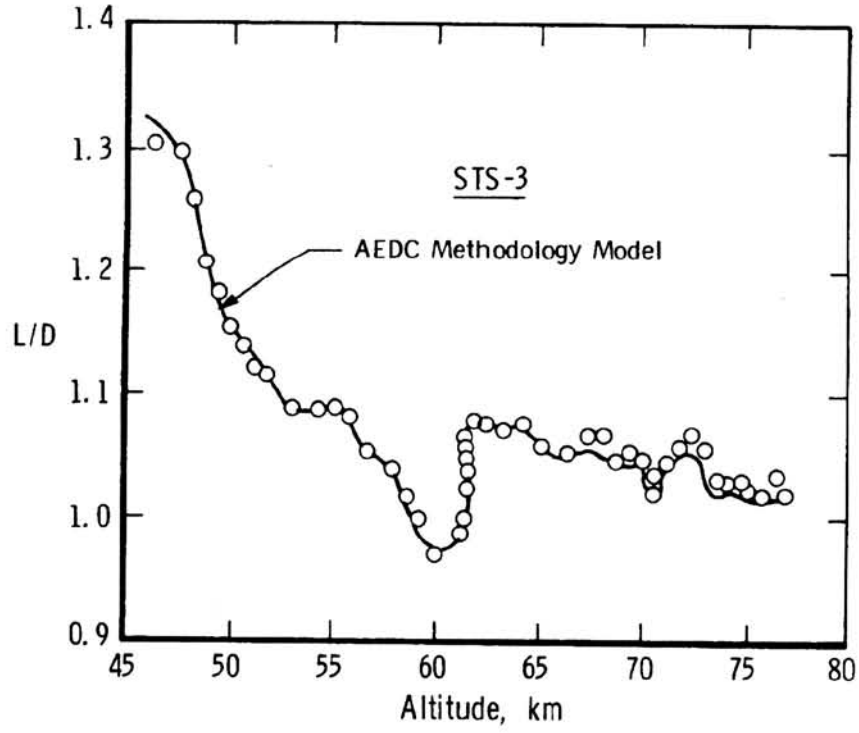

Figure 37.- Comparison of flight L/D with AEDC methodology.

- LACK OF ACCURATE VALIDATION OF REAL-GAS AND MACH EFFECTS
- COMPUTATIONAL MODEL GEOMETRY DIFFERENCES
- CODE MATING PROBLEMS
- LIMITED COMPUTATIONS ESPECIALLY PNS (α = 20 DEG ONLY)
  (SOME SEMI-EMPIRICAL ANALYSIS IS REQUIRED WHICH DEGRADES THE CFD RESULTS)
- SEVERAL CODES REQUIRED TO DEVELOP METHODOLOGY MODEL
- LEE-SIDE FLOW NOT TREATED ACCURATELY OR IN SOME CASES NOT AT ALL
- BODY-FLAP FLOW SEPARATION AND VISCOUS PROBLEMS NOT ADDRESSED

Figure 38.- CFD uncertainties.

SPACE SHUTTLE ORBITER REACTION CONTROL SUBSYSTEM FLIGHT DATA ANOMALIES

J. S. Stone and J. J. Baumbach
Space Transportation and Systems Group
Rockwell International
Downey, California

B. B. Roberts
NASA Johnson Space Center
Houston, Texas

SUMMARY

Shuttle orbiter vehicle flight data obtained during operation of the reaction control subsystem (RCS) were compared with predictions derived from RCS wind tunnel test data. This paper reviews the derivation of the wind tunnel data base and discusses how it was used to predict the full-scale RCS effects. Flight and predicted data comparisons include the lateral and directional aerodynamic effects of firing the side jets, longitudinal aerodynamics for pitch jets, and lateral aerodynamics for roll jets. Flight data anomalies resulting from wind tunnel limitations in representing portions of the entry flight trajectory are presented. The cause of each data anomaly is described, as well as a requirement for additional technical analysis to establish RCS effect simulation parameters that can be used to update jet effect technology.

INTRODUCTION

The forward and aft RCS jets, shown in figure 1, are used during Shuttle missions to control the orbiter vehicle. During entry, only the aft RCS jets are fired. The side-firing jets are used for directional control down to Mach 1.0, at which time the rudder becomes fully effective for directional control. The up- and down-firing jets are active for vehicle pitch control down to a dynamic pressure of 20 psf and to 10 psf for roll control.

The RCS engines operate on monomethlhydrazine (MMH) for fuel and nitrogen tetroxide (N_2O_4) as an oxidizer. The resultant jet exhaust not only creates thrust but also affects the local flow field in the vicinity of the jet. This interference of the RCS jet exhaust with orbiter aerodynamics was predicted from wind tunnel test data (reference 1). Comparison of these data with flight data revealed a number of anomalies.

During the orbiter entry phase, a series of bank reversals is executed to maintain a navigational heading and to manage vehicle energy. These maneuvers

require extensive use of the RCS side-firing jets. During the first flight of the space transportation system (STS-1), the execution of the first bank resulted in damped oscillations in sideslip angle (β) that were in excess of the predicted values (± 4 deg in flight compared to ± 1 deg predicted). Initial computer simulations of this portion of the entry trajectory indicated that the rolling moment jet interactions (JI's) for the side-firing jets were overpredicted. A more rigorous analysis using a flight data reduction program defined this and other RCS data anomalies in detail.

A flight data reduction program that employs a motion-matching technique was used to calculate the resulting flight aerodynamic forces and moments. This program (a modified version of the program discussed in reference 2) is called the Modified Maximum Likelihood Estimator (MMLE) program. Program results indicated by the initial analysis of the vehicle motions during the first bank maneuver showed the side-jet rolling moment interactions at high flight altitudes to be overpredicted. It was also determined that the side-jet yawing moment and side-force interactions were larger than predicted at all altitudes. In addition, the side-jet rolling moment interactions were found to be dependent on the number of jets firing; there was a large, sudden decrease in the magnitude of this rolling moment JI term at relatively low flight altitudes ($M \approx 5$). Analysis of flight aerodynamics for up- and down-firing jet combinations revealed that the pitching-moment interactions were overpredicted for a negative pitch command (one down-firing jet per side) and that the rolling moment interaction was overpredicted for a positive roll command (one left down-firing jet and one right up-firing jet).

These observations represent deviations from the predicted jet effect data published in the Orbiter Aerodynamic Design Data Book (reference 1). Since these data discrepancies were not anticipated by the orbiter flight control system, vehicle motions induced by the jet firings had to be balanced by additional jet usage. This increased usage depleted RCS fuel margins and thus became a primary concern with regard to understanding the limitations of the wind-tunnel-derived RCS data.

SYMBOLS

A_j	jet nozzle exit area ($in.^2$)
C_D	nozzle discharge coefficient (P_{o_j} actual/P_{o_j} theoretical)
$C\ell_{JI}$	RCS rolling-moment jet-interaction coefficient
IMP	plume impingement
JI	jet aerodynamic interaction
M	Mach number
m_j/m_∞	jet-to-free-stream mass flow ratio

n	number of jets firing
P	pressure (psi)
q	dynamic pressure (psf)
R	gas constant (ft-lb/slug-deg Rankine)
Re	Reynolds number based on mean aerodynamic chord
S_{ref}	reference area ($in.^2$)
T	temperature (deg Rankine)
α	angle of attack (deg)
β	angle of sideslip (deg)
δBF	body flap deflection angle
δe	elevon deflection angle
γ	ratio of specific heats
θn	nozzle exit lip angle (deg)
$\phi j/\phi_\infty$	jet-to-free-stream momentum ratio

Subscripts:

j	exit plane jet gas conditions
ℓ	local flow conditions external to plume
o	stagnation conditions
∞	free-stream conditions

SIMULATION OF JET EFFECTS

The classical case of a jet exhausting from a flat plate into a cross flow produces a flow structure that is well defined in the literature. However, the complex flow field in the vicinity of the RCS jets on the Shuttle orbiter makes the aerodynamic influence of the jets difficult to predict analytically. Thus, a wind tunnel test program is mandatory to develop jet effect data.

Wind tunnel testing requires the definition of jet simulation parameters to ensure that the modeled jet effects will be equivalent to full-scale flight, and the proper format for these parameters is subject to debate. Since wind tunnel

models are scaled versions of the flight vehicle, the simulation parameter must account for the relation between the jet exhaust size and the vehicle size. Because of cost and safety considerations, the parameter must also include the effects of wind tunnel testing with jet gases that are not the actual flight vehicle jet gases.

More specifically, documentation on the subject suggests a number of scaled jet effect simulation parameters, including jet penetration or Mach disk height, energy ratio, thrust ratio, momentum ratio (jet to free stream), mass flow ratio, etc. Thus, the jet aerodynamic interaction on the test model is equal to that on the flight vehicle when the correct value of the simulation parameter is achieved. The proper simulation parameters or combination of parameters was selected in the Shuttle program through analysis of an extensive RCS wind tunnel data base.

WIND TUNNEL DATA BASE

A number of simulation variables were tested before the current format was selected. Early in the test program, jet simulation parameters were limited primarily to ratios of momentum, nozzle expansion, and jet pressure. Other parameters from the list of prospects previously discussed were also investigated.

Exact scaling of flight conditions and vehicle geometry was not always possible because of limitations imposed by model constraints, wind tunnel capabilities, and RCS jet gas restrictions. The RCS test program is summarized in table I. The largest model tested was 1.5 percent of full scale, which created a problem in manufacturing geometrically scaled RCS nozzles that could properly discharge a gaseous medium without becoming contaminated. Therefore, nozzle expansion ratios larger than full scale were tested. Wind tunnel test conditions were limited to Mach numbers less than or equal to 10.0, and free-stream pressure levels were generally higher than those in flight. Reynolds numbers tested were lower than full-scale flight.

Because it was impractical as well as hazardous to test with the actual engine oxidizer and fuel (nitrogen tetroxide and monomethlhydrazine), a number of gases were tested in the wind tunnel to determine what effects such parameters as specific heat ratio, gas molecular weight, and gas temperature would have on the simulated jet effects.

The extensive wind tunnel data base was examined to determine the best data correlation parameters. This effort was completed under NASA contract by General Dynamics, Convair (reference 3). Test data were examined in terms of jet firing groups (side jets, up-firing jets, and down-firing jets). During wind tunnel testing, the up- and down-firing jet plumes impinged on orbiter surfaces to generate loads and created a jet interaction with the local flow field. The impingement of these plumes on the model was calculated with a computer program (reference 4) and subtracted from the model balance output so that only the jet interaction effect remained. The side-firing jets, exhausting parallel to the wing, created a JI only. The resultant JI data were correlated with various plume simulation parameters to determine the most accurate fit. The data correlation included the effects of all test variables--Mach number, Reynolds number, angle of attack, angle of sideslip, elevon deflection, body flap deflection angle, nozzle geometry, jet chamber pressure, and jet gas properties.

The results indicated that the side-jet data correlated best with a modified mass flow ratio and angle of attack, whereas the up- and down-firing jet data correlated best with momentum ratio and angle of attack:

$$\text{Mass flow ratio} = m_j/m_\infty = \left[\frac{\gamma_j R_\infty T_\infty (C_D P_j M_j A_j)^2 \sin\theta_n}{\gamma_\infty R_j T_j (P_\infty M_\infty S_{ref})^2}\right]^{1/2} \quad (1)$$

$$\text{Momentum ratio} = \phi j/\phi_\infty = \frac{\gamma_j P_j C_D M_j{}^2 \Sigma A_j}{\gamma_\infty P_\infty M_\infty{}^2 S_{ref}} \quad (2)$$

Note that the mass flow ratio was derived independent of the number of jets firing and is a function of the sine of the nozzle lip angle. The final data base is summarized in table II. Thus, the JI's, given in reference 1, are functions of angle of attack and simulation parameter only, with a secondary influence of elevon deflection and body flap deflection. These data were used to calculate flight jet interactions for the required jet group, given the known value of the simulation parameter, angle of attack, and elevon and body flap deflections. Flight plume impingement was analytically determined as a function of the ambient pressure and pertains mainly to high-altitude flight ($q<20$ psf).

The curve fit of the test data with mass flow ratio for the side-firing jets and with momentum ratio for the up- and down-firing jets resulted in a certain amount of test data scatter. General Dynamics then calculated a tolerance based on the scatter of the test data about the mean for each of the six aerodynamic force and moment coefficients. Since these tolerances included the effects of such a large range of JI simulation variables, they were thought to provide adequate variations in the prediction of actual RCS flight values based on wind tunnel test data.

The RCS JI data were based on test data obtained for Mach numbers between 2.5 and 10. However, after the RCS data correlation was completed and published (reference 1), the need to use the side-firing jets for directional control down to Mach 1.0 became apparent. Although data as a function of mass flow ratio down to Mach 1.0 were available and considered independent of Mach number, a special wind tunnel test (OA-255) was necessary for verification.

RCS test OA-255 utilized a balance selected for its sensitivity to lateral and directional forces and moments to measure the small anticipated loads accurately. Test results were compared with the existing side-jet data base. Although previously unobserved trends were apparent in OA-255, the data were still within the data base uncertainties for the nominal JI data. Hence, the OA-255 test results were not included in the current data base (reference 1).

FLIGHT DATA REDUCTION

During Shuttle orbiter entry, the aft RCS jets are fired as often as necessary until the control surfaces become effective. Because the jet-on times are generally quite short, reducing the jet effect data is a difficult task. To establish the vehicle aerodynamic characteristics, a series of planned test maneuvers was

executed that increased jet-on times to provide better RCS data. These maneuvers, called programmed test inputs (PTI's), constitute the best source of full-scale RCS effectiveness data.

The RCS effectiveness data were extracted from flight by using the NASA DFRC-developed MMLE program, which produced the best estimate of aerodynamic derivatives to match the observed flight motion. The Rockwell version of this program was slightly modified to use RCS forces and moments in dimensional form and thus remove the dynamic pressure dependence for these terms. The RCS was initially modeled as described in reference 1 but was later changed to a more general independent jet model in which each two-, three-, or four-yaw-jet group produced an independent estimate of its effectiveness.

The PTI maneuvers produced the most reliable results for casual maneuvers or bank reversals. This determination was based on the scatter in the results and the lower uncertainty bounds computed by MMLE for each point during analysis of the PTI maneuvers. The fairings of the data results tend to favor these PTI points, and the overall uncertainties tend to bound these points.

RCS AERODYNAMIC DATA ANALYSIS

Side-Firing Jets

Flight rolling moment JI effects for the side-firing jets in the high-altitude portion of entry were smaller than predicted (figure 2). For lower flight altitudes, i.e., less than Mach 20, the flight data show better agreement with the orbiter RCS data base (reference 1). The explanation for this high-altitude jet simulation error lies in the description of the flow field surrounding the side jet exhaust. At high altitudes, the vehicle angle of attack is approximately 40°, which causes flow separation on the upper surface of the wing. When the RCS side jets are fired, the exhaust enters this separated flow region and pressurizes the volume defined by the wing upper surface and the flow separation wake boundaries.

The aerodynamic flow field for this high-altitude flight environment cannot be properly simulated in the wind tunnel. For example, at the first bank maneuver (Mach 24), the flight dynamic pressure (q) is approximately 14 psf. The RCS wind tunnel data base was limited to a maximum Mach number of 10 and minimum q of 75 psf. The higher pressure level in the wind tunnel creates not only a higher pressure for the jet exhaust to penetrate but also a wake boundary that is more rigid than that normally encountered during flight. This boundary constraint traps the jet exhaust over the wing surfaces while allowing a portion to escape through the downstream structure of the wake. The flight-wake boundary, on the other hand, is much less rigid because of the low pressure levels associated with the high-altitude flight condition; q = 14 psf for the first bank maneuver. The wake boundary is much more easily deflected on the flight vehicle than on the wind tunnel model. This difference in high-altitude pressure levels strongly influences the differences observed between flight and predicted side-jet rolling moment JI.

The available literature was reviewed to ascertain the influence of free-stream pressure levels on wake structure in high-altitude flight conditions. The only related geometry application came from the exhaust of a jet into a base flow region. The majority of the information obtained dealt with low Mach and high pressures; it did not focus on the problem of wake structure influenced by low free-stream pressure levels during a constant jet-to-free-stream simulation. Additional analyses will be required to define the observed phenomenon.

In addition to the overprediction of the side-jet rolling moment JI, it was determined that the rolling moment JI flight data depend on the number of side jets firing. The test data used to generate the existing data base indicated that all side-jet interactions were independent of the number of jets firing. However, as shown in figure 2, flight data for two and four jets firing indicate that there are two distinct levels in the rolling moment JI. These differences were not evident in the test data because of testing constraints and balance accuracy.

Test OA-255 included an investigation of the effects of the number of jets firing, and OA-255 results tend to substantiate flight results. Data from OA-255 are presented in figure 3 for three-jet mass flow ratios. As indicated, there is a distinct difference between the three-jet case and the single-jet case. This seems to be more in line with the physics of the jet exhaust flow interacting with the orbiter flow field. That is, an increase in the amount of fluid exhausting from a jet group, be it from an increase in jet chamber pressure (causing an increase in $\dot{m}_j/\dot{m}_\infty$) or an increase in the number of jets firing, should give the same result. As presented in figure 3, both an increase in the number of jets firing and an increase in mass flow ratio result in an increase in rolling moment JI.

Another data anomaly appears as an abrupt decrease in side-jet rolling moment JI in the late-entry flight regime (Mach ≈ 5). As shown in figure 2, this anomaly occurs during the decreasing angle-of-attack phase of entry. The present data base (reference 1) consists primarily of test data at a mass flow ratio greater than 0.001. Below this ratio, the JI data were linearly extrapolated to zero at a mass flow ratio of zero. Since reference 1 presents these data as a function of angle of attack, terms controlling the shape of the decrease in the rolling moment JI (figure 2) are angle of attack, the linear decay in mass flow ratio, and the decrease in entry dynamic pressure. The resultant Aerodydnamic Design Data Book (ADDB) JI exhibits a smooth decay for mass flow ratios less than 0.001. Test OA-255 included mass flow ratios of less than 0.001, and results indicate a significant reduction in side-jet rolling moment interaction with decreasing angle of attack.

Figure 3 shows that the point at which the JI goes to zero in test OA-255 depends on both angle of attack and jet mass flow ratio. For the high-angle-of-attack condition, the jets exhaust into the wake generated by the wing and produce a significant rolling moment JI through pressurization of the upper wing surface. For the low-angle-of-attack case, the separation wake boundary passes underneath the side-jet exhaust plume and the problem becomes one of a jet exhausting into free-stream cross flow. The side-firing jets are then unable to affect the wing upper surface, since the exhaust is "washed" away and the influence is no longer felt on the wing. The resultant rolling moment JI becomes small. Thus, results of OA-255 agree with the effects of angle of attack in flight test side-jet rolling moment JI.

The uncertainty in the flight data is a measure of the scatter observed in that data for all the sample flight maneuvers. The orbiter uncertainties in reference 1, on the other hand, represent the anticipated differences between predicted and actual flight data. As expected, the scatter in the flight data is much less than the reference 1 uncertainties. Figure 4 compares flight and predicted rolling moment JI for four jets firing, including the uncertainties for each set of data. The use of the small flight uncertainties becomes apparent when trajectory performance margin studies are of interest.

The side force and yawing moment JI flight data are presented in figures 5 and 6. Where the side jet rolling moment JI is produced primarily on the wing upper surface, the side force and yawing moment are produced on the side of the orbiter fuselage. The exhaust from the side jets affects the pressure level on the side of the fuselage essentially by pressurizing the flow in the separated wake on the fuselage. The position of the flow separation point, as in flat-plate flow, is sensitive to Reynolds number.

Using a flat-plate analogy, figure 7 depicts the separation point on the fuselage as influenced by the free-stream Reynolds number. A higher Reynolds number causes the separation point to move aft so that the jet exhaust pressurizes a smaller volume, resulting in higher pressures on the side of the fuselage. Thus, the flight vehicle flow field consists of high fuselage pressures acting on the aft portion of the orbiter and producing higher than predicted side force and yawing moment. The wind tunnel flow field, on the other hand, has a flow separation point on the forward part of the vehicle (figure 7) that allows the jet-induced pressurization to dissipate aft and/or above the vehicle, resulting in lower side force and yawing moment. Hence, the flight side force and yawing moment data were, for the most part, underpredicted. Better agreement with predicted values is observed at high flight altitudes where the Reynolds numbers of flight and test are in closer agreement.

The data anomalies observed for the side-jet rolling moment JI regarding angle of attack and effects of number of jets firing were not seen in the side force or yawing moment data. The vehicle angle of attack had no discernable influence, since the relative angle of the fuselage side with respect to the velocity vector did not change with angle of attack. Although sideslip angle could cause a change in the fuselage separation point, data are insufficient to validate this possibility with any degree of certainty. The increase in the number of jets firing had no effect on the fuselage side loads because the leading, upstream jet is the primary driver on local near-field pressures immediately in front of the jets. The forward jets act to shield the forebody from the effects of additional downstream jets. For this reason, the side force and yawing moment are independent of the number of side jets firing (verified by the flight data in figures 5 and 6). The on-orbit impingement data are considered the most accurate. Figure 8 indicates impingement is the major portion of the measured flight data jet effect. Since there is a relatively high degree of confidence in the on-orbit plume impingement terms, the conclusion may be drawn that the JI terms were overpredicted.

The uncertainties in the side force and yawing moment flight data presented in figures 5 and 6 are significantly less than the reference 1 values. Data outside of these uncertainties have large MMLE tolerance bands; therefore, they were weighted less in constructing the flight data uncertainties. It should be noted that the yawing moment JI uncertainties are not symmetrical about the mean-flight JI fairing because the uncertainty data are derived independently by a number of flight data reduction groups that use distinct, individual, nominal flight data curves. Each uncertainty limit was constructed to include data from each group. These uncertainties are considered an adequate representation of the flight data scatter.

Up and Down Firing Jets

During the entry phase, the up- and down-firing jets are used as required for pitch and roll control. As mentioned earlier, RCS pitch commands are possible for dynamic pressures less than or equal to 20 psf and RCS roll commands are possible for dynamic pressures less than or equal to 10 psf. These pressure levels occur at high flight altitudes and high Mach numbers with the orbiter at an angle of attack of 40°. The separated flow field in the vicinity of the up- and down-firing jets is analogous to the wake flow associated with the side-firing jets. The up- and down-firing jets exhaust into the wakes generated by the fuselage and wing. The result is similar to that encountered with the side jets exhausting into the wake from the wing; the JI's are overpredicted. The rolling moment of the roll jets (one left up-firing and one right down-firing) and the pitching moment of the pitch jets (one down-firing, both sides) in flight are smaller than predicted (figure 8).

When an up or a down jet is fired, a large portion of the jet loads is a result of the jet exhaust impingment on the orbiter. These terms were predicted for entry by using an analytical model and for on-orbit vacuum back-pressure by using the plume impingement computer program (reference 4).

CONCLUSION

The generation of the orbiter RCS data base required the development of simulation parameters to correlate the RCS wind tunnel test data. A number of parameters suggested in the literature were investigated. It was determined that jet mass flow ratio, based on one side-jet firing, best correlated the side-jet data and that jet momentum ratio, based on the number of jets firing, best correlated the up- and down-firing jet data. Results from Shuttle flights STS-1 through -4 indicate that a number of discrepancies existed between the flight and predicted RCS JI data.

The side-firing RCS jets exhaust over the wing upper surface, influencing the aerodynamics on that surface in both the high-angle-of-attack regime (when the jets are exhausting into the wing wake) and the low-angle-of-attack regime (when the jets exhaust into a cross flow). The flight rolling-moment JI effect at high altitudes and high angles of attack is smaller than predicted by the wind tunnel test.

Similarly, the high-altitude operation of the up- and down-firing jets indicates that the jet effects are less than predicted. These results show the limitations of the wind tunnel data base in predicting high-altitude jet effects; vehicle wake-flow parameters such as ambient pressure cannot be duplicated in the tunnel. Further analysis is required to develop simulation parameters that can be used to predict the high-altitude jet effects in the wind tunnel.

The side-firing jet aerodynamic interaction terms that originate on the side of the orbiter fuselage (side force and yawing moment) are larger than predicted. The inability to duplicate the flow on the side of the fuselage in the wind tunnel produced the observed data anomaly and accented the need for better simulation of flow separation regions during RCS wind tunnel testing. The sensitivity of the flow separation point to a Reynolds number appears to play a strong part in the magnitude of the wind-tunnel-derived jet effects originating on the side of the fuselage.

The Shuttle orbiter RCS flight data have been used to describe a number of deficiencies in the existing wind-tunnel-derived jet effect data base. High-altitude jet effect simulation appears to be difficult, if not impossible, in existing wind tunnel facilities. Further development in the technology, in conjunction with knowledge of flight data results, is required to establish simulation parameters that will define primary candidates to be duplicated during testing.

REFERENCES

1. Preoperational Aerodynamic Design Data Book, Vol. 1, Orbiter Vehicle. Space Division, Rockwell International, SD72-SH-0060, Vol. 1L-6 (Apr. 1982).

2. Users Manual for MMLE 3, a General Fortran Program for Maximum Likelihood Parameter Estimation. NASA Dryden Flight Research Center, Technical Paper 1563 (Nov. 1980).

3. Space Shuttle Orbiter Rear Mounted Reaction Control System Jet Interaction Study, Final Report. Convair Aerospace Division, General Dynamics, CASD-NSC-77-003 (May 1977).

4. Rocket Exhaust Plume Computer Program Improvement, Volume I - Final Report. Huntsville Research and Engineering Center, Lockheed Missiles and Space Company, Inc., LMSC/HREC D162220-1 (Jan. 1972).

TABLE I.-RCS TEST DATA BASE FOR ENTRY

Test No.	Test Type	Model	Scale	Test Facility	Remarks
MA7	Force and heat transfer	PRR	0.015	LaRC/UPWT	Convair test
OA70	Force	139B	0.015	LaRC/UPWT	Yaw RCS data only
OA73	Force	139B	0.015	ARC 3.5 ft	--
OA85	Force and limited pressure	139B	0.010	LaRC/CFHT	Tabulated pressure only
LA25	Force	139B	0.010	LaRC/CFHT	Jet location and cant angle study
OA82	Force	139B	0.010	LaRC/CFHT	--
MA22	Force	139B	0.010	LaRC/CFHT	--
OA99	Force and limited pressure	139	0.0175	LaRC/vacuum	On-orbit impingement
OA93	Force	140A/B	0.010	CALSPAN	High Mach no.
OA169	Force	2C	0.0125	AEDC/VKF B	Forward and aft jets
OA-255	Force and limited base pressure	2C	0.0125	LaRC/UPWT	Aft side jets

TABLE II.-RCS JI AND IMPINGEMENT DATA BASE (LHS JETS)

Force or moment component	Up-firing jets		Down-firing jets						Side-firing jets		
	JI	IMP	JI	IMP	δe_{JI}	δBF_{JI}	δe_{IMP}	δBF_{IMP}	JI	IMP	δe_{JI}
Axial force	X		X	X	X		X	X	X	X	X
Side force	X	X	X	X			X		X	X	
Normal force	X		X	X	X	X	X	X	X	X	X
Rolling mom.	X	X	X	X	X		X	X	X	X	X
Pitching mom.	X		X	X	X	X	X	X	X	X	X
Yawing mom.	X	X	X	X			X	X	X	X	

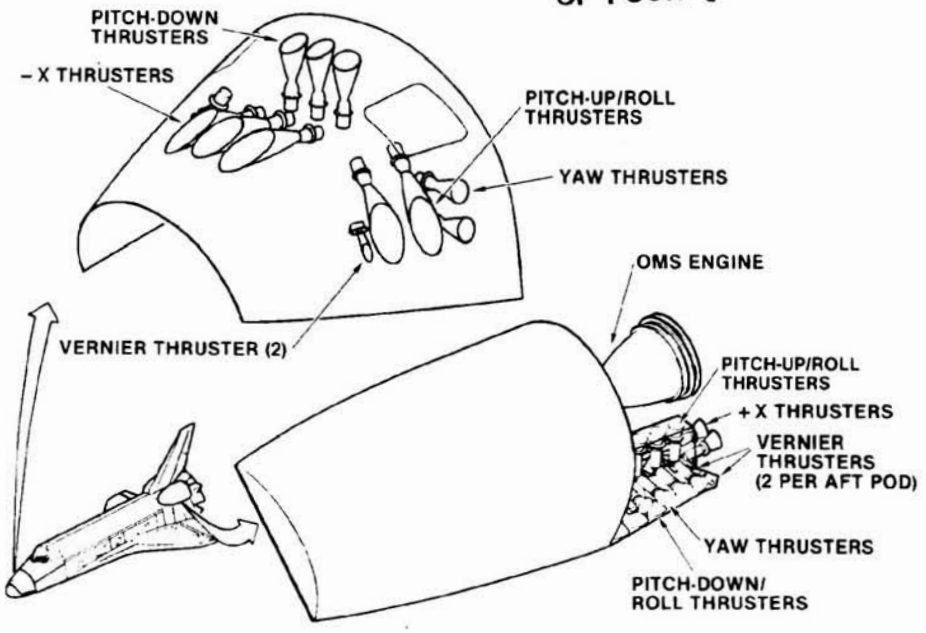

Figure 1.- Space Shuttle orbiter forward and aft RCS.

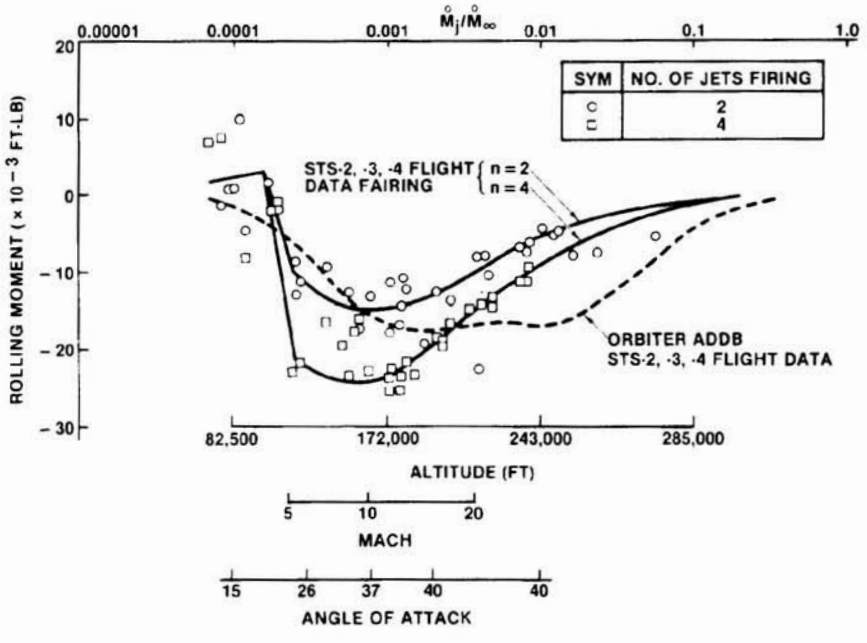

Figure 2.- Yaw jet rolling moment interaction.

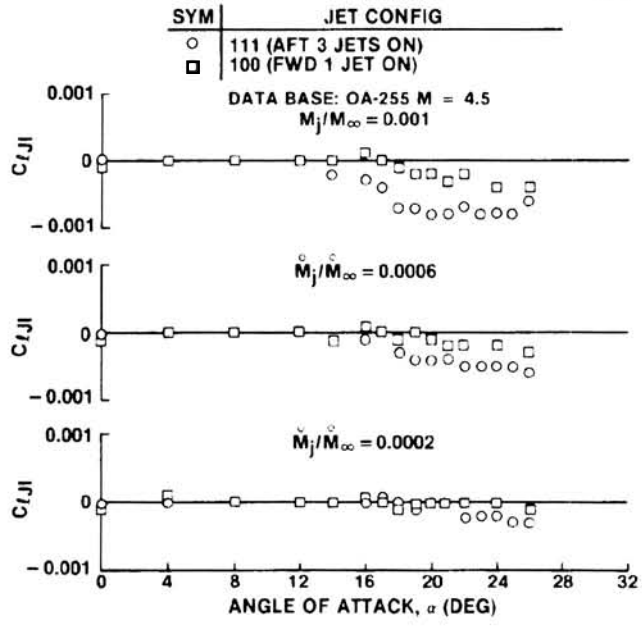

Figure 3.- Effects of angle of attack and number of jets on rolling moment JI.

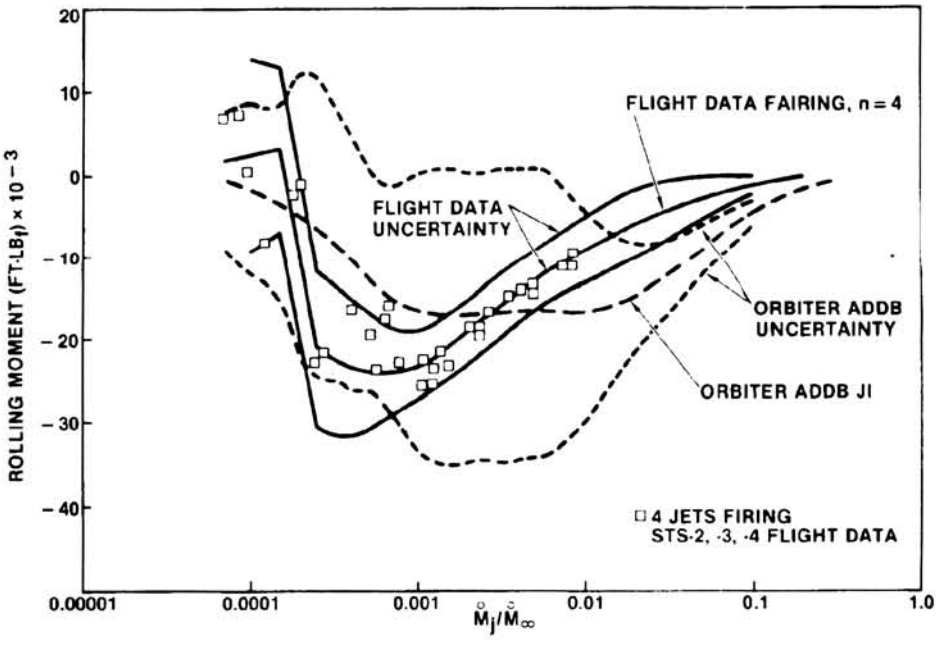

Figure 4.- Comparison of flight and orbiter ADDB-derived rolling moment JI and uncertainties. Four side jets firing.

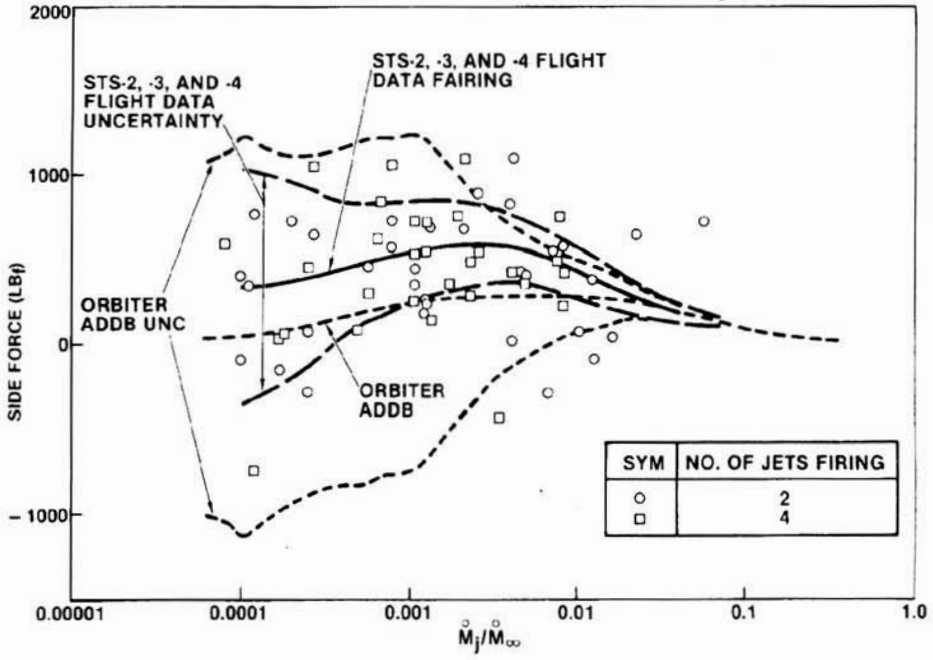

Figure 5.- Yaw jet side force interactions.

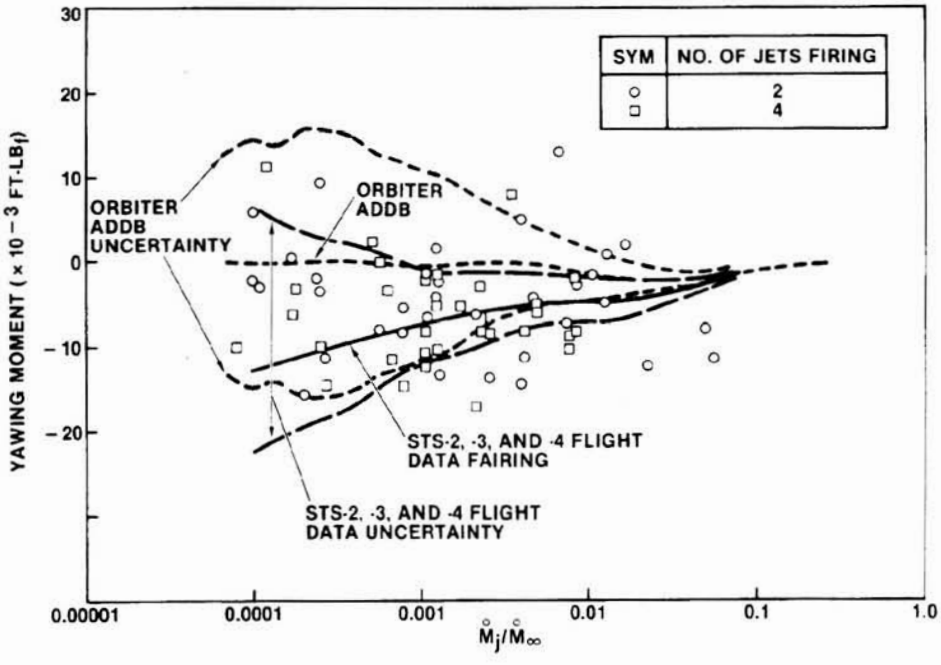

Figure 6.- Yaw jet yawing moment interactions.

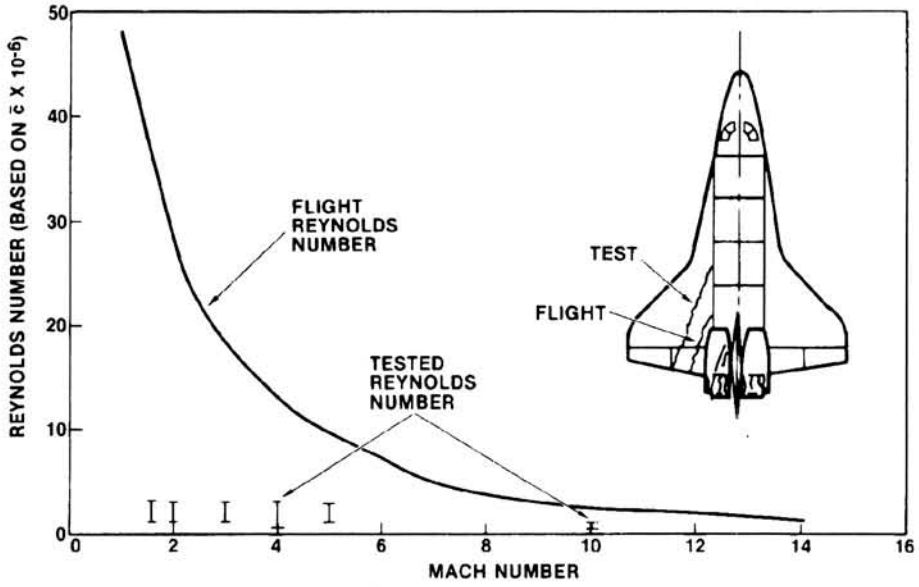

Figure 7.- Effect of Reynolds Number on fuselage flow separation.

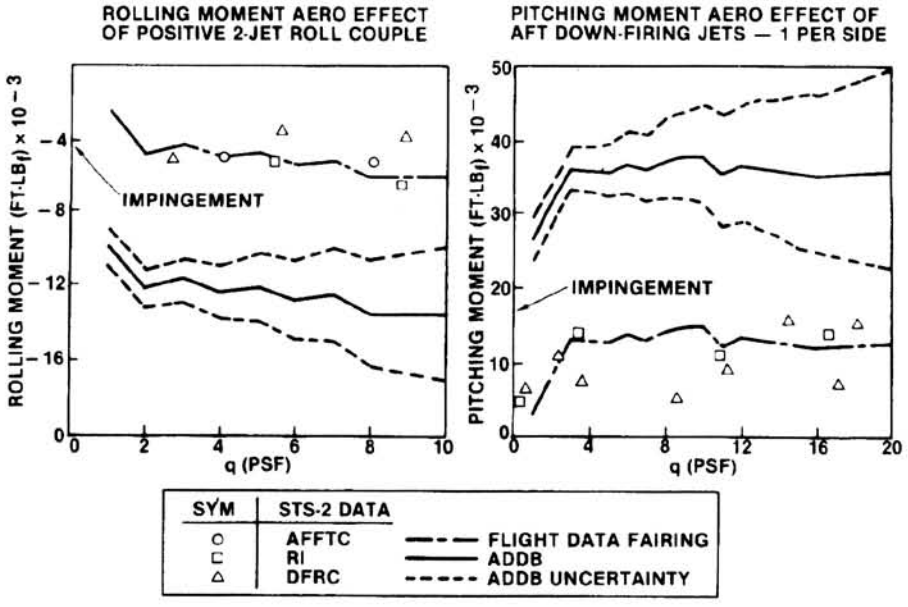

Figure 8.- Up/down-firing jet effects.

ANALYSIS OF SHUTTLE OSCILLATION IN THE MACH NUMBER = 1.7 TO MACH NUMBER = 1.0 RANGE

William T. Suit, Harold R. Compton, William I. Scallion,
James R. Schiess, and L. Sue Gahan
NASA Langley Research Center
Hampton, Virginia

INTRODUCTION

The first five flights of the Space Transportation System (STS) have exhibited unexpected lateral oscillations in the Mach Number = 1.7 to Mach Number = 1.0 region of the descent trajectory. These oscillations can be split into two parts: a predominantly rolling oscillation referred to as the "quarter hertz" motion (reference 1) and a long-period, large-amplitude oscillation in sideslip, roll rate, and yaw rate (reference 2). During the long-period oscillation, sideslip shows the largest increase in amplitude over that observed for the "quarter hertz" motion. The "quarter hertz" motion begins at about Mach Number = 1.7 and ends at about Mach Number = 1.4. The long-period oscillation begins at about Mach 1.4 and ends at about Mach Number = 1.0 with a period of twenty to thirty seconds and runs for about one and a half to two cycles.

These motions are analyzed in this paper in order to determine their source and the mechanism driving them. They will first be examined to determine how much of the motion can be explained using the set of equations that contain linear aerodynamic parameters whose values are given in reference 3. Then differences between measured moments and those calculated using linear aerodynamics which are considered to be due to unmodeled moments (reference 2) will be examined. Possible error sources such as not including nonlinear aerodynamics in the vehicle model, measurement errors, and the effect of pressure gradients will be considered. Based on these analyses, conclusions as to the nature and cause of the Shuttle lateral oscillations will be drawn. Comments will also be made on the deficiencies of the analysis and how the analysis can be improved with better instrumentation.

SYMBOLS

b	wing span, ft
$I_{x,y,z}$	moment of inertia about longitudinal, lateral, and vertical body axes, respectively, slug-ft^2
I_{xz}	product of inertia, slug-ft^2
M	moment where subscript indicates type, ft-lb
p,q,r	roll rate, pitch rate, and yaw rate, respectively, rad/sec or deg/sec
$\bar{q}$	dynamic pressure $1/2\ \rho\ V^2$, lb/ft^2
S	wing area, ft^2
V	vehicle total velocity, ft/sec
α	angle of attack, rad or sec
β	sideslip angle, rad or sec
$\delta a, \delta r$	aileron and rudder deflection, rad or deg
ρ	air density, slug/ft^3

C_ℓ rolling moment coefficient

$$C_{\ell_\beta} = \frac{\partial C_\ell}{\partial \beta} \qquad C_{\ell_{\delta_r}} = \frac{\partial C_\ell}{\partial \delta_r}$$

$$C_{\ell_p} = \frac{\partial C_\ell}{\partial \frac{pb}{2V}} \qquad C_{\ell_{\beta\alpha}} = \frac{\partial^2 C_\ell}{\partial \beta \partial \alpha}$$

$$C_{\ell_r} = \frac{\partial C_\ell}{\partial \frac{rb}{2V}} \qquad C_{\ell_\beta 3} = \frac{1}{3!} \frac{\partial^3 C_\ell}{\partial \beta^3}$$

$$C_{\ell_{\delta_a}} = \frac{\partial C_\ell}{\partial \delta_a}$$

A dot over a symbol signifies a derivative with respect to time.

ANALYSIS AND RESULTS - APPLICATION OF DETERMINISTIC METHODS

The lateral oscillations of the Shuttle vehicle for flights STS-2, -3, and -5 are shown in figures 1, 2, and 3. Flights 1 and 4 showed similar oscillatory patterns. The oscillation is in two parts, the "quarter hertz" rolling motion followed by the long period motion. The "quarter hertz" motion was not obvious during STS-2 (figure 1) because test inputs were initiated at about the Mach number where the motion had started on STS-3 and STS-5.

The deterministic analysis discussed in reference 2 was applied to the Mach number = 1.7 to Mach number = 1.0 region of the Shuttle flights. Only the analysis of the moments about the x-body axis will be presented in this paper. Roll rate is the predominant motion in the "quarter hertz" oscillation and for the long-period motion and an analysis of moments about the x body axis is sufficient to illustrate the conclusions that will be made concerning the lateral oscillation problem. The general form of the equations used for moments about the vehicle x-axis is:

$$M_{TOTAL} = M_{RCS} + M_{AERO} + M_{UK}$$

where

$$M_{TOTAL} = \dot{p} I_x + rq(I_z - I_y) - (pr + \dot{r}) I_{xz}$$

$$M_{AERO} = \bar{q} S b \left[C_{\ell_\beta} \beta + C_{\ell_{\delta r}} \delta r + C_{\ell_p} \frac{pb}{2V} + C_{\ell_r} \frac{rb}{2V} + C_{\ell_{\delta a}} \delta a \right]$$

M_{RCS} is the measured moment from the Reaction Control System (RCS)

M_{UK} is the unmodeled moment

In this calculation the aerodynamic parameters come from reference 3 and the states and controls are measured during the Shuttle flights.

The results of calculating the various moments for STS-2, -3, and -5 are shown in figures 4, 5, and 6. During the "quarter hertz" portion of the flight, the forms of M_{TOTAL} and M_{AERO} were similar, but M_{AERO} appeared to be biased and the peak-to-peak variations were different (figures 4, 5, and 6). This implies that the form of the model, which is nonlinear in the states but linear in the aerodynamic parameters, is correct. However, to match the M_{TOTAL} time history the values of the aerodynamic parameters from reference 3 will have to change. Also, during the "quarter hertz" portion of the time history M_{UK} was small compared to its value during the long-period oscillation. Examination of the moment components indicate that during the long period oscillation, the moments resulting from sideslip, roll rate, and yaw rate in the M_{AERO} term were not reflected in the angular acceleration terms of M_{TOTAL} resulting in a large M_{UK} term. An interpretation of these results and how they lead to a possible explanation of the oscillatory motions of the Shuttle vehicle follows.

ANALYSIS OF "QUARTER HERTZ" MOTION

The small unmodeled moment shown in figures 5 and 6 implies this motion can be largely explained using a linear aerodynamic model and the measured data. The questions of what starts the motion and what other factors influence it, still must be answered. One possible influence is pressure gradients on the wings and vertical tail resulting from flow separation. The pressure data was examined and no pressure variations of the proper frequency occurred during the time of the "quarter hertz" oscillation. The pressure variation patterns seen on the wings did not appear to significantly effect vehicle moments. However, pressure patterns were seen on the vertical tail that could be significant. These patterns are shown for STS-3 and STS-5. Typical of the patterns are those for stations along the .1 chord of the vertical tail (figures 7 and 8).

Time histories from STS-3 show various vehicle states during the "quarter hertz" motion (figure 2). Initially the yaw rate builds gradually (step 1 figure 9) and the rudder changes to stop the yaw rate increase (step 2 figure 9). This rudder change causes a roll rate and also creates a side force on the vehicle (step 2 figure 9). The resulting lateral acceleration is fed into the control system, multiplied by a large gain, and summed with the yaw rate. When this combined signal reaches a threshold value the yaw RCS fires to drive the yaw rate to zero (step 3 figure 9). However, the roll component of the yaw jet is in a direction that increases the roll rate introduced by the rudder deflection. Now the aileron is activated to suppress the roll rate. The aileron deflection over-corrects and the roll rate changes sign (step 4 figure 9). The aileron then also changes to suppress the roll rate, but since the rudder and aileron are coupled the rudder also moves and helps create a yaw rate so that the cycle begins again. In the case of STS-3 this sequence is repeated three times (figure 2). The rates then tend to stabilize, but the yaw rate starts to become more negative, causing the rudder to deflect. The rudder deflection now introduces a negative lateral acceleration and a negative roll rate. Again, when the combined yaw rate and lateral acceleration terms in the control system become large enough the yaw RCS fires to reduce the yaw rate. In so doing the roll rate is increased, the aileron over-corrects and another oscillation cycle is introduced (figure 2). A similar pattern is seen for STS-5 (figure 3).

A question still remains relative to the "quarter hertz" oscillation. What causes the yaw rate buildup preceding the control sequence discussed, and why does the yaw rate build up after the RCS inputs to suppress it? In each of these cases the yaw rate is greater than might be expected from the aerodynamic control deflections seen. A possible solution to this question will now be discussed.

The pressures on the wings and vertical tail did not show an oscillatory pattern that could drive the "quarter hertz" oscillations directly, however, there were pressure patterns on the vertical tail that could possibly explain the yaw rate pattern that was seen in figure 2. Figures 7 and 8 show representative pressure patterns on the vertical tail for STS-3 and STS-5. An estimate of the pressure change due to altitude change is plotted on the figure. If the average slope of the measured pressures is less than the altitude change curve, this represents a reduced pressure at the measurement points. The pressure points shown on figures 7 and 8 are all on the left side of the vertical tail so a reduced pressure at these locations could imply a movement of the tail to the left or a positive yaw rate.

Simultaneous examination of figures 2 and 7 for STS-3 shows that for time 0 to 11 seconds the pressure is reduced and when there is no RCS firing and the rudder deflection is small, the vehicle tends to have a positive yaw rate. From 11 to 18 seconds there are two slope changes and the yaw rate stays close to zero. Then at a time of about 18 seconds the pressure changes so that its slope is greater than the nominal, implying a negative yaw rate, and the change in yaw rate occurs. Figures 3 and 8 show similar trends for STS-5. So a connection between pressure changes on the vertical tail and the onset and persistence of the "quarter hertz" oscillation has been established. Even fairly small pressure variations acting on a large surface such as the Shuttle vertical tail for a five to ten second interval can introduce a significant rate. However, the rates generated are long-term effects and the short-period motions seen are a function of the control system. For this reason the linear model and the data book aerodynamics explain most of the "quarter hertz" motion.

Analysis of Long Period Oscillation

For all the Shuttle flights examined (figures 4, 5, and 6) the deterministic analysis shows a large unmodeled error during the long-period motion. This implies that the linear aerodynamic model in conjunction with the measured flight data does not describe the vehicle motions.

The change in character of the lateral oscillation for short to long period is coincident with the reduction of the gain on lateral acceleration so that the RCS does not fire as often, if at all. Three possible causes considered for the long-period oscillation were the effect of nonlinear aerodynamic terms which were not included in the mathematical model describing the vehicle motions, errors in the measured data, and unmodeled moments caused by pressure gradients on the wings and vertical tail. These error sources will be examined and a probable cause of the unmodeled error determined.

Unmodeled Nonlinear Aerodynamics

This effect was thought to be small since the angle of attack was less than 15° and its variations were less than 3°. Also, rates and displacements were small. However, for completeness two possible nonlinear terms were considered. The possible effects of a $C_{\ell_{\beta\alpha}}$ term were discussed in reference 4 and if a higher order sideslip term were required, $C_{\ell_{\beta^3}}$ should be included to maintain a consistent trend of C_ℓ with beta. These two terms were included in the aerodynamic model. A regression program which is used to select the aerodynamic parameters that most affect the vehicle motion (reference 5) was applied to flight data from STS-2 and STS-3. The two nonlinear terms were not found to have any significant effect on the vehicle

motions. As an additional check, various values of $C_{\ell_{\beta\alpha}}$ were used in a maximum-likelihood parameter extraction program and the results showed the vehicle response to be insensitive to large changes in $C_{\ell_{\beta\alpha}}$.

Measurement Error

Since the unmodeled error was small for the "quarter hertz" motion, any measurement errors that existed during that time were small. The long-period motion immediately follows the "quarter hertz" motion so the probability that the measurement error would suddenly increase enough to account for the unmodeled error is remote. However, again for completeness, the possibility of a significant measurement error will be examined. The states that will be checked will be the roll acceleration and sideslip. If the roll acceleration is in error, since it is the primary term in M_{TOTAL}, this would directly affect the value of the unmodeled moment. The rolling acceleration was measured directly for STS-3 and STS-5, but not for STS-2. Therefore, for STS-2 the roll acceleration was calculated by using a spline fit to the roll rate and differentiating the resulting time history. To check the accuracy of this method the roll acceleration was obtained by both methods for STS-5. The comparison is shown in figure 10. The differences are small and any unmodeled error seen in figures 4, 5, and 6 is much larger than any possible error in roll acceleration.

Possible sideslip errors will now be considered. Figures 4, 5, and 6 show a pattern in unmodeled moments indicating that sidelip is the largest contributor to M_{AERO} and is, therefore, the primary contributor to the unmodeled moment. There is no measured RCS or aerodynamic control input that would cause a disturbance in M_{TOTAL} so that it would have a shape similar to M_{AERO} in the long-period oscillation region. This was independently illustrated when a maximum-likelihood parameter program was applied to data from STS-3. A fairly good fit was obtained for the "quarter hertz" part of the data but when the long-period sideslip oscillation data were added the fit was poor for roll rate and sideslip because the measured control inputs were not sufficient to cause the responses that could fit both sets of data (figure 11).

The development of the corrected sideslip time history will now be discussed. The raw measured sideslip was thought for some flights to be in error by as much as 6° because wind corrections had not been applied. After applying corrections for winds based on the best meteorological data available, a sideslip time history based on vehicle rates and accelerations was generated. The reconstructed sideslip represents the best estimate of sideslip consistent with the other measured data (reference 6). This sideslip is thought to be good to at least half a degree.

To check this supposition, the method discussed in reference 7 was used. The measured roll rate, yaw rate, and lateral acceleration were treated as known quantities and time histories of sideslip and bank angle were calculated. As can be seen from figure 12, the match with the measured sideslip and bank angle was good. This result implies that the best estimate of sideslip is consistent with the measured roll rate, yaw rate, and lateral acceleration and is probably more accurate than half a degree. If, however, there was a consistent sideslip error of half of degree, this would account for about 45,000 ft-lb of the over 150,000 ft-lb

unmodeled moment seen in figure 5. The maximum possible sideslip error can account for at most one-third of the unmodeled moment.

PRESSURE GRADIENTS ON THE WINGS AND VERTICAL TAIL

An examination of figures 4, 5, and 6 shows that the forces that cause the long-period oscillation do not excite the angular acceleration significantly. Continuing the analysis begun when discussing the "quarter hertz" oscillations we look at the pressure trends on the vertical tail. Pressure data from STS-2, -3, and -5 will be used in this analysis.

The STS-2 unmodeled moment compares very well in form and timing with the pressure data along the 0.1 chord line (figures 4 and 13). The comparisons between the unmodeled moments and the pressure data were not as good for STS-3 and 5 (figures 5, 6, 7, and 8). The pressure trends and times between changes in trends were generally similar to those of the unmodeled moments, but the timing was different. The trend changes seen in the pressure data tended to lead those of the unmodeled moments. However, the similarities are close enough to suggest that a portion of the unmodeled moment is due to pressure gradients on the vertical tail. A similar analysis of the wing pressures did not show the same relationship between pressure patterns and the unmodeled moments.

Approximate calculations were made to determine the possible rolling moment from the pressure gradients on the vertical tail. The calculations showed that rolling moments with magnitudes from one-half to two-thirds of the unmodeled moment could arise from pressure gradients on the vertical tail. The difficulty in drawing conclusions from these results arises from the assumptions made when the moment calculations were made. The most critical assumption arises from the fact that the Shuttle vehicle only has pressure points on the left side of the vertical tail. Therefore, in making the moment calculations the pressure on the right side of the vertical tail was assumed constant and all moments resulted from the gradients on the left side.

Based on the data available, the greatest part of the unmodeled moment appears to come from the pressure gradient on the vertical tail. A 10 to 15 percent change in the data book values for C_{ℓ_β} and $C_{\ell_{\delta a}}$ along with a quarter of a degree error in β could account for the rest of the unmodeled moment.

One final comment on the effect of the pressure gradients acting on the vertical tail of the Shuttle: an examination of the region from time 53 sec to time 67 sec of figure 1 shows that for STS-2, the roll rate and yaw rate are opposite from the rates that would be expected from the control inputs shown. In the same time period of figure 13, a pressure change profile is seen that almost exactly corresponds to the roll rates seen on figure 1 and shows the same trends as the yaw rate, but with about a one second lead in time. Specifically, for the roll rate case at 54 seconds the aileron is close to zero but the roll rate is becoming negative. At this time the pressure shows a reducing trend on the left side of the vertical tail which would create a negative roll. At about 57 seconds the roll rate starts to become more positive and at this same time the pressure on the vertical tail becomes sharply higher. At 60 seconds the roll rate turns more negative and the pressure begins to decrease relative to the nominal line. At 65 seconds the roll rate increases and again the pressure trend shows increased pressure on the vertical tail. Finally, at 66 seconds the roll rate decreases and the pressure also begins to decrease. The aerodynamic controls are active and have the effect of slowing the

angular rates so that the maximum rates attained are suppressed, but the driver of the rates during this part of STS-2 is the pressure gradient on the vertical tail.

CONCLUDING REMARKS

The preceding analysis leads to the following conclusions: (1) the "quarter hertz" oscillation, while initiated by pressure gradients, is sustained by the reaction of the control system to the externally induced rates; (2) the long-period oscillation which follows the "quarter hertz" oscillation is apparently caused by pressure gradients on the vertical tail; (3) the separation between the long- and short-period lateral motions appears to be related to the reduction in the gain on lateral acceleration; (4) the large unmodeled moment seen during the long-period oscillation occurs because there is no control input to the vehicle that would cause an angular acceleration compatible with the rates and displacements measured; (5) since the pressure gradients do not account for all the unmodeled moment, the rest is thought to be caused by sideslip error and error in the assumed data book aerodynamic parameters; and (6) in the flight regime investigated, the motions generated by the pressure gradients should be controllable by the aerodynamic controls. The maximum control deflections seen, regardless of the magnitude of the pressure gradients, were about twenty percent of full scale for the rudder and between ten and fifteen percent of full scale for the aileron. These deflections in most cases were sufficient to stop the increase of the angular rates and larger deflections could completely suppress them.

Finally, how could we do better next time?

1. The problem of analyzing the lateral oscillations in the Mach Number = 1.7 to Mach Number = 1.0 region of the Shuttle flights was made very difficult because of inadequate data.

2. Without pressure information on both sides of the vehicle any analysis is speculation.

3. Without an accurate air data system there is potential error in angle of attack and angle of sideslip. These errors directly affect all aerodynamic analysis.

4. If there is serious interest in the analysis of Shuttle-type vehicles at low Mach numbers, pressure sensors with sufficient range so that they will not saturate must be provided.

5. The results of any investigation are only as good as the data available and at this point in the investigation of the lateral motions of the Shuttle vehicle in the Mach Number = 1.7 to Mach Number = 1.0 range, the results are questionable.

REFERENCES

1. Underwood, Jimmy M.: Correlation of Flight with Wind Tunnel Stability and Control Aerodynamics of the Space Shuttle Orbiter. Paper presented at the 13th Congress of the International Council of the Aeronautical Sciences/AIAA Aircraft Systems and Technology Conference, Seattle, Washington, August 22-27, 1982.

2. Suit, W. T.; Compton, H. R.; Scallion, W. I.; and Schiess, J. R.: Simplified Analysis Techniques to Support the Determination of Shuttle Aerodynamics. AIAA Paper 83-0117, 1983.

3. Whitnah, Authur M.; and Hillje, Ernest R.: Space Shuttle Wind-Tunnel Testing Program. AIAA Paper 82-0562, 1982.

4. Raper, J. L.: Rolling Motion of 79-Degree Clipped Delta Wing Configuration at Supersonic Speed - Free Flight Investigation. NASA TN D-2017, 1963.

5. Klein, V.; Batterson, J. G.; and Murphy, P. C.: Determination of Airplane Model Structure from Flight Data by Using Modified Stepwise Regression. NASA TP-1916, 1981.

6. Kelly, G. Mel; Findlay, John T.; Compton, H. R.: Wind Estimates Using Air Data Probe Measurements to Evaluate Meteorological Measurements Made During Space Shuttle Entries. AIAA Paper 82-1333, 1982.

7. Klein, Vladislav; and Schiess, James R.: Compatibility Check of Measured Aircraft Responses Using Kinematic Equations and Extended Kalman Filter. NASA TN D-8514, 1977.

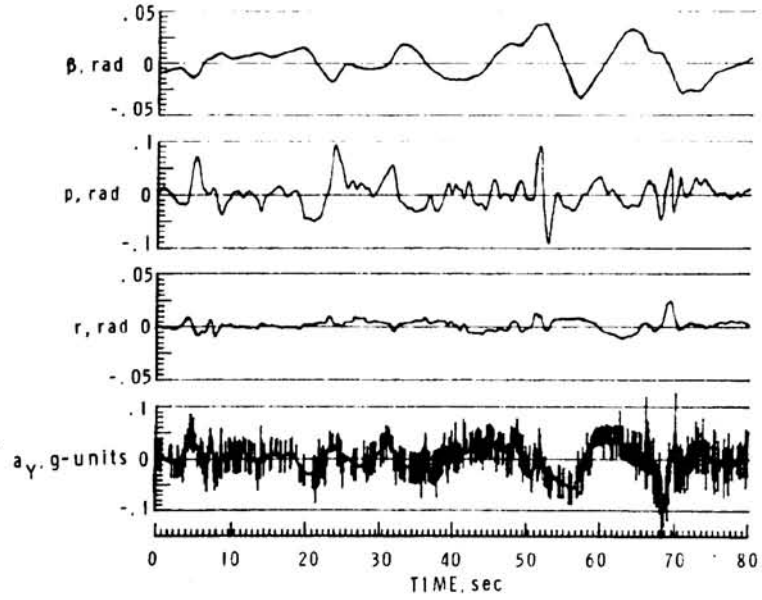

(a) Responses.

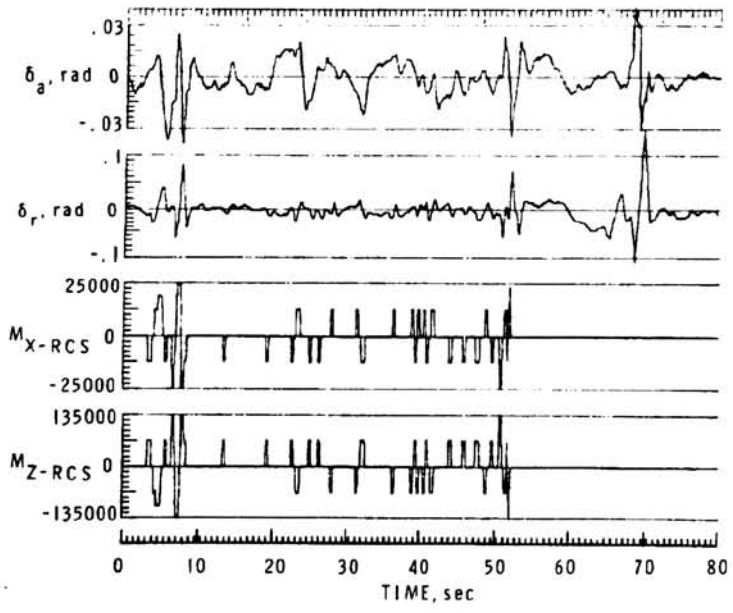

(b) Inputs.

Figure 1.- STS-2 flight data time histories.

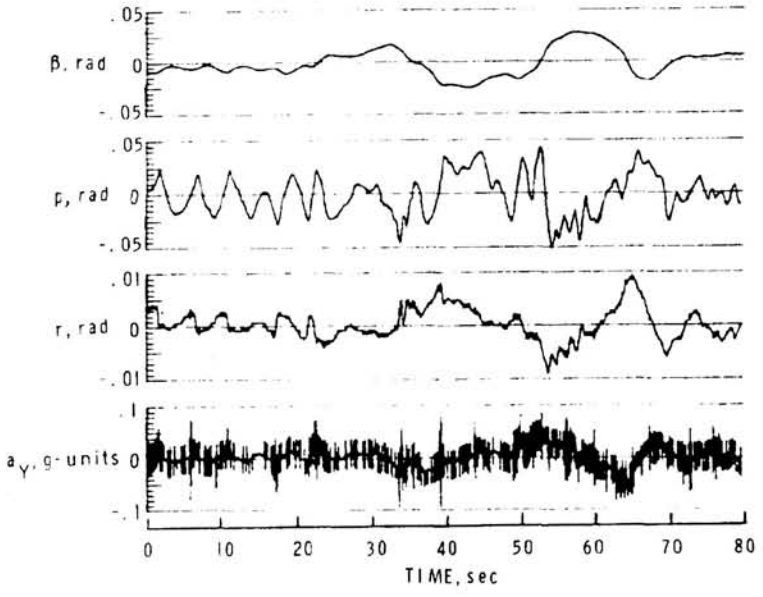

(a) Responses.

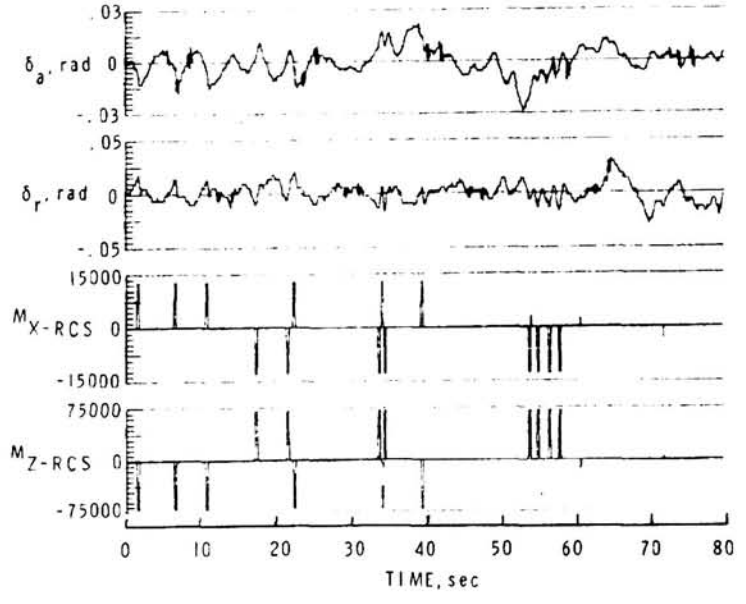

(b) Inputs.

Figure 2.- STS-3 flight data time histories.

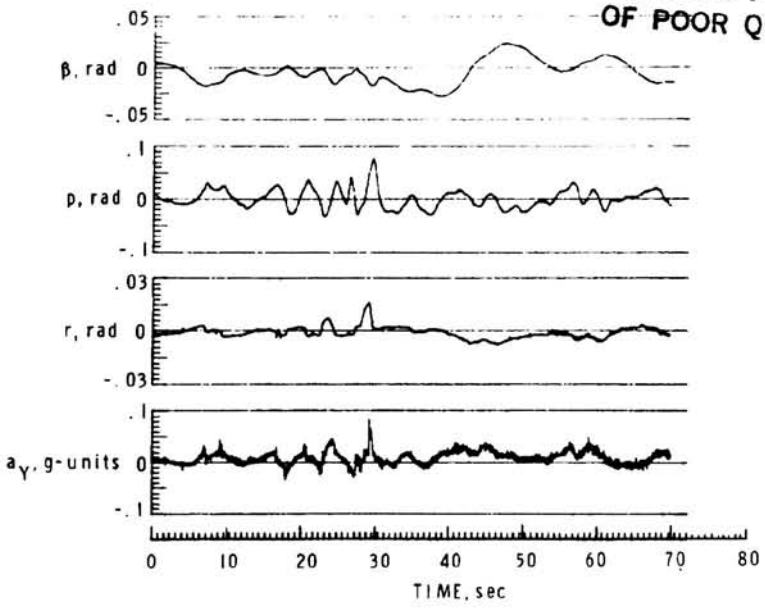

(a) Responses.

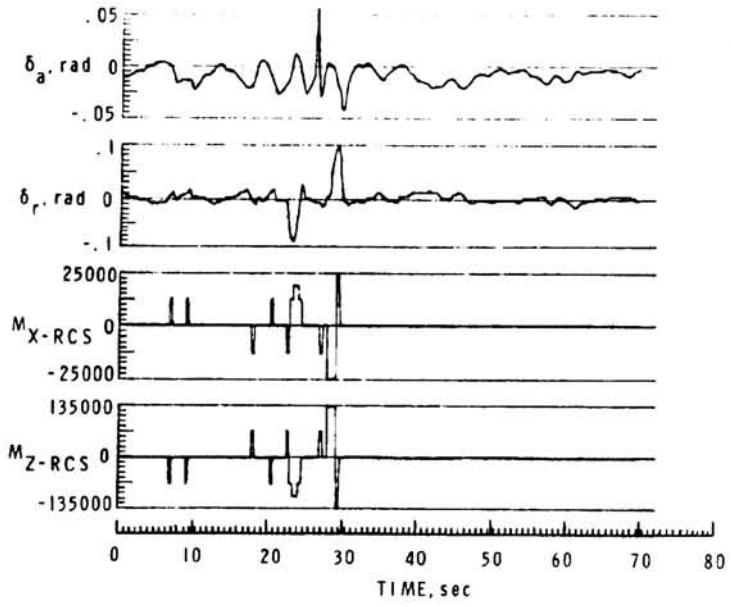

(b) Inputs.

Figure 3.- STS-5 flight data time histories.

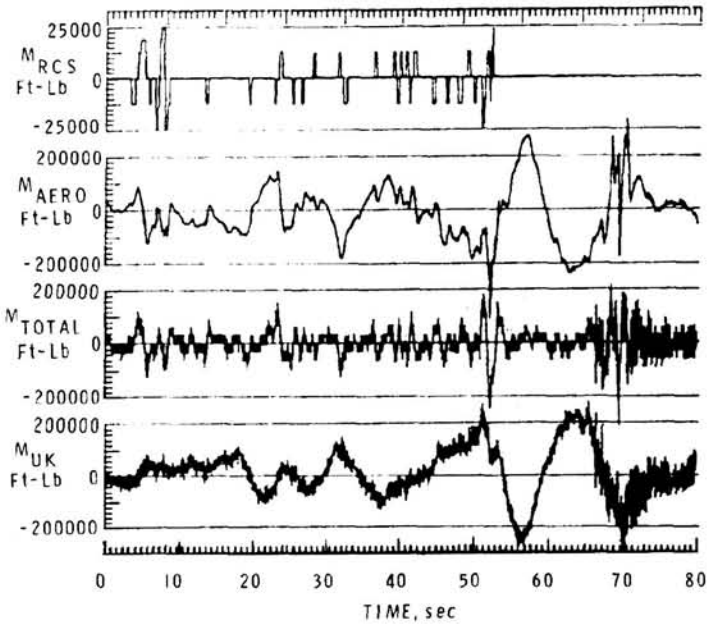

Figure 4.- Vehicle moments from STS-2 flight data.

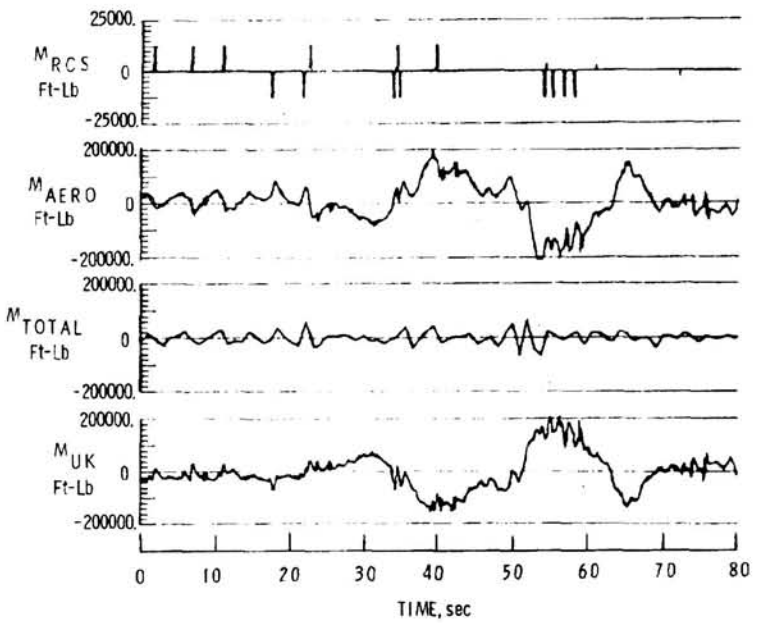

Figure 5.- Vehicle moments from STS-3 flight data.

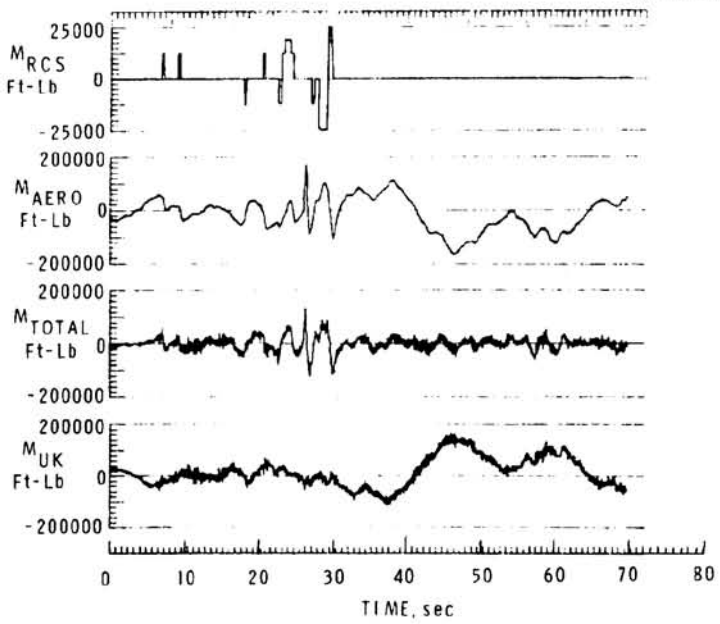

Figure 6.- Vehicle moments from STS-5 flight data.

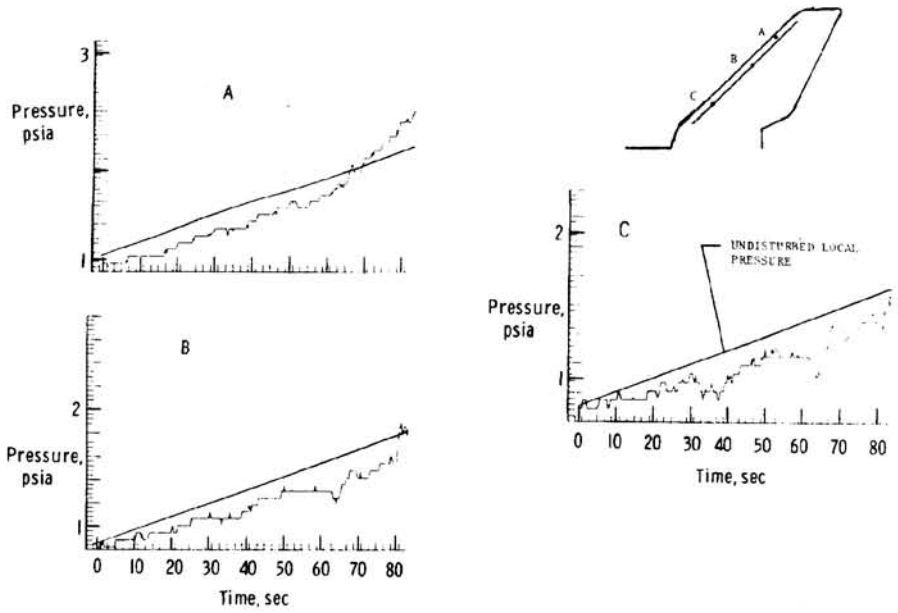

Figure 7.- STS-3 pressure time histories for various locations on the Shuttle vertical tail.

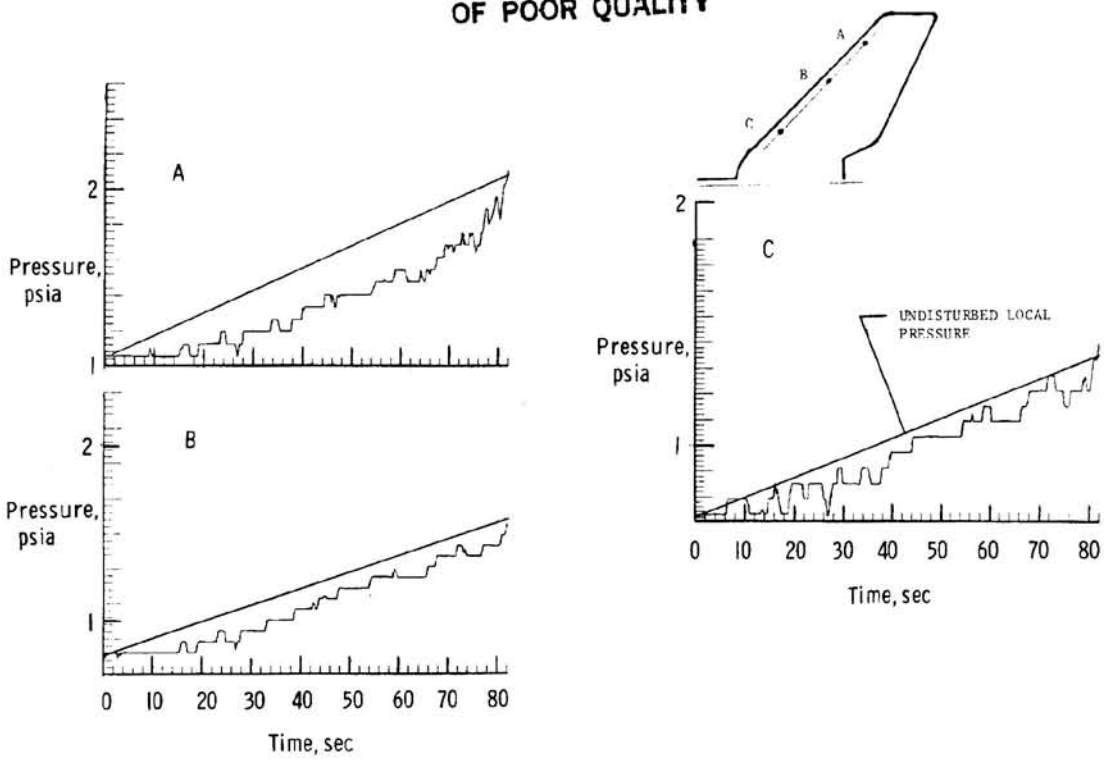

Figure 8.- STS-5 pressure time histories for various locations on the Shuttle vertical tail.

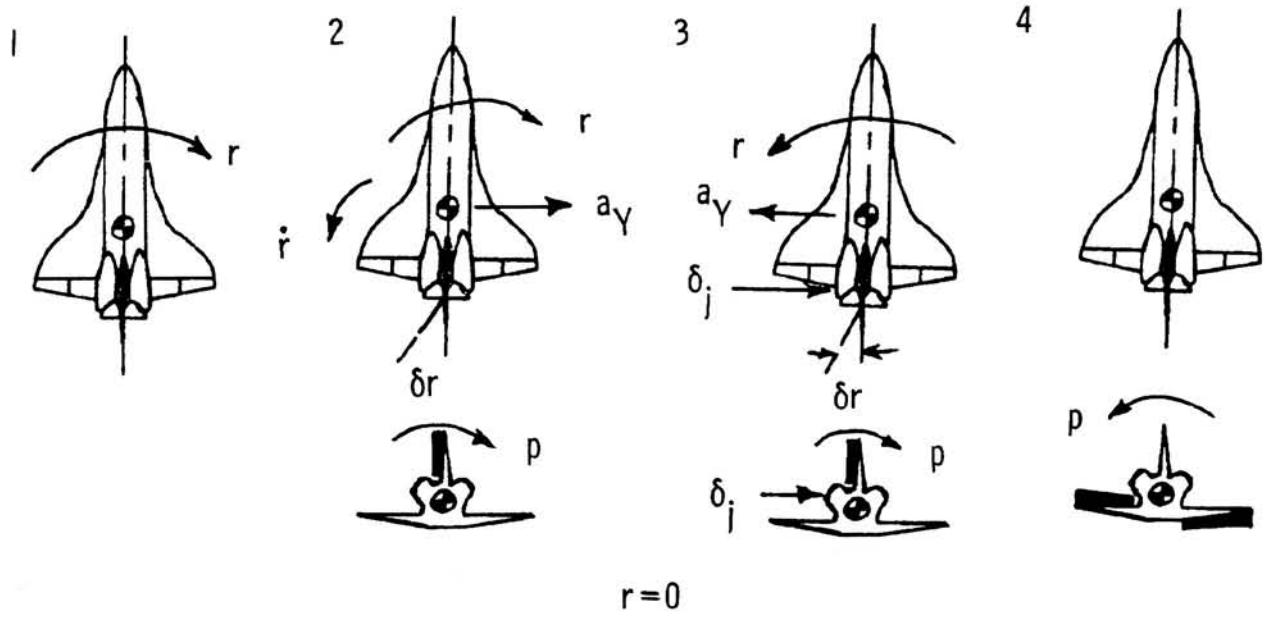

Figure 9.- Vehicle dynamics during "quarter hertz" motions.

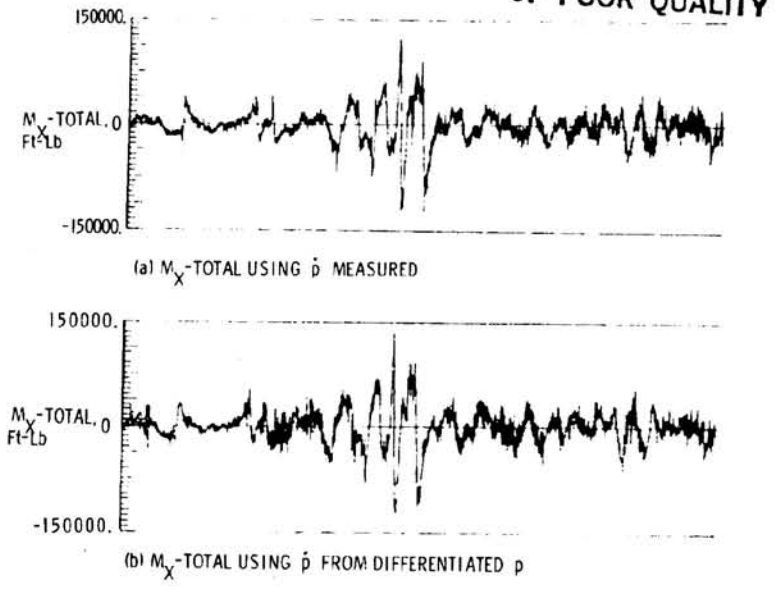

Figure 10.- Comparison of M_{TOTAL} about the X-body axis using two different sources of $\dot{p}$.

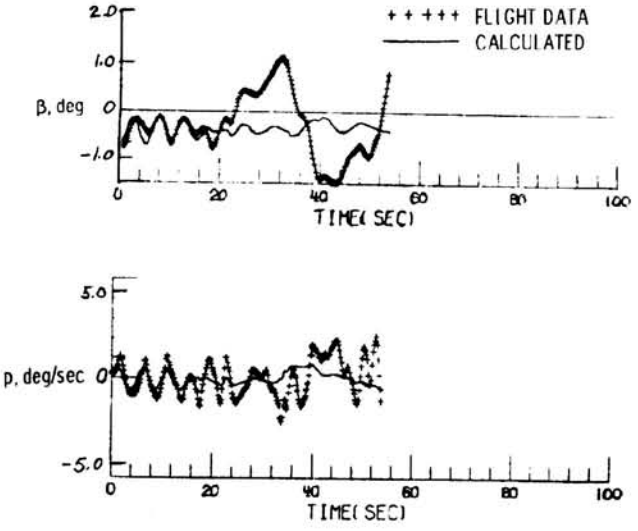

Figure 11.- Maximum-likelihood fit to sideslip and roll rate flight data.

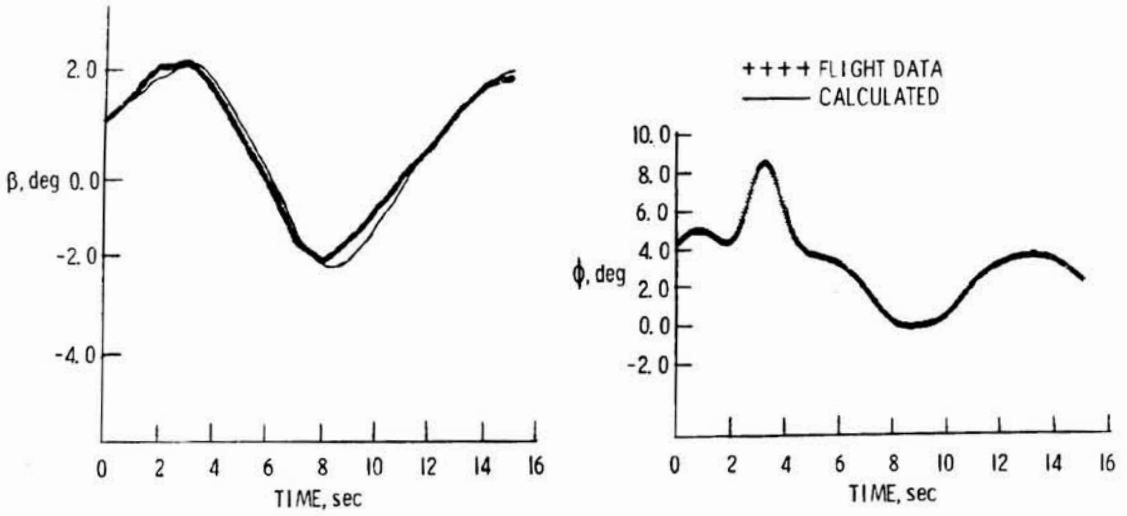

Figure 12.- Sideslip and roll attitude compatibility using roll rate, yaw rate, and lateral acceleration as known inputs to the vehicle kinematic equations.

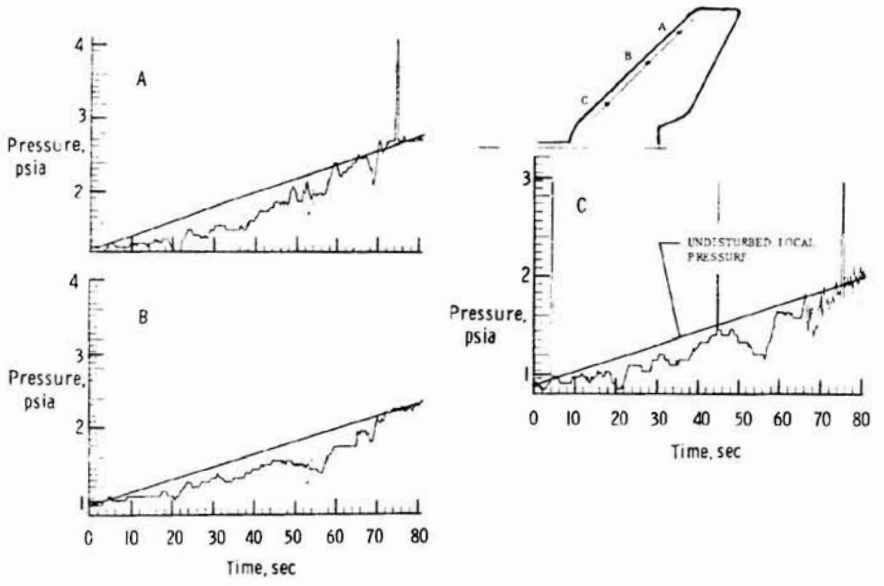

Figure 13.- STS-2 pressure time histories for various locations on the Shuttle vertical tail.

APPROACH TO ESTABLISHING THE EFFECT OF AEROELASTICITY ON AERODYNAMIC CHARACTERISTICS OF THE SPACE SHUTTLE ORBITER

D. C. Schlosser and D. F. Dominik
Space Transportation and Systems Group
Rockwell International
Downey, California

SUMMARY

The static aeroelastic effects on the longitudinal stability and elevon/aileron effectiveness of the space transportation system (STS) Space Shuttle orbiter were estimated by a simplified approach called the elevon torsional stiffness (ETS) method. This method employs rigid model wind tunnel test results to predict aeroelastic effects. Lateral/directional stability and rudder effectiveness were based on results of a wind tunnel test in which a flexible tail model was used. Comparisons with selective flight data are made in this paper. Results of correlations with flight data (although limited at the present time) verify the predicted aeroelastic effects for the orbiter.

The orbiter's structural characteristics are such that the effects of aeroelasticity, whether estimated using analytical techniques or simplified methods, do not appear to affect the vehicle performance to any great extent. The large amount of scatter in the flight-extracted data made verification of the aeroelastic corrections very difficult. Generally, the simplified elevon torsional stiffness method provided better correlation with flight test results than the analytical method and reduced the verification effort and cost.

INTRODUCTION

The aerodynamic characteristics of the STS orbiter are influenced by elastic deformation of the airframe as it is subjected to airloads. Early in the Space Shuttle program, a requirement was identified to verify these aeroelastic characteristics on the orbiter and a systematic approach was developed. At the beginning of the program, theoretical methods involving Woodward panel lifting surface calculations (ref. 1) were used to predict aeroelastic effects on the orbiter's aerodynamic characteristics. These early attempts at predicting the aeroelastic effects proved to be costly, time consuming, and could only be verified by other analytical methods; therefore, sensitivity studies were conducted to isolate major contributors and thereby aid in understanding the aeroelastic effects. The current ETS method used to estimate the longitudinal stability and control, elevator/aileron effectiveness, and elevon hinge moments evolved from these studies.

The vertical tail fin was isolated as the major contributor to aeroelastic effects on lateral/directional stability and rudder effectiveness. It was considered necessary to verify the effects of the vertical tail aeroelastic contribution by means of a flexible-tail wind tunnel model because of the limitations of the analytical methods employed.

This paper presents a discussion of the aforementioned aeroelastic methods, which were incorporated in the orbiter aerodynamic design data base (ref. 2). Comparisons are made with selective flight data and verification problems with flight data are addressed.

SPACE SHUTTLE ORBITER VEHICLE AEROELASTICITY

Configuration

The Space Shuttle orbiter configuration is shown in figure 1. The principal components relating to the aeroelastic analyses presented in this paper are identified and control surface areas and maximum deflections are given. During a normal end-of-mission entry, the expected operating envelope for dynamic pressure is 125 psf to 300 psf. At high Mach numbers, dynamic pressure diminishes to zero; therefore, aeroelastic effects are a concern only when dynamic pressure becomes significant, i.e., in the low supersonic and transonic Mach ranges.

Flight Environment

The environment experienced by the orbiter has been well within the expected operating envelope. During free-flight 4 (FF-4), dynamic pressure was varied from 100 psf to 300 psf in the Mach 0.4 to 0.5 range during a push-over pull-up (POPU) maneuver. The orbital flight test (OFT) program was benign, with a dynamic pressure reaching 225 psf near Mach 3.0, decaying to approximately 170 psf at Mach 1.0. The four flights were very similar with dynamic pressure excursions of approximately +35 psf or less. This repeatability did not enhance the ability to correlate or verify aeroelastic characteristics since this type of verification requires a greater range of dynamic pressure.

Aeroelastic Methodology

Early studies conducted to define the orbiter vehicle aeroelastic characteristics used advanced linear theory, as presented in reference 1. It was not considered necessary to model fuselage volume and wing or vertical tail thickness because panel deflection caused by aerodynamic loading is a function of the net load only. The orbiter was panelled (174 total panels) as shown in figure 2. The static influence coefficient method included aerodynamic and structural cross-coupling terms for all panels.

Longitudinal

The aeroelastic effects on the longitudinal aerodynamic characteristics were calculated by:

$$C_L^F = \frac{1}{\bar{q}\ S} \left[1 \right] \left\{ L^F \right\} \tag{1}$$

$$C_m^F = \frac{1}{\bar{q}\ S\ \bar{c}} \left[X - X_{CG} \right] \left\{ L^F \right\} \tag{2}$$

where

$$\left\{ L^F \right\} = \bar{q} \left[S_{LONG} \right] \left[\left[A \right]^{-1} - \bar{q} \left[s \right] \left[S \right] \right]^{-1} \left\{ \alpha^R \right\} \tag{3}$$

$$\left\{ \alpha^R \right\} = \text{Local panel angle of attack} \tag{4}$$

$$\left[A \right] = \begin{array}{c} \\ W \\ B \\ T \end{array} \begin{array}{c} \begin{array}{ccc} W & B & T \end{array} \\ \begin{bmatrix} A_{WW} & A_{WB} & A_{WT} \\ A_{BW} & A_{BB} & A_{BT} \\ A_{TW} & A_{TB} & A_{TT} \end{bmatrix} \end{array}$$

= Aerodynamic influence coefficient matrix based on symmetric boundary conditions (5)

$$\left[s \right] = \begin{array}{c} \\ W \\ B \\ T \end{array} \begin{array}{c} \begin{array}{ccc} W & B & T \end{array} \\ \begin{bmatrix} S_{WW} & S_{WB} & S_{WT} \\ S_{BW} & S_{BB} & S_{BT} \\ S_{TW} & S_{TB} & S_{TT} \end{bmatrix} \end{array}$$

= Structural influence coefficient matrix based on symmetric boundary conditions (6)

$\left[S_{LONG} \right]$ = Planform projection panel areas (7)

A typical wing deflection caused by elevon or aileron deflection is presented in figure 3. The major portion of the wing deflection occurs slightly ahead of the elevon hinge line (FS 1387). To verify that the wing was the primary contributor to the longitudinal aeroelastic effects, the SIC matrix was partioned such that various regions of the wing could be stiffened (wing box, elevon panels, and wing leading-edge reinforced carbon-carbon [RCC] panels) by a factor of 1.5. Results of these sensitivity studies are summarized in table I in terms of percentage change in the aeroelastic effect. It was concluded from these results and the deflection pattern shown in figure 3 that the longitudinal (and similarly the aileron) characteristics could be related to elevon deflection under load and could, therefore, be expressed as a function of the elevon hinge moment. This method was called the ETS method.

ETS Method

The math model for the ETS method is presented in figure 4. This method assumes that the elevon is attached to the wing by means of a spring having a constant, K. Application of a rigid hinge moment would cause the elevon to deflect in a manner tending to reduce the hinge moment. The corresponding change in elevon deflection results in a change to the aerodynamic load. The resulting flexible elevon deflection (δ_e^F) can be used with the rigid aerodynamic characteristics to solve directly for the flexible aerodynamics or to compute flex-to-rigid ratios by using both flexible and rigid elevon deflections.

Development and Verification of Elevon Spring Constants

The elevon spring constants were first developed using the static structural influence coefficient matrix and applying a unit load on the individual panels to determine deflection at all the panels. Analysis of the resulting deflections yielded the in- and out-board spring constants presented in figure 5. The value of K is dependent on the location of the spanwise load because the elevon torsional load is transmitted to the wing through the actuator. The value of K to be used in the ETS method is the value at the actuator station. The values of K delineated in figure 5 were used to predict the effects of aeroelasticity. Verification of the spring constants, which were developed by this analytical method, was obtained during the structural test article (STA) loadings performed on Orbiter 099 with dummy actuators and the actual static calibrations performed on Orbiter 101 during calibration of the elevon deflection with a powered-up hydraulic system used during the Approach and Landing Test (ALT) program.

Comparison of Results

The difference between results of the analytical method and the ETS method is presented in figures 6 and 7 at a dynamic pressure of 300 psf for the longitudinal characteristics. The ETS method consistently produced a lower value of the aeroelastic effect. Aileron derivatives are presented in figure 8, and again the ETS method produced lower aeroelastic effects than the analytical method.

To better understand the differences between the analytical method and the ETS method, the relationship between the theoretical rigid and flexible normal force, pitching moment, and elevon hinge moment was examined.

The flexible elevon hinge moment (figure 9) pivots about the rigid $C_{h_e} = 0$ point, indicating the aeroelastic effect is directly related to elevon load. Similarly, the aeroelastic pitching moment increment changes sign as elevon hinge moment passes through zero. Application of the analytical method results (e.g., ΔC_{m_o}, $\Delta X_{ac}/\bar{c}, \eta_{m_e}$) to rigid experimental data produces the results shown in figure 10. The experimental data had a significantly lower absolute level and the relationship to elevon hinge moment is not maintained because of the large theoretical $\Delta C_{m_o}^F$, $\Delta C_{L_o}^F$, $\Delta C_{h_o}^F$, which is being applied. The ETS method intrinsically preserves the elevon hinge moment relationship and the corresponding aeroelastic pitching moment effects, as shown in figure 11. The reduction in aeroelastic effects by using the ETS method is also consistent with the smaller experimental aerodynamic loadings.

Lateral/Directional

The effect of aeroelasticity on the lateral/directional aerodynamic characteristics was calculated by:

$$C_Y^F = \frac{1}{\bar{q}\,S} \left[1\right] \left\{SF^F\right\} \tag{8}$$

$$C_n^F = -\frac{1}{\bar{q}Sb} \left[X' - X_{CG}\right] \left\{SF^F\right\} \tag{9}$$

$$C_\ell^F = -\frac{1}{\bar{q}Sb} \left[Y - Y_{CG}\right] \left\{L^F\right\} + \frac{1}{\bar{q}Sb} \left[Z - Z_{CG}\right] \left\{SF^F\right\} \tag{10}$$

where

$\left\{L^F\right\}$ = same as longitudinal equation (3) except based on asymmetric and antisymmetric boundary conditions

$$\left\{SF^F\right\} = \left[S_{LAT-DIR}\right] \left[\left[A\right]^{-1} - \bar{q}\left[s\right]\left[S\right]\right]^{-1} \left\{\alpha^R\right\}_\beta \tag{11}$$

$$\left\{\alpha^R\right\}_\beta = \text{local panel sideslip angle} \tag{12}$$

$$\left.\begin{matrix}[A] = \\ [s] =\end{matrix}\right\} \text{same as longitudinal matrix, except based on asymmetric and antisymmetric boundary conditions} \quad (5,6)$$

$$\left[\widehat{S_{LAT-DIR}}\right] = \text{side-view projection panel areas} \quad (13)$$

Based on the aeroelastic sensitivity studies conducted using the method just described, it was concluded that the majority of the aeroelastic losses in the lateral/directional stability and rudder effectiveness parameters were coming from the fin portion of the vertical tail. Typical deflection patterns of the vertical tail caused by sideslip and rudder deflection are presented in figures 12 and 13. The fuselage and wing were small contributors and parametric stiffening studies of the aft fuselage, rudder/speed brake panels and actuators showed only minor changes in the aerodynamic losses caused by aeroelasticity. The results of these stiffening studies are summarized in table II; therefore, it was concluded that only the fin portion of the vertical tail needed to be modeled.

Flexible Vertical Tail Design and Verification

Selection of the vertical tail structure to be modeled was based on the fact that the wind tunnel model could only be tested at a constant load factor; therefore, mass and inertia relief effects should not be included. A summary of the differences between a wind tunnel model and a full-scale flight vehicle is presented in figure 14; therefore, the vertical tail SIC matrix model selected for the wind tunnel model was the restrained or fixed SIC model. Because of the model scale selected (0.03), it was impossible to attempt a structural replication of the full-scale structure and a simple beam model was selected.

The steps taken to define and verify the test article prior to wind tunnel testing are outlined in figure 15. Having selected the appropriate SIC matrix for the vertical tail design, the first step was to reduce the SIC matrix to a spanwise variation of bending stiffness (EI) and torsional stiffness (GJ) about an elastic axis (EA). The EI and GJ specifications were used to design a simple beam model that would produce deflections matching those from the SIC matrix. A requirement also existed for the chordwise stiffness of the model to be equal to or greater than that of the full-scale orbiter. This requirement also applied to the rudder/speed brake panels, although no attempt to model their flexibility was made. As the design of the model progressed, it became apparent that the model lacked chordwise stiffness and thus the chordwise stiffeners were added.

Having produced a beam design representative of the full-scale vehicle, it then had to be scaled to model dimensions and wind tunnel dynamic pressures. The aeroelastic scaling laws utilized to reduce the full-scale beam to model scale are presented in the following equations:

$$\left(\frac{q_M}{q_A}\right)\left(\frac{E_A I_A}{E_M I_M}\right)\left(\frac{S_M}{S_A}\right)^2 = 1.0$$

$$\left(\frac{q_M}{q_A}\right)\left(\frac{G_A J_A}{G_M J_M}\right)\left(\frac{S_M}{SA}\right)^2 = 1.0$$

thus

$$\left(\frac{E_A I_A}{E_M I_M}\right) = \left(\frac{G_A J_A}{G_M J_M}\right)$$

and if airplane and model are constructed of the same material

$$\left(\frac{E_A}{E_M}\right) = \left(\frac{G_A}{G_M}\right) = 1.0$$

therefore

$$\left(\frac{I_A}{I_M}\right) = \left(\frac{J_A}{J_M}\right) \text{ and } \left(\frac{J_M}{I_M}\right) = \left(\frac{J_A}{I_A}\right)$$

Satisfactory testing of an aeroelastic model requires the selection of wind tunnels that have the capability of varying free-stream dynamic pressure at constant Mach numbers. The facilities selected for testing the orbiter model had the capability of varying dynamic pressure from 300 to 900 psf over a Mach range of 0.6 to 3.5. A $\bar{q}_m/\bar{q}_A$ ratio of 3.0 was used in the scaling equations so that at a wind tunnel free-stream dynamic pressure of 900 psf the model deflections would correspond to full-scale deflections at a dynamic pressure of 300 psf. After the model was designed and built, it was necessary to calibrate and tune it to the desired EI and GJ distributions. The design requirements for EI and GJ and the as-measured values are given in figure 16. Calibrations were made with the rudder/speed brake panels attached. No differences in the calibration were observed because of speed brake angle (i.e., 25 or 55 degrees). The beam of the model had to be extended 0.90 inch below the fuselage outer moldline (OML) in order to match root deflections resulting from the aft fuselage flexibility. The calibration was the first step toward verification of the tail design.

Additional steps in verifying the model tail design were done analytically. First, the tail geometry was modeled in the NASTRAN (ref. 3) program and an SIC matrix was generated for the as-built tail. Secondly, the as-built SIC matrix was reduced to EI and GJ by the same procedure used to reduce the design to SIC matrix. These checks constituted the static verification of the flexible vertical tail model design prior to installation of the rubber coating on the beam, which gave the tail an airfoil shape. No attempt was made to verify the effect of the rubber coating prior to testing.

An additional requirement for a flutter analysis was imposed on the flexible tail model to ensure that it would be free of any significant dynamic loadings because at maximum design loads a factor of safety of 5.0 could not be demonstrated. Results indicated that the first divergence occurred in the second bending mode at a speed of approximately 1000 knots. This was equivalent to a wind tunnel dynamic pressure of 2000 psf, well above the anticipated maximum during the test program.

Additional static calibrations of the tail have been conducted since the completion of the wind tunnel tests. The flexible tail model was statically loaded in locations similar to those used on the STA and the corresponding deflections were measured. These load points and deflection measurement points are illustrated in figure 17. Two types of loadings were made at load points 21, 22, and 23. Instead of loading at a single point, a plate, as outlined on the figure, was used to distribute the load similar to the STA, which was not loaded at a single load point. Deflections at load points 22 and 23 showed little difference because of the method of loading; therefore, a single load point was used for loading points 24, 25, and 26. Comparisons of the STA results and the wind tunnel model (scaled to full scale) are presented in figures 18 through 23. Again, it was concluded that the flexible-tail model was an excellent representation of the actual Orbiter 102 vertical tail.

From the extensive pre-test design and pre- and post-test verification efforts, it can be concluded that the orbiter flexible tail model used during the orbiter aeroelastic verification test program will produce results that can be used to verify analytical methods and/or be used to estimate orbiter full-scale aeroelastic characteristics.

The flexible tail model underwent extensive wind tunnel testing in the NASA Ames Research Center (ARC) and Air Force Arnold Engineering Development Center (AEDC) facilities. Analysis of these data forms the basis for the current lateral/directional aeroelastic characteristics. The flexible-tail wind tunnel test program and the Mach/dynamic pressure range of the facilities used are presented in figure 24.

Comparison of Results

Comparisons between the analytical predictions and the results of the flexible tail wind tunnel test program (at a dynamic pressure of 300 psf) are given in figures 25 and 26. Sideslip derivative flex-to-rigid ratios show a larger loss caused by aeroelasticity than the analytical results do. Rudder derivatives are in close agreement. As stated earlier, it is believed the analytical method is deficient in describing the vertical-tail flow field because of sideslip angle, thereby causing the difference in the sideslip effects. The rudder effect was analyzed at zero sideslip and is less dependent upon the local flow field, resulting in closer agreement.

Correlation with Flight Test Results

The orbiter aerodynamic characteristics are being verified in two ways. The low-speed aerodynamics were verified during the ALT phase using Orbiter 101 and the present high-speed verification is being conducted using Orbiter 102 during the OFT program. Flight test results from the ALT and first four flights of the OFT programs are presented.

Two ALT flights were conducted with the tailcone off, FF-4 and FF-5. Specific maneuvers were performed to extract the low-speed aerodynamic stability and control characteristics. A POPU maneuver during FF-4 provided an angle of attack variation from 3 to 15 degrees and, simultaneously, dynamic pressure varied from 300 to 100 psf. Since the aeroelastic effects are a function of dynamic pressure, this maneuver provided the dynamic pressure change necessary to correlate the aeroelastic methods. Assuming that the rigid effect of angle of attack could be predicted with reasonable accuracy through the use of wind tunnel test data, the effect of aeroelasticity at low dynamic pressure should be small. It should be large at high dynamic pressures. The aeroelastic methods can be compared by plotting elevon deflection required to trim as a function of trimmed lift coefficient (figure 27). The theoretical effect of aeroelasticity on elevon deflection required to trim does not correlate with the flight test results as well as the ETS method or the rigid data. The largest contributor to the difference in the theoretical data is caused by the C_{m_o} and C_{L_o} increments. The ETS method estimated these increments to be much smaller.

Elevon and aileron effectiveness ($C_{N_{\delta_e}}$, $C_{m_{\delta_e}}$ and $C_{Y_{\delta_a}}$, $C_{n_{\delta_a}}$, and $C_{\ell_{\delta_a}}$) were extracted during the ALT program and are presented in figures 28 and 29. Either aeroelastic method could adequately predict these derivatives. The preflight uncertainties for which the vehicle was stress-tested are shown on the right-hand side of these figures. The effect of aeroelasticity is only a fraction of the total uncertainty and not critical to low-speed handling qualities. It was clearly evident that the method of applying theoretical aeroelastic effects (C_{m_o} and C_{L_o}) was producing too large an effect at the conclusion of the ALT program. The ETS method provided a more reasonable effect; therefore, it was the method used to derive the Orbiter 102 aeroelastic effects.

The correlation of the sideslip and rudder derivatives with ALT flight test results are presented in figures 30 and 31. The rigid results and the theoretical method produce about the same aeroelastic effect for the sideslip derivative while the wind tunnel results indicate a large loss. The derivative, C_{ℓ_β}, does appear to be more accurately predicted by the wind tunnel results than by theory. The design uncertainty is indicated on the right-hand side of the figure and either method of estimating aeroelastic effects on the sideslip derivatives is well within the design-to uncertainty.

Rudder effectiveness is not affected by the estimating technique as much as the sideslip derivatives. The aeroelastic effects on $C_{\ell_{\delta_R}}$ approach the preflight uncertainty at high dynamic pressure and had to be accounted for.

It was concluded from these correlations that the ETS method did provide better agreement in longitudinal trim characteristics and the sideslip and rudder derivatives, derived from the flextail wind tunnel test program, should be used for the OFT program planning.

OFT Results (STS-1 Through STS-4)

During a normal end-of-mission entry, aeroelastic effects do not become significant until Mach 5 is reached and dynamic pressure has increased to approximately 200 psf. Angle of attack, dynamic pressure, elevon deflection, and center of gravity location have not differed significantly (figure 32) during the first four STS flights. The majority of trajectory differences and dispersions have occurred at Mach numbers less than 1.0. The speed brake schedule has been the same and body flap deflection does not influence the ETS method. The dynamic pressure was reduced to 150 psf and the elevon scheduled near zero hinge moment in the transonic Mach range, thus providing maximum control surface deflection rate capability. These conditions also combine to produce negligible aeroelastic effects in the transonic Mach number range.

In the Mach 5 to 2 region, dynamic pressure was 180 psf or more and the elevon hinge moments were allowed to increase as the elevon schedule was controlled to optimize the yawing moment derivative, $C_{n_{\delta_a}}$. The flight test results from STS-2 have been selected to illustrate the elevon hinge moment (figure 33) and longitudinal aerodynamic (figure 34) correlation. The differences between flexible and rigid prediction are very small; the largest aeroelastic correction appears in pitching moment. The increments (flight minus predicted) for both flexible and rigid estimates (figure 35) are within preflight uncertainties in the Mach 5 to 2 region, with the flexible estimate minutely better. The flight increments are much larger than the flex-to-rigid increments and obscure any effort to verify the longitudinal aeroelastic effects.

Lateral/directional flight-minus-predicted increments for the aileron, rudder, and sideslip derivatives are summarized in figures 36 through 38. These derivatives are extracted from programmed test inputs (PTI) or bank reversal motion time histories recorded during the entry flight phase. There were no PTI's during STS-1; therefore, only data from STS-2 through STS-4 are presented. Again, the flight-minus-predicted increments greatly exceed the aeroelastic increment and the data scatter precludes verification of the lateral/directional aeroelastic effects.

CONCLUDING REMARKS

The orbiter structural characteristics and entry dynamic pressure profile result in minimal aeroelastic effects relative to preflight design-to uncertainties and flight test measurement accuracies. The required fidelity of the aeroelastic analysis should consider these uncertainties in addition to flight control system sensitivity requirements.

Theoretical analysis was used to understand the relationship between flexible and rigid aerodynamic characteristics, including resulting aeroelastic deformations. This resulted in a simplified aeroelastic estimation procedure (ETS method), which utilized the high-fidelity, experimentally derived aerodynamic characteristics.

Theoretical analysis also initiated the flexible vertical tail wind tunnel test program and supported the simplified flexible tail design approach. Step-by-step coordination of model design requirements, fabrication, and verification produced a quality test article.

Verification of the aeroelastic effects has been difficult with the current flight test program results and limited trajectory dispersions in dynamic pressure.

SYMBOLS

ac	aerodynamic center
b	reference wing span, in.
c	mean aerodynamic chord, in.
C_A	axial force coefficient
C_D	drag coefficient
C_L	lift coefficient
C_N	normal force coefficient
C_Y	side force coefficient
C_h	hinge moment coefficient
C_ℓ	rolling moment coefficient
C_m	pitching moment coefficient
C_n	yawing moment coefficient
K	spring constant, deg/in.-lb
$\bar{q}$	dynamic pressure, lb/ft^2
S	reference wing area, ft^2
α	angle of attack, deg
β	angle of sideslip, deg
Δ	increment
δ	control surface deflection, deg
η	flex-to-rigid ratio
$\lfloor \rfloor$	row vector
$\{ \}$	column vector
$[ ]$	rectangular or square matrix

Subscripts

a	aileron
bf	body flap
e	elevon
r	rudder
sb	speed brake
o	zero angle of attack, $\alpha = 0$

B	body
T	tail
W	wing
LAT-DIR	lateral/directional
LONG	longitudinal

Superscripts

F	flexible
R	rigid

Acronyms

ADDB	Aerodynamic Design Data Book (ref. 2)
AEDC	Arnold Engineering Development Center
ARC	Ames Research Center
CG	center of gravity
EA	elastic axis
EI	bending stiffness parameter
ETS	elevon torsional stiffness
FF	free-flight
GJ	torsional stiffness parameter
NASA	National Aeronautics and Space Administration
NASTRAN	NASA structural analysis
OFT	orbital flight test
OML	outer moldline
POPU	push-over pull-up
psf	lb/ft^2
PTI	programmed test inputs
RCC	reinforced carbon-carbon
SIC	structural influence coefficient
STA	structural test article
STS	Space Transportation System

REFERENCES

1. Bonner, E.; Clever, W.; and Dunn, K.: Aerodynamic Preliminary Analysis System II, Part I - Theory. NASA CR-165626, Apr. 1981.

2. Aerodynamic Design Data Book (Volume I) Orbiter Vehicle, STS-1. SD 72-SH-0060-1M, Rockwell International, Space Transportation Integration and Operations Division, Downey, California, Nov. 1980.

3. NASTRAN - NASA Structural Analysis System (CDC Version). HQN-10952, COSMIC, University of Georgia.

TABLE I.- EVALUATION OF STIFFENED WING/ELEVON STUDY

[$\bar{q}$ = 300 psf]

Region Stiffened	C_{m_α} (%)	$C_{m_{\delta_e}}$ (%)	$C_{\ell_{\delta_a}}$ (%)
Wing	16	13	16
Inboard elevon	6	5	4
Outboard elevon	6	2	3
Wing leading edge	< 5	--	--
Rigid actuators	—	<1	--

TABLE II.- EVALUATION OF STIFFENED VERTICAL TAIL STUDY

[$\bar{q}$ = 300 psf]

Region Stiffened	C_{n_β} (%)	C_{ℓ_β} (%)	$C_{n_{\delta_R}}$ (%)	$C_{\ell_{\delta_R}}$ (%)
Fin	26	26	29	29
Rudder/panels	--	--	< 2	< 2
Aft fuselage	3	6	< 2	< 2
Rigid actuators	--	--	< 1	< 1

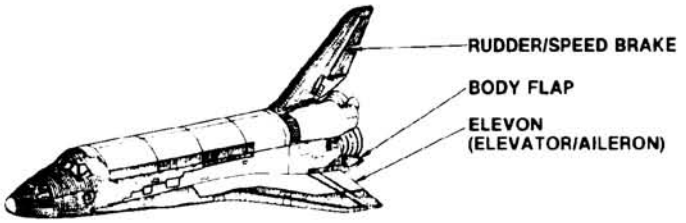

GEOMETRY	COMPONENT	
	WING	VERTICAL TAIL
AREA	2690.00 FT²	413.25 FT²
SPAN	936.68 IN.	315.72 IN.
ASPECT RATIO	2.265	1.675
TAPER RATIO	0.20	0.404
SWEEP L.E.	81/45 DEG	45 DEG
DIHEDRAL	3.5 DEG	—
INCIDENCE	0.5 DEG	—
MAC	474.81 IN.	199.81 IN.

CONTROL SURFACE	AREA (FT²)	MAX DEFLECTION (DEG)
ELEVON (1 SIDE)	206.570	-35 TO +20
BODY FLAP	135.750	-11.7 TO +22.5
SPEED BRAKE	97.148	0 TO 87.2
RUDDER	97.148	-22.8 TO +22.8

Figure 1.- Space Shuttle orbiter configuration.

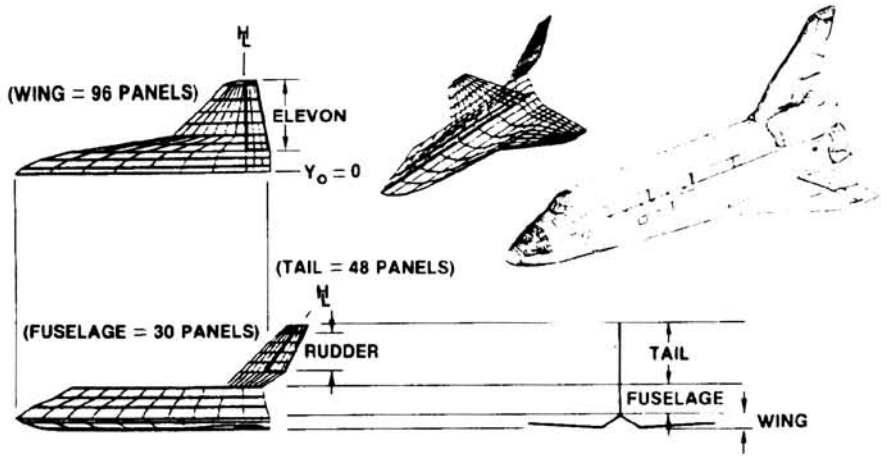

Figure 2.- Orbiter vehicle paneling.

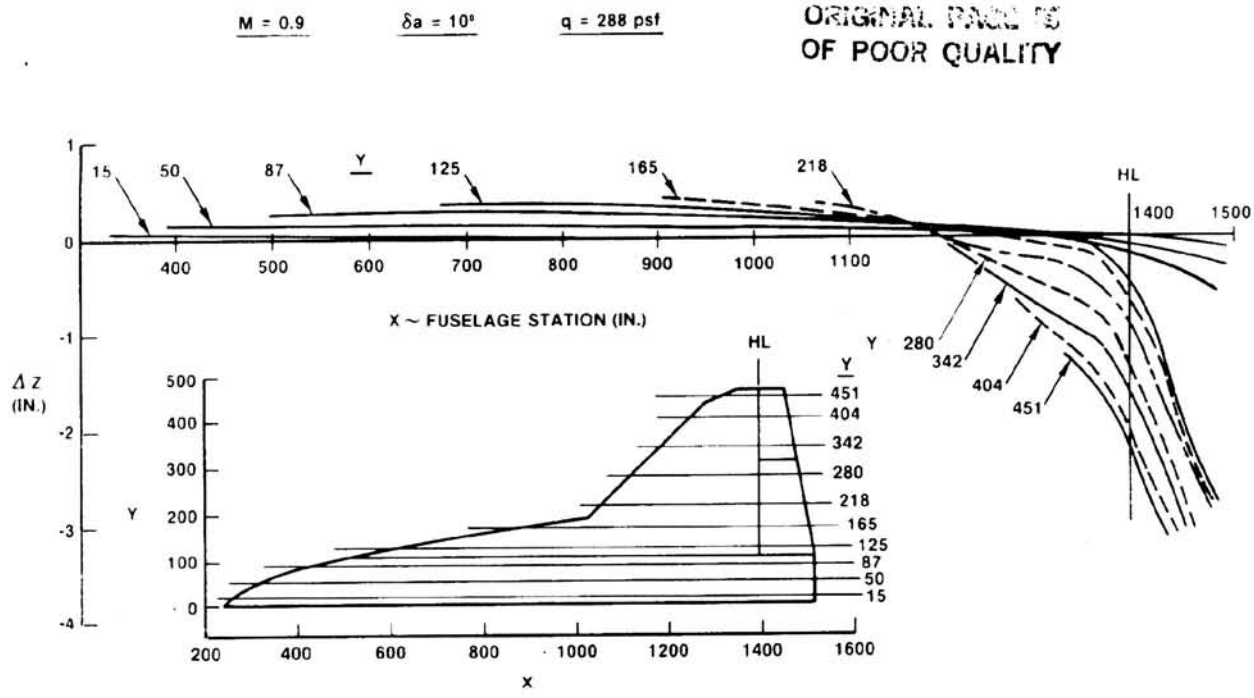

Figure 3.- Wing deflection caused by elevon deflection.

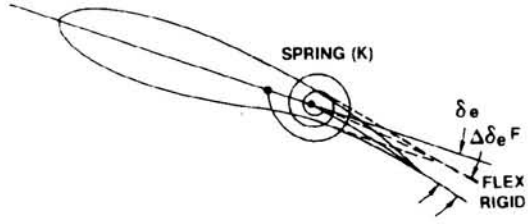

$$C_h^F = C_h^R + \Delta C_h^F \quad (1)$$

$$\Delta C_h^F = C_{h_{\delta e}}^R \Delta\delta_e^F \quad (2)$$

$$\Delta\delta_e^F = Kq\, S_e \bar{c}_e\, C_h^F \quad (3)$$

$$C_h^F = C_h^R + C_{h_{\delta e}}^R Kq\, S_e \bar{c}_e\, C_h^F$$ SUBSTITUTE (2) AND (3) INTO (1)

$$C_h^F = \frac{C_h^R}{1 - C_{h_{\delta e}}^R Kq\, S_e \bar{c}_e} \quad (4)$$

$$\delta_e^F = \delta_e^R + \Delta\delta_e^F$$

$$\delta_e^F = \delta_e^R + \frac{Kq\, S_e \bar{c}_e\, C_h^R}{1 - C_{h_{\delta e}}^R Kq\, S_e \bar{c}_e}$$ SUBSTITUTE (4) INTO (3)

Figure 4.- Elevon torsional stiffness math model.

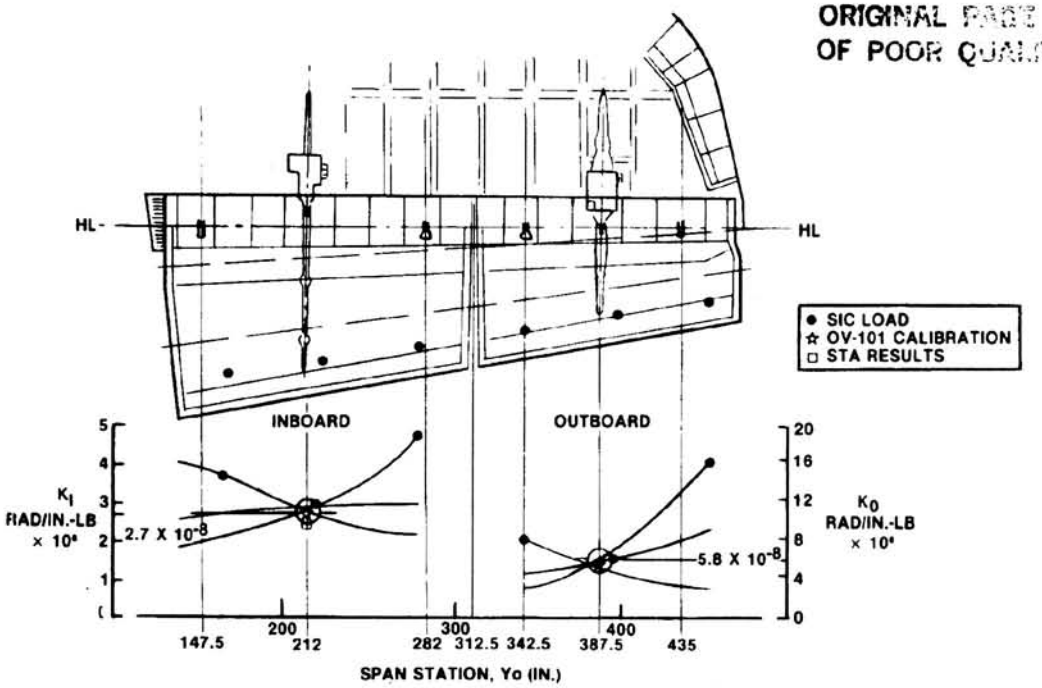

Figure 5.- Elevon hinge/actuator arrangement.

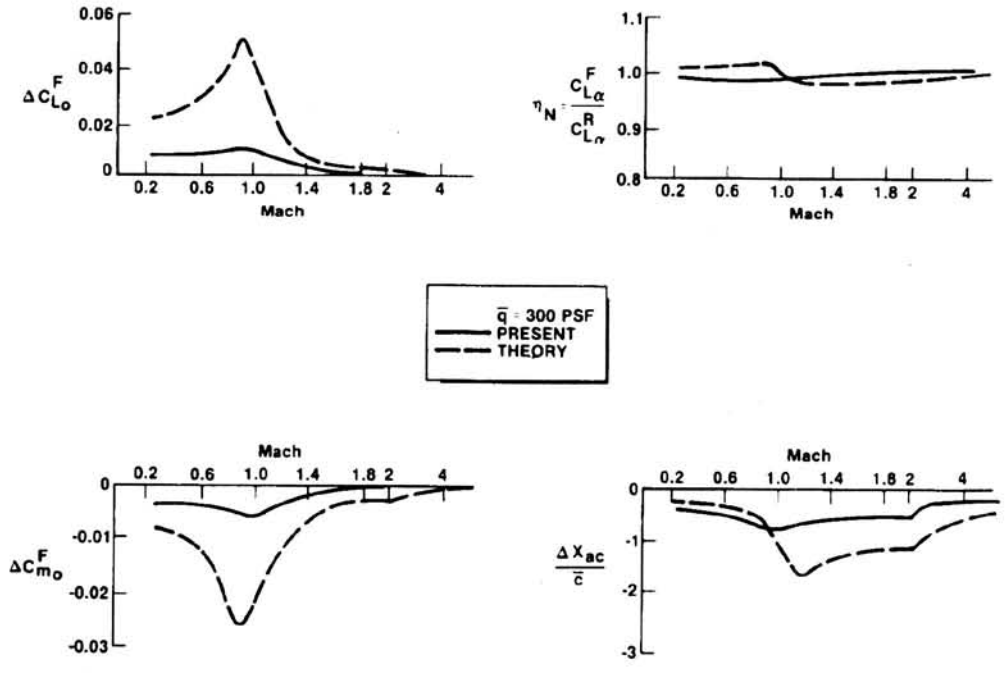

Figure 6.- Comparison of aeroelastic methods on lift and pitching moment.

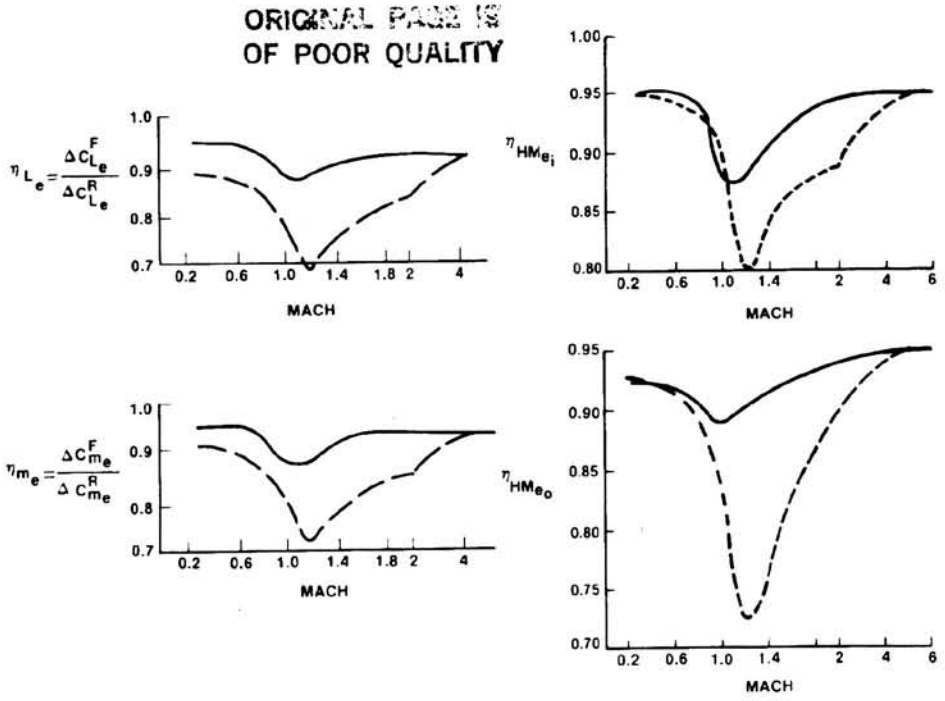

Figure 7.- Comparison of aeroelastic methods on elevon effectiveness and hinge moments.

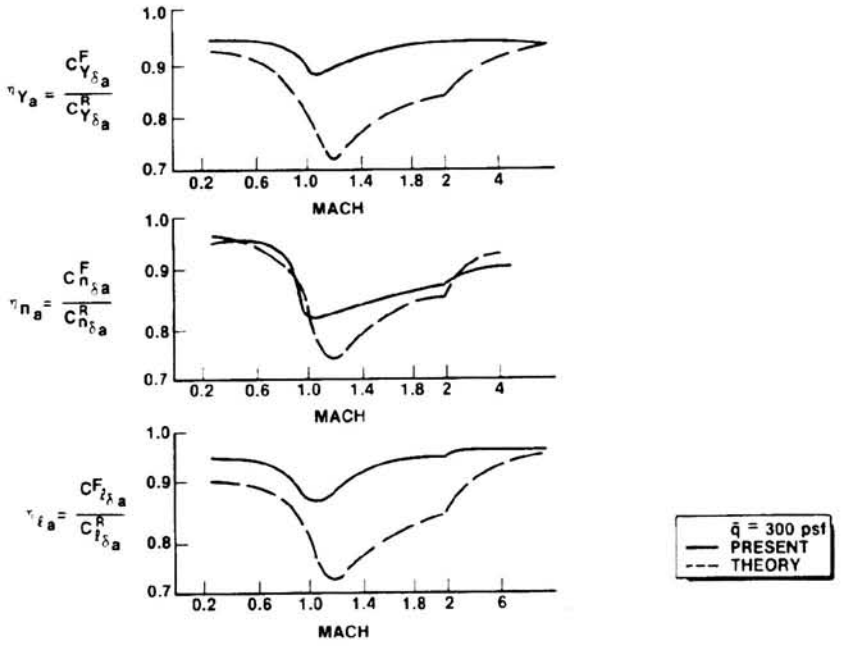

Figure 8.- Comparison of aeroelastic methods on aileron derivatives.

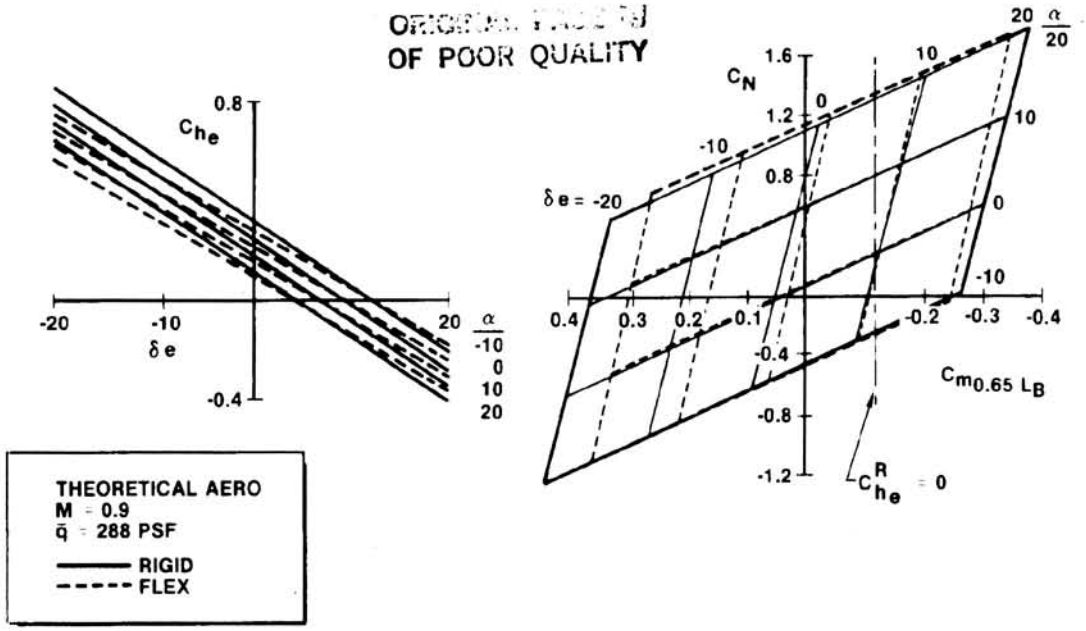

Figure 9.- Relationship between theoretical rigid and flexible aerodynamics.

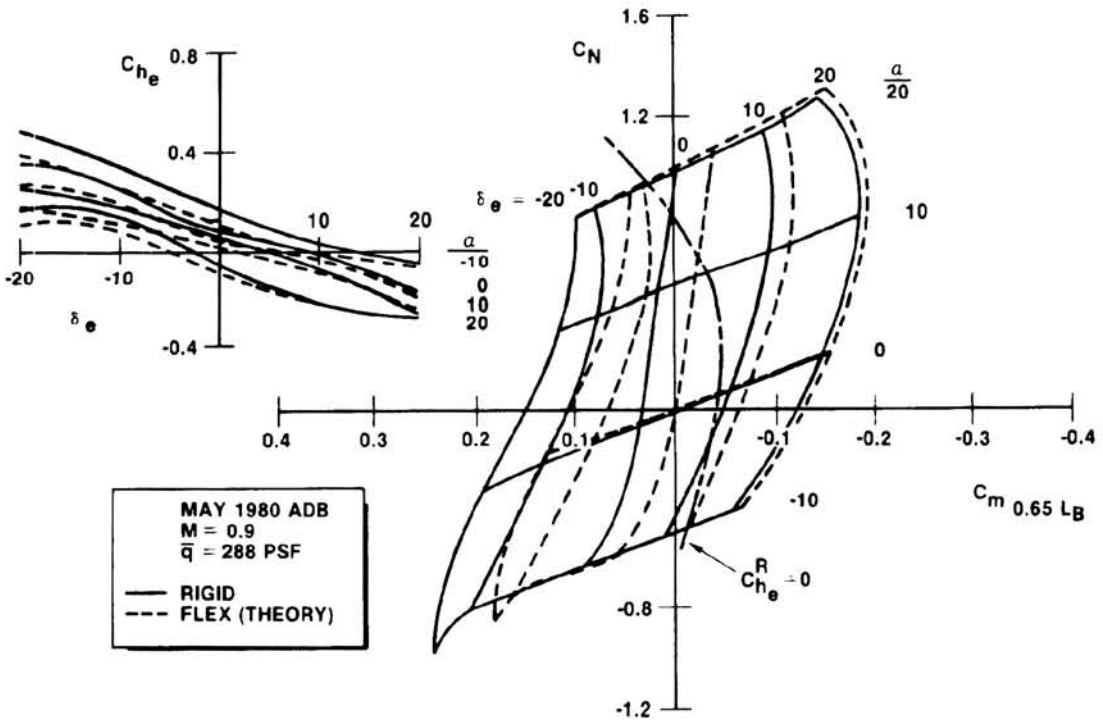

Figure 10.- Rigid and flexible aerodynamics using theoretical results.

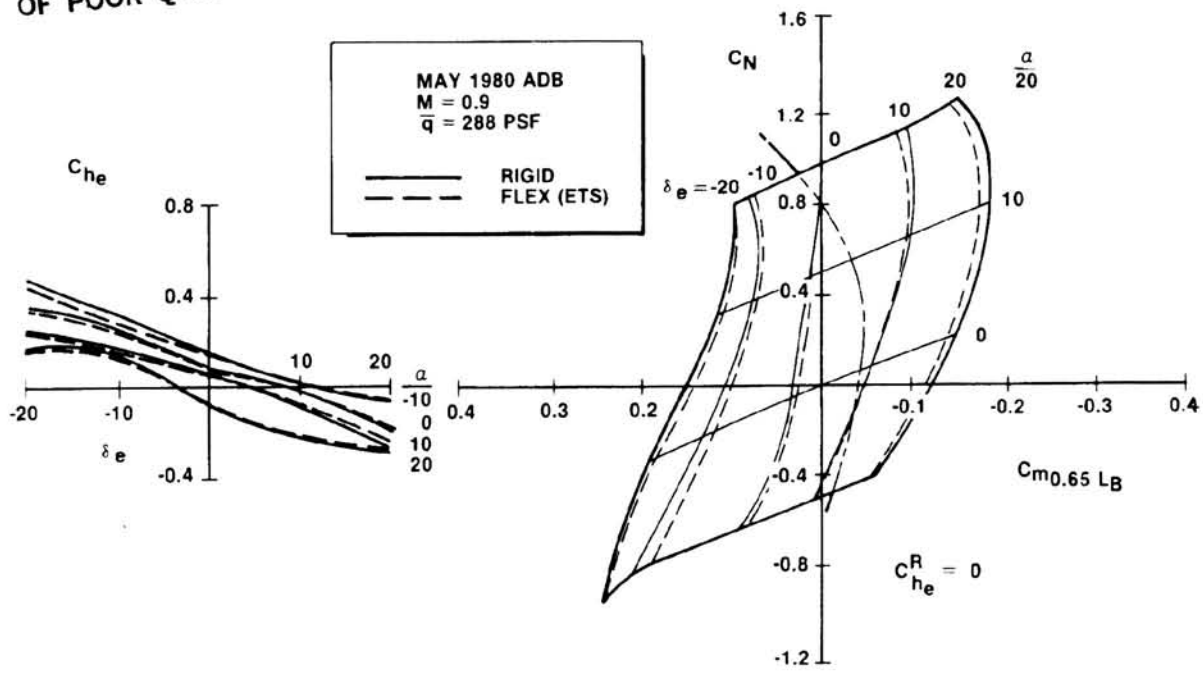

Figure 11.- Rigid and flexible aerodynamics using elevon torsional stiffness method.

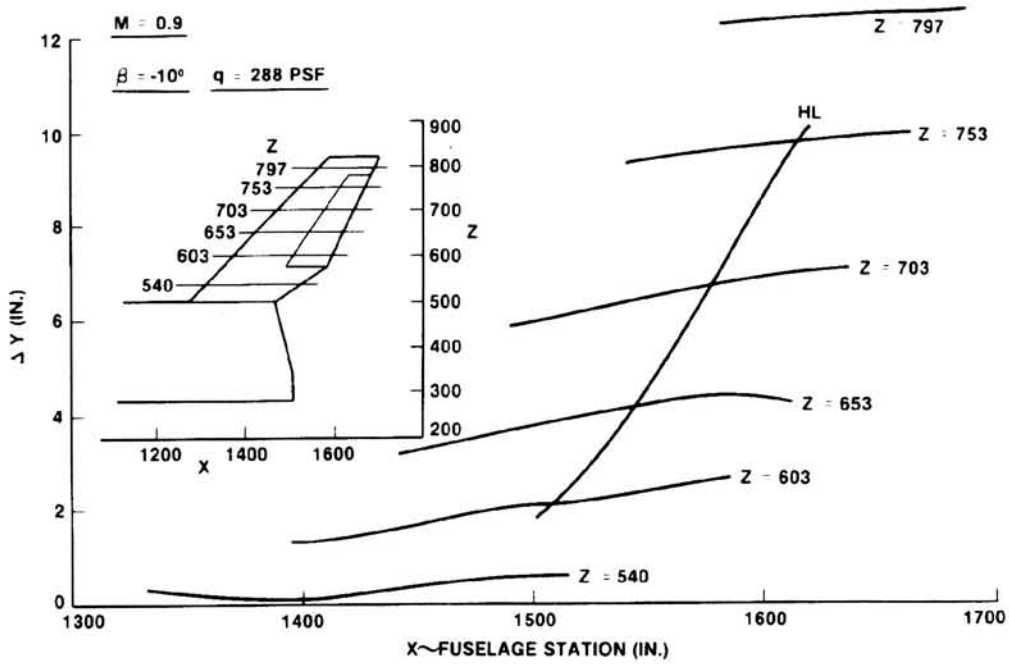

Figure 12.- Vertical tail deflection caused by sideslip loading.

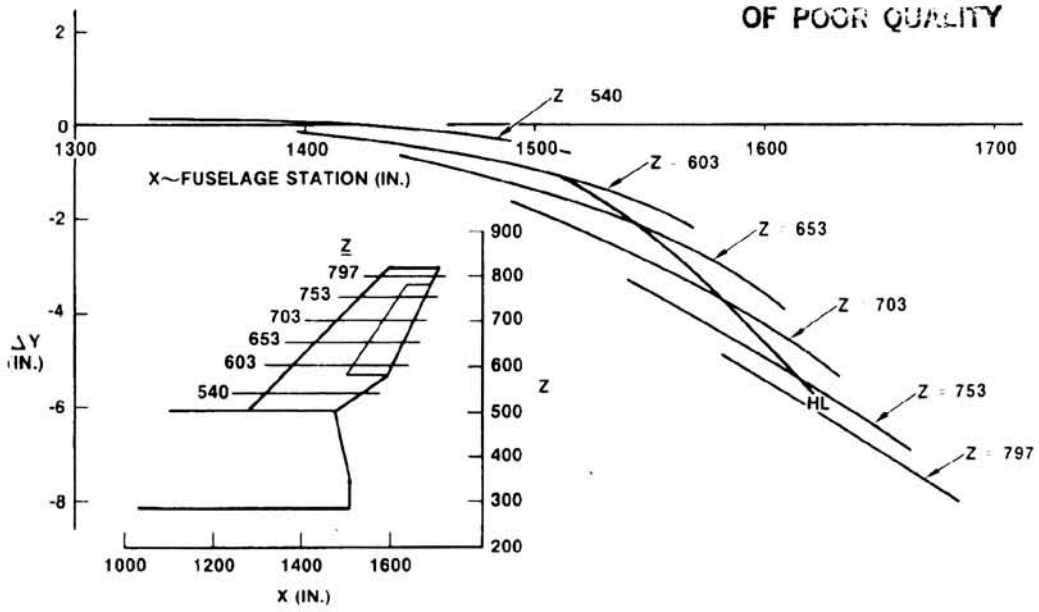

Figure 13.- Vertical tail deflection caused by rudder loading.

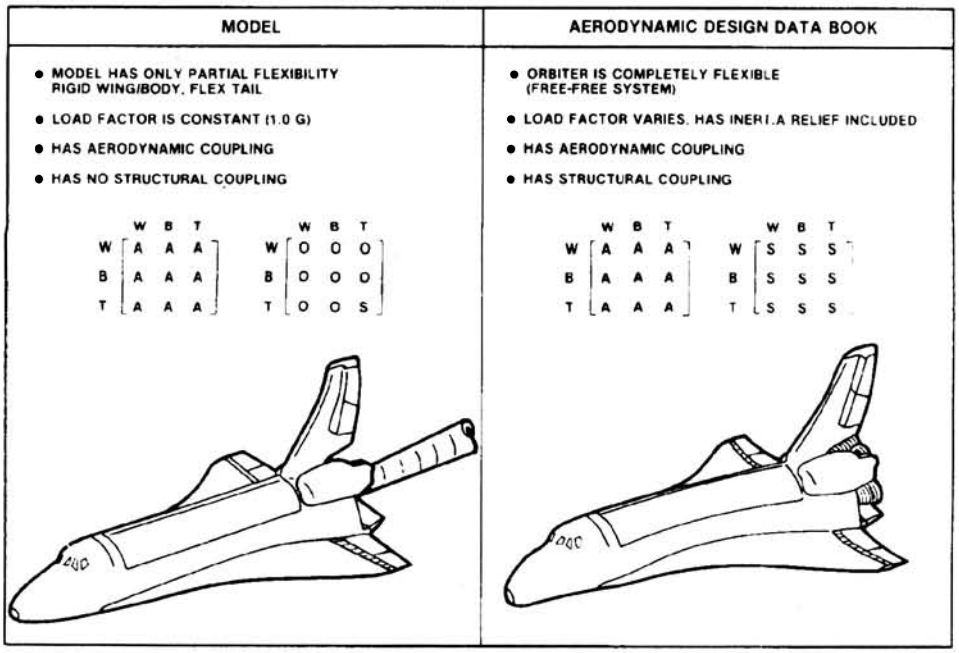

Figure 14.- Differences between model and orbiter.

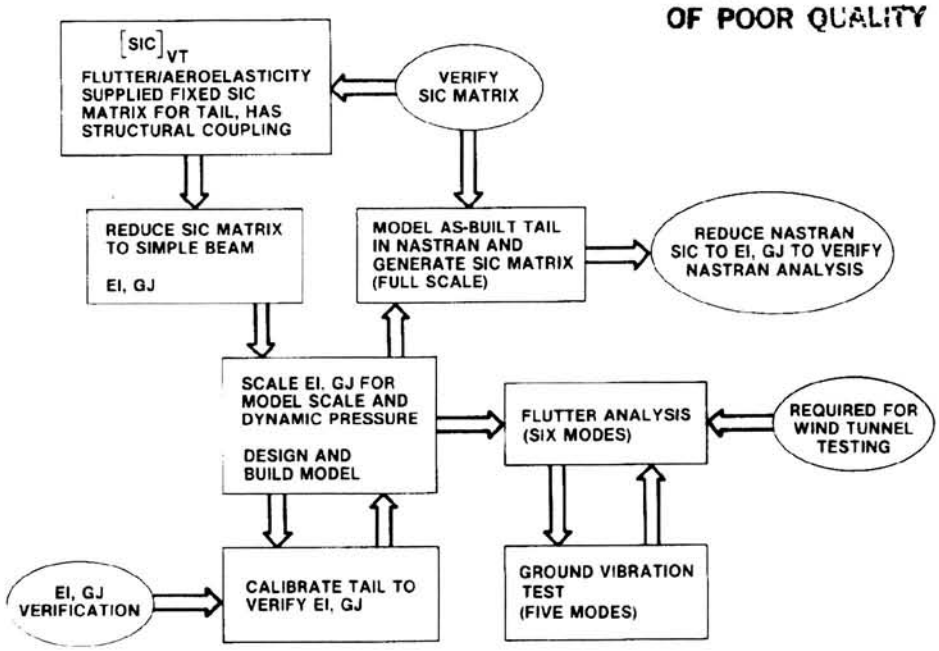

Figure 15.- Model design process and verification.

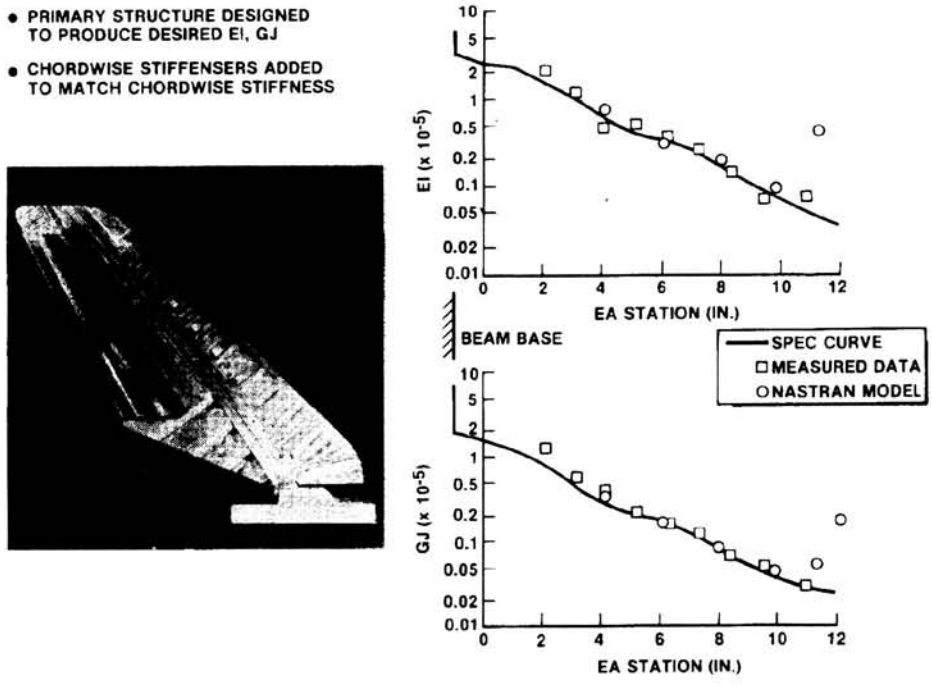

Figure 16.- Model design verification.

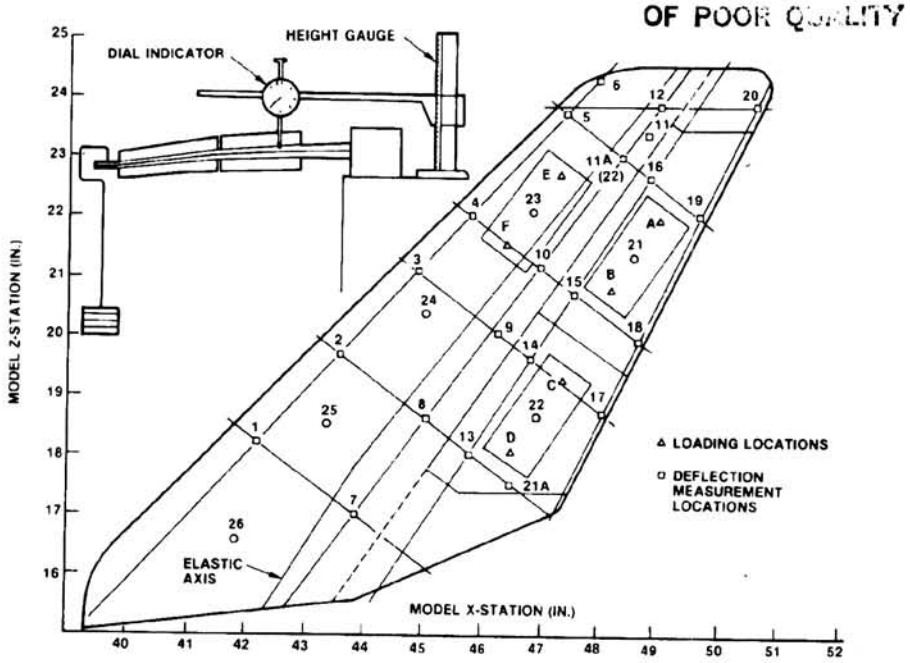

Figure 17.- Distributed loading locations.

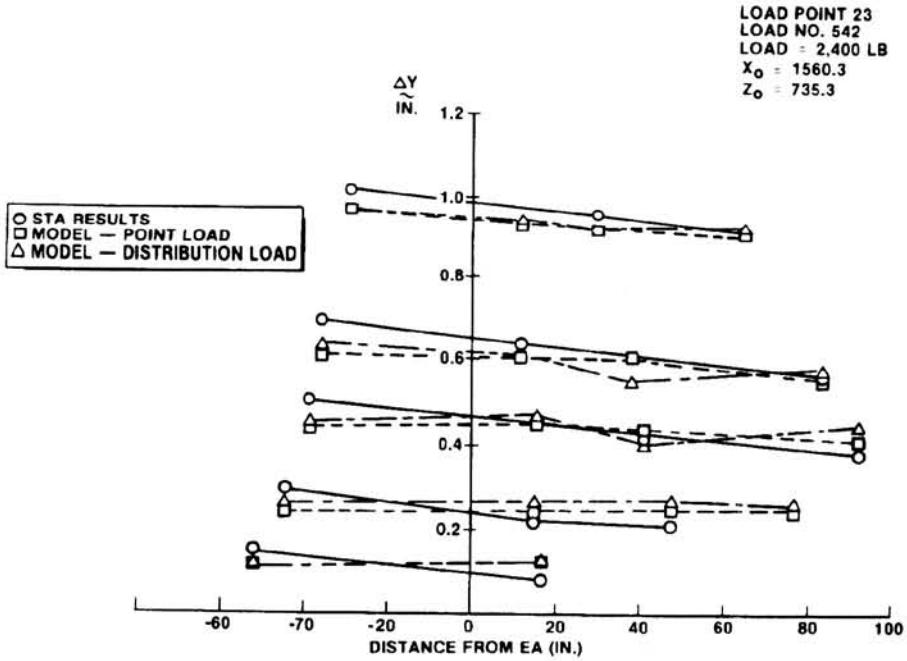

Figure 18.- Deflections caused by loading point 23.

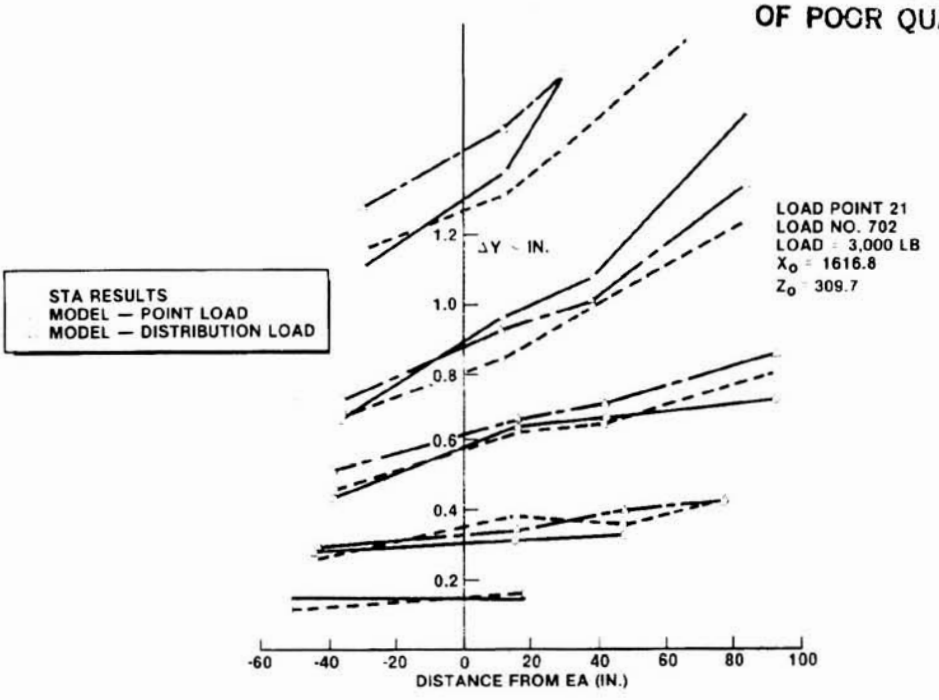

Figure 19.- Deflections caused by loading point 21.

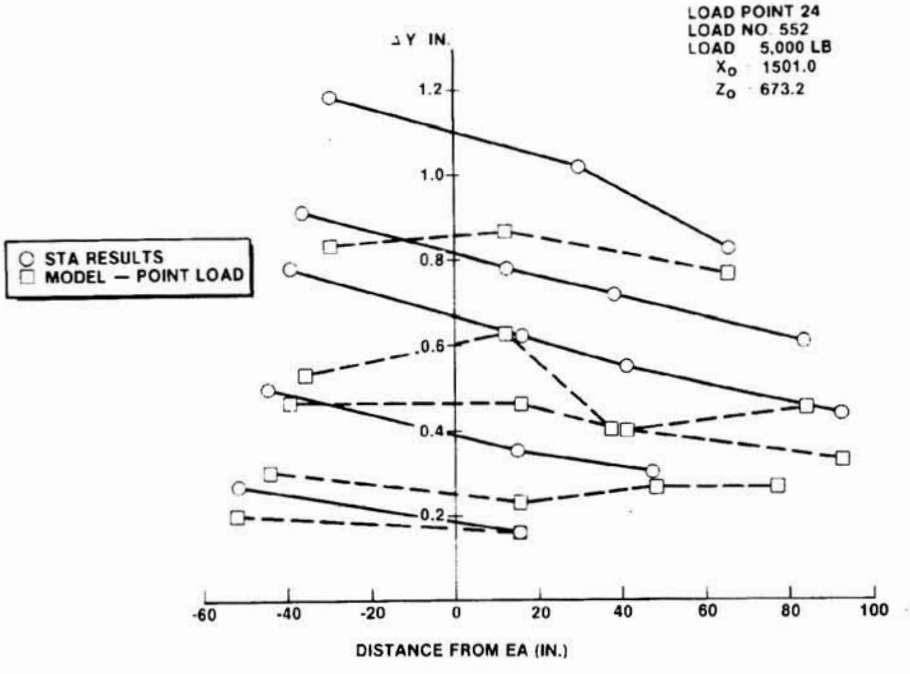

Figure 20.- Deflections caused by loading point 24.

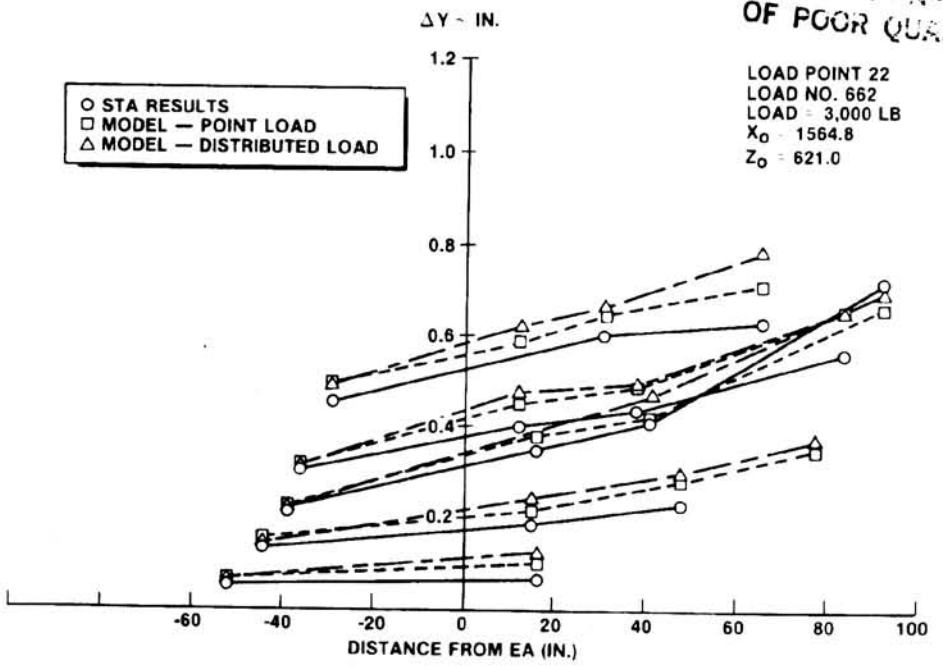

Figure 21.- Deflections caused by loading point 22.

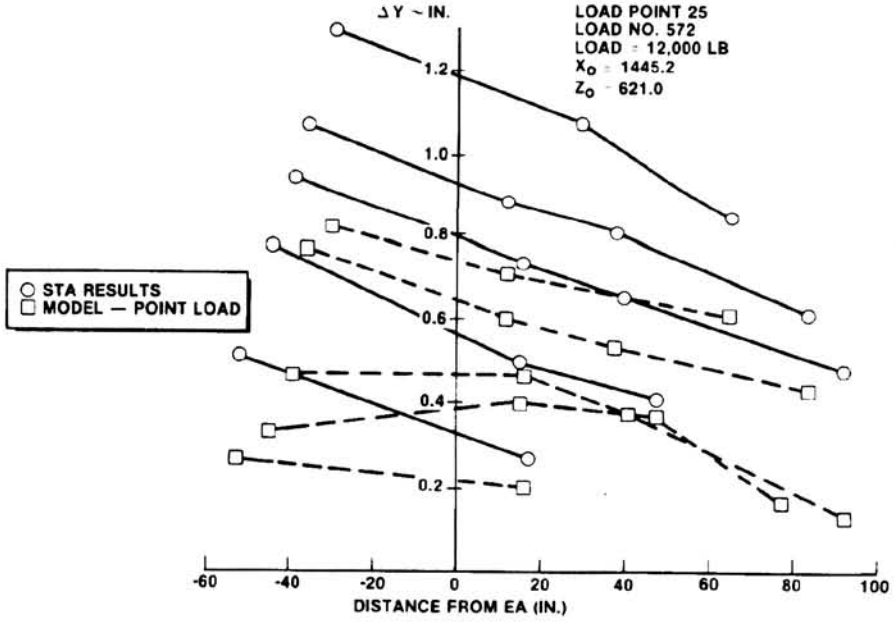

Figure 22.- Deflections caused by loading point 25.

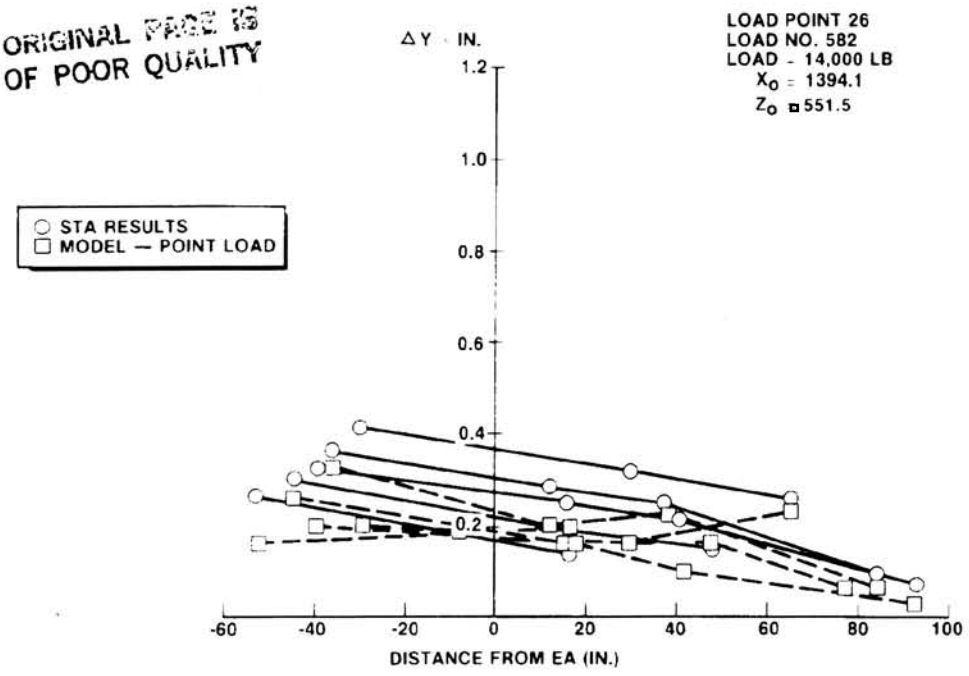

Figure 23.- Deflections caused by loading point 26.

TEST NO.	OBJECTIVE	FACILITY	DOCUMENTATION
OA-126A	AEROELASTIC STABILITY & CONTROL	ARC 11 FT	DMS-DR-2424
OA-126B	AEROELASTIC STABILITY & CONTROL	ARC 9x7 FT	DMS-DR-2424
OA-126C	AEROELASTIC STABILITY & CONTROL	ARC 8x7 FT	DMS-DR-2447
OA-129	AEROELASTIC STABILITY & CONTROL	AEDC 16T	DMS-DR-2434
OA-400	AEROELASTIC STABILITY & CONTROL	ARC 11 FT	DMS-DR-2482

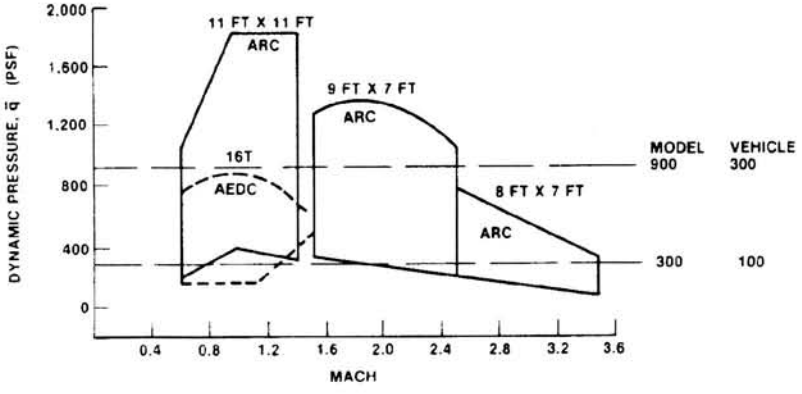

Figure 24.- Flexible tail wind tunnel test program.

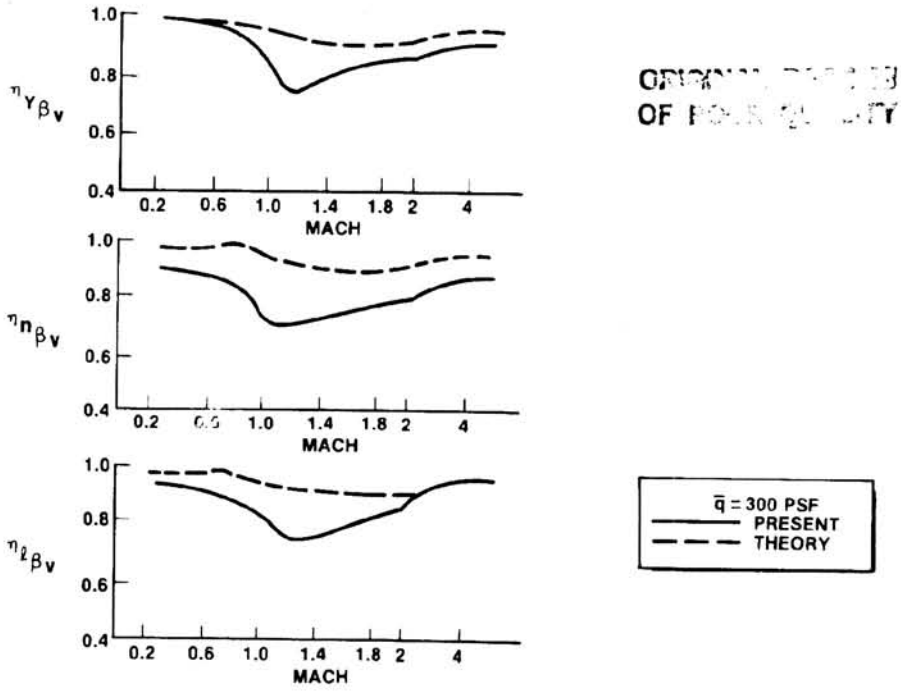

Figure 25.- Comparison of aeroelastic methods on vertical tail component sideslip.

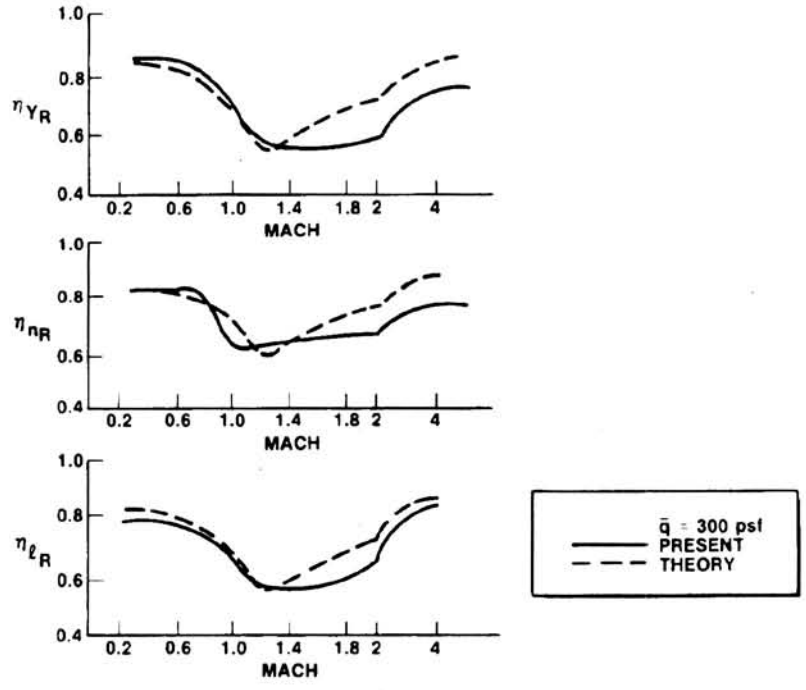

Figure 26.- Comparison of aeroelastic methods on rudder derivatives.

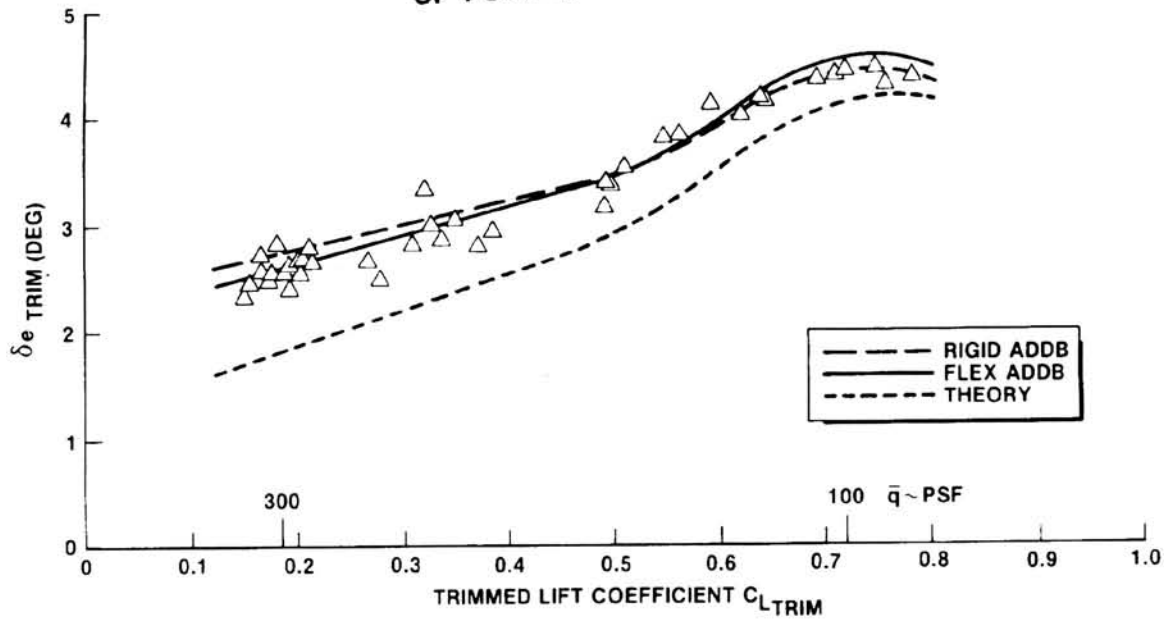

Figure 27.- ALT longitudinal trim characteristics.

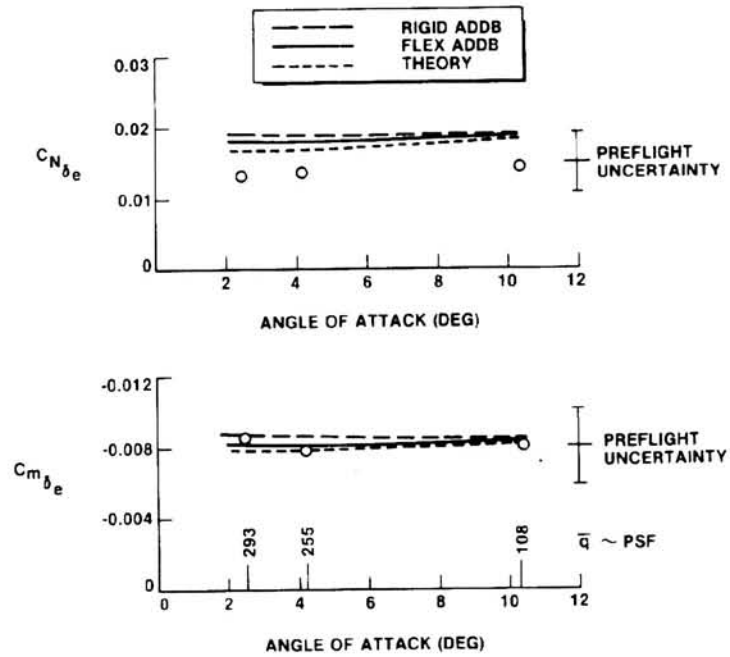

Figure 28.- ALT elevon effectiveness.

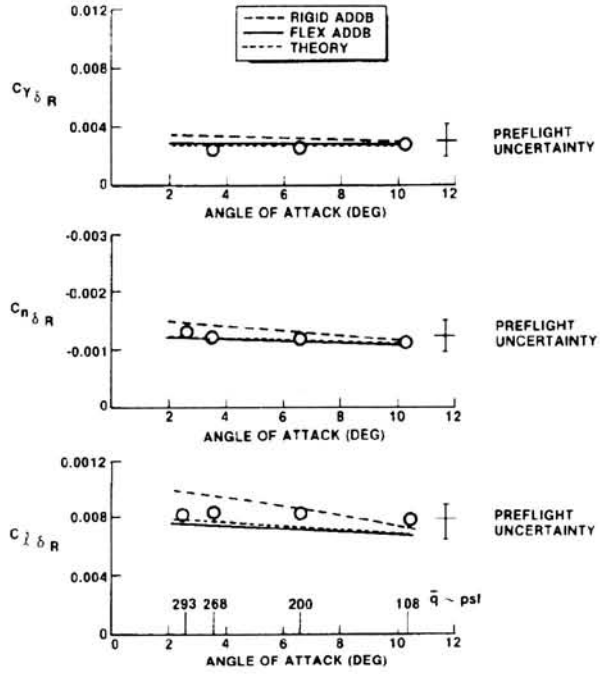

Figure 31.- ALT rudder stability derivative results.

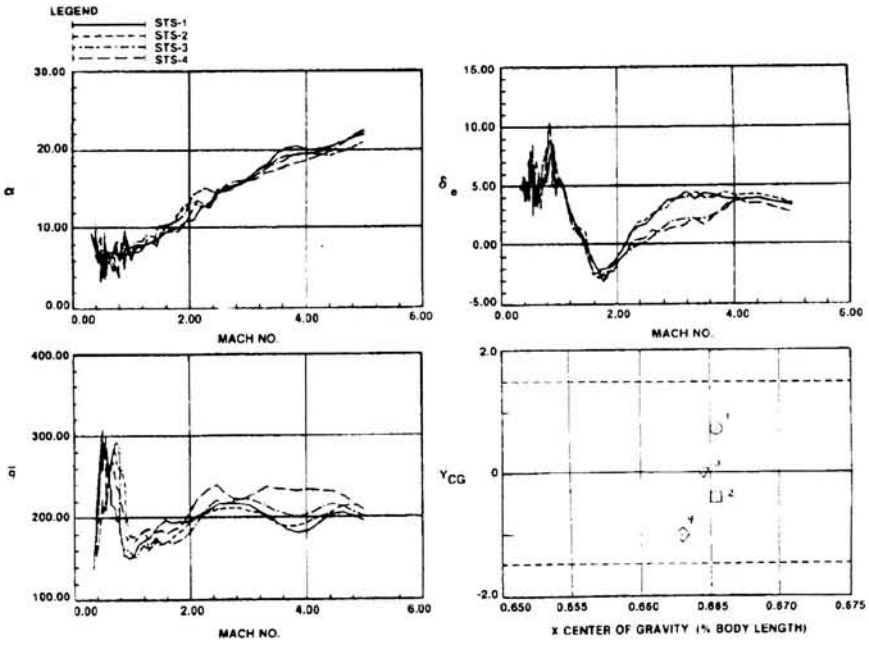

Figure 32.- STS-1 through STS-4 trajectory parameters.

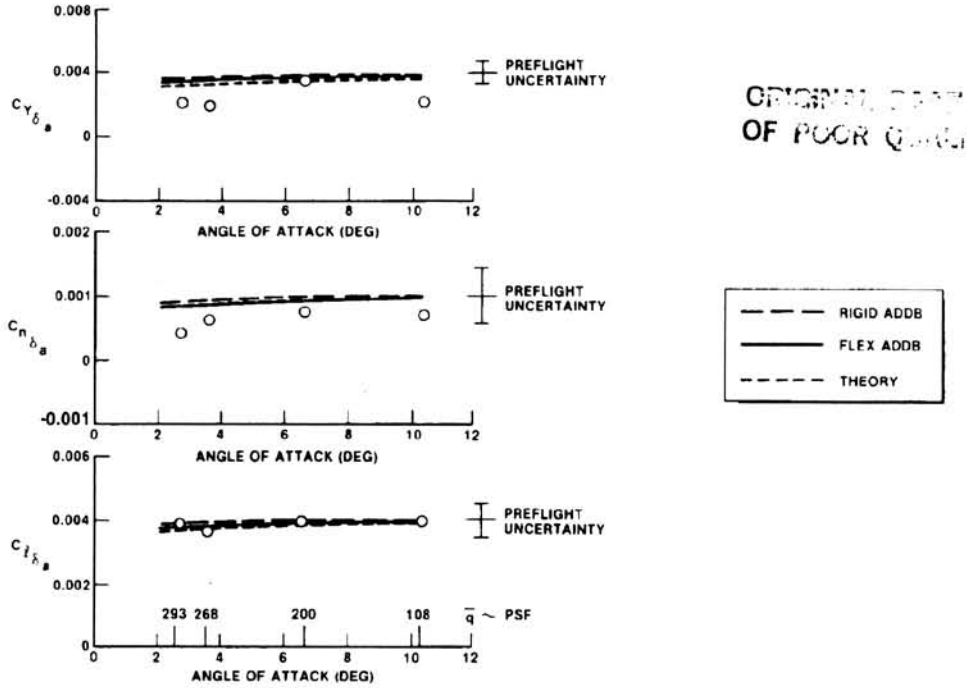

Figure 29.- ALT aileron stability derivative results.

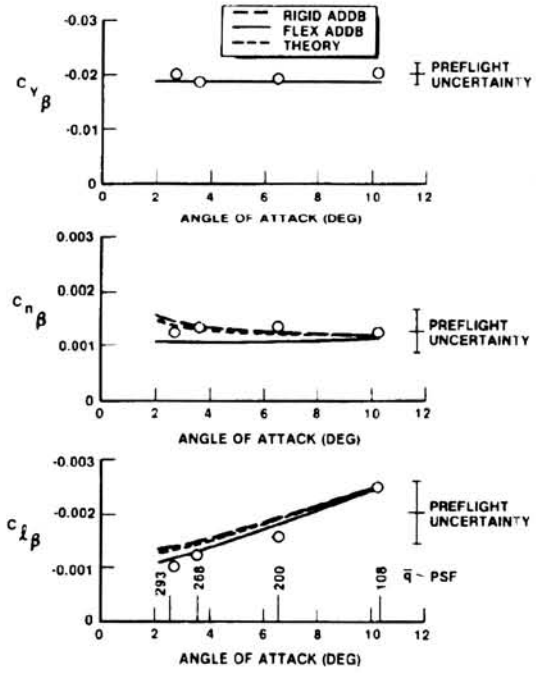

Figure 30.- ALT sideslip stability derivative results.

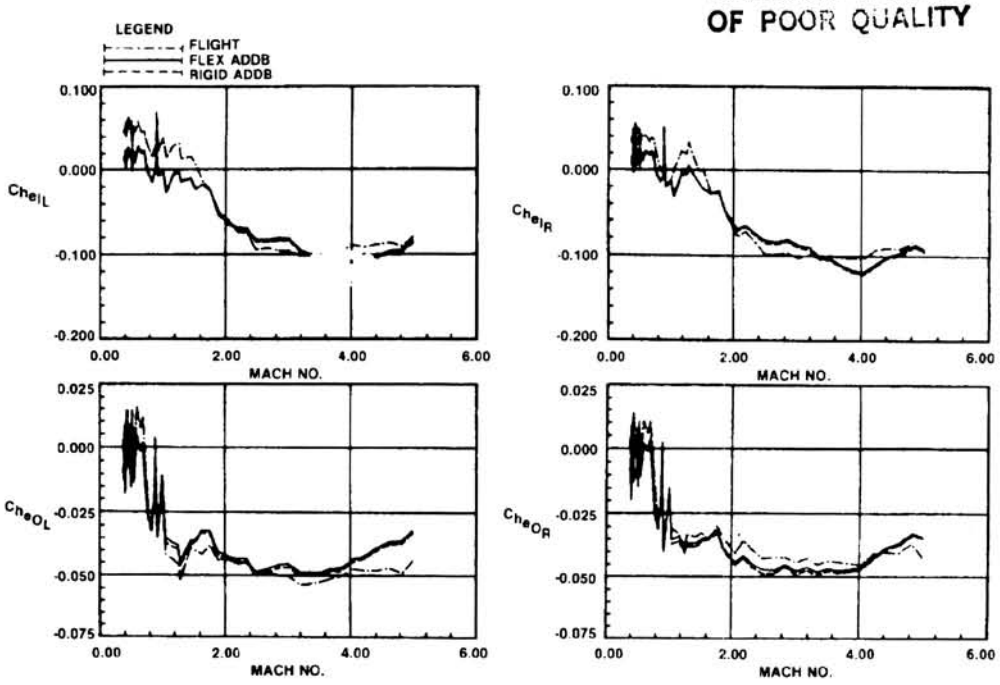

Figure 33.- STS-2 elevon hinge moments (flight versus predicted).

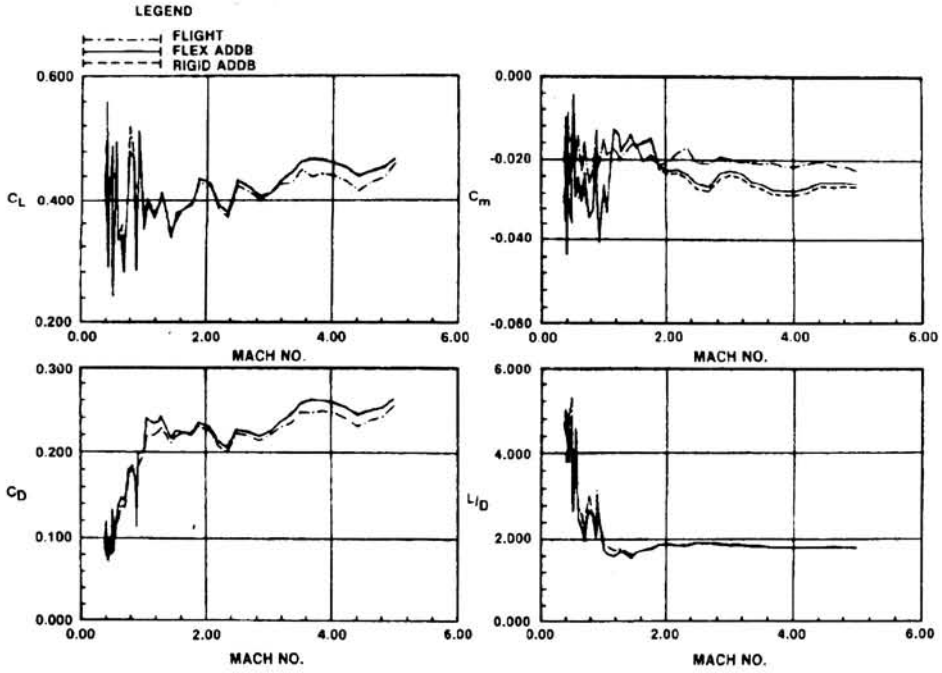

Figure 34.- STS-2 longitudinal aerodynamics (flight versus predicted).

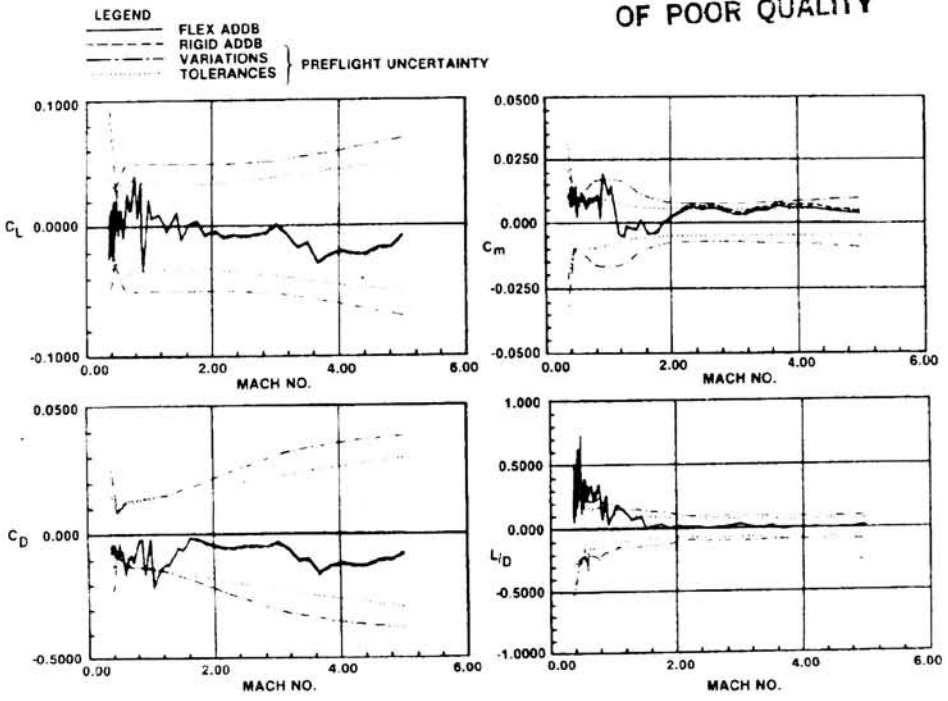

Figure 35.- STS-2 longitudinal aerodynamics (flight minus predicted).

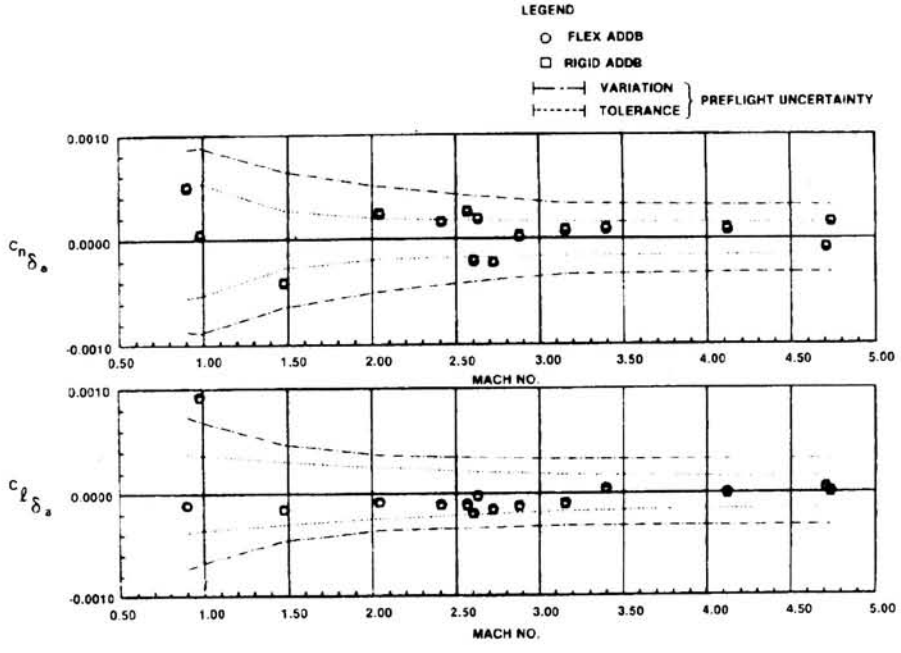

Figure 36.- Flight minus predicted aileron derivatives.

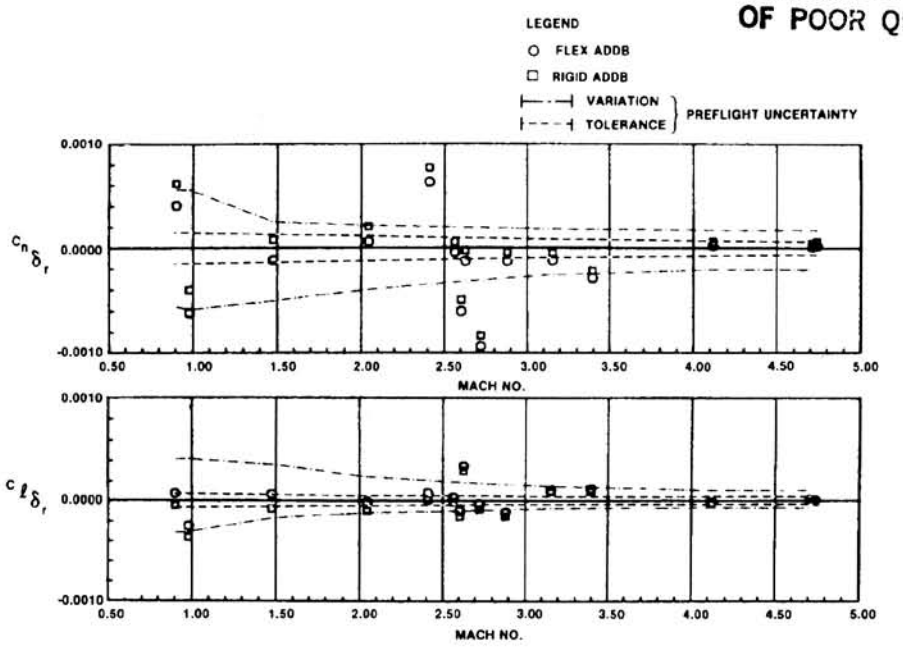

Figure 37.- Flight minus predicted rudder derivatives.

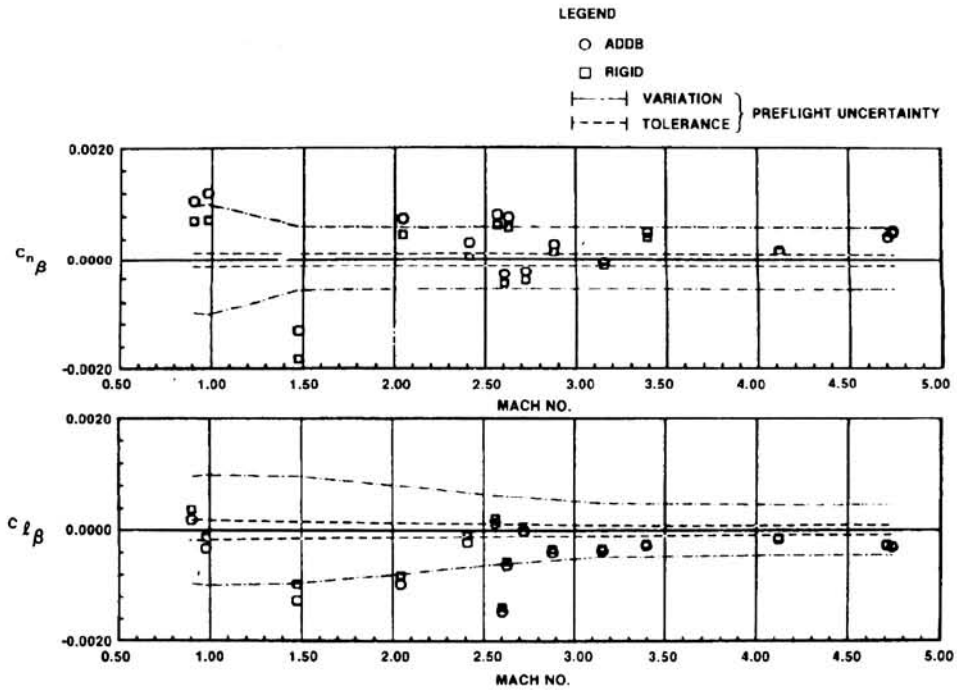

Figure 38.- Flight minus predicted sideslip derivatives.

MINIMUM TESTING OF THE SPACE SHUTTLE ORBITER FOR STABILITY AND CONTROL DERIVATIVES

Douglas R. Cooke
Lyndon B. Johnson Space Center
Houston, TX

SUMMARY

A unique approach has been developed for stability and control derivative testing of the Space Shuttle orbiter during entry. Shuttle Program requirements have necessitated a minimum of testing. Therefore, flight tests concentrate on potential control problem areas predicted from wind tunnel data as well as anomalies discovered during flight testing. The object is to use the test data to remove center of gravity (cg), angle of attack, and elevon placards which are a function of these potential control problems. To ensure successful aerodynamic extraction from a minimum of testing, the following special measures have been taken. Exact maneuvers are designed pre-flight on Shuttle simulators. These maneuvers are duplicated and implemented during the flight by onboard software. An onboard instrumentation system was designed especially for aerodynamic parameter identification. State-of-the-art techniques are used in extracting aerodynamics. The 17 flight test schedule is designed for a minimum number of maneuvers to provide stability and control data over the Shuttle operational ranges of expected angles of attack, elevon deflection, and cg location. Where differences between wind tunnel and flight data occur, aerodynamic coefficient deltas are provided to simulators, which verify the safety of upcoming flights. The status of this test plan and results from accomplished testing are presented in this paper.

NOMENCLATURE

A	Amplitude, deg/sec or g's
An	Normal acceleration, g's
Ax	Axial acceleration, g's
Ay	Lateral acceleration, g's
C_{ℓ_β}	Coefficient of roll due to sideslip, per deg
$C_{\ell_{\delta_a}}$	Coefficient of roll due to aileron deflection, per deg
$C_{\ell_{\delta_r}}$	Coefficient of roll due to rudder deflection, per deg

C_{n_β}	Coefficient of yaw due to sideslip, per deg
$C_{n_{\delta_a}}$	Coefficient of yaw due to aileron deflection, per deg
$C_{n_{\delta_r}}$	Coefficient of yaw due to rudder deflection, per deg
$C_{n_{\delta_e}}$	Coefficient of normal force due to elevon deflection, per deg
C_m	Pitching moment
C_{m_o}	Pitching moment at zero angle of attack
$C_{m_{\delta_{BF}}}$	Coefficient of pitching moment due to bodyflap deflection, per deg
$C_{m_{\delta_e}}$	Coefficient of pitching moment due to elevon deflection, per deg
C_{m_α}	Coefficient of pitching moment due to angle of attack, per deg
C_{Y_β}	Coefficient of side force due to sideslip, per deg
$C_{Y_{\delta_a}}$	Coefficient of side force due to aileron deflection, per deg
$C_{Y_{\delta_r}}$	Coefficient of side force due to rudder deflection, per deg
L_B	Body length, in.
L/D	Lift-to-drag ratio
M	Mach number
T	Time, sec
V	Velocity, ft/sec
X	Body axis axial coordinate, in.
Y	Body axis lateral coordinate, in.
Z	Body axis vertical coordinate, in.
α	Angle of attack, deg
β	Sideslip angle, deg
δ_a	Aileron deflection, deg
δ_{BF}	Bodyflap deflection, deg
δ_e	Elevon deflection, deg
δ_r	Rudder deflection, deg
δ_{SB}	Speedbrake deflection, deg

ACIP	Aerodynamic Coefficient Identification Package
cg	Center of gravity
GPC	General purpose computer
IMU	Inertial Measurement Unit

MMLE3	Modified maximum likelihood estimator, version 3
POPU	Pushover Pullup Maneuver
PTI	Programmed test input
RCS	Reaction control system
STS-1	Space Transportation System, flight one

INTRODUCTION

Stability and control testing of the Space Shuttle is driven by conflicting program desires, while limited by unique problems. Space Shuttle flights are very costly when compared with test flights of other aircraft. There is an intense desire within the program to bring the Shuttle to an operational mode, where payloads can begin to make the Shuttle cost effective. On the other hand it is important to assure the safety of entry flight and to identify the real limitations of the Shuttle through flight testing. This conflict in goals has resulted in the need for a minimum amount of highly productive testing.

Conventional flight test techniques and computer programs have formed the basis for the Shuttle flight test program. Modifications to these techniques have been necessary, however, due to the inherent constraints in Shuttle testing. Measures have been taken to ensure the quality of maneuvers and the data from them, so that the number of repeat maneuvers can be minimized.

The flight test plan developed for the Shuttle contains very few test points when compared to test programs of military aircraft. Enough maneuvers are scheduled only to verify the safety of the Shuttle entry, not enough to build a flight test data base. Where significant differences exist between the flight data and the wind tunnel data base, further test points are scheduled.[1]

The stability and control derivatives are obtained from the onboard sensor data through the MMLE3 parameter identification program.[2] This program was developed at Dryden Flight Research Facility and is a state-of-the-art method of extracting derivatives from flight data. MMLE3 is the latest version of a program which has been used in many test programs for all types of aircraft.

Derivative deltas calculated between flight and values from the Shuttle Aerodynamic Design Data Book are provided to Shuttle simulators to demonstrate the safety of further testing on upcoming flights and to assure the safety of flying cg's associated with planned payloads.[1]

SHUTTLE CONFIGURATION

The Space Shuttle orbiter configuration for entry is shown in figure 1. The orbiter uses a combination of several control devices during entry for both longitudinal and lateral directional control and trim. The full span elevons, of which there are two panels on each side, are deflected together to act as an elevator. The left and right panels are deflected differentially to operate as ailerons. The bodyflap is hinged at the lower aft edge of the fuselage. The elevons and bodyflap work together during entry to perform the trim function. The elevon is scheduled to fly a specific profile in the flight software. The bodyflap trims the vehicle to keep the elevon on schedule. However, the bodyflap moves slowly, and the elevons move off schedule to trim pitch transients and perform longitudinal maneuvers. The combination rudder/speedbrake on the vertical tail has two panels which move together as a rudder. These panels separate to form a speedbrake, which is used as a drag device subsonically. The speedbrake also contributes to longitudinal trim control from Mach .9 to 10.

In addition to control surfaces, the orbiter has a reaction control system (RCS), located in pods on either side of the aft end of the vehicle. These jets contribute to trim and control capability during entry. Four side firing jets on each side are used for yaw control. On each of the two aft pods there are three up- and three down-firing jets, which are used in combinations to provide roll and pitch control.

The control effectors are phased in and out by the flight control system to utilize them where their effectiveness is predictable and significant. Figure 2 illustrates how the flight control system uses the controls during entry.

TEST REQUIREMENTS

Aerodynamic test requirements have arisen from two sources. The original source is the preflight wind tunnel data and the associated uncertainties. The other source of requirements is the flight data from the initial flights, during which anomalies occurred. The types of problems identified involve either potentially excessive RCS fuel usage for longitudinal and lateral trim, or potential loss of control.

Preflight Test Requirements

Preflight wind tunnel data for the orbiter is very extensive and provided sufficient confidence to fly the initial missions under benign conditions and within a limited range of Xcg[3]. From wind tunnel test data, a preflight data base was developed for use in simulators and for design of the entry guidance and flight control

systems.[1] Uncertainties on these data were developed because of wind tunnel to flight differences noted in previous flight test programs on other aircraft. Uncertainties were also assessed for high Mach number, low dynamic pressure flight regimes where wind tunnels were heretofore either unverified or not capable of reproducing flight conditions.

Design specifications require that the orbiter be able to fly safely with a cg range of 65 to 67.5% of the reference body length. Extremes of this range result in the limits of trim capability necessary to operate the vehicle. At the cg extremes, analysis indicates combinations of the uncertainties in pitching moment and the stability and control derivatives result in potential control problems. The problem areas defined from preflight data were the drivers in setting entry flight placards. A summary of these issues is listed in figure 3, items A through E.

From entry interface to a dynamic pressure of 20 lbs per sq ft, uncertainties in basic pitching moment and in pitch jet, bodyflap, and elevon effectiveness indicated a possible problem in longitudinal trim at the cg extremes. Such a trim problem would result in excessive use of RCS fuel by the pitch jets.

From Mach 7 to 4.5, uncertainties in lateral trim and possible reversal in the sign of $C_{n_{\delta_a}}$ could cause excessive use of RCS fuel by the yaw jets. The reversed sign of $C_{n_{\delta_a}}$ is possible where the cg is at the forward limit, causing the elevons to be in the most up position. In this position, the elevons are up out of the predictable flow in the lee of the wings.

The most critical flight control regime occurs between Mach 4.5 to 1.0. The effectiveness of the aileron and jet trim capability continue to be of concern for the forward cg case. In addition, the angle of attack is ramping down, and the vertical tail begins to be exposed to flow past the vehicle. As the tail becomes exposed, uncertainty exists as to where the rudder becomes effective. Worst case combinations of uncertainties in this regime, with a forward cg, can potentially result in a loss of control.

Flight testing is planned between Mach numbers of .9 and .75 due to uncertainties in rudder effectiveness at minimum speedbrake settings. The rudder is aft of the maximum thickness point on the vertical tail, and effects of the flow past the rudder panels become less certain with a closed speedbrake.

Flight Test Requirements from Flight Data

Anomalies in the actual flight data have extended the test requirements as originally conceived. These anomalies have in some

cases accentuated the need for certain data already planned for. Others have pointed to a need for more concentrated investigation of certain flight regimes. A summary of flight anomalies is shown in figure 3, items 1 through 7.

During the initial bank maneuver on flight 1, at a dynamic pressure of 14 lbs per sq ft, a large oscillation occurred in sideslip. Studies have indicated that the primary cause was a missed prediction in roll due to yaw jet firing.[4]

Another flight anomaly is a longitudinal trim difference from what was predicted. This occurs both in the hypersonic regime with a pitch up difference and in the transonic regime, where the difference is a pitch down moment.[4] Because the pitching moment anomaly causes more up (-) elevon trim transonically, the aileron effectiveness data required in this regime has become even more important. The hypersonic anomaly has caused an increased need for longitudinal stability and control data to ascertain the contributions of $C_{m_{\delta_e}}$, $C_{m_{\delta_{BF}}}$, C_{m_α}, and C_{m_o} to this problem. Figure 4 indicates the range of elevon settings required for trim based on attributing the pitching moment difference to C_{m_o} alone.

Causing additional interest in the Mach 2 to 1 regime is an anomaly which has been observed on the first five flights. The anomaly is in the form of an undamped low amplitude roll oscillation, which has a frequency of approximately 1/4 hertz. This problem has not resulted in additional test requirements, since intensive testing is already planned for this regime.[4]

Additional stability and control testing in the hypersonic regime has resulted from flight one data. These data indicated that lateral stability was different than expected. Specifically C_{n_β} was more (+) than expected.[3,5,6] In addition, aileron trim was observed to have an offset between Mach 23 and 12. This offset changed signs, indicating possible flow asymmetries.

Another important anomaly has occurred hypersonically. Above Mach 10, where the elevon schedule has been varied between -1 and +5 on flights 1-4, the flight data indicate that the aileron is more effective than predicted at positive elevon deflections. The data also indicate the effectiveness to be close to nominal at 0^o elevon setting. While this is beneficial for positive deflections, the trend indicates that the aileron may be less effective at negative deflections. This accentuates the need for data which will clarify the dependence of aileron on elevon deflection.

These anomalies have not restricted the flight placards further. However, they have accentuated the need for data in certain flight regimes. They have also caused the planning of further testing in specific areas.

SHUTTLE FLIGHT TEST PROGRAM

The Shuttle test program is the product of significant planning and integration with other program requirements. The flight test requirements from wind tunnel uncertainties and flight anomalies dictated the flight conditions at which maneuvers would be done. Sufficient maneuvers were planned at nominal conditions to indicate repeatability of results. Additional maneuvers were planned over the ranges of elevon and angle of attack that will be seen operationally to check coefficient sensitivities to these parameters. The test plan has been modified to provide additional information in areas where anomalies have occurred. This is necessary to establish an understanding of the anomaly and to develop a database for simulators, in areas where the wind tunnel data is deficient.

The tests planned for each flight are limited by the nature of the Shuttle entry and by other program requirements. Only one maneuver at each flight condition is possible on a given flight, since the Shuttle glides from 400,000 ft in altitude at Mach 25 to touchdown in the span of 30 minutes. The crew has monitoring functions and other tasks during entry that also limit the number of maneuvers that can be performed. This has resulted in a limit of 8 to 10 maneuvers per flight and in a ground rule which requires that maneuvers be spaced to the satisfaction of the flight crew. Another limitation is the amount of RCS fuel available for doing maneuvers. Entry tests must compete in priority with other mission objectives for RCS fuel. This includes on-orbit activities such as rendezvous tests and payload deployment. Other entry tests such as structural flutter tests and aerothermal test maneuvers (POPU) have taken priority over stability and control maneuvers, because instrumentation for these tests was available on flights 1-5 only. When a conflict occurs, guidance maneuvers and guidance phase changes take priority over test maneuvers.

The flight testing has been planned to meet program objectives. The first and most important is to open the cg placards as quickly as possible, to verify the safety of flying planned payloads. In addition, data resulting from tests is scheduled to support planned flight control system changes, which will improve control where in-flight aerodynamic anomalies have occurred.

Sensor Data for Testing

Sensor data used in stability and control analysis is obtained from two basic sources. The primary source of data is the aerodynamic coefficient identification package (ACIP), which is located in the

wing carry-through structure (figure 1). It was designed specifically for aerodynamic data extraction. The other source is the onboard data system, which provides real-time data for the guidance and flight control systems.

Because of the limited test data in the Shuttle test program, it is important to ensure high quality data. The ACIP was designed to provide the most critical extraction parameters with the quality necessary. It contains body axis x, y, and z linear accelerometers, rate gyros, and angular accelerometers. Also routed through the ACIP data handling equipment are position signals from each elevon panel, the rudder, and one yaw jet. All of this sensor data is processed together in the ACIP data handling equipment through matched prefilters and is time tagged. This is done to assure that time skews between the most important extraction parameters do not occur. Another feature of the package is that the data is recorded with high resolution, utilizing a 14 bit system as opposed to an 8 bit system available for other Shuttle data. The sample rate of the data is 173 sample per sec. The sensors chosen for the package were of the highest quality available.

The onboard data system provides the remaining data. The 20 pitch, roll, and yaw jet signals are included. One yaw jet is routed through ACIP so that the signals in the onboard data can be aligned in time. Bodyflap, speedbrake, and air data parameters are also included in the onboard data. The air data probes are not deployed until Mach 3.5, providing angle of attack, dynamic pressure, true airspeed, and Mach number. Before the probes are deployed, air data parameters are calculated from the onboard inertial measurement unit (IMU) data in the General Purpose Computers (GPC) (figure 1). Also calculated from the IMU data are the Euler angles, which are used in data extraction. The data from the onboard instrumentation is of lower resolution and sample rate than that from ACIP. The data is recorded with an 8 bit system. The sample rate of the jet data is 25 hertz. The Euler angles and air data are at 5 hertz.

Stability and Control Maneuvers

Maneuvers for stability and control data have been carefully developed to provide the maximum amount of information possible. It is important in this testing to excite the motion defined by the derivatives in question, so as to identify them from the flight data. Because of the limited testing of the Shuttle and the characteristics of the flight control system, precise maneuver design and execution are very important. Poorly performed maneuvers can be costly to the program in the form of further required testing.

The flight control system of the Shuttle heavily modifies inputs through the stick and is designed to damp oscillations and transients. This design causes difficulty in pulsing a control effector and allowing motion to damp as is done with most aircraft. In pulsing the Shuttle, the control system modifies the stick input with filters, responds to rate and acceleration feedback values, and damps the

response with further surface motion. In general, when the vehicle is pulsed all control effectors available are put into action to quickly damp the vehicle motion. This can cause difficulty in separating out the effectiveness of the various control effectors. It makes it almost impossible to identify damping derivatives.

To overcome this important problem and to provide exact designed inputs, programmed test inputs (PTI) were developed. This type of maneuver is input directly to the flight control system through onboard software. The amplitude and timing are governed by programmed variables to generate a specific input at a predesignated flight condition.

The crew involvement in the maneuvers is almost entirely a monitoring function. The maneuver sequencing is initiated by the crew before the first maneuver, and the software automatically executes the predefined maneuvers within specified windows. These windows are defined by dynamic pressure or Mach number. The software avoids executing maneuvers close to bank reversals and other guidance phase changes. The crew monitors trajectory and trim parameters and important entry flight systems to assure safe maneuver conditions. The crew can quickly stop the maneuver sequence by moving the stick or selecting the control stick steering (CSS) mode. They have full visibility into the testing status through items on their displays.

The inputs are made through the flight control system, and go to an integrator at the point where the surface deflection is commanded. The input is added to the current command. The command, a surface rate, is then processed through a maximum rate limit function. Signals can be sent to the elevon, aileron, rudder, and pitch, yaw, and roll jets. Because of the direct input capability, maneuvers are input in the automatic guidance mode. The input is in the form of a doublet. The doublet commands surface rate in one direction and then the opposite direction providing only a pulse from the control effector. These doublets can be strung together in combinations to provide various inputs from each of the control effectors. There is a capability to define 25 PTI windows, and there are 45 doublets that can be grouped in the windows as desired.

The input from the automatic PTI is not completely free of flight control system interference, but the design does allow for enhanced maneuvers. An example of a maneuver for Mach 5.8 is illustrated in figure 5. The inputs are defined by amplitudes, times, and the effector to be pulsed. The flight control system continues to respond to the motion feedback, but direct input can be made to the control effector. In this example it is possible to make the aileron input while there are no yaw jet firings.

Direct input to the surfaces in a "bare airframe" sense is not possible in the program at present. With the basic lack of stability of the Shuttle, it would not be safe to maneuver the vehicle without an active control system. The automatic PTI design offers the most feasible alternative that is available.

Maneuvers, once designed for the optimum motion for data extraction, are assessed for flight control and guidance safety. Although potential problem areas are approached carefully, care must be taken in maneuvering not to excite an undamped or diverging oscillation. It is also important not to perturb the trajectory so as to disturb the ranging capability during the Shuttle's gliding descent.

Maneuvers are studied extensively for flight control safety. Both off-line and real-time simulators are used to study maneuvers with worst case aerodynamic uncertainty combinations. Maneuver amplitudes are increased to assess safety margins. Loss of RCS jets is also simulated. Flight test aerodynamic results are fed through this same process to ascertain maneuver safety margins with data that is the best possible representation of actual Shuttle characteristics.

Maneuver guidance impacts and entry timeline conflicts are assessed in a similar manner. Simulations are run to determine conflicts between stability and control maneuvers and guidance maneuvers and phase changes. Shuttle pilots assess maneuver conflicts with other important pilot functions. If conflicts arise from these studies, maneuver windows are adjusted or are deleted. In general the short, low amplitude, PTI maneuvers have a negligible impact on guidance capability, but they are studied nonetheless. When combined with other maneuver sequences, guidance impacts can occur. RCS jet fuel budgets for maneuvers are developed during these simulations to provide the pilots with fuel "red lines" that must not be violated, in order to continue initiating maneuvers. Usage of RCS fuel during maneuvers is significant. Loss of vehicle control is possible if the RCS fuel is depleted.

Shuttle Maneuver Test Plan

The maneuvers planned or already flown on each flight are listed in figure 6. The left-hand column lists the flight conditions at which the tests are planned. The other columns are labeled by flight number. Flight one had no planned maneuvers other than bank reversals required for ranging. The first entry was designed to be as benign as possible. Flight 2 had 25 maneuvers, including pitch and roll maneuvers for stability and control data, a pushover pullup maneuver, and bodyflap pulses. Subsequent to STS-2, decisions were made to reduce the number of maneuvers per flight so as to decrease crew workload during entry. As a result fewer maneuvers are shown on flights 3-17. The test program has therefore evolved from an initial 10 flights into a 17-flight program in order to obtain sufficient data. It can be observed in figure 6 that the most concentrated testing is from Mach 6 to .9. This is because it is the most critical regime with respect to potential problems in stability and control.

The test plan for stability and control data is designed to provide sufficient information to remove forward and aft cg constraints. The forward center of gravity travel is limited primarily by aileron characteristics at negative elevon settings. To

verify the aileron characteristics before flying a forward cg, the vehicle trim of a forward cg is simulated by appropriate scheduling of the elevon. Elevon schedules for flights 1-17 are shown in figure 7. Also shown are the locations of the maneuvers from figure 6 along these schedules. The schedules cover the range of expected values for the full range of cg's. These elevon schedules are attained during flight by onboard software programming of the elevon settings. The bodyflap is used to trim the vehicle at the given setting. A backup elevon schedule is also programmed to be more benign, so that it can be switched to if a control problem is anticipated or discovered during the flight. The schedule shown for flight 2 is the most benign schedule and provides the most positive aileron control between Mach 6 to 1. As the flights progress and more data is obtained, the elevons are to be scheduled gradually more up (-) until the most forward cg is simulated on flights 14-17. Hypersonically, the elevon is being trimmed beyond what is required during normal entry for a forward cg (figure 4). This is due to the data already obtained which indicated anomalous aileron effectiveness as a function of elevon position. The settings shown on flights 14 to 17 should shed additional light on this problem and the results can be used to assess certain abort profiles which use more negative elevon positions for trim.

Angle of attack will be varied on a limited number of flights. Figure 8 illustrates the nominal angle of attack profiles to be flown on particular flights. Maneuvers will be executed along these profiles to verify predicted angle-of-attack trends in stability and control parameters. Flights 6, 8, and 12 will be flown with an elevon schedule that has been flown previously so as to vary only one parameter at a time. Flights 14, 16, and 17 will be flown with an elevon setting that represents the trim requirements for a forward cg. The symbols represent where maneuvers will occur along the profile on flights where the profile is off-nominal. Stability derivatives C_{ℓ_β} and C_{n_β} are of particular interest as a function of angle of attack. In addition, an understanding of the possibility of aileron effectiveness being a function of the angle of attack of the elevon is to be studied. This will require deviations in both angle of attack and elevon position for various maneuver test points.

Additional factors in the planning will contribute to the necessary understanding of the stability and control characteristics of the Shuttle. Figure 9 shows speedbrake schedules for the nominal entry, and planned schedules for flights 5 through 17. With these different schedules, rudder sensitivities can be obtained. With the automatic maneuvers beginning on flight 5, a rudder pulse can be input at any point regardless of whether or not the rudder is active in the flight control system. The rudder normally becomes active at Mach 3.5. With this capability, the rudder effectiveness will be tested 1/2 Mach number higher per flight, beginning on flight 5 at Mach 4. To obtain further data on possible aerodynamic asymmetric characteristics of the Shuttle Ycg, offsets are planned through payload placement. Ycg values of .5 to .9 inches have been flown on flights 4 and 5. A Ycg value of 1.5 inches is planned for flights 7

and 11, with the sign of the offset reversing between the two flights. Although POPU maneuvers were planned primarily to obtain aerodynamic performance and aerothermal data, these maneuvers were also a valuable source of additional longitudinal stability and control data. Bodyflap pulses were flown only on STS-2. During these maneuvers the crew manually changed bodyflap trim down (+) to move the elevons up (-). A PTI was then performed. This was to provide early indications of aileron effectiveness with more (-) elevon settings.

FLIGHT DATA ASSESSMENTS

An important product of the flight test program is the confidence that is gained from flight test results in assessing the safety of upcoming flights. Vehicle cg's associated with specific payloads must be shown to be safe. In addition, further testing in the flight test program depends on values of derivatives obtained from previous tests. For instance, it is important to understand as much as possible about stability and control characteristics for down elevon positions, before it is safe to fly with elevons at more negative settings. To accomplish this, fairings are developed for the flight test results and are provided to the Shuttle flight control system community. These fairings or "assessment" values are incorporated into simulators which are used to verify the safety of upcoming flights. Exact maneuvers and trajectory profiles are simulated with correct cg's. In addition, stability analyses are performed using the flight derived aerodynamic data to update cg placards for the vehicle.

STS-1 Through -4 Flight Assessment Values

Flight test results in the form of stability and control derivatives have been output for use in simulators after flights 1, 2, and 4. Some of the most significant of these derivatives are shown in figures 10 to 17. These figures show derivative values for various types of maneuvers from flights 1 to 4. It is important to note that the highest quality maneuvers are the PTI's, which have darkened symbols. In the plots preflight 1 Aerodynamic Design Data Book values (solid line) and the associate uncertainties are drawn.[1] The uncertainty brackets on the derivatives are Cramer Rao bounds, which provide information on the relative accuracy of data extraction between data points.[2] Also drawn on the plots are the STS-2 and -4 assessment values, where they exist. These assessment values are the fairings that have been published from flights 2 and 4 for these derivatives.

For C_{ℓ_β} in figure 10 the assessment values for flight 4 are identical to those for flight 2. Above Mach 10 the flight test values are shown to be significantly more positive than what was predicted. This is of no particular concern, however, to the safety of the

Shuttle through this Mach regime. Below Mach 6 the C_{ℓ_β} fairing is shown to be approximately halfway between nominal and the lower value of the uncertainties. This value of C_{ℓ_β} by itself is not of concern for Shuttle safety of flight.

Aileron effectiveness above Mach 10 is shown for PTI's in figures 11 through 13. These values are plotted as a function of elevon position. Because of the spread of elevon between flights 1 through 4 in this Mach regime (figure 7), a difference in the effect of elevon on aileron effectiveness has been discovered. All the aileron derivatives, $C_{y_{\delta_a}}$, $C_{\ell_{\delta_a}}$, and $C_{n_{\delta_a}}$, indicate increased effectiveness with down elevon deflections. The assessment values for elevon settings above 0° were set to nominal, because of the lack of data. If the trend for positive elevon deflections extends to negative elevon deflections, the aileron may be less effective than predicted. Although this difference between predicted and actual aileron effectiveness has little effect on safety hypersonically, the impact to cg placards could be important if the trend continues at lower Mach numbers. Testing on later flights, where the elevon will be scheduled with more negative settings, will provide the necessary data to determine Shuttle cg impacts. This example points out the importance of obtaining derivative sensitivities to elevon and angle of attack profiles. Between Mach 2 and 1 (figure 14) the flight values of roll due to aileron are shown to be less effective than predicted. In this region the elevon has been above 0° deflection due to overshooting the elevon schedule (figure 7). Because there has been no spread in the elevon deflections on flights 1 to 4, it is not yet possible to attribute this anomaly to effectiveness due to elevon position. Later flights will provide the spread necessary to determine this function.

The most significant updates in stability and control aerodynamics are the assessment values and new uncertainties for yaw jet effectiveness. Figures 15 through 17 show very consistent flight test results for RCS yaw jet effectiveness. After STS-4 sufficient data was available to update nominal values and reduce RCS jet effectiveness uncertainties from early entry through Mach 1, where the yaw jets are turned off. The jets were shown to be more effective than predicted. These results have had a dramatic effect on cg expansion.

Center of Gravity Expansion

The primary goal of the entire data extraction effort is to open cg placards for the Shuttle, so that the full payload carrying capability can be utilized. Through the planned maneuvers, and elevon and angle-of-attack schedules, sufficient data is to be obtained to verify the Shuttle operational safety during entry. The operational limits for cg have been specified to be from 65 to 67.5 percent of the

reference body length. This represents a cg travel of 32.32 inches. It is the goal of the test program to relax cg placards to these operational limits. Figure 18 shows the expansion of the Xcg that has taken place as a result of flight test data from STS-1 through -4. Opening of the aft cg boundary as well as initial opening of the forward boundary is primarily a result of the confidence that has been gained in the knowledge of the basic pitching moment of the vehicle. This information resulted in the known elevon and bodyflap trim requirements shown in figure 4. Pitch jet trim requirements were also determined. The most restrictive boundary is the forward cg limit, because of the critical potential problem areas between Mach 6 and 1. The most significant relaxation of this forward boundary occurred because of the yaw jet flight test results. The more effective jets along with the reduced uncertainties resulted in the change shown in the placard between STS-5 and -6. This has proved the safety of flying payloads planned for STS-7 and -9. Also shown in figure 18 are aft cg flight test limits, which must be honored in order to fly the elevon schedules planned for these flights. Relaxation of the boundary to the full forward limit of 65-percent body length will occur as a result of decreases in other stability and control derivative uncertainties by the end of the flight test program. Optimistically these data will prove that predicted potential control problems do not exist.

CONCLUSIONS

Placards on the Space Shuttle during entry are to be reduced after 17 flights, based on high quality data from carefully designed maneuvers. The maneuvers are planned to verify data base predictions at critical flight conditions and reduce uncertainties in the corresponding aerodynamics. The plan provides for maneuvers at safe centers of gravity while simulating control surface settings for critical cg values. The plan takes into account findings from test data already analyzed. The approach is optimistic and ambitious, but every effort is being made to ensure its success through careful maneuver design, data quality and safety analyses. The experience gained and techniques employed in the Shuttle program are applicable to future flight test planning in programs where testing must be limited due to time constraints or expense.

REFERENCES

1. "Aerodynamic Design Data Book, Orbiter Vehicle 102, Vol. 1," SD72-SH-0060, Vol. 1M, Space Systems Group, Rockwell International, November 1980.

2. Maine, Richard E.; and Iliff, Kenneth W.: User's Manual for MMLE3, a General FORTRAN Program for Maximum Likelihood Parameter Estimation. NASA TP-1563, 1980.

3. Underwood, Jimmy M.; and Cooke, Douglas R.: A Preliminary Correlation of the Orbiter Stability and Control Aerodynamics from the First Two Space Shuttle Flights (STS-1 and -2) with Preflight Predictions. AIAA Paper 82-0564, March 1982.

4. Cooke, Douglas R.: Space Shuttle Stability and Control Test Plan. AIAA Paper 82-1315, August 1982.

5. Iliff, Kenneth W.; Maine, Richard E.; and Cooke, Douglas R.: Selected Stability and Control Derivatives from the First Space Shuttle Entry. AIAA Paper 81-2451, November 1981.

6. "Evaluation of the Space Shuttle Orbiter First Flight Descent Phase," AFFTC-TR-81-21, Office of Advanced Manned Vehicles, Air Force Flight Test Center, July 1981.

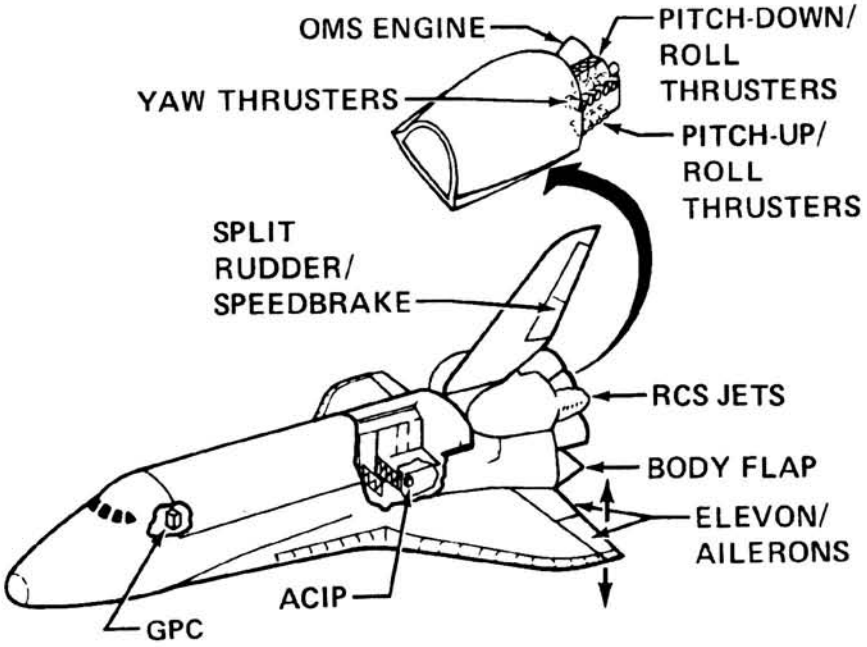

Figure 1.- Shuttle configuration.

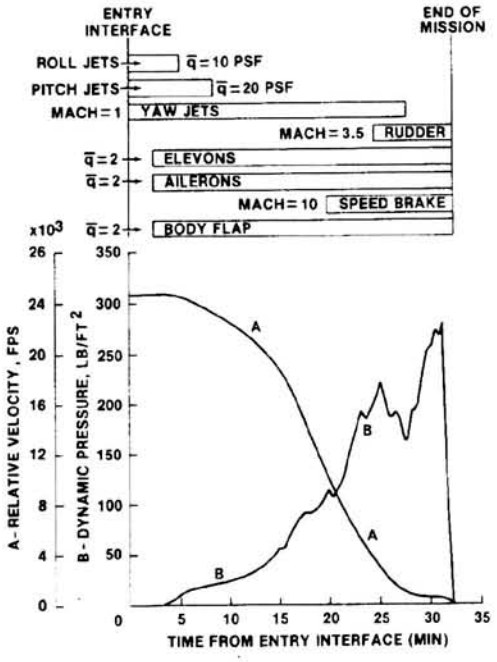

Figure 2.- Control effector phasing.

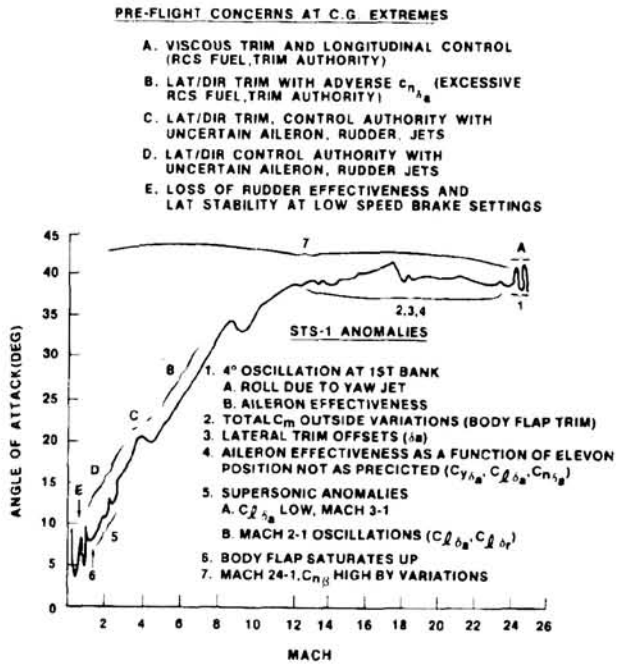

Figure 3.- Preflight test requirements and flight anomalies.

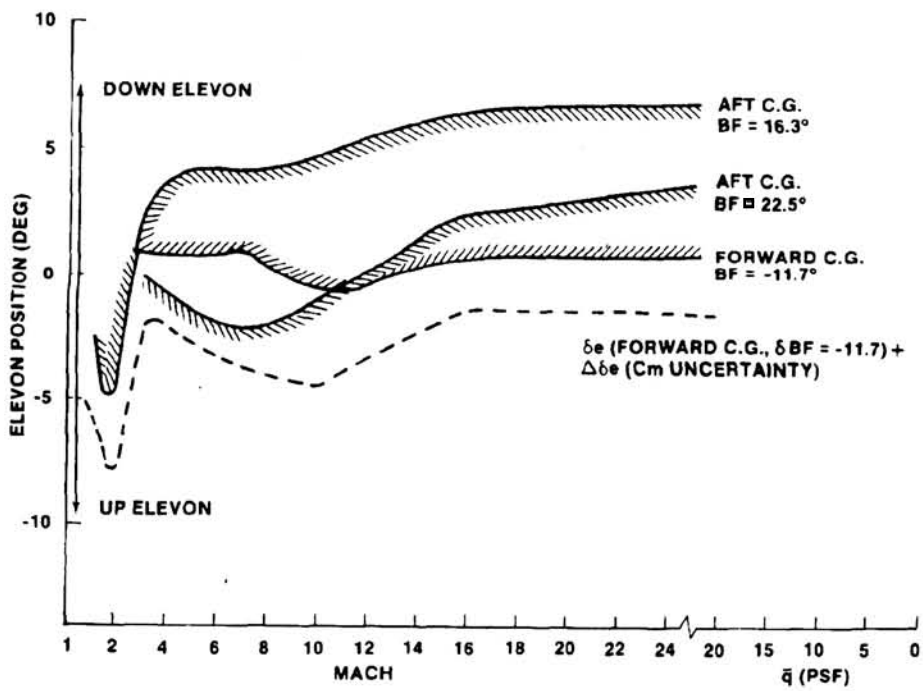

Figure 4.- Elevon trim capability.

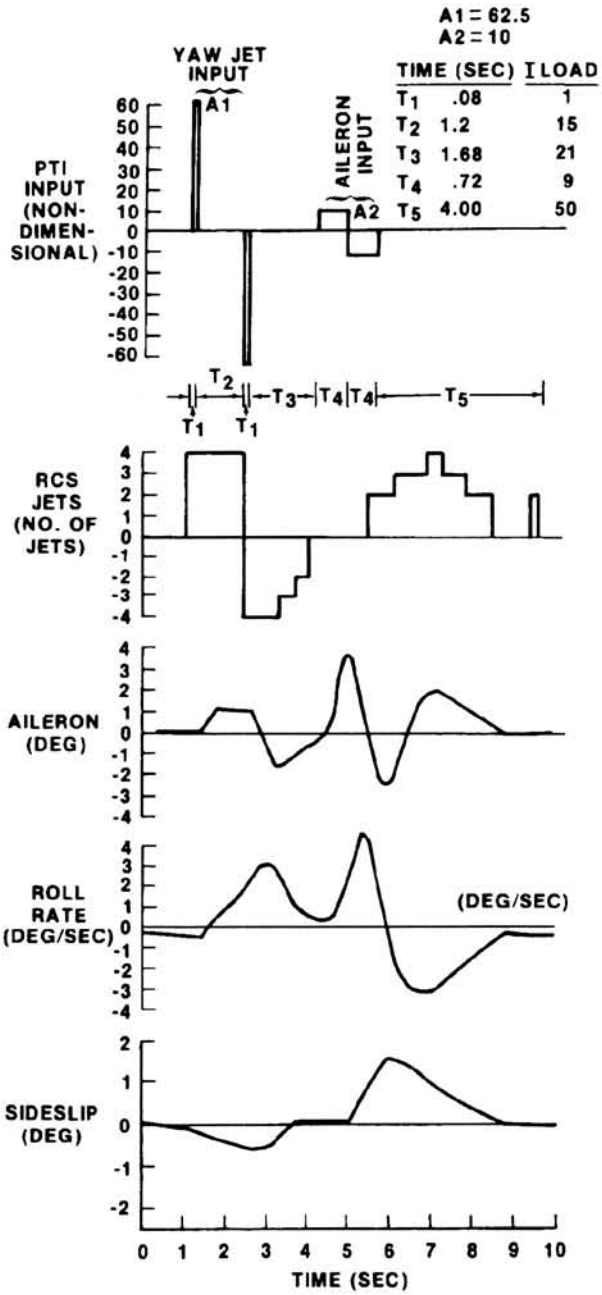

Figure 5.- Automatic PTI capability.

FLT COND \ FLT #	1	2	3	4	5	6	7	8	9	10	11	12	13	14	15	16	17
q = .3		P															
q = 3		P							P								L,P
q = 4		L			L		L										
q = 8		L				L				L,P	L,P					L,P	
q = 10		P															
q = 16		P			P			P		L,P		L,P	L,P		L,P		L,P
q = 18		R															
q = 22		R	L	L	L	L		L	L				L		L		L,P
M = 21.5		P,L,BF POPU	L,P	L,P	L,P		L,P	L,P		L,P	L,P	L,P	L,P	L,P			
M = 18		L,BF	L	L	POPU	L,P	L,P	L,P		L,P	L,P	L,P	L		L,P		L,P
M = 15				L					L,P					L,P			
M = 14		L,BF	L	POPU			L,P			L,P	L	L,P	L,P				L,P
M = 8.4		L	L	POPU		L,P		L,P	L,P	L,P	L	L	L	L	L,P	L	L
M = 5.8		L			L	L	L	L	L		L	L		L	L,P	L	
M = 4.0		L	L		L	L,P		L	L				L	L	L,P	L	
M = 3.2		L		L	L	L	L			L	L	L	L	L	L	L	L
M = 2.2		L	S	S			L,P	L,P	L	L	L	L	L				L
M = 1.6		L		L	L,P	L		L,P	L	L,P	L,P	L		L	L	L	L
M = 1.1		L				L	L		L	L	L		L	L	L	L	
M = .9		L					L,P		L			L		L		L	

P - PITCH MANEUVER
L - LATERAL DIRECTIONAL
BF - BODY FLAP PULSE
POPU - PUSHOVER - PULLUP

S - STRUCTURAL PTI
✗ - MANEUVER NOT EXECUTED

Figure 6.- Maneuver test plan.

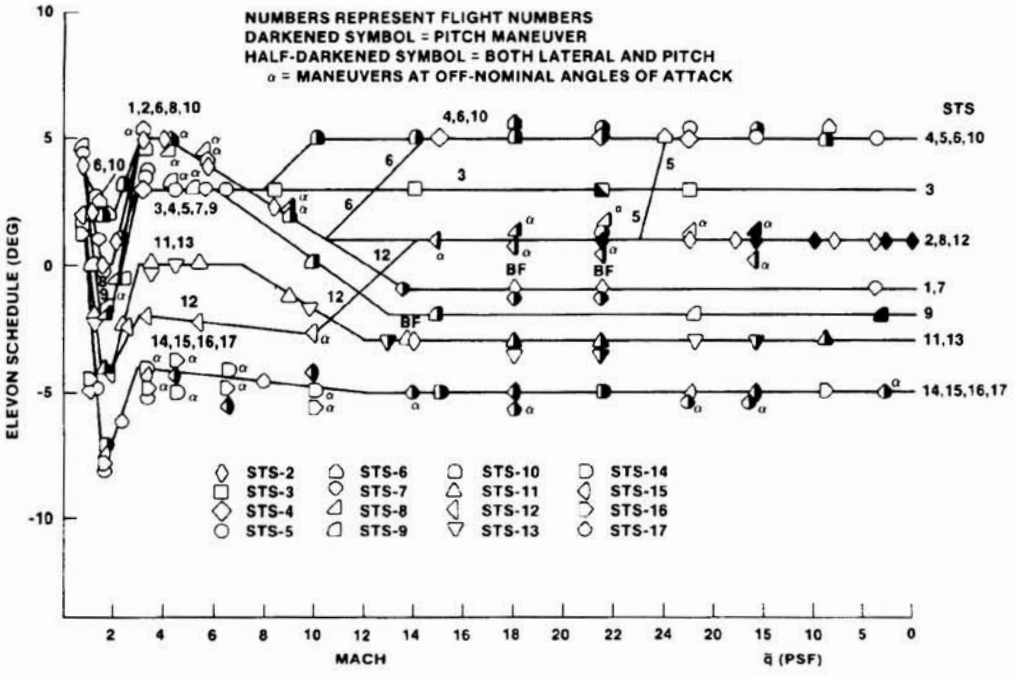

Figure 7.- Flight test elevon profiles.

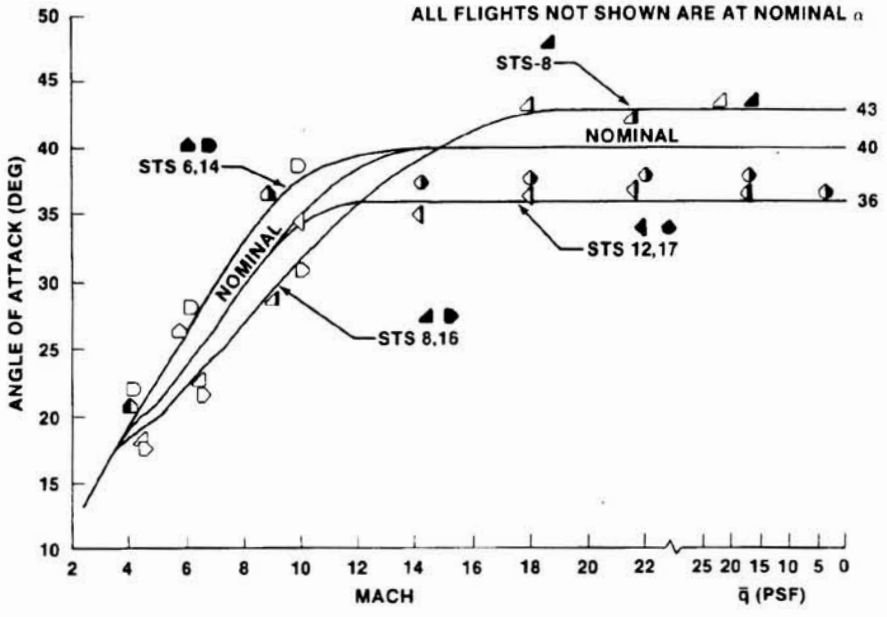

Figure 8.- Flight test angle-of-attack profiles.

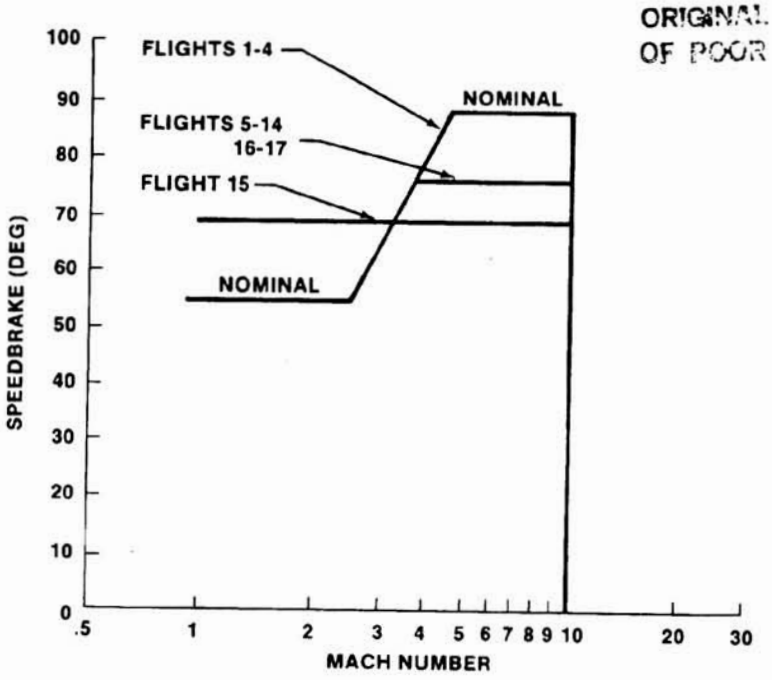

Figure 9.- Speedbrake schedule for testing.

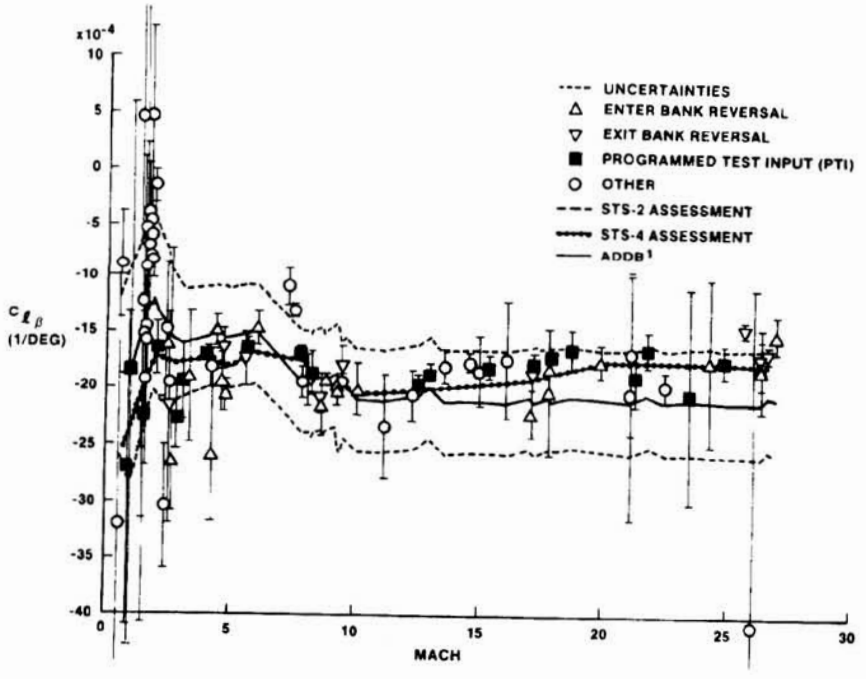

Figure 10.- C_{ℓ_β}, STS 1-4.

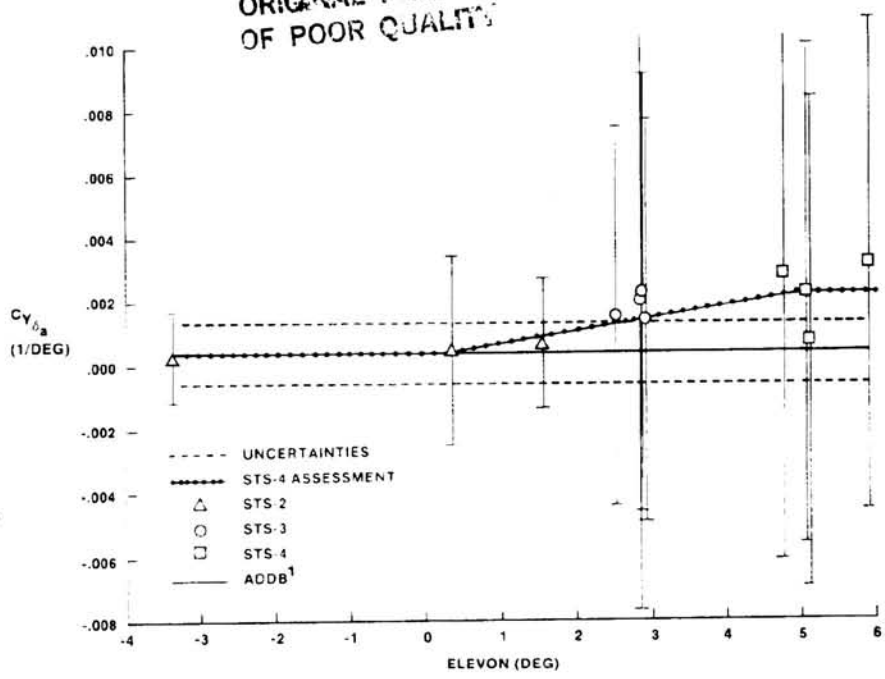

Figure 11.- $C_{Y_{\delta_a}}$ as a function of elevon position for M > 10, STS 1-4.

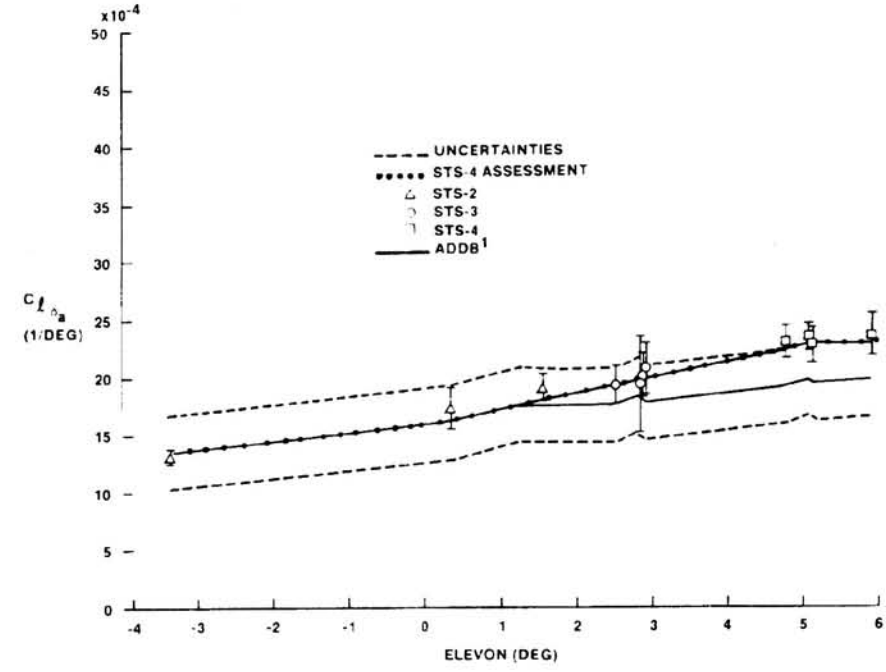

Figure 12.- $C_{\ell_{\delta_a}}$ as a function of elevon position for M > 10, STS 1-4.

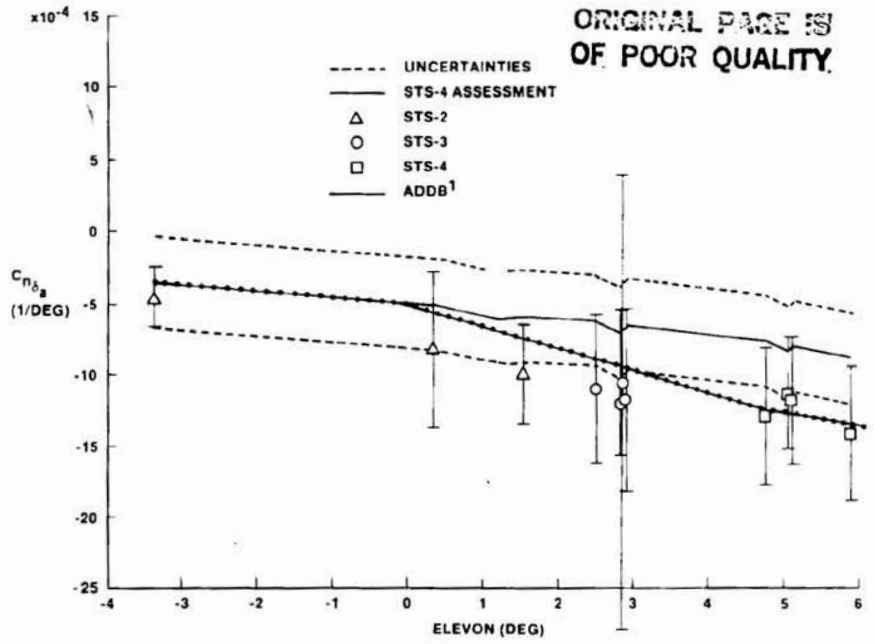

Figure 13.- $C_{n_{\delta_a}}$ as a function of elevon position for M > 10, STS 1-4.

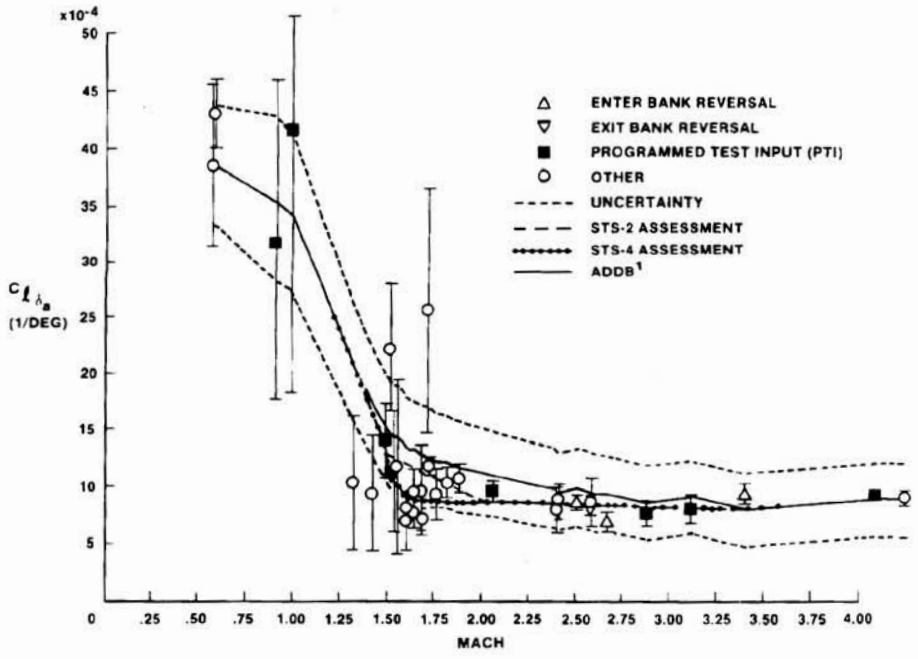

Figure 14.- Rolling moment due to aileron, STS 1-4.

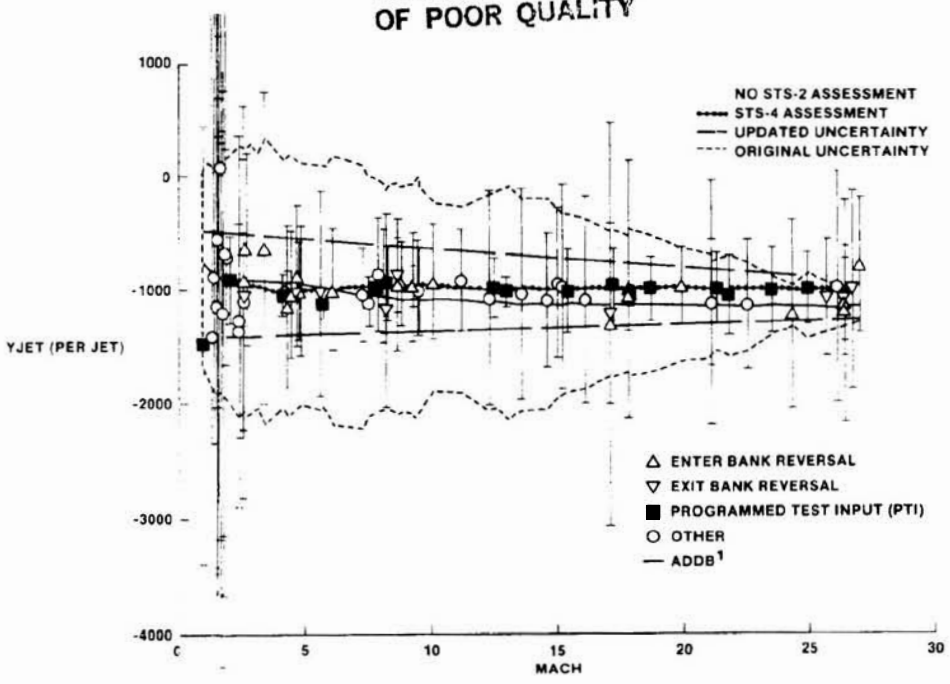

Figure 15.- Side force due to yaw jets, STS 1-4.

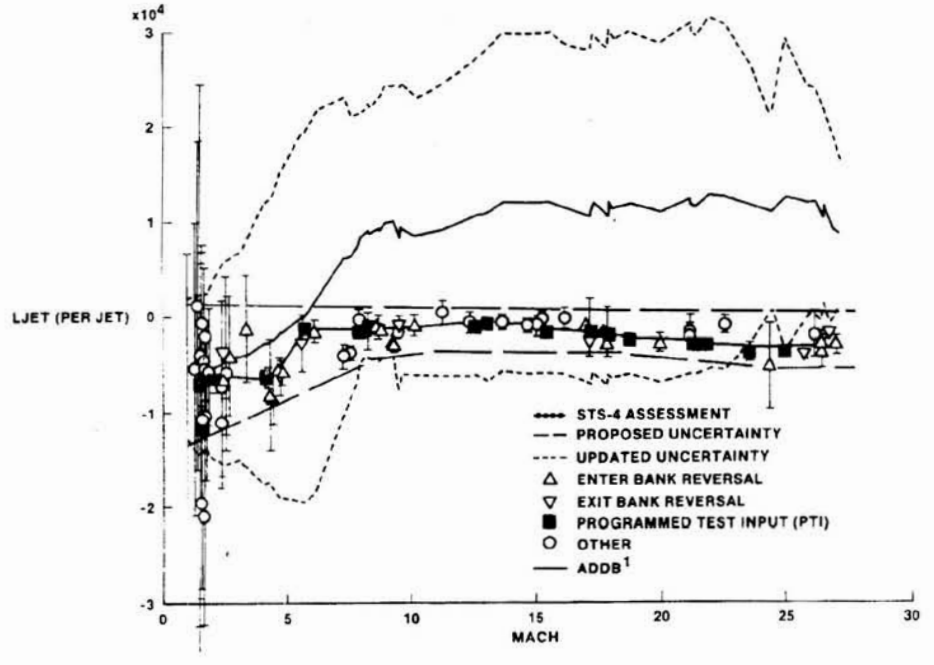

Figure 16.- Rolling moment due to yaw jets, STS 1-4.

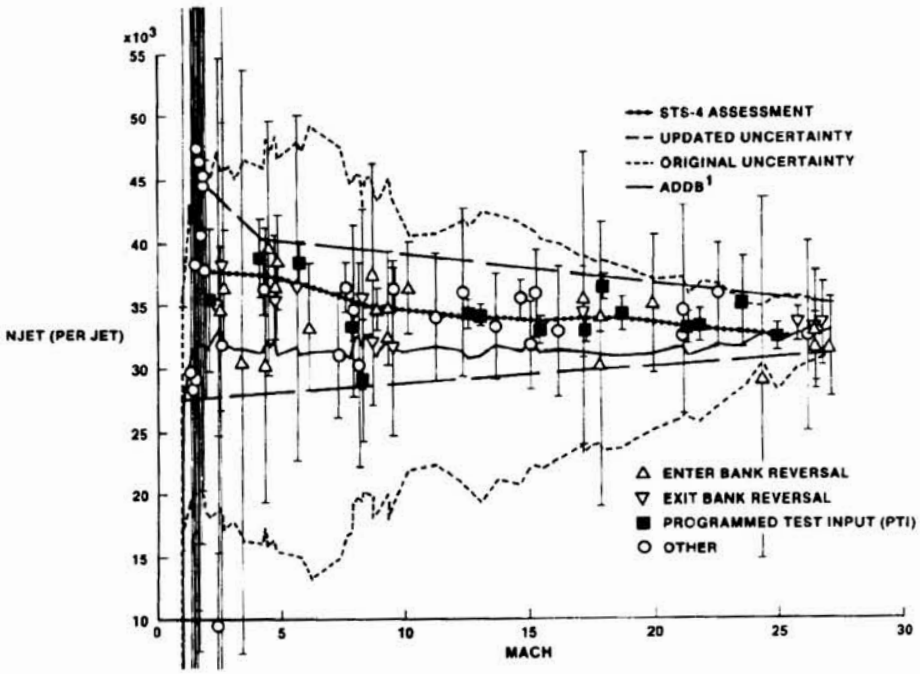

Figure 17.- Yawing moment due to yaw jets, STS 1-4.

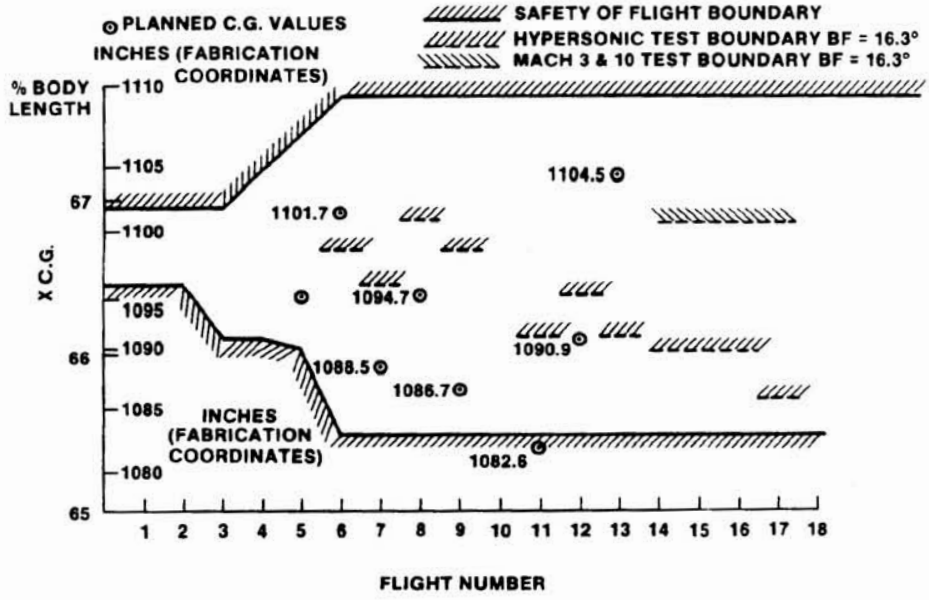

Figure 18.- Shuttle center of gravity placards (M = 3.5).

D20

STABILITY AND CONTROL OVER THE SUPERSONIC AND HYPERSONIC SPEED RANGE

Harold R. Compton, James R. Schiess, William T. Suit,
William I. Scallion, and JoAnn W. Hudgins
NASA Langley Research Center
Hampton, Virginia

SUMMARY

The performance and aerodynamic characteristics of the Space Shuttle Columbia are analyzed over the speed range from Mach 2 to 26 using flight data taken from the first five Space Transportation System (STS) flights. These data are used to reconstruct the entry trajectory, calculate vehicle performance, and estimate lateral stability and control derivatives including those associated with the onboard Reaction Control System (RCS). The trajectory reconstruction process is discussed in its relationship to the determination of the vehicle flight characteristics. Vehicle performance results are presented which show that lift and drag were generally overpredicted by 3 percent and that the lift-to-drag ratio was underpredicted by 1 percent. Anomalies in pitching-moment trim characteristics are shown and noted to be due to real-gas and Mach-number effects. Lateral stability and control derivatives estimated using programmed test input maneuvers are correlated with preflight predictions and are usually within the uncertainties associated with the predictions. The lateral reaction-control system effectiveness is evaluated. In terms of side force and yawing moment, the lateral side firing (yaw) jets are virtually 100 percent effective. However, the rolling moment due to yaw jet firings is significantly different from what had been predicted due to jet plume interaction effects.

INTRODUCTION

The five flight STS test plan was recently concluded with the safe entry and recovery of the Space Shuttle Columbia from its fifth flight. Each of these flights was unique in that it met specific requirements of the integrated test plan for expanding the STS flight envelope in terms of aerodynamics and aerothermodynamics. They were also unique as an ensemble in that they offered repeated opportunities for aerodynamic and aerothermodynamic research related to a full-scale winged vehicle moving through a real environment over the entire flow regime from free-molecule through transition to the hypersonic continuum and then to subsonic flow. Thus it follows naturally that the Space Systems Division (SSD) at the Langley Research Center (LaRC) was extremely interested in these opportunities because of the long-time engagement of SSD in research that centers around applications to future space transportation systems. Hence, members of SSD with specific expertise support from other research divisions have analyzed and are continuing to analyze flight data from the ensemble of flights in support of ongoing aerodynamic and

aerothermodynamic research related to future space transportation systems. Only the research activity related to aerodynamics will be discussed in this paper. This activity is proceeding, with a few minor modifications, as planned (refs. 1, 2, and 3) prior to the first test flight. The proposed methods and techniques have made maximum use of onboard measurement data and have proven extremely flexible in the use of alternative data sources in cases of data loss for an entire flight or data dropouts during down-link telemetry. Generally, the onboard measurement systems have functioned very well except for some disappointing losses of Development Flight Instrumentation (DFI) pressure data on STS-1, 2, and 4.

The purpose of this paper is to present recent results from analyses of STS-4 and 5 flight data and to summarize overall results from the five flights. Detailed results from STS-1, 2, and 3 have been previously presented (ref. 4, 5) and are discussed in this paper only in the context of the overall research objectives. In addition, and in keeping with the theme of the current forum, Shuttle performance and lessons learned will be highlighted in this paper. Specifically, Shuttle trajectory and aerodynamic performance are presented, and flight-extracted lateral stability and control derivatives are compared with preflight predictions of the same quantities. Alternative methods and flight data for extracting some of these derivatives are discussed with the relative merits of each of them being pointed out. The results in this paper should prove useful for applications to future STS programs and for the development of numerical and analytical methods of computational fluid dynamics.

METHOD AND APPROACH

General Discussion

For the most part, two basic approaches have been used to obtain the results presented in this paper. They are generally referred to as deterministic and estimation (statistical) approaches, and they have been discussed in detail in a previous publication (ref. 4). Therefore, only the basic differences are noted here. The deterministic method requires that measured values of vehicle accelerations and rates during entry be combined with corresponding measured values of atmospheric density to make straightforward analytical calculations of vehicle performance in terms of total force and moment coefficients. In the statistical or estimation approach, the measured accelerations and rates are combined with various trajectory parameters and the measured atmosphere in a maximum likelihood estimate to determine stability and control derivatives including those that relate to the reaction control system (RCS). The flight-derived coefficients from either approach are analyzed for flight anomalies and compared with preflight predictions to obtain a measure of how well the vehicle performed. These comparisons also provide a check on wind-tunnel-to-flight-prediction techniques which in turn allows an expansion of the STS flight envelope on a flight-to-flight basis. In addition, the flight-derived results have proven useful for comparison with theory via comparisons with results from various Computational Fluid Dynamic (CFD) codes.

Two basic types of parameters are common to both the deterministic and estimation approaches. They are the measured parameters (accelerations, rates, and atmospheric pressure, density, temperature, and winds) and the trajectory-related parameters such as altitude, velocity, attitude, dynamic pressure, Mach number, etc. The trajectory parameters come from a postflight reconstruction of the entry trajectory, usually referred to as the BET or Best Estimated Trajectory. Each of these two types of parameters is respectively discussed in the following two sections of this paper.

Accelerations and Rates

Onboard measurements of the Shuttle accelerations and rates are fundamental to all of the results presented in this paper and are illustrated in figure 1, which also shows the body axis system used in this paper. There are three possible sources of these measurements from the various Shuttle onboard instruments, each of which has its own merits. The first source, known as the Aerodynamic Coefficient Instrumentation Package (ACIP), measures the three components of linear and angular accelerations and the three components of angular velocity. The triply redundant Inertial Measuring Units (IMU) constitute a second source, and a third source for linear accelerations and angular rates is the Rate Gyro and Accelerometer Assembly (RGA,AA).

The relative merits of each of these sources have been discussed in detail in reference 4. Thus it is sufficient to say that the ACIP has a resolution (1 percent full-scale) and measurement frequency (170 Hz) designed specifically for analyses of Shuttle stability and control. The IMU's are high-fidelity instruments designed for space navigation and have performed extremely well in the intended tasks. They have also been used for postflight reconstruction of the entry trajectory and in some cases for analyses of stability and control. The RGA,AA instruments are an integral part of the flight guidance and control but have been pressed into service for stability and control analyses in lieu of ACIP. However, the RGA,AA does not have a longitudinal (X axis) accelerometer and when used for stability and control work must be augmented by longitudinal accelerations from the IMU.

Examples of the measured accelerations and rates are given in figure 2, which shows the body axis linear accelerations and angular rates from STS-5 as a function of time. Similar information is shown in reference 5 for the previous four flights.

Best Estimated Trajectory (BET)

In order to make either a deterministic or statistical calculation of the flight-derived aerodynamic coefficients and to compare them with preflight predictions, an accurate knowledge of the trajectory air-relative parameters is required. Thus the STS entry trajectory was reconstructed postflight for each of the first five STS flights. The approach chosen for the reconstruction was unique in that prior knowledge of the STS aerodynamics and the entry atmosphere was not required. In fact, this separation of spacecraft dynamics, spacecraft aerodynamics, and the ambient atmosphere afforded the independent assessment of vehicle performance, and stability and control.

The basic reconstruction approach begins with an assumed set of initial conditions and proceeds with an integration of the onboard measurements of acceleration and rates to obtain a trajectory. The trajectory is constrained in an iterative-weighted least-squares process to fit ground-based S-band, C-band, and theodolite tracking data. This produces a planet-relative trajectory which is then melded with measured ambient atmospheric parameters to obtain a final air-relative BET (ref. 6).

Prior to STS-1, it was anticipated that the trajectory reconstruction process would make use of the ACIP measurement data. The strapped-down (body-axis oriented) ACIP, with its high frequency measurement response, seemed a natural choice for Shuttle trajectory reconstruction. Therefore, the Entry Trajectory Estimation (ENTREE) program was formulated for ACIP measurements and the associated error models. This formulation was based on the assumption that the ACIP measurement accuracy would be equivalent to the specified measurement resolution. This was not to be. In fact, the ACIP measurement accuracy specifications turned out to be 1 percent of the full-scale range of the instrument, which was fine for aerodynamic-derivative extraction. However, parametric analyses showed that this accuracy level would not be adequate for Shuttle trajectory reconstruction and thus it became necessary to search for alternative sources for the acceleration and rate measurements. Whatever was chosen had to be usable in the ENTREE program. There was not sufficient time to completely reformulate all software. The IMUs were finally settled upon and preprocessing programs were built which reformatted the inertial output from the IMUs to emulate ACIP measurements (ref. 7). It was also necessary to rework the basic error models to allow the use of IMU data in the strapped-down ENTREE program. This was perhaps the first lesson learned; i.e., anticipation of what was not to be.

As stated earlier, the air-relative trajectory parameters are obtained by combining measured values of the ambient-atmosphere parameters with the planet-relative trajectory. The source of these measurements was generally through the National Oceanographic and Atmospheric Administration (NOAA). They were obtained by NOAA via various types of atmospheric probes (rawinsondes, datasondes, robin spheres, etc.) launched as close as possible to the time of entry and the vehicle-entry ground track. However, the measurements are further analyzed at the LaRC using the Langley Atmospheric Information Retrieval System (LAIRS) program to account for proper spatial, diurnal, and semidiurnal corrections (ref. 8). Included with the NOAA measurements were measured values of wind speed and directions. These measurements were generally good except for regions in the lower altitudes where even small prevailing winds can combine with large gusts to produce large errors in some of the atmosphere-related parameters such as angle of attack and sideslip (ref. 9). In addition, wind speed and direction are usually not stable even for short periods of time, especially at the Shuttle landing site. Thus one can expect considerable variations of the prevailing winds from the time of measurement to landing time. Hence in all cases after each flight, considerable effort was made to insure a BET based on an accurate wind analysis. In fact, wind-estimation techniques were formulated using measurements of α, β, and true air speed, V_T, from the onboard Air Data System (ADS) measurements (ref. 10). These estimates were usually confined to altitudes below 50,000 feet because of limitations on the ADS operations and accuracy, but this included the region for critically accurate knowledge of the winds. At higher altitudes the effect of winds is not so important because the spacecraft

velocity usually is very large compared to wind velocity thus tending to minimize wind perturbations. In any case, the estimated winds are compared with the measured winds and a judicious choice of which to use in the BET is made.

It is estimated that the altitude and velocity at the epoch time is accurate to less than 500.0 feet and 0.5 feet per second. The corresponding accuracies near touchdown are 5.0 feet and 0.2 feet per second. The spacecraft attitude is known to within 0.1 degrees through the entry. Sideslip and angle-of-attack errors are each approximately 0.1 degrees at the higher altitudes, but in the lower altitudes, from approximately 50,000 feet down, could be as large as 0.5 degrees. Again this lower altitude region is where wind uncertainties have the largest effects. The errors quoted in this paragraph are equivalent to one standard deviation, σ.

Generally the nominal-entry flight path and dynamics for each of the five STS flights have been very similar except that STS-3 landed at an alternate landing site in White Sands, New Mexico. They each made a gliding entry from deorbit to touchdown with an entry angle of attack at 400,000 feet of about 40 degrees. The angle of attack was held constant to about 175,000 feet (Mach 13.5) at which time the spacecraft was gradually pitched down to angles of attack of about 10 degrees at 75,000 feet (Mach 1.5). The entry ground track from STS-4 is illustrated in figure 3 along with pertinent ground-based tracking coverage. The figure shows time and altitude marks throughout the entry where time is trajectory time from an epoch of 55821 GMT seconds from midnight on the day of landing. This track is typical of the five flights. Usually either Guam or the Hawaii S-band tracking station provided excellent coverage at the higher altitude region between 475,000 and 700,000 feet, whereas the C-band network gave continuous overlap coverage at altitudes below approximately 170,000 feet. No ground-based tracking was available between approximately 170,000 feet and 450,000 feet. To date this has not proven to be a serious limitation for the reconstruction process. The approach and landing ground track from C-band acquisition to touchdown is illustrated in figure 4, which also shows the heading alignment circle and the various theodolite camera-tracking stations. Again time and altitude marks are given to illustrate the tracking coverage from the various stations.

Some of the entry trajectory parameters from STS-4 are shown in figures 5, 6, and 7. They are altitude (h), air-relative velocity (V_A), flight path angle (γ), angle of attack (α), angle of sideslip (β), dynamic pressure ($\bar{q}$), and Mach number (M). These parameters are typical of each of the five STS flights. This will be discussed in a later section of the paper.

STS PERFORMANCE

General Discussion

Flight-extracted coefficients for the body axes total force and moment coefficients are determined using the BET parameters, which include the remotely measured atmosphere, combined with the accelerations and angular rates measured by the IMUs. They are determined in each instance over the Mach range from about 0.5 to 26.0 and are straightforward deterministic

calculations using the basic aerodynamic force and moment equations. For example, the normal-force (C_N) and pitching-moment (C_M) equations can be written as

$$C_N = \frac{m\ A_{ZB}}{\bar{q}\ S} = \frac{2m\ A_{ZB}}{\rho V_A^2 S} \tag{1}$$

$$C_M = \frac{\dot{q}\ I_{yy} + (p^2-r^2)I_{xz} + pr(I_{xx}-I_{zz})}{\bar{q}\ SC} \tag{2}$$

where the mass (m), reference area (S), chord (C), and inertia moments (I_{xx}, I_{yy}, I_{zz}, I_{xz}) are known from engineering data. The air-relative velocity (V_A) is obtained from trajectory reconstruction, the atmospheric density (ρ) from the measured atmosphere, and the remaining acceleration and rate terms (A_{ZB}, p, q, r) from IMU measurements. Only the cross-product inertia term I_{xz} is retained in equation (2) since the other terms are assumed negligible. Similar expressions hold for the remaining body axes force and moment equations.

One can see that the forces and moments are inversely proportional to the density and the square of the velocity and directly proportional to the measured accelerations and rates. Because of the quality of the other terms in equations (1) and (2) it is generally thought that the principal error source in the extracted coefficients is the measured density which has been estimated by Mr. Mel Gelman of NOAA to be known to within $\pm$ 7 percent. However, it will be shown later in very local regions on some of the flights that comparisons with the preflight data book (ref. 11) indicate coefficient discrepancies which far exceed 7 percent. In fact, the discussions lead to postulates of density shears or spacecraft flow-field phenomena.

The Shuttle preflight data-book values of the aerodynamic coefficients represent the primary benchmark for comparisons with the flight results. This data base represents an assembly of some 27,000 hours of wind tunnel testing (ref. 12) and is the best available information for extrapolating test data to flight conditions. It also provides a measure of uncertainty associated with the data base via the concept of variations (ref. 13). The variations are based on differences between flight and predicted results experienced by previous aircraft and extrapolated to the STS configuration and flight environment. In a sense they represent the flight envelope for Shuttle and suggest the level of improvement that might be obtained via flight-derived results. The version of the data base used in this paper was provided by Mr. R. Powell at the LaRC (ref. 11). As stated by Findlay and Compton (ref. 5) only the aileron and rudder effects are modeled as linear controllers. Due to nonlinearities, incrementals for elevator, body flaps, and speed brakes are modeled. The model provides for basic airframe aerodynamics (assuming undeflected controls) to which the various control increments are added.

Lift and Drag

Since the data-base predictions have been developed in terms of lift and drag coefficients, the flight-derived axial-force coefficients have been rotated to the stability axis to obtain the corresponding C_L and C_D coefficients. The BET α was used in the rotations and is estimated to be accurate to within 0.2 degrees. The lift and drag performance for all five flights is summarized in figures 8-13. The coefficients have been compared with preflight predictions, and the comparison is shown on each figure via percentile differences between the flight and data-book values, i.e., flight minus data book. The ΔC_L and ΔC_D plots include the uncertainties associated with the data book in terms of variations. It should be noted again that the variations represent the approximate maximum level of improvement that one could expect to obtain from the flight-derived coefficients. Also shown in figures 11 and 12 are the actual values of the flight and predicted L/D, C_L, and C_D for STS-4 and 5. Values for STS-1, 2, and 3 have been previously given by Compton et al. in reference 4.

Considering first the lift-to-drag ratio, one can see a very consistent pattern from flight to flight. First, the flight and data book are in excellent agreement throughout the supersonic and hypersonic regime. Second, the sense of the differences shown is such that the L/D is slightly underpredicted in the hypersonic regime and slightly overpredicted in the supersonic region where supersonic has been somewhat arbitrarily picked to be less than Mach 6. Shown on each of the plots is the mean (μ) and standard deviation (σ) of the differences over both the supersonic and hypersonic regime. These statistics have been included in Table I which also shows the mean and standard deviation for the hypersonic regime exclusively for each flight and the corresponding means and standard deviations for the ensemble of flights. The ensemble statistics show that the mean L/D difference over both the supersonic and hypersonic region is 0.69 ± 1.24 percent. Above Mach 6 the mean and standard deviation are respectively $\overline{1}.16$ and 0.51 percent. Thus one can conclude that L/D is generally known to within 2.0 percent.

The consistent patterns and differences noted for L/D cannot be seen flight to flight for the individual C_L and C_D coefficients except that usually the sense of differences is such that the coefficients were overpredicted. The flight results seem to fall into two categories. First, with the exception of a narrow region on STS-1 (Mach 18 to 20), flights 1, 3, and 5 differences were well within variations over both the supersonic and hypersonic regime. Second, STS-2 and 4 differences exhibited very radical departures from predictions above approximately Mach 20. It will be noted later that even STS-3 showed some of this radical departure when using $\bar{q}$ from the NOAA-measured atmosphere. Over the entire flight regime from Mach 2 to 26 the ensemble statistics show that the C_L and C_D mean differences are -4.50 ± 4.38 percent and -5.24 ± 4.55 percent, respectively. In the altitude interval below Mach 20 (80,000 ft < h < 220,000 ft) the computed mean differences are -3.3 ± 2.5 percent and -3.7 ± 2.4 percent for C_L and C_D, respectively (ref. 5). Above Mach 20, where the large discrepancies were noted on STS-2 and 4, similar computations yield -9.0 ± 6.1 percent and -10 ± 6.1 percent for the lift and drag statistics. In some cases for STS-2 and 4 the coefficients were as much as 25 percent overpredicted.

Pitching Moment C_m

For each of the five flights, a significant difference between the hypersonic predicted trim with the known control-surface deflections and that derived from flight was noted. Figure 14, which shows C_m from STS-5 referenced to the flight c.g. as a function of Mach number is typical of all five flights. The maximum difference occurs at approximately Mach 16 and is generally constant at 0.03 up to Mach 26 (0.035 on STS-2 and 3). Below Mach 16 the difference decreases to about 0.002 at Mach 8 and remains constant at that value through Mach 2. Early speculations on this difference include (1) overprediction of body flap effectiveness, (2) uncertainties in c.g. location, (3) real-gas effects, and (4) errors in the predicted basic pitching moment. Current thinking is that it is an error in the basic pitching-moment (C_{m_o}) prediction due primarily to real-gas and Mach-number effects. The Air Force Flight Test Center has shown that with an updated C_{m_o} in their simulation that they are able to obtain good agreement between simulator predictions and flight-derived characteristics. In addition, they have shown that body flap and elevon effectiveness agree well with preflight test results (ref. 16). The findings of Maus et al. (ref. 17) tend to support the C_{m_o} error. They show that real-gas and Mach-number effects on C_{m_o} at flight conditions are on the order of 0.022. Using the Mach-number and real-gas effects as corrections to the wind tunnel C_{m_o} they work backward to show the body-flap deflections required to trim the Shuttle vehicle at the high angles of attack. Their results agree with the flight-derived body-flap deflections to within 2 degrees. Thus it would appear that real-gas and Mach-number effects are primarily responsible for the flight compared to data-book differences shown in figure 14. However, it should be noted that the differences indicated in figure 14 at the high Mach numbers are on the order of 0.03 or approximately 30 percent larger than the real-gas and Mach-number effect and as yet are unaccounted for. This may be due to the vintage data-book values that were used for comparisons or may, in fact, indicate that control surface effectiveness is slightly overpredicted. Some preliminary calculations tend to support a combination of real-gas, Mach-number, and control-surface effects as the cause for the differences shown in figure 14, the principal part of which is due to real-gas and Mach-number effects.

LATERAL STABILITY AND CONTROL

General Discussion

Flight-extracted lateral stability and control results are presented in the remaining sections of this paper. In most cases the estimated stability and control derivatives have been obtained using the Modified Maximum Likelihood Estimation (MMLE-3) program developed by Iliff and Maine (ref. 18). This program has had widespread use in the Shuttle flight-data analysis user community in addition to numerous applications to commercial and military aircraft. However, the results obtained from MMLE often reflect the experience of the analyst, his choice of input data, and the program options which are used. For this reason, the authors have used independent methods and programs as well as alternate data sources to provide balances and checks on the MMLE solutions. This has been discussed in detail in reference 4, and only a few of these alternate results will be discussed in this paper.

With few exceptions, the stability and control results were estimated assuming the rotary derivatives fixed at zero and $C_{Y_{\delta a}}$ fixed at the preflight data-book value of 0.00042 per degree. The MMLE option for estimating the weighting matrix was used. All mass properties and c.g. information were provided by the Johnson Space Center (JSC).

The results presented in this section of the paper have been derived using only the Programed Test Inputs (PTI's) from flights 2, 3, 4, and 5. There were no PTI's on STS-1. Although there were bank reversal maneuvers for energy management on each flight and astronaut stick-input maneuvers on some of the flights, the PTI's which are performed automatically by the vehicle are considered to be the most optimum for stability and control estimation. The flight-derived results are presented along with equivalent preflight predictions and variations all corrected to the flight c.g.

Lateral-Directional Derivatives

C_{ℓ_β}.- The rolling moment due to the angle of sideslip is presented in figure 15 as a function of Mach number. Both flight and predicted values of C_{ℓ_β} are shown along with variations associated with the predicted values. In addition, as will be the case for all results presented in this paper, the Cramer-Rao bounds associated with the flight data multiplied by a factor of 10 are shown in the figure. It should be noted that the true Cramer-Rao bound is the lower limit of the variances of the estimated parameters and is the measure of efficiency of an estimator. The factor of 10 is generally accepted as a conservative multiplicative factor for association with STS extraction results.

If one ignores the obvious outliers shown in figure 15 in the region below Mach 5, the solutions for C_{ℓ_β} are for the most part well within predicted variations. In the region above Mach 8, the results indicate a definite Mach number effect, contrary to the predicted results. In this same region the flight results are slightly more positive than predicted indicating less than predicted stability. Similar results were reported by Kirsten et al. (ref. 16) and Maine and Iliff (ref. 19). In the Mach 25 region the flight results were estimated using maneuvers in the very low $\overline{q}$ (4-10 psf) region where it is difficult to estimate the stability and control derivatives, and this may partially account for them being outside of variations. Below Mach 8, especially in the interval below Mach 4, the solutions are very scattered making it difficult to understand the trend in the flight data. However, STS-2 results would indicate that the vehicle is more stable than predicted: i.e., more negative than predicted. The STS-5 results would indicate values slightly more positive than predicted, but it is known in some cases that reasonably high correlations exist between some of the estimated parameters for STS-5. For example, at Mach 21.5 C_{ℓ_β} is highly correlated with $C_{\ell_{\delta a}}$ and $C_{\ell_{\delta J}}$; i.e., with roll due to aileron and the RCS jets. These high correlations could degrade some of the solutions and are still being analyzed at this time. The scatter in the solutions below Mach 4 is likely due to couplings in the estimation software

(math model) resulting in statistical correlations between the various control-surface parameters that are being estimated. Quite often in this region the various control surfaces are simultaneously active, especially the rudder and aileron. With the present control system, it is not possible to perform maneuvers which isolate one control surface at a time, and thus it is difficult for the extraction program to accurately allocate the effects of each surface. The results shown in figure 15 by the circle symbols with dots inside are indicative of such cases. For these cases solutions were obtained which included the rudder parameters. These results can be compared to the open symbols for the same maneuver where rudder parameters were not estimated. Significant differences in the solutions can be noted. It should also be noted that there are a few other cases where more than one solution is shown for the same maneuver. This usually results from dividing a maneuver into two segments or from using an alternate computer program with a different analyst estimating the coefficients.

In terms of lessons learned, the ACIP measurements were not available from STS-2 due to flight recorder problems, and yet we were able to obtain good lateral solutions using the RGA,AA measurements.

C_{n_β}.- Flight results for the yawing moment due to sideslip shown in figure 16 present a pattern similar to that given for C_{ℓ_β} in that solutions above Mach 8 are generally well within variations and solutions below Mach 8 especially from Mach 4 down are very scattered and sometimes outside of variations. The error bounds in this region are also very large. Values of C_{n_β} above Mach 8 are more negative than predicted and below Mach 8 more positive. In the higher Mach region, this is contradictory to what has been given in references 19 and 20 where it is shown that C_{n_β} is slightly more positive than predicted. Reasons for this discrepancy are not known at this time except one could argue that error bounds associated with the three solution sets are such as to overlap the various solutions. A reasonable fairing of the values above Mach 8 would not show the constancy indicated by the predicted values.

$C_{\ell_{\delta a}}$.- The rolling moment due to aileron is presented in figure 17. Ignoring the obvious outliers below Mach 4 and the solutions outside of variations above Mach 4, the solutions compare very well with the data book. The trend below approximately Mach 5 shows aileron effectiveness to be slightly less than predicted. Above Mach 5 and ignoring results outside of variations, the aileron effectiveness generally agrees with the data book with some indications that the ailerons may be slightly more effective than predicted. However, one must be careful here since the data-book values used for all the comparisons have been taken from flight 5 and are necessarily different from the other flights. In fact, the individual flight comparisons shown in reference 4 for all maneuvers on flights 1, 2, and 3 tend to support a slightly less than predicted aileron effectiveness throughout the flight. If in fact the aileron effectiveness in the Mach 1 to Mach 3 region proves to be less than predicted, it may be the cause of the small amplitude lateral directional oscillation (ref. 19) that has been noted in this flight regime. However, a more detailed analysis is required to substantiate such a conclusion.

$C_{n_{\delta a}}$.- Figure 18 shows yaw due to aileron. The many outliers and large Cramer-Rao bounds are indicative of the difficulty in estimating this coefficient. Above Mach 5 the flight results agree reasonably well with the data book. The flight 2 results tend to support yaw-aileron effectiveness less than predicted. Flight 3 results are a little more negative than those for flight 2 and are perhaps due to a more downward deflection of the elevators. The flight 4 values appear to be outliers in every case. This may be partially due to the density problem previously noted, but it is not clear at this time why this occurs and is still under investigation by the authors. The results shown here are in no way conclusive. A more detailed analysis is required to accurately define $C_{n_{\delta a}}$.

The lateral derivatives associated with the rudder have been reported in reference 4 and no new information has been obtained to date for these coefficients. Recall that the rudder is only active below Mach 3.5. It was shown that roll due to the rudder ($C_{\ell_{\delta r}}$) is close to what has been predicted. However, in the Mach 1.5 to 2.5 region the yaw due to rudder ($C_{n_{\delta r}}$) shows less effectiveness than predicted but agrees very well with predictions in the close vicinity of Mach 1 and Mach 3.

LATERAL REACTION CONTROL JET EFFECTIVENESS

General Discussion

The RCS jets have been modeled in MMLE as if they are another aerodynamic controller and solutions are obtained throughout the speed range for the side force, rolling moment, and yawing moment due to yaw-jet firings. For the purposes of this paper, the yaw-jet evaluation is presented as a function of Mach number on a per jet basis. Comparisons are made to preflight values which are based on known vacuum thrust corrected for altitude effects. Since the altitude profiles are slightly different for each flight, two sets of predicted values (STS-2 and 4) are noted on the plots in the following section.

RCS Derivatives

$C_{Y_{\delta J}}$.- The side force due to a yaw-jet firing is shown in figure 19 as a function of Mach number. The predicted values are on a per jet basis and since they are based on a known thrust per jet, the difference between predicted and flight can be attributed to jet interaction effects. Here the interactions are defined to include the combination of flow-field interactions and vehicle impingements. The flight results are in very good agreement with the predicted side force even though significantly large error bounds are shown for the estimates. These uncertainties should not detract from the goodness of the results since they are due primarily to the small signal-to-noise ratio in the data for estimating side force. The results indicate that the yaw jets are a little more than 100 percent effective in terms of side force. This is perhaps due to interaction effects, but with

the uncertainties as shown one can conclude that RCS side-force jet effectiveness is virtually 100 percent.

$C_{n_{\delta J}}$.- The yawing moment due to a yaw jet firing shown in figure 20 has been evaluated in the same manner as $C_{Y_{\delta J}}$, and the results obtained are very similar in that they agree very well with the predicted values, usually within 10 percent. However, the uncertainties associated with the flight derived $C_{n_{\delta J}}$ are substantially smaller. The results indicate that the yaw jets are from 90 to 100 percent effective in terms of yawing moment produced.

$C_{\ell_{\delta J}}$.- Evaluations of the rolling moment due to a yaw jet present a significantly different story as can be seen in figure 21. Here the difference between flight and predicted values indicates large interaction effects which vary significantly over the Mach-number range. Determinations of the interaction effects have varied significantly among the various researchers and in many cases differed significantly from preflight predictions. No attempt is made here to compare the interactions with the data book, but one can quickly see the significance of accurately identifying the interactions. In fact, it is tempting here to state that the interactions are well determined from these results. However, it appears to be more prudent to search for other means of verifying the interactions. This has been attempted by using the DFI pressure measurements on the upper surface of the wing from STS-3 and STS-5. The details of this process are given in reference 21 where it is shown that the measured pressure distribution on the upper wing surface is integrated both chordwise and spanwise to obtain a direct experimental calculation of the interaction. This can be added to the predicted $C_{\ell_{\delta J}}$ in figure 21 to obtain a $C_{\ell_{\delta J}}$ which can be directly compared with the estimated flight results. This calculation has been completed for a limited number of cases and is shown on figure 21 as the solid symbols. The agreement with the other solutions indicate that the DFI pressure measurements may be an excellent way for determining the interactions and that the estimated interactions are reasonable.

CONCLUDING REMARKS

The STS aerodynamic performance and stability have been analyzed over the speed range from Mach 2 to 26 using flight mesaurement data from STS flights 1-5. Stability results were obtained using only the PTI's from STS flights 2-5. There were no PTI's on STS-1. Generally, the performance and stability correlated well with preflight predictions. There were some significant differences noted in the lift and drag comparisons with preflight predictions at the higher Mach number. These differences are probably due to errors in the measured density but may be due to a flow-field phenomenon as yet unexplained. The lift-to-drag ratio, which is independent of density, was shown to be in excellent agreement with the predictions over the entire hypersonic regime for all five flights. In the very localized vicinity of Mach 4 in the supersonic region, the lift-to-drag ratio difference was 3 to 5

percent. Vehicle trim anomalies were noted on all five flights with the largest differences occurring above Mach 8. These differences are thought to be due primarily to unpredicted Mach-number and real-gas effects. Stability and control results were usually well within one variation of the data book except in the region below approximately Mach 4 where the flight solutions exhibited quite a bit of scatter and oftentimes large uncertainties. Aileron effectiveness below Mach 3 appears to be slightly less than predicted. The yaw jet evaluation shows that they are virtually 100 percent effective in terms of side force and from 90 to 100 percent effective in terms of yawing moment. This evaluation also indicated significant yaw-jet rolling-moment interactions.

It is felt that estimates of the stability and control derivatives can be improved by a more detailed analysis of each maneuver for removal of parameter correlations especially in the region below Mach 5 and especially for all those maneuvers from flight 4. The flight 4 stability results may be biased in the high Mach region by what has been noted as a possible density error or flow-related phenomenon. It is also felt that additional flight maneuvers are required before comprehensive and meaningful data-book updates to the stability and control derivatives can be made.

REFERENCES

1. Compton, H. R., Blanchard, R. C., and Walberg, G. D.: An Experiment for Shuttle Aerodynamic Force Coefficient Determination From Inflight Dynamical and Atmospheric Measurements. AIAA Paper 78-795, 1978.

2. Compton, Harold R., Blanchard, R. C., and Findlay, John T.: Shuttle Entry Trajectory Reconstruction Using Inflight Accelerometer and Gyro Measurements. AIAA Paper 79-0257, 1979.

3. Jones, Jim J.: OEX--Use of the Shuttle Orbiter as a Research Vehicle. AIAA Paper 81-2512, 1981.

4. Compton, Harold R., Scallion, W. I., Suit, W. T., and Schiess, J. R.: Shuttle Entry Performance and Stability and Control Derivatives Extraction From Flight Measurement Data. AIAA Paper 82-1317, 1982.

5. Findlay, John T. and Compton, Harold R.: On the Flight Derived/ Aerodynamic Data Base Performance Comparisons for the Space Shuttle Entries During the Hypersonic Regime. AIAA Paper 83-0115, 1983.

6. Findlay, J. T., Kelly, G. M., and Heck, M. L.: Reconstruction of the First Space Shuttle (STS-1) Entry Trajectory. NASA CR-3561, 1982.

7. Heck, M. L., Findlay, J. T., Kelly, G. M., and Compton, H. R.: The Adaptation of a Strap Down Formulation for Processing Inertial Platform Data. AIAA Paper 82-1332, 1982.

8. Price, Joseph M.: Atmospheric Definition for Shuttle Investigations. Journal of Spacecraft and Rockets, Vol. 20, pp. 133-140, March-April 1983.

9. Compton, Harold R., Findlay, John T., Kelly, George M., and Heck, Michael L.: Shuttle (STS-1) Entry Trajectory Reconstruction. AIAA Paper 81-2459, 1981.

10. Kelly, G. Mel; Findlay, John T., and Compton, Harold R.: Wind Estimation Using Air Data Probe Measurements to Evaluate Meteorological Measurements. AIAA Paper 82-1333, 1982.

11. Aerodynamic Design Data Book. Vol. I - Orbiter Vehicle. Report No. SD72-SH-0060-1L, Rockwell International, Oct. 1978.

12. Whitnah, Authur M. and Hillje, Ernest R.: Space Shuttle Wind Tunnel Testing Program. AIAA Paper 82-0562, 1982.

13. Young, James C. and Underwood, Jimmy M.: The Development of Aerodynamic Uncertainties for the Space Shuttle Orbiter. AIAA Paper 82-0563, 1982.

14. Siemers, P. M. III, Wolf, H., and Flanagan, P. F.: Shuttle Entry Air Data System Concepts Applied to Space Shuttle Orbiter Flight Pressure Data to Determine Air Data - STS 1-4. AIAA Paper 83-0118, 1983.

15. Leurs, J. K.: A Method of Computing Winds, Density, Temperature, Pressure, and Their Associated Errors From the High Altitude Robin Sphere Using an Optimum Filter. Report No. AFCRL-70-0366, Air Force Cambridge Research Laboratories, July 1970.

16. Kirsten, P. W., Richardson, D. F., and Wilson, Charles M.: Predicted and Flight Test Results of the Performance, Stability and Control of the Space Shuttle From Reentry to Landing. Shuttle Performance: Lessons Learned, NASA CP-2283, Part 1, 1983, pp. 509-524.

17. Maus, J. R., Griffith, B. J., and Szema, K. Y.: Hypersonic Mach Number and Real Gas Effects on Space Shuttle Orbiter Aerodynamics. AIAA Paper 83-0343, 1983.

18. Maine, Richard E. and Iliff, Kenneth W.: User's Manual for MMLE-3, A General FORTRAN Program for Maximum Likelihood Parameter Estimation. NASA TP-1563, 1980.

19. Maine, R. E. and Iliff, K. W.: Selected Stability and Control Derivatives From the First Three Space Shuttle Entries. AIAA Paper 82-1318, 1982.

20. Kirsten, Paul W. and Richardson, David F.: Predicted and Flight Test Results of the Performance and Stability and Control of the Space Shuttle From Reentry to Landing. Paper presented at the AGARD 61st Flight Mechanics Panels Meeting, Symposium on Ground/Flight Test Techniques and Correlation, Cesme, Turkey, Oct. 11-15, 1982.

21. Scallion, W. I., Compton, H. R., Suit, W. T., Powell, R. W., Blackstock, T. A., and Bates, B. L.: Space Shuttle Third Flight (STS-3) Entry RCS Analysis. AIAA Paper 83-0116, 1982.

TABLE I. - LIFT AND DRAG COMPARISON STATISTICS

EVENT	ΔC_L		ΔC_D		$\Delta L/D$	
	μ	σ	μ	σ	μ	σ
STS 1						
MACH 2-26	-5.94	3.34	-6.46	3.36	0.48	1.08
MACH 6-26	-5.85	3.62	-6.72	3.51	0.82	0.56
STS 2						
MACH 2-26	-6.86	6.45	-7.60	7.03	0.65	1.29
MACH 6-26	-8.10	6.53	-9.37	6.64	1.15	0.45
STS 3						
MACH 2-26	-2.66	2.10	-3.59	1.94	0.90	1.29
MACH 6-26	-2.42	1.69	-3.83	1.76	1.36	0.45
STS 4						
MACH 2-26	-4.24	4.32	-4.97	4.56	0.68	1.31
MACH 6-26	-4.09	4.78	-5.37	5.00	1.21	0.51
STS 5						
MACH 2-26	-2.52	1.76	-3.32	1.59	0.77	1.18
MACH 6-26	-2.11	1.58	-3.41	1.52	1.25	0.38
STS 1-5						
MACH 2-26	-4.50	4.38	-5.24	4.55	0.69	1.24
MACH 6-26	-4.61	4.73	-5.83	4.74	1.16	0.51

μ = mean, % σ = standard deviation, %

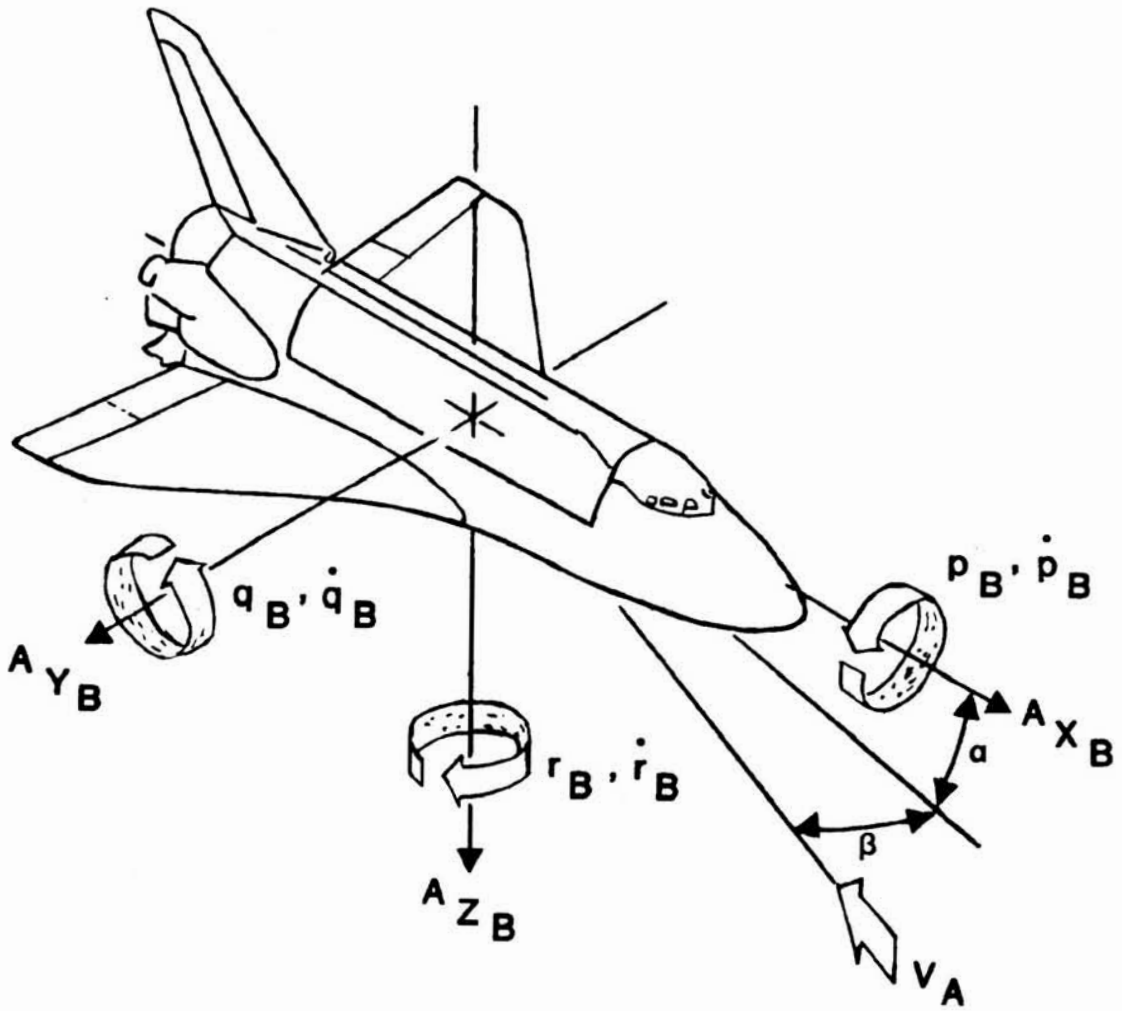

Figure 1.- Schematic of STS body axes, accelerations, and rates.

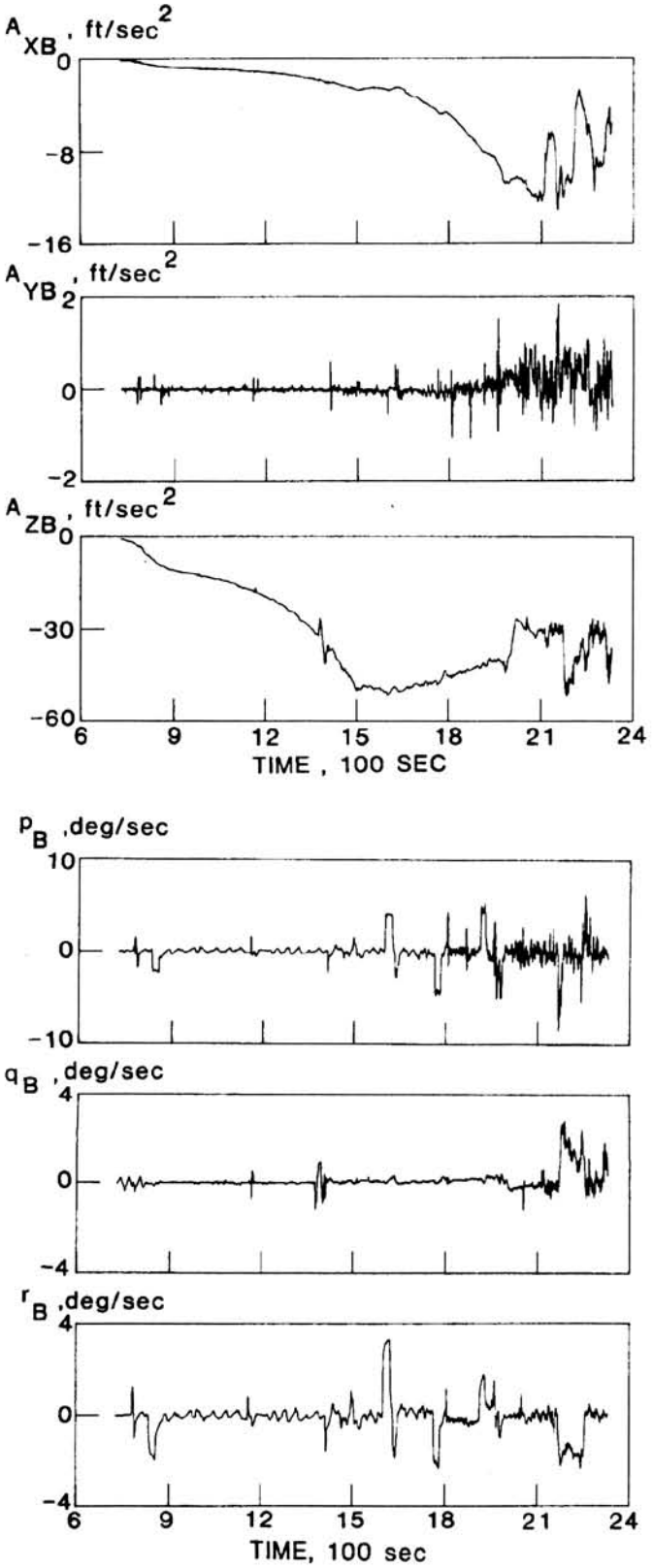

Figure 2.- IMU measured accelerations and rates.

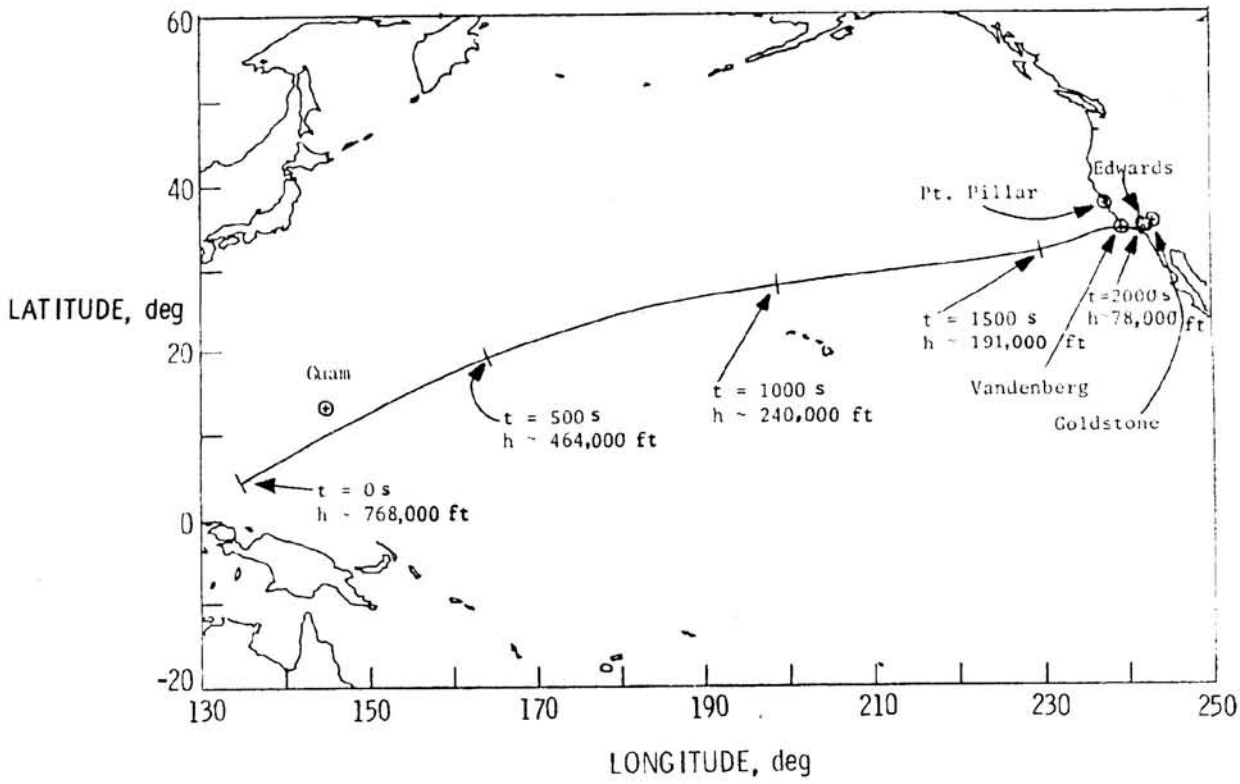

Figure 3.- STS-4 entry ground track.

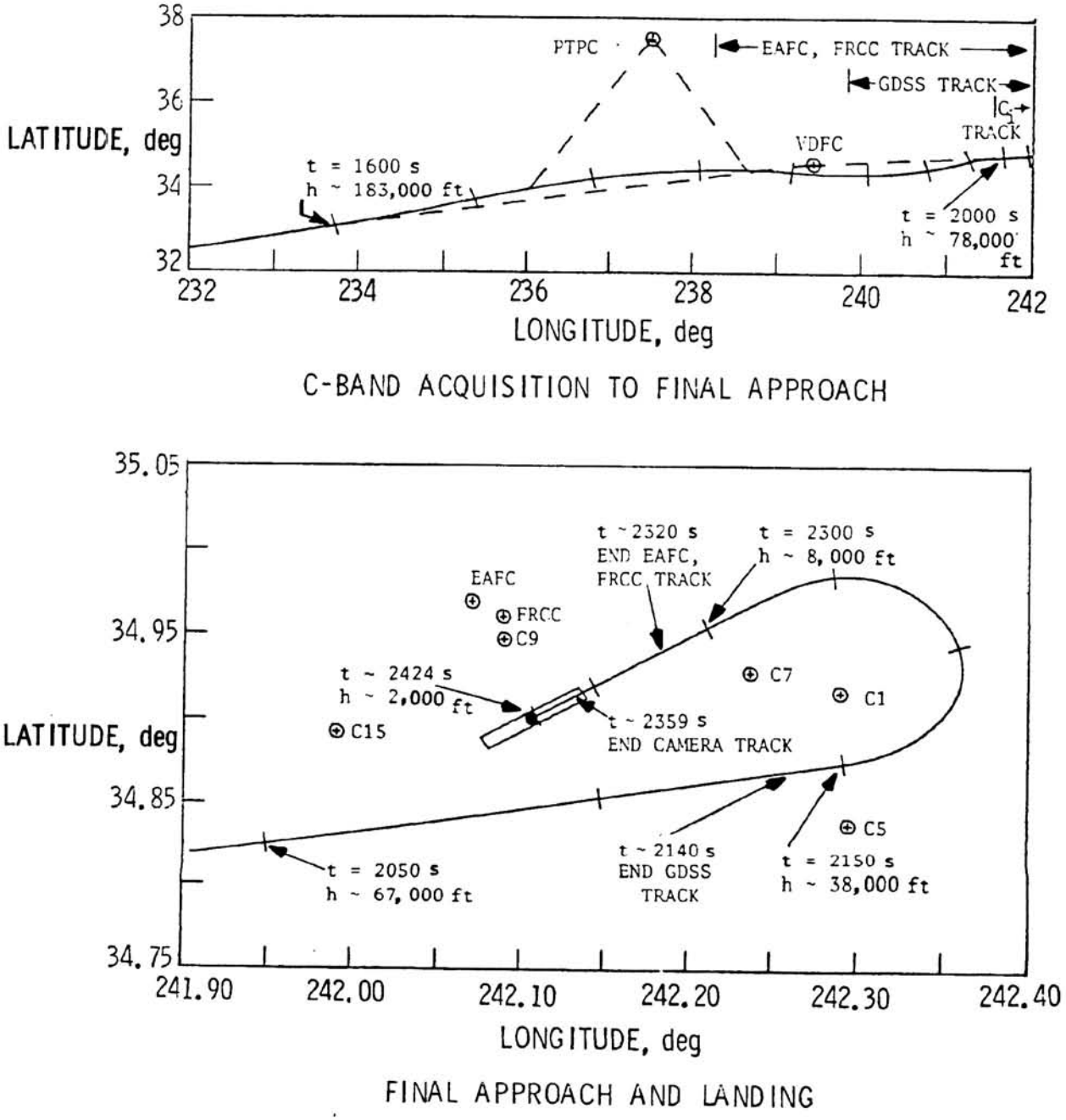

Figure 4.- STS-4 ground track from C-band acquisition to landing.

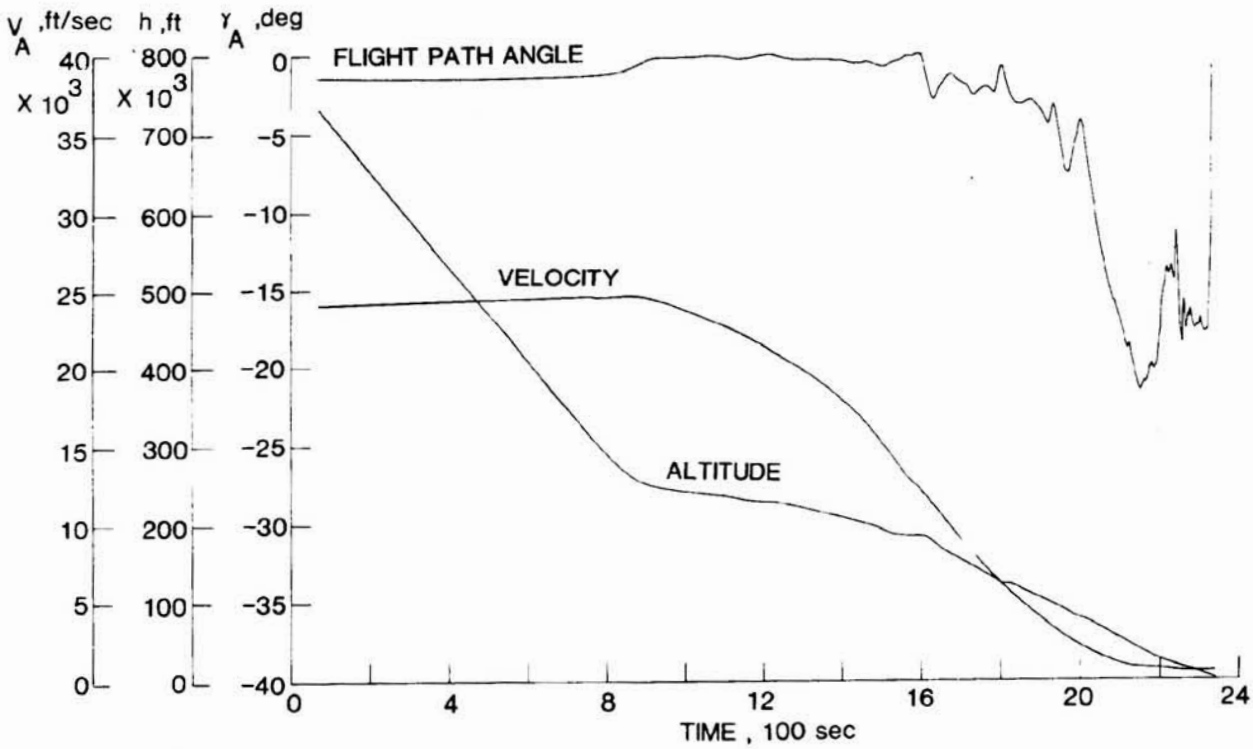

Figure 5.- Variation of STS-4 in plane state parameters with time from epoch.

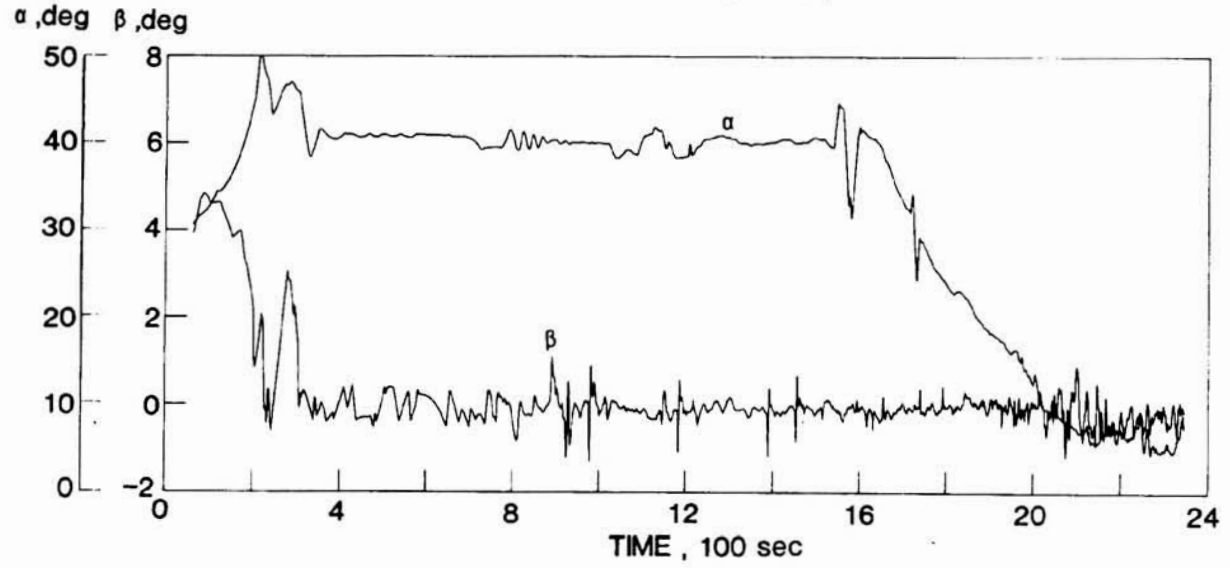

Figure 6.- Variation of STS-4 angles of attack and sideslip with time from epoch.

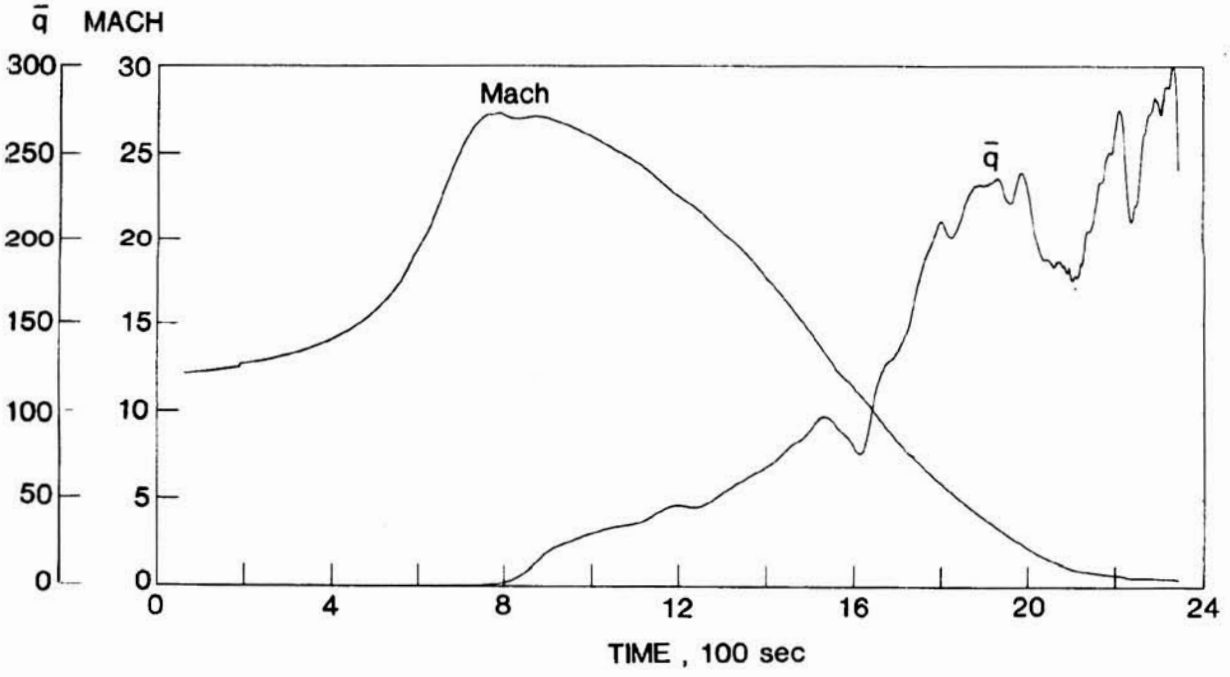

Figure 7.- Variation of STS-4 dynamic pressure and Mach number with time from epoch.

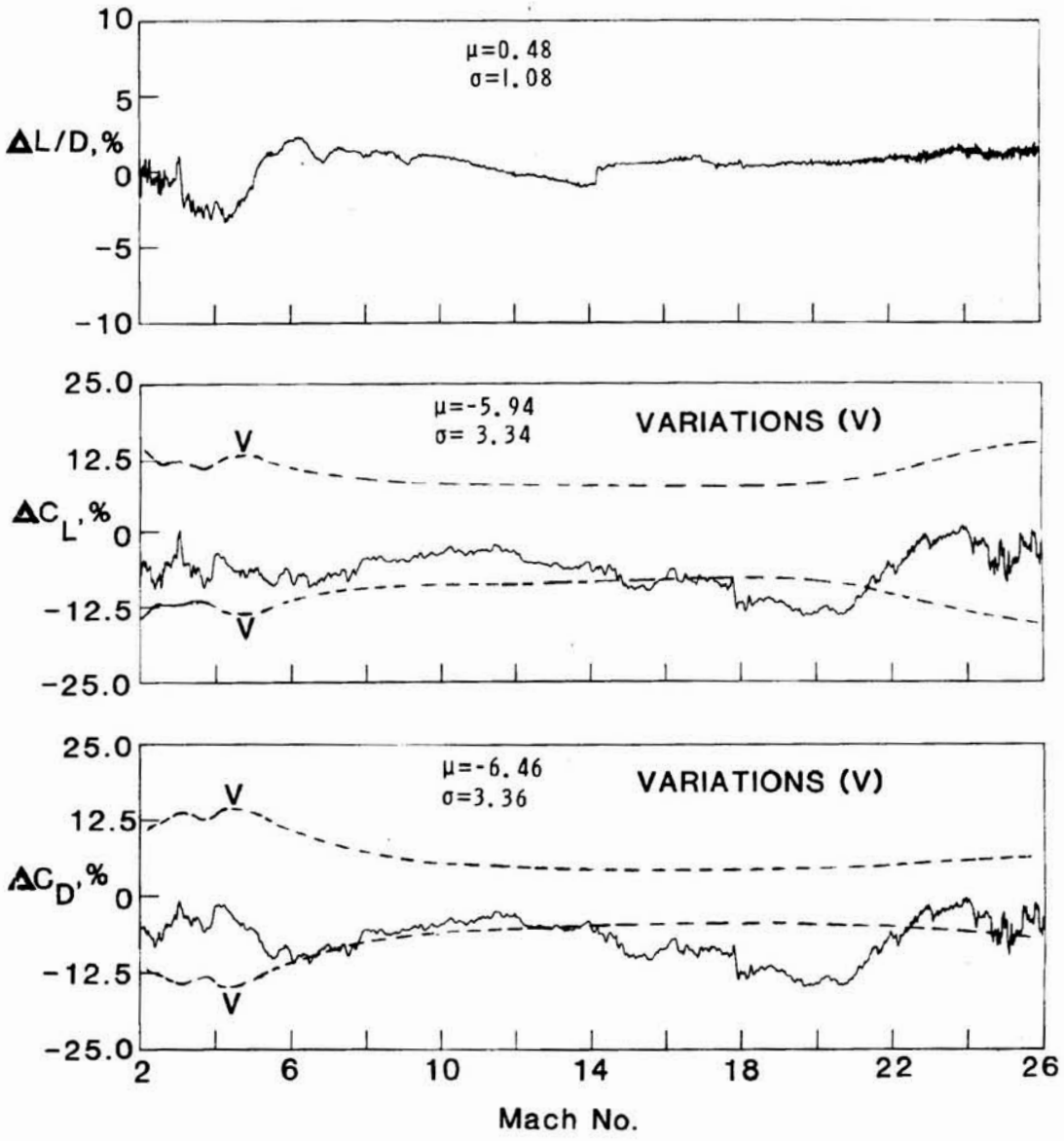

Figure 8.- STS-1 lift and drag comparisons with preflight predictions.

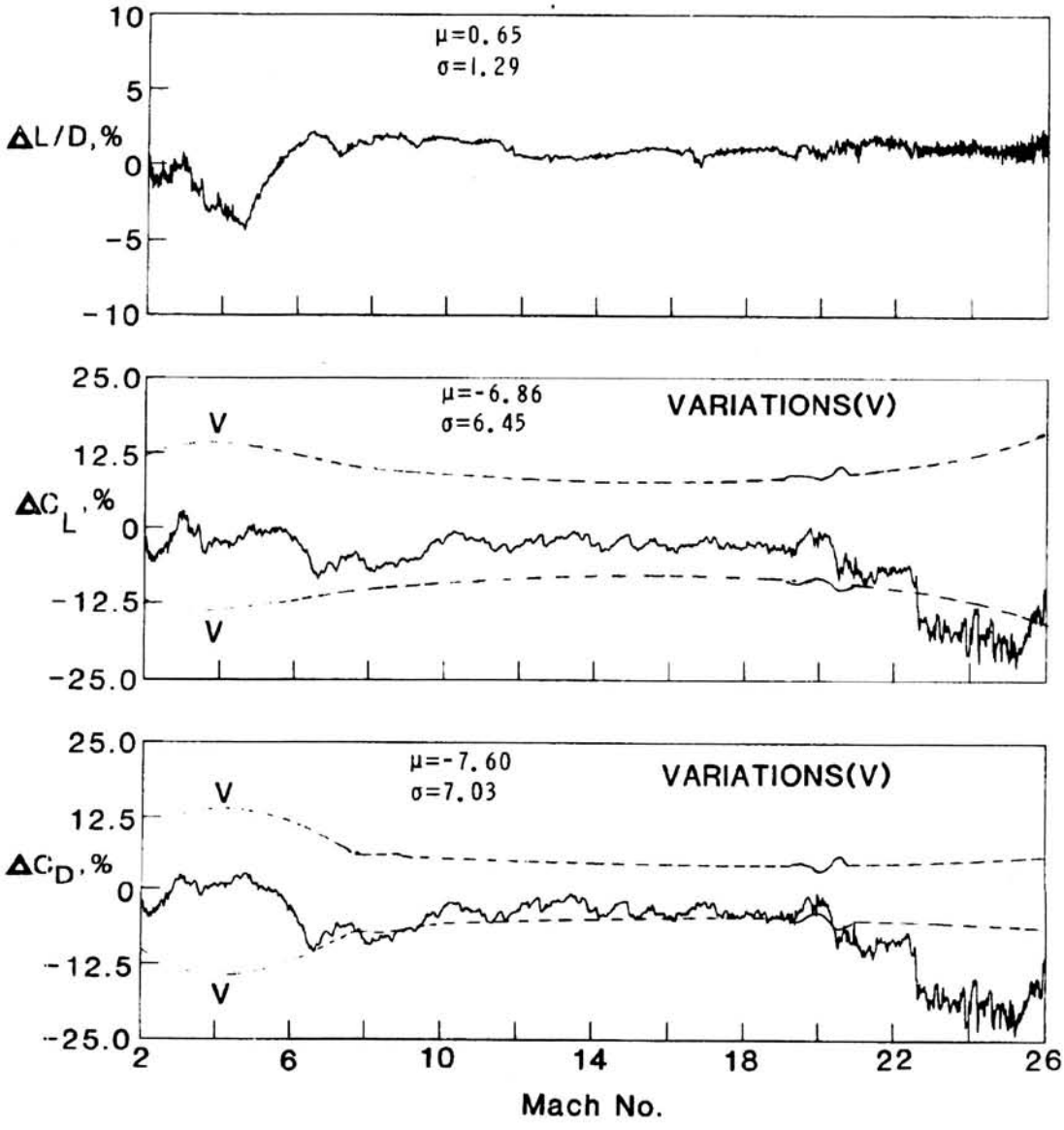

Figure 9.- STS-2 lift and drag comparisons with preflight predictions.

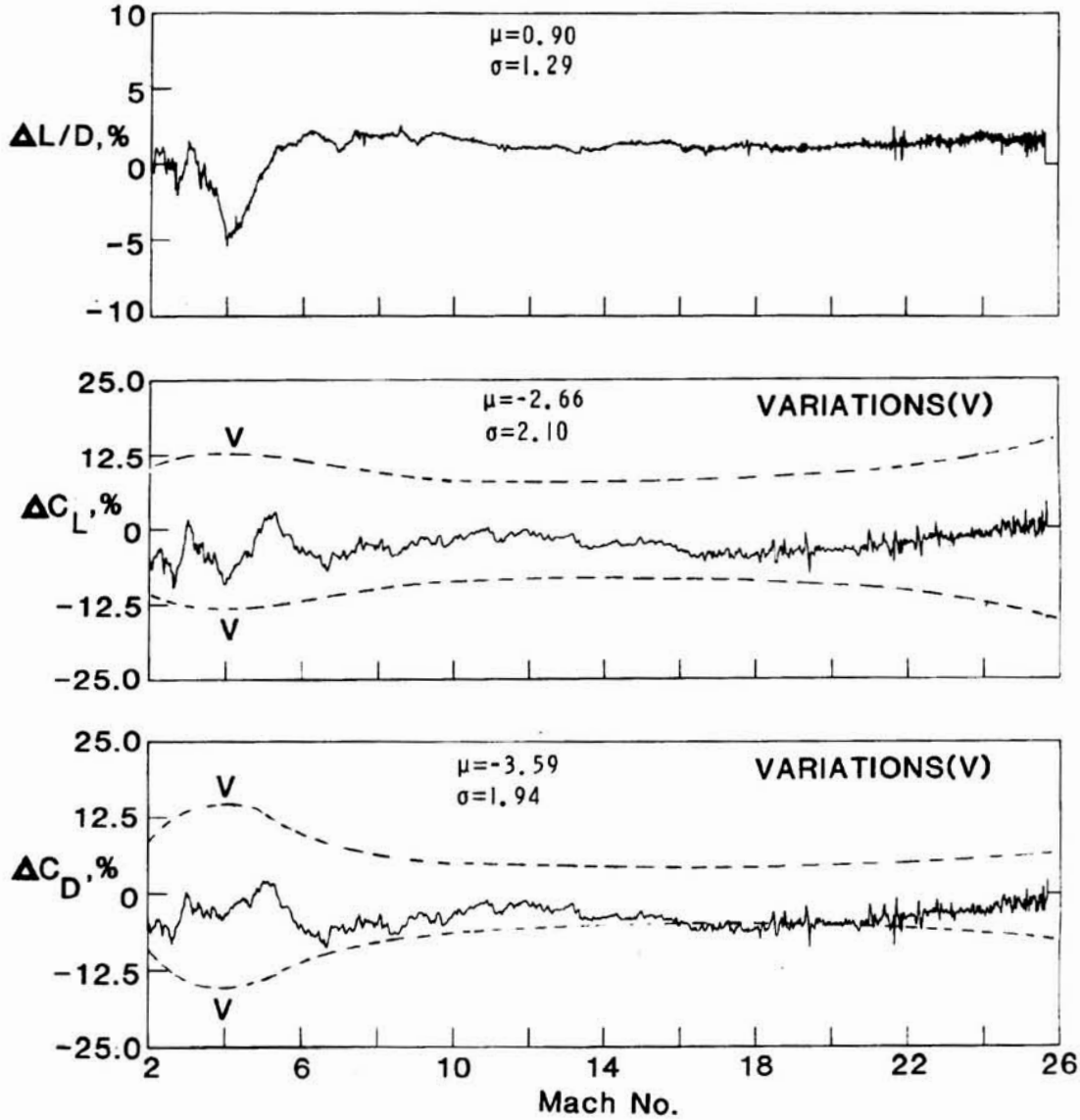

Figure 10.- STS-3 lift and drag comparisons with preflight predictions.

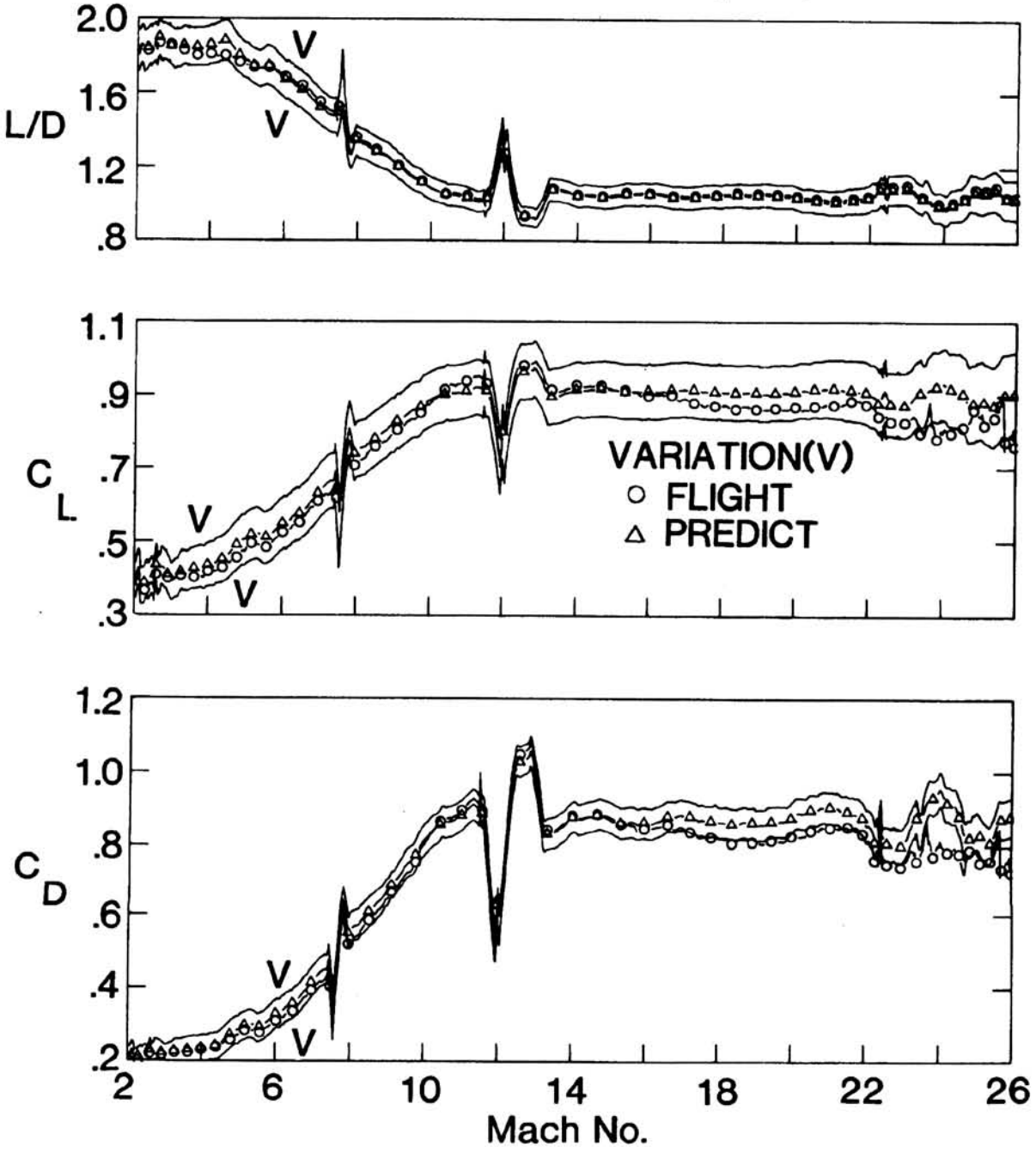

Figure 11.- STS-4 lift and drag comparisons with preflight predictions.

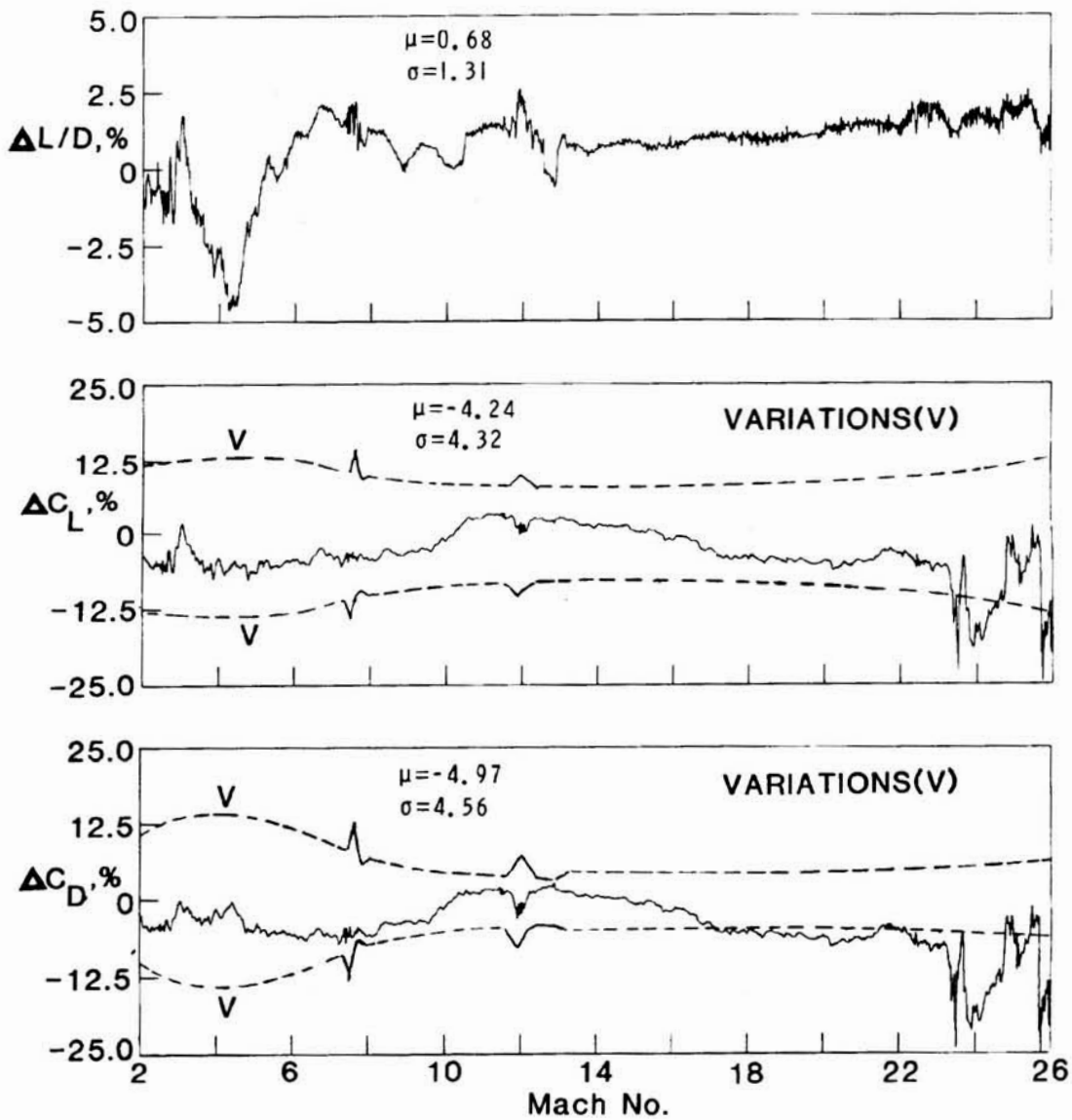

Figure 11.- Concluded.

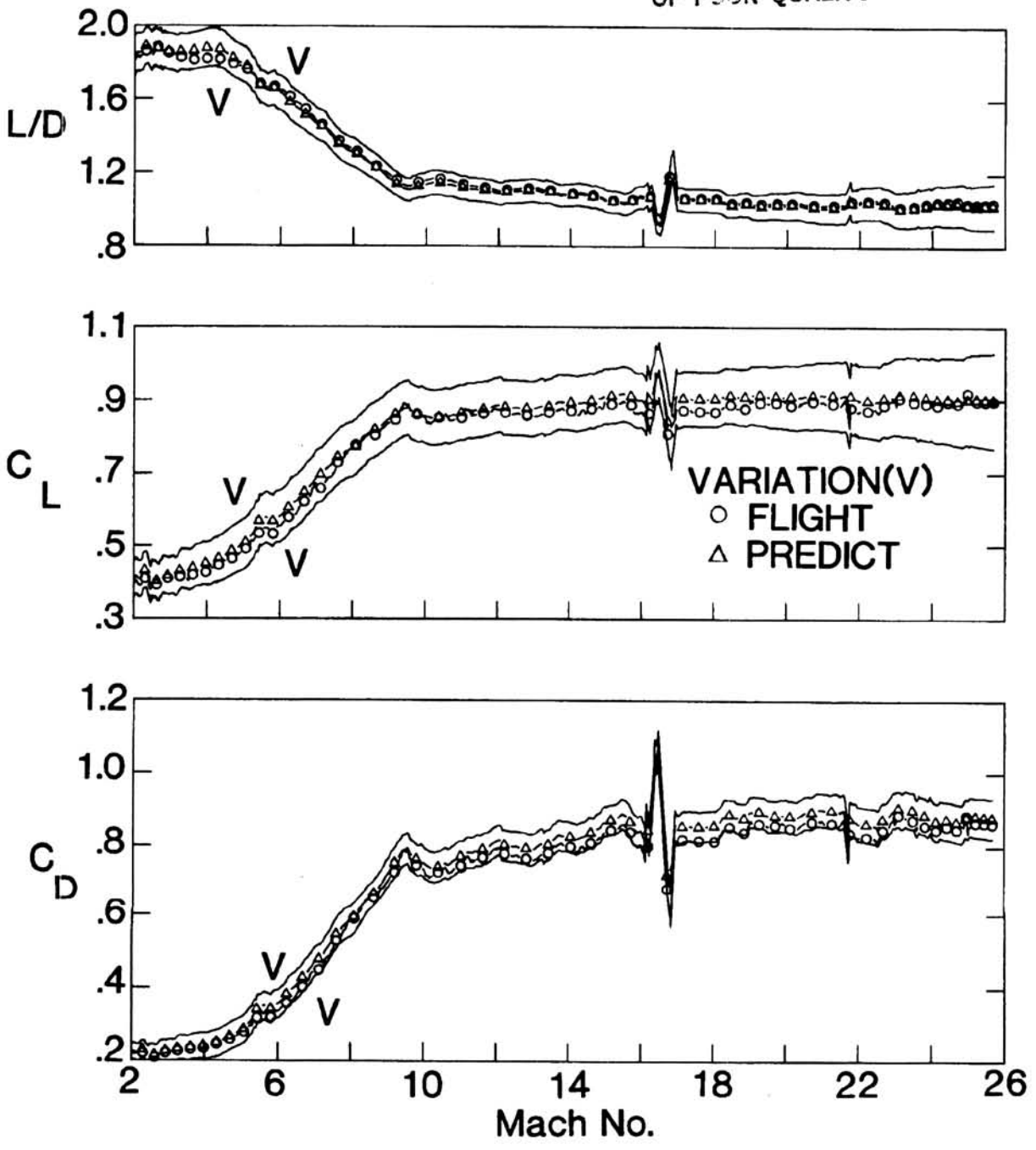

Figure 12.- STS-5 lift and drag comparisons with preflight predictions.

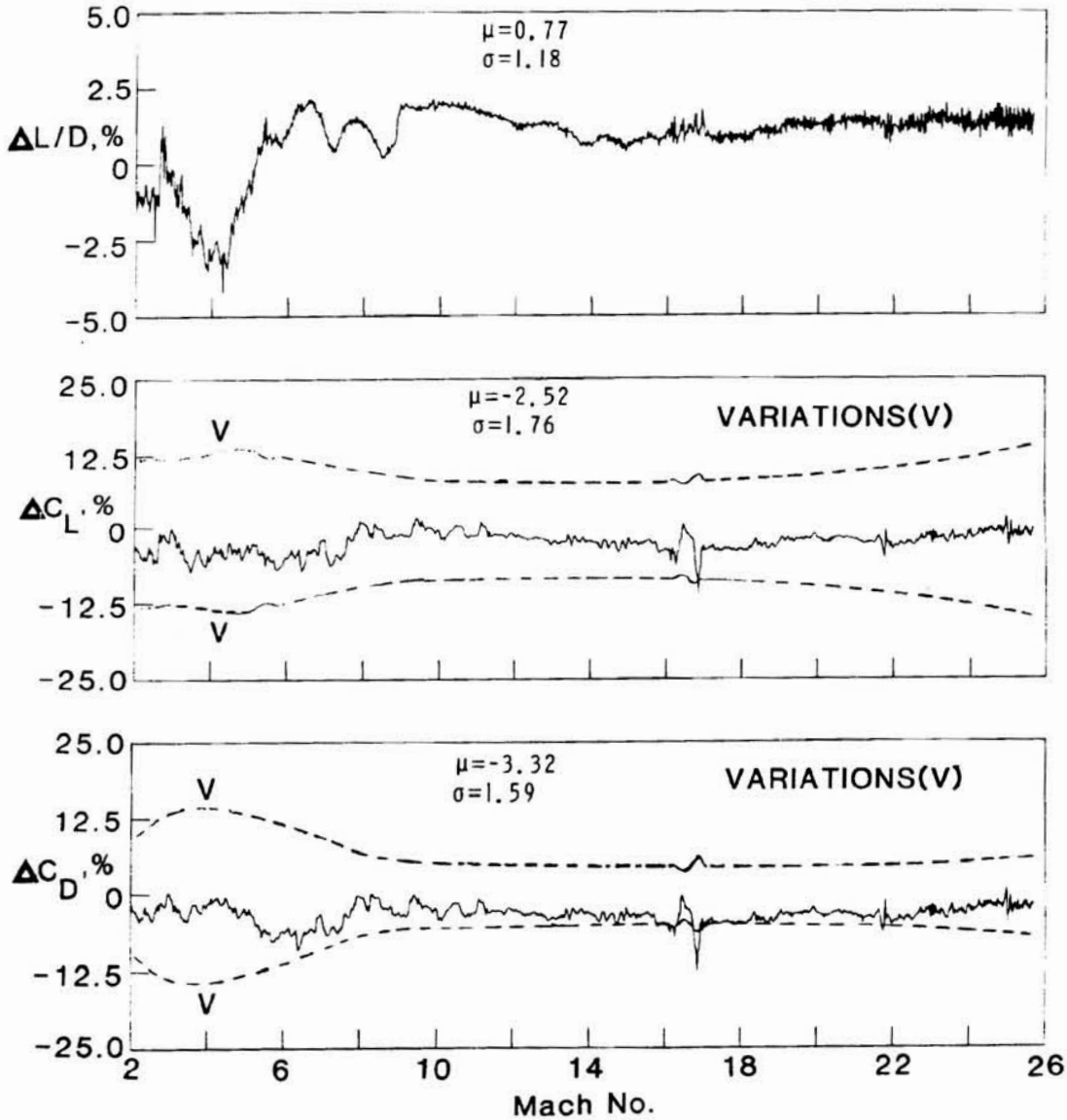

Figure 12.- Concluded.

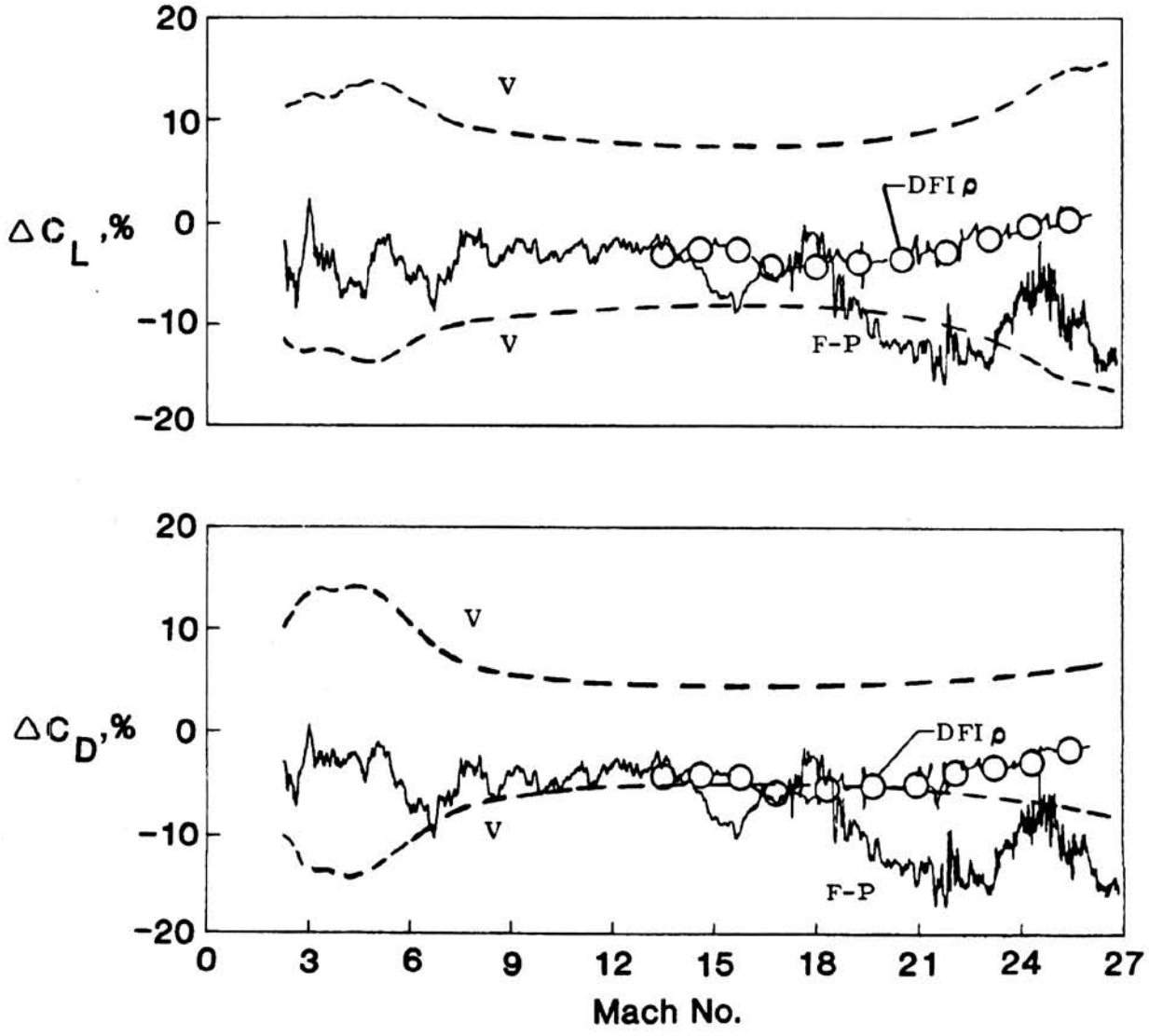

Figure 13.- STS-3 lift and drag comparisons with preflight predictions using DFI derived density (ρ).

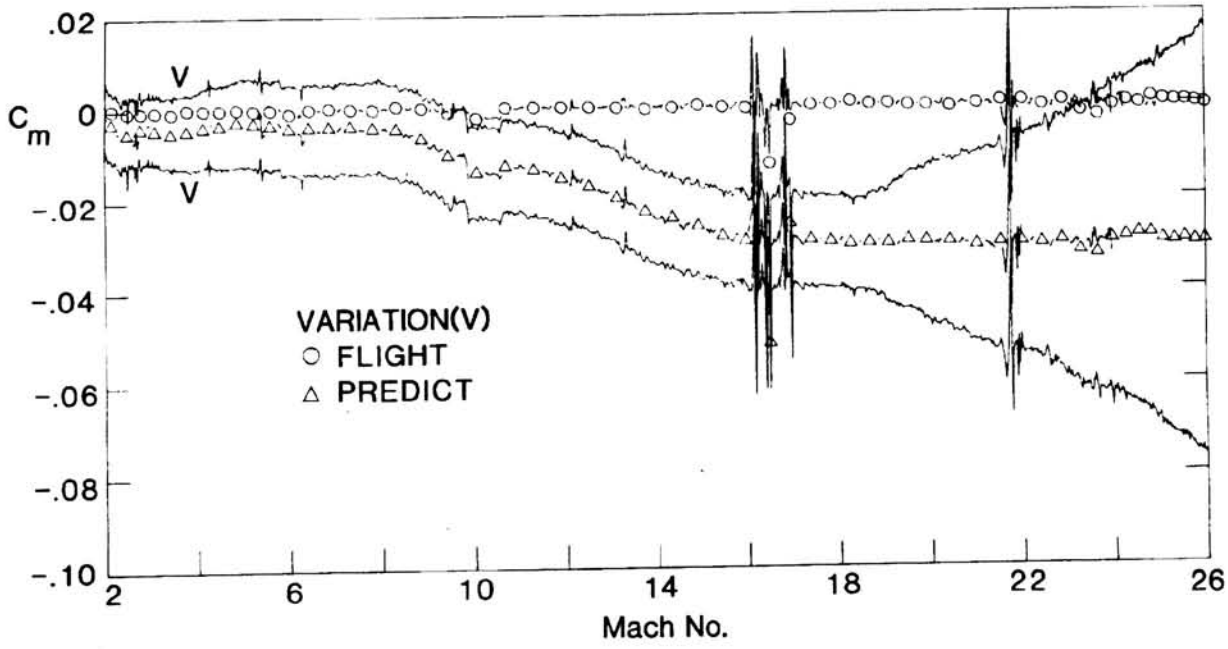

Figure 14.- STS-5 pitching moment.

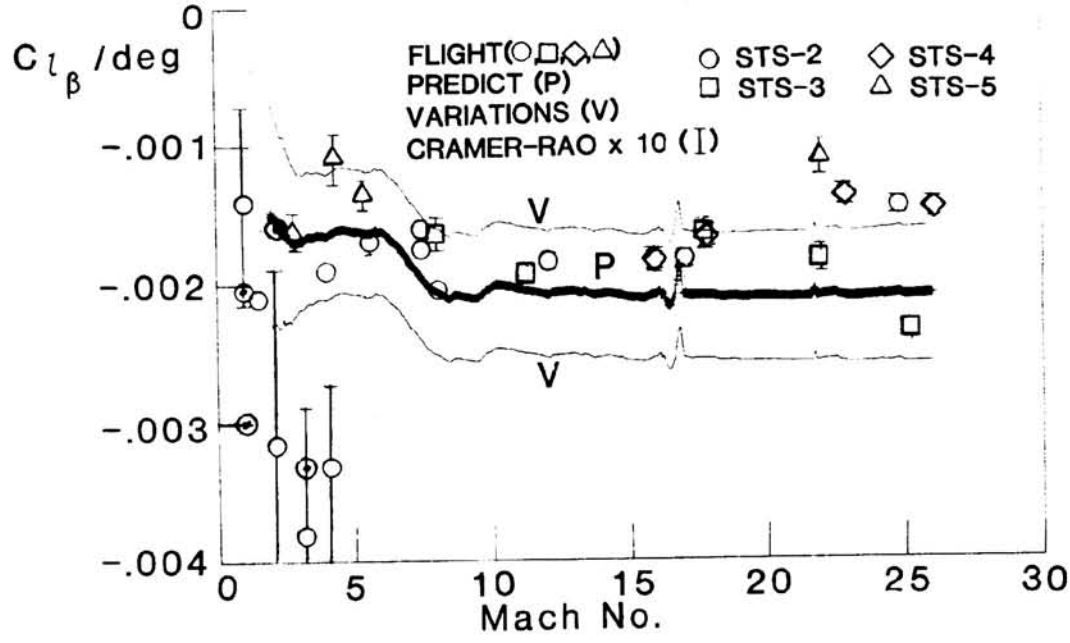

Figure 15.- Rolling moment due to sideslip.

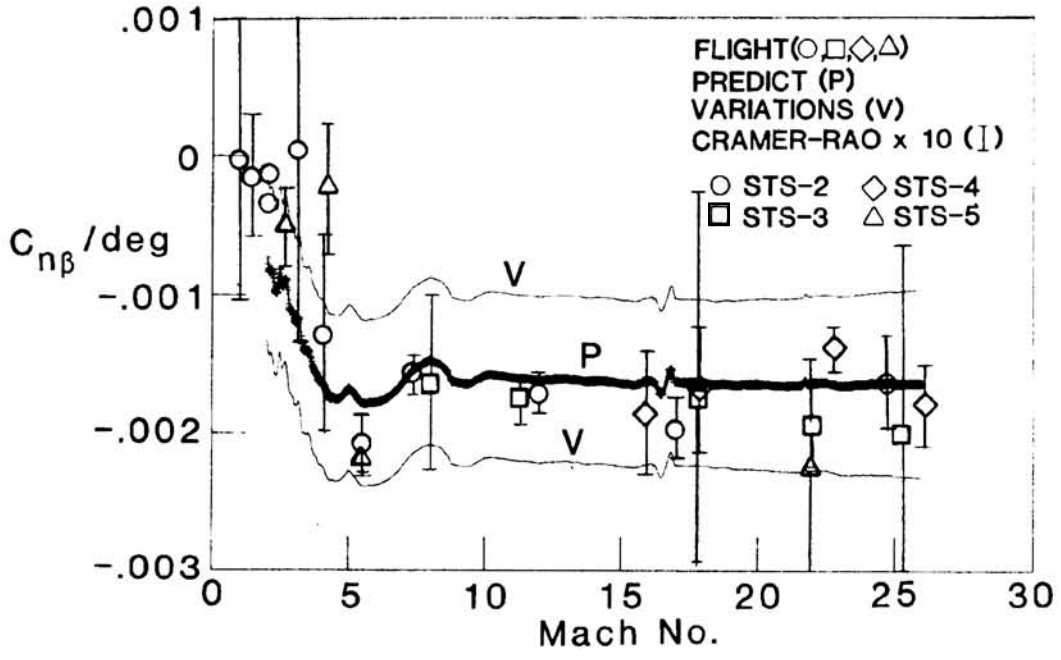

Figure 16.- Yawing moment due to sideslip.

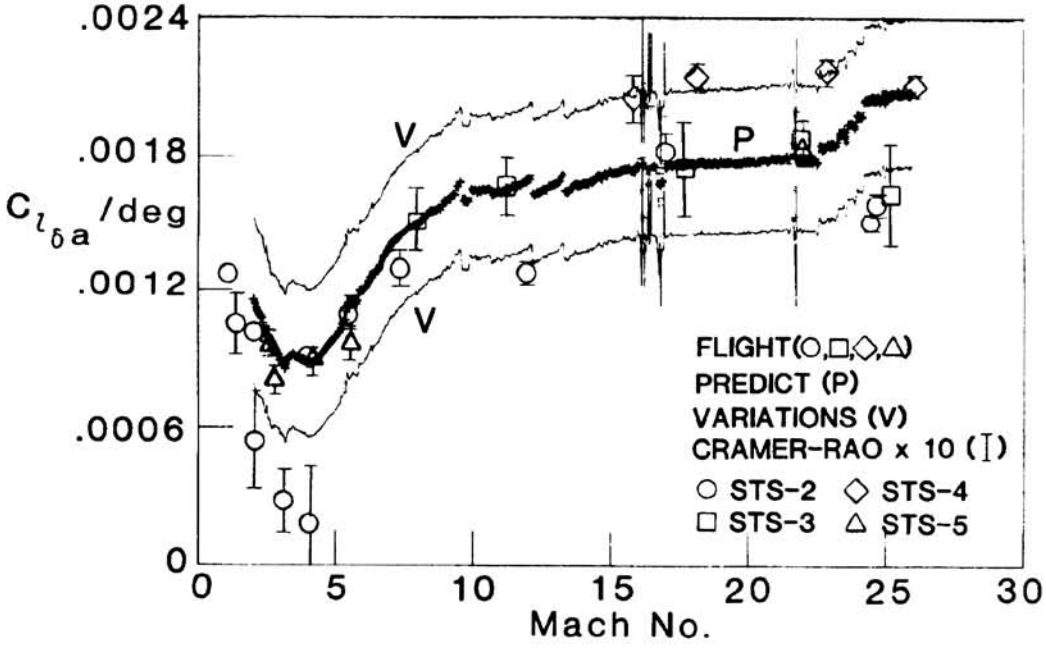

Figure 17.- Rolling moment due to aileron.

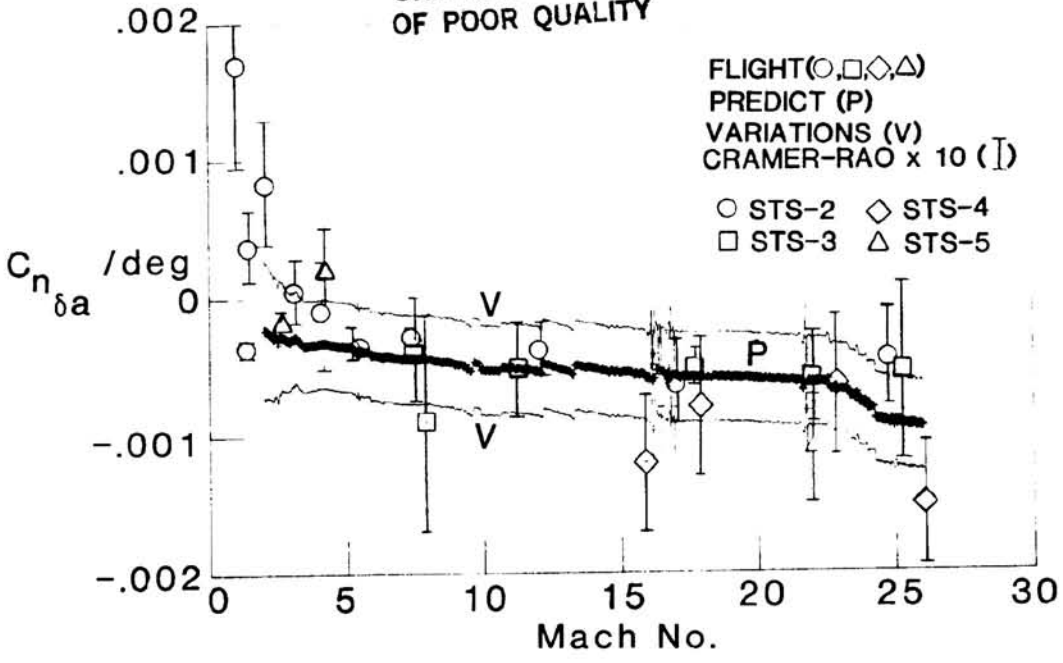

Figure 18.- Yawing moment due to aileron.

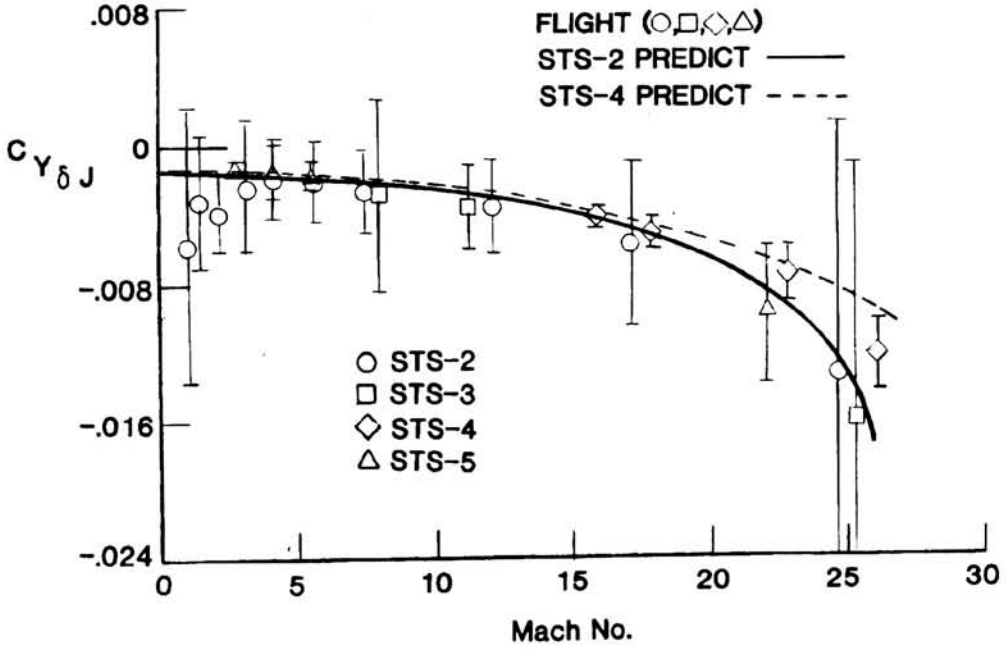

Figure 19.- Side force due to RCS.

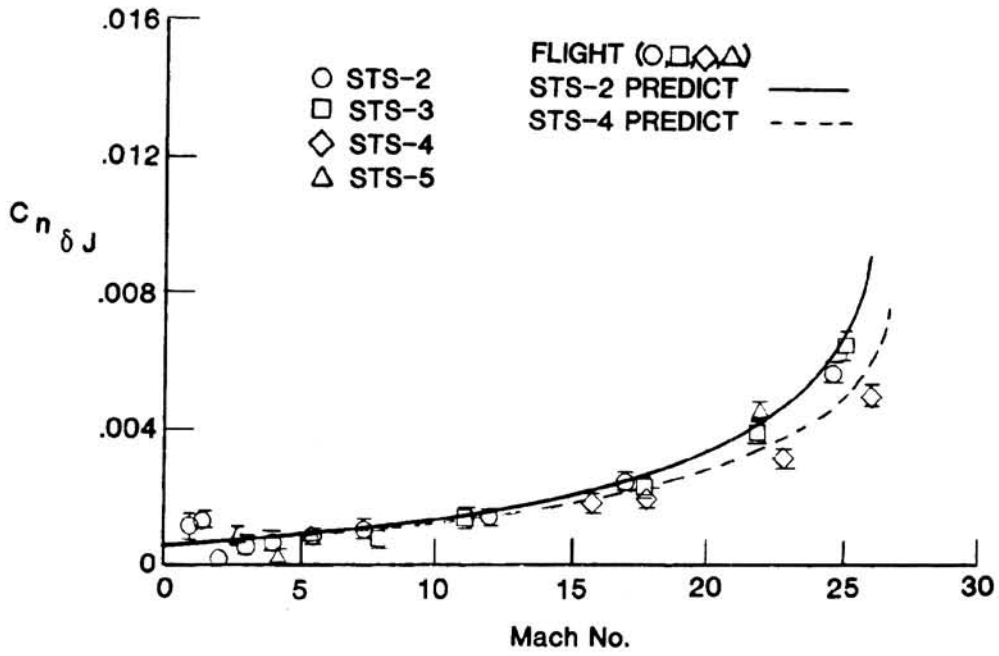

Figure 20.- Yawing moment due to RCS.

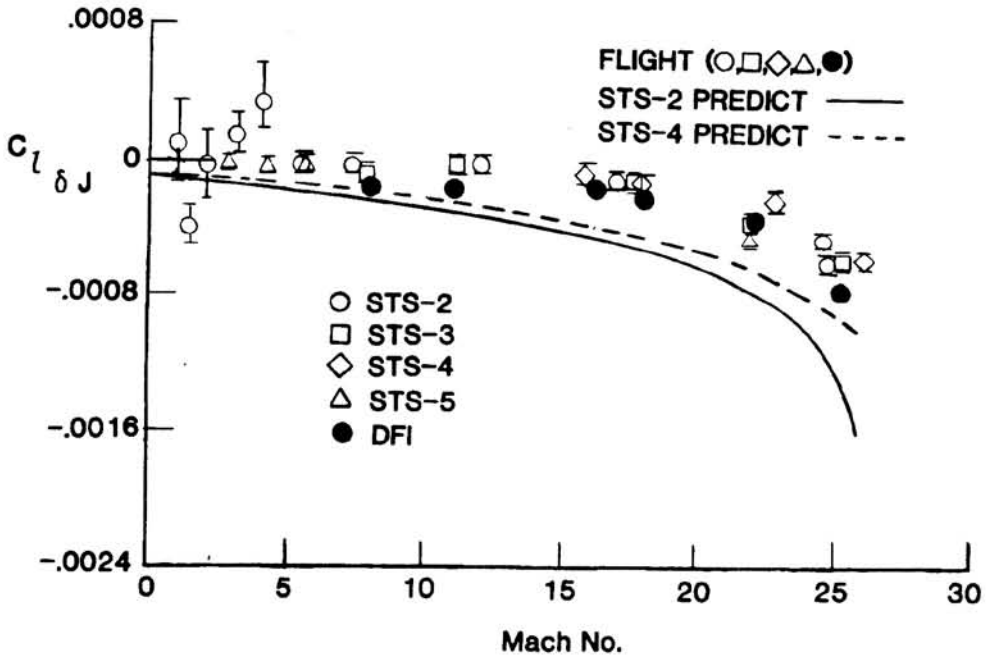

Figure 21.- Rolling moment due to RCS.

PREDICTED AND FLIGHT TEST RESULTS OF THE PERFORMANCE, STABILITY AND CONTROL OF THE SPACE SHUTTLE FROM REENTRY TO LANDING

Paul W. Kirsten, David F. Richardson,
and Charles M. Wilson
Air Force Flight Test Center
Edwards Air Force Base, California

SUMMARY

This paper presents aerodynamic performance, stability and control data obtained from the first five reentries of the Space Shuttle orbiter. Flight results are compared to predicted data from Mach 26.4 to Mach 0.4. Differences between flight and predicted data as well as probable causes for the discrepancies are given.

INTRODUCTION

The United States Space Shuttle orbiter offers a unique opportunity to correlate ground and flight test data for a manned maneuvering aerodynamic vehicle over a wide range of hypersonic velocities. Thus for the first time ground aerodynamic prediction techniques can be evaluated for extremely high velocities. In addition, the evaluation can be conducted using state-of-the-art ground and flight techniques. The Shuttle wind tunnel test program was one of the largest ever conducted, incorporating high-fidelity test facilities and wind tunnel models. Instrumentation sensors and reentry flight test maneuvers were specifically designed for the orbiter to obtain high quality flight results. Analytical computer programs which have been proven reliable on numerous flight test programs in the past were used to extract the flight data. It is therefore felt that a meaningful comparison of predicted and flight aerodynamic data can be made throughout the orbiter's reentry envelope.

ABBREVIATIONS AND SYMBOLS

AFFTC	Air Force Flight Test Center
C_A	axial force coefficient
C_D	drag force coefficient
C_L	lift force coefficient
C_ℓ	rolling moment coefficient
C_m	pitching moment coefficient
C_{m_o}	basic pitching moment coefficient

C_N	normal force coefficient
C_n	yawing moment coefficient
fps	feet per second
L/D	lift-to-drag ratio
M	Mach number
MMLE	modified maximum likelihood estimator
m_j/m_∞	yaw jet mass flow ratio ($8.296 \times 10^{-6}\ V_\infty/\bar{q}_\infty$)
NASA	National Aeronautics and Space Administration
psf	pounds per square foot
q	pitch rate, deg/sec
$\bar{q}$, $\bar{q}_\infty$	dynamic pressure, psf
STS-1,2,3,4,5	Space Transportation System flights 1, 2, 3, 4, and 5
$\bar{V}$	viscous interaction parameter
YJI	yaw jet interaction effects
α	angle of attack, degrees
β	sideslip angle, degrees
δa	aileron deflection, degrees
δBF	bodyflap deflection, degrees
δe	elevator deflection, degrees
δr	rudder deflection, degrees
δSB	speedbrake deflection (x-axis), degrees
Δ	prefix meaning increment
Subscripts:	
q, YJI, α, β, δa, δBF, δe, δr	partial derivatives with respect to the subscripted variables

DATA ACQUISITION AND ANALYSIS TECHNIQUES

One of the largest wind tunnel programs in history was conducted for the Space Shuttle (Reference 1). Over 27,000 occupancy hours were spent obtaining performance, stability and control characteristics for the orbiter from virtually every major wind tunnel facility in the United States. A significant amount of this time was spent testing the final flight configuration. Two high fidelity wind tunnel models were constructed and tested to permit accurate modeling of all aerodynamic surfaces and simulation of all aerodynamically relevant cavities, gaps, and protuberances.

Most wind tunnel testing was performed at Mach 8 and below. There were a few tests conducted above Mach 8 from which viscous interaction effects were obtained. Theoretical estimates at high altitudes (above 300,000 feet) were added to the basic wind tunnel data base to account for low density effects. Also, theoretical estimates of aeroelastic effects were incorporated at higher dynamic pressures, primarily in the transonic and subsonic regions. Real gas effects, which would primarily occur in the 150,000 to 270,000 foot altitude range, were not accounted for in the predicted data. Thus, the data referred to as "predicted" data in this report consists primarily of an extensive wind tunnel data base up to Mach 8, a limited number of wind tunnel tests above Mach 8 to obtain viscous interaction effects and high Mach effects, and theoretical estimates of low density and aeroelastic effects (Reference 2). None of the flight data contained in this report were obtained above 300,000 feet; therefore, low density effects were not applicable. Also, aeroelastic effects for most of the data presented were small in relation to the rigid wind tunnel data. Nevertheless the data must be referred to as "predicted" rather than wind tunnel data due to the extensive engineering interpretation that was applied to the basic wind tunnel data to account for such things as extrapolation of Reynolds number effects, differences between tunnels and models, and linear interpolation between test conditions.

Three types of test maneuvers specifically designed for obtaining aerodynamic data were performed during orbiter reentries: (1) pushover-pullup maneuvers to obtain longitudinal performance data as a function of angle of attack, (2) bodyflap sweeps to obtain bodyflap effectiveness, and (3) longitudinal and lateral-directional control pulses to obtain stability and control derivatives. All three maneuvers were designed on ground based simulators and practiced extensively by the flight crews prior to flight.

Lift, drag, and longitudinal trim data were computed from flight test through the use of a Flight Test Performance Data Extraction program. This program required high resolution body axis accelerometers to compute performance data. Since the orbiter is a gliding vehicle, there were not any thrust terms that had to be considered.

During a pushover-pullup maneuver, the pitch rate is sustained by an elevator deflection which also contributes to lift and drag. Therefore, the flight-derived lift, drag, and elevator deflection were corrected to zero pitch rate and pitch acceleration to obtain trimmed (equilibrium flight) data. These data were also corrected to a standard center of gravity position (66.7 percent) for comparison with the predicted data. The performance data were corrected and standardized using predicted values for elevator effectiveness ($C_{m_{\delta e}}$, $C_{N_{\delta e}}$, and $C_{A_{\delta e}}$) and predicted pitch damping coefficient data (C_{m_q}).

Stability and control derivatives were extracted from flight data through the use of a Modified Maximum Likelihood Estimator (MMLE) program (Reference 3). This program has been extensively used on numerous aircraft and lifting body vehicles in the past, and has produced reliable and accurate results. In addition to providing an estimate of the value of the derivatives, the program also computes an estimation of the accuracy of each derivative. These accuracy estimations can be invaluable in assessing the quality of the results. However, the final assessment of accuracy should be obtained from the repeatability of the results as a function of a particular flight parameter such as Mach number or angle of attack.

The input data to the performance and MMLE programs were measurements from the orbiter onboard instrumentation system with appropriate post flight calibrations/ corrections applied. The Mach number and dynamic pressure were updated based on the NASA Langley Research Center Best Estimated Trajectory analysis for STS-1 through STS-4. Orbiter weight and balance calculations were provided by NASA.

COMPARISON OF FLIGHT AND PREDICTED DATA

Selected aerodynamic data obtained from flight are compared to predicted data in this section. Additional orbiter aerodynamic flight test results were presented in an AGARD paper (Reference 4) and all the AFFTC analysis results will be published in a technical report at some future date.

Longitudinal Performance

The predicted performance and longitudinal trim data are for a rigid orbiter and are presented in Figures 1 through 8 as solid lines. Uncertainties in the predicted data are presented as dashed lines above and below the predicted data where applicable. These uncertainties were referred to as "variations" in the Shuttle program, and were obtained by comparing the differences between flight and predicted data on previous aircraft and lifting body flight test programs.

The hypersonic lift-to-drag ratio (L/D) data obtained from pushover-pullup maneuvers at Mach numbers of 7.7 and 12.4 are presented in Figure 1. These data showed excellent agreement with predictions. Similar results were obtained from pushover-pullup maneuvers at Mach 17.0 and 20.3.

The hypersonic lift and drag coefficient flight test data in general have been less than predicted due primarily to an error in the prediction of normal force coefficient (C_N) (Figure 2). Axial force coefficient (C_A) is very small (Figure 3) and consequently does not contribute significantly to the error in C_L and C_D. These data indicate that the direction of the resultant total force acting on the orbiter was predicted correctly but the magnitude was wrong. The data shown in Figures 2 and 3 are for Mach numbers of 7.7 and 12.4. The C_N and C_A data obtained from the Mach 17.0 and 20.3 maneuvers showed a similar trend.

The subsonic L/D data computed from a guidance-induced pitch maneuver are presented in Figure 4. The higher-than-predicted L/D out-of-ground effect is due primarily to the lower-than-predicted drag coefficient. The flight data values of C_L were very close to predictions. The primary cause of this error in C_D is thought to be an overprediction of the drag due to surface irregularities in the Thermal Protection System (TPS). The drag increment (.0038) to account for TPS gaps and steps was

based on theoretical calculations and was not verified with wind tunnel tests. Preliminary flight test data also indicated that the L/D in-ground effect was also higher than predicted. The higher subsonic performance required some refinements to the landing approach (revised glide slope aim points) in order to touch down at the desired point on the runway.

The trimmed flight data from a speedbrake sweep at 0.5 Mach number were corrected to a common elevator deflection (6 degrees) to obtain the normal and axial force coefficient (C_N and C_A) increments due solely to the speedbrake. This correction accounted for the contribution of C_N and C_A due to elevator which was deflected to counteract the longitudinal trim change from the speedbrake. These data were corrected to a common angle of attack (6 degrees). The resultant corrected increments were plotted as a function of speedbrake deflection in Figure 5. These data indicate that the speedbrake effectiveness was slightly greater than predicted for deflections above 50 degrees. The normal force decrement due to speedbrake was less than predicted. Note that both of these increments were dependent upon the values for the longitudinal derivatives that were used to correct the flight data to the standard elevator and angle of attack. Predicted values were used for these derivatives and will be updated whenever flight test data become available.

The orbiter flight control software logic contains a bodyflap-elevator interconnect designed to maintain the elevator on a predefined schedule as a function of Mach number by automatic trimming of the bodyflap. A significant error in longitudinal trim in the hypersonic Mach regime was apparent on all five orbiter reentries. For example, during STS-1 the trim bodyflap was 16 degrees rather than 7 degrees at Mach numbers greater than 17 (Figure 6). Analysis of the bodyflap sweeps and the pitch pulse performed during the second orbiter reentry established that the major contributor to the trim error was an error in the basic pitch curve, C_{m_o}, rather than an error in elevator or bodyflap effectiveness. Figure 7 contains trim data obtained during the bodyflap sweep at a Mach number of 21.5. These data were corrected to a constant α of 39 degrees and are presented at the flight center of gravity. Note that the slope of the flight test data is similar to, or slightly greater than predicted. Similar results were obtained from bodyflap sweeps at Mach 16.6 and 12.1. The trim elevator data obtained from the pushover-pullup maneuvers at Mach numbers of 20.3 and 17.0 (Figure 8) showed that the orbiter was statically stable and the slopes indicated that the combined elevator effectiveness/pitch static stability was close to predictions. The foregoing tends to confirm that the mispredicted longitudinal trim at hypersonic Mach numbers is attributable to an error in basic pitching moment (C_{m_o}). The error in C_{m_o} for Mach numbers greater than 16 varied between 0.026 and 0.029 (average of .0275) depending on the flight from which the data were obtained (Figure 8). This flight to flight difference corresponds to an uncertainty in the longitudinal center of gravity of $\pm$2.0 inches.

The primary cause of the error in the predicted hypersonic values of C_{m_o} is felt to be real gas effects. Real gas effects are the aerodynamic effects resulting from deviations of real air thermodynamic properties from ideal gas with constant specific heat. These effects were not fully simulated in wind tunnel tests and were not accounted for in the predicted aerodynamic data base of the orbiter. Real gas

effects are most significant between 150,000 and 270,000 feet (Mach numbers greater than 8.0). Recent analytical studies performed by the Arnold Engineering Development Center, which are the subject of a separate paper in this conference, indicate real gas effects could produce a pitch-up increment of .024 above Mach 18, which is very close to the difference between flight and predicted results (Reference 5).

The remaining small difference between flight and predicted values of C_{m_o} could be caused by viscous interaction and high Mach number effects. These effects are thought to be small in comparison to real gas effects, however, and tend to cancel each other.

The most significant effect of the error in the prediction of hypersonic trim will be increased heating on the bodyflap and/or elevon due to the more downward deflection required. Additional downward deflection, and increased heating, would be required for more aft longitudinal centers of gravity. However, it appears that heating margins are adequate to achieve the most aft center of gravity required in the Shuttle program provided that a suitable elevon schedule is used.

Lateral-Directional Derivatives

Lateral-directional derivative results obtained from pulse maneuvers during STS-2, 3, 4, and 5 are contained in Figures 9 through 12. Uncertainty estimates for the predicted and flight data are also shown. The predicted data is represented by a solid line, while the short dashed line represents a fairing of the flight data. Flight data uncertainties are presented as vertical bars about the derivative value. Predicted data uncertainties are presented as dashed lines. Since the orbiter's reentry profile for the parameters which affect derivative results was very similar for the first five flights, predictions appropriate for only the STS-2 trajectory are presented in the figures and the flight test data from the other flights are corrected to the STS-2 trajectory.

The dihedral effect (C_{ℓ_β}) is presented in Figure 9. Flight results varied with Mach number above Mach 12 and were considerably less negative than predicted at very high Mach numbers. The consistency of the flight results as a function of Mach number, and the flight uncertainty estimates, were considerably smaller than the uncertainty of the predicted data for most maneuvers, indicating high confidence in the flight results in this regime. Large uncertainties were contained in the STS-2, 3, and 4 flight results below Mach 3.5. The primary cause for this was that three control effectors (rudder, aileron, and yaw jets) were activated simultaneously during the pulse maneuvers performed on these flights. Extraction of accurate lateral-directional derivatives was not possible from these maneuvers. Independent control effector pulses were performed on STS-5, and the uncertainty estimates of the flight results were considerably smaller. The STS-5 flight value of C_{ℓ_β} was close to predicted at Mach 2.75 but more negative than predicted at Mach 1.6. A small amplitude lateral-directional oscillation always occurs around Mach 1.6 in flight. The higher-than-predicted dihedral effect is a possible contributor to this oscillation. Another possible cause of the oscillation has been postulated to be shock detachment and reattachment on the vertical fin which results in movement of the center of pressure on the fin.

Flight results for the directional stability derivative (C_{n_β}) were slightly less negative than predicted throughout most of the Mach range. Nonlinearities in the derivative as a function of sideslip angle may be causing some of the apparent scatter in the flight results below Mach 10. Insufficient flight data has been obtained thus far to determine the nonlinearity.

Aileron derivatives are presented in Figure 10. The predicted curves for $C_{\ell_{\delta a}}$ and $C_{n_{\delta a}}$ were based on the STS-2 reference elevator bias schedule. All flight data have been corrected to the STS-2 reference schedule using predicted values of elevator effects. STS-2, 3, and 4 were flown at elevator bias positions of 1, 3, and 5 degrees respectively above Mach 12. Flight values of the aileron effectiveness derivative ($C_{\ell_{\delta a}}$) obtained at elevator positions of 3 and 5 degrees were higher than predicted above Mach 12, while flight data obtained at all other elevator positions were close to predicted. Although not shown, trends in the data indicate that the high Mach number wind tunnel data obtained at zero degrees of elevator deflection may be correct, while the data obtained at five degrees may be inaccurate.

Flight values of $C_{\ell_{\delta a}}$ were lower than predicted between Mach 3 and 1. Low aileron effectiveness is another possible cause of the small amplitude lateral-directional oscillation which occurs in this flight regime. Wind tunnel data obtained after the first flight at the precise conditions and vehicle configurations experienced in flight produced lower $C_{\ell_{\delta a}}$ values in the Mach 3 to 1 region than the preflight predicted tunnel data and agreed well with flight results.

Flight results for $C_{n_{\delta a}}$ followed the trend of those for $C_{\ell_{\delta a}}$ at high Mach numbers. Flight results for $C_{n_{\delta a}}$ were close to predicted below Mach 8. Data obtained from sharp, independent pulsing of individual control effectors at Mach 1.6 on STS-5 were considered to be much more accurate than data obtained on STS-2 in the transonic regime.

Rudder derivatives are presented in Figure 11. Flight results for $C_{\ell_{\delta r}}$ were slightly greater than predicted. More positive roll due to rudder is another possible contributor to the small amplitude lateral-directional oscillation in the Mach 1.6 flight regime. The flight fairing was weighted heavily toward the more accurate STS-5 results. Flight results for $C_{n_{\delta r}}$ agreed very well with predictions. The rudder is presently used in the orbiter's flight control system only from Mach 3.5 to landing. The new automatic pulse logic used on STS-5 allowed a rudder pulse to be applied just prior to the actuator and bypass the flight control system rudder disconnect logic. A rudder pulse was performed at Mach 4.4 on this flight to obtain higher Mach number rudder derivatives. Some effectiveness was obtained for the rudder from the Mach 4.4 pulse. These results could allow the rudder to be activated sooner on future flights.

Since the aft reaction control jets are located above the wing at the base of the vertical tail of the orbiter, the plume produced when the jets are fired can interact with the flow field over the vehicle and alter the basic aerodynamic forces and moments. These effects are referred to as jet interaction effects, and are presented in derivative form in this report. Jet interaction effects are presented as a function of mass flow ratio, a parameter used to extrapolate Mach 10 wind tunnel data to higher Mach numbers. (Jet interaction effects were not obtained at Mach numbers greater than 10 in wind tunnel tests.) The derivative values presented are a measure of the jet plume interaction with the aerodynamic flow only, and do not contain the basic thrust and moment components of the jets. The AFFTC model for the yaw axis reaction control jets used in the MMLE analysis assumes the interaction effects produced by these jets to be a function of the number of jets fired.

Yaw jet interaction effects are presented as a function of yaw jet mass flow ratio in Figure 12. Flight fairings for two and four jets are presented. Three jets rarely fired long enough during a maneuver to obtain accurate data. The three-jet value was usually held fixed while analyzing these maneuvers. The predicted data were independent of the number of jets firing, and are presented as a single line.

Flight values for the roll-due-to-yaw-jet interaction effect ($C_{\ell_{YJI}}$) were significantly less than predicted at high values of mass flow ratio. The two and four jet values were fairly consistent with mass flow ratio, and high confidence is therefore placed in the flight fairings. The smaller-than-predicted value of $C_{\ell_{YJI}}$ was the major cause of a large amplitude, lightly damped lateral-directional oscillation which occurred during the initial bank maneuver performed on STS-1 at a mass flow ratio of .015 (Mach = 26, dynamic pressure = 14 psf). Yaw jet interaction wind tunnel data were obtained at a maximum Mach number of 10.3 and a minimum dynamic pressure of 75 psf. The extrapolation of this data to high Mach, low dynamic pressure flight conditions was probably invalid due to the differences in wing wake boundary static pressure levels during the wind tunnel tests and in the actual flight environment. The first bank maneuver on STS-1 was performed in the automatic flight control system mode. On subsequent flights, the maneuver was performed manually by the commander at a slower rate to avoid the large oscillation. A flight control system modification was made on STS-5 which provided adequate control in either mode.

The four-jet flight value of $C_{\ell_{YJI}}$ was greater than predicted between mass flow ratios of .0027 and .0002. A discontinuity exists in the flight data at a mass flow ratio of .0002. At this point in the trajectory, the angle of attack is approximately 22 degrees. The flight data implies that the yaw jet interaction effects do not exist below 22 degrees angle of attack, possibly because the jets are out of the wing wake and in the free stream at these angles of attack.

Flight values of yaw-due-to-yaw-jet interaction effect ($C_{n_{YJI}}$) were slightly greater than predicted throughout reentry. The difference was much smaller than that obtained for $C_{\ell_{YJI}}$, however, and had little effect on the orbiter's flying qualities.

CONCLUDING REMARKS

Aerodynamic performance and stability data have been successfully obtained from the first five reentries of the Space Shuttle orbiter. Generally good correlation was achieved between flight results and the orbiter's predicted data base. Some differences did occur, primarily at high Mach numbers and altitudes. The basic normal force at hypersonic Mach numbers was less than predicted. Also, the basic pitching moment was significantly different than predicted above Mach 8. These differences are thought to be caused by real gas effects at high altitudes.

The interaction of the yaw reaction control jets with the aerodynamic flow field was overpredicted at low dynamic pressures, and caused a lightly damped oscillation during a bank maneuver performed early in the reentry. The overprediction was due to incorrect extrapolation from wind tunnel test conditions to very low dynamic pressure flight conditions. A flight control system modification was made on STS-5 which provided adequate control during this maneuver.

Three primary lateral-directional derivatives, C_{ℓ_β}, $C_{\ell_{\delta a}}$, and $C_{n_{\delta a}}$, have been inaccurately predicted above Mach 12. It appears that Mach number, viscous interaction, real gas or low density effects have not been properly accounted for in the prediction of C_{ℓ_β}. Also, apparently the wind tunnel aileron data obtained at an elevator setting of five degrees was inaccurate at high Mach numbers.

The small amplitude lateral-directional oscillation which has occurred near Mach 1.6 during the reentries may be the result of decreased lateral-directional stability due to lower-than-predicted aileron effectiveness ($C_{\ell_{\delta a}}$), higher-than-predicted dihedral effect (C_{ℓ_β}), and more positive roll due to rudder ($C_{\ell_{\delta r}}$). Another possible cause has been postulated to be shock detachment and reattachment on the vertical fin which results in movement of the center of pressure. The bodyflap was deflected to its upper limit at Mach 1.6 during flight. Thus more forward longitudinal center of gravity movement would require the elevator to be deflected further up to maintain the desired trim angle of attack. An increased up elevator deflection would decrease $C_{\ell_{\delta a}}$ somewhat, which could in turn degrade the lateral-directional stability. The transonic oscillation could therefore restrict the forward center of gravity limit of the orbiter until the causes of the oscillation are more completely understood.

The subsonic lift-to-drag ratio was greater than predicted due primarily to an overprediction of the drag due to the roughness of the thermal protection system. The landing approach pattern was altered somewhat after STS-1 to compensate for the increased L/D.

In summary, the aerodynamic mispredictions have not been of major consequence to the reentry because of the conservative design of the orbiter. Also, training simulators have been updated in a timely manner with flight results, allowing the crews to train with the best available aerodynamics. In general, the aerodynamic predictions have been good considering the extensive Mach number range of the

orbiter. However, some predictions need improvement which once again points out the value of adequate flight testing. It is apparent that future reentry vehicles will rely heavily on state-of-the-art analytical prediction techniques to fill areas outside the wind tunnel capabilities.

REFERENCES

1. Underwood, Jimmy M. and Cooke, Douglas R., A Preliminary Correlation of the Orbiter Stability and Control Aerodynamics from the First Two Space Shuttle Flights (STS-1 and 2) with Preflight Predictions, AIAA Paper 82-0564, March 1982.

2. Aerodynamic Design Data Book, Orbiter Vehicle 102, SD2-SH-0060, Volume 1L, October 1978, plus Revisions 1, 2, and 3, Rockwell International, Space Division, Downey, California.

3. Maine, Richard E. and Iliff, Kenneth W., User's Manual for MMLE-3, A General Fortran Program for Maximum Likelihood Parameter Estimation, NASA Technical Paper 1563, November 1980.

4. Kirsten, Paul W. and Richardson, David F., Predicted and Flight Test Results of the Performance and Stability and Control of the Space Shuttle from Reentry to Landing, Paper presented at the AGARD 61st Flight Mechanics Panels Meeting, Symposium on Ground/Flight Test Techniques and Correlation, Cesme, Turkey, October 11-15, 1982.

5. Griffith, B. J., Maus, J. R., and Best, J. T.: Explanation of the Hypersonic Longitudinal Stability Problem, Shuttle Performance: Lessons Learned, NASA CP-2283, Part 1, 1983, pp. 347-381.

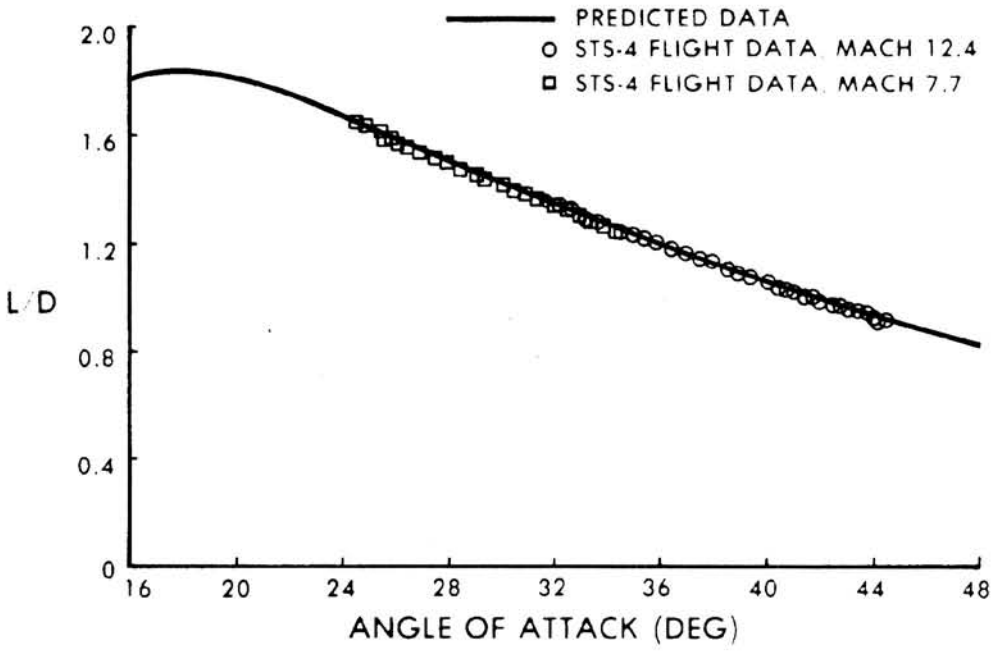

Figure 1.- Hypersonic lift-to-drag ratio data.

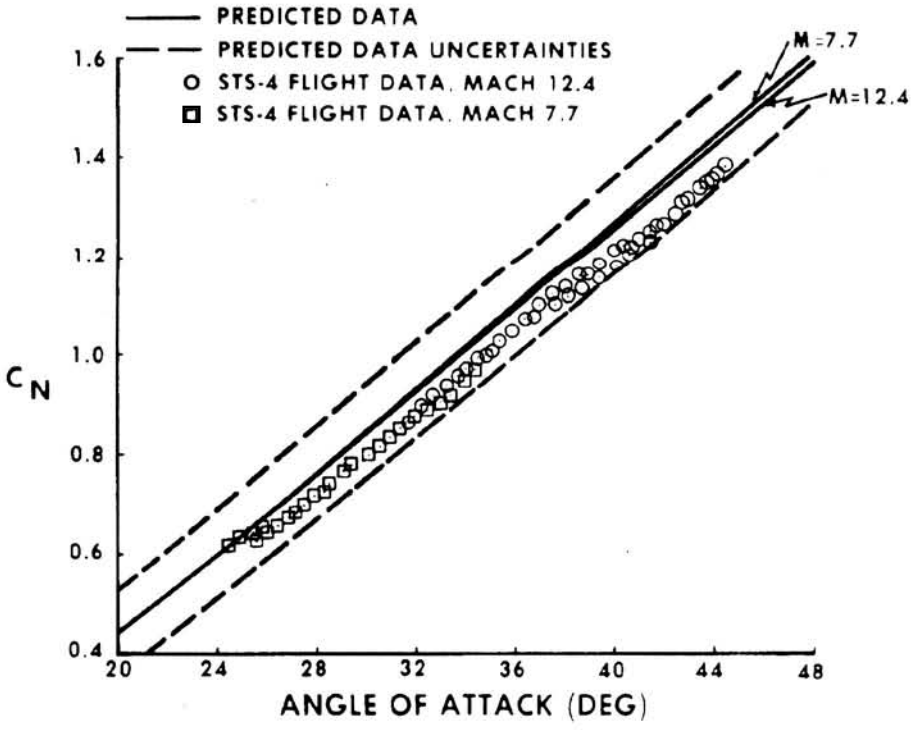

Figure 2.- Hypersonic normal force data.

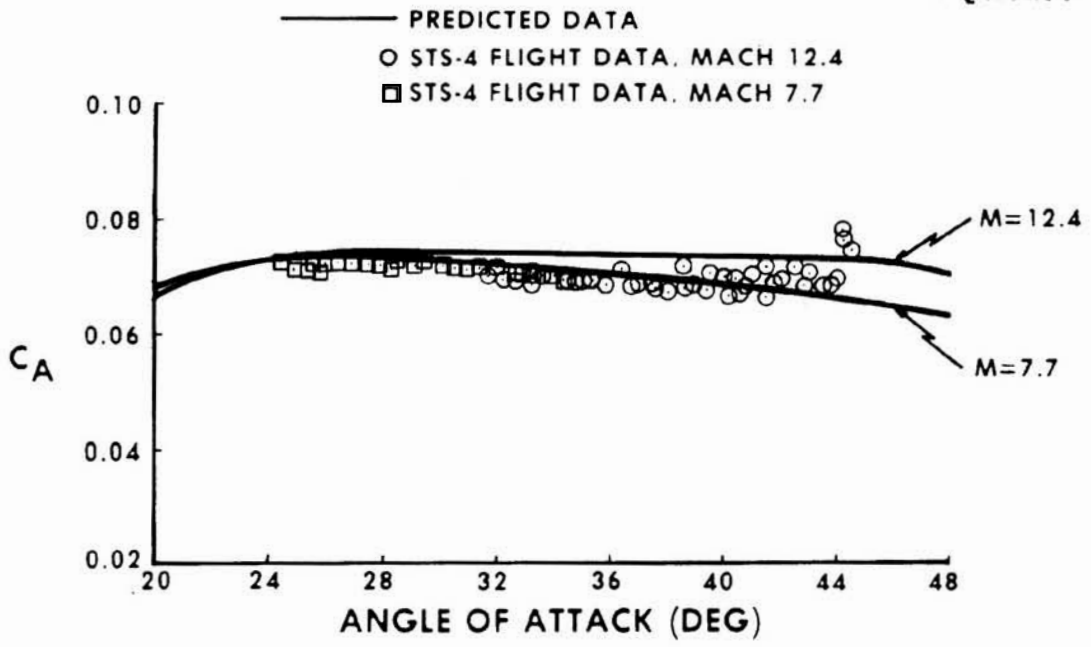

Figure 3.- Hypersonic axial force data.

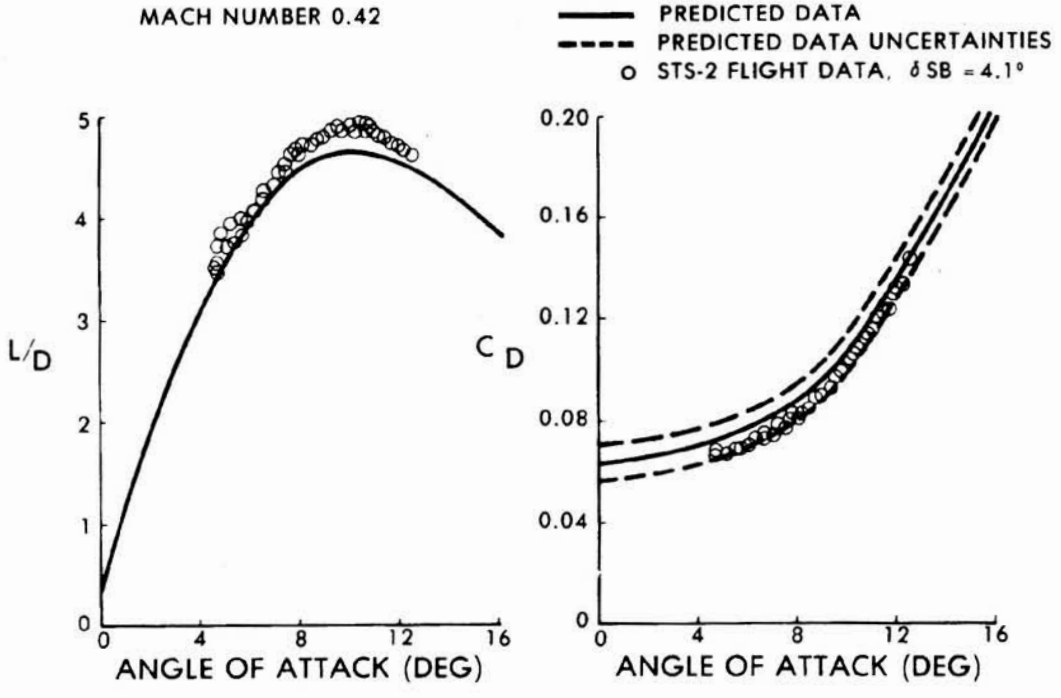

Figure 4.- Subsonic performance data.

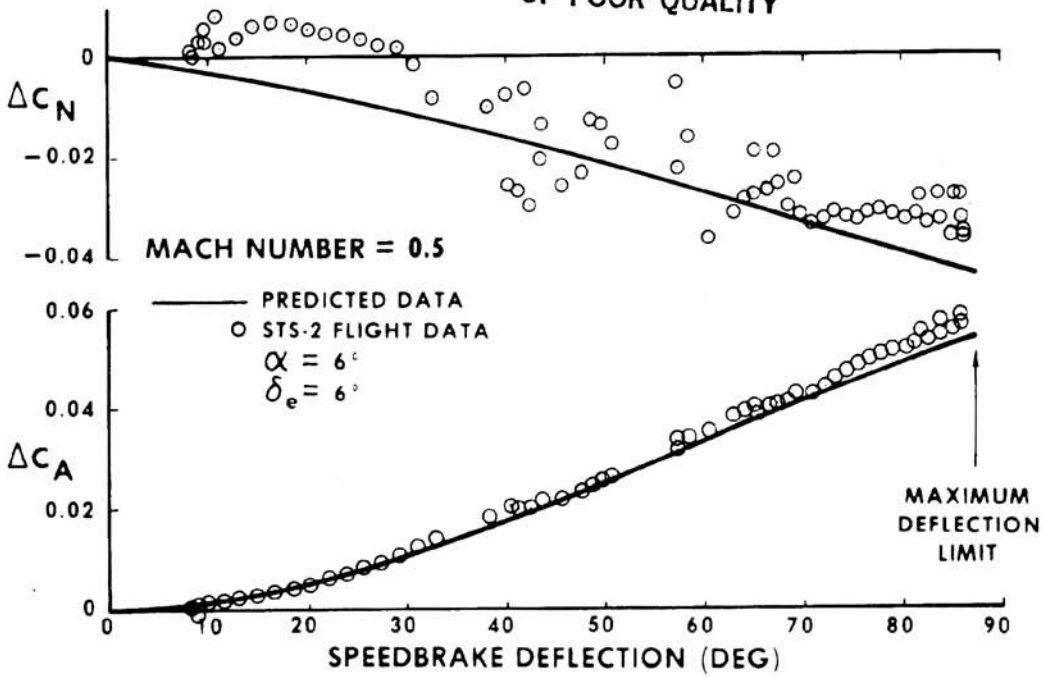

Figure 5.- Subsonic speedbrake effectiveness.

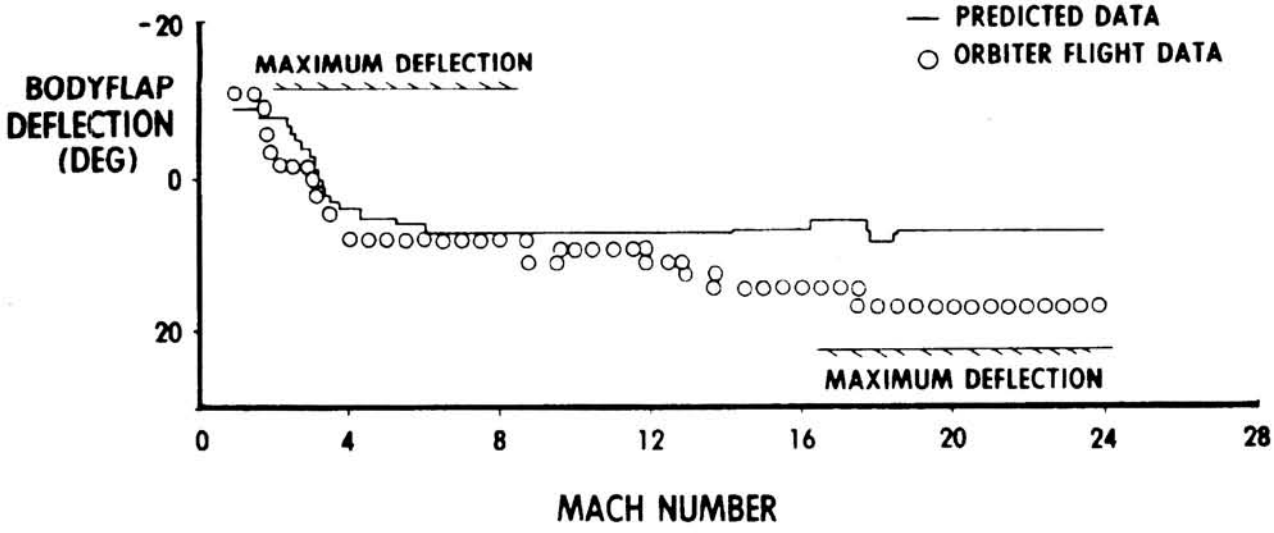

Figure 6.- Longitudinal trim characteristics.

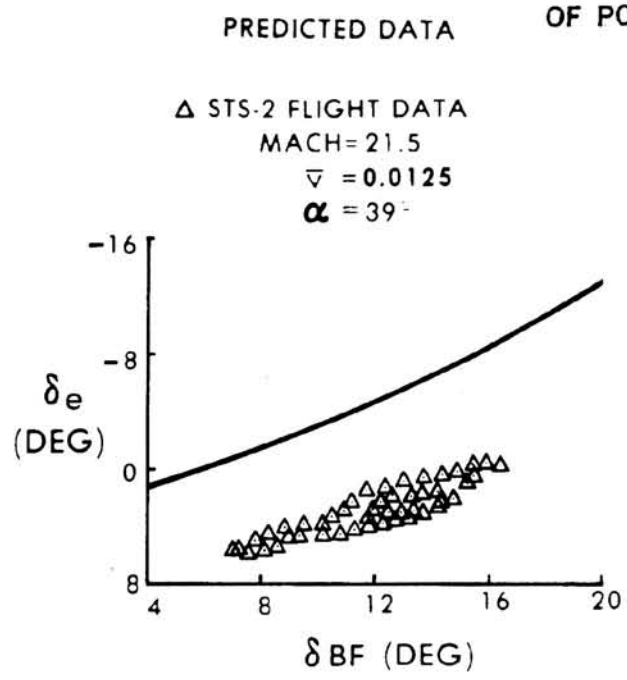

Figure 7.- Hypersonic longitudinal trim data.

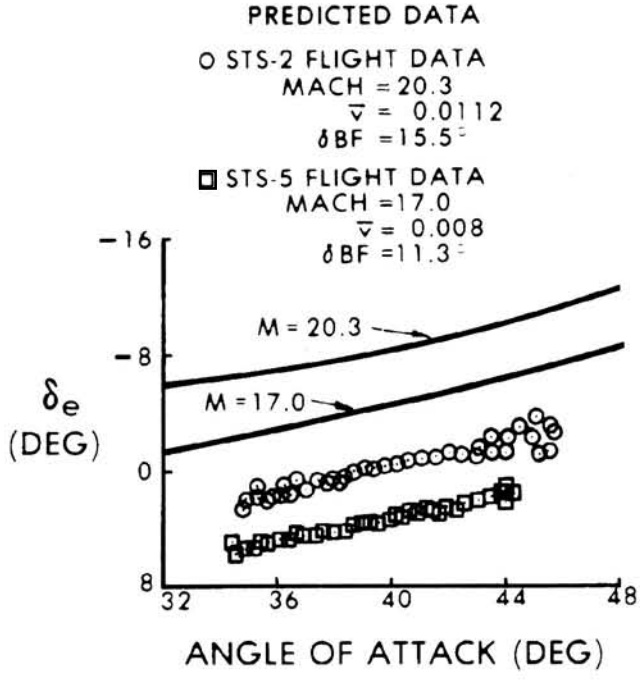

Figure 8.- Elevator trim angles during pushover-pullup maneuvers.

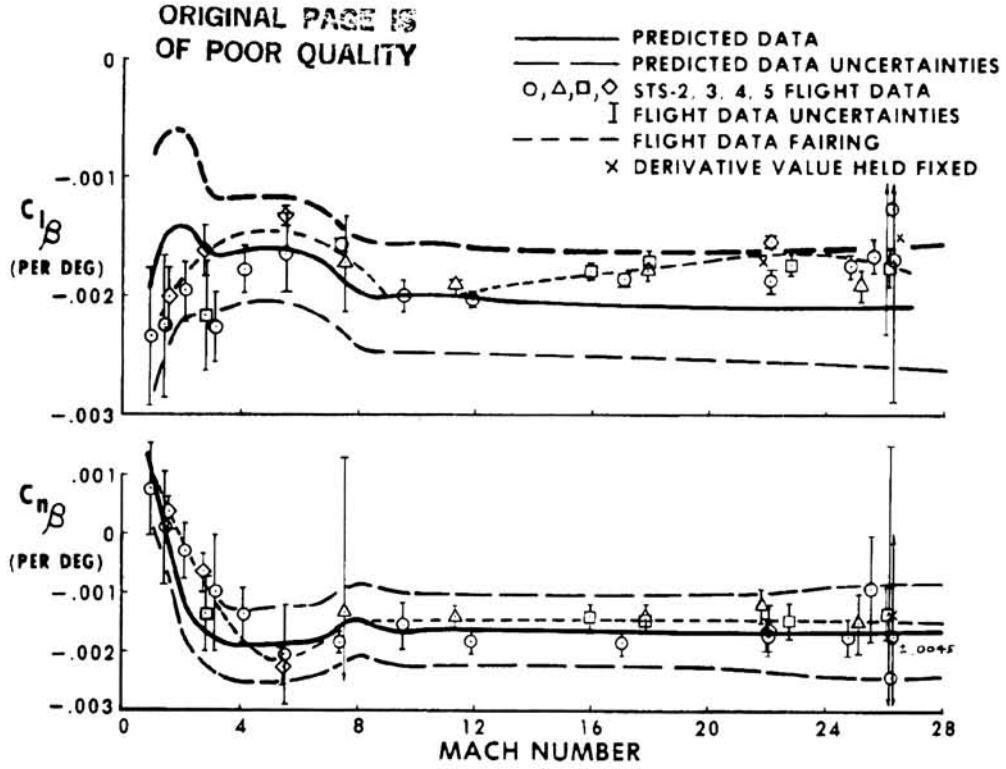

Figure 9.- Sideslip derivatives.

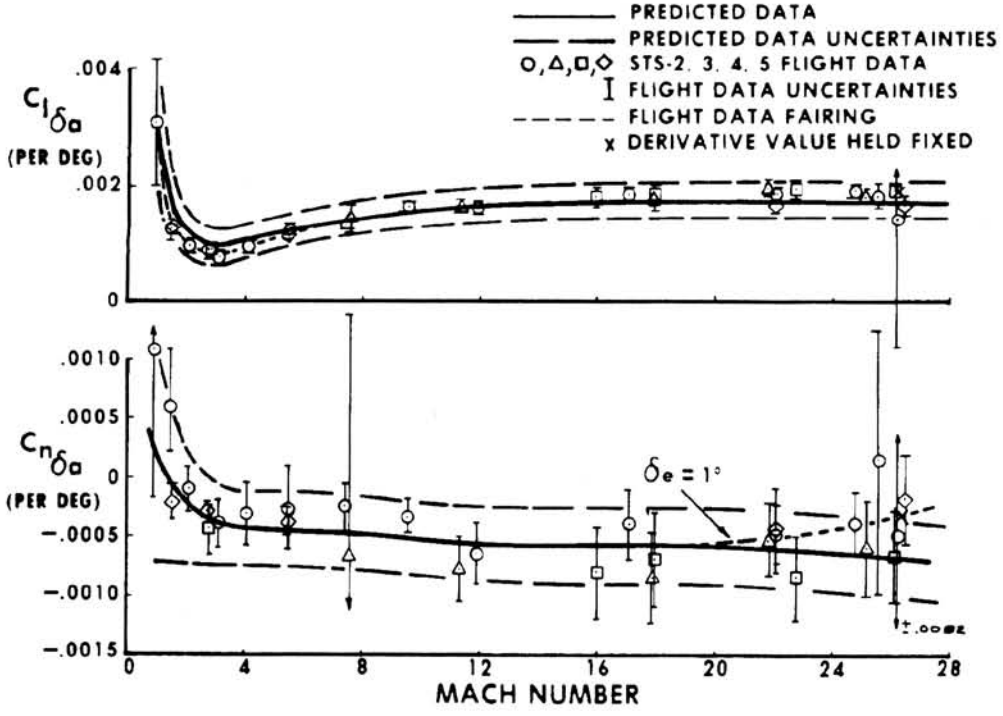

Figure 10.- Aileron derivatives.

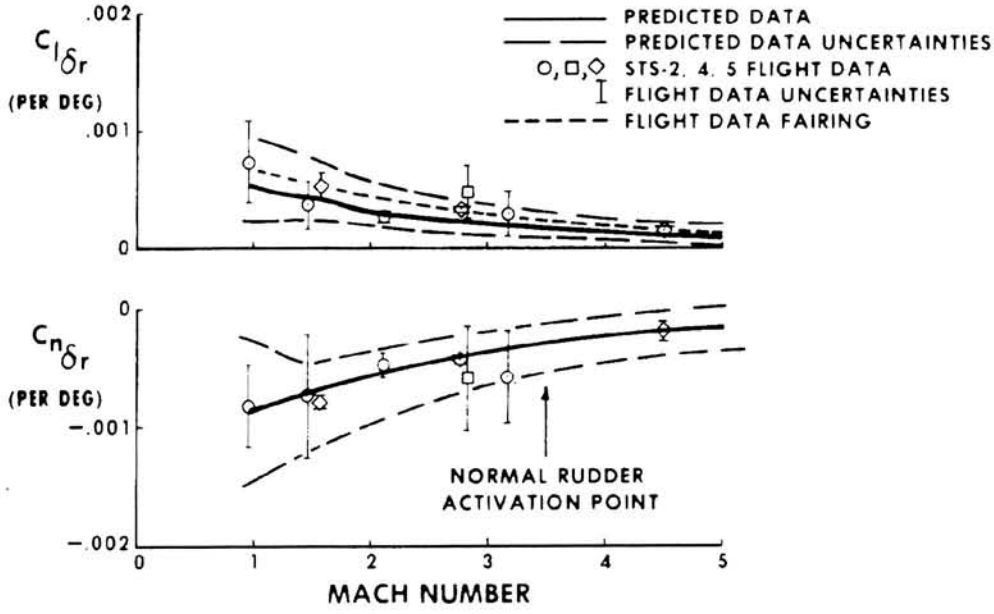

Figure 11.- Rudder derivatives.

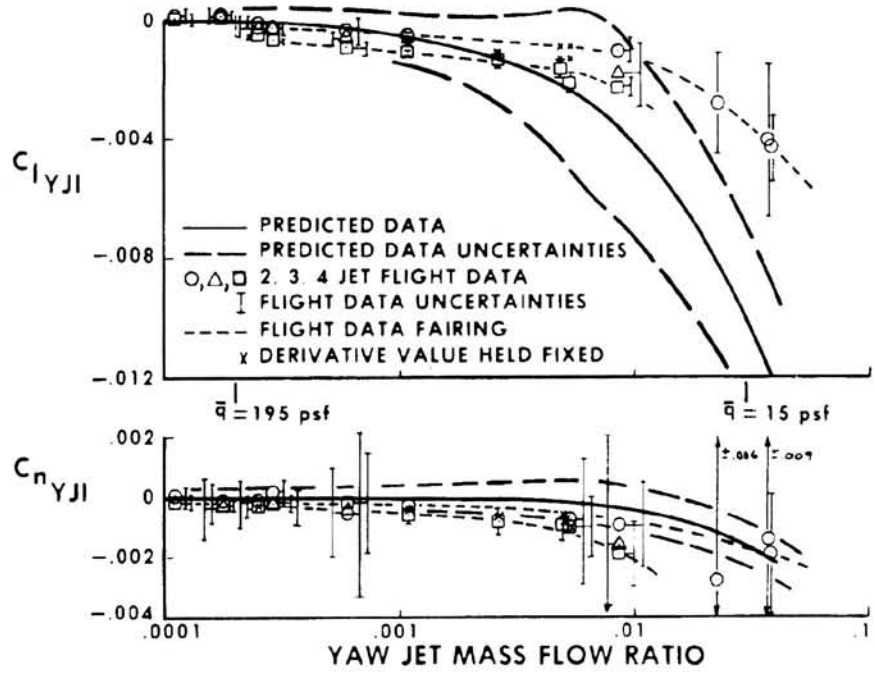

Figure 12.- Yaw jet interaction derivatives.

LATERAL-DIRECTIONAL STABILITY INVESTIGATION OF THE SPACE SHUTTLE ORBITER AT MACH 6

Robert L. Calloway
NASA Langley Research Center
Hampton, Virginia

SUMMARY

Lateral-directional aerodynamic data and oil-flow visualization results are presented from four tests (conducted in two facilities using three models) which were designed to verify the hypersonic aerodynamics of the Space Shuttle orbiter at M=6. Comparisons of measured lateral-directional stability data and oil-flow results between the tests show excellent agreement, especially considering the nonuniform, unpredictable flow which occurs in the vicinity of the vertical tail. Results were shown to be sensitive to Reynolds number with the higher Reynolds number cases producing more stable values and also showing good agreement with flight values. The results also show that the effects of Reynolds number, angle of attack, and angle of sideslip on the lateral-directional stability of future entry configuration should be carefully assessed for non-linearities.

INTRODUCTION

The Shuttle orbiter is the most complex configuration that has reentered our atmosphere. In the hypersonic regime, where the angle of attack changes from approximately 40° to 20° while the Mach number changes from 30 to 4, the flow field around the orbiter is extremely complex. The Aerodynamic Design Data Book (ref. 1) did an excellent job predicting (indirectly) the levels of control input needed to conduct a safe return to Earth. The ADDB values were based on numerous wind-tunnel tests on various models. Much time was spent to assess the effects of flow-field parameters, model fidelity, and wind-tunnel repeatability/accuracy on the hypersonic aerodynamics of the orbiter. Since no prototype orbiter was built for testing at hypersonic speeds and since there are no facilities which can duplicate all hypersonic entry conditions, final determination of the ADDB values was a mixture of experimental and theoretical data and appropriate extrapolations to flight conditions.

For the Mach 5 to Mach 8 region, ADDB values were based on tests conducted at the Arnold Engineering Development Center's VKF Tunnel B at those Mach numbers, with interpolations for cases within those values. The tests were conducted on a 0.02-scale model, and Reynolds number effects were not assessed. At the request of the Shuttle Program Office, a 0.004-scale model was tested in the Langley 20-Inch Mach 6 Tunnel to verify Mach 6 interpolated ADDB values and to investigate abort maneuver aerodynamics. Langley test results showed significant lateral-directional instabilities at flight attitudes and control surface settings. Further oil-flow visualization and aerodynamic testing showed that these instablities were sensitive to Reynolds number, angle of sideslip, and angle of attack. At the lower test Reynolds numbers, large nonlinearities and aerodynamic hysteresis were observed in the measured yawing-moment and rolling-moment coefficient results, making the data acquisition technique critical.

As a result of the Langley tests, a new series of tests was scheduled. These tests were designed to answer the questions of lateral-directional instabilities completely by testing at Vought's 4' x 4' Tunnel (M=2 → 4.75), AEDC's Tunnel B (M=6 and 8), and Langley's 20-Inch Mach 6 Tunnel, using a high fidelity 0.02-scale model and medium fidelity 0.01-scale model. All tests were conducted at maximum Reynolds numbers to approach flight conditions and at other Reynolds numbers to assess those effects. Oil-flow tests were conducted on the 0.02-scale model at AEDC's Tunnel B and on the 0.01-scale model at Langley's 20-Inch Mach 6 Tunnel to better understand the flow phenomena responsible for the measured changes in lateral-directional stability. To further understand this flow phenomena, component buildup studies on the OMS pods and vertical tail were conducted. Results from this series of tests produced the so-called "Pre-op ADDB" for the Mach 2.5 to 8 range (ref. 2). Although the Pre-op ADDB values are within the ADDB variations, flight data showed better agreement with the Pre-op ADDB.

The purpose of this paper is to present a portion of the M=6 results from the series of wind-tunnel tests just described and show comparisons with flight data. The effects of Reynolds number, angle of sideslip, angle of attack, speedbrake setting, and component buildup on the lateral-directional stability of the orbiter are assessed for angles of attack of 20°, 25°, and 30° and speedbrake settings of 87° and 0°. Also, comparisons of the aerodynamic data and the oil-flow visualization results from tests in the two facilties using three different-sized models over a range of length Reynolds numbers are made.

SYMBOLS

b wing span, in

C_ℓ rolling-moment coefficient, $\dfrac{\text{Rolling moment}}{q\ S\ b}$

C_{ℓ_β} lateral-stability parameter, $\Delta C_\ell/\Delta\beta$, per deg

C_n yawing-moment coefficient, $\dfrac{\text{Yawing moment}}{q\ S\ b}$

C_{n_β} directional-stability parameter, $\Delta C_n/\Delta\beta$, per deg

$\bar{c}$ wing mean aerodynamic chord, in

M free-stream Mach number

q free-stream dynamic pressure, psi

$Re_{\bar{c}}$ Reynolds number based on wing chord and free-stream conditions

S wing planform area, in^2

α angle of attack, deg

β angle of sideslip, deg

δ_{SB} speedbrake deflection angle, deg

ACRONYMS

ADDB Aerodynamic Design Data Book

OMS Orbital Maneuvering System

VKF Von Karman Facility

V.T. Vertical Tail

DESCRIPTION OF TESTS

The pertinent information for the four tests discussed herein is presented in Table 1. Model-to-model and tunnel-to-tunnel comparisons were possible for the aerodynamic data and the oil-flow visualizations. Although testing for the series concentrated on maximum Reynolds numbers (approximately one-half of flight values) and the planned flight speedbrake setting (87°), a multitude of runs were also conducted at other Reynolds numbers, speedbrake deflections, configurations, and attitudes. Detailed pre-test checks of models and balances were also made to help ensure data accuracy. Assessments of tunnel-flow accuracy and repeatability along with model construction accuracy for both the 1 percent and 2 percent models led to a high degree of confidence in this series of tests.

For the most accurate determination of the static lateral-directional stability, fine cut β-sweeps at essentially constant α's were conducted for all cases. Runs to examine hysteresis were performed for conditions near those for flights. Slopes of the C_n and C_ℓ vs β curves were determined over a β-range of $\pm 0.5°$.

Total measurement accuracies of the lateral-directional data presented are within the data symbol sizes. Although detailed balance checks did show them to be quite accurate, the total accuracies were constrained by accuracies of the tunnel flow, model dimensions, and model attitude measurement. The data were reduced using the following reference values:

Model Scale (%)	S (in^2)	$\bar{c}$ (in)	b (in)
0.4	6.198	1.899	3.747
1	38.736	4.748	9.367
2	154.944	9.496	18.734

The body flap and elevons were set at 0° for all runs.

The oil-flow runs were conducted with the models painted black using white pigment (titanium oxide) and oil. A base coat of plain oil and then a mixture of pigment and oil were applied for each run. For the tests in the 20-Inch M-6 tunnel, the oil-flow patterns were photographed after the run; for the Tunnel B tests, the photographs were made during the runs.

RESULTS AND DISCUSSION

At M=6 reentry conditions, the vertical tail of the orbiter is located in a very complex, relatively high energy leeside flow field. (See fig. 1.) The wing-body juncture vortex combines with separated flow from the body and wing to form the feather-like pattern on the side of the fuselage which impinges on the OMS pods. The flow on the upper surface of the fuselage is dominated by a pair of primary vortices (caused by the canopy) which produce the feather-like pattern on the centerline. Also, a pair of secondary vortices exist outboard and downstream of the primary ones, as shown in figure 1. These vortical regions, combined with the other separated flow regions, unquestionably present a very nonuniform, unpredictable flow approaching the OMS pods and vertical tail, and flow on the vertical tail is further complicated by large speedbrake deflections. Reference 3, which discusses the flow approaching the vertical tail in more detail, illustrates recirculating flow patterns which occur in front of the vertical tail as shown in figure 1 and further exemplifies this complex flow region. Measurement of lateral-directional stability data becomes exceedingly difficult in this type of flow environment where small changes in model attitudes, configurations, and free-stream flow conditions can greatly influence measured stability levels.

Effect of Speedbrake Deflection on C_{n_β}

In figure 2, C_{n_β} values are presented vs $Re_{\bar{c}}$ for $\alpha=20°$, $25°$, and $30°$ and for $\delta_{SB}=0°$ and $87°$. The dashed lines between values for $\delta_{SB}=87°$ at $Re_{\bar{c}}=0.4 \times 10^6$ and 0.8×10^6 result from the C_n vs β curves being non-linear near $\beta=0°$. The spread in the C_{n_β} values is less as $Re_{\bar{c}}$ approaches 3×10^6 where the basic data are approximately linear with β. For $\alpha=20°$ (fig. 2(a)) and $\delta_{SB}=87°$, there is increased stability with increasing $Re_{\bar{c}}$, and the trend of the curve flattens, which indicates less sensitivity to changes in Reynolds number at the higher values. For $\delta_{SB}=0°$ and $\alpha=20°$, little or no change in stability level is seen for the range of Reynolds numbers tested. For $\alpha=25°$ (fig. 2(b)) and $\delta_{SB}=87°$, a stabilizing trend is again shown as the Reynolds number increases. Also, the result of non-linear directional data is observed, though at higher $Re_{\bar{c}}$ ranges than for $\alpha=20°$. The C_{n_β} for a speedbrake value of $0°$ is relatively insensitive to $Re_{\bar{c}}$ at $\alpha=25°$, as it was for $\alpha=20°$. The flight data presented on figure 2(b) show better agreement with the lower Reynolds number stability values. The flight values also indicate less stability than predicted by the ADDB. Note that the spread in the C_{n_β} caused by the non-linearities in the C_n vs β curves is larger than the range of the variations. For $\alpha=30°$ (fig. 2(c)), a reverse trend from the two previous α's is shown. For both $0°$ and $87°$ speedbrake, more stable C_{n_β} values are obtained for the lower $Re_{\bar{c}}$'s, and the stability level for both speedbrakes is relatively

insensitive to the $Re_{\bar{c}}$'s. At 30° angle of attack, the directional instability phenomenon is probably dominated by more conventional, delta-wing-type separations which do not interact with the tail region of the orbiter.

Effect of Speedbrake Deflection on C_{ℓ_β}

The C_{ℓ_β} values at α=20° (fig. 3(a)) are consistent with the C_{n_β} trends shown in figure 2(a). For the lower $Re_{\bar{c}}$ values, more unstable C_{ℓ_β}'s are shown for δ_{SB}=87°, but there is increased stability with increasing $Re_{\bar{c}}$. The stability levels measured for δ_{SB}=0° are relatively insensitive to changes in $Re_{\bar{c}}$. The positive C_{ℓ_β} value at $Re_{\bar{c}}=0.8 \times 10^6$ was obtained from a case where the basic data were very non-linear and exhibited hysteresis. Lateral stability results for the 87° and 0° speedbrake shown in figure 3(b) for α=25° are similar to the directional stability results of figure 2(b) and the results shown in figure 3(a). There is increasing stability with increasing Reynolds numbers for δ_{SB}=87°, and the C_{ℓ_β} values for the 0° speedbrake are less sensitive to $Re_{\bar{c}}$. The flight data shown in figure 3(b) compare well with the lateral stability data for $Re_{\bar{c}}$ above 0.8×10^6. Also, there is excellent agreement between the flight data and the ADDB for C_{ℓ_β} (well within the variations). The spread of the C_{ℓ_β} values caused by the non-linearity in the C_ℓ vs β curves is outside the variations band, as it was for C_{n_β} in figure 2(b). For α=30° (fig. 3(c)), little or no effect on stability is shown for both speedbrake settings over the range of Reynolds numbers tested, which supports the conclusion drawn from figure 2(c). Generally, the lateral stability data of figure 3 show significantly less sensitivity to changes in $Re_{\bar{c}}$ than do the directional stability data of figure 2, probably because the lateral stability values are inherently stable.

Effect of Configuration Buildup on C_{n_β}

The C_{n_β} vs $Re_{\bar{c}}$ results for baseline, OMS pods off, vertical tail off, and both OMS pods and vertical tail off configurations are presented in figure 4 for all three α's. The C_{n_β} values for δ_{SB}=87° were averaged at common $Re_{\bar{c}}$'s to simplify the figure. Although configuration buildup runs were not made for all cases, the limited results are quite important. Taking off the OMS pods at α=20° (fig. 4(a)) increased the stability level significantly at $Re_{\bar{c}}=0.4 \times 10^6$. When the vertical tail was also removed, only a small gain in stability was measured, which indicates that the OMS pods have a large destabilizing effect on the 87° speedbrake at $Re_{\bar{c}}=0.4 \times 10^6$. At $Re_{\bar{c}}=0.9 \times 10^6$, removing either the V.T. or the OMS pods results in a slight increase in stability, but when both are removed no change was measured, which indicates an interaction effect between these two components. Removing only the vertical tail increased the stability for all $Re_{\bar{c}}$'s, except for a small trend reversal at $Re_{\bar{c}}=3 \times 10^6$. At $Re_{\bar{c}} \geq 3 \times 10^6$ the baseline configuration appears to be the most stable. For α=25°(fig. 4(b)), and $Re_{\bar{c}}=0.9 \times 10^6$ and 3×10^6, the OMS pods appear to have a stabilizing effect as the stability is significantly reduced when they are removed. There is a definite stabilizing trend over the lower range of $Re_{\bar{c}}$'s when the vertical tail is removed at this angle of attack. For α=30° (fig. 4(c)), the removal of the vertical tail is shown to decrease or have no effect on the stability level.

Trends of figure 4(c) are similar with those of figure 2(c) and 3(c) where it was shown that at $\alpha=30°$ the effects of the speedbrake deflection angle on the stability are small.

Effect of Configuration Buildup on C_{ℓ_β}

The C_{ℓ_β} vs $Re_{\bar{c}}$ results for the various configurations are presented in figure 5 for all three α's. The C_{ℓ_β} values are generally less sensitive to changes in Reynolds number than the C_{n_β} values. This conclusion was also drawn from an observation of the speedbrake deflection results shown in figures 2 and 3. The most significant change in lateral stability incurred by removal of a configuration component is shown in figure 5(b) ($\alpha=25°$) for $Re_{\bar{c}}=0.9 \times 10^6$. The removal of the OMS pods in this case reduces the stability level, which is expected from the C_{n_β} results shown in figure 4(b) for the same test case. For $\alpha=20°$ and 25° (figs. 5(a) and (b)), the stability level is shown to increase slightly with the removal of the vertical tail, especially for the lower values of $Re_{\bar{c}}$. This agrees with the results of figures 4(a) and (b), and verifies the conclusion that the vertical tail with the 87° speedbrake contributes to the lateral-directional instability at both $\alpha=20°$ and 25° and $Re_{\bar{c}} \leq 1.7 \times 10^6$. At $\alpha=30°$ (fig. 5(c)), little or no effect on stability is observed over the range of $Re_{\bar{c}}$'s, as expected.

Basic Lateral-Directional Aerodynamic Data

Results from three tests (0A-258, 0A-259, and 0A-257) can be compared at $Re_{\bar{c}}$ values of $\approx 0.8 \times 10^6$ and 1.7×10^6. Although the slopes of the basic data curves (figs. 6, 7, 8, and 9) did produce a range of values as shown in figures 2 and 3 (especially for $\alpha=20°$ and 25°), the overall shape of the curves agrees very well from test to test. For several runs, however, the spread in the measured stability level was outside the ADDB variations values.

For $Re_{\bar{c}} \approx 0.8 \times 10^6$ (fig. 6), results show the presence of hysteresis and non-linearities at $\alpha=20°$. Besides the excellent agreement between tests, the C_n and C_ℓ values for $\alpha=20°$ (figs. 6(a) and 7(a)) are very closely coupled, with the hysteresis and discontinuous regions matching identically. Hysteresis as shown in Test 0A-259 would probably have been obtained in the other two tests had the β-sweep direction been reversed. For $\alpha=25°$ and 30° (figs. 6(b) and (c)), the C_n vs β comparisons are also quite good. Results from Test 0A-259 do indicate a more non-linear character than do the other test results. There is a general tendency, as expected, of the C_n vs β curves to become more linear at $\alpha=30°$. Good test-to-test agreement is also shown for C_ℓ vs β in figure 7(b) at $\alpha=25°$.

For $Re_{\bar{c}}=1.7 \times 10^6$ and $\alpha=20°$ (figs. 8(a) and 9(a)), no hysteresis was observed for either C_n or C_ℓ, and the test-to-test data comparisons are good. At $\alpha=25°$, both the C_n and C_ℓ curves (figs. 8(b) and 9(b)) show excellent test-to-test agreement. Both figures show an abrupt slope change in the curves at $\beta \approx -0.25°$, which is especially obvious for tests 0A-259 and 0A-257. A non-linear, nonsymmetrical region was observed from the results from test 0A-257, as shown in figure 8(c) for $\alpha=30°$ and $\beta>1$. Similar results were obtained by another run from test 0A-257 which had only an insignificant model change as a difference.

No basic data comparisons for $Re_{\bar{c}}=3 \times 10^6$ are made here. Although tests OA-257 and OA-258 can be compared at this $Re_{\bar{c}}$ value, the curves from both tests are basically very linear, and the stability values are shown to agree very well as reflected in figures 2 and 3.

Oil-Flow Results

Although oil-flow runs were conducted to help understand the flow phenomenon responsible for the measured lateral-directional stability results, this series of tests also provided the opportunity to conduct oil-flow tests in two facilities using three models with matching Reynolds numbers for some cases. All oil-flow pictures were taken of the leeside, particularly on the vertical tail, since early test results from LA-141B showed large changes in the patterns on the vertical tail for small changes in β (from 0 to +0.5°) and for changes in $Re_{\bar{c}}$ from 0.4×10^6 to 1.3×10^6. The pattern that was observed and which helped lead to an understanding of the lateral-directional stability phenomenon was the extent of the separated region on the vertical tail. For cases where large non-linearities and high levels of instability were observed (usually for α's$\leq$25° and $Re_{\bar{c}} \leq 1.7$), the separated region on the windward side of the vertical tail (right side for β=+0.5°) was very large compared to the leeward side and compared to the pattern observed in the same region for β=0°. The separated surface flow regions are accompanied by surface pressures in that region which are low compared to regions of attached flow. Therefore, destabilizing yawing moments and rolling moments are applied by the vertical tail when the vehicle is yawed with separated flow on the windward side and attached flow on the leeward side.

Oil-flow photographs for α=20°, β=+0.5°, δ_{SB}=87°, and for three $Re_{\bar{c}}$'s (one run from each test for which oil flows were obtained) are presented in figure 10 to illustrate the trend just discussed. For the two lower $Re_{\bar{c}}$'s, the windward side of the vertical tail has significantly larger separated regions, which cause the measured instability levels. For $Re_{\bar{c}}=3 \times 10^6$, separated regions from one side to the other are not significantly different, which is consistent with the results of figures 4 and 5 where it is shown that the vertical tail does not contribute to the instability level at this $Re_{\bar{c}}$ value.

The angle of sideslip is varied from -0.5° to 0° to +0.5° in figure 11 for $Re_{\bar{c}}=0.4 \times 10^6$, α=20°, and δ_{SB}=87°. The relatively large separated region moves to the windward side of the vertical tail for both $\beta \neq 0$ cases. For β=0°, there is no significant difference in the relative areas of separated flow. These oil-flow runs depict the unpredictable surface flows which cause the measured hysteresis and non-linearities along with the level of lateral-directional stability shown in figures 2(a) and 3(a) at $Re_{\bar{c}}=0.4 \times 10^6$.

A test-to-test comparison of an oil-flow run for α=25°, β=+0.5°, δ_{SB}=87° and $Re_{\bar{c}} \approx 0.8 \times 10^6$ is made in figure 12. First, note that the regions of separated flow and the flow reattachment patterns compare well for both tests. Secondly, the relatively large separated regions on the windward side of the vertical tail are indicative of the unpredicatable leeside flows which cause the non-linearities shown in figures 6(b) and 7(b) and produce the high level of instability and the uncertainty band shown in figures 2(b) and 3(b).

Another test-to-test comparison of an oil-flow run for $\alpha=20°$, $\beta=+0.5°$, $\delta_{SB}=87°$ and $Re_{\bar{c}}=3 \times 10^6$ is made in figure 13. These pictures also show excellent test-to-test agreement with significant difference in the separated regions from one side to the other. These observations support the results of figures 4(a) and 5(a) which show that the vertical tail has little or no effect on the lateral-directional stability at $Re_{\bar{c}}=3 \times 10^6$.

CONCLUSIONS

Lateral-directional aerodynamic data and oil-flow visualization results are presented from four tests (conducted in the Langley 20-Inch Mach 6 Tunnel and AEDC's Tunnel B with three models) which were designed to verify the hypersonic aerodynamics of the orbiter at M=6. Comparisons of measured lateral-directional stability data and oil-flow results between the tests show excellent agreement, especially considering the nonuniform, unpredictable flow which occurs in the vicinity of the vertical tail. These results indicate that both facilities are capable of producing similarly accurate and reliable lateral-directional stability data and oil-flow visualization up to the same length Reynolds numbers.

For the comparisons made with both flight data and the ADDB, the lateral stability values showed excellent agreement. As for the directional stability, flight data showed less stable trends than both the ADDB and the present data at the highest Reynolds number, though all values were within variations.

Lateral and directional stability for a speedbrake deflection angle of 87° was shown to increase (and become insensitive to Reynolds number) as the Reynolds number was increased to its maximum value or as the angle of attack was increased to 30°. Changing the speedbrake deflection angle from 0° to 87° produced a significant decrease in directional stability at the lower Reynolds numbers and angles of attack. Component buildup studies showed that the vertical tail contributed to the measured lateral and directional instabilities at the lower Reynolds numbers and angles of attack.

Oil-flow results showed the relative separated flow regions on the vertical tail which cause the high directional instability levels and depicted the flow patterns which produce the non-linear measurements of yawing moments and rolling moments. The oil-flow results were also consistent with the stability data which showed that the vertical tail does not contribute to the instability at the maximum test Reynolds number.

For the design and development of future entry vehicles, the results of these tests show that no assumptions of linearity should be made on the effects of Reynolds number, angle of attack, and angle of sideslip on the lateral-directional stability. Also, the lateral-directional stability is shown to be configuration dependent and is strongly influenced by aft leeside components. It is anticipated that these effects will become more critical as future flight envelopes expand to include maneuvers over larger ranges of Reynolds numbers.

REFERENCES

1. Aerodynamic Design Data Book, Vol I - Orbiter Vehicle. Rept. No. SD72-SH-0060-1M, Rockwell International, Nov. 1980.

2. Underwood, Jimmy M.; and Cook, Douglas R.: A Preliminary Correlation of the Orbiter Stability and Control Aerodynamics From the First Two Space Shuttle Flights (STS-1&2) With Preflight Predictions, AIAA Paper 82-0564, March 1982.

3. Helms, Vernon T., III: An Empirical Method for Computing Leeside Centerline Heating on the Space Shuttle Orbiter, AIAA 81-1043, June 1981.

TABLE I.- DESCRIPTION OF MACH 6 TESTS

TESTS	FACILITY	MODEL	$Re_{\bar{c}} \times 10^6$	DATA RUNS	OIL-FLOW RUNS
LA141B	LaRC 20-INCH M-6	0.4% #74 (140C)	0.4, 0.7, 1.3	130	13
OA-258	VKF TUNNEL B	2% #106 (OV102)	0.8, 1.7, 3.0	300	21
OA-259	VKF TUNNEL B	1% #72 (OV102)	0.8, 1.7	137	--
OA-257	LaRC 20-INCH M-6	1% #72 (OV102)	0.9, 1.7, 3.0	200	15

TABLE II.- FLIGHT DATA

FLIGHT	M	C_{n_β}	C_{ℓ_β}	MANEUVER
STS-2	5.7	-0.00183	-0.00165	Programmed Test Input
STS-4	5.6	-0.00212	-0.00175	Bank Reversal
	6.1	-0.00255	-0.00147	Bank Reversal
STS-5	5.6	-0.00221	-0.00164	Programmed Test Input

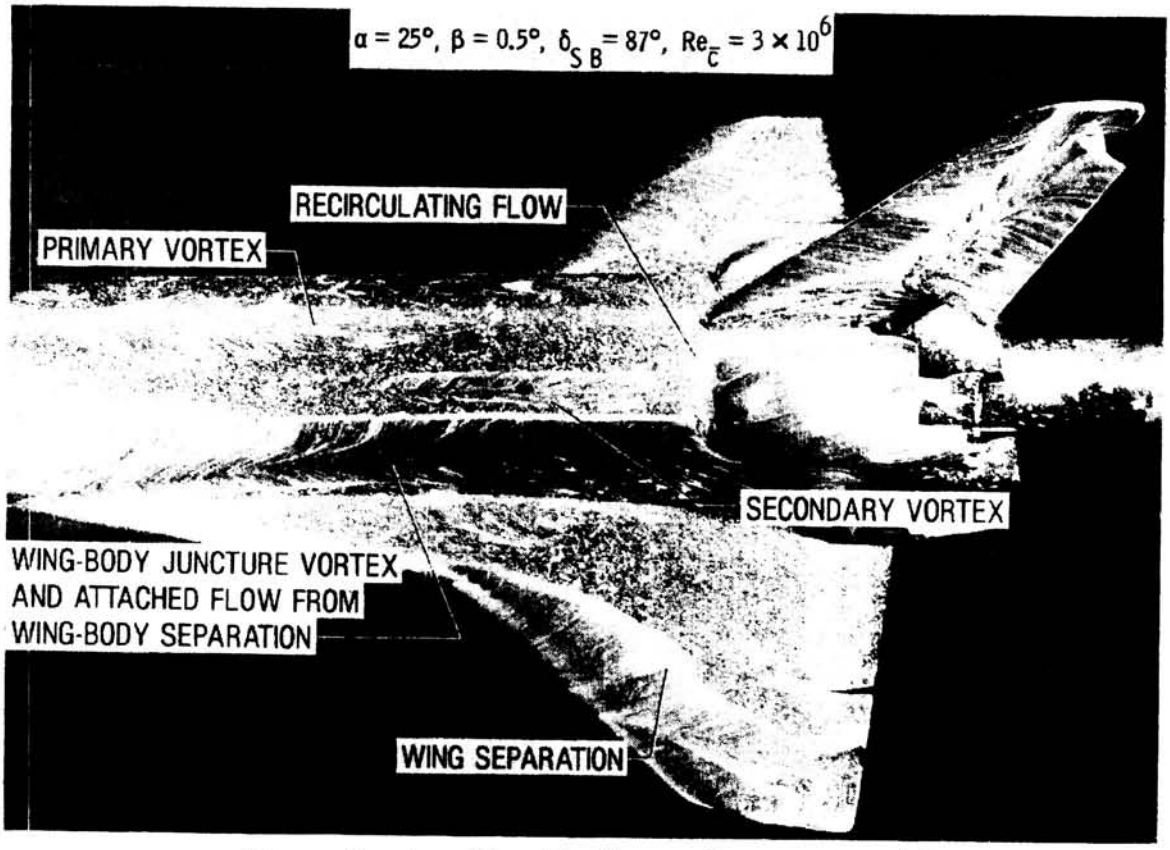

Figure 1.- Leeside oil flow on 1-percent model.

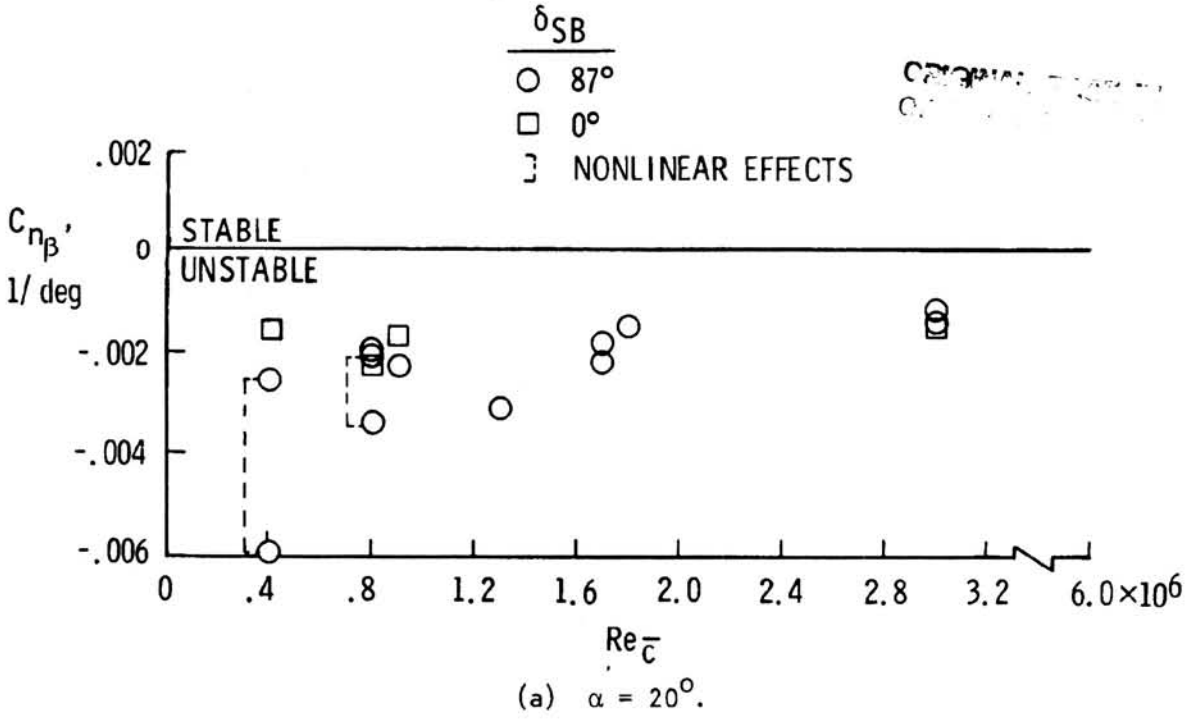

(a) $\alpha = 20^{\circ}$.

Figure 2.- Effect of speedbrake deflection on directional stability.

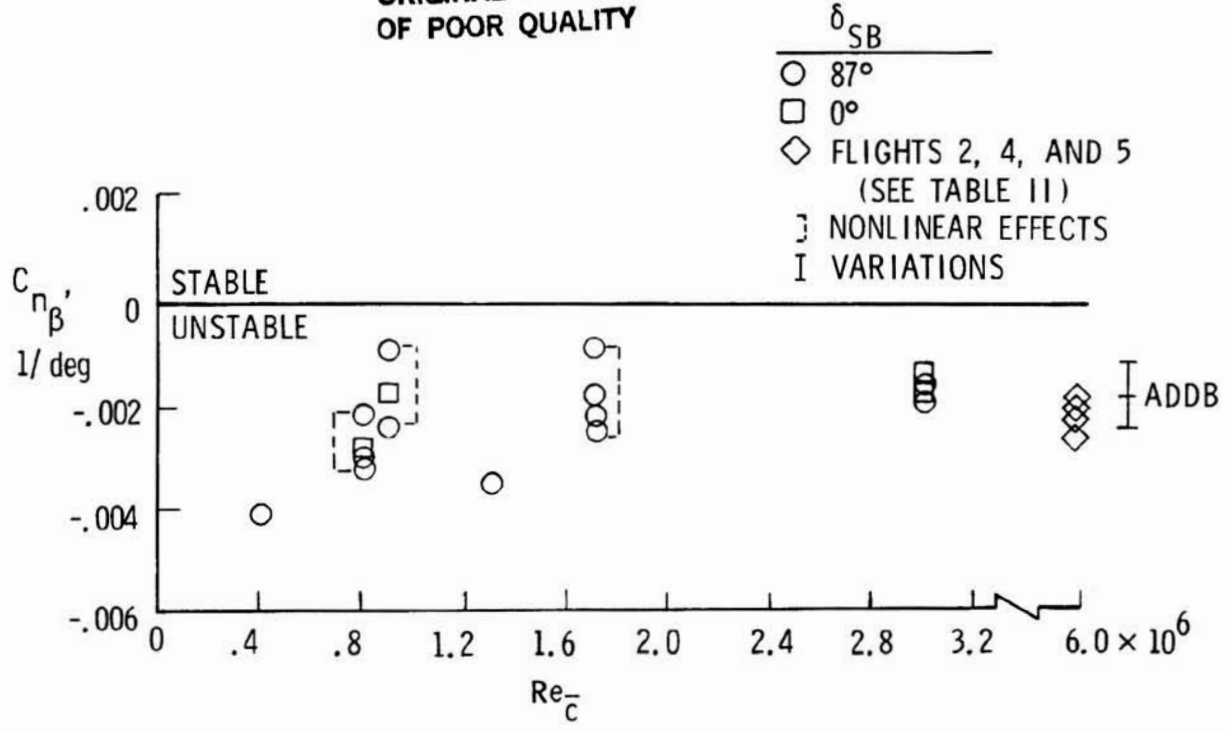

(b) $\alpha = 25^{\circ}$.

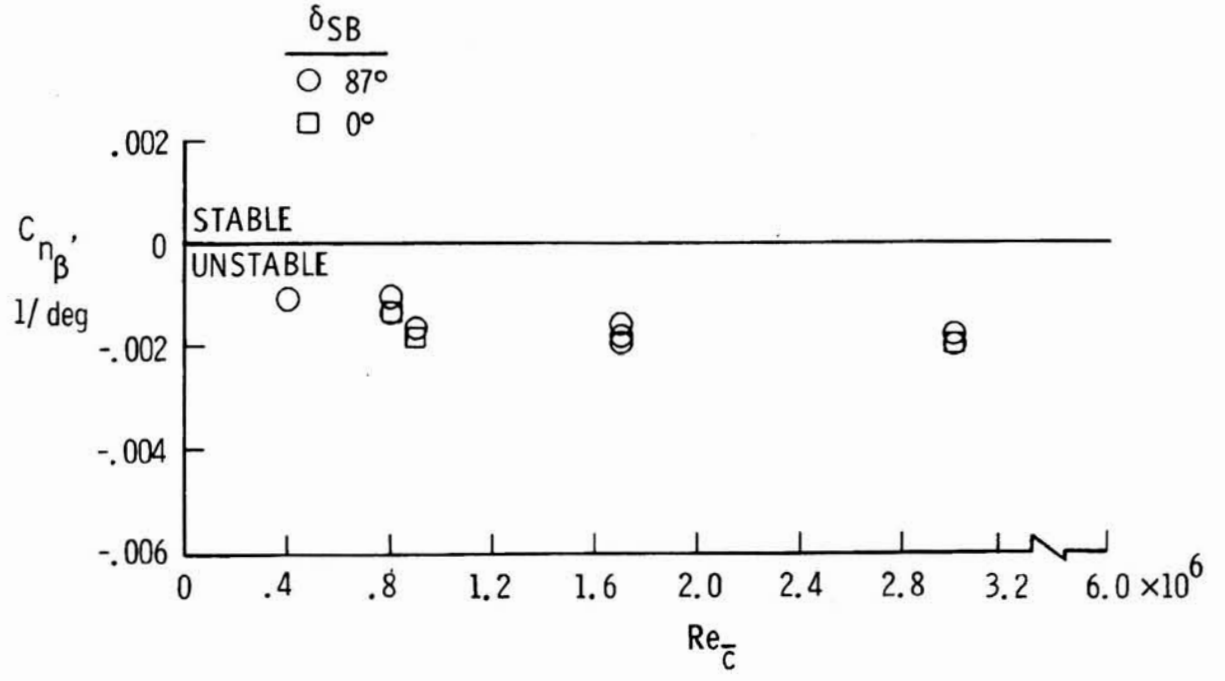

(c) $\alpha = 30^{\circ}$.

Figure 2.- Concluded.

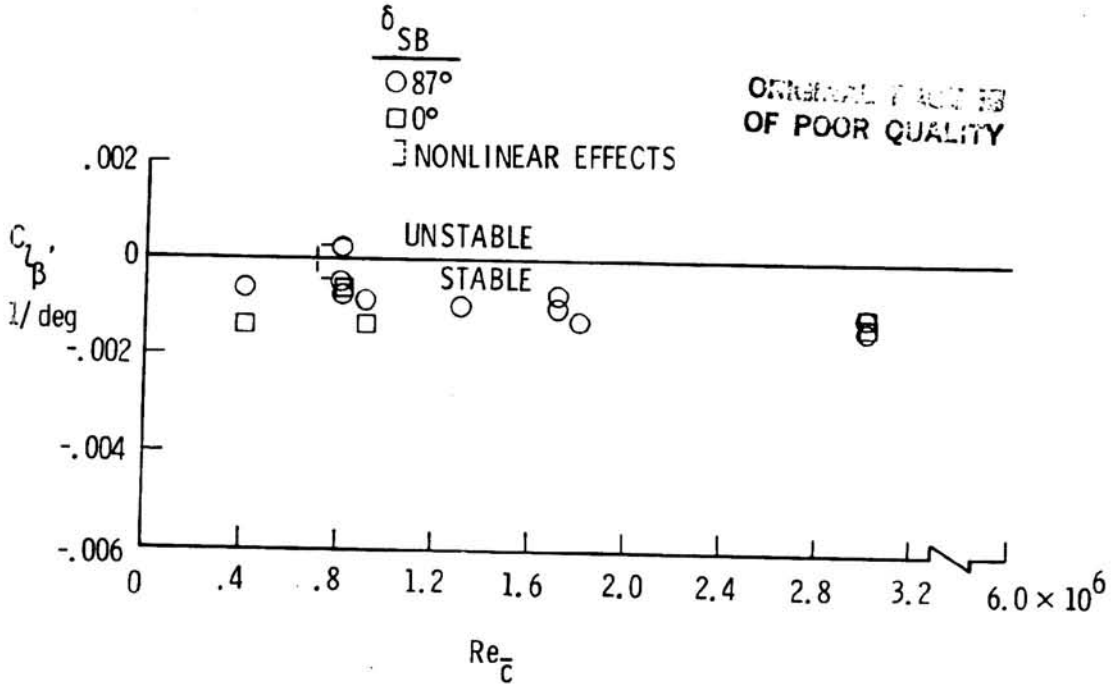

(a) $\alpha = 20^{\circ}$.

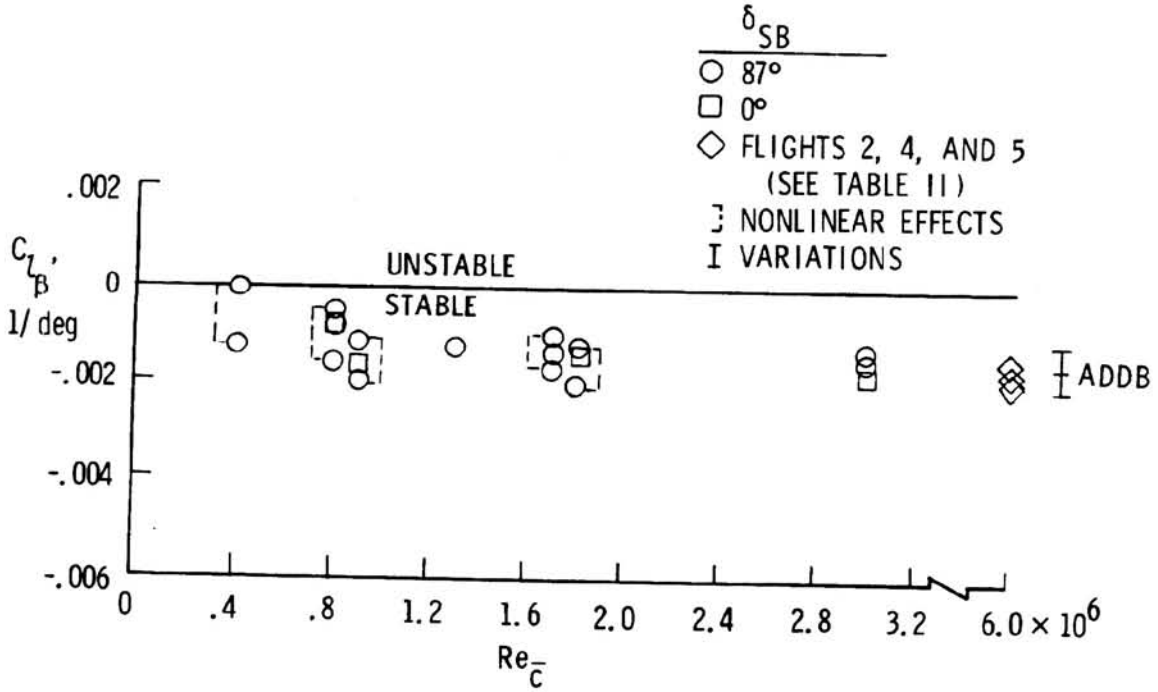

(b) $\alpha = 25^{\circ}$.

Figure 3.- Effect of speedbrake deflection on lateral stability.

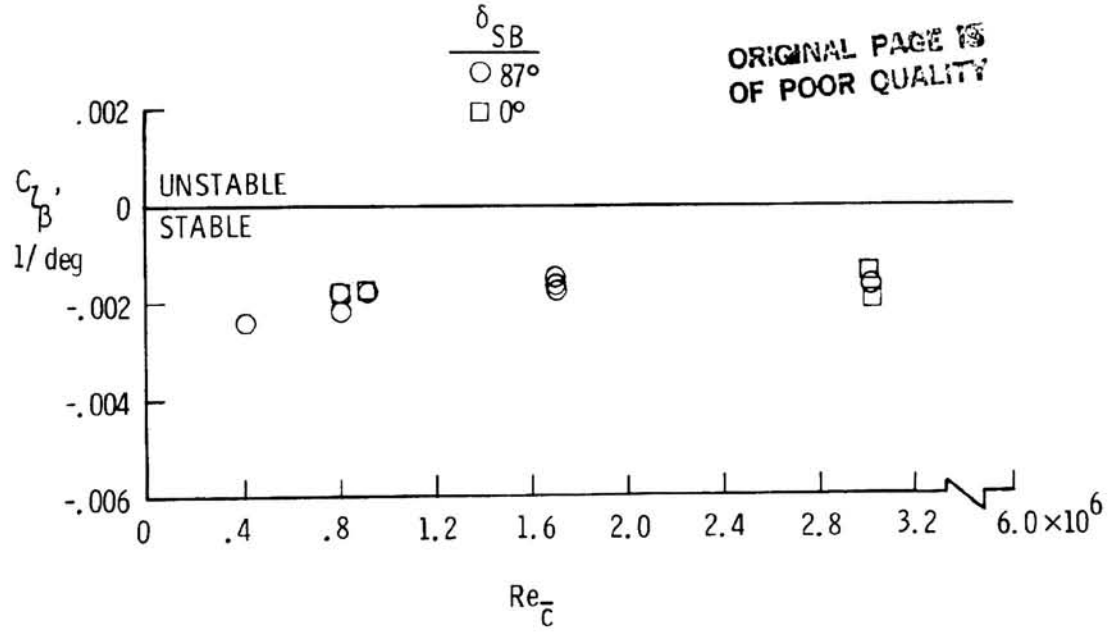

(c) $\alpha = 30^{\circ}$.

Figure 3.- Concluded.

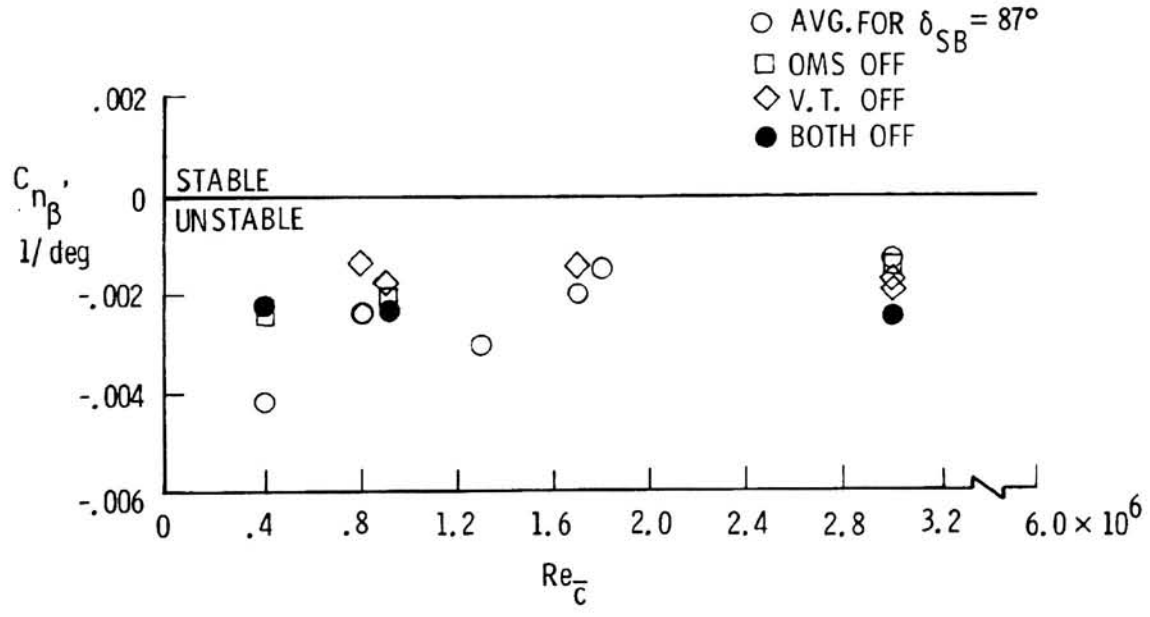

(a) $\alpha = 20^{\circ}$.

Figure 4.- Effect of configuration change on directional stability.

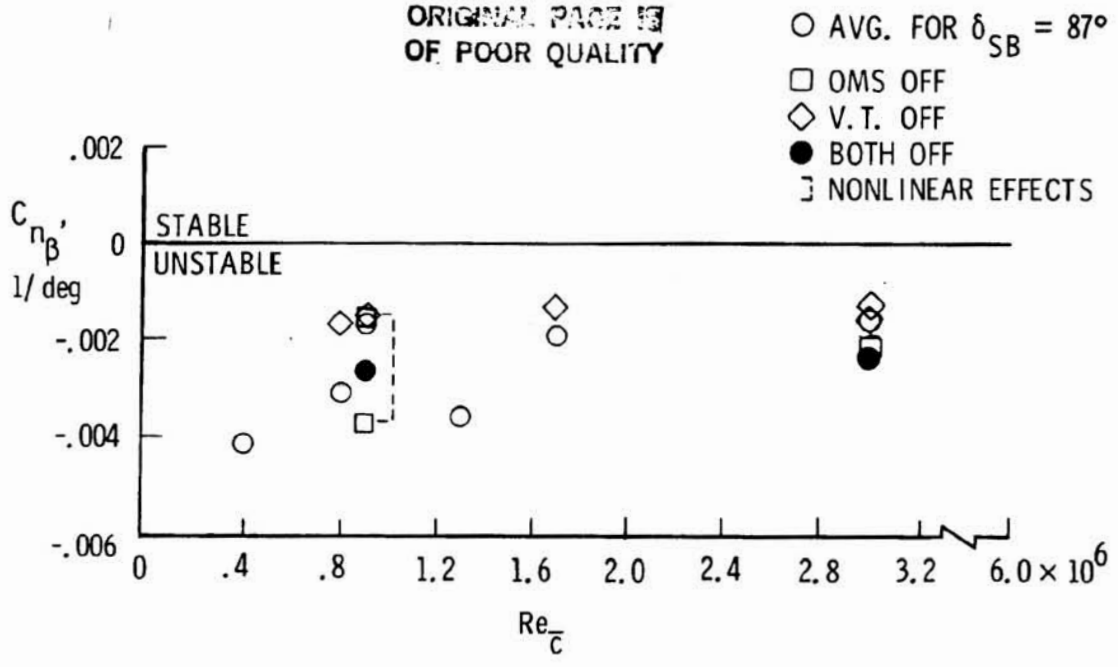

(b) $\alpha = 25^\circ$.

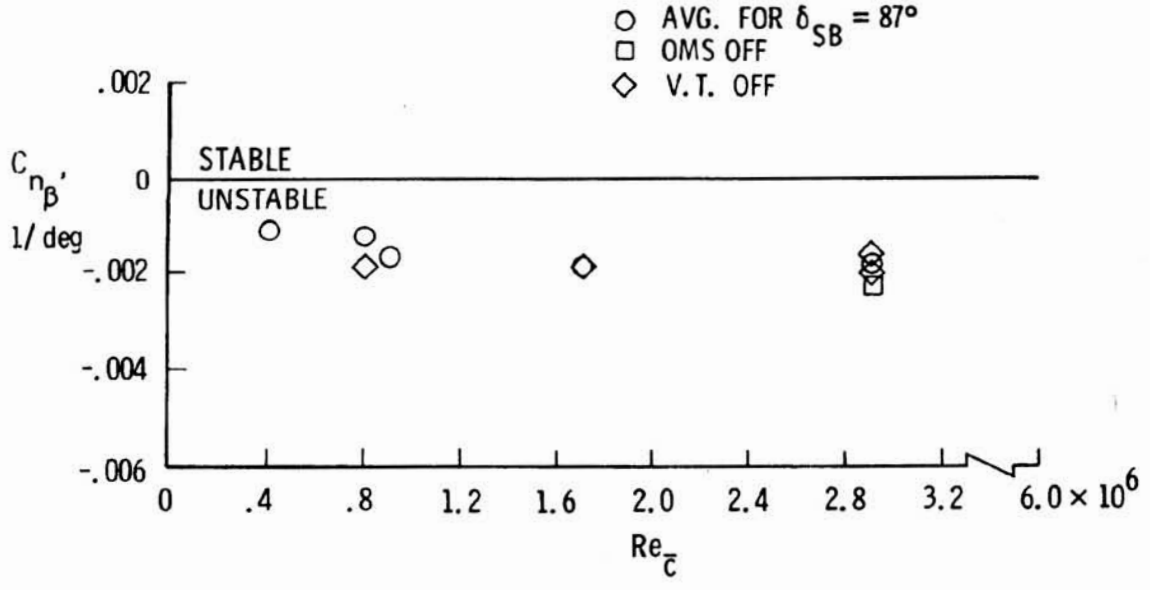

(c) $\alpha = 30^\circ$.

Figure 4.- Concluded.

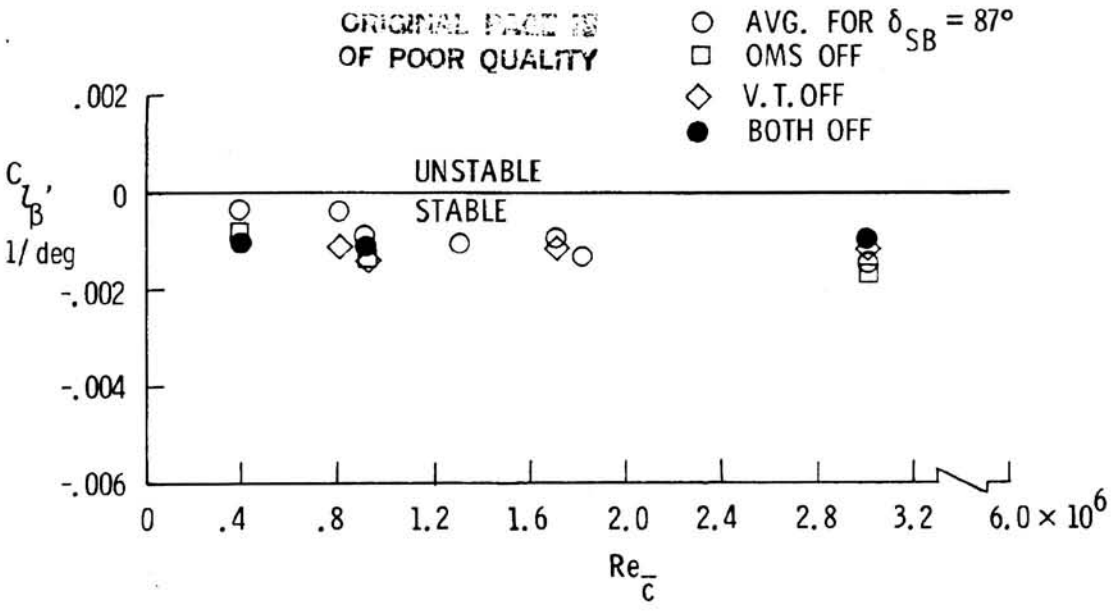

(a) $\alpha = 20^{\circ}$.

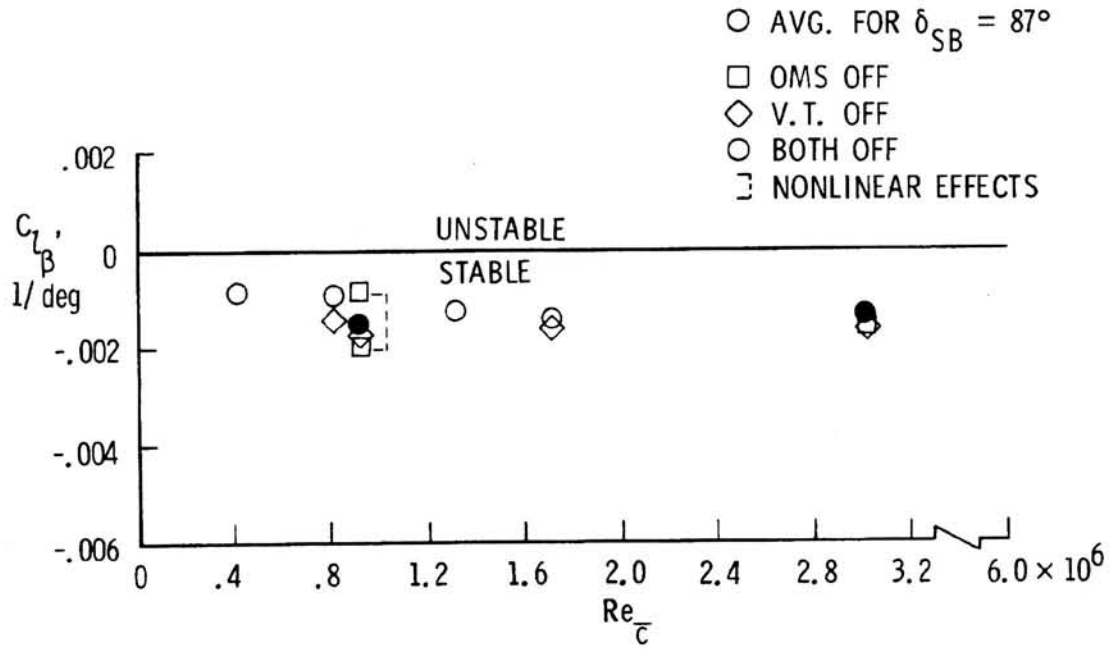

(b) $\alpha = 25^{\circ}$.

Figure 5.- Effect of configuration change on lateral stability.

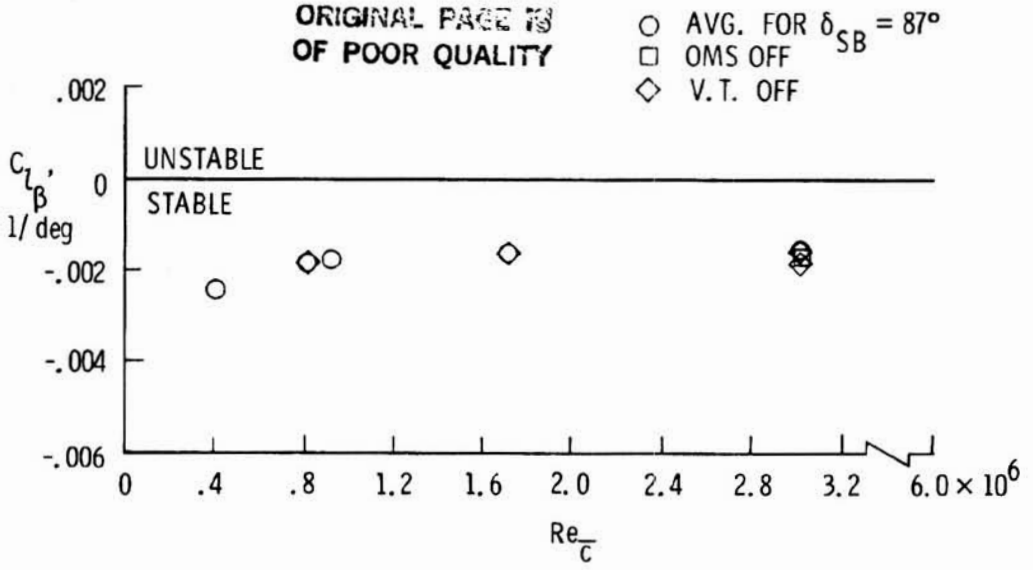

(c) $\alpha = 30^\circ$.

Figure 5.- Concluded.

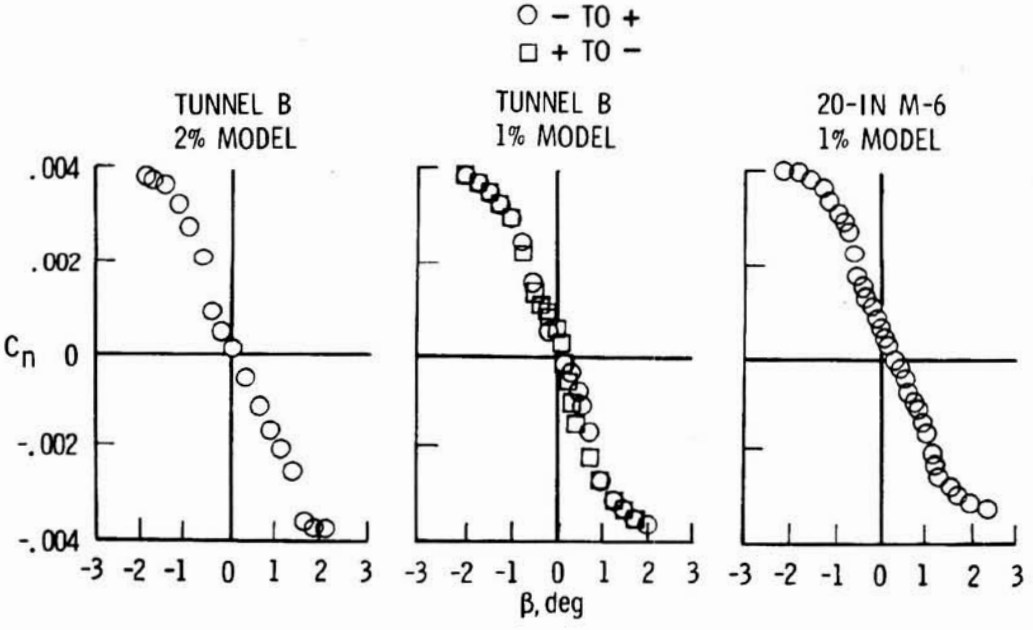

(a) $\alpha = 20^\circ$.

Figure 6.- Test-to-test comparisons of basic directional data at $Re_c = 0.8 \times 10^6$.

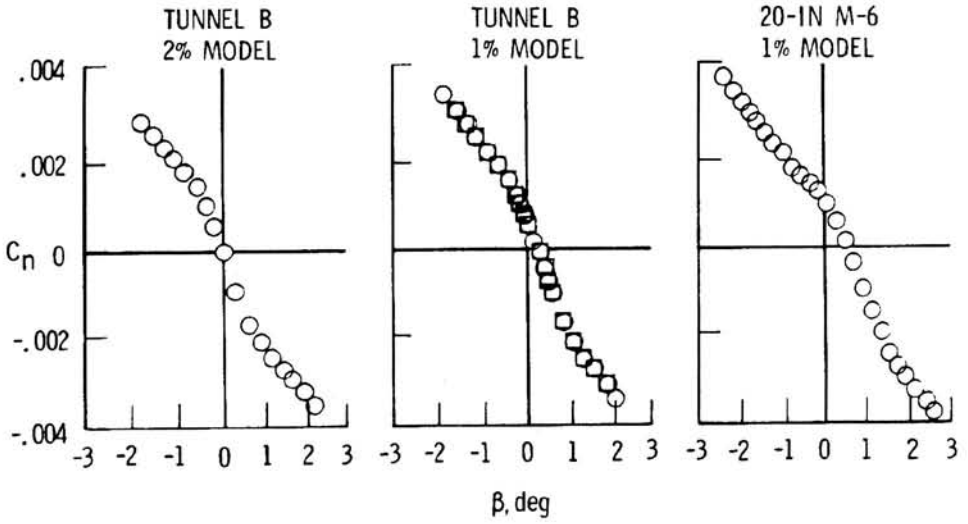

(b) $\alpha = 25^{\circ}$.

SWEEP DIRECTION
○ – TO +
□ + TO –

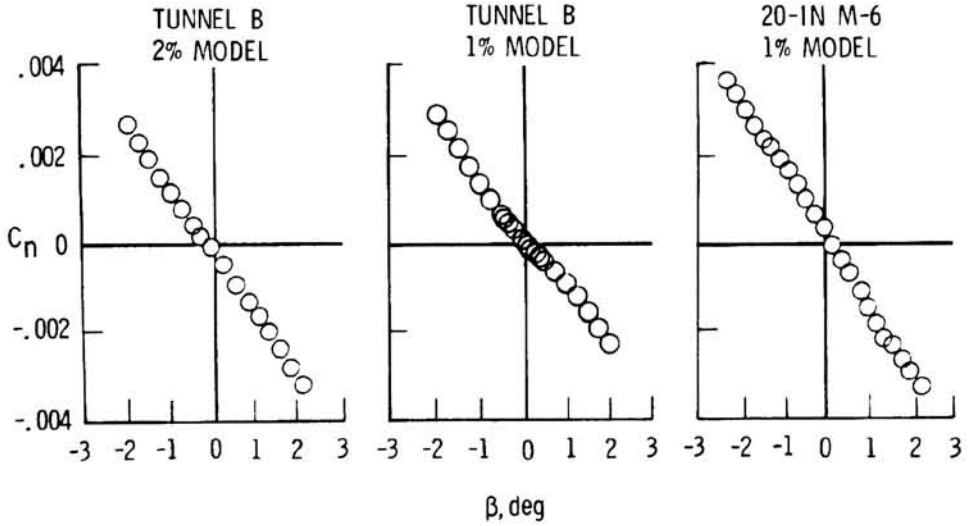

(c) $\alpha = 30^{\circ}$.

Figure 6.- Concluded.

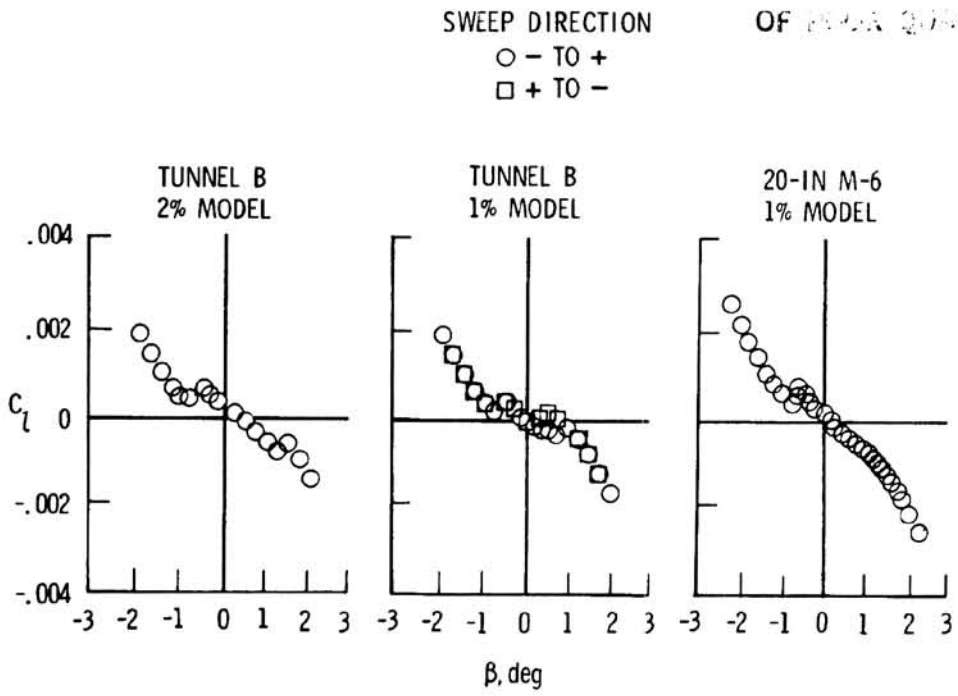

(a) $\alpha = 20^{\circ}$.

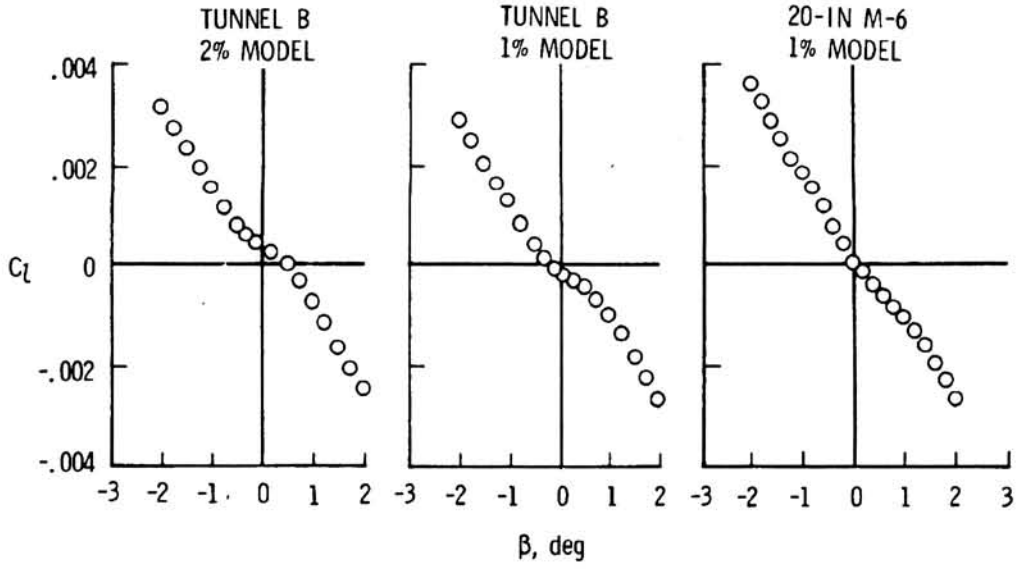

(b) $\alpha = 25^{\circ}$.

Figure 7.- Test-to-test comparisons of basic lateral data at $Re_c = 0.8 \times 10^6$.

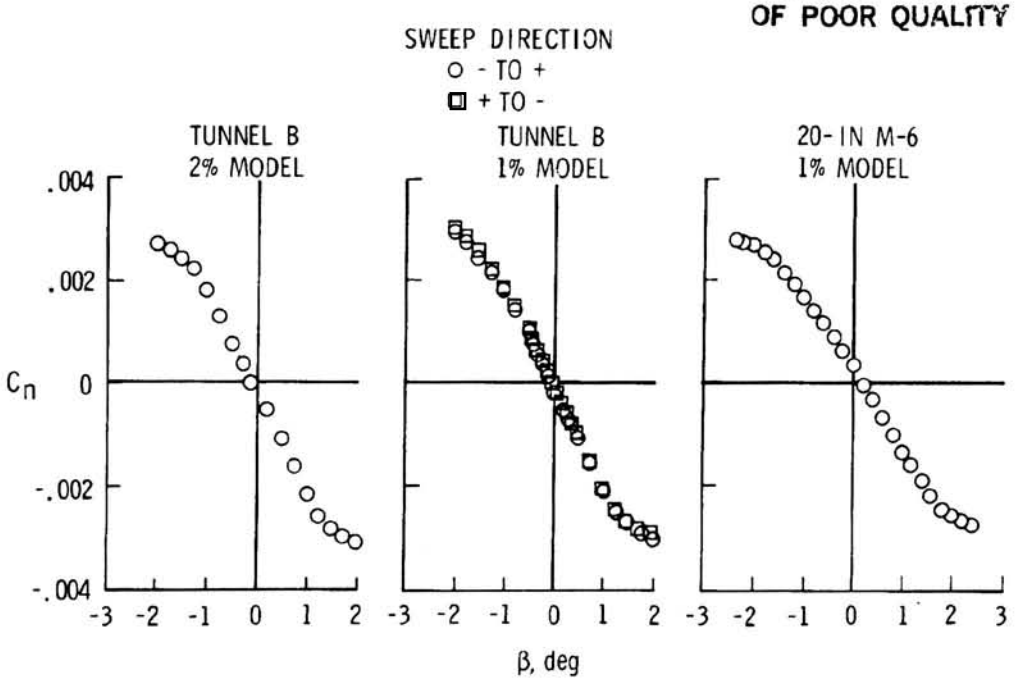

(a) $\alpha = 20^{\circ}$.

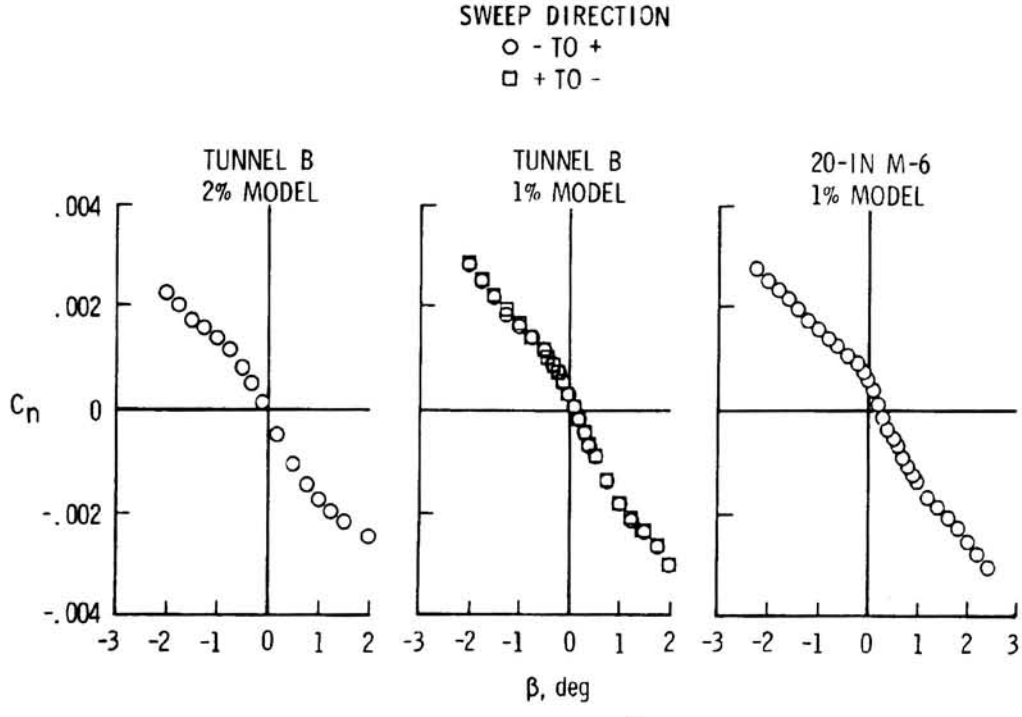

(b) $\alpha = 25^{\circ}$.

Figure 8.- Test-to-test comparisons of basic directional data at $Re_c = 1.7 \times 10^6$.

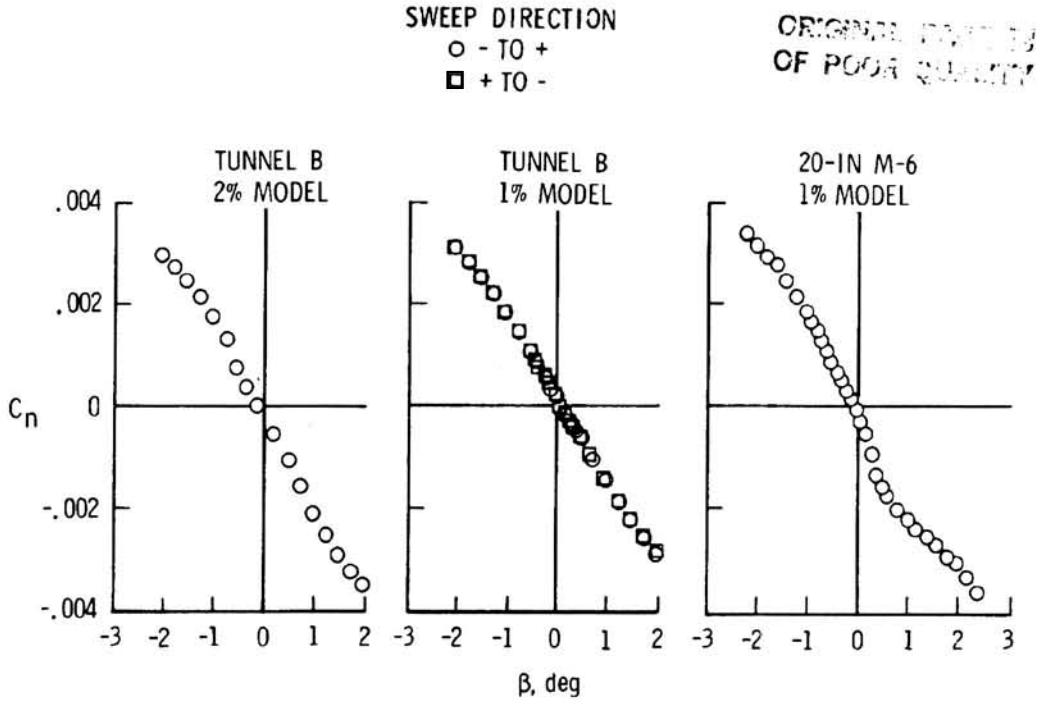

(c) $\alpha = 30^{\circ}$.

Figure 8.- Concluded.

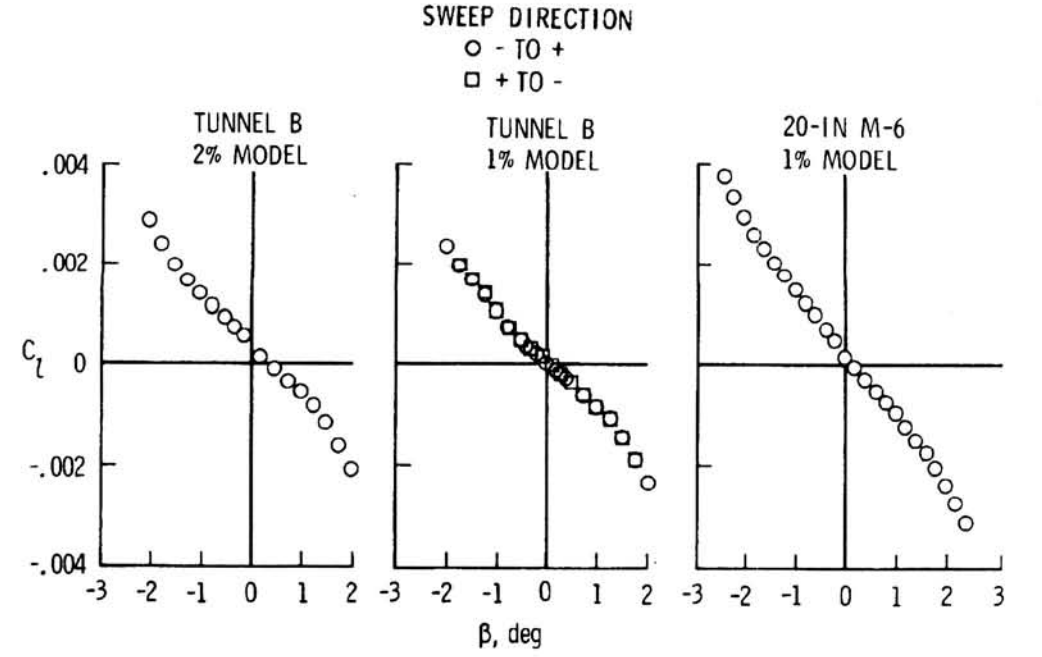

(a) $\alpha = 20^{\circ}$.

Figure 9.- Test-to-test comparisons of basic lateral data at $Re_c = 1.7 \times 10^6$.

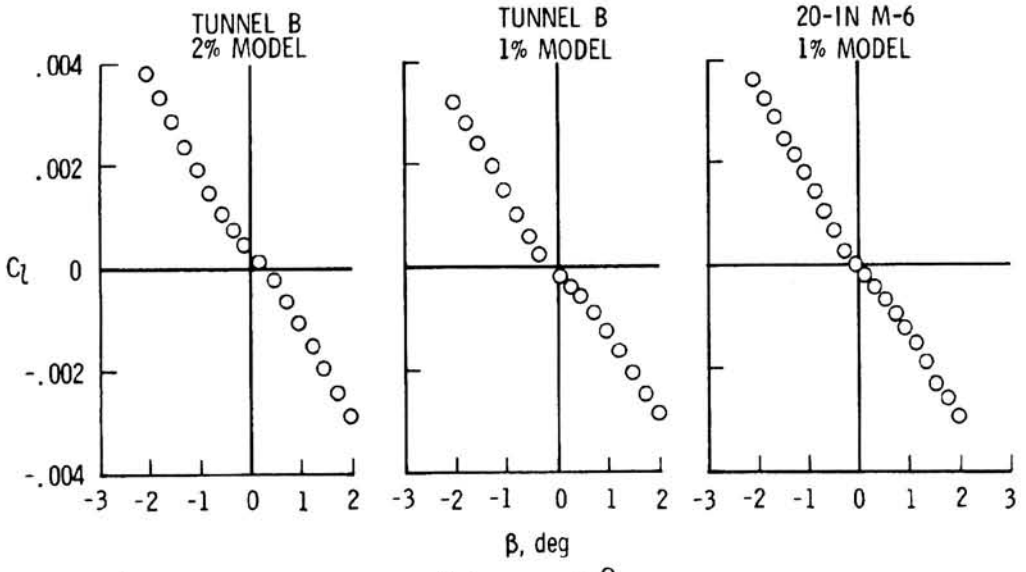

(b) $\alpha = 25^{\circ}$.

Figure 9.- Concluded.

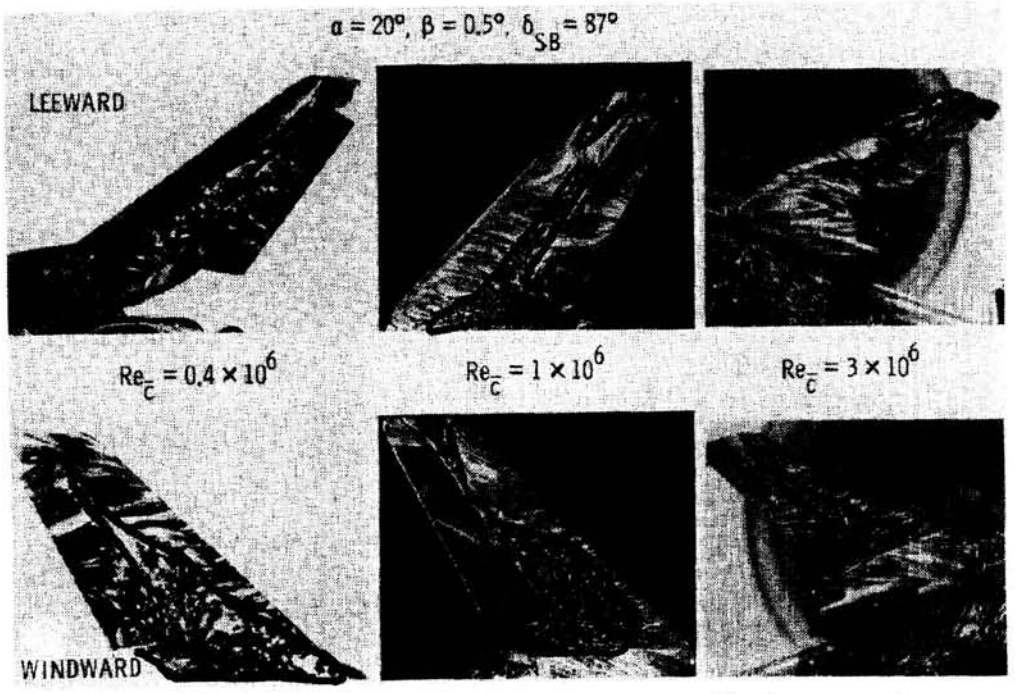

Figure 10.- Effect of Reynolds number on oil-flow results. Separated flow regions are outlined.

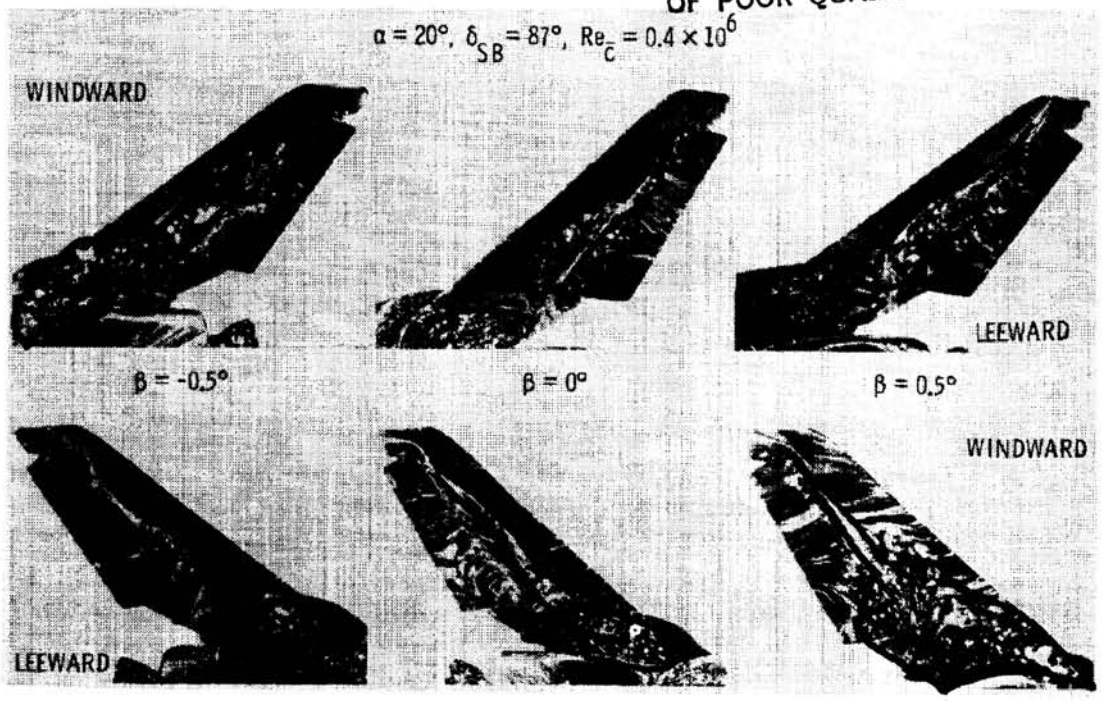

Figure 11.- Effect of sideslip on oil-flow results.
Separated flow regions are outlined.

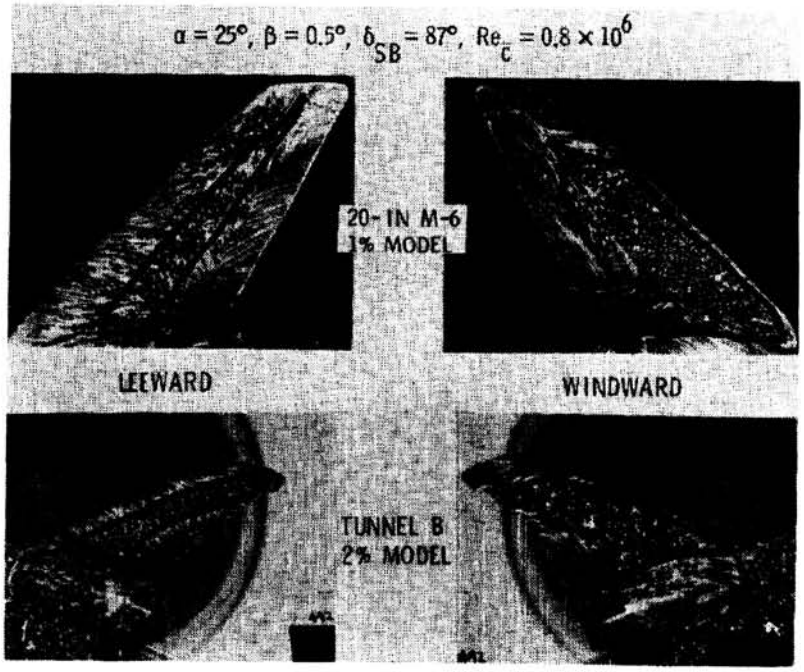

Figure 12.- Test-to-test oil-flow comparison.
Separated flow regions are outlined.

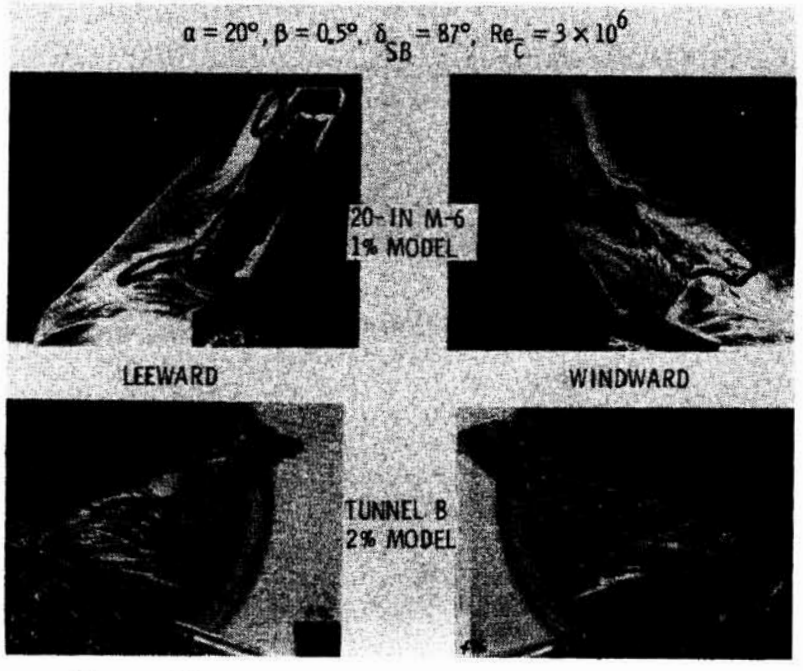

Figure 13.- Test-to-test oil-flow comparisons. Separated flow regions are outlined.

AERODYNAMIC COEFFICIENT IDENTIFICATION PACKAGE DYNAMIC DATA ACCURACY DETERMINATIONS - LESSONS LEARNED*

Michael L. Heck and John T. Findlay
Analytical Mechanics Associates, Incorporated
Hampton, Virginia

Harold R. Compton
NASA Langley Research Center
Hampton, Virginia

SUMMARY

The errors in the dynamic data output from the Aerodynamic Coefficient Identification Packages (ACIP) flown on Shuttle flights 1, 3, 4, and 5 have been determined using the output from the Inertial Measurement Units (IMU). A weighted least-squares batch algorithm was employed. Using an averaging technique, signal detection was enhanced; this allowed improved calibration solutions. Global errors as large as 0.04 deg/sec for the ACIP gyros, 30 mg for linear accelerometers, and 0.5 deg/sec^2 in the angular accelerometer channels were detected and removed with a combination of bias, scale factor, misalignment, and g-sensitive calibration constants. No attempt was made to minimize local ACIP dynamic data deviations representing sensed high-frequency vibration or instrument noise. Resulting 1σ calibrated ACIP global accuracies were within 0.003 deg/sec, 1.0 mg, and 0.05 deg/sec^2 for the gyros, linear accelerometers, and angular accelerometers, respectively.

INTRODUCTION

Shuttle postflight analysts have at their disposal three separate measurement sources of the reentry vehicle dynamics. These are:

1) the tri-redundant Inertial Measurement Unit (IMU) data

2) the Aerodynamic Coefficient Identification Package (ACIP) data

3) the quadredundant measurements from the Rate Gyro and Accelerometer Assemblies (RGA/AA)

The IMUs are utilized onboard for navigation. The RGA/AA are utilized for guidance and control. The ACIP instrument was developed principally to provide aerodynamicists with high-frequency strapped-down measurements of the vehicle rates, linear accelerations, and angular accelerations for aerodynamic coefficient extraction. For reasons of accuracy, the IMU data have been utilized extensively for entry trajectory reconstruction (ref. 1) and, though the downlist frequency is only ~1 Hz, they have been used by Modified Maximum Likelihood Estimation (MMLE) investigators to

*This work was performed under NASA Contract NAS1-16087.

extract control surface and stability derivatives (ref. 2). Methods have been developed to derive the equivalent body axis (strapped-down) data from the raw IMU measurements of sensed inertial velocity changes and quaternion attitude information (ref. 3). The RGA/AA data are available at 25 Hz, but the AA is devoid of an axial accelerometer, and the quantization levels on both the RGA and AA data are significant. However, data from these instruments have also been utilized with good results for MMLE purposes (ref. 2).

Perhaps the best source for MMLE investigations is the Aerodynamic Coefficient Identification Package data. The ACIP is a body-mounted instrument consisting of linear accelerometers, rate gyros, and angular accelerometers used to sense external accelerations and attitude rates onboard the Shuttle. It is located approximately 9 feet behind and 6 feet below the vehicle's center of gravity. The output data consist of digitized counts which are converted to volts and then scaled to engineering units. For example, linear accelerations a_x, a_y, and a_z are output in g's, angular rates P, Q, and R in deg/sec, and angular accelerations $\dot{P}$, $\dot{Q}$, and $\dot{R}$ in rad/sec^2; all are expressed in the ACIP instrument coordinate system which is nominally aligned with the Shuttle body coordinate system (figure 1). With ACIP data, MMLE analysts can utilize trajectory (state and attitude) information completely consistent with the available high-frequency dynamic data source. Data are recorded at ~170 Hz through a band-pass filter of 20 Hz which is employed onboard. Thus "real" frequency content of 20 Hz is measured (some higher frequency components might be aliased (folded-back) into the lower ranges).

In agreement with reference 4, the ACIP data were found to be accurate to within 1% full scale (table 1). As was indicated previously, early analysis showed this to be unacceptable for purposes of trajectory reconstruction. However, the data have been successfully utilized for aerodynamic coefficient extraction. Actual ACIP flight measurements to date have exhibited the following:

1) structural frequencies (7-12 Hz) appearing as "pseudo-random" noise

2) "large" biases when compared with the alternate sources of data, specifically the IMU

The former, though apparently aggravated by the particular location of the instrument within the vehicle, exists because of the requirement to operate at frequencies sufficiently large to enable aerodynamic and, particularly, reaction jet effectiveness studies postflight. The latter varies from instrument to instrument and results in part from the limited amount of preflight test data to adequately define the full error correction model (ref. 4).

The tri-redundant IMU data used to calibrate the ACIP data are available postflight at about a 1-Hz rate and are known to be quite accurate. The IMU-derived dynamic data in body coordinates are translated from the nav base location in the nose of the Shuttle vehicle to the ACIP instrument location, and are derived at a rate equal to the ACIP data rate. Due primarily to the effects of instrument quantization over a 1-second time interval, the IMU-derived angular rates are accurate to about 0.01 deg/sec, the linear accelerations to about 1 mg, and the angular accelerations to about 0.01 deg/sec^2. These values represent the latent accuracy of the IMU and hence represent the best level of improvement that could be expected for ACIP data calibration. For a more complete discussion of the technique for converting the inertial dynamic data into equivalent body accelerations and rates, and the resulting accuracies, see reference 3.

The purpose of this paper is to rigorously determine the errors associated with the ACIP instruments flown on Shuttle flights 1, 3, 4, and 5.* With this "lesson learned," the ACIP data can be calibrated, and aerodynamic investigators will have a more accurate dynamic data input source to extract aerodynamic coefficients.

METHOD OF STUDY

A weighted least-squares batch estimation algorithm was employed. The highly accurate, low-rate, Inertial Measurement Unit data were converted to high-rate body axis angular rates and accelerations, and linear accelerations, using the technique described in reference 3. The IMU data were the observables with which the ACIP data were differenced to determine the coefficients of a modified error calibration model (ref. 5). The coefficients represent physical error sources associated with the ACIP instrument, such as constant and temperature-dependent bias, linear and quadratic scale factor, static and dynamic misalignment and g-sensitivity. The 170-Hz ACIP data were "thinned" to 25 Hz for the purposes of this study.

Due to the noisy nature of the ACIP data, resulting primarily from vehicle structural vibrations, an extremely low signal-to-noise ratio was obtained comparing the IMU-ACIP differences at the 25-Hz rate. Thus, an averaging technique was applied to the data, effectively smoothing over the high-frequency noise and enhancing the signal detection capabilities. The error coefficients determined in this manner represent the calibrations which best match the ACIP data to the IMU data, in a least-squares sense.

The bias portion of the ACIP error was determined from an examination of the IMU-ACIP averaged differences during the approximately 20-minute quiescent mode following the termination of the de-orbit burn. In the absence of any significant external accelerations or angular rates, the only error contribution to the ACIP output would be a constant bias value. The on-orbit biases thus determined were those values which resulted in a zero-mean ACIP error during that 20-minute period. These biases were then held constant during the estimation of the remaining ACIP calibration coefficients over the entire reentry trajectory to permit determination of the remaining (potential) systematic errors.

The bias error consists of a constant component and a temperature dependent component (ref. 4). During the Shuttle reentries examined, the change in temperature throughout the 20-minute quiescent mode was quite small, on the order of 10°F, or less than 0.01°F/second on the average. Thus, although the total bias could be easily obtained, it was difficult to separate out the constant and temperature-dependent portions on any one flight. However, with two or more flights available with the same ACIP instrument package, a least-squares fit can be applied to the total biases and average temperatures to obtain the constant and temperature dependent components that best match the total biases from all flights examined. This technique was successfully accomplished with the STS-3, 4, and 5 data. However, for the STS-1 flight (with the different ACIP package), the total bias is attributed to the constant

*A different ACIP instrument package was flown on STS-1 as opposed to the package which flew on flights 3, 4, and 5. Due to an onboard recorder failure, no ACIP data was available for postflight analysis following STS-2.

term, and no temperature dependent terms are estimated. As it turns out, the STS-1 linear accelerometer and rate gyro biases were much smaller than those seen on the ACIP instrument which flew in flights 3, 4, and 5.

It should be mentioned that prior to any ACIP error calibration determinations, the recorded ACIP input data were carefully edited to remove all blunder points which were present.

RESULTS

Complete tables of results appear at the end of this paper. In addition, the data from selected components of the STS-3 ACIP instrument package are plotted to give the reader graphical insight into the calibration process. In particular, the yaw rate, R, has been chosen to exemplify rate gyro results, y-axis acceleration, a_y, to demonstrate linear accelerometer results, and roll angular acceleration, $\dot{P}$, to show angular accelerometer results. Time 0 corresponds to de-orbit burn ignition minus 10 seconds. The vehicle rolled to a stop some 3162 seconds later on STS-3.

Figures 2, 3, and 4 show the residuals for STS-3 IMU-edited yaw rate, y-body rate, and roll-angular accelerator rate, respectively. Figures 2(a), 3(a), and 4(a) show the noisy nature of the recorded ACIP data due in part to high-frequency structural vibration induced rates not sensed by the (comparatively low-rate) IMU. The plots show the difference between the edited (but uncalibrated) ACIP measured dynamic data and the IMU #1 derived dynamic data.

Figures 2(b), 3(b), and 4(b) show the IMU-ACIP averaged residuals that are plotted to the same scale and that use the averaging technique described earlier, with 100-second intervals. As it turns out, for the yaw rate gyro, there was not much of a residual global error as evidenced by the small 0.00022 deg/sec mean, and the 0.00109 deg/sec standard deviation in the 100-second means as shown in figure 2(b).

Figure 3(a) shows the IMU-ACIP y-linear accelerometer actual residuals. Figure 3(b) shows the underlying signal via the averaged residuals plotted to the same scale. Note the relatively large 27.96-mg mean error in the y-accelerometer, as well as the curved signature, indicating detectable error in the ACIP signal. Likewise, the average roll angular accelerometer residual, μ_{PDOT}, plot of figure 4(b) shows the mean signal which is nearly masked by the actual angular accelerometer residual plot (fig. 4(a)). Figures 2, 3, and 4 illustrate the need for residual averaging and improved signal detection capability.

Figures 5, 6, and 7 illustrate the IMU-ACIP differences, with on-orbit bias calibrations only applied to the ACIP dynamic data (figures (a)) versus fully calibrated ACIP data (figures (b)). Fully calibrated here means that combination of bias scale factor, misalignment and/or g-sensitive terms that best fits the ACIP data to the IMU data. This and all subsequent plots represent 100-second "averaged" residuals. As described earlier, instrument biases were determined from a period approximately 20 minutes in length following the de-orbit burn cutoff, in a quiescent environment with no measurable ongoing rates or accelerations.

Before proceeding to examine individually the ACIP component calibration solutions, some introductory comments on the overall results obtained are in order. By and large, the major portion of the IMU-ACIP differences results from a bias in the ACIP data. Thus, application of the on-orbit bias solutions to the linear calibration data generally removes most of the IMU-ACIP differences. (An exception is the $\dot{P}$

angular accelerometer). Nevertheless, a smaller, but detectable signal remains after application of the on-orbit bias, as will be shown in figures 5, 6, and 7. Thus, "fine tuning" of the ACIP data by application of calibration coefficients beyond on-orbit bias is recommended only for relatively large (compared to nominal) and consistent (flight-to-flight) estimated values obtained.

Table 2 lists the results of the application of the on-orbit bias terms and additional calibration constants for the rate gyros for Shuttle missions 3, 4, and 5. Looking at the STS-3 roll gyro rate P, for example, shows that the application of on-orbit bias values of 37.8E-3 deg/sec, and -0.37E-3 deg/sec/°F, results in an IMU-ACIP fit with 2.3E-3 deg/sec mean, and 3.0E-3 deg/sec dispersion about the mean. The fit was further improved from 3.0E-3 to 2.0E-3 deg/sec, with the application of the g-sensitive calibration corrections. Similar improvement was noted for the STS-4 and STS-5 results.

Smaller biases were ascertained for the pitch gyros. Not only did the bias remove almost all of the ACIP error, the application of no other optimally determined calibration coefficient was able to significantly improve the fit.

The yaw rate gyro channel, R, yielded results similar to the pitch gyro. Small on-orbit biases (0.5E-3 deg/sec and -0.13E-3 deg/sec/°F) were determined and are recommended for application to the linear calibration ACIP data. In addition, the application of a small positive scale factor yielded a somewhat improved fit. The STS-3 yaw rate, R, differences are plotted in figure 5. As can be seen, there was some improvement in going from the on-orbit bias calibration only (fig. 5(a)), to the bias plus scale factor solution (fig. 5(b)).

Thus, in general, the STS-3, 4, and 5 ACIP gyros were well behaved. The application of bias terms only was sufficient to achieve a good fit compared to the IMU data. With resulting fits on the order of the inherent accuracy of the IMU data, it is not surprising that additional calibration corrections yielded little or no fit improvements.

Figure 6(a) shows the signal remaining in the STS-3 y-accelerometer with an on-orbit bias of 30.7 mg, and -0.14 mg/°F applied. Familiarity with the linear acceleration time history of STS-3 shows a striking similarity between the difference plot of figure 6(a) and the Z-body axis acceleration. And in fact, the application of a somewhat large value of 17.0 $\widehat{\text{min}}$ of static misalignment (Z onto Y) results in figure 6(b), which shows a significant fit improvement (from 3.10 mg above, to 0.42 mg below) with most of the difference signal removed. Table 3 lists the linear accelerometer calibration results for the 3 flights. No additional calibration beyond static misalignment resulted in any substantial fit improvement for a_y. Again, as was true for the gyros, the resulting fit is on the same order as the accuracy of the IMUs themselves, and hence the application of additional calibration coefficients would not be expected to produce significant additional fit improvements. The x and z linear accelerometers are also tabulated in table 3. There was a significant improvement in the ACIP x-accelerometer signal fit applying linear scale factor calibrations. No additional improvement was obtained by solving for static misalignment or quadratic scale factor coefficients. The a_z linear accelerometer fit was not improved with the application of any calibration coefficient beyond constant and temperature dependent bias. Thus, a constant bias of 16.0 mg and a temperature dependent bias value of -0.08 mg/°F are recommended for application to the a_z data. Such a calibration application results in 0.3-mg mean, and 0.5-mg sigma for STS-3,

-0.1-mg mean with a 0.5-mg sigma for STS-4, and a 0.0-mg mean with a 0.4-mg sigma for STS-5.

Figure 7(a) shows the remaining signal in the $\dot{P}$ roll angular accelerometer data with on-orbit bias calibrations only applied. Figure 7(b) plotted to the same scale reveals a sizeable improvement in signal fit with the application of a g-sensitive calibration coefficient solution. Although much improved, the signal fit is still rather large as indicated by the 0.05453 deg/sec^2 σ_μ. Figure 8(a), with expanded scales, depicts more clearly the residual error signal. The results of the angular accelerometer calibration studies are listed in table 4. Note that no calibration constants other than bias improves the $\dot{Q}$ or $\dot{R}$ angular accelerometer fits. It should be pointed out that, despite averaging, the remaining signal-to-noise ratio in the angular accelerometer channels was still too small to permit any meaningful scale factor calibration or static misalignment solutions.

Compared to the gyro and linear accelerometer results, the optimally calibrated ACIP angular accelerometer data fits contained significantly more residual error signal. Therefore, in an attempt to improve the IMU-ACIP angular accelerometer data fit, the modified Bendix error model (ref. 4) was expanded to allow for g-sensitive contributions along the angular accelerometer axis, and angular rate term contributions along any of the 3 instrument axes. Unfortunately, this model augmentation did not appreciably reduce the signal present in the IMU-ACIP averaged differences.

As an experiment, the uncalibrated ACIP angular rate gyro data were back differenced (at the 25-Hz frequency) to create pseudo $\dot{P}$, $\dot{Q}$, and $\dot{R}$ angular accelerometer data. These were then differenced with the IMU data. The results for the "$\dot{P}$" data are plotted in figure 8(b). Note the significant improvement in fit. The utility of this incestuously derived angular acceleration data is outside the scope of this report; it is clear, however, that the ACIP angular accelerometers themselves have sizeable errors which can be easily detected when compared to IMU-generated angular accelerations. The ACIP gyro-derived angular accelerations, on the other hand, have hardly any error in signal whatsoever. For purposes of comparison, the STS-3 $\dot{P}$, $\dot{Q}$, and $\dot{R}$ IMU-calibrated ACIP angular accelerometer σ's are 0.055, 0.018, and 0.018 deg/sec^2, respectively (obtained from table 4). The IMU-uncalibrated ACIP gyro-derived angular acceleration σ's are 0.0058, 0.0002, and 0.0003 deg/sec^2 for $\dot{P}$, $\dot{Q}$, and $\dot{R}$, respectively.

The next series of plots, figures 9, 10, and 11, are presented to demonstrate that the signal remaining after application of the optimally determined calibration coefficients are nevertheless due to the ACIP model itself, and not the IMU data. The top plots are repeated from figures 5(b), 6(b), and 7(b) (showing the IMU#1 fully calibrated ACIP data), while the bottom plots show the IMU#2 ACIP differences. As can be seen, the upper and lower plots are nearly identical, thus indicating that all remaining signals are due to limitations of the current calibration equations to completely model the ACIP error sources.

Tables 5, 6, and 7 summarize the STS-1 calibration study results using 100-second averaging time intervals. Generally speaking, the on-orbit biases were smaller than those determined from the ACIP package flown on flights 3, 4, and 5 (one exception was the pitch rate, $\dot{Q}$, angular accelerometer). Also, even though the STS-1 results represent a different instrument package, and different trajectory, the IMU-ACIP data fits were comparable (again, with the exception of the $\dot{Q}$ fit which was larger for STS-1). In other words, the ACIP data was fit equally well to the IMU data for all 3 flights examined.

The roll rate, P, gyro showed some error signal which was successfully reduced from a fit of 6.7E-3 deg/sec to 1.0E-3 deg/sec with the application of both x and $\dot{z}$ g-sensitive calibration coefficient solutions as well as linear scale factor (table 5). The pitch rate, Q, gyro had a very accurate fit of 1.5E-3 deg/sec with on-orbit bias only applied. Thus, further calibration is not warranted. A linear scale factor solution of 1.0061 deg/sec/volt is recommended for application to the yaw rate, R, gyro, as the fit was improved from 2.9E-3 deg/sec to 1.1E-3 deg/sec (table 5). Thus, all 3 STS-1 gyros were calibrated to global fits on the order of 0.001 deg/sec.

Table 6 shows that the x linear accelerometer ACIP output fit was significantly improved by the application of a constant linear scale factor term only (0.14787 g/volt vs a nominal value of 0.15 g/volt), but nothing much else. Improvement of the y accelerometer output was obtained only with a z-channel static misalignment solution of 3.9 $\widehat{\text{min}}$. A relatively large improvement was obtained for the STS-1 ACIP a_z linear accelerometer with the application of a scale factor coefficient value of 0.29900 g/volt (nom = 0.30 g/volt). The 3 STS-1 ACIP linear accelerometers were all calibrated to global accuracies of less than 1 mg.

Table 7 reveals that the roll angular acceleration, $\dot{P}$, IMU-ACIP data fit was improved by over an order of magnitude (from 0.31 deg/sec^2 to 0.023 deg/sec^2) with the application of an a_z g-sensitive calibration coefficient value of -2.7E-3 rad/second^2/volt. No other calibration solutions significantly improved this resulting fit. The $\dot{Q}$ pitch angular accelerometer had one of the largest constant bias value seen of the 4 flights examined: 0.40 deg/sec^2. The application of the bias correction resulted in an IMU-ACIP fit of 0.14 deg/sec^2 (table 7). Additional improvement was obtained with the application of g-sensitive calibration coefficients, yielding a resultant fit of 0.052 deg/sec^2. Finally, the $\dot{R}$ yaw angular accelerometer fit was improved with the application of an a_x g-sensitive term of 2.1E-3 rad/sec^2/volt, resulting in an IMU-ACIP fit of 0.039 deg/sec^2. Thus the 3 STS-1 ACIP angular accelerometers were calibrated to global accuracies on the order of 0.05 deg/sec^2.

Unlike the ACIP package flown in flights 3, 4, and 5, the STS-1 ACIP has no other flight data with which to compare. Thus, all on-orbit bias determinations were attributed to the constant component of the bias term, i.e., all temperature dependent biases are zero by definition, as was mentioned previously.

CONCLUSIONS

The results of this study showed that significant systematic errors were present in the Aerodynamic Coefficient Identification Package flown on Shuttle flights STS-3, STS-4, and STS-5, and, to a somewhat lesser extent, the ACIP flown on STS-1. These errors were extracted with the use of calibration coefficients estimated with a weighted least-squares batch filter algorithm. Identified were error sources such as constant and temperature dependent biases, linear scale factors, static misalignment, and g-sensitivity terms. The resultant calibrated data showed a considerable accuracy improvement in most components over the uncalibrated data. Nevertheless, a small amount of signal remains which cannot be accounted for with the current modified error model.

The angular accelerometers had the largest error residual signatures remaining after calibration. Extensions of the angular accelerometer error model were

investigated without success. An examination of ACIP gyro-derived angular accelerations yielded a much closer fit to the IMU-derived angular accelerations than did the ACIP angular accelerometers themselves.

Thus, having completed several Shuttle flights, one of the "lessons learned" was the uncalibrated accuracy associated with the ACIP dynamic data. It remains for aerodynamic investigators to determine the effect of the dynamic data errors identified in this paper upon aero coefficient extraction.

REFERENCES

1. Findlay, J. T.; Kelly, G. M.; and Heck, M. L.: Reconstruction of the First Space Shuttle (STS-1) Entry Trajectory. NASA CR-3561, 1982.

2. Compton, H. R.; Scallion, W. I.; Suit, W. T.; and Schiess, J. R.: Shuttle Entry Performance and Stability and Control Derivatives Extraction From Flight Measurement Data. AIAA Paper No. 82-1317, August 1982.

3. Heck, M. L.; Findlay, J. T.; Kelly, G. M.: The Adaptation of a Strap Down Formulation for Processing Inertial Platform Data. AIAA Paper No. 82-1332, August 1982.

4. ACIP Error Correction Models, Final Report. BSR4426, Bendix Corporation, Communications Division, Oct. 1980.

5. Heck, M. L.: Aerodynamic Coefficient Identification Package Calibration Study Results Using Inertial Measurement Units. AMA Report No. 83-1, Analytical Mechanics Assoc., Inc., 1983.

TABLE 1.- ACIP OUTPUT RANGE

Component	Counts	Volts	Engineering Units
a_x	0 → 16383	±10	± 1.5 g
a_y	0 → 16383	±10	± 0.5 g
a_z	0 → 16383	±10	± 3.0 g
P	0 → 16383	±10	± 30 deg/sec
Q	0 → 16383	±10	± 10 deg/sec
R	0 → 16383	±10	± 10 deg/sec
$\dot{P}$	0 → 16383	±10	± 2 rad/sec^2
$\dot{Q}$	0 → 16383	±10	± 1 rad/sec^2
$\dot{R}$	0 → 16383	±10	± 1 rad/sec^2

TABLE 2.- STS-3, 4, AND 5 RATE GYRO CALIBRATION RESULTS

	ACIP CALIBRATION COEFFICIENT SET		VALUE	GLOBAL FIT (deg/sec)					
				STS-3		STS-4		STS-5	
				μ	σ	μ	σ	μ	σ
P	NO CALS			39.4E-3	2.3E-3	44.7E-3	1.6E-3	44.6E-3	1.5E-3
	BIAS CALS ONLY	CONSTANT TEMPERATURE DEP.	37.8E-3 deg/sec -0.37E-3 deg/sec/°F	2.3E-3	3.0E-3	2.6E-3	3.6E-3	2.5E-3	2.9E-3
	BIAS PLUS FULL CALS	G-SENSITIVITY to a_x G-SENSITIVITY to a_y	-2.6E-3 deg/sec/volt -6.5E-4 "	0.4E-3	2.0E-3	0.7E-3	2.8E-3	0.4E-3	1.0E-3
Q	NO CALS			1.7E-3	0.8E-3	3.3E-3	0.9E-3	3.2E-3	1.4E-3
	BIAS CALS ONLY	CONSTANT TEMPERATURE DEP.	2.5E-3 deg/sec -0.10E-3deg/sec/°F	-0.4E-3	0.6E-3	-0.3E-3	0.7E-3	-0.3E-3	1.2E-3
	BIAS PLUS FULL CALS	NO IMPROVEMENT BEYOND BIAS ONLY							
R	NO CALS			0.2E-3	1.1E-3	2.2E-3	1.6E-3	2.2E-3	1.9E-3
	BIAS CALS ONLY	CONSTANT TEMPERATURE DEP.	0.5E-3 deg/sec -0.13E-3deg/sec/°F	0.1E-3	0.9E-3	-0.0E-3	1.7E-3	0.1E-3	1.5E-3
	BIAS PLUS FULL CALS	LINEAR SCALE FACTOR (nominal = 1.0)	1.004 deg/sec/volt	-0.0E-3	0.6E-3	0.0E-3	1.3E-3	0.4E-3	0.8E-3

TABLE 3.- STS-3, 4, AND 5 LINEAR ACCELEROMETER CALIBRATION RESULTS

	ACIP CALIBRATION COEFFICIENT SET		VALUE	GLOBAL FIT (mg)					
				STS-3		STS-4		STS-5	
				μ	σ	μ	σ	μ	σ
a_x	NO CALS			-24.8	1.8	-21.6	1.5	-21.6	1.6
	BIAS CALS ONLY	CONSTANT TEMPERATURE DEP	-26.8 mg -0.21 mg/°F	1.4	2.2	1.5	2.4	1.6	2.3
	BIAS PLUS FULL CALS	LINEAR SCALE FACTOR (nominal = 0.15)	0.1466 g/volt	-0.0	0.7	0.3	1.2	0.2	0.7
a_y	NO CALS			28.0	3.6	31.1	3.0	30.7	3.7
	BIAS CALS ONLY	CONSTANT TEMPERATURE DEP	30.7 mg -0.14 mg/°F	-2.5	3.1	-1.7	2.2	-2.1	2.9
	BIAS PLUS FULL CALS	STATIC MISALIGNMENT w.r.t. a_z	17.0 min	0.0	0.4	-0.0	0.5	0.2	0.3
a_z	NO CALS			16.1	0.5	17.0	0.8	17.1	0.8
	BIAS CALS ONLY	CONSTANT TEMPERATURE DEP	16.0 mg -0.08 mg/°F	0.3	0.5	-0.1	0.5	0.0	0.4
	BIAS PLUS FULL CALS	NO IMPROVEMENT BEYOND BIAS ONLY							

TABLE 4.- STS-3, 4, AND 5 ANGULAR ACCELEROMETER CALIBRATION RESULTS

	ACIP CALIBRATION COEFFICIENT SET		VALUE	GLOBAL FIT (deg/sec^2)					
				STS-3		STS-4		STS-5	
				μ	σ	μ	σ	μ	σ
$\dot{P}$	NO CALS			-0.115	0.284	0.037	0.257	0.031	0.235
	BIAS CALS ONLY	CONSTANT TEMPERATURE DEP	-0.27 deg/sec^2 -0.012 $deg/sec^2/°F$	0.256	0.318	0.254	0.300	0.272	0.315
	BIAS PLUS FULL CALS	G-SENSITIVITY to a_z	-2.8E-3 $rad/sec^2/volt$	-0.006	0.055	0.018	0.037	0.012	0.055
$\dot{Q}$	NO CALS			-0.212	0.017	-0.199	0.012	-0.167	0.013
	BIAS CALS ONLY	CONSTANT TEMPERATURE DEP.	-0.21 deg/sec^2 -0.15E-2 $deg/sec^2/°F$	-0.000	0.018	-0.006	0.015	0.028	0.016
	BIAS PLUS FULL CALS	NO IMPROVEMENT BEYOND BIAS ONLY							
$\dot{R}$	NO CALS			-0.396	0.042	-0.419	0.044	-0.401	0.028
	BIAS CALS ONLY	CONSTANT TEMPERATURE DEP	-0.40 deg/sec^2 0.13E-2 $deg/sec^2/°F$	-0.012	0.018	-0.021	0.020	0.005	0.028
	BIAS PLUS FULL CALS	NO IMPROVEMENT BEYOND BIAS ONLY							

TABLE 5.- STS-1 RATE GYRO CALIBRATION RESULTS

	ACIP CALIBRATION COEFFICIENT SET		VALUE	GLOBAL FIT (deg/sec) μ	GLOBAL FIT (deg/sec) σ
P	NO CALS			-9.0E-3	6.7E-3
	BIAS CALS ONLY	CONSTANT	-1.4E-3 deg/sec	-7.6E-3	6.7E-3
	BIAS PLUS FULL CALS	LINEAR SCALE FACTOR G-SENSITIVITY wrt a_x G-SENSITIVITY wrt a_z	3.0155 deg/sec/volt 5.8E-3 deg/sec/volt 1.6E-3 deg/sec/volt	-0.1E-3	1.0E-3
Q	NO CALS			-0.4E-3	1.5E-3
	BIAS CALS ONLY	CONSTANT	-0.2E-3 deg/sec	-0.2E-3	1.5E-3
	BIAS PLUS FULL CALS	NO IMPROVEMENT BEYOND BIAS ONLY			
R	NO CALS			4.7E-3	2.9E-3
	BIAS CALS ONLY	CONSTANT	5.1E-3 deg/sec	-0.4E-3	2.9E-3
	BIAS PLUS FILL CALS	LINEAR SCALE FACTOR (nominal = 1.0)	1.0061 deg/sec/volt	0.0E-3	1.1E-3

TABLE 6.- STS-1 LINEAR ACCELEROMETER CALIBRATION RESULTS

	ACIP CALIBRATION COEFFICIENT SET		VALUE	GLOBAL FIT (mg) μ	GLOBAL FIT (mg) σ
a_x	NO CALS			2.5	1.8
	BIAS CALS ONLY	CONSTANT	1.3 mg	1.2	1.8
	BIAS PLUS FULL CALS	LINEAR SCALE FACTOR (nominal = 0.15)	0.14787 g/volt	-0.1	0.6
a_y	NO CALS			-0.2	0.6
	BIAS CALS ONLY	CONSTANT	0.8 mg	-1.0	0.6
	BIAS PLUS FULL CALS	STATIC MISALIGNMENT w.r.t. a_z	3.9 $\widehat{\text{min}}$	-0.2	0.4
a_z	NO CALS			3.7	1.9
	BIAS CALS ONLY	CONSTANT	1.4 mg	2.3	1.9
	BIAS PLUS FULL CALS	LINEAR SCALE FACTOR (nominal = 0.3)	0.29900 g/volt	0.0	0.3

TABLE 7.- STS-1 ANGULAR ACCELEROMETER CALIBRATION RESULTS

	ACIP CALIBRATION COEFFICIENT SET		VALUE	GLOBAL FIT (deg/sec^2)	
				μ	σ
$\dot{p}$	NO CALS			0.29	0.31
	BIAS CALS ONLY	CONSTANT	-0.06 deg/sec^2	0.35	0.31
	BIAS PLUS FULL CALS	G-SENSITIVITY to a_z	-2.7E-3 rad/sec^2/volt	-0.006	0.023
$\dot{Q}$	NO CALS			0.25	0.14
	BIAS CALS ONLY	CONSTANT	0.40 deg/sec^2	-0.15	0.14
	BIAS PLUS FULL CALS	G-SENSITIVITY to a_z	1.2E-3 rad/sec^2/volt	0.002	0.052
$\dot{R}$	NO CALS			0.18	0.08
	BIAS CALS ONLY	CONSTANT	0.26 deg/sec^2	-0.08	0.08
	BIAS PLUS FULL CALS	G-SENSITIVITY to a_x	2.1E-3 rad/sec^2/volt	-0.013	0.039

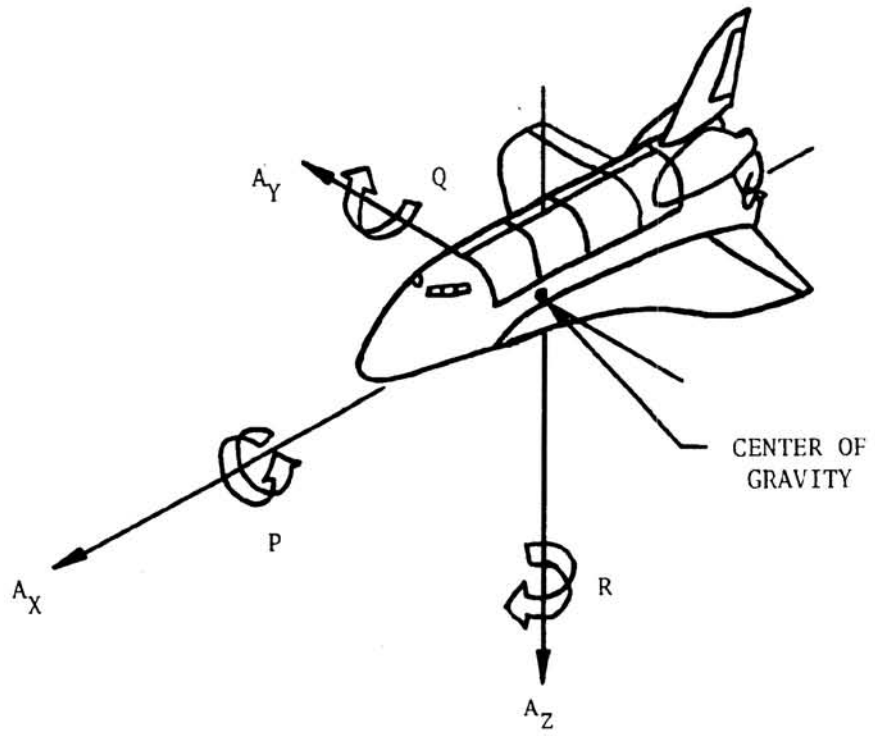

Figure 1.- Definition of body axis accelerations and attitude rates.

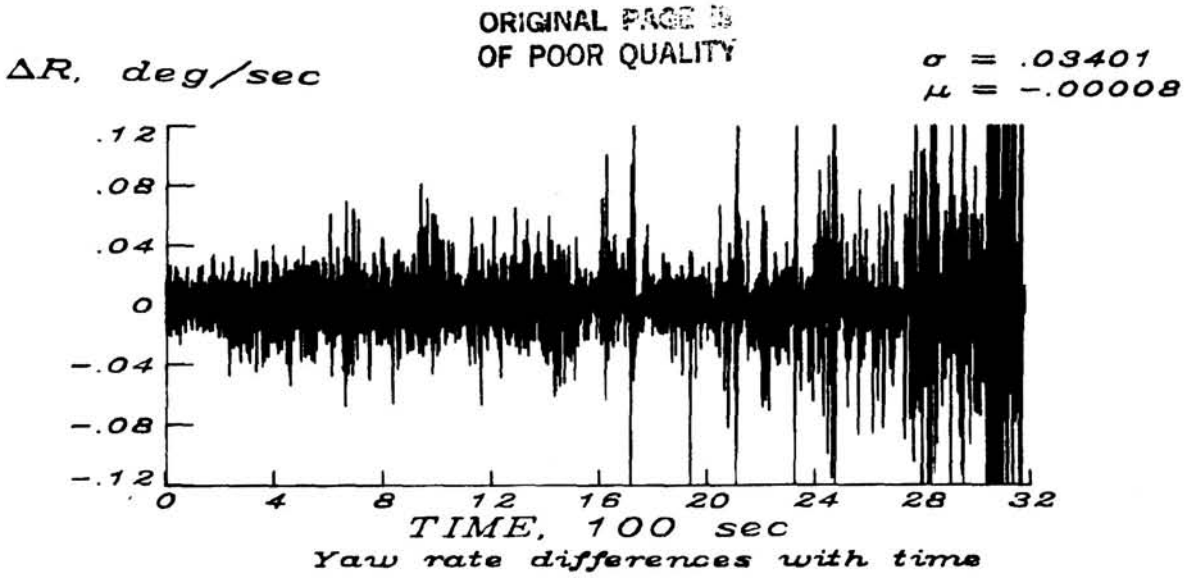

(a) Actual residuals.

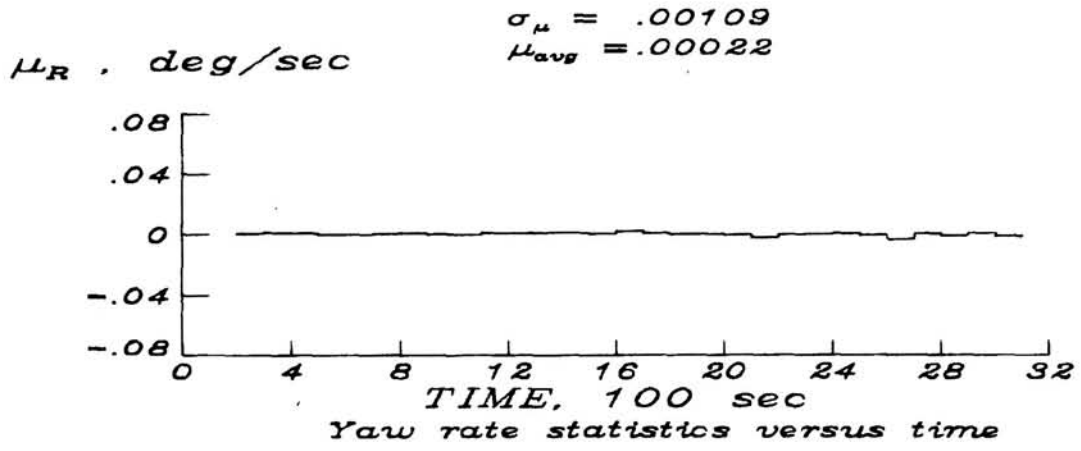

(b) Averaged residuals.

Figure 2.- STS-3 IMU-edited ACIP yaw rate residuals.

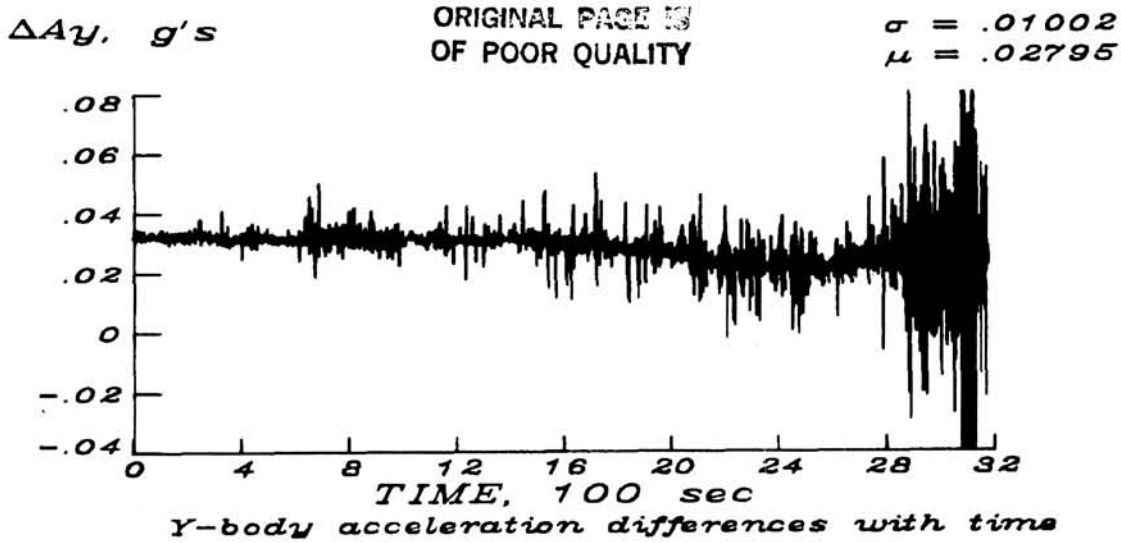

(a) Actual residuals.

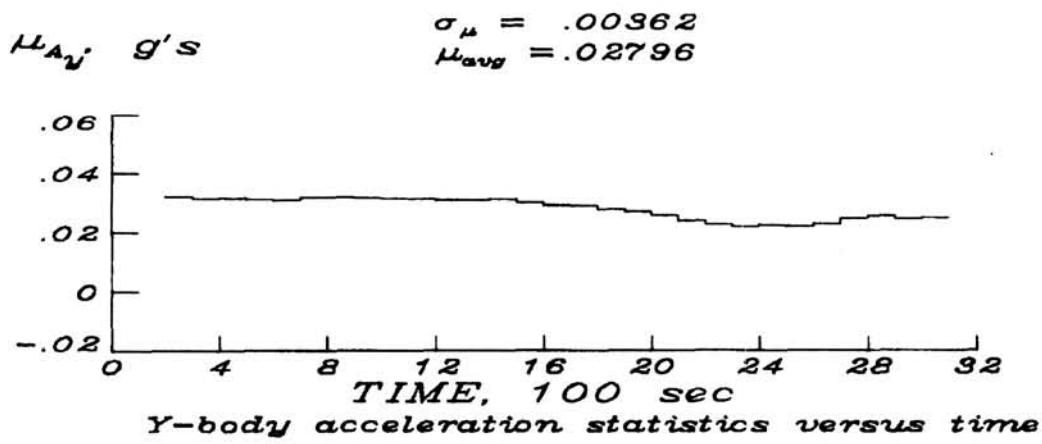

(b) Averaged residuals.

Figure 3.- STS-3 IMU-edited ACIP y-body rate residuals.

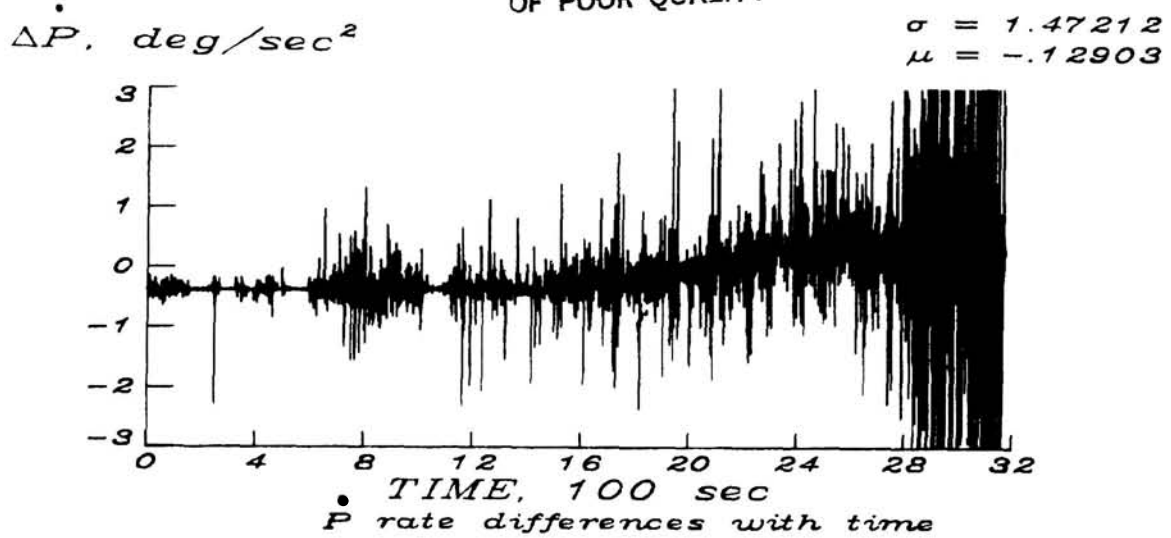

(a) Actual residuals.

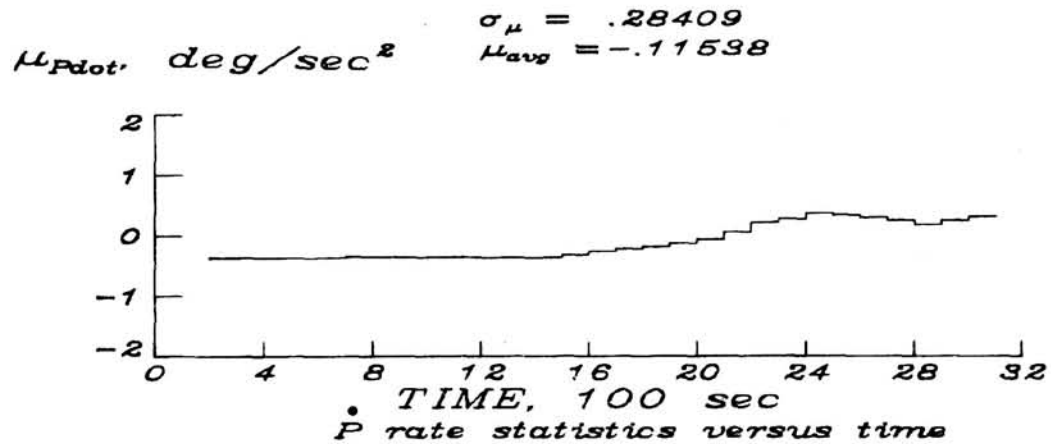

(b) Averaged residuals.

Figure 4.- STS-3 IMU-edited ACIP $\dot{P}$ rate residuals.

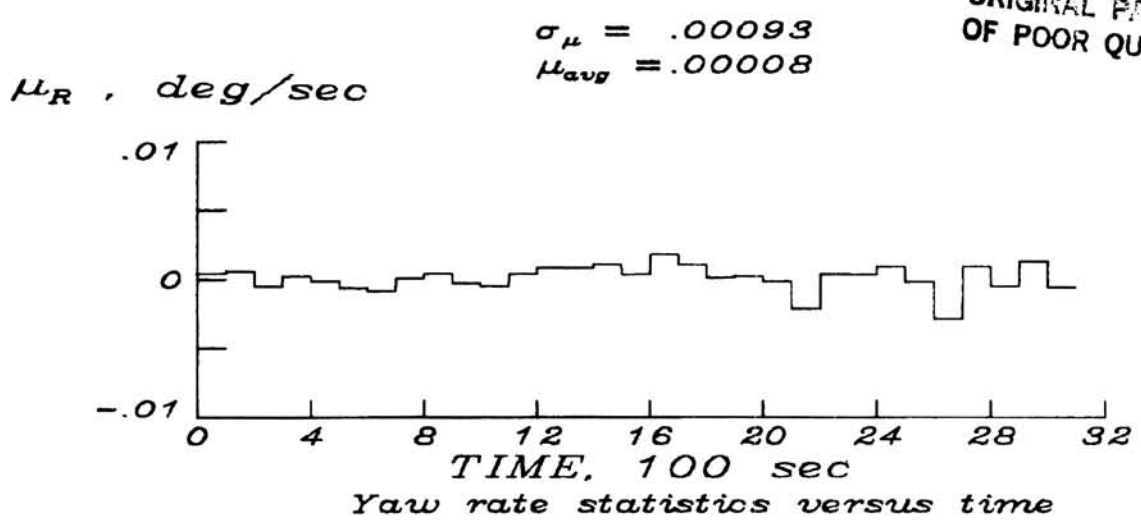

(a) On-orbit bias calibrations only.

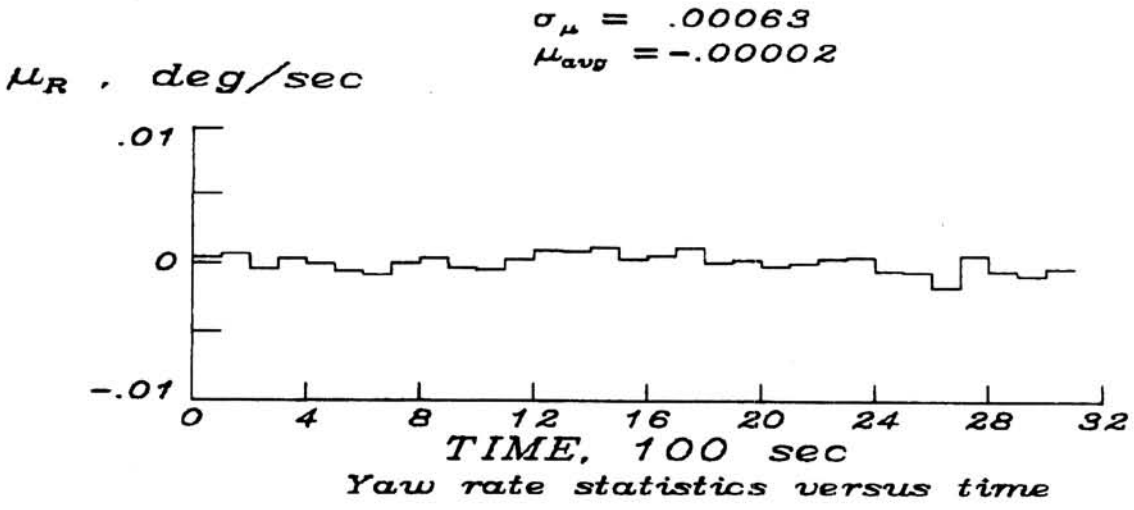

(b) On-orbit bias plus scale factor calibrations.

Figure 5.- Mean differences in STS-3 IMU-ACIP yaw rate.

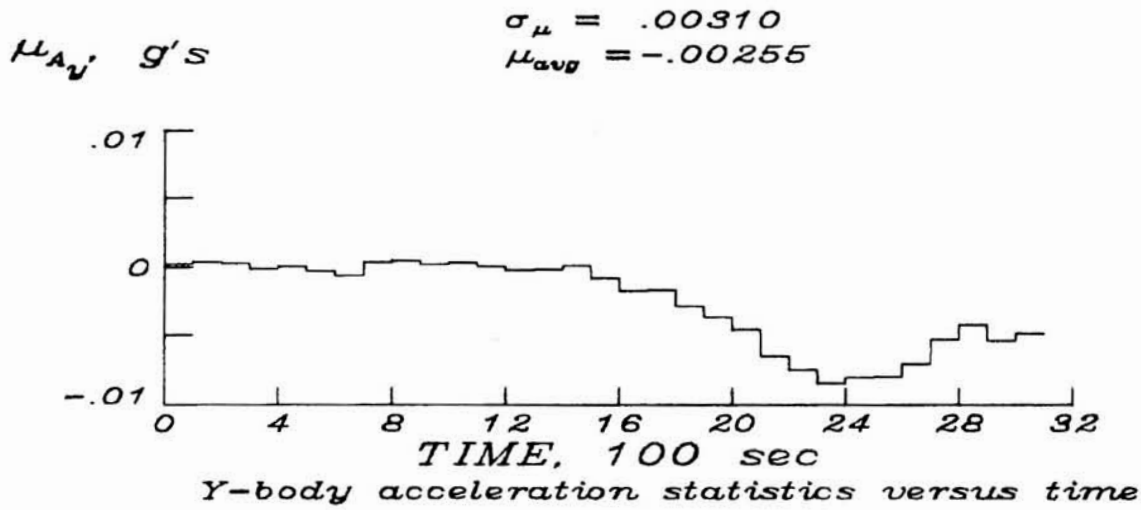

(a) On-orbit bias calibrations only.

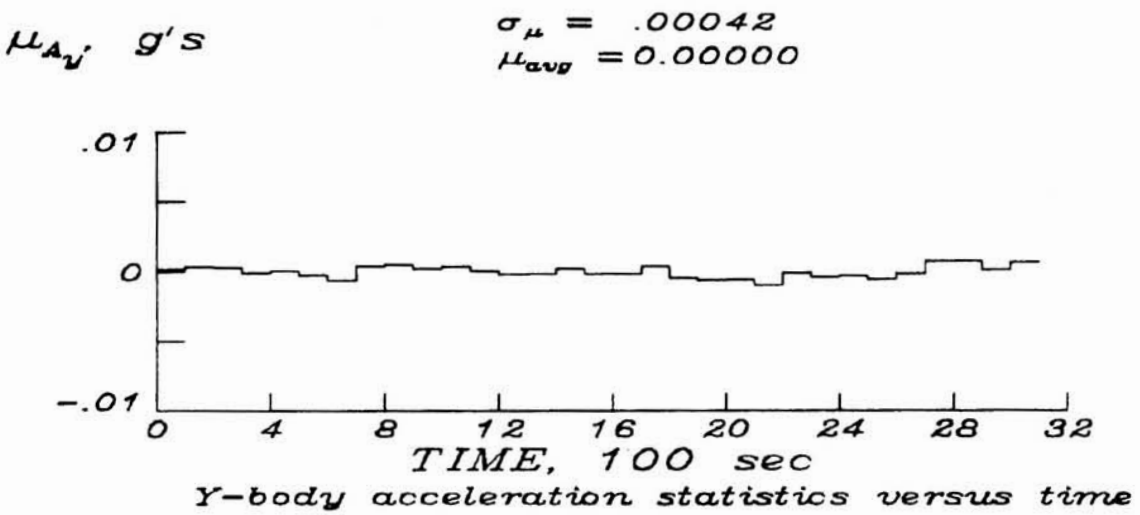

(b) On-orbit bias plus static misalignment calibrations.

Figure 6.- Mean differences in STS-3 IMU-ACIP y-body rate.

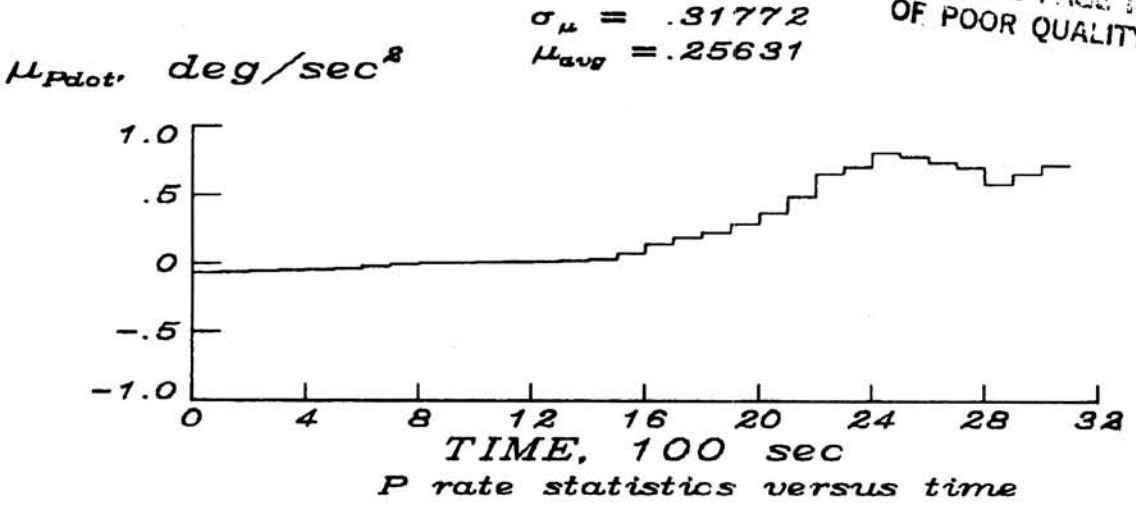

(a) On-orbit bias calibrations only.

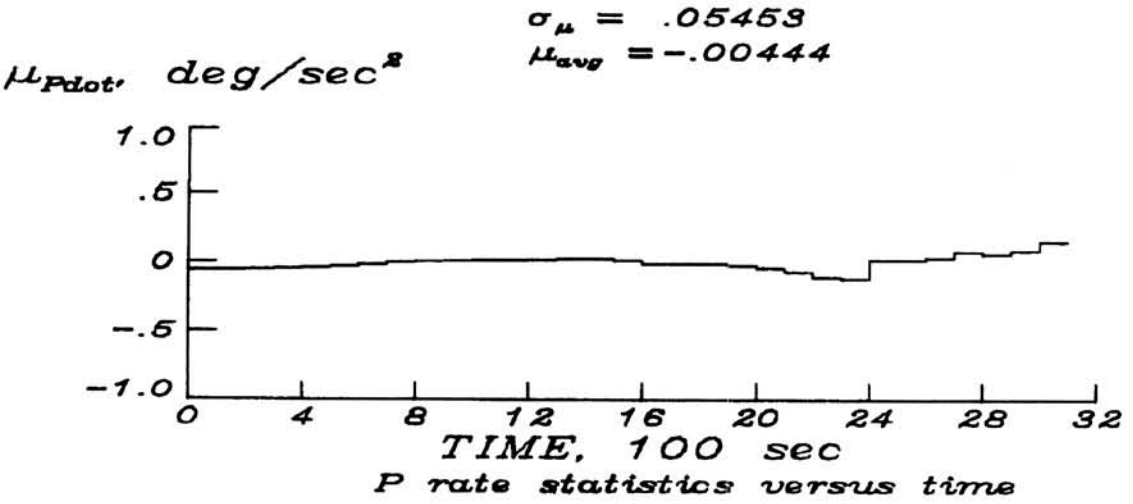

(b) On-orbit bias plus g-sensitive calibrations.

Figure 7.- Mean differences in STS-3 IMU-ACIP $\dot{P}$ rate.

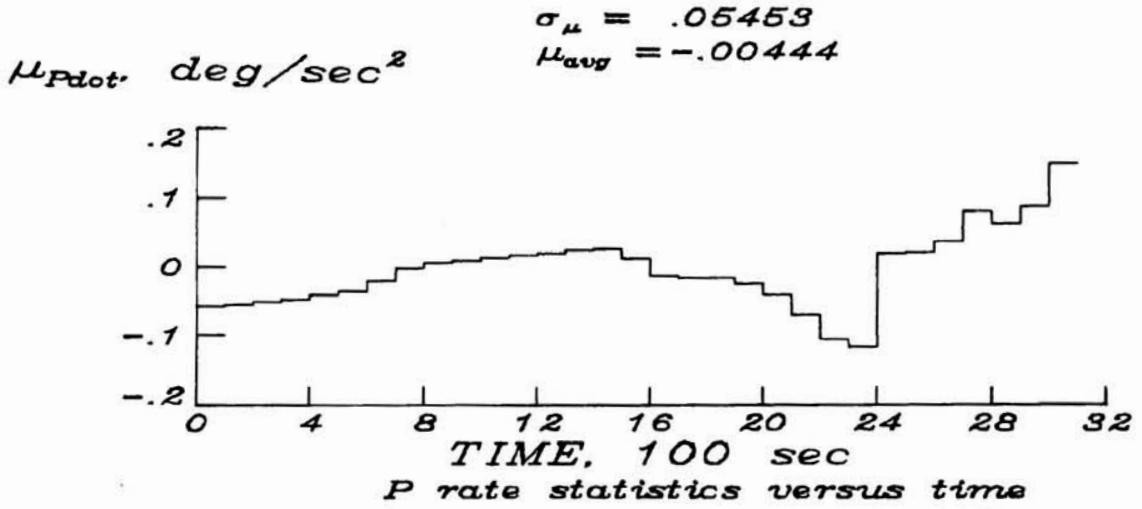

(a) STS-3 IMU-ACIP on-orbit bias plus g-sensitive calibrations.

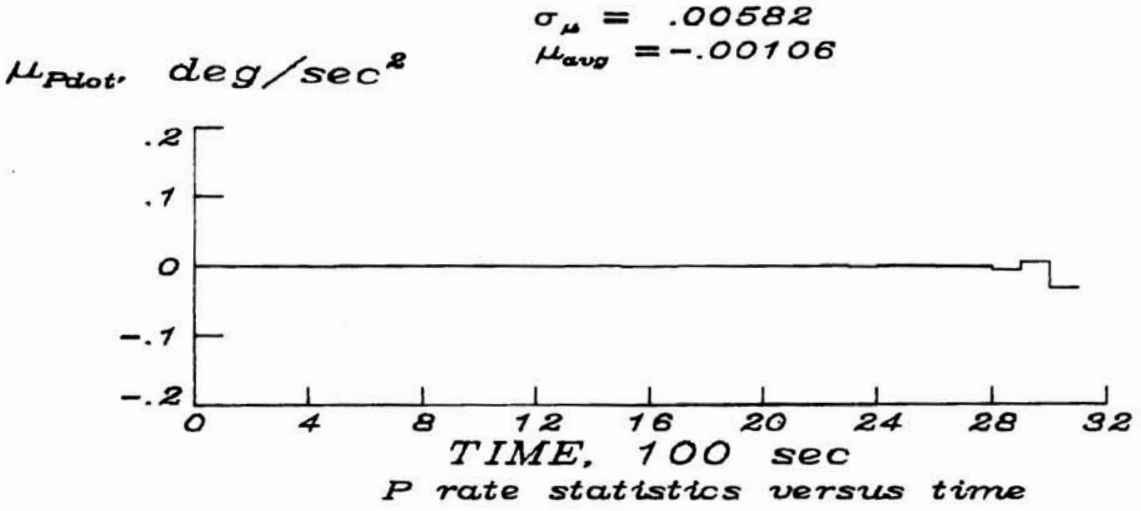

(b) STS-3 IMU-back-differenced P from ACIP (no calibrations).

Figure 8.- Mean differences in STS-3 IMU-ACIP $\dot{P}$ rate with expanded scales.

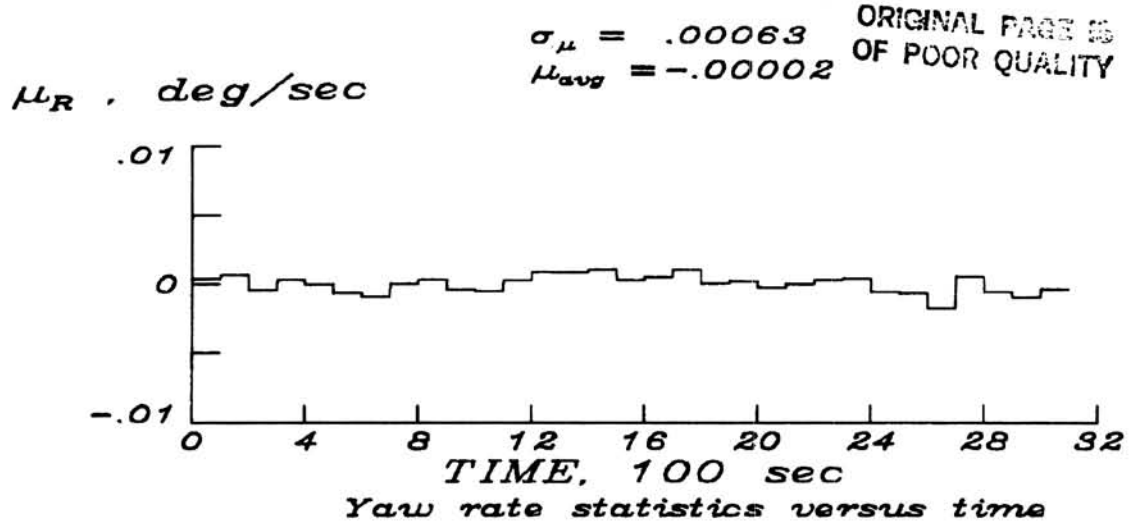

(a) STS-3 IMU number 1.

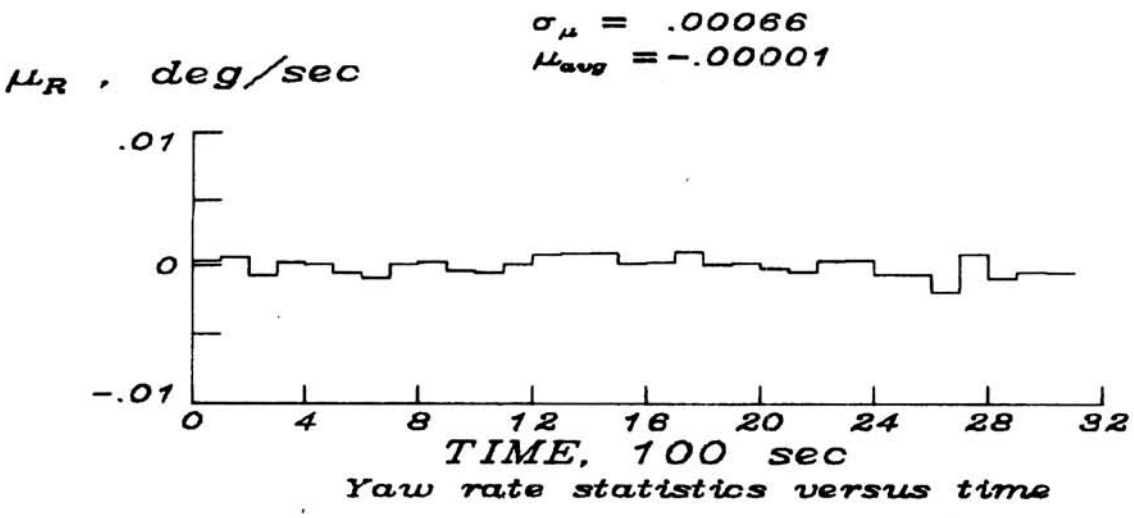

(b) STS-3 IMU number 2.

Figure 9.- Mean differences in STS-3 IMU number 1 and IMU number 2 - ACIP on-orbit bias plus scale factor calibrations.

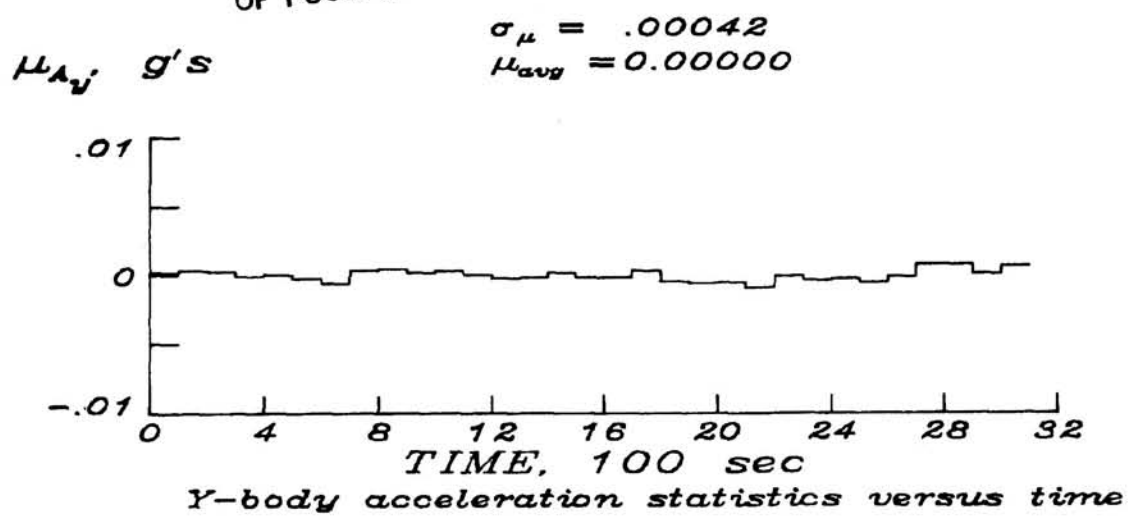

(a) STS-3 IMU number 1.

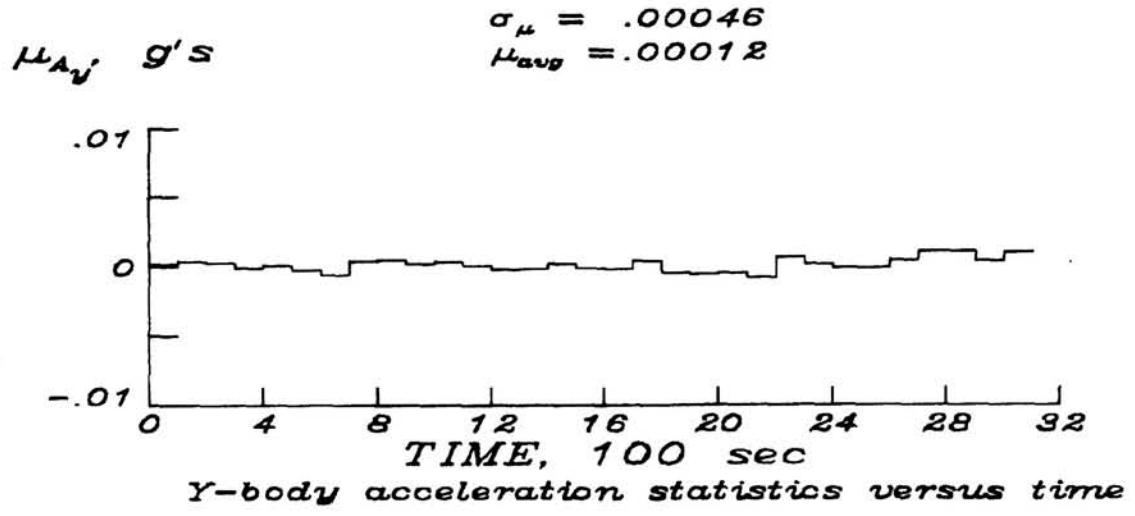

(b) STS-3 IMU number 2.

Figure 10.- Mean differences in STS-3 IMU number 1 and IMU number 2 - ACIP (on-orbit bias plus static misalignment calibrations).

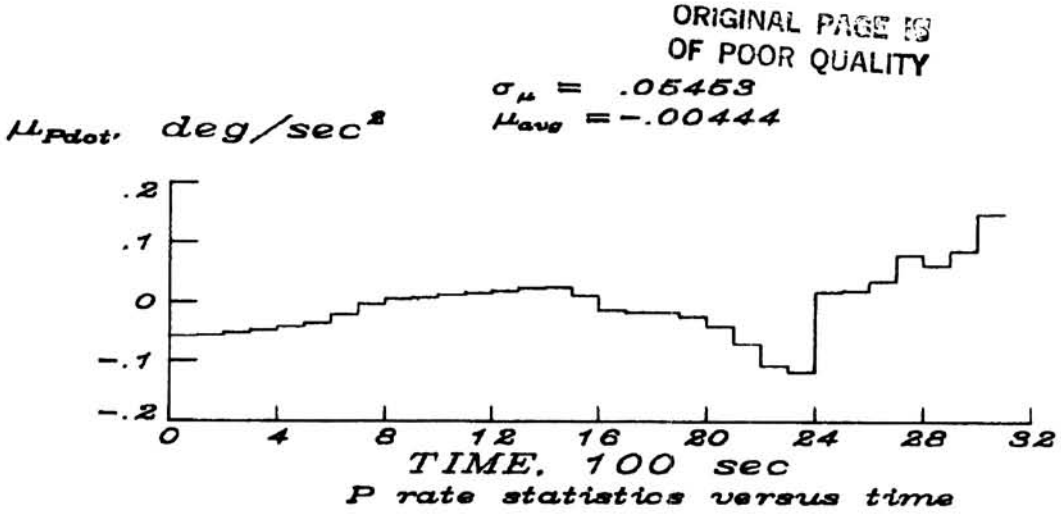

(a) STS-3 IMU number 1.

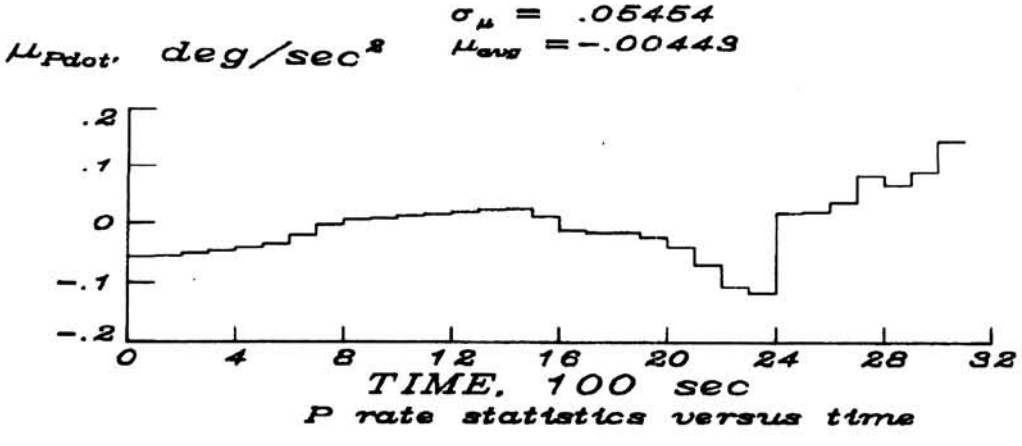

(b) STS-3 IMU number 2.

Figure 11.- Mean differences in STS-3 IMU number 1 and IMU number 2 - ACIP (on-orbit bias plus g-sensitive calibrations).

REMOTELY DRIVEN MODEL CONTROL SURFACES FOR EFFICIENT WIND-TUNNEL OPERATIONS*

George M. Ware, Bernard Spencer, Jr.,
and L. Raymond Gentry
NASA Langley Research Center
Hampton, Virginia

Abstract

A remote control system for wind-tunnel model control surfaces was developed during the Space Shuttle program to make more efficient use of wind-tunnel occupancy time and to aid in gathering the large force test data base necessary for the definition of the Shuttle aerodynamic characteristics. This paper presents a history of the development of the remote system, details of the system and associated equipment, and results from wind-tunnel tests showing the effect of system improvements on experimental data. Wind-tunnel test rate and cost comparisons are made between conventional models with bracketed control surfaces and remote models.

Introduction

Models using remotely driven control surfaces have been used in wind-tunnel tests for many years with varying degrees of success. The inherent problems of remote-control systems--the cost, complexity, and, more importantly, reliability--have generally led most experimenters to continue to use conventional angle brackets for positioning model control surfaces. Currently, however, the high cost of energy has focused attention on more efficient wind-tunnel operations. A remote-control system offers the possibility of markedly reducing the wind-tunnel time and cost required to define the aerodynamics of a configuration.

In support of the Space Shuttle Program, the Langley Research Center has designed, built, and tested several wind-tunnel models with remotely-driven elevons, body flap, and rudder. The models have been tested at Mach numbers from 0.30 to 4.5 and at dynamic pressures greater than 2,000 pounds per square foot. Although a reduction in wind-tunnel occupancy time from a cost and program scheduling standpoint was desirable, this was not the primary reason for constructing the remote-controlled Shuttle models. Because the Shuttle development plan did not include a conventional flight test program where the flight characteristics could be progressively explored but would have the vehicle perform the total mission on its first flight, the ground-based testing was extremely important. Therefore, a great deal of attention was directed to defining the aerodynamic characteristics of the Shuttle across its operating range through wind-tunnel tests.

*Presented at the AIAA 21st Aerospace Sciences meeting, Reno, Nevada, January 10-13, 1983.

Particular emphasis was placed on determining the vehicle control effectiveness and linearity, since the operational flight mode would be, to a large degree, computer controlled and require precisely known control characteristics. To build and test a model with numerous fixed brackets to adequately describe the control effectiveness was impractical, and, as a result, the remote system was developed. During the course of Shuttle development, several wind-tunnel models were built by the Langley Research Center with remote systems. The current system uses off-the-shelf electric motors and high-quality potentiometers mounted inside the model. The electrical control box has the capability to preselect as many as 80 control positions for as many as six different control surfaces. This paper presents a history of the development of several remote-controlled Shuttle models and gives a brief description of the drive system and position read-out equipment. Results from the wind-tunnel tests are given which illustrate improvements in the control system. Comparisons are made for wind-tunnel test rates using conventional bracketed control surface models and the remotely driven control models. The paper presents data showing the accuracy obtained in setting and holding control position during a test and the rapidity of changing settings. Cost comparisons are also being made between conventional and remote models.

History of the Langley Shuttle Remote Control Models

The design of a remote control model system grew out of the Shuttle program. Particular problems investigated during the development of the Shuttle lent themselves to a remote system, and as experience was gained, the system was developed and improved.

Split Elevon Model

Early in the Shuttle program (1973), heating and structural considerations led to the decision that the trailing-edge elevons on the vehicle be divided into four segments, each powered by a separate actuator system. The question then arose, "Is there an aerodynamic advantage to differentially deflect the segments?" For instance, the inboard surfaces could be used for pitch control, and the outboard surfaces for roll control. Another suggestion was to set the inboard elevons such that the outboard elevons would always be at a neutral or slightly positive deflection. This would maintain consistent roll/yaw characteristics from the outboard surfaces even at high angles of attack.

The problem of testing a control system such as this in a wind tunnel is obvious. A multitude of brackets for the four elevon segments would have to be constructed, and the test time would be unusually long because of the number of bracket changes necessary to complete a test matrix. The solution to the problem was a remotely driven elevon system. This first attempt was an extremely ambitious undertaking to drive four elevon segments independently. Fortunately, the Shuttle configuration has a large fuselage that could accommodate four small electric motors with reduction gear boxes and still have sufficient space available for a strain-gage balance and sting. (See Fig. 1.)

The elevons were driven by the motors through four individual systems of bellcranks and push rods. The outboard elevons rotated on a shaft passing through the shaft of the inboard elevons. To measure the position of the surfaces, a potentiometer was attached to the end of the gear box of each drive motor. The signals from these onboard potentiometers were received on four separate 10-turn potentiometers mounted on a console in the wind-tunnel control room. The elevon position, calibrated against potentiometer output, could be adjusted by operating the drive motors from the remote console. The system worked remarkably well for a first attempt. Over 120 runs in 30 hours of operation were made in the Langley 8-Foot Transonic Wind Tunnel and in the Unitary Plan Wind Tunnel. The system had several shortcomings, however. The potentiometers located on the gear box shaft did not read the "play" or "slop" in the bellcrank/push-rod system or the torsional bending of the elevon shaft as the elevon was aerodynamically loaded. Recognizing these problems, care was taken to insure close tolerances in construction of the assembly and the system was adjusted between tunnel entries. The accuracy of setting and the surface nevertheless deteriorated during the test as the controls were cycled.

Another weakness of the test technique was the human engineering aspect. It was quickly discovered that two operators were required to control the elevons, one for the right side and one for the left. Testing became a labor intensive activity resulting from the need for close coordination between the model control, tunnel, and data acquisition system operators and the need to constantly change or monitor the model surface positions. As experience was gained with the remote system, the tunnel time on-line increased until over 6 hours out of the 8-hour shift was spent taking data. Even with the problems of this first remote system, a large amount of meaningful data was obtained in a relatively short time that could not have been obtained to such an extent using a conventional bracketed model.

"Bang-Bang" Model

As the Shuttle entry flight plan developed, a concern was expressed that the combination of high angle of attack and high negative elevon deflection required for trim and control through the Mach range from 2 to 5 could induce flow separation over the upper surface of the wings. If the flow separated over one wing panel and not the other, the vehicle might diverge in a roll. In addition, this phenomena could be aggravated by a rapid roll control input. To investigate this potential problem, tests were planned using the Langley remote-control model. Since the flow separation could be initiated by the motion of the elevons, it was necessary to dynamically scale the movement of the surfaces. The Shuttle orbiter elevon deflection rate is 20° per second. This value scaled to the model size resulted in such an extremely high control rate that the use of an electric drive motor was impractical. The motors were, therefore, replaced by a pair of double acting pneumatic pistons. This system could drive the right and left elevons (the inboard and outboard segment having been pinned together) independently to their full up or down position almost instantaneously. The name "Bang-Bang" refers to a system that is either full on or full off and describes the modified model. The investigation was conducted in the Langley Unitary Plan Wind Tunnel. A photograph of the model prior to installation in the tunnel is presented in Fig. 2.

A typical example of the results of this test is shown in Fig. 3. The test procedure was to hold the model at a fixed angle of attack and deflect the control surfaces in both the positive and negative direction while taking continuous data. For each test condition, the force and moment data repeated consistently with mirror image values resulting from increasing and decreasing control deflections. The test progressed smoothly with no indication of asymmetric flow separation over the model.

The development of the pneumatically driven elevons was an unusual step in remote control development but added to the overall knowledge of such systems.

"Fine-Cut" Model

The next remote-control model resulted from the need to define in detail the aerodynamic characteristics of the final Shuttle orbiter configuration as construction began on the full-size vehicle. Because the Shuttle had to perform the complete mission on its first launch, care would have to be taken that there were no aerodynamic surprises. Therefore, a "fine-cut" series of wind-tunnel tests was initiated to define angle of attack, angle of sideslip, Mach number, and each control effectiveness parameter in small increments across the flight profile to insure that no nonlinear characteristics or other unknowns had been overlooked. For these tests, Langley Research Center used an existing Rockwell International 0.015-scale model and added a new wing with a remote left and right elevon system. (By this time the decision had been made to operate the inboard and outboard elevons as a single unit.) The model is shown in Fig. 4.

Several major improvements were made to the remote drive system on this new model. A small, accurate potentiometer was mounted directly into each elevon shaft on its axis of rotation. Any change in elevon angle, therefore, would be read directly by the potentiometer and eliminate all inaccuracies because of "play" in the drive system. The accuracy of the elevon setting, neglecting the very minute torsional bending in

the elevon shaft, was the accuracy of the potentiometer and its readout system. A second area of attention was the control console. A simple feedback system was installed to sense the position of the elevons and, if not at the proper angle, command the drive motor to return the surface to the desired position.

The data of Fig. 5 dramatically show the advantage of the feedback system. These data were taken in the Vought high-speed blowdown tunnel at a dynamic pressure of 2,000 pounds per square foot. The test technique was to start the run with the model at zero angle-of-attack and pitch through the angle-of-attack range at a constant rate. A run would generally take less than 30 seconds. As a result, the load on the model was constantly changing which caused the elevons to shift. Because of the short time interval, an operator could not adjust the surfaces during the run. As shown in Fig. 5, when feedback control was not employed, the elevons drifted off the desired condition several degrees. With feedback, there was almost no change in elevon angle. This was a most successful model with 16 tests comprising 2,744 runs in seven facilities in the time period from September 1975 to August 1977.

ALT Model

When the Shuttle Approach and Landing Tests (ALT) were planned, the first flights were scheduled with the body tailcone in place to reduce the drag and turbulence. This new configuration required another series of wind-tunnel tests. Since the tests would only be made in relatively large subsonic-transonic tunnels, a larger model than had previously been used could be accommodated. The resulting 0.30-scale model allowed sufficient room to expand the remote system to drive the body flap and rudder as well as the left and right elevon surfaces. At this time the control console was completely redesigned. The console (Fig. 6) now had four rows of 10 dial potentiometers that would allow the deflection schedule of each driven control surface to be preset to as many as 80 different positions. During a test, only a stepping switch was used to change control position. As with the previous model, the feedback system held the model surfaces at a fixed position.

The feedback system was also used in another manner. In this alternate mode of operation, the force and moment information from the internal strain-gage balance is sent to the control console where the feedback system drives the control surfaces to null out an unbalanced moment. For instance, the elevon surfaces could be driven to maintain zero pitching moment as the model was moved through an angle-of-attack range to obtain a trimmed pitch polar, or the rudder could be driven to balance out a yawing moment from aileron deflection. Results from such a test are illustrated in Fig. 7. It was then possible to "fly" the sting-mounted model in the wind tunnel.

High-Fidelity Model

Near the end of the aerodynamic development phase of the Shuttle program, Rockwell built a 0.02-scale high-fidelity orbiter model to the "as built" full-size Shuttle outer mold lines complete with protuberances such as recessed windshields, payload bay hinges, and control jet openings. This model was used to verify the aerodynamic data previously obtained using models of less fidelity. After completing this task, the model was sent to the Langley Research Center to be used in the event that analysis of Shuttle flight results might indicate a need for additional wind-tunnel tests. A remote system has been added to the model, and the latest improvements have been incorporated. To improve the drive mechanism, the bellcrank/pushrod design has been replaced with a screw action system. The arrangement is shown in Fig. 8. The motor turns a precision micrometer-like threaded rod and follower which rotate the control surface through a single bellcrank machined as part of the elevon. Misalignment during operation is handled by a precision universal joint. The model was equipped with remotely driven right and left elevons, body flap, and rudder. Because of the size of this model, it was necessary to locate the rudder drive motor in the nose portion and drive the rudder through a long shaft and a right-angle gear box at the rudder (Fig. 9). It was realized that there might be a need to test this model in facilities at operating temperature so high that internal motors and potentiometers could not be used. In order to retain as much of the control positioning mechanism as possible, the system was designed so that the motors could be replaced by a "Jacob's chuck" mechanical drive that was adjusted through a hole in the lower fuselage. The threaded drive link produced a positive lock on control position. A photograph of the model, which represents the evolution of the remote control model system to date, is shown mounted in the Langley Unitary Plan Wind Tunnel in Fig. 10.

Efficiency of Wind-Tunnel Operation With Remote Models

A study was made of the efficiency of using the remote Shuttle models as opposed to conventional models with bracket-mounted controls. A typical operation of the Langley 8-foot transonic pressure tunnel for the two types of models is shown in Fig. 11. This tunnel is representative of continuously operating closed-circuit tunnels. The tunnel is brought up to test conditions, a series of pitch and sideslip polars are made with the model controls at a specified position and at Mach numbers of interest. In the case of a conventional model, the tunnel is then shut down and opened up, model controls are repositioned, and the tunnel is brought back to test conditions. This is unnecessary, of course, for the remote-control model. As a result, the time required to complete a typical double-shift operation with a running time of 12 hours is reduced to 5-1/2 hours for a remote model with a manually operated control console and only 3-1/2 hours with an automated feedback control console. The fully implemented remote model therefore requires only about one-third of the tunnel time and power for control effectiveness tests.

Not all tests or models, however, are adaptable for a remote system. The chart in Fig. 12 is a depiction of types of tests conducted in the

8-Foot TPT in a typical year. As can be seen, approximately 70 percent of the tests could have benefited by the use of a remote model. This result is of course contingent on the model being able to accept the drive mechanism. A comparison of conventional bracketed model run rate versus remote model run rate in three Langley facilities is shown in Fig. 13. These results are for complete test programs that involve conditions other than control surface variation. The tests were also conducted before the construction of the automated console and, thus, are extremely conservative. Even so, the data indicate about a 50-percent saving in time and, therefore, energy. In facilities such as high Reynolds number tunnels that require time and energy to pump to elevated test pressures, the savings may be even greater. Power costs are becoming a more important factor in total wind-tunnel test cost. In order to get more "research per dollar" a remote control model system should be considered. Currently, the Langley Research Center is in the process of adapting the remote model to operate at cryogenic temperatures for use in the National Transonic Facility. If the modification is successful, it can significantly reduce configuration test time.

Cost of Remote Models

A study of the cost of the relatively sophisticated remote-control model compared to a bracketed model was made. Since the external lines of the models were assumed to be the same, the cost comparison is merely the cost of the purchase of motors, potentiometers, and construction of the drive mechanism as opposed to construction of numerous control surface brackets. The expense of the control console, which could be used with many models and might be considered a part of the wind-tunnel data acquisition system, is not included in the comparison. Obviously, the cost of the bracketed model is dependent on the number of different control settings selected for investigation. Plotted in Fig. 14 is the time required to build a three-control (left and right elevon and body flap) remote drive system and the cost of machining brackets. As can be seen, the remote system becomes less expensive if more than 15 control settings are required. It is possible, therefore, that a remote model may be less expensive than a bracketed model.

Accuracy of Control Settings

The capability of the remote system to set and hold a precise control position was continually improved as experience was gained with the various models. The latest model with screw-drive, precision potentiometers mounted on the axis of rotation of the control surface, and a feedback readout console has produced position accuracy within about $\pm 0.1°$. This is approximately the accuracy of the potentiometer itself. A calibration of a control surface to its maximum expected load is shown in Fig. 15. The total deflection of the elevon under full load is only about 0.25°. This deflection compares well with measured deflection of bracketed control surfaces. No direct comparison can be made, however, because of the variety of bracket designs and attachment methods. The repeatability of the control setting with the remote system is superior to brackets. With each control position bracket change, the chance of improper installation exists with the possible introduction of debris between mating surfaces and from differences in tightening the bracket. The remote system constantly displays control position and repeatability has been excellent.

Concluding Remarks

The development of a remote-control system for wind-tunnel models was a by-product of the Space Shuttle program. It was born of the necessity to obtain more data more quickly during wind-tunnel tests. The major advances in remote control systems were: 1) direct reading of the control angle by mounting a potentiometer on the axis of rotation of the surface, 2) a precision micrometer-like screw drive link that was self locking and almost entirely free of "play," and 3) a feedback system that maintained or set close tolerance control positions.

The results of tests with the remote system indicated that test time for control effectiveness investigations could be reduced by about two-thirds in a conventional continuously operating tunnel and by about 50 percent for more general wind-tunnel tests. In high Reynolds number facilities that operate at high pressure or cold temperatures, the savings may be even greater. Because of the increasing cost of wind-tunnel operation, it will be necessary in the future to take advantage of every means possible to improve efficiency. The wind-tunnel model with remotely driven control surfaces has been shown to be an effective means of increasing wind-tunnel efficiency.

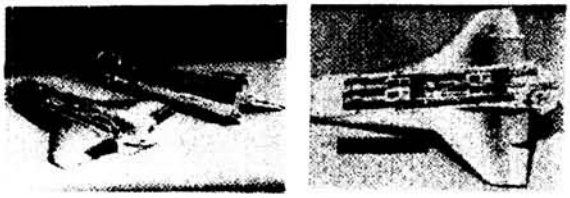

a) Complete model. b) Drive system.

Fig. 1 Split elevon model.

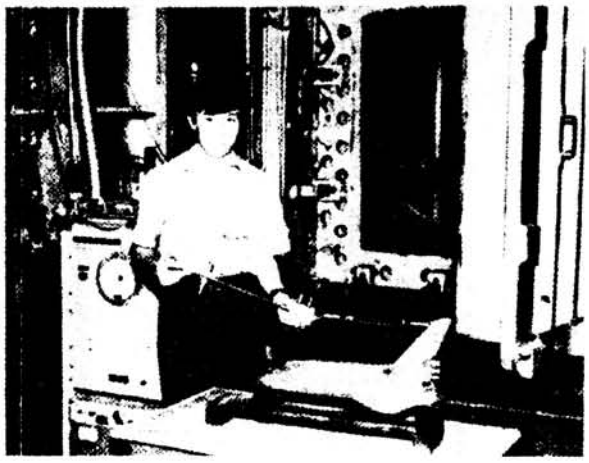

Fig. 2 "Bang-bang" model ready for installation in the Unitary Plan Wind Tunnel.

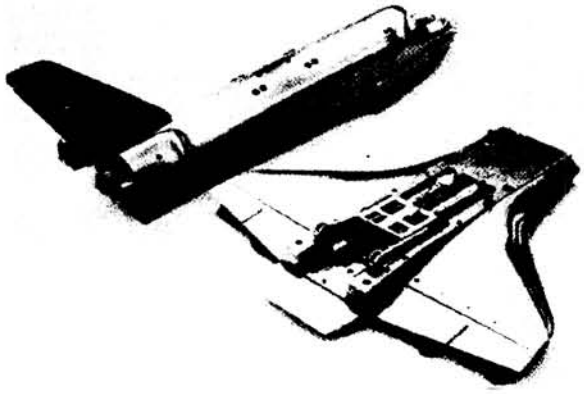

Fig. 4 "Fine-cut" model.

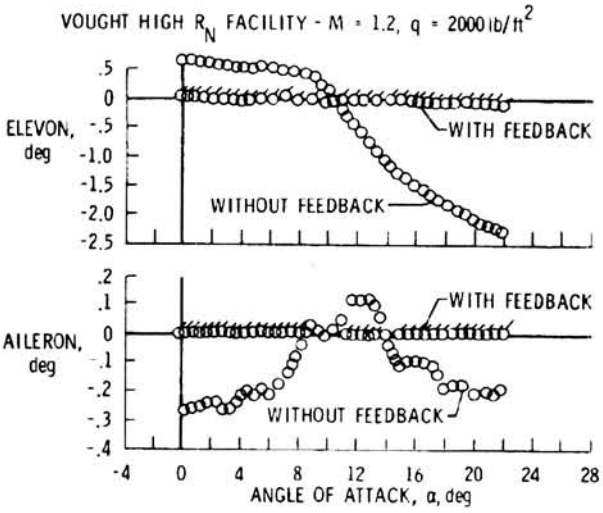

Fig. 5 Effect of feedback system on elevon position.

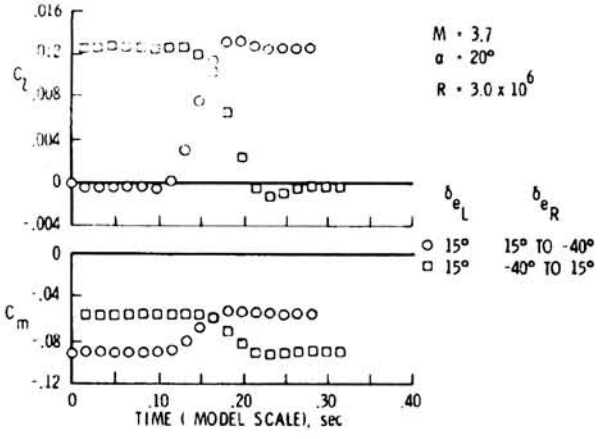

Fig. 3 Effect of rapid full travel elevon deflection on pitching- and rolling-moment coefficients.

Fig. 6 Model control console and 0.03-scale ALT model.

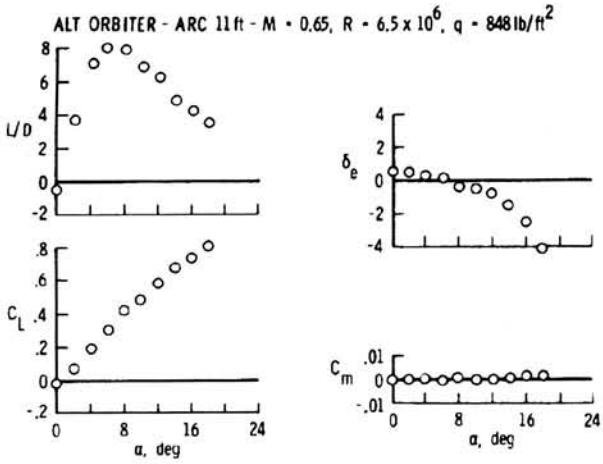

Fig. 7 Effect of feedback system on pitch trim.

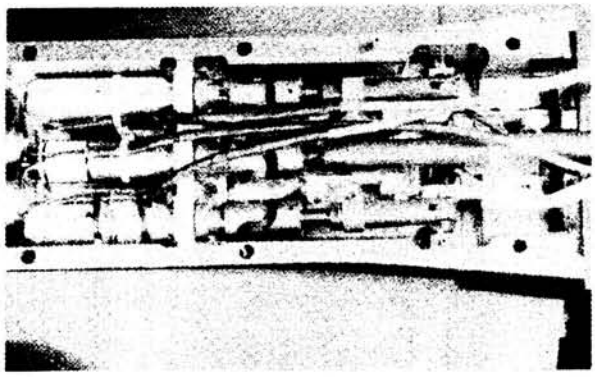

Fig. 8 Detail of elevon and body-flap drive system of the 0.02-scale high-fidelity model.

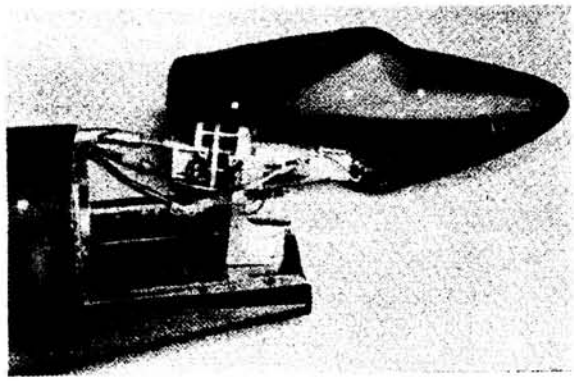

Fig. 9 Nose section of the high-fidelity model showing rudder drive motor.

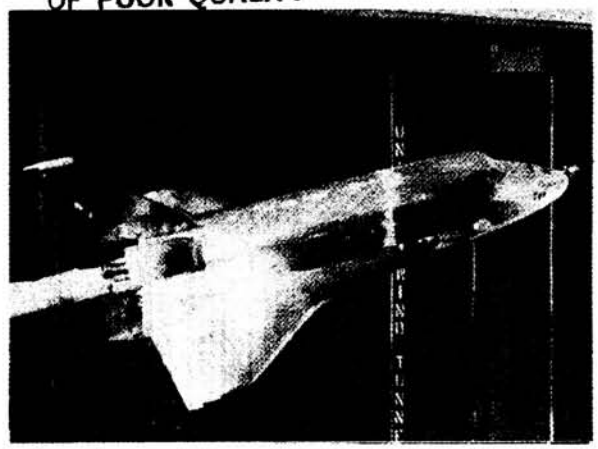

Fig. 10 High-fidelity model mounted for tests in the Unitary Plan Wind Tunnel.

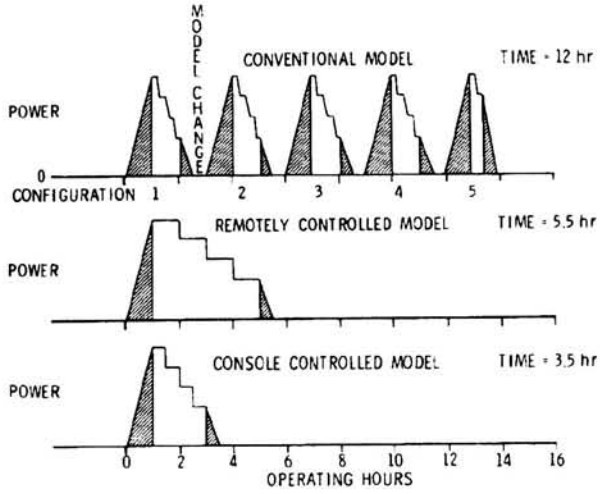

Fig. 11 Typical operation - Langley 8-Foot Transonic Pressure Tunnel. Shaded area represents tunnel start/stop time.

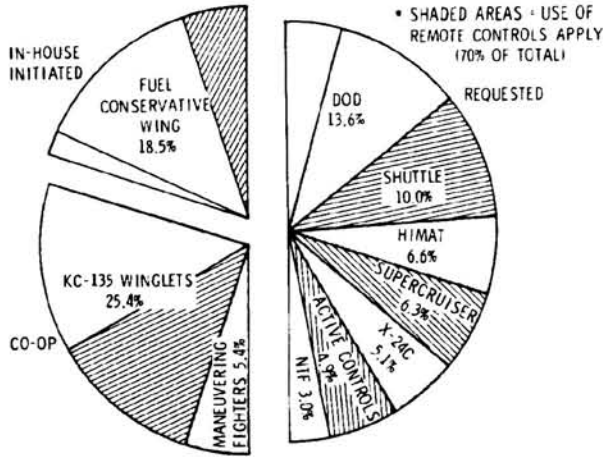

Fig. 12 Typical yearly operation - Langley 8-Foot Transonic Pressure Tunnel.

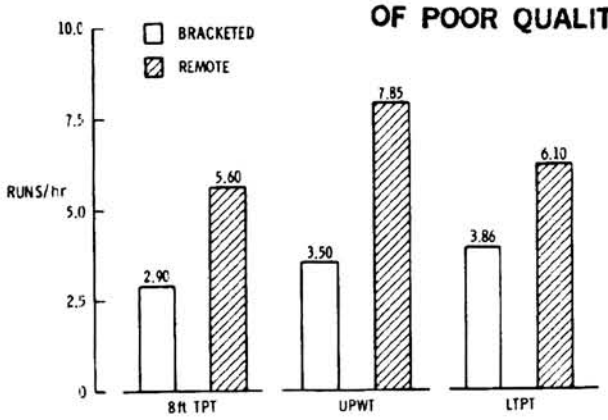

Fig. 13 Comparison of model test rates.

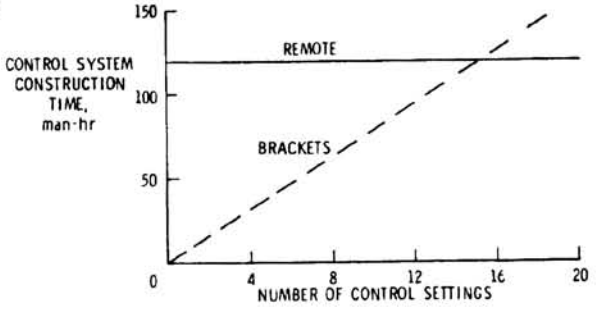

Fig. 14 Comparison of time to construct control systems.

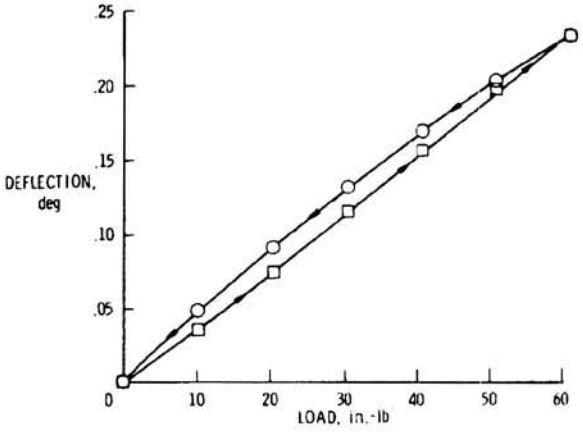

Fig. 15 Typical deflection characteristics of remote control surface under load.

SHUTTLE ASCENT GN&C POSTFLIGHT RESULTS

Gene McSwain
NASA Johnson Space Center
Houston, Texas

ABSTRACT

This paper describes the key features of the ascent GN&C system and examines how well this system performed during the orbital flight test program. Flight results are compared with preflight predictions and postflight reconstructions. Variations from expected performance are identified as well as flight-to-flight trends. The most notable variation was the lofted trajectory observed on STS-1.

The lessons learned from the OFT program are being used to enhance the overall system performance for future Shuttle flights. Several of the planned GN&C system enhancements are discussed.

INTRODUCTION

Launch of the STS-1 from launch complex 39A on April 12, 1981, marked the beginning of a nearly flawless Shuttle test flight program. In each of the subsequent flights, the ascent flight envelope was expanded. After the fourth flight, the vehicle was verified fully operational.

First flight came after more than a decade of design, development, and verification activities leading to certification of a rather complex vehicle avionics system. The quad-redundant, fly-by-wire digital GN&C system provides automatic steering for ascent. Four GPC's each perform identical computations in a synchronized manner, using inputs from redundant sensors. TVC and aerosurface actuators thus receive four parallel commands which are force-summed at the power valve.

Since the avionics system is designed to be two-fault tolerant (fail operational-fail safe), redundancy management is an integral part of the GN&C system. Redundant sensor inputs are sampled at the user rate (25 Hz for rate gyros and accelerometers) and the middle value is selected for use by the flight control system. Fault detection and isolation algorithms are processed at lower rates and once a sensor is declared failed, the high rate selection process is moded accordingly and fault annunciation is displayed to the crew and telemetered to the ground. Since the GPC's do not have adequate memory capability for the entire mission profile, the software has been structured into several memory loads including ground checkout, ascent, on-orbit, on-orbit checkout, and entry. These load blocks are stored on redundant mass memory units and GPC memory is reloaded at appropriate points along the mission profile. The ascent load provides GN&C software for use throughout the terminal count starting at T-20 minutes through orbit circularization. A portion of the GPC memory is preserved across the phase transitions which include the operating system software, state vector, sensor and effector configuration, and failure status and initialization data.

SYMBOLS AND ACRONYMS

h	altitude (ft)
t	time (sec)
$\bar{q}$	dynamic pressure (lb/ft^2)
α	angle of attack
β	side slip angle
MECO	main engine cutoff
GN&C	guidance, navigation, and control
OFT	orbital flight test
GPC	general purpose computer
TVC	thrust vector control
Hz	cycles per second
RTLS	return to the launch site
SRB	solid rocket booster
OMS	orbital maneuvering system
ET	external tank
RCS	reaction control system
IMU	inertial measurement unit
V_{REL}	relative velocity, feet/sec
DAP	digital autopilot
STS	space transportation system
rad	radian
δ	flight path angle, deg.
V	velocity, feet/sec

ASCENT TRAJECTORY DESCRIPTION

The ascent phase begins with ignition of the SRB's and terminates at orbit insertion or at landing at KSC in the case of an RTLS abort which would be required with an orbiter engine failure early in powered flight. Three subphases of a normal ascent include stage 1 from liftoff to SRB separation, stage 2 from separation to MECO, and a coasting phase which includes two OMS engine burns for orbital circularization (see Figure 1).

The Space Shuttle is launched from a vertical position with the tail south on the KSC launch pad. Following a short vertical rise to clear the launch tower, a 3-axis maneuver is performed to orient the vehicle to the desired flight azimuth. A programmed pitch maneuver continues for the remainder of first stage flight until SRB staging. During staging a constant attitude is maintained to minimize the probability of recontact with the spent solids. The Shuttle flies in a "tail-down" attitude so that the orbiter thrust, inclined 12 degrees to the vehicle centerline, lifts the vehicle trajectory at zero angle of attack. The characteristic dynamic pressure profile is achieved by shaping the stage 1 pitch command profile appropriately and throttling the main engines through the high $\bar{q}$ region. Nominal $\bar{q}$ maximum was designed to be less than 600 lb/ft^2 for STS-1 to minimize aerodynamic loads and was increased incrementally through the remainder of the flight test program. Orbiter aerodynamic surfaces are not used for control during ascent but the elevons follow an open-loop position profile in first stage to avoid excessive hinge moment

and wing bending and torsion loads. A closed-loop elevon load relief feature is available to command the elevons away from the open-loop profile, if required, based on measured actuator differential pressure.

Approximately 6 seconds after SRB staging, the stage 2 closed-loop guidance is initiated to steer the vehicle to the desired MECO target conditions on velocity, flight path angle, altitude, and orbital plane. Late in stage 2, the guidance commands throttling of the main engines to limit vehicle acceleration to 3 g's. At MECO the vehicle is still on a suborbital trajectory to allow disposal of the ET in the Indian Ocean.

Eighteen seconds after MECO, the orbiter is separated from the ET and the coast phase transitional autopilot commands the down-firing RCS thrusters on to provide a vertical velocity increment of 4 ft/sec, providing comfortable clearance from the separated tank. At MECO plus 2 minutes, a short OMS burn (approximately 2 minutes duration) is performed to raise both apogee and perigee. Thirty minutes later, a second OMS burn raises perigee to circularize at the desired orbital altitude. During the first OMS burn, residual propellant in the main engines and manifolds is dumped overboard and the main engines are commanded to a stowed position prior to deactivation of the orbiter hydraulic systems.

ASCENT GN&C OVERVIEW

A simplified GN&C software overview is shown in Figure 2. The sensors used for ascent include rate gyros, normal and lateral accelerometers and inertial measurement units. GPC computations of flight control inner-loop errors are performed at 25 Hz and transport delay is kept to less than 20 milliseconds to preserve adequate closed-loop autopilot phase margin. Less time-critical navigation and guidance functions are processed at lower sample rates to keep the overall computing demand within the capabilities of the GPC.

The ascent navigation function uses selected IMU data and a model of the Earth's gravitational acceleration to maintain a current estimate of the Shuttle state vector. State initialization occurs at T-8 seconds and a precise state computation is calculated approximately every 4 seconds. IMU accelerometers are sampled at a 1 Hz rate and higher rate user demands are fulfilled by a propagation algorithm so that a velocity estimate is available for guidance at 6.25 Hz. During the coast phase following MECO, the IMU sensed acceleration is not used if below a noise threshold and an atmospheric drag model is used instead. Also, a more accurate model of the Earth's gravity is used by including higher order terms in addition to those used in powered flight.

First-stage guidance computations are processed at 6.25 Hz and consist of a table look-up of pitch, yaw, and roll attitudes and main engine throttle commands as a function of navigated relative velocity. Velocity is used as the independent variable to provide a pitch profile which produces a desired angle of attack vs. Mach number relationship dictated by aerodynamic loads requirements in the high $\bar{q}$ region. Alternate pitch tables provide the necessary steering changes required for loss of a main engine in first stage.

The fuel optimum second-stage guidance cyclically computes the desired thrust pointing direction based on the difference between the targeted MECO state and the current navigated state. Stage 2 guidance is processed at 0.5 Hz and consists of three major subtasks of predictor, corrector, and steering parameter computation. A constant thrust is assumed early in second stage and constant 3 g acceleration in the latter portion. Stage 2 guidance provides desired thrusting direction and thrust turning rate information to the flight control system and issues throttle commands to the main engines late in second stage to limit acceleration to no more than 3 g's. As MECO is approached, the position constraints are released and guidance computational rate is increased to provide an accurate velocity cutoff.

The ascent digital autopilot design is based on a conventional two-loop closure on attitude and attitude rate. A simplified software overview is shown (see Fig. 3). During the high $\bar{q}$ region of first stage, an additional loop closure on normal and lateral acceleration is used to provide structural load alleviation. Attitude errors are calculated at 12.5 Hz and rate and acceleration errors at 25 Hz. Gains are scheduled against relative velocity for stage 1 and updated at 6.25 Hz as are the reference thrust vector control trim angle, normal acceleration, and elevon schedule profiles. Gain and trim profiles for stage 2 are scheduled as a function of calculated vehicle mass provided by stage 2 guidance. The rigid body closed-loop control frequency is slightly greater than 1.0 rad/sec to provide adequate steering response to guidance commands while maintaining sufficient propellant slosh phase margin. The oxidizer slosh mode near 3 rad/sec is phase stabilized. Flexible mode compensation is provided by multiple digital filters (as high as 9th order end-to-end in stage 1) and the filter coefficients are switched at transition to stage 2. The bending modes are gain stabilized across their frequency spectrum beginning at 12 rad/sec early in first stage. A software module called RECON provides the necessary moding of TVC biases, mixing logic changes, limiters, and faders based on mission timeline events and subsystem failure status. An example of the control law signal flow topology is shown for the stage 1 pitch channel (see Fig. 4). Note that a forward path integration of attitude error is used as an autotrim function to wash out the effects of sensor bias or steady state mistrim due to thrust level imbalance or thrust vector misalignment.

FLIGHT RESULTS

The ascent guidance and control system performed as designed throughout the OFT program and during the first operational mission (STS-5). Several deviations from expected vehicle behavior were observed. A reconstruction of the ascent trajectory for each flight was made to explain these deviations and to provide essential information required to upgrade the Shuttle vehicle and environmental math models. These upgraded models are now used to provide better performance prediction capability and an upgraded test bed for evaluation of future hardware and software changes. Table I lists the major deviations from expected behavior observed on the first five Shuttle flights.

The most notable deviation was the lofted trajectory that occurred on STS-1. The predicted and actual SRB staging conditions given in Table II indicate that the vehicle was about 9000 ft higher and 68 ft/sec slower than predicted. The actual wind experienced during the STS-1 flight was near the mean monthly wind; therefore, the lofting was not wind induced. There was no indication from attitude errors early in flight that a significant SRB thrust misalignment existed. The pitch attitude error (Figure 5) began to build up later during the load relief phase and

peaked at -5 degrees. This error is indicative of an "unplanned for" negative pitch moment with a peak value of about -9 million foot pounds. The only explanation that fits the observed behavior is a significant shift from wind tunnel predictions for the pitch aerodynamic coefficients.

A minor software change to compensate for about half of the lofting was introduced on STS-2. On STS-3 and subsequent flights, the first stage aerodynamics extracted from flight data was used in the development of the stage 1 steering, reference acceleration, and SRB trim profiles. A comparison of SRB staging conditions (Table III) and the pitch attitude error (Fig. 5) for STS-1 and -2 with subsequent flights indicates that the lofting was eliminated by this approach. Note the trend toward positive attitude errors of flights 3, 4, and 5 is probably the result of (1) a slight overcorrection in the aerodynamics, (2) a low SRB burn rate on each flight and a slight headwind relative to the mean wind. An enhancement to the software which will compensate for SRB dispersions is discussed later in this paper. A dispersion in the trajectory is the expected result of the first stage load relief scheme in the presence of wind deviations from the monthly mean. Headwind deviations tend to depress the trajectory, whereas tailwind deviations tend to loft it. Crosswind deviations produce out-of-plane velocity and position errors at SRB staging.

There is an indication of an unknown moment operating on the vehicle near the end of first stage flight. The effect on the vehicle is slight: a negative pitch rate which builds to -.5 degrees per second and is damped out prior to staging. The origin of this phenomenon is unknown at the present time.

Examination of the second stage attitude error histories that existed on all five flights reveals an obvious thrust vector misalignment due to structural deformation. The autotrim function of the autopilot gradually washed out these errors following the start of closed-loop guidance. Table IV gives the thrust misalignment required to reconstruct the second-stage attitude errors. These errors had no significant effect on the overall trajectory performance. The overall accuracy of the G&C system thrust vector pointing during the second-stage maneuver is demonstrated by the accuracy with which the MECO target was achieved on all flights (Tables V and VI). For future flights, the second-stage pitch trim table will be adjusted slightly to compensate for the structural deformation.

Successful completion of the orbital flight test program demonstrated conclusively that the ascent GN&C system performance is adequate for operational Shuttle missions. But the need to make the overall Shuttle operation more efficient to support future higher flight rates and to increase payload capability make enhancements to the Shuttle inevitable. The next section of this paper discusses some of the currently planned ascent GN&C enhancements.

ASCENT GN&C ENHANCEMENTS

A summary of the proposed GN&C enhancements is given in Table VII. Major Shuttle system enhancements such as the filament-wound case have a significant effect on the ascent GN&C system but are beyond the scope of this paper. The remainder of this section is dedicated to two proposed changes which are approved for the STS-8 flight software.

First-Stage Adaptive Guidance

Currently, first-stage guidance employs a table look-up scheme to obtain pitch, yaw, and roll attitude and main engine throttle commands as a function of relative velocity. The design of the attitude and throttle command profiles assumes a mean environment (atmosphere, winds, SRB temperature) and nominal system performance. Deviations from the mean environment and/or off-nominal system performance can cause excessive aerodynamic loads. To avoid this, the first-stage trajectory is designed to a nonoptimum dynamic pressure profile that is conservative enough to allow the vehicle to tolerate three-sigma systems dispersions in the presence of two-sigma adverse winds.

Since SRB performance variations are the major contributor to the systems dispersions, a technique to measure and correct for inflight SRB performance dispersions would increase payload capability by permitting the first-stage trajectory to be designed closer to the optimum. The technique proposed consists of checking the time required to achieve a predefined velocity point early in ascent (about 20 seconds after SRB ignition). The aerodynamic force on the vehicle during this phase is small compared to the thrust force so any dispersion in the time required to achieve the reference velocity is directly attributable to dispersions in thrust (mainly SRB thrust). A one-shot correction proportional to the delta time required is then made. If the reference velocity is achieved earlier than predicted, then the SRB performance is higher than predicted. In this case, the pitch profile is biased higher (more thrust along the local vertical) and the MPS throttle profile is biased lower. Both measures reduce dynamic pressure. If the reference velocity is achieved later than predicted, then the SRB performance is lower than predicted. In this case, the pitch profile is biased lower and the MPS throttle profile is biased higher. This reduces the payload performance loss that would have otherwise occurred. This technique will increase payload capability on certain missions by as much as 1000 pounds.

First-Stage Engine Out Pitch Biasing

First-stage guidance uses two additional pitch tables to accommodate a top or side engine failure. The tables are required to satisfy aerodynamic load constraints and to provide suitable initial conditions for a return-to-the-launch-site abort. The increased altitude rate at staging that these tables provide compensates for the reduced thrust-to-weight ratio with an engine out. The resultant more lofted trajectory eliminates RTLS guidance convergence problems as well as aerodynamic heating problems that are associated with low altitude powered flight.

The proposed enhancement replaces the two engine out tables with a computed bias to the nominal pitch table, which is a function of the velocity at the time of engine failure. The advantage of this technique is twofold: (1) it provides additional lofting of the first stage trajectory with an engine out, thus providing a greater margin of safety for the RTLS maneuver, and (2) it eliminates two 30-point tables.

CONCLUSIONS

During the orbital flight test program, all major test objectives of the ascent GN&C system were satisfied. The safe ascent of the vehicle, crew, and payload was demonstrated. The GN&C system maintained the vehicle loads within acceptable bounds, provided acceptable SRB and ET separation conditions, and steered the vehicle to the desired orbital conditions.

The deviations from expected behavior that were observed during the OFT program have been explained using postflight reconstruction techniques. Improved vehicle and environmental models that resulted from this reconstruction process are now being used for flight performance predictions and as a test bed for proposed hardware and software changes.

Lessons learned from the Shuttle design phase and the flight test program are reflected in the currently proposed enhancements to the ascent GN&C system.

TABLE I.- DEVIATION FROM EXPECTED PERFORMANCE

DESCRIPTION	EFFECT ON GN&C	PROBABLE CAUSE
UNMODELED AERODYNAMIC BIAS	• -5 DEG PITCH ATTITUDE ERROR • LOFTED TRAJECTORY ON STS-1 & -2	INACCURATE PREDICTION OF AERODYNAMIC PITCHING MOMENT FROM WIND TUNNEL TESTS
LATE SRB STAGING	• 1-2 DEG + PITCH ATTITUDE ERROR • DEPRESSED TRAJECTORY	SLOW BURNING SRB'S & LOWER SRB ISP
MPS THRUST MISALIGNMENT	2ND STAGE TRIM INTEGRATOR SHOWS CONSISTENT BIAS FOR ALL FIVE FLIGHTS	MPS THRUST STRUCTURE DEFORMATION
UNMODELED PITCHING MOMENT NEAR END OF FIRST STAGE	UNEXPECTED PITCH RATE & ATTITUDE ERROR	UNKNOWN

TABLE II.- SRB STAGING CONDITIONS FOR STS-1

	PREDICTED	STS-1	DIFFERENCE
TIME, SEC	131.68	130.82	-0.86
ALTITUDE, FT	164736	173957	+9221
RELATIVE VELOCITY, FT/SEC	4178.56	4110	-68.56
INERTIAL VELOCITY, FT/SEC	5216.77	5127	-89.8
INERTIAL FLIGHT PATH ANGLE, DEG	26.13	28.73	+2.60

TABLE III.- SRB STAGING CONDITIONS FOR FIRST FIVE FLIGHTS

	h, FT		V_{REL}, FPS		γ_I, DEG	
MISSION	FLT	SIM	FLT	SIM	FLT	SIM
1	173957	172615	4110	4093	28.7	28.47
2	166904	168632	4184	4218	26.0	25.9
3	160155	159554	4220	4218	25.3	25.32
4	154000	155169	4276	4296	21.9	21.91
5	155216	154300	4345	4339	21.4	21.7

TABLE IV.- STAGE 2 MPS THRUST MISALIGNMENT

PITCH 1 = +0.1 DEG	YAW 1 = -0.40 DEG
PITCH 2 = -0.4 DEG	YAW 2 = -0.25 DEG
PITCH 3 = +0.8 DEG	YAW 3 = -1.45 DEG

TABLE V.- MECO CONDITIONS FOR FIRST FIVE FLIGHTS

	RADIUS, FT		INERTIAL VEL, FPS		FLIGHT PATH ANG, DEG	
MISSION	TARGET	FLIGHT	TARGET	FLIGHT	TARGET	FLIGHT
1	21290308	21291633	25668	25665	.50	.499
2	21290308	21291779	25668	25671	.50	.502
3	21272055	21273258	25680	25681	.65	.638
4	21259927	21261628	25677	25678	.76	.757
5	21272079	21273684	25670	25672	.65	.647

TABLE VI.- SUMMARY OF MECO TARGET MISSES FOR FIRST FIVE SHUTTLE FLIGHTS

FLIGHT	Δh, FT	$\Delta\gamma_I$, DEG	ΔV_I, FPS
1	1325	-.001	-3.20
2	1471	+.003	2.68
3	1203	-.012	.66
4	1701	-.001	1.23
5	1605	-.002	1.75

TABLE VII.- ASCENT GN&C ENHANCEMENTS

ENHANCEMENT	DESCRIPTION
(1) FIRST STAGE ADAPTIVE GUIDANCE	ONE SHOT ADJUSTMENT TO PITCH STEERING AND MAIN ENGINE THROTTLE COMMANDS TO COMPENSATE FOR OFF-NOMINAL SRB PERFORMANCE.
(2) FIRST STAGE ENGINE OUT PITCH BIASING	A PITCH BIAS THAT IS A FUNCTION OF THE VELOCITY AT THE TIME OF ENGINE FAILURE IS USED TO SATISFY AERODYNAMIC LOAD CONSTRAINTS AND TO LOFT THE FIRST STAGE TRAJECTORY.
(3) PARALLEL MAIN ENGINES DURING 2ND STAGE	MAIN ENGINES ARE PARALLELED IN PITCH AS WELL AS YAW TO AVOID COSINE LOSS IN THRUST PERFORMANCE.
(4) TRANSATLANTIC ABORT MECO PLANE TARGET	AN ONBOARD FUEL OPTIMUM TARGET PLANE COMPUTATION IS USED TO INCREASE TRANSATLANTIC ABORT PERFORMANCE FOR HIGH INCLINATION MISSIONS.
(5) SRB RGA REMOVAL	BLENDED FORWARD AND AFT ORBITER RGA SIGNALS USED TO REPLACE SRB RGA, MAY USE DERIVED RATE FROM ORBITER IMU INSTEAD OF FORWARD RGA.

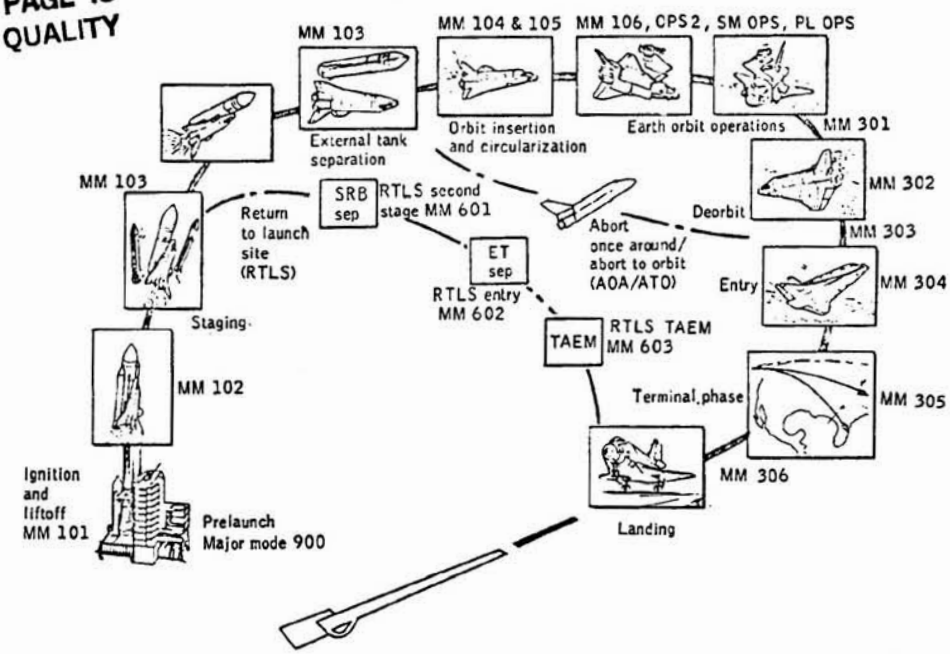

Figure 1.- Shuttle mission profile.

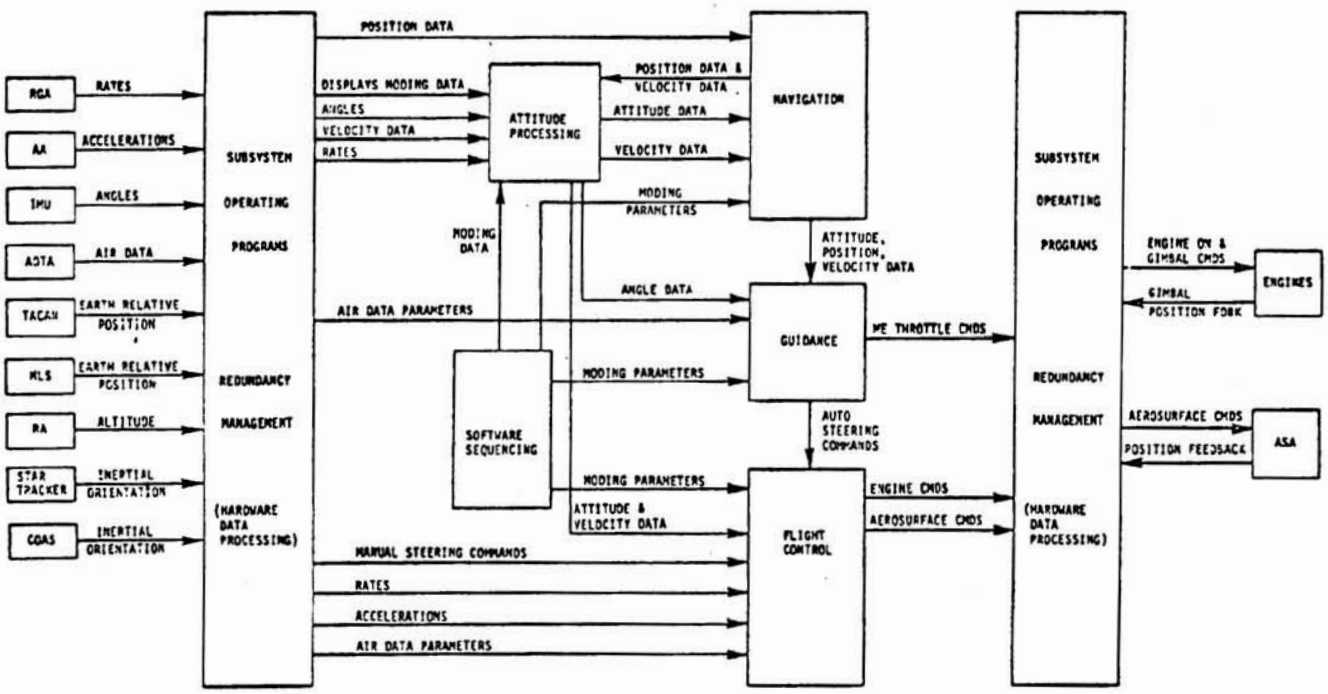

Figure 2.- Ascent GN&C software overview.

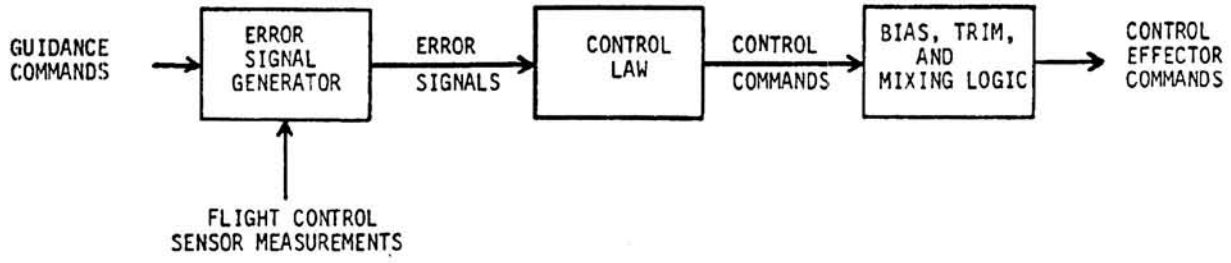

Figure 3.- Simplified flight control software overview.

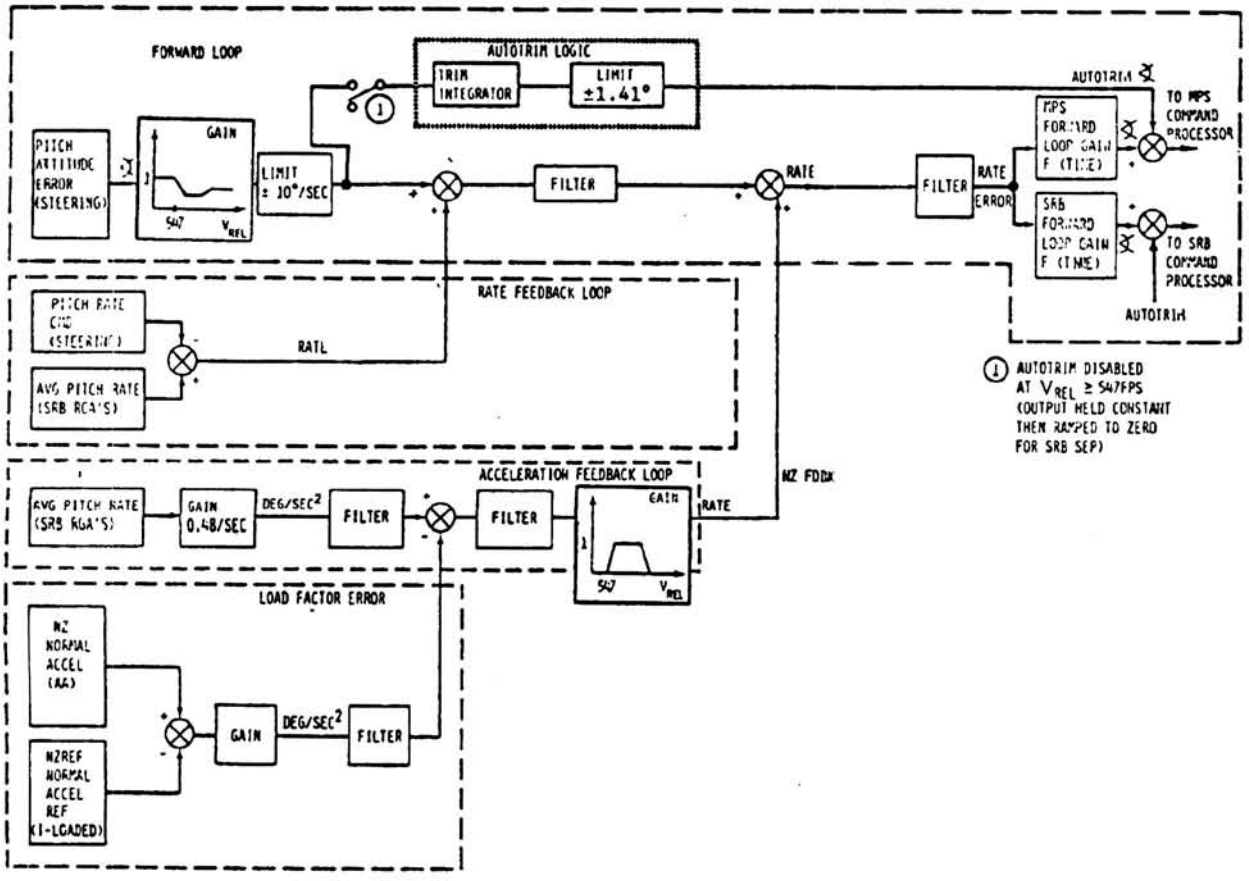

Figure 4.- First stage pitch loop.

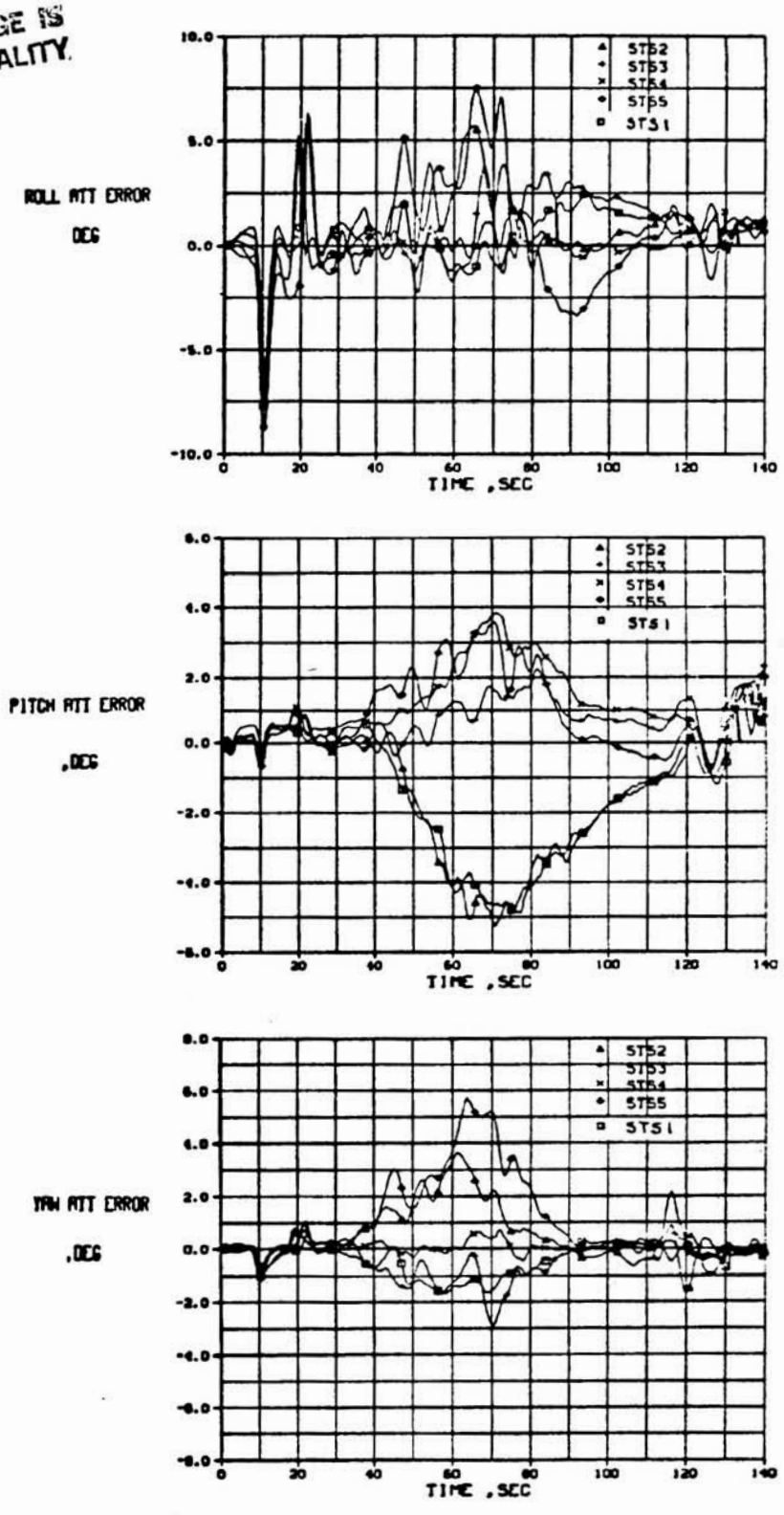

Figure 5.- Comparison of first stage attitude errors for first five Shuttle flights.

THE APPLICATION OF AERODYNAMIC UNCERTAINTIES IN THE DESIGN OF THE ENTRY TRAJECTORY AND FLIGHT CONTROL SYSTEM OF THE SPACE SHUTTLE ORBITER

Joe D. Gamble
Lyndon B. Johnson Space Center
Houston, TX

ABSTRACT

The process used in the application of aerodynamic uncertainties for the design and verification of the Space Shuttle Orbiter Entry Flight Control System is presented. The uncertainties were used to help set center of gravity, angle of attack and dynamic pressure placards for the entry of the first Shuttle flight. A form of the lateral control divergence parameter as well as C_{n_β} dynamic were instrumental in setting these placards.

NOMENCLATURE

Symbols

α	Angle of attack, degrees
β	Angle of sideslip, degrees
C_m	Pitching moment coefficient
C_{m_o}	Pitching moment coefficient which is independent of α
C_{Y_β}	Derivative of side force due to angle of sideslip, per degree
$C_{Y_{\delta_a}}$	Derivative of side force due to aileron, per degree
$C_{Y_{\delta_R}}$	Derivative of side force due to rudder, per degree
C_ℓ	Rolling moment coefficient, body axis
C_{ℓ_β}	Derivative of rolling moment due to angle of sideslip, per degree
$C_{\ell_{\delta_a}}$	Derivative of rolling moment due to aileron, per degree
$C_{\ell_{\delta_R}}$	Derivative of rolling moment due to rudder, per degree
$\Delta C_{\ell_{JI}}$	Increment in rolling moment coefficient due to RCS exhaust plume flowfield interaction

C_n	Yawing moment coefficient, body axis
C_{n_β}	Derivative of yawing moment due to angle of sideslip, per degree
C_{n_β} dynamic	Stability axis dynamic directional stability parameter
$C_{n_{\delta_a}}$	Derivative of yawing moment due to aileron, per degree
$C_{n_{\delta_R}}$	Derivative of yawing moment due to rudder, per degree
δ_{BF}	Bodyflap position, degrees
δ_R	Rudder angle, degrees
δ_{SB}	Speedbrake angle, degrees
δ_a	Aileron angle, degrees
δ_e	Elevon angle, degrees
$\bar{q}$	Dynamic pressure, psf
ω_d	Undamped natural frequency of the dutch roll oscillation
ω_ϕ	Undamped natural frequency of the numerator of ϕ/δ_a transfer function

Acronyms

cg	Center of gravity
FCS	Flight control system
FSL	Flight Software Laboratory
MXRCS	RCS roll moment
MZRCS	RCS yaw moment
RCS	Reaction control system
SPS	Shuttle Procedures Simulator
STS	Space Transportation System
STS-1	First Flight of the Space Shuttle
STS-2	Second Flight of the Space Shuttle
WOW	Worse on worse combination of errors

INTRODUCTION

The decision for Shuttle to perform an orbital, manned mission on the first launch raised the general question of how to maximize the mission safety without the benefit of either a graduated flight test program (as used by the aircraft industry) or an initial unmanned flight concept (as used in the early space program). The consequence of this decision was to adopt a philosophy of providing a reasonable estimate of maximum possible errors in the preflight predicted aerodynamics, and certify the flight control system (FCS) using the errors prior to STS-1. However, the estimated errors must not be so great as to completely invalidate the FCS design. Thus, a set of "worst case" aerodynamic uncertainties, defined as variations, was

developed. As part of the first flight certification, variations, combined with other system uncertainties, were used to "stress" the FCS through a multitude of simulations. As a consequence, the initial entry was flown at a center of gravity and with FCS gains which maximized the aerodynamic margins thereby maximizing mission safety for these systems.

This paper will discuss some of the criteria that were used to identify the critical aerodynamic uncertainty cases and show how these cases were used in setting entry placards for the first STS flight. The procedure that was established for verification of the entry FCS with uncertainties applied will also be discussed.

ENTRY MISSION DESCRIPTION

The Space Shuttle Orbiter is designed to perform an unpowered gliding entry. In order to minimize entry heating the initial angle of attack is maintained at approximately 40°. After the initial high angle entry a gradual pitchdown is initiated at Mach 12 and is completed around Mach 2. From Mach 2 to touchdown the angle of attack is defined by energy and structural load requirements and normally stays between 4° and 10°. Figure 1 shows a typical (STS-1) entry angle of attack profile.

FLIGHT CONTROL SYSTEM FUNCTIONAL OPERATION

The entry FCS provides augmentation for both longitudinal and lateral directional axes throughout the entry profile. Angle of attack and pitch rate feedback provide stability augmentation and damping for the pitch axis while side acceleration, roll rate and yaw rate feedback are used to augment the roll and yaw axes. The flight control gains are scheduled as a function of Mach number, angle of attack and dynamic pressure and are designed to provide good flying qualities throughout entry. A detailed description of the FCS is given in references 1 and 2.

VARIATIONS DEVELOPMENT

Two types of aerodynamic uncertainties were defined during the Space Shuttle Orbiter program. A set of smaller uncertainties which were to be representative of the minimum error expected were defined as tolerances. A set of "worst case" uncertainties, defined as variations, was developed to provide an estimate of the maximum error expected. The variations were developed by analyzing the wind tunnel to flight differences of past aircraft programs and fairing these differences as a function of Mach number. Since selection of the configurations and the fairing process are subjective in nature, a

team of aerodynamicists from the Air Force Flight Test Center, NASA Dryden Flight Research Facility, NASA Johnson Space Center, and Rockwell International was formed to conduct the analysis and reach a consensus on variations. The team's flight-to-predicted correlation and their recommended variation fairings are presented in reference 3. A more detailed development is presented in reference 4.

APPLICATION OF AERODYNAMIC VARIATIONS

A programmatic decision was made to use aerodynamic variations in the Orbiter FCS design evaluation and verification process. For the initial FCS design evaluation and simulation studies, a "worst on worst" combination of variations was used. For the formal entry verification at the Flight Software Laboratory (FSL) at Rockwell, variation sets were used which correlated the roll and yaw moment coefficients for the sideslip, aileron and rudder coefficients.

Because of the wide range of flight conditions the orbiter was to encounter during the first reentry flight test, it was required to evaluate as many combinations of aerodynamic uncertainties as possible. However it was also desirable to select a more limited set of uncertainties for concentrated analysis and simulation efforts. It thus became necessary to define those aerodynamic uncertainty combinations that presented the most potential problems to the orbiter and to make certain that the flight control system could maintain control of the orbiter with these combinations. In the initial FCS evaluation, a total of 26 lateral directional variation sets were evaluated in a series of almost 600 piloted simulation runs on the Shuttle Procedures Simulator (SPS) at the Johnson Space Center (JSC). These 26 cases were selected using various trim, controllability and handling qualities criteria. Based on the results of these simulation runs plus additional trim and stability analyses, a subset of 7 cases was chosen and used for the majority of the formal verification process.

Figure 2 shows a vector diagram of the aero coefficients and RCS jets for the roll and yaw axes at Mach 3.5. The numbers shown on the diagram indicate the nomenclature used for identifying the 7 cases selected for the verification process. The corners shown indicate the WOW or "rectangular" variation sets which were used in the FCS development while the ellipses represent the correlated variations. The elliptical variation sets were generally selected from points on the ellipses that were close to the rectangular counterparts. Some of the history and logic involved in the selection of the cases used for the FCS verification will now be discussed.

A significant portion of the analysis effort devoted to aero variations was applied to two controllability criteria. These were the lateral control departure parameter (LCDP) and C_{n_β} dynamic as given in references 5 and 6.

Lateral Control Departure Parameter

The LCDP was the first controllability criterion that was systematically applied to the orbiter. During the early stages of the orbiter development, most of the reentry was performed using an all aerodynamic control concept. Prior to rudder activation which then occurred around Mach 5, the aileron was the only aerodynamic control effector for lateral directional control and trim. A reverse aileron control (negative aileron for positive roll) that required a negative value for the LCDP, $C_{n_\beta} C_{\ell_{\delta_a}} - C_{\ell_\beta} C_{n_{\delta_a}} < 0$, was utilized prior to rudder activation. The lateral trim logic was also configured so that a negative value of the LCDP was required prior to rudder activation. Some of the early simulations using aerodynamic uncertainties on the aileron and beta derivatives resulted in lateral trim and controllability problems prior to rudder activation. Analysis indicated that the problem was caused by a sign change in the LCDP in the Mach 5 region. As a partial result of this problem, several changes were made to the FCS. The basic FCS design was changed from the aileron bank control to a system utilizing the yaw RCS jets to initiate bank maneuvers and the ailerons to coordinate the maneuvers prior to activation of the rudder. After the rudder became active, a gradual FCS gain change produced the conventional aileron bank control with rudder coordination.

Since use of the yaw jets for trim would result in excessive propellant requirements, the aileron was still required for trim. To improve the aileron trim capability in the critical Mach region, changes were made to the angle of attack and elevon schedules. With aero variations applied, Mach 3.5 was the highest Mach number at which the rudder could be considered effective and this Mach number was chosen as the activation point for the rudder. It was then considered a requirement that aileron trim be available down to Mach 3.5 with minimal yaw RCS requirements.

Figure 3 shows the sensitivity of the Orbiter LCDP to angle of attack for several Mach numbers with the worst case aero variations applied. It is obvious that in the Mach greater than 3 region an angle of attack of more than 15° is desirable in order to maintain a negative LCDP. The early flights of the Orbiter were tailored so that the angle of attack remained above 15° for Mach greater than 3.5.

Another significant factor in the LCDP is the elevon trim position. This is due to the effect of elevon position on the aileron derivatives. A desired elevon trim position of $+5^\circ$ (down) was eventually selected for STS-1 in the Mach 3-4 region. In the higher Mach region where elevon heating is a concern, the elevon was scheduled at -1 degree (up) and in the transonic region where there was some concern about hinge moments, a schedule close to zero was selected. The elevon position is maintained by the bodyflap through a feedback from the elevon which drives the bodyflap to maintain the pre-set elevon schedule.

In the longitudinal axis the primary problem associated with aero uncertainties was the pitching moment uncertainty, C_{m_o} and its effect on elevon trim position. Figure 4 shows the pre STS-1 capability to position the elevon for the design cg body length extremes of 65 percent (forward) and 67.5 percent (aft) with pitching moment variations and with the bodyflap positioned at its extreme limits to aid the desired trim. Also shown on figure 4 is the STS-1 elevon schedule. It is obvious that with C_m variations the orbiter could not achieve the desired elevon schedule over the design range of cg's. Based on the desired elevon schedule and the effect of pitching moment variations, the STS-1 cg was selected at 66.7 percent body length. Figure 5 shows the elevon envelope at the 66.7 percent cg with C_m variations while figure 6 shows the effect of cg on the LCDP at Mach 3.5 for the worst case variation set. The cg envelope adopted for STS-1 mission rules is shown in figure 7. STS-1 proved the 66.7 percent location to be near optimum as the bodyflap reached the maximum desired down position ($+16^{\circ}$) in the Mach 20 area and saturated up (-11.7°) in the Mach 1-2 region. The elevon maintained the desired schedule except for a brief period in the Mach 1.5 region where it was 2° to 3° more up than scheduled.

In the Mach region greater than 0.9 the speedbrake followed a preset schedule that was designed to improve the lateral directional control. From activation of the speedbrake at Mach 10 down to Mach 4 the speedbrake was full open to provide more down elevon capability with a resultant improvement in the LCDP. Between Mach 4 and Mach 3 the speedbrake was ramped to 65 percent open to provide a more effective rudder when it became active at Mach 3.5. The 65 percent value was maintained down to Mach .9 where the guidance assumes control of the speedbrake for subsonic energy management.

Thus, application of the LCDP in the Mach range from approximately 3-8 was a driver in the angle of attack, elevon and speedbrake schedules as well as the longitudinal cg location for STS-1.

C_{n_β} Dynamic

Another criterion that was used to evaluate the FCS and to shape the entry trajectory was C_{n_β} dynamic which was defined as $C_{n_\beta} \cos\alpha - C_{\ell_\beta} \sin\alpha \frac{I_z}{I_x}$. Figure 8 presents C_{n_β} dynamic versus Mach number for the nominal aerodynamics and shows that the STS-1 entry trajectory resulted in a predicted stable value of C_{n_β} dynamic throughout entry. Since C_{n_β} dynamic is the stability term for coupled lateral

directional motion, it was considered a requirement to have a stable value for this parameter throughout entry.

There is a significant reduction in C_{n_β} dynamic around Mach 2 because of aeroelastic effects on the vertical fin and a subsequent reduction in C_{n_β}. This effect is aggravated by higher dynamic pressures which can result from flying a lower angle of attack profile as is illustrated by the curves for 5° and 7.5° alpha in figure 8. Angle of attack and dynamic pressure limits were established for STS-1 in the lower supersonic region because of this concern. Figure 9 shows C_{n_β} dynamic in the lower Mach region for the worst case aero variation set for 1-g flight at 7.5° α. The unaugmented C_{n_β} dynamic is unstable from about Mach 1.2 to 3.2 at these flight conditions.

The orbiter FCS utilizes a side acceleration feedback to the rudder and yaw jets to provide stability augmentation. An approximate β feedback gain to the rudder can be computed and from this gain a rudder "augmented C_{n_β} dynamic" can be calculated. For the Mach 2 region the equivalent gain for β feedback to the rudder is approximately -1.5 to -2. Additional augmentation is provided by the yaw RCS jets and although the system is nonlinear, an approximation to an augmented C_{n_β} can be obtained which is valid for sideslip angles less than that required to fire all 4 jets (approximately 1° to 2°). Figure 9 shows the effective C_{n_β} dynamic for both rudder and RCS augmentation. Very little improvement is shown for the rudder augmentation. This is due to the small rudder effectiveness which results from the aeroelasticity effects and from application of aerodynamic variations. It is evident that the RCS provides a significant improvement. However after the jets are saturated additional augmentation is not available and there is a β limit beyond which control is not possible. For STS-1, angle of attack and dynamic pressure limits were established based on the ability of 2 yaw jets to control the orbiter at 1.5° sideslip for the worst case aero variations. Figure 10 shows the lower angle of attack boundary established for the flight rules based on lateral trim concerns above Mach 3 and C_{n_β} dynamic concerns below Mach 3. In the Mach 2 region STS-1 had a dynamic pressure limit of 250 psf programmed into the guidance laws and the trajectory was shaped to provide ample margin above the lower alpha limits.

Because of a possible RCS malfunction associated with jet firings at lower altitudes, it is eventually planned to turn the jets off around Mach 2. However, before this can be safely accomplished, it will be necessary to ascertain that the aero variations do not exist.

The Orbiter 17 flight test program is designed to verify the aerodynamics so that both the trim and stability concerns are eliminated.

Additional Criteria

While the aero variation sets associated with the LCDP and with C_{n_β} dynamic received considerable attention during the FCS design and verification process, other combinations of variations shown on figure 2 were also extensively analyzed. Diagrams similar to figure 2 were widely used in helping to select which variation sets to use at different flight conditions. This was particularly true of cases involving coalignment of effectors and/or stability derivatives. For example, with the variation set numbered 19, the beta and aileron vectors align which corresponds to the LCDP going to zero. This would require the use of yaw jets to trim. Variation set 19 was used for the worst case LCDP analysis. Variation set 20 was used for the minimum C_{n_β} dynamic case and results in both minimum β and rudder stability. Variation set 20 resulted in another problem at higher Mach numbers which required a change to the FCS. At the hypersonic Mach numbers and 40° angle of attack when variations were applied to 1 yaw jet, a coalignment of the jet and β vectors occurred. Since the bank control is achieved through the combination of jets and β, a control criterion similar to the LCDP results. The form of this criterion used for the orbiter was $C_{n_\beta} M_{X_{RCS}} - C_{\ell_\beta} M_{Z_{RCS}} > 0$. With one yaw jet firing a control reversal resulted which was similar to the case for the aileron control problem associated with the LCDP. As a result of this problem, the FCS was changed so that a minimum of two yaw jets were always fired. Another case that received considerable attention was variation set 12 which is a high gain case utilizing the most stable sideslip derivatives in combination with the most effective control surfaces and jets. This case provided a balance for the low gain cases and resulted in FCS gains that covered the potential extremes in the aero variations. Case 9 was similar to case 20, but in the presence of large winds around Mach 5, a long period oscillation was observed under certain flight conditions.

In general cases 2, 11, and 23 produced less severe problems than the previously mentioned cases and were eventually dropped from the formal verification for STS-2. Case 2 was originally selected because it produced the largest value for $(\omega_\phi / \omega_d)^2$ and there was some concern about creating pilot induced oscillations (PIO) with this set of variations. However, there was no indication in any of the piloted simulations that this case produced any PIO tendencies. Case 11 was originally selected because it was thought to give the minimum value of the LCDP for the conventional aileron control mode. However, in the critical Mach region around Mach 2, case 9 usually resulted in a

lower value of the LCDP. Case 23 was selected because it generated a maximum sideslip angle during the high heating region.

A problem that was observed with cases 9, 11 and 23 was an occasional tendency for the aileron and rudder to trim against each other after the rudder became active. From figure 2 it can be observed that the aileron and rudder vectors are almost coaligned for these cases and is the probable cause for the trim problem. A procedure was utilized for STS-1 which required the crew to check the trim after the rudder became active and to trim the aileron back toward zero if a force fight resulted between the aileron and rudder.

FCS VERIFICATION PROCESS

As mentioned previously, the initial comprehensive FCS evaluation using aero variations was in a series of 570 piloted simulation runs conducted at JSC on the SPS. These runs were completed in December 1977 and nine fairly significant problems were identified. After it became evident that FCS/aero problems were occurring, key representatives from the flight control groups at Rockwell and Honeywell came to JSC to participate in the simulations. As a result of close coordination between these experts and the FCS and aero community at JSC, as well as inputs from the Langley Research Center, several FCS modifications were made and a change request was submitted and approved early in 1978. These changes were incorporated and another series of 400 simulation runs were made on the SPS in April and May. Some additional FCS changes were made during this series of simulations including modifications to the elevon and speedbrake schedules and a more aft shift in the recommended STS-1 X cg location to 66.7% body length. The resulting FCS was able to maintain control for all combinations of aerodynamic variations except for one case in the Mach 6 region. This problem occurred when a variation set with minimum values of C_{n_β} dynamic was combined with large winds resulting in errors in the navigation derived angle of attack. Because angle of attack terms are present in the bank coordination logic of the FCS, errors in the angle of attack result in miscoordination during bank maneuvers and a resulting buildup in sideslip angle. If RCS jet failures occurred, control problems resulted for angle of attack errors greater than approximately 3°. In order to accommodate this problem the flight rules for the early flights required manual bank reversals at reduced roll rates in the Mach 6 region if RCS jet failures occurred.

The formal integrated guidance, navigation and control (GN&C) verification testing began at the FSL in September 1979. A total of 35 runs were made before the simulation was suspended due to several significant problems that resulted. Forty-one flight software anomalies were identified of which 21 were related to the FCS. In general the problems occurring on the FSL had not been observed in the nonintegrated FCS simulations or were of a much smaller magnitude.

As a result of the FSL results extensive analysis of the FCS was done to attempt to identify and correct the observed anomalies. The launch schedule slip due to the loose tile problem provided the FCS community an opportunity to perform a major review of the FCS design. Some of the problems were related to excessively large uncertainties applied to the GN&C line replaceable units (LRU) and some related to the FSL models. However, several additional changes were made to the FCS and the Orbiter Software Control Board approved the change requests in April 1980.

Figure 11 from reference 7 shows the test matrix that was proposed for the FCS verification. The matrix includes aerodynamic uncertainties, winds, and tolerances on the GN&C LRU's. Most of the simulation runs were performed using the upper left box (nominal) and the lower right box (worst case). Figure 12 from reference 7 outlines the verification process that was approved by the orbiter Configuration Control Board (CCB) prior to the final integrated verification testing at the FSL.

The GN&C was tested first with nominal aerodynamics and then with the variations. If no problems occurred with worst case variations, verification was considered complete. If problems resulted with variations, the case was repeated with tolerances. If the system could not handle tolerances a design change was required and the process repeated. A case that passed with tolerances but failed with variations resulted in a review with the aero group to discuss the validity of the specific variation case. The problem was then presented to the CCB who made the decision to either accept the risk associated with the case or to require a design change.

Formal verification was done on the FSL in August and September of 1980. The GN&C performance was greatly improved compared to the previous verification runs. A week long post simulation review by personnel from Rockwell, Honeywell, and JSC was conducted to thoroughly analyze the results of each run. A total of 16 anomalies were identified, but most of these were relatively minor and required no substantive action. The most significant problems were associated with the low C_{n_β} dynamic cases in the presence of design case winds around Mach 5. The program managers eventually accepted these cases after it was shown that the design winds for the STS-1 flight date of April resulted in less severe problems than the worst case winds used for the FSL verification. The flight rule requiring manual bank maneuvers in this Mach region following RCS jet failures also tended to alleviate the problem.

FLIGHT TEST RESULTS

The flight results from STS-1 showed the validity of applying aero variations in the FCS design and verification process. In the early entry region the pitching moment coefficient was outside the

variations in the positive direction while in the Mach 1-2 region C_m approached the negative variation limit as can be seen from figure 13. Thus the longitudinal cg location for STS-1 was near optimum. Figures 14-19 show some of the preliminary lateral directional data derived from the first four flights (ref. 8) compared to those from the Aerodynamic Data Book (ref. 9). It is anticipated that additional changes will occur in the data base as more flight data is obtained in the proposed 17 flight test program.

The results from figures 13-19 show that each of the seven coefficients approached or exceeded the variation level at some point in the entry trajectory. In addition to the pitching moment problem which has already been mentioned, two other problems were noted on STS-1. At the first bank maneuver which occurred very early in the entry, a large sideslip oscillation developed with β reaching a value of 3.5^{o}. Post flight analysis showed the primary culprit to be the rolling moment RCS jet interaction shown in figure 18. This coefficient was about twice the variation level and if the FCS had not been designed for acceptable control with variations applied, a more serious problem could have developed on STS-1. For STS-2 through -4 the problem was circumvented by having the crew manually perform the maneuver at a slower rate and on STS-5 the FCS flight software was changed to provide acceptable performance with the revised data. In the Mach 1.5 region a low amplitude roll oscillation has been noted on each of the orbiter flights. Additional flight data is required to determine the source of the oscillation, but the reduced $C_{\ell_{\delta_a}}$ shown in figure 16 is a possible contributor. Changes to the FCS in this Mach region are planned once the aero data is more accurately defined.

CONCLUSIONS

The successful flight of STS-1 in April 1981 proved the success of the FCS design and verification process. A key factor in this success was the selection and application of the aerodynamic variations. A comparison of the flight data with the predicted data (ref. 9) indicates that the magnitude of the variations used was not overly conservative. In fact, it can reasonably be concluded that for an individual coefficient, the variation represented an expected value at some point during the entry trajectory. However since the entry covers a large Mach region and the stability and control problems generally required a combination of adverse aerodynamics in a specific Mach region, the application of aero variations for the orbiter entry probably represented a combined probability approaching a 3σ case. Based on this reasoning, the aero variation magnitudes used for the orbiter should be considered reasonably valid for future programs.

A definite need exists for defining the appropriate controllability criteria for heavily augmented vehicles to help define the correct combinations of aero variations. It would appear that use

of equivalent augmented coefficients similar to the augmented C_{n_β} dynamic discussed in this paper may provide some guidance in selecting these criteria.

A final factor that undoubtedly contributed to the success of the FCS design was the close coordination and cooperation of the Rockwell, Honeywell, and JSC control and aerodynamic groups throughout the orbiter program. This coordination allowed rapid response from several different organizations whenever a problem arose and permitted evaluation and changes to occur in a relatively short time period.

REFERENCES

1. Kafer, G. C.: Space Shuttle Entry/Landing Flight Control Design Description, AIAA Paper 82-1601 CP, August 9, 1982.

2. Kafer, G. C. and Wilson, D.: Space Shuttle Descent Flight Control Design Requirements and Experiments, Shuttle Performance: Lessons Learned, NASA CP- 2283, Part 1, 1983, PP. 617-628.

3. Young, James C. and Underwood, Jimmy M.: The Development of Aerodynamic Uncertainties for the Space Shuttle Orbiter, AIAA Paper 82-063, 1982.

4. Weil, Joseph and Powers, B.: Correlation of Predicted and Flight Derived Stability Derivatives with Particular Application to Tailless Delta Wing Configurations, NASA TM-81361, July 1981.

5. Moul, M. T. and Paulson, J. W.: Dynamic Lateral Behavior of High-Performance Aircraft, NACA RML58E16, August 1958.

6. Weissman, R.: Status of Design Criteria for Predicting Departure Characteristics and Spin Susceptibility, J. Aircraft, Vol. 12, No. 12, December 1975, pg. 989-993.

7. Bayle, G. P.: Entry Flight Control Off-Nominal Design Considerations, AIAA paper 82-1602CP, August 9, 1982.

8. Underwood, J. M.: STS-4 Flight Assessment Package Orbiter Aerodynamics, JSC Report No. 18699, October 1982.

9. Aerodynamic Design Book (Space Shuttle Program). Vol.I- Orbiter Vehicle STS-1. Report No. SD72-SH-0060-1M, Rockwell International, Nov. 1980.

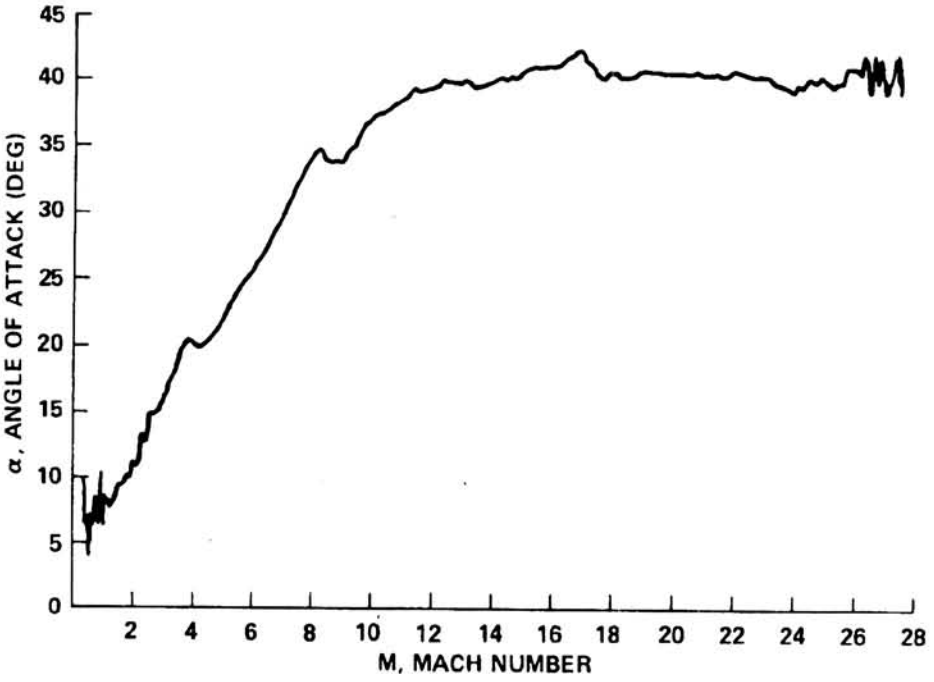

Figure 1.- STS-1 angle of attack history.

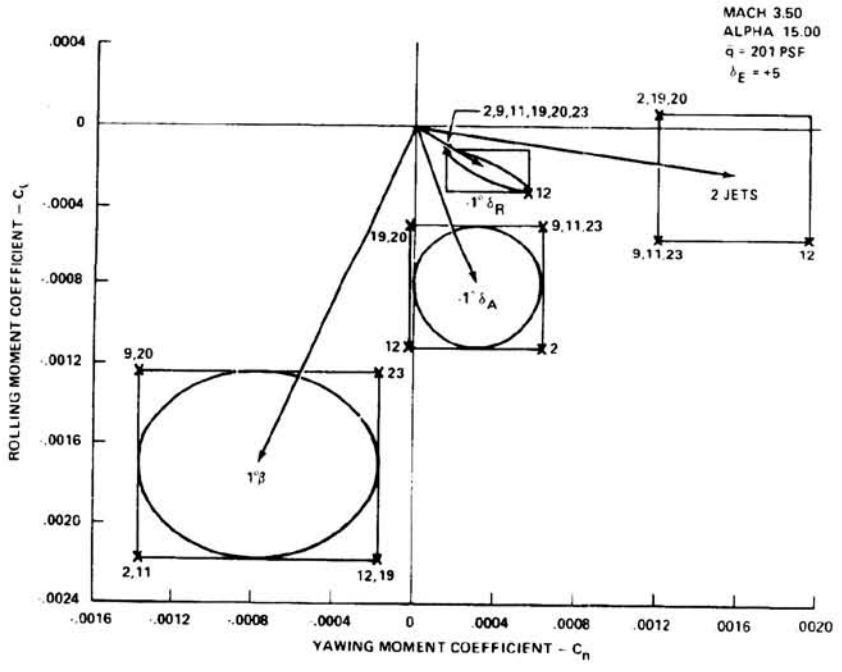

Figure 2.- Aerodynamic vectors at Mach 3.5 showing variation sets.

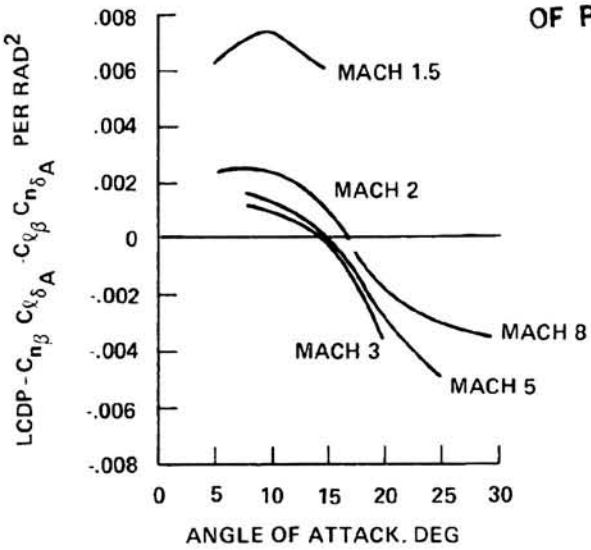

Figure 3.- Effect of angle of attack on LCDP for aero variation set 19.

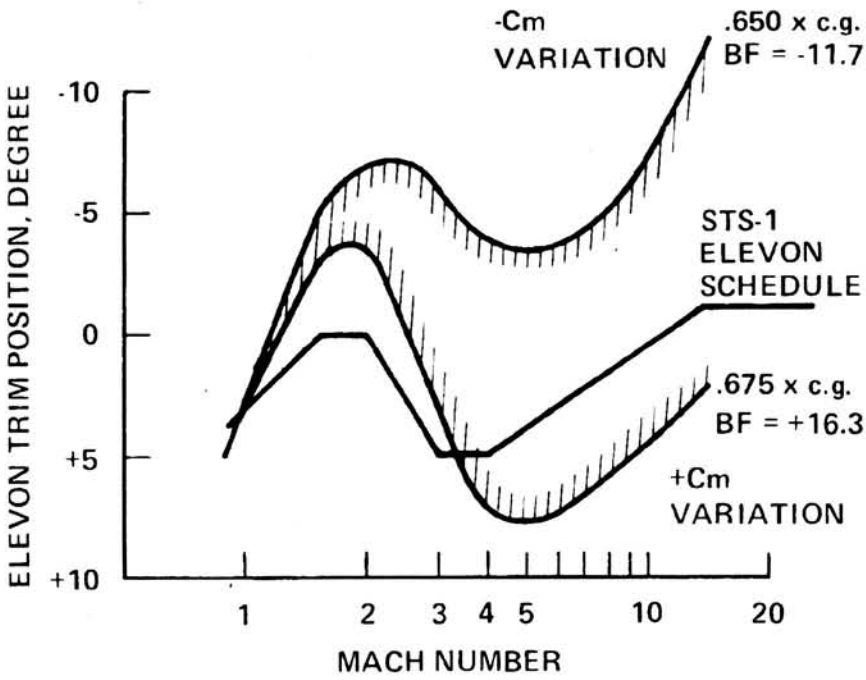

Figure 4.- Elevon trim envelope for design cg limits with pitching moment variations.

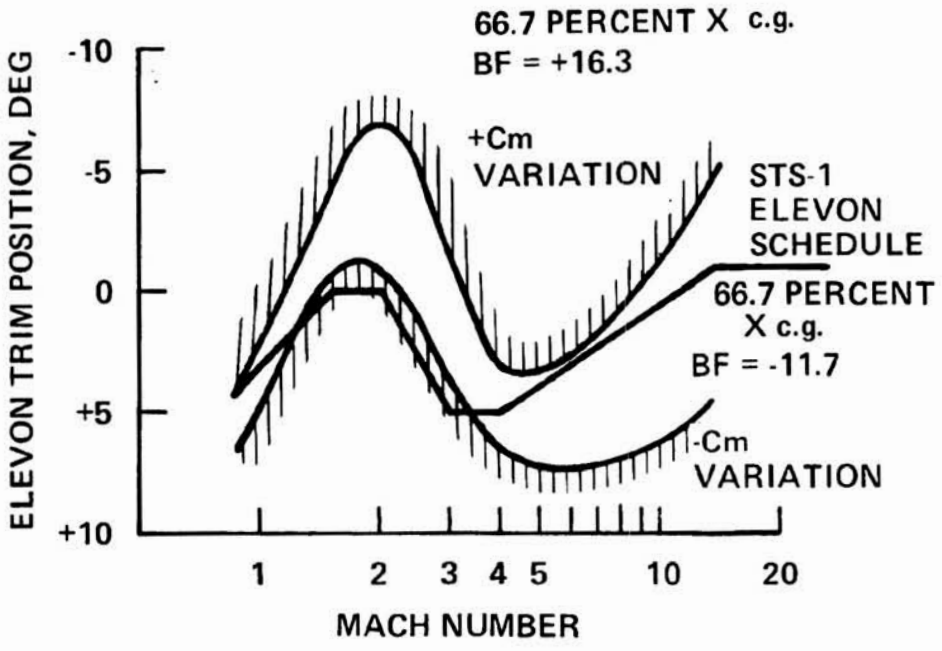

Figure 5.- Elevon trim envelope for 66.7 percent L_B X_{cg} with pitching moment variations.

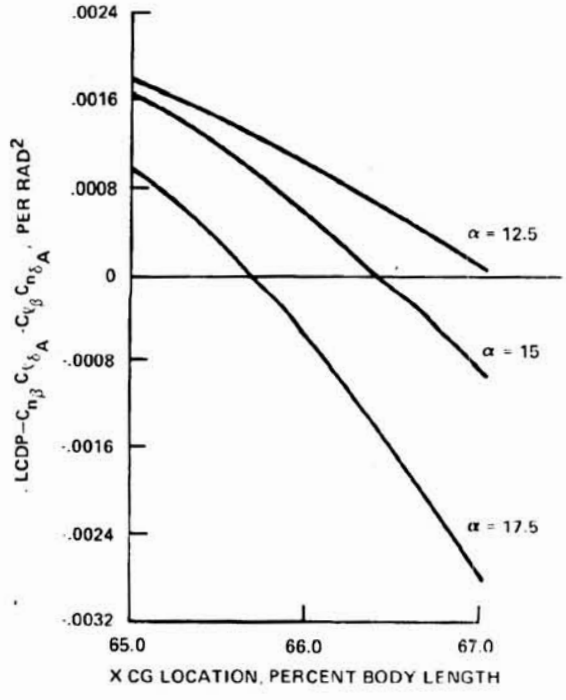

Figure 6.- Effect of cg and angle of attack on LCDP at Mach 3.5 with aero variation set 19.

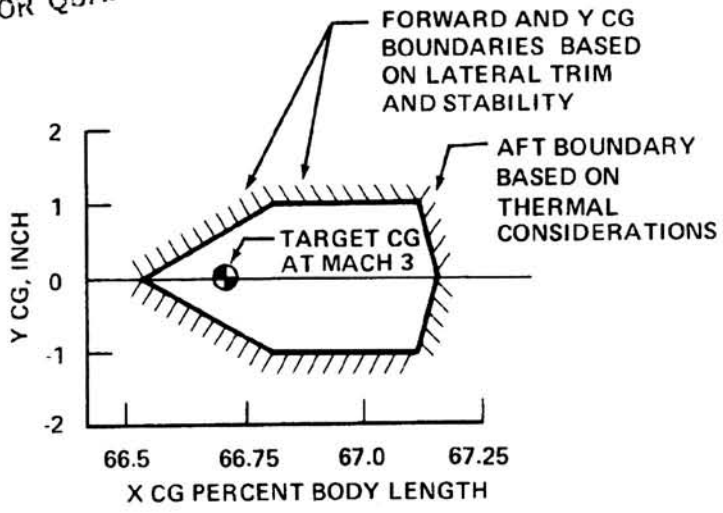

Figure 7.- Recommended cg envelope contained in flight rules document for STS-1.

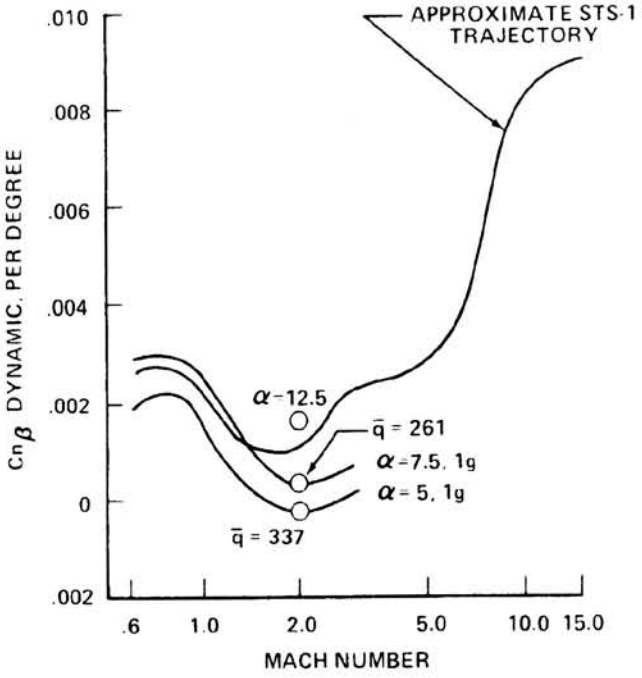

Figure 8.- C_{n_β} dynamic for nominal aerodynamics.

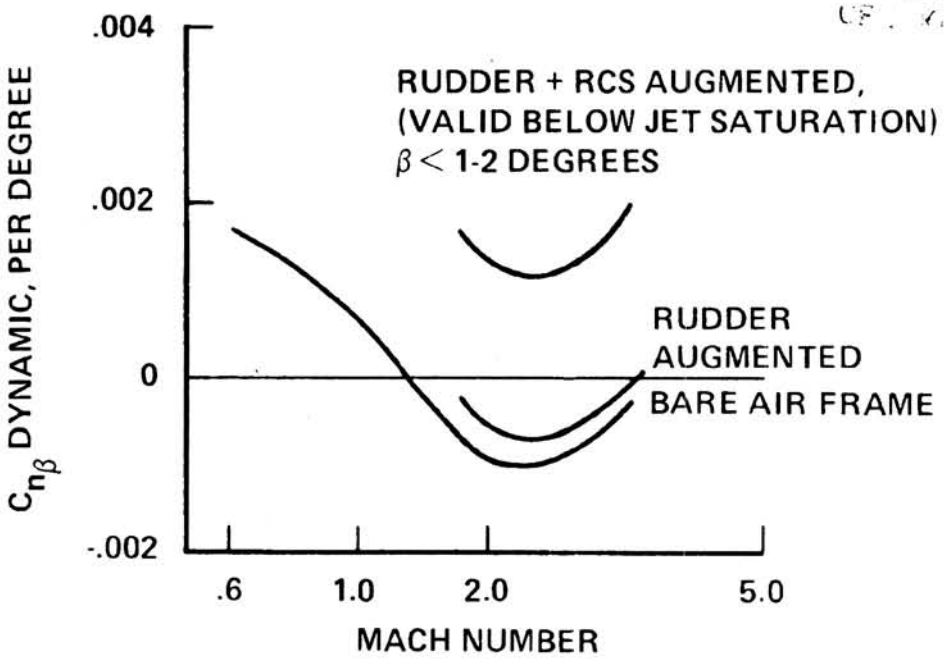

Figure 9.- C_{n_β} dynamic for worst case variation set (LVAR20), 1-g flight at 7.5 degrees alpha.

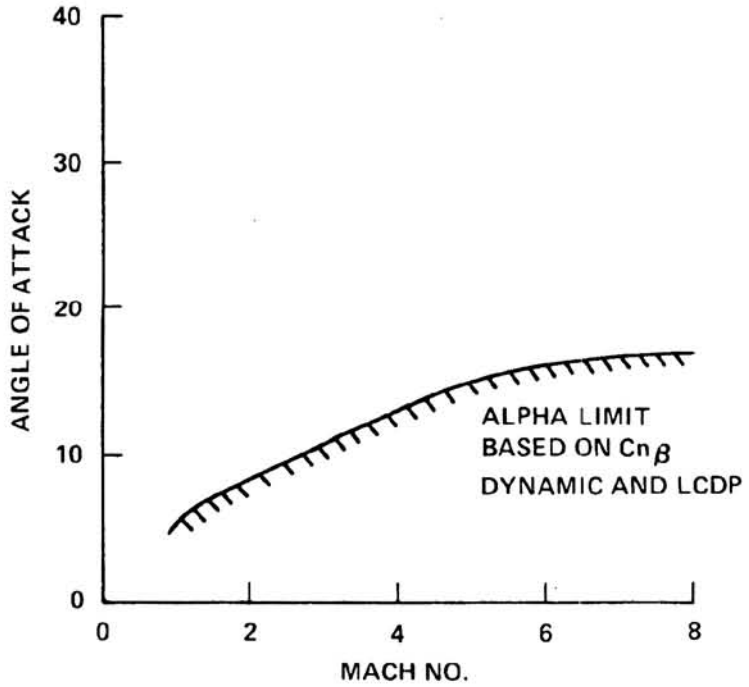

Figure 10.- Lower angle-of-attack boundary contained in flight rules document for early orbiter flights.

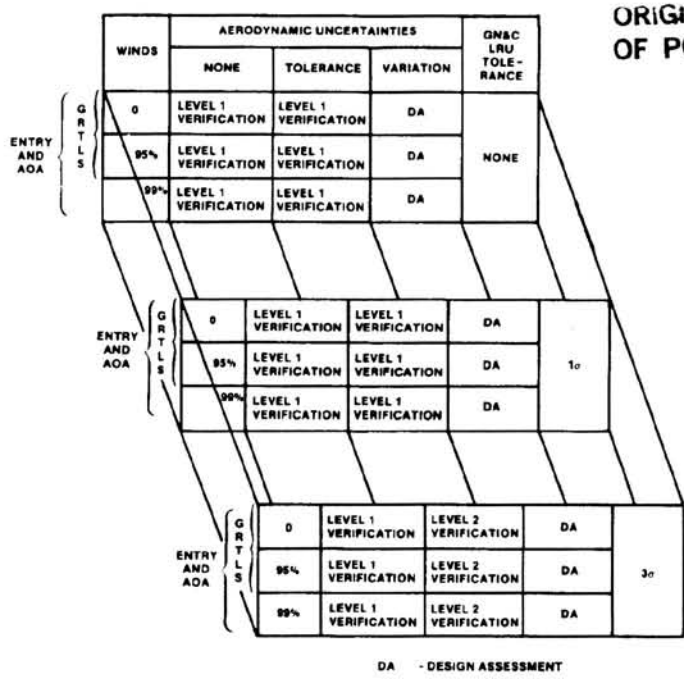

Figure 11.- Entry verification test matrix.
(From ref. 7.)

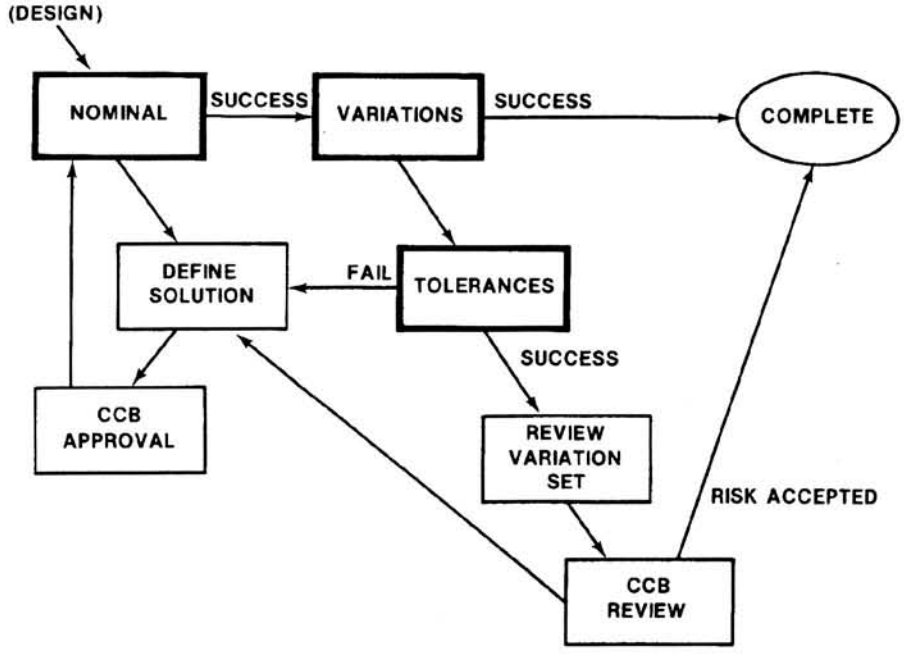

Figure 12.- GN&C/FCS formal verification process.
(From ref. 7.)

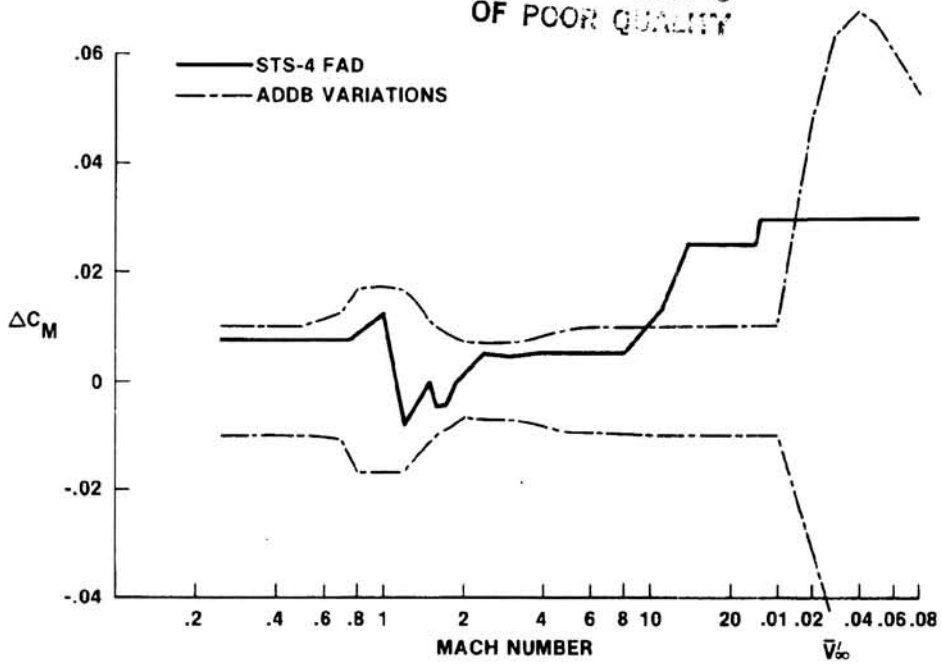

Figure 13.- STS-4 flight assessment delta for pitching moment coefficient.

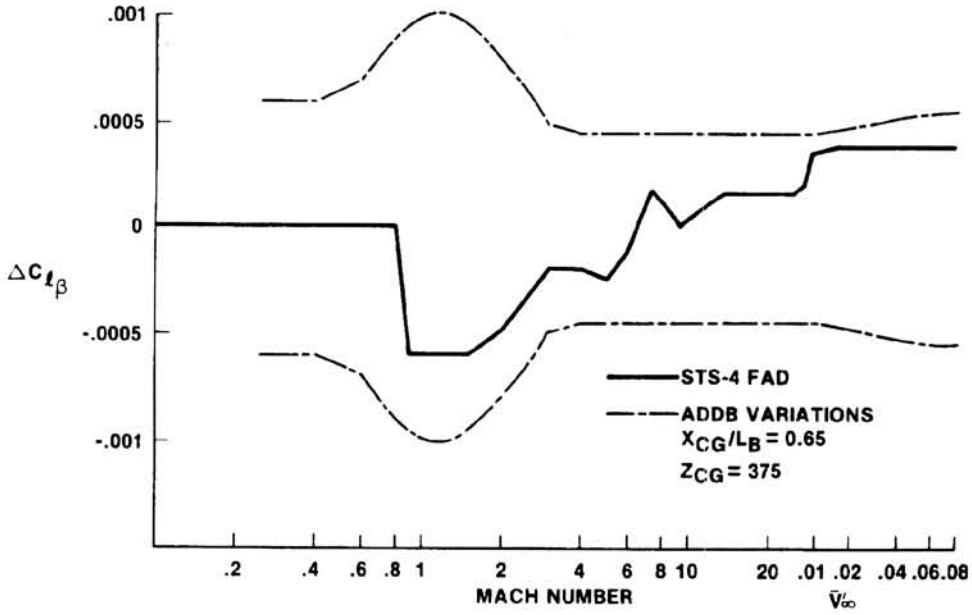

Figure 14.- STS-4 flight assessment delta for C_{ℓ_β}.

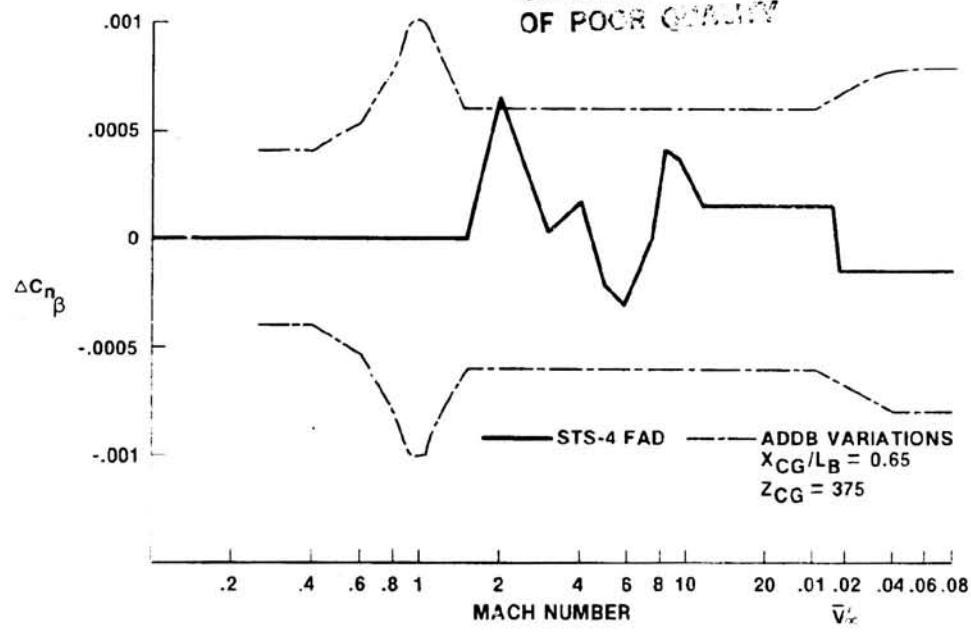

Figure 15.- STS-4 flight assessment delta for C_{n_β}.

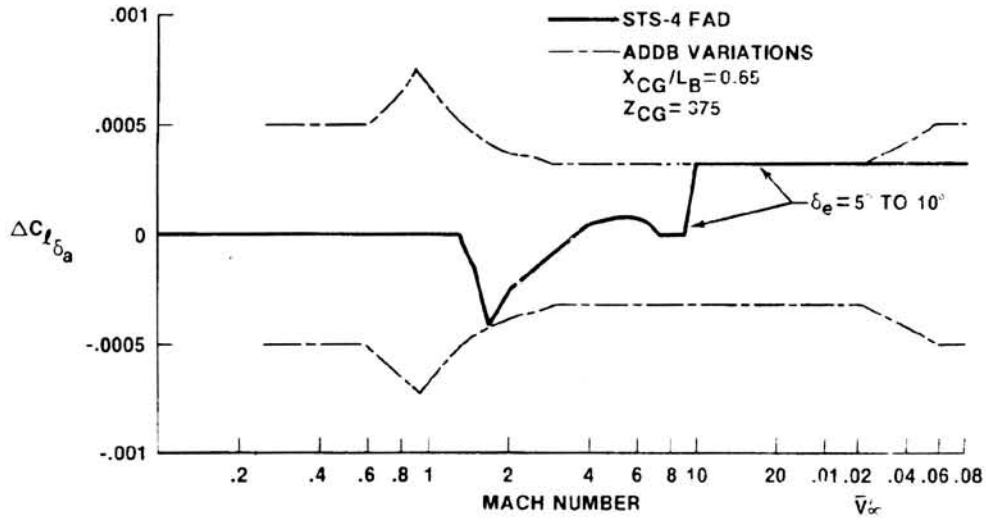

Figure 16.- STS-4 flight assessment delta for $C_{\ell_{\delta_a}}$.

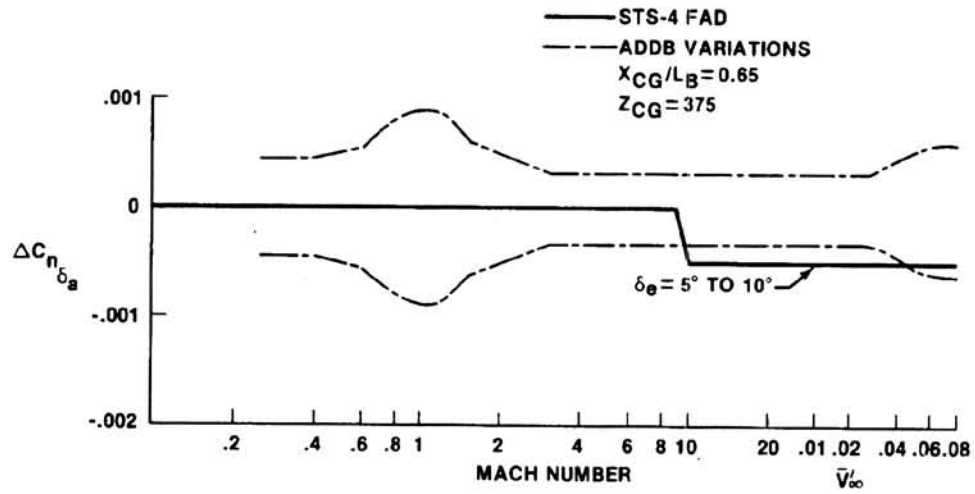

Figure 17.- STS-4 flight assessment deltas for $C_{n_{\delta_a}}$

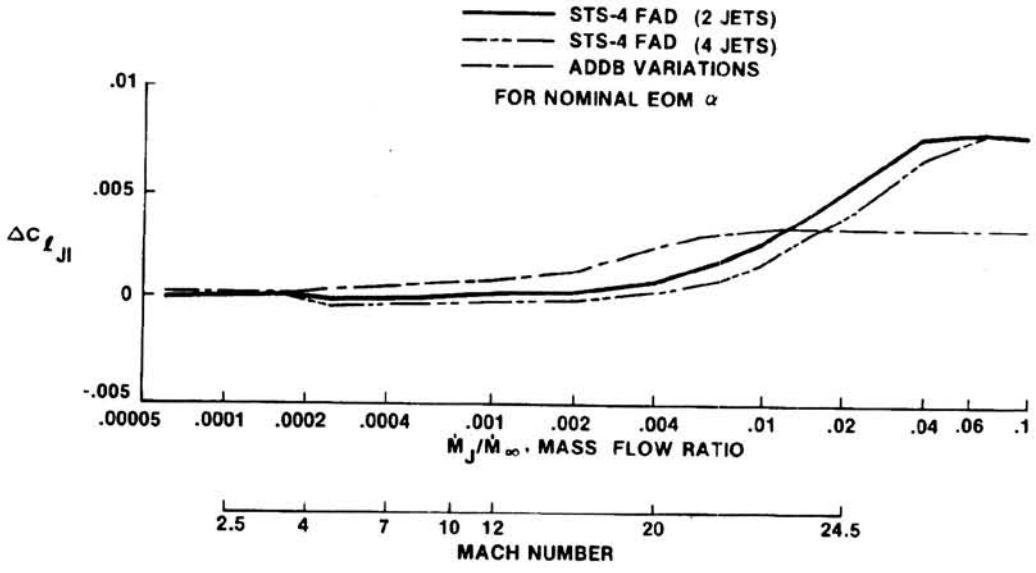

Figure 18.- STS-4 flight assessment deltas for rolling moment RCS interaction due to yaw jets.

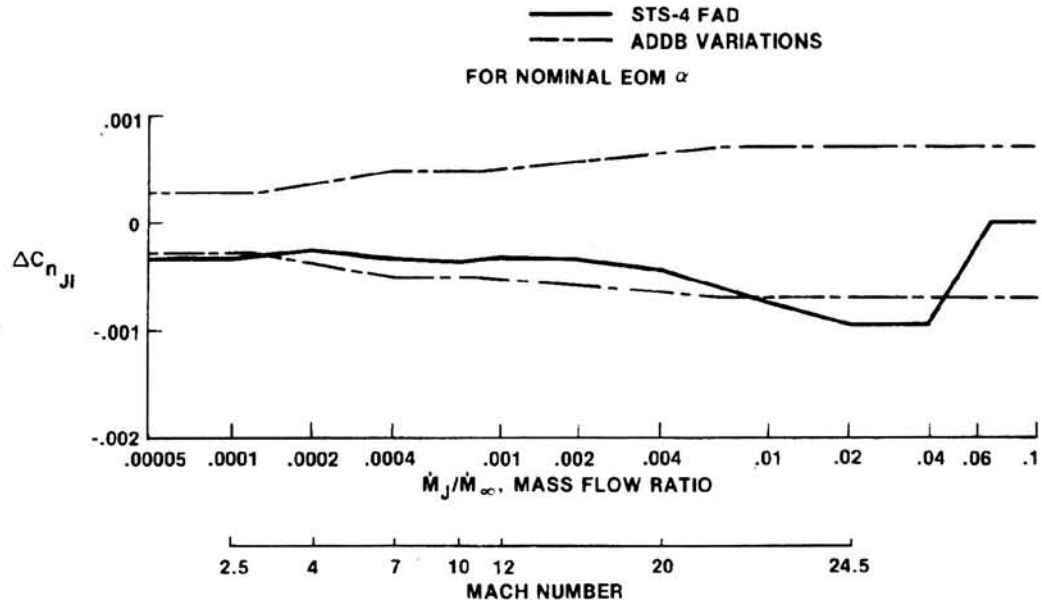

Figure 19.- STS-4 flight assessment deltas for yawing moment RCS.

SPACE SHUTTLE DESCENT FLIGHT CONTROL DESIGN REQUIREMENTS AND EXPERIMENTS

G. Kafer and D. Wilson
Honeywell Inc.
Clearwater, FL

SUMMARY

This paper reviews some of the lessons learned during the development of the Space Shuttle descent flight control system. Examples were selected to emphasize the scope of the FCS design problem, and to confirm the importance for requirements definition, systems level analyses, and testing. In so doing these experiences may have implication for future designs or suggest the discipline required in this engineering art.

INTRODUCTION

The performance of the Space Shuttle Entry/Landing (E/L) Flight Control System (FCS) has been outstanding. The successful flights in the OV101 - Approach/Land Test (ALT) and OV102 - Operational Flight Test (OFT) have demonstrated the basic system capability. In addition, the validity of most preflight design assumptions, and system analyses, test predictions has been confirmed.

This paper provides an overview of some of the lessons learned during the development of the FCS. Examples were selected to emphasize the scope of the FCS design problem, and to confirm the importance for requirements definition, systems level analyses and testing. In so doing, these experiences may have implication for future designs and/or suggest the discipline required in this engineering art.

The examples focus on the following elements of the controlled configured vehicle (CCV) FCS represented in Figure 1. They are: the digital fly-by-wire autopilot (DAP), the stabilization of the vehicle dynamics, both flexible and rigid body, and the quad redundant sensor interface. In addition, certain landing performance characteristics are summarized to introduce a "lesson learned" on the need for adequate specifications of flying qualities.

STABILIZATION OF VEHICLE DYNAMICS

The development and lessons learned relating to the stabilization of the orbiter during descent has confirmed the need, importance, and benefit of system level requirements, analyses, and testing. In particular, the design to wide margins to satisfy stability requirements represents a considerable development effort. Yet it is an essential step to eliminate FCS anomalies which can result when margins are inadequate due to unexpected uncertainties.

Combinations of design uncertainties in the following parameters indicate the complexity of the modeling, analyses, design and test. Key parameters are vehicle aerodynamic, structural, configuration effects; mission and flight phase characteristics; and system integration - trades between low frequency rigid stability and high frequency flexible mode attenuation.

Flexible Vehicle Dynamics

Test results to date have confirmed the structural/controller body bending modes are stable. As indicated in Table 1, however, this achievement resulted from numerous lessons learned during the analytic design and ground test experience. Table 2 is included as reference to provide an overview compilation of the structural/payload mode characteristics. Note that: 1) the orbiter bending modes are sufficiently high, relative to the approximate 1.5 Hz rigid control bandwidth, to permit a classical rigid versus flexible body model/analyses formulation; and, 2) payload modes, however, are approaching the rigid control bandwidth and represent future FCS challenges to provide acceptable system-level dynamics.

STS flight performance to date, for Entry/Landing nominal end-of-mission, has confirmed the modes are stable. Yet to be tested are the GRTLS and certain weight-on-wheels (WOW) controller performance.

GRTLS Stability

The Glide-Return-To-Launch Site (GRTLS) abort performance, based upon analyses and simulation, exhibits degraded flexible and rigid mode stability relative to similar low dynamic pressure ($\bar{q}$<70 psf) entry, aerojet DAP conditions. In particular, initial stability predictions for STS-9, Spacelab payload, indicate a limit cycle will occur; no attenuation or phase margin is predicted at an approximate 3.9 Hz mode. Similarly, minor rigid performance anomalies and waivers on low frequency stability and response requirements have been predicted during the OFT analytic verification. Though overall performance has been judged acceptable for flight, these effects prompted a DAP redesign study. Table 3 presents key development control features of this redesign. In summary, they typify the complex FCS requirements to provide:

1. 12 dB low frequency gain margin, 6 dB high frequency gain margin, and 6 dB flex mode attenuation

2. High proportional and integral pitch DAP gains to achieve acceptable response, accuracy and trajectory control performance

3. Integrated force effector operation, aero and reaction control jets (RCS)

The feasibility of a GRTLS DAP update has been demonstrated via analyses and the February 1983 NASA/SES simulation. A high frequency gain reduction was achieved. The candidate update provides acceptable overall FCS performance for both manual and automatic control modes. Currently a baseline software change request is being developed for program approval and resolution of the rigid/flex performance interaction concerns.

WOW Performance

Weight on wheels (WOW) FCS stability (i.e., interactive gear, rigid, flex, payload, DAP control modes) is receiving concerted attention because of 1) critical need for adequate performance in this mission phase, 2) uncertain past ability, and experience in predicting actual system performance coupled with the need to extrapolate and/or assess new, operational system effects (heavy orbiter, mission payloads), 3) absence of analyses and test results for operational configuration, and 4) concurrent DAP redesign to effect landing improvements.

Table 4 provides an overview of certain pertinent engineering data. As indicated, along with Table 1, test results have provided confidence in the design for actual flight; there has been no evidence of ground instabilities from the ALT and OFT landings. Nevertheless, vehicle level testing, OV102 and OV099 DST, has produced low frequency mode instabilities due to either new unmodeled effects or procedural effects. For this reason attention is warranted to assure continued acceptability of performance. A lesson learned has been to anticipate structural resonances, and conduct analyses and test activities to eliminate the associated risk.

RIGID VEHICLE DYNAMICS

Operational flight test performance has correlated very well with predicted, and in most cases, nominal results. For the exceptions in the STS-1, first roll maneuver sideslip oscillation, and the ¼ Hz lateral oscillation, it has been demonstrated that the principal cause is the basic design data base and uncertainty definition.

First Roll Maneuver, Sideslip Oscillation

Analyses subsequent to the STS-1 flight, with the flight derived data base (Figure 2), matched the flight results, and determined that the low damped system response was due to the roll-due-to-yaw jet aerodynamic interaction. A digital control law update based upon these data base assumptions was formulated and flown on STS-5. As evidenced by Figure 3 significant performance improvement was achieved through the deliberate and precise analyses, and test development process. In-flight instrumentation made it possible to refine the design data base assumptions, and improve performance and flight safety.

1/4 Hz Lateral Oscillation

The lateral oscillation in the Mach 1.6 flight regime has been the subject of a significant number of analytic and test investigations. To date there has been no successful matching of both the programmed test input (PTI) response and small amplitude rolling divergence using the baseline models and data base. Results indicate that the large amplitude motion (PTI) is nominal and can be emulated by the baseline models. But this is not the case for the small amplitude response. This in turn suggests some unmodeled, nonlinear effect. The oscillation develops from a small amplitude aileron-rudder loop divergence (i.e., instability for yaw RCS off, control signal errors inside the jet command deadbands). While the overall performance (yaw jets active control the response) is acceptable, model and problem definition remains a concern, and is being addressed in the planned flight testing through STS-17.

Another facet of this performance problem is evidenced in Figures 4 and 5. Figure 4, with a superimposed plot of the roll axis forward loop gain (Ref. 1 - FSSR GDA module), gives strong evidence to support an increase in the loop gain. Analyses and simulations have demonstrated that this improved gain schedule provides a significant reduction (factor of 2 to 3) in the amplitude of the 1/4 Hz oscillation. After additional flight test and analyses firm problem definition and resolution will result. This, in turn, could permit earlier termination of the RCS and expansion of the performance envelope.

SENSOR INTERFACE

The QMVS (quad mid-value select) selection filter and fault detection, identification and reconfiguration algorithms (References 2, 3) selects a single output for the DAP from four sensor inputs. Sensors that fail at full amplitude (hardover failures) and those that drop to near zero output (null failures) are detected, removed and substituted with functioning sensors.

The QMVS function reconfigures channels when the difference between midvalue select signals exceeds an I-load, "C-VALUE" constant. A large C-VALUE is desirable for the no fault case to prevent transients due to inadvertent switching between channels with large sensor bias errors. Conversely for the dual null fault case a small C-VALUE is desirable; the smaller the C-VALUE the smaller the selection filter output deadband and switching transient. Some development concerns relating to this FCS function are described below.

QMVS Effect on Residual Oscillations/RCS Propellant

During the course of testing and analysis in support of STS-2 and STS-3 verification (Reference 4) it was found that the RCS propellant consumption can more than double with worst case undetected dual pitch rate gyro or dual yaw rate gyro null failures. This is because selection filter output nonlinearities in combination with signal noise and quantization effects can cause vehicle/system residual oscillations. The following comparison of baseline descent analyses results illustrates this and shows the performance sensitivity to the vehicle data base.

Comparative 1/4 Hz Oscillation Characteristics

Yaw Rate Gyro Failures Status	Vehicle Data Base	Roll Rate Oscillation Frequency	Amplitude
None	Pre STS-1 Flight	.14 Hz	0.4 deg/sec
None	STS-1 Flight	.21	2.0
Dual	STS-1 Flight	.21	6.0

Because of these performance effects candidate software design updates to the baseline QMVS have been developed for future implementation. The development was aided by the fact that performance could be predicted and accurately correlated by using the describing function - linear stability analyses, nonlinear time history simulation, and real time trajectory simulation testing.

PERFORMANCE REQUIREMENTS/SPECIFICATION

Emphasis on system level requirements (References 5, 6) and verification of these requirements can result in a usable system and reduce in-service resolution of design deficiencies. Evidence of this is demonstrated by the successful operation and performance of the Space Shuttle ENTRY/LANDING FCS.

One lesson learned, and not entirely unique to the orbiter, is the continuing need for research, definition, and utilization in FCS design of flying qualities criteria (References 7-10). For example, current studies, somewhat similar to post ALT flight test efforts (Reference 11), are again addressing landing performance, e.g., induced oscillation tendencies, sluggish response, control sensitivity, and authority. Potential problems have been identified in the airborne pitch axis control and weight-on-wheels derotation stability. These concerns in combination with operational requirements to effect short field or spot landings without exceeding tire, gear, brake constraints indicate a: 1) challenge to the STS, and 2) lesson that there are yet man/machine relations to be learned.

CONCLUSION

The accomplishments and lessons learned have been generally consistent with tradition. Program success goes back to the basics; i.e., the increasing complexity of flight control increases the need for requirements set to provide adequate subsystem and system level design margins, and the need for analyses, design, verification and test. Basic leadership, technical and communication skills, along with a dedicated team with a commitment to discipline, hard work and quality bring about success. What has been obvious, and a tribute to those contributing to the FCS development, is the dependency of program success on people.

REFERENCES

1. Functional Subsystem Software Requirements (FSSR); Part C - Flight Control Entry - GRTLS. Rockwell International Baseline Document: STS81-0007A, May 1982.

2. Gelderloos, H. C., and Wilson, D. V., Redundancy Management of Shuttle Flight Control Sensors, Proceedings of the IEEE Conference on Decision and Control and Symposium on Adaptive Processes, December 1976, pp. 462-475.

3. Gelderloos, H. C., and Young, D. J., Redundancy Management of Shuttle Flight Control Rate Gyroscopes and Accelerometers; American Control Conference Proceedings, vol. 2, June 1982, pp. 808-811.

4. STS-3 Verification Test Report, Flight Systems Laboratory: Rockwell International Baseline Document: STS81-0710, February 1982.

5. Requirements/Definition Document; Flight Control, Part 1 Configuration, Performance and Functional Requirements. Rockwell International Baseline Document: SD72-SH-0105, Vol. 1, Book 2, Part 1B; December 1980.

6. Bayle, G. P., Entry Flight Control Off-Nominal Design Considerations, Proceedings of the AIAA Guidance & Control Conference, August 1982, pp. 538-545.

7. Berry, D. T., Flying Qualities: A Costly Lapse in Flight Control Design? Astron. & Aeron., vol. 20, no. 4, April 1982, pp. 54-57.

8. Myers, T. T., McRuer, D. T., Johnston, D. E., Space Shuttle Qualities and Flight Control System Assessment. Proceedings of the AIAA Guidance & Control Conference, August 1982, pp. 561-570.

9. Ashkenas, I. L., Hoh, R. H., Teper, G. L., Analyses of Shuttle Orbiter Approach and Landing. Proceedings of the AIAA Guidance & Control Conference, August 1982, pp. 810-820.

10. Flying Qualities Design Criteria. Proceedings of AFFDL Symposium at Wright Patterson AFB. AFWAL-TR-80-3067, May 1980.

11. AFFTC Evaluation of the Space Shuttle Orbiter and Carrier Aircraft (see pages 101-105). AFFTC-TR-78-14, May 1978.

TABLE 1. FLEX STABILITY RELATED GROUND TESTS

TEST	DESCRIPTION	FCS RESULTS
Hot Fire November 1979	OV102, FCS active	o Not modelled/predicted high gain instability o Not modelled pitch/yaw coupling o Relocate outboard rate gyros o Redesign FCS filters for STS-1
Dynamic Stability August 1980	OV102, FCS active	o Not modelled/predicted gear/tire high gain instability o Obtained data for use in STS-1 verification
Inertial Upper Stage Dynamic Stability	OV099, FCS active IUS payload/damper	o Stable with nominal and high gain o Correlated with predictions, model confirmed o Procedural error instability; i.e., FCS on, air bags not activated

Lesson Learned

High frequency dynanic interactions, model difficulties require design to wide margins, analyses and test.

TABLE 2. FLEX DATA BASE OVERVIEW REPRESENTATIVE STRUCTURAL/PAYLOAD MODES

PLANE-AXIS	DESCRIPTION	FREQUENCY
Symmetric (Pitch)	Fuselage	4.5 Hz
	Wing	6.1 Hz
	Vertical Tail	6.4 Hz
	Payload Modes	2.5 - 3 Hz
Antisymmetric (Lateral)	Vertical Tail	3.6 Hz
	Wing/Fuselage	6.9 Hz

	Design Tolerances (5.4F Model)	Verification Tolerances (6.0B Model)
Damping:	1% all modes except 0.5% symmetric vertical tail	1% all modes except: Mode 2 - 2 % Mode 3 - 1.5% Mode 4 - 1.5% Mode 6 - 2 % Mode 7 - 2 %
H-Parameters:	±50% (3σ)	±30% (3σ)
RCS Displacements:	±50% (3σ)	±30% (3σ)
Gyro Slopes	±50% (3σ)	Pitch ±15% ϕ'_2 (3σ) Roll ±25% ϕ'_3 (3σ) Yaw ±30% ϕ'_7 (3σ)
Accelerometer	±50% (3σ)	N_Z ±15% ϕ_2(3σ) N_Y ±15% ϕ_7(3σ)
Mode Frequency	±12% (3σ) except ± 5% antisymmetric vertical tail	±10% All Modes except 2 & 5

TABLE 3. GRTLS LOW $\bar{Q}$ PITCH AXIS DESIGN OVERVIEW

Configuration	Key Control Features (Vehicle Pitch-Up to $\alpha = 50^{o}$)	Comment
Pre STS-1	Proportional plus integral gains (FSSR GDQ, GTRE) like Entry; unlike Entry no function to convert jet commands into elevon trim command.	
STS-1	Entry reduced high integral gain, auto mode (α) error gain (FSSR GQAL and GQALR), and added α filter to improve rigid body response/stability. GRTLS minimum change retained high integral, auto mode gains to maintain tight trajectory control; increased (6 dB) proportional gain (GDQ) to maintain stability, improve system damping.	Increased GDQ directly reduces flex mode margins 6 dB.
Current		Minor spec violations, e.g., STS-5: 10 vs. required 12 dB low frequency gain margin, 26^{o} vs. required 30^{o} phase margin. $0 \leq MA^{*} \leq 4$ dB at $\bar{Q} < 40$ psf, for STS-9 Spacelab payload.
Candidate Redesign	Reduce GTRE and thereby allow proportional, GDQ, gain reduction to maintain rigid stability and improve flex mode attenuation. Extend use of pitch RCS jets to improve low frequency control especially for operational, forward CG configurations. Add GJET to obviate need for high integral gain, GTRE and minimize elevon/RCS force fight.	Pre-simulation analyses and February '83 NASA/SES evaluation indicates significant performance improvements, and 6 dB decrease in high frequency gain, are feasible.

*MA = 3.9 Hz Mode Attenuation

TABLE 4. IUS/DST TEST

ACTUAL GROUND TEST			ACTUAL FLIGHT
Gains Tested		Axis/Gain	Operational Gains
Nominal	High Gain	Pitch/GDQ	Range*
10^{o}/o/s	20^{o}/o/s	o CSS	1.2 - 1.65^{o}/o/s
-	-	o AUTO	3.3 - 6.0
2	4	Roll/GDA	.26 - .48
7.5	15	Yaw/GDRC	5.5 - 10

*Maximum value limited by air-data $\bar{Q}$ limit equal to 90 psf

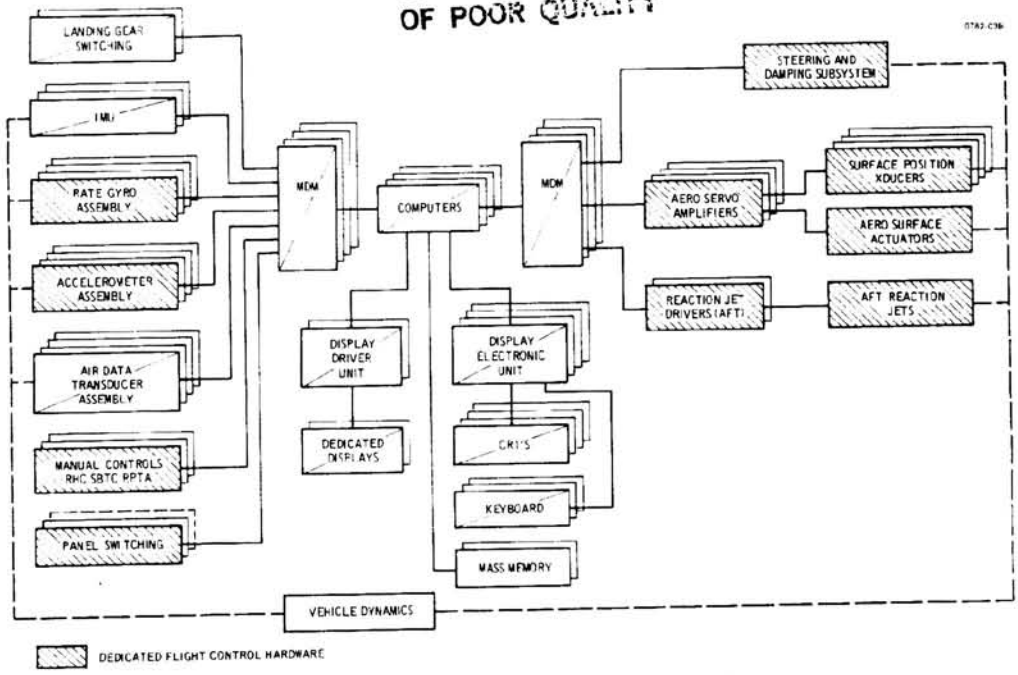

Figure 1.- Flight Control System.

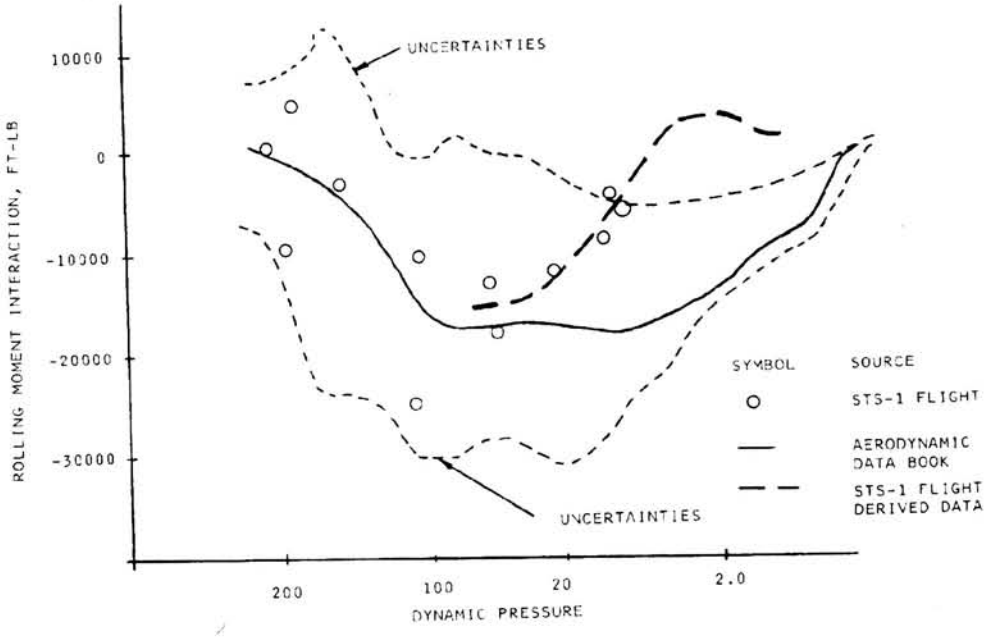

Figure 2.- Rolling moment thruster interaction.

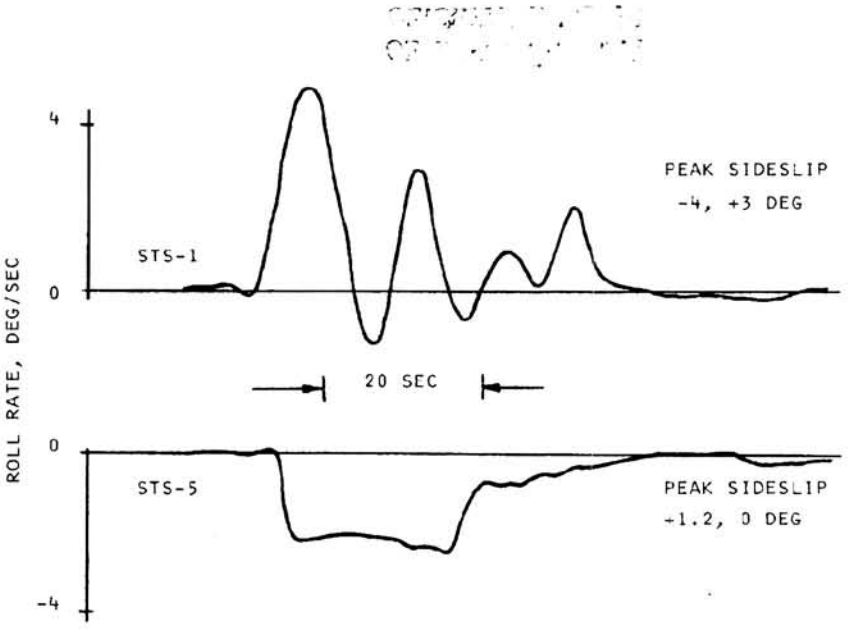

Figure 3.- Comparison of STS-1 and STS-5 first roll maneuver.

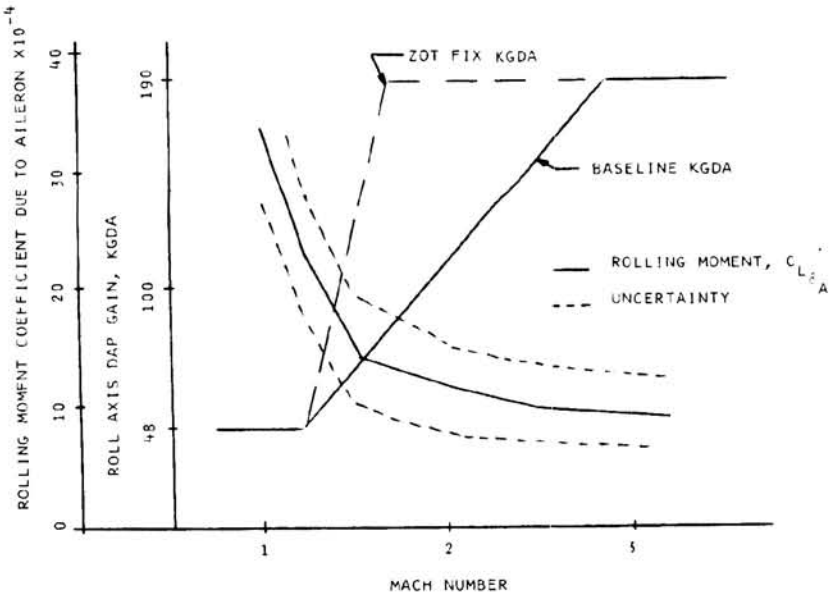

Figure 4.- Aileron effectiveness, roll DAP gain characteristics.

CONDITIONS: MACH 1.64
DYNAMIC PRESSURE 269 PSF
ANGLE OF ATTACK 8 DEG
STS-1 FLIGHT DATA

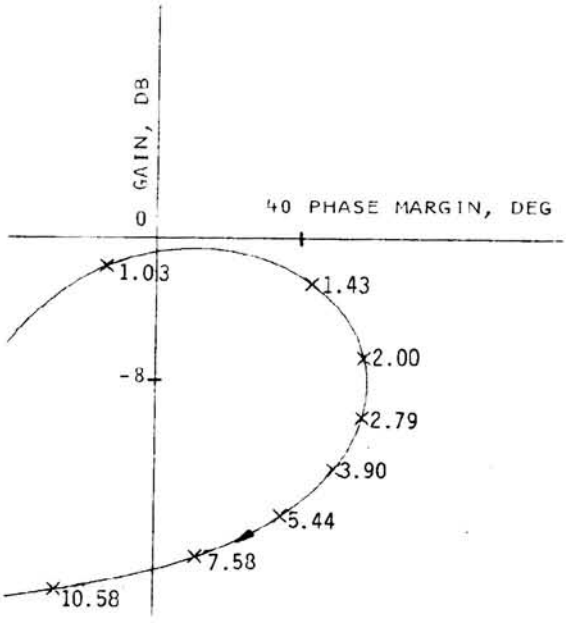

BASELINE (UNSTABLE)

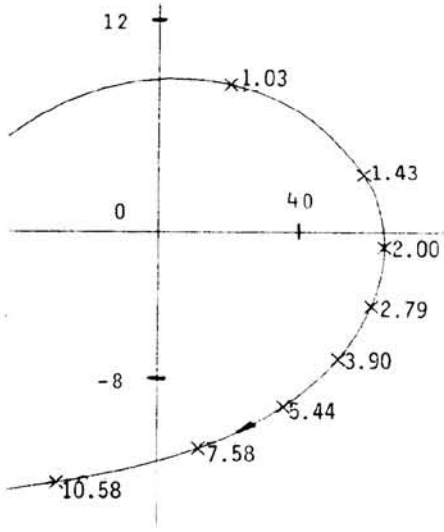

ZOT FIX (ADEQUATE MARGINS)

Figure 5.- Comparative auto mode aileron loop stability. Yaw jets off.

USE OF NONLINEAR DAMPERS TO SUPPRESS SPACE SHUTTLE PAYLOAD MODES*

Clint C. Browning
Avionics Division, Honeywell Inc.,
Clearwater, Florida

and

Gordon E. Hunter
Rockwell International,
Space Transportation Systems Group,
Downey, California

Abstract

This paper presents the analysis methodology and major results in use of nonlinear coulomb dampers to suppress payload modes. A problem arises from large, cantilevered, soft-mounted payloads with low-frequency payload modes that are only slightly higher than the rigid body control bandwidth of the entry mission phase. Unacceptable stability and control result. Additional attenuation was obtained from two coulomb dampers plus digital bending filters. Discussed are coulomb damper and simple payload models, failures, force unbalances, limit cycles, and optimum force level. Open- and closed-loop linear and non-linear methods of analyses are presented. The IUS/TDRS (interim upper stage/tracking and data relay satellite) payload is used as a case study.

Introduction

Large, soft-mounted, cantilevered payloads can exert a major impact on Shuttle vehicle stability and control. The low-frequency dominant payload modes (2.5 to 3 Hz) are about twice the rigid-body control bandwidth (1.5 Hz). The only effective damping on the modes is structural damping. Stability and control are unacceptable during the low-dynamic-pressure reentry phase of the mission.

Assessments were made at 25 flight conditions, 14 above Mach 1 and 11 below Mach 1, including 4 cases of glide return to launch site (GRTLS). Fig. 1 presents the portions of the mission that are the problem areas. The two regions are, in essence, abort regions. If the payload cannot be deployed on orbit, it must be carried through reentry back to earth. Both the early GRTLS and early reentry phases involve low-$\bar{Q}$ conditions and relatively low-control capabilities. In those phases, coulomb dampers, in conjunction with digital filters, are used to suppress the low-frequency payload modes. In all other mission phases, digital filters are sufficient to attenuate the bending modes.

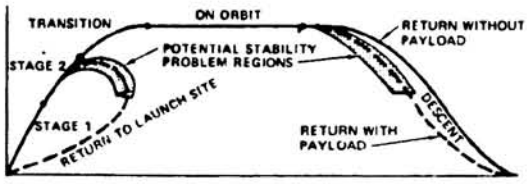

Fig. 1 Potential stability problem regions.

Of several proposed solutions that could provide structural stiffening and/or increased damping, coulomb dampers offer the advantages of reliability, availability, ease of installation, and negligible structural redesign. A critical design requirement is limit-cycle amplitude control to preserve auxiliary power unit (APU) fuel margins. In this paper element models, analysis methodology, and major results for the chosen solution are discussed. And the IUS/TDRS payload, which is the first large, soft-mounted payload scheduled to fly on the Shuttle (Flight 6), is used as a case study.

Summary of Trade Studies and Solution for IUS/TDRS Payload

This study involved assessment of Shuttle control system stability with a heavy payload, supported by an underdamped suspension system, installed in the cargo bay. A ground rule established early was to maintain the existing auto-pilot design in the low-frequency range and not impact either the gain or phase at frequencies below 10 radians per second (RPS).

System trade studies were conducted to evaluate both hardware and flight control system (FCS) software modifications. Four options were identified as the most promising for improving stability. These hardware modifications in general were an attempt either to stiffen the payload support structure to increase the mode frequencies or to provide additional modal damping. The options investigated were:

1. Airborne support equipment (ASE) modification (stiffening to increase payload mode frequencies, linear dampers, etc.) plus FCS software modifications
2. FCS software modifications only
3. Orbiter rate gyro blending plus FCS software modifications
4. Damper kit plus FCS software modification

*Reprinted from August 9-11, 1982 AIAA Guidance and Control Conference under permission granted by AIAA.

The main conclusion from the trade studies was that the interaction problem would require a combination of hardware and software changes to achieve stability. An underlying principle that drove the analysis was the desire to retain the essential rigid body control system design and the vehicle handling qualities in order to avoid additional man-in-the-loop simulations. The solution ultimately selected by NASA, in December of 1980, was addition of two coulomb dampers attached at the centers of the spreader beams on the aft airborne support cradle in conjunction with pending filter redesign (Option 4).

Orbiter Coulomb Friction Damper Kit

Addition of two vertical (Z) direction dampers at the center of the aft cradle spreader beams (Fig. 2) provides additional damping for modes below 5 Hz.

The coulomb friction dampers were chosen because they are efficient at low velocities and are reliable, economical, and adjustable, thus providing different damping forces for use with other payloads.

An existing commercial and Army coulomb damper design was modified for certification and orbiter use.

Follow-on activities included a coulomb damper requirement assessment consisting of the following study areas:

- Nonlinear damper modeling
- Worst-flight-condition assessment
- Nominal system and tolerance analyses (limit cycles, optimum damper force, force unbalances, etc.)
- Single damper failures (failed free or locked)
- Linear equivalent damper model

The models, approaches, and areas of major concern are discussed below.

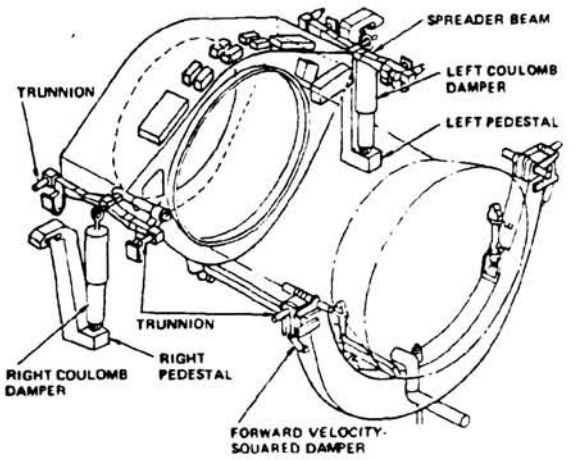

Fig. 2 Paylond support cradle with damper installation.

Models Used for Analysis

A simplified block diagram is shown in Fig. 3. The plant is represented by a structural model of the orbiter plus payload. The model is a finite element model with specific cargo-element attach points. The mode shapes at various node points on the vehicle are computed from the 6-degree-of-freedom modal point model.

The plant also contains the nonlinear dampers. There are six velocity-squared dampers supplied with the airborne support equipment. These were sized for large force levels (lift-off and landing) and are not efficient at low velocities. Two coulomb dampers are attached to the aft cradle spreader beams.

The equations for the bending modes and dampers are given in Appendix A. The coulomb damper and its support structure are characterized by free play, S, stiffness, K, and constant force level, F_t, as illustrated in Fig. 4.

The primary tool used was a nonlinear time domain simulation, which includes models of sensors, actuators, the digital flight control system, and 6-degree-of-freedom vehicle dynamics.

A simple 2-degree-of-freedom payload model was developed to provide insight and help evaluate nonlinear dampers.[1] The model is a rigid mass on two (forward and aft) unbalanced springs, giving coupled plunge and rotation motion. The excitation was applied to a rigid base (orbiter).

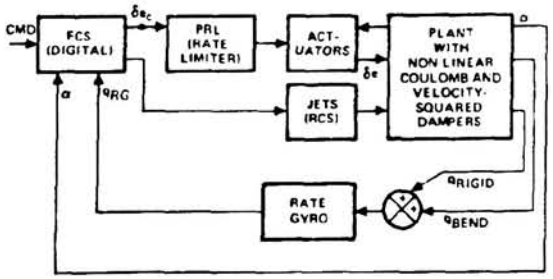

Fig. 3 Simplified block diagram.

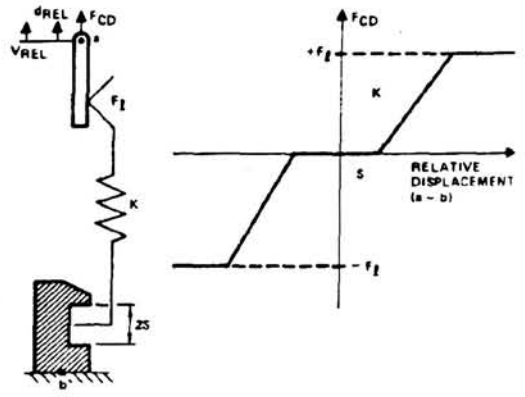

Fig. 4 Coulomb damper kit model.

The descent structural model showed the system payload modes (orbiter plus IUS/TDRS payload) to be the same frequency as the constrained payload modes (payload on rigid base); therefore, the simple model results were considered good approximations. The equations of motion are given in Appendix B. The nonlinear coulomb damper model used in the large time-domain simulation was also used in the simple payload model.

Study Approaches

The decision to use two coulomb dampers to help solve the problem provided the impetus to determine the best methods for analysis. The first part of the study involved identifying the operating states of the damper. The two primary states of the damper were identified as the locked and unlocked conditions. In other words, for small displacements, the coulomb damper is not broken out, and the motion remains within the free play and compliance of the damper and its supporting structure (locked condition). For large displacements, the dampers break loose and absorb energy. This condition is referred to as the unlocked condition.

Three structural models were used to generate modal data for the analysis. The first contained a rigid link for the damper. The second model had no link or damper in it. The third model contained a rigid link on one side to simulate a damper failure. Each set of modes was surveyed to determine the 16 or 17 dominant modes, and those modes were used in the analysis programs.

The second part of the study involved open-loop frequency sweeps. Nichols' (and Bode) plots were first constructed from the linear frequency response. The system was linearized (with no dampers and reaction jets) and the loop opened at the input to the actuator (Fig. 3). The time response program could then be used to run the frequency sweeps to evaluate the impact of adding first the nonlinear coulomb dampers and then the velocity squared dampers to the linear model. Variations in input amplitude and damper force levels were also evaluated.

The full nonlinear, closed-loop analysis was the third major part of the study. The approach not only provides a check of overall stability and limit cycles, but also helps define the damper operating point for a given orbiter maneuver. This operating point is then used to define the approximate operating point for the linear studies discussed above.

Major Areas of Concern and Study

Damper Influence on System Response

Adding dampers at the center of the spreader beams on the aft cradle produces a stiffening effect on the system. This stiffening of the aft cradle tends to increase the frequencies of the dominant payload modes—the plunge mode and the pitch mode—and it tends to transfer the energy of motion from the plunge mode to the pitch mode. The higher the coulomb damper force, the stiffer the system is at the aft cradle and the more dominant the rotational mode becomes.

Payload mode attenuation and mode frequency are altered by the damper operating point, which is a function of input amplitude, A_O, dead space, S, damper stiffness, K, and damper force, F_ℓ. An effective stiffness, K, is established, which then determines the frequency and damping (Fig. 5).

The coulomb dampers also add damping to the payload modes (primarily the plunge mode); the amount of damping is dependent upon input amplitude, A_O, and damper force level. Lower damper forces, in general, provide more energy dissipation in the lower amplitude (A_O) operating regions. These points are illustrated in Figs. 5 and 6.

Optimum Damper Size

An optimum damper force can be defined for a given operating region. This is based upon an attempt to provide maximum mode attenuation for both the plunge and pitching modes. The crossover point A (Fig. 6) represents the optimum damper force for the IUS/TDRS payload. However, tolerances and other considerations might dictate a somewhat higher force level.

Influence of Input Amplitude, A_O

The nonlinear, closed-loop results were used to determine the open-loop input amplitude, A_O (i.e., the approximate operating point). The system response is highly dependent on

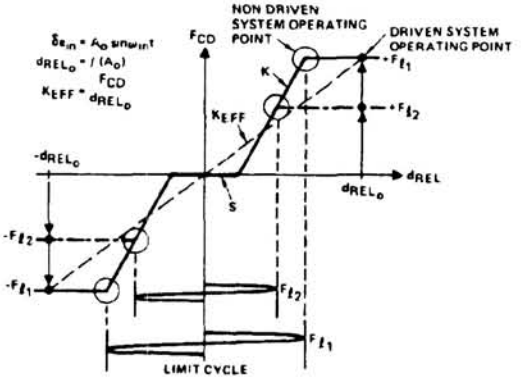

Fig. 5 Damper characteristics.

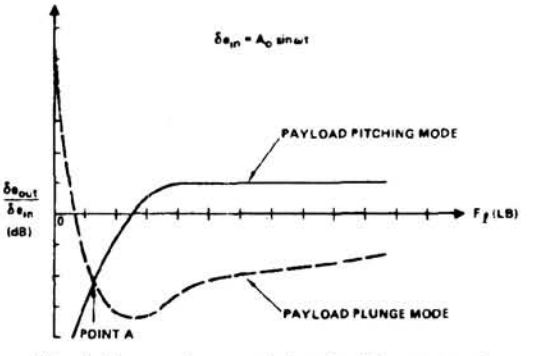

Fig. 6 Damper force optimization (A_O constant).

A_O, especially in the low-amplitude region. Open-loop results, mode attenuation as a function of input amplitudes, A_O, at a constant frequency, are presented in Fig. 7. These results show that there is a point where essentially no damping occurs, and larger inputs add damping.

Payload Modes Additional Damping

Additional damping due to the coulomb damper (Fig. 8) is dependent on input amplitude, A_O, and force level, F_{CD}. These plots show the total plunge mode damping (1 percent structural plus the additional coulomb damping) as a function of A_O and F_{CD}. For a given damper force level, larger disturbances will add damping. The motion will then decrease to a smaller amplitude and thus to the operating point, where little or no additional damping is added. Limit cycles then become the principal concern.

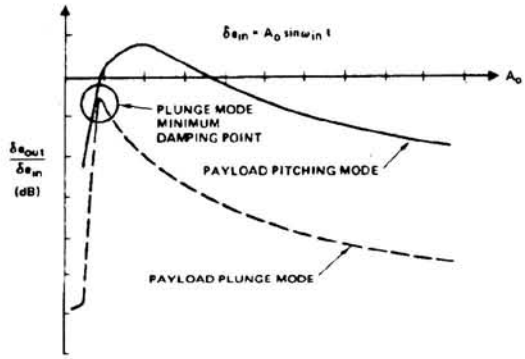

Fig. 7 Influence of input amplitude, A_O (F_ℓ and ω_{IN} constant).

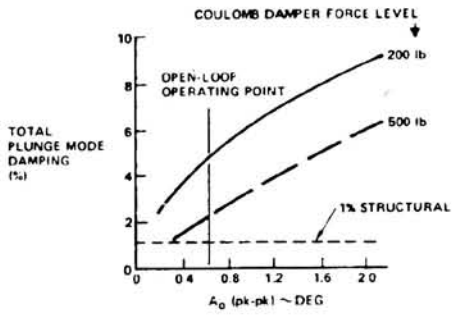

Fig. 8 Total payload plunge mode damping versus input amplitude, A_O.

Limit Cycles

While the stability of the system was, at the outset, the main problem, after the addition of the dampers and the redesigned software, the principal problem became the magnitude of the limit cycles. The criteria for the acceptability of the limit cycles are the acceptability of the g level at the crew station and the depletion of the consumables used in generation of hydraulic power.

The key limit cycle contributors for this system are as follows:

1. Payload/damper-kit related
   - Coulomb damper parameters set the limit cycle due to bending (for an unstable elevator loop at low $\bar{Q}$ flight conditions due to a payload mode) (Fig. 5)
     - Free play, S
     - Damper support structure stiffness, K
     - Damper force level, F_ℓ
2. Structural-model/data-base-related (orbiter plus payload)
   - Payload mode structural damping, ζ
   - Rate gyro mode slopes, mode frequencies, and control surface inertia parameters
   - Damper attach points mode shapes, $\Delta\phi_{ab}$
3. Nonpayload/damper-kit-related (these also contribute to an apparent limit cycle during a maneuver when the payload mode is stable)
   - Flight control system
     - Digital (quantization, A/D, D/A)
     - Body-bending filter attenuation
     - Forward loop gain
   - Nonlinear rate gyro (hysteresis)
   - Nonlinear actuator

To evaluate limit cycle sets of key parameters (S, K, F_{CD}, etc.) were defined as best-guess and worst-case values. A third set of extreme values was chosen for sensitivity runs. For the worst case and sensitivity runs, parameters were varied in their worst direction, giving the largest limit cycle.

Runs were made at several flight conditions along the entry trajectory from Mach 27 ($\bar{Q}$ = 5 psf) down to Mach 1.1 ($\bar{Q}$ = 90 psf). This covered a flight time of about 25 minutes from aero-surface activation ($\bar{Q}$ = 2 psf). In each case, a pitch maneuver (-4 degree α step) was executed to excite the limit cycle. A limit cycle occurred if the aero surface loop was unstable due to the payload plunge mode.

A quantitative evaluation of the impact of the limit cycles on auxiliary propulsion unit (APU) fuel consumption and crew comfort could then be made. A fuel integral was defined and computed as follows:

$$\dot{\delta}_{e_{AVG}} = \frac{1}{2}\,\frac{\left[\int_{t_o}^{t_F} |\dot{\delta}_{e_1}|\,dt + \int_{t_o}^{t_F} |\dot{\delta}_{e_o}|\,dt\right]}{t_F - t_o}\left(\frac{deg}{sec}\right)$$

where,

$\dot{\delta}_{e_{AVG}}$ = degrees of travel per surface per second of time (integral of surface rate per Δt)

$\dot{\delta}_{e_I}, \dot{\delta}_{e_O}$ = inboard and outboard aero surface rate

t_O, t_F = initial and final time, Δt, over which limit cycle is evaluated

The $\dot{\delta}_{e_{AVG}}$ is plotted against flight time, and the area under the curve is proportional to APU fuel consumed. In this way, best guess and worst case can be converted into fuel consumption rates and their acceptability evaluated.

The normal acceleration due to the limit cycle was monitored at the crew station. "Human response to accelerations" data from Reference 2 were used in evaluation of the peak g levels.

Coulomb Damper Failures and Mismatches

This section briefly describes the various damper failures and mismatches considered. Two types of single damper failures were studied:

1. One side locked and one side active
2. One side free and one side active

Two types of force unbalances were considered:

1. Right-side versus left-side force unbalance
2. Each side: tension and compression differences

An asymmetric simulation with 23 bending modes was used for the force unbalance and failure investigations. All loops were closed (pitch, roll, and yaw) and various pitch and lateral excitations used. No problems were found for the damper failures and unbalanced forces used.

Design Modifications

The coulomb damper evaluation studies for Shuttle flight control resulted in several hardware and software design modifications.

Major inputs were made to the damper kit design specification. Study results showed the need for the following hardware modifications:

1. Smaller damper kit end-to-end free play (design value: $S \leq \pm 0.007$ inches; was ± 0.04 in).
2. Stiffer end-to-end damper/support structure (design value: $K \geq 20{,}000$ lb/in.; was $\approx 6{,}000$ lb/in.)
3. Lower force level (design value: 250 pounds per damper; was 500 pounds)

The digital bending filters flown on Flights 1, 2, and 3 were also modified for the possibility of a return with a payload. Fig. 9 shows the mode suppression compromises between low-frequency (payload) and higher-frequency (orbiter) bending modes in the filter design. Version 18 software (Flights 1, 2, 3, and 4) and Version 19 software

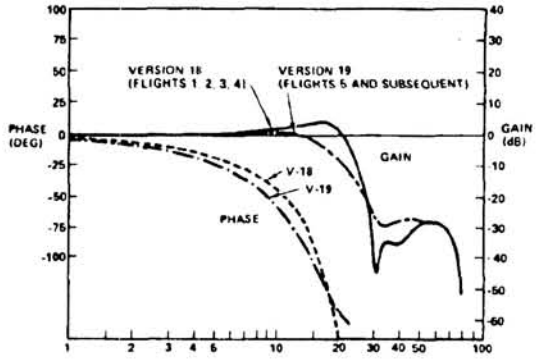

Fig. 9 Pitch supersonic body-bending filters.

(Flights 5 and subsequent) pitch, Mach >1, body-bending filter frequency responses are shown. The Version 19 filter attenuates more than the Version 18 filter in the 15 to 25 RPS range, while giving up some at higher frequencies. Additional attenuation could not be achieved at low frequencies without impacting the rigid-body control bandwidth. The coulomb dampers will provide additional attenuation between 15 and 25 RPS.

Conclusions

The evaluation and use of nonlinear dampers to suppress Shuttle payload modes have revealed the following important points:

- There is need for a damper model that gives output force as a function of free play, stiffness, sliding force, and relative displacement.
- The location and duration of the worst flight condition should be found.
- Nominal and tolerance analyses should be used to evaluate the following:
  - Change in payload mode frequencies
  - Control surface amplitude to determine the approximate operating point
  - Optimum damper location and force level
  - Limit cycle influence on fuel consumption, loads, and crew comfort
  - Force unbalances (left versus right and tension versus compression)
  - Single damper failures (failed free or locked)
- A simple spring and mass model of the payload using nonlinear dampers can provide valuable insight and confirm trends seen in the larger simulations.

Results from the IUS/TDRS payload studies have shown that:

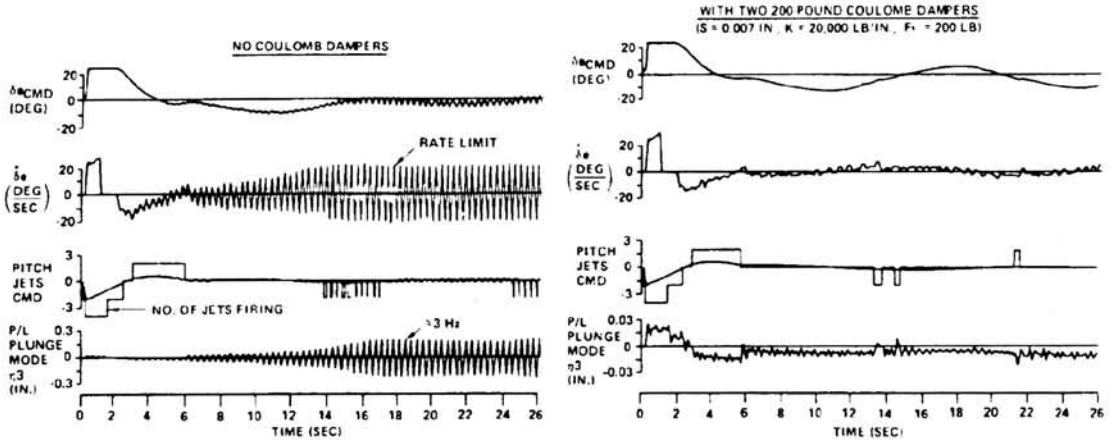

Fig. 10 Change in -4-deg alpha step response with addition of coulomb dampers.

- The optimum damper force is approximately 200 pounds.
- For an unstable aero-surface control loop (due to payload plunge mode), the key limit-cycle parameters are the coulomb damper end-to-end free play, support structure stiffness, and force level. These parameters determine the limit cycle amplitude and frequency.
- Worst-case variations of key damper/data base limit cycle parameters failed to produce any APU fuel or acceleration concerns.
- The worst-case payload mode instability region lasts for about 15 minutes during the reentry phase.
- The system is relatively insensitive to force unbalances and single damper failures.
- The coulomb dampers plus digital filter modification effectively suppress the payload and orbiter flex modes. The "before" (without coulomb dampers) and "after" (with 200-lb coulomb dampers) closed-loop responses are illustrated in Fig. 10.

Acknowledgement

The authors wish to express their appreciation to Terry Mulkey, Tony Gecan, and Dr. John Lee of Honeywell for their valuable contribution to this paper. Thanks is also due Maria Guerrera, who typed the manuscript.

References

1. Ruzicka, J. E., and Derby, T. F., "Influence of Damping in Vibration Isolation," SVM-7, The Shock and Vibration Information Center, Naval Research Laboratory, Washington, D.C. (1971).
2. "Human Response to Vertical Vibration," Aviation Age (July 1954).

Appendix A

Generalized Bending Modes and Damper Equations

The flex portion of the plant is represented by generalized modes (up to 40):

$$\ddot{\eta}_i = -2\zeta_i \omega_i \dot{\eta}_i - \omega_i^2 \eta_i - \frac{F^{TWD}_{\eta_i}}{m_i} + \frac{F^{RCS}_{\eta_i}}{m_i} + \frac{F^{AERO}_{\eta_i}}{m_i} - \frac{F^{V^2}_{\eta_i}}{m_i} - \frac{F^{COULOMB}_{\eta_i}}{m_i}$$

where:

η_i = i^{th} mode generalized coordinate

ζ_i = i^{th} mode structural damping

ω_i = i^{th} mode frequency

m_i = i^{th} mode generalized mass

$F^{TWD}_{\eta_i}$ = i^{th} mode generalized force contribution from "tail-wag-dog" (control surface influence on bending)

$F^{RCS}_{\eta_i}$ = i^{th} mode generalized force contribution from reaction control jets

$F^{AERO}_{\eta_i}$ = i^{th} mode generalized force contribution from aerodynamics

$F^{V^2}_{\eta_i}$ = i^{th} mode generalized force contribution from velocity squared dampers

$F^{COULOMB}_{\eta_i}$ = i^{th} mode generalized force contribution from coulomb dampers

The damper forces are given by:

$$F^{V2}_{\eta i} = \sum_{j=1}^{N} C_j \; \Delta\phi^{i}_{ab_j} \left(\sum_{K=1}^{M} \Delta\phi^{K}_{ab_j} \; \dot{\eta}_K \right) \left(\left| \sum_{K=1}^{M} \Delta\phi^{K}_{ab_j} \; \dot{\eta}_K \right| \right)$$

N = Number of V^2 dampers

M = Number of bending modes

C_j = j^{th} V^2 damper coefficient (j=1 to 6)

$\Delta\phi_{ab}$ = Mode shape (delta between attach points a and b) at j^{th} damper

$$F^{COULOMB}_{\eta i} = \sum_{j=1}^{N} f\,(F_\ell, S, K, d_{rel})$$

N = Number of coulomb dampers

F_ℓ = Mean effective force across the coulomb damper (sliding region)

2 S = Total free play (slop) between "a" and "b"

K = Total spring constant between "a" and "b"

$$d_{REL} = \sum_{i=i}^{M} \Delta\phi^{i}_{ab} \; \eta_i$$

= relative displacement across each damper and support structure (between points "a" and "b")

"a" = IUS ASE spreader beam attach point

"b" = Orbiter longeron point

(+) d_{REL} = Expansion of "a" relative to "b"

(-) d_{REL} = Compression of "a" relative to "b"

Appendix B

Simple Payload Model with Base Excitation

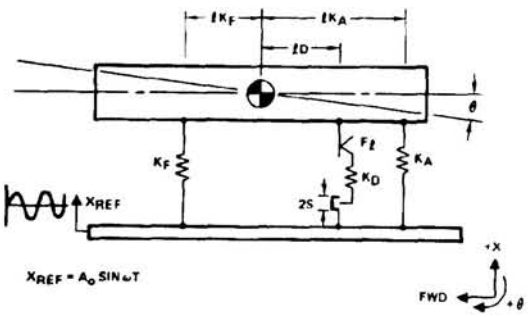

Equations of Motion

1. $M\ddot{X} = -(K_F + K_A)(X - X_{REF}) - (K_F \ell_{K_F} - K_A \ell_{K_A})\theta - F_{CD}$

$J_\theta \ddot{\theta} = -(K_F \ell_{K_F} - K_A \ell_{K_A})(X - X_{REF}) - (K_F \ell^2_{K_F} + K_A \ell^2_{K_A})\theta + \ell_D F_{CD}$

where:

M = mass of payload

J_θ = moment of inertia of payload

$F_{CD} = f\,(F_\ell, S, K_D, d_{REL})$

$d_{REL} = X - \ell_D \theta - X_{REF}$

APPROACH AND LANDING CHARACTERISTICS OF THE SPACE SHUTTLE ORBITER

Cynthia A. Bourne and Paul W. Kirsten
Air Force Flight Test Center
Edwards Air Force Base, California

SUMMARY

The first five Space Shuttle orbiter landings during the Orbital Flight Test (OFT) program are analyzed with respect to the unique requirement to perform routine unpowered landings within the confines of a 15,000 foot concrete runway. Landing experience during the Approach and Landing Tests (ALT) is also considered. Results are presented on energy control, handling qualities, and landing distance.

INTRODUCTION

The orbiter approach and landing technique has evolved from the technique that was first developed for rocket powered, low lift-to-drag ratio (L/D) research aircraft. Over the years, the technique has been successfully adapted to each particular vehicle (X-15, X-24, orbiter). The technique consists of flying an overhead pattern to a steep, high energy, straight-in final approach followed by a flare, landing gear deployment, and deceleration to touchdown. The adaptation of this technique for the orbiter and the associated guidance nomenclature are shown in Figure 1.

The Space Shuttle landing pattern consists of the following phases: Heading Alignment Circle (HAC), steep glide slope, preflare, shallow glide slope, and final flare. The automatic guidance system for the landing phase includes the Terminal Area Energy Management (TAEM) and Autoland.

The orbiter has the capability to be landed manually by the crew or automatically by the Autoland guidance system. In lieu of monitoring an automatic approach, the crew can elect to manually fly by reference to the guidance error needles on the Attitude Direction Indicator (ADI). These guidance errors are generated by TAEM (above 10,000 feet) and Autoland guidance systems. When the needles are kept centered during a manual approach, the trajectory is essentially the same as an automatic approach.

Achieving the desired touchdown conditions is highly dependent on flying an appropriate landing pattern for the existing conditions. Variations in any phase can result in energy dispersions at touchdown unless corrected in subsequent phases. The Air Force Flight Test Center (AFFTC) approach to evaluating orbiter landing performance was to compare the planned landing pattern with the actual for each flight beginning at the HAC and progressing through landing rollout. Proceeding in this manner allowed for analysis of each phase of the approach and determination of all factors that caused variations from the desired profile and the relative success

of subsequent corrections. Analysis of the different phases of the landing pattern led to the selection of three general topics which carry through all the phases: energy control, handling qualities, and landing and stopping distance.

ABBREVIATIONS AND SYMBOLS

ADI	Attitude Direction Indicator
AFB	Air Force Base
AFFTC	Air Force Flight Test Center
AGL	above ground level
ALT	Approach and Landing Tests
HAC	Heading Alignment Circle
HUD	Head Up Display
JSC	Johnson Space Center
KEAS	knots equivalent airspeed
L/D	lift-to-drag ratio
NASA	National Aeronautics and Space Administration
N_z	normal acceleration
OFT	Orbital Flight Test
PAPI	Precision Approach Path Indicator
PIO	pilot induced oscillation
STS-1,2,3,4,5	Space Transportation System flights 1, 2, 3, 4, and 5
TAEM	Terminal Area Energy Management
TIFS	Total In-Flight Simulator

OVERVIEW OF LANDINGS

A summary overview of the first five landing patterns is shown in conceptual form in Figure 2. On STS-1, the pilot manually flew the orbiter around the HAC through touchdown. Touchdown occurred well past the predicted point. Following this flight, the aimpoints were adjusted to compensate for performance mispredictions. On STS-2, the groundtrack around the HAC was purposely altered by the crew to compensate for known high upper altitude winds. Autoland was engaged down to preflare in roll/yaw and through the preflare maneuver in pitch. A low energy situation developed on final due to the combination of high winds and inadvertent speedbrake deployment on the HAC which resulted in touchdown short of the predicted point. A right hand 90 degree pattern was flown on STS-3 at Northrup Strip. Again, the pilot took manual control prior to the HAC to compensate for winds. Automatic guidance was engaged on final and Autoland was exercised down through preflare after which the pilot took manual control. A high energy condition developed on final and, in combination with a late manual takeover, resulted in touchdown short of predicted but at a high

airspeed. The decision was made to revert to manual control at or above preflare altitude on subsequent flights. STS-4 was the first OFT landing on a concrete runway. The pilot took manual control prior to the HAC to gain a feel for the orbiter's handling qualities. Automatic guidance was engaged prior to rolling out on final and the subsequent Autoland test was followed by a manual preflare and landing. The landing occurred short of the predicted point. The STS-5 pattern was flown manually prior to the HAC through touchdown as was done on STS-1. The landing was short of the predicted point. STS-5 was the first flight requiring the orbiter to penetrate a cloud layer in the landing pattern. A summary of Autoland engagements is shown in Figure 3. The effect of transitioning to and from the automatic mode is discussed in subsequent sections.

DISCUSSION

Energy Control

The TAEM and Autoland guidance concepts are based on essentially a fixed geometry landing pattern and airspeed schedule starting with the first tangent point to the HAC. Wind or off-energy compensation is accomplished by adjustments to bank angle, g level, or speedbrake position as necessary to achieve the desired pattern geometry. In the presence of high upper altitude winds, this leads to flight conditions close to the edge of the design envelope (i.e., g limits and maximum or minimum glide capability).

AFFTC simulator studies confirm that the TAEM guidance concept does compensate for winds using bank angle, g level, and speedbrake modulation. However, as shown in Figure 4, large compensations are required when flying through high winds. In a high tailwind situation while approaching the HAC intercept point, it is possible for the orbiter to exceed the operational g limit in a steeper than nominal bank as TAEM guidance attempts to keep the orbiter on the guidance-computed HAC trajectory. This can result in a low energy condition once established on final approach. Conversely, with a high headwind when approaching the HAC, if the orbiter follows the computed HAC trajectory, it will be in a high energy condition on final approach. If either one of these conditions exists, the burden of correcting to the right energy level is placed on judicious use of the speedbrake by either the pilot or Autoland on final in the last few minutes of flight. Stable energy conditions may or may not be achieved prior to preflare depending on the magnitude of energy loss or gain around the HAC. On two of the five OFT flights, real time decisions were made to fly the HAC in the manual mode when high winds were present to allow the pilot to adjust the pattern geometry and thus avoid the possibility of exceeding the normal acceleration limits.

A scheme is being sought that will allow for the incorporation of anticipated high upper altitude winds into TAEM guidance and will allow the automatic system to compensate for winds in the same manner as the pilot. The guidance logic could be altered to accept crew inputs of the latest upper altitude wind values at the selected landing site prior to deorbit. The pattern geometry would then be automatically adjusted to account for the wind effects on the orbiter and allow final approach to be flown with a nominal speedbrake setting. In this way, speedbrake

modulation on final will compensate only for errors in the predicted wind rather than for the entire magnitude of the wind vector. For an approach in a tailwind at the start of the HAC, the groundtrack around the HAC could be adjusted in toward the runway to allow for wind compensation while using essentially the nominal bank angle and speedbrake schedules. Conversely, for an approach into a headwind at the start of the HAC, the groundtrack could be shifted farther away from the runway to compensate for the high winds while flying the nominal bank angle and speedbrake. The magnitude of the correction to be used can be determined through simulator studies. Winds at three different altitude levels (possibly at 50,000, 35,000, 10,000 feet) would probably be sufficient to approximate the wind profile that the orbiter would encounter in its descent to landing. Current AFFTC simulator studies are being conducted to define a specific approach for wind incorporation into TAEM guidance.

Speedbrake modulation provides airspeed control on final (10,000 feet and below) in both manual and automatic modes. The long final approach is designed to allow a relatively stabilized airspeed and glide slope to be established at the preflare point. For a nominal landing, the speedbrake is commanded fully closed just prior to preflare. In the automatic mode, the speedbrake retract logic is based on a combination of altitude and the current speedbrake position as shown in Figure 5. If, at the decision altitude, the speedbrake is open less than the designated angle for that altitude, the speedbrake is commanded closed by the automatic system. Following STS-2, the speedbrake logic was changed to allow for the first automatic retract command to be at 4,000 feet instead of 2,500 feet. This caused the speedbrake to be commanded closed by Autoland guidance at 4,000 feet on STS-3 due to the effects of flying through a wind shear at a slightly higher altitude as shown in Figure 6. Once commanded closed, the logic does not allow for the speedbrake to be reopened at a lower altitude in the automatic mode. The result of the early retraction on STS-3 was an unstable energy condition (airspeed increasing to preflare) which partially accounted for the high energy landing. The flight conditions were duplicated in an AFFTC simulator study which used flight winds. The speedbrake logic was then changed in the simulator back to the original schedule so that the first speedbrake retract command was at 2,500 feet. As compared with the flight data in Figure 6, the speedbrake closed near 4,000 feet but then continued to modulate down final toward the desired approach airspeed of 285 KEAS. As can be seen in the figure, the airspeed was almost back to the desired value when the speedbrake was commanded closed at 2,500 feet. The speedbrake retract logic is not yet optimized, but has been changed in attempts to improve airspeed control on final.

Another concern is that the speedbrake extend/retract rate cannot provide good airspeed control on final in other than nominal conditions (no wind or steady wind) in either manual or automatic. Large airspeed excursions around the desired approach airspeed have been seen in the flight data. A stabilized energy condition is highly desirable in order to achieve consistent approaches and landings. To provide more positive energy control on final, it is necessary to reduce the dispersions and accurately bracket the approach airspeed. An AFFTC simulator study was conducted to determine what possible software changes could be implemented to accomplish this. The speedbrake gain and opening rate were both increased and produced positive results. The gain was changed from 2 to 6 and the opening rate was increased from 6.1 degrees/second to 12 degrees/second. With both changes incorporated, the speedbrake became more responsive (less delay) to commands. This was seen in both the

automatic and manual modes. The faster response eliminated gross airspeed undershoots and overshoots. In Figure 7, two AFFTC simulator Autoland runs using STS-5 software are compared. Both were flown in no wind and began with the speedbrake closed. As the airspeed increased above 295 KEAS, automatic speedbrake was selected and, as can be seen in the figure, opened full out initially to reduce the airspeed back to the desired approach airspeed of 285 KEAS. In the run in which the gain and opening rate were increased, the speedbrake returned the airspeed back to nominal much faster in comparison to the other run which incorporated the current software gain and opening rate. This same result was observed in other simulator runs in which variable winds were incorporated.

Handling Qualities

The landing of the final flight of the Space Shuttle ALT program was made on the concrete main runway at Edwards AFB. Time histories of the landing are presented in Figure 8. A Pilot Induced Oscillation (PIO) occurred in the pitch axis just prior to touchdown followed by a bounce and subsequent PIO in the lateral-directional axis before the vehicle finally settled on the runway. This landing precipitated numerous fixed and moving base simulator studies, inflight simulator evaluations, and independent contractor and consultant analytical studies.

The lateral-directional oscillation which occurred after the bounce was determined to be caused by elevon rate limiting. The orbiter's software rate limit was increased for combined elevator and aileron deflections. Lateral-directional low speed handling qualities are now considered acceptable. The conclusion of all engineering analysts involved in the handling qualities evaluations was that the orbiter's low speed longitudinal handling qualities were acceptable for well-trained pilots performing lakebed landings, but unacceptable for general operational use.

Longitudinal pilot ratings and comments obtained from a study conducted in 1978 using the Total Inflight Simulator (TIFS) variable stability aircraft are contained in Figure 9. These results are considered typical of the numerous studies conducted. The pilot ratings exemplify the need for extensive pilot training. Most NASA Johnson Space Center (JSC) pilots rated the orbiter in the 3 to 4 range, while most other pilot ratings were 5 to 7. NASA JSC pilots had many years of orbiter simulator training. All others were highly experienced test pilots, but did not have extensive orbiter simulator training. The most objectionable deficiencies of the aircraft are listed under typical pilot comments. Primary causes of the orbiter's poor low speed longitudinal handling qualities are felt to be inadequate pitch attitude visual reference cues and long time delays for normal acceleration cues. A one-half second delay occurs between pitch stick command input and normal acceleration response at the cockpit partly due to the digital control system and partly due to vehicle geometry.

A PIO suppression filter was added in the pitch axis prior to STS-1. The suppressor reduced pilot command inputs as a function of pitch command frequency. Pilot comments obtained from a 1980 moving base study on the NASA Ames Vertical Motion Simulator indicated that the suppressor reduced the tendency to develop a rapidly divergent PIO and avoided control system saturation. However, some PIOs were encountered and the basic longitudinal deficiencies are still felt to exist.

No major subsonic handling qualities problems have occurred during the first five orbital flights. A primary reason for this was that all pilots had received several years of simulator training which allowed them to follow the nominal energy profile and avoid aggressive inputs during the landing phase. Nevertheless, the incident-free landings were not achieved without considerable pilot effort. Although the STS-4 landing to the concrete runway at Edwards AFB was smooth and without incident, the commander stated that the workload was extremely high. There was possibly some degradation in his performance caused by the on-orbit stay. He expressed some concern that future pilots may not receive adequate training to perform the landing task routinely.

Several potential improvements for the orbiter's low speed handling qualities are currently under consideration for evaluation. These include a normal acceleration feedback and other flight control system modifications, a Head Up Display (HUD), and ball/bar system for pitch attitude reference during the final landing phase. It is not anticipated that any single item will provide a dramatic improvement, but hopefully a combination may be found which allows adequate low speed longitudinal handling qualities for general operational use.

The ball/bar system is the latest visual landing aid to receive acceptance into the orbiter flying community. The system was originally tested for the orbiter as a lighting aid for future night landings, but was first used operationally on STS-5. The ball/bar system is situated 50 feet from the runway edge near the approach end as shown in Figure 10. It consists of a single white source light (ball) and a row of six red lights (bar). The bar is positioned 500 feet down the runway from the ball. The ball height is about 13 feet above the ground and the bar rests within three feet of the ground. When the pilot visually aligns the ball with the bar, the Orbiter is on the 1.5 degree inner glide slope. This allows for a smoother and accurate manual (visual) transition from the outer glide slope using the Precision Approach Path Indicator (PAPI) lights to the inner glide slope. Due to its favorable acceptance, current NASA policy is to have the system available for use on all future flights.

Two HUDs have been installed in the Challenger and will be used on STS-6. The HUD allows the pilot to fly a manual approach or monitor an Autoland approach visually while receiving selected information (airspeed, altitude, speedbrake position) from the HUD. It is hoped that the addition of this aid in the landing pattern will provide more positive energy control, and better attitude information, and reduce handling qualities problems.

Landing and Stopping Distance

To date, all orbiter landings have been performed manually. A comparison of orbiter landing rollouts is made in Figure 11. It should be noted that no attempt was made to demonstrate minimum stopping distance, although brief braking tests were performed on STS-4 and STS-5. On STS-1, the touchdown occurred well past the planned point. Post flight analysis revealed that the subsonic L/D was higher than predicted, ground effect was greater than predicted, and the approach airspeed was

25 KEAS higher than desired. To compensate for the aerodynamic effects on subsequent flights, the approach geometry was altered to bleed off the energy during the shallow glide slope and final flare by moving the outer glide slope aimpoint 1,000 feet farther from the threshold and the inner glide slope 500 feet closer to the threshold. On STS-2, touchdown occurred near the planned airspeed but short of the predicted location. This was due to a low energy condition on final that resulted from inadvertent speedbrake deployment and flying through high winds around the HAC. On STS-3, the orbiter landed earlier than expected and at a high airspeed, 220 KEAS. The early touchdown was attributed to a late manual takeover (143 feet) and inadequate height perception. On STS-4, manual control was initiated at 2,300 feet. The touchdown on the concrete runway occurred sooner than planned also due to poor height perception as reported by the pilot. On STS-5, manual control was initiated prior to reaching the HAC and was maintained throughout the approach and landing. STS-5 touchdown was slightly short of predicted due to poor height perception.

The derotation phase of the landing between main gear and nose gear touchdowns required careful pitch control by the pilot to avoid exceeding either main gear or nose gear loads. No braking could occur during this phase of the rollout. The long roll prior to nose gear touchdown on STS-3 was due to an intentional effort to decelerate to the desired nose gear touchdown speed and an unexpected nose rise in response to a manual pitch command.

For the three lakebed landings, considerably more than 15,000 feet was available for landing and rollout so there was no effort made to limit rollout distance. Light braking was used on STS-1, 2, and 3. On STS-4, a moderate (8 fps^2) braking test was performed from 135 KEAS to 40 KEAS. A maximum braking test was performed between 120 KEAS and 80 KEAS on STS-5. One main gear wheel locked up during the last 50 feet of rollout due to brake component failure.

Brake problems have been seen periodically throughout the test program. Brake chattering accompanied by vehicle shuddering and brake lining damage were noted during the ALT program. During OFT, axle flexing during touchdown and rollout permitted interference between the wheel and brake assemblies which caused damage to both. A fix to minimize flexing and eliminate the interference will be flown on STS-6. While the exact cause for the brake failure on STS-5 is still under investigation, preliminary analysis indicates that high energy and brake pressure profiles are contributing factors. Additional development and test activities may be necessary to ensure that an operational brake system is available on future flights.

CONCLUDING REMARKS

Although performance has been satisfactory thus far, improvements in the approach and landing are being identified for both the manual and automatic modes to enhance the orbiter landing performance. Optimum energy control is important if consistent approaches and landings are to be achieved. Several software modifications are being explored for improving energy control. Deficiencies in the low speed handling qualities have been isolated and solutions are being investigated.

Effective braking capability must be available for each flight. Research into fixes to the cause(s) of the recurring brake damage is continuing. By reducing the allowable variations from the desired profile in each of these areas, more consistent and repeatable approaches and landings are expected.

The AFFTC feels that an approach and landing technique is evolving which will be an acceptable method for operational use. This was demonstrated on STS-5 where the pilot took over manual control prior to intercepting the HAC. He flew around the HAC and penetrated a cloud layer essentially by reference to the guidance error needles. He transitioned to a visual approach once he acquired the visual landing aids on final. The long stick time afforded the pilot prior to touchdown by this technique appears to allow the pilot to adapt to the orbiter's low speed handling qualities. The visual aids available - PAPI, ball/bar - provide invaluable cues to the pilot while flying a manual approach. The additional stick time and the landing aids will become even more important to future orbiter crews whose training will be substantially less than that received by the first several crews.

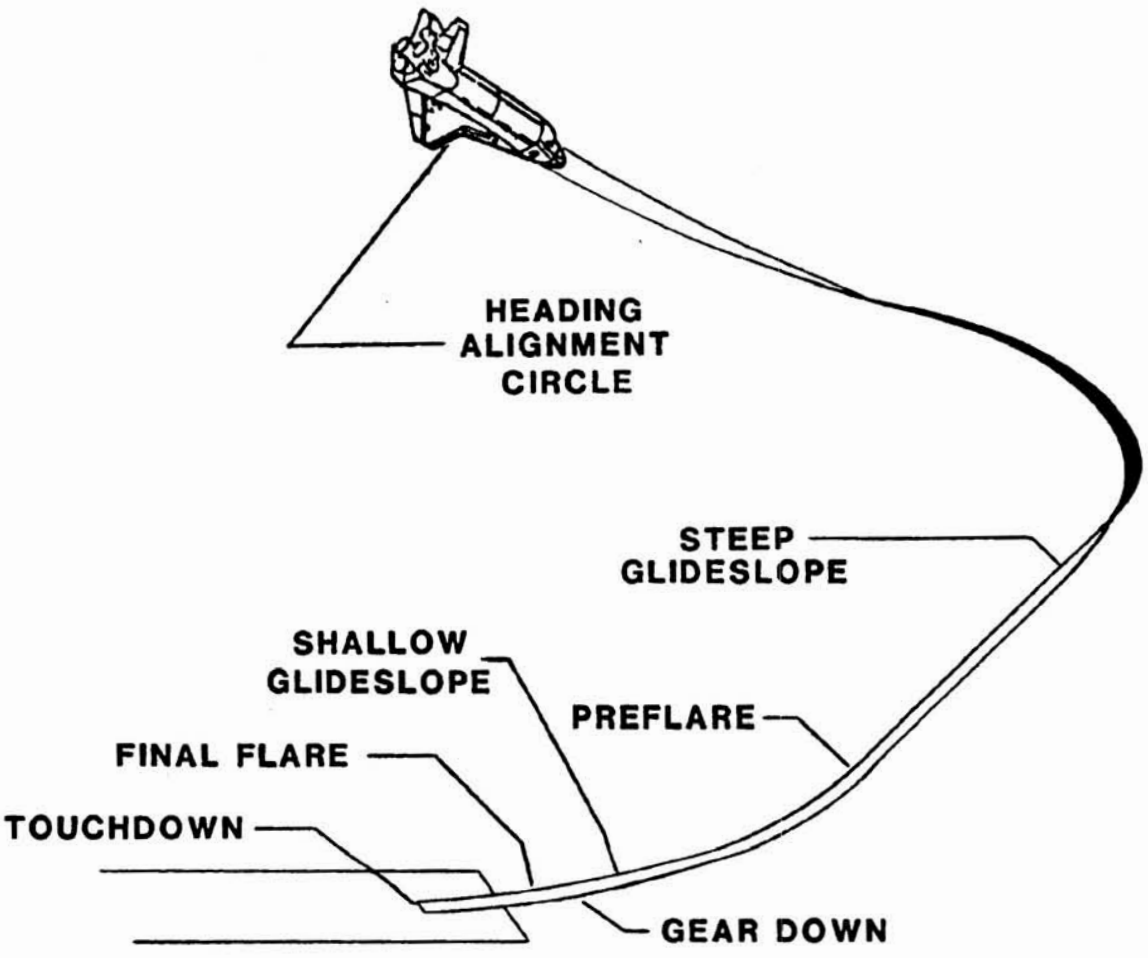

Figure 1.- Typical landing approach for orbiter.

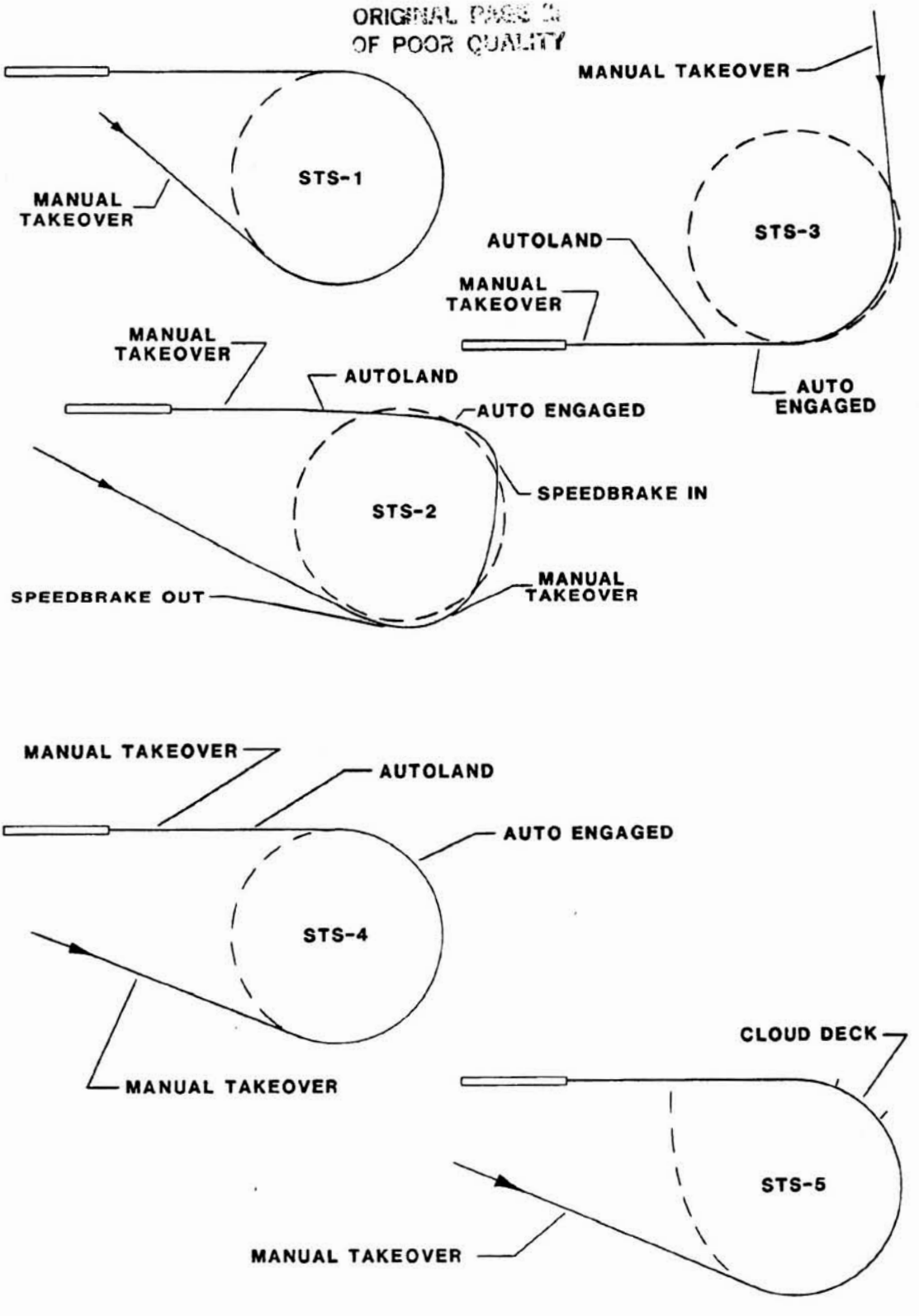

Figure 2.- Approach and landing patterns.

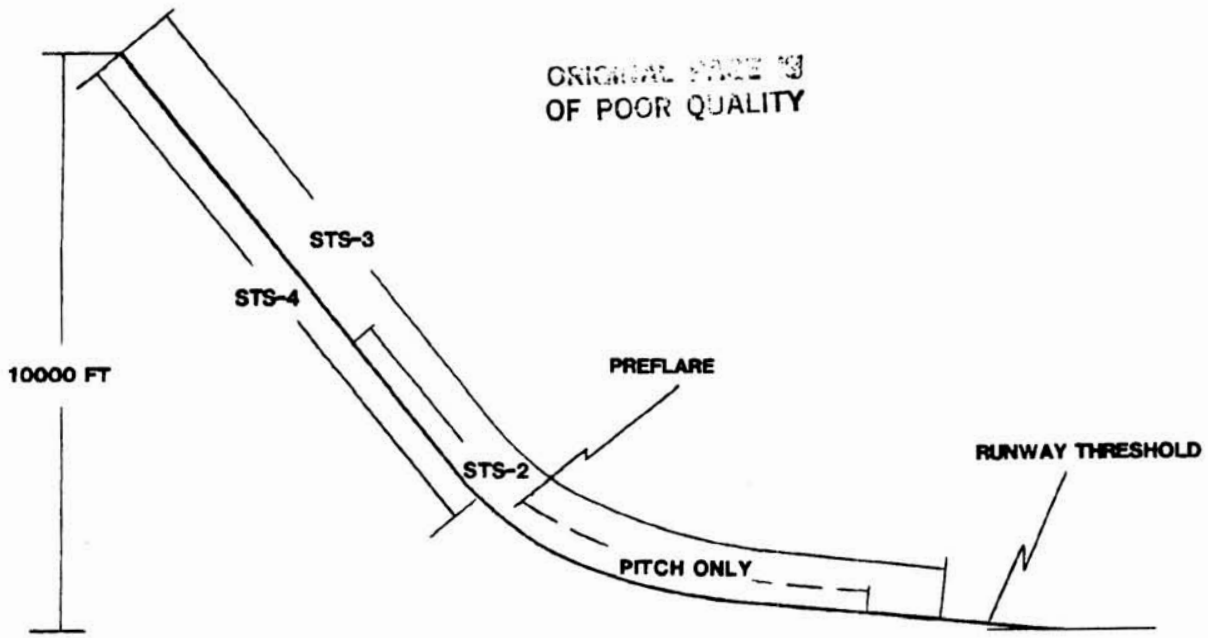

Figure 3.- Autoland engagements.

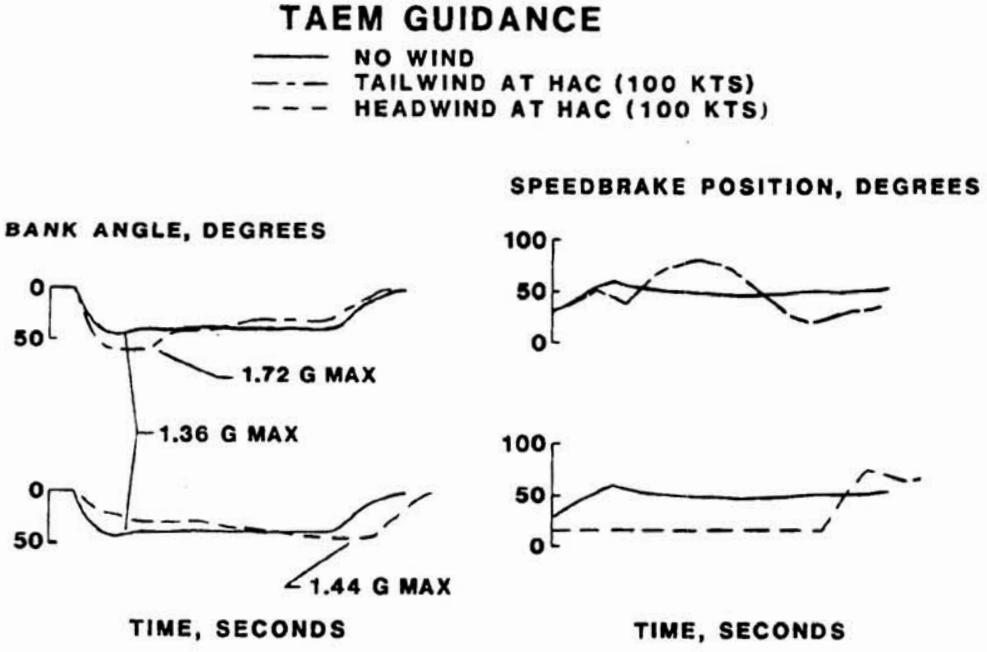

Figure 4.- Comparison of AFFTC simulator runs.

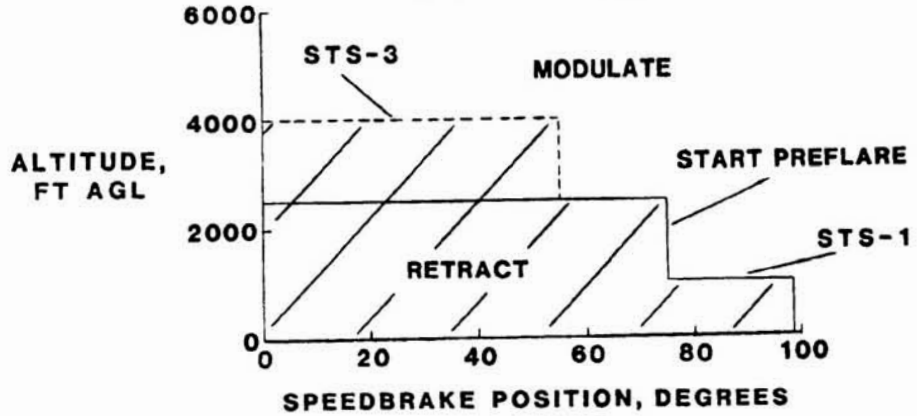

Figure 5.- Speedbrake retract logic.

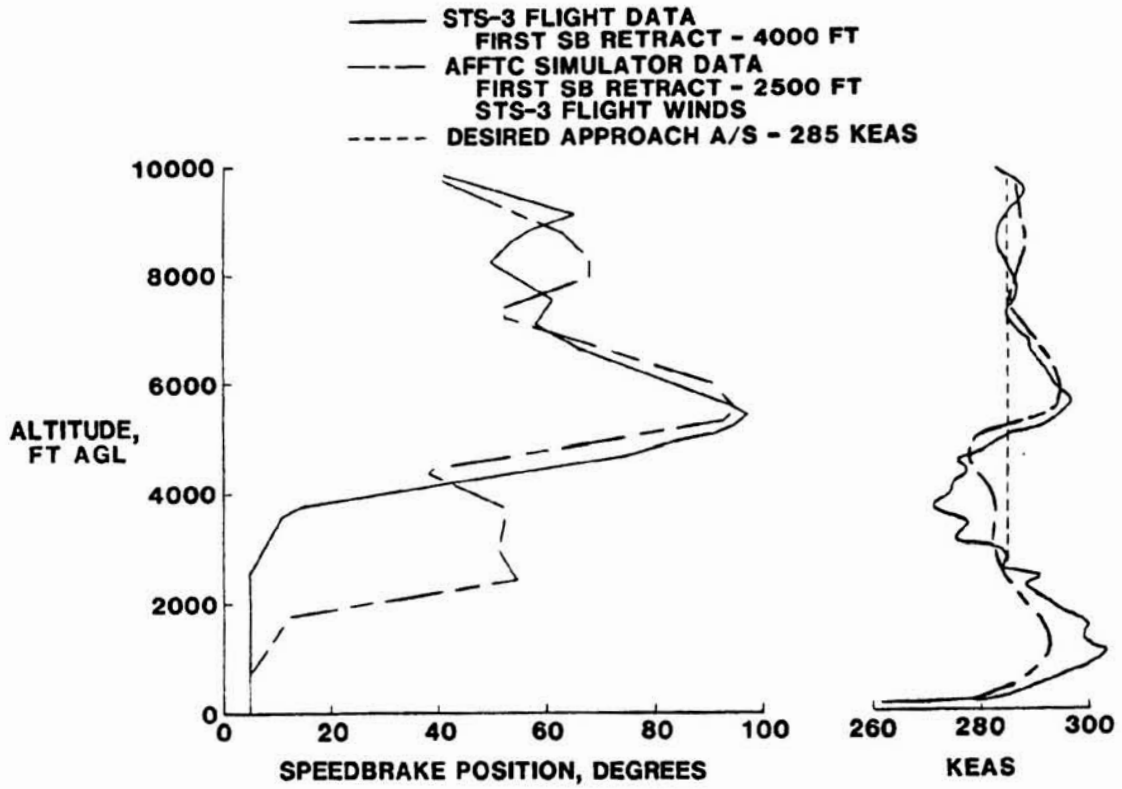

Figure 6.- Comparison of flight and simulator data.
Autoland guidance.

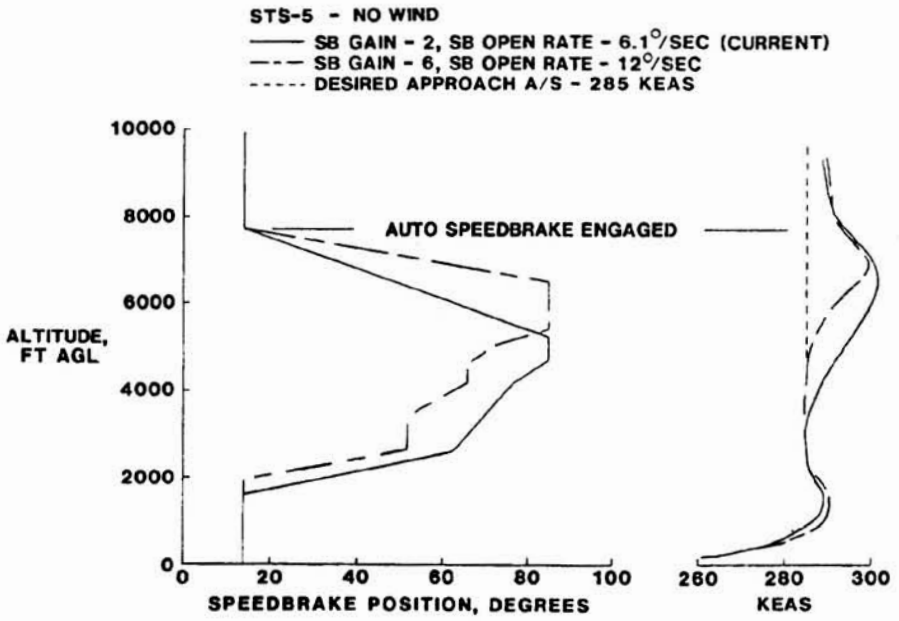

Figure 7.- Comparison of AFFTC simulator runs. Autoland guidance.

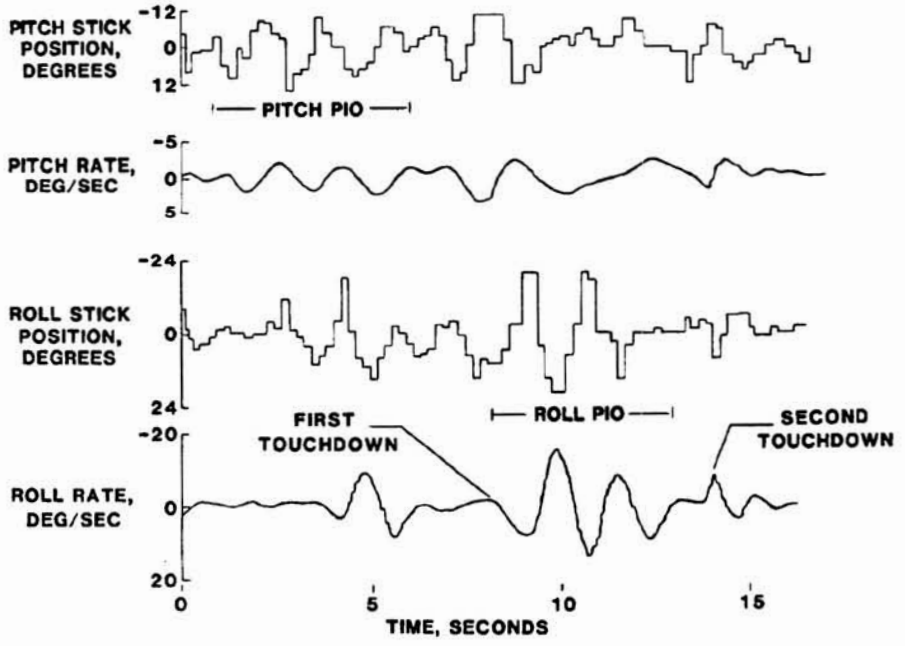

Figure 8.- ALT landing PIO.

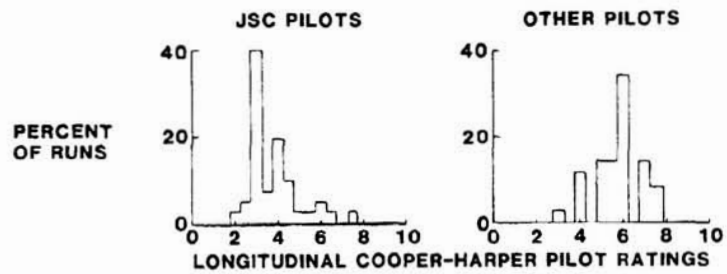

TYPICAL PILOT COMMENTS

LACK OF PRECISE FLIGHT PATH AND SINK RATE CONTROL
UNPREDICTABLE RESPONSE TO PILOT INPUTS
TENDENCY TO OVERCONTROL AND BALLOON

PIO SUPPRESSOR ADDED PRIOR TO STS-1

REDUCED TENDENCY FOR EXPLOSIVE PIO
BASIC DEFICIENCIES STILL EXIST

Figure 9.- TIFS evaluation results.

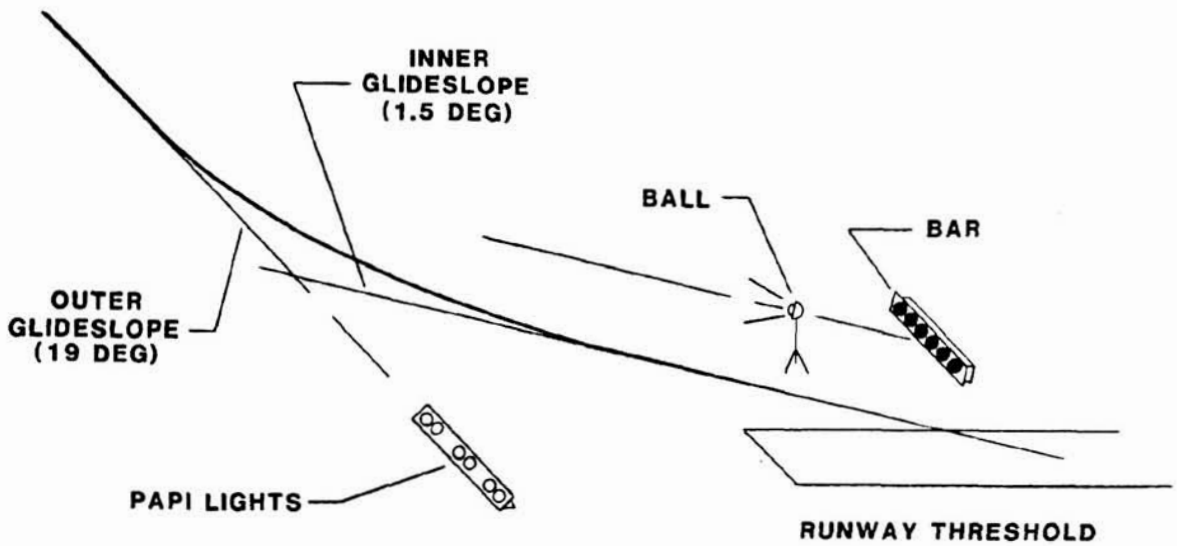

Figure 10.- Visual landing aids.

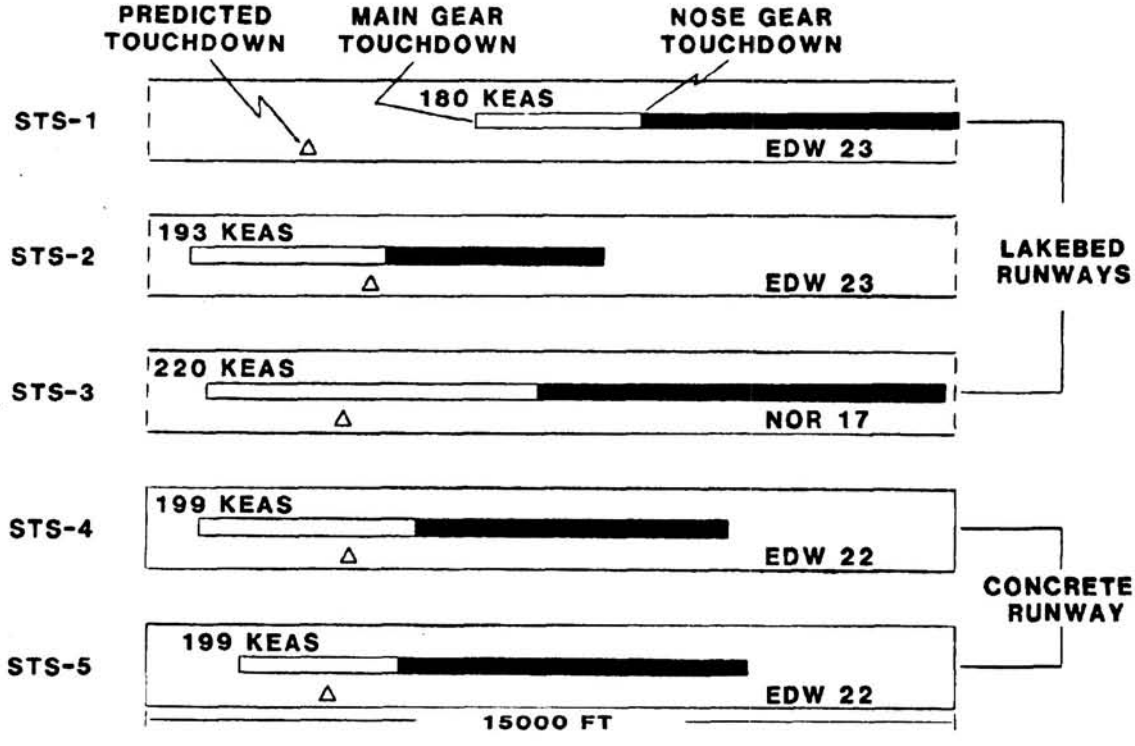

Figure 11.- Orbiter landing rollout.

☆U.S. GOVERNMENT PRINTING OFFICE:1983 -639 -008/ 31